2018 TAPPI JOURNAL YEARBOOK

Copyright© 2019 by



TAPPI PRESS
15 Technology Parkway South, Suite 115
Peachtree Corners, GA. 30092 U.S.A. www.tappi.org
All rights reserved

The Association assumes no liability or responsibility in connection with the use of this information or data, including, but not limited to, any liability or responsibility under patent, copyright, or trade secret laws. The user is responsible for determining that this document is the most recent edition published.

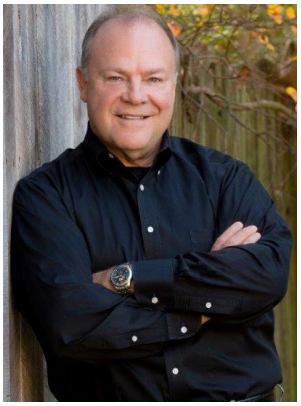
To obtain copyright permission to photocopy pages from this publication for internal or personal use, contact Copyright Clearance Center, Inc. (CCC) via their website at www.copyright.com. If you have questions about the copyright permission request process, please contact CCC by phone at +1-978-750-8400.

To obtain copyright permission to use excerpts from this publication in another published work, send your specific request in writing to TAPPI PRESS, 15 Technology Parkway South, Suite 115, Peachtree Corners, GA 30092 U.S.A. or by fax to +1-770-446-6947.

ISBN: 978-1-59510-291-1
TAPPI PRESS Order Number: 0101R359EL
Printed in the United States of America

Please note: The following TAPPI Journal pages are sequenced chronologically according to publication order. Therefore, you can expect breaks in page numbering, as time sensitive, full-page advertisements have been removed for your convenience.

Welcome to the 2018 TAPPI *Journal* Yearbook



I believe that the progress of TAPPI is vitally connected to the progress of our industry as a whole—and vice versa. Both reflect growth that is focused on our industry's future and its people. Both depend on knowledge sharing to fuel innovation and enrich the professional lives of those involved.

This philosophy has driven our association's success for more than 100 years. It is why we publish *TAPPI Journal (TJ)*, a leading research publication. In eleven issues a year, *TJ* reflects the research many scientists and students are doing to advance our industry. Last year, *TJ* included peer-reviewed papers on lignocellulosics, coating, nanotechnology, tissue, and biorefining—all areas of exciting innovation.

As an association, TAPPI's efforts also support growth through knowledge-sharing and peer connection. The past year offered many opportunities for me to marvel at the dedication of our members, volunteer leaders, and the TAPPI staff. Look at what we achieved together during 2018:

In September 2018, we launched **TAPPI Connect Open Forum**, which provides a valuable point of communication and insight for members and nonmembers. Since its launch, the TAPPI Connect Open Forum has hosted 212 discussions where professionals can post questions and receive answers in real-time from others in the industry. We'll continue to grow in 2019 with the addition of engaging new communities. Look for monthly committee highlights and an "Ask the Experts" feature on the horizon.

Our **Mentor Match** program is going strong. Our most recent signup was in April, 2019. We hope you'll join the 35+ Mentors and 30+ Protégés already involved!

TAPPI Press launched three new publications in both print and electronic format: Advances in Papermaking Wet End Chemistry Application Technologies; Nanocellulose: A Guide for Producers, Products and Applications; and Nanocellulose Challenges and Opportunities: End User Perspectives. Look for three important new publications in 2019.

In June 2019, more than 400 industry professionals gathered in Chiba, Japan, for the largest International Conference on **Nanotechnology for Renewable Materials** ever. TAPPI was excited to co-locate TAPPI Nano with the Nanocellulose Forum (NCF) Exhibition in Chiba, Japan. It was the first TAPPI Nano Conference held in Asia.

Our **TAPPI courses**—such as January's Kraft Recovery course, led by 17 industry experts—continue to receive high marks and strong attendance, and we've received many inquiries into our convenient **Company Classroom** program.

TAPPI continues its support of industry safety. In 2018, **TAPPISAFE** grew its student base by 12 percent and expanded its course offerings into new segments, including Converting and

Timber. ***Paper360°*** continued to spotlight a manufacturer's safety journey in every Jan/Feb issue (featuring Domtar in 2019) as its commitment to putting "Safety First."

In May, more than 2,100 attended **PaperCon 2019** in Indianapolis, IN, with a host of co-located events for a truly customizable experience. Also at PaperCon, our **Young Professionals Division** sponsored a community service project for Rise Against Hunger.

We were excited by the response to the inaugural **Women's Summit** in April 2018, and we held our second event in May of 2019 following PaperCon. More than 50 attendees participated in roundtable discussions on issues salient to women in the pulp and paper industry. TAPPI's **Women In Industry Division** also continued its webinar series highlighting vital professional skills.

Other 2018 events also fostered outstanding opportunities for knowledge and connection. Former Governor Scott Walker proclaimed Paperweek in Wisconsin October 1-5, 2018, which included the TAPPI/RISI **Tissue 2018** event in Appleton. In Indianapolis, IN, TAPPI's Corrugated Division and AICC held a successful **Corrugated Week** joint event, attracting 1,700 attendees. In November, the co-located **PEERS & IBBC** events in Portland, OR offered attendees 10 technical tracks and 37 technical sessions, including industry-leading keynote speakers. The newly branded **International Flexible Packaging and Extrusion Division** held their annual event in Charlotte, NC and attracted nearly 200 flexible packaging industry attendees.

In 2018, TAPPI was pleased to increase its **member** retention rate over the previous year, and we added a new Local Section for members: the Four States section, which held its first meeting in December. We welcomed 14 new **sustaining member** companies by adding two valuable new benefits; a charitable donation of five student memberships and discount on TAPPISAFE Site Employee Safety Orientation. Through the charitable portion of their membership, sustaining members help support future generations of industry professionals.

What's in store for TAPPI in 2019 and beyond? In large part, that's up to you. Our members' talent, knowledge, experience, and passion for innovation drive our Association forward and provide a tremendous resource for our industry. As I look back on 2018, I see an Association committed to the future of its members, and of our industry, as shown through our achievements. Each and every TAPPI member, sponsor, staff member, and supporter played a role in that success. Thank you, all!

If you are a new TAPPI member, welcome. I firmly believe you've made a career-building decision to join us, and I hope you'll take full advantage of all that our association offers. If you're a returning member, welcome back. May 2019 bring you even more opportunities to grow your professional knowledge and networks through TAPPI.

Sincerely,



Larry N. Montague
TAPPI President & CEO

Bleaching

Decreased water usage in a softwood ECF bleaching sequence— full mill simulations

By: Pia Jour, Karin Lindgren, Katarina Gutke, Johan Wallinder

June, pp. 353 - 360 In this study, an elemental chlorine free (ECF) bleach plant with a $D_0(EOP)D_1(EP)D_2$ sequence was studied with the aim of identifying options for significantly decreasing (fresh) water usage in the bleach plant and decreasing the effluent volume. A base-case simulation model for a softwood kraft market pulp mill was made based on a reference model representing the best available techniques as well as data produced in an extensive laboratory pulp bleaching study. This model was used to evaluate increased closure within the bleach plant and the recirculation of bleach plant effluent to the brownstock system and their effects on both the bleach plant and the recovery cycle. The results indicate that it is possible to reduce the fresh water consumption from 15 metric tons/a.d. metric ton in the base case to about 2 metric tons/a.d. metric ton, without increasing the carryover of chemical oxygen demand (COD) to the pulp machine. Nonprocess elements in wood contribute to the levels of metals found in the bleach plant and thus to the risk of precipitates such as calcium oxalate, barium sulfate, and calcium carbonate. The risk of precipitates forming is a key factor determining the possible degree of closure. In addition, chloride concentration in the black liquor is another important factor that is affected by recirculating bleach plant filtrate to the brownstock washer and by the grade of the sodium hydroxide used in the mill.

Application: The intention of this work is to give input for possible steps than can be taken in order to reduce the water use in a pulp mill applying ECF bleaching technology.

Jour is a scientist and Gutke is a research engineer with AkzoNobel Pulp and Performance Chemicals, Bohus, Sweden. Lindgren is a senior research associate and Wallinder is a research engineer with RISE Bioeconomy, Stockholm, Sweden. Email Jour at pia.jour@akzonobel.com .

Laboratory method for determining the source of brightness loss at a southern United States bleached paperboard mill

By: Aru Timwari, Ashok Ghosh, Peter W. Hart

October, pp. 547 - 554 Bleached pulp is known to lose some brightness between the end of the bleach plant and the paper machine reel. An ISO brightness drop of 1–3 points is often experienced. There are many reasons for the brightness loss; however, the usual suspects tend to be water quality, metallurgy, and process chemicals.
One bleached paperboard mill in the southern United States had been experiencing brightness losses in the 6–8 point range for several years. A systematic study was
conducted to determine the potential sources for this bright-ness loss. A laboratory simulation technique was developed to demonstrate the potential causes for the brightness loss along the process.

Application: This study examines how to define the relevant aspects of a pulp/papermaking process, followed by systematically modeling the effect of process chemicals on paper brightness. The concepts of this study may be used by process engineers to model their process in a laboratory, and to investigate the root cause for changes in many paper properties.

Tiwari is a co-operative education student from Virginia Polytechnic Institute, Ghosh is research engineer, and Hart is director, Fiber Technology and Innovation, at WestRock, Richmond, VA, USA. Email Ghosh at ashok.ghosh@westorck.com .

Understanding the risks and rewards of using 50% vs. 10% strength peroxide in pulp bleach plants

By: Alan W. Rudie, Peter W. Hart

November, pp. 601 - 607 The use of 50% concentration and 10% concentration hydrogen peroxide were evaluated for chemical and mechanical pulp bleach plants at storage and at point of use. Several dangerous occurrences have been documented when the supply of 50% peroxide going into the pulping process was not stopped during a process failure. Startup conditions and

leaking block valves during maintenance outages have also contributed to explosions. Although hazardous events have occurred, 50% peroxide can be stored safely with proper precautions and engineering controls. For point of use in a chemical bleach plant, it is recommended to dilute the peroxide to 10% prior to application, because risk does not outweigh the benefit. For point of use in a mechanical bleach plant, it is recommended to use 50% peroxide going into a bleach liquor mixing system that includes the other chemicals used to maintain the brightening reaction rate. When 50% peroxide is used, it is critical that proper engineering controls are used to mitigate any risks.

Application: By understanding the risk/reward benefit, chemical pulp mills should realize there is no justification for using 50% peroxide in an extraction stage. If they lower the concentration of peroxide to 10%, their operation will be much safer.

Rudie is assistant director, U.S. Department of Agriculture Forest Products Laboratory, Madison, WI, USA. Hart is director, Fiber Technology and Innovation, at WestRock, Richmond, VA, USA. Email Hart at peter.hart@westrock.com .

Understanding the pulping and bleaching performances of eucalyptus woods affected by physiological disturbance

By: Juliana Marangon Jardim, Carolina Marangon Jardim, Jorge Luiz Colodette

November, pp. 633-642 The wood quality is a factor of extreme importance when the pulping process is targeting high yield, low cost, and high pulp quality. Thus, wood knowledge is crucial for process optimization. In some northeastern Brazilian eucalyptus plantations, a physiological disturbance caused by water stress has been observed. Up to now, there have been no studies concerning the effects of such disturbances on the wood quality or on the pulping and bleaching process performance. The present work is aimed at understanding the impact of the stress on the production of bleached pulp. The wood quality of two clones (one tolerant to the disturbance and another sensitive), cultivated in sites where the disturbance is present and absent, was evaluated. Kraft pulps of kappa number 20 were produced and bleached by the sequence DHT (EP) D_1 to a brightness of 90% ISO, which allowed for assessment of the wood pulpability and bleachability. It was concluded that the disturbance affects the wood quality, and overall it showed a negative impact on the production of bleached eucalyptus kraft pulp, with significant potential economical setbacks.

Application: This research is a case study of how bleached pulp production is affected by wood quality. Eucalyptus woods affected by physiological disturbances were studied, as well as their performance during kraft pulping and elemental chlorine-free (ECF) bleaching. Mills could use this information to better understand the wood consumption, chemicals, and energy demands on the process when using those woods in the pulp manufacturing.

J. Marangon Jardim is a Ph.D. student in the Department of Forest Biomaterials at North Carolina State University, Raleigh, NC, USA. C. Marangon Jardim is a researcher at Federal University Viçosa in Viçosa, Brazil. Colodette is full professor in the Department of Forest Engineering at Federal University of Viçosa. Email J. Marangon Jardim at jmjardim@ncsu.edu .

Using multistage models to evaluate how pulp washing after the first extraction stage impacts elemental chlorine-free bleach demand

By: Brian N, Brogdon, Lucian A. Lucia

November, pp. 621 - 630 Steady-state models were constructed to predict the response of a southern U.S. softwood brown-stock to three- and five-stage elemental chlorine-free (ECF) bleach sequences. The models provided insight into how typical (EO) washing efficiencies from a vacuum drum unit affected pulp brightening and total chlorine dioxide con-sumption. When (EO) carryover was between 15% and 30%, the chlorine dioxide needed to reach target brightness increased by 8% to 15% for the $D_0(EO)D_1(EP)D_2$ sequence (89% ISO) and by 15% to 23% for the $D_0(EO)D_1$ sequence (86% ISO) versus perfect washing. Use of (EO) filtrate as D_0 shower water, such as in split-flow countercurrent

washing, caused the bleach uptake to increase by 1.5 to 3.0 kg chlorine dioxide (ClO_2)/ton pulp when compared to using cleaner D_0 shower water sources. The ClO_2 consumed by 15% to 30% (EO) washer carryover is comparable to that consumed by typical carryover levels from brownstock washing (~10 kg Na_2SO_4/ton pulp). High (EO) carryover made ECF bleaching to higher brightness targets more difficult.

Application: Multistage models are employed to estimate how typical levels of extraction washer carryover, as well as how extraction washer filtrate reuse in countercurrent washing, affects chlorine dioxide consumption and brightness development of a softwood kraft pulp when bleached with ECF sequences. These models could be adapted to simulate mill data, used to optimize bleaching operations, and used in process control strategies.

Brogdon is owner of Future Bridge Consulting Services LLC, Marietta, GA, USA. Lucia is associate professor in the Department of Forest Biomaterials at North Carolina State University, Raleigh, NC, USA. Email Brogdon at Brian.Brogdon@gmail.com .

Coating

Discrete element method to predict coating failure mechanisms

By: Daniel H. Varney, Douglas W. Bousfield

January, pp. 21 – 28 The mechanical properties of coating layers are critical for post-application processes such as calendering, printing, and folding. Discrete element methods (DEM) have been used to simulate basic deformations such as tensile and compression, but have not been used as a tool to predict cracking-at-the-fold (CAF) or picking. DEM has the potential to increase our understanding of these failure mechanisms at the particle level. We propose a method to model the three-point bending of a coating layer and also the out-of-plane picking event during printing (using a z-direction scenario and an approach involving a moving force/velocity). Properties of the binder and the binder concentration are input parameters for the simulation. The model predicts the crack formation of the layer, the flexural modulus, and the maximum flexural strain during bending. The model also predicts the forces required for picking to occur. Results are compared with those of complimentary studies.

Application: Mills can use the findings of this study to better understand the mechanical properties of these coatings and to adjust coating formulations to better meet product needs.

Varney is technical service manager, OMYA, Proctor, VT, USA. Bousfield is professor, Paper Surface Science Program, University of Maine, Orono, ME, USA. Email Bousfield at bousfld@maine.edu .

Contrasting underlying mechanisms of different barrier coating types

By: Bryan McCulloch, John Roper, Kaitlin Rosen

January, pp. 31 - 37 Barrier coatings are used in applications including food packaging, dry goods, and consumer products to prevent transport of different compounds either through or into paper and paperboard substrates. These coatings are useful in packaging to contain active ingredients, such as fragrances, or to protect contents from detrimental substances, such as oxygen, water, grease, or other chemicals of concern. They also are used to prevent visual changes or mechanical degradation that might occur if the paper becomes saturated. The performance and underlying mechanism depends on the barrier coating type and, in particular, on whether the barrier coating is designed to prevent diffusive or capillary transport. Estimates on the basis of fundamental transport phenomena and data from a broad screening of different barrier materials can be used to understand the limits of various approaches to construct barrier coatings. These estimates also can be used to create basic design rules for general classes of barrier coatings.

Application: Barrier coatings can be designed with unique performance profiles optimized for customer requirements.

McCulloch is an associate research scientist, Roper is a fellow, and Rosen is a senior chemist at Dow

Chemical Company, Collegeville, PA, USA. Email McCulloch at BMcCulloch@dow.com .

Corrosion

A hundred years of corrosion in the pulp and paper industry

By: Max Moskal

May, pp. 253 - 258 Through the decades, the pulp and paper industry greatly expanded production capacity to meet increasing demands. Correspondingly, the cost of corrosion damage soared. The most serious corrosion control challenges were researched and met by university and governmental researchers, and by task groups within the TAPPI Engineering Division's Corrosion and Materials Engineering Committee. Today, thanks to material and process advances, mills encounter less corrosion than in the past. This overview takes a historical look back, covering many decades, at how corrosion problems have been managed in the pulp and paper industry. Yet, corrosion keeps on going, and today mills appear less able to manage corrosion problems for which known solutions are available. This paper also addresses the significant yet underrated task of optimizing corrosion control management in the present and into the future. Discussion is provided on best practices needed to mitigate new and ongoing corrosion problems.

Application: This review should help mills better realize the importance and benefits of systematic corrosion management.

Moskal is principal engineer, M&M Engineering Associates, Division of Acuren Inspection Inc., Indian Head Park, IL, USA. Email Moskal at max_moskal@mmengineering.com .

Corrugated Containers

Importance of specimen preparation for edgewise compressive strength (ECT) testing

By: Jerry Loza, Doug Cash, Benjamin Frank

April, pp. 219 - 227 While more than 50 years of published studies recognize the importance of rectangular, parallel edgewise compressive strength (ECT) specimens, none of the existing test methods address the degree to which a sample specimen is defined as sufficiently parallel. We present a detailed exploration of ECT results for specimens whose edges deviate from parallel with varying severity. We work to identify causes of variation in dimensional measurements and the corresponding ECT values across several industry standard cutters. These variations present a significant challenge to the industry in satisfying customer expectations for performance-based packaging, as well as to the development of improved predictive models for packaging performance.

Application: This work serves as an early step for identifying or developing more optimal test methodologies to measure the inherent compressive strength of corrugated materials.

Frank is senior manager, Technical Operations and Resources, Loza is senior technician, and Cash is contract technician, Packaging Corporation of America, Mundelein, IL, USA. Email Frank at bfrank@packagingcorp.com .

Delignification

Using online bubble size and total dissolved solids measurements to investigate the performance of oxygen delignification

By: Riku Kopra, Heikki Mutikainen, Olli Dahl

June, pp. 343 - 350 The main target of oxygen delignification is to continue delignification that started in cooking in a more selective manner than occurs in the digester (i.e., remove a substantial fraction of the residual lignin using oxygen and alkali at a moderate temperature). Delignification with oxygen is a gentler way of reducing the kappa number than extended cooking. Lowering inlet kappa to bleaching also decreases bleaching chemicals consumption and, because of this, reduces organic wastewater load from bleaching. We studied the performance of oxygen delignification by installing bubble size imaging systems and refractometers, which measure dissolved dry solids in the oxygen stage feed. Based on these measurements, we gathered information

about gas dispersion (bubble size distribution) and the behavior of dissolved matter in the hardwood mill's oxygen delignification stage. Our goal was to investigate the effects of different variables on the oxygen stage's gas dispersion, kappa reduction, yield, and pulp quality. Gas dispersion improved (i.e., average bubble size decreased) when the chemical mixer speed increased. Increasing the mixer speed and the amount of oxygen yielded higher kappa number reductions and increased the amount of dissolved organic matter.

Application: Methods described here could help mills adjust the oxygen charge and gas dispersion in delignification processes and allow for future monitoring and controlling of the oxygen process.

Kopra is RDI scientist, Fiber Laboratory, Southeastern Finland University of Applied Sciences, Savonlinna, Finland. Mutikainen is R&D engineer, Fiber Technologies Division, Andritz Ltd., Kotka, Finland. Dahl is professor, Clean Technologies Group, Department of Bioproducts and Biosystems, School of Chemical Engineering, Aalto University, Espoo, Finland. Email Kopra at riku.kopra@xamk.fi .

Effects of lignin chemistry on oxygen delignification performance

By: Valeria Juste Gomes, Hasan Jameel, Hou-Min Chang, Robert Narron, Jorge Colodette, Peter W. Hart

July, pp. 373 - 381 The present work focused on characterizing the chemical and structural properties of isolated lignin from six hardwoods and their kraft pulps in an attempt to better understand the relationship between lignin's chemical properties and resultant oxygen delignification performance. Several hardwood samples were cooked under the same conditions with varying alkali charges to obtain unbleached pulps with kappa numbers between 19 and 20. These pulps were then subjected to an oxygen delignification stage. Both processes were evaluated for pulp quality, residual lignin, and O-stage delignification efficiency. The oxygen delignification stage was carried out under fixed conditions and evaluated with regards to kappa number, which was corrected for hexenuronic acid (HexA) contributions. Results revealed that different hardwood species exhibited differing oxygen delignification efficiencies. A high correlation was found between the O-stage delignification efficiency and the content of phenolic groups in the unbleached lignin, which confirmed that free phenolic groups are the reactive site for molecular oxygen attack. When different hardwood species were compared, the HexA contents were not found to affect O-stage delignification efficiencies.

Application: The authors are attempting to understand how the structure of different hardwood species impacts oxygen delignification performance. If they can develop this understanding, the performance of the oxygen stage can be tailored to specific seasonal changes in the wood hardwood species being harvested.

Juste Gomes is visiting scholar, Jameel is professor, Chang is professor, and Narron is a Ph.D. candidate at North Carolina State University in Raleigh, NC, USA. Colodette is professor at University Federal de Viçosa, in Viçosa, MG, Brazil. Hart is director, Fiber Science and Innovation at WestRock in Richmond, VA, USA. Email Hart at peter.hart@westrock.com .

Emissions

Factors affecting particulate removal efficiency of kraft recovery boiler electrostatic precipitators: a technical review

By: Ezzat Jaroudi, Ivan Sretenovic, Greg Evans, Honghi Tran

May, pp. 273 - 283 Electrostatic precipitators (ESPs) are used in most pulp mills to remove particulate from recovery boilers, power boilers, and lime kilns. As environmental regulations have become increasingly stringent in recent years, maintaining high ESP performance is of vital importance in mill operation. This paper discusses results of a literature review of the ESP technology used in industrial combustion units, including recovery boilers, as well as results of a parametric study using the well-known Deutsch-Anderson equation to correlate recovery boiler operat-ing

conditions with ESP collection efficiency. The results show that for particles up to about 0.3 μm, the ESP collec-tion efficiency decreases drastically with increased particle size and with decreased temperature. For particles larger than 0.5 μm, however, the trend reverses; the collection efficiency increases with increased particle size and decreased temperature. The results also suggest that the particle concentration (or loading) in the flue gas has no effect on collection efficiency and that sodium chloride particles are more readily captured than sodium sulfate particles. The latter prediction, however, appears to be in contradiction with mill experience that sodium chloride particles are more difficult to capture.

Application: Mills can maximize their boiler throughputs by better understanding key operating factors that affect electrostatic precipitator performance.

Jaroudi is a graduate student, Evans is a professor, and Tran is Frank Dottori Professor of Pulp and Paper Engineering in the Department of Chemical Engineering and Applied Chemistry, University of Toronto, Toronto, ON, Canada. Sretenovic is product manager-ESP, Air Pollution Control Product Division, Clyde Bergemann Power Group Americas Inc., Hanover, MD, USA. Email Tran at honghi.tran@utoronto.ca .

Photo-catalytic degradation of gaseous pollutants in paper mills of southern China

By: Xin Tong, Jiao Li, Jun Ma, Xiaoquan Chen, Wenhao Shen

March, pp. 167 - 178 Studies were undertaken to evaluate gaseous pollutants in workplace air within pulp and paper mills and to consider the effectiveness of photocatalytic treatment of this air. Ambient air at 30 sampling sites in five pulp and paper mills of southern China were sampled and analyzed. The results revealed that formaldehyde and various benzene-based molecules were the main gaseous pollutants at these five mills. A photo-catalytic reactor system with titanium dioxide (TiO_2) was developed and evaluated for degradation of formaldehyde, benzene and their mixtures. The experimental results demonstrated that both formaldehyde and benzene in their pure forms could be completely photo-catalytic degraded, though the degradation of benzene was much more difficult than that for formaldehyde. Study of the photo-catalytic degradation kinetics revealed that the degradation rate of formaldehyde increased with initial concentration fitting a first-order kinetics reaction. In contrast, the degradation rate of benzene had no relationship with initial concentration and degradation did not conform to first-order kinetics. The photo-cat-alytic degradation of formaldehyde-benzene mixtures indicated that formaldehyde behaved differently than when treated in its pure form. The degradation time was two times longer and the kinetics did not reflect a first-order reaction. The degradation of benzene was similar in both pure form and when mixed with formaldehyde.

Application: The developed photo-catalytic system had an excellent degradation performance on the gaseous pollutants in the paper mills. The findings from this work will be useful in the further development of workplace air conditioning devices.

Tong is a post-doctoral student, Li is a doctoral student, Chen is associate professor, and Shen is professor at the State Key Laboratory of Pulp and Paper Engineering, South China University of Technology, Guangzhou, China. Email Shen at ppwhshen@scut.edu.cn .

Fiber Properties

Enzymatic treated viscose fibers functionalized by chitosan

By: Urška Vrabič Brodnjak, Diana Gregor-Svetec, Maja Klančnik,

August, pp. 447 - 457 Our research focused on the sorption properties of enzymatically treated viscose/chitosan and viscose fibers treated with enzymes and chitosan. To improve sorption properties of viscose fibers and to obtain the characteristics similar to viscose/chitosan fibers, we performed two different treatments. First, we treated both fibers with enzyme cellulase for 60 min and afterwards treated viscose fibers with the chitosan in an ultrasonic bath. In our research, structural characteristics and the accessibility of free

adsorption places were investigated. We noted a noticeable change in the structure (degree of polymerization, crystallinity, and molecular orientation) of treated viscose and viscose/chitosan fibers. Changes that occurred in the morphology and in the structural properties of both types of tested fibers were also reflected in their physical and chemical properties. Research showed that the sorption properties of enzymatic treated fibers were improved.

Application: This study provides structure and sorption properties of viscose/chitosan fibers and viscose fibers treated with chitosan and analyzes the improvement of sorption properties of fibers, based on enzymatic treatment. Such treated fibers could be used in paper, packaging, hygiene towels, pads, and other applications.

Brodnjak is assistant professor, Gregor-Svetec is professor, and Klančnik, is assistant professor, University of Ljubljana, Faculty of Natural Sciences and Engineering, Department of Textiles, Ljubljana, Slovenia. Email Gregor-Svetec at diana.gregor@ntf.uni-lj-si .

Lignocellulose

Activated carbon from potassium hydroxide spent liquor lignin using phosphoric acid

By: Mamon Sarkar, Chao Tian, M. Sarwar Jahan

February, pp. 63 - 69 Activated carbon was prepared by phosphoric acid (H_3PO_4) activation of potassium hydroxide (KOH) pulping spent liquor lignin from rice straw and compared with KOH hydroxide activation. The process parameters, such as impregnation ratio, activation temperature, and activation time were varied and their effects on the yield of activated carbon and iodine number were studied. The activated carbon prepared by H_3PO_4 at 800°C for 60 min at an impregnation ratio of 2.5 reached a Brunauer-Emmett-Teller (BET) surface area of 1063 m^2/g, including pore diameter of 14.4 nm, iodine number of 525 mg/g, and yield of 49.2%. Yield and BET surface area in KOH activation was much lower than that of H_3PO_4.

Application: Potassium hydroxide spent liquor lignin can be used in producing activated carbon. In the biorefinery, this can be integrated with pulp production based on agricultural wastes.

Jahan is chief science officer and Sarkar is a research chemist, Pulp and Paper Research Division, BCSIR Laboratories, Dhaka, Bangladesh. Tian is director, China National Pulp and Paper Research Institute, Beijing, China. Email Jahan at sarwar2065@hotmail.com .

Static and dynamic sorption of lignin removed **Populus euramericana**

By: Haizhen Zhou, Jingyu Li, Erni Ma

February, pp. 71 - 77 To investigate the effect of lignin on moisture sorption behaviors of wood under static and dynamic conditions, Populus euramericana cultivars measuring 20 mm tangentially × 20 mm radially × 4 mm along the grain was divided into three groups: untreated, extractives removed, and lignin removed. All the samples were subjected to static sorption where relative humidity (RH) was controlled at 11%, 45%, and 75%, and dynamic sorption where RH changed sinusoidally between 45% and 75% for cyclic periods of 1 h and 24 h, both conditions kept at 25C°. Moisture changes were measured during the adsorption and desorption processes. Moisture of the samples varied rapidly at the initial stage during static sorption. The rate decreased gradually until equilibrium was reached. Moisture changes for dynamic condition were generally sinusoidal but lagged behind the imposed RH. The moisture content difference (ΔMC45-75) and moisture sorption coefficient (Z) were higher under static conditions, whereas the hysteresis ratio showed greater values in the dynamic environment. Among the three groups, the lignin-removed samples exhibited the highest ΔMC45-75, Z, and hysteresis ratio, followed by the extractives removed and untreated samples.

Application: Results from this study provide further insights into the physical properties of the chemical components of wood and sorption relative to the main components of wood.

Zhou and Li are post-graduate students and Ma is associate professor, Beijing Key Laboratory of Wood Science and Engineering, MOE Key Laboratory of Wooden Material Science and Application, Beijing Forestry University, Beijing, China. Email Ma at maerni@bjfu.edu.cn

Lignocellulose fibers elaborating super-swollen three-dimensional cellulose hydrogels from solution in N, N-dimethylacetamide/lithium chloride

By: Aleksandra Mikhailidi, Shahriar Karim Saurov, Seppo Andersson, Nina Kotelnikova

February, pp. 81 - 88 Super-swollen hydrogels were prepared in vitro from lignocelluloses of various origins via direct dissolving in N,N-dimethylacetamide/lithium chloride (DMAc/LiCl) followed by regeneration from solutions. The hydrogels retained a large amount of water (up to 2500 wt%) and had high porosity and specific surface areas. Superabsorbance of the hydrogels was confirmed with a wide angle X-ray scattering method. The hydrogels seem to be smart matters due to PH-dependent behavior by swelling and pH change experiments. The gelation mechanism includes spontaneous self-assembly from the solutions in DMAc/LiCl, due to the reconstruction of new hydro-gen bond webs between lignocellulose chains and water. The hydrogels exhibited high stability but their morphology changed while drying due to water removal and the collapse of the H-bonds.

Application: Super-swollen hydrogels have potential for biomedical, pharmaceutical, and industrial purposes. Applications might include scaffolds for tissue engineering and composite hydrogels with organic and inorganic substances for surgical interventions.

Mikhailidi is a Ph.D. and lecturer, High School of Printing and Media Technologies, St. Petersburg State University of Industrial Technologies and Design, St. Petersburg, Russia. Saurov is a Master's Degree student and Andersson is a Ph.D. and laboratory engineer, Department of Physics, University of Helsinki, Helsinki, Finland. Kotelnikova is a professor, Institute of Macromolecular Compounds, Russian Academy of Sciences, St. Petersburg, Russia. Email Mikhailidi at amikhailidi@yahoo.com

Lignin — a promising biomass resource

By: Yong Qian, Hongming Lou, Weifeng Liu, Dongjie Yang,Xinping Ouyang, Yuan Li, Xueqing Qiu

March, pp. 125 - 141 Lignin, the second most abundant component in plants, is a class of complex aromatic polymer. Industrial lignin is a major byproduct of pulp and paper production and biorefineries, with more than 50 megatons generated annually. However, more than 98% of industrial lignin is either burned as fuel or discharged as wastewater, causing serious environmental pollution. From a sustainable feedstock perspective, finding additional high-volume and high-value applications for lignin is an extremely important and long-term pursued objective. Thus, lignin resources deserve to be further exploited as biorenewable raw materials for energy-saving and low-carbon polymer production. Inspired by the natural three-dimensional structure, excellent ultraviolet-blocking and antioxidant properties of lignins, the authors have focused their research on lignin-based biorenewable resources. This review summarizes research achievements of the recent decade. Progress has been made in several aspects, such as nonionic and amphoteric lignin-based surfactants, lignin-based functional materials, lignin-based photoelectric materials, lignin-based resins and polymer composites, and catalytic depolymerization of lignin.

Application: This review summarizes recent research and provides some novel strategies for the application and understanding of lignin.

Qian is professor, Lou is professor, Liu is associate professor, Yang is professor, Ouyang is professor, Li is associate professor, and Qiu is professor and vice pres-ident, School of Chemistry and Chemical Engineering, South China University of Technology, Guangzhou, China. Qian, Lou, and Qiu are also associated with the State Key

Laboratory of Pulp and Paper Engineering, South China University of Technology. Email Qiu at xueqingqiu66@163.com .

Microfibrilated Cellulose

Mineral/microfibrillated cellulose composite materials: High performance products, applications, and product forms

By: David Skuse, Mark Windebank, Tafadzwa Motsi,
Guillaume Tellier

September, pp. 507 - 515 When pulp and minerals are co-processed in aqueous suspension, the mineral acts as a grinding aid, facilitating the cost-effective production of fibrils. Furthermore, this processing allows the utilization of robust industrial milling equipment. There are 40000 dry metric tons of mineral/microfbrillated (MFC) cellulose composite production capacity in operation across three continents. These mineral/MFC products have been cleared by the FDA for use as a dry and wet strength agent in coated and uncoated food contact paper and paperboard applications. We have previously reported that use of these mineral/MFC composite materials in fiber-based applications allows generally improved wet and dry mechanical properties with concomitant opportunities for cost savings, property improvements, or grade developments and that the materials can be prepared using a range of fibers and minerals. Here, we: (1) report the development of new products that offer improved performance, (2) compare the performance of these new materials with that of a range of other nanocellulosic material types, (3) illustrate the performance of these new materials in reinforcement (paper and board) and viscosification applications, and (4) discuss product form requirements for different applications.

Application: The benefits of using mineral/MFC composite materials can include cost savings by filler increase; optical and print quality improvements; coating holdout improvements; improvements in many mechanical proper-ties; and improved wet strength and runnability. In addition, these materials offer opportunities for grade development.

Skuse is vice president of Technology, Windebank is senior research engineer, Motsi is senior research engineer, and Tellier is vice president of Manufacturing at FiberLean Technologies Ltd., Cornwall, UK. Email Skuse at david.skuse@fiberlean.com .

Nanotechnology

Slot die coating of nanocellulose on paperboard

By: Vinay Kumar, Douglas W. Bousfield, Martti Toivakka

January, pp. 11 - 19 Constantly growing interest in nanocellulose usage and applications is pushing the scientific community to search for suitable production and processing techniques. One example is use of nanocellulose as a barrier material in packaging applications, which requires processing of nanocellulose into films and coatings. It is challenging to coat nanocellulose suspensions using conventional pigment coating techniques due to their yield stress behavior and very high viscosity, even at low solids concentration. This work demonstrates a novel roll-to-roll coating method of nanocellulose on paperboard using slot die geometry. The rheology of nanocellulose suspensions in pressure-driven flow is found to play a critical role in enabling their coating using the said process. In this work, the slot die is used in an unconventional manner where the shearing and metering elements are combined to aid wet film formation and application of nanocellulose suspension onto the paperboard. Barrier performance of the nanocellulose coated paperboards against air, water, heptane vapor, grease, and oils was found to be reasonable and warrants further research on the subject.

Application: The modified slot die coating method reported here could be utilized for roll-to-roll coating of web materials with a large variety of highly viscous materials such as cellulose nanofibers.

Kumar is doctoral researcher and Toivakka is professor at the Laboratory of Paper Coating and Converting, and Center for Functional Materials, at Åbo Akademi University, Turku, Finland. Bousfield is professor in the Department of Chemical and Biological Engineering and director of the Paper Surface Science Program at the University of Maine, Orono, ME, USA. Email Toivakka at Martti.Toivakka@abo.fi .

Functionalization of wood/plant-based natural cellulose fibers with nanomaterials: a review

By: Charu Agarwal, Levente Csóka

February, pp. 92 - 111 Being the most abundant natural biopolymer on earth, cellulose has been vastly exploited in a range of applications, from writing paper to high-end biosensors. Natural cellulose fibers can be isolated from wood or non-woody plants such as hemp, jute, flax, and bamboo by chemical or mechanical treatments. To make it suitable for targeted applications, cellulose fibers are modified with functional moieties in the nanometer scale. Cellulose has been functionalized with noble metals such as silver and gold nanoparticles for catalysis and antimicrobial applications. A number of metal oxides, such as zinc oxide, titanium dioxide, and tin dioxide have been incorporated into cellulose. The porosity, hydrophilicity, and roughness of cellulose surface makes it an ideal substrate for a plethora of sensing applications. Further, it can be made into a lightweight, portable, foldable, and dis-posable device, which provides an excellent platform for various point-of-care purposes. Cellulose fibers have also been immobilized with carbon nanomaterials, including carbon nanotubes and graphene oxide. For optical applications, $[Fe(hptrz)_3](OTs)_2$ spin-crossover nanoparticles have also been immobilized on cellulose fibers. Likewise, many enzymes, macromolecules, and some polymers have been used to modify natural cellulose for specific end uses. This review focuses on recent developments in the modification or immobilization of functional materials on cellulose fibers, in macro-scale only, obtained from wood or plant sources.

Application: Manufacturers are developing a growing range of products based on combinations of nanomaterials and cellulose fibers.

Agarwal is a Ph.D. scholar and Csóka is professor, Cellulose and Biomacromolecules Research Group, Institute of Wood Based Products and Technologies, University of Sopron, Hungary. Email Csóka at levente. csoka@skk.nyme.hu or csoka.levente@uni-sopron.hu .

Controlling porosity and density of nanocellulose aerogels for superhydrophobic light materials

By: Chenghua Yu, Feng Wang, Shiyu Fu, Lucian A. Lucia

March, pp. 145 - 153 A very low-density oil-absorbing hydrophobic material was fabricated from cellulose nanofiber aerogels–coated silane substances. Nanocellulose aerogels (NCA) superabsorbents were prepared by freeze drying cellulose nanofibril dispersions at 0.2%, 0.5%, 0.8%, 1.0%, and 1.5% w/w. The NCA were hydrophobically modified with methyltrimethoxysilane. The surface morphology and wettability were characterized by scanning electron microscopy and static contact angle. The aerogels displayed an ultralow density (2.0–16.7 $mg \cdot cm^{-3}$), high porosity (99.9%–98.9%), and superhydrophobicity as evidenced by the contact angle of ~150° that enabled the aerogels to effectively absorb oil from an oil/water mixture. The absorption capacities of hydrophobic nanocellulose aerogels for waste engine oil and olive oil could be up to 140 $g \cdot g^{-1}$ and 179.1 $g \cdot g^{-1}$, respectively.

Application: Mills might sell pulps for production of nanocellulose-based aerogels for oil spill remediation.

Yu is a Ph.D. student, Wang is an undergraduate student, and Fu is a professor at the State Key Laboratory of Pulp and Paper Engineering, South China University of Technology, Guangzhou, China. Lucia is associate professor in the

Department of Forest Biomaterials, North Carolina State University, Raleigh, NC, USA. Email Fu at shyfu@scut.edu.cn

An effective method for determining the retention and distribution of cellulose nanofibrils in paper handsheets by dye labeling

By: Shengdan Wang, Wenhua Gao, Kefu Chen, Jinsong Zeng,
Jun Xu, Bin Wang

March, pp. 157 - 164 Cellulose nanofibrils (CNF) were prepared by cellulase in conjunction with mechanical disintegration from the bleached softwood kraft pulp and labelled by Congo red dye. The labelled CNF were used to investigate the retention and distribution of CNF in paper handsheets. The retention of the labelled CNF was obtained by measuring the absorbance of white water using an ultraviolet-visible spectrophotometer. The results showed that this method for measuring the retention was rapid, feasible, and sensitive, owing to the high correlation coefficient R^2 (0.9993) of the standard curve. The labelled CNF showed even distribution in paper handsheets. The colorimetric values of paper handsheets were explored with a residual ink analyzer.

Application: In the laboratory, the dye labeling method is a feasible and effective approach to indicate the retention and distribution of CNF in paper handsheets.

S. Wang is a Ph.D. student; Gao, Xu, and B. Wang are associate professors; Chen is an academician; and Zeng is a professor at State Key Laboratory of Pulp and Paper Engineering, South China University of Technology, Guangzhou, China. Email Gao at segaowenhua@scut.edu.cn .

Wet-end addition of nanofibrillated cellulose pretreated with cationic starch to achieve paper strength with less refining and higher bulk

By: Matthew C. Rice, Lokendra Pal, Ronalds Gonzalez, Martin A. Hubbe

July, pp. 395 - 403 Nanofibrillated cellulose (NFC) treated with cationic starch was evaluated as a bonding system to permit lower degrees of refining and lower apparent density of high-mass handsheets made from bleached kraft pulp. Mixed pulp (70% hardwood, 30% softwood) was formed into sheets with the optional addition of 5% by dry mass of NFC. The default addition of NFC was compared with a system in which the NFC had been pretreated either with cationic starch (at various levels) or optionally followed by colloidal silica. Comparative tests also were carried out with separate addition of cationic starch to the main furnish. Unrefined fibers (514 mL CSF) were compared with low-refined (473 mL CSF) and high-refined (283 mL CSF) pulp mixtures. The NFC that had been pretreated with cat-ionic starch at a high level was especially effective at boosting the tensile strength and stiffness of sheets prepared from pulp that had been refined at a low level, thus achieving improved strength at relatively low apparent density (high bulk) of the handsheets. The results support a strategy, for applicable grades of paper, of using cationic starch-pretreated NFC in place of refining energy applied to the main fiber furnish. It was further established that colloidal silica can be employed as a further pretreatment of the cationic starch–treated NFC as a means of promoting dewatering in the combined system.
Application: Higher caliper at a defined basis weight, while maintaining tensile strength and stiffness, can be achieved by use of cationic starch–pretreated nanofibrillated cellulose, while decreasing the main refining of kraft fibers. Mills can consider this technology for paper and board grades for which low apparent density and maintaining stiffness are primary goals.

Rice is a student, Pal and Gonzalez are associate professors, and Hubbe is a professor in the Department of Forest Biomaterials, North Carolina State University, Raleigh, NC, USA. Email Hubbe at hubbe@ncsu.edu .

Nonwood Pulping

Does the kappa number method accurately reflect lignin content in nonwood pulps?

By: Sabrina Burkhardt

November, pp. 611 - 617 The traditional kappa number method was developed in 1960 as a way to more quickly determine the level of lignin remaining in a completed or in-progress pulp. A significantly faster approach than the Klason lignin procedure, the kappa number method is based on the reaction of a strong oxidizing agent ($KMnO_4$) with lignin and small amounts of other organic functional groups present in the pulp, such as hexenuronic acid. While the usefulness of the kappa number for providing information about bleaching requirements and pulp properties has arguably transformed the pulp and paper industry, it has been mostly developed for kraft, sulfite, and soda wood pulps. Nonwood species have a different chemical makeup than hardwood or softwood sources. These chemical differences can influence kappa and Klason measurements on the pulp and lead to wide ranges of error. Both original data from Sustainable Fiber Technologies' sulfur and chlorine-free pulping process and kappa and Klason data from various nonwood pulp literature sources will be presented to challenge the assumption that the kappa number accurately represents lignin content in nonwood pulps.

Application: The information provided in this study closely examines typical results of the analysis of lignin in nonwood pulps and encourages researchers in this area to measure both kappa number and Klason lignin separately to determine if a consistent correlation can be applied.

Burkhardt is director of Chemical Development at Sustainable Fiber Technologies, Renton, WA, USA. Email Burkhardt at Sabrina@sustainablefibertechnologies.com .

Packaging

Production of polyhydroxyalkanoates (PHA)-based renewable packaging materials using photonic energy: A bench and pilot-scale study

By: Michael Joyce, Lokendra Pal, Tom Tran

October, pp. 557 - 565 This work describes the utilization of a new photonic heat treatment technology in combination with polyhydroxyalkanoates (PHA) materials for the development of biofriendly packaging and coated substrate materials. This technology advances the use of aqueous PHA coatings as a replacement for less environmentally friendly extruded plastic and fluorotreated packaging papers and boards. The new technology utilizes short burst photonic energy to heat PHA latex coatings. Utilizing a rapid pulse of photonic energy enables PHA particles to melt and form a film within milliseconds, as compared to conventional equilibrium drying that takes several minutes. Coatings were applied to commercially produced papers in order to validate the combined use of photonic treat-ment technology with PHA materials for commercial applications. Photonic treatment for both bench-top and roll-to-roll pilot-scale studies resulted in kit values of 12, and 2 min Cobb values of <2 g/m^2. Repulpability studies showed the material to be completely repulpable, having 100% accepts after screening. The results demonstrate that the photonic treatment of PHA polymers could be used in current commercial settings to produce environmentally friendly packaging and coated products.

Application: By combining aqueous based PHA coating with photonic drying technology, it is now possible to implement PHA in commercial applications pertaining to environmentally friendly barrier coatings for the manufacture of functional paper and paperboard products, specifically for moisture vapor, moisture, and grease resistance. It presents an alternative to conventional non-renewable extruded polyethylene, petroleum-based latex coatings, and fluorochemical and chromium-containing coatings. Industry impacts for the introduction of this technology include: introduction of green chemistry formulations into coating processes, reduction of plastic waste in the recycle stream, increased utilization of renewable and sustainable product lines, and decreased carbon footprints.

Joyce is a post-doctoral student, Pal is associate professor, and Tran is director, Product Innovation,

at North Carolina State University, Raleigh, NC, USA. Email Joyce at Michael@snpinc.com .

Paper Physics

Evaluation of the out-of-plane response of fiber networks with a representative volume element model

By: Yujun Li, Zengzhi Yu, Stefanie Reese, Jaan-Willem Simon

June, pp. 329 - 339 Many natural and synthetic materials have fibrous microstructures, including nonwoven fabrics, paper, and fiberboard. Experimentally evaluating their out-of-plane mechanical behavior can be difficult because of the small thickness compared with the in-plane dimension. To properly predict such properties, network-scale models are required to obtain homogenized material mechanics by considering fiber-scale mechanisms. We demonstrate a three-dimensional representative volume element (RVE) for fiber networks using the finite element method. We first adopted the classical deposition procedure to generate fiber networks with random or preferential fiber orientations and then an artificial compression to achieve the practical fiber volume fraction. The hollow fibers, described with elastic-plastic brick elements, were joined by interface-based cohesive zone elements introduced in all fiber-fiber contact areas. Thereafter, the fiber networks were subjected to displacement boundary conditions, and their apparent mechanical response was evaluated by a homogenized stress. To determine the RVE dimension, we further conducted an RVE size convergence study for the out-of-plane compression and tension (varying specimen length while keeping the specimen thickness constant). Finally, we evaluated the apparent out-of-plane response of the obtained RVE for four loading cases: out-of-plane compression, tension, simple shear, and pure shear. The results show a quite different mechanical behavior of fiber networks between all these out-of-plane loading cases, particularly between tension and compression.

Application: Virtual fiber networks can be generated to evaluate the out-of-plane mechanical properties.

Li is assistant professor, School of Mechanical Engineering, Northwestern Polytechnical University, Xi'an, China. Yu is engineer, Schlaich Bergermann Partner GmbH, Shanghai, China. Reese is professor and head of institute, and Simon is composite materials and structures group leader, Institute of Applied Mechanics, RWTH Aachen University, Aachen, Germany. Email Li at li.yujun@hotmail.com .

Prediction of box failure from paper data for asymmetric corrugated board

By: Heinz Joachim Schaffrath, Felix Reichenbach, Samuel Schabel

August, pp. 429 - 434 The well-known McKee formula was derived in 1963 for symmetric fluting constructions. This paper presents investigations showing the influence of asymmetric properties, either geometric or concerning the elastic moduli. Paper properties of the base papers used are taken to calculate the panel properties of corrugated boards. From these results, the box failure is predicted. To do this, a model approximating the corrugated medium by triangles is presented. With this assumption, the bending stiffness of corrugated board, no matter how many flutes, can be predicted from paper data. Machine direction and cross direction are treated separately. The theoretical considerations are verified by measuring paper parameters such as short compression test (SCT), thickness, and bending stiffness, as well as edge compression test (ECT) and bending stiffness of corrugated board and box compression test (BCT) of the boxes. It can be stated that the prediction of using paper data instead of corrugated board data may lead to even better prediction results, as the measuring of bending stiffness at the board may sometimes be influenced by sampling inconveniences. Finally, thickness of the used base papers, as well as thickness of the manufactured board, appear to be the main influencing parameters. The McKee formula is robust enough to be applied for asymmetric corrugated board as well.

Application: The results here help to predict the BCT values from paper data.

Schaffrath is senior researcher, Reichenbach is a Master's student, and Schabel is professor in the Department of Mechanical Engineering at the Technical University of Darmstadt, Darmstadt, Germany. Email Schaffrath at schaffrath@papier.tu-darmstadt.de .

Paper Testing

Dielectric spectroscopic studies of biological material evolution and application to paper

By: Mary Kombolias, Jan Obrzut, Karl Montgomery, Michael T. Postek, Dianne L. Poster, Yaw S. Obeng

September, pp. 501 - 505 Current product composition and quality test methods for the paper and pulp industry are mainly based on manual ex-situ wet-bench chemistry techniques. For example, the standard method for determining the furnish of paper, TAPPI T 401 "Fiber analysis of paper and paperboard," relies on the experience and visual acuity of a specially trained analyst to determine the individual plant species present and to quantify the amount of each constituent fiber type in a sheet of paper. Thus, there is a need for a fast, nondestructive analytical technique that lever-ages intrinsic attributes of the analytes. In this paper, we demonstrate an application of dielectric spectroscopy (DS) as a potential metrology to differentiate between nonwood pulp and wood pulp fibers. This in-situ, noncontact and nondestructive assessment method has inherent forensic capabilities and is also amiable to quality assurance techniques such as gauge capability studies and real-time statistical process control (SPC).

Application: The dielectric spectroscopy results presented in this paper can nondestructively determine the amount of lignin in paper products and are in principle comparable to the performance specifications of the TAPPI Standard Test Method T 401. This DS method should enable the sources of printing substrates to be both authenticated and validated in real time in a paper testing laboratory environment.

Kombolias is senior chemist in Testing and Technical Services, Plant Operations, at the United States Government Publishing Office, Washington, DC, USA. Obrzut is materials research engineer and Poster is research chemist in the Materials Measurement Laboratory, National Institute of Standards and Technology, Gaithersburg, MD, USA. Montgomery is engineering student trainee, Postek is senior scientist, and Obeng is research chemist in the Physical Measurement Laboratory, National Institute of Standards and Technology, Gaithersburg, MD, USA. Email Kombolias at mary.kombolias@nist.gov .

Paperboard

On the nominal transverse shear strain to characterize the severity of creasing

By: Douglas W. Coffin, Joel C. Panek

April, pp. 231 - 240 A transverse shear strain was utilized to characterize the severity of creasing for a wide range of tooling configurations. An analytic expression of transverse shear strain, which accounts for tooling geometry, correlated well with relative crease strength and springback as determined from 90° fold tests. The experimental results show a minimum strain (elastic limit) that needs to be exceeded for the relative crease strength to be reduced. The theory predicts a maximum achievable transverse shear strain, which is further limited if the tooling clearance is negative. The elastic limit and maximum strain thus describe the range of interest for effective creasing. In this range, cross direction (CD)-creased samples were more sensitive to creasing than machine direction (MD)-creased samples, but the differences were reduced as the shear strain approached the maximum. The presented develop-ment provides the foundation for a quantitative engineering approach to creasing and folding operations.

Application: The provided equation characterizing the shear experienced by the paperboard increasing can be used to determine multiple crease tool configurations that yield the same effect on creasing (relative crease strength or springback). The range of interest in shear strain is identified for practical evaluation and further studies of creasing and

folding. The differences between MD and CD creasing is further illuminated.

Coffin is professor in the Department of Chemical, Paper, and Biomedical Engineering at Miami University in Oxford, OH, USA. Panek is research scientist with WestRock in Richmond, VA, USA. Email Coffin at coffindw@miamioh.edu .

Impact of fiber structure on edge-wicking of highly-sized paperboard

By: Lebo Xu, Jeremy Meyers, Peter W. Hart

August, pp. 437 - 443 Coffee edge-wicking testing was conducted on two groups of highly-sized paperboard manufactured at two mills with similar manufacturing processes, but with vastly different local fiber sources. Although the Hercules size test (HST) indicated similar internal size levels between the two types of board, the edge-wicking behavior was noticeably different. Analysis of fiber structure revealed that the board with more edge-wicking had fibers with thicker fiber walls, which kept the fiber lumen more open after pressing and drying on a paper machine. It was demonstrated that liquid penetration through voids between fibers in highly-sized paperboard was limited, because the fiber surface was well protected by the presence of sufficient sizing agent. Nevertheless, freshly exposed fiber walls and lumens at the cut edge of the sheet were not protected by sizing material, which facilitated edge-wicking. The correlation between fiber structure and edge-wicking behavior was highlighted in this work to inspire development of novel sizing strategies that protect the freshly cut edge of the sheet from edge-wicking.

Application: The current work shows the contribution of fiber structure to the edge-wicking process for highly-sized paperboard after all the surfaces are protected with size. Understanding the impact of fiber structure on edge-wicking should inspire the development of novel sizing strategies to further reduce edge-wicking.

Xu is senior research chemist and Hart is director, Fiber Science and Innovation, for WestRock, Richmond, VA, USA. Meyers is assistant papermill superintendent, WestRock, Evadale, TX, USA. Email Hart at peter.hart@westrock.com .

Papermaking

Factors affecting the free shrinkage of handsheets: apparent density, fines content, water retention value, and grammage

By: Nader Mayeli

June, pp. 317 - 325 Industrial papermaking is a high-speed process during which a suspension of cellulosic fibers is formed into a continuous web via dewatering followed by drying. Dewatering in the paper machine occurs mechanically in the forming and pressing sections; however, most of the remaining water, whose removal requires applying high temperatures, evaporates in the dryer section. As a result, the paper web shrinks, due to the shrinkage of individual fibers in the paper web. On the paper machine, the paper web is under restraint in the machine direction (MD), whereas it can shrink in the cross-machine direction (CD). The edges of the web shrink more than the center of the web. A shrinkage profile is therefore created in the CD of the web. All machine-made papers exhibit a CD shrinkage profile. The CD shrinkage profile is significant because it affects the final product quality and manufacturing efficiency.
The prime cause of the CD shrinkage profile during drying is free shrinkage. The effects of several wood pulp fibers on the free shrinkage of handsheets were investigated to obtain deeper understanding of the mechanism of paper shrinkage during drying processes.

Application: Mlls can better understand the role of different fiber types, density, fines content, water retention value, and grammage on the free shrinkage of handsheets formed from a selection of softwood and hardwood pulps.

Mayeli was a Ph.D. researcher at the University of Manchester, Manchester, UK. Email Mayeli at nader.mayeli@hotmail.com .

Rewet in wet pressing of paper

By: J. David McDonald, Richard J. Kerekes

September, pp. 479 - 487 Wet pressing in papermaking removes water by pressure applied over time, but some of the expelled water may

return to the web in an action called "rewet." This water, and the other remaining water, must be removed by drying. To understand the underlying factors of rewet, we have developed a mathematical model of it comprised of a time-dependent term that accounts for water flow from the felt to paper and a time-independent term that accounts for splitting of interfacial water between the felt and paper. Our model is consistent with measurements from the literature and can be used to understand how paper properties, press operation, and felt design can minimize rewet.

Application: This paper provides a physical model that can describe and quantify rewet. This model can be used to guide work to minimize rewet by means of operational changes and through press and fabric design.

McDonald is president, JDMcD Consulting Inc., Vaudreuil-Dorion, QC, Canada, and Kerekes is professor emeritus, University of British Columbia, Pulp and Paper Centre, Vancouver, BC, Canada. Email McDonald at mcdonald.jdavid@gmail.com .

Boosting the elongation potential of paper by mechanical refining and additives

By: Anders Strand, Jarmo Kouko, Antti Oksanen, Kristian Salminen,
Annika Ketola, Elias Retulainen, Anna Sundberg

September, pp. 489 - 498 The procedures used in restraining the web during drying will severely affect paper properties. In this work, the main differences between restrained drying and unrestrained drying on paper properties were identified. The mechanical properties of paper were studied as a function of low-consistency mechanical refining energy; wet-end additions of carboxymethyl cellulose (CMC) with cationic starches; as well as spray addition of alginate, chitosan, and cationic guar gum. After restrained drying, the tensile index and tensile stiffness increased with increasing refining energy, but the elongation at break was severely limited. After unrestrained drying, the elongation at break increased linearly with increasing refining energy. However, unrestrained drying also resulted in significantly lower tensile index and tensile stiffness values. After restrained drying, the largest increases in tensile index and stiffness were obtained by sequential wet-end addition of CMC and cationic starches. Certain combinations could mitigate all of the decrease in tensile index from unrestrained drying, while maintaining the distinctively high elongation potential of the paper. Wet-end addition of CMC and cationic starches could mitigate some of the decrease in tensile stiffness, but not completely. Spray addition of alginate, chitosan, or cationic guar gum increased the tensile index after both restrained and unrestrained drying. Spray addition of alginate resulted in significant increases in elongation at break and two-dimensional formability of the handsheets after unrestrained drying. After restrained drying, the tensile stiffness increased after spray addition of all of the different polysaccharides. After unrestrained drying, however, stiffness was unaffected by all of the tested polysaccharide spray additions. The same pulp treatment/additives will increase either stiffness or stretch, depending on the drying technique, but both properties could not be maximized simultaneously.

Application: Increased elongation of paper could lead to new packaging products. Altering the drying technique increases elongation but also affects other paper properties. Mills can benefit from understanding the effects of different treatments after unrestrained and restrained drying.

Turku, Finland. Kouko and Oksanen are senior scientists and Ketola is a research scientist at VTT Technical Research Centre of Finland, Jyväskylä, Finland. Salminen is a senior scientist at VTT, Tampere, Finland. Retulainen is principle scientist at VTT and adjunct professor at South China University of Technology, Jyväskylä, Finland. Email Sundberg at anna.sundberg@abo.fi .

Printing

Print quality of flexographic printed paperboard related to coating composition and structure

By: E. Bohlin, C. Johansson

January, pp. 43 - 51 Ink transfer and setting influence the achievable print quality and visual appearance. The pressure in the printing nip and the porosity of the substrate regulate the amount of ink that penetrates into a porous coating structure. The purpose of this study was to understand how print quality aspects could be related to ink penetration of water-based flexographic ink into coatings of differently engineered structures: calcium carbonate (GCC) of various particle size distribution (PSD), coatings with different amounts of latex binder, and coatings with various blends of GCC and kaolin. Calcium carbonate with broad pigment PSD resulted in a lower print density compared to coatings of narrowly distributed particle sizes. Coatings of larger pore volume and greater dominating pore radius showed a higher amount of z-directional ink penetration. A high ratio of uncovered areas (UCA) could be detected for samples with high amount of latex. However, increased printing force eliminated these artefacts. Increased printing force increased the print density to a higher degree than did a reduced ink viscosity for coatings with pure GCC. For coating layers containing both GCC and kaolin clay, decreased ink viscosity had a stronger impact on the print density than increased printing force. Print density was also affected by ink penetration, suggesting that the optical response is sensitive to the ink-substrate interaction layer. The result presented in this work also suggests that the print gloss decreases with increased amount of penetrated ink due to a higher rate of ink vehicle removal.

Application: By fine-tuning the coating composition and structure and by a proper selection of printing parameters, it was demonstrated that print quality defects can be addressed by fundamental studies of ink transfer and subsequent ink setting. The detailed understanding of mechanisms of ink-substrate interactions is a requirement for maintaining competitiveness in the packaging industry based on renewable materials.

Bohlin is development engineer and Johansson is specialist, chemical additives, at BillerudKorsnäs Gruvön, Grums, Sweden. Email Johansson at caisa.johansson@billerudkorsnas.com .

Pulping

Online measurement of bulk, tensile, brightness, and ovendry content of bleached chemithermomechanical pulp using visible and near infrared spectroscopy

By: Matthew R. Tomkins, Wesley Gilbert, Thanh Trung

April, pp. 207 - 216 Current pulp mill practice to determine the pulp properties of bleached chemithermomechanical pulp (BCTMP) is to prepare and test handsheets for properties of interest. While the use of handsheets is well established, tests require well trained technical staff and introduce a significant lag before test results can be acted upon. In this report, a prototype online visible and near infrared (Vis-NIR) sensor that complements handsheet testing was trialed for 16 months at a BCTMP mill. The system consists of a cabinet located near a probe installed on a conveyor belt between a slab press and a bale press. When a bale stops on the conveyor belt, the probe rises and comes into contact with the bale, taking a spectral measurement and predicting its bulk, tensile strength, brightness, and ovendry (o.d.) content. The data presented here covers a period of 100 days of real-time measurements that correlated with laboratory tests with an R^2 of 0.88 for bulk, 0.87 for tensile, and 0.92 for brightness. Bulk, tensile strength, and brightness measurements had root mean square error of prediction (RMSEP) values of 0.19 cm^3/g, 3.994 Nm/g, and 0.96 brightness points, respectively. Ovendry content measurements trended with the mill's existing online moisture measurement system and had an R^2 of 0.36 and an RMSEP value of 1.04%. The quality of the correlation for o.d. content was substantially impacted because of difficulties with synchronizing the time stamps between the mill's existing online measurements and the online system reported here. The online Vis-NIR sensor provides information in real time and has the potential to be used to reach target grade properties more quickly, assist in the identification of inefficient chemical dousing, reduce the effect of operator bias during testing, allow for the prioritizing of laboratory tests, and

improve segregation of final products according to customer needs. However, further development would be necessary to use these measurements as part of a process control strategy.

Application: New Vis-NIR sensor technology can provide mills with more information about pulp properties.

Tomkins is an engineer, Sensor Development and Applications, and Gilbert is a senior control engineer, FP Innovations, Vancouver, BC, Canada. Trung is vice president of technology, FITNIR Analyzers Inc., Vancouver, BC, Canada. Email Tomkins at matthew.tomkins@fpinnovations.ca .

Dry chip feedrate control using online chip moisture

By: Wesley Gilbert, Ivan Trush, Bruce Allison, Randy Reimer, Howard Mason

May, pp. 295 - 305 Normal practice in continuous digester operation is to set the production rate through the chip meter speed. This speed is seldom, if ever, adjusted except to change production, and most of the other digester inputs are ratioed to it. The inherent assumption is that constant chip meter speed equates to constant dry mass flow of chips. This is seldom, if ever, true. As a result, the actual production rate, effective alkali (EA)-to-wood and liquor-to-wood ratios may vary substantially from assumed values. This increases process variability and decreases profits. In this report, a new continuous digester production rate control strategy is developed that addresses this shortcoming. A new noncontacting near infrared–based chip moisture sensor is combined with the existing weightometer signal to estimate the actual dry chip mass feedrate entering the digester. The estimated feedrate is then used to implement a novel feedback control strategy that adjusts the chip meter speed to maintain the dry chip feedrate at the target value. The report details the results of applying the new measurements and control strategy to a dual vessel continuous digester.

Application: A new method of dry chip feedrate control could help mills stabilize and potentially increase production rates and achieve better production quality when combined with existing liquor dosing controls. *Bohlin is development engineer and Johansson is specialist, chemical additives, at BillerudKorsnäs Gruvön, Grums, Sweden. Email Johansson at caisa.johansson@billerudkorsnas.com .*

Gilbert is senior control engineer and Allison is research leader at FPInnovations, Vancouver, BC, Canada. Trush is process control specialist, Reimer is business unit leader for fiberline/pulp finishing, and Mason is fiberline area specialist at Alberta Pacific, Boyle, AB, Canada. Email Gilbert at Wesley.gilbert@fpinnovations.ca .

Influence of tensile straining and fibril angle on the stiffness and strength of previously dried kraft pulp fibers

By: John M. Long, Warren J. Batchelor

July, pp. 383 - 392 It has long been known that in individual wood fibers, the tensile mechanical properties are heavily determined by the nature of the cellulose chains in the fibers. Both elastic tensile modulus and strength are directly related to the fibril angle, which is the steepness with which the cellulose chains wind their way around the fiber in the secondary wall of the middle layer, named the S_2 layer. Classic work from the 1970s measured modulus and strength in wood fibers as a function of the fibril angle and compared the results with theoretical models. The measurements were hampered by the presence of defects in the fibers, some which occurred naturally and others which resulted from pulp processing. In this study, we performed more accurate measurements of strength and modulus in single fibers of radiata pine by loading the fibers in cycles, gradually pulling some of the defects out of the fibers in an attempt to obtain defect-free values of modulus and strength. We then plotted these properties against measured fibril angle and compared our results with theoretical models. The results show that even when the fiber had reached maximum load before fracture, at a given value of fibril angle, it still had a measured modulus that is around half the theoretically expected value. The results suggest that the load required to fully remove defects from

the fibers may be larger than the fibers can bear before fracturing.

Application: Information contained in this investigation will help paper researchers and engineers better understand the relationship between processing defects and mechanical properties of single wood fibers.

Long is senior lecturer in the School of Engineering, Deakin University, Geelong, Victoria, Australia. Batchelor is associate professor in the Department of Chemical Engineering, Monash University, Clayton, Victoria, Australia. Email Long at john.long@deakin.edu.au

Recovery Cycle

Monitoring the free lime content in lime mud using zeta potential

By: Wei Ren, Honghi Tran

April, pp. 197 - 204 The presence of unreacted lime (free lime) in the lime mud can cause many problems in the chemical recovery operation of kraft pulp mills. There are currently no standards for free lime determination. Conventional methods used in mill laboratories require extensive preparations and give inconsistent and sometime erroneous results. A systematic study was performed to determine if zeta potential, a dispersion characteristic of the lime mud and liquor slurry, can be used to indirectly indicate the amount of free lime in the lime mud. Lime mud with different free lime contents was produced in the laboratory by causticizing green liquors with lime at different liming ratios. The results show that zeta potential changes from negative to positive when the free lime in lime mud exceeds a critical value. This unique characteristic enables a rapid detection of free lime.

Application: This research can help mills take appropriate actions to avoid problems associated with "overliming" in the recovery process.

Ren is research engineer with FPInnovations in Vancouver, BC, Canada. Tran is Frank Dottori Professor of Pulp & Paper Engineering, Department of Chemical Engineering and Applied Chemistry, at the University of Toronto, Toronto, ON, Canada. Email Tran at honghi.tran@utoronto.ca .

Use of vent stack temperature as a feedforward variable for dissolver total titratable alkali (TTA) control

By: Wei Ren, Brennan Dubord, Jason Johnson, Bruce Allison

May, pp. 261 - 269 Tight control of raw green liquor total titratable alkali (TTA) may be considered an important first step towards improving the overall economic performance of the causticizing process. Dissolving tank control is made difficult by the fact that the unknown smelt flow is highly variable and subject to runoff. High TTA variability negatively impacts operational costs through increased scaling in the dissolver and transfer lines, increased deadload in the liquor cycle, under- and over-liming, increased energy consumption, and increased maintenance. Current practice is to use feedback control to regulate the TTA to a target value through manipulation of weak wash flow while simultaneously keeping dissolver density within acceptable limits. Unfortunately, the amount of variability reduction that can be achieved by feedback control alone is fundamentally limited by the process dynamics. One way to improve upon the situation would be to measure the smelt flow and use it as a feedforward control variable. Direct measurement of smelt flow is not yet possible. The use of an indirect measurement, the dissolver vent stack temperature, is investigated in this paper as a surrogate feedforward variable for dissolving tank TTA control. Mill trials indicate that significant variability reduction in the raw green liquor TTA is possible and that the control improvements carry through to the downstream processes.

Application: Implementing feedforward control at the dissolving tank can reduce raw green liquor TTA variability, which leads to improved operation at the slaker. Feedforward control can also minimize the impact of smelt runoffs and improve safety at the dissolving tank.

Ren is research engineer and Allison is principal research engineer and research leader at FPInnovations in Vancouver, BC, Canada. Dubord is process engineer and Johnson is control systems coordinator, Steam & Recovery, at Cariboo Pulp & Paper in Quesnel, BC, Canada. Email Ren at wei.ren@fpinnovations.ca .

Effect of ring formation on burner flame stability in lime kilns

By: Girish Mohanan, Honghi Tran, Markus Bussmann, Richard Manning

May, pp. 285 - 293 Ring formation in lime kilns is a common problem in pulp mills. Unstable burner operation that causes wide temperature variations within the kiln has been shown to be a main contributor. As rings grow thicker and longer, they are expected to affect the burner flame pattern, alter the temperature distribution, and further aggravate the problem. This study systematically examines the effect of rings on burner operation as a function of primary air and ring characteristics, using a laboratory mock kiln. The results show that primary air greatly affects the burner flame pattern and stability. Without a ring, the flame is brighter and shorter, with an increase in primary air (PA) up to 17%, and blows out at 20% PA or higher. In the presence of a ring, the flame becomes unstable and blows out when the ring is placed near the burner, but it is more stable when the ring is placed away from the burner. Thick and long rings destabilize the flame more than thin and short rings.

Application: Pulp mill engineers may use the information in this study to help stabilize the lime kiln burner flame.

Mohanan is a graduate student and Tran is Frank Dottori Professor of Pulp & Paper Engineering in the Department of Chemical Engineering and Applied Chemistry at the University of Toronto, Toronto, ON, Canada. Bussmann is professor in the Department of Mechanical and Industrial Engineering at the University of Toronto, Toronto, ON, Canada. Manning is director and chief technology officer at KFS in High Wycombe, U.K. Email Tran at honghi.tran@utoronto.ca .

A review of green liquor scale formation

By: Peter W. Hart

October, pp. 571 - 578 Green liquor scale is a recurring problem in most kraft mills. Several types of scale, e.g., pirssonite, calcite, sodium aluminosilicates, etc., have been identified in various green liquor scales. The mechanisms of formation and potential operational methods to control the formation of these scales is reviewed.

Application: For mills, understanding ways to prevent scale formation will benefit the process area.

Hart is director, Fiber Science and Innovation, for WestRock, Richmond, VA, USA. Email Hart at peter.hart@westrock.com .

RECYCLING

Effect of pH and enzymes on strength of recycled fibers during refining

By: Ashok Ghosh, Breland Thornton, Peter W. Hart

July, pp. 407 - 415 Recycled fiber-based papermaking in America is experiencing a persistent reduction in the strength of the incoming fiber. To maintain paper strength properties, paper mills respond by increasing basis weight, dry strength, etc. On average, the fiber cost component in recycled paper is approximately 40% of the total manufacturing cost. Increased fiber weight results in higher operating cost and has a negative effect on production rate, especially on dryer-limited paper machines. Increased pH and use of certain enzymes can improve strength during subsequent refining. The ProLab refiner was used to generate laboratory refining curves to evaluate changes in fiber bonding. The effect of pH and enzymes pretreatment on the strength development and change in drainage of recycled fibers with refining was evaluated.

Application: This study can demonstrates potential uses and net positive effects of enzyme treatments of recycled fiber.

Ghosh is senior R&D engineer and Hart is director, Fiber Technology and Innovation, WestRock Company, Richmond, VA, USA. Thornton is a chemical engineering student at Virginia Commons University, Richmond, VA, USA. Email Ghosh at ashok.ghosh@westrock.com .

Effect of pulper consistency on stickies size distribution

By: Mahendra Doshi, Salman Aziz, Robert De Jong, Carl Houtman

August, pp. 461 - 468 Pulper consistency affects production capacity, defibering efficiency, and particle size distribution of contaminants, and in particular, stickies and inks. The effect of pulper consistency on stickies size distribution, though important, has not been studied in detail. In this project, pressure-sensitive adhesive (PSA)-containing furnish was pulped in a laboratory at 5%, 10% and 15% consistency. Results show that 15% consistency pulp produced many more small-sized stickies compared to pulps produced at 5% and 10% consistency. This is contrary to the generally accepted hypothesis and needs further investigation. Calcium carbonate, usually present in varying proportions in many recovered paper grades, is known to have some pacifying effect on stickies. A new pacifying agent prepared from silicone release liner, called desiliconized pulp (DSP), behaves like bleached virgin hardwood kraft pulp. DSP seems to have a pacifying effect similar to that of calcium carbonate. Thus, DSP may potentially replace a small amount of bleached virgin hardwood kraft pulp, with a bonus stickies-pacifying effect.

Application: Stickies size distribution is important for paper recycling mills. The goal is to keep stickies particles large enough for easy removal by screens, cleaners, and flotation. Small-sized stickies or microstickies may be pacified by the new additive—desiliconized pulp (DSP).

Doshi is president, Doshi & Associates Inc., Appleton, WI, USA. Aziz is ex-president and founder, Integrated Paper Services Inc., Appleton, WI, USA. De Jong is president, 2 Fiber Consulting, Appleton, WI, USA. Houtman is research chemical engineer, U.S. Department of Agriculture Forest Products Laboratory, Madison, WI, USA. Email Doshi at mahen@aol.com .

Sustainability

Regulatory and sustainability initiatives lead to improved polyaminopolyamide epichlorohydrin (PAE) wet-strength resins and paper products

By: Mark T. Crisp, Richard J. Riehle

September, pp. 519 - 532 Polyaminopolyamide-epichlorohydrin (PAE) resins are the predominant commercial products used to manufacture wet-strengthened paper products for grades requiring wet-strength permanence. Since their development in the late 1950s, the first generation (G1) resins have proven to be one of the most cost-effective technologies available to provide wet strength to paper. Throughout the past three decades, regulatory directives and sustainability initiatives from various organizations have driven the development of cleaner and safer PAE resins and paper products. Early efforts in this area focused on improving worker safety and reducing the impact of PAE resins on the environment. These efforts led to the development of resins containing significantly reduced levels of 1,3-dichloro-2-propanol (1,3-DCP) and 3-monochloropropane-1,2-diol (3-MCPD), potentially carcinogenic byproducts formed during the manufacturing process of PAE resins. As the levels of these byproducts decreased, the environmental, health, and safety (EH&S) profile of PAE resins and paper products improved. Recent initiatives from major retailers are focusing on product ingredient transparency and quality, thus encouraging the development of safer product formulations while maintaining performance. PAE resin research over the past 20 years has been directed toward regulatory requirements to improve consumer safety and minimize exposure to potentially carcinogenic materials found in various paper products. One of the best known regulatory requirements is the recommendations of the German Federal Institute for Risk Assessment (BfR), which defines the levels of 1,3-DCP and 3-MCPD that can be extracted by water from various food contact

grades of paper. These criteria led to the development of third generation (G3) products that contain very low levels of 1,3-DCP (typically <10 parts per million in the as-received/delivered resin). This paper outlines the PAE resin chemical contributors to adsorbable organic halogens and 3-MCPD in paper and provides recommendations for the use of each PAE resin product generation (G1, G1.5, G2, G2.5, and G3).

Application: Paper manufacturers and their customers have key information needed for the proper choice of PAE resin to meet regulatory and sustainability initiatives.

Riehle is a Research Fellow at Solenis LLC, Wilmington, DE, USA. Crisp is a Research Fellow at Solenis Netherlands BV, Capelle aan den Ijessel, The Netherlands. Email Riehle at rjriehle@solenis.com .

Effect of pulper consistency on stickies size distribution

By: Mahendra Doshi, Salman Aziz, Robert De Jong, Carl Houtman

August, pp. 461 - 468 Pulper consistency affects production capacity, defibering efficiency, and particle size distribution of contaminants, and in particular, stickies and inks. The effect of pulper consistency on stickies size distribution, though important, has not been studied in detail. In this project, pressure-sensitive adhesive (PSA)-containing furnish was pulped in a laboratory at 5%, 10% and 15% consistency. Results show that 15% consistency pulp produced many more small-sized stickies compared to pulps produced at 5% and 10% consistency. This is contrary to the generally accepted hypothesis and needs further investigation. Calcium carbonate, usually present in varying proportions in many recovered paper grades, is known to have some pacifying effect on stickies. A new pacifying agent prepared from silicone release liner, called desiliconized pulp (DSP), behaves like bleached virgin hardwood kraft pulp. DSP seems to have a pacifying effect similar to that of calcium carbonate. Thus, DSP may potentially replace a small amount of bleached virgin hardwood kraft pulp, with a bonus stickies-pacifying effect.

Application: Stickies size distribution is important for paper recycling mills. The goal is to keep stickies particles large enough for easy removal by screens, cleaners, and flotation. Small-sized stickies or microstickies may be pacified by the new additive—desiliconized pulp (DSP).

Doshi is president, Doshi & Associates Inc., Appleton, WI, USA. Aziz is ex-president and founder, Integrated Paper Services Inc., Appleton, WI, USA. De Jong is president, 2 Fiber Consulting, Appleton, WI, USA. Houtman is research chemical engineer, U.S. Department of Agriculture Forest Products Laboratory, Madison, WI, USA. Email Doshi at mahen@aol.com .

Wastewater Treatment

Removal of phthalate from papermaking wastewater by MIL-101(Fe) in the presence of persulfate

By: Xueming Lin, Zeyu Guan, Jinquan Wan, Yongwen Ma,Yan Wang

March, pp. 181 - 186 Phthalates are found in most papermaking wastewater, as are various other pollutants. Phthalates such as diethyl phthalate (DEP) and dibutyl phthalate (DBP) are endocrine-disrupting compounds (EDCs). The objective of this research was to use metal organic frameworks (MOFs) MIL-101(Fe) as a new-style adsorbing material and persulfate (PS) activator for removing DEP and DBP from artificial aqueous model solutions. We used X-ray diffractometer, scanning electron microscope, and Fourier transform infrared spectroscopy technologies to characterize the MIL-101(Fe). More than 80% of the DEP and DBP were removed with a MIL-101(Fe)/PS system over a 5 h period when the initial concentrations of the pollutants (DEP or DBP) were around 3 ppm. MIL-101(Fe) was able to absorb the pollutants and activate persulfate, which together contributed to phthalate removal. As the amount of MIL-101 and PS was increased, the percentage of removed phthalate increased gradually. We concluded that

the MIL-101(Fe)/PS system removed phthalate effectively from papermaking wastewater.

Application: Metal organic frameworks MIL-101(Fe) could be applied to activate persulfate for phthalate removal, which would reduce the risk for exposure to EDCs from papermaking wastewater.

Lin is post-doctoral researcher, College of Natural Resources and Environment, South China Agricultural University, Guangzhou, China. Guan is research assistant, Wan is professor, Ma is professor, and Wang is associate professor, South China University of Technology, Guangzhou, China. Email Guan at guanzeyu1@126.com .

TAPPI JOURNAL
WWW.TAPPI.ORG
THE PAPER AND PACKAGING INDUSTRIES' TECHNICAL RESOURCE
JANUARY 2018 | VOL. 17 NO. 1



SLOT DIE COATING 11
Slot die coating of nanocellulose on paperboard
Vinay Kumar, Douglas W. Bousfield, and Martti Toivakka

COATING FAILURE 21
Discrete element method to predict coating failure mechanisms
Daniel H. Varney and Douglas W. Bousfield

BARRIER COATING 31
Contrasting underlying mechanisms of different barrier coating types
Bryan McCulloch, John Roper, and Kaitlin Rosen

PRINTING 43
Print quality of flexographic printed paperboard related to coating composition and structure
E. Bohlin and C. Johansson

Special Coating Content

January 2018

TABLE OF CONTENTS VOL. 16 NO. 11

5 EDITORIAL
The changing face of the coated paper industry
Steven P. Ottone

11 SLOT DIE COATING
Slot die coating of nanocellulose on paperboard
Vinay Kumar, Douglas W. Bousfield, and Martti Toivakka

21 COATING FAILURE
Discrete element method to predict coating failure mechanisms
Daniel H. Varney and Douglas W. Bousfield

31 BARRIER COATING
Contrasting underlying mechanisms of different barrier coating types
Bryan McCulloch, John Roper, and Kaitlin Rosen

43 PRINTING
Print quality of flexographic printed paperboard related to coating composition and structure
E. Bohlin and C. Johansson

»COVER CREDIT: Researchers Kumar et al. of Åbo Akademi University in Turku, Finland, have demonstrated a novel roll-to-roll coating method for nanocellulose on paperboard using slot die geometry. This modified slot die coating method could be utilized for a range of highly viscous materials, including cellulose nanofibers (p. 11).

TAPPI JOURNAL
WWW.TAPPI.ORG

Editor-in-Chief
Scott Rosencrance scott.rosencrance@kemira.com
+1 770 429-2753

Associate Editor
Brian N. Brogdon brian.brogdon@gmail.com
+1 678 581-9114

Editorial Director
Monica Shaw mshaw@tappi.org
+1 770 367-9534

PRESS Manager
Jana Jensen jjensen@tappi.org
+1 770 209-7242

Webmaster
Trina Heath theath@tappi.org
+1 770 209-7416

***TJ* EDITORIAL BOARD**

Randy Branston, BASF
randy.branston@basf.com, +1 704 819-4251

Brian N. Brogdon, FutureBridge Consulting & Training LLC
brian.brogdon@gmail.com, +1 678 581-9114

David A. Carlson, Carlson Consulting
dacarlson39@aol.com, +1 847 323-2685

Mahendra Doshi, Doshi and Associates
mahen@aol.com, +1 920 832-9101

Marc Foulger, GL&V USA Inc.
Marc.foulger@glv.com +1 315 767-2920

Peter W. Hart, WestRock
peter.hart@westrock.com, +1 409 276-3465

Carl J. Houtman, USDA Forest Products Laboratory
choutman@fs.fed.us, + 1 608 231-9445

John A. Neun, John A. Neun LLC
john.neun@gmail.com, +1 518 275-8139

Jim Niemiec, Verso Corporation
jim.niemiec@versoco.com, +1 715 422-7404

Steven P. Ottone, Omya
steven.ottone@omya.com, +1 919 641-7854

Gaurav Pranami, Imbed Biosciences
gpranami@imbedbio.com, +1 515 230-7005

Arthur Ragauskas, Oak Ridge National Laboratory
aragausk@utk.edu

Gerard J.F. Ring, University of Wisconsin—Stevens Point
gerrryring@wi-net.com, +1 715 592-3732

Scott Rosencrance, Kemira Chemicals
scott.rosencrance@kemira.com, +1 770 429-2753

Paul Wiegand, NCASI
pwiegand@ncasi.org, +1 919 941-6417

Junyong Zhu, USDA Forest Products Laboratory
jzhu@fs.fed.us, +1 608 231-9520

Join TAPPI *today!*
TAPPI JOURNAL is a free benefit of TAPPI membership, and is only available to members. To join TAPPI, to renew your TAPPI Membership, or to learn about other valuable benefits, visit www.tappi.org.

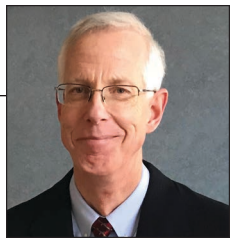
TAPPI, 15 Technology Parkway S., Suite 115, Peachtree Corners, GA 30092, publishes *TAPPI JOURNAL* monthly.

ATTENTION PROSPECTIVE AUTHORS: All papers published are subject to *TAPPI JOURNAL's* peer-review process. Not all papers accepted for review will be published. Before submitting, check complete author guidelines at http://www.tappi.org/s_tappi/doc.asp?CID=100&DID=552877.

Statements of fact and opinions expressed are those of individual authors. TAPPI assumes no responsibility for such statements and opinions. TAPPI does not intend such statements and opinions or construe them as a solicitation of or suggestion for any agreed-upon course of conduct or concerted action of any sort.

Copyright 2017 by TAPPI, all rights reserved. For copyright permission to photocopy pages from this publication for internal or personal use, contact Copyright Clearance Center, Inc. (CCC) via their website: www.copyright.com. If you have questions about the copyright permission request process, please contact CCC by phone at +1 978 750-8400. To obtain copyright permission to use excerpts from this publication in another published work, send your specific request in writing to Editor, TAPPI JOURNAL, 15 Technology Parkway S., Suite 115, Peachtree Corners, GA 30092, USA; or by fax to +1 770 446-6947. Send address changes to TAPPI, 15 Technology Parkway S., Suite 115, Peachtree Corners, GA 30092, USA; Telephone +1 770 446-1400, or FAX +1 770 446-6947. www.tappi.org

Editorial



STEVEN P. OTTONE
TAPPI Journal
Editoral Board Member

The changing face of the coated paper industry

Editor's Note: *TAPPI would like to thank Steven P. Ottone, Randy Branston, and Jim Niemiec of the* TAPPI Journal *Editorial Board, as well as Guest Editor Gregory Welsch of Trinseo, for selecting these papers from PaperCon 2017 and overseeing their peer review for this special Coating issue.*

– Monica Shaw, Editorial Director

As a key contributor to the printing and writing (P&W) papers industry, *TAPPI Journal* has a long history of publishing groundbreaking research, as with the information presented in this special coating issue. Keeping pace with this research is vital to the face of our industry, which is evolving with changes in the way a new generation of people consumes information, goods, and services. Some of the challenges include:

- *The steady drumbeat of decay in the demand for P&W papers in the face of more and more consumption of electronic information:* Printing and writing papers consumption continues to decline on a year over year basis. The 2016 drop in North America demand was 3.9% across all P&W papers, with a faster-than-expected 5.9% loss in 2017 [1].
- *The continuing transition of how goods are purchased from brick-and-mortar to online:* This transition produces ever-increasing pressures for innovative shipping solutions. Key among these pressures is in the luxury packaging arena, which is focused on creating a "wow" factor for package recipients [2].
- *The effects of changing lifestyles and demographics on how food is purchased and consumed [3-5]:* Some of the important changes are the continually increasing number of meals consumed outside the home; growth in consumption of carryout over in-restaurant; and high growth predictions for delivered foods beyond pizza.
- *Sustainability of the food value chain is an ever more important factor [6-9]. This includes:*
  - Public perception of the key points in the life cycle of packaged foods: 1) in the field; 2) in the packaging; and 3) at the end of life.
  - The facets of packaging sustainability: 1) raw materials derived from sustainable sources; 2) "right-sized" for each application; 3) reducing food waste by protecting against damage and spoilage; and 4) recoverable, non-landfill end of life.
  - Non-landfill disposal options will follow collection and processing infrastructure development. Recycling will be an immediate solution to bolster while composting infrastructure develops on the horizon.
  - Sustainability and cost top a list of 2022 projected consumer food packaging concerns (% citing each): sustainability (48), cost (41), food safety and security (31), and packaging performance (28).

Looking to the future

Moving forward, the growth for our industry looks to be in the specialty and packaging arenas. Key growth areas are projected to be stiff and flexible barrier food packaging, label, release liner, and décor papers [10].

The face of folding carton packaging is changing as more and more of it migrates from recycled boxboard to solid bleached sulfate (SBS) and coated unbleached kraft (CUK) paperboard [11]. Another change in the folding carton realm is the increasing use of microflute corrugated, a structure that allows high strength, high graphic quality, and lightweight packaging solutions.

As for the print technology of choice for many of these specialty applications, digital, particularly ink jet, appears to be the most prominent [12]. Water based flexography will also assume a bigger share of the package printing market.

Leading the industry forward

As paper coating scientists, it is our duty to lead our industry into this uncertain future with innovative coatings built on the understanding of chemistry, applications, process, and requirements. This special coating issue of *TAPPI Journal* is a step in that direction, as readers will have the opportunity to examine works on four coating topics with impacts on our industry.

In this issue, we look at concepts in modeling, coating structure effects on flexographic print quality, coating with nanocellulose, and the mechanisms of gaining performance with aqueous barrier coatings. It is our pleasure to be able to publish these fine works for your review. Read, absorb, understand, and most of all, look to the future! **TJ**

Steven P. Ottone is a member of the TAPPI Journal *Editorial Board and a technical service manager, Market Development and Innovation, for Omya Inc., Cincinnati, OH, USA.*

REFERENCES

1. PPPC, North American Printing & Writing Paper Statistics Flash Report, Pulp and Paper Products Council, Montreal, December 2016 and December 2017.
2. Gendell, A., "Brands roundtable," *Sustainable Packaging Coalition Fall Meeting*, Sustainable Packaging Coalition, Charlottesville, VA, USA, September 2017.
3. Harvey, A., "Growth opportunities in convenience retailing," *Foodservice Packaging Institute Spring Meeting*, Foodservice Packaging Institute, Falls Church, VA, USA, June 2017.
4. Kaiser, T., "Food on demand: What's driving this unstoppable trend," *Foodservice Packaging Institute Spring Meeting*, Foodservice Packaging Institute, Falls Church, June 2017.
5. Williams, G., "How millennials will shape food in 2017," *Forbes Blog*, Forbes, New York, 31 December 2016.
6. Peterson, W., "The future of paper-based food packaging," *Focal Point 2017*, Wisconsin Institute for Sustainable Technology, Stevens Point, WI, USA, October 2017.
7. Humes, A., "Packaging's positive influence on sustainability," *Focal Point 2013*, Wisconsin Institute for Sustainable Technology, Stevens Point, October 2013.
8. Nielson, "Green generation: millennials say sustainability is a shopping priority," Nielson, New York, 5 November 2015. Available [Online] http://www.nielsen.com/us/en/insights/news/2015/green-generation-millennials-say-sustainability-is-a-shopping-priority.html <24Jan2018>.
9. Morgan, L., "The changing waste stream," *Focal Point 2017*, Wisconsin Institute for Sustainable Technology, Stevens Point, October 2017
10. Moore, G., "How will the specialty paper sector fare in the next five years? A market view," *Specialty Papers Conference*, Smithers Pira/TAPPI, Leatherhead, UK/Peachtree Corners, GA, USA, September 2017
11. RISI, *Paper Packaging Monitor*, RISI, Bedford, MA, USA, November 2017.
12. Pennington, J., "Production inkjet for tomorrow," *Specialty Papers Conference*, Smithers Pira/TAPPI, Leatherhead /Peachtree Corners, September 2017.

Thanks! to our Peer Reviewers

TAPPI and the *TAPPI Journal* Editorial Board and staff would like to recognize the following peer reviewers for their input and participation in the *TJ* peer review process during 2017. The thoughtful comments and critiques provided by our peer reviewers reflect the expertise of individuals, academic institutions, and research facilities from around the world. We sincerely thank them for their time and dedication to this process, which serves to advance science within the forest products and related industries.

Larry N. Montague
President and CEO, TAPPI

TAPPI JOURNAL

Tom Allen
John Andrews
Johan Backstom
Cesar Basilio
Haoxi Ben
Yuxia Ben
Karyn Biasca
Yaman Boluk
Randy Branston
Garnet Bremner
Marc Brink
Brian N. Brogdon
Nicolas Brosse
Sabrina Burkhardt
Clay Campbell
Richard Chandra
Shih-Chin Chen
Gang Cheng
Douglas W. Coffin
John M. Considine
Emily Cranston
Dennis Crawshaw
Francides Da Silva, Jr.
Hongqi Dai
Christopher Demler
Yulin Deng
Subhash Deodhar
Anita Doepke
Lloyd Donadson
Mahendra Doshi
Monica Ek
Zach Emerson
Martin Fairbank
Yimin Fam
Guigang Fang
Neale Fetterly
Celso Foelkel
Jim Frederick
Shiyu Fu
Patrick Gane
Jerry Gargulak
Andy Garner
Paul Gatenholm
Ashok Ghosh
Roland Gong
Ronalds Gonzalez
Shisei Goto
Hongmei Gu
Marko Hakovirta
Peter W. Hart
Jun'ichi Hayashi
Danny Haynes
Ted Heindel
Gunnar Henriksson
Ryan Henry
Matti Hietaniemi
Ulrich Hirn
Feng Hong
Richard Hordyke
Carl Houtman
Martin Hubbe
Chris Hunt
Long Jiang
Sudheer Jinka
Dewey Johnson
David Jones
Margaret Joyce
D. Steven Keller
Richard Kerekes
David Kittel
Mika Korkko
Matyas Kosa
Jarmo Kouko
William Krepps
Artem Kulachenko
Matti Kurki
Jussi Lahtinen
Stan Lebow
Koon-Yang Lee
Kaichang LI
Mi Li
Mikael Lindstrom
Thomas Lindstrom
Eric Linvill
Dalton Longue, Jr.
Hongming Lou
Kai Luder
Enrique Mateos-Espejel
Sherry Mayo
Steven McDonald
Thomas McDonough
Maulik Mehta
Carson Meredith
Christian Mora
Jean Morin
Maryam Moshkelani
Humphrey Moynihan
Tom Mullen
Lee Nester
Jim Niemiec
James Olson
Al Osgood
Steve Ottone
Joel Panek
Tim Patterson
Magnus Paulsson
Joel Pawlak
Kimmo Peltonen
Hermant Pendse
Bill Pitman
Gaurav Pranami
Yunqiao Pu
Hans Putz
Scott Renneckar
Michelle Ricard
John Roper
Troy Runge
Ronald Sabo
Tsuguyuki Saito
Samuel Schabel
Adya Singh
Vinitkumar Singh
Mark Sorenson
Qining Sun
Nisrag Tambe
Takis Taousakis
Satoru Tsuchikawa
Carl Richard Ullrich
Esa Vakkilainen
Donghai Wang
Siqun Wang
Gregory Welsch
Mark Wolfinger
Chang-Yu Wu
Charles Xu
Lebo Xu
Philip Ye
Chang Geun Yoo
Zhirun Yuan
Xiao Zhang
Haifeng Zhou
Junyong Zhu



Slot die coating of nanocellulose on paperboard

VINAY KUMAR, DOUGLAS W. BOUSFIELD, AND MARTTI TOIVAKKA

ABSTRACT: Constantly growing interest in nanocellulose usage and applications is pushing the scientific community to search for suitable production and processing techniques. One example is use of nanocellulose as a barrier material in packaging applications, which requires processing of nanocellulose into films and coatings. It is challenging to coat nanocellulose suspensions using conventional pigment coating techniques due to their yield stress behavior and very high viscosity, even at low solids concentration.

This work demonstrates a novel roll-to-roll coating method of nanocellulose on paperboard using slot die geometry. The rheology of nanocellulose suspensions in pressure-driven flow is found to play a critical role in enabling their coating using the said process. In this work, the slot die is used in an unconventional manner where the shearing and metering elements are combined to aid wet film formation and application of nanocellulose suspension onto the paperboard. Barrier performance of the nanocellulose coated paperboards against air, water, heptane vapor, grease, and oils was found to be reasonable and warrants further research on the subject.

Application: The modified slot die coating method reported here could be utilized for roll-to-roll coating of web materials with a large variety of highly viscous materials such as cellulose nanofibers.

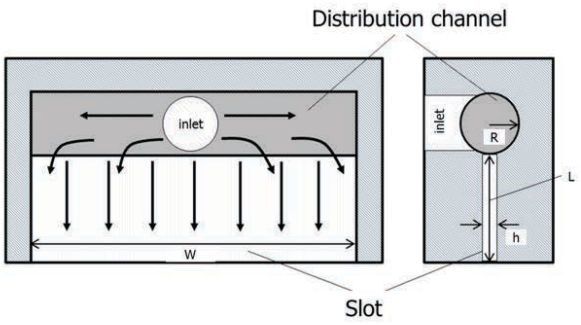
Replacement of oil-based materials with those produced from renewable material sources has attracted considerable interest in recent years. An example is the use of bio-based barriers in food packaging [1-3]. One candidate material for renewable barrier applications is nanocellulose, which has been found to possess excellent impermeability, especially against grease, oils, and oxygen. Numerous reviews [4-17], doctoral theses [18-21], and book chapters [22-25] have covered various fundamental aspects of nanocellulose manufacturing, properties, and applications. For packaging applications, large scale production of nanocellulose-based films and coatings is needed. However, most of the research related to potential future applications that has been presented so far is based on small, batch-produced freestanding films [26,27] and coatings [28-38]. Reports on continuous processing into films or coatings, which is required for large-scale and low-cost production, are few [39-41]. One such example is coating of co-ground pigment-microcellulose suspension on a wet paper web in the wet end of a paper machine, as demonstrated recently by Svending et al. [42]. For the successful operation of a coating process, the rheology of the coating material needs to be understood and controlled. Rheology studies based on boundary driven flow of nanocellulose suspensions have been very extensive and are comprehensively covered in a recent review by Nechyporchuk et al. [43] and a book chapter by Naderi and Lindström [25]. However, high deformation rate rheology of nanocellulose, which is relevant for high speed coating operations, has received very little attention [44]. The lack of work on large scale processing of nanocellulose suspensions into coatings and relevance of their high shear rheology in the same calls for more research effort on the subject.

The slot die coating technique is well known in production of, for example, magnetic tapes, pressure sensitive adhesives, photovoltaics, and functional coatings. Slot die has also been demonstrated to be useful for coating of shear-thinning suspensions [45,46]. Fundamentals of the technique can be found, for example, in the book chapter by Durst and Wagner [47]. However, slot die coating has not become a common technique for paper coating, and one potential reason is the swelling of base paper fibers, which can lead to non-uniform coatings for thin coating layers. This is less of a problem when coating with low solids content fluids, as is the case with nanocellulose suspensions. Nanocellulose suspensions have been reported as highly shear thinning in many previous studies [25,44,48,49], and their shear-thinning behavior was utilized to process them into coatings in a roll-to-roll manner in earlier work by the authors [39,40].

The objectives of the current work are to demonstrate the usefulness of slot die geometry for determining high shear rheology of nanocellulose suspensions and enabling their coating on paperboard in a roll-to-roll process. Barrier properties of the nanocellulose-coated paperboard, including oil, grease, water, and heptane vapor barriers, are reported to illustrate potential future applications.

EXPERIMENTAL

The nanocellulose produced by mechanical treatment of cellulose fibers is commonly called micro- or nanofibrillated cellulose (MFC or NFC). Other terms, such as cellulose



Newtonian Flow:

$$\Delta P_{slot} = \frac{12\eta LQ}{Wh^3}$$

$$\sigma_w = \frac{-\Delta P}{L}\frac{h}{2}$$

$$\dot{\gamma}_w = \frac{6Q}{Wh^2}$$

$$\eta = \frac{\sigma_w}{\dot{\gamma}_w} = \frac{-\Delta P}{L}\frac{Wh^3}{12Q}$$

Non-Newtonian Flow:

$$\dot{\gamma} = \left(\frac{2Q}{Wh^2}\right)\left(2+\frac{1}{n}\right)$$

$$\eta_a = \frac{\sigma_w}{\dot{\gamma}} = \frac{-\Delta P}{L}\frac{Wh^3}{4Q\left(2+\frac{1}{n}\right)}$$

Kinetic Energy Correction:

$$P_{kE} = \frac{27f\rho Q^2}{35h^2W^2}$$

Rabinowitch Correction:

$$n = \frac{d[log(\sigma_w)]}{d[log(6Q/Wh^2)]}$$

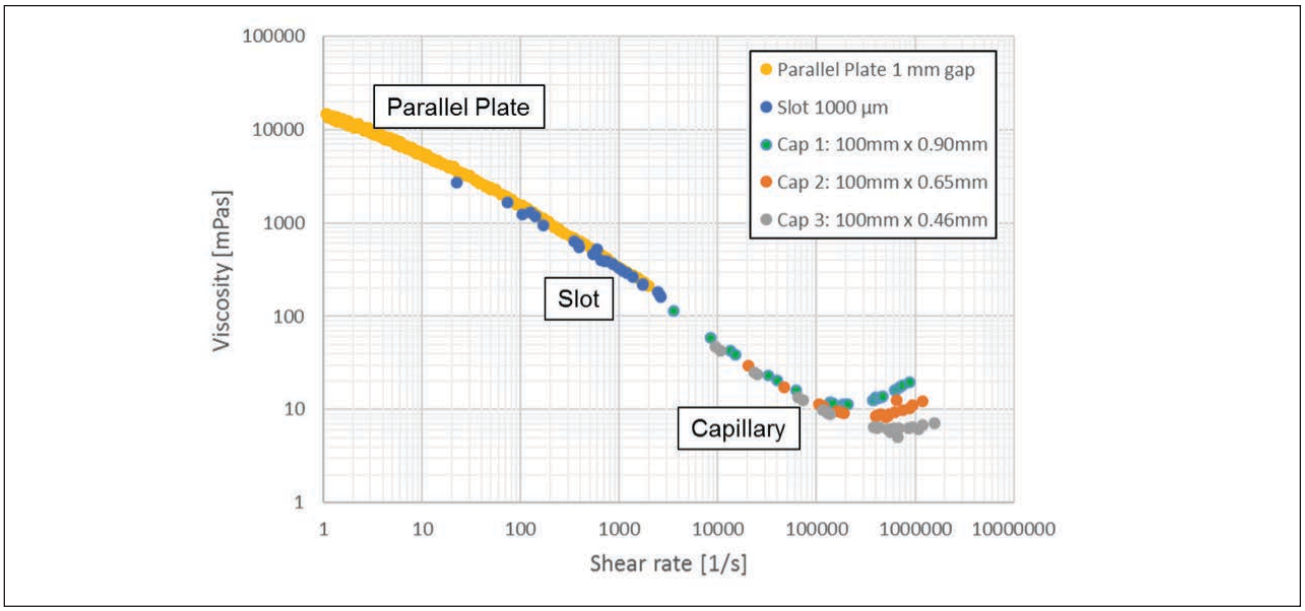
1. Slot die geometry and equations to calculate viscosity.

nanofibers (CNF) and micro-nanofibrillated cellulose (MNFC) are also in use. Turbak et al. [50] and Herrick et al. [51] were first to report production of this type of nanomaterial. The mechanical defibrillation process can be combined with chemical [52-54] and/or enzymatic [55] pretreatments to reduce the energy consumption in MFC production, and/or to provide higher fibrillation level with finer material. Nanocellulose, referred to as CNF in this work, was produced at the University of Maine's Process Development Center (Orono, ME, USA) using mechanical treatment with a refiner as described in detail in Kumar et al. [26]. CNF suspension was diluted to 3% solids for rheology determinations and coating with slot die. A JEOL JEM-1400 Plus (JEOL; Tokyo, Japan) transmission electron microscope (TEM) operating at 80 kV acceleration voltage was used to obtain electron micrographs of CNF. The suspension (0.05% w/v) was drop cast on Form-var/carbon-coated 400 MESH copper grids and negatively stained with 1% (w/v) uranyl acetate in water for 40 s before imaging.

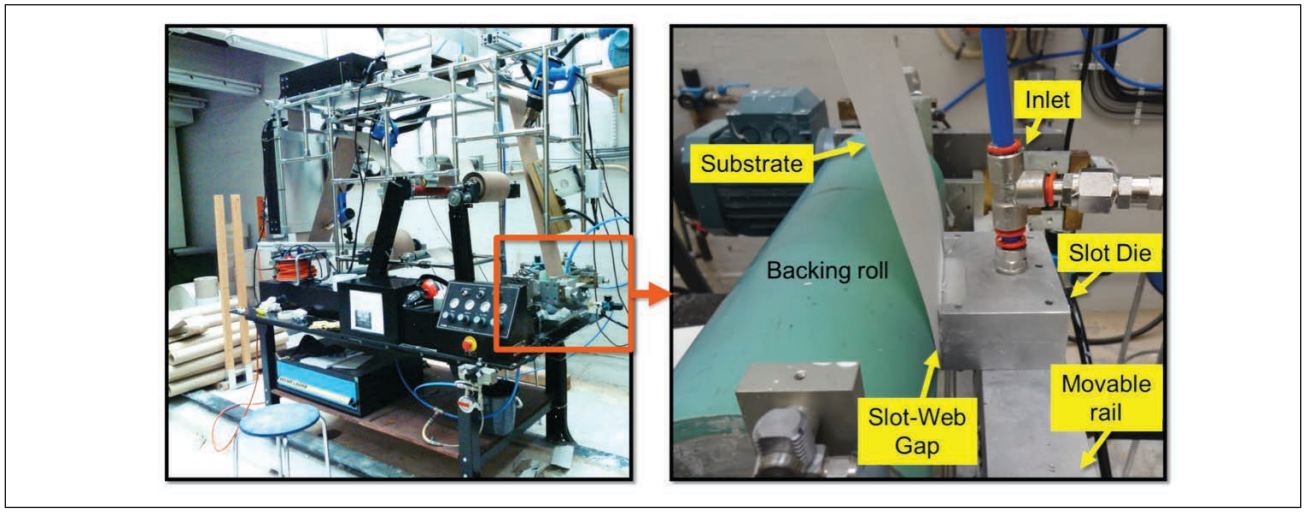
Due to experimental problems, viscosity of CNF suspensions has usually been reported only for very low shear rates, typically up to 1000 s^{-1}. Sample ejection from the measurement gap, potentially due to repeated shear, is a common problem when measuring with rotational viscometers. In order to reach higher shear rates, the current work utilizes slot viscometry with a simple, custom-built slot die, as shown in **Fig. 1**. By measuring the inlet pressure and the outflow, the viscosity of the test material can be calculated with well-known equations for narrow gap flow as detailed in Kumar et al. [44]. Corrections to account for fluid acceleration, slot end/exit effects, and non-Newtonian behavior can be applied in a manner similar to capillary viscometry. Correct operation of the slot viscometry device was verified by measuring Newtonian oils and honey water solutions of known viscosities and by comparing to flow curves for a non-Newtonian carboxymethyl cellulose (CMC) solution measured with rotational parallel plate and capillary viscometry as shown in **Fig. 2**.

Figure 3 shows the experimental setup for slot die coating of CNF on paperboard used in the current work. The custom-built slot die (slot width = 74 mm, slot length = 34 mm, slot gap = 500–1000 µm, lip lengths = 5 mm) is placed at the three o'clock position on a movable rail against the backing roll. The nanocellulose suspension is fed into the coating head from an air-pressurized vessel. For a chosen slot gap, the coating process can be controlled by changing the web speed (1–50 m/min), feeding pressure (0–10 bar), and the slot-web gap (SWG; 0–2000 µm). Utilizing the slot die geometry, a recycled fiber paperboard (grammage 178 ± 4 g/m^2 and thickness 190 ± 5 µm) was coated with CNF suspension at 2% solids concentration using 5 pph CMC (FINNFIX 4000G, CP Kelco; Atlanta, GA, USA) as an additive. All the CNF-coated paperboards were calendered with a laboratory soft nip calender, keeping the back side towards the soft roll, using a line load of 100 kN/m and temperature of 60°C. Samples were conditioned (23°C, 50% relative humidity [RH]) for at least 24 h before testing.

CNF-coated paperboards were characterized for coating coverage and barrier properties. Surface images of the coated paperboards were obtained using a Leo (Zeiss) 1530 Gemini scanning electron microscope (SEM; Carl Zeiss, Oberkochen, Germany) operating in secondary electron mode. A working distance of 11 mm and an acceleration voltage of 10 kV were used to obtain surface images at different magnifications. The specimens were sputtered with a thin layer of gold before imaging. For barrier performance of CNF-coated paperboards, water vapor transmission rate (WVTR) tests were performed according to the ASTM Standard Test Method E96/E96M-05 "Standard test methods for water vapor transmission of mate-



2. Comparison of slot, rotational, and capillary viscometry using a 2% carboxymethyl cellulose (CMC) suspension.

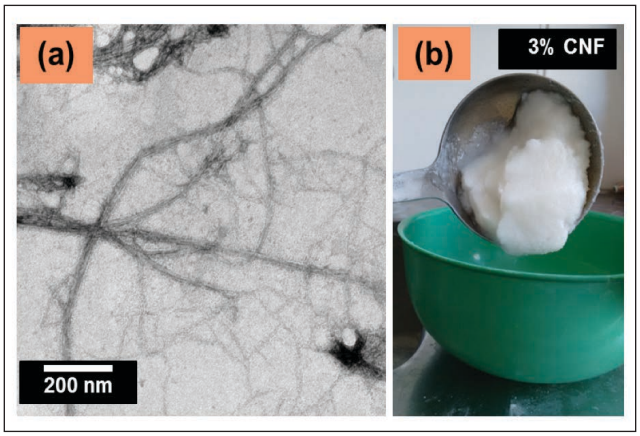


3. Experimental setup for roll-to-roll slot die coating of nanocellulose (CNF) suspension.

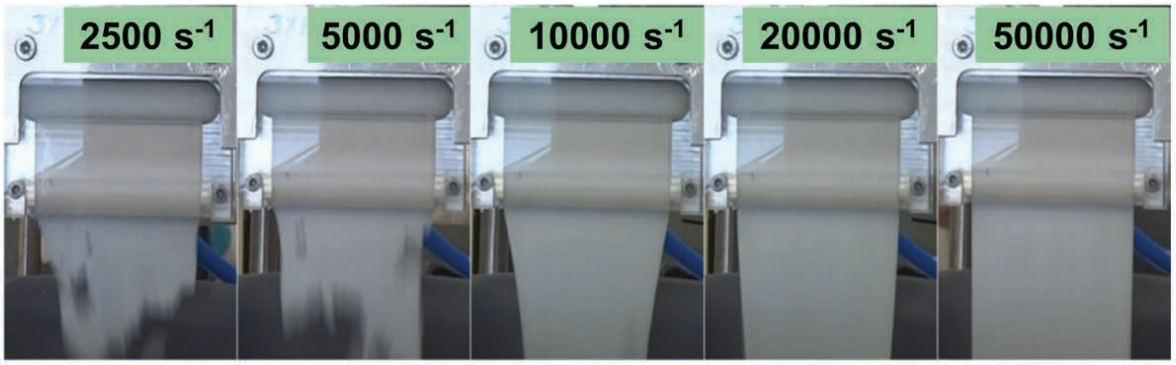
rials." Heptane vapor transmission rate (HVTR) was determined using a similar method and has been described in detail by Kumar et al. [39]. Air permeability tester SE-166 (L&W; Kista, Sweden) with a measurement range of 0.003–100 µm/(Pa•s) was used to determine the air permeance. Five parallel measurements were performed on different areas of each sample. Grease resistance was determined using the KIT Test following the TAPPI Standard Test Method T 559 "Grease resistance test for paper and paperboard."

RESULTS

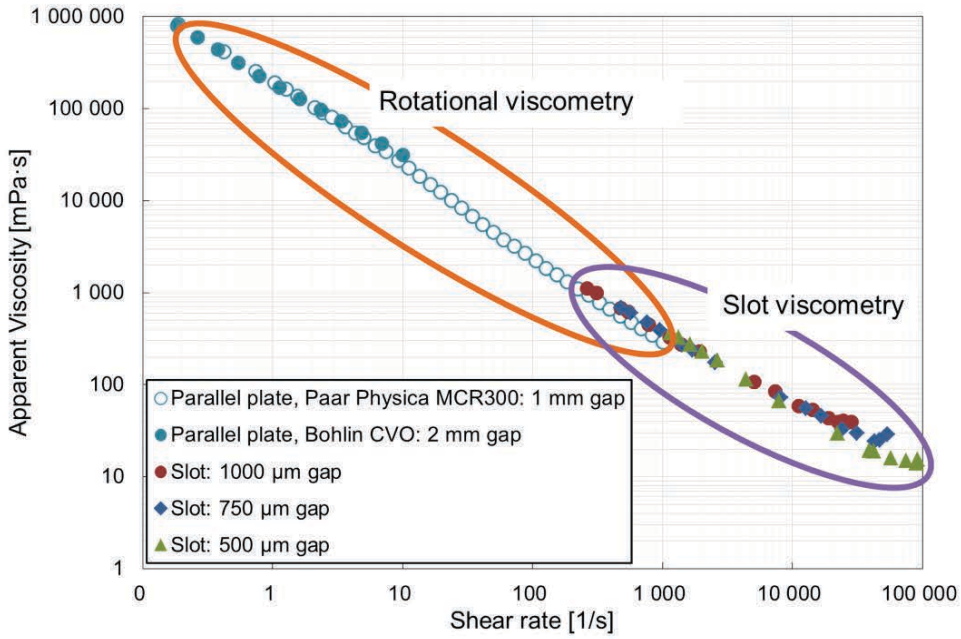
CNF used in the current work was produced without any chemical pretreatment. Therefore, the fibril diameter varies greatly, from less than 100 nm to microns, and the length can reach tens of microns, as shown in the electron micrograph in **Fig. 4a**. Much smaller sized nanocellulose can be pro-



4. (a) Transmission electron micrograph (TEM) of CNF and (b) CNF suspension at 3% solids.



5. A 3% CNF suspension flowing through the slot die at different shear rates.



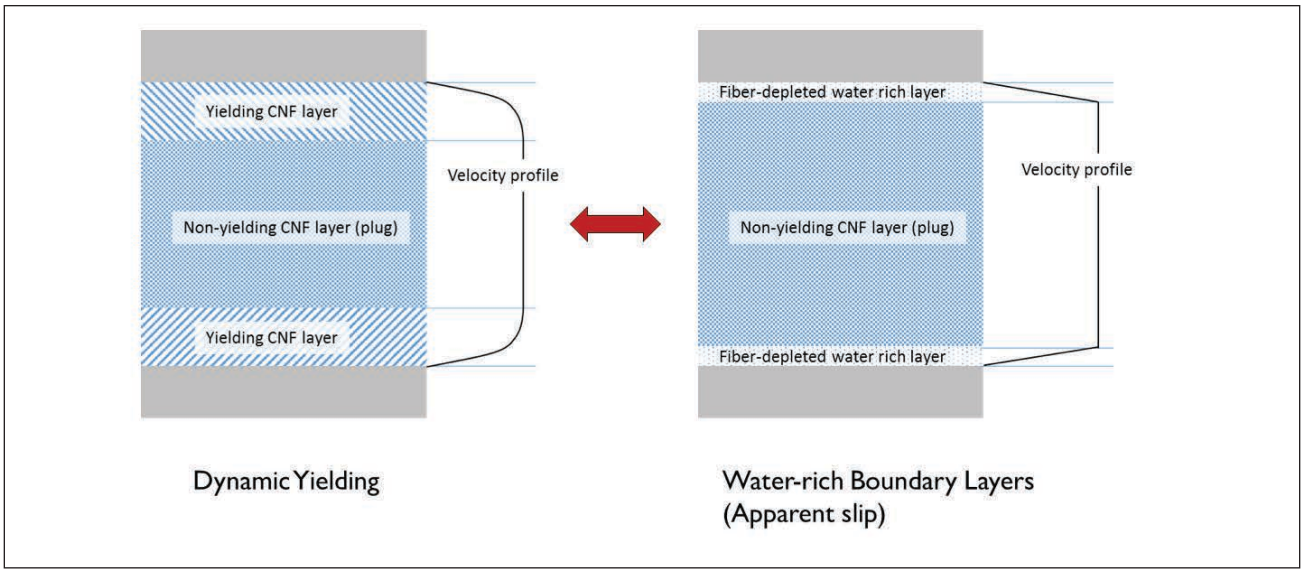
6. Apparent viscosity of 3% CNF suspension with parallel plate and slot geometries. Data reproduced from Kumar et al. [44].

duced by using, for example, TEMPO-mediated oxidation or acid hydrolysis prior to defibrillation. CNF suspensions are typically gel-like, and demonstrate very high viscosities and yield stress already at low solids concentrations, as exemplified in Fig. 4b. The high viscosity, the large amount of water to be dried, and water absorption into paper during coating challenge the CNF coating on paper.

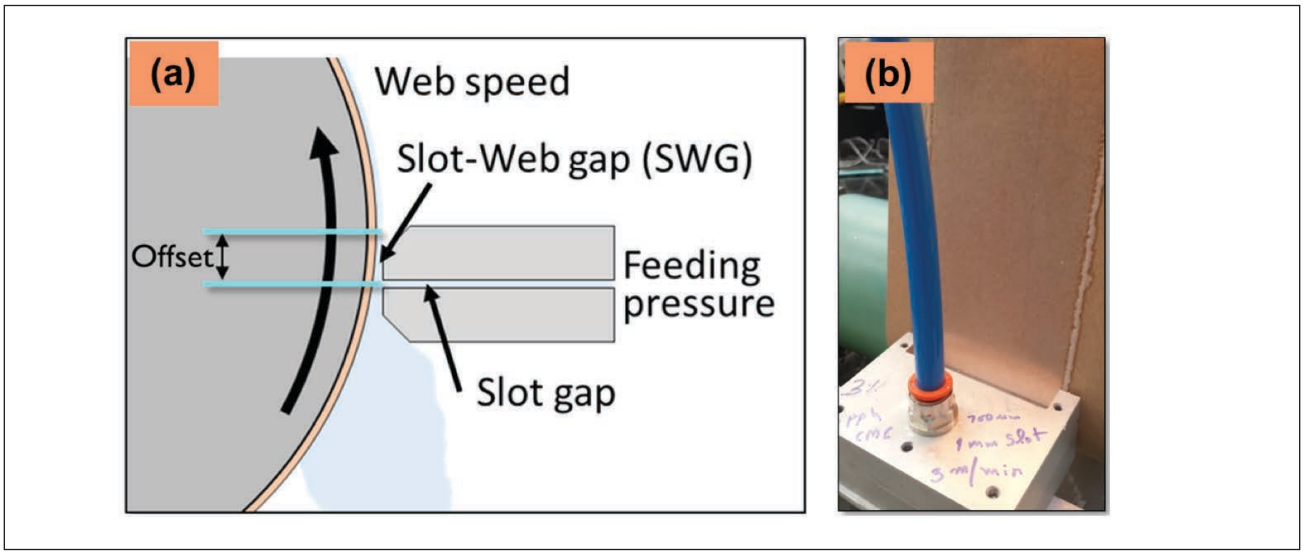
Rheology

Figure 5 shows the 3% CNF suspension at different flow rates in the slot die. One can observe the highly shear-thinning behavior as the deformation rates increase. At shear rates 50000 s^{-1} and beyond, the CNF suspension seems to flow without much resistance. With slot geometry, it is possible to reach high deformation rates, as shown in **Fig. 6**, which plots the apparent viscosity of 3% CNF suspension over six decades of shear rate. The viscosity from the boundary-driven parallel plate devices at low shear rates agrees reasonably with that from the slot geometry at high shear rates. The three different used slot gaps—500 µm, 750 µm, and 1000 µm—give the same result. Noteworthy is the extension of the apparent shear thinning to high shear rates, where the apparent viscosity approaches 10 mPas. The shear thinning can be explained by dynamic yield behavior, where a non-yielding center plug is surrounded by yielded, flowing suspension layers at the boundaries as illustrated to the left in **Fig. 7**.

An alternative explanation for the apparent shear thinning can be provided by apparent slip at the boundaries (Fig. 7, right). Optical coherence tomography measurements for Couette flow of nanocellulose by Haavisto et al. [48] provide experimental evidence for existence of fiber-depleted watery boundary layers. Assuming a non-deforming center plug sur-



7. Alternative mechanisms for apparent shear-thinning behavior in slot flow of CNF.



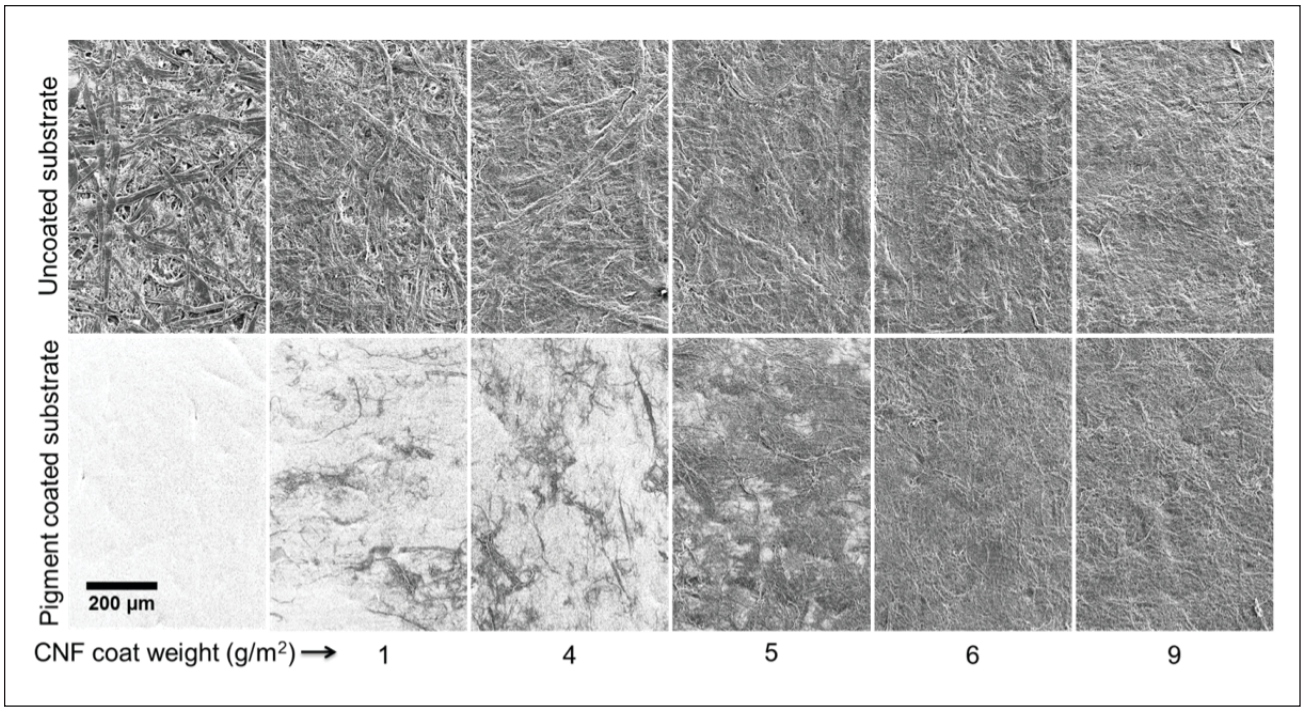
8. (a) Position of the slot die relative to the backing roll, and (b) slot die in operation.

rounded by water layers, the thickness of the water layer calculated for 3% CNF suspension in the current experiments varies from less than one micron up to 5 microns. While the current work cannot separate the two mechanisms causing the high apparent shear thinning, the low flow resistance does suggest the possibility of using slot die coating for processing of CNF suspensions into coatings and films.

Slot die coating of CNF suspension

Several process parameters, such as slot gap, SWG, feeding pressure, and web speed, affect the slot die coating process. Occasional large aggregates in the CNF material forces one to use relatively large slot gaps to avoid clogging of the slot entrance. At the same time, high flow rates through the slot are needed to produce low apparent (process) viscosity and uniform flow. Therefore, to obtain low coat weights at relatively low coater speeds (required by slow drying) the slot die has to be run in an unconventional mode in which part of the coating material is metered off.

For well-controlled metering, it was found to be beneficial to offset the slot die 6 mm below the center line of the backing roll, as shown in **Fig. 8a**. This creates a converging geometry between the substrate and the slot die lips, which enables coat weight control by changing the SWG. The split (i.e., the percentage of CNF coated on paperboard vs. being metered off) is determined by the balance between the pressure-driven extrusion flow forcing the coating both upward and downward, and the shear drag of the moving paper web pulling the coating along upwards. In the converging narrow gap geometry, the pressure-driven flow scales to the third



9. SEM images of CNF coatings with increasing coat weight on recycled fiber paperboard (top) and pigment coated paperboard (bottom).

power of the gap distance, whereas the shear drag upward is directly proportional to the inverse of the gap distance. Closing the SWG, increasing the feeding pressure, and lowering the web speed all reduce the *relative* proportion of coating transferred to the paper. The final coat weight, which depends on the web speed and the amount of coating that is not metered off, increases with increasing SWG, feeding pressure, and lowering of the web speed. The coat weight was controlled by adjusting the web speed, the CNF suspension feeding pressure, and the SWG to obtain dry CNF coat weights varying from 1 to 16 g/m². The option to control the coat weight with both the SWG and the feeding pressure was found useful, because the flow profile in the slot-paper gap seemed to influence the visual coating quality of the fibrous nanocellulose. Furthermore, CMC addition was found to improve the CNF dispersion and increase the water retention, leading to overall improvement in the final coating quality as observed earlier by Kumar et al. [39]. The quality of wet CNF film formed on the paperboard can be seen in Fig. 8b, which shows the slot die in operation.

Coat Weight, g/m²	Air Permeance, µm/Pa•s	Water Vapor Transmission Rate, g/m²/day	Heptane Vapor Transmission Rate, g/m²/day	KIT Number**
0	1.72 ± 0.0321	688 ± 43	9031 ± 417	0
1	0.3680 ± 0.0304	502 ± 9	6852 ± 315	0
4	0.0567 ± 0.0129	376 ± 9	858 ± 304	1
5	0.0159 ± 0.0029	323 ± 31	338 ± 249	4
6	0.0030*	216 ± 3	23 ± 16	8
9	0.0030	115 ± 10	0	9
11	0.0030	92 ± 3	0	10
13	0.0030	103 ± 15	0	10
16	0.0030	120 ± 12	0	10

* Detection limit of the instrument.
** Grease resistance measurement.

I. Barrier properties of the nanocellulose (CNF)-coated paperboard.

Coating coverage and barrier properties

Figure 9 shows surface SEM images of the CNF-coated paperboards with increasing coat weight. Because it is difficult to visualize the fibrous CNF coating on top of the uncoated paperboard, pigment-coated board was also used as a substrate to improve the coating coverage visualization. The SEM images suggest that full coverage is reached at coat weights higher than 5 g/m². The incomplete coverage at low coat weights is also apparent in the barrier properties shown in **Table I**. Air permeability values indicate a fully closed surface by CNF at 6 g/m². Both the high surface roughness of the substrate (PPS 7.3 μm) and the coarse CNF quality used in the current work contribute to the insufficient coverage when applying thin coatings. Once the paperboard surface is fully covered, beyond 6 g/m², the barrier properties improve considerably. At 9 g/m², the water vapor barrier reaches a constant value of approximately 100 g/m²/day, a reasonable value considering the hydrophilic nature of the CNF material. At high coat weights, the coating provides a grease barrier with KIT values of 9 or more and no detectable heptane vapor transmission. No vegetable oil penetration was detected within 4 weeks, after which the test was aborted. Similarly, no penetration of a non-polar solvent, dichlorobenzene, was found within the tested 1-week time period. The high solvent barrier suggests potential uses in paper-based electronics such as supercapacitors and batteries. Oxygen barrier was measured, but most samples did not show any oxygen barrier, probably due to pin holes in the relatively large tested areas.

CONCLUSIONS

The current work measured high shear rate viscosity of CNF suspensions utilizing slot die geometry. The results agree with those obtained with parallel plate devices and demonstrate that, in pressure-driven flow, the highly shear-thinning behavior observed with rotational instruments at low shear rates extends to high shear rates. The high apparent shear-thinning behavior can be explained by dynamic yielding or fiber-depleted water-rich boundary layers (apparent wall slip) controlling the flow. The highly shear-thinning process viscosity of CNF suspensions in slot flow enables roll-to-roll coating of these viscous, high-yield stress, gel-like suspensions on paper. Offset slot die placement enables easy metering with slot-to-paper gap control. Provided there is a full coverage of the paper by the CNF material, the barrier properties of paperboard improved considerably. The insufficient coverage issue at low coat weights could potentially be addressed by using a substrate with lower surface roughness and nanocellulosic material with smaller fiber size. Attention needs to be paid to possible pinholes in the coating. Potential solutions include use of multilayer coatings and finer grade nanocellulose. Future work should address moisture sensitivity of the CNF. The current results were obtained at 50% RH, and it is well known that at high humidity the swelling of CNF deteriorates the barrier properties.

Although this work demonstrates a successful use of slot die for coating of nanocellulose suspensions, there are still process challenges that need addressing. For example, higher concentrations of nanocellulose suspensions may lead to air entrainment and difficulties in their pumping to the slot die. Also, an even distribution of these highly viscous and high-yield stress suspensions in wide slot dies at industrial scale may become challenging. **TJ**

ACKNOWLEDGEMENTS

We acknowledge the financial support from KAUTE Foundation for the research reported in this paper. Behzad Nazari is thanked for the parallel plate rheology measurements. Alex Elfving, Rajesh Koppolu, and Aayush Kumar Jaiswal are thanked for helping with CNF coatings.

LITERATURE CITED

1. Azeredo, H.M.C., Rosa, M.F., and Mattoso, L.H.C., *Ind. Crops Prod.* 97: 664(2016).
2. Khan, A., Huq, T., Khan, R.A., et al., *Crit. Rev. Food Sci. Nutr.* 54(2): 163(2014).
3. Rastogi, V.K. and Samyn, P., *Coatings* 5(4): 887(2015).
4. Abitbol, T., Rivkin, A., Cao, Y., et al., *Curr. Opin. Biotechnol.* 39: 76(2016).
5. Brodin, F.W., Gregersen, O.W., and Syverud, K., *Nord. Pulp Pap. Res. J.* 29(1): 156(2014).
6. Dufresne, A., *Mater. Today* 16(6): 220(2013).
7. Eichhorn, S.J., Dufresne, A., Aranguren, M., et al., *J. Mater. Sci.* 45(1): 1(2010).
8. Isogai, A., Saito, T., and Fukuzumi, H., *Nanoscale* 3(1): 71(2011).
9. Isogai, A., *J. Wood Sci.* 59(6): 449(2013).
10. Klemm, D., Kramer, F., Moritz, S., et al., *Angew. Chem., Int. Ed.* 50(24): 5438(2011).
11. Lavoine, N., Desloges, I., Dufresne, A., et al., *Carbohydr. Polym.* 90(2): 735(2012).
12. Lindström, T., Naderi, A., and Wiberg, A., *J. Korea Tech. Assoc. Pulp Pap. Ind.* 47(6): 5(2015).
13. Moon, R.J., Martini, A., Nairn, J., et al., *Chem. Soc. Rev.* 40(7): 3941(2011).
14. Osong, S.H., Norgren, S., and Engstrand, P., *Cellulose* 23(1): 93(2015).
15. Plackett, D.V., Letchford, K., Jackson, J.K., et al., *Nord. Pulp Pap. Res. J.* 29(1): 105(2014).
16. Siró, I. and Plackett, D., *Cellulose* 17(3): 459(2010).
17. Hubbe, M., Ferrer, A., Tyagi, P., et al., *BioResources* 12(1): 2143(2017).
18. Dimic-Misic, K., "Micro and nanofibrillated cellulose (MNFC) as additive in complex suspensions: influence on rheology and dewatering," Ph.D. thesis, Aalto University, Helsinki, 2014.
19. Hua, K., "Nanocellulose for biomedical applications," Ph.D. thesis, Uppsala University, Uppsala, Sweden, 2015.
20. Richmond, F., "Cellulose nanofibers use in coated papers," Ph.D. thesis, University of Maine, Orono, ME, USA, 2014.

21. Rodríguez, M.H., "Preparation and characterization of nanocellulose films and coatings from industrial bio-residues," Ph.D. thesis, Luleå University of Technology, Luleå, Sweden, 2015.
22. Aspler, J., Bouchard, J., Hamad, W., et al. in *Biopolymer Nanocomposites: Processing, Properties, and Applications* (A. Dufresne, S. Thomas, and L.A. Pothen, Eds.) 1st edn., John Wiley & Sons, Hoboken, NJ, USA, 2013, pp. 461-508.
23. Bardet, R. and Bras, J. in *Handbook of Green Materials: Processing Technologies, Properties and Applications* (K. Oksman, A.P. Mathew, A. Bismarck, et al., Eds.) 1st edn., World Scientific, Hackensack, NJ, USA, 2014, pp. 207-232.
24. Habibi, Y. and Lucia, L.A. in *Polysaccharide Building Blocks: A Sustainable Approach to the Development of Renewable Biomaterials* (Y. Habibi and L.A. Lucia, Eds.) 1st edn., John Wiley & Sons, Hoboken, 2012, pp. 105-125.
25. Naderi, A. and Lindström, T. in *Cellulose and Cellulose Derivatives: Synthesis, Modification and Applications* (M.I.H. Mondal, Ed.) 1st edn., Nova Science, New York, 2015, pp. 187-202.
26. Kumar, V., Bollström, R., Yang, A., et al., *Cellulose* 21(5): 3443(2014).
27. Syverud, K. and Stenius, P., *Cellulose* 16(1): 75(2009).
28. Aulin, C., Gällstedt, M., and Lindström, T., *Cellulose* 17(3): 559(2010).
29. Beneventi, D., Chaussy, D., Curtil, D., et al., *Ind. Eng. Chem. Res.* 53(27): 10982(2014).
30. Amini, E., Azadfallah, M., Layeghi, M., et al., *Cellulose* 23(1): 1(2016).
31. Hamada, H. and Bousfield, D.W., "Nano-fibrillated cellulose as a coating agent to improve print quality on synthetic fiber sheet," *TAPPI Adv. Coat. Fundam. Symp., 11th*, TAPPI Press, Peachtree Corners, GA, USA, 2010.
32. Hamada, H., Beckvermit, J., and Bousfield, D.W., "Nanofibrillated cellulose with fine clay as a coating agent to improve print quality," *PaperCon*, TAPPI Press, Peachtree Corners, 2010.
33. Hamada, H., Tahara, K., and Bousfield, D.W., "The effects of nanofibrillated cellulose as a coating agent for screen printing," *TAPPI Adv. Coat. Fundam. Symp., 12th*, TAPPI Press, Peachtree Corners, 2012.
34. Hamada, H. and Mitsuhashi, M., *Nord. Pulp Pap. Res. J.* 31(2): 255(2016).
35. Lavoine, N., Desloges, I., Khelifi, B., et al., *J. Mater. Sci.* 49(7): 2879(2014).
36. Lavoine, N., Bras, J., and Desloges, I., *J. Appl. Polym. Sci.* 131(8): 40106(2014).
37. Song, H., Anderfors, M., Hoc, M., et al., *Nord. Pulp Pap. Res. J.* 25(4): 495(2010).
38. Bousfield, D.W., "Strength and barrier enhancement of paperboard properties with cellulose nanofibrils applied by blade coater," *Int. Conf. Nanotechnol. Renewable Mater.*, TAPPI Press, Peachtree Corners, 2017.
39. Kumar, V., Elfving, A., Koivula, H., et al., *Ind. Eng. Chem. Res.* 55(12): 3603(2016).
40. Ottesen, V., Kumar, V., Toivakka, M., et al., *Nord. Pulp Pap. Res. J.* 32(2): 179(2017).
41. Kinnunen-Raudaskoski, K., Hjelt, T., Kenttä, E., et al., *TAPPI J.* 13(7): 9(2014).
42. Svending, P., Skuse, D., and Phipps, J., "New applications for microfibrillated cellulose in and on paper and board," *PTS Pap. Board Symp.*, Papiertechnische Stiftung, Munich, Germany, 2016.
43. Nechyporchuk, O., Belgacem, M.N., and Pignon, F., *Biomacromolecules* 17(7): 2311(2016).
44. Kumar, V., Nazari, B., Bousfield, D.W., et al., *Appl. Rheol.* 26(4): 43534(2016).

ABOUT THE AUTHORS

We chose to study this topic because continuous roll-to-roll coating on paperboard can potentially enable commercialization of nanocellulosic materials. For large-scale and, therefore, low-cost production, a roll-to-roll coating is needed. However, previous work by others has been limited to small, batch processes.

The most difficult aspect of this study was finding a suitable coating technique, as well as the practical operation of it. The most interesting finding was the very low apparent viscosity of nanocellulose at high deformation rates in pressure-driven flow. Through this research, we gained a better understanding of flow properties for high-yield stress, gel-like materials, such as nanocellulose.

Mills might benefit from the information in this study by gaining a better understanding of the potential to use nanocellulose as a coated barrier. Our next step is to use other types of nanocellulose and to find end-use demonstrators.



Kumar



Toivakka



Bousfield

Kumar is doctoral researcher and Toivakka is professor at the Laboratory of Paper Coating and Converting, and Center for Functional Materials, at Åbo Akademi University, Turku, Finland. Bousfield is professor in the Department of Chemical and Biological Engineering and director of the Paper Surface Science Program at the University of Maine, Orono, ME, USA. Email Toivakka at Martti.Toivakka@abo.fi.

45. Bhamidipati, K., Didari, S., and Harris, T.A.L., *Chem. Eng. Sci.* 80: 195(2012).

46. Kim, D., Shin, H., Ko, E., et al., *Sci. Rep.* 6: 34322(2016).

47. Durst, F. and Wagner, H. in *Liquid Film Coating* (S.F. Kistler and P.M. Schweizer, Eds.) 1st edn., Springer Netherlands, Dordrecht, Netherlands, 1997, pp. 401-426.

48. Haavisto, S., Salmela, J., Jäsberg, A., et al., *TAPPI J.* 14(5): 291(2015).

49. Nazari, B., Kumar, V., Bousfield, D.W., et al., *J. Rheol.* 60(6): 1151(2016).

50. Turbak, A.F., Snyder, F.W., and Sandberg, K.R., *J. Appl. Polym. Sci.: Appl. Polym. Symp.* 37: 815(1983).

51. Herrick, F.W., Casebier, R.L., Hamilton, J.K., et al., *J. Appl. Polym. Sci.: Appl. Polym. Symp.* 37: 797(1983).

52. Saito, T., Nishiyama, Y., Putaux, J., et al., *Biomacromolecules* 7(6): 1687(2006).

53. Saito, T., Kimura, S., Nishiyama, Y., et al., *Biomacromolecules* 8(8): 2485(2007).

54. Wågberg, L., Decher, G., Norgren, M., et al., *Langmuir* 24(3): 784(2008).

55. Pääkkö, M., Ankerfors, M., Kosonen, H., et al., *Biomacromolecules* 8(6): 1934(2007).

ABOUT THIS PAPER

Cite this article as:
Kumar, V., Bousfield, D., Toivakka, M. *TAPPI J.* 17(1): 11(2018).
https://doi.org/10.32964/TJ17.01.11

DOI: https://doi.org/10.32964/TJ17.01.11

ISSN: 0734-1415

Publisher: TAPPI Press

Copyright: ©TAPPI Press 2018

About this journal

Discrete element method to predict coating failure mechanisms

DANIEL H. VARNEY AND DOUGLAS W. BOUSFIELD

ABSTRACT: The mechanical properties of coating layers are critical for post-application processes such as calendering, printing, and folding. Discrete element methods (DEM) have been used to simulate basic deformations such as tensile and compression, but have not been used as a tool to predict cracking-at-the-fold (CAF) or picking. DEM has the potential to increase our understanding of these failure mechanisms at the particle level. We propose a method to model the three-point bending of a coating layer and also the out-of-plane picking event during printing (using a z-direction scenario and an approach involving a moving force/velocity). Properties of the binder and the binder concentration are input parameters for the simulation. The model predicts the crack formation of the layer, the flexural modulus, and the maximum flexural strain during bending. The model also predicts the forces required for picking to occur. Results are compared with those of complimentary studies.

Application: Mills can use the findings of this study to better understand the mechanical properties of these coatings and to adjust coating formulations to better meet product needs.

Coated paper and board undergo various process steps after coating application which, depending on the coating mechanical strength, can negatively affect final quality. Such post-application steps include calendering, printing, and folding. The potential quality problems that can result from these processes are cracking, picking, and cracking-at-the-fold (CAF), respectively. These issues result from compression (calendering), z-direction tension (printing), and bending (folding). The proper balance of the mechanical properties of the coated substrate must be achieved to avoid such problems.

The discrete element method (DEM) and the finite element method (FEM) have been used extensively for modeling free-standing coating layers. DEM has been used for modeling coating layers under tension [1-4], under compression [5-7], and, just recently, during bending [8]. FEM has been used to model all three types of events [9-11]. Lyons and Peshave [12] used a unique approach to model the bending of coated paper. They proposed calculating coating stiffness by using a three-point bending technique in conjunction with modeling the coated paper as a multilayer construct as opposed to an I-beam. Although this work has great potential to help us understand the macroscopic behavior of these systems, that does not extend to an understanding of behavior at a pigment level.

Because the finite element method normally treats the coated paper as a composite material, it does not make the "connection" between events on the micro-scale and the responses on a macro-scale (as can the DEM). FEM can be used to develop particle-level models [13], but the computational complexity and the computing time increase significantly as the number of particles goes up.

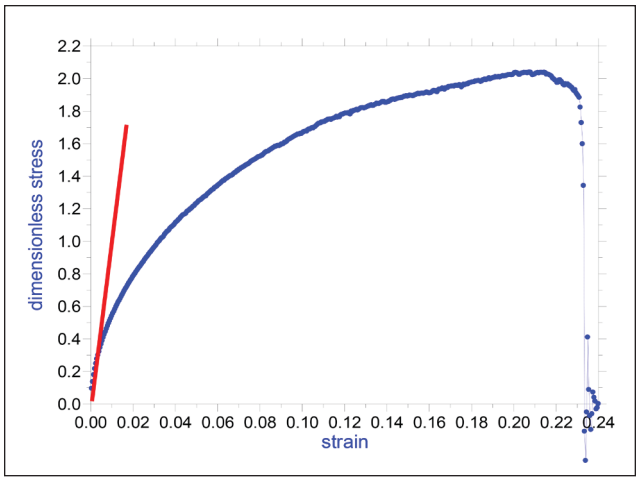
This current paper will build on the recent work of Varney and Bousfield [4,8]. The nonlinear tension model will be applied to out-of-plane (z-direction) tension, which is a modification to the in-plane tensile modeling of the first paper referenced. This effort will simulate picking. Two picking simulations will be studied: the traditional out-of-plane z-direction approach and a novel moving force/velocity situation. In addition, the same tension and compression equations outlined in the second paper will be applied to a three point bending simulation for latex and latex/starch binder systems. For both the picking and bending scenarios, the model will be compared to the experimental data of Hashemi-Najafi et al. [14].

MODEL DEVELOPMENT

As outlined in two earlier papers [4,8], a set of equations were developed to provide a better fit with the nonlinear stress-strain results seen during tension experiments [15-17]. The force equation evolved into the following:

$$F = A(1-e^{-B\varepsilon})\pi R_b^2 \quad (1)$$

where F is the tensile force between particles, A and B are parameters that depend on the pure binder, ε is the local strain between particles, and R_b is the radius of the binder bridge between particles. The bridge radius and the spacing of the particles depend on the pigment volume concentration (PVC), which is defined as the ratio of total volume of pigments to the volume of pigments plus the volume of binder. When the local strain between particles is larger than the strain-to-failure of the pure binder, the binder is assumed to fail cohesively and the force is set to zero. As confirmed with



1. Typical nonlinear response from tension simulation [4].

the data of Zhu et al. [17], the model provides a nonlinear response, as depicted in **Fig. 1**.

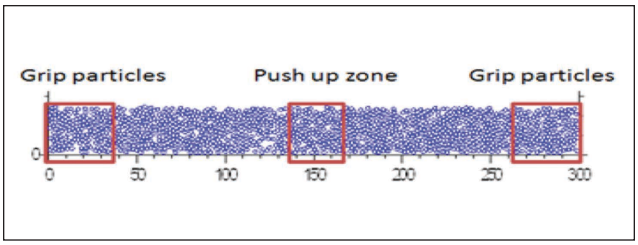
For compression, a repulsive force is calculated as:

$$F = \frac{Eh_i}{h} \varepsilon \pi R_b^{\,2} \tag{2}$$

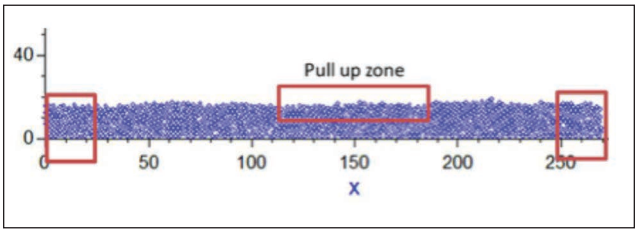
where h and h_i are the current and initial gaps between particles, respectively, and E is the elastic modulus of the binder. The ratio of initial to current gaps is needed in this expression to give a large force as the current gap goes toward zero. This large force would come from the compression of high points on the particles and is important to keep particles from overlapping. The difference between tension and compression is that, in compression, the force has to go to a large value as the gap is small to keep particles from overlapping each other while, in tension, the force follows the behavior seen in tensile tests and goes to zero when the critical strain is reached.

The bending simulation is done by holding two groups of particles in place, not allowing motion, while another group of particles is set to move upward (**Fig. 2**). This arrangement simulates a three-point bending test. Other types of deformation are also possible with the model, such as moving a group of particles at one end upward and not allowing some particles on the other end to move, as in a cantilever. Particles in the "push-up" zone are moved upward with a dimensionless velocity of 1. The grip particles can be either not allowed to move at all or not allowed to move in the vertical direction. This latter condition lets the particles in the grip zones slide and simulates a three-point bending test where the sample is supported loosely with a support structure.

The flexural force on each particle is calculated as it moves relative to its neighboring particles. If particles move away from each other, Eq. 1 is used to calculate the tension force between these particles. If particles are pushed together, then a repulsive force is applied to keep the particles from overlapping, as in Eq. 2. The net vertical force on the left and right



2. Boundary conditions for a bending simulation. Particles in push-up zone are set to move upward.



3. Picking simulation by applying an out-of-plane velocity in the pull-up zone. Either bottom layer of particles is held stationary or the side particles are not allowed to move.

grip particles are summed. This upward force should equal the net downward force on the particles that are moving upward to balance the forces. The flexural stress and strain are defined respectively as:

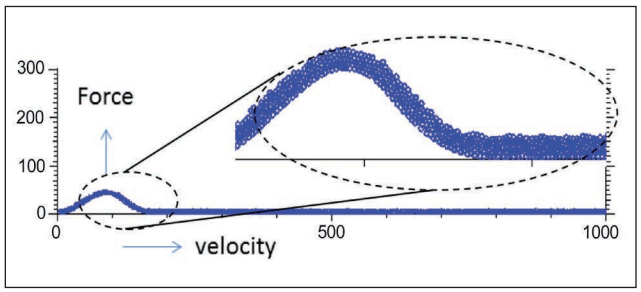
$$\sigma_f = \frac{3PL}{2bd^2} \tag{3}$$

and

$$\varepsilon_f = \frac{6Dd}{L^2} \tag{4}$$

where P is the sum of the forces on the grip particles (or the load force), L is the distance between grips, D is the displacement of the upward moving particles at the center of the sample, b is the width of the sample, and d is the thickness of the sample. The stress, σ_f, reported here is made dimensionless with the elastic modulus of the binder. The goal is to predict the bending behavior of these systems and to predict the crack propagation.

Similarly to the bending simulation, the picking model sets the velocity of the top couple of layers of particles to an upward direction in the "pull-up" zone (**Fig. 3**). Two conditions are compared for other particles: 1) the particles along the bottom of the region are assigned zero velocity or 2) the particles on the sides are not allowed to move. The first condition does not let the paper flex or bend during printing, as when printing on both sides of the sample. The second condition would represent single-sided printing, where the paper might bend slightly at the nip exit as ink tack forces pull on the paper. This condition might be similar to standard tests, such as the IGT pick test that prints an ink layer on one side



4. Conditions to simulate the exit of a printing nip. A force is applied to a region of particles and moves along the web. Upper right part of the figure is an enlargement of the region that is experiencing an upward force or velocity.

of the paper. The net force on the bottom particles predicts the force event that the coating will see as it fails.

The length scales for the simulations for bending and for picking are scaled with pigment radius. If the particles have a radius of 1 μm, then the length in Fig. 3 would represent a 270 μm × 20 μm region; the height of this region would be typical of a paper coating layer thickness. The length scale is much smaller than typical bending tests or production scales, but representative paper and board deformations of these sorts can be modeled by increasing the number of particles in the matrix. Regardless of the length scale, the results should be similar because the parameters input into the model would be the same.

Another way to simulate picking takes a long layer of particles with a force or velocity dynamically applied to various regions of this sample. **Figure 4** illustrates this condition. The force is applied to a region of the particles. The position of this applied force or velocity then moves from left to right at some known velocity. This would represent the paper moving from right to left. This scenario should be close to the condition where the tack force is applied to a small region of the paper for a short amount of time as the web exits the printing nip.

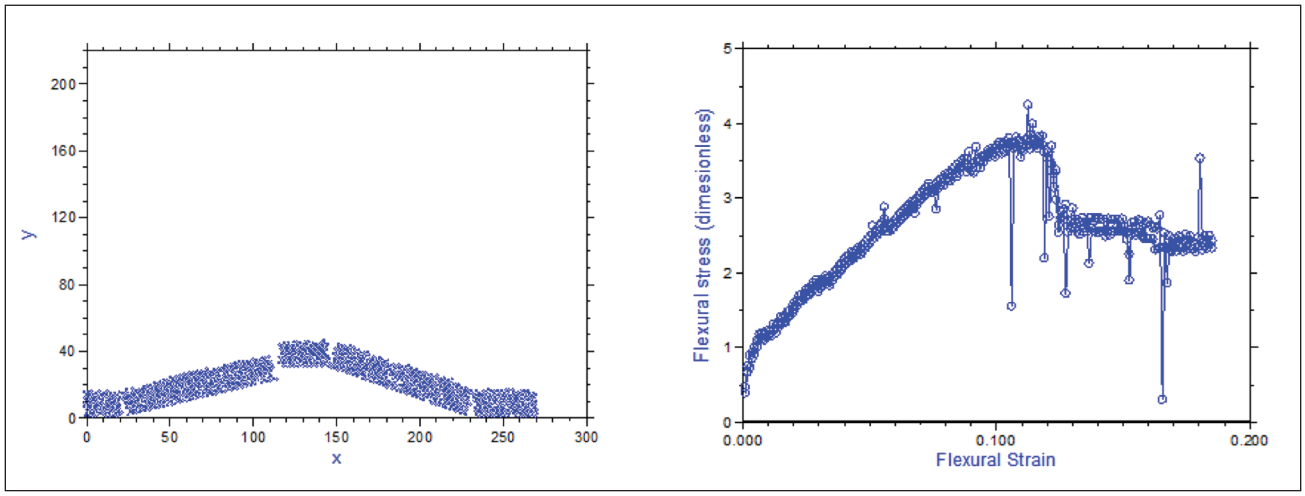
A model of this nature involves a number of assumptions. The results presented here are limited to equal-sized spheres that are confined in a mono-layer. The spheres are assumed to be rigid particles and all of the deformation is either compression or tension of the latex bridges between particles. The model in this current form neglects the rotation and shear between particles; they can be included if these types of deformation are found to be important.

Figure 5 shows the results of a bending simulation for a system near the critical pigment volume concentration for a binder package of 40% latex and 60% starch. As expected, the coating layer fractures earlier than the latex-only binder properties at around 10% strain. The flexural stress increases to a maximum and drops sharply when a crack develops. The shape of these predictions is similar to the experimental results.

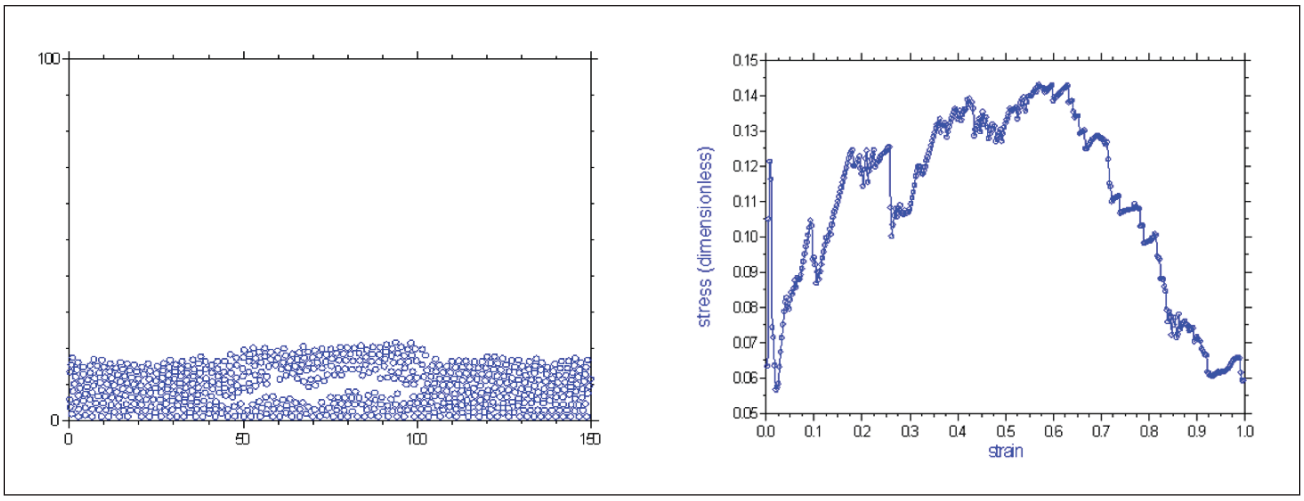
Figure 6 shows typical results for the picking simulations, where the bottom particles are held stationary. A group of particles are forced to "pick" from the coating layer. In the real situation, the top surface of a coating layer would be subject to a normal-acting tack force instead of a velocity. If the force is less than the maximum shown in Fig. 6, the particles will deform some amount but then remain as part of the coating layer.

Figure 7 shows results obtained when the picking simulation is done by allowing the bottom particles to move but by holding the ends stationary. Again, this situation should represent the case where the web is allowed to deflect a small amount during printing, as would happen with one-sided printing. Note that quite a different behavior is obtained in that the coating layer cracks through the entire depth instead of a small region being picked from the coating layer. In addition, the strain-to-failure is larger in this case because the bottom layers of the particles are not being held stationary, which allows some level of movement.

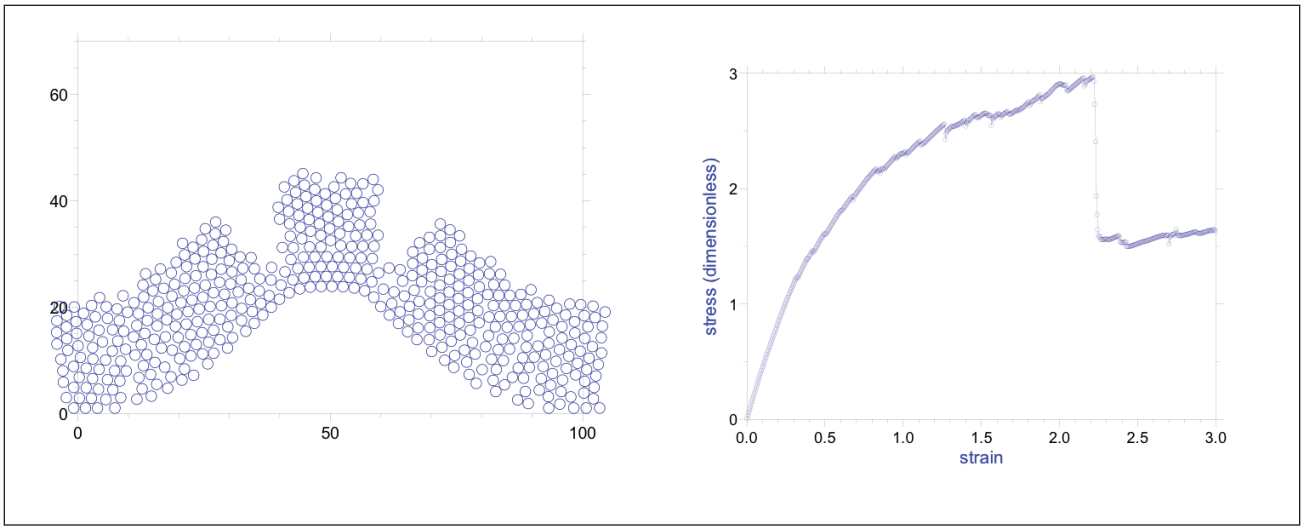
Figure 4 shows typical results of the moving force boundary conditions. For the conditions used, the coating layer de-



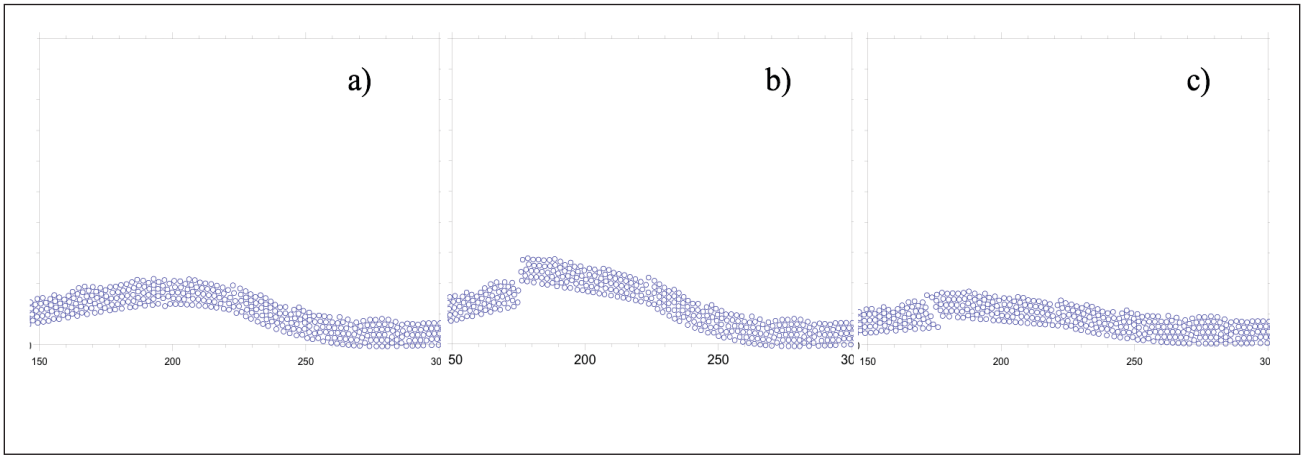
5. Typical results for 62 pigment volume concentration (PVC; 20 pph binder) for binder properties that resemble 40% latex and 60% starch. Left are the particle positions near the end of the simulation and right is the stress-strain prediction.



6. Typical results of the picking simulation for pure latex binder properties and PVC of 62 (20 pph binder). Left are the particle positions near the end of the calculation and right is the stress-strain prediction.



7. Typical picking results when the ends of the coating layer are fixed for similar binder properties as in Fig. 6. Left are the particle positions near the end of the calculation and right is the stress-strain prediction.



8. Results for binder properties that contain 80% latex and 20% starch at 20 pph binder content with a) net displacement of 10 units, b) net displacement of 12.5 units, and c) binder composition of 60% latex and 40% starch and a net displacement of 10 units.

forms and does not crack. In general, the model predicts that as the elastic modulus of the binder becomes large, the force needed to crack the layer increases. This behavior does not agree with the common experience and the companion study [14] in that as starch is added, the coating layer elastic modulus increases, but the picking velocity decreases.

Figure 8 shows another key result for the moving velocity condition. In this case, a region of the coating layer is forced to deflect a certain distance because an upward velocity boundary condition is set on a region of the coating layer. The location of this condition moves from left to right (Fig. 8). Regardless of the elastic modulus of the coating, the layer must deflect. Figure 8 shows that coating layers that contain starch are more prone to crack. Therefore, even though coating layers become stronger with the addition of starch, they also become more brittle. The cracking shown in Figs. 8b and 8c illustrate the crack formation that occurs.

COMPARISON WITH EXPERIMENTAL DATA

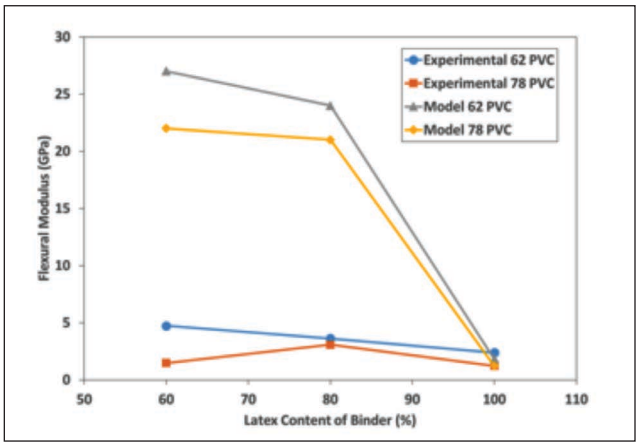
We compared the results of the model simulations with the experimental work of Hashemi-Najafi et al. [14,18]. Their efforts involved three-point bending and picking experiments. The pigment used in their coatings was a ground calcium carbonate (GCC) (60 w/w%, <2 μm) and various ratios of a latex/starch binder system (latex/starch ratios were 100/0, 80/20, and 60/40). The GCC used in this study would approximate the aspect ratio of the spheres used in the model but would not have the same particle size distribution. The properties of binder-only films were characterized by tensile tests. **Table I** lists the parameters that fit the nonlinear binder deformation, where A and B are the parameters in Eq. 1, E is the elastic modulus of the binder, and A*=A/E. As expected, as the starch level increases, the elastic modulus increases, but the strain to failure decreases. Hashemi-Najafi et al. [18] report some tensile properties of the latex-only and coating layers with latex as the binder.

Bending simulations

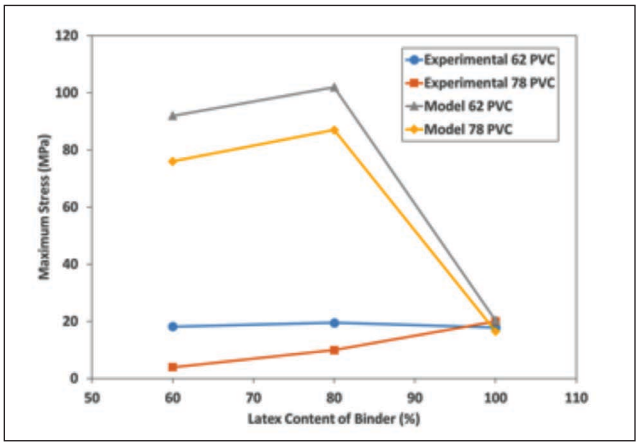
Figures 9-11 compare the model predictions with the bending experiments. For the 100% latex cases, the model predicts

Parameters	Pure Binder			
	Pure Latex	80L-20S	60L-40S	40L-60S
A	1.5	4.9	4.8	11.0
B	2	15	35	60
E, Mpa	3	73.5	168	660
STF, %	200	80	22	5
A*	0.5	0.067	0.029	0.017

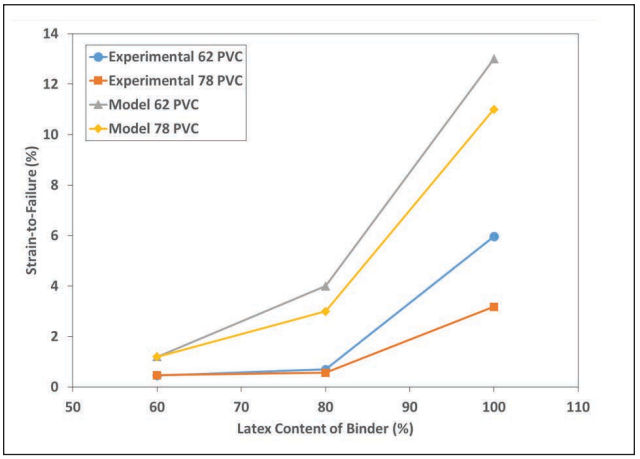
I. Properties of the pure binder films from tensile tests. Strain-to-failure (STF) is given as a percent. 80L-20S is 80% latex and 20% starch on a weight basis from companion paper.



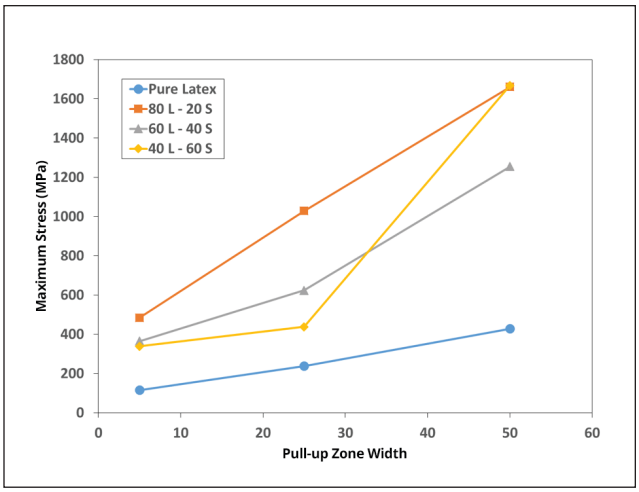
9. Flexural modulus as a function of the latex content of the binder system for two pigment volume concentrations (62 PVC corresponds to 20 parts of binder and 78 PVC corresponds to 10 parts of binder).



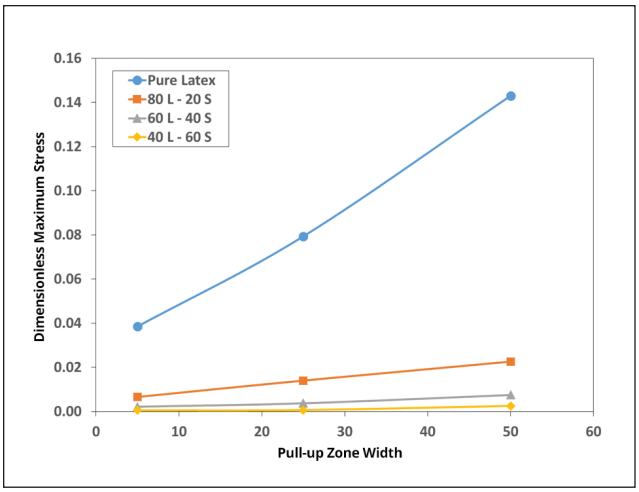
10. Maximum stress as a function of the latex content of the binder system at two pigment volume concentrations (62 PVC corresponds to 20 parts of binder and 78 PVC corresponds to 10 parts of binder).



11. Strain-at-failure as a function of the latex content of the binder for two pigment volume concentrations (62 PVC corresponds to 20 parts of binder and 78 PVC corresponds to 10 parts of binder).



12. Maximum dimensional picking stress against pull-up zone width for four binder systems. The 80L-20S is 80% latex and 20% starch on a weight basis.



13. Maximum dimensionless picking stress against pull-up zone width for four binder systems. The 80L-20S is 80% latex and 20% starch on a weight basis.

the flexural elastic modulus within 20% and maximum stress within 25%. The strain at failure is overpredicted by the model by up to 100%. This overprediction of the model can easily come from its failure to predict minor defects in the experimental samples that lead to early cracking. The model overpredicts the elastic modulus, the maximum stress, and the strain at failure for all of the starch-containing binder systems by a large amount. This result is similar to the predictions for tensile properties given by Varney and Bousfield [4,8]. The starch is a likely cause of this overprediction by:

- acting to reduce the adhesion of the binder to the pigments,
- altering the packing properties or the initial separation of the particles (induced flocculation), or
- causing a number of fine scale defects (shrinkage during drying).

The maximum stress predictions are similar to the elastic modulus.

The overprediction of the elastic modulus and the stress at failure is at first surprising, but can be expected from looking just at the experimental results. As the pure binder films are changed from all latex to 60% starch, the elastic modulus of the binder increases by a factor of 50, but the elastic modulus of the coating only increases by a factor of 1.5. Similar results are found in the data of Zhu et al. [17] where the elastic moduli, in tension, of the pure binder films increase by a factor of 100, yet the moduli of the coating layers, even below the critical pigment volume concentration (CPVC), increase by a modest amount.

As discussed by Zhu et al. [17], starch seems to be acting more like a pigment than a binder. Adjusting the PVC calculation to take this idea into account results in improved predictions, but a good match with the experiments is lacking. The strain-to-failure still overpredicts the data.

Another issue that caused the overpredictions at high starch levels might be the adhesive strength of the binder to the pigments. Starch might reduce this adhesive property. Therefore, as the binder elastic modulus increases with starch addition, the adhesive properties of the binder to the pigment might decrease. This adhesive behavior could be studied by measuring the adhesion of binder to calcium carbonate crystals. The adhesive parameter has been incorporated into the current model, but the correct value of this parameter needs to be determined from adhesive type tests.

The best predictions are obtained by assuming that the starch acts as a pigment, by using the binder properties of pure latex, and by using the strain-to-failure properties of the starch-latex binder film. This method of using the pure binder properties underpredicts the elastic modulus of the starch-containing coating by around 20%, underpredicts the maximum stress by 15%, and overpredicts the strain at failure by 80%.

Picking simulations

Figures 12 and 13 show results of the picking simulations when the bottom layer of pigments are held stationary. These simulations were done using the four binder packages from the experimental work of Hashemi-Najafi et al. [1] and three "pull-up" zone widths in the model. Changing the widths would represent different ink halftone dot sizes in an offset press, for example. The model particle size is such that the range of up-zone widths chosen in this simulation would represent a typical halftone dot size of about 20–50 μm. This set of data is for a pigment volume concentration at the critical value (CPVC).

The maximum stresses plotted in Fig. 12 were taken from the peak on the stress/strain curves, such as those in Figs. 6 and 7 (right side), and were converted from dimensionless stress to dimensional stress. Figure 12 shows how the maximum stress at failure would increase directly with the width of the pull-up zone. This plot also shows that the latex-only

binder system had the lowest stress values while the trends for the starch-containing systems generally increased in stress indirectly with starch levels. Figure 13 is similar to Fig. 12, except that the dimensionless stress is plotted instead. In this case, the latex-only binder system had the highest values while the addition of starch caused the maximum dimensionless stress to decrease. The predicted stress before the coating cracks is well above the ink tack stress values measured by Harrison and Bousfield [19]. This result indicates that these coating layers would be strong enough to withstand normal offset printing forces.

The picking results of Hashemi Najafi et al. [14] show that the IGT velocity at picking increases with the binder level and decreases with the addition of starch. The model also predicts that increasing binder level increases the force required to cause picking. However, the increase in starch content, corresponding to the amount used in the experiments, should also increase the force required to generate picking. This result is opposite to what was found in the experiments, where increasing starch decreases the pick velocity.

The ability of the coating layer to deform, even a small amount, to a bending motion explains this outcome. As seen with the moving force condition and the picking simulation that allows bending of the coating layer, the addition of starch in the binder system decreases the strain at failure even if the coating layer is stronger.

CONCLUSIONS

A discrete element model is proposed to describe the bending and picking events for a coating layer. This model has the potential to predict cracking events when the sample is bent or picking phenomena during printing. The model incorporates the mechanical properties obtained from binder-only films.

For the bending results, the model well predicts the behavior of coatings that contain only latex as the binder in terms of the elastic modulus, of the maximum stress, and of the strain at failure. For coatings that contain starch, the model overpredicts the elastic modulus and maximum stress. If starch is treated as a pigment, and the properties of latex are used for the binder, the predictions are improved.

In the picking simulations, the model predicts the correct trend in terms of binder level. The model also predicts that starch-containing coatings should be stronger than coatings that contain only latex, but the experiments show that the latex-only coatings are more resistant to picking. If a deflection or bending of the coating layer is imposed in the model, the cracking of the coating layer is found to increase with starch content. This result agrees with the experiments. **TJ**

ACKNOWLEDGEMENTS

The authors thank the University of Maine, the Paper Surface Science Program, and the program's various industry sponsors for their financial support of this project.

LITERATURE CITED

1. Alam, P., Toivakka, M., Lazarus, E., et al., "On the mechanisms of wet and dry strength of paper coatings: Part II – modelling and simulation," *PaperCon*, TAPPI Press, Peachtree Corners, GA, USA, 2012.
2. Toivakka, M. and Bousfield, D., *Adv. Coat. Fundam. Symp.*, TAPPI Press, Peachtree Corners, 2001, pp. 197-211.
3. Toivakka, M., Alam, P., Touatti, F., et al., "Molecular and microscopic level understanding of coating strength," *PaperCon*, TAPPI Press, Peachtree Corners, 2014.
4. Varney, D. and Bousfield, D., "Improved discrete element method model to predict coating layer mechanical properties," *PaperCon*, TAPPI Press, Peachtree Corners, 2016.
5. Azadi, P., Farnood, R., and Yan, N., *Comput. Mater. Sci.* 42(1): 50(2008).
6. Azadi, P., Farnood, R., and Yan, N., *Comput. Chem. Eng.* 32(12): 3084(2008).

ABOUT THE AUTHORS

We chose this topic to study because cracking at the fold and cracking of barrier layers are important topics for the industry. This study builds on our past modeling work. It connects with work by others who have studied the mechanical properties of coating layers.

The most challenging part of the study was trying to make accurate predictions for starch-containing coatings. Those predictions were not so good, and the reasons were hard to explain. This was an interesting finding, in that starch-containing coatings do not act as one would expect. However, we did discover a pattern to coating flexing properties and tension.

Mills can use the findings of this study to better understand the mechanical properties of these coatings and to adjust coating formulations to better meet product needs. Future work will focus on two-layer and three-dimensional modeling.



Varney



Bousfield

Varney is technical service manager, OMYA, Proctor, VT, USA. Bousfield is professor, Paper Surface Science Program, University of Maine, Orono, ME, USA. Email Bousfield at bousfld@maine.edu.

7. Ma, D., Carter, D., and Bousfield, D., "Prediction of coating structure change during calendering," *TAPPI Adv. Coat. Fundam. Symp.*, TAPPI Press, Peachtree Corners, 2008.
8. Varney, D. and Bousfield, D., "Discrete element method to predict bending and cracking," *Adv. Coat. Fundam. Symp.*, TAPPI Press, Peachtree Corners, 2016.
9. Alam, P., Toivakka, M., Carlsson, R., et al., *J. Compos. Mater.* 43(11): 1265(2009).
10. Barbier, C., Larsson, P-L, Ostlund, S., *Compos. Struct.* 67(4): 383(2005).
11. Salminen, P., Carlsson, R., Sandas, S., et al., "Combined modeling and experimental studies to optimize the balance between fold crack resistance and stiffness for multilayered paper coatings—Part 2: pilot coater experimental studies," *PaperCon*, TAPPI Press, Peachtree Corners, 2008.
12. Lyons, A. and Peshave, C., *TAPPI Adv. Coat. Fundam. Symp.*, TAPPI Press, Peachtree Corners, 2014, pp. 11-17.
13. Barbier, C., Rättö, P., and Hornatowska, J., "Coating models for an analysis of cracking behavior between folded paper and creased board," *TAPPI Adv. Coat. Fundam. Symp.*, TAPPI Press, Peachtree Corners, 2012.
14. Hashemi-Najafi, S.M., Tajvidi, M., and Bousfield, D.W., "Measurement of tensile and bending properties of free standing coating layers," *PaperCon*, TAPPI Press, Peachtree Corners, 2017.
15. Prall, K., Shaler, S., and LePoutre, P., *Nord. Pulp Pap. Res. J.* 15(5): 564(2000).
16. Raman, K., Bousfield, D.W., and Shaler, S.M., "Analyzing the effects of binder content on the mechanical properties of paper coatings," *TAPPI Coat. Conf.*, TAPPI Press, Peachtree Corners, 1998.
17. Zhu, Z., Salminen, P., Chen, G., et al., "Mechanical properties of pigment coating composites containing starch," *TAPPI Adv. Coat. Fundam. Symp.*, TAPPI Press, Peachtree Corners, 2014.
18. Hashemi-Najafi, S.M., Tajvidi, M., and Bousfield, D.W., "Mechanical properties of free standing coating layers: bending and tensile properties," *TAPPI Adv. Coat. Fundam. Symp.*, TAPPI Press, Peachtree Corners, 2016.
19. Gates, H. and Bousfield, D., "Pressure pulse measurements for coating and printing," *PaperCon*, TAPPI Press, Peachtree Corners, 2015.

ABOUT THIS PAPER

Cite this article as:
Bousfield, D., Varney, D. *TAPPI J.* 17(1):21(2018). https://doi.org/10.32964/TJ17.01.21

DOI: https://doi.org/10.32964/TJ17.01.21

ISSN: 0734-1415

Publisher: TAPPI Press

Copyright: ©TAPPI Press 2018

About this journal

Contrasting underlying mechanisms of different barrier coating types

BRYAN MCCULLOCH, JOHN ROPER, AND KAITLIN ROSEN

ABSTRACT: Barrier coatings are used in applications including food packaging, dry goods, and consumer products to prevent transport of different compounds either through or into paper and paperboard substrates. These coatings are useful in packaging to contain active ingredients, such as fragrances, or to protect contents from detrimental substances, such as oxygen, water, grease, or other chemicals of concern. They also are used to prevent visual changes or mechanical degradation that might occur if the paper becomes saturated. The performance and underlying mechanism depends on the barrier coating type and, in particular, on whether the barrier coating is designed to prevent diffusive or capillary transport. Estimates on the basis of fundamental transport phenomena and data from a broad screening of different barrier materials can be used to understand the limits of various approaches to construct barrier coatings. These estimates also can be used to create basic design rules for general classes of barrier coatings.

Application: Barrier coatings can be designed with unique performance profiles optimized for customer requirements.

Barrier coatings are a growing market because they are well aligned with consumer trends toward increasing demands in packaging. In general, there is interest in using paper products for packaging because of their low cost, inherent recyclability, and biodegradability. Unfortunately, paper products typically present very poor intrinsic barriers and require additional functionality to compete with barrier properties provided by plastic packaging. Many different approaches have been used, including impregnation of the paper substrate or lamination of a metal foil or plastic film to the surface of the paper. A wide range of different products exists for every class of barrier coatings, depending on the exact requirements of the application. Because of the highly fragmented, complex, and segmented barrier coatings market, there are opportunities to produce higher-performance products, lower-cost options, or custom products that fit unique customer demands.

There are many ways to divide the different applications for barrier coatings and the technologies or materials used to produce these coatings. Some of the most common barrier coating markets for paper and paperboard include products that provide barriers to water, oil and grease, water vapor, mineral oil, and various gases. While all of these barrier coatings typically try to slow transport of a material through or into the paper substrate, the targets and modes of action can be quite different. To better understand the mode of action for these diverse barrier coatings, it is important to recognize the three primary modes of transport relevant to barrier coatings. These modes are (1) capillary transport, driven by a difference in surface energy that causes liquid to wet the paper substrate; (2) diffusive transport, driven by a concentration gradient occurring by fickian diffusion; and (3) pressure-driven flow, which can occur from pressure differences within a package or by hydrostatic pressure exerted onto the coating surface.

Barrier coatings for liquids are designed differently than those for vapor or gases. An effective way of classifying barrier coatings is to look at the relevant underlying transport mechanisms because this can drive the choice of barrier coating technology. It is convenient to group barrier coatings that work against liquids by preventing capillary or wicking transport and barrier coatings against gases, which operate by decreasing the rate of diffusive transport through the substrate. The barrier coatings for water or oil are often required to prevent the product from becoming saturated by the liquid, which changes the opacity and visual appearance of the product or degrades the mechanical strength of the packaging. Typically, performance requirements associated with these applications emphasize measurement of mass change (e.g., Cobb—water saturation) or visual changes from saturation of the underlying fibers (e.g., 3M kit—oil saturation) after exposure to the liquids of interest. Alternatively, barrier coatings for gases are used to prevent the slow diffusion of molecules into or out of the packaged product. The relevant performance requirement for these products is the quantity or flux of molecules through the barrier coating, which is directly related to the shelf life of the product.

In this paper, the differences between these two fundamentally different classes of barrier coatings (gas versus liquid) will be examined and general relationships will be drawn for materials within these classes. Theoretical estimates will be made for the diffusive and capillary mass transport rates

to support these conclusions. Existing literature and experimental data will be used to calculate reasonable expectations of maximum performance and failure mechanisms for some barrier materials.

BARRIER COATINGS

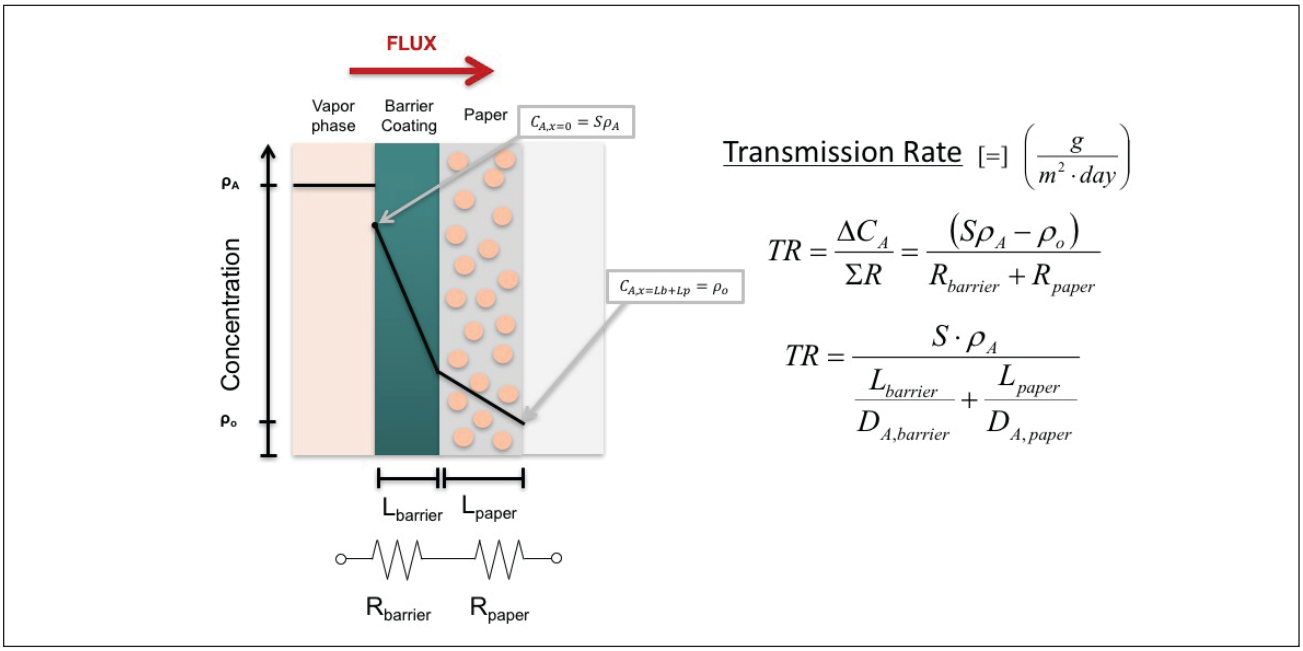
Barrier coatings against gases (slowing diffusive transport)

Barrier coatings used to prevent or slow the transmission of molecules into a package function by decreasing the flux of the target molecule through the package to provide sufficient shelf life for the product. It is impossible to completely prevent diffusion regardless of the barrier type; therefore, it is important to develop accurate performance targets for these products. Water vapor barrier coatings are the most common application for these types of barriers in paper, although oxygen barrier coatings are also widely used in plastic packaging. Often the performance targets for these barrier coatings are difficult to achieve without using relatively thick coatings or might even require metal foil for oxygen barrier performance.

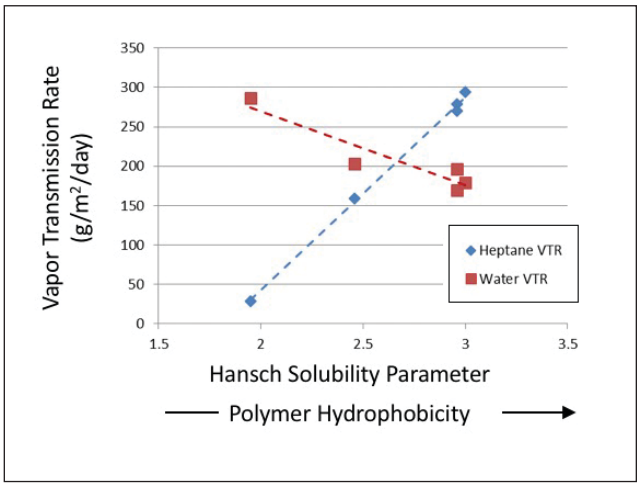
The performance of these coatings can be described by using a fickian diffusion model and related mass transport equations [1]. Typically, measured moisture transmission rates for a paper substrate containing a barrier coating are represented with units such as g/m²/day, although the units might vary for other materials. This is a useful way to express these results to a customer because if the geometry of the package (surface area) and the total tolerated mass of water is known, then the shelf life of the product can be calculated. While a useful way to express performance to the customer, it is not an inherent property of the coating itself and can make comparison of different barrier coatings difficult because many variables such as the test conditions (temperature/humidity), paper substrate porosity, paper basis weight, and barrier coat weight also have a direct impact on this metric.

As seen in **Fig. 1**, the performance of a barrier coating can be described by modeling a coating that lies between a region containing a higher level of the target molecule (outside the package) and the interior of the package that contains little to none of this molecule. Diffusion occurs because of this concentration gradient and will occur until the interior of the package is equilibrated with the exterior environment. The flux of material is directly related to the diffusion coefficient and solubility of the molecule in the barrier coating and is inversely proportional to the coating thickness, assuming that the paper represents an insignificant resistance to mass transport. For papers that are very thick or have low porosity, this assumption might not be valid; for this instance, the total experimentally measured flux is the combination of the resistances resulting from the barrier coating and the underlying paper substrate. Understanding this helps us to decouple the performance of the barrier coating material, coating thickness, and paper substrate to translate performance data between applications and better predict performance in new applications.

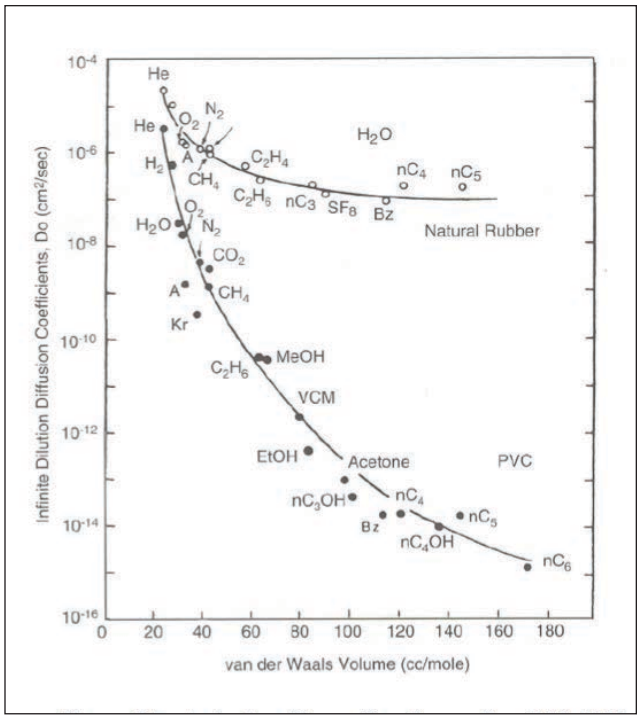
Several important factors affect the performance of this class of barrier coatings. In general, three major variables can be altered to improve performance. The simplest is to increase the thickness of the barrier coating. Transport is inversely proportional to coating thickness if the composition of the coating is held fixed. Unfortunately, the cost of a barrier coating also increases roughly linearly with coat weight so while



1. Schematic and mass transport equation for the diffusive transport of a material across a barrier coating layer and through the paper substrate. For a highly porous paper the mass transport resistance is negligible and can be eliminated from the above expression.



2. Experimentally measured vapor transmission rates for heptane and water through 10 g/m² acrylic coatings where all coating and polymer process variables such as glass transition and molecular weight are held constant while the solubility parameter is varied.



3. Experimentally determined diffusion coefficients of common small molecules in either natural rubber or poly(vinyl chloride) (PVC) plotted as a function of molecular size. Reproduced with permission from American Chemical Society [2].

this might be relatively easy to achieve, it is often impractical as a method to significantly improve barrier performance. The other two variables are more often used when designing effective solutions by choosing materials with a low diffusion coefficient and low solubility of the active component in the barrier material. Transport varies linearly with both of these variables; however, these parameters can vary by many orders of magnitude, depending on material choice.

The previous discussion of diffusion is relevant for steady-state flux of materials through a barrier coating; however, for some barrier coatings such as for mineral oil, which might be present in recycled paperboard, the customer's desire is that steady-state transport is never achieved and no significant diffusion of any mineral oil reaches the product within a package. In this case, the steady-state flux of mineral oil is not important and a parameter referred to as the breakthrough time should be considered. The breakthrough time represents the characteristic time that there is an inflection point in the flux, where the diffusion front begins to penetrate the barrier coating. The breakthrough time does not depend as strongly on the solubility of mineral oil and only strongly depends on the diffusion rate of mineral oil and the coating thickness. This has important implications to design of the product, because the polymer composition is much less critical for these systems. Rather, effort should be focused on decreasing the effective diffusion coefficient of the barrier coating (e.g., increasing glass transition, increasing crystallinity, including impermeable inorganics) or increasing the thickness of the coating.

The solubility of a material in polymeric barrier coatings is primarily controlled by the intermolecular interactions between the active component and the polymeric matrix. There are many ways to describe these interactions according to the material polarity or structure, and typically it is easily measured. In **Fig. 2**, water vapor and heptane vapor transmission rates are plotted as a function of barrier coating solubility. As the polymer phase becomes more hydrophobic we observe a decrease in water transmission rate and an increase in the heptane transmission rate. This effect can be seen when looking at the barrier coatings market where polyethylene (extremely hydrophobic) is often used for water vapor barrier coatings and poly(vinyl alcohol) (very hydrophilic) can be used as a mineral oil barrier coating. While polymer chemistry can dictate to a large degree the solubility parameter of the coating, the degree of crosslinking or crystallinity in the film can also prevent uptake and swelling. Likewise, inclusion of additives such as pigments, rheology modifiers, or wetting aids can affect the morphology of the coatings and the solubility in the final coating.

It may not always be possible to design a coating with the desired hydrophobicity/hydrophilicity to achieve suitable transport. In this case, altering the material to produce lower diffusion coefficients can have a large impact on performance. In a polymeric material, the diffusion coefficient is related to the free volume (open space between atoms) within the polymer, the molecular size of the molecule diffusing through the coating, and the degree of mobility in the polymer. **Figure 3** [2] illustrates that the diffusion coefficient can vary by several orders of magnitude by varying the size of the molecule, which means that it is easier to design barrier coatings to block large molecules than small gases. Also, rubbery polymer materials have significantly higher diffusion

coefficients (D_{AB} ~10^{-5} to 10^{-7}) than materials above their glass transition (D_{AB} ~10^{-8} to 10^{-12}) [3,4]. Halogenated polymers such as poly(vinyl chloride) and poly(vinylidene chloride) also have lower free volume compared with polyolefins; however, their use is under pressure in the market because of the sustainability of chlorinated polymers. Increasing the glass transition of a polymer can improve barrier performance by dramatically decreasing the diffusion coefficient; however, this also changes the mechanical properties of the coating and can produce a coating with more defects due to poor film formation or that is more prone to cracking. The other implication of this dependence is that the diffusion coefficient is strongly dependent on temperature such that small changes in temperature can lead to order of magnitude changes in performance [3,4]. Similarly, materials that can plasticize the barrier coating can dramatically increase the diffusion coefficient by diluting the polymer density and decreasing the polymer glass transition temperature (Tg) [3,4]. For example, hydrophilic polymers such as poly(vinyl alcohol) or functionalized starches can provide good vapor or gas barrier performance because of their high Tg and low gas solubility; however, in the presence of atmospheric moisture, their gas barrier properties can be reduced by several orders of magnitude as the coating absorbs moisture from the air.

Barrier coatings against liquids (preventing capillary transport)

Barrier coatings designed to block liquids such as water or oils are typically used to prevent the saturation of the underlying paper substrate, which can alter its appearance and decrease the packaging structural integrity. Typically, the goal of these materials is not to prevent the diffusion of small levels of molecules through the package but to prevent catastrophic failures of the packaging when contacted with liquids. This is because the life of a coffee cup or food wrapper is typically measured in minutes to hours instead of months to years. For most applications, the diffusion of the liquid is sufficiently slow to prevent saturation of the underlying substrate during the life of the paper product. Wicking or capillary forces are driven by the surface tension and liquid contact angle with the substrate and are powerful forces at nano- to micrometer-length scales. Water and oils wet untreated paper fiber and quickly spread and wick into most paper substrates. Therefore, liquid barrier coatings must be designed to prevent the capillary transport. Only in packaging that requires long shelf life would it be important to design barrier coatings to prevent diffusive transport.

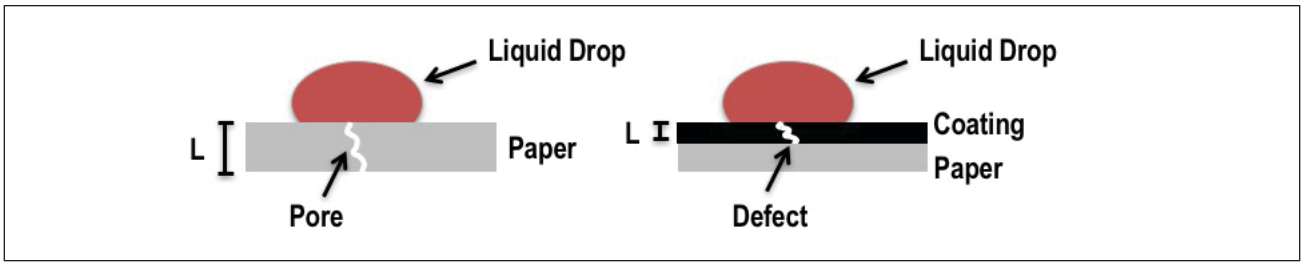
To better understand the relevant time scales for wicking versus diffusive transport, the time to failure can be estimated for capillary transport using the Washburn equation, which describes the rate at which liquid is transported through a pore [5]:

$$t = \frac{4L^2\eta}{r^2\left(P + \frac{2\gamma Cos\theta}{r}\right)}$$

where L is pore length, η is viscosity, r is pore radius, P is hydrostatic pressure, γ is liquid-air surface tension, $2\gamma\cos\theta/r$ is capillary pressure, θ is liquid-solid contact angle, $P = pgh$ is hydrostatic pressure, p is liquid density, and h is droplet height. In this equation, if the liquid does not wet the substrate, then failure will never occur unless a large hydrostatic pressure is applied to literally push the liquid through the pore. This is the mechanism by which hydrophobic sizing provides a water barrier, and fluorocarbon treatments can give oil and grease resistance. Unfortunately, most liquids (water, oils, and solvents) typically will wet untreated paper; therefore, it can be difficult to prevent wetting unless high levels of high-performance sizing agents are used. In addition,

Transport Mechanism	Diffusion	Capillary	Pressure
Breakthrough Time (s)	$t \sim \frac{L^2}{6D_{A,B}}$	$t = \frac{2L^2\eta}{\gamma r \cos\theta}$	$t = \frac{4L^2\eta}{\rho g h r^2}$
Mass Flux (g/s)	$Q = \frac{\Delta C D_{A,B} A}{L}$	$Q = \frac{\pi\rho\gamma r^3 \cos\theta}{4\eta L}$	$Q = \frac{\pi\rho^2 g h r^4}{8\eta L}$

I. Comparison of transport equations defining the approximate breakthrough time and mass transport rates for different mechanisms in barrier coatings. Diffusion is assumed to be occurring over a circular coating surface with radius (r). Capillary and pressure driven flow are assumed to be occurring within a pore of radius (r) and pore size of length (L). Pressure-driven flow also assumes a droplet of liquid is exerting a gravitational pressure which is a function of liquid density (ρ), gravitational acceleration (g), and height (h).



4. Pathways for capillary failures for sized paper (left) and paper using a barrier coating (right). For sized paper, the failure mechanism is through pores in the paper substrate that are not sufficiently treated to prevent wetting. In coated materials, failure occurs through defects, pinholes, or cracks in the coating.

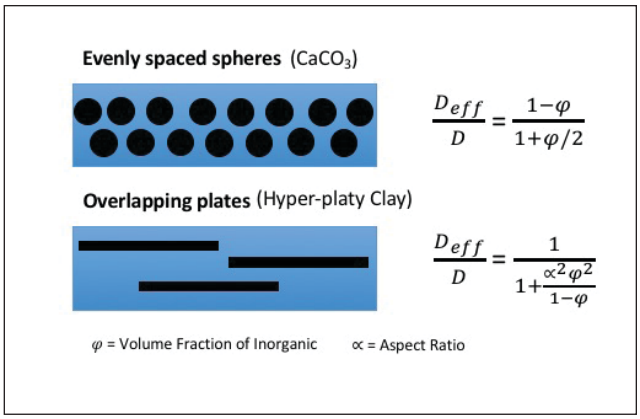
even if sufficient sizing is used to treat the fiber surface, nonuniform paper with large pores might allow liquid to travel through the paper because of a different dependence on pore radius in the Washburn equation. In instances where the paper is wetted, the length scales associated with most paper products lead to very rapid capillary transport and will result in saturation on time scales of seconds to minutes. These rates are much faster than diffusive transport and therefore indicate that failure of barrier coatings for liquids are dominated by wicking through defects or pores in the coating and paper substrate. While the Washburn equation is a good first approximation of the wetting of porous substrates, it only holds for the capillary wicking in a cylindrical pore. Non–steady state capillary transport in paper substrates with a distribution of pore sizes can be significantly more complex [6].

Using the mass transport equations in **Table I**, we can estimate the transport rates for a given barrier coating. As an example, consider a barrier coating designed to limit the transport of water (e.g., cup stock). Assume various properties of liquid water (density, surface tension, viscosity) and a polymeric barrier coating with a thickness of ~10 µm, contact angle ~60°, diffusion coefficient ~$1x10^{-7}$ cm^2/s, and water height of 1 cm. The initial concentration gradient across the barrier coating can be estimated to be the difference between the solubility of water in the polymer at the surface of the barrier coating (assumed ~1 wt%) and no water on the inner side of the barrier coating. The relative rates of transport can be compared between these various types of transport by assuming that diffusion is occurring over a surface area of 1 cm^2 and that capillary- or pressure-driven flow is occurring in a single pinhole (pore diameter = 10 µm). Using these estimates, the breakthrough time for all mechanisms are all very short (diffusion = 1.7 s, capillary = 0.001 ms, pressure = 0.2 ms), which is not surprising given the estimation of how quickly water will begin to move through a very thin coating. Estimation of the mass flux indicates better differentiation in transport rates (diffusion = 0.09 $g/cm^2/day$, capillary = 33.1 g/pore/day, pressure = 0.2 g/pore/day), which helps to show that capillary transport is extremely rapid for a material that contains small defects and is wetted by a liquid. This also indicates the importance of low defect rates in barrier coatings because the rate of transport through a single 10-µm defect can overwhelm a barrier coating when trying to design coatings to resist liquids. These fundamental mass transport equations are a simple subset of the mathematical models that define mass transport in barrier coatings. However, they have powerful implications in designing new barrier coatings materials, because they help to dictate design rules for barrier coatings depending on the application and customer requirements.

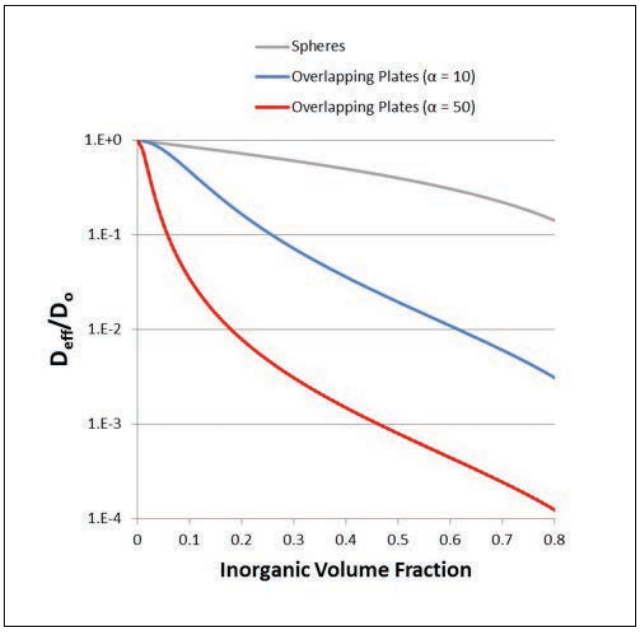
The speed at which capillary transport occurs makes these applications much more sensitive to defects in the coatings. A single pinhole, crack, or untreated area on the surface of the paper can produce rapid failures in any of the common test methods used to evaluate these materials. This means that the coating application process, coating rheology, film formation properties, base sheet uniformity, and flexibility of the coating can have a massive impact on barrier performance because any defect will result in rapid failure. To prevent this, a sizing agent can be applied to the surface of the paper or to the wet end of the papermaking process to change the liquid–paper contact angle and prevent wetting (**Fig. 4**). Capillary transport can be effectively shut down by application of surface sizing agents that increase the contact angle to >90°, which will shut down liquid flow as long as the hydrostatic pressure is not high enough to force liquid through the pore. We have not focused on the details of sizing methods in this discussion; rather, we will focus on coatings applied to the surface of the paper to prevent the liquid from reaching the underlying paper substrate.

Impact on barrier performance using hard/impermeable inorganic pigments

Barrier coatings used in the market today can be made of a single material (e.g., extruded low-density polyethylene, alkyl ketene dimer sizing) but can also be formulated with other materials to make more complex structured barrier coatings. Often, inorganic pigments such as clay, talc, or calcium carbonate are added to reduce the cost of the coating or enhance the performance by introducing relatively impermeable material. When semicrystalline polymers are used, they also contain crystals that are quite impermeable but embedded in a matrix of amorphous polymer. These structured materials can dramatically decrease the effective diffusion coefficient for barrier coatings used to block diffusive transport. Mathematical models exist, as seen in **Fig. 5**, that can be used to calculate the impact of impermeable additives on the diffusion



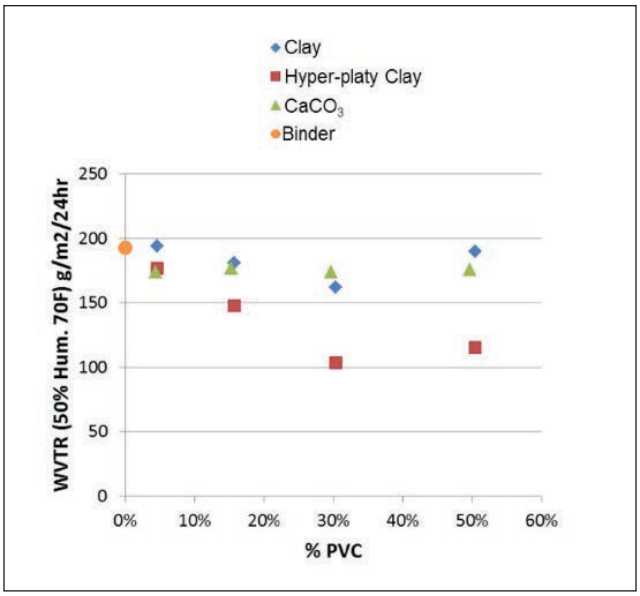
5. Mathematical relationships for the effective diffusion coefficient as a function of volume fraction and aspect ratio for either evenly distributed spheres (left) or plate-like structures that are perfectly overlapping (right). These models assume an ideal distribution, perfect orientation, and no aggregation in the coating, and therefore are a best case prediction for a real barrier coating ($CaCO_3$ = calcium carbonate).



6. The ratio of the effective diffusion coefficient (D_{eff}) to the original diffusion coefficient (D_o) in the continuous phase is plotted as a function of impermeable inorganic volume fraction for an ideal distribution of spheres or plates of different aspect ratio. These predictions are only valid up until the critical pigment concentration at which voids/pores are formed in the coating (~30%–60% volume fraction), which can dramatically increase the diffusivity.

coefficient by accounting for the increase in the tortuosity or path length that a molecule must travel through the continuous phase [7]. These models are plotted in **Fig. 6**, giving the ideal predictions for how the introduction of inorganics can affect the performance of these barrier coatings by a reduction in the effective diffusion coefficient.

Theoretically, it is possible to achieve large improvements



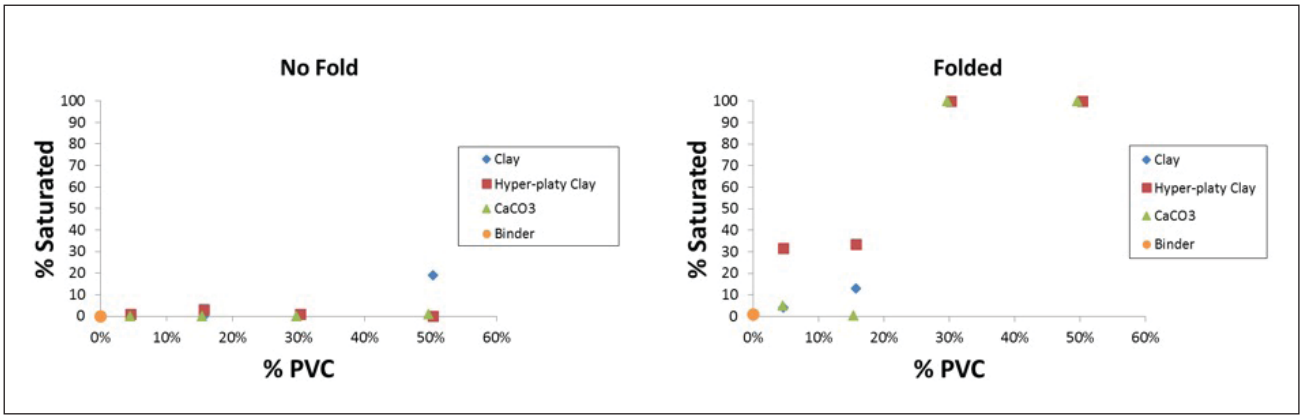
7. Water vapor transmission rate (WVTR) as a function of pigment volume concentration (PVC) at constant coating thickness in a barrier coating using an acrylic binder. Small improvements (~50% reduction) in performance are observed up until the coating reaches a critical level at which not enough binder is present to prevent voids in the coating.

in performance of several orders of magnitude by reduction of the diffusion coefficient by using very high aspect ratio pigments; however, to achieve these performance enhancements it is important to achieve perfect alignment, dispersion, and distribution of these materials in the coating. As seen in **Fig. 7**, the use of these materials often gives much less improvement in performance compared with theoretical predictions and rigorous formulation, and coating optimization is needed to achieve further improvements.

The use of inorganic additives in coatings to prevent liquid transport via capillary mechanisms does not have the same impact on performance. Because inorganics do not help with film formation and might give rise to voids in coatings when used at high levels, they increase the chance that defects can occur, which should lead to rapid failure. In addition, they are not flexible, which puts additional stress on the remaining polymer and leads to a greater chance of cracking after flexing or folding the paper coating (**Fig. 8**). While these additives have value in liquid barrier coatings by reducing cost and improving properties such as blocking or runnability, they do not generally improve the barrier performance of the coating.

CONCLUSIONS

Barrier coatings represent a large yet diverse market for specialty paper products with a wide variety of customer requirements and applications. When designing a barrier coating to meet specific customer requirements, it is important to recognize the underlying mechanism and coating chemistry to understand the maximum performance of the coating and the possible modes of failure. The performance of barrier coatings



8. Percentage of saturation of paper substrate underneath a barrier coating as a function of inorganic type and loading. A flat substrate is unaffected by inorganic volume fraction content until high levels are reached (left). The barrier performance is dramatically decreased after folding the coating, because introduction of inorganics leads to cracking of the coating (right).

that prevent diffusive transport is inherently related to the diffusion coefficient and solubility of the target molecule in the coating, as well as the coating thickness. Dramatic improvements are possible by optimization of the polymer chemistry, and theoretically large improvements can also be achieved through formulation with impermeable inorganic pigments. Barrier coatings that are used against liquids should be thought of differently because they are primarily focused on preventing wicking, which makes them significantly more sensitive to defects. Creation of a uniform film across the surface of a paper substrate is essential for liquid barrier coatings, and prevention of defects through adjustment of coating application and rheology is critical in producing an effective barrier. By understanding the potential performance and limits of these technologies, new barrier coatings with unique performance profiles optimized for customer requirements can be brought to market. **TJ**

LITERATURE CITED

1. Bird, R.B., Stewart, W.E., and Lightfoot, E.N., *Transport Phenomena*, John Wiley & Sons, Hoboken, NJ, USA, 1960.
2. Chern, R.T., Koros, W.J., Hopfenberg, H.B., et al., *ACS Symp. Ser., Vol. 269*, 1985, Chap. 2.
3. Duda, J.L., Vrentas, J.S., Ju, S.T., et al., *AIChE J.* 28(2): 279(1982).
4. Vrentas, J.S. and Vrentas, C.M., *Macromolecules* 27(17): 4684(1994).
5. Washburn, E.W., *Phys. Rev.* 17(3): 273(1921).
6. Schoelkopf, J., Gane, P.A.C., and Ridgway, C.J., *Nord. Pulp Pap. Res. J.* 15(5): 422(2000).
7. Cussler, E.L., *Diffusion: Mass Transfer in Fluid Systems*, Cambridge University Press, Cambridge, UK, 2009.



McCulloch



Roper



Rosen

ABOUT THIS PAPER

Cite this article as: McCulloch, B., Roper, J., Rosen, K. *TAPPI J.* 17(1):31(2018). https://doi.org/10.32964/TJ17.01.31

DOI: https://doi.org/10.32964/TJ17.01.31

ISSN: 0734-1415

Publisher: TAPPI Press

Copyright: ©TAPPI Press 2018

About this journal

ABOUT THE AUTHORS

New barrier coatings are an important need for the industry. This work supports our efforts to develop new barrier coating materials for the paper and paperboard market.

Research in this area continues to provide insights to better develop and test new materials. We have found that, in many instances, improving application methods or optimization of the underlying paper substrate for barrier coatings is as important as choosing the correct barrier coating material. This requires time, commitment, and collaboration between customers and suppliers to be successful. Moving forward to develop lower cost, higher performance or more sustainable barrier coatings technologies will require an understanding of how all of these components work together.

Work is still needed to improve materials that are used today and to test theoretical conclusions and predictions that have been made.

McCulloch is an associate research scientist, Roper is a fellow, and Rosen is a senior chemist at Dow Chemical Company, Collegeville, PA, USA. Email McCulloch at BMcCulloch@dow.com.

Print quality of flexographic printed paperboard related to coating composition and structure

E. BOHLIN AND C. JOHANSSON

ABSTRACT: Ink transfer and setting influence the achievable print quality and visual appearance. The pressure in the printing nip and the porosity of the substrate regulate the amount of ink that penetrates into a porous coating structure. The purpose of this study was to understand how print quality aspects could be related to ink penetration of water-based flexographic ink into coatings of differently engineered structures: calcium carbonate (GCC) of various particle size distribution (PSD), coatings with different amounts of latex binder, and coatings with various blends of GCC and kaolin.

Calcium carbonate with broad pigment PSD resulted in a lower print density compared to coatings of narrowly distributed particle sizes. Coatings of larger pore volume and greater dominating pore radius showed a higher amount of z-directional ink penetration. A high ratio of uncovered areas (UCA) could be detected for samples with high amount of latex. However, increased printing force eliminated these artefacts.

Increased printing force increased the print density to a higher degree than did a reduced ink viscosity for coatings with pure GCC. For coating layers containing both GCC and kaolin clay, decreased ink viscosity had a stronger impact on the print density than increased printing force. Print density was also affected by ink penetration, suggesting that the optical response is sensitive to the ink-substrate interaction layer. The result presented in this work also suggests that the print gloss decreases with increased amount of penetrated ink due to a higher rate of ink vehicle removal.

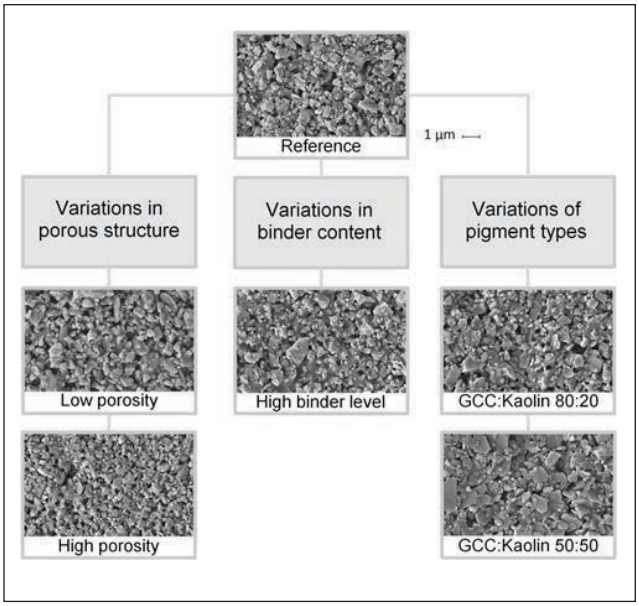
Application: By fine-tuning the coating composition and structure and by a proper selection of printing parameters, it was demonstrated that print quality defects can be addressed by fundamental studies of ink transfer and subsequent ink setting. The detailed understanding of mechanisms of ink-substrate interactions is a requirement for maintaining competitiveness in the packaging industry based on renewable materials.

Competitiveness in the packaging industry increases the demands on end-user requirements and sustainability of the printing process. Coating is widely utilized in the paper industry to improve optical properties and printability. Even though smoothness, gloss, and printability improve after coating, the relatively rough base substrates cause local coating thickness variations, with subsequent gloss variations, at a sub-millimeter scale [1-5]. Calendering causes reduction of pore volume and average pore size [6]. Due to the thickness variations of the coating layer, variations in porosity can occur with low porosity regions, or closed areas, developing as a result of the consolidation and compression processes [7]. Such closed areas are often located in low coat weight regions, caused by the unevenness of the paper substrate [8].

The major constituent of a coating color is the pigment. Calcium carbonate, kaolin clay, talc, or a mixture of these are the most commonly used pigments. Commercial coating pigments are available in a wide range of particle sizes, particle shapes and particle size distributions. By mixing different pigments, coating layers with broad variations in porosity, structure and surface properties can be created.

High gloss of printed areas is often desired to give aesthetically attractive images. Print gloss is related to the rate of ink vehicle removal and the rate of ink levelling before it sets on the surface. Both the coating pore diameter and the pore density of the coating are factors that strongly influence the ink setting rate [9-12]. Smaller pores and higher pore density increase the ink setting capacity in case of a capillary driven process.

The amount of latex binder used in the coating recipe and the fraction of latex that eventually ends up on the surface affect the coating layer structure and porosity. This effect has been explored in several studies where both the appearance of the surface and distribution of the latex particles have been investigated [13-16]. Olsson et al. [17] showed how the dot gain and mottling were influenced by coating structure and ink viscosity. By means of changes in viscosity, it was demonstrated that the influence of coating structure variations could be overridden, allowing for local variations in ink setting. Barros et al. [18,19] studied the influence of topography on the occurrence of uncovered areas (UCA) and missing dots in



1. Overview of investigated coating structures, including scanning electron microscope (SEM) micrographs (top images).

flexographic printing on linerboard and showed that the depth and opening size of impressions were important factors for the UCA frequency.

Upon ink setting, a certain amount of ink penetration also takes place. Due to capillary forces and mechanical forces in the printing nip, ink pigments move downwards into the substrate together with the ink vehicle and form a mixed layer of coating material and ink pigment. A higher surface porosity often results in a faster ink setting, thus leading to a greater ink penetration in the z-direction and lower print gloss [20,21].

Recently, Kim et al. [22] studied ink transfer of functional nanoparticle inks by means of engineered nanoporous microstructures ("stamps") to form ultrathin printing layers, a technology mainly developed for fabrication of printed electronic devices. As in conventional flexographic printing, the contact pressure between the nanoporous stamp and the substrate is crucial to form a uniform printing layer without loss of printed features or damage of the application unit.

Numerous publications concerning ink transfer and ink setting of oil-based or solvent-based offset and inkjet inks can be found in the literature [9,11,20], whereas rather few articles deal with this topic when it comes to water-based flexographic ink. This paper is thus an attempt to provide a broader picture about mechanisms controlling ink-substrate interactions in flexographic printing by comparing the findings in our previously published articles [23-25].

Print quality aspects related to ink penetration of water-based flexographic ink into pilot coated paperboard with variations in porosity and surface structure was the objective of this study. As a reference coating, a standard GCC-based coating color was prepared. Variation in porous structure was achieved by using calcium carbonate pigments of different particle size distribution (PSD), thus rendering coating layers with either low or high porosity (**Fig. 1**), which were further treated by calendering. Impact of binder content was studied by varying the fed amounts of styrene-butadiene latex, medium level (reference coating) or high level: whereas, effects of pigment types were investigated from blends of calcium carbonate and kaolin clay.

These pilot-coated paperboard structures comprising a palette of varying surface porosity, surface roughness, and surface energy were then further printed in a laboratory flexographic printer, with ink viscosity and printing force as variables. The ink penetration was determined by visual evaluation of microscopic cross-sectional images and the print quality was measured as print density, fraction of uncovered areas, and print gloss. The print quality was strongly affected by the ink-substrate interactions, especially to the ink penetration in the z-direction. By fine-tuning the coating composition and structure and by a proper selection of printing parameters, it was demonstrated that problems with print quality defects can be overcome.

MATERIALS AND METHODS

Three-ply cartonboard (Duplex) with a basis weight of 179 g/m^2 with a core of unbleached sulfate pulp sandwiched between a bleached top layer and an unbleached bottom layer (supplied by BillerudKorsnäs AB; Frövi, Sweden) was used as the substrate for coating. The cartonboard was precoated with a 95/5 blend of calcium carbonate (GCC)/kaolin pigment at a coat weight of 11 g/m^2 using a stiff ceramic blade. The coating was performed on the pilot machine at BillerudKorsnäs AB in Frövi, Sweden, at a speed of 500 m/min using a bent ceramic blade held at a blade angle of 19°. Calendering of GCC-based coatings with varying PSD was performed online in a soft nip with line load of 100 kN/m using a rubber roll of hardness 65°Shore D and a steel roll held at a temperature of 100°C.

For the reference coating color, a standard grade GCC (Hydrocarb 90, Omya AB; Malmö, Sweden) was used. The latex used in all colors was a styrene-butadiene latex (Eka Polymer Latex Oy; Oulu, Finland) with Tg 24°C and particle diameter 120 nm. The thickener Sterocoll FD (BASF Paper Chemicals; Ludwigshafen, Germany) was added to all colors at 0.3 parts dry per hundred parts of pigment.

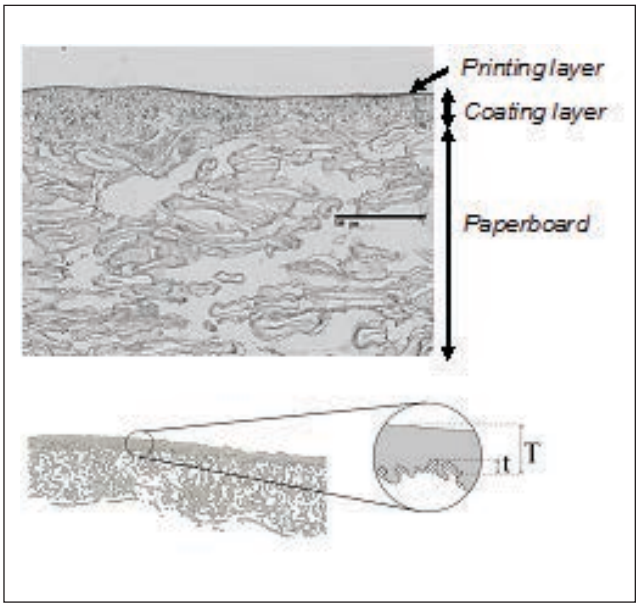
Variations in porous structure were achieved by using calcium carbonate pigments of either broad (Setacarb HG) or narrow (Covercarb 75) particle size distribution (both from Omya AB; Malmö, Sweden), thus rendering a coating layer with either low or high porosity (Fig. 1). Impact of binder content was studied by varying the fed amounts of styrene-butadiene latex binder: the medium level of 12 parts latex used in the reference coating was compared to a high level, corresponding to 18 parts per hundred parts of standard grade GCC. Effects of pigment types were investigated from blends of the standard grade GCC (Hydrocarb 90) and kaolin clay (Capim DG, Imerys Minerals Ltd.; Cornwall, UK) at 80:20 or 50:50 ratios respectively. Data for all coating formulations are given in **Table I**.

Coating	GCC Grade, pph		Kaolin Grade, pph		Latex, pph
Reference	Hydrocarb 90	100	-	-	12
Low porosity	Setacarb HG	100	-	-	12
High porosity	Covercarb 75	100	-	-	12
High binder level	Hydrocarb 90	100	-	-	18
GCC:Kaolin 80:20	Hydrocarb 90	80	Capim DG	20	12
GCC:Kaolin 50:50	Hydrocarb 90	50	Capim DG	50	12

I. Coating recipes.

Pore size distribution was characterized by an AutoPore III mercury porosimeter (Micromeritics; Norcross, GA, USA). The top surface structure and the percentage areas covered with latex and pigment, respectively, were evaluated from microscopic images (Jeol JSM-6700F cold field emission scanning electron microscope [SEM]; Tokyo, Japan).

The coated paperboard grades were printed with a water-based cyan ink (Sun Chemical Inks A/S; Skovlund, Denmark), with a viscosity of 25 s (Zahn cup no. 2). Printing was done by a laboratory flexographic printer (IGT-F1 laboratory flexographic printer, IGT Testing Systems; Amsterdam, NL), using an anilox roll (volume 2.7 ml/m^2 and screen ruling 235 lines/cm) and a printing plate with hardness 57° Shore A and thickness 1.7 mm (Miller Graphics; Sunne, Sweden). Full-tone areas were printed at either 25 or 50 N at constant speed of 0.3 m/s. Impact of ink viscosity was studied by heating the ink from its normal temperature of use (23°) up to 50°C. The corresponding viscosities as measured by a controlled shear stress rheometer (MCR 300, Physica Messtechnik GmbH; Stuttgart, Germany) were 52 mPas (23°C) and 31 mPas (50°C), respectively, at a shear rate of 100 s^{-1}.



2. Upper: cross-section image showing the printing layer, coating layer and paperboard structure. Lower: definitions of printing layer thickness (T) and ink penetration depth (t).

Print density was assessed by a GretagMacbeth D19C densitometer (Regensdorf, Switzerland) at 10 points per sample. The fraction of uncovered areas (UCA) was evaluated by STFI Mottling Expert v1.2 (Innventia AB; Stockholm, Sweden) from scanned images of printed, full-tone areas (8 measurements). Gloss measurements of coated and printed surfaces were performed by means of a gloss meter (Zehntner glossmeter, 20°–75°; Shropshire, UK) at 75° (ISO 8254-1 "Paper and board — Measurement of specular gloss — Part 1: 75 degree gloss with a converging beam, TAPPI method") at 10 points per sample. Ink penetration depth was evaluated by optical cross-section microscopy (Leica DMRX, Leica Mikroskopie & Systeme GmbH; Wetzlar, Germany) with assistance of software processing utilizing a method described elsewhere [23], which is illustrated in **Fig. 2**. The evaluation covered 12 measurement points on five cross-sectional images, i.e., 60 points in total for each printed sample.

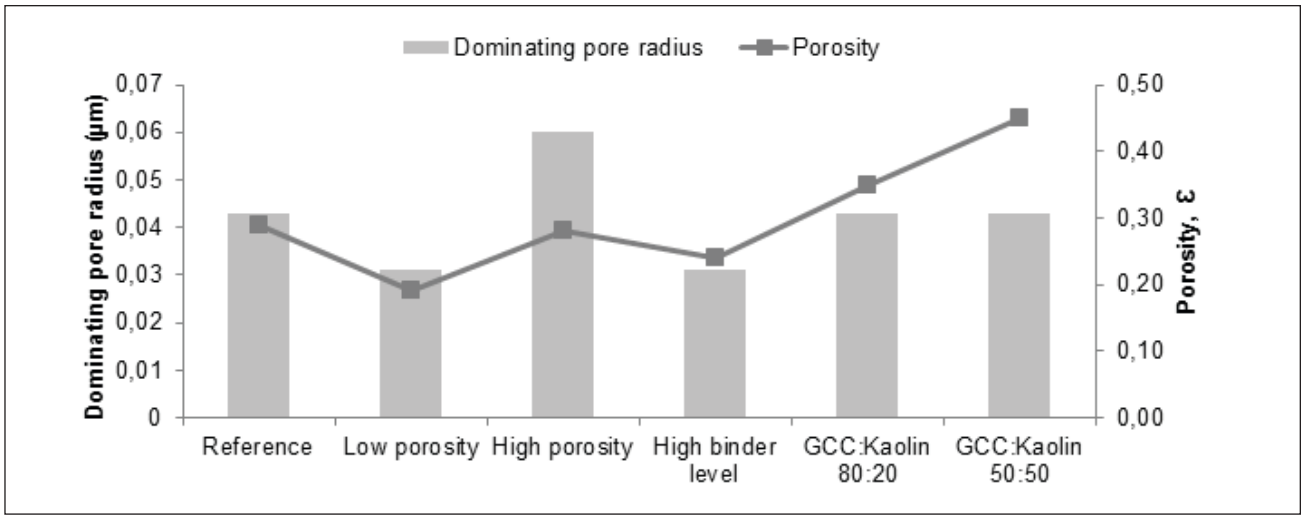
SEM (Jeol 6700F cold field emission SEM) was used to investigate the distribution of pigment and latex on the coated cartonboard surfaces. The percentage area covered with latex was determined by software analysis in a procedure described elsewhere [25].

RESULTS AND DISCUSSION

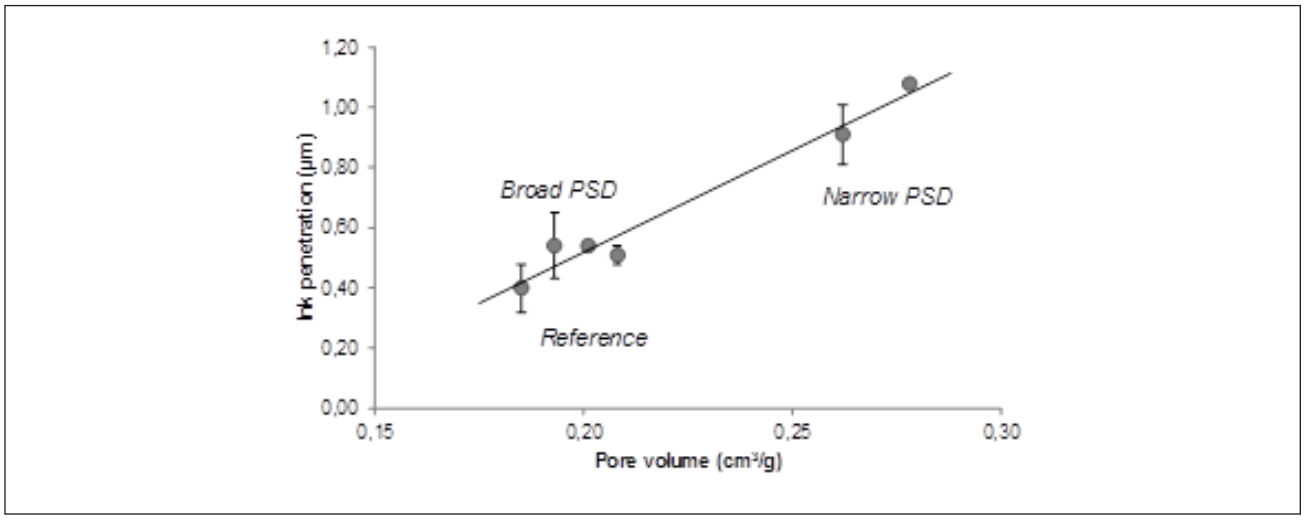
SEM images of all coated surfaces are shown in Fig. 1, while dominating pore radius and porosity determined by mercury porosimetry are summarized in **Fig. 3**. The impacts of porous structure, binder content, and pigment type are discussed under relevant headings in the following sections.

Variations in porous structure

From the SEM images in Fig. 1, differences in surface structure depending on the choice of GCC grade are clearly seen. The dominating pore radius was, as expected, smallest for the coating containing the GCC grade with broad PSD and largest for the grade with narrow PSD, while the reference coating showed a pore radius between these two (Fig. 3). The GCC with broad PSD resulted in a coating layer porosity of 0.19,



3. Dominating pore radius and porosity for different coating structures (GCC = ground calcium carbonate).



4. Ink penetration depth at a printing force of 50 N as a function of pore volume for GCC-based coatings with various particle size distribution (PSD). Average of 60 measurements with standard deviations. Data from Bohlin et al. [23] for both calendered and uncalendered surfaces.

whereas the GCC with narrow PSD and the reference coating both resulted in porosities near 0.28.

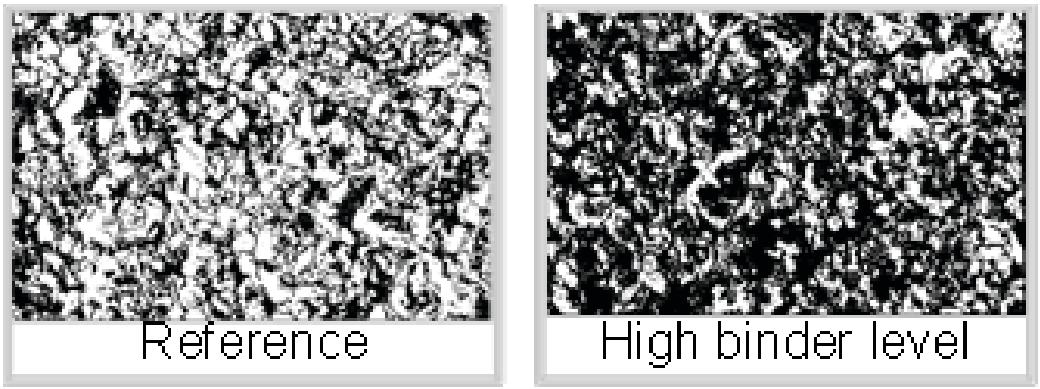
Figure 4 shows the ink penetration depth in micrometers plotted against pore volume in cm^3/g evaluated for the three coatings printed at a printing force of 50 N, both before and after calendering. Calendering resulted in a significant reduction in pore volume, with a subsequent reduction in ink penetration for the reference coating and the coating based on the GCC grade with narrow PSD. The pore structure of the coating with broad PSD (which already showed small pore radius and porosity) turned out, however, to be less affected by calendering, which also was illustrated by an almost unchanged degree of ink penetration.

From Figs. 3 and 4, it is obvious that greater pore radius and larger pore volume of the coating layer formed by selection of a calcium carbonate grade with narrow particle size distribution result in significantly higher z-directional ink penetration.

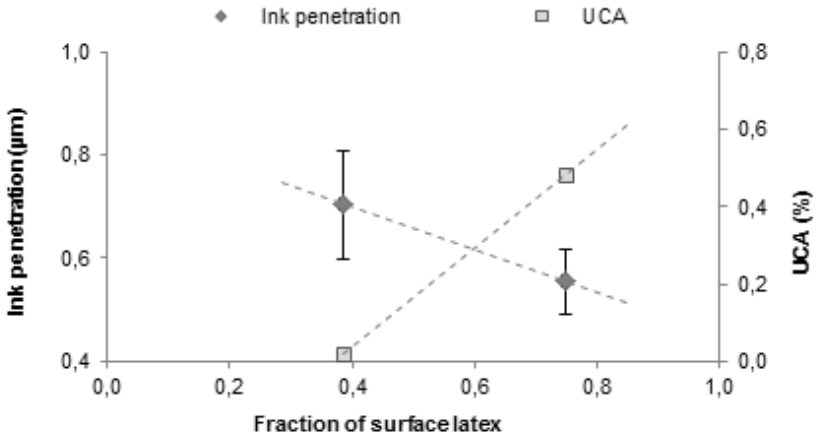
Variations in binder content

SEM micrographs of the top surfaces of the reference coating with 12 pph latex showed a coarse and porous structure consisting mainly of the GCC pigment (Fig. 1). Increasing the amount of latex to 18 pph resulted in enlarged regions comprised of a smoother texture, indicating a structure with GCC particles embedded in a latex film. This increased fraction of latex located near the top surface rendered a more closed surface structure. Figure 3 shows that the porosity decreased from 0.29 to 0.24 while going from 12 to 18 pph latex. At the same time, the dominating pore radius decreased from 0.043 to 0.031 µm.

The software processing method for estimation of percent-



5. SEM images of reference coating and coating with high binder level after software processing to determine the percentage area covered with latex (colored black). Compare with original images in Fig. 1. Data from Bohlin et al. [25].



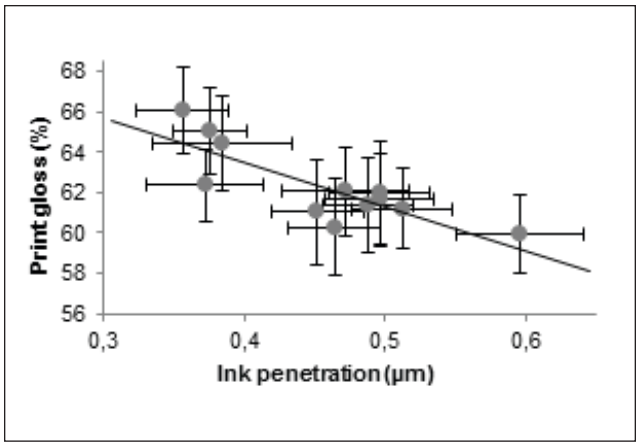
6. Ink penetration depth and uncovered areas (UCA) at printing force 25 N as a function of surface fraction of latex for GCC-based coatings with varying latex content. Dotted lines are inserted as a guide for the eye only. Average of 3 measurements (surface latex), 60 measurements (ink penetration), and 8 measurements (UCA) with standard deviations. Data from Bohlin et al. [25].

age area covered by latex and pigment, respectively, is illustrated in **Fig. 5** where the latex parts are colored black. The estimated fraction of the surface covered with latex increased from roughly 0.38 for the reference coating to 0.75 for the 18 pph sample.

This rather small increase of SB-latex in the coating recipe thus resulted in a tremendous increase in the fraction of latex located at the topmost surface. Higher fraction of surface latex in turn resulted in lower z-directional ink penetration (**Fig. 6**), which is easily explained by the more closed coating structure. The effect is strongest at the lowest printing force (25 N); increasing the printing force to 50 N aided in pressing more ink into the coating structure due to increased mechanical forces and a larger contact area between substrate and printing plate. The results are consistent with other studies on relationship between nip force and ink transfer ratio [26]. Higher fraction of surface latex also resulted in an increased amount of uncovered areas (UCA), Fig. 6, due to local variations in wettability. However, increasing the printing force from 25 N to 50 N compensated for this effect, since no visible UCAs were detected at the higher printing force [25]. This points to the ambiguity in designing coatings for either higher printing speeds (i.e., quicker setting) or for minimizing print quality defects. Striving to retain ink on the surface for print density, less UCA, etc., by means of porous structure and surface energetics can be challenging when higher printing speeds are desired for multicolor printing [27,28].

Variations of pigment types

The change in surface structure by incorporation of higher



7. Print gloss as a function of ink penetration depth for GCC/kaolin clay-based coatings. Average from 10 measurements (print gloss) and from 60 measurements (ink penetration) with standard deviations. Redrawn from Bohlin et al. [24].

fractions of disc-shaped kaolin particles among the more sphere-shaped GCC particles is clearly shown in the SEM images (Fig. 1). Increased ratio of kaolin clay resulted in increased porosity, from 0.29 (reference) to 0.35 (GCC:Kaolin ratio 80:20) to 0.45 (GCC:Kaolin ratio 50:50), while the dominating pore radius remained constant at 0.043 µm (Fig. 3).

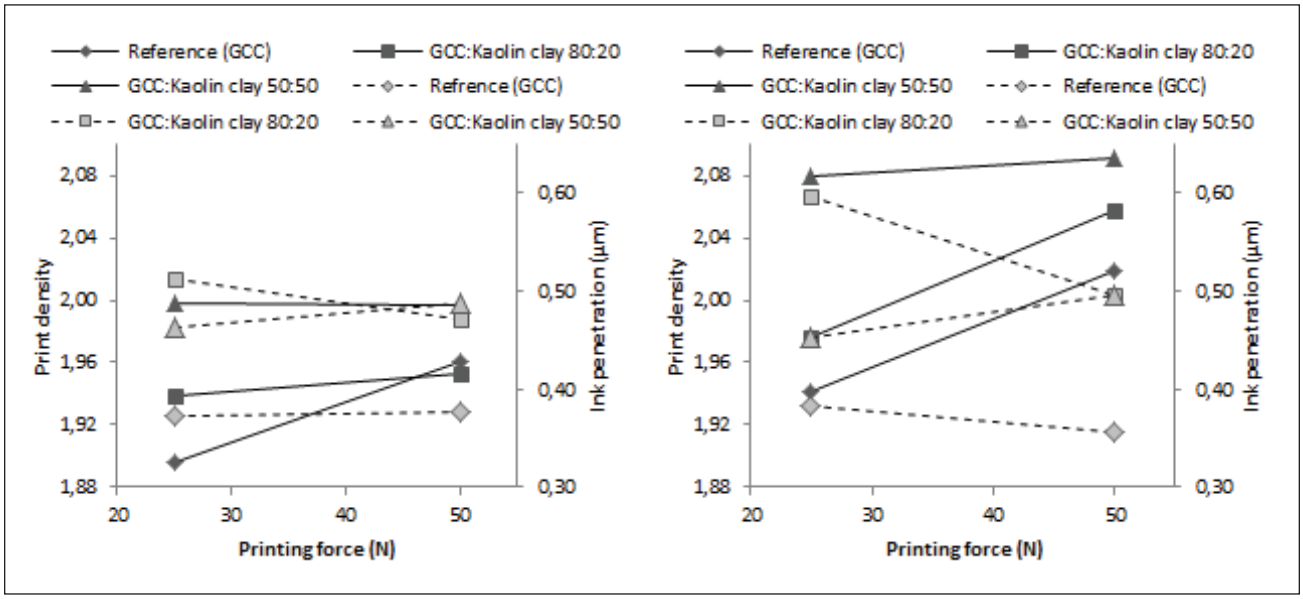
In **Fig. 7**, print gloss is plotted against ink penetration depth for the complete series of samples where pigment type was studied: reference coating and coatings with GCC:Kaolin ratio of 80:20 and 50:50—all printed at printing forces 25 N or 50 N with ink viscosity of either 52 mPas or 31 mPas. Increased ink penetration resulted in decreased print gloss (Fig. 7) due to a higher rate of ink vehicle removal and thereby a higher ink surface roughness. This lends credit to investigations made by Olsson et al. [29], where lower gloss and higher ink penetration resulted when the ink temperature was raised.

In **Fig. 8**, print density and ink penetration are plotted as a function of printing force (25 N and 50 N) for an ink viscosity of 52 mPas (23°C; left diagram) and 31 mPas (50°C; right diagram). Higher printing force did not increase the depth of penetrated ink to any greater extent; instead, higher printing force led to an improved distribution of the ink, with increased print density as a result. Higher printing force also resulted in a decreased amount of uncovered areas [25]. The effects were more pronounced at a lower ink viscosity (right diagram).

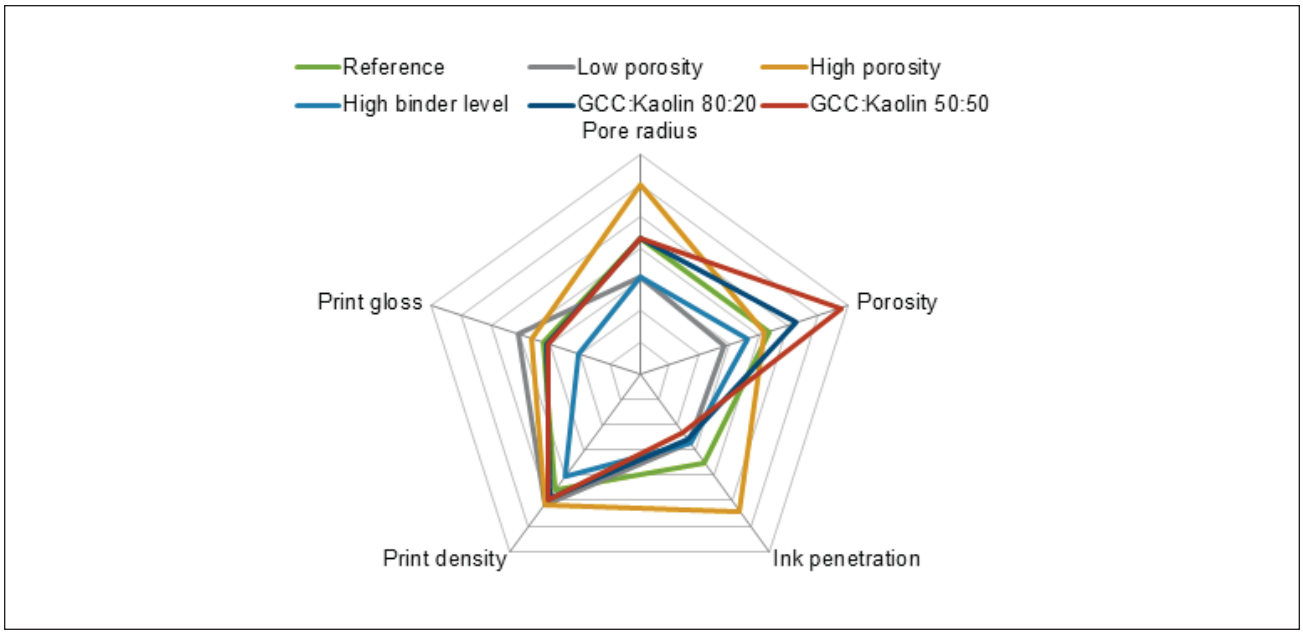
Overall impact of studied properties

Our attempt with this paper was to evaluate the overall impact on flexographic print quality by comparing the findings of three separate research studies. The pore radius and porosity were shown to differ considerably depending on the choice of pigment particle size, amount of binder, and type of pigment (Fig. 3). Furthermore, the ink penetration depth evaluated by our method from cross-section images of printed paperboard could easily be related to the observed variations in porous structure. A strong relationship between surface structure and ink-substrate interactions with subsequent impact on print quality was found.

The impact of various parameters in relation to each other is schematically depicted in the diagram in **Fig. 9**, where pore radius, porosity, ink penetration depth, print density, and print gloss are plotted (in arbitrary units) for the complete series of coating structures printed at a printing force of 50 N.



8. Print density and ink penetration as a function of printing force and ink viscosity for GCC/kaolin clay-based coatings. Data from Bohlin et al. [24]. Left diagram: ink viscosity ~52 mPas; right diagram: ink viscosity ~31 mPas. Average from 10 measurements (print density) and 60 measurements (ink penetration). Error bars are hidden to enhance readability of the diagrams. Lines are inserted as a guide for the eye. Solid lines: print density; dotted lines: ink penetration.



9. Schematic diagram showing the pore radius, porosity, ink penetration depth, print density and print gloss for the complete series of coating structures printed at a printing force of 50 N. Arbitrary units.

The porosity increases in the following order: low porosity<high binder level<high porosity <reference <GCC:kaolin ratio 80:20<GCC:kaolin ratio 50:50. However, ink penetration depth was highest for the coating with the largest pore radius (i.e., the sample named high porosity), followed by the reference coating. This may be ascribed to a combined effect of capillary and mechanical forces, as discussed in our previous paper [23]. The samples showing smallest overall pore radius and lowest porosity (low porosity and high binder level) also were the ones showing lowest ink penetration depth.

Lower ink penetration with increased amount of kaolin can be related to an increased degree of tortuosity with the incorporation of flaky kaolin particles, even though the dominating pore radius was equal within this series.

The coating with high binder level showed the poorest print quality, both in terms of lowest print density and lowest print gloss among all investigated samples, which is understood by the negative impact from the high fraction of surface latex on ink transfer and setting.

Using a GCC grade with either broad or narrow PSD (i.e., low or high porosity), or a coating formulation with blends of GCC and kaolin, all resulted in slightly higher print density compared to the reference coating (Fig. 9). The highest overall value of print gloss was achieved by using the GCC grade with broad PSD, giving a coating layer of low porosity, which can be explained by the smooth surface of this coating created by the very small pigment particles [23]. Using a GCC grade with narrow PSD (high porosity) resulted in a higher print gloss than the reference coating, whereas the print gloss decreased slightly with increased fraction of kaolin clay.

Interactions between printing inks and substrates have been the topic of some recent studies: Thorman et al. [30] developed a method for studying the absorption uniformity based on short-time absorption of a colored liquid, followed by blotting of excess liquid and characterization of the pattern of the stain. They analyzed a set of coatings with different compositions and could ascribe absorption nonuniformity to variations in coating layer thickness and/or wettability where different pore structures between thinner and thicker coating areas were claimed to affect the results.

The mercury porosimetry method has been used for decades for determination of porosity of coating layers. Recent approaches involve 3D-modeling of the pore structure by tomography: Aslannejad et al. [31] very recently presented a sophisticated method for modelling the three-dimensional pore space within a coating structure based on focused ion beam SEM. The authors reported a good agreement between mercury porosity measurements and the modelling based on SEM imaging and claimed the method to be useful for macroscale modelling of ink penetration during inkjet printing and, further, a valuable tool for optimization of the ink penetration depth and ink spreading on and within coated paper structures. Such an approach would also strongly add to the understanding of ink-substrate interactions when it comes to water-based flexographic inks used in our study.

Gomez et al. [32] developed a new method to study the distribution of ink components (oil and pigment) from cold-set inks in printed newspaper of thickness about 70 µm. Attenuated total reflectance-Fourier transform infrared (ATR-FTIR) spectroscopy analysis was performed on printed and unprinted sides of several consecutive layers separated by delamination of the paper. With this procedure, it was possible to determine the portion of each component at various

locations; oil was mainly found below half the paper thickness (i.e., penetration depth >45 µm), whereas pigment was detected in the layers close to the printed surface (penetration depth <15 µm). A drawback with this method lies in difficulties to differentiate components in the printing ink from components in the paper and coating layers due to overlapping peaks in the ATR-FTIR spectra.

Thus, further investigation of water-based flexographic ink-coated paper substrate interactions with the application of such newly developed analysis techniques will most likely provide deeper insights into these very intriguing aspects on print quality.

CONCLUSIONS

Overall, the results demonstrated that the print quality was strongly affected by the ink-substrate interactions. The ink penetration depth was related to the porosity of the coating; a coating layer with larger pore volume and larger pore size created by the use of a calcium carbonate grade with narrow particle size distribution resulted in higher ink penetration in the z-direction. The ink penetration depth was also related to the binder content in the coating color; higher fraction of surface latex generated a more closed surface (lower porosity), thus hindering ink from penetrating into the coating structure.

The print quality was furthermore related to the ink penetration depth, which in turn was related to the pigment type in the coating color; increased ink penetration resulted in decreased print gloss. Higher printing force resulted in increased print density; for coatings with both GCC and kaolin clay (more porous structures), decreased ink viscosity had a greater impact on print density than increased printing force. This study has shown that by fine-tuning the coating composition and structure and by a proper selection of printing parameters, problems with print quality defects can be overcome. **TJ**

ACKNOWLEDGEMENTS

The Swedish Governmental Agency for Innovation Systems (VINNOVA) and the industry participants in the PaperOpt project are gratefully acknowledged for financial support. BillerudKorsnäs Frövi is thanked for performing the pilot coating. The authors are indebted to Eka Synthomer Oy and Omya for supplying materials, and SCA and Imerys for performing measurements on both coated and printed cartonboard materials, as well as for valuable discussions on the experimental results. Professor Magnus Lestelius is thanked for valuable comments on this work.

LITERATURE CITED

1. MacGregor, M.A., Johansson, P., and Beland, M., *TAPPI Int. Print. Graphic Arts Conf.*, TAPPI Press, Peachtree Corners, GA, USA, 1994, p. 33.
2. Caner, E., Farnood, R., and Yan, N., *TAPPI J.* 7(4): 19(2008).
3. Dahlström, C. and Uesaka, T., *Ind. Eng. Chem. Res.* 48:(23): 10472(2009).
4. Engström, G. and Morin, V., *TAPPI J.* 79(9): 120(1996).
5. Engström, G., *TAPPI J.* 77(4): 160(1994).
6. Larsson, M., Engström, G., Vidal, D., et al., *TAPPI Adv. Coat. Fundam. Symp.*, TAPPI Press, Peachtree Corners, 2006, p. 6.19.
7. Chinga, G. and Helle, T., *J. Pulp Pap. Sci.* 29(6): 179(2003).
8. Xiang, Y., Coleman, P., Bousfield, D., et al., *TAPPI Coat. Conf. Trade Fair*, TAPPI Press, Peachtree Corners, 2000, p. 45.
9. Cummings, D.O. and Lyons, A.V., *TAPPI Coat. Conf.*, TAPPI Press, Peachtree Corners, 1996, p. 16.
10. Preston, J.S., Daun M., Nutbeem, C., et al., *Wochenbl. Papierfabr.* 5: 252(2000).
11. Preston, J.S., Elton, N.J., Legrix, A., et al., *TAPPI Adv. Coat. Fundam. Symp.*, TAPPI Press, Peachtree Corners, 2001, p. 21.
12. Olsson, R., Yang, L., and Lestelius, M., *Nord. Pulp Pap. Res. J.* 22(3): 287(2007).
13. Al-Turaif, H.A. and LePoutre, P., "Entwicklung der Oberflächenstruktur und–chemie von Pigmentstrichen während des Trocknungsvorganges," *PTS Coat. Symp., 19th*, Papiertechnische Stiftung, Munich, 1999.

ABOUT THE AUTHORS

Print quality of flexographic printed paperboard is an interesting area of research in the paper industry, and this research study summarizes and explains observations from several studies on the topic.

The most difficult aspect of this research was that paper is a nonuniform material that gives rise to variations in measured parameters. To address this, a broad number of replicates were tested. We found that many different parameters affect the final result in a complicated manner. The most interesting finding was the connection between ink penetration and print



Bohlin



Johansson

Mills might benefit from this information in terms of their choice of materials and process conditions for optimization of product performance. Our next step is to explore new analytical techniques.

Bohlin is development engineer and Johansson is specialist, chemical additives, at BillerudKorsnäs Gruvön, Grums, Sweden. Email Johansson at caisa.johansson@billerudkorsnas.com.

14. Al-Turaif, H., Bousfield, D.W., and LePoutre, P., *Prog. Org. Coat.* 44: 307(2002).
15. Al-Turaif, H., *J. Coat. Technol. Res.* 5(1): 85(2008).
16. Al-Turaif, H., *Prog. Org. Coat.* 65: 322(2009).
17. Olsson, R., Yang, L., and Lestelius, M., "Flexographic print quality of pilot coated paperboard," *Adv. Printing Media Technol.* 35: 169(2008).
18. Barros, G.G., Fahlcrantz, C.M., and Johansson, P.Å., *TAGA J.* 2(1): 43(2005).
19. Barros, G.G. and Johansson, P.Å., *Nord. Pulp Pap. Res. J.* 21(2): 172(2006).
20. Preston, J.S., Elton, N.J., Legrix, A., et al., *TAPPI J.* 1(5): 3(2002).
21. Preston, J., Hiorns, A., Parsons, D.J., et al., *Pap. Technol.* 49(3): 27(2008).
22. Kim, S., Sojoudi, H., Zhao, H., et al., *Sci. Adv.* 2: e1601660: 1(2016).
23. Bohlin, E., Lestelius, M., and Johansson, C., *Nord. Pulp Pap. Res. J.* 28(4): 573(2013).
24. Bohlin, E., Johansson, C., and Lestelius, M., *IARIGAI Int. Res. Conf., 41st*, International Association of Research Organizations for the Information, Media and Graphic Arts Industries, Darmstadt, Germany, 2014, p. 57.
25. Bohlin, E., Johansson, C., and Lestelius, M., *TAPPI J.* 15(4):253(2016).
26. Nguyen, H.A.D., Keehyun, S., and Changwoo, L., *Int. J. Precis. Eng. Manuf.* 16(3):517(2015).
27. Mešić, B., Edholm, B., Engström, G., et al., *Int. Print. Graphic Arts Conf.*, PAPTAC, Montreal, 2004, p. 179.
28. Hallberg, E., Lestelius, M., and Rättö, P., *Nord. Pulp Pap. Res. J.* 21(1):111(2006).
29. Olsson, R., Yang, L., van Stam, J., et al., *IARIGAI Int. Res. Conf., 34th*, "Effects of elevated temperature on flexographic printing," International Association of Research Organizations for the Information, Media and Graphic Arts Industries, Darmstadt, Germany, 2007.
30. Thorman, S., Ström, G., Hagberg, A., et al., *Nord. Pulp Pap. Res. J.* 27(2): 459(2012).
31. Aslannejad, H., Hassanizadeh, S.M., Raoof, A., et al., *Chem. Eng. Sci.* 160: 275(2017).
32. Gomez, N., Molleda, C., Quintana, E., et al., *Appl. Spectrosc.* 70(9): 1537(2016).

ABOUT THIS PAPER

Cite this article as: Bohlin, E., Johannson, C. *TAPPI J.* 17(1): 43(2018). https://doi.org/10.32964/TJ17.01.43

DOI: https://doi.org/10.32964/TJ17.01.43

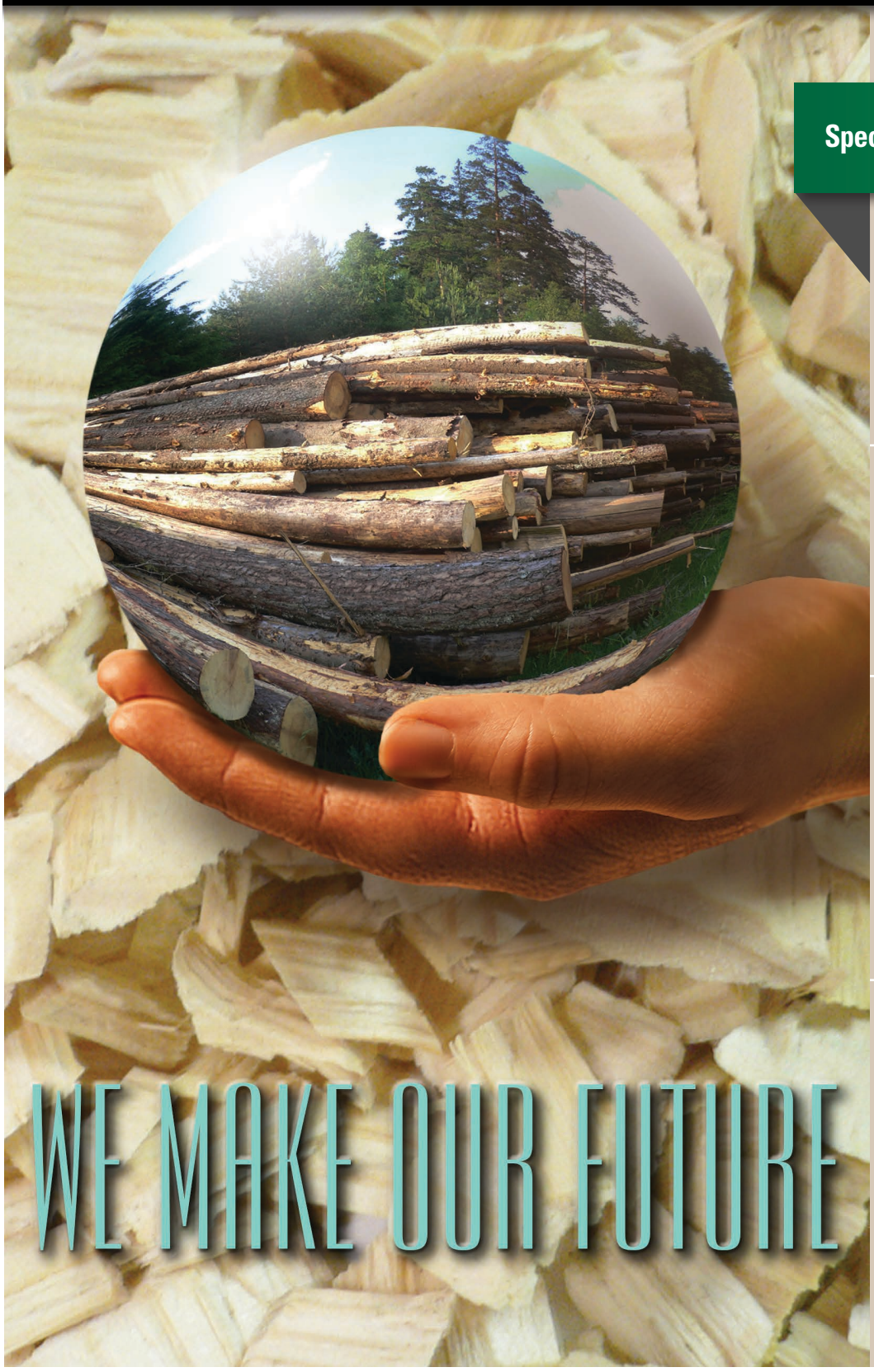
ISSN: 0734-1415

Publisher: TAPPI Press

Copyright: ©TAPPI Press 2018

About this journal

TAPPI JOURNAL
WWW.TAPPI.ORG
THE PAPER AND PACKAGING INDUSTRIES' TECHNICAL RESOURCE
FEBRUARY 2018 | VOL. 17 NO. 2



Special Lignocellulosics Content

LIGNIN PRODUCTS 63
Activated carbon from potassium hydroxide spent liquor lignin using phosphoric acid
Mamon Sarkar, Chao Tian, and M. Sarwar Jahan

MOISTURE SORPTION 71
Static and dynamic sorption of lignin removed *Populus euramericana*
Haizhen Zhou, Jingyu Li, and Erni Ma

LIGNOCELLULOSE 81
Lignocellulose fibers elaborating super-swollen three-dimensional cellulose hydrogels from solution in N,N-dimethylacetamide/lithium chloride
Aleksandra Mikhailidi, Shahriar Karim Saurov, Seppo Andersson, and Nina Kotelnikova

NANOMATERIALS 92
Functionalization of wood/plant-based natural cellulose fibers with nanomaterials: a review
Charu Agarwal and Levente Csóka

February 2018

TABLE OF CONTENTS VOL. 17 NO. 2

59 **EDITORIAL**
New lignocellulosics address consumer expectations and industry prosperity
Arthur J. Ragauskas and Yunqiao Pu

63 **LIGNIN PRODUCTS**
Activated carbon from potassium hydroxide spent liquor lignin using phosphoric acid
Mamon Sarkar, Chao Tian, and M. Sarwar Jahan

71 **MOISTURE SORPTION**
Static and dynamic sorption of lignin removed *Populus euramericana*
Haizhen Zhou, Jingyu Li, and Erni Ma

81 **LIGNOCELLULOSE**
Lignocellulose fibers elaborating super-swollen three-dimensional cellulose hydrogels from solution in N,N-dimethylacetamide/lithium chloride
Aleksandra Mikhailidi, Shahriar Karim Saurov, Seppo Andersson, and Nina Kotelnikova

92 **NANOMATERIALS**
Functionalization of wood/plant-based natural cellulose fibers with nanomaterials: a review
Charu Agarwal and Levente Csóka

»COVER CREDIT: This *TAPPI Journal* cover, a collaborative design from Robert Davies at Renewable Bioproducts Institute at Georgia Institute of Technology and Dr. Arthur J. Ragauskas at the University of Tennessee, captures the exciting future opportunities available in processing woody biomass.

TAPPI JOURNAL
WWW.TAPPI.ORG

Editor-in-Chief
Brian N. Brogdon brian.brogdon@gmail.com
+1 678 581-9114

Associate Editor
Peter W. Hart peter.hart@westrock.com
+1 409 276-3465

Editorial Director
Monica Shaw mshaw@tappi.org
+1 770 367-9534

PRESS Manager
Jana Jensen jjensen@tappi.org
+1 770 209-7242

Webmaster
Trina Heath theath@tappi.org
+1 770 209-7416

***TJ* EDITORIAL BOARD**

Randy Branston, BASF
randy.branston@basf.com, +1 704 819-4251

Brian N. Brogdon, FutureBridge Consulting & Training LLC
brian.brogdon@gmail.com, +1 678 581-9114

David A. Carlson, Carlson Consulting
dacarlson39@aol.com, +1 847 323-2685

Mahendra Doshi, Doshi and Associates
mahen@aol.com, +1 920 832-9101

Marc Foulger, GL&V USA Inc.
Marc.foulger@glv.com +1 315 767-2920

Peter W. Hart, WestRock
peter.hart@westrock.com, +1 409 276-3465

Carl J. Houtman, USDA Forest Products Laboratory
choutman@fs.fed.us, + 1 608 231-9445

Lucian Lucia, North Carolina State University
lucian.lucia@gmail.com, +1 919 889-7059

John A. Neun, John A. Neun LLC
john.neun@gmail.com, +1 518 275-8139

Jim Niemiec, Verso Corporation
jim.niemiec@versoco.com, +1 715 422-7404

Steven P. Ottone, Omya
steven.ottone@omya.com, +1 919 641-7854

Gaurav Pranami, Imbed Biosciences
gpranami@imbedbio.com, +1 515 230-7005

Arthur Ragauskas, Oak Ridge National Laboratory
aragausk@utk.edu

Gerard J.F. Ring, University of Wisconsin—Stevens Point
gerrryring@wi-net.com, +1 715 592-3732

Scott Rosencrance, Kemira Chemicals
scott.rosencrance@kemira.com, +1 770 429-2753

Paul Wiegand, NCASI
pwiegand@ncasi.org, +1 919 941-6417

Junyong Zhu, USDA Forest Products Laboratory
jzhu@fs.fed.us, +1 608 231-9520

Join TAPPI *today!*
TAPPI JOURNAL is a free benefit of TAPPI membership, and is only available to members. To join TAPPI, to renew your TAPPI Membership, or to learn about other valuable benefits, visit www.tappi.org.

TAPPI, 15 Technology Parkway S., Suite 115, Peachtree Corners, GA 30092, publishes *TAPPI JOURNAL* monthly.

ATTENTION PROSPECTIVE AUTHORS: All papers published are subject to *TAPPI JOURNAL's* peer-review process. Not all papers accepted for review will be published. Before submitting, check complete author guidelines at http://www.tappi.org/s_tappi/doc.asp?CID=100&DID=552877.

Statements of fact and opinions expressed are those of individual authors. TAPPI assumes no responsibility for such statements and opinions. TAPPI does not intend such statements and opinions or construe them as a solicitation of or suggestion for any agreed-upon course of conduct or concerted action of any sort.

Copyright 2018 by TAPPI, all rights reserved. For copyright permission to photocopy pages from this publication for internal or personal use, contact Copyright Clearance Center, Inc. (CCC) via their website: www.copyright.com. If you have questions about the copyright permission request process, please contact CCC by phone at +1 978 750-8400. To obtain copyright permission to use excerpts from this publication in another published work, send your specific request in writing to Editor, TAPPI JOURNAL, 15 Technology Parkway S., Suite 115, Peachtree Corners, GA 30092, USA; or by fax to +1 770 446-6947. Send address changes to TAPPI, 15 Technology Parkway S., Suite 115, Peachtree Corners, GA 30092, USA; Telephone +1 770 446-1400, or FAX +1 770 446-6947. www.tappi.org

Editorial



ARTHUR J. RAGAUSKAS
TAPPI Journal
Editoral Board Member



YUNQIAO PU
Guest Editor

New lignocellulosics address consumer expectations and industry prosperity

Editor's Note: *TAPPI would like to thank Arthur J. Ragauskas of the* TAPPI Journal *(*TJ*) Editorial Board, as well as Guest Editor Yunqiao Pu, for developing this special Lignocellulosics issue.*
– Monica Shaw, Editorial Director

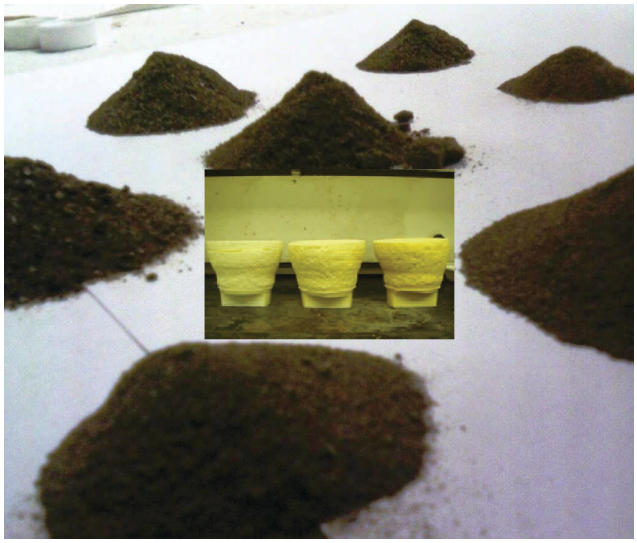
A walk down a grocery store aisle is an amazing lesson in the creativity and productivity of the pulp and paper industry. There, you can realistically show students interested in a forest products career where we are in the production of lignocellulosic products and where we may well be headed. Many of the issues that have and will drive innovations are clearly illustrated in a grocery aisle, including:

- Recycling
- Sustainable/environmentally friendly production practices
- Convenient, high-performance products, including paper, packaging, filtration, towel, tissue, hygiene, and healthcare items
- Issues of physical strength properties, as well as barrier and optical properties

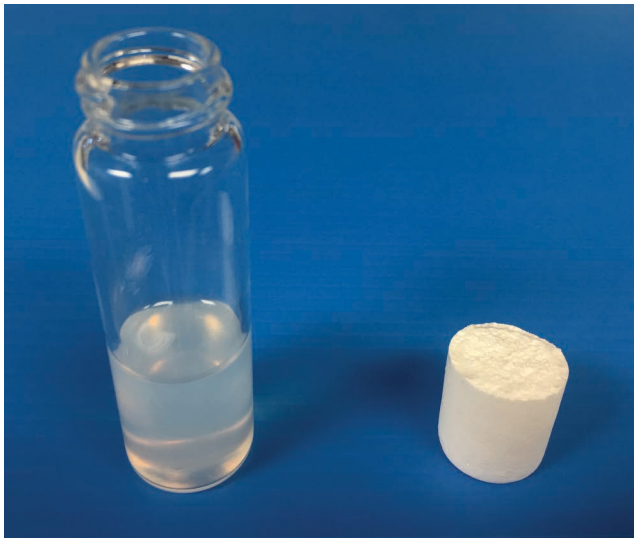
Yet even as we examine existing products, it is clear that today's consumers have expectations that significantly differ from former generations, and this provides new opportunities and challenges for the pulp and paper industry.

Lignocellulosics for new consumer patterns

With development of new materials and changes in consumer patterns, there is a constant challenge for chemical and mechanical pulps to address these demands and to evolve into improved/new physical



Polyurethane made from lignin.



Current studies by L. Liang and A.J. Ragauskas are directed at designing lightweight nanocellulosic foams.

attributes and properties. Certainly, this has been a growing theme in lignocellulosic research over the past few decades, and it seems to only have accelerated as illustrated in the patent realm, with a few examples exemplified below:

- Kuo, C.K. and Huang, C.H., "Paper box with wireless signal transmission component and manufacturing method thereof," *U.S. Pat. Appl.*, 2016, US 20160010285 A1 20160114.
- Lee, J.H. and Lee, H.J., "Nanocellulose from non-lignocellulosic biomass for use in moisturizers and superabsorbents," *Repub. Korean Kongkae Taeho Kongbo*, 2017, KR 2017011697 A 20170202.
- Lou, X., Feng, Z., and Feng, X., "Antibacterial paper for daily use and its making method," *Faming Zhuanli Shenqing*, 2017, CN 107524052 A 20171229.
- Hong, W., Zhou, J., Kanungo, M., et al., "Design of biomedical paper sensor," *U.S. Pat.*, 2016, US 20160051980 A1 20160225.
- Honnorat, A., "Paper that cannot be forged using solvents," *U.S. Pat. Appl.*, 2014, US 20140027078 A1 20140130.
- Hasani, M., Mesic, N., Soederqvist L.M., et al., "Cellulose nanocrystal-containing cellulosic product," *Eur. Pat. Appl.*, 2013, EP 2639351 A1 20130918.
- Samec, J., Enquist, K., and Cordova, A., "Method for improving properties of cellulose-based fibrous sheet-formed materials for use in medical goods," *Eur. Pat. Appl.*, 2011, EP 2309059 A1 20110413.

Coupled with this pathway of innovation is the question of how we can improve the production process and garner greater value from wood resources; hence, there is the ongoing focus on evolving a pulp mill to a biorefinery whereby waste streams in pulp production are fractionated and these process streams become a valuable bioresource for the production of new materials and chemicals [1]. This special issue of *TAPPI Journal* examines some of the challenges in lignocellulosics and helps illustrate the exciting new pathways available in research. **TJ**

Arthur J. Ragauskas is a member of the TAPPI Journal *Editorial Board and is professor/Governor's Chair in Biorefining, Oak Ridge National Laboratory; Department of Chemical and Biomolecular Engineering; Department of Forestry, Wildlife, and Fisheries; and BioEnergy Science Center; University of Tennessee, Knoxville, TN, USA.*

Pu is senior R&D staff in the Biosciences Division, Joint Institute for Biological Science, Oak Ridge National Laboratory, Oak Ridge, TN, USA.

REFERENCES

1. Chakar, F.S. and Ragauskas, A.J., "Review of current and future softwood kraft lignin process chemistry," *Ind. Crops Prod.* 20(2): 131(2004).

Activated carbon from potassium hydroxide spent liquor lignin using phosphoric acid

MAMON SARKAR, CHAO TIAN, AND M. SARWAR JAHAN

ABSTRACT: Activated carbon was prepared by phosphoric acid (H_3PO_4) activation of potassium hydroxide (KOH) pulping spent liquor lignin from rice straw and compared with KOH hydroxide activation. The process parameters, such as impregnation ratio, activation temperature, and activation time were varied and their effects on the yield of activated carbon and iodine number were studied. The activated carbon prepared by H_3PO_4 at 800°C for 60 min at an impregnation ratio of 2.5 reached a Brunauer-Emmett-Teller (BET) surface area of 1063 m^2/g, including pore diameter of 14.4 nm, iodine number of 525 mg/g, and yield of 49.2%. Yield and BET surface area in KOH activation was much lower than that of H_3PO_4.

Application: Potassium hydroxide spent liquor lignin can be used in producing activated carbon. In the biorefinery, this can be integrated with pulp production based on agricultural wastes.

Bangladesh is a densely populated forest-deficient agricultural country. Consequently, forests can no longer supply fibrous raw material for pulp production. In this context, agricultural wastes can be an alternative to fibrous raw materials. Rice straw is the largest agricultural waste generated in Bangladesh, but recovery is the main drawback of rice straw pulping in the conventional process. The pulping process is not environmental friendly without chemical recovery. Therefore, many studies have been carried out on alternative pulping, such as potassium hydroxide (KOH) or ammonia-based pulping, where black liquor can be used as fertilizer. The spent liquor of pulp and cellulose industries contains large quantities of lignin as byproducts. In our previous study, KOH-based pulping of rice straw and wheat straw was proposed in a biorefinery concept [1]. In the KOH pulping process, lignin, part of hemicellulose, and silica were dissolved. Silica was precipitated from the alkaline liquor by reducing pH to 7 [2-3]. Ultrafiltration and nanofiltration can separate and recover lignin and hemicellulosic sugars from the black liquor [4-5]. After the separation of silica and the potassium-rich liquor, dissolved biomass could be used in irrigation. In this work, dissolved lignin in the KOH pulping was used as starting material for the production of activated carbon. Lignin is mostly beneficial for the production of activated carbon because of its higher percentage of phenolic content, which provides higher yield of carbon than any kind of biomass [6-7].

Activated carbon is a highly porous materials with high surface area used in gas purification, water purification, medicinal applications, and air filtration. Activated carbon is also used as a catalyst support. The demand for activated carbon is increasing because of its multipurpose industrial applications. Activated carbon is mainly prepared in two ways: physical and chemical activation. In physical activation, carbonization is done for the precursor and activation of char is done by carbon dioxide or steam gasification. In chemical activation, both the carbonization and the activation steps proceed simultaneously. Generally, activated carbon prepared by water vapor gasification creates micropores that are suitable for the adsorption of small molecular impurities. Therefore, researchers focus on chemical activation for the preparation of mesopores in activated carbon with high surface area [8]. A wide range of chemical compounds, such as KOH, sodium hydroxide, potassium carbonate (K_2CO_3), sodium carbonate, zinc chloride ($ZnCl_2$), and phosphoric acid (H_3PO_4), are used as activating agents. Because of their corrosive nature, environmental disadvantages associated with metal hydroxides and $ZnCl_2$ are not preferred for activation [9-10]. On the other hand, KOH reduces the yield of the final product. For the green-environment concept and preparation of high surface area, H_3PO_4 is preferred as an activating agent. Phosphoric acid is less corrosive and more efficient in chemical recovery than other strong acids [11].

Phosphoric acid has a double role in impregnating materials [12]. First, it hydrolyzes the lignocellulosic materials and subsequently extracts of some components, thus weakening the materials and swelling the precursor materials. Second, the acid takes up a volume that slows the contraction of the material during the heat treatment by forming phosphate and polyphosphate bridges that connect and cross-link biopolymer fragments. As a consequence, it produces porosity when it is extracted by washing after carbonization. Hayashi et al. [13] investigated the possibility of chemical activation of kraft

lignin with H_3PO_4 at 500°C–900°C for 1 h under N_2 inert atmosphere. They found that 600°C is the optimum carbonization temperature. The observed maximum surface area was almost 1000 m^2/g. Fierro et al. [14] observed the carbonization efficiency using H_3PO_4 from kraft lignin. They achieved surface area greater than 1300 m^2/g. Jin et al. [15] examined the activation efficiency using KOH and K_2CO_3 as activation agents for alkali pulping straw lignin and achieved iodine number 1100 at 700°C and 1300 at 800°C. Myglovets et al. [16] observed the preparation of activated carbon from lignosulfonates using H_3PO_4 and observed the maximum surface area of 1373 m^2/g at 1000°C. However, the carbonization efficiency from KOH pulping lignin as a precursor has not been performed.

The objective of this study was to optimize conversion of KOH pulping liquor lignin into activated carbon by H_3PO_4 through chemical activation at varying activation times, temperatures, and impregnation ratios. Pore size, surface chemistry, and yield of the produced activated carbon were determined and compared with KOH activation.

MATERIAL AND METHODS

Materials

KOH spent liquor from rice straw pulping was collected and silica, which was settled and filtered, was separated by reducing pH to 7. The pH of silica-separated liquor was further reduced to 2 and lignin was precipitated. The lignin was collected by filtration and dried for further experiments.

Methods

For preparation of activated carbon, 10 g o.d. lignin was collected in a crucible and then impregnated with 85% H_3PO_4 at different predetermined impregnation ratios (1-3). The impregnated slurry was soaked for 2 h with the activating agent and then dried in an oven at 105°C for 24 h so that the reagents were totally adsorbed by precursor. After the 24-h period, the crucible was stored in a desiccator until the furnace attained the set temperature. Then, the impregnated materials were transferred into the furnace with a suitable lid at predetermined variations in time (60–120 min) and temperature (600°C–850°C) for auto carbonization. At the end of carbonization, the activated carbons were washed with 500 mL hot water, followed by extensive washing with distilled water until the pH of the filtrate reached neutrality. Finally, the activated carbon was dried in an oven overnight at 105°C. A few experiments were also performed with KOH as the activating agent and compared with the results of H_3PO_4 activation.

Characterization

The yield of the activated carbon was calculated using (Eq. 1):

$$Y = (M_1/M_2) \times 100\% \quad (1)$$

where M_1 is the weight of the o.d. activated carbon and M_2 is the weight of the o.d. lignin.

For the characterization of activated carbon, iodine number was measured, which represents the surface area contributed by the pores larger than 10 Å [17]. Iodine number is widely used for activated carbon testing for its simplicity and ability to rapidly assess adsorbent quality. The iodine number is defined as the milligrams of iodine adsorbed by one gram of material when the iodine residual concentration of the filtrate is 0.02N (0.01 mol L^{-1}), according to ASTM D4607 "Standard test method for determination of iodine number of activated carbon," which is based on a three-point isotherm.

The total surface area was observed using a Brunauer-Emmett-Teller (BET) surface area analyzer. Surface morphology of activated carbon was studied using an S-3400N scanning electron microscope (SEM) (Hitachi; Tokyo, Japan). For observing the functional group, fourier-transform infrared spectroscopy (FTIR) studies were also performed.

Carbon, hydrogen, and nitrogen contents of the activated carbons were measured using an elemental analyzer at the Institute of Analytical Research & Services, Bangladesh Council of Scientific and Industrial Research. Surface area and pore size distributions were determined with an automatic instrument (ASAP 2020, Micromeritics; Norcross, GA, USA) using corresponding nitrogen adsorption-desorption isotherms obtained at 77 K. The samples were previously outgassed at 523 K for several hours. The N2 adsorption data at relative pressures ranging from 105 to 0.99 (in a set of values previously fixed) were analyzed.

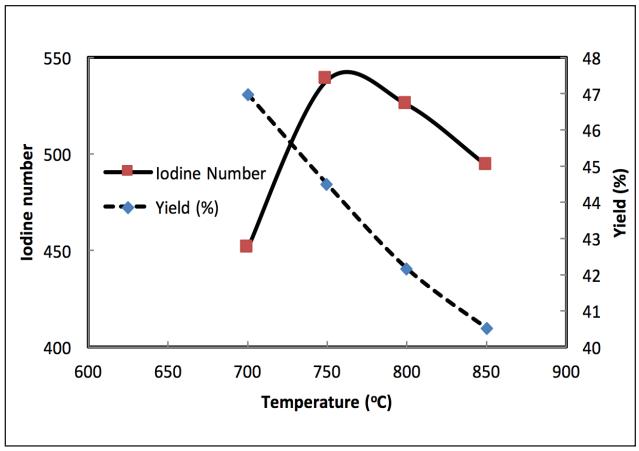
RESULTS AND DISCUSSION

Analysis of KOH lignin

Table I shows the proximate and ultimate analysis of KOH black liquor lignin. The carbon content was 55.4%. Hayashi et al. [13] found that carbon content in the kraft liquor lignin from softwood was 59.8%, while Jin et al. [15] showed that

Proximate Analysis	
Moisture, %	11.72
Ash, %	11.97
Klason lignin, %	74.70
Ultimate Analysis	
Carbon, %	55.37
Hydrogen, %	4.92
Silicon, %	6.03
Calcium, %	4.95
Potassium, %	2.12
Iron, %	1.41

I. Analysis of potassium hydroxide (KOH) black liquor lignin.



1. Effect of temperature on yield and iodine number (time = 90 min and impregnation ratio = 2.0).

carbon content in wheat straw lignin was 51.8%. Carbon content in our lignin is acceptable for activated carbon preparation. The Klason lignin content accounted for 74.7% of KOH black liquor lignin, which was higher compared with wheat straw lignin obtained by Jin et al. [15]. As shown in Table I, the ash content in KOH lignin was higher (12%) than the ash content in wheat straw lignin [15], but comparable to kraft lignin (11.2%) reported by Fierro et al. [14].

Iodine number and yield

The effects of the preparation conditions on the activated carbon produced from KOH lignin–H_3PO_4 activation (temperature 700°C–850°C, H_3PO_4-to-lignin impregnation ratio of 1.0–3.0, and impregnation time 60–120 min) were varied. **Fig. 1** shows the effect of temperature on the yield and iodine number of the produced activated carbon by H_3PO_4 chemical activation. The activation time (90 min) and impregnation ratio of 2.0 were kept constant to explore the effects of activation. As shown in Fig. 1, the yield of activated carbon decreased gradually with increasing temperature because of the burn off, which created more numerous pores formed in higher activation temperature. The pores would widen and consequently, the adsorption capacity of activated carbon increased to a certain value and then decreased with increasing temperature. As compared with H_3PO_4 activation, KOH showed much lower yield and higher iodine number (**Table II**). At the condition of 850°C for 90 min of activation in the impregnation ratio of 2.0, KOH produced activated carbon of 10.4% with iodine number 1115, which is not economically viable. In comparison, H_3PO_4 activation in the same conditions produced yield of 40.5% with iodine number 494 (experiment 4). The maximum yield in H_3PO_4 activation was 50.5% with iodine number 515.7 at the conditions of 800°C for 60 min of activation and impregnation ratio of 2.0 (experi-

Experiment No.	Temperature, °C	Activating Agent	Ratio	Time, min	Yield, %	In, mg/g
1	700	H_3PO_4	2.0	90	47.00	451.10
2	750	H_3PO_4	2.0	90	44.50	538.27
3	800	H_3PO_4	2.0	90	42.17	525.70
4	850	H_3PO_4	2.0	90	40.52	494.22
5	800	H_3PO_4	2.0	60	50.68	515.71
6	800	H_3PO_4	2.0	90	42.17	525.70
8	800	H_3PO_4	1.0	60	—	—
9	800	H_3PO_4	2.0	60	50.68	515.71
10	800	H_3PO_4	2.5	60	49.25	524.99
11	800	H_3PO_4	3.0	60	48.16	541.61
12	800	KOH	2.0	60	40.25	—
13	800	KOH	1.0	120	29.9	403.50
14	800	KOH	2.0	90	18.63	393.42
15	900	KOH	1.0	120	14.70	732.70
16	900	KOH	1.5	120	13.90	938.40
16	850	KOH	2.0	90	10.38	1,115.21

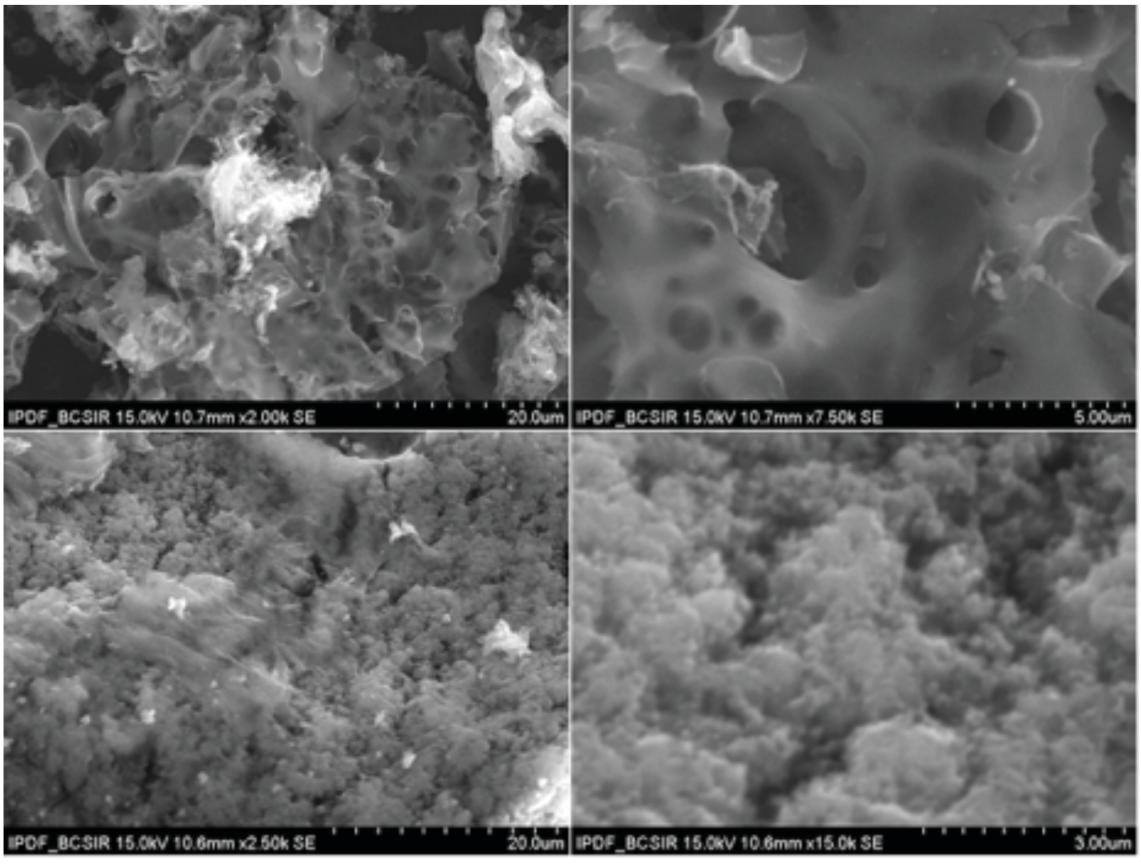
H_3PO_4 = phosphoric acid; KOH = potassium hydroxide.

II. Optimization of activated carbon production from KOH pulping liquor from rice straw.

Experiment No.	Activating Agent	Ratio	Time, min	Temperature, °C	S_{BET}, m^2/g	Pore Volume, cc/g	Pore Diameter, nm	Total Pore Volume, cc/g
1	H_3PO_4	2.0	90	700	688	0.790	14.309	7.860e-01
2	H_3PO_4	2.0	90	750	981	0.703	14.195	8.487e-01
3	H_3PO_4	2.0	90	800	822	0.795	14.353	9.017e-01
4	H_3PO_4	2.0	90	850	827	0.578	14.156	7.676e-01
5	H_3PO_4	2.0	60	800	1016	0.910	14.401	1.039e+00
7	H_3PO_4	2.0	120	800	854	0.641	14.161	7.569e-01
8	H_3PO_4	1.0	60	800	7.2	0.028	37.868	2.144e-02
10	H_3PO_4	2.5	60	800	1063	1.059	14.385	1.097e+00
11	H_3PO_4	3.0	60	800	976	0.698	14.170	8.923e-01
12	KOH	1.0	120	800	358	0.350	19.420	3.591e-01
14	KOH	1.0	120	900	599	0.239	14.195	4.276e-01
15	KOH	1.5	120	900	927	0.646	14.373	7.574e-01

H_3PO_4 = phosphoric acid; KOH = potassium hydroxide.

III. Surface area of prepared activated carbon.



2. Scanning electron microscope (SEM) micrograph of activated carbon with phosphoric acid (H_3PO_4; top) and as potassium hydroxide (KOH; bottom) activation (experiments 10 and 16).

ment 5). At this optimum condition of H_3PO_4 activation, KOH activation produced yield of 40.2% but iodine number was not measurable (experiment 12). Therefore, activation with H_3PO_4 needs to be optimized to increase iodine number. The lower yield in KOH activation can be explained by the fact that the increased amount of KOH will drop the yield of the final product as potassium ions adhere on the surface of carbon and act as a catalyst and intensify the gasification of self-generated carbon dioxide [10]. Impregnation is a more effective method than mixing precursors with solid KOH, which increased BET surface area of the produced activated carbon [10].

Table II also shows the effect of time on the yield and iodine number of the produced activated carbon (experiments 5–7). The activation temperature (800°C) and H_3PO_4-to-lignin ratio (2:1) were set and the activation time was varied from 90 to 120 min to examine the effects of activation time on yield and iodine number. The yield of activated carbon decreased with increased activation time. The iodine number increased gradually from 515 to 560 mg/g with increasing activation time from 90 to 120 min.

The ratio of H_3PO_4 to lignin was varied from 1.0 to 3.0 and its effect on yield and iodine number were studied (Table II, experiments 8–11), while the activation temperature (800°C) and activation time (60 min) were kept constant. A ratio of H_3PO_4 to lignin below 1.5 led to insufficient activated carbons (i.e., the iodine adsorption value was relatively low). However, higher values led to materials with too wide pores (i.e., the iodine adsorption value was also low). Consequently, on increasing the ratio of H_3PO_4 to lignin, more pores would be formed. When the ratio reached a certain value, the pores would be widened and burnt off. Therefore, adsorption capacity of the activated carbon would increase to a certain value and then decrease with the H_3PO_4-to-lignin ratio.

BET surface area and pore volume

Some of the produced activated carbon was further analyzed for BET surface area (**Table III**). The reaction of lignin with H_3PO_4 starts as soon as the components are mixed together [7]. Lai [18] reported the cleavage of aryl ether bonds accompanied by dehydration, degradation, and condensation reactions together with the formation of ketones by hydrolysis of ether linkages at low temperatures. The activation of lignin with H_3PO_4 at 800°C for 60 min with the impregnation ratio of 1.0 produced very low surface area of 7 m^2/g and pore volume of 0.028 cm^3/g. The surface area increased with the increase of carbonization temperature, time, and impregnation ratio. Increasing activation temperature from 700°C to 800°C for 90 min with an impregnation ratio of 2.0 increased BET surface area from 688 m^2/g to 822 m^2/g. Further increase of temperature did not increase BET surface area (experiment 4). BET surface area increased dramatically to 1016 m^2/g with the reduction of activation time to 60 min (experiment 5) and further increased to 1063 m^2/g with increased impregnation ratio (experiment 10).

The surface area of activated carbon from lignin was up to 1063 m^2/g with H_3PO_4 activation under the conditions of 60 min activation time at 800°C and an impregnation ratio of 2.5. At these conditions, the pore volume was 1.059 cm^3/g. The surface area and pore volume were considerably reduced with the increase of impregnation time, temperature, and ratio. Phosphate and polyphosphate bridges could degrade with higher temperature, time, and impregnation ratio [7,19], consequently weaken the structure and result in collapse, and ultimately lower both the BET surface area and the pore volume. It can also be interpreted to cause contraction and collapse of pores at higher time and temperature; consequently, pore volume and surface area became smaller [20]. Fierro et al. [7,14] showed that 600°C is the optimum temperature for surface development in activated carbon prepared by orthophosphoric acid activation of kraft lignin. In our study, raw material was KOH lignin, which might explain different conditions for maximum surface area. Similarly, Hayashi et al. [13] also observed that at temperatures greater than 600°C, alkali metal compounds work effectively as activating agents, but $ZnCl_2$ and H_3PO_4 activation do not.

When compared with KOH activation, surface area was much lower than H_3PO_4 activation (**Table III**). The maximum surface area and pore volume with KOH activation was 927 m^2/g and 0.646 cm^3/g at 120 min activation time at 900°C and an impregnation ratio of 1.5.

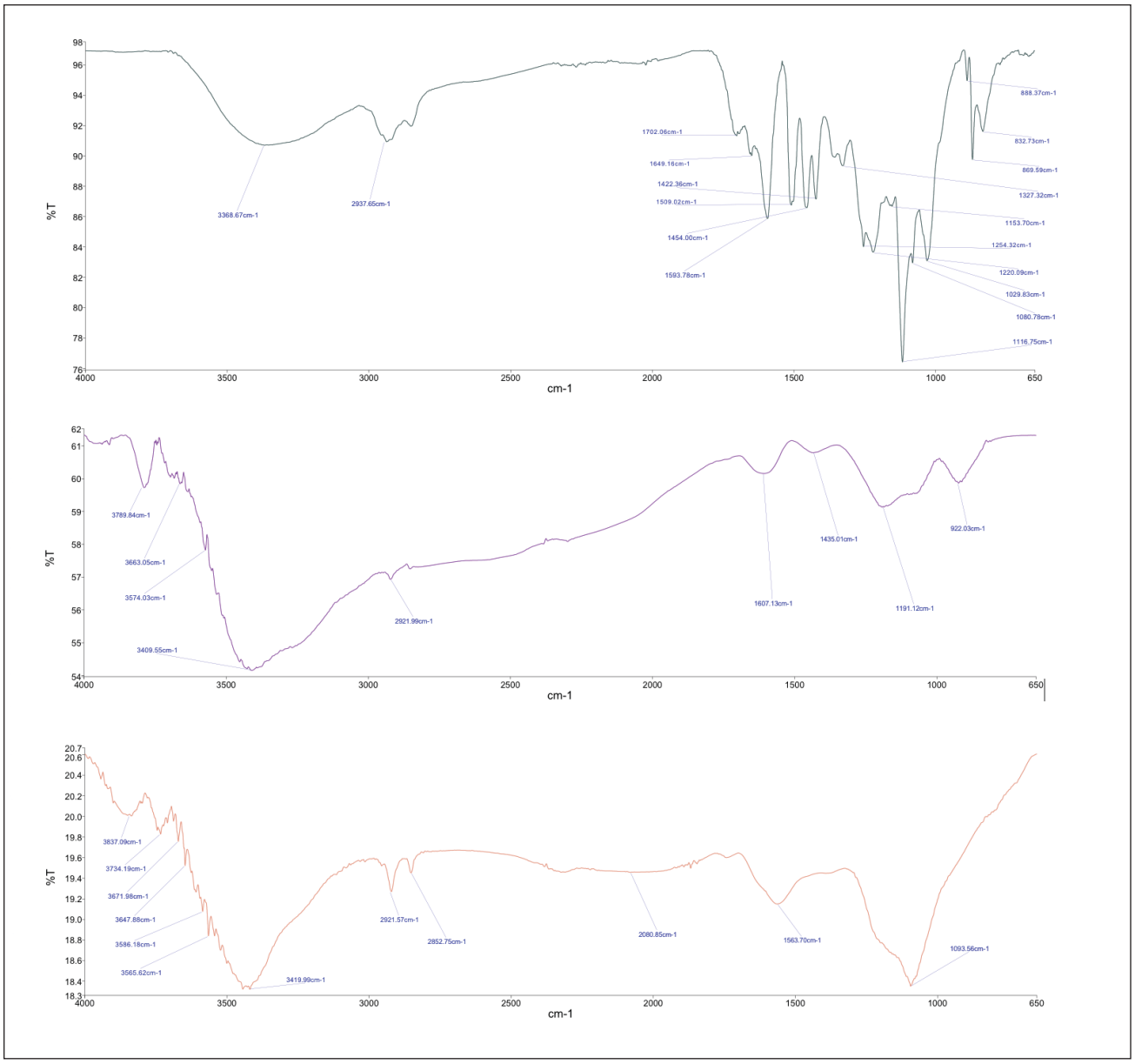
Surface morphology

Figure 2 shows an SEM micrograph of activated carbon produced from KOH liquor lignin by H_3PO_4 and KOH (experiments 10 and 15) activation. Relatively homogenous particle size distribution with cavities and pores was observed for activated carbon with H_3PO_4. Similar cavity and pore structure was observed for activated carbon with H_3PO_4 activation of corncob residue [21]. As shown in Fig. 2, KOH activation produced a surface with small pores of about 1–3 μm. This phenomenon suggested that the activating agent was effective in producing pores.

Fourier-transform infrared spectroscopy

FTIR analysis was carried out to determine functional groups of starting lignin and activated carbon produced from H_3PO_4 and KOH activation of experiments 5 and 16. The spectra are shown in **Fig. 3**.

The band at 2938 and 2850 cm^{-1} in the FTIR spectrum (Fig. 3, top), corresponding to C-H stretching in aliphatic moieties, indicated a significant contamination of lignin with lipophilic substances [23]. The bands at 1702 cm^{-1} designated carbonyl stretching–unconjugated ketones and carbonyl group in KOH lignin. The band at 1509 cm^{-1} assigned to the aromatic skeletal vibrations coupled with C-H in-plane deformations, 1454 cm^{-1}, assigned to C-H deformations (asymmetric in methyl, methylene, and methoxyl groups). KOH lignin showed strong absorbance near 1330 cm^{-1} (syringyl), which is typical for nonwood lignin [24]. The intensity of the band at 1116 cm^{-1} indicated



3. Fourier-transform infrared (FTIR) spectroscopy spectra of KOH lignin (top), activated carbon with H_3PO_4 (middle), and KOH (bottom) activation (experiments 5 and 16).

dominant syringyl structure of the KOH lignin [23]. The bands at 1220 and 1029 and shoulder at 1153 cm^{-1} indicated the presence of both guaiacyl units in the lignin molecule.

The peak at 1600 cm^{-1} present in both H_3PO_4 and KOH activated carbon is due to carboxyl group (Fig. 3, middle and bottom). There is no peak at 1410 cm^{-1}, which indicated alcoholic hydroxyl might be converted to carboxyl group. The wide peak near 1000 cm^{-1} in activation with H_3PO_4 might be due to C=P and C-P [22]. In conclusion, the results indicate that chemical activation with H_3PO_4 and KOH does not destroy aromatic structure.

CONCLUSION

Activated carbon was produced by chemical activation with H_3PO_4 of KOH lignin. The results showed that pyrolysis of KOH lignin with H_3PO_4 produced activated carbon with high BET surface areas and good carbon yields, while lignin with KOH produced lower BET surface areas and yields. Increasing activation temperature from 700°C to 800°C increased iodine number and consequently increased BET surface area. Temperatures higher than 800°C decreased both the BET surface areas and pore volumes because of shrinkage and oxidation of the material. **TJ**

ACKNOWLEDGEMENT

The authors thank the Ministry of Science and Technology, government of Bangladesh, for providing funds from the Special Allocation Project to carry out this research.

LITERATURE CITED

1. Jahan, M.S., Haris, F., Rahman, M.M., et al., *Bioresour. Technol.* 219(21): 445(2016).
2. Jahan, M.S., Sutradhar, S., Rahman, M.M., et al., *Nord. Pulp Pap. Res. J.* 30(4): 562(2015).
3. Minu, K., Jiby, K.K., and Kishore, V.V.N., *Biomass Bioenergy* 39: 210(2012).
4. Ahsan, L., Jahan, M.S., and Ni, Y., *Bioresour. Technol.* 155: 111(2014).
5. Toledano, A., Garcia, A., Mondragon, I., et al., *Sep. Purif. Technol.* 71(1): 38(2010).
6. Ariyadejwanich, P., Tanthapanichakoon, W., Nakagawa, K., et al., *Carbon* 41(1): 157(2003).
7. Fierro, V., Torné-Fernández, V., Montané, D., et al., *Thermochim. Acta* 433(1): 142(2005).
8. Kang, S., Jiang, J.C., and Xincheng, L., *J. Chem. Ind. For. Prod.* 29(B 10): 77(2009).
9. Lillo-Ródenas, M.A., Juan-Juan, J., Cazorla-Amorós, D., et al., *Carbon* 42(7): 1371(2004).
10. Guo, J. and Luaa, A.C., *J. Colloid Interface Sci.* 254(2): 227(2002).
11. Guo, Y. and Rockatraw, D.A., *Microporous Mesoporous Mater.* 100(1): 12(2007).
12. Jagtoyen, M. and Derbyshire, F., *Carbon* 36(7–8): 1085(1998).
13. Hayashi, J., Kazehaya, A., Muroyama, K., et al., *Carbon* 38(13): 1873(2003).
14. Fierro, V., Torné-Fernández, V., and Celzard, A., *Microporous Mesoporous Mater.* 92(1-3): 243(2006).
15. Jin, X.J., Yu, Z.M., and Wu, Y.U., *Cellul. Chem. Technol.* 46(1-2): 79(2012).
16. Myglovets, M., Poddubnaya, O.I., Sevastyanova, O., et al., "Preparation of carbon adsorbents from technical lignins by phosphoric acid activation," *Nord. Wood Biorefinery Conf.*, VTT Technical Research Centre of Finland, Helsinki, 2014.
17. Bansal, R.C., Donnet, J.B., and Stoeckli, F., *Active Carbon*, Marcel Dekker, New York, 1988.
18. Lai, Y.Z., in *Wood and Cellulosic Chemistry, vol. 10* (D.N.S. Hon and N. Shirashi, Eds.), Marcel Dekker, New York, 1991, p. 455.
19. Montané, D., Torné-Fernández, V., and Fierro, V., *Chem. Eng. J.* 106(1): 1(2005).
20. Wang, L., Guo, Y., Zou, B., et al., *Bioresour. Technol.* 102(2): 1947(2011).
21. Chen, J., Zhang, L., Yang, G., et al., *BioResources* 12(3): 5928(2017).
22. Li, C. and Kumar, S., *Biomass Convers. Biorefin.* 6(4): 407(2016).
23. Faix, O., *Holzforschung* 45(s1): 21(1991).
24. Jahan, M.S., Chowdhury, D.N., Islam, M.K., et al., *Bioresour. Technol.* 98(2): 465(2007).

ABOUT THIS PAPER

Cite this article as: Sarkar, M., Tian, C., Sarwar Jahan, M. *TAPPI J.* 17(2):63(2018). https://doi.org/10.32964/TJ17.02.63

DOI: https://doi.org/10.32964/TJ17.02.63

ISSN: 0734-1415

Publisher: TAPPI Press

Copyright: ©TAPPI Press 2018

About this journal

ABOUT THE AUTHORS

Small-scale potassium hydroxide (KOH) pulping generates black liquor, which contains lignin. Use of this lignin will produce biobased products and protect the environment. This research is a continuation of our nonwood biorefinery work. In this research, lignin fraction is used. It is the first time KOH liquor lignin has been used for activated carbon production.

Activated carbon washing was the most difficult task. We solved it by filtration followed by repeated centrifugation. KOH lignin can add value to different products, and our work showed that higher activated carbon yield with good surface area can be obtained from KOH lignin.

Small-scale pulp mills, especially in the Asian region, can use this concept to add value to products and reduce environmental problems. The next step is to scale up the study.



Jahan



Sarkar



Tian

Jahan is chief science officer and Sarkar is a research chemist, Pulp and Paper Research Division, BCSIR Laboratories, Dhaka, Bangladesh. Tian is director, China National Pulp and Paper Research Institute, Beijing, China. Email Jahan at sarwar2065@hotmail.com.

Static and dynamic sorption of lignin removed Populus euramericana

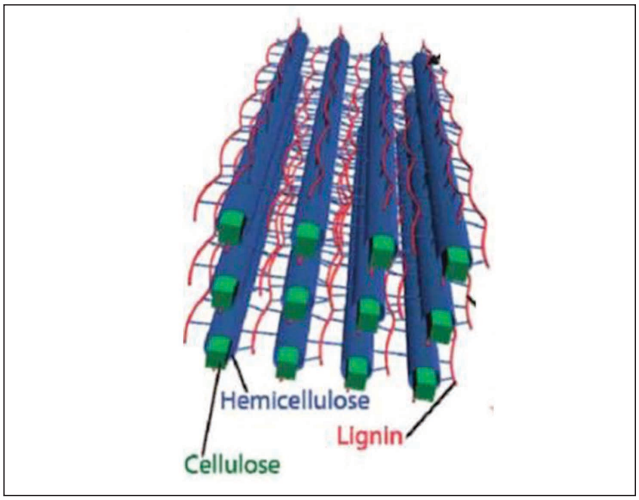
HAIZHEN ZHOU, JINGYU LI, AND ERNI MA

ABSTRACT: To investigate the effect of lignin on moisture sorption behaviors of wood under static and dynamic conditions, *Populus euramericana* cultivars measuring 20 mm tangentially × 20 mm radially × 4 mm along the grain was divided into three groups: untreated, extractives removed, and lignin removed. All the samples were subjected to static sorption where relative humidity (RH) was controlled at 11%, 45%, and 75%, and dynamic sorption where RH changed sinusoidally between 45% and 75% for cyclic periods of 1 h and 24 h, both conditions kept at 25C°. Moisture changes were measured during the adsorption and desorption processes. Moisture of the samples varied rapidly at the initial stage during static sorption. The rate decreased gradually until equilibrium was reached. Moisture changes for dynamic condition were generally sinusoidal but lagged behind the imposed RH. The moisture content difference ($\Delta MC_{45\text{-}75}$) and moisture sorption coefficient (Z) were higher under static conditions, whereas the hysteresis ratio showed greater values in the dynamic environment. Among the three groups, the lignin-removed samples exhibited the highest $\Delta MC_{45\text{-}75}$, Z, and hysteresis ratio, followed by the extractives removed and untreated samples.

Application: Results from this study provide further insights into the physical properties of the chemical components of wood and sorption relative to the main components of wood.

Wood is a natural material with hygroscopicity. The moisture content in wood is always changing, and this significantly affects the physical and mechanical properties as well as biological deterioration performances of wood [1-3]. This inevitably affects the performance of wood products. The interaction between wood and water is therefore an important consideration that can provide theoretical guidance for developing modifications and treatments and ensuring the durability and sustainability of woodwork.

As a natural polymer, wood is mostly composed of cellulose, hemicellulose, and lignin, and a minor amount of extractives. Cellulose and hemicellulose are polysaccharides that are rich in free hydroxyl groups, which are capable of absorbing moisture by forming hydrogen bonds. Therefore, the amount of cellulose and hemicellulose in the wood contributes to its hygroscopicity. On the other hand, lignin is relatively hydrophobic because of the networks developed by phenylpropane units mainly through ether bonds, leading to most hydroxyl groups being not available to water molecules. Furthermore, lignin exists outside of cellulose and hemicellulose (**Fig. 1**) [4], and covalently cross-links with hemicellulose to form lignin-carbohydrate complex (LCC). As a result, delignification causes an increasing exposure of hydroxyl groups and then weakens the water resistance capabilities of wood [5,6]. In addition, removing extractives will encourage wood sorption because extractives deposit in the cell cavity, which could block the passage for water [7]. Small extractive molecules can even enter the internal spaces in the cell wall and occupy the sites for water adsorption [8]. Therefore, the chemical components play a key role in wood hygroscopicity through free hydroxyl groups and their combination status.



1. The arrangement of chemical components in the cell wall of wood [4].

Various studies on wood hygroscopicity have been conducted using constant temperature and relative humidity (RH). They used static conditions, with equilibrium of moisture content, sorption isotherm [9], moisture diffusion coefficient [10], and sorption hysteresis [11]. At the same time, various sorption theories have been proposed to characterize the sorption isotherm of wood, including the Brunauer–Emmett–Teller (BET) [12], Hailwood and Horrobin [13], and Dent [14] theories. Among those, the Hailwood and Horrobin model was shown by Simpson [15] to give the best fit

to experimental data. Research under static conditions can simplify the experimental operations and theoretical analyses. However, wood materials in daily life are exposed to dynamic conditions in which changes in atmospheric RH and temperature may be sinusoidal [16]. Therefore, this practical condition plays a much more important role and should be highlighted for further refinement of wood-water interaction analysis.

As early as 1983, dynamic moisture sorption had been first discussed by Chomcharn and Skaar [17]. After that, a series of research involving dimensional response [18], moisture sorption coefficient [19], and sorption hysteresis [20] were reported. On the other hand, some works focused on the mechanical properties under dynamic condition after a removal of chemical components from wood, including the creep behavior of delignified wood during RH cyclic changing processes [21] and the stress relaxation of matrix (hemicellulose and lignin) removed wood responding to periodic changes of temperature [22]. However, the moisture sorption of chemical removed samples under dynamic conditions, as a basic research, gained less attention.

In a previous study [11], the moisture changes of hemicellulose-removed wood flour during adsorption and desorption processes were studied. Based on this, the effect of hemicellulose on moisture sorption of wood was clarified. This paper further dealt with the effect of lignin. Moisture changes of the samples were measured and compared between the static and dynamic condition. Results from this study could not only provide some fundamental data for the physical properties of chemical components of wood, but also prompt a new insight into wood sorption through the interactions between the main components of wood.

EXPERIMENTAL

Materials

The test material was poplar (*Populus euramericana* cultivar) sapwood without clear defects, measuring 4 mm along the grain and 20 mm in tangential and radial directions.

Chemical treatment

The samples were dried at 105°C until a constant weight (m0) was obtained, and then divided into three groups: untreated (control), extractives removed (DE), and lignin removed (DL), Chemical treatments were conducted as follows:

- **Extractives removed**: The samples were extracted with a mixture of ethanol and benzene (1:2 volume ratio) for 48 h and then boiled for 3 h at 60°C in the same solution heated by water bath to remove soluble extractives. They were then washed with distilled water, air-dried, and finally dried at 105°C until a constant weight (m_1) was achieved [22].
- **Lignin removed**: The DE was further delignified with a mixture of 967 mL distilled water, 20 g sodium chlorite ($NaClO_2$), and 13 mL acetic acid (CH_3COOH) at 40°C in a water bath for 30 h and then washed with distilled water, air-dried, and dried at 105°C until a constant weight (m_2) was achieved [21].

The ratio of extractives loss (P_1) and lignin loss (P_2) was calculated according to Eqs. 1 and 2:

$$P_1 = \frac{m_0 - m_1}{m_0} \times 100\% \quad (1)$$

$$P_2 = \frac{m_0 - m_2}{m_0} \times 100\% \quad (2)$$

Approximately 3% of extractives in DE and 10% of the lignin in DL were removed, each based on the oven-dried weight of the sample. After chemical treatment, all the samples were kept in a sealed container for later use.

Fourier transform infrared spectroscopy (FTIR)

The samples were pulverized (100 mesh), mixed with potassium bromide (KBr), and pressed as pellets before being examined by Fourier transform infrared spectroscopy (FTIR) (Bruker VERTEX 70V; Ettlingen, Germany) in the scanning range of 400 cm^{-1} to 4000 cm^{-1}, and a resolution of 4 cm^{-1}, and 32 scans per sample were used.

Static sorption

Samples at the fiber saturation point (conditioned at 100% RH) and the over-dried condition were separately exposed to three RH conditions for desorption and adsorption: 11%, 45%, and 75% at 25°C. Moisture changes were measured at certain time intervals during the processes. The moisture content (MC) of the samples was calculated as follows:

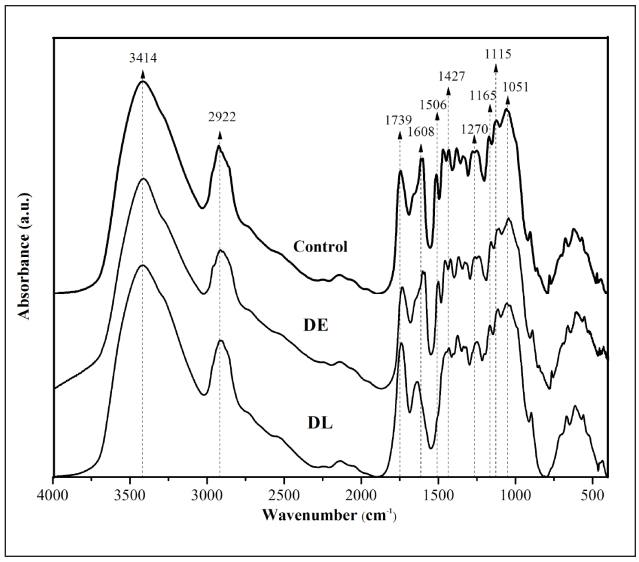
$$MC = \frac{M_n - M_0}{M_0} \times 100\% \quad (3)$$

where the M_0 and M_n are weights for over-dried samples and samples after n hours of desorption or adsorption.

The three RH conditions were obtained using saturated salt solutions of lithium chloride, potassium carbonate, and sodium chloride, respectively [23]. Sorption isotherms of the samples were then calculated from the equilibrium moisture content measured under the three RH conditions according to Hailwood and Horrobin sorption theory [13].

Dynamic sorption

The samples were subjected to 45% RH conditions controlled by a saturated salt solution of potassium carbonate [23] at 25°C. They were then moved into a conditioning oven (DHS 225, Beijing Yashilin Test Equipment Co.; Beijing, China) for the dynamic cyclic tests, where RH was changed sinusoidally between 45% and 75% (±3%), cycled at two periods of 1 h and 24 h at 25°C. The cycle at the period of 1 h was aimed to investigate moisture responses to rapid RH variation. The



2. Fourier transform infrared spectroscopy (FTIR) spectra for different chemical component-removed samples.

period of 24 h was designed to simulate daily RH change. During the process, weight changes were monitored every 1 min and 15 min for each of the two periods, respectively.

RESULTS AND DISCUSSION

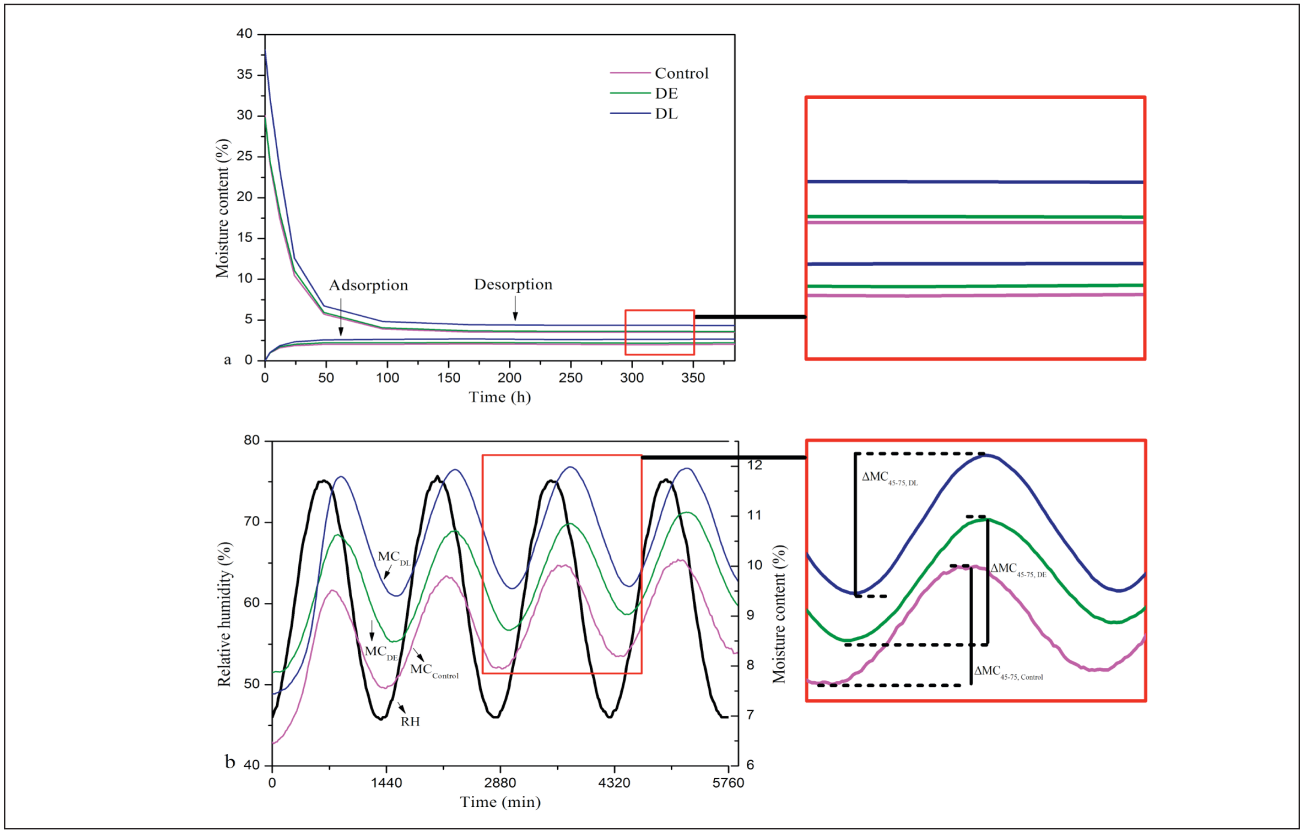
Analysis of chemical components based on FTIR

Figure 2 shows the FTIR spectra for various chemical component-removed samples; all of them were normalized based on the highest peak of around 3414 cm^{-1}, which is assigned to O-H stretching. Generally, O-H stretching absorption bands and C-H absorption bands (around 2922 cm^{-1}) play a limited role in the analysis of changes in wood chemical components because the three main chemical constituents of wood all contain hydroxyl and methylene [24].

The intensity of the peaks at 1608 and 1427 cm^{-1} in Fig. 2 are assigned to benzene ring vibration originating mainly from lignin [25] in DL. As compared with the DE, these intensity peaks decrease significantly. Another characteristic peak of lignin at 1506 cm^{-1} (C=C stretching vibration) [26] disappears after lignin removal treatment, suggesting a decrease in the relative amount of lignin for the DL. The absorbance at 1270 cm^{-1} is characteristic of argon-oxygen (Ar-O) stretching [27] or α, β-aryl ether [28] in lignin. The intensity of this absorption in DL fades, indicating that an ether cleavage reaction occurred in DL during the delignification. What's more, the positive signal at 1739 cm^{-1} assigned for C=O stretch originating mainly from hemicellulose [29] shows an increase in the relative amount of hemicellulose within the DL caused by lignin removal.

Moisture responses at static and dynamic conditions

Figure 3 shows moisture responses of samples to a given humidity, 11% at 25°C (static condition), and sinusoidally varying RH cycled for 24 h at 25°C (dynamic condition) as exam-



3. Moisture changes of the samples at static (11% relative humidity [RH]) and dynamic (b: 24 h, 45%–75% RH) conditions.

ples. Moisture changes rapidly for all three groups at the initial stage during static sorption, after which the rate gradually decreases until a state of equilibrium is reached (Fig. 3a). On the other hand, the moisture content for all three groups is generally sinusoidal, but lags behind the imposed RH for dynamic sorption (Fig. 3b).

Among the three groups, the lignin-removed samples had the highest moisture content, followed by the extractives-removed samples and the untreated samples. As mentioned previously, extractives exist in cell lumen and cell walls, which can slightly restrain the moisture sorption of wood. In the case of lignin, because it mainly locates outside of the hydrophilic polysaccharides (cellulose and hemicellulose) (Fig. 1), delignification might provide more accessible spaces for water molecules, and thus increase the capacity to accommodate water in cell walls. Another reason for this is that most of the lignin is believed to covalently cross-link the hemicelluloses to form a lignin-carbohydrate complex [30]. As a result, removal of lignin would cause an increasing exposure of hydroxyl groups from hemicellulose [31], which would intensify wood hygroscopicity.

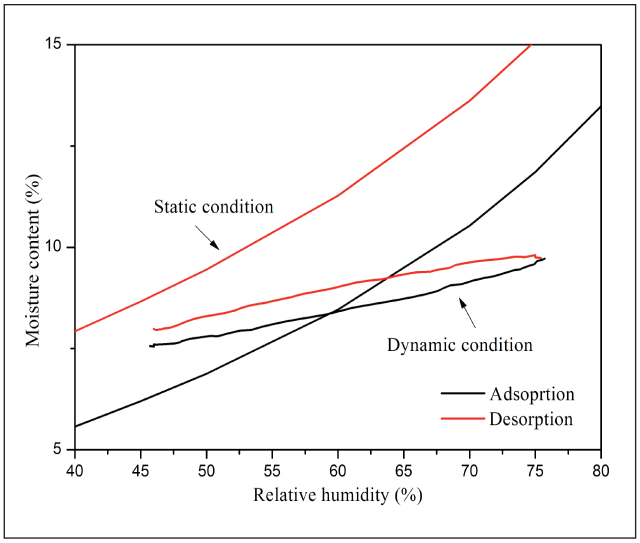
Comparison of moisture content difference

Moisture contents measured at 45% RH and 75% RH for adsorption were selected. Their differences were worked out and defined as $\Delta MC_{45\text{-}75}$ (Fig. 3). **Table I** lists the $\Delta MC_{45\text{-}75}$ under static and dynamic conditions. It is apparent that $\Delta MC_{45\text{-}75}$ at static condition is significantly larger than that from the dynamic condition. This is because the sorption time is sufficient to respond to a constant RH at static state rather than the varying RH under dynamic condition, where $\Delta MC_{45\text{-}75}$ (amplitude) is greater for all the groups exposed to a longer cyclic period (24 h). This agrees with the results reported by Chomcharn and Skaar [17]. On the other hand, a comparison of $\Delta MC_{45\text{-}75}$ among different sample groups demonstrates that DL is larger than the control and DE, suggesting that delignified would enhance moisture change through increasing hygroscopicity, based on the two reasons discussed previously.

Comparison of moisture sorption coefficient Z

Figure 4 shows sorption isotherms of the control at static and dynamic conditions. The slope of the isotherms illustrates variation in moisture content per unit RH change. Skaar [32] refers to this as the moisture sorption coefficient Z, which can be used as an index to evaluate wood hygroscopicity [33]. **Table II** shows the coefficient of the samples within the RH range of 45% to 75% in this study. The Z of the control at static condition is 0.189, which is similar to results of previous research on mean values for 28 wood species [34]. What's more, the Z at static condition is larger than that of the dynamic condition, suggesting much stronger hygroscopic ability for the samples under static condition.

Additionally, the Z of the samples is characterized by a trend that the DL shows the highest value, followed by the DE and control. This indicates that delignified treatment would promote hygroscopicity as well.



4. Sorption isotherms of the control at static (calculated by Hailwood and Horrobin sorption theory) and dynamic (45%–75% relative humidity, the second cycle of 24 h) conditions.

Comparison of moisture sorption hysteresis

As shown in Fig. 4, moisture sorption hysteresis exists in static state as well as dynamic conditions. To quantitatively investigate the sorption hysteresis, the hysteresis ratio A/D

		Control	DE	DL
Static condition[a]		5.66 (0.0014)	5.68 (0.0015)	5.93 (0.0043)
Dynamic condition[b]	1 h	1.12 (0.0388)	1.15 (0.0290)	1.20 (0.0479)
	24 h	2.10 (0.1571)	2.14 (0.0951)	2.44 (0.0817)

DE = extractives removed; DL = lignin removed.
[a] Average values (standard deviation) for adsorption from three replicates.
[b] Average values (standard deviation) of all cycles.

I. A comparison of the moisture content difference ($\Delta MC_{45\text{-}75}$ [%]) between static condition and dynamic condition for the samples.

		Control	DE	DL
Static condition[a]		0.189 (0.0047)	0.189 (0.0049)	0.198 (0.0143)
Dynamic condition[b]	1 h	0.0304 (0.0006)	0.0308 (0.0004)	0.0359 (0.0005)
	24 h	0.0649 (0.0018)	0.0678 (0.0022)	0.0778 (0.0007)

DE = extractives removed; DL = lignin removed.
[a] Average values (standard deviation) for adsorption from three replicates.
[b] Average values (standard deviation) of all cycles.

II. A comparison of moisture sorption coefficient Z between static condition and dynamic condition for the samples.

		Control	DE	DL
Static condition[a]	11%	0.581 (0.0127)	0.618 (0.0113)	0.625 (0.0140)
	45%	0.715 (0.0040)	0.718 (0.0009)	0.741 (0.0074)
	75%	0.785 (0.0023)	0.774 (0.0013)	0.805 (0.0052)
Dynamic condition[b]	1 h	0.925 (0.0020)	0.923 (0.0026)	0.929 (0.0025)
	24 h	0.944 (0.0135)	0.945 (0.0077)	0.947 (0.0031)

DE = extractives removed; DL = lignin removed.
[a] Average values (standard deviation) for adsorption from three replicates.
[b] Average values (standard deviation) of all cycles.

III. A comparison of adsorption/desorption (A/D) ratio between static condition and dynamic condition for the samples.

($MC_{adsorption}/MC_{desorption}$) for each condition was calculated (**Table III**). Specifically, maximum hysteresis, namely the minimum A/D ratio of every cycle, was considered for dynamic tests. Table III shows that the A/D ratio of the samples increases at the static condition with an increase in relative humidity, indicating a reduction in sorption hysteresis. This was because an increase in RH promoted the softening of hemicellulose [35], which weakened the difference in MC between adsorption and desorption, causing sorption hysteresis to decrease. What's more, A/D ratio is in a positive relation with cyclic period, indicating that moisture sorption hysteresis decreases with the cyclic period in this dynamic condition, which is in accordance with the previous research by Yang and Ma [36]. Compared with the static condition, the A/D ratio of the samples in the dynamic condition is remarkably larger. This could be attributed to a diminution of hygroscopic response ability of wood to the changing environment.

In addition, the DL show maximum A/D ratios among the three groups, implying a reduction in sorption hysteresis caused by deligninfication. Matrix stiffness is imparted by lignin; therefore, the flexibility of all macromolecules in the glassy state is lowered. On adsorption, water molecules cause swelling of glassy materials, resulting in the creation of nanopores and new sorption sites. On desorption, lignin prolongs the time lag between the water molecules departing and matrix relaxation because of its stiffness effect [37]. Fibers with higher lignin contents, and consequently with a higher stiffness of the matrix macromolecules, display greater hysteresis [38]. Thus, lignin significantly contributes to the extent of hysteresis.

CONCLUSIONS

Moisture responses of delignified wood under static condition and dynamic condition were investigated in this study, giving the following results:

1) At a given range of RH condition, the moisture content difference, moisture sorption coefficient, and sorption hysteresis of the samples were higher under static conditions because of a relative longer response time compared with dynamic conditions.
2) The lignin-removed samples exhibited the highest moisture difference, moisture sorption coefficient, and hysteresis ratios at static and dynamic conditions, followed

by the extractives samples and untreated samples. This implies an increase in hygroscopicity and a reduction in sorption hysteresis after delignification because of the depositon outside of the wood cell wall and relative hydrophobicity for lignin. **TJ**

ACKNOWLEDGEMENTS

We thank the Fundamental Research Funds for the Central Universities of China (No.2017ZY47. No. 2015ZCQ-CL-01) and the Beijing Higher Education Young Elite Teacher Project (No.YETP0762) for their financial support.

LITERATURE CITED

1. Widehammar, S., *Exp. Mech.* 44(1): 44(2004).
2. Stefanie, E., Stanzl, T., and Navi, P., *Holzforschung.* 63(2): 139(2009).
3. Thybring, E.E., *Int. Biodeterior. Biodegrad.* 82(82): 87(2013).
4. Zakzeski, J., Bruijnincx, P.C., Jongerius, A.L., et al., *Chem. Rev.* 110(6): 3552(2010).
5. Zhou, H.Z., Xu, R., and Ma, E.N., *Chin. Agric. Sci. Bull.* 30(25): 49(2014).
6. Ou, R., Xie, Y., Wolcott, M.P., et al., *Mater. Des.* 58(6): 339(2014).
7. Ma, E.N. and Zhao, G.J., *Special Topics on Wood Physics*, China Forestry Publishing House, Beijing, 2012.
8. Panshin, A.J. and Zeeuw, C.D., *Textbook of Wood Technology*, McGraw-Hill Book Company, New York, 1980.
9. Liu, Y.X. and Zhao, G.J., *Wood Resources in Materials Science*, China Forestry Publishing House, Beijing, 2004.
10. Stamm, A.J., *For. Prod. J.* 9(1): 27(1959).
11. Zhou, H.Z., Xu, R., and Ma, E.N., *BioResources* 11(2): 3110(2016).
12. Brunauer, S., Emmett, P.H., Teller, E., *J. Am. Chem. Soc.* 60(2): 309(1938).
13. Hailwood, A.J., and Horrobin, S., *Trans. Faraday. Soc.* 42(B): 84(1946).
14. Dent, R.W., *Text. Res. J.* 40: 145(1977).
15. Simpson, W.T., *Wood Fiber* 5(1): 41(1973).
16. Schniewind, A.P., *Wood Sci. Technol* 1(4): 278(1967).
17. Chomcharn, A. and Skaar, C., *Wood Sci. Technol.* 17(4): 259(1983).
18. Ma, E.N., Nakao, T., Zhao, G.J., et al., *Wood Sci. Technol.* 42(2): 229(2010).
19. Yang, T.T. and Ma, E.N., *BioResources* 10(1): 1675(2015).
20. Yang, T.T., Ma, E.N., and Zhang, J., *Holzforschung.* 70(12): 1191(2016).
21. Zhang, W.B., Tokumoto, M., Takeda, T., et al., *J. Jpn. Wood Res. Soc.* 52(1): 19(2006).
22. Xie, M.H., "Stress relaxation of chemically treated wood," Ph.D. thesis, Beijing Forestry University, Beijing, 2006.
23. Macromolecule Academy, *Physical Properties of Macromolecules*, Kyoritsu Press, Tokyo, 1958.
24. Zhang, F.D., Xu, C.H., Li, M.Y., et al., *J. Mol. Struct.* 1069(1): 89(2014).

ABOUT THE AUTHORS

Chemical components play a key role in wood hygroscopicity, which can significantly affect the processing and use of wood products.

In a previous study, the moisture changes of hemicellulose-removed wood flour during adsorption and desorption processes were studied. This paper further dealt with the effect of lignin. Moisture changes of the samples were measured and compared between the static and dynamic conditions.

In this research, the most difficult aspect was to find a suitable way to remove lignin from *Populus*. Through literature searches and various tests, we identified the most appropriate method of lignin-removal for use.

The study showed that the moisture content difference, moisture sorption coefficient of the samples, was higher under static conditions. In contrast, the hysteresis ratio showed greater values in a dynamic environment.

One of the most interesting findings from this study is that delignified treatment would promote hygroscopicity in static and dynamic conditions.

Results from this study could not only provide some fundamental data for the physical properties of chemical components of wood, but also prompt a new insight into wood sorption through the interactions between the main components of wood.

In future work, we will attempt to improve the dimensional stability of wood through lignin impregnation. The idea is to use the hydrophobic effect of lignin and the formation of covalent bonds between small lignin molecules with chemical components of wood cell wall to block water passageways in cell lumen.



Zhou



Li



Ma

Zhou and Li are post-graduate students and Ma is associate professor, Beijing Key Laboratory of Wood Science and Engineering, MOE Key Laboratory of Wooden Material Science and Application, Beijing Forestry University, Beijing, China. Email Ma at maerni@bjfu.edu.cn.

25. Huang, Y.X., Ma, E.N., and Zhao, G.J., *Ind. Crops Prod.* 69: 447(2015).
26. Moniruzzaman, M. and Ono, T., *Bioresour. Technol.* 127(1):132(2013).
27. Cheng, X.B., "The influence of incipient brown rot on the properties of Chinese fir at macroscopic and tissue level," M.S. thesis, Chinese Academy of Forestry, Beijing, 2011.
28. Sui, X.J., "Study on the catalytic liquefaction of industrial kraft lignin for the production of phenols," Ph.D. thesis, South China University of Technology, Guangzhou, China, 2011.
29. Labbé, N., Rials, T.G., Kelley, S.S., et al., *Wood Sci. Technol.* 39(1): 61(2005).
30. Ralph, J., Grabber, J.H., and Hatfield, R.D., *Carbohydr. Res.* 275(1): 167(1995).
31. Iversen, T., *Wood Sci. Technol.* 19(3): 243(1985).
32. Skaar, C., *Wood-Water Relations*, Springer, Berlin, 1988.
33. Yang, T.T. and Ma, E.N., *Funct. Mater.* 44(24): 3055(2013).
34. Noack, D., Schwab, E., and Bartz, A., *Wood Sci. Technol.* 7(3): 218(1973).
35. Engelund, E.T., Thygesen, L.G., Svensson, S., et al., *Wood Sci. Technol.* 47(1): 141(2013).
36. Yang, T.T. and Ma, E.N., *J. Korean Wood Sci. Technol.* 44(2): 191(2016).
37. Hosseinpourpia, R., Adamopoulos, S., and Mai, C., *Wood Sci. Technol.* 50(1): 1(2016).
38. Hill, C.A.S., Norton, A., and Newman, G., *J. Appl. Polym. Sci.* 112(3): 1524(2009).

ABOUT THIS PAPER

Cite this article as: Zhou, H., Li, J., Ma, E. *TAPPI J.* 17(2): 71(2018). https://doi.org/10.32964/TJ17.02.71

DOI: https://doi.org/10.32964/TJ17.02.71

ISSN: 0734-1415

Publisher: TAPPI Press

Copyright: ©TAPPI Press 2018

About this journal

Lignocellulose fibers elaborating super-swollen three-dimensional cellulose hydrogels from solution in N,N-dimethylacetamide/lithium chloride

ALEKSANDRA MIKHAILIDI, SHAHRIAR KARIM SAUROV, SEPPO ANDERSSON, AND NINA KOTELNIKOVA

ABSTRACT: Super-swollen hydrogels were prepared in vitro from lignocelluloses of various origins via direct dissolving in N,N-dimethylacetamide/lithium chloride (DMAc/LiCl) followed by regeneration from solutions. The hydrogels retained a large amount of water (up to 2500 wt%) and had high porosity and specific surface areas. Superabsorbance of the hydrogels was confirmed with a wide angle X-ray scattering method. The hydrogels seem to be smart matters due to PH-dependent behavior by swelling and pH change experiments. The gelation mechanism includes spontaneous self-assembly from the solutions in DMAc/LiCl, due to the reconstruction of new hydrogen bond webs between lignocellulose chains and water. The hydrogels exhibited high stability but their morphology changed while drying due to water removal and the collapse of the H-bonds.

Application: Super-swollen hydrogels have potential for biomedical, pharmaceutical, and industrial purposes. Applications might include scaffolds for tissue engineering and composite hydrogels with organic and inorganic substances for surgical interventions.

Cellulose-based hydrogels have attracted much attention because these biodegradable polymers have numerous advantages. Cellulose-based hydrogels prepared from suspensions of nanofibrillar cellulose have been studied extensively [1]. Plant-derived cellulose has been broadly applied in the paper, textile, and food and cosmetic industries, as well as in biomaterials in medicine [2-4]. The hydrogels can be also formed from solutions of cellulose derivatives (e.g., hydroxypropylcellulose, carboxymethycellulose, and methylcellulose [5]), from cellulose-based composites or cellulose/synthetic hybrid polymers [6-11], and many others. Other than cellulose, the composites have included various types of natural (e.g., chitosan, agarose, collagen, proteins, and deoxyribonucleic acid) [9,12,13] and synthetic components (e.g., polyvinyl alcohol, polyethylene glycol, peracetic acid, or polymethacrylic acid) [2,8] and have exhibited a wide range of properties.

The majority of studies have been made on bacterial celluloses that formed the hydrogels due to the peculiarities of the synthesis and shapes [2]. Plant-derived cellulose rarely has been applied to prepare the hydrogels. Natural cellulose has poor solubility due to the strong hydrogen bonding between the hydroxyl groups involved in the cellulose chains [14]. Numerous complex solvent systems have been applied to directly dissolve the cellulose fibers to decrease the hydrogen bonding. Some of them are sodium hydroxide (NaOH)/urea aqueous solution [15], ionic liquids [16], N-methyl-2-pyrrolidinone/lithium chloride (LiCl), N,N-dimethylacetamide/LiCl (DMAc/LiCl) [17], and others.

The solvent system DMAc/LiCl is one of the most popular [18,19]. Saito and others [20] prepared the transparent cellulose hydrogels from various solutions of cellulose samples in DMAc/LiCl and studied the impact of regeneration conditions on physical properties of the cellulose hydrogels. The hydrogel obtained from the solution in a mixed water/organic medium contained 80% water but was very thin and was rather a film but not a gel [20]. Ishii and others [21] studied dissolving of cellulose in DMAc/LiCl and aggregation behavior from the solutions with small-angle X-ray scattering and polarized optical microscopy. The prepared gels were shaped as spherical particles. The particle formation depended on the concentration of the cellulose and of gelation method [21]. The relationship between the structure of cellulose in dissolved and gelled states has been determined as originating in large-scale fluctuations of the cellulose chain density. Obradovic et al. [17] prepared three-dimensionally shaped cellulosic materials via a two-step procedure: swelling of softwood pulp in DMAc/LiCl followed by molding. Swollen gels were precipitated with two antisolvents: distilled water and a combination of 2-propanol/deionized water that resulted in various X-ray structures and mechanical properties

of the precipitates. Scanning electron microscope (SEM) studies showed that the samples exhibited a change in morphology of the surface of the cellulose.

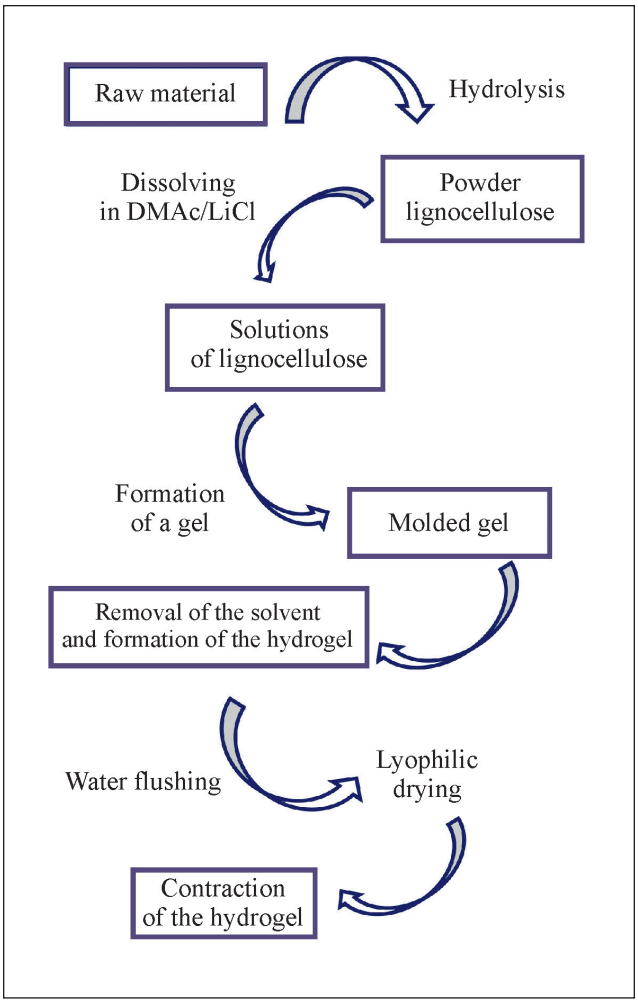
Typically, the processing of cellulose gels involves the following steps: pretreatment of starting cellulose samples to activate them, dissolution of the samples, regeneration of the cellulose, and solvent removal while avoiding cellulose agglomeration. Detailed studies on the formation of the hydrogels from DMAc/LiCl solutions and the properties of the hydrogels have been made to a lesser extent [18,20,21]. The aim of the present study was to explore the formation of self-assembled hydrogels that occurred in solutions of lignocelluloses of various origins in DMAc/LiCl. The impact of factors (e.g., the method of drying on a gelation behavior) was also a study objective. We focused mainly on the stages providing the regeneration from the dissolved state, the spontaneous gelation accompanied by the formation of the hydrogels, and subsequent drying of the hydrogels. The main chemical properties of the hydrogels were evaluated on the basis of various experimental methods.

EXPERIMENTAL

Materials and processing

Powder samples were isolated from short-length flax fibers (PF), bleached sulfite hardwood pulp (PH), and cotton cellulose (MCC). The pulp and cotton celluloses were purchased from chemical plants in Russia. All chemicals including anhydrous lithium chloride, purum p.a., purchased from Honeywell Fluka (Morristown, NJ, USA) and N,N-dimethylacetamide purchased from Sigma-Aldrich (St. Louis, MO, USA) were analytical grade.

The processing, which included the hydrolysis of the powder lignocellulose samples, the pretreatment and the dissolving of the powders in the solutions of DMAc/LiCl, and the regeneration of the samples from the solutions and spontaneous gelation, was performed as described elsewhere [19,22-25]. The PF, PH, and MCC were hydrolyzed with an aqueous solution of nitric acid with a concentration of 10 wt% to prepare the powder cellulose samples. The dissolving of lignocelluloses in DMAc/LiCl required a pretreatment of the samples. The pretreatment was processed by solvent exchange (i.e., infusing and rinsing of the powder celluloses with deionized water and then with DMAc). The dissolving procedure included heating of the pretreated samples in the solution of DMAc to 165°C. Lithium chloride was added to suspension of the cellulose samples in DMAc in the calculated quantity to achieve a concentration of LiCL of 8.0 wt% in slurry. The mixture was continuously stirred, yielding a clear or semiclear solution that was cooled to room temperature and filtered through a glass filter. To find the optimal gelation conditions, we used the solutions of the samples in DMAc/LiCl with concentrations in the range of 0.5 wt% to 5.0 wt%. Ten milliliters of every solution were poured into dishes or plastic vessels and left at ambient conditions. Spontaneous thickening of the solutions occurred gradually over 5–7 days. Upon thickening,



1. Schematic of multistage hydrogel processing.

the solutions were completely absorbed and the massive swollen samples were formed. The prepared gels were rinsed with cold and hot water several times. At this point, the solvent was replaced with the water and thus hydrogel was obtained. We controlled whether the solvent remained in the regenerated samples. The purity of the hydrogels has been confirmed with Fourier-transform infrared (FTIR) spectroscopy and with the energy-dispersive X-ray analyzer of the SEM. The regenerated samples did not contain the traces of chloride ions. Depending on the objectives, the hydrogels were air dried, dried in a vacuum oven, or freeze dried (**Fig. 1**).

Characterizations

The dissolving ability of the powder samples (D_a, %) was monitored by estimating a decrease in weight of the samples at the dissolving point (Eq. 1):

$$D_a = [(W_p - W_r) \cdot W_p^{-1}] \cdot 100 \quad (1)$$

where W_p is the weight of the powder sample and W_r is the weight of the insoluble remainder. The powder samples were dissolved to 94.8 wt%–98.7 wt%. After dissolving, the solu-

tions were filtered through a glass filter to separate the insoluble solids. These specimens were rinsed with distilled water to remove the remainder of the solvent and were dried to constant weight. The measurements of D_a were duplicated.

The solvent absorbed by the gels or water absorbed by the hydrogels quantitatively represented by equilibrium solvent content (ESC) or equilibrium water content (EWC) was calculated using Eq. 2 [26]:

$$\text{ESC or EWC} = (m_s - m_0) \cdot m_s^{-1} \quad (2)$$

where m_s is a mass of the swollen gel or hydrogel at time t at the equilibrium, and m_0 is a mass of the dried specimen to a constant weight in the vacuum.

The overall porosity of the hydrogels, P_t (i.e. proportion of sample volume occupied by pores), was calculated according to Eq. 3:

$$P_t = (1 - m_0) \cdot P^{-1} \cdot L^{-1} \cdot \varrho^{-1} \quad (3)$$

where m_0 is a weight of the hydrogel dried; P is a square of the surface of the hydrogel, cm^2; L is a thickness of the hydrogel, cm; and ϱ is a density of cellulose (ϱ = 1.561 kg m^{-3}) [27]. The hydrogels were regenerated from the solutions of PF, PH, or MCC with the concentration of 3 wt%.

Dye sorption equilibrium of the powder samples PF, PH, and MCC; the hydrogels; and the freeze-dried hydrogels was analyzed by batch sorption studies [23] using a direct dye methylene blue (MB). The maximum value of MB uptake (i.e., maximum absorption capacity of the hydrogels [A_{max}, mg•g^{-1}]) was calculated using Eq. 4 [28]:

$$A_{max} = (c_0 - c_{eq}) \cdot V \cdot W_p^{-1} \quad (4)$$

where c_0 is a concentration of the solution of MB before the absorption, mg•L^{-1}; c_{eq} is a concentration of the solution of MB after the absorption, mg•L^{-1}; V is a volume of the solution of MB taken to the absorption, L; and W_p is a mass of the powder of the hydrogel or the freeze-dried hydrogel, g.

Specific surface area of the hydrogels (SSA, g•m^{-2}) was calculated as the total surface of the sample that was in contact with the solution of MB (Eq. 5) [27,29]:

$$SSA = X_m \cdot N \cdot A_{max} \cdot M_w^{-1} \quad (5)$$

where X_m is a monolayer capacity of MB, mole g^{-1}. The mean area occupied at the solid-liquid interface by the molecule of MB corresponding to a monomolecular layer on the surface was used as 130 Å; N is Avogadro's number, $mole^{-1}$; A_{max} is a maximum absorption capacity of the hydrogel; and M_w is the molecular weight of MB.

The solubility of the freeze-dried hydrogels was examined in the water and in the solvents, including 17.5% aqueous solution of NaOH, ethanol, acetone, toluene; 86% solution of phosphoric acid (H_3PO_4); and 72% solution of sulfuric acid (H_2SO_4) and cadmium ethylenediamine solvent (cadoxen).

Swelling studies of the dried hydrogels were carried out with the freeze-dried hydrogels after immersing in media with various pH from pH 2.0 to 10.0 and then rinsed with the water. The equilibrium swelling ratios (Q) were calculated using Eq. 6:

$$Q = (m_g - m_r) \cdot m_r^{-1} \quad (6)$$

where Q is a swelling ratio, g•g^{-1}; m_r is a mass of removed hydrogel; and m_g is a mass of the swollen hydrogel at equilibrium at given pH.

Wide angle X-ray scattering measurements were performed on a 4circle goniometer (J.M. Huber; Edison, NJ, USA) using CuKα_1 radiation (λ = 1.541Å). The diffractometer was applied in a symmetrical transmission mode. The intensity was measured as a function of the scattering angle 2θ by θ–2θ scan, which was obtained from 5°–55°. The powder samples (100 mg) were pressed in an ad hoc mold to form pellets. The swollen samples were measured between Mylar thin films. To determine the degree of crystallinity (DC) of the samples, amorphous fitting analysis was used [30]. The peak width was calculated according to the Scherrer equation [31].

Macroscopic digital images of the samples were obtained in normal light with Canon Power Shot SX20 IS camera (Canon; Tokyo, Japan).

RESULTS AND DISCUSSION

Stages of the gelation

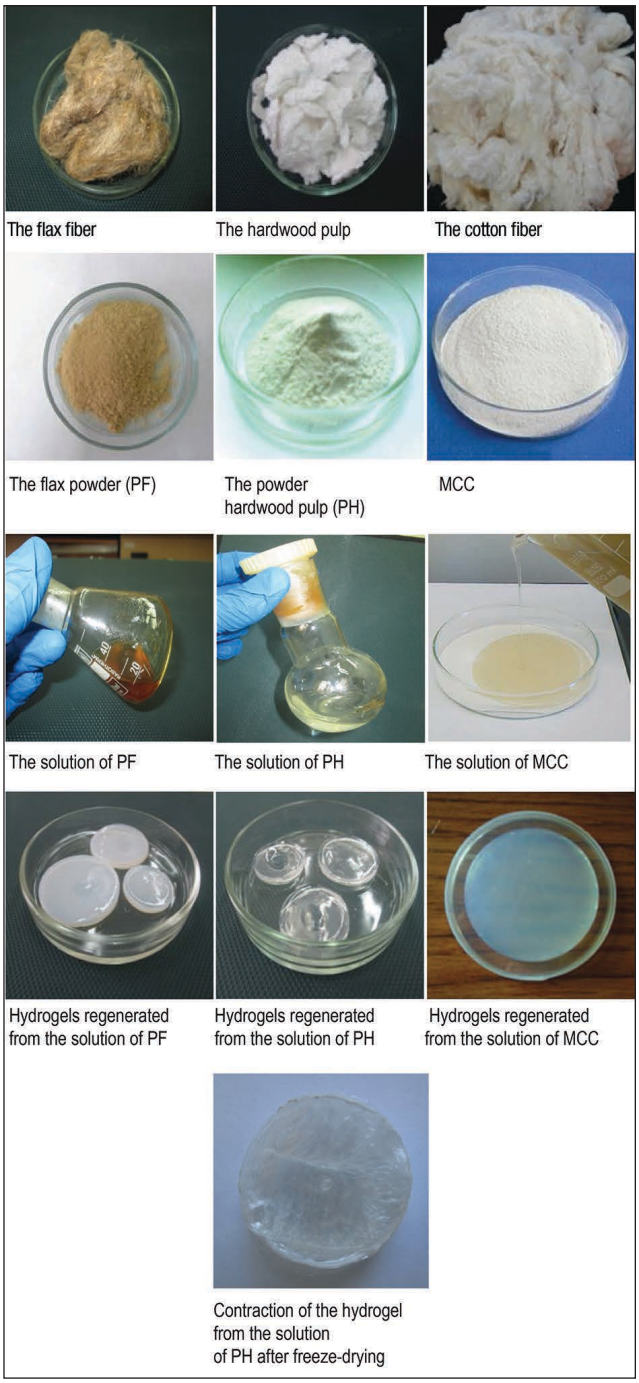
The multistage experimental processing to prepare the hydrogels is depicted in Fig. 1. Digital images of the processing are shown in **Fig. 2**. The following are the five main stages:

1. Hydrolysis of raw materials and the preparation of the powder samples.
2. Pretreatment of the powder samples and the dissolving in solution of DMAc/LiCl.
3. Slow aggregation of the solutions at the ambient atmosphere accompanied by the spontaneous gelation and the formation of the gels.
4. Removal of the solvent by rinsing with water and replacement of the solvent with the water to get the hydrogels.
5. Drying or freeze drying of the hydrogels.

The entire process was adequate and feasible.

Characteristics of the powder samples and dissolving values

Properties of the powder samples have been described elsewhere [19]. The properties are listed in **Table I**. MCC was chemically purer and had a lower degree of polymerization (DP_v) compared with PF and PH. However, PF and PH exhibited higher dissolving ability, and MCC dissolved to a lesser extent. Ordered supramolecular structure and high crystallinity of MCC essentially affected the dissolving ability. Neverthe-



2. Digital images of the hydrogel processing (DMAc/LiCl = N,N-dimethylacetamide/lithium chloride).

less, the samples dissolved to 94.8 wt%–98.7 wt% [22]. After dissolving, the solution of PH was optically clear and colorless, the solution of PF was dark yellow and slightly opalescent, and the solution of MCC was somewhat turbid (Fig. 2).

Equilibrium solvent content in the gels and water content in the hydrogels

Table II shows the data for the gels containing the solvent (ESC) and for the hydrogels containing the water (EWC) [23]. The gels and the hydrogels seemed to be super-swollen systems and retained large amounts of the solvent or the water. The EWC of the hydrogel of PF was 2500 wt%. The EWC of the hydrogel of PH was 2800 wt%. MCC had lower EWC (2000 wt%). The EWC values are similar to those of bacterial cellulose [32].

Porosity of the hydrogels

The overall porosity values for the hydrogels are shown in Table II [23]. The hydrogel of PH had the highest P_t and these values were lower for the hydrogels of PF and MCC. The P_t values also correspond to those for bacterial cellulose and are higher than for bead cellulose and for some modified or cross-linked celluloses [11,32,33].

Specific surface area of the hydrogels

Specific surface area of the PF, PH, and MCC powders; the hydrogels; and the freeze-dried hydrogels due to MB uptake are listed in **Table III** [23]. Specific surface area values for the powder celluloses were highest for MCC, followed by PH and PF. Specific surface area for the hydrogels and for the dried hydrogels was highest for PH, followed by PF and MCC. The SSA was highest for the hydrogel of PH in both the swollen and dried states. Thus, the results of the P_t study were confirmed with the dye SSA data.

Cellulose is known to belong to a class of capillary-porous systems contained in a highly branched inner and outer surface of macro- and micropores, as well as in dead-end pores voids. The values of EWS, P_t, SSA, and A_{max} showed that the hydrogels, due to the porous system, can be successful in applications for medical purposes because of the absorption of significant liquid content.

Dissolving ability of the dried hydrogels

While drying, the swollen hydrogels collapsed. The drying affected the properties of the hydrogels, especially their dissolving

Samples	Content of Main Components		Degree of Polymerization (DP_v)	Dissolving Ability (D_a), %
	Lignin	α-cellulose		
Short-length flax fibers (PF)	3.4	88.4	270	97.7
Bleached sulfite hardwood pulp (PH)	4.0	79.5	240	98.7
Cotton cellulose (MCC)	0	98.7	170	94.8

I. Characteristics of powder samples and solubility in N,N-dimethylacetamide/lithium chloride.

Samples	Equilibrium Solvent Content (ESC), wt%	Equilibrium Water Content (EWC), wt%	Porosity (Pt), %
Short-length flax fibers (PF)	2700	2500	98.9
Bleached sulfite hardwood pulp (PH)	3300	2800	97.4
Cotton cellulose (MCC)	2150	2000	86.8

II. Maximum values of equilibrium solvent content and equilibrium water content in the hydrogels and porosity of the hydrogels.

Source	Specific Surface Area (SSA), $m^2 \cdot g^{-1}$			Maximum Absorption Capacity (A_{max}), $mg \cdot g^{-1}$	Swelling Ratio (Q), $g \cdot g^{-1}$		
	Powders	Swollen Hydrogels	Freeze-dried Hydrogels		pH 2.0	pH 6.0	pH 10.0
Short-length flax fibers (PF)	4.7	41	5.5	4.1	4.2	3.1	5.7
Bleached sulfite hardwood pulp (PH)	5.7	45	6.2	4.8	4.4	3.4	5.5
Cotton cellulose (MCC)	12.7	38	4.8	3.9	3.8	2.8	4.9

III. Specific surface area of of the samples, maximum absorption capacity of swollen hydrogels, and and swelling ratio of freeze-dried hydrogels.

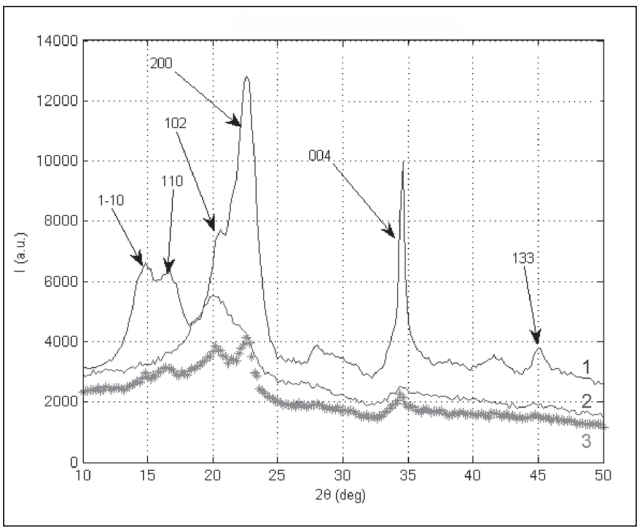
ability. The dissolving study of the freeze-dried hydrogels in the water; 17.5% aqueous solution of NaOH, ethanol, acetone, toluene; 86% solution of H_3PO_4; and 72% solution of H_2SO_4 showed that they were insoluble in almost all listed liquids. In addition, they were partly hydrolyzed in the solution of H_2SO_4 and were partly dissolved in the solution of H_3PO_4. Moreover, the dried hydrogels were insoluble in the solution of DMAc/LiCl that was applied for the dissolving of the lignocellulose powders. Strong bonds between structural links or macromolecules of the regenerated samples were formed. When a three-dimensional structure is formed, the solubility of the samples would be low but the swelling capacity might be maintained. To confirm this assumption, the solubility of the freeze-dried hydrogels in cadoxen was controlled and we found that the samples only swelled partly but remained insoluble.

Equilibrium swelling of the dried hydrogels in solutions with different pH

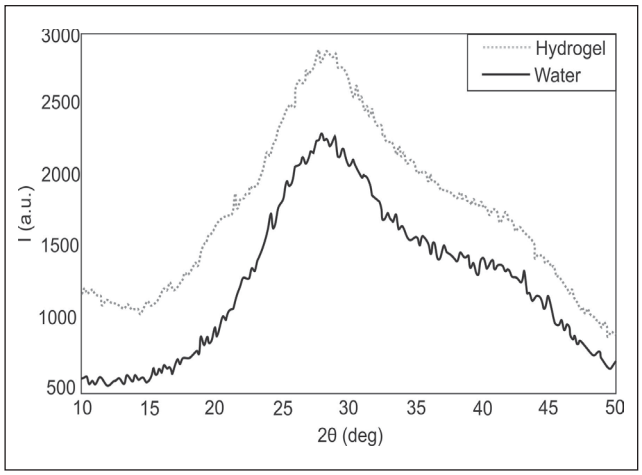
To determine the effect of pH on the swelling capacity (Q) of the hydrogels, equilibrium swelling studies were performed. We found that Q values depend on pH of the solutions. The highest Q values were observed for all hydrogels at pH 10.0, Q values were lower at pH 2.0, and the lowest Q values were at pH 6.0 (Table III) [23]. Because the chemical processing is usually accompanied by the swelling, hydrogels can be referred to as smart substances (i.e., chemical properties are pH dependent). This specificity of the hydrogels allows for their application for a wide range of practical purposes.

Comparison of X-ray crystal structure of the powder lignocellulose and of the hydrogel

X-ray diffraction intensity profiles (XDP) of the powder PH, of the hydrogels, and of the freeze-dried hydrogels are shown in **Fig. 3**. X-ray pattern of the powder PH (line 1) had the reflections characteristic of the cellulose I crystal structure, which is the native cellulose allomorph [34]. The XDP of the hydrogel of PH (line 2) did not reveal any reflections of cellu-



3. X-ray diffraction intensity profiles of powder bleached sulfite hardwood pulp (PH) (line 1), of the hydrogel of PH (line 2), and of the freeze-dried hydrogel of PH (line 3).

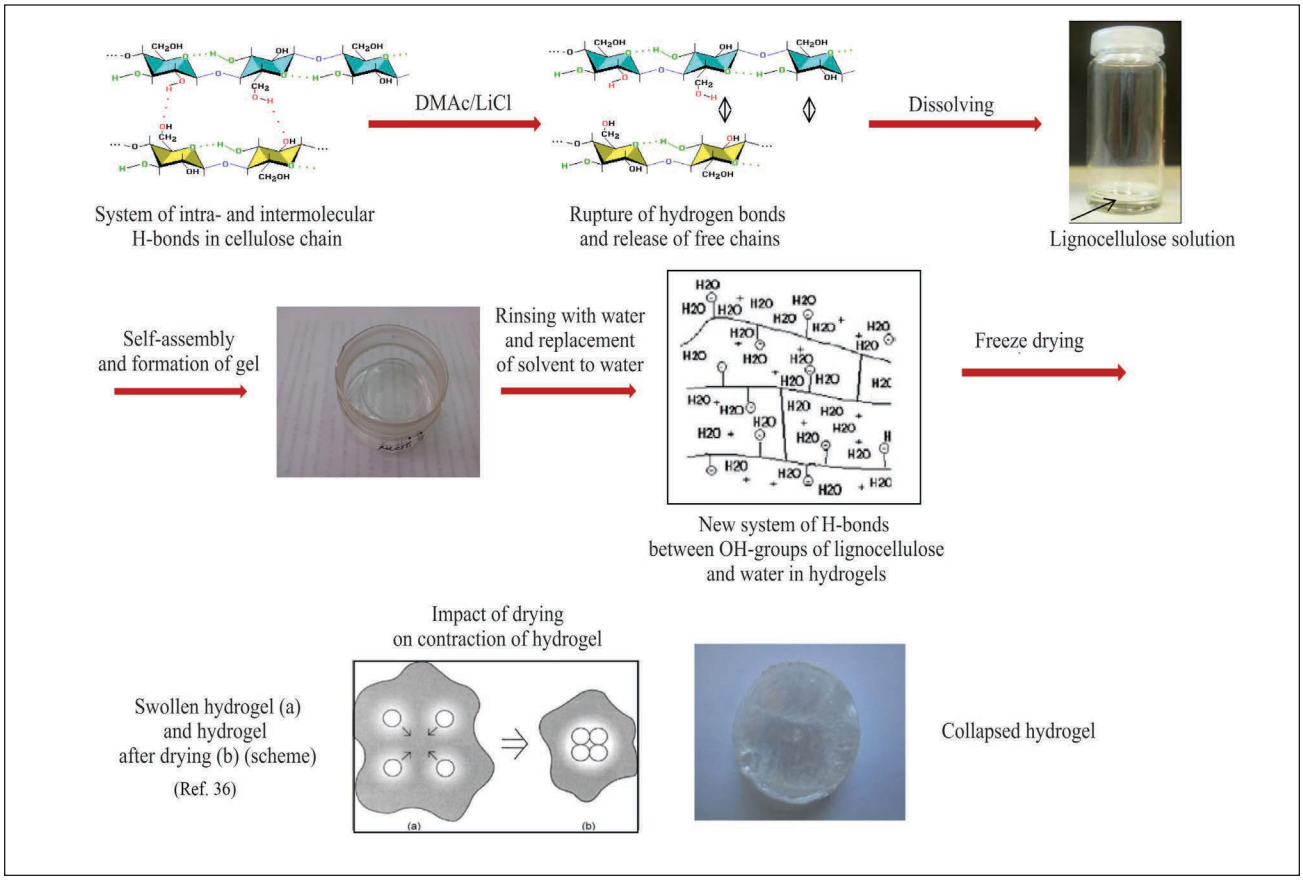


4. X-ray diffraction intensity profiles of bleached sulfite hardwood pulp (PH) hydrogel and water.

lose lattice. The XDP of the freeze-dried hydrogel of PH (line 3) had the reflections characteristic of cellulose II. DC values of the powder, hydrogel, and partly dried hydrogel were 0.46, 0.21, and 0.23, respectively, and the width of the peak reflection [200] of PH was 4.15 Å.

For more detailed characterization of the hydrogels, **Fig. 4** shows the XDP of the super-swollen hydrogel of PH and of the water. Both patterns contained smear halos at a 2θ range from 20°–45°, although they revealed no difference between both XDP. This means that the concentration of PH in the hydrogel was very low, although this small amount of the HP absorbed and held a great amount of the water. Obradovic et al. [17] studied swelling of softwood pulp in DMAc/LiCl followed by molding and regeneration and also showed that the crystalline structure of the pulp was lost after swelling. Duchemin and others [35] studied the transformation of MCC due to partial dissolution in DMAc/LiCl and assumed disappearance of the crystalline diffraction in regenerated specimens indicated that the slow solidification produced crystallites of small sizes.

The described processing was a multistage process schematically shown in **Fig. 5**. The first stage was the dissolving of the reference powder lignocelluloses in DMAc/LiCl solution. The web of intra- and intermolecular H-bonds in lignocellulose chains ruptured in the solutions and free cellulose chains were released. The next stage was gelation and after the rinsing with water, the formation of the hydrogels. These stages were performed by spontaneous self-assembly and aggregation of lignocellulose chains in the ambient conditions without any anticoagulants. The super-swollen hydrogels retained large amounts of the water and were stable as long as needed. A new web of H-bonds between OH-groups and the water was reconstruct-



5. Detailed scheme and visualization of hydrogel processing.

ed. However, the stable materials collapsed while drying and slightly accessible structures were formed.

CONCLUSIONS

We have successfully obtained in vitro stable super-swollen hydrogels. The hydrogels were prepared from powder celluloses of various origins via direct dissolving in DMAc/LiCl followed by regeneration from the solutions. The hydrogels retained large amounts of water (up to 2500 wt%) and had high porosity and specific surface areas. The hydrogels seemed to be smart materials resulting from pH-dependent behavior by swelling. The formation of hydrogels occurred via spontaneous self-assembly from the solutions because of reconstruction of a new hydrogen bond web between the lignocellulose chains and the water. The hydrogels were stable but their morphology changed after drying due to the collapse of the H-bonds formed. These findings demonstrated the lignocellulose hydrogels as novel materials with wide potential applications. **TJ**

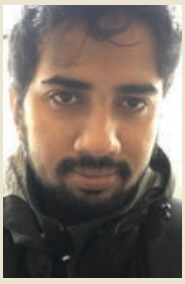
LITERATURE CITED

1. Beck-Candanedo, S., Roman, M., and Gray, D.G., *Biomacromolecules* 6(2): 1048(2005).
2. Sekiguchi, Y., Sawataria, C., and Kondo, T., *Carbohydr. Polym.* 53(2): 145(2003).
3. Qing, Y., Wu, Y., Cai, Z., et al., *J. Nanomaterials*, 2013. Available [Online] http://dx.doi.org/10.1155/2013/594734 <14Feb2018>.
4. Watanabe, J., Kiritoshi, Y., Nam, K.W., et al., in *Encyclopedia of Biomaterials and Biomedical Engineering*, Marcel Dekker, New York, 2004.
5. Pasqui, D., De Cagna, M., and Barbucci, R., *Polymers* 4(3): 1517(2012).
6. Sannino, A., Demitri, C., and Madaghiele, M., *Materials* 2(2): 353(2009).
7. Kono, H., Fujita, S., and Oeda, I., *J. Appl. Polym. Sci.* 127(1):478(2013).
8. Wang, W.B., Xu, J.X., and Wang, A.Q., *eXPRESS Polym. Lett.* 5(5): 385(2011).
9. Salah El-Din, T.A., Elzatahry, A.A., Aldeyab, S.S., et al., *Afr. J. Biotechnol.* 11(66): 13058(2012).
10. Chen, Y., Liu, Y., and Tan, H.-M. *BioResources* 3(1): 247(2008).
11. Pandey, M., Amin, M.C.I.M., Ahmad, N., et al., *Int. J. Polym. Sci.*, 2013. Available [Online] http://dx.doi.org/10.1155/2013/905471 <14Feb2018>.
12. Wickleinab, B. and Salazar-Alvarez, G., *J. Mater. Chem. A* 1: 5469(2013).
13. Kono, H. and Zakimi, M., *J. Appl. Polym. Sci.* 128(1): 572(2013).
14. Gulrez, S.K.H., Al-Assaf, S., and Phillips, G.O., in *Progress in Molecular and Environmental Bioengineering—From Analysis and Modeling to Technology Applications* (A. Carpi, Ed.), InTechOpen, London, 2011, Chap. 5.
15. Zhou, J., Chang, C., Zhang, R., et al., *Macromol. Biosci.* 7(6): 804(2007).
16. Arin, R., Brodin, M., Boldizar, A., et al., *BioResources* 8(2): 2209(2013).
17. Obradovic, J., Wondraczek, H., Fardim, P., et al., *Cellulose* 21(6): 4029(2014).
18. Aono, H., Tatsumi, D., and Matsumoto, T., *J. Polym. Sci., Part B: Polym. Phys.* 44(15): 2155(2006).

ABOUT THE AUTHORS



Mikhailidi



Saurov



Andersson



Kotelnikova

We chose this research topic because we wanted to grab readers' attention as to the possibility of preparing in vitro super-swollen hydrogels of unmodified cellulose with a simple and low-cost spontaneous method. This research complements our previous study by developing our idea of a self-organization of cellulose chains in the solutions of DMAc/LiCl during gelation.

The most difficult aspect of our research was to obtain the hydrogels of a given morphological form. In solving this, a new paradigm to prepare a rather highly organized system from the very dilute solutions of cellulose was discovered. The most surprising finding was the possibility of obtaining the hydrogels of various morphological forms.

One can get much benefit from our results by using the obtained hydrogels as functional materials in various applications. The next step is to study the materials based on hydrogels and other components.

Mikhailidi is a Ph.D. and lecturer, High School of Printing and Media Technologies, St. Petersburg State University of Industrial Technologies and Design, St. Petersburg, Russia. Saurov is a Master's Degree student and Andersson is a Ph.D. and laboratory engineer, Department of Physics, University of Helsinki, Helsinki, Finland. Kotelnikova is a professor, Institute of Macromolecular Compounds, Russian Academy of Sciences, St. Petersburg, Russia. Email Mikhailidi at amikhailidi@yahoo.com.

19. Kotelnikova, N.E., Bykhovtsova, Y.V., Mikhailidi, A.M., et al., *Cellul. Chem. Technol.* 48(7-8): 643(2014).
20. Saito, H., Sakurai, A., Sakakibara, M., et al., *Appl. Polym. Sci.* 90(11): 3020(2003).
21. Ishii, D., Tatsumi, D., Matsumoto, T., et al., *Macromol. Biosci.* 6(4): 293(2006).
22. Shcherbakova, T.P., Kotelnikova, N.E., and Bykhovtsova, Y.V., *Russ. J. Bioorg. Chem.* 38(7): 689(2012).
23. Kotelnikova, N.E., Mikhailidi, A.M., and Martakova Yu, V., *Polym. Sci., Ser. A* 59(1): 76(2017).
24. Henniges, U., Kostic, M., Borgards, A., et al., *Biomacromolecules* 12(4): 871 (2011).
25. Potthast, A., Rosenau, T., Buchner, R., et al., *Cellulose* 9(1): 41(2002).
26. Kundakci, S., Karadag, E., and Üzüm, Ö.B., *J. Encapsulation Adsorpt. Sci.* 1: 7(2011).
27. Gregg, S.J. and Sing, K.S.W., *Adsorption, Surface Area, and Porosity*, Academic Press, London, 1967.
28. Tewari, B.B. and Thornton, C.O., *Rev. Soc. Quím. Peru* 76(4): 330(2010).
29. Asghari, F., Jahanshahi, M., and Ghoreyshi, A.A., *J. Chromatogr. A* 1242: 35(2012).
30. Ahvenainen, P., Kontro, I., and Svedström, K., *Cellulose* 23(2): 1073(2016).
31. Scherrer, P., *Göttinger Nachrichten Gesell.* 2: 98(1918).
32. Fu, L., Zhang, Y., Zhang J., et al., in *Biomedical Engineering—Frontiers and Challenges* (R. Fazel, Ed.), InTechOpen, London, 2011, pp. 249-275.
33. Huo, J., Zheng, Y., Pang, S., et al., *Cellulose* 20(2): 841(2013).
34. Leppanen, K., Andersson, S., Torkkeli, M., et al., *Cellulose* 16(6): 999(2009).
35. Duchemin, B.J.C.Z., Newman, R.H., and Staiger, M.P., *Cellulose* 14(4): 311(2007).

ABOUT THIS PAPER

Cite this article as: Mikhailidi, A., Suarov, S., Andersson, S. *TAPPI J.* 17(2):81(2018). https://doi.org/10.32964/TJ17.02.81

DOI: https://doi.org/10.32964/TJ17.02.81

ISSN: 0734-1415

Publisher: TAPPI Press

Copyright: ©TAPPI Press 2018

About this journal

Functionalization of wood/plant-based natural cellulose fibers with nanomaterials: a review

CHARU AGARWAL AND LEVENTE CSÓKA

ABSTRACT: Being the most abundant natural biopolymer on earth, cellulose has been vastly exploited in a range of applications, from writing paper to high-end biosensors. Natural cellulose fibers can be isolated from wood or non-woody plants such as hemp, jute, flax, and bamboo by chemical or mechanical treatments. To make it suitable for targeted applications, cellulose fibers are modified with functional moieties in the nanometer scale. Cellulose has been functionalized with noble metals such as silver and gold nanoparticles for catalysis and antimicrobial applications. A number of metal oxides, such as zinc oxide, titanium dioxide, and tin dioxide have been incorporated into cellulose. The porosity, hydrophilicity, and roughness of cellulose surface makes it an ideal substrate for a plethora of sensing applications. Further, it can be made into a lightweight, portable, foldable, and disposable device, which provides an excellent platform for various point-of-care purposes. Cellulose fibers have also been immobilized with carbon nanomaterials, including carbon nanotubes and graphene oxide. For optical applications, $[Fe(hptrz)_3](OTs)_2$ spin-crossover nanoparticles have also been immobilized on cellulose fibers. Likewise, many enzymes, macromolecules, and some polymers have been used to modify natural cellulose for specific end uses. This review focuses on recent developments in the modification or immobilization of functional materials on cellulose fibers, in macro-scale only, obtained from wood or plant sources.

Application: Manufacturers are developing a growing range of products based on combinations of nanomaterials and cellulose fibers.

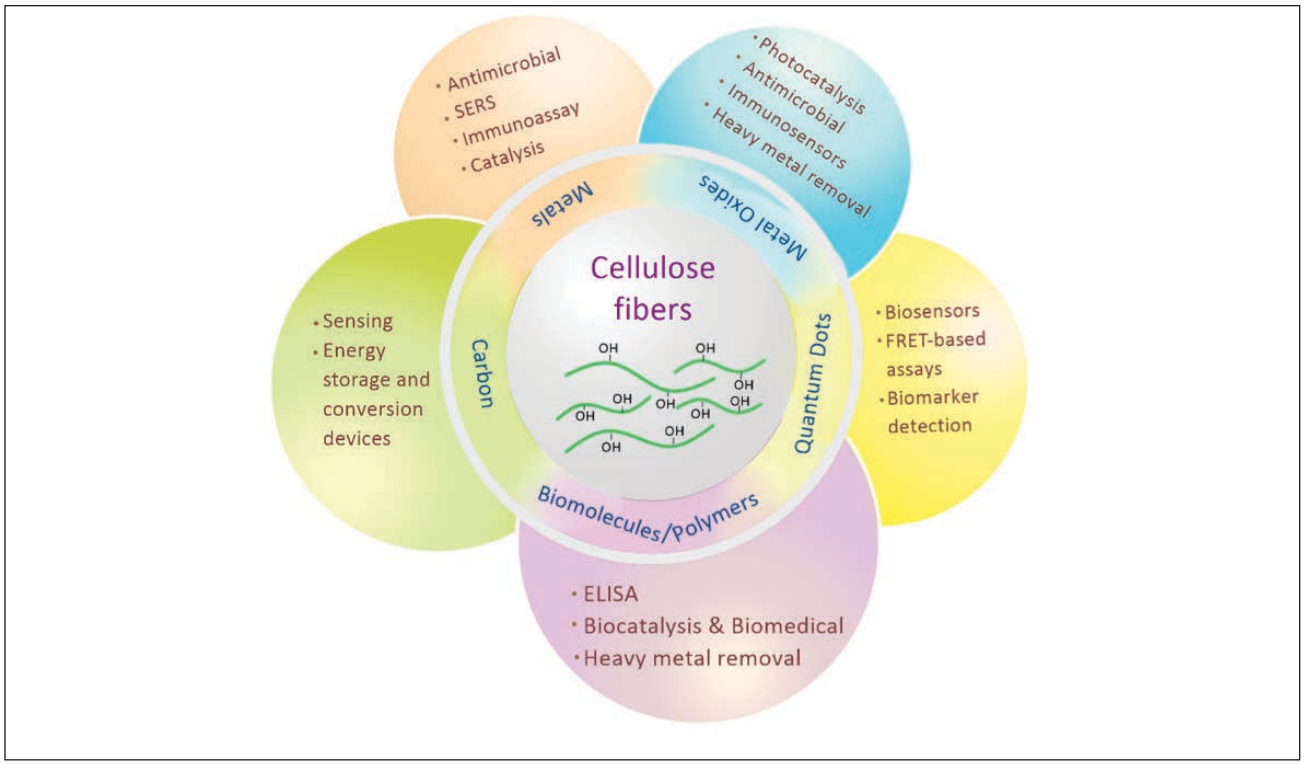
In view of the growing concerns on sustainable and economic development, natural materials such as cellulose have drawn significant attention from scientists in various fields in recent years. Cellulose, the most abundantly available biopolymer on earth, was first isolated from plants by Anselme Payen in 1838 [1,2]. Since then, cellulose has become an attractive biomaterial for a plethora of applications, ranging from simple wound-healing bandages to complex immunosensors, owing to the many advantages it offers.

Cellulose consists of β-D-glucopyranose units joined by β-(1-4) linkages, with the chemical formula of $(C_6H_{10}O_5)_n$, in which the "n" ranges from 10000 to 15000 [2,3]. It has crystalline and amorphous regions, which strongly influence its properties. Being the fundamental strengthening component of plant cell walls, cellulose forms an inexhaustible source of raw material fround predominantly in trees and nonwoody plants such as cotton, bamboo, hemp, flax, jute, sisal, ramie, etc. [3,4].

The biodegradability and biocompatibility of cellulose make it ideal for a number of biomedical applications. Further, the cellulose fibers are naturally hydrophilic as the result of hydroxyl groups, which allow capillary wicking of fluids required in many lateral flow immunoassays (LFIAs) [1]. The porosity of cellulose fiber networks, as in paper, is also immensely useful for incorporating and diffusing materials [5]. The structure of cellulose allows its surface to be chemically modified by processes such as oxidation, amination, and esterification. This plays an instrumental role in the immobilization of materials by imparting new properties to cellulose without destroying its appealing intrinsic properties [1].

The immobilization of nanomaterials onto substrates such as paper, polymer, metal, and glass can prevent their dispersal in the environment and aid their recovery [6]. The immobilization of an entity simply refers to its attachment to a surface, leading to a reduction or loss of its mobility. It can occur by different approaches, including physical, chemical, biological, or a combination of these processes [1,7]. Cellulose fiber substrates, such as paper, are an inherently oriented and organized network of fibers [8] that provide an ideal platform for immobilization by favoring the growth of nanostructures.

Within the fast-growing field of nanotechnology, metal, metal oxide, quantum dots, and carbon nanomaterials are gaining the increasing interest of researchers [6,9,10]. Cellulosic substrates have been widely explored for embedding these nanomaterials for building simple, portable, and disposable devices in theranostics (molecular diagnostic tests and targeted therapeutics), electronics, microfluidics, and environmental and point-of-care (POC) applications (**Fig. 1**) [1,5]. Paper, being a sheet of randomly interwoven cellulose fibers, possesses all the aforementioned intriguing features of cellu-



1. Applications of cellulose fibers modified with nanomaterials.

lose, which make an excellent platform for anchoring of materials. It also easily complies with the requirements of World Health Organization (WHO) for diagnostic devices, which should be ASSURED: affordable, sensitive, specific, user-friendly, rapid and robust, equipment-free, and deliverable to end-users [1].

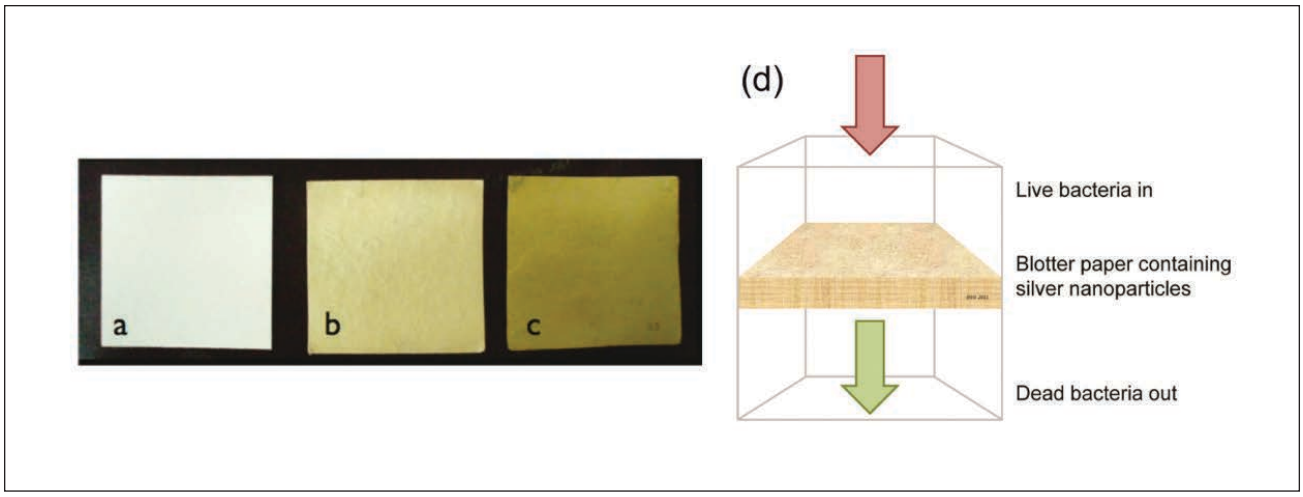
This review covers the most recent works about the incorporation or immobilization of different nanomaterials onto cellulose fibers, with emphasis on their functional applications, particularly in the ongoing decade. The nanomaterials have been broadly divided into five categories: 1) metals, 2) metal oxides, 3) quantum dots, 4) carbon, and 5) others, including biomolecules and polymers. A brief overview of the immobilizing strategy on cellulose is discussed, along with applications of the functionalized cellulose materials. Considering the vast potential and demand of natural and renewable resources in virtually every sector, functionalized cellulosic materials show promise to overcome many hurdles and challenges posed during material synthesis and application.

FUNCTIONALIZATION WITH METALS

Cellulose fibers have been incorporated with noble metals, such as silver, gold, platinum, and palladium, and with other metals, such as copper and cobalt, for catalytic, sensing, electronic, and biomedical applications. Different approaches have been used to fabricate metal/cellulose nanocomposites, including ex situ and in situ reduction techniques, with or without the use of external linking or binding agents. A simple in situ synthesis of silver, gold, platinum, and palladium nanoparticles (NPs) under 10 nm in size was achieved by immersing cellulose paper in metal precursor solution, followed by subsequent reduction with aqueous sodium borohydride [11]. The reduction of metal salts can also be achieved by terminal reducing groups in cellulose, such as aldehyde and carboxylic groups, thus preventing the need for external agents that might hinder the accessibility of active sites by blocking the exposed surface of the nanomaterials and reducing efficiency [6,12]. Further, the ether and hydroxyl groups in cellulose play an important role in the in situ synthesis of metal nanoparticles by anchoring the metal ions tightly onto the fibers via ion-dipole interactions, and by stabilizing the synthesized NPs via surface interactions [12]. Metal nanoparticles can also be immobilized on modified cellulose surfaces by grafting functional moieties onto it. Electrostatic assembly mediated the synthesis of gold and platinum nanoparticles capped with negative citrate ions onto cationic cellulose grafted with positive ammonium ions [13].

Of late, several nonconventional methods for fabricating nanocomposites have gained popularity owing to their many advantages. For instance, microwave-assisted synthesis of silver nanoparticles (AgNPs) onto cellulose fibers was achieved using 6-O chitosan sulfate as a reducing and capping agent to prevent the agglomeration of nanoparticles. On comparing it with a conventional heating method, no appreciable differences were observed on the strength properties of the nanocomposites or on the particle morphology of the AgNPs under the same conditions of reaction temperature and time [14].

Numerous works have modified cellulose fibers with



2. a) Untreated paper; b) paper with 0.2 mg Ag/g; c) paper with 5.8 mg Ag/g; and d) bactericidal paper with silver nanoparticles (AgNPs) for purification of potable water against pathogenic bacteria [20]. (Adapted with permission from ref. 20 © 2011 ACS publisher).

AgNPs, with bactericidal application being the most explored [15-18]. Silver has been one of the strongest antimicrobial agents against a wide range of microorganisms. The most commonly accepted mechanisms behind its antimicrobial activity are:

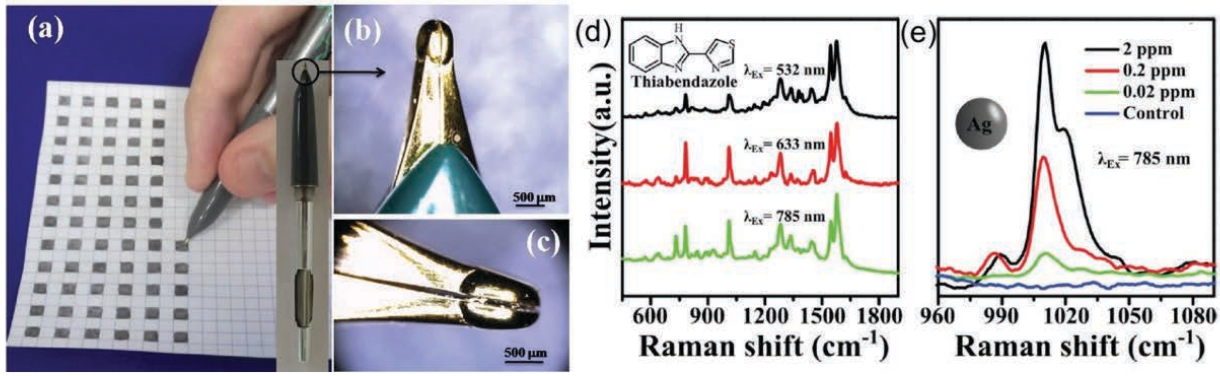
1. Gradual release of free Ag^+ ions, leading to disruption of adenosine triphosphate (ATP) production and deoxyribonucleic acid (DNA) replication.
2. Direct damage to cell membranes by AgNPs.
3. Generation of reactive oxygen species by AgNPs and Ag^+ ions [19].

A simple method of deposition of AgNPs by in situ reduction of silver nitrate on a blotting paper was used to fabricate bactericidal paper for point-of-use treatment of water contaminated with pathogenic microbes [20]. As shown in **Fig. 2**, increasing concentrations of precursor silver ions yielded different colors on paper because of surface plasmon resonance of AgNPs. The inactivation of bacteria was achieved by percolation of contaminated water through the paper rather than removal by filtration. The log reduction values obtained for *Escherichia coli* and *Enterococcus faecalis* in the effluent were log 6 and log 3, respectively. Further, less than 0.1 ppm of silver leached out into the effluent, which was within the standard limits [20].

In an ex situ impregnation method, a colloidal solution of AgNPs was first prepared using D-glucose as the reducing agent. The solution was then added to suspensions of cellulose fibers from three different sources: pine, linter, and recycled fibers [19]. The cell viability test showed remarkable microbicidal activity against common pathogenic strains of gram-negative *E. coli*, gram-positive *Staphylococcus aureus*, and *Candida albicans*. Over 99% reduction in the cell count of all the strains was obtained with pine fibers after 1 h of exposure to the AgNP-impregnated sheet. This might be because the silver trapped into the cellulose fibers released gradually as Ag^+ ions or AgNPs causing microbial lethality. Further, significant improvement was observed in the mechanical and viscoelastic properties of sheets loaded with about 0.1 wt% of silver. This was evident from the higher values of tensile indices and storage moduli of the Ag-modified sheets against the unmodified ones [19].

The noble metal nanoparticles show interesting phenomena, such as surface-enhanced Raman scattering (SERS) and surface plasmon resonance (SPR). These optical phenomena are influenced by the aggregation state of the nanoparticles as well as their adsorption on the substrate. Paper has been used as SERS substrate; nevertheless, its roughness and porosity hinder the uniform distribution of the nanoparticles [9]. Many groups have reported AgNPs deposited on paper as SERS substrates for nanoplasmonic sensing [21,22]. Various techniques—such as dip-coating, screen-printing, laser-induced deposition, and physical vapor deposition—have been used to impregnate paper with plasmonic nanostructures [23]. For instance, a filter paper was modified with chloride ions to facilitate the chemisorption of AgNPs using dip-coating by overcoming the electrostatic repulsion between AgNPs and paper. The SERS substrate had an enhancement factor of 6.4×10^5 with a limit of detection of 10^{-8} M for 4-mercaptobenzoic acid. Further, the substrate showed good stability over more than 2 months because of the shielding effect of chloride ions on AgNPs, thus weakening the oxidation [24]. Another study used a simple "pen-on-paper" approach to make SERS substrate using silver nanospheres [25]. SERS arrays were created on paper using a fountain pen filled with plasmonic ink containing metal nanoparticles of arbitrary shape and size. As shown in **Fig. 3**, the ink in the pen could be dispensed on paper through the nib via a combination of gravity and capillary action. Detection limits down to 20 ppb were achieved for thiabendazole, a pesticide, using the SERS paper substrate at 785 nm excitation of the AgNPs [25].

AgNPs have been widely used as sensing platforms [26,27]



3. a) A fountain pen with plasmonic nanoparticle ink and surface-enhanced Raman scattering (SERS) paper substrates (inset: inner part of the pen); b & c) optical microscopy images of the nib; d) AgNPs SERS spectra of thiabendazole (20 ppm) at excitation wavelengths of 532 nm, 633 nm, and 785 nm; and e) AgNPs SERS spectra of thiabendazole with varying concentrations at 785 nm [25]. (Adapted with permission from ref. 25 © 2014 JWS publisher).

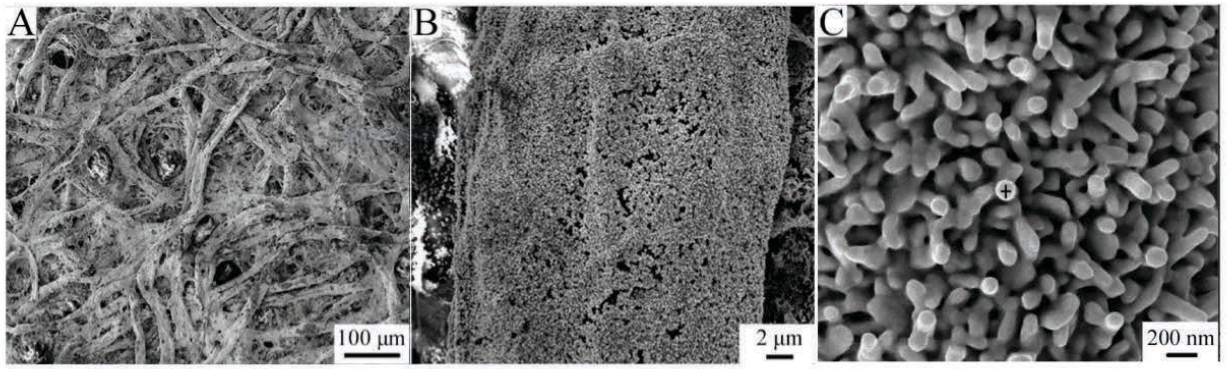
or for analyte labeling [28] in biosensors or immunodevices. A paper electrode was modified with silver through a seed-mediated growth approach for the attachment of antibodies. Metal ion-coated nanoporous silver-chitosan served as labels, which greatly amplified signals for the detection of cancer antigen 125 and carcinoma antigen 199 down to 0.08 mU mL^{-1} and 0.1 mU mL^{-1}, respectively [27]. In another paper-based analytical device, an AgNP-labeled analyte provided 250,000-fold amplification for the electrochemical detection of proteins. The AgNPs eliminated the need for enzymatic amplification, thereby improving device stability and response time [28].

Inkjet-printed AgNPs on paper were used for SERS detection of odors of trinitrotoluene (TNT), a crystalline explosive, using Raman spectroscopic approach. The silver paper was modified with *p*-aminobenzenethiol in order to collect the airborne TNT and to enhance its scattering by multiple spectral resonances. The layer-by-layer printing ensured a uniform sensitivity of AgNP-printed paper to a limit of 1.6×10^{-17} g/cm^2 TNT [29]. Silver colloid-deposited paper enhanced the fluorescence emission of fluorophores for high-throughput surface analysis and anti-counterfeiting applications [30].

The hydroxyl groups on the surface of cellulose can be paired with various functional groups to give chemically modified fibers. Cotton cellulose fibers were modified using lecithin and thiol groups to achieve uniform particle size and high loading of silver and gold nanoparticles (AuNPs) [31]. Strong electrostatic interactions between the negatively charged hydroxyl groups of cellulose with the positively charged quaternary ammonium groups of lecithin, followed by similar interactions between phosphate groups of lecithin and metal ions, led to their adsorption on the cellulose fibers. It resulted in AgNPs 10-30 nm and AuNPs 20-30 nm in size. The surface loading density was found to be 25 wt% for AgNPs and 15 wt% for AuNPs, as determined from energy dispersive x-ray (EDX) analysis. On the other hand, the thiol modification was brought about by treatment of cellulose by mercaptoactetic acid in the presence of a catalyst (p-toulene sulfonic acid), which converted the hydroxyl groups into mercaptoacetate groups. Although similar particle size distribution was observed for thiol-modified fibers, the surface loading for gold had dramatically improved to 43 wt%, while that for silver had dropped to a meagre 13 wt%, attributed to lower affinity of silver for thiol. The thiol-modified cellulose fibers loaded with AuNPs were found to be an active catalyst for the conversion of 4-nitrophenol to 4-aminophenol [31].

Gold is another noble metal extensively investigated in combination with cellulose. Different morphologies of gold nanostructures have been widely explored for sensing applications. Recently, gold nanorods (AuNRs) were grown from seed solution by adsorption on the surface of cellulose fibers [32]. As can be seen from **Fig. 4**, a dense layer of AuNRs, which resulted after hydrothermal treatment of the solution under the self-catalytic reduction mechanism, entirely covered the fiber surface. The excellent conductivity of AuNRs, combined with the porosity of paper, provided an electrode/scaffold system for fabrication of an electrochemical immunosensor to capture antibodies for the detection of prostate specific antigen [32]. Several other studies have used paper substrate embedded with AuNPs as sensing platforms for developing electrochemiluminescent assays for biomarkers like ATP or proteins such as human immunoglobulin G [33,34], electrochemical immunosensor for carbohydrate antigen [35], electrochemical sensor for cancer cells [36], and cyanotoxin immunoassay [37].

Cellulosic platforms offer numerous advantages for developing SERS substrates by embedding plasmonic nanostructures onto paper, such as high specific surface area, excellent wicking property, compatibility with common printers, low



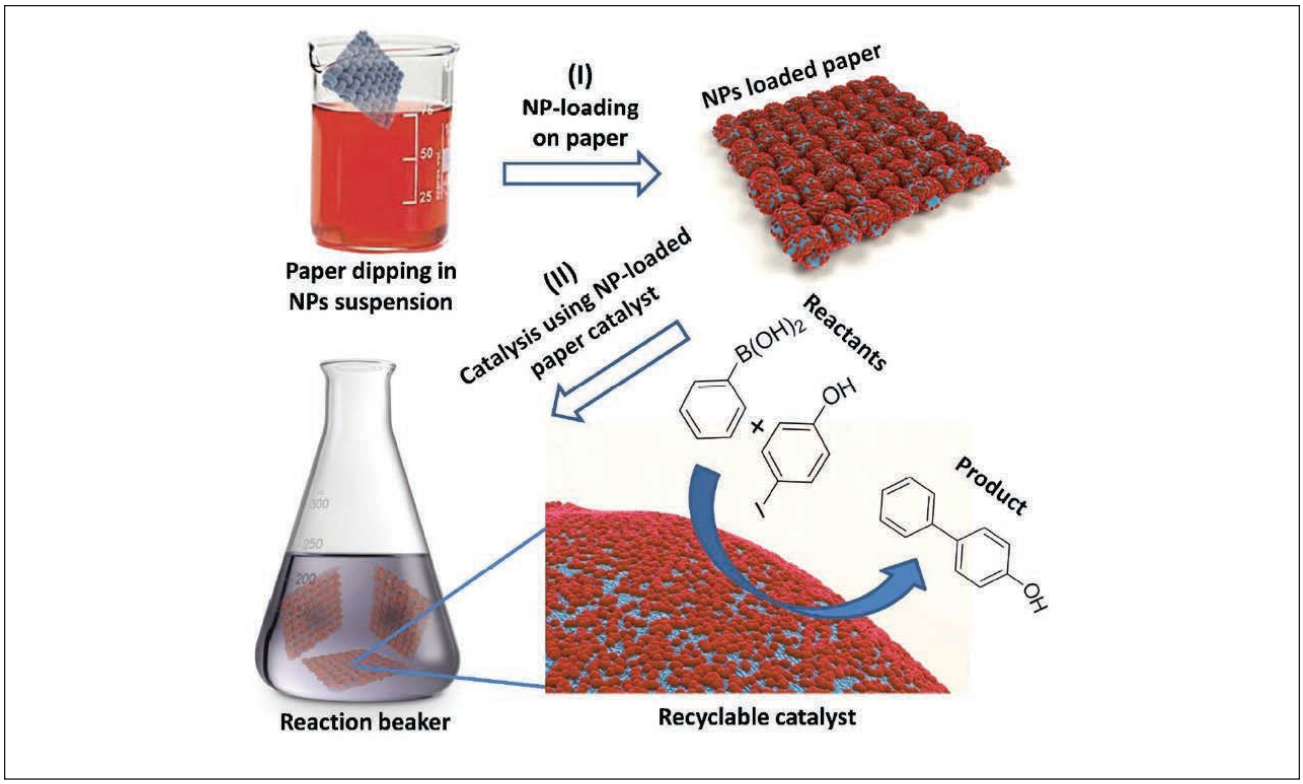
4. a) Scanning electron microscopy (SEM) image of gold nanorod (AuNR)-immobilized paper; and b & c) high magnification images of AuNRs grown on cellulose surface [32]. (Adapted with permission from ref. 32 © 2015 RSC publisher)

cost, and easy disposability. Gold nanorods, 60 nm long and 18 nm in diameter, were deposited on filter paper to make SERS substrate with high sensitivity to detect 0.5 nM of trans-1,2-bis(4-pyridyl)ethene and excellent reproducibility [38]. The SERS properties are governed by the manner in which the nanoparticles are immobilized onto the substrate and their state of aggregation [39,40]. A generic SERS platform for bio-diagnostic purposes was built by functionalizing a series of biomolecules on AuNP-embedded paper. Streptavidin, a bacterial protein, was bound onto the AuNP-treated paper using biotinylated-thiol. Subsequently, the biotinylated-antibody was anchored onto streptavidin for antigen detection. The SERS spectra confirm the presence of the analyte, with the peak intensity giving its concentration [41].

AuNPs exhibit remarkable optical properties in the visible and near infrared regions, due to the so-called localized surface plasmon resonances (LSPRs) arising from the coherent oscillation of their conduction band electrons. This has been used to study reactions by monitoring the time-dependent SERS signals of the reactants or products. A bifunctional dip-catalyst based on AuNPs loaded on filter paper exhibited unchanged catalytic efficiency for over 20 consecutive cycles, along with high SERS efficiency, to keep track of the progress of the reaction through SERS signals [42]. In a similar fashion, a paper catalyst was fabricated by physical adsorption of an aqueous suspension of polyethyleneimine (PEI)-entrapped AuNPs onto a filter paper via electrostatic interaction between the oppositely charged entities. Abundant amine groups on the molecular periphery of PEI were used as a template to entrap AuNPs with a core size of 3.2 nm. Excellent catalytic activity was obtained for the transformation of 4-nitrophenol to 4-aminophenol with a conversion rate of 97% in 36 min [43].

Other metals, including copper, nickel, platinum, and palladium, anchored to cellulose fibers, have also been explored for diverse applications. Antibacterial coatings were formed by in situ deposition of copper nanoparticles (CuNPs) on cotton cellulose fibers using the layer-by-layer self-assembly approach [44]. Preconditioning of the cellulose substrate (carboxymethylation) imparted negative surface charges for binding Cu^{2+} ions, which were then reduced to yield sub-5 nm CuNPs. It showed remarkable potential for wound dressings by efficient inhibition of *Acinetobacter baumannii*, a multi-drug resistant wound pathogen, achieving an 8-log reduction in bacterial growth in 10 min contact time. Interestingly, analogous silver coatings exhibited a far too inferior performance, with a 5-log reduction in bacterial growth even after 24 h of contact [44]. Similarly, filter paper dip-coated in a colloidal solution of nickel nanoparticles (NiNPs) was used to immobilize proteins to develop it into a biosensing platform [45]. The in situ self-assembly of NiNPs adsorbed on the filter paper served as docking sites for the selective immobilization of proteins. This bio-conjugation assembly with cellulose-based scaffold demonstrated the ability to effectively bind anti-*Salmonella* antibodies, allowing the immuno-capture of *Salmonella* bacteria [45]. A rechargeable battery was developed using paper as a support and electrolyte, which also served to separate the thin metallic layers of anode and cathode. A battery with copper and aluminum deposited on opposite sides of paper lead to an output voltage of 0.70 V and a current density between 150 nA/cm² and 0.5 mA/cm², subject to the paper composition, thickness, and the degree of OHx species adsorbed on the paper matrix [46].

Similarly, a layer of platinum nanospheres was grown from nanoparticle seed solution onto a fiber surface to create a working electrode for H_2O_2 determination from cancer cells [47] and protein/antigen detection [48]. Using a simple dip-coating method, paper catalysts were prepared by adsorption of oleylamine-stabilized palladium nanoparticles (PdNPs) on filter paper. The PdNPs with an average diameter of 3 nm were immobilized on the paper substrate via strong van der Waals forces and hydrophobic interactions between the two. As shown in **Fig. 5**, to produce palladium-loaded paper, paper strips were dipped into the nanoparticle dispersion, pulled out for solvent evaporation, dried overnight, and then washed. The paper catalysts demonstrated high catalytic activity with excellent reusability and recyclability for a number



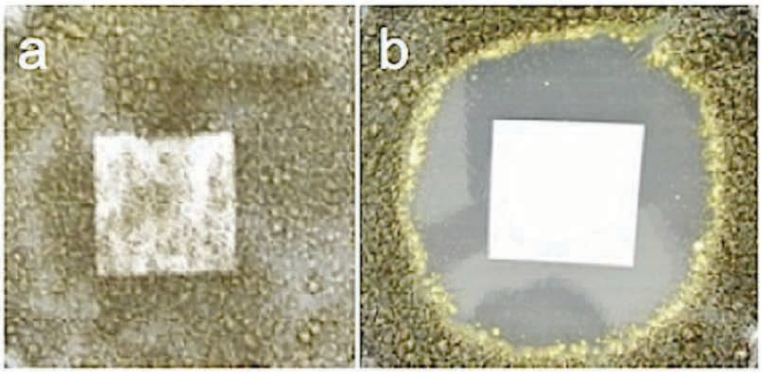
5. Schematic representation showing assembly of oleylamine-capped palladium nanoparticles (PdNPs) on filter paper by dip-coating (I) and nanoparticle-loaded paper immersed in a reaction mixture to catalyze a cross-coupling reaction (II) [49]. (Adapted with permission from ref. 49 © 2015 ACS publisher).

of organic reactions such as the Suzuki cross-coupling reaction, the oxidative homocoupling of arylboronic acids, and nitro to amine reduction [49].

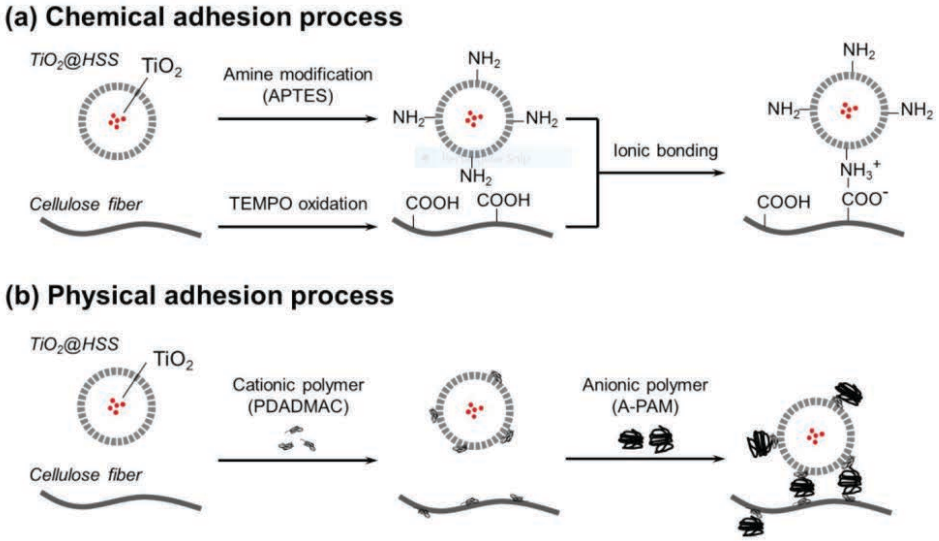
FUNCTIONALIZATION WITH METAL OXIDES

Metal oxide nanomaterials have gained an immense commercial significance because of their unique optical, chemical, and electrical properties. A variety of metal oxides, including titanium, zinc oxide, iron oxides, and silica, have been immobilized on cellulose fibers for sensing, packaging, catalysis, electronics, and a host of other applications. Metal oxide semiconductors with wide band-gaps, such as titanium and zinc oxide, generate electron-hole pairs through photonic excitation. This allows efficient mineralization of toxic organic pollutants and hazardous inorganic substances and microbial disinfection of pathogenic bacteria or fungi [50]. Because of the self-agglomerating tendency of the metal oxide nanomaterials, they often lose a good fraction of their intended surface area for practical applications. Moreover, their loss or entrainment might also be a barrier for environmental remediation. Immobilizing the nanomaterials on suitable substrates circumvents these issues to a certain extent. Recent studies have thus focused on developing hybrids that have synergistic effects between the nanomaterials and their immobilizing substrates to mitigate the drawbacks of their individual use. In this regard, natural fibers, such as cellulose, are gaining attention because of their network forming ability, porosity, and hydrophilicity, for which the nano-metal oxides have an affinity [51,52].

Zinc oxide (ZnO) is a wide band-gap (E_g = 3.37 eV) transition metal oxide with excellent photochemical, catalytic, and antimicrobial properties. Its high isoelectric point enables adsorption or immobilization of antibodies, proteins, and enzymes [53,54]. Various techniques, such as an in situ hydrothermal route [8,55,56], ex situ synthesis of NPs using stabilizing or binding agents [57], and ultrasound-assisted deposition of NPs [58], have been used to incorporate nano-ZnO into the cellulose fibers. Several studies have investigated the antimicrobial action of nano-ZnO-modified cellulose [53,55,57,58]. ZnO nanorods (ZnO NRs) were grown in situ by the hydrothermal method on fiber surfaces to fabricate an antimicrobial paper, taking advantage of the hygroscopic nature of cellulose [50]. The moisture adsorbed from the atmosphere contributes to the gradual seepage of Zn^{2+} ions, leading to the production of hydroxyl radicals (·OH). Exposure to light enhances the inhibition through photocatalysis, resulting in the production of hydrogen peroxide (H_2O_2). These species are harmful to living cells and are the major contributors to the antimicrobial effect. Inhibition zones up to 2.8 cm and 2.1 cm were observed for *E. coli* and *S. aureus*, respectively, under room lighting conditions. The inhibition of bacterial growth occurred because of the bactericidal effects of the ZnO NRs rather than their bacteriostatic effects. The ZnO-embedded paper also inhibited the growth of common airborne fungus,



6. Growth of **Aspergillus niger** *after 72 h of incubation on a) untreated paper and b) paper modified with zinc oxide (ZnO) nanorods [50].*



7. Fabrication of photocatalytic paper by a) chemical and b) physical adhesion processes [68]. (Adapted with permission from ref. 68 © 2017 ACS publisher).

Aspergillus niger, with zone of inhibition of 2.6 cm after 72 h of incubation (**Fig. 6**) [50]. The same group has also reported visible light-induced degradation of organic dyes using paper functionalized with ZnO NRs [59].

Because of high surface-to-volume ratios, fast electron transfer, and good biocompatibility, ZnO nanomaterials have outstanding capacities for sensing applications and have been used in microfluidic paper-based analytical devices (μPADs) [60]. Paper substrates embedded with nano-ZnO also have been used to fabricate photoconductive ultraviolet (UV) sensor [61], piezoelectric strain sensor [62], electrochemical (EC) immunosensor [63], and photoelectrochemical (PEC) immunosensors [64,65]. ZnO nanowires (ZnO NWs) were synthesized on paper via a low-temperature hydrothermal method to develop a biosensor for detection of glucose on human serum [60]. The high isoelectric point (≈9.5) of ZnO NWs helped immobilize glucose oxidase, an enzyme, via electrostatic attraction. The paper-based electrochemical biosensor showed higher sensitivity, lower limits of detection, and enhanced stability. It is also economical, portable, and easy to operate [60].

Another widely used metal oxide, titanium dioxide (TiO_2), has been immobilized into cellulose and used to develop self-cleaning paper, food packaging, biomedical, and other applications that are low cost, non-toxic, stable, and easily available. It is well-known for its photoactivity on exposure to light, which makes it an excellent photocatalyst for degradation of organic pollutants in wastewaters. Several studies have investigated the photocatalytic properties of nano-TiO_2-modified cellulose, following the pioneering work of Matsubara et al. [66-70]. A photocatalytic paper was fabricated with nano-TiO_2 encapsulated in hollow silica spheres (TiO_2@HSS) via two dif-

ferent processes. As shown in **Fig. 7**, the chemical adhesion was caused by ionic bonding between the –COOH groups of TEMPO (2,2,6,6-tetramethylpiperidine-1-oxyl radical)-oxidized cellulose fibers and the $-NH_2$ groups anchored to TiO_2@HSS particles, while a dual polymer system resulted in physical adhesion between them. The TiO_2@HSS had a yolk-shell structure, with TiO_2 NPs of 20 nm size enveloped by 100–200 nm silica NPs. Ample void space within shielded the TiO_2 and the substrate. The porous nature of the silica shell improved the adsorption capacity for the degradation of 2-propanol in comparison with bare TiO_2. Moreover, the immobilization of TiO_2@HSS on paper enhanced adsorption by providing a reticular fiber network for uniform particle dispersion. The air permeability of paper profoundly influenced the photocatalytic functionality of the immobilized photocatalyst [68].

TiO_2 nanomaterials incorporated with cellulose have also shown potential as promising adsorbents for removal of toxic contaminants such as heavy metals and organic pollutants from aqueous environments. The adsorption of lead ion (Pb^{2+}) and copper ion (Cu^{2+}) has been studied on cellulose fibers immobilized with TiO_2 NPs [52,71,72]. TiO_2 nanocrystals were generated in situ on cellulose fibers by hydrolysis of the precursor, titanium oxysulfate ($TiOSO_4$), for selective adsorption and removal of Pb^{2+} from water [73]. Interestingly, cellulose served as a scaffold for the TiO_2 NPs and as a chemical template directing crystal growth for the formation of spindle-shaped TiO_2 crystals. The hydroxyl groups on cellulose adsorbed TiO^+ to create sites for nucleation, leading to the formation of TiO_2 nuclei by hydrolysis condensation and their subsequent growth into nanocrystals. The TiO_2 spindles, with an average length of 180 nm and diameter of 50 nm, after 4.5 h of reaction were well-dispersed on the fiber surface and oriented along the fiber direction. Increasing the reaction time, however, led to particle agglomeration, even though the crystals became larger. The composite displayed good adsorption characteristics and good regenerability [73]. Other methods, such as synthesis using binding agents like sodium alginate [74], bioconjugation using streptavidin-biotin interaction [75], sol-gel process [76], hydrothermal route [67], and microwave-assisted synthesis [72] have also been used to functionalize cellulose fibers with TiO_2.

Other metal oxides have also been functionalized on cellulose fibers for various applications (**Table I**). Various groups have reported synthesis of silica (SiO_2)/cellulose hybrids using the sol-gel approach [77-80]. A dense network of SiO_2 formed over cellulose fibers by hydrolysis and condensation of the precursors, followed by the addition of cellulose pulp. The hybrid was subsequently functionalized with polyoxometlates (POMs) via electrostatic interactions between them. SiO_2-modified cellulose served as a support for POMs, which demonstrated catalytic activity for oxidation of volatile organic compounds [80]. Another study investigated the effect of process variables on the deposition of SiO_2 NPs on cellulose fiber surfaces by the sol-gel method by varying reaction times and precursor contents. These variables directly influenced the size and amount of deposition of SiO_2 NPs and their thermal stability and moisture adsorption [79].

Manganese dioxide (MnO_2) synthesized in situ on cellulose had excellent catalytic activity for the oxidation decomposition of formaldehyde (HCHO) [81]. The fibers were first impregnated with potassium permanganate ($KMnO_4$) solution, then reduced by oleic acid to MnO_2 NPs in ambient conditions. The color intensity rose with increasing molar concentrations of $KMnO_4$, indicating the formation of MnO_2 (**Fig. 8a**). Cellulose with 8.86 wt% of MnO_2 showed the highest catalytic efficiency, which depended not only on the MnO_2 content but also on the adsorption of HCHO on the surface of cellulose. The conversion of HCHO of 8.86 wt.% MnO_2 paper (for 1 mg of MnO_2) was up to 17 times higher than that of hydrothermally prepared MnO_2 powder from birnessite (Fig. 8b) [81].

A portable patch-type sensor was fabricated taking advantage of the co-existent dual oxidation states of cerium oxide (CeO_2) for detection of common food antioxidants [82]. The CeO_2 NPs were immobilized by soaking filter paper disks in a colloidal solution of CeO_2 NPs, followed by drying. The underlying principle involved the ability of antioxidants to reduce cerium on the nanoparticle surface from Ce^{4+} to Ce^{3+}, leading to a change in color that served as a "signature" of the antioxidant power and its type. The color change occurred because of changes in the physicochemical and spectroscopic properties of the NPs in the presence of antioxidants. The calibration curves in **Fig. 9** for gallic and ascorbic acids show that the color intensity was linearly dependent on the concentration of antioxidant. It was also found to be influenced by the chemical structure and the oxidation potential of the antioxidants [82]. The same group has reported similar work using different metal oxides [83].

FUNCTIONALIZATION WITH QUANTUM DOTS/ UPCONVERTING DONORS

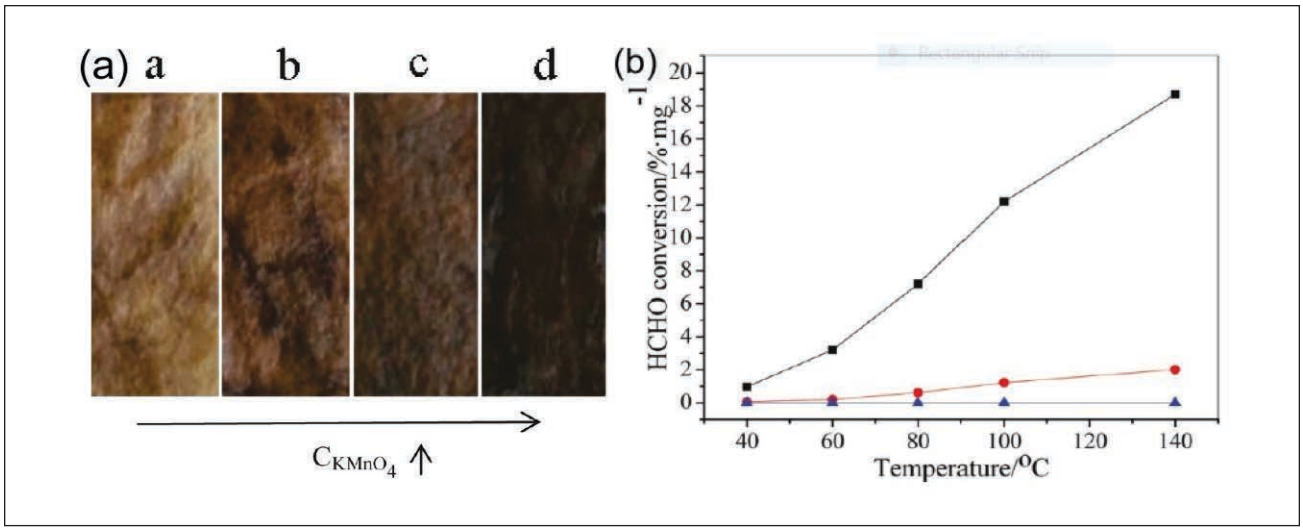
Quantum dots (QDs) or semiconductor nanocrystals typically have dimensions of 2-6 nm and unique electro-optical properties lying between the molecular and bulk semiconductor regimes. The striking effect of size on the properties of QDs is an outcome of the phenomenon of quantum confinement, which makes them ideal for a number of electronic and biomedical applications including solar cells, transistors, light-emitting diodes (LEDs), medical imaging, and quantum computing [101,102]. Their size-tunable properties have been exploited for developing optical probes for biological sensing. QDs have broad absorption spectra, photoluminescence spectra with large Stoke's shifts, and good photostability, which have been used to build glucose biosensor [103] and nucleic acid hybridization assay [104].

Cellulose paper, surface-modified with silane and chitosan, was investigated for its physicochemical compatibility with carboxyl group functionalized CdS_xSe_{1-x}/ZnS-alloyed QDs (λ_{em}= 630 nm). The surface modification of paper introduced

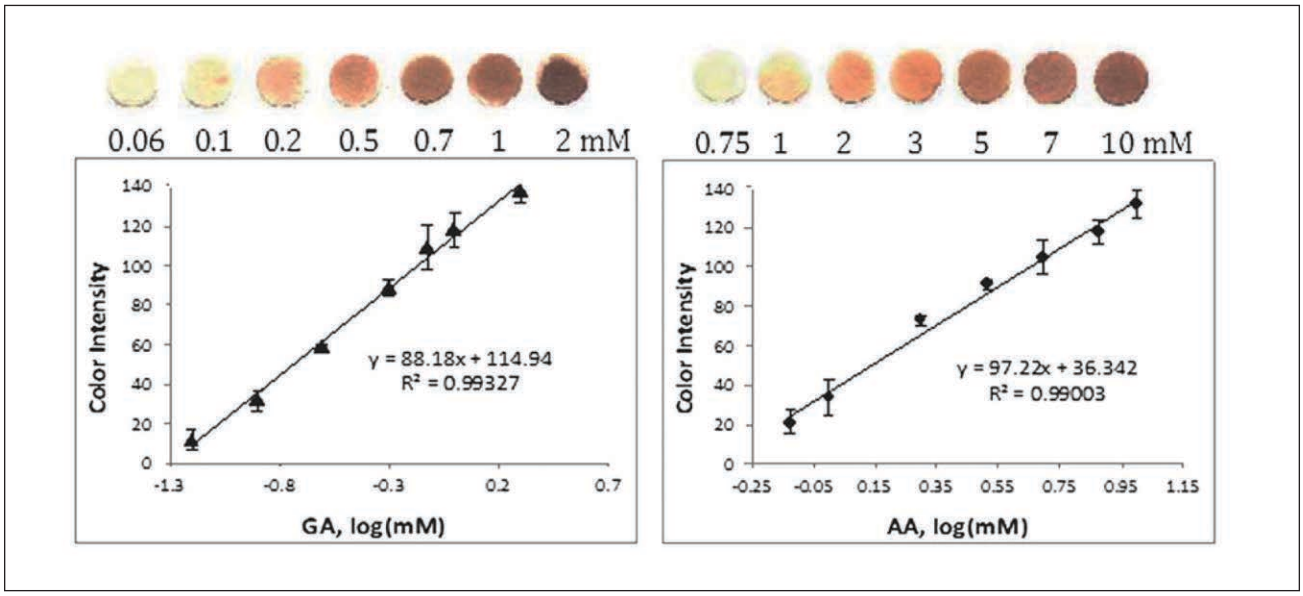
No.	Metal oxide	Method of immobilization/application	Reference
1.	ZnO	ZnO NPs synthesized using surfactants and deposited on cotton via ultrasound with antibacterial and antifungal activities	[58]
2.	ZnO	ZnO NPs impregnated on cellulose fibers with sodium alginate manifested good antibacterial activity against *Escherichia coli*	[57]
3.	ZnO	Ex situ synthesis of ZnO NPs using carbohydrates as capping agents for immobilization of antibodies; also showing antimicrobial activity and superior mechanical properties	[53]
4.	ZnO	Complete inhibition of *E. coli* under 9 h of visible light exposure with hydrothermally immobilized ZnO nanowires on paper sheet	[55]
5.	ZnO	Ultraviolet-vis-induced degradation of methylene blue and eosin yellowish by ZnO NPs deposited on cellulose using the sol-gel process	[84]
6.	ZnO	ZnO NPs grown in situ by seeding AgNPs on the surface of cotton fibers so as to prevent clustering	[85]
7.	ZnO	Hydrothermally grown ZnO nanowires on paper to build piezoelectric touch pads	[56]
8.	TiO_2	Adsorption of Pb^{2+} by mesoporous TiO_2 agglomerates synthesized under microwave irradiation on cellulose fibers	[72]
9.	TiO_2	Cellulose fibers modified with poly(ethyleneimine)–TiO_2–anthocyanin as a support for dye-sensitized solar cells	[86]
10.	TiO_2	TiO_2 NPs impregnated on cotton fibers for in situ photoreduction of Ag^+ ions to AgNPs with excellent antibacterial activity	[87]
11.	TiO_2	Photocatalytic degradation of methyl orange by TiO_2 NPs-loaded carbon fibers on cellulose fibers	[88]
12.	TiO_2	Hydrothermally synthesized TiO_2 layer with in situ formation of Cu_2O NPs on paper as efficient hybrid photocatalyst for solar light-induced degradation of toluidine	[89]
13.	TiO_2	Hydrothermally prepared TiO_2 nanobelts and AgNPs formed by in situ reduction on paper for efficient degradation of methyl orange and antibacterial activity	[90]
14.	TiO_2	TiO_2 synergistically modified with graphene on cotton fibers for photo-degradation of methylene blue and excellent antibacterial and antifungal activities	[91]
15.	TiO_2	Nano-TiO_2 sols functionalized on cotton fabrics for photo-degradation of rhodamine B to get self-cleaning textiles	[51]
16.	SiO_2	Ethanol suspension of superhydrophobic SiO_2 (immobilized by dodecyltrichloro groups) NPs spray-coated on paper	[92]
17.	SiO_2	In situ growth of NPs on cotton cellulose fibers to generate dual-scaled surface roughness for hydrophobicity	[93]
18.	CeO_2	CeO_2 NPs co-immobilized with enzyme on filter paper by silanization developed as colorimetric probes for bioanalysis	[94]
19.	Bi_2O_3	Bi_2O_3 NPs hydrothermally immobilized on cellulose to make antibacterial paper	[95]
20.	CuO	In situ deposition of CuO nanoleaves by soaking cellulose paper metal salt solution giving paper with antibacterial activity against gram-negative and gram-positive bacteria	[96]
21.	Mn_2O_3	In situ chemical synthesis of Mn(III) oxide on cellulose for Pb^{2+} removal	[97]
22.	Ag_2O	Ag_2O NPs loaded-graphite fibers on cellulose matrix to fabricate a full spectrum photocatalytic paper also showing bactericidal effect	[98]
23.	WO_3, MoO_3	Particulate WO_3 and MoO_3 dispersed in mashed filter paper to make electrochromic paper	[99]
24.	Indium tin oxide	Indium tin oxide NPs deposited with polyelectrolytes on coated wood fibers using layer-by-layer assembly to fabricate conductive paper	[100]

ZnO = zinc oxide; NPs = nanoparticles; AgNPs = silver nanoparticles; TiO_2 = titanium dioxide; Pb^{2+} = lead ion; Cu_2O = cuprous oxide; SiO_2 = silica; CeO_2 = cerium oxide; Bi_2O_3 = bismuth(III) oxide; Mn_2O_3 = manganese(III) oxide; Ag_2O = silver oxide; WO_3 = tungsten trioxide; MoO_3 = molybdenum trioxide.

I. Metal oxides immobilized on cellulose fibers for different applications.



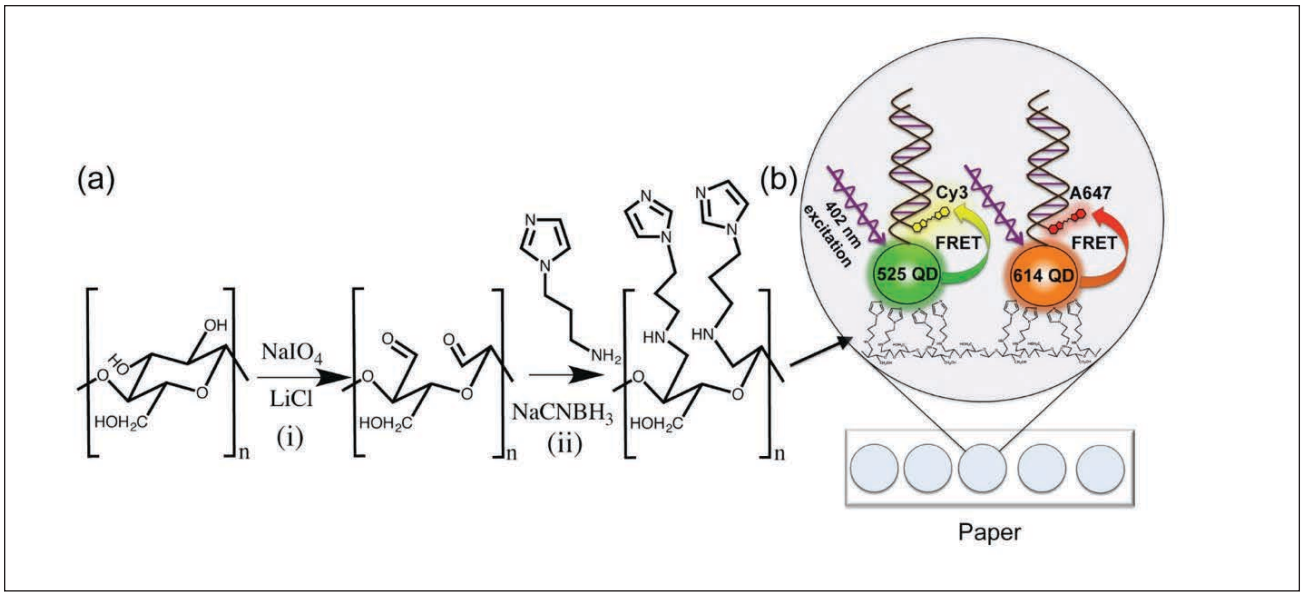
8. a) Photographs showing manganese dioxide (MnO_2)-immobilized cellulose papers prepared from different concentrations of aqueous potassium permanganate ($KMnO_4$): (a) 6.33 mM, (b) 12.6 mM, (c) 19 mM, and (d) 25.3 mM. b) Catalytic decomposition of formaldehyde (HCHO) by MnO_2 nanoparticle-coated cellulose fibers prepared from aqueous $KMnO_4$ of 12.6 mM (black squares), birnessite MnO_2 powder (red circles), and control without any catalyst (blue triangles) [81]. (Adapted with permission from ref. 81 © 2011 ACS publisher).



9. Colorimetric responses of cerium oxide (CeO_2) paper sensors to varying concentrations of gallic acid (GA) and ascorbic acid (AA) [82]. (Adapted with permission from ref. 82 © 2012 RSC publisher).

active functional groups, thereby improving the charge interaction between paper and QDs. In contrast, the QDs migrated with the solvent phase in the untreated paper. The fluorescence images captured a very weak red color for the untreated paper, whereas clear red signals were obtained for both modified paper samples. The chitosan-modified paper was used to design an analytical device for detection of glucose based on the quenching effect of the enzymatic product on the fluorescent emission of QDs [103]. Based on the same phenomenon of quenching, polymer QD-enzyme hybrid film deposited on a paper substrate was used as a versatile platform for biorecognition of glucose and phenol [105].

A different study developed a multiplexed nucleic acid hybridization assay based on fluorescence resonance energy transfer (FRET) by immobilizing multicolor quantum dot-probe oligonucleotide conjugates on paper surfaces modified with imidazole groups [104]. FRET monitors binding interactions based on the detection of proximity between a fluorescent energy donor and an acceptor [106]. Green-emitting QDs (gQDs) and red-emitting QDs (rQDs) served as donors with Cyanine 3 (Cy3) and Alexa Fluor 647 (A647) acceptors, respectively. The former donor/acceptor pair acted as an internal standard and the latter served as a detection channel to combine the control and analytical test zones in one location.

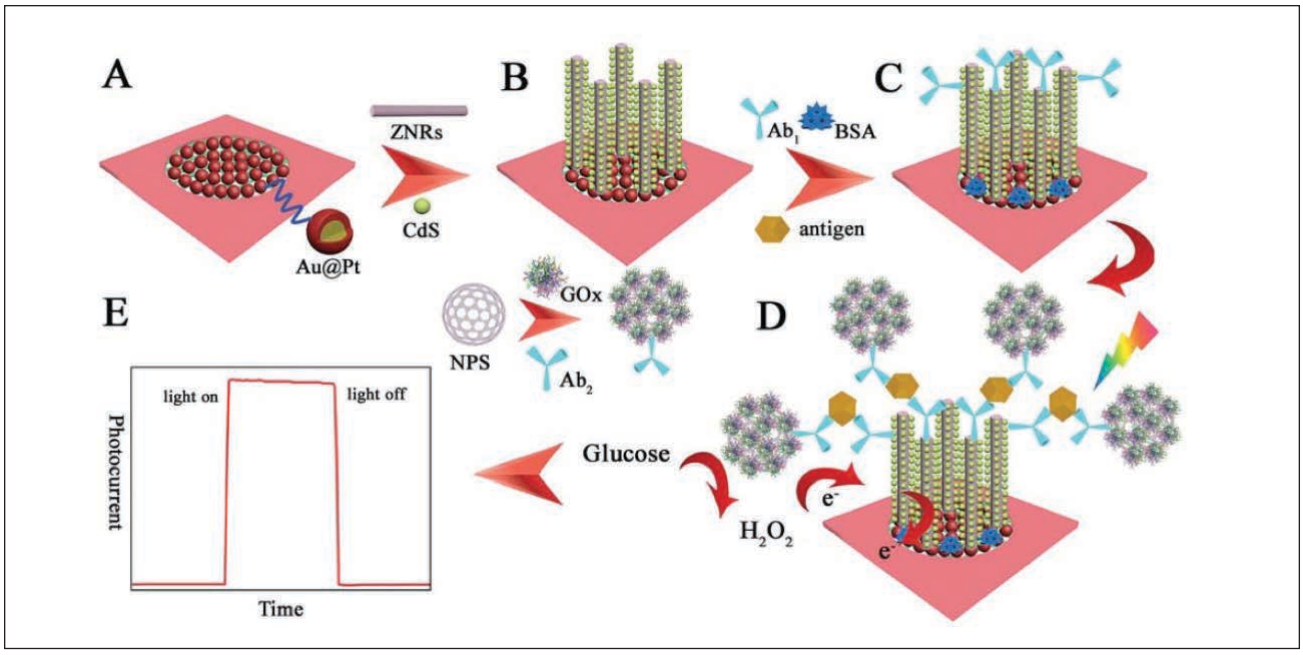


10. a) Step-wise surface modification of paper with imidazole ligands for the immobilization of green-emitting quantum dots (gQDs) and red-emitting quantum dots (rQDs) modified with SMN1 and uidA oligonucleotide probes, respectively; and b) design of the paper-based nucleic acid hybridization assay using gQDs and rQDs as donors in FRET [104]. (Adapted with permission from ref. 104 © 2013 ACS publisher).

Hybridization with Cy3 labeled SMN1 and A647 labeled uidA target oligonucleotides provided the proximity for FRET sensitized emission from Cy3 and A647 dyes when excited with a 402 nm laser, which served as an analytical signal (**Fig. 10**) [104]. Later, the same group integrated QD-FRET methods with digital imaging for a ratiometric transduction of nucleic acid hybridization on a paper-based platform [107]. Similarly, CdSeS/ZnS QDs immobilized on paper surface modified with thiol ligands were used as probes in paper-based diagnostic assay for proteolytic activity [108]. Recently, the researchers also demonstrated proof-of-concept by integrating QDs, smartphone imaging, and FRET on a paper-in-chip to develop a bioassay for detection of hydrolase activity in serum and whole blood using thrombin as an analyte [109]. Another work reported using highly luminescent CdTe QDs-cellulose composites with controlled emission to make LEDs, taking advantage of the high color purity from the narrow emission of QDs [110].

A microfluidic origami photoelectrochemical immunodevice (μ-OPECI) was developed using CdS QD-sensitized ZnO nanorods (ZNRs) as a photoactive matrix for the detection of tumor markers, carcinoembryonic antigen (CEA), and α-fetoprotein (AFP) [111]. The paper working electrode (PWE) was modified with core-shell type Au@Pt nanoparticles with subsequent in situ growth of ZNRs. The scanning electron microscopy (SEM) confirmed a dense and uniform film of CdS QDs, which was galvanostatically electrodeposited onto ZNR surfaces. The coupling with QDs provided enhanced excitation and conversion efficiency. Additionally, the fast electron migration from excited QDs to the ZNR/Au@Pt-PWE when irradiated improved the sensitivity through effective matching of energy levels between QDs and ZNRs. Further amplification in the photocurrent signal was achieved by nanoporous silver (NPS)-labeled glucose oxidase (GOx), which catalyzed the conversion of glucose into H_2O_2 for efficient electron donation. The antibody, Ab_1, was immobilized onto CdS/ZNR/Au@Pt-PWE via a coupling reaction. Another antibody, Ab_2, was conjugated with GOx/NPS for subsequent interaction with antigen biomarkers, CEA and AFP (**Fig. 11**). The dual-signal amplification strategy for detection resulted in excellent performance with good reproducibility and stability [111].

A few studies have reported the use of upconverting energy donors such as upconverting phosphors (UCPs) [112] and upconversion nanoparticles [113] in paper-based bioassays using luminescence resonance energy transfer (LRET). In simple terms, during upconversion, a sample is excited by light of lesser energy than that which it emits [106]. UCPs, when irradiated with near-infrared radiation, produce strong anti-Stokes photoluminescence of narrow bandwidth. The long excitation wavelengths have little interaction with biomolecules, thereby eliminating autofluorescence and scattered incident light, resulting in improved sensitivity of the assay. UCPs functionalized with streptavidin and adsorbed onto paper were conjugated with biotinylated oligonucleotide probes via streptavidin-biotin linkage to develop a paper-based DNA hybridization assay [112]. All these paper-based analytical devices (PADs) take advantage of the three-dimensional microstructure of paper, which promotes easy fluid transport through capillary action within the pores, thus reducing assay time. The porosity of paper serves as a filtering medium to separate particles and aggregated materials from the reaction zone. Moreover, the paper surface can be modified with functional groups that can be further conjugated



11. Schematic of the fabrication of a microfluidic origami photoelectrochemical immunodevice (μ-OPECI): (a) Au@Pt-PWE, growth of Au@Pt layer on the cellulose surface in bare paper working electrode (PWE); (b) CdS/ZNR/Au@Pt-PWE; (c) immobilization with Ab_1 and blocking with bovine serum albumin (BSA); (d) capturing, washing, and incubating with the corresponding bioconjugate; and (e) photoelectrochemical (PEC) detection of the μ-OPECI [111]. (Adapted with permission from ref. 111 © 2015 RSC publisher).

with various biomolecules and nanomaterials. On the whole, paper substrates provide inexpensive, portable, easy-to-develop, disposable, eco-friendly, and biocompatible platforms for PADs [112].

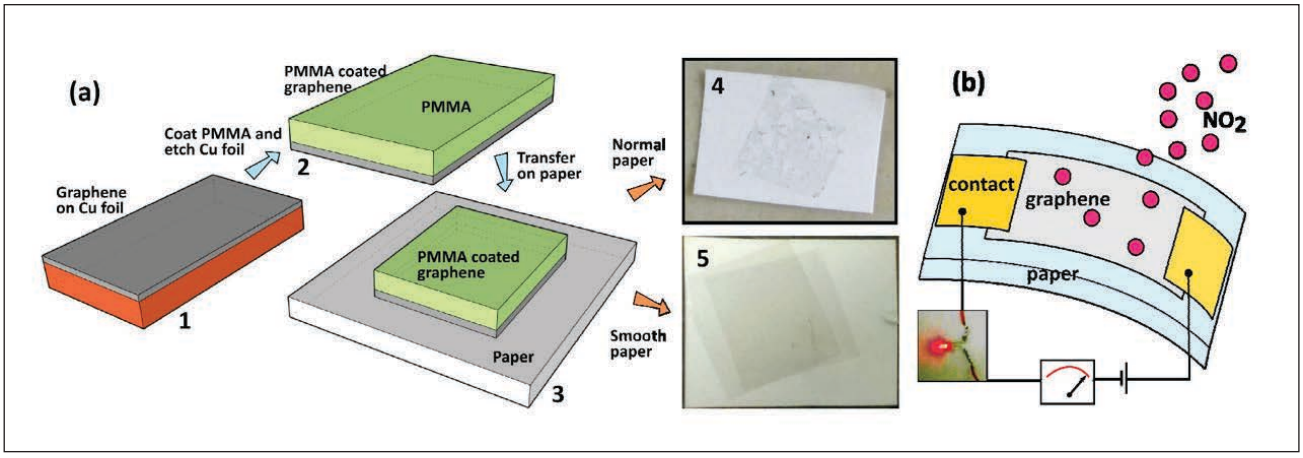
FUNCTIONALIZATION WITH CARBON NANOMATERIALS

Various nanomaterials based on carbon, such as fullerenes, graphene, and carbon nanotubes (CNTs) have attracted significant attention in the past three decades. In view of their extraordinary mechanical, optical, electrical, thermal, and chemical properties, they have been extensively explored for use in electronics, optoelectronics, photovoltaics, and sensing applications [10]. Since the discovery of CNTs by Iijima in 1991, considerable efforts have been devoted to uncovering their underlying potential. CNTs are seamless cylinders of single or layered graphene, with an aspect ratio ranging from 10^2 to 10^7. Apart from having a high surface area, CNTs have shown remarkable mechanical properties, good electrical conductivity, high thermal conductivity and stability, and unique mesoporosity. These attributes have made them very attractive for various piezoelectric and thermoelectric energy-harvesting devices, cells, batteries, and sensors [114]. Graphene is a two-dimensional, single atom-thick building block for other carbon materials. It consists of planar sheets of sp^2-bonded carbon atoms that are closely packed in a honeycomb crystal lattice. It has many similarities to CNTs in structure and property, which make it a promising candidate for use in similar areas as CNTs, including supercapacitors, solar cells, lithium-ion batteries, fuel cells, actuators, and transistors [114,115].

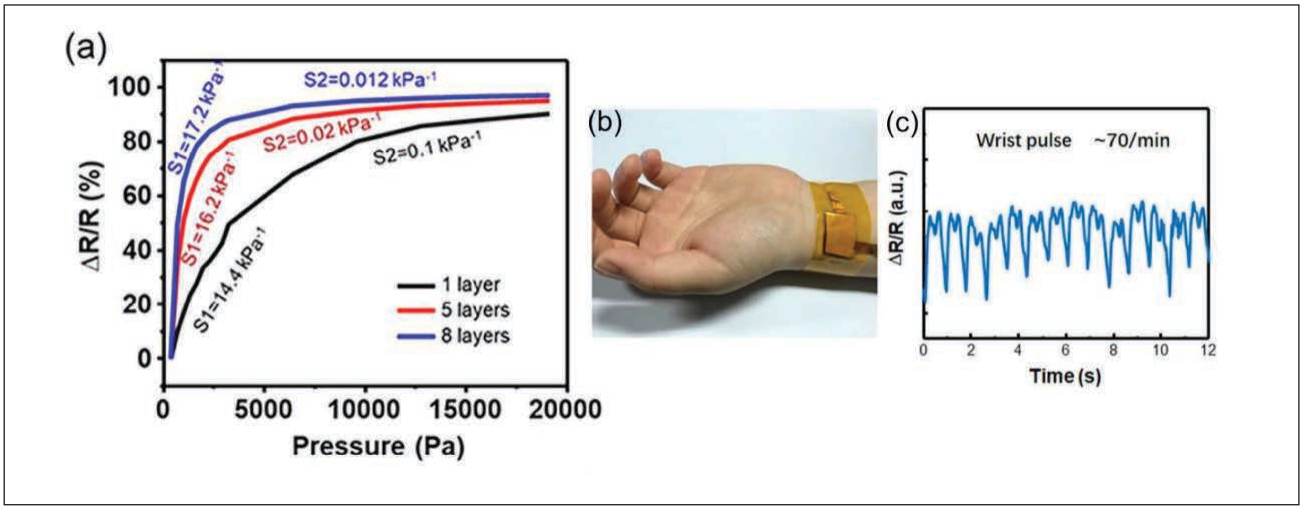
Carbon nanomaterials have been widely used to sense a variety of analytes, including gases, solvents, and biomolecules. Cellulose-based sensors using CNTs have been developed for the detection of glucose [116], ammonia [117, 118], tumor markers [119-122], chemical vapors [123], environmental toxins [124], water [125-127], and ions [128]. Different approaches used to anchor CNTs to cellulosic substrates include simple papermaking techniques [127,129], coating [130], mechanical drawing [118], and ink-jet printing [123].

A humidity sensor was fabricated by conformally coating single-walled CNTs (SWCNTs) functionalized with carboxylic acid on a paper surface [130]. The roughness and porosity of paper were advantageous because they increased the contact area with the ambient air and promoted adhesion to CNTs. SEM images confirmed firm entanglement of the CNTs with the cellulose fibers. A shift in conductance of the CNT network entangled on the fibers was used for humidity sensing. Because cellulose is an insulator, no current flowed in the bare paper up to 80% relative humidity (RH). Current, however, began to flow at higher RH because of ionic conduction from the dissociation of water. On the other hand, the CNT-coated paper showed a linear decrease in conductance with increasing RH, up to 75% RH, after which the rise in conductance was marginal. In comparison with a control sensor on glass substrate, cellulose aided the charge transport on the paper substrate, thus enhancing its sensitivity. The wettability of paper also allowed it to soak the CNT suspension, leading to better adhesion [130].

In another study, ink-jet printed films of CNTs on 100%



12. a) Schematic depicting transfer of graphene onto paper, b) graphene paper strip in action as a gas sensor may glow a light-emitting diode (LED) bulb [141]. (Adapted with permission from ref. 141 © 2015 ACS publisher).

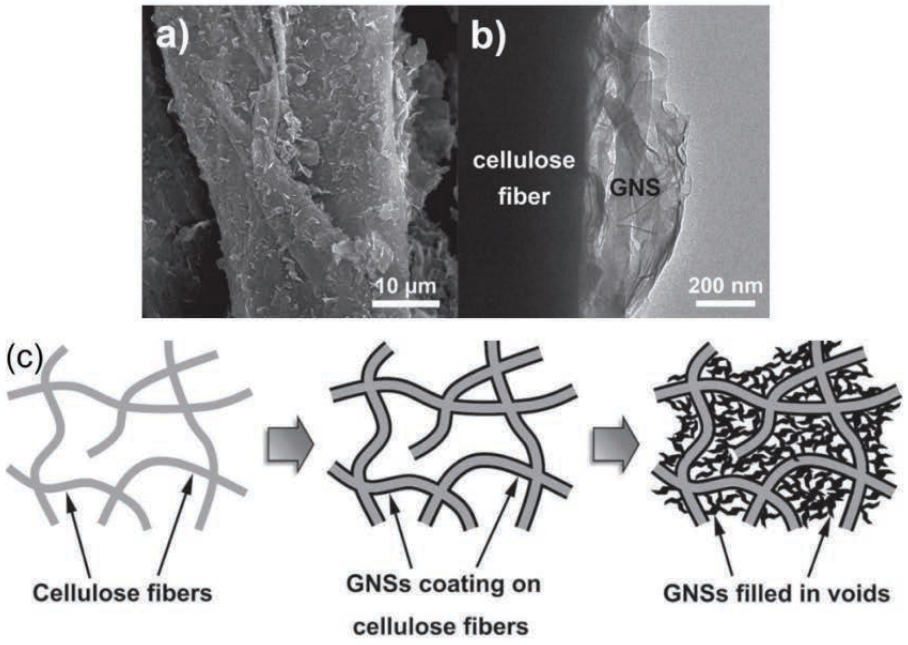


13. a) Increase in resistance change with pressure for graphene-based pressure sensor for different number of layers of tissue paper; b) sensor application for detection of wrist pulse; and c) pulse waveform of the sensor [133]. (Adapted with permission from ref. 133 © 2017 ACS publisher).

acid-free paper demonstrated the use of cellulose as a substrate for sensing chemically aggressive vapors [123]. The study showed that the instability of cellulose toward highly oxidizing vapors is not intrinsic, but instead, it is an outcome of the surface finishes used during paper manufacture. The detection of NO_2 and Cl_2 vapors up to 250 ppb and 500 ppb, respectively, was made possible by acid-free paper in ambient conditions by recording the resistance changes. Unlike polyethylene terephthalate (PET)-based substrates, the paper sensor exhibited spontaneous signal recovery and repeated use over multiple cycles, without loss of functionality. Study results suggested that cellulosic substrates can meaningfully mitigate the aggressive behavior of vapors such as Cl_2 toward thin organic films by reducing the residence time of vapors [123].

Like CNTs, graphene [131-134], reduced graphene oxide [135, 136], graphene quantum dots [137,138], and carbon nanodots [139,140] anchored to cellulosic substrates have shown extraordinary sensing potential. Graphene stands out as a material for sensing because of its single atom thickness, which makes it extremely sensitive to changes in its environment.

Graphene layers were directly transferred on paper for resistive sensing of NO_2 with remarkably low limit of detection at 300 ppt [141]. As shown in **Fig. 12**, graphene on copper foil was spin-coated with a layer of poly-(methyl methacrylate) (PMMA) and etched to foil. The PMMA-graphene film was then dredged onto paper and the PMMA was dissolved with acetone. Normal paper yielded a patchy coverage; complete transfer occurred on smooth glossy paper [141]. A pressure sensor was developed by soaking tissue paper in graphene oxide (GO) solution and subsequently reducing it thermally into reduced GO (rGO paper) [133]. Optimization between sensor sensitivity and working range was achieved in the range of 0–20 kPa and sensitivity up to 17.2 kPa^{-1}. Significant differences in sensor performance were observed with differ-

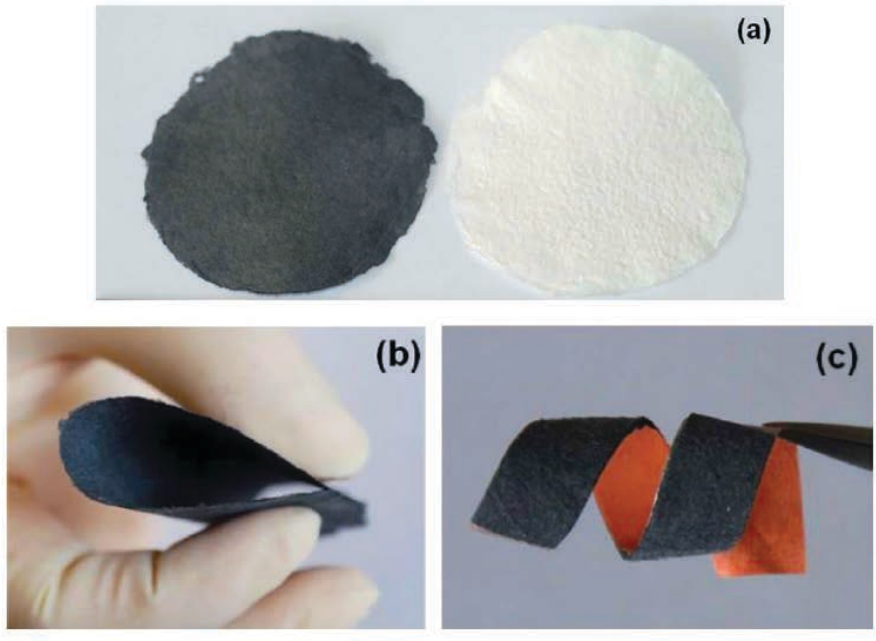


14. a) SEM and b) transmission electron microscopy (TEM) images of a cellulose fiber in a graphene-cellulose paper (GCP) membrane showing graphene nanosheets (GNSs) anchored on the fiber surface; and c) cellulose-graphene nanosheets binding in GCP [150]. (Adapted with permission from ref. 150 © 2011 JWS publisher).

ent numbers of tissue layers (**Fig. 13a**). As the number of layers increased, the sensitivity rose 17.2 kPa^{-1} in the range of 0–2 kPa, but fell to 0.1 kPa^{-1} in the range of 2–20 kPa. This was attributed to the presence of air gaps between the layers of tissue paper, resulting in poor contact, which led to a large origin resistance when no pressure was applied on the sensor. The sensor showed good response for detection of pulse, respiration, and other human movements (Fig. 13 b & c) [133]. Likewise, rGO on paper with AuPd alloy nanoparticles has been used for real-time and in situ analysis of hydrogen sulfide released from cancer cells [142]. An rGO-paper electrode modified with ZnO nanorods was used as an electrochemical sensor platform for various antigens [143]. A flower-like rGO-modified paper biosensor showed a good linear response for the detection of Pb^{2+} from 0.005 nM to 2000 nM [144]. Long graphene nanoribbons (150 nm wide) synthesized via nanoscale cutting of graphite were cleaved to produce graphene quantum dots (100–200 nm) for humidity and pressure sensors [145]. Electrochemical immunoassays with graphene-based sensing have been used to detect biomolecules such as DNA and biomarker [146-148].

Apart from sensing, carbon nanomaterials have found a plethora of applications in energy storage and energy conversion devices. Cellulose modified with fullerene has shown improved sorption efficiency for the recovery of copper, nickel, and cadmium ions from aqueous solutions [149]. Supercapacitors fabricated from graphene/cellulose composites as flexible electrodes have shown good capacitance, low resistance, and high strength [115,150]. The graphene-cellulose paper (GCP) was prepared by simply filtering a suspension of graphene nanosheets (GNSs) through a filter paper under vacuum. Electrostatic attraction between the functional groups on cellulose fibers and the negatively charged graphene caused the GNSs to strongly bind to fibers and penetrate the voids to form a conductive interwoven network (**Fig. 14**). The low strength and porosity of graphene was overcome by combining it with the cellulose matrix. The GCP also inherited mechanical flexibility from paper and could endure more than 1000 repeated bend tests, with little increase in resistivity for good supercapacitor performance [150]. Similarly, a GNS/paper composite was synthesized by dispersing chemically synthesized GNSs in a cellulose pulp, followed by infiltration. The tough paper composite could be bent and restored fully, forming good contact with the copper foil while remaining flexible without separation (**Fig. 15**). It also showed higher modulus of elasticity than pure cellulose paper because of the mechanical locking of the cellulose fibers by the GNS coating, making it less vulnerable to inter-fiber sliding. It exhibited high electrochemical activity as an electrode in a supercapacitor and lithium battery with a promising electrochemical performance [151]. Likewise, flexible electrodes from graphene/polyaniline composite paper have been reported [152].

Paper-based supercapacitors were prepared by depositing SWCNTs on a paper substrate via Meyer rod coating and inkjet printing. The paper was treated with polyvinylidene fluoride before printing of CNTs to prevent short circuiting and yet allow it to function as an electrolyte membrane and sepa-



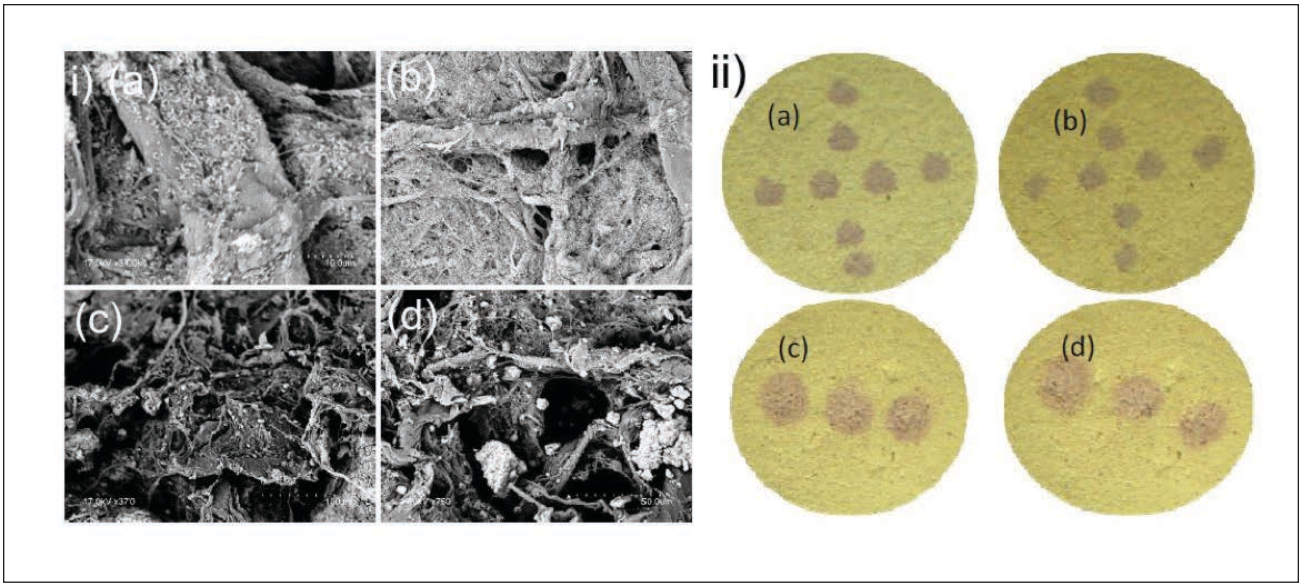
15. a) Graphene nanosheets/cellulose composite paper (black) against pure cellulose paper (white); b) the bent composite paper, showing flexibility of the paper; and c) composite paper adhered to conducting copper foil to make a flexible supercapacitor [151]. (Adapted with permission from ref. 151 © 2012 RSC publisher).

rator [153]. Earlier, the researchers had deposited a combination of SWCNTs and silver nanowires on paper using a printable solution processing technique. The values of specific capacitance, energy, power, and life were found to be better than those of devices that used plastic substrates. Those higher values were attributed to the intrinsic properties of paper, such as high solvent absorption and strong binding with nanomaterials. Superior mechanical properties resulted from the porous nature of paper, which relaxed the bending strain. Additionally, the conductive paper also showed potential as a current collector in lithium-ion batteries to replace the metallic counterparts [154]. Similar studies of CNT-coated paper supercapacitors have been reported [155-157].

FUNCTIONALIZATION WITH OTHER MATERIALS

Cellulosic substrates, such as paper, have attracted great attention from the scientific community for point-of-care diagnostic devices and on-site environmental monitoring. In this context, biomolecules such as enzymes, antibodies, bacteriophages, and aptamers have been embedded onto cellulose to render it bioactive for sensing and other purposes. Various methods, including physical attachment, covalent bonding, entrapment, and immobilization of carriers, have been used to anchor these biological entities onto cellulosic substrates [158]. Very recently, glucose oxidase from *A. niger* was covalently immobilized onto the surface of cellulose fibers premodified with amino functional groups to give biocatalytic fibers [159]. Similarly, lysozyme [160] and trypsin [161] were covalently anchored onto modified cotton for biomedical uses. Another study reported physical adsorption of glucose oxidase on filter paper disks to fabricate amperometric glucose sensors with a limit of detection of 0.18 mM [162]. An alternate layer-by-layer assembly of laccase and urease on cellulose was used to make biocomposites with catalytic activity [163]. Lysostaphin-functionalized cellulose with activity against *S. aureus* showed good biocompatibility for wound healing applications [164]. Antibodies covalently immobilized onto paper were used to build enzyme-linked immunosorbent assay (ELISA) with a limit of 100 ng/mL for immunoglobulin G detection [165]. Peptide conjugated to cellulose has been used for the fluorescent detection of human neutrophil elastase [166].

Several reports have focused on anchoring of polymers on cellulose fibers for applications such as sensing and adsorption. Colorimetric sensors for pH and ammonia were built by in situ polymerization of pyrrole on a paper matrix modified with bromophenol blue (BPB), an acid-basic indicator dye. The morphological analysis confirmed that the cellulose fibers were uniformly covered by polypyrrole, a stable conducting polymer, and strongly bound to BPB [167]. An acid-sensitive material was fabricated by depositing polyaniline nanoparticles on a cellulose sheet via a chromatographic process for colorimetric detection of acids [168]. Likewise, polyethyleneimine-functionalized paper has been used for adsorptive removal of hazardous pollutants such as Cr^{6-} anions, Ni^{2+}, Cd^{2+}, and Cu^{2+} cations [169]. Surface modification of cellulose was achieved by grafting it with various monomers, such as



16. i) SEM images showing spin-crossover particles in composite 1 (a & b) and composite 2 (c & d); ii) thermochromism of composite 1 before (a) and after (b) 275 print/erase cycle and that of composite 2 before (c) and after (d) 105 print/erase cycle [174]. (Adapted with permission from ref. 174 © 2015 RSC publisher).

methyl methacrylate, styrene, and glycidyl methacrylate, using atom transfer radical polymerization (ATRP) based on "activators regenerated by electron transfer" [170]. Cellulose fibers grafted with poly(N,N-dimethyl aminoethyl methacrylate) showed potential as an anion adsorbent for removal of fluoride and arsenic from aqueous media, even at low concentrations [171]. The wettability properties of cellulose were modified by atmospheric pressure plasma enhanced chemical vapor deposition of acrylic acid on a paper substrate [172].

Cellulose fibers functionalized with spin-crossover nanoparticles (SCO NPs), $[Fe(hptrz)_3](OTs)_2$ where hptrz = 4-heptyl-1,2,4-triazole and OTs = para-toluenesulfonyl, were used to fabricate sheets with specific optical properties [173]. The SCO NPs, known to display an abrupt spin transition with a hysteresis loop close to room temperature, were physically adsorbed onto linter fibers from a preformed colloidal solution. The modified sheets showed significant thermochromic and thermofluorescent effects associated with the spin transition phenomenon, and they could have potential applications in paper thermometry and anti-counterfeiting [173]. The same group also reported other works on spin crossover particles conjugated to cellulose [174,175]. Composites were fabricated with strong viscoelastic coupling between $[Fe(Htrz)_2(trz)](BF_4)$ microparticles (where Htrz = 1,2,4-4H-triazole and trz = 1,2,4-triazole) and the cellulose fiber matrix, combining the functionality of compliant, free-standing polymer materials with the actuating force arising with the spin transition in SCO particles [175]. Similarly, $[Fe(Htrz)_2(trz)]BF_4$ and $[Fe(NH_2trz)_3]Br_2$ particles were embedded onto linter fibers to form composite sheets 1 and 2, respectively, by the standard papermaking process [174]. The SEM micrographs taken in the backscattered electron mode (BSE) show randomly dispersed particles over the cellulose fibers as indicated by the brighter objects, along with some particle agglomeration (**Fig. 16i**). The composite sheets showed perceptible thermochromic effects associated with a memory effect (Fig. 16ii). They were rewritable by laser heating and completely erasable over several hundred printing cycles [174].

Additionally, few studies have investigated the anchoring of pigments and metal organic frameworks (MOFs) on cellulose. Hydrothermally synthesized magnesium hydroxide nanoparticles were deposited on cellulose fibers with different refining degrees using spraying and immersion methods to prevent them from aging [176]. The degree of refining significantly influenced the morphology of the sheets and the dispersion of the nanoparticles. In another work, silane modified-magnesium hydroxide was immobilized onto the surface of bromo end-functional cellulose fiber by surface-initiated ATRP. Cellulose grafted with the hybrid pigment showed improved thermal properties by absorbing four times more heat than the native fiber [177]. Cellulose hybrids with enhanced thermal properties were prepared by grafting with polyhedral oligomeric silsesquioxane (POSS) using a cross-linking agent [178]. MOF crystals anchored onto cellulose fibers have exhibited complete inhibition of *E. coli* on agar plates and liquid cultures [179]. Likewise, copper benzene-1,3,5-tricarboxylate (Cu-BTC) MOF crystals have shown preferential adsorption of ethylene over ethane and the ability to adsorb ammonia from air [180]. Cotton fabrics coated with an amine-functionalized titanium-bearing MOF (NH_2-MIL-125) displayed excellent antimosquito properties by attracting and killing those insects [181].

CONCLUSION

An exhaustive review based on the functionalization of cellulose fibers with various types of nanomaterials, including metals, metal oxides, QDs, carbon, biomolecules, and poly-

mers is presented. The last two decades have witnessed immense growth in the use of cellulose and its modification, providing huge scope for a wide array of applications. Cellulose is an attractive material owing to its huge abundance, easy availability, low-cost, biocompatibility, and non-toxicity, while cellulose-based devices are promising due to their flexibility, portability, disposability, and eco-friendliness. The chemical structure of cellulose with end hydroxyl groups has facilitated its surface modification with functional species. The hydrophilic nature and porosity of native cellulose play a key role to anchor the nanomaterials by way of either physical sorption or covalent linkage. Cellulose has been exploited as a substrate for the development of paper-based immunoassays for signal amplification and detection of target analytes. The immobilization of metal and metal oxide nanomaterials onto cellulose fibers has opened new avenues for various point-of-care devices like biosensors and antibacterial coatings, and for environmental remediation applications, such as photocatalysis of organic pollutants and adsorption of heavy metals. Carbon nanotubes and graphene incorporated into cellulose have been vastly explored for energy harvesting devices like supercapacitors, apart from sensing. Nevertheless, challenges still exist in their synthesis, applications, and large-scale commercialization from laboratory-scale, which can be resolved to some extent by collaborative efforts between various disciplines of science, engineering, and industry. **TJ**

ACKNOWLEDGEMENT

We thank the Tempus Public Foundation (TPF) for providing financial assistance under the Stipendium Hungaricum Programme. This review was also supported through "EFOP-3.6.1-16-2016-00018 – Improving the role of research +development+innovation in the higher education through institutional developments assisting intelligent specialization in Sopron and Szombathely."

LITERATURE CITED

1. Credou, J. and Berthelot, T., *J. Mater. Chem. B* 2(30): 4767(2014).
2. Hokkanen, S., Bhatnagar, A., and Sillanpaa, M., *Water Res.* 91: 156(2016).
3. Moon, R.J., Martini, A., Nairn, J., et al., *Chem. Soc. Rev.* 40(7): 3941(2011).
4. Siqueira, G., Bras, J., and Dufresne, A., *Polymers* 2(4): 728(2010).
5. Ge, S., Zhang, L., Zhang, Y., et al., *Nanoscale* 9(13): 4366(2017).
6. Chauhan, I., Aggrawal, S., Chandravati, C., et al., *RSC Adv.* 5(101): 83036(2015).
7. Liu, Y. and Chen, J.Y., *J. Bioact. Compat. Polym.* 31(6): 553(2016).
8. Tiwari, S., Vinchurkar, M., Rao, V.R., et al., *Sci. Rep.* 7: 43905(2017).
9. Ngo, Y.H., Li, D., Simon, G.P., et al., *Adv. Colloid Interface Sci.* 163(1): 23(2011).
10. Jariwala, D., Sangwan, V.K., Lauhon, L.J., et al., *Chem. Soc. Rev.* 42(7): 2824(2013).
11. He, J., Kunitake, T., and Nakao, A., *Chem. Mater.* 15(23): 4401(2003).
12. Pinto, R.J., Neves, M.C., Neto, C.P., et al., in *Nanocomposites-New Trends and Developments*, InTech, Rijeka, Croatia, 2012, Chap. 4.
13. Dong, B.H. and Hinestroza, J.P., *ACS Appl. Mater. Interfaces* 1(4): 797(2009).
14. Breitwieser, D., Moghaddam, M.M., Spirk, S., et al., *Carbohydr. Polym.* 94(1): 677(2013).
15. Tang, F., Zhang, L., Zhang, Z., et al., *J. Macromol. Sci. Part A: Pure Appl. Chem.* 46(10): 989(2009).
16. Zhu, C., Xue, J., and He, J., *J. Nanosci. Nanotechnol.* 9(5): 3067(2009).
17. Park, S.Y., Chung, J.W., Priestley, R.D., et al., *Cellulose* 19(6): 2141(2012).
18. Shateri Khalil-Abad, M., Yazdanshenas, M.E., and Nateghi, M.R., *Cellulose* 16(6): 1147(2009).
19. Csóka, L., Bozanic, D.K., Nagy, V., et al., *Carbohydr. Polym.* 90(2): 1139(2012).
20. Dankovich, T.A. and Gray, D.G., *Environ. Sci. Technol.* 45(5): 1992(2011).
21. Yu, W.W. and White, I.M., *Anal. Chem.* 82(23): 9626(2010).
22. Tseng, S.C., Yu, C.C., Wan, D., et al., *Anal. Chem.* 84(11): 5140(2012).
23. Polavarapu, L. and Liz-Marzan, L.M., *Phys. Chem. Chem. Phys.* 15(15): 5288(2013).
24. Hasi, W.-L.-J., Lin, X., Lou, X.-T., et al., *Appl. Phys. A* 118(3): 799(2014).
25. Polavarapu, L., Porta, A.L., Novikov, S.M., et al., *Small* 10(15): 3065(2014).
26. Li, W., Li, L., Ge, S., et al., *Chem. Commun. (Cambridge, U.K.)* 49(70): 7687(2013).
27. Li, W., Li, L., Ge, S., et al., *Biosens. Bioelectron.* 56: 167(2014).
28. Scida, K., Cunningham, J.C., Renault, C., et al., *Anal. Chem.* 86(13): 6501(2014).
29. Wang, J., Yang, L., Liu, B., et al., *Anal. Chem.* 86(7): 3338(2014).
30. Zhang, Y., Aslan, K., Previte, M.J.R., et al., *Dyes Pigm.* 77(3): 545(2008).
31. Ashraf, S., Saif ur, R., Sher, F., et al., *Cellulose* 21(1): 395(2013).
32. Sun, G., Liu, H., Zhang, Y., et al., *New J. Chem.* 39(8): 6062(2015).
33. Yan, J., Yan, M., Ge, L., et al., *Chem. Commun. (Cambridge, U.K.)* 49(14): 1383(2013).
34. Wu, L., Ma, C., Zheng, X., et al., *Biosens. Bioelectron.* 68: 413(2015).
35. Wu, K., Zhang, Y., Wang, Y., et al., *ACS Appl. Mater. Interfaces* 7(43): 24330(2015).
36. Ge, S., Zhang, Y., Zhang, L., et al., *Sens. Actuators, B* 220: 665(2015).
37. Ge, S., Liu, W., Ge, L., et al., *Biosens. Bioelectron.* 49: 111(2013).
38. Lee, C.H., Hankus, M.E., Tian, L., et al., *Anal. Chem.* 83(23): 8953(2011).
39. Ngo, Y.H., Li, D., Simon, G.P., et al., *Langmuir* 28(23): 8782(2012).
40. Ngo, Y.H., Li, D., Simon, G.P., et al., *J. Colloid Interface Sci.* 392: 237(2013).
41. Ngo, Y.H., Then, W.L., Shen, W., et al., *J. Colloid Interface Sci.* 409: 59(2013).

42. Zheng, G., Polavarapu, L., Liz-Marzan, L.M., et al., *Chem. Commun. (Cambridge, U.K.)* 51(22): 4572(2015).
43. Liu, L., Zhao, Y., Chen, Q., et al., *RSC Adv.* 5(126): 104239(2015).
44. Cady, N.C., Behnke, J.L., and Strickland, A.D., *Adv. Funct. Mater.* 21(13): 2506(2011).
45. Bodelón, G., Mourdikoudis, S., Yate, L., et al., *ACS Nano* 8(6): 6221(2014).
46. Ferreira, I., Bras, B., Correia, N., et al., *J. Disp. Technol.* 6(8): 332(2010).
47. Liu, F., Ge, S., Yu, J., et al., *Chem. Commun. (Cambridge, U.K.)* 50(71): 10315(2014).
48. Li, L., Kong, Q., Zhang, Y., et al., *J. Mater. Chem. B* 3(14): 2764(2015).
49. Zheng, G., Kaefer, K., Mourdikoudis, S., et al., *J. Phys. Chem. Lett.* 6(2): 230(2015).
50. Jaisai, M., Baruah, S., and Dutta, J., *Beilstein J. Nanotechnol.* 3: 684(2012).
51. Ortelli, S., Blosi, M., Albonetti, S., et al., *J. Photochem. Photobiol., A* 276: 58(2014).
52. Li, Y., Li, L., Cao, L., et al., *Chem. Eng. J.* 283: 1145(2016).
53. Khatri, V., Halasz, K., Trandafilovic, L.V., et al., *Carbohydr. Polym.* 109: 139(2014).
54. Zhao, S.-W., Zheng, M., Zou, X.-H., et al., *ACS Sustainable Chem. Eng.* 5(8): 6585(2017).
55. Chauhan, I., Aggrawal, S., and Mohanty, P., *Environ. Sci. Nano* 2(3): 273(2015).
56. Li, X., Wang, Y.H., Zhao, C., et al., *ACS Appl. Mater. Interfaces* 6(24): 22004(2014).
57. Varaprasad, K., Raghavendra, G.M., Jayaramudu, T., et al., *Carbohydr. Polym.* 135: 349(2016).
58. El-Nahhal, I.M., Elmanama, A.A., El Ashgar, N.M., et al., *Ultrason. Sonochem.* 38: 478(2017).
59. Baruah, S., Jaisai, M., Imani, R., et al., *Sci. Technol. Adv. Mater.* 11(5): 055002(2010).
60. Li, X., Zhao, C., and Liu, X., *Microsyst. Nanoeng.* 1: 15014(2015).
61. Gimenez, A.J., Yáñez-Limón, J.M., and Seminario, J.M., *J. Phys. Chem. C* 115(1): 282(2011).
62. Gullapalli, H., Vemuru, V.S., Kumar, A., et al., *Small* 6(15): 1641(2010).
63. Sun, G., Yang, H., Zhang, Y., et al., *Biosens. Bioelectron.* 74: 823(2015).
64. Zhang, Y., Ge, L., Li, M., et al., *Chem. Commun. (Cambridge, U.K.)* 50(12): 1417(2014).
65. Sun, G., Yang, H., Ma, C., et al., *New J. Chem.* 39(9): 7012(2015).
66. Adjimi, S., Sergent, N., Roux, J.C., et al., *Appl. Catal., B* 154-155: 123(2014).
67. Chauhan, I. and Mohanty, P., *RSC Adv.* 4(101): 57885(2014).
68. Fujiwara, K., Kuwahara, Y., Sumida, Y., et al., *Langmuir* 33(1): 288(2017).
69. Jiao, Y., Wan, C., and Li, J., *Funct. Mater. Lett.* 10(03): 1750018(2017).
70. Matsubara, H., Takada, M., Koyama, S., et al., *Chem. Lett.* 24(9): 767(1995).
71. Li, S.X., Lin, X., Zheng, F.Y., et al., *Anal. Chem.* 86(14): 7079(2014).
72. Zhang, J., Li, L., Li, Y., et al., *Chem. Eng. J.* 313: 1132(2017).
73. Li, Y., Cao, L., Li, L., et al., *J. Hazard. Mater.* 289: 140(2015).
74. Abdel Rehim, M.H., El-Samahy, M.A., Badawy, A.A., et al., *Carbohydr. Polym.* 148: 194(2016).
75. Ye, L., Filipe, C.D.M., Kavoosi, M., et al., *J. Mater. Chem.* 19(15): 2189(2009).
76. Venkataramanan, N.S., Matsui, K., Kawanami, H., et al., *Green Chem.* 9(1): 18(2007).
77. Hou, A., Yu, Y., and Chen, H., *Carbohydr. Polym.* 79(3): 578(2010).
78. Xie, K., Yu, Y., and Shi, Y., *Carbohydr. Polym.* 78(4): 799(2009).
79. Raabe, J., de Souza Fonseca, A., Bufalino, L., et al., *Carbohydr. Polym.* 114: 424(2014).
80. Gamelas, J.A.F., Evtyugina, M.G., Portugal, I., et al., *RSC Adv.* 2(3): 831(2012).
81. Zhou, L., He, J., Zhang, J., et al., *J. Phys. Chem. C* 115(34): 16873(2011).
82. Sharpe, E., Frasco, T., Andreescu, D., et al., *Analyst* 138(1): 249(2013).
83. Sharpe, E., Bradley, R., Frasco, T., et al., *Sens. Actuators, B* 193: 552(2014).
84. Moafi, H.F., Shojaie, A.F., and Zanjanchi, M.A., *Thin Solid Films* 519(11): 3641(2011).
85. Barani, H., *New J. Chem.* 38(9): 4365(2014).
86. Csóka, L., Dudić, D., Petronijević, I., et al., *Cellulose* 22(1): 779(2014).
87. Milošević, M., Radoičić, M., Šaponjić, Z., et al., *Cellulose* 21(5): 3781(2014).
88. Zhang, J., Liu, W., Wang, P., et al., *J. Environ. Chem. Eng.* 1(3): 175(2013).
89. Sboui, M., Bouattour, S., Gruttadauria, M., et al., *RSC Adv.* 6(90): 86918(2016).
90. Wang, J., Liu, W., Li, H., et al., *Chem. Eng. J.* 228: 272(2013).
91. Karimi, L., Yazdanshenas, M.E., Khajavi, R., et al., *Appl. Surf. Sci.* 332: 665(2015).
92. Ogihara, H., Xie, J., Okagaki, J., et al., *Langmuir* 28(10): 4605(2012).
93. Chen, X., Liu, Y., Lu, H., et al., *Cellulose* 17(6): 1103(2010).
94. Ornatska, M., Sharpe, E., Andreescu, D., et al., *Anal. Chem.* 83(11): 4273(2011).
95. Aggrawal, S., Chauhan, I., and Mohanty, P., *Mater. Express* 5(5): 429(2015).
96. Yoosefi Booshehri, A., Wang, R., and Xu, R., *Chem. Eng. J.* 262: 999(2015).
97. Maliyekkal, S.M., Lisha, K.P., and Pradeep, T., *J. Hazard. Mater.* 181(1-3): 986(2010).
98. Chen, H. and Liu, W., *J. Bioresour. Bioprod.* 1(4): 192(2016).
99. Monk, P.M., Delage, F., and Vieira, S.M.C., *Electrochim. Acta* 46(13): 2195(2001).
100. Peng, C.Q., Thio, Y.S., and Gerhardt, R.A., *Nanotechnology* 19(50): 505603(2008).

101. Rogach, A.L., *Semiconductor Nanocrystal Quantum Dots*, Springer, New York, 2008.
102. Algar, W.R., Tavares, A.J., and Krull, U.J., *Anal. Chim. Acta* 673(1): 1(2010).
103. Guan, L., Tian, J., Cao, R., et al., *BioResources* 10(1): 1587(2015).
104. Noor, M.O. and Krull, U.J., *Anal. Chem.* 85(15): 7502(2013).
105. Yuan, J., Gaponik, N., and Eychmuller, A., *Anal. Chem.* 84(11): 5047(2012).
106. Morgan, C.G., Dad, S., and Mitchell, A.C., *J. Alloys Compd.* 451(1-2): 526(2008).
107. Noor, M.O. and Krull, U.J., *Anal. Chem.* 86(20): 10331(2014).
108. Petryayeva, E. and Algar, W.R., *Anal. Chem.* 85(18): 8817(2013).
109. Petryayeva, E. and Algar, W.R., *Analyst* 140(12): 4037(2015).
110. Zhou, D., Zou, H., Liu, M., et al., *ACS Appl. Mater. Interfaces* 7(29): 15830(2015).
111. Ge, S., Li, W., Yan, M., et al., *J. Mater. Chem. B* 3(12): 2426(2015).
112. Zhou, F., Noor, M.O., and Krull, U.J., *Anal. Chem.* 86(5): 2719(2014).
113. Zhou, F., Noor, M.O., and Krull, U.J., *Nanomaterials (Basel)* 5(4): 1556(2015).
114. Dai, L., Chang, D.W., Baek, J.B., et al., *Small* 8(8): 1130(2012).
115. Liu, W.-W., Yan, X.-B., Lang, J.-W., et al., *J. Mater. Chem.* 22(33): 17245(2012).
116. Figueredo, F., Garcia, P.T., Corton, E., et al., *ACS Appl. Mater. Interfaces* 8(1): 11(2016).
117. Han, J.-W., Kim, B., Li, J., et al., *RSC Adv.* 4(2): 549(2014).
118. Mirica, K.A., Weis, J.G., Schnorr, J.M., et al., *Angew. Chem. Int. Ed. Engl.* 51(43): 10740(2012).
119. Liu, W., Yang, H., Ding, Y., et al., *Analyst* 139(1): 251(2014).
120. Wang, P., Ge, L., Yan, M., et al., *Biosens. Bioelectron.* 32(1): 238(2012).
121. Ge, S., Ge, L., Yan, M., et al., *Chem. Commun. (Cambridge, U.K.)* 48(75): 9397(2012).
122. Feng, Q.M., Pan, J.B., Zhang, H.R., et al., *Chem. Commun. (Cambridge, U.K.)* 50(75): 10949(2014).
123. Ammu, S., Dua, V., Agnihotra, S.R., et al., *J. Am. Chem. Soc.* 134(10): 4553(2012).
124. Wang, L., Chen, W., Xu, D., et al., *Nano Lett.* 9(12): 4147(2009).
125. Qi, H., Liu, J., Deng, Y., et al., *J. Mater. Chem. A* 2(15): 5541(2014).
126. Qi, H., Mäder, E., and Liu, J., *Sens. Actuators, B* 185: 225(2013).
127. Dichiara, A.B., Song, A., Goodman, S.M., et al., *J. Mater. Chem. A* (5)38: 20161(2017).
128. Guinovart, T., Parrilla, M., Crespo, G.A., et al., *Analyst* 138(18): 5208(2013).
129. Anderson, R.E., Guan, J., Ricard, M., et al., *J. Mater. Chem.* 20(12): 2400(2010).
130. Han, J.-W., Kim, B., Li, J., et al., *J. Phys. Chem. C* 116(41): 22094(2012).
131. Ruecha, N., Rangkupan, R., Rodthongkum, N., et al., *Biosens. Bioelectron.* 52: 13(2014).
132. Li, L., Li, W., Yang, H., et al., *Electrochim. Acta* 120: 102(2014).
133. Tao, L.Q., Zhang, K.N., Tian, H., et al., *ACS Nano* 11(9): 8790(2017).
134. Yang, G., Lee, C., Kim, J., et al., *Phys. Chem. Chem. Phys.* 15(6): 1798(2013).
135. Kumar, S., Kumar, S., Srivastava, S., et al., *Biosens. Bioelectron.* 73: 114(2015).
136. Ling, Y., Li, X., Zhou, S., et al., *J. Mater. Chem. A* 3(14): 7422(2015).
137. Zhang, L., Li, L., Ma, C., et al., *Sens. Actuators, B* 221: 799(2015).
138. Carrasco, P.M., García, I., Yate, L., et al., *Carbon* 109: 658(2016).
139. Kim, Y., Jang, G., and Lee, T.S., *ACS Appl. Mater. Interfaces* 7(28): 15649(2015).
140. Wang, Y., Wang, S., Ge, S., et al., *Anal. Methods* 5(5): 1328(2013).
141. Kumar, S., Kaushik, S., Pratap, R., et al., *ACS Appl. Mater. Interfaces* 7(4): 2189(2015).
142. Yang, H., Zhang, Y., Li, L., et al., *Biosens. Bioelectron.* 87: 53(2017).
143. Sun, G., Zhang, L., Zhang, Y., et al., *Biosens. Bioelectron.* 71: 30(2015).
144. Ge, S., Wu, K., Zhang, Y., et al., *Biosens. Bioelectron.* 80: 215(2016).
145. Sreeprasad, T.S., Rodriguez, A.A., Colston, J., et al., *Nano Lett.* 13(4): 1757(2013).
146. Li, M., Wang, Y., Zhang, Y., et al., *Biosens. Bioelectron.* 59: 307(2014).
147. Zhang, Y., Li, L., Yang, H., et al., *RSC Adv.* 3(34): 14701(2013).
148. Li, L., Zhang, L., Yu, J., et al., *Biosens. Bioelectron.* 71: 108(2015).
149. Alekseeva, O.V., Bagrovskaya, N.A., and Noskov, A.V., *Russ. J. Appl. Chem.* 88(3): 436(2015).
150. Weng, Z., Su, Y., Wang, D.-W., et al., *Adv. Energy Mater.* 1(5): 917(2011).
151. Kang, Y.R., Li, Y.L., Hou, F., et al., *Nanoscale* 4(10): 3248(2012).
152. Wang, D.W., Li, F., Zhao, J., et al., *ACS Nano* 3(7): 1745(2009).
153. Hu, L., Wu, H., and Cui, Y., *Appl. Phys. Lett.* 96(18): 183502(2010).
154. Hu, L., Choi, J.W., Yang, Y., et al., *Proc. Natl. Acad. Sci. USA* 106(51): 21490(2009).
155. Kang, Y.J., Chung, H., Han, C.-H., et al., *Nanotechnology* 23(28): 289501(2012).
156. Kang, Y.J., Kim, B., Chung, H., et al., *Synth. Met.* 160(23-24): 2510(2010).
157. Ge, L., Wang, P., Ge, S., et al., *Anal. Chem.* 85(8): 3961(2013).
158. Sicard, C. and Brennan, J.D., *MRS Bulletin* 38(04): 331(2013).
159. Vega Erramuspe, I.B., Fazeli, E., Nareoja, T., et al., *Biomacromolecules* 17(10): 3188(2016).
160. Edwards, J.V., Prevost, N.T., Condon, B., et al., *Cellulose* 18(5): 1239(2011).
161. Nikolic, T., Kostic, M., Praskalo, J., et al., *Carbohydr. Polym.* 82(3): 976(2010).
162. Kuek Lawrence, C.S., Tan, S.N., and Floresca, C.Z., *Sens. Actuators, B* 193: 536(2014).
163. Xing, Q., Eadula, S.R., and Lvov, Y.M., *Biomacromolecules* 8(6): 1987(2007).
164. Miao, J., Pangule, R.C., Paskaleva, E.E., et al., *Biomaterials* 32(36): 9557(2011).
165. Peng, Y., Gelder, V.V., Amaladoss, A., et al., *J. Visualized Exp.* 116: e54111(2016).

166. Edwards, J.V., Fontenot, K.R., Haldane, D., et al., *Cellulose* 23(2): 1283(2016).

167. Gonçalves, D., *Open Chem.* 14(1): 404(2016).

168. Souza, F.G., Oliveira, G.E., Anzai, T., et al., *Macromol. Mater. Eng.* 294(11): 739(2009).

169. Setyono, D. and Valiyaveettil, S., *J. Hazard. Mater.* 302: 120(2016).

170. Hansson, S., Ostmark, E., Carlmark, A., et al., *ACS Appl. Mater. Interfaces* 1(11): 2651(2009).

171. Tian, Y., Wu, M., Liu, R., et al., *J. Hazard. Mater.* 185(1): 93(2011).

172. Garcia-Torres, J., Sylla, D., Molina, L., et al., *Appl. Surf. Sci.* 305: 292(2014).

173. Nagy, V., Halász, K., Carayon, M.-T., et al., *Colloids Surf., A* 456: 35(2014).

174. Nagy, V., Suleimanov, I., Molnár, G., et al., *J. Mater. Chem. C* 3(30): 7897(2015).

175. Rat, S., Nagy, V., Suleimanov, I., et al., *Chem. Commun. (Cambridge, U.K.)* 52(75): 11267(2016).

176. Sierra-Fernandez, A., Gomez-Villalba, L.S., Rabanal, M.E., et al., *RSC Adv.* 6(57): 51583(2016).

177. Wang, X., Zhang, Y., Lv, L., et al., *Appl. Surf. Sci.* 363: 189(2016).

178. Xie, K., Zhang, Y., and Yu, Y., *Carbohydr. Polym.* 77(4): 858(2009).

179. Rodríguez, H.S., Hinestroza, J.P., Ochoa-Puentes, C., et al., *J. Appl. Polym. Sci.* 131(19): 40815(2014).

180. Bunge, M.A., Ruckart, K.N., Leavesley, S., et al., *Ind. Eng. Chem. Res.* 54(15): 3821(2015).

181. Abdelhameed, R.M., Kamel, O.M.H.M., Amr, A., et al., *ACS Appl. Mater. Interfaces* 9(27): 22112(2017).

ABOUT THIS PAPER

Cite this article as: Agarwal, C., Csoka, L. *TAPPI J.* 17(2): 92(2018). https://doi.org/10.32964/TJ17.02.92

DOI: https://doi.org/10.32964/TJ17.02.92

ISSN: 0734-1415

Publisher: TAPPI Press

Copyright: ©TAPPI Press 2018

About this journal

ABOUT THE AUTHORS

This review aims to throw light on the various ways cellulose fibers can be functionalized for desired applications. Cellulose is an emerging biomaterial that is being explored for new applications by modifying it with functional nanomaterials. Its inherent properties will make it a next-generation material in virtually every sector, from electronics to aeronautics.

We have worked with natural cellulose fibers and their functional modification with nanomaterials. The review will go a long way in supporting our research on developing cellulose fiber-based novel materials.

It was challenging to categorize the review systematically and create a continuity of ideas. Efforts were put forth to create methodological filters and to logically structure and organize the information so as to reach the readers in a simple yet impactful way.

The review has broadened our outlook towards cellulose. Going through the review makes one realize the innumerable possibilities in which this simple natural fiber can be modified to suit a targeted application.

It was very interesting to note how the methods for immobilization of nanomaterials have evolved over time, addressing the limitations of conventional ways.

Mills might look into the scale-up/commercialization aspects of essential cellulose/paper-based devices, such as the diagnosis kits for point of care applications, to cater to wider and needy sections of society and bring down the overall costs of manufacture/testing/diagnosis kits. Further, it may lead to potential savings in energy and resources by limiting the need for expensive tests and state-of-art infrastructure.



Agarwal



Csóka

The next steps may look into the limitations of the current works and try to address them by using different ways of synthesizing materials and processing or using them.

Agarwal is a Ph.D. scholar and Csóka is professor, Cellulose and Biomacromolecules Research Group, Institute of Wood Based Products and Technologies, University of Sopron, Hungary. Email Csóka at levente.csoka@skk.nyme.hu or csoka.levente@uni-sopron.hu.

TAPPI JOURNAL
WWW.TAPPI.ORG
THE PAPER AND PACKAGING INDUSTRIES' TECHNICAL RESOURCE
MARCH 2018 | VOL. 17 NO. 3



LIGNIN PRODUCTS **125**
Lignin — a promising biomass resource
Yong Qian, Hongming Lou, Weifeng Liu, Dongjie Yang, Xinping Ouyang, Yuan Li, and Xueqing Qiu

NANOCELLULOSE **145**
Controlling porosity and density of nanocellulose aerogels for superhydrophobic light materials
Chenghua Yu, Feng Wang, Shiyu Fu, and Lucian A. Lucia

NANOCELLULOSE **157**
An effective method for determining the retention and distribution of cellulose nanofibrils in paper handsheets by dye labeling
Shengdan Wang, Wenhua Gao, Kefu Chen, Jinsong Zeng, Jun Xu, and Bin Wang

EMISSIONS **167**
Photo-catalytic degradation of gaseous pollutants in paper mills of southern China
Xin Tong, Jiao Li, Jun Ma, Xiaoquan Chen, and Wenhao Shen

WASTEWATER TREATMENT **181**
Removal of phthalate from papermaking wastewater by MIL-101(Fe) in the presence of persulfate
Xueming Lin, Zeyu Guan, Jinquan Wan, Yongwen Ma, and Yan Wang

March 2018

TABLE OF CONTENTS VOL. 17 NO. 3

121 EDITORIAL
China's State Key Laboratory of Pulp and Paper Engineering
Fachuang Lu

125 LIGNIN PRODUCTS
Lignin — a promising biomass resource
Yong Qian, Hongming Lou, Weifeng Liu, Dongjie Yang, Xinping Ouyang, Yuan Li, and Xueqing Qiu

145 NANOCELLULOSE
Controlling porosity and density of nanocellulose aerogels for superhydrophobic light materials
Chenghua Yu, Feng Wang, Shiyu Fu, and Lucian A. Lucia

157 NANOCELLULOSE
An effective method for determining the retention and distribution of cellulose nanofibrils in paper handsheets by dye labeling
Shengdan Wang, Wenhua Gao, Kefu Chen, Jinsong Zeng, Jun Xu, and Bin Wang

167 EMISSIONS
Photo-catalytic degradation of gaseous pollutants in paper mills of southern China
Xin Tong, Jiao Li, Jun Ma, Xiaoquan Chen, and Wenhao Shen

181 WASTEWATER TREATMENT
Removal of phthalate from papermaking wastewater by MIL-101(Fe) in the presence of persulfate
Xueming Lin, Zeyu Guan, Jinquan Wan, Yongwen Ma, and Yan Wang

»COVER CREDIT: Established in 1995, the State Key Laboratory of Pulp and Paper Engineering (SKLPPE) at South China University of Technology (SCUT), in Guangzhou is the only state key laboratory in the fields related to pulping, papermaking, biomass science, and engineering in China. It offers experimental education and training, primarily at the graduate level.

TAPPI JOURNAL
WWW.TAPPI.ORG

Editor-in-Chief
Brian N. Brogdon brian.brogdon@gmail.com
+1 678 581-9114

Associate Editor
Peter W. Hart peter.hart@westrock.com
+1 409 276-3465

Editorial Director
Monica Shaw mshaw@tappi.org
+1 770 367-9534

PRESS Manager
Jana Jensen jjensen@tappi.org
+1 770 209-7242

Webmaster
Trina Heath theath@tappi.org
+1 770 209-7416

***TJ* EDITORIAL BOARD**

Randy Branston, BASF
randy.branston@basf.com, +1 704 819-4251

Brian N. Brogdon, FutureBridge Consulting & Training LLC
brian.brogdon@gmail.com, +1 678 581-9114

David A. Carlson, Carlson Consulting
dacarlson39@aol.com, +1 847 323-2685

Mahendra Doshi, Doshi and Associates
mahen@aol.com, +1 920 832-9101

Marc Foulger, GL&V USA Inc.
Marc.foulger@glv.com +1 315 767-2920

Peter W. Hart, WestRock
peter.hart@westrock.com, +1 409 276-3465

Carl J. Houtman, USDA Forest Products Laboratory
choutman@fs.fed.us, + 1 608 231-9445

Lucian Lucia, North Carolina State University
lucian.lucia@gmail.com, +1 919 889-7059

John A. Neun, John A. Neun LLC
john.neun@gmail.com, +1 518 275-8139

Jim Niemiec, Verso Corporation
jim.niemiec@versoco.com, +1 715 422-7404

Steven P. Ottone, Omya
steven.ottone@omya.com, +1 919 641-7854

Gaurav Pranami, Imbed Biosciences
gpranami@imbedbio.com, +1 515 230-7005

Arthur Ragauskas, Oak Ridge National Laboratory
aragausk@utk.edu

Gerard J.F. Ring, University of Wisconsin—Stevens Point
gerrryring@wi-net.com, +1 715 592-3732

Scott Rosencrance, Kemira Chemicals
scott.rosencrance@kemira.com, +1 770 429-2753

Paul Wiegand, NCASI
pwiegand@ncasi.org, +1 919 941-6417

Junyong Zhu, USDA Forest Products Laboratory
jzhu@fs.fed.us, +1 608 231-9520

Join TAPPI *today!*

TAPPI JOURNAL is a free benefit of TAPPI membership, and is only available to members. To join TAPPI, to renew your TAPPI Membership, or to learn about other valuable benefits, visit www.tappi.org.

TAPPI, 15 Technology Parkway S., Suite 115, Peachtree Corners, GA 30092, publishes *TAPPI JOURNAL* monthly.

ATTENTION PROSPECTIVE AUTHORS: All papers published are subject to *TAPPI JOURNAL's* peer-review process. Not all papers accepted for review will be published. Before submitting, check complete author guidelines at http://www.tappi.org/s_tappi/doc.asp?CID=100&DID=552877.

Statements of fact and opinions expressed are those of individual authors. TAPPI assumes no responsibility for such statements and opinions. TAPPI does not intend such statements and opinions or construe them as a solicitation of or suggestion for any agreed-upon course of conduct or concerted action of any sort.

Copyright 2018 by TAPPI, all rights reserved. For copyright permission to photocopy pages from this publication for internal or personal use, contact Copyright Clearance Center, Inc. (CCC) via their website: www.copyright.com. If you have questions about the copyright permission request process, please contact CCC by phone at +1 978 750-8400. To obtain copyright permission to use excerpts from this publication in another published work, send your specific request in writing to Editor, TAPPI JOURNAL, 15 Technology Parkway S., Suite 115, Peachtree Corners, GA 30092, USA; or by fax to +1 770 446-6947. Send address changes to TAPPI, 15 Technology Parkway S., Suite 115, Peachtree Corners, GA 30092, USA; Telephone +1 770 446-1400, or FAX +1 770 446-6947. www.tappi.org

Guest Editorial



FACHUANG LU
Director, SKLPPE
Guest Editor

China's State Key Laboratory of Pulp and Paper Engineering

Editor's Note: *TAPPI would like to thank Junyong (J.Y.) Zhu of the* TAPPI Journal *(*TJ*) Editorial Board, as well as Guest Editor Fachuang Lu, for developing this special issue featuring research from South China University of Technology and the State Key Laboratory of Pulp and Paper Engineering in Guangzhou, China.*
– Monica Shaw, Editorial Director

The State Key Laboratory of Pulp and Paper Engineering (SKLPPE) at the School of Light Industry and Engineering, South China University of Technology (SCUT), is the only state key laboratory in the fields related to pulping, papermaking, biomass science, and engineering in China. Located at the SCUT campus and hosted by the School of Light Industry and Engineering, the laboratory was established in 1995 and approved by the China State Ministry of Science and Technology. Since it officially began operating in 1996, SKLPPE has witnessed visits and collaborative research from thousands of scholars and experts in the field of pulp and papermaking from all over the world. SKLPPE has become the most important platform for scientific research, academic idea exchange, and education in pulping and paper-related programs in China.

The laboratory was built around three key disciplines, including one national first-class discipline, Light Industry Technology and Engineering, and two national second-class disciplines, Pulp and Paper Engineering and Chemical Engineering, as well as several other related subjects. The laboratory motto is "Open, Dynamic, Collaborative and Competitive". An excellent working environment for academic activities has been built through establishment of comprehensive management regulations. The laboratory's goal is to lead sustainable developments in paper science and serve the nation's paper industry.



State Key Laboratory of Pulping and Paper Engineering at South China University of Technology in Guangzhou, China.

The laboratory now has 66 full-time personnel, including one academician of the Chinese Academy of Engineering and over 40 professors awarded with provincial or national honors. Most of the experts have a background in the field of pulping and papermaking, and the others are majored in material science, chemical engineering, food science and technology, resource and environmental science, and related fields. The laboratory's academic committee consists of 13 members who are all distinguished and outstanding scholars and experts in pulping and papermaking-related fields in China. The current committee chair, Professor Kefu Chen, is also the academician of the Chinese Academy of Engineering.

Flagship educational programs, outstanding graduates

SKLPPE offers experimental education and training primarily at the graduate level. Graduate students, especially students from the School of Light Industry and Engineering at SCUT, take advantage of the laboratory's

state-of-the-art facilities, performing research projects with the support of their supervisors. As an affiliate of the School of Light Industry and Engineering, the laboratory offers Master's and Ph.D. education to students with two programs: Pulp and Paper Engineering and Biomass Science and Technology. Most faculty members work as researchers and teachers for the undergraduate and graduate programs in the school. In the last five years, SKLPPE has matriculated over 300 doctoral students and over 750 Master's students. Currently, about 100 doctoral students and 230 Master's students are associated with the laboratory.

Graduates of SKLPPE from the Pulp and Paper Engineering program mostly find careers in pulping, papermaking, and related industries. For some time now, SKLPPE graduates have been found in virtually every major company in such fields. They have shown strong leadership and capabilities, playing important roles involving technology and management for these companies. Because of this, SKLPPE has been recognized as the flagship school in the field of pulping and papermaking in China.

Graduates from the program of Biomass Science and Technology have broader choices for their professional employment. Most graduates find careers as researchers at universities and research institutes throughout the world, and others find their professional paths in bioprocess industries, chemical industries, and related fields. Many SKLPPE graduates have had great success. In the past 10 years, over 40 distinguished scholars from SKLPPE have been awarded national honors.

Major research areas and accomplishments

Research at SKLPPE is primarily based on its two strong graduate programs, with total research funding in the past five years of more than US$12.5 million from the government, Ministry of Education of China, Guangdong Province, and SCUT. SKLPPE members also receive funding from other foundations. SKLPPE keeps a very close relationship with industries and other institutes.
In the past five years, SKLPPE has secured more than 360 national projects and 700 others, with total funding of about US$55 million, from which almost US$9 million comes from industries.

The laboratory has focused on solving problems associated with pulping and papermaking, including effluent management, environmental protection, plant resources, processing equipment, and energy savings. In recent years, SKLPPE has expanded its research interests to biorefinery, bio-based materials, bioenergy, biochemicals, and other related topics. Based on the fractionation-transformation-application strategy for plant fiber utilization, the laboratory emphasizes fundamental and applied research in four primary areas: 1) pulping and pollution control; 2) papermaking and paper-based functional material; 3) processing equipment and intelligent management; and 4) biomass refinery, plant-derived bio-based chemical and nanomaterial technologies.

In the last five years, SKLPPE has matriculated over 300 doctoral students and over 750 Master's students. Currently, about 100 doctoral students and 230 Master's students are associated with the laboratory.

Through continual efforts, SKLPPE members have made significant progress in several major fields related to pulping technology, reducing effluent discharge, lignin utilization, paper-based functional materials, and cellulose nanomaterials. Some of these advances include:

- The optimal terminal point of cooking (transitional point from cooking to oxy-bleaching) was determined with comprehensive analysis and process modeling, allowing a major reduction in the overall operational cost of pulping.
- The scaling problem associated with nonwood pulping was solved thanks to our recent identification of the cause of scaling and methods to monitor it.
- Black liquor containing mainly kraft lignins has been processed to effectively produce fuel and chemicals using our patented technologies.
- Sophisticated treatment processes involving physiochemical, biological, and deep (advanced) oxidation for wastewaters discharged from paper mills have been developed, allowing the treated water to be reused or discharged along with satisfying the nation's strict regulations.
- Recycled paper/paperboard are important fibrous resources for papermaking, so SKLPPE members identified major influences on the quality of paper made from recycled fibers and invented a technology to improve/assure quality paper.

- A series of specialty paper products and fibrous paper-based composite materials have been developed in the laboratory, reducing the nation's dependence on imported products used by military, aerospace, rail transportation, and more.
- The integrated biorefinery concept for pulping and papermaking operations is a new direction that has been added to our research on traditional pulp and paper science. SKLPPE has brought in faculty/research members from disciplines of material science, renewable energy, biotechnology, food science, chemistry, and related fields to conduct fundamental and applied studies on biomass-related subjects.
- Great progress has been made in preparing metal catalysts, bio-based carbonaceous materials, organic-inorganic hybrid composites, bio-based films, and bio-based optoelectronic materials for various applications.

As a result of these and other efforts, over 1,700 scientific papers and 17 books have been published in the last five years. According to a Chinese scientific consulting service, SKLPPE was ranked in 2017 as the No. 2 worldwide research institute in the field of pulping and papermaking after Aalto University in Finland.

Expansive facilities and equipment

SKLPPE is comprised of more than 13,000 m^2 of space filled with over 800 instruments. The laboratory has both traditional and advanced equipment for education and research. The traditional equipment includes machines for pulping, papermaking, screening, bleaching, and more. These instruments are mainly for educating students from the Pulp and Paper Engineering program, after which they are directed to become professionals in pulping and papermaking industries. In addition, this traditional equipment is available for researchers to study pulping and papermaking processes. The advanced equipment includes machines like microfluidizers, homogenizers, freezing microtomes, and various reactors that are intended for biomass-related research and education. All instruments, including the testing instruments for pulp and paper, gas chromatography–mass spectrometry (GC-MS), liquid chromatography–mass spectrometry (LC-MS), high performance liquid chromatography (HPLC), and biochemical analyzers, as well as different types of electro-microscopes, are employed for the education and research of both students and researchers.

All SKLPPE facilities are open to the public and shared with researchers from other institutes, universities, and industries around the world under agreement, which creates a strong platform of support for research and education in pulping, papermaking, and related disciplines.

Global collaboration

Researchers and experts from institutes, universities, and industries around the world are welcome to the laboratory for academic idea exchange and collaborative research. The laboratory also provides funding for post-doctoral and visiting researchers. Many projects are conducted through collaborations with domestic or overseas companies. In the last five years, the laboratory has had 17 international collaborative projects with total funding of about US$1 million.

Hosting/organizing international conferences is another approach for connecting with scientists and engineers. The laboratory has held several international conferences, including the 5th International Symposium on Emerging Technologies of Pulping and Papermaking and the 3rd International Papermaking and Environment Conference held in 2016, as well as the Sino-German Symposium on Polysaccharides: New Chemistry and Materials in 2017.

Legendary Chinese papermaking moves toward future frontiers

It is well known that papermaking technology is one of the greatest ancient inventions originating from China. SKLPPE is determined to inherit the ancestor's wisdom and stand at the frontier of the pulping and papermaking field to solve problems encountered by the modern pulping and papermaking industry; develop novel processes for pulping, papermaking and related products; and make substantial contributions to the sustainable development of society and mankind. **TJ**

Fachuang Lu, Ph.D., is professor and director, State Key Laboratory of Pulping and Paper Engineering and dean, School of Light Industry Science and Engineering, at South China University of Technology, Guangzhou, China.

Lignin — a promising biomass resource

YONG QIAN, HONGMING LOU, WEIFENG LIU, DONGJIE YANG, XINPING OUYANG, YUAN LI, AND XUEQING QIU

ABSTRACT: Lignin, the second most abundant component in plants, is a class of complex aromatic polymer. Industrial lignin is a major byproduct of pulp and paper production and biorefineries, with more than 50 megatons generated annually. However, more than 98% of industrial lignin is either burned as fuel or discharged as wastewater, causing serious environmental pollution. From a sustainable feedstock perspective, finding additional high-volume and high-value applications for lignin is an extremely important and long-term pursued objective. Thus, lignin resources deserve to be further exploited as biorenewable raw materials for energy-saving and low-carbon polymer production. Inspired by the natural three-dimensional structure, excellent ultraviolet-blocking and antioxidant properties of lignins, the authors have focused their research on lignin-based biorenewable resources. This review summarizes research achievements of the recent decade. Progress has been made in several aspects, such as nonionic and amphoteric lignin-based surfactants, lignin-based functional materials, lignin-based photoelectric materials, lignin-based resins and polymer composites, and catalytic depolymerization of lignin.

Application: This review summarizes recent research and provides some novel strategies for the application and understanding of lignin.

In response to environmental problems and energy concerns, the development and use of biomass energy has aroused wide attention [1]. Lignin, a biopolymer derived from trees and crops, is the second-most abundant component in the plants [2]. Historically, the majority of lignin was burned as fuel or used in low-value applications such as activated carbons, [3-5] dispersants [6-10], and adhesive agents [11-13]. In the past few years, lignin has risen to stardom because of its remarkable properties. Scientists have noticed that high-value use of lignin, based on its inherent features, is the most effective and green strategy [14,15].

Qiu and coworkers have dedicated more than 20 years researching value-added uses of industrial lignin. After chemical modifications of industrial lignin by sulfonation, sulfomethylation, carboxylation, amination, and so on, they developed a series of lignin-based macromolecular amphphilic surfactants successfully used in areas such as construction, agriculture, and energy [6-10]. To counter the competition of surfactants derived from oil in the last 10 years, they developed a new lignin adjuvant to enhance the enzymatic hydrolysis of cellulose. They also developed methods to depolymerize lignin into aromatic chemicals and explored new applications in cosmetics, photoelectric, and polymer areas.

LIGNIN FOR ENHANCING ENZYMATIC HYDROLYSIS

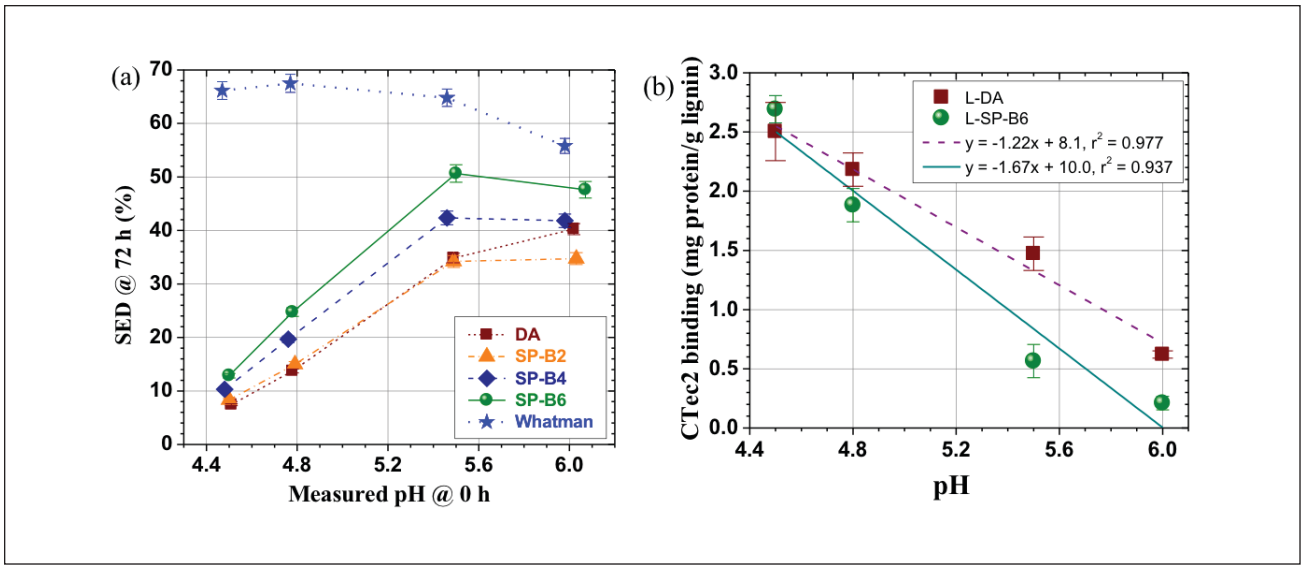
In the production of cellulosic ethanol, lignin in lignocellulosic substrates has significant effects on the enzymatic hydrolysis of cellulose [16-18]. Previous studies have suggested that lignin would affect the activity of cellulase and then inhibit the enzymatic hydrolysis of cellulose [19,20]. Several methods have been developed to improve the enzymatic hydrolysis of cellulose. Those include reducing the non-productive adsorption of cellulase on lignin and covalent or noncovalent modification of lignin [16,21]. Meanwhile, enzymatic hydrolysis has generated a large amount of enzymatic hydrolysis lignin (EHL). Recycling and improving the efficiency of using EHL is an urgent problem to be solved [22]. In that regard, some new methods and technologies to enhance the enzymatic hydrolysis and to increase the use of EHL are introduced.

Enhancing the enzymatic hydrolysis of lignocelluloses by adjusting pH

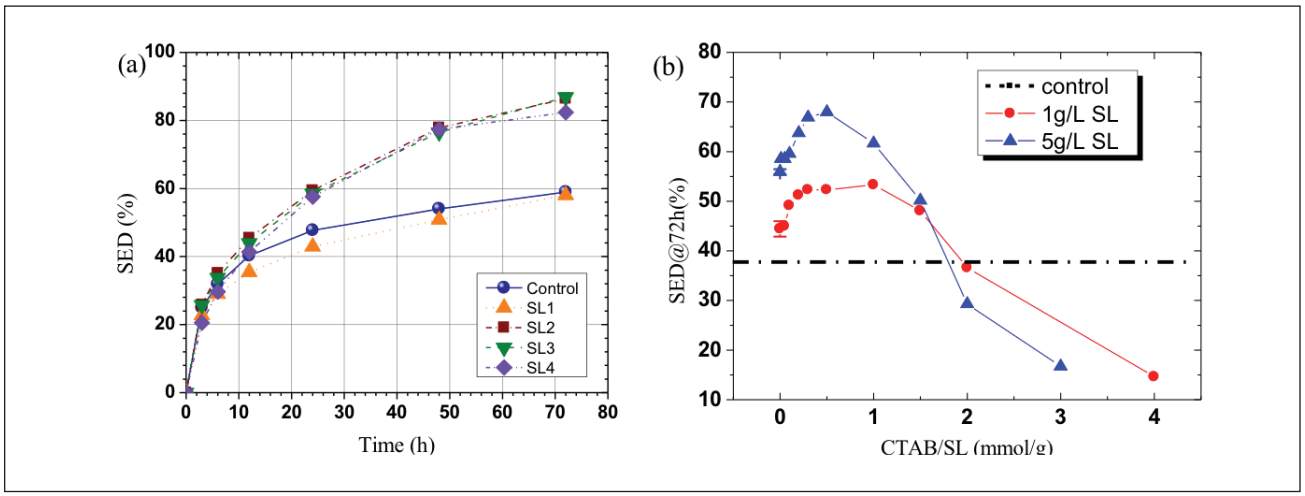
Cellic CTec2 (Novozymes; Bagsvaerd, Denmark) cellulase exhibited best activity at the pH value of about 4.8 [23], but lignocellulosic substrates had higher substrate enzymatic digestibility (SED) at pH 5.5~6.0 (**Fig. 1a**). Especially when softwood substrates were pretreated by sulfuric acid, the SED value at pH = 5.5 was one time higher than that at pH = 4.8 [24]. By comparison, it was found that higher pH could increase the hydrophilicity and negativity of lignin in lignocellulosic substrates, thereby weakening the affinity of lignin to cellulase and reducing the non-productive adsorption of cellulase on lignin [25]. Simultaneously, the higher pH increased the negative charge of cellulase and the electrostatic repulsion between lignin and cellulase (Fig. 1b). Because the higher pH helps reduce the cost of enzymatic hydrolysis and fermentation, it is of great value to improve the enzymatic efficiency by simply changing the pH.

Sodium lignosulfonate in the enzymatic hydrolysis of lignocelluloses

Sulfite pretreatment to overcome recalcitrance of lignocelluloses (SPORL) is a recently developed method for pretreat-



1. (a) Effects of pH on enzymatic saccharification of four lignocelluloses and Whatman paper , and (b) effects of pH on CTec2 binding to enzymatic hydrolysis lignin residues (SED = substrate enzymatic digestibility).

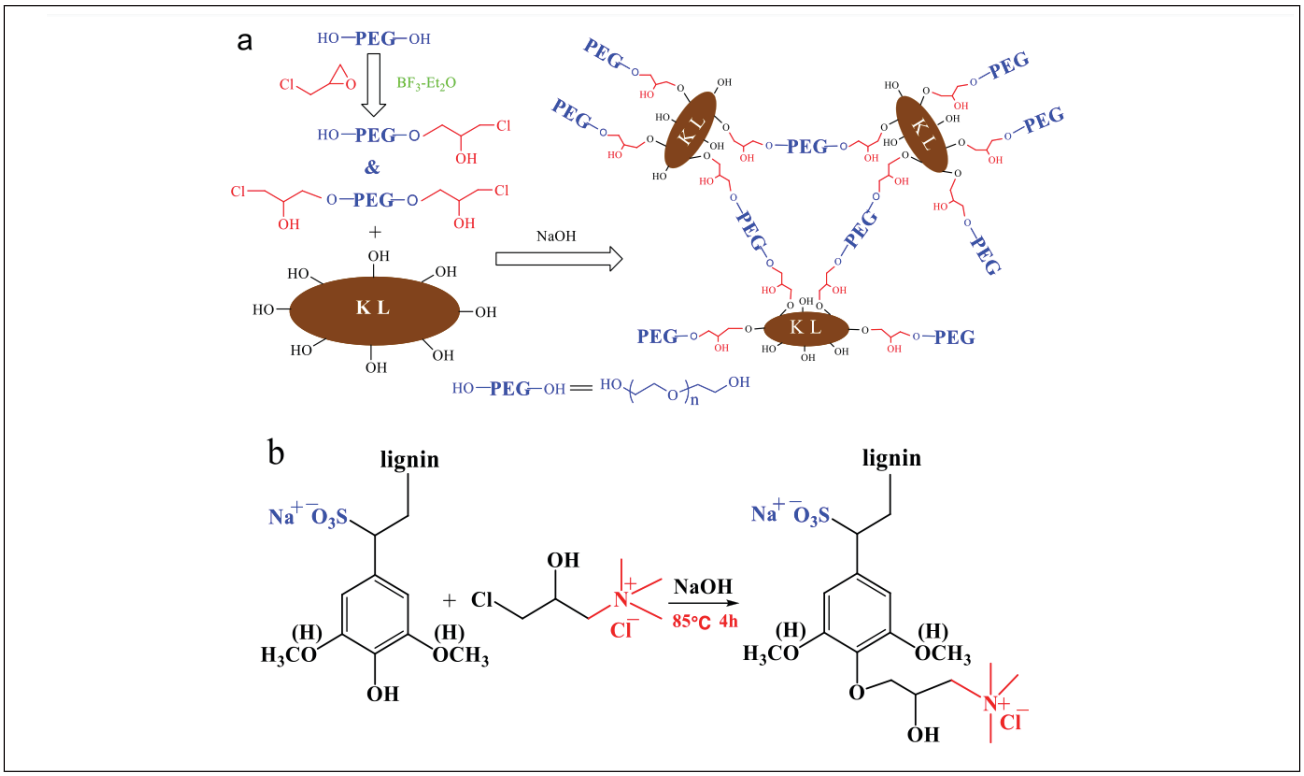


2. (a) Effects of different sodium lignosulfonate (SL) fractions on the SED of Whatman paper at CTec2 enzyme loading of 10 FPU/g glucan, and (b) effect of SL-cetyltrimethyl ammonium bromide (CTAB) on the SED of lignocelluloses.

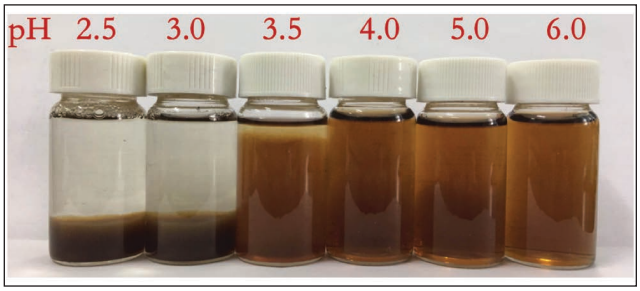
ment of lignocelluloses, which facilitated the biotransformation of softwoods. Lignocelluloses can release water-soluble sodium lignosulfonate (SL) when pretreated by SPORL. SLs with small molecular weight and high sulfonation have very good effects on the enzymatic hydrolysis of different lignocellulosic substrates [4]. **Figure 2a** shows the effects of different SL fractions on the SED of Whatman paper. Adding 5 g/L of SL2 or SL3 increases the SED of filter paper from 59% to 85% [26]. Further study found that SL compounded with cationic cetyltrimethyl ammonium bromide (CTAB) could further improve the SED of lignocelluloses (Fig. 2b) [27]. CTAB was thought to increase the adsorption of SL on lignin to form more effective steric hindrance and reduce the non-productive adsorption of cellulase on lignin by neutralizing the negative charge of SL.

Modification of EHL and its use in enzymatic hydrolysis

To improve the value of using insoluble lignin, lignin-based polyoxyethylene ether (enzymatic hydrolysis lignin and polyethylene glycol; EHL-PEG) and pH-responsive lignin amphoteric surfactant (TCSL-N25) were synthesized by modifying the EHL (**Fig. 3**), and their application in enzymatic hydrolysis was studied. The results showed that EHL-PEG could effectively reduce the particle size of cellulase while reducing the non-productive adsorption of cellulase on lignin compared with PEG [28]. TCSL-N25 had a sensitive pH response (**Fig. 4**); it was dissolved at pH 4.5~6.0, which was for normal enzymatic hydrolysis and precipitated when pH was less than 3.5. When it precipitated, it could recover the cellulase in solution through electrostatic forces. The addition of 2 g/L of



3. Synthesis mechanisms of (a) enzymatic hydrolysis lignin-PEG copolymer and (b) pH-responsive lignin amphoteric surfactant (TCSL-N25).



4. The solubility of TCSL-N25 changes with pH. The concentration of TCSL-N25 is 2 g/L.

TCSL-N25 could increase the SED of eucalyptus pretreated by dilute acid from 33.4% to 83.2% at a cellulase loading of 5 FPU/glucan. After enzymatic hydrolysis, more than 85% of TCSL-N25 and 30% of cellulase activity could be recovered by adjusting the pH of enzymatic hydrolysate to 3.0.

Generally, pretreatments of lignocelluloses are operated under high temperature and low pH conditions [29]. Furfural and 5-hydroxymethyl furfural are formed from hexose degradation [30], and lignin is degraded into cinnamic acid, vanillin, and other kinds of phenols [31]. These degradation products will aggregate in pre-hydrolysates and inhibit the enzymatic hydrolysis and fermentation of lignocelluloses. Therefore, the pre-hydrolysates usually must be separated before enzymatic hydrolysis and fermentation [32].

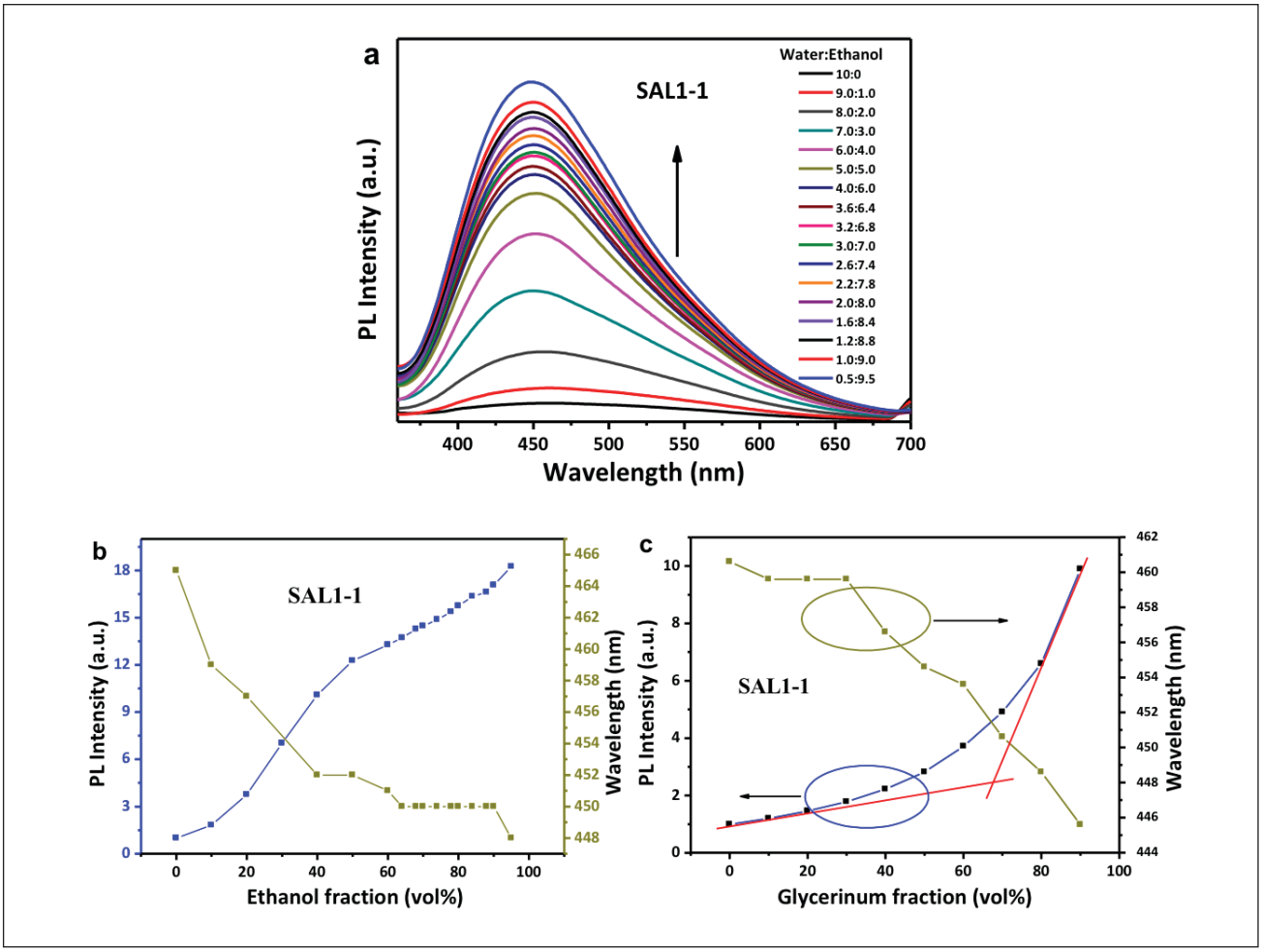
Effects of EHL on the adsorption and removal of the inhibitor in the pre-hydrolysate have been studied experimentally [33]. EHL had good adsorption and removal ability to furfural and 5-hydroxymethylfurfural. The adsorption process was in agreement with the Freundlich model and was exothermic. The adsorption capacity of EHL for furfural was stronger than that for 5-hydroxymethylfurfural. It is feasible for EHL to remove furfural and 5-hydroxymethylfurfural in the pre-hydrolysate.

LIGNIN FOR PHOTOELECTRIC APPLICATION

The origin of lignin fluorescence

Plant cell walls containing lignin exhibit fluorescence when exposure to ultraviolet (UV) or visible light excitation of the aromatic rings in lignin. The fluorescent feature enables the lignin to be used as a sensitive probe for lignin constituent analysis. The fluorescence of lignin was discovered many years ago, but the UV/visible-excited lignin fluorophore remains elusive. Still, the origin of its fluorescence has been periodically proposed: an anion of coniferyl alcohol, stilbene structures, and phenylcoumarone structures [34-37]. However, the real origin of lignin fluorescence is still unclear.

Inspired by the fluorescence of wood cell walls, which might come from the presence of lignin, we are interested in the mechanism of the emission of lignin, because it is almost non-conjugated. In the wood cell walls, the molecular structure of raw lignin is fixed by cross-linking with hemicelluloses, which is similar to the aggregation in the solid state. Lignin becomes relatively highly luminescent in poor solvents



5. (a) Photoluminescent (PL) spectra of sulfonated alkali lignin fraction (SAL1-1) in water and water-ethanol mixtures (100 mg/L, λ_{ex} = 350 nm); b) the fluorescent image of SAL1-1 in water and water-ethanol (1:9) mixtures and the change curves of PL intensity (yellow line) and emission peak (blue line) in water and water-ethanol mixtures; and (c) the change curves of PL intensity (yellow line) and emission peak (blue line) in water and water-glycerinum mixtures.

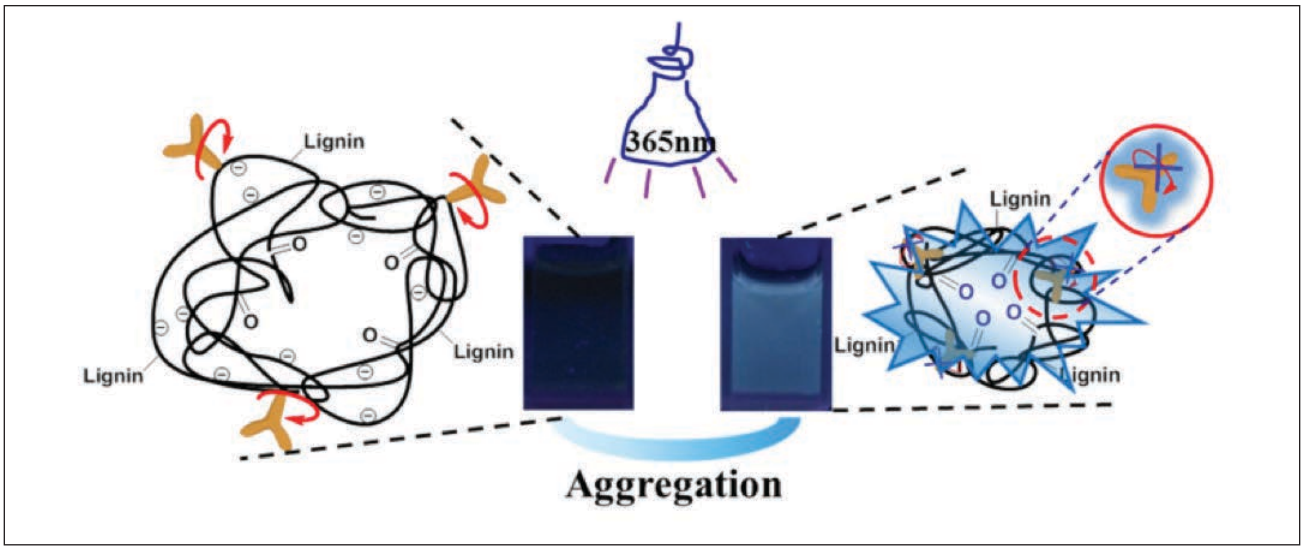
or in the solid state as aggregates. The fluorescent behaviors of sulfonated alkali lignin (SAL) were studied and evaluated in mixed solvent systems (**Fig. 5**) [38]. SAL fraction (SAL1-1) showed a weak blue light emission at 450 nm under the excitation of 350 nm in distilled water. With the increase of ethanol fraction, the fluorescence intensity showed a sustained increase until the ethanol fraction reached 95%, accompanied by a blue shift of 17 nm. We proposed that the fluorescence of lignin might come from its aggregation. A similar phenomenon was observed in a water-glycerin system.

The aggregation-induced emission (AIE) property of SAL was also observed after adding CTAB, which promoted the aggregation of SAL [38]. We proposed that AIE played a role in the origin of blue lignin fluorescence because of clustering of the carbonyl groups and restriction of intramolecular rotation (**Fig. 6**). Large conjugated ϖ electron systems of SAL were well established by the aggregation of nonconventional luminogens, which contained electron-rich atoms, such as oxygen and sulfur. These results provided a new perspective to understand the fluorescence in lignin and explore novel potential application for the AIE activity of lignin.

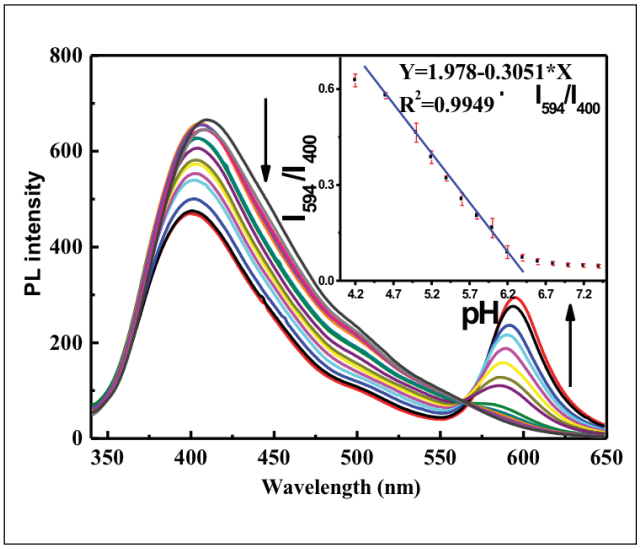
As an inexpensive and environmentally friendly fluorescent chromophore, the application based on the fluorescent property of lignin is rarely reported. Lignin has a broad fluorescence emission range and can be excited with UV and visible light. This indicates that lignin has potential as a donor in fluorescence resonance energy transfer (FRET)-based probes.

A water-soluble, ratiometric fluorescent pH probe was synthesized by grafting spirolactam rhodamine B (SRhB) to SL (L-SRhB) [39]. SL serves as the donor, whereas the SRhB works as a recognition element for hydrogen ions (H^+) and acts as the energy acceptor when the long-wavelength fluorophore, Rhodamine B, is generated. L-SRhB showed a rapid response to pH changes from 4.60 to 6.20, with a *pKa* of 5.35 (**Fig. 7**), which indicated that L-SRhB has the potential for pH detection of acidic organelle.

Encouraged by the pH-responsive property of L-SRhB, the biological application of the probe was also studied [39]. The



6. Mechanism model diagram of lignin fluorescence.



7. Fluorescence spectra of spirolactam rhodamine B (L-SRhB) in phosphate-buffered saline (PBS) (0.2 mg/mL) at various pH values. Inset is the linear plots of fluorescence intensity to pH (4.60-6.20). λ_{ex} = 330 nm.

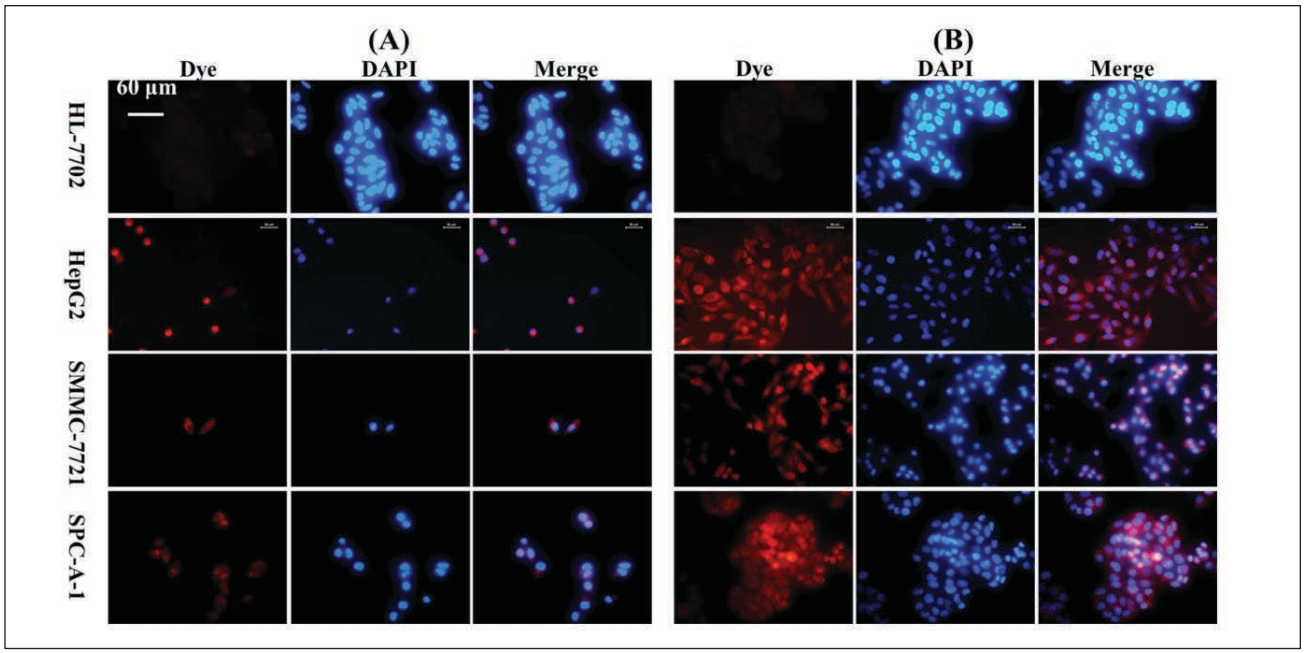
L-SRhB was successfully internalized by living cells through the endocytosis pathway. This is good for acidic organelle detection by the fusion of cytomembrane. Rhodamine B is known as a mitochondrion localization agent. However, the pH of mitochondrion is alkalescent. The alkaline environment would have a negative effect on the cell staining experiment because the *pKa* of the reversible ring-opening reaction of L-SRhB is 5.35. The ring-opening product of L-SRhB with red fluorescence might be stabilized by the interaction between sulfur triopxide (-SO_3^-) and quaternary ammonium salt, which came from SL and the ring-opening product of L-SRhB, respectively, in alkalescent condition. In addition, L-SRhB could distinguish normal cells from cancer cells by the different staining times. There was almost no red fluorescence in the normal cells after incubation for 8 h with L-SRhB and fuchsia L-SRhB (FL-SRhB), respectively, whereas an obvious red fluorescence from the probes was observed in the cancer cells in the same condition (**Fig. 8**). Our results provide an interesting design strategy for bioimaging dyes based on lignin.

Even though the fluorescence quantum yield of lignin is relatively low, such AIE mechanisms should have strong implications for understanding the structure of lignin. Meanwhile, high value-added use of lignin on the basis of its autofluorescence also shows enormous potential.

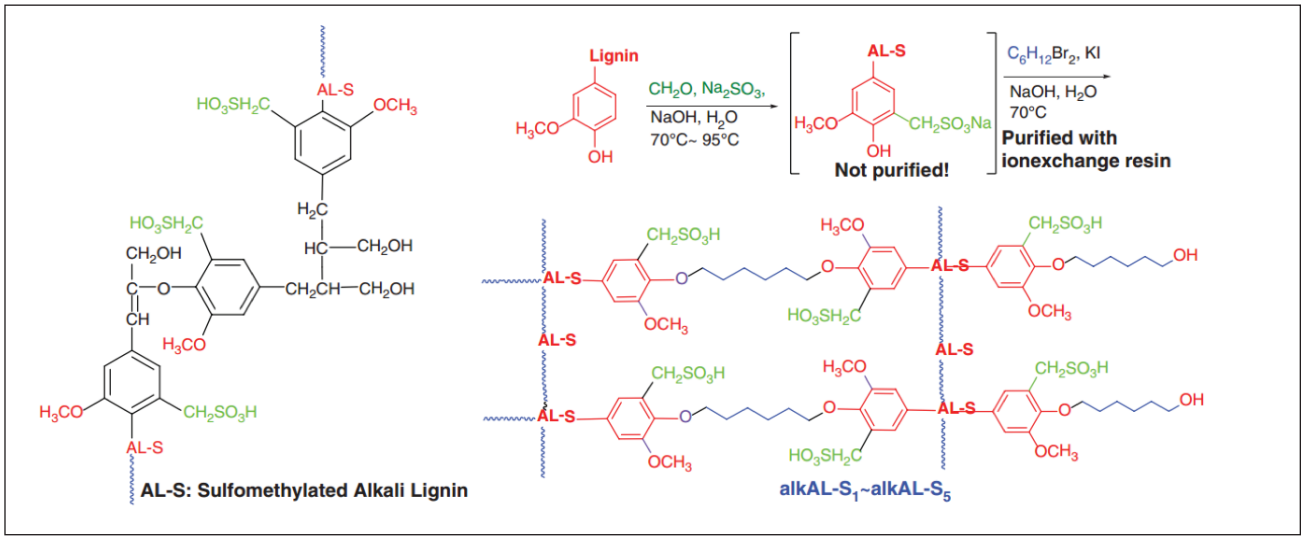
Sulfobutylated SL with ultra-high molecular weight and high sulfonation

Increasing the molecular weight of SL is highly desirable to improve its dispersion ability [40]. Graft copolymerization, graft sulfonation, and enzyme catalysis reaction are suitable for increasing the molecular weight of SL. Graft sulfonation is an effective way to improve the sulfonation degree and molecular weight of SL [41-43]. However, these methods still could not obtain SL with a molecular weight over 50 kDa, which is required in many industrial applications.

To address this problem, Qiu et al. developed a one-pot modification method that includes two steps: sulfomethylation of alkali lignin (AL) as raw material leading to AL-S and alkylation with different proportions of 1,6-dibromohexane ($C_6H_{12}Br_2$) in sodium hydroxide aqueous solutions leading to alkAL-S samples [44]. Sulfomethylation of AL rendered products with water solubility, and the subsequent alkyl chain reaction led to the increment in molecular weight via polymerization. They hypothesized that sulfomethylation occurs in ortho-position to the phenolic hydroxyl groups and the alkylation proceeds better via the phenolic hydroxyl groups (**Fig. 9**). As a result, a significant increase of molecular weight from 5200 Da of AL-S to 201000 Da of alkAL-S with high degree of alkylation was obtained. The relatively high molecular weight of alkAL-S yielded unexpected viscosity



8. Images of human hepatocyte cell (HL-7702), human hepatocellular liver carcinoma cell (SMMC-7721, HepG2) and human lung adenocarcinoma cancer cells (SPC-A-1) treated with (a) spirolactam rhodamine B (L-SRhB) and (b) FL-SRhB for 8 h.



9. Synthetic approach of ultrahigh molecular weight alkAL-S polymers via sulfomethylation and reaction with 1,6-dibromohexane (C6H12Br2).

reducing effect, stability and good rheological properties on a low-rank coal-water slurry.

Application of lignin in organic optoelectronic devices

During the past decades of development of organic electronic devices, including organic light-emitting diodes (OLEDs), organic solar cells (OSCs), perovskite solar cells and polymer solar cells, interface engineering has been of critical importance to improve the performance of these optoelectronic devices. Poly(3,4-ethylenedioxythiophene):poly(styrene sulfonic acid) (PEDOT:PSS) is the most widely used commercial water-soluble conductive polymer, which is used as an anode interlayer for high performance organic electronic devices. The PSS dopes PEDOT through protonic acid doping and PSS acts as a polyanion to stabilize the p-doped PEDOT [45-47]. However, it is known that PEDOT:PSS could corrode indium tin oxides (ITO) at elevated temperatures because of its high acidity. New solution-processable hole transporting materials (HTMs) are still in demand and chemistry scientists have made great effort.

There were very few studies aiming to produce better conducting PEDOT by replacing PSS with new dopants. Inspired by the electron transfer process during the oxidation of the phenol

Sample	Thickness (L), nm	Slope (ρ)	Hole-mobility, $cm^2V^{-1}s^{-1}$
SL	110	2.90	3.75×10 -6
SL	100	2.95	2.91×10 -6
SL	35	14.96	3.21×10 -6
ASL	30	6.46	4.57×10 -6

I. The hole mobilities of the samples of sodium lignosulfonate (SL) and alkyl chain cross-linked SL (ASL).

Anode Modifier	V^{on}, V*	CEmax, cd/A†	PEmax, lm/W‡
None	4.6	14.5	5.82
PEDOT: PSS	4.5	25.09	8.25
PEDOT: ASLS-1:1	4.2	37.65	12.84
* turn-on voltages, † maximum current, ‡ power efficiency.			

II. Performances of organic light-emitting diodes with no anode modifier, with oly(3,4-ethylenedioxythiophene):poly(sty rene sulfonic acid) (PEDOT:PSS), and with PEDOT: alkyl chain sulfobutylated sodium lignosulfonate (ASLS) as anode modifier, respectively.

derivatives of lignin, in which radicals are produced, we explore a series of lignin derivatives as dopants to replace PSS as conducting PEDOT materials. SL and alkyl chain cross-linked SL polymer (ASL) exhibited unexpected hole mobility because of phenolic oxidation and J-aggregation behavior [48,49]. This unexpected hole mobility provides a novel perspective for the application of SL and ASL as potential polymeric p-type semiconductors. A novel water solution-processable hole transport material, which was prepared from the oxidation of EDOT dispersed in SL or ALS. For comparison, commercial PEDOT:PSS 4083 was studied as a control for the hole transport performance test. **Table I** shows SL with a higher phenolic group content having higher hole mobility than ASL with a lower phenolic group content, which further suggests that phenolic groups are conducive to the hole transporting property.

As a hole-transport material in organic photovoltaic (OPV) with a power conversion efficiency (PCE) of 5.79%, PEDOT:SL showed comparable performance to that of the conventional PEDOT:PSS with a device structure of ITO/HTM/PTB7:PC71BM/Al. We found that the performance of PEDOT:SL is not very dependent on the mass ratio of PEDOT in PEDOT:SL.

Furthermore, we explored grafted sulfonated-acetone-formaldehyde lignin (GSL) as a dopant to replace PSS. An unexpected hole mobility of 2.27×10^{-6} cm^2 $V^{-1}s^{-1}$ was achieved. GSL is a potential water soluble polymeric p-type semiconductor. Taking advantage of the hole transporting property of GSL, PEDOT:GSLs with controllable work functions were developed and applied as a hole transport layer (HTL) in organic electronic devices, including OLEDs, OPVs, and perovskite solar cells [50,51].

Based on the previously mentioned works [48-51], alkyl chain sulfobutylated SL (ASLS) with phenol derivative was expected to have an intrinsic hole transport property [52]. Water processable PEDOT:ASLS was applied as a hole injection layer (HIL) to modify ITO in Firpic-based phosphorescent OLEDs. This new HIL material showed improved device performance compared to that of PEDOT:PSS under the same device structure (**Table II**). Comparing with PSS with regular structure, strong aggregation and oxidation behavior of ASLS contribute to the hole injection capability of PEDOT:ASLS.

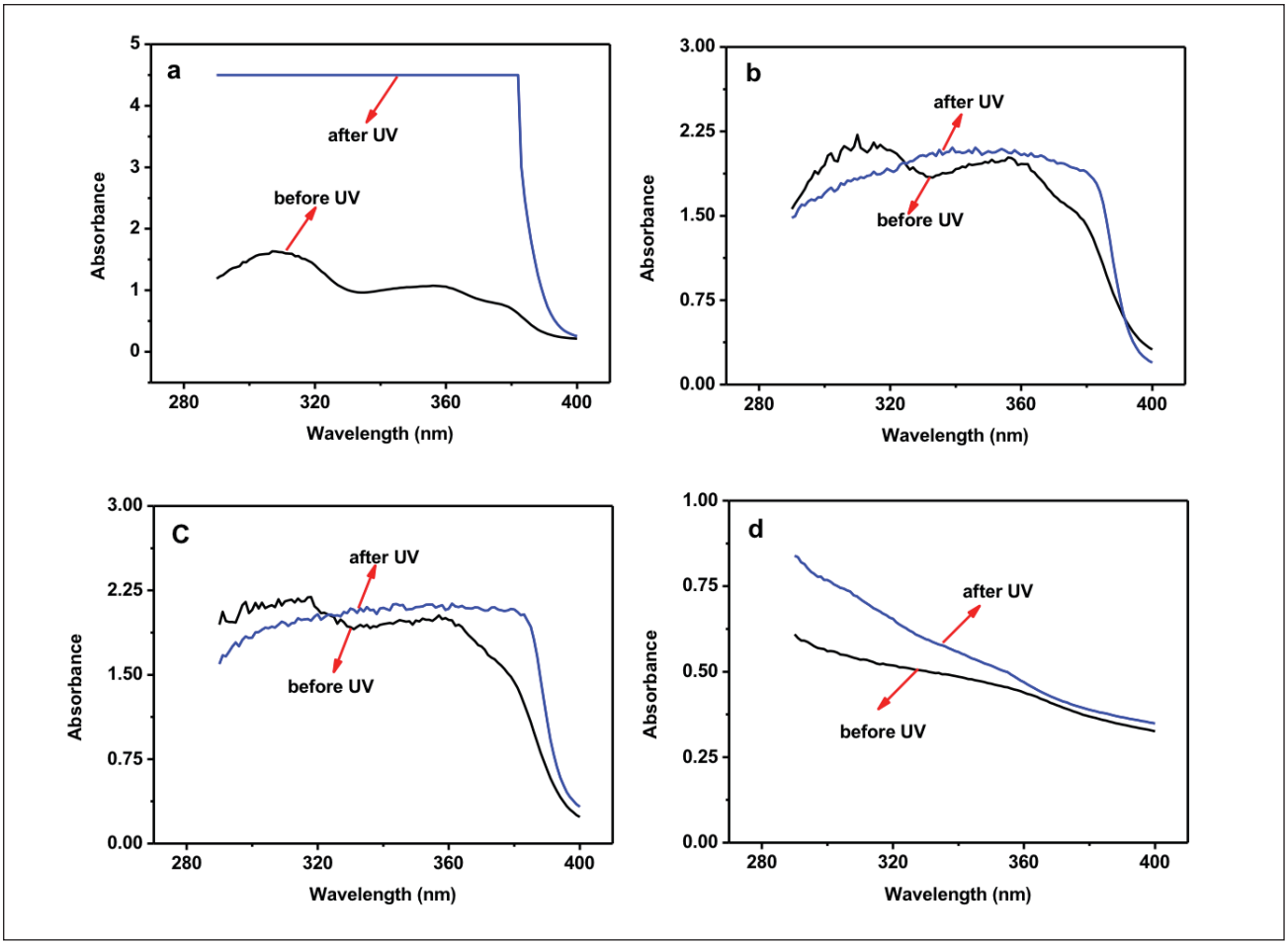
In this section, we explored a series of lignin derivatives as a dopant to replace PSS as dispersant and template for water soluble polymeric semiconductor PEDOT. Our results provide a novel concept for the application of bi-radicals containing polyaromatic hydrocarbons and provide a promising scaffold for the design and feasible synthesis of HTMs based on the interconversion between phenol and benzoquinone for organic electronics in the future.

LIGNIN FOR NATURE-INSPIRED SUN BLOCKER

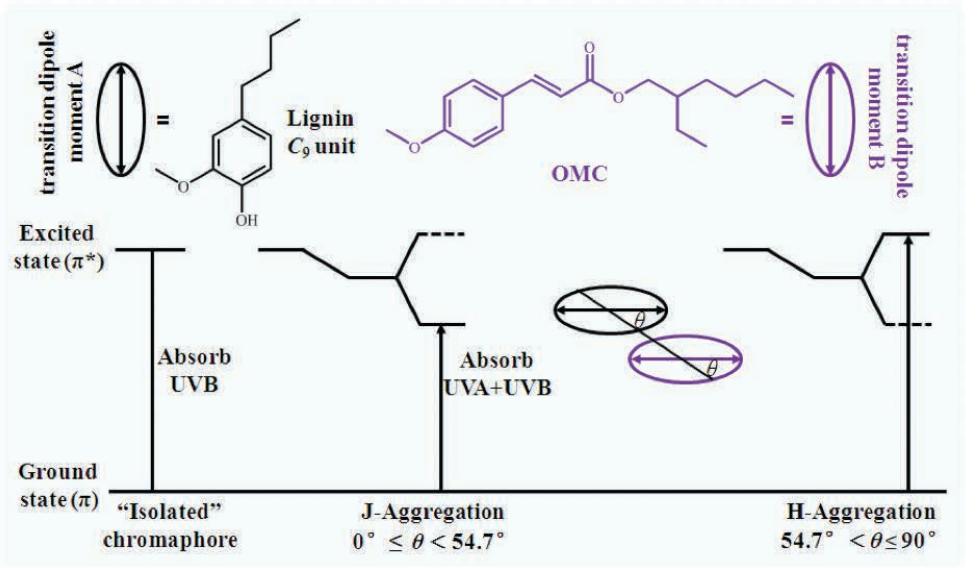
Lignin is a unique aromatic polymer in plants. It exhibits excellent ultraviolet (UV)-blocking and antioxidant properties because of its functional groups such as phenols, ketones and other chromophores. Recently, Qiu and co-workers demonstrated lignin could be used as a highly efficient nature-inspired sun blocker [53].

When lignin was added into commercial sunscreen products, significant enhancements in UV absorbance were observed. The sunscreen performance of the cream with sun protection factor (SPF) 15 could reach that of the cream with SPF 30 when 2 wt% lignin was added. Adding 10 wt% lignin made SPF 15 cream outperform SPF 50 cream. The synergistic effect between lignin and chemical sunscreen was found first and was more obvious after UV irradiation (**Fig. 10**). This means lignin-based sunscreens could improve the duration of protection from sunshine. Further, Qian el al. demonstrated lignin from different technical resources has a general synergistic effect with sunscreen actives in the commercial lotion and tried to elucidate radical mechanisms of the synergy [54]. Their exploration suggested that the synergistic effect in the lignin-modified sunscreen lotions could be attributed to the $\pi-\pi^*$ stacking between lignin and chemical sunscreen actives (**Fig. 11**) and the formation of UV radiation-induced conjugated chromophores. However, they also found that the sunscreen performance of pure lignin could not meet the daily requirement and the color should be whitened.

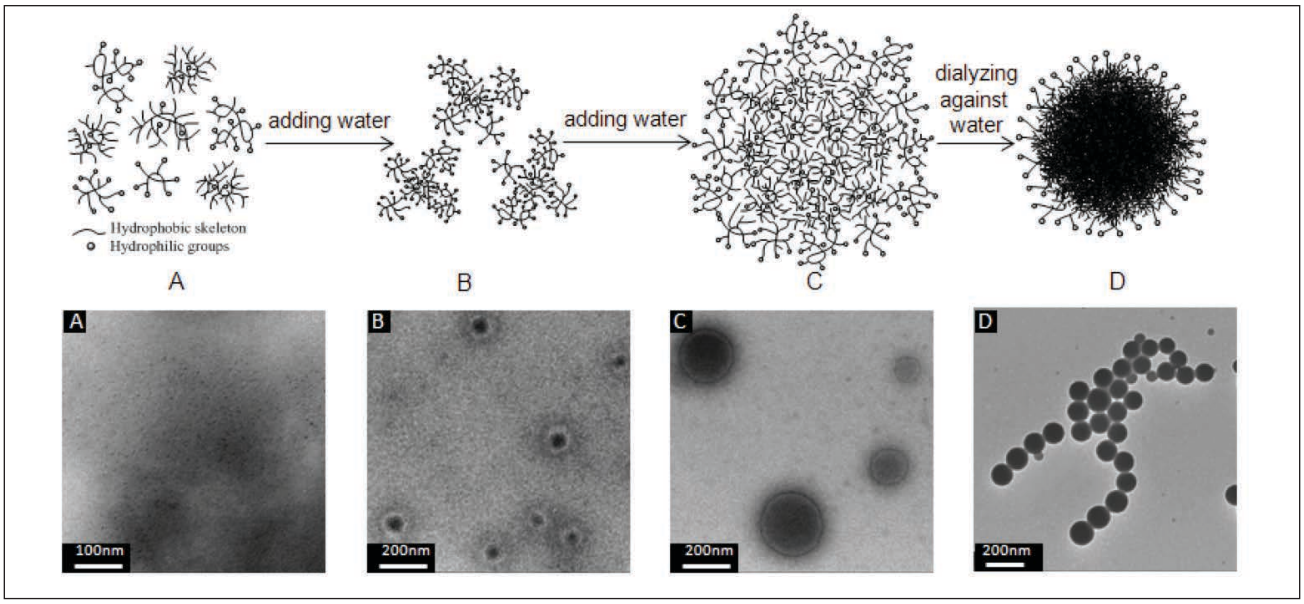
The dark color of industrial lignin is the main obstacle for its high value-added uses in areas such as sunscreen products or dyestuff dispersants. By acetylating modification and self-assembling in selective solvents, Qian et al. first fabricated uniform lignin colloidal spheres and the formation mechanism was evaluated (**Fig. 12**) [55]. Because of the blocking of phenolic hydroxyl chromophores and effect of the Mie



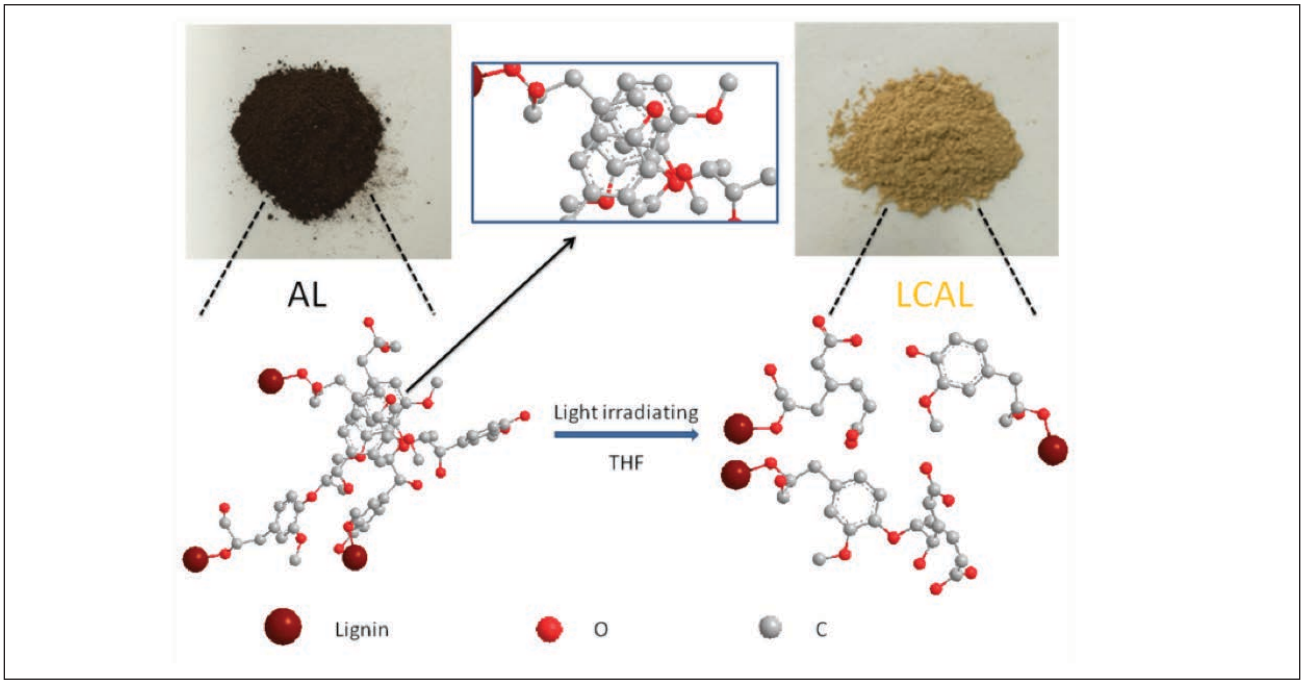
10. Ultraviolet (UV) absorbance of the sunscreens before and after 2 h UV radiation: (a) sun protection factor (SPF) 15 cream + 10 wt% lignin, (b) SPF 15 cream, (c) SPF 30 cream, and (d) pure cream +10 wt% lignin.



11. Typical energy diagram of π-π stacking between lignin and chemical sunscreen active octyl methoxycinnamate.*



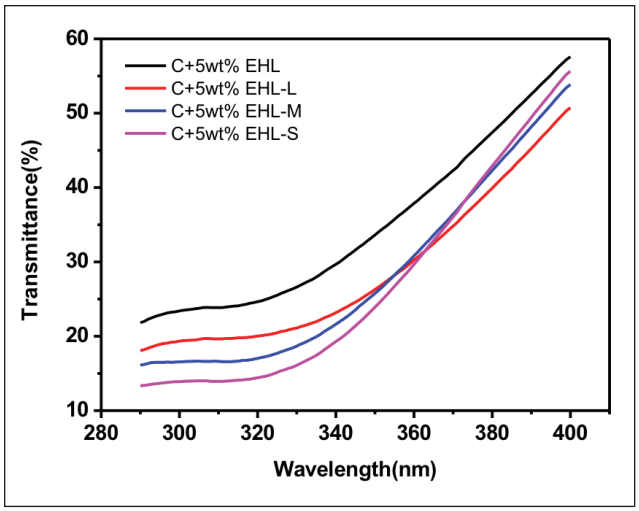
12. Schematic representation of the colloid formation process of the actylated lignin in a tetrahydrofuran-water (THF–H_2O) medium and transmission electron microscopy (TEM) images of the samples obtained from the dispersions with different water contents. Water content: (A) 0–13 vol%, (B) 13–44 vol%, (C) 44–67 vol%, and (D) >67 vol%, removing THF for recycling.



13. Schematic representation of whitening lignin via ultraviolet radiation.

scattering, lignin was obviously whitened [56]. Furthermore, they presented a one-step UV radiation method to reduce the color of lignin and characterized the structural changes of the whitened lignin [57]. When lignin was exposed to UV in solvents producing peroxides, its content of aromatic ring, methoxyl and phenolic hydroxyl groups would decrease, while the content of carboxylic groups increased. Lignin was not only intermolecular and intramolecular disaggregated, but also partially depolymerized (**Fig. 13**).

However, both whitening methods sacrificed the phenolic hydroxyl groups of lignin, which are not only responsible for scavenging free radicals, but also helpful for blocking UV radiation. Thus, Qian el al. prepared lignin colloidal spheres with different sizes and structures by self-assembling without chemical modification, and then blended with pure skin cream to develop lignin-based sunscreens [58]. The sunscreen performance of lignin colloidal spheres was better than that of original lignin (**Fig. 14**). The SPF value of the



14. Ultraviolet (UV) transmittance of pure cream blended with 5 wt% lignin and lignin colloidal spheres in UVA and UVB.

sunscreen containing 10 wt% lignin colloidal spheres with the size of about 50 nm reached 15. The SPF value of sunscreen containing 10 wt% middle size lignin colloidal spheres (~200 nm) can be boosted from 11 to 48 by adding 2 wt% UVA and 2 wt% UVB chemical sunscreens.

Further research in this area is being carried out. Whitening without sacrifice of the UV blocking performance is practically important for many applications, not only for the sunscreen creams but also for its use as functional fillers in polymer applications.

LIGNIN FOR POLYMER COMPOSITES APPLICATION

Lignin-based phenol-formaldehyde resin

As a natural polyphenol compound rich in phenol hydroxyl groups, lignin has attracted much attention for partial or even complete replacement of phenol in phenol-formaldehyde (PF) resin production. In our early research, we developed lignin-based phenol-formaldehyde (LPF) resin using wheat straw soda lignin (WSSL) as partial substitute of phenol. WSSL was first modified by phenolation in alkaline medium [59,60]. After modification, the content of methoxyl group in lignin decreased from 11.04% to 8.72%, and the content of phenolic hydroxyl increased from 2.64% to 4.20%. The molecular weight of WSSL also decreased, which resulted in improved WSSL reactivity and decreased LPF viscosity. The adhesive strength and storage stability of LPF were also improved compared with non-phenolated LPF adhesive. When 70% of phenol was replaced by the phenolation-modified WSSL, the adhesive strength of LPF (1.9 MPa) was comparable to traditional PF adhesives (2.1 MPa). Therefore, the modification of WSSL by phenolation increased its reactivity and improved the performance of lignin-based phenol-formaldehyde adhesive.

To study the effect of WSSL molecular weight on the performance of LPF, ultrafiltration was conducted to fractionate WSSL, and three fractions with different molecular weight ranges were obtained [61]. Analysis results showed that WSSL with lower molecular weight contained less methoxy group and more phenolic hydroxyl group, thus exhibiting higher reactivity in the synthesis of LPF. Further experiments showed that as the molecular weight of WSSL decreased, the adhesive strength of LPF increased, but the free formaldehyde content and the viscosity decreased; therefore, better performance of LPF was achieved. When 2%~3% of urea was added into the LPF with the WSSL-to-phenol ratio of 70:30, the adhesive performance could be further improved. The adhesive strength improved from 2.0 MPa to 2.2 MPa, the free formaldehyde content decreased from 0.16% to 0.05%, and the viscosity of LPF reduced from 858 mPa.S to 306 mPa.s [62,63]. The overall performance has reached that of traditional PF resins.

Later research showed that hydroxymethylation modification could also increase the reactivity of WSSL [64,65]. With 50% of phenol substituted by hydroxymethylation modified WSSL, the adhesive strength of LPF could reach 2.0 MPa. Without need of purification, the residual content of formaldehyde and phenol was much lower than the national standard. In comparison with traditional PF adhesives, the prepared LPF had lower curing temperature but faster curing rate.

Recently, researchers developed new demethylation techniques to improve the content of phenolic hydroxyl groups of lignin and enhance their reactivity for preparation of LPF [66-69]. Ma et al. found that the content of phenolic hydroxyl groups of EHL could increase 20% after high-intensity ultrasound processing for 20 min [66]. Sawamura et al. investigated demethylation efficiency of 1-dodecanethiol (DSH), hydroiodic acid (HI), and iodocyclohexane (ICH) on guaiacyl-type synthetic lignin (GDHP) [67]. ICH was the most effective demethylation reagent for increasing the phenolic hydroxyl levels in GDHP. GDHP demethylated with ICH showed higher tannin-like properties. Using rhodium chloride ($RhCl_3$) in the presence of a promoter as a catalyst, Mei et al. demonstrated that more than 80% of the methoxyl group in lignin could react with carbon monoxide and water to generate acetic acid, and the lignin was modified to be rich in phenolic hydroxyls [68]. Li et al. demethylated AL under different mild conditions using sodium sulfite as a catalyst [69]. The methoxyl group content decreased from 1.93 mmol/g to 1.09 mmol/g, whereas the phenolic hydroxyl group content increased from 0.56 mmol/g to 0.82 mmol/g. Prepared LPF resins exhibited faster curing rate and shorter gel time.

Lignin-based polymer composites

Preparing lignin/polymer composites is another way to efficiently use the abundant renewable lignin on a large scale. Rubber, one of the most important polymer materials widely used in daily life, usually needs large quantities of filler (e.g., carbon black) for reinforcement. Considering the abundance of technical lignin produced annually, blending lignin with rubber as a partial substitute for traditional filler is a good choice for massive application of lignin. However, direct

blending results in poor performance because of weak compatibility and severe aggregation of lignin particles in the rubber matrix.

We have studied the influence of three EHL pretreatment methods — ball milling (EHL-BD), spray drying (EHL-SD), and jet milling (EHL-JM) — on their nitrile rubber (NBR) reinforcement ability [70]. EHL-JM gave the finest particle size, averaging 2~3 μm. The particle size from spray drying was about 23 μm, and ball-milling generated coarse particles with a broad size distribution from 4 μm to 300 μm. When the pretreated EHL was blended with NBR in an open roller mill, the viscosity of rubber composite increased with the lignin content. Extending the mixing time could facilitate the distribution of lignin particles in the rubber matrix and shorten the vulcanizing time. EHL could delay the rubber vulcanization process. As the EHL content increased, the delay/inhibiting effect was more obvious. From the dynamic thermomechanical analysis and differential scanning calorimetry analysis, only one glass transition temperature was observed for all the EHL/NBR composites, showing that lignin has a certain degree of compatibility with NBR. The glass transition temperature of rubber composites increased as the lignin content increased, indicating the obvious constraining effect of lignin particle on the NBR chains. Mechanical performance studies revealed that all the EHL pretreated with different methods could reinforce the rubber. EHL-JM showed the best strengthening effect and had better compatibility and stronger interphase adhesion with the NBR matrix. When 40 parts per 100 rubber (phr) EHL-JM was added, the tensile strength of NBR reinforced by EHL-JM was 24% and 61% higher than that of EHL-BM and EHL-SD, respectively. Thermogravimetry results and the analysis of thermal-oxidative aging mechanical properties revealed that EHL could also enhance the thermal stability and anti-aging properties of NBR/EHL blends.

When the EHL-JM was added together with the carbon black, the mechanical properties could be significantly improved [71]. This is because the specific surface area and the particle size of carbon black is much smaller than that of lignin. The NBR composite with 20 phr EHL-JM and 20 phr carbon black showed the best mechanical properties, with a tensile strength of 21 MPa and an elongation at break of 650%, which reached the mechanical requirement of some special rubber applications. However, increasing the proportion of EHL-JM in the composite filler system decreased the tensile strength, the tear strength, and the break elongation. Adding an interfacial modifier, such as a silane coupler, contributed little to the mechanical properties of the NBR/lignin composite, but could improve the anti-thermal oxidative aging property.

Because polyolefin occupies more than half of the global polymer market, our group has also studied lignin-based polyolefin composites. The pretreated AL by ball milling (AL-BM) and jet milling (AL-JM) methods with different sizes were separately blended with high-density polyethylene (HDPE) [72]. AL-JM had the finest particle size of about 3 μm. The results showed that the tensile strength of composite increased with the AL content. When containing the same addition, the composite prepared by finer AL particles had higher tensile strength. The tensile strength of composite produced by 40 wt% AL-JM reached 26 MPa, higher than the blank HDPE sample (about 22 MPa). However, the elongation at break of composites decreased sharply compared with the blank HDPE sample. The more AL added, the smaller the elongation at break. The rheological properties showed that the addition of AL increased the apparent viscosity (η) and complex viscosity (η*) of the composites, the linear viscoelastic region turned narrow, and the storage modulus (G') and the loss modulus (G") also gradually declined with the increasing AL content. The thermogravimetric analysis showed that AL lowered the thermostability of composites.

The effect of plasticizer on the properties of AL/HDPE composites was also systematically studied [73]. With AL content fixed at 20 wt%, the AL/HDPE composites were prepared separately with dioctyl phthalate (DOP), dibutyl phthalate (DBP), and epoxidised soybean oil (ESO). The results showed that these plasticizers could increase the elongation at break of composites, and DOP had the best effect. When we added 7.5 g DOP, the elongation at break of composites reached about 150%. Increasing the DOP dosage helped increase elongation at break and toughness. The fracture surfaces of composites became coarser with the addition of DOP, as verified by scanning electron microscopy. The apparent viscosity (η) and complex viscosity (η*) of the composites were lowered after the addition of DOP, compared with the composites with only AL added. DOP was shown to adsorb on the surface of AL particles and suppress the agglomeration of AL particles in HDPE, which improved the dispersion of AL particles in HDPE, thus the mechanical properties and rheological performance of the composites were improved.

Similarly, the addition of maleic anhydride grafted polypropylene (PP-*g*-MAH) significantly improved the tensile strength of lignin/PP composites [74]. We also correlated the lignin content to the water absorption of lignin-plastic composite. With the increase of lignin content, the water absorption of the composite indicated a increasing trend. At a lignin content less than 30 wt%, the water absorption of the composites was lower than 1.0%, except for spray-dried AL. We also found that the water absorption of the AL composites was lower than that of the EHL composites [74].

The antioxidant performance of lignin in plastics

Because of its rich functional groups, including phenolic, ketone, and other chromophores, lignin also can be used as an excellent antioxidant for polyolefin plastics. We have systematically studied the effect of lignins on the antioxidant properties of polyolefin [75]. As a result of lignin addition, the thermal aging resistance and UV resistance abilities of polyolefin improved. Pine wood alkali lignin (PAL) had the best protective effect performance in terms of thermal oxidative aging and UV aging. The efficiency of UV absorption of lignin had a positive correlation with its anti-UV effect. In the high tem-

perature environment, the oxidation induction time (OIT) of polyolefins could be significantly increased. For HDPE, adding 1% lignin could increase the OIT up to 22 min. However, 3% lignin was needed for low-density polyethylene (LDPE) and PP to increase their oxidation induction period up to 15 min or more.

In the UV aging environment, an improvement in toughness of HDPE composite with 2% lignin was achieved, and the conservation rate of fracture tensile rate reached 168%, which was comparable to industrial light stabilizer. In the thermal oxidative aging environment, the conservation rate of fracture tensile rate of HDPE, LDPE, and PP with 2% lignin reached about 90%, 54%, and 68%, respectively. Rheological tests showed that lignin could reduce the aging rate of polyolefin in the high temperature condition.

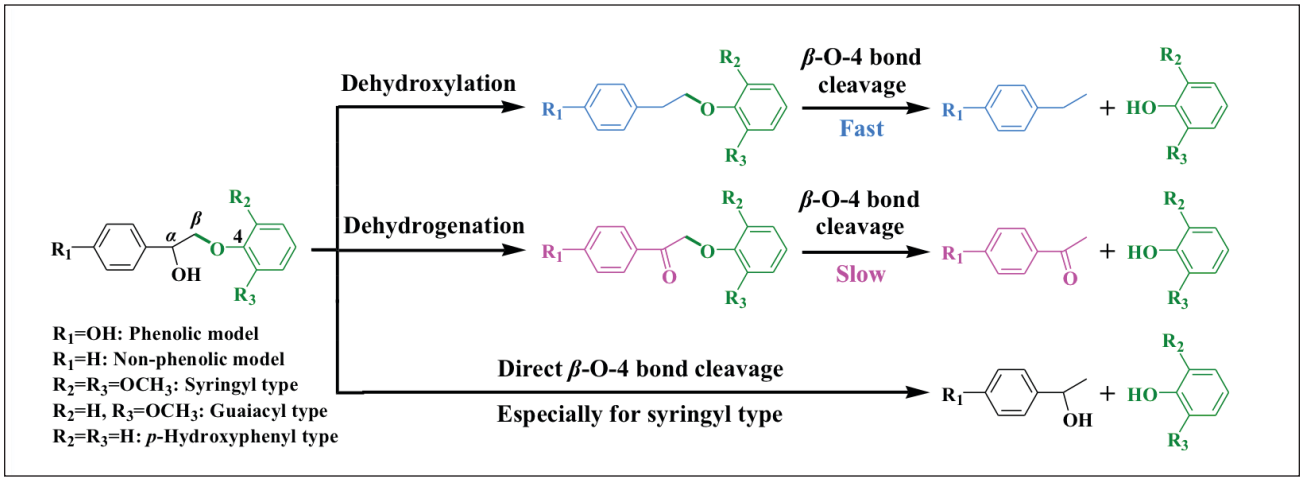
The mechanism for the antioxidant property of lignin was attributed to that the phenolic compounds in lignin that could capture free radicals and prevent the automatic oxidation cycle in polyolefin under the action of thermal oxygen [75]. The conjugated structure in lignin could absorb UV light, and played the role of UV shielding under the action of UV irradiation. Therefore, high purity and high content of phenolic hydroxyl in the lignin from pine wood resulted in low transmission of UV light, which was more suitable for polyolefin antioxidant. Unfortunately, the anti-aging performance of lignin was still poor compared with that of industrial antioxidant Irganox 1010 ($C_{73}H_{108}O_{12}$). To conquer the insufficient protection ability of lignin under the thermal aging condition of polyolefin, additives such as aluminum stearate, stearic acid, and maleic anhydride grafted polyethylene (PE-MA) could be used to improve the dispersion effect of lignin in polyolefin and the anti-aging effect of polyolefin. Commercial Irganox1010 also could be compounded with lignin to realize the synergistic effect. The results showed that the OIT of LDPE compounded with 1% lignin and 0.05% Irganox1010 reached 36.5 min, which could meet the basic requirements of industrial production. Our work has shown that lignin could be used as a co-antioxidant in polyolefin plastics [75].

LIGNIN-DERIVED CHEMICALS

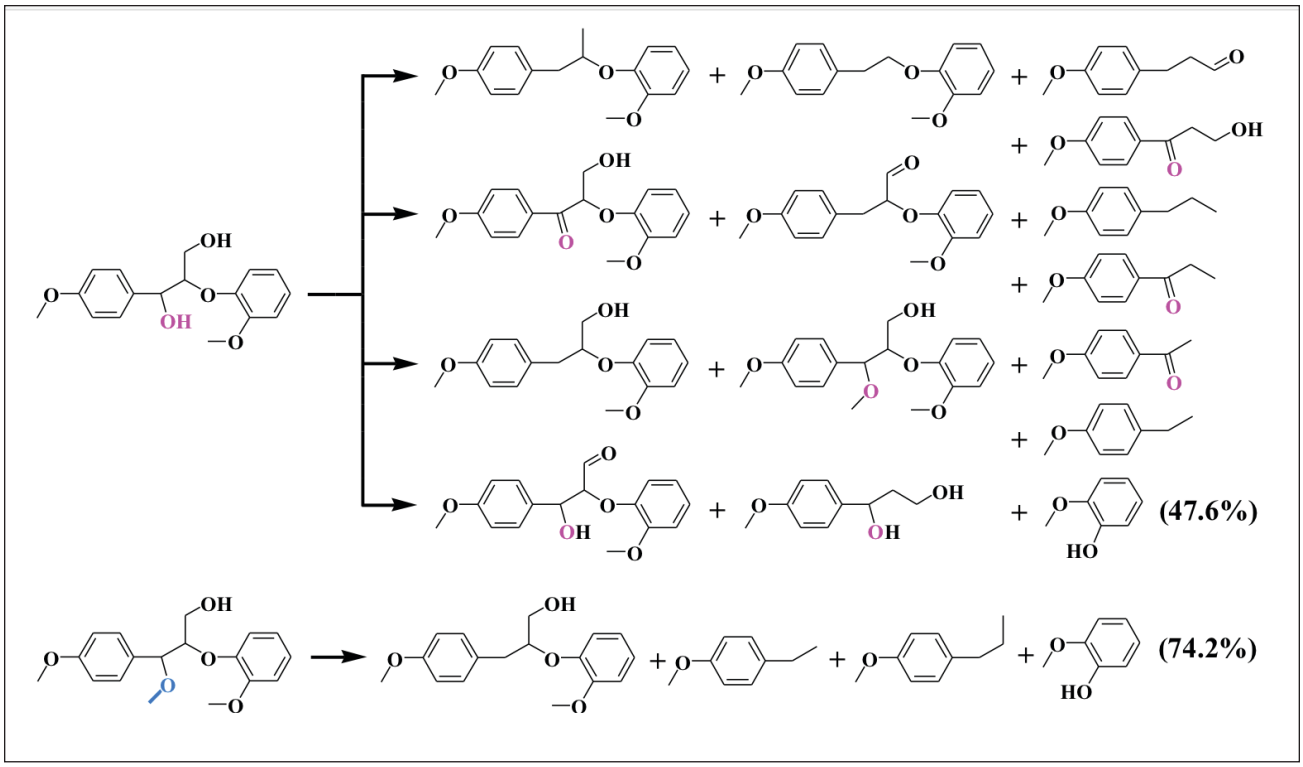
Because lignin is an abundant natural compound rich in aromatic rings, full use of lignin as a raw material for platform chemicals is one promising path for saving petrochemical resources. Therefore, we have also conducted research in the hydrogenolysis of lignin for producing aromatic monomers.

Hydrogenolysis is considered the most promising depolymerized technology for the production of aromatic monomers from lignin [76]. β-O-4 linkage is the predominant linkage in lignin. It is important to understand how three major functional groups of lignin — benzylic alcohol group (C_a—OH), aromatic methoxyl group (C_{aryl}—OCH_3), and phenolic hydroxyl group (C_{aryl}—OH) — affect the behavior of lignin hydrogenolysis [77]. In hydrogenolysis systems, the β-O-4 bond cleavage of lignin with the C_a—OH followed three reaction routes (**Fig. 15**). First, dehydroxylation of the C_a—OH led to C_a—H, followed by a fast cleavage of the β-O-4 bond. Second, dehydrogenation of the C_a—OH easily led to C_a=O, followed by a slow β-O-4 bond cleavage. Third, the β-O-4 bond was cleaved directly, and the cleavage route tended to occur on the β-O-4 bond linked with a syringyl unit. The occurrence of the three reaction routes resulted in a complex product distribution from lignin with the C_a—OH. Both C_{aryl}—OH and C_{aryl}—OCH_3 were stable under the hydrogenolysis condition below 180°C and less than 10 min, so they had no effect on the cleavage route of the β-O-4 bond and product distribution.

To avoid the primary dehydrogenation of C_a—OH during hydrogenolysis, a new two-step lignin depolymerization strategy was developed in which the C_a—OH of lignin was methylated to C_a—OCH_3, followed by hydrogenolysis of methylated lignin [78]. Iron (III) sulfate, $Fe_2(SO_4)_3$, and aluminum sulfate $Al_2(SO_4)_3$, were excellent catalysts in C_a—OH methylation under microwave irradiation. An efficient methylation was achieved with various lignin models under a mild reaction condition. A protonation between C_a—OH and methanol solvent was induced under an acidic environment [79], which resulted in methylation of the C_a—OH. The protonation preferred the C_a—OH to C_y—OH or C_{aryl}—OH under the acidic



15. The cleavage routes of the β-O-4 bond in hydrogenolysis system.



16. Evaluation of hydrogenolysis reactivity; 0.10 mmol of lignin model, 10 mL of methanol, 1.0 mmol of formic acid, 0.0165 g of 10% palladium on carbon (Pd/C), 160°C, 30 min, and microwave heating.

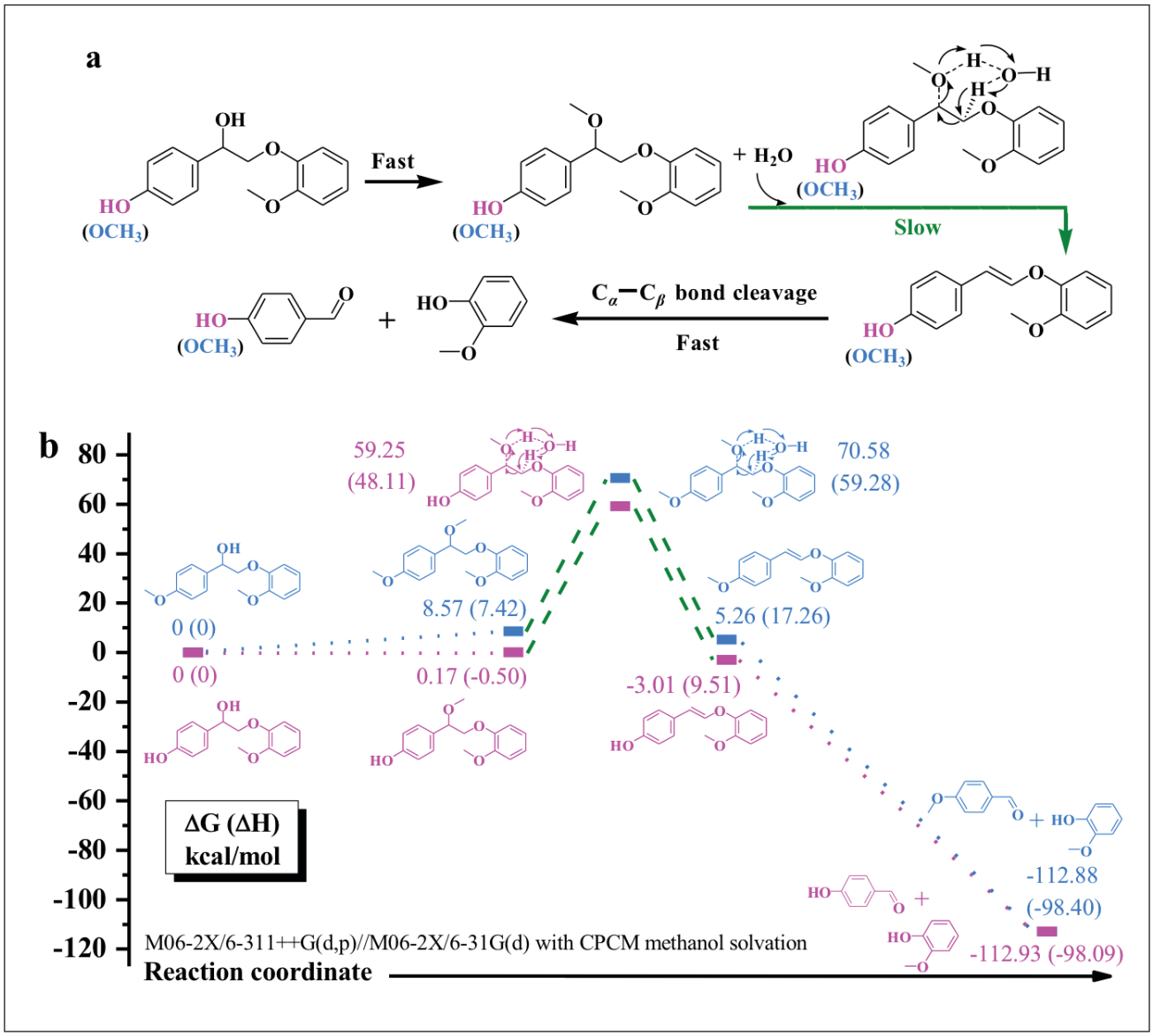
condition, so the methylation selectively occurred only at C_a—OH rather than C_y—OH or C_{aryl}—OH.

C_a—OH was methylated to improve the hydrogenolysis reactivity of the β-O-4 bond. Methylation of C_a—OH improved product selectivity in decomposition, yielding only four products instead of 15 products from unmethylated compound (**Fig. 16**). The formation of C_a=O from the dehydrogenation of C_a—OH was inhibited through replacement of C_a—OCH_3, resulting in the β-O-4 bond cleavage reactivity increasing by 55.9%. These results provided an important foundation for the hydrogenolysis of lignin into aromatic monomers. A methylation pretreatment of lignin allowed for increasing the degree of lignin depolymerization by 24.7% to about 28.7%, and the yield of aromatic monomers by 43.1% to about 54.1%.

The oxygen atom in the C_a position of aromatic monomers was generally retained when the β-O-4 bond was cleaved [80,81], resulting in a higher oxygen content of alkyl side chain. However, none of the oxygen atoms in the C_a position were found in aromatic monomers from methylated compounds (Fig. 16). Aromatic monomers with low oxygen content were conducive to further preparation of advanced bioalkane fuels. The results highlighted the prospect of a reduction of oxygen content of aromatic monomers. Whether or not the C_a—OH was methylated to C_aOCH_3, lignin yielded 18 major aromatic monomers, which included low and high oxygen content of alkyl side chain of aromatic monomers. However, methylation pretreatment contributed to a reduction of the oxygen content of aromatic monomers, whose ratio of low and high oxygen content of alkyl side chain of aromatic monomers increased to about 6.5–7.4:1 from the ratio of about 1.6–1.8:1 generally obtained on unmethylated lignin.

In addition to the relatively low yield of aromatic monomers from lignin depolymerization, a complicated distribution of aromatic monomers also hinders the large-scale conversion of lignin into aromatic monomers. Hence, we must narrow the distribution of aromatic monomers to achieve the selective production of aromatic monomers from lignin. A complicated distribution of aromatic monomers is derived from an irregular phenyl C3 side-chain, so it is important to unify the side-chain of aromatic monomers. The C_a—C_β bond was the most vulnerable among C—C bonds on the phenyl C3 side-chain [82]. Therefore, we also targeted selective C_a—C_β bond cleavage of the phenyl C3 side-chain [83]. The cleavage of the C_a—C_β bond was achieved with $Fe_2(SO_4)_3$ as a catalyst under microwave irradiation, and a conversion process with the free energy and enthalpy profile was shown for microwave-assisted cleavage of the C_a—C_β bond (**Fig. 17**).

An acidic environment promoted rapid methylation of the C_a—OH with methanol into methylated product. A further elimination of C_a—OCH_3 with C_β—H in the methylated product occurred to form alkenyl product, and the formation of alkenyl product was a decomposition-determining step. Density functional theory calculations indicated that a phenolic lignin model was more thermodynamically favorable to form alkenyl product than a non-phenolic lignin model, so the pres-

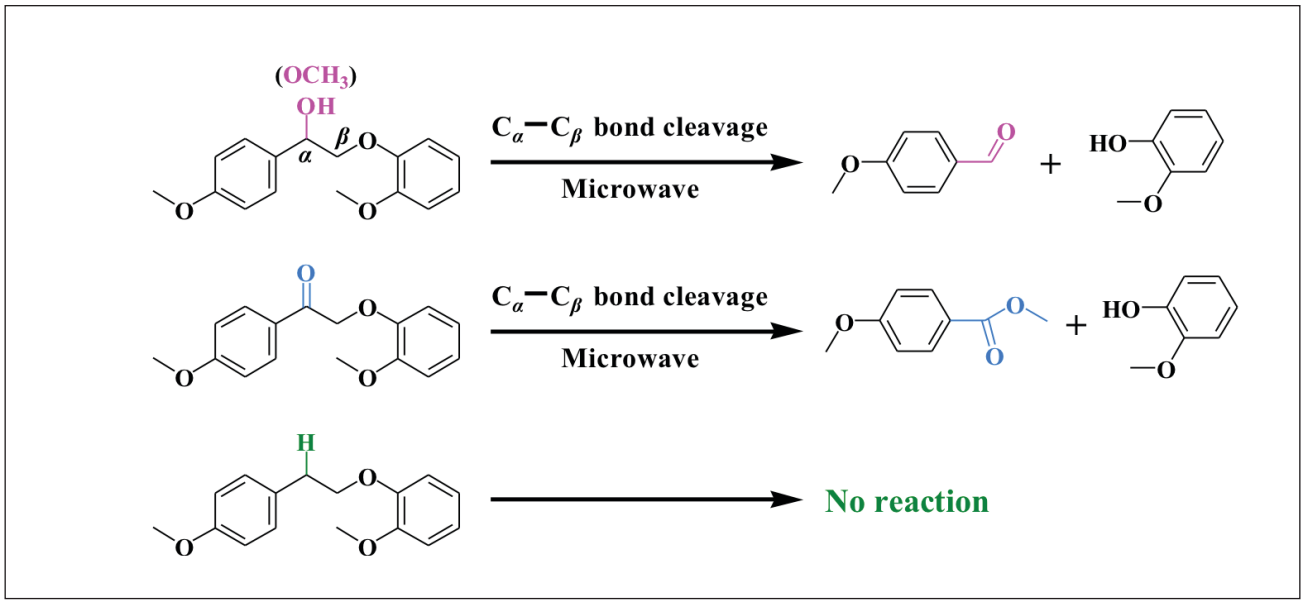


17. (a) Decomposition process and (b) reaction energy diagrams for microwave-assisted selective cleavage of the C_a—e_β bond.

ence of C_{aryl}—OH enhanced the C_a—C_β bond cleavage reactivity in nature.

The result highlighted the prospect of selective C_a—h_β bond cleavage of lignin. Compared with conventional heating, microwave heating promoted lignin depolymerization and allowed for increasing the degree of lignin depolymerization by 17.3% to about 28.4%. Meanwhile, microwave heating markedly facilitated C_a—C_β bond cleavage of lignin, and the cleavage percentage of the C_a—C_β bond in lignin increased to about 65.2% to 96.3% from about 19.3% to 34.0% generally obtained using conventional heating. An excellent microwave-assisted selective cleavage of the C_a—C_β bond allowed for a narrowing of aromatic monomers, which only contained four main aromatic monomers (vanillin, syringaldehyde, methyl vanillate, and methyl syringate).

Inspired by the process of the C_a—C_β bond cleavage (Fig. 17), a fundamental understanding of how the benzyl functionality of C_a—OH to C_a=O, C_a—H, or C_a—OCH_3 controlled the microwave-assisted selective cleavage of the C_a—C_β bond was further investigated [84]. The oxidization, reduction, and etherification of C_a—OH to C_a=O, C_a—H, and C_a—OCH_3 had little influence on the bond length and bond dissociation enthalpies of the C_a—C_β bond. Hence, it was still difficult to cleave the C_a—C_β bond under mild thermal condition [85]. However, dynamic analysis showed that the oxidization of C_a—OH to C_a=O increased the decomposition rate constant by 16.3%. The decomposition determining step was enolate isomerization when C_a—OH was oxidized to C_a=O. The density functional theory calculations indicated that ΔG and ΔH of the decomposition determining step decreased by 35.8% and 44.9%, respectively. An increase of the decomposition rate constant and a decreased barrier of the decomposi-



18. Effect of benzyl functionality on the formation of aromatic monomers.

tion determining step improved the C_a—C_β bond cleavage. Methylation of C_a—OH to C_a—OCH_3 had no effect on the cleavage reactivity of the C_a—C_β bond. Meanwhile, the microwave-assisted selective cleavage of the C_a—C_β bond followed first-order kinetic and radical reaction mechanisms. No reaction occurred between the compound whose C_a—OH was reduced to C_a—H with hydroxyl free radical, which resulted in the C_a—C_β bond cleavage being hindered. Additionally, benzyl functionality had an obvious effect on the formation of aromatic monomers (**Fig. 18**). The presence of C_a—OH or C_a—OCH_3 allowed for the production of aromatic aldehyde, whereas aromatic ester would be produced when C_a—OH was oxidized to C_a=O.

OUTLOOK

Value-added usage of lignin is booming. However, how to improve the technologies, simplify the experimental procedures, and realize industrialization are still obstacles. Our work is developing in several directions. Fabrication of lignin-based adjuvant that can enhance the enzyme hydrolysis of cellulose and make it easy to recycle the cellulase could be more popular. Improving the stability of aggregation-induced fluorescence and efficiency of the transfer free electron is the key for the application of lignin in photoelectrics. To realize the application of lignin in skin-care products, the dark color of lignin should be whitened. The sunscreen performance of lignin itself cannot meet the daily requirement. Physical or chemical modification should be tested, but should not sacrifice the phenolic hydroxyl groups, which are very important for UV-blocking and antioxidant performance. To break through the original depolymerizaiton of lignin to platform chemicals, key technical issues include making clear the dynamic relation of activating mechanisms of lignin molecules, catalytic active center, and catalyst supporter. Several technologies are expected to result after several years' exploration. **TJ**

ACKNOWLEDGEMENT

We gratefully acknowledge financial support from the National Natural Science Foundation of China (21606089, 21436004), the Guangdong Province Science and Technology Research Project of China (2014B050505006), the Guangzhou Science and Technology Research Project of China (201704030126), and the Open Fund of the State Key Laboratory of Pulp and Paper Engineering (201701).

LITERATURE CITED

1. Goldemberg, J., *Science* 315(5813): 808(2007).
2. Ragauskas, A.J., Beckham, G.T., Biddy, M.J., et al., *Science* 344(6185): 1246843(2014).
3. Montané, D., Torné-Fernández, V., Fierro, V., *Chem. Eng. J.* 106(1): 1(2005).
4. Hayashi, J.I., Kazehaya, A., Muroyama, K., et al., *Carbon* 38(13): 1873(2000).
5. Carrott, P.J.M. and Carrott, M.R., *Bioresour. Technol.* 98(12): 2301(2007).
6. Ouyang, X.P., Ke, L.X., Qiu, X.Q., et al., *J. Dispersion Sci. Technol.* 30(1): 1(2009).
7. Qin, Y.L., Yang, D.J., Guo, W.Y., et al., *J. Ind. Eng. Chem.* 27: 192(2015).
8. Qin, Y.L., Yang, D.J., Qiu, X.Q., *ACS Sustainable Chem. Eng.* 3(12): 3239(2015).
9. Li, Z.L., Pang, Y.X., Ge, Y.Y., et al., *J. Phys. Chem. C* 115(50): 24865(2011).

10. Zhou, H.F., Qiu, X.Q., Yang, D.J., et al., *ACS Sustainable Chem. Eng.* 4(3): 1248(2016).
11. Graupner, N., *J. Mater. Sci.* 43(15): 522(2008).
12. Mansouri, N.E.E., Pizzi, A., and Salvado, J., *J. Appl. Polym. Sci.* 103(3): 1690(2007).
13. Khan, M.A., Ashraf, S.M., and Malhotra, V.P., *Int. J. Adhes. Adhes.* 24(6): 485(2004).
14. Kadla, J.F., Kubo, S., Venditti, R.A., et al., *Carbon* 40(15): 2913(2002).
15. Zhang, M. and Ogale, A.A., *Carbon* 69: 626(2014).
16. Lou, H.M., Wang, M.X., Lai, H.R., et al., *Bioresour. Technol.* 146: 478(2013).
17. Zhou, H.F., Lou, H.M., Yang, D.J., et al., *Ind. Eng. Chem. Res.* 52(25): 8464(2013).
18. Nakagame, S., Chandra, R.P., and Saddler, J.N., in *Sustainable Production of Fuels, Chemicals, and Fibers from Forest Biomass*, American Chemical Society, Washington, DC, USA, 2011, ACS Symposium Series, Vol. 1067, Chap. 6, pp. 145-167.
19. Nakagame, S., Chandra, R.P., and Saddler, J.N., *Biotechnol. Bioeng.* 105(5): 871(2010).
20. Pan, X.J., *J. Biobased Mater. Bioenergy* 2(1): 25(2008).
21. Zhang, J.Z., Laguna, A., Clemons, C., et al., *BioEnergy Res.* 8(1): 464(2015).
22. Rinaldi, R., Jastrzebski, R., Clough, M.T., et al., *Angew Chem., Int. Ed.* 55(29): 8164(2016).
23. Lin, X.L., Cai, C., Lou, H.M., et al., *Cellulose* 24(1): 61(2017).
24. Lou, H.M., Zhu, J.Y., Lan, T.Q., et al., *ChemSusChem* 6(5): 919(2013).
25. Wang, Z.J., Zhu, J.Y., Fu, Y.J., et al., *Biotechnol. Biofuels* 6(1): 156(2013).
26. Lou, H.M., Zhou, H.F., Li, X.L., et al., *Cellulose* 21(3): 1351(2014).
27. Cai, C., Qiu, X.Q., Lin, X.L., et al., *Bioresour. Technol.* 216: 968(2016).
28. Lin, X.L., Qiu, X.Q., Yuan, L., et al., *Bioresour. Technol.* 185: 165(2015).
29. Ye, X.K. and Chen, Y.C., *Biotechnol. Bioprocess Eng.* 20(2): 242(2015).
30. Palmqvist, E. and Hahn-Hagerdal, B., *Bioresour. Technol.* 74(1): 17(2000).
31. Ximenes, E., Kim, Y., Mosier, N., et al., *Enzyme Microb. Technol.* 46(3-4): 170(2010).
32. Palmqvist, E. and Hahn-Hagerdal, B., *Bioresour. Technol.* 74(1): 25(2000).
33. Lou, H.M., Liu, H.Y., Wu, S., et al., *Fine Chem.* 31(6): 711(2014).
34. Shen, Z.G., Luo, Y.Q., Wang, Q., et al., *ACS Appl. Mater. Interfaces* 6(18): 16147(2016).
35. Liitiä, T.M., Maunu, S.L., Hortling, B., et al., *J. Agric. Food Chem.* 51(8): 2136(2003).
36. Zakzeski, J., Bruijnincx, P.C., Jongerius, A.L., et al., *Chem. Rev.* 110(6): 3552(2010).
37. Albinsson, B., Li, S., Lundquist, K., et al., *J. Mol. Struct.* 508(1): 19(1999).
38. Xue, Y.Y., Qiu, X.Q., Wu, Y., et al., *Polym. Chem.* 7(21): 3502(2016).
39. Xue, Y.Y., Liang, W.S., Li, Y., et al., *J. Agric. Food Chem.* 7: 3502(2016).
40. Yang, D.J., Qiu, X.Q., Pang, Y.X., et al., *J. Dispersion Sci. Technol.* 29(9): 1296(2008).
41. Zhou, H.F., Yang, D.J., and Qiu, X.Q., *Appl. Microbiol. Biotechnol.* 97(24): 10309(2013).
42. Li, Z.L., Pang, Y.X., Lou, H.M., et al., *BioResources* 4(2): 589(2009).
43. Lou, H.M., Lai, H.R., Wang, M.X., et al., *Ind. Eng. Chem. Res.* 52(46): 16101(2013).
44. Hong, L.N., Yu, W., Xue, Y.Y., et al., *Holzforschung* 70(4): 297(2016).
45. Hau, K., Yip, H.L., Baek, N.S., et al., *Appl. Phys. Lett.* 92(25): 253301(2008).
46. Kawano, K., Pacios, R., Poplavskyy, D., et al., *Sol. Energy Mater. Sol. Cells* 90(20): 3520(2006).
47. Hains, A.W., Liang, Z.Q., Woodhouse, M.A., et al., *Chem. Rev.* 110(11): 6689(2010).
48. Hong, N.L., Qiu, X.Q., Deng, W.Y., et al., *RSC Adv.* 5(110): 90913(2015).
49. Li, Y. and Hong, N.L., *J. Mater. Chem. A* 3(43): 21537(2015).
50. Hong, N.L., Xiao, J.Y., Li, Y.D., et al., *J. Mater. Chem. C* 4(23): 5297(2016).
51. Wu, Y., Wang, J.Y., Qiu, X.Q., et al., *ACS Appl. Mater. Interfaces* 8(19): 12377(2016).
52. Li, Y., Wu, Y., Zeng, W.M., et al., *ACS Sustainable Chem. Eng.* 4(4): 2004(2016).
53. Qian, Y., Qiu, X.Q., and Zhu, S.P., *Green Chem.* 17(1): 320(2015).
54. Qian, Y., Qiu, X.Q., and Zhu, S.P., *ACS Sustain. Chem. Eng.* 4(7): 4029(2016).
55. Qian, Y., Deng, Y.H., Qiu, X.Q., et al., *Green Chem.* 16(4): 2156(2014).
56. Qian, Y., Deng, Y.H., Li, H., et al., *Ind. Eng. Chem. Res.* 53(24): 10024(2014).
57. Wang, J.Y., Deng, Y.H., Qian, Y., et al., *Green Chem.* 18(3): 695(2016).
58. Qian, Y., Zhong, X.W., Li, Y., et al., *Ind. Crops Prod.* 101: 54(2017).
59. Liu, G.Y., Qiu, X.Q., and Xing, D.S., *J. Chem. Eng. Chinese U.* 21(4): 678(2007).
60. Liu, G.Y., Qiu, X.Q., and Yang, D.J., *J. Shaanxi U. Sci. Technol. (Nat. Sci. Ed.)* 26(4): 5(2008).
61. Liu, G.Y., Qiu, X.Q., and Yang, D.J., *J. Chem. Ind. Eng.* (China) 59(6): 1590(2008).
62. Liu, G.Y., Qiu, X.Q., Yang, D.J., et al., *Fine Chem.* 25(9): 922(2008).
63. Liu, G.Y., Qiu, X.Q., Yang, D.J., et al., *Fine Chem.* 26(4): 399(2009).
64. Ouyang, X.P., Zhan, L., Chen, K., et al., *J. South China Univ. Technol., Nat. Sci.* 39(11): 22(2011).
65. Lin, Z.X., Ouyang, X.P., Yang, D.J., et al., *World Sci-Tech. R&D* 32(3): 348(2010).
66. Ma, Z.M., Li, S.J., Fang, G.Z, et al., *Int. J. Biol. Macromol.* 93: 1279(2016).
67. Sawamura, K., Tobimatsu, Y., Kamitakahara, H., et al., *ACS Sustainable Chem. Eng.* 5(6): 5424(2017).
68. Mei, Q.Q., Liu, H.Z., Shen, X.J., et al., *Angew. Chem., Int. Edit.* 129(47): 15064(2017).
69. Li, J.J., Zhang, J.Z., Zhang, S.F., et al., *Polymers* 9(9): 428(2017).

70. Zhou, M.S., Mo, X.K., Lou, H.M., et al., *J. Chem. Eng. Chinese U.* 28(4): 830(2014).
71. Mo, X.K., Zhou, M.S., Lou, H.M., et al., *Polym. Mater.: Sci. Eng.* 31(1): 51(2015).
72 Zhou, M.S., Sun, J.Z., Huang, J.H., et al., *Polym. Mater.: Sci. Eng.* 7(29): 39(2013).
73. Zhou, M.S., Sun, J.Z., Yang, D.J., et al., *Acta Polym. Sin.* 2: 210(2014).
74. Huang, J.H., "Preparation and evaluation of lignin-plastic composite," Master's thesis, South China University of Technology, Guangzhou, China, 2012.
75. Chen, J.H., "Study of lignin on the anti-aging properties of polyolefin," Master's thesis, South China University of Technology, Guangzhou, China, 2016.
76. Pandey, M.P. and Kim, C.S., *Chem. Eng. Technol.* 34(1): 29(2011).
77. Zhu, G.D., Ouyang, X.P., Jiang, L.F., et al., *Fuel Process. Technol.* 154: 132(2016).
78. Zhu, G.D., Ouyang, X.P., Jiang, L.F., et al., *Bioresour. Technol.* 218: 718(2016).
79. Sturgeon, M.R., Kim, S., Lawrence, K., et al., *ACS Sustainable Chem. Eng.* 2(3):472(2013).
80. Hanson, S.K., Wu, R.L., and Silks, L.A.P., *Chem. Int. Ed.* 51(14): 3410(2012).
81. Wu, A., Lauzon, J.M., and James, B.R., *Catal. Lett.* 145(2): 511(2015).
82. Hu, L.B., Luo, Y.P., Cai, B., et al., *Green Chem.* 16(6): 3107(2014).
83. Zhu, G.D., Jin, D.X., Zhao, L.S., et al., *Fuel Process. Technol.* 161: 155(2017).
84. Zhu, G.D., Lin, M.L., Fan, D., et al., *J. Phys. Chem. C* 121(3): 1537(2017).
85. Zhu, G.D., Ouyang, X.P., Yang, Y., et al., *RSC Adv.* 6(22): 17880(2016).

ABOUT THIS PAPER

Cite this article as: Qian, Y., Lou, H., Liu, W., et al. *TAPPI J.* 17(3): 125(2018). https://doi.org/10.32964/TJ17.03.125

DOI: https://doi.org/10.32964/TJ17.03.125

ISSN: 0734-1415

Publisher: TAPPI Press

Copyright: ©TAPPI Press 2018

About this journal

ABOUT THE AUTHORS

We chose to research this topic because lignin is one of the world's most promising biomass resources. This research differs from previous research in that we take an application-oriented basic approach.

The most difficult aspect of this research was developing lignin as a natural UV blocker for the very first time. It was surprising to discover that lignin is a natural macromolecular sunscreen and that it can be used in high-end cosmetic applications. Also, it was interesting to find that lignin can be used at large scale in polymeric materials.

Mills should consider that their lignin byproduct may become more appealing for a range of applications in the future. Our next step is developing lignin-based products and pushing their use in cosmetic and materials areas.



Qian



Lou



Liu



Yang



Ouyang



Li



Qiu

Qian is professor, Lou is professor, Liu is associate professor, Yang is professor, Ouyang is professor, Li is associate professor, and Qiu is professor and vice president, School of Chemistry and Chemical Engineering, South China University of Technology, Guangzhou, China. Qian, Lou, and Qiu are also associated with the State Key Laboratory of Pulp and Paper Engineering, South China University of Technology. Email Qiu at xueqingqiu66@163.com.

Controlling porosity and density of nanocellulose aerogels for superhydrophobic light materials

CHENGHUA YU, FENG WANG, SHIYU FU, AND LUCIAN A. LUCIA

ABSTRACT: A very low-density oil-absorbing hydrophobic material was fabricated from cellulose nanofiber aerogels–coated silane substances. Nanocellulose aerogels (NCA) superabsorbents were prepared by freeze drying cellulose nanofibril dispersions at 0.2%, 0.5%, 0.8%, 1.0%, and 1.5% w/w. The NCA were hydrophobically modified with methyltrimethoxysilane. The surface morphology and wettability were characterized by scanning electron microscopy and static contact angle. The aerogels displayed an ultralow density (2.0–16.7 mg·cm^{-3}), high porosity (99.9%–98.9%), and superhydrophobicity as evidenced by the contact angle of ~150° that enabled the aerogels to effectively absorb oil from an oil/water mixture. The absorption capacities of hydrophobic nanocellulose aerogels for waste engine oil and olive oil could be up to 140 g·g^{-1} and 179.1 g·g^{-1}, respectively.

Application: Mills might sell pulps for production of nanocellulose-based aerogels for oil spill remediation.

As oil spills become more frequent, the catastrophic events within a marine environment demand immediate and effective responses [1]. Currently, chemical, physical, and biological approaches are the common remediation solutions to deal with such calamities [2-4]. Among these, using absorbents to adsorb oil from water is one of the most promising approaches due to convenience, simplicity, and efficiency [3,4]. Various natural absorbents with low cost, biocompatibility, and effectiveness (e.g., rice husks [5], cotton fibers [6], coconut husks, sugar cane bagasse [7], and wool fibers [8]) have been developed. However, inherent problems such as poor buoyancy, low absorption capacity, poor oil/water selectivity, and poor recyclability [4,5] restrict them for practical applications.

Recently, aerogels made of carbon (e.g., carbon nanotubes, graphene, or cellulose) have been used as oil/water separation materials due to their low density, high specific surface area, and high porosity [9]. Aerogels based on cellulose, such as cotton fibers, cellulose fibers, or bacterial cellulose, are especially favored for treating petroleum spills because of their superior physical and chemical properties and low cost. Cellulose nanofibrils (CNF), derived from cellulose, have attracted widespread attention in many arenas because of their outstanding mechanical properties as evidenced by their elastic modulus of 140 GPa [10]. Their renewability, good mechanical properties, low density, high porosity, natural biodegradability, and environmental friendliness [11,12] make CNF an ideal raw material for oil sorbents.

In this study, a superhydrophobic nanocellulose-based aerogel was fabricated for dealing with oil spills via a simple and green method. The nanocellulose aerogels (NCA) were produced by freeze drying and subsequently modified with methyltrimethoxysilane (MTMS) through chemical vapor deposition. The obtained aerogels displayed ultralow density, high porosity, and excellent oil absorption capacity.

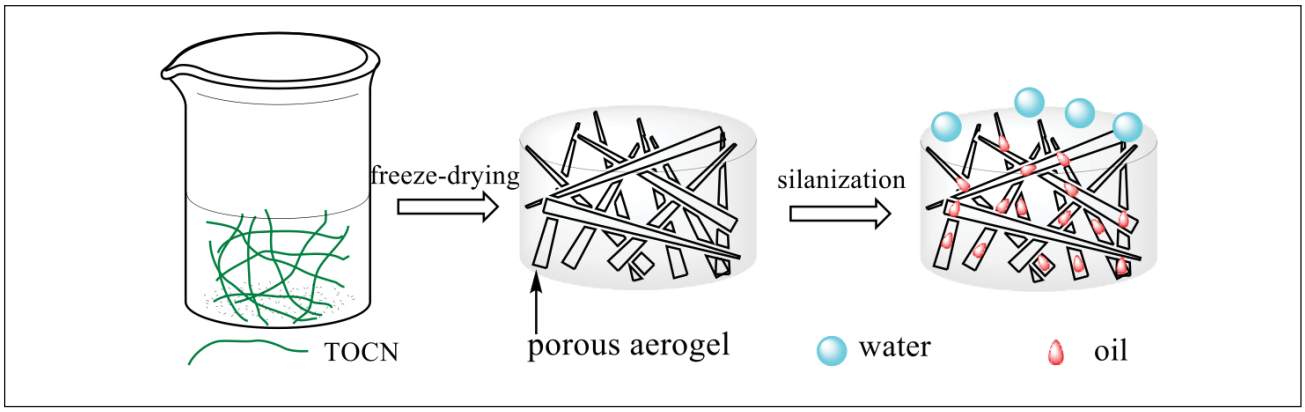
EXPERIMENTAL

Materials

Bleached kraft softwood pulps were used as the raw materials for 2,2,6,6-Tetramethyl-1-piperidinyloxy (TEMPO)-oxidized cellulose nanofibrils (TOCN) preparation. The pulps were provided by Yueyang Forest & Paper Co. Ltd., Yueyang, China. Methyltrimethoxysilane (98%, MTMS) and 2,2,6,6-Tetramethyl-1-piperidinyloxy (98%, TEMPO) were purchased from Aladdin Chemistry Co. Ltd., Shanghai, China. Pump oil and olive oil were supplied by Yu Shao Trading Co. Ltd., Guangzhou, China. All other chemicals were commercially purchased and used as received without further purification.

Preparation of nanocellulose

On the basis of previous work [13], 10 g (dry weight, d.w.) of softwood pulp was first dispersed into 1 L of deionized water with continuous mechanical stirring at 300 rpm for 10 min. Fixed amounts of sodium bromide (0.1 g/g d.w. pulp) and TEMPO (0.015 g/g d.w. pulp) were sequentially added. The reaction was started by the addition of sodium hypochlorite solution (12%, 6 mmol/g d.w. pulp), after which the pH of the reaction was maintained at 9.8–10 by adding 0.5 mol/L sodium hydroxide until the pH was no further changed. Subsequently, the TEMPO-oxidized cellulose was washed with a large amount of deionized water. Finally, the obtained TEMPO-oxidized cellulose was treated by high-pressure homogenization to provide TOCN dispersions that were stored at 4°C.



1. Preparation of porous aerogel and the process of oil/water separation.

Fabrication of nanocellulose aerogels

The concentrations of TOCN dispersions were controlled as 0.2%, 0.5%, 0.8%, 1.0%, and 1.5% w/w. The TOCN dispersions were frozen in a refrigerator at -20°C for 24 h then freeze dried at -50°C for 48 h to obtain various NCA (**Fig. 1**).

Preparation of superhydrophobic nanocellulose aerogels

For the superhydrophobic NCA to address oil absorption, the as-prepared samples were treated with MTMS through vapor phase deposition [3]. The samples were placed in a 500 mL metal bottle that contained two small open bottles with 200 µL of MTMS and 800 µL of deionized water. The metal bottle was then sealed and put in an 80°C oven for 8 h to ensure the reaction was complete. Subsequently, the MTMS-modified samples were put in a 60°C vacuum oven for more than 4 h to remove the unreacted MTMS. Then, the obtained MTMS-modified samples were stored in a desiccator for further use.

Morphology and nanostructure

The NCA were first sectioned into pieces. These pieces were fixed on sample holders and then coated with gold for scanning electron microscope (SEM) observation. The morphological images of the samples were observed by an EVO 18 SEM (Zeiss; Oberkochen, Germany).

Density and porosity of nanocellulose aerogels

The densities of the NCA were calculated using Eq. 1:

$$\rho = \frac{m}{v} \quad (1)$$

where m and v were the mass (g) and volume (cm³) of the aerogels, respectively. The porosities of the NCA were calculated using Eq. 2:

$$P = (1 - \frac{\rho_a}{\rho_c}) \times 100\% \quad (2)$$

where ρ_a was the density of the aerogel and ρ_c was the density of crystalline cellulose (1.528 g/cm³) [14].

X-ray photoelectron spectroscopy analysis

The surface composition of NCA and MTMS-modified NCA were analyzed by X-ray photoelectron spectroscopy (XPS) using an Axis Ultra DLD instrument (Kratos Analytical; Manchester, UK).

Compressive properties

Compressive properties of NCA were performed using an Instron 5565 (Instron; Norwood, MA, USA) with a loading cell of 200 N. The samples were placed in the specimen holder and then compressed to 70% of their initial thickness at a speed of 50 mm/min.

Contact angle measurement

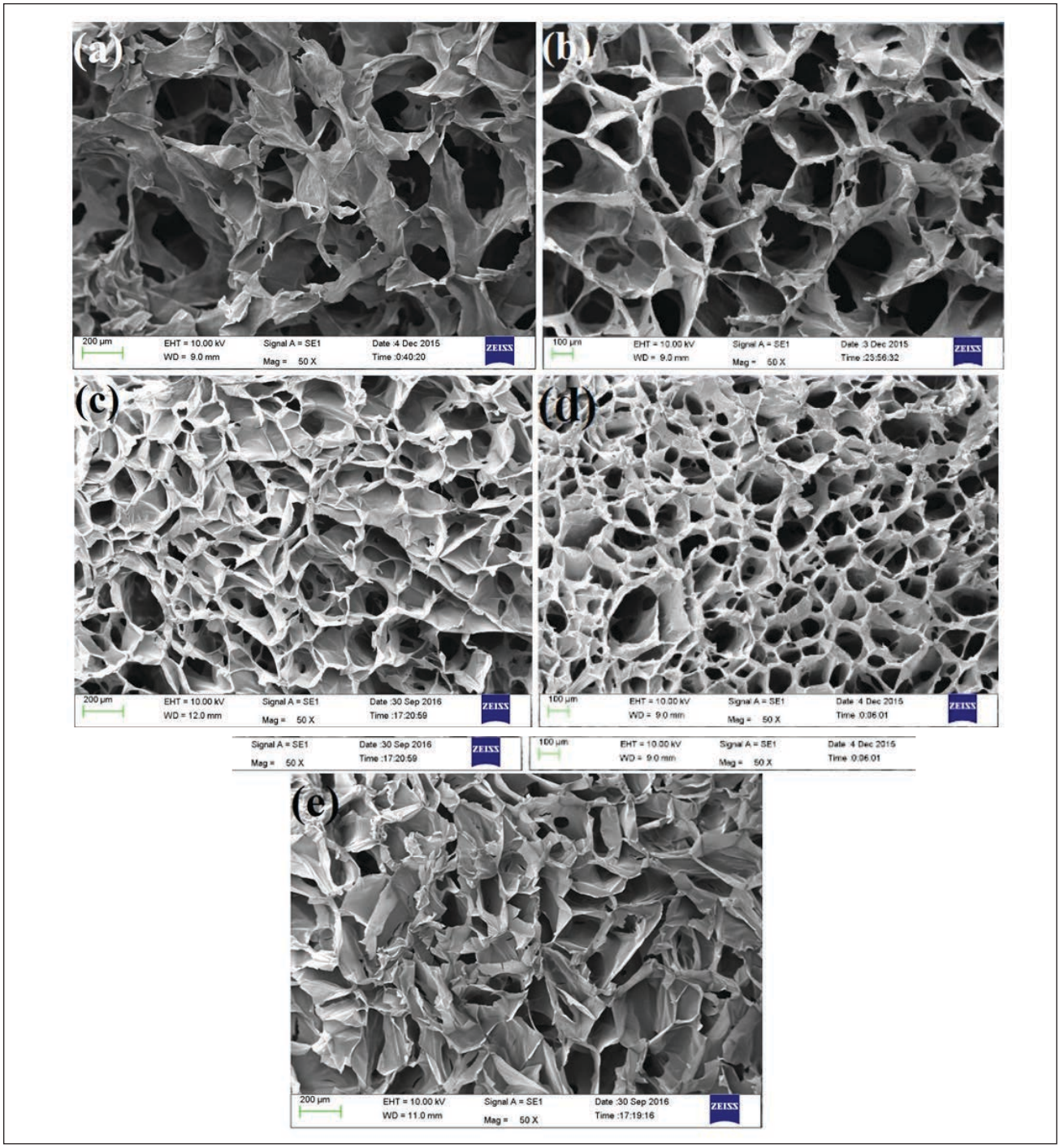
Measurements of water contact angle were performed to evaluate the hydrophobicity of MTMS-modified NCA by an OCA20 Micro (DataPhysics Instruments GmbH; Filderstadt, Germany) using 5 µL of deionized water as an indicator.

Oil absorption test

Pump oil and olive oil were used to examine the oil absorption capabilities of the MTMS-modified NCA. Preweighed hydrophobic MTMS-modified NCA samples were put in oil for 60 min to allow for oil absorption equilibrium. The samples were taken out and drained for 30 s to remove the unabsorbed oil by a stainless-steel colander. The absorption of oil was calculated according to Eq. 3:

$$Q = \frac{m_a - m_b}{m_b} \quad (3)$$

where Q (g·g) is the oil absorption capacity of the NCA, m_a (g) is the weight of the NCA after absorption, and m_b (g) is the weight of the NCA before absorption. Adsorption kinetics experiments were performed using 0.8 wt% MTMS-modified NCA and the oil absorption capacities were measured at several time intervals.



2. Scanning electron microscope images of the aerogels: (a) 0.2 wt% nanocellulose aerogels (NCA), (b) 0.5 wt% NCA, (c) 0.8 wt% NCA, (d) 1.0 wt% NCA and (e) 1.5 wt% NCA.

Recyclability

The recyclability of the NCA was determined by immersing the samples in 50 mL of toluene three times to remove absorbed oil. The samples were then dried in a 60°C oven to remove the absorbed toluene and reweighed. Subsequently, the samples were directly used for oil absorption tests.

RESULTS AND DISCUSSION

Formation of the nanocellulose-based aerogel

Images of the morphologies of NCA were obtained and are shown in **Fig. 2**. The NCA were formed by the self-assembly of nanocellulose fibers as governed by hydrogen-bond interactions after subsequent freeze drying [15,16]. The randomly intertwined nanocellulose fibers formed a three-dimensional porous

structure. It was found that some porous structure collapses happened at a concentration of NCA = 0.2 wt% in Fig. 2a, suggesting poor mechanical strength. The aerogels prepared at a concentration range of 0.5 wt%–1.0 wt% had a highly and integrally porous structure consisting of a network of self-assembled nanocellulose fibers, as shown in Fig. 2b–d. At higher nanocellulose concentrations (1.5 wt%), the aerogels displayed a more compact network and smaller porous structure in which the nanocellulose fibers were tightly entangled to cause poor porosity. The pore sizes of the aerogels in Fig. 2 were determined by Nano Measure software (Keithley Instruments; Solon, OH, USA) and the average pore diameters were measured in order of 350 µm, 300 µm, 205 µm, 178 µm, and 183 µm.

Density and porosity

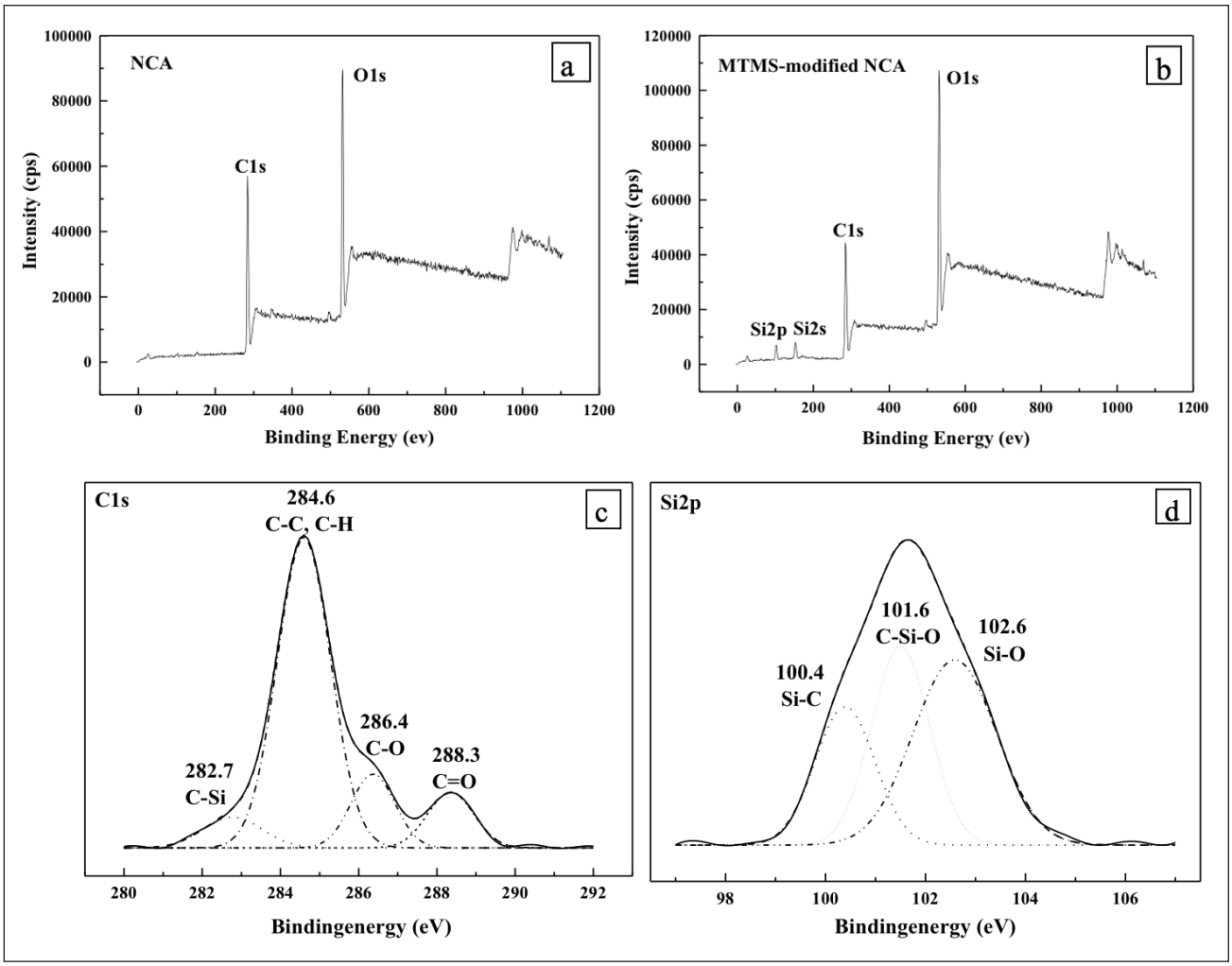
Table I shows the densities and porosities of the aerogels from various concentrations of nanocellulose suspension. The densities of NCA increased from 2.0 mg·cm^{-3} to 16.7 mg·cm^{-3} with increasing nanocellulose concentration from 0.2 wt% to 1.5 wt% as calculated from Eq. 1. The density of 0.2 wt% NCA was lower than other NCA. The density of 1.5 wt% NCA was as high as 16.7 mg·cm^{-3}. Meanwhile, all aerogels had very high porosity (>98%), which changed from 99.9% to 98.9% when using nanocellulose concentration from 0.2 wt% to 1.5 wt%. The results indicated that low concentrations of nanocellulose lead to high porosities. The reason is that higher nanocellulose concentration (1.5 wt%) has a more compacted network between nanocellulose fibers during freeze drying (Fig. 2) that resulted in higher density and lower porosity.

Samples	0.2 wt%	0.5 wt%	0.8 wt%	1.0 wt%	1.5 wt%
Density, mg·cm^{-3}	2.0	6.3	9.0	10.5	16.7
Porosity, %	99.9	99.6	99.4	99.3	98.9

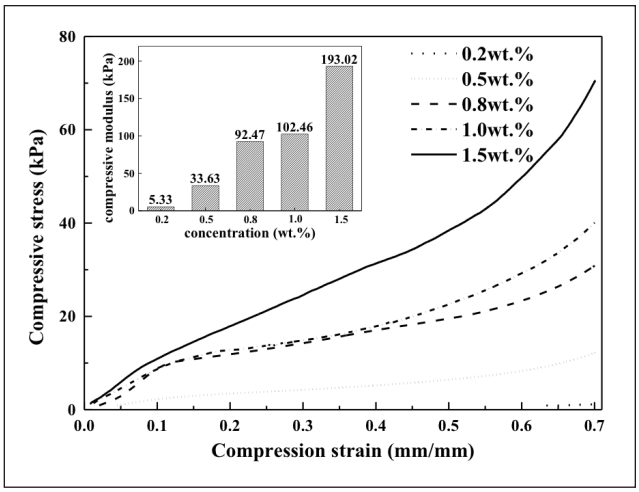
I. Densities and porosities of the aerogels.

Surface modification of aerogels

The surface elemental composition of NCA and MTMS-modified NCA were examined using XPS (**Fig. 3**). XPS spectra



3. X-ray photoelectron spectroscopy spectra of (a) NCA, (b) methyltrimethoxysilane (MTMS)-modified NCA, (c) high resolution C1s of MTMS-modified NCA, and (d) high resolution Si2p of MTMS-modified NCA.



4. Compression stress-strain curves of nanocellulose aerogels.

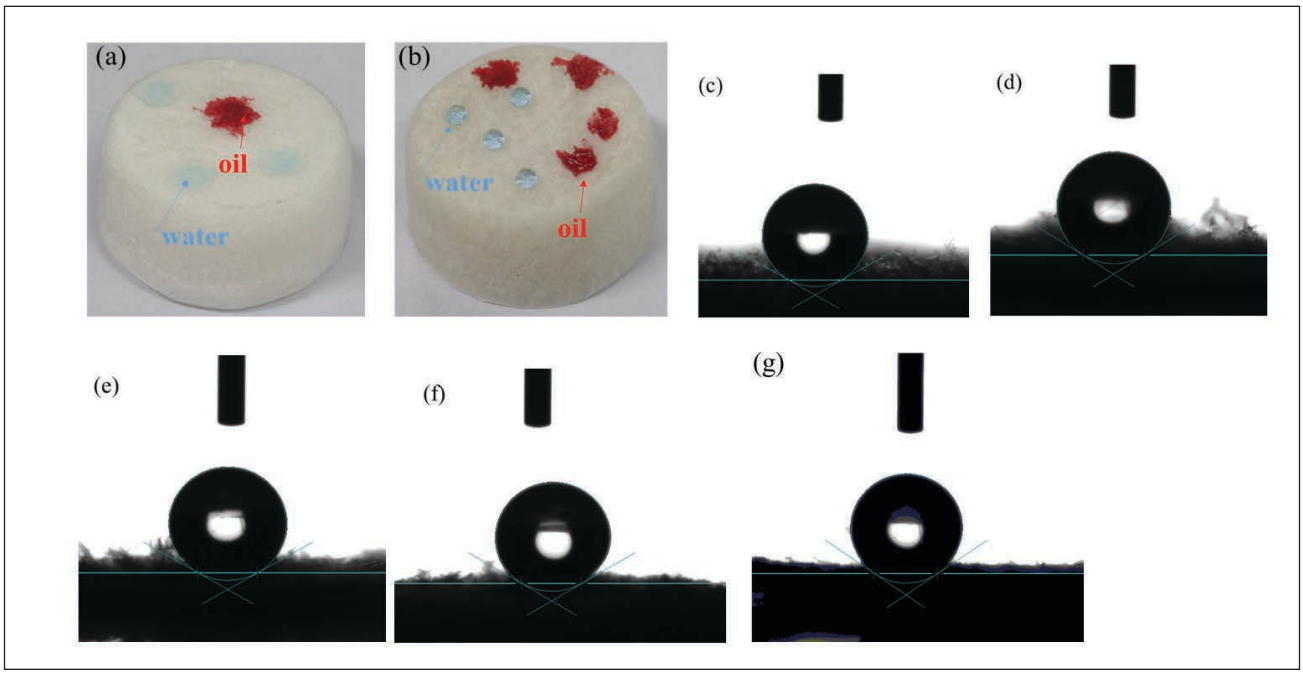
of the NCA (Fig. 3a) and MTMS-modified NCA (Fig. 3b) show that both contained high resolution C1s and O1s peaks. As expected, there were two new typical peaks at 101.9 eV and 152.8 eV on the MTMS-modified NCA surface from Si2p and Si2s, respectively, confirming the presence of silicon on the surface and further confirming that MTMS was bound on the NCA surface. Furthermore, in the high resolution C1s of MTMS-modified NCA (Fig. 3c), the carbon signal can be resolved into four component peaks: 288.3 eV was ascribed to C=O bonds, 286.4 eV is from C-O bonds [17], 284.6 eV corresponded to C-C and/or C-H bonds, and an exceptionally high peak at 282.7 eV was assigned to C-Si [18]. For the high resolution Si2p of MTMS-modified NCA (Fig. 3d), 100.4 eV was due to Si-C bonds [17], 101.6 eV corresponded to C-Si-O bonds [19], and 102.6 eV corresponded to Si-O bonds. The silicon content was estimated to be 7.1% for the MTMS-modified NCA.

Composite properties

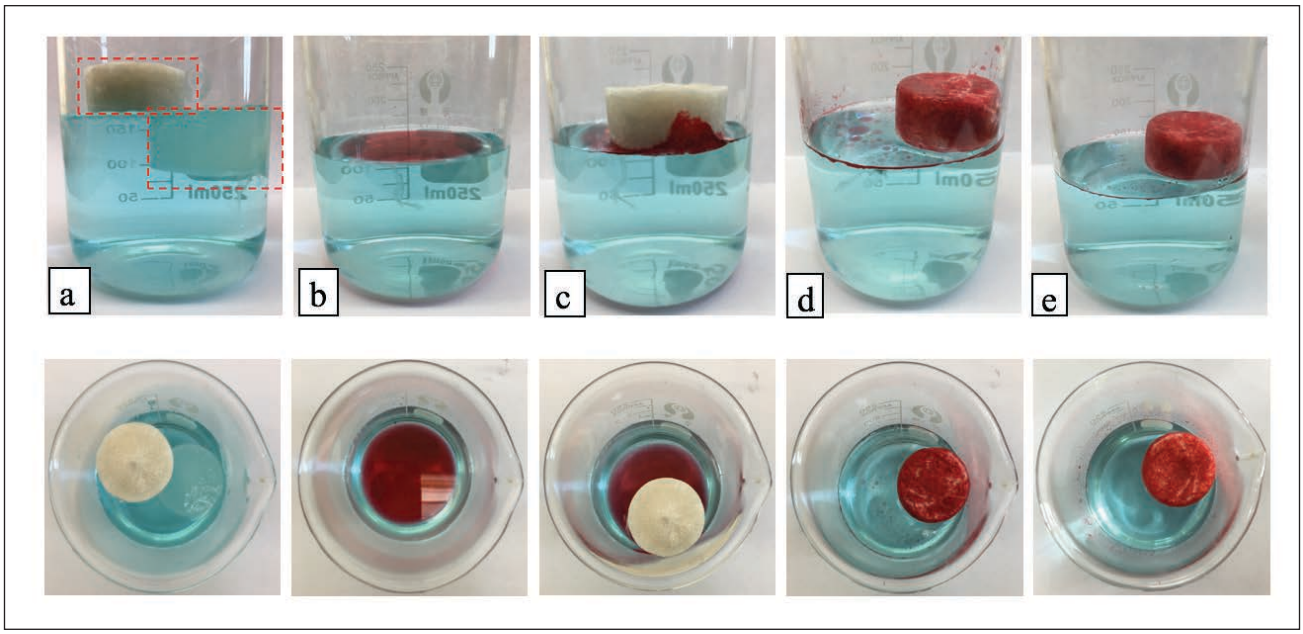
Figure 4 illustrates the compressive stress-strain and compressive modulus of NCA when compressed to 0.7 strain. When the nanocellulose concentration increased from 0.2 wt% to 1.5 wt%, the compressive stress of aerogels augmented from 1.2 kPa to 70.6 kPa. Furthermore, the elastic modulus changed from 5.3 kPa to 193.0 kPa. The compression strain and compressive modulus increased when aerogel densities increased, revealing better mechanical strength with smaller pores or more compacted network structure [20]. As shown in Table I, at higher nanocellulose concentrations, the density of NCA increased from 2.0 to 16.7 mg·cm^{-3}.

Wettability

Cellulose chains mainly consist of hydrophilic hydroxyls and hydrophobic pyranose rings [21] so that natural cellulose fibers have amphiphilic properties. The amphiphilic NCA were modified with MTMS via chemical vapor distribution to make them hydrophobic and oleophilic for selective adsorption of water/oil mixtures. **Fig. 5a** shows that both water droplets and oil droplets were rapidly soaked into the unmodified NCA, indicating that the NCA could not be directly used as water/oil separation materials. Conversely, Fig. 5b shows that the water droplets could be detained on the surface of the MTMS-modified NCA, while oil was immediately absorbed. The water contact angles were measured to evaluate the hydrophobicity of the MTMS-modified NCA and



5. Photographs of water and oil droplets on the (a) unmodified NCA, (b) MTMS-modified NCA, (c) water contact-angle images of 0.2 wt% NCA, (d) 0.5 wt% NCA, (e) 0.8 wt% NCA, (f) 1.0 wt% NCA, and (g) 1.5 wt% NCA.

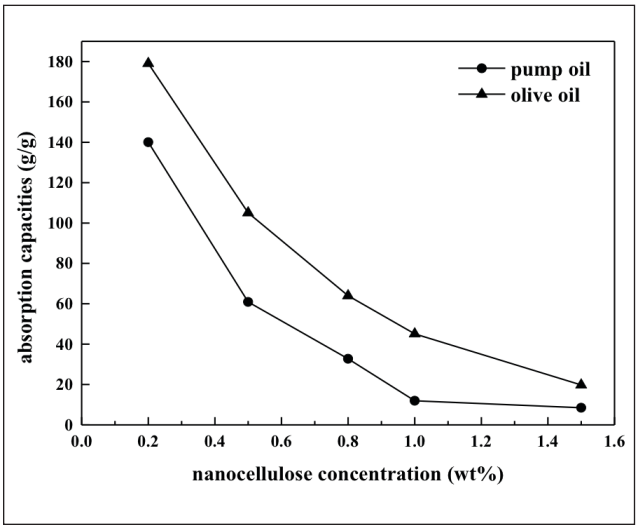


6. Photographs of selective sorption of oil (oil stained with oil red O dye) with MTMS-modified NCA.

are shown in Fig. 5c–g. The water contact angles for 0.2 wt%–1.5 wt% MTMS-modifier NCA were 150.8°, 148.0°, 150.7°, 150.0°, and 146.3°, respectively, implicating the hydrophobic nature of the MTMS-modified NCA.

Oil absorption capabilities of the aerogels

The selective oil absorption capacities are shown in **Fig. 6**. When unmodified NCA was placed in water (stained with methylene blue), it quickly sank into the water. The MTMS-modified NCA floated on the water (Fig. 6a) and showed excellent hydrophobicity. When MTMS-modified NCA was placed in olive oil stained with oil red O and water mixture, it floated on the water surface (Fig. 6c) and completely absorbed oil selectively (Fig. 6e). The pump oil and olive oil were further used to evaluate the oil absorption capabilities of the MTMS-modified NCA. The results are shown in **Fig. 7**. It can be clearly observed that by decreasing nanocellulose concentration from 1.5% to 0.2% for aerogels, the absorption capacities of hydrophobized aerogels for pump oil and olive oil increased from 8.5 to 140 $g \cdot g^{-1}$ and 19.8 to 179.1 $g \cdot g^{-1}$, respectively. The NCA formed by a lower nanocellulose concentration possessed much higher oil absorption capacity. As shown in Table I, the densities of NCA increased from 2.0 $mg \cdot cm^{-3}$ to 16.7 $mg \cdot cm^{-3}$ with nanocellulose concentration from 0.2 wt% to 1.5 wt%, while the aerogel porosity changed from 99.9% to 98.9%. The increase of the oil absorption capacity might be due to the lower density and higher porosity of the NCA [1]. Previous research indicated that aerogels with lower density possessed higher oil absorption capacity [3], as higher porosity could provide more dead volume in the aerogel for oil invasion [1]. On the other hand, the adsorption capacity for olive oil was distinctly higher than for pump oil. This adsorption difference might relate to the density and



7. The pump oil and olive oil absorption capacities for the MTMS-modified NCA.

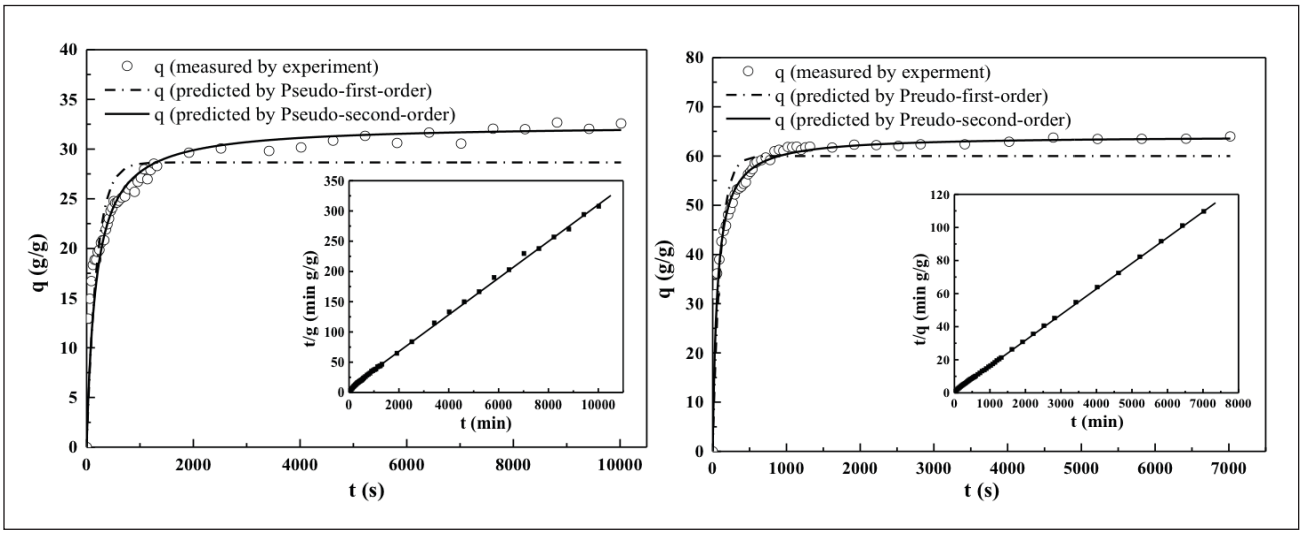
volatility of the oils [22,23]. High density for the oils has a positive effect on the volume retained in the NCA, thus resulting in higher oil adsorption capacity.

Varieties of carbon-based absorbents for oil/water separation and their absorption capacities are shown in **Table II**. N-doped graphene [24] and carbon nanotube (CNT)/graphene oxide (GO) sponges [25] demonstrate superior absorption capacities for both oils and organics, up to 200–600 $g \cdot g^{-1}$ and 215–743 $g \cdot g^{-1}$, respectively. Most carbon-based absorbents, such as reduced GO foam [23], CNT sponges [26], microfibrillated cellulose sponges [3], bacterial cellulose aerogels [4], and carbon fiber aerogels [27], showed high absorption capacities for oils and organics, at 122 $g \cdot g^{-1}$,

Absorption Materials	Oil	Absorption Capacity, $g \cdot g^{-1}$	Reference
Nanocellulose aerogels	Pump oil	8.5–140.0	Current paper
	Olive oil	19.8–179.1	19.8–179.1
Microfibrillated cellulose sponges	Pump oil Motor Oil	88–228	[3]
Bacterial cellulose aerogels	Oils/organics	86–185	[4]
Silylated nanocellulose sponges	Oils/organics	102	[15]
Recycled cellulose aerogels	Motor oils	95	[1]
Magnetic cellulose/TiO_2 aerogel	Paraffin oil	28	[28]
Aerogels from paper waste	Crude oils	24.4	[29]
Polystyrene/Fe_3O_4/graphene aerogel	Crude oil	40	[30]
Carbon fiber aerogel	Pump oil	192	[27]
Reduced graphene oxide foam	Olive oil	122	[23]
Carbon nanotube [CNT] sponge	Diesel oil	143	[26]
N-doped graphene framework	Oils/organics	200–600	[24]
CNT/graphene oxide sponges	CCl_4	215–743	[25]

TiO_2 = titanium dioxide; Fe_3O_4 = iron oxide; CCl_4 = tetrachloromethane.

II. Comparison of the absorption capacities of different materials.



8. Absorption kinetics of MTMS-modified NCA for pump oil and olive oil. The inset shows fitting results of the pseudo second-order model for oil absorption.

143 $g \cdot g^{-1}$, 88–228 $g \cdot g^{-1}$, 86–185 $g \cdot g^{-1}$, and 192 $g \cdot g^{-1}$, respectively. In this work, the obtained NCA also have high absorption capacities for pump oil and olive oil (up to 140 $g \cdot g^{-1}$ and 179 $g \cdot g^{-1}$, respectively). Therefore, as a low density and highly efficiency absorbent, MTMS-modified NCA represents a promising absorbent for treating oil spills.

Absorption kinetics

The time-dependent absorption capacities of MTMS-modified NCA on pump oil and olive oil were measured and the pseudo first-order and pseudo second-order models were used to fit the experimental data (**Fig. 8**). Two typical models could be expressed by Eq. 4 and Eq. 5, respectively:

Sample	qe,expa, g·g^{-1}	Pseudo First-order Kinetics			Pseudo Second-order Kinetics		
		qe, cal, g·g^{-1}	k_1	R^2	qe, cal, g·g^{-1}	k_2	R^2
Pump oil	32.6	28.6	5.34×10^{-3}	0.7687	32.5	1.78×10^{-4}	0.9992
Olive oil	64.0	60.0	9.97×10^{-3}	0.8901	64.1	2.53×10^{-4}	0.9999

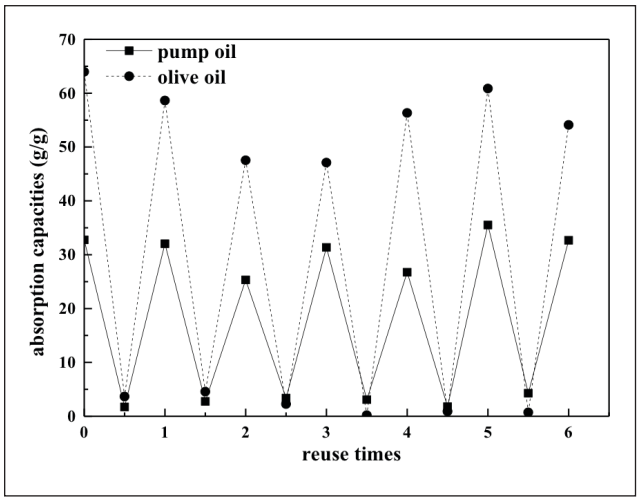
III. Fitting of the pseudo first-order model and pseudo second-order model for pump oil and olive oil absorption.

$$Ln[(q_e - q_t)/q_e] = -k_1 t \quad (4)$$

$$t/q_t = 1/k_2 q_e^2 + t/q_e \quad (5)$$

where k_1 (min^{-1}) and k_2 (g·mg^{-1}·min^{-1}) are the rate constants of the pseudo first-order and pseudo second-order absorption kinetics, respectively; R^2 are the correlation coefficient values; q_e (mg·g^{-1}) and q_t (mg·g^{-1}) are the amount of oil absorbed on NCA at equilibrium and at time t (min), respectively. The value of k_1 is calculated from the slope of plots of Ln(q_e-q_t) versus t, while k_2 is calculated from t/q_t versus t.

The absorption of pump oil by 0.8 wt% MTMS-modified NCA was rapid in the first 1000 s and a pseudo static state was reached at ~2000 s, whereas that of the olive oil was more rapid and a pseudo static state was reached at ~1000 s. The fitting results (k_1, k_2, R^2, q_e) of the absorption kinetic data are presented in **Table III**. Obviously, the R^2 of the pseudo second-order model (0.9992 and 0.9999 for pump oil and olive oil, respectively) was much higher than that of the pseudo first-order model (0.7687 and 0.8901) for the two kinds of oils, indicating that the oil absorption behavior was better fitted by a pseudo second-order kinetic model as well as predicting that the total absorption rate was limited by the rate of adsorbate diffusion into the pores of the MTMS-modified NCA. Furthermore, the equilibrium adsorption capacities ($q_{e,cal}$, 32.5 g·g^{-1}, and 64.1 g·g^{-1}, respectively) calculated by Eq. 5 were very close to the experimental values ($q_{e,exp}$, 32.6 g·g^{-1}, and 64.0 g·g^{-1}, respectively). In addition, the k_1 and k_2 of olive oil were higher than those of pump oil, implying that the absorption rate of the olive oil was faster than that of the pump oil.



9. The reusability of MTMS-modified NCA.

Reusability

Figure 9 illustrates the adsorption and desorption capabilities of pump oil and olive oil by 0.8 wt% MTMS-modified NCA over six recycles. The adsorption capacities of pump oil were measured to be 32.0, 25.3, 31.4, 26.7, 35.5, and 32.7 g·g for six cycles and those of olive oil were 58.6, 47.5, 47.1, 56.3, 60.9, and 54.1 g·g. The reuse efficiencies were high, up to 99.7% (pump oil) and 84.6% (olive oil) after six cycles, respectively, indicating that the absorption efficiency of MTMS-modified NCA remained at a high level for numerous reuses.

CONCLUSIONS

A unique hydrophobic nanocellulose-based superabsorbent was prepared by freeze drying nanocellulose, following modification with MTMS. The obtained aerogels possessed ultralow densities (2.0–16.7 mg·cm^{-3}), high porosities (99.9%–98.9%), and water contact angles of 146.3°–150.8°. Furthermore, the MTMS-modified aerogels exhibited excellent oil absorption capacities (up to 140 g·g^{-1} and 179.1 g·g^{-1}), strongly implicating MTMS-modified nanocellulose aerogels as promising candidates for oil spills remediation. **TJ**

ACKNOWLEDGEMENTS

The work was supported by the National Natural Science Foundation of China (31570569), the key project of the Science and Technology Ministry of Guangzhou, China (201607020025), and the Guangdong-Hong Kong Joint Innovation Program (2014B050505019).

LITERATURE CITED

1. Feng, J., Nguyen, S.T., Fan, Z., et al., *Chem. Eng. J.* 270: 168(2015).
2. Mauter, M.S. and Elimelech, M., *Environ. Sci. Technol.* 42(16): 5843(2008).
3. Wang, S., Peng, X., Zhong, L., et al., *J. Mater. Chem. A* 3(16): 8772(2015).
4. Sai, H., Fu, R., Xing, L., et al., *ACS Appl. Mater. Interfaces* 7(13): 7373(2015).
5. Angelova, D., Uzunov, I., Uzunova, S., et al., *Chem. Eng. J.* 172(1): 306(2011).

6. Deschamps, G., Caruel, H., Borredon, M.E., et al., *Environ. Sci. Technol.* 37(5): 1013(2003).
7. Wahia, R., Chuah, L.A., Choong, T.S.Y., et al., S*ep. Purif. Technol.* 37(5): 1013(2003).
8. Radeti, M.M., Joci, D.M., Iovanti, P.M., et al., *Environ. Sci. Technol.* 37(5): 1008(2003).
9. Wu, Z., Li, C., Liang, H., et al. *Sci. Rep.–UK* 4: 4079(2014).
10. Iwamoto, S., Kai, W., Isogai, A., et al., *Biomacromolecules* 10(9): 2571(2009).
11. Yang, X. and Cranston, E.D., *Chem. Mater.* 26(20): 6016(2014).
12. Sehaqui, H., Zhou, Q., and Berglund, L.A., *Compos. Sci. Technol.* 71(13): 1593(2011).
13. Meng, Q., Li, H., Fu, S., et al., *React. Funct. Polym.* 85: 142(2014).
14. Cai, J., Kimura, S., Wada, M., et al., *ChemSusChem* 1(1–2): 149(2008).
15. Zhang, Z., Sèbe, G., Rentsch, D., et al., *Chem. Mater.* 26(8): 2659(2014).
16. Silva, T.C.F., Habibi, Y., Colodette, J.L., et al., *Cellulose* 19(6): 1945(2012).
17. Yamamoto, K., Koga, Y., and Fujiwara, S., *Diamond Relat. Mater.* 10(9–10): 1921(2001).
18. Yang, J., Cao, L., Guo, R., et al., *J. Hazard. Mater.* 184(1–3): 782(2010).
19. Veres, M., Koós, M., Tóth, S., et al., *Diamond Relat. Mater.* 14(3–7): 1051(2005).
20. Jiang, F. and Hsieh, Y., *J. Mater. Chem. A* 2(18): 6337(2014).
21. Glasser, W.G., Atalla, R.H., Blackwell, J., et al., *Cellulose* 19(3): 589(2012).
22. Bi, H., Xie, X., Yin, K., et al., *Adv. Funct. Mater.* 22(21): 4421(2012).
23. He, Y., Liu, Y., Wu, T., et al., *J. Hazard. Mater.* 260: 796(2013).
24. Zhao, Y., Hu, C., Hu, Y., et al., *Angew. Chem.* 124(45): 11533(2012).
25. Sun, H., Xu, Z., and Gao, C., *Adv. Mater.* 25(18): 2554(2013).
26. Gui, X., Wei, J., Wang, K., et al., *Adv. Mater.* 22(5): 617(2010).
27. Bi, H., Yin, Z., Cao, X., et al., *Adv. Mater.* 25(41): 5916(2013).
28. Chin, S.F., Binti Romainor, A.N., and Pang, S.C., *Mater. Lett.* 115: 241(2014).
29. Nguyen, S.T., Feng, J., Le, N.T., et al., *Ind. Eng. Chem. Res.* 52(51): 18386(2013).
30. Zhou, S., Jiang, W., Wang, T., et al., *Ind. Eng. Chem. Res.* 54(20): 5460(2015).

ABOUT THIS PAPER

Cite this article as: Yu, C., Wang, F., Fu, S., Lucia, L. *TAPPI J.* 17(3):145(2018). https://doi.org/10.32964/TJ17.03.145

DOI: https://doi.org/10.32964/TJ17.03.145

ISSN: 0734-1415

Publisher: TAPPI Press

Copyright: ©TAPPI Press 2018

About this journal

ABOUT THE AUTHORS



Yu



Wang



Fu



Lucia

The application of nanocellulose, produced from fiber, is a topic that is attracting interest. Our previous research focused on the pulping process, but this work focused on the alternative application of fiber to prepare nanocellulose for high-value products.

By controlling the concentration of nanocellulose, it is possible to obtain superhydrophobic aerogels modified with silane agents that have low density and high absorption capacity. We found that the high density of aerogels positively affected the volume of oils retained in the nanocellulose aerogels so that the aerogel had higher oil adsorption capacity. This had not been previously reported. The superhydrophobic aerogels were found to be very good for waste oil absorption.

Mills might sell pulps for nanocellulose production. The method for aerogels is very useful, and the next step is to find an easier manufacturing process for them.

Yu is a Ph.D. student, Wang is an undergraduate student, and Fu is a professor at the State Key Laboratory of Pulp and Paper Engineering, South China University of Technology, Guangzhou, China. Lucia is associate professor in the Department of Forest Biomaterials, North Carolina State University, Raleigh, NC, USA. Email Fu at shyfu@scut.edu.cn.

An effective method for determining the retention and distribution of cellulose nanofibrils in paper handsheets by dye labeling

SHENGDAN WANG, WENHUA GAO, KEFU CHEN, JINSONG ZENG, JUN XU, AND BIN WANG

ABSTRACT: Cellulose nanofibrils (CNF) were prepared by cellulase in conjunction with mechanical disintegration from the bleached softwood kraft pulp and labelled by Congo red dye. The labelled CNF were used to investigate the retention and distribution of CNF in paper handsheets. The retention of the labelled CNF was obtained by measuring the absorbance of white water using an ultraviolet-visible spectrophotometer. The results showed that this method for measuring the retention was rapid, feasible, and sensitive, owing to the high correlation coefficient R^2 (0.9993) of the standard curve. The labelled CNF showed even distribution in paper handsheets. The colorimetric values of paper handsheets were explored with a residual ink analyzer.

Application: In the laboratory, the dye labeling method is a feasible and effective approach to indicate the retention and distribution of CNF in paper handsheets.

Cellulose nanofibrils (CNF) are abundant biodegradable polymers manufactured from lignocellulose by mechanical disintegration with or without chemical [1-4] or enzymatic treatment [5-9]. CNF have obtained increased attention because of their desirable properties, such as high mechanical strength and stiffness, high thermal stability, exceptional barrier properties, high surface area, high optical transparency, low density, and renewability [10-13]. Applications of CNF have been investigated in many areas, such as reinforcement in biocomposites, production of hydrogels, linting control agents, high-technology devices, and paper additives in papermaking [13-17].

There are quite a number of reports on the applications of CNF in the papermaking industry [18], many of which have focused on the effects of CNF on paper properties. For example, CNF were used as additives to enhance the physical properties of paper or paperboard (e.g., tensile strength, barrier properties, gloss property) or to produce smart packaging (e.g., security papers) [16,19-21]. There are also some reports on the effects of CNF as flocculants and filler retention agents in papermaking [22,23]. It seems possible that CNF can be applied in the papermaking industry in the near future. However, to the best of our knowledge, there has not been a reported method that is feasible and effective to measure the retention of CNF in paper sheets formed, due to their small size and shared components between CNF and fines. Therefore, it is necessary to investigate the retention of CNF in paper sheets, which is a key factor affecting the production efficiency and quality of paper [24].

In this study, we explored an effective and feasible method to determine the retention of CNF in paper handsheets. CNF were prepared from a bleached softwood kraft pulp (BSKP) and labelled by a traditional Congo red dye labeling method. A standard curve was prepared for determining the labelled CNF content in the white water using an ultraviolet-visible (UV-Vis) spectrophotometer. Meanwhile, the distribution of the labelled CNF in paper handsheets was elucidated by measuring the colorimetric values of paper sheets using a residual ink analyzer. This study provided a basis for measuring the retention and distribution of CNF produced by enzymatic and mechanical treatment in paper handsheets. In particular, this method is for laboratory use only and is not commercially viable in its current form.

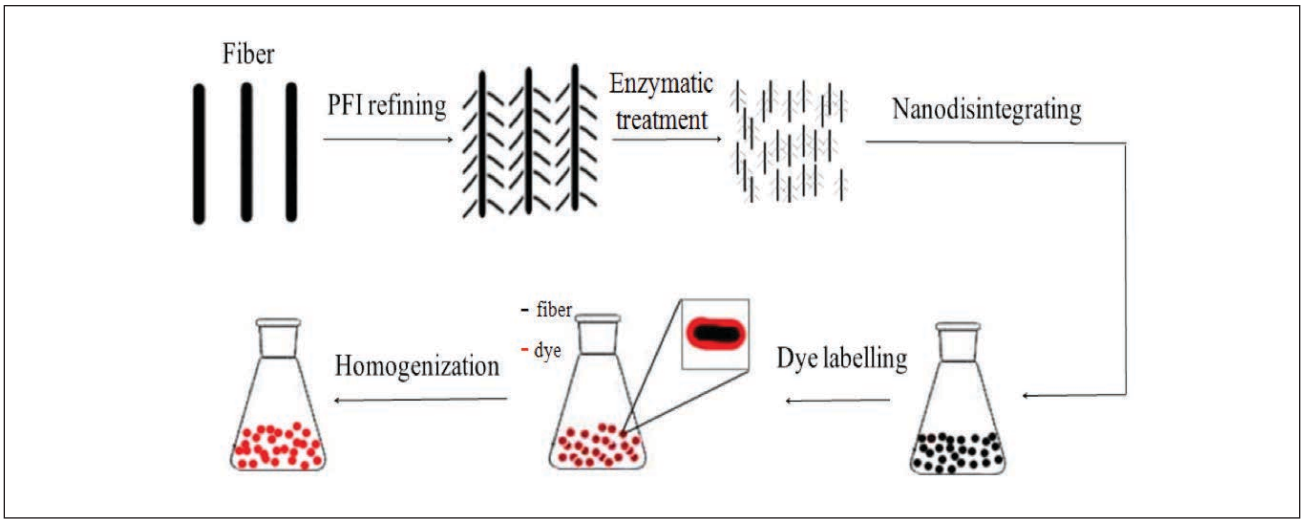
EXPERIMENTAL

Materials

Commercial dried BSKP was obtained from a paper mill (Guangdong Province, China). Commercial cellulase (Celluclast 1.5 L, activity 250 FPU/g) from *Tricoderma reesei* was purchased from Sigma (Beijing, China). The dye of Congo red 4B was delivered by Yutong Packaging & Printing Co. Ltd. (Shenzhen, China). The Congo red dye solution was prepared by dissolving 2 g in 60 mL of deionized water at 60°C.

Preparation of the labelled CNF

The pulp was treated by a laboratory PFI mill (Hamjern Maskin; Hamar, Norway) according to TAPPI T 248 "Labora-



1. Preparation of the labelled cellulose nanofibrils (CNF).

tory beating of pulp (PFI mill method)" with two modifications: 40 g pulp was diluted with water to a total weight of 266 g (15% dry content) and the pressure shearing line pressure of the disk refiner was 1.0 N/mm. After mechanical beating for 1000 revolutions, the enzymatic treatment of the pulp was conducted according to the procedure in our previous work [25]. Briefly, 5% (w/v) pulp was dispersed in 50 mmol citrate acid-sodium citrate buffer (pH 4.8) with cellulase loading of 5 FPU/g (substrate). The slurry was incubated at 50°C for 5 h and then incubated at 100°C for 5 min to inactivate the enzyme. After that, the slurry was washed in a Buchner funnel until the pH value of the filtrate approached 7.0. Under those conditions, the yield of enzymatic pretreatment samples was 90.13%. After that, 1% pulp suspensions were subjected to the nanodisintegrating action of a laboratory disintegrator. The suspension was passed four times through the disintegrator at the slit pressure of 5000 psi. Then, 60 mL dye solution was added to the pulp suspension. The mixture was heated to 70°C in a preheated water bath at 300 rpm for 12 h. After cooling to 25°C, deionized water was added to the slurry with an agitation rate of 250 rpm for 30 min. The mixture was filter washed with deionized water several times until a colorless filtrate was obtained. Then, 1% filtering cake suspension in water was subjected to homogenization by a high-pressure Nano DeBEE slit homogenizer (BEE International; South Easton, MA, USA) with a slit pressure of 25000 psi. The labelled CNF were obtained and stored at 4°C for the following process. **Fig. 1** summarizes the experimental flow described previously.

Characterizations of the labelled CNF

A standard curve of labelled CNF was prepared for the assay of the CNF in the white water. The curve was constructed using different standard concentrations of the CNF (100 mg/mL, 200 mg/mL, 400 mg/mL, 600 mg/mL, 800 mg/mL, and 1000 mg/mL). The absorbance was measured at 504 nm using a spectrophotometer. Additional dilution was carried out if the absorbance value measured was >1.0.

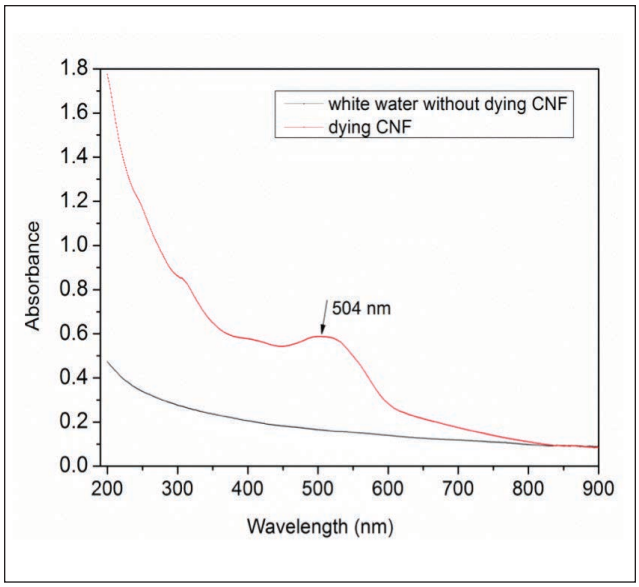
The water fastness was measured by dispersing the labelled CNF into deionized water for 12 h without stirring, and the supernatant was assayed at 504 nm by the spectrophotometer.

The widths of the labelled CNF were investigated by atomic force microscopy (AFM). A drop of dilute CNF suspension (0.05 wt%) was allowed to dry on a clean mica substrate at room temperature for 12 h. The scan was performed in tapping mode in air. The sizes of the images were 2 μm × 2 μm and 5 μm × 5 μm. AFM images were shown in the height mode without other image processing, except flattening.

Making composite paper handsheets

The wet BSKP and disintegrated labelled CNF were mixed with different ratios, including 0%, 1%, 2%, 3%, 4%, 5%, 7%, 9%, 12%, 15%, 20%, 30%, 40%, 50%, or 60% (proportion of labelled CNF was based on the total fiber dry weight). The grammage of each handsheet was controlled at 60 (dry weight). The preparation process of paper sheets was performed in the following steps:

1. The wet BSKP was dispersed with a standard pulp disintegrator at a consistency of 1.5% (w/w).
2. The suitable amount of the labelled CNF suspension at 0.5 wt% was added to the pulp slurry.
3. The mixture was stirred with a blender for 1 min to obtain a homogeneous suspension.
4. Paper handsheets were made from the mixed pulp through a Rapid-Koethen model RK3AKWT semiautomatic sheet former (Xell GmbH; Eberstalzell, Austria) with 200-mesh copper screen, and the white water was collected to detect the nonretention CNF during the formation of the handsheets.
5. Paper handsheets were dried at 90°C for 15 min and equilibrated for 24 h at constant temperature (23±1°C) and humidity (50±2%) prior to physical tests.



2. The absorption spectra of white water without and with labelled CNF.

Characterizations of paper handsheets and white water

The absorbance of the white water was measured for retention analyses at 504 nm using the UV-Vis spectrophotometer. The absorption of white water without the labelled CNF was very low (**Fig. 2**). The absorbance measurements were repeated at least five times for each sample and averaged. Each sample was recycled back into the white water. The retention has been calculated using Eq. 1 and Eq. 2:

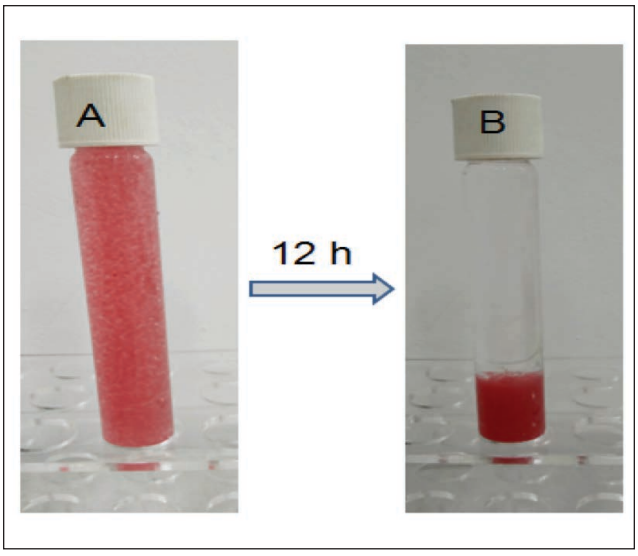
$$R_A = \frac{W_1 - W_2}{W_1} \times 100 \quad (1)$$

$$W_2 = \frac{A_1 - A_0}{K} \times V \quad (2)$$

where R_A is the retention of CNF in paper handsheets measured by spectrum method (SM), W_1 is the theoretical mass of the labelled CNF added to the slurry, W_2 is the mass of the labelled CNF in white water, A_1 is the absorbance of white water, A_0 is the absorbance of white water without labelled CNF added to the slurry, V is the volume of white water, and K is the extinction coefficient of the labelled CNF at 504 nm. The extinction coefficients were calculated by preparing standard curves of the slope of the labelled CNF absorbance.

The white water was centrifuged to separate the solids (nonretention samples). The precipitate was dried in an air oven for 12 h and weighed. The retention has been calculated using Eq. 3:

$$R_w = \frac{W_3 - W_4}{W_3} \times 100 \quad (3)$$



3. Labelled CNF (a) dispersion and (b) aggregation in water.

where W_3 is the theoretical mass of the labelled CNF added to the slurry, and W_4 is the mass of white water without labelled CNF added to the slurry measured by weighing method (WM).

The distributions of the labelled CNF in the handsheets for the wire side and felt side were evaluated by colorimetric values (L, a*, b*) using a Color Touch PC residual ink analyzer (Technidyne Corp.; New Albany, IN, USA), including transparency and relative standard deviation (RSD). The colorimetric value measurement was taken at five different points for each side of the paper handsheets, and every measurement was repeated at least three times for each point and averaged.

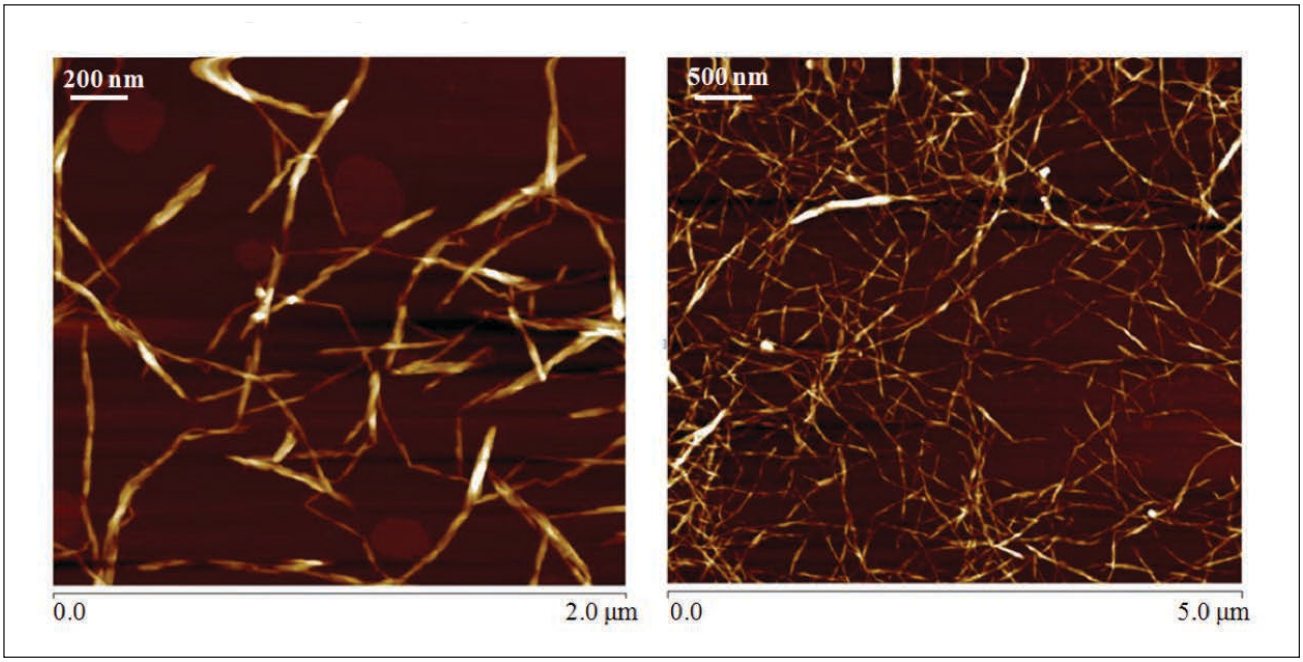
The surface morphologies of paper handsheets were observed using an EVO-18 scanning electron microscope (Zeiss; Oberkochen, Germany). The samples were coated with a thin layer of gold to ensure conductivity before testing.

RESULTS AND DISCUSSION

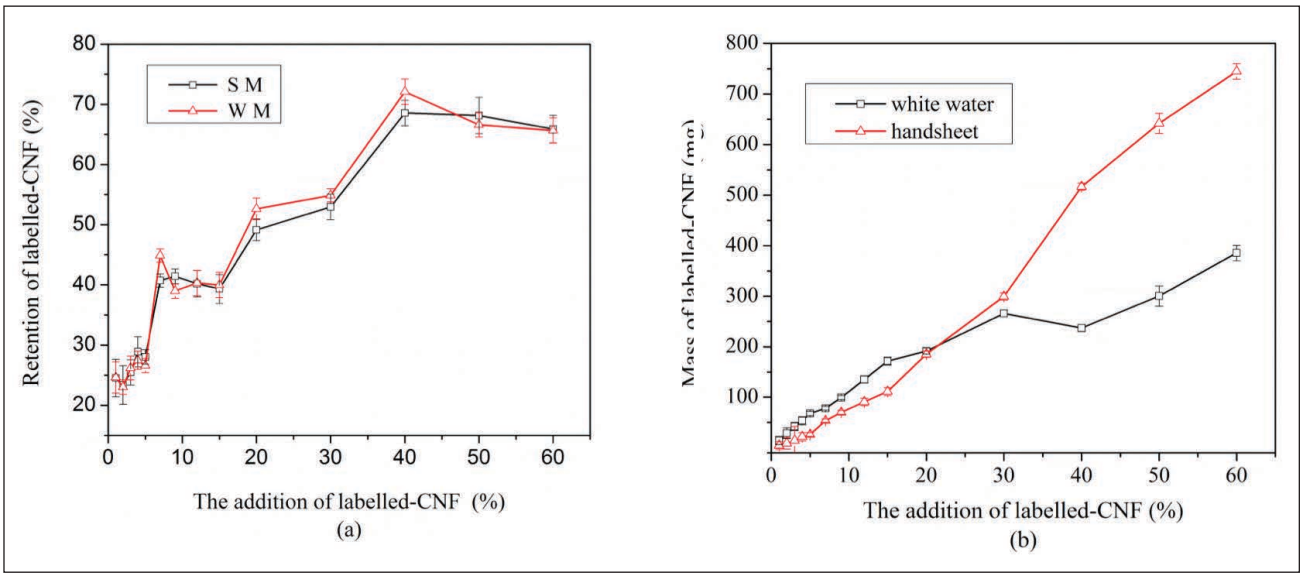
Characterization of labelled CNF

A standard curve of the labelled CNF y = 0.0015x (n = 6, R^2 = 0.9993, the labelled CNF concentration <1000 mg/mL) was obtained by a linear regression model. In this equation, y and x represent the absorbance and concentration of the labelled CNF, respectively. The states of the labelled CNF dispersion and aggregation were shown in **Fig. 3**. The absorbance of supernatant in tube B (Fig. 3) was measured at 504 nm and was about 0.02. The low absorption value (0.02) indicated that the labelled CNF showed superior water fastness (no fading). Therefore, the detection of subsequent retention by the dye labeling method might have high sensitivity and good linearity, on the basis of the superior water fastness and higher R^2 (0.9993).

Figure 4 shows AFM images of the labelled CNF after 25000 psi through a high-pressure slit homogenizer. The size of the sample was estimated to be within the range of 15–30 nm in width, while the length was up to several microns.



4. Atomic force microscopy (AFM) images of the labelled CNF.



5. Retention characterization of the labelled CNF in paper handsheets: (a) Retentions of the labelled CNF in paper handsheets detected by spectrum method (SM) and weighing method (WM), where the y coordinate "retention of CNF %" and the x coordinate "CNF added %" were relative to the CNF added and the dry pulp, respectively; and (b) the mass of the labelled CNF in paper handsheets and white water.

Therefore, the sample has been referred to as cellulose nanofibers [17]. The weblike network structure of the labelled CNF can be seen in Fig. 4.

Retention of the labelled CNF in paper handsheets

The retention of the labelled CNF in paper handsheets was detected using an UV-Vis absorption spectrum method and weighing method, as shown in **Fig. 5a**. The contents of the labelled CNF in paper handsheets and white water are shown in Fig. 5b. A control group without CNF loading also was evaluated to prevent the influence of fine fibers from BSKP on retention. The retention values of the labelled CNF in paper handsheets by spectrum method were consistent with that of WM (Fig. 5a). This consistency further indicated that the dye labeling method was a feasible and effective approach to determine the retention of CNF during paper handsheets formation. In addition, SM was faster (2 min), simpler, and more economical than WM (12 h) for the retention measuring of the labelled CNF.

C (%)	CV	Replica No.					Av	RSD (%)	C (%)	CV	Replica No.					Av	RSD (%)
		1	2	3	4	5					1	2	3	4	5		
0	L^f	95.56	95.55	95.60	95.54	95.39	95.53	0.08	5	L^f	79.16	79.05	79.08	79.15	79.16	79.12	0.05
	a^{*f}	0.22	0.24	0.21	0.23	0.24	0.23	5.72		a^{*f}	30.12	30.05	30.25	30.24	29.97	30.13	0.40
	a^{*w}	0.21	0.23	0.20	0.25	0.23	0.22	8.70		a^{*w}	29.50	29.79	29.81	29.61	29.43	29.63	0.57
	b^{*f}	4.15	4.18	4.10	4.28	4.27	4.20	1.85		b^{*f}	9.27	9.48	9.43	9.53	9.36	9.41	0.97
	T_r	29.23	34.95	35.24	35.09	34.50	33.80	7.61		T_r	37.70	37.99	37.81	37.59	37.87	37.79	0.41
1	L^f	89.54	89.65	89.61	89.71	89.66	89.63	0.07	7	L^f	75.05	75.01	74.96	74.84	74.91	74.95	0.11
	a^{*f}	12.01	12.16	12.16	12.03	12.16	12.10	0.64		a^{*f}	34.35	34.64	34.65	34.48	34.71	34.57	0.43
	a^{*w}	11.89	11.81	11.99	11.89	11.97	11.91	0.61		a^{*w}	34.39	34.41	34.06	34.25	34.12	34.25	0.46
	b^{*f}	4.95	4.99	5.01	4.90	4.90	4.95	1.02		b^{*f}	11.63	11.86	11.67	11.69	11.79	11.73	0.81
	T_r	37.00	35.85	36.1	36.36	37.31	36.52	1.68		T_r	37.16	37.83	38.91	37.1	37.60	37.72	1.94
2	L^f	86.06	86.13	86.06	86.12	86.05	86.08	0.04	9	L^f	72.57	72.83	72.29	72.38	72.21	72.46	0.34
	a^{*f}	18.39	18.47	18.52	18.22	18.64	18.45	0.57		a^{*f}	37.70	37.99	37.81	37.59	37.87	37.79	0.41
	a^{*w}	18.13	18.02	18.01	17.98	17.96	18.02	0.51		a^{*w}	37.65	37.52	37.63	37.29	37.22	37.46	0.51
	b^{*f}	6.47	6.42	6.51	6.37	6.33	6.42	1.01		b^{*f}	12.56	12.47	11.45	11.42	11.61	11.90	4.75
	T_r	36.66	35.96	37.97	36.19	36.93	36.74	2.27		T_r	37.51	37.83	38.21	37.96	37.05	37.71	1.18
3	L^f	82.54	82.77	82.62	82.56	82.57	82.61	0.10	12	L^f	69.50	69.74	69.67	69.69	69.52	69.62	0.15
	a^{*f}	24.03	23.81	23.81	24.06	23.93	23.93	0.49		a^{*f}	39.91	39.22	39.37	39.35	39.28	39.43	0.64
	a^{*w}	23.61	23.87	23.76	23.99	23.85	23.82	0.59		a^{*w}	38.98	38.87	39.01	38.96	39.11	38.99	0.22
	b^{*f}	7.6	7.57	7.56	7.51	7.70	7.59	0.83		b^{*f}	13.45	13.64	13.38	13.51	13.45	13.49	0.72
	T_r	36.86	37.49	36.20	36.42	35.90	36.57	1.51		T_r	37.72	37.38	38.23	37.16	38.01	37.70	1.16
4	L^f	79.42	79.43	79.51	79.39	79.53	79.46	0.06	60	L^f	47.24	47.6	47.74	47.54	47.65	47.55	0.40
	a^{*f}	29.08	29.32	28.96	29.19	28.94	29.10	0.54		a^{*f}	52.39	52.05	52.25	52.67	51.97	52.27	0.54
	a^{*w}	28.46	28.51	28.69	28.88	28.7	28.65	0.59		a^{*w}	50.72	51.01	51.2	51.18	50.09	50.84	0.91
	b^{*f}	9.70	9.72	9.61	9.84	9.68	9.71	0.77		b^{*f}	23.89	23.72	24.06	24.72	23.74	24.03	1.71
	T_r	37.10	37.38	37.21	37.23	37.23	37.23	0.24		T_r	42.86	43.15	43.6	44.47	41.54	43.12	2.49

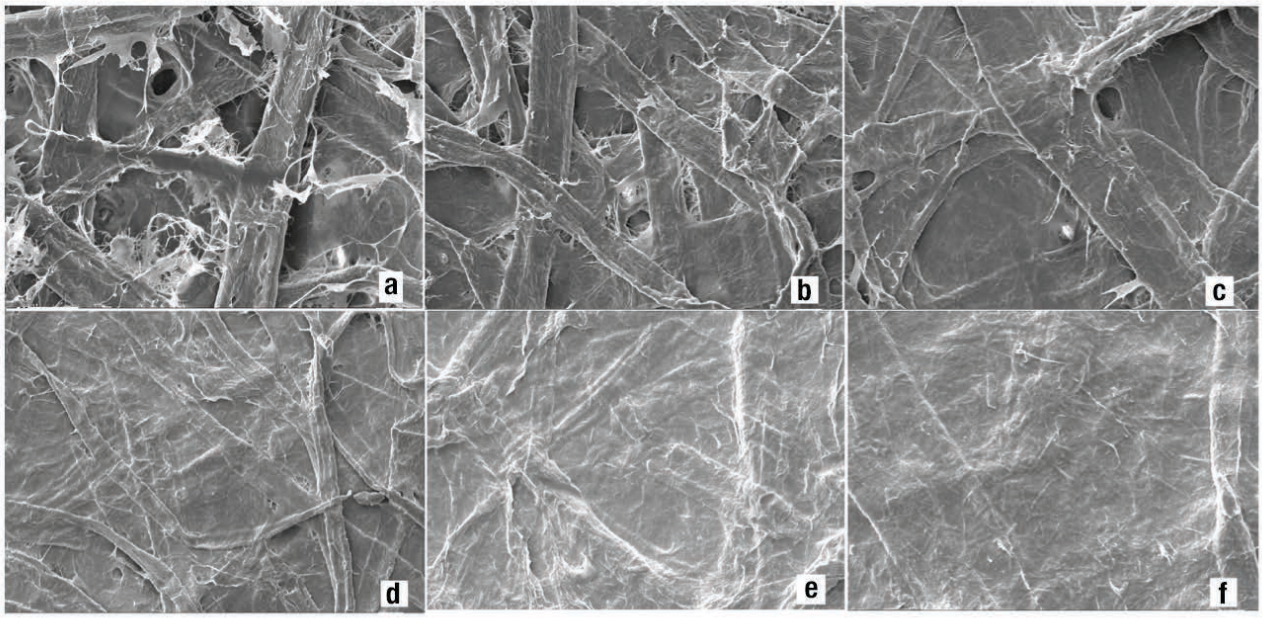
C = CNF loading (%); CV = colorimetric values; Av = average; RSD = relative standard deviation; T_r = transparency; f = the felt side of the sheet; w = the wire side of the sheet; L = the colorimetric values of darkness or lightness; a* = the colorimetric values of red or green; b* = the colorimetric values of yellow to blue.

I. Colorimetric values of each side of paper handsheets filled with labelled CNF.

As the CNF loading was increased from 1% to 60%, the retention of the labelled CNF in paper handsheets increased from 24.5% to 68.5% (Fig. 5a), and the contents of the labelled CNF in paper handsheets increased almost linearly, from 4.6 mg to 744.8 mg (Fig. 5b). Although the labelled CNF are smaller than the copper screen mesh, great amounts of them were retained when the additive amount of the labelled CNF exceeded 20% (Fig. 5a). Regrettably, the drainage time increased almost linearly with increasing the labelled CNF addition during the preparation of paper handsheets. This result indicated that the retention of the labelled CNF in paper handsheets was enhanced with the labelled CNF addition, which might be due to the clogging of the porous configuration of paper handsheets caused by the entanglement and interactions of the weblike network structure of the labelled CNF [26].

Distribution of the labelled CNF in paper handsheets

Paper handsheets made with various labelled CNF additions (0%, 1%, 2%, 3%, 4%, 5%, 7%, 9%, 12%, and 60%) were selected to investigate the distribution of the labelled CNF. The colorimetric values (L: 0–100, darkness to lightness; a*: from +a* to –a*, red to green; b*: from +b* to –b*, yellow to blue) of the two sides of those paper handsheets were examined, as shown in **Table I**. The distribution of the labelled CNF in paper handsheets was illustrated using the colorimetric values



6. Scanning electron microscopy (SEM) images of felt side of handsheets filled without and with labelled CNF: (a) 0%, (b) 5%, (c) 9%, (d) 20%, (e) 30%, and (f) 50% labelled CNF.

of five different points. This method was determined mainly by the changes of the colorimetric values, which were highly sensitive to the dye amount [27,28].

The main factor affecting the colorimetric values was a* because the labelled CNF were colored by Congo red dye. With no addition of the labelled CNF, the average of L was 95.53, and the average and RSD of a* for the felt side of handsheets (a^{*f}) were 0.23% and 5.72%, respectively (Table I). This revealed that the neat handsheets exhibited nearly saturated lightness with little or no redness. As the labelled CNF addition increased from 0% to 1%, the average of a^{*f} rapidly increased from 0.23 to 12.10, whereas the RSD of a^{*f} decreased from 5.72% to 0.64%. These findings indicated that the labelled CNF had a remarkable effect on the colorimetric values (higher a^{*f}) of the handsheets and had an even distribution (lower RSD) on the felt side of the sheet. Surprisingly, all of the values of a^{*f} were higher than the values of the wire side of paper handsheets (a*w); the RSD of a^{*f} were <0.64%, with the labelled CNF addition increasing from 1% to 60%. Therefore, the filter caking effect of the labelled CNF was further clarified during the paper handsheets forming. In addition, all of the RSD of a^{*f} were less than 0.64%, with the labelled CNF addition increasing from 1% to 60%. The lower RSD of a^{*f} confirms the even distribution of the labelled CNF on the felt side of the sheet. Otherwise, the RSDs of a* could be higher.

The RSD for transparency decreased from 7.61% to 2.49% as the labelled CNF addition increased from 0% to 60% (Table I), whereas the average transparency values of paper handsheets increased from 33.80 to 43.12. Theoretically, due to the colorless cellulose fibers, paper handsheets made of BSKP should be more transparent than paper handsheets containing the labelled CNF. In fact, the average transparency of paper handsheets was apparently higher with extra addition of the labelled CNF. This phenomenon could be attributed to the porous structure of paper handsheets that evokes light scattering at the fiber–air interface [29,30]. Therefore, the low RSD of transparency inferred that the pores of paper handsheets were evenly clogged by the labelled CNF.

Fig. 6 shows the felt side of paper handsheets filled (a) without dye-labelled CNF and (b) 5%, (c) 9%, (d) 20%, (e) 30%, and (f) 50% the labelled CNF. The rough and porous structure of the control handsheets is apparently observed (Fig. 6a). As the labelled CNF loading increased, the porous structure of paper handsheets gradually disappeared and the surface of paper handsheets became smoother. In addition, the labelled CNF might initially fill the porous configuration of the paper handsheets and subsequently homogeneously deposit on the paper handsheets surface. Therefore, the labelled CNF should be good for improving the gas barrier properties of papers.

CONCLUSIONS

A feasible and effective method has been developed to determine the retention and distribution of CNF in paper handsheets by dye labeling. The retention of CNF in paper handsheets increased as the loading of CNF increases. The filter caking effect of the CNF was a pronounced presence during formation of paper handsheets. The CNF initially fill the porous configuration of paper handsheets and subsequently evenly deposit on the surface. In addition, the transparency of paper handsheets with CNF addition was improved compared to those of the control paper handsheets without CNF addition. **TJ**

ACKNOWLEDGEMENTS

The authors are grateful for the support of the National Natural Science Foundation of China (Grant No. 31400512), State Key Laboratory of Pulp and Paper Engineering (201716), Fundamental Research Funds for the Central Universities (2017MS099), 111 plan, and the Guangdong Provincial Science and Technology Plan Projects (No. 2015B020241001).

LITERATURE CITED

1. Missoum, K., Belgacem, M.N., and Bras, J., *Materials* 6(5): 1745(2013).
2. Saito, T., Nishiyama, Y., Isogai, A., et al., *Biomacromolecules* 7(6): 1687(2006).
3. Wang, R., Chen, L., Zhu, J.Y., et al., *ChemNanoMat* 3(5): 328(2017).
4. Qin, Y., Qiu, X., and Zhu, J.Y., *Sci. Rep.* 6: (2016). DOI:10.1038/srep35602.
5. Zhu, J.Y., Sabo, R., and Luo, X., *Green Chem.* 13(5): 1339(2011).
6. Pääkkö, M., Ankerfors, M., Lindström, T., et al., *Biomacromolecules* 8(6): 1934(2007).
7. Wang, W., Mozuch, M.D., and Sabo, R.C., *Cellulose* 22(1): 351(2015).
8. Yarbrough, J.M., Zhang, R., Mittal, A., et al., *ACS Nano* 11(3): 3101(2017).
9. Henriksson, M., Henriksson, G., Berglund, L.A., et al., *Eur. Polym. J.* 43(8): 3434(2007).
10. Berglund, L.A. and Peijs, T., *MRS Bull.* 35(03): 201(2010).
11. Alcala, M., González, I., Boufi, S., et al., *Cellulose* 20(6): 2909(2013).
12. Liu, D.Y., Sui, G.X., and Bhattacharyya, D., *Compos. Sci. Technol.* 99: 31(2014).
13. Tunç, S. and Duman, O., *LWT--Food Sci. Technol.* 44(2): 465(2011).
14. Abe, K. and Yano, H., *Carbohydr. Polym.* 85(4): 733(2011).
15. Balea, A., Blanco, A., Merayo, N., et al., *Appita J.* 69(2): 148(2016).
16. Osong, S.H., Norgren, S., and Engstrand, P., *Cellulose* 23(1): 93(2016).
17. Zhu, H., Luo, W., Ciesielski, P.N., et al., *Chem. Rev.* 116(16): 9305(2016).
18. Brodin, F.W., Gregersen, O.W., and Syverud, K., *Nord. Pulp Pap. Res. J.* 29(1): 156(2014).
19. Gonzalez, I., Boufi, S., Pelach, M.A., et al., *BioResources* 7(4): 5167(2012).
20. Lavoine, N., Desloges, I., and Bras, J., *Carbohydr. Polym.* 103(1): 528(2014).
21. Lindström, T., Aulin, C., Gimåker, M., et al., *IPPTA* 26(1): 53(2014).
22. Ämmälä, A., Liimatainen, H., Burmeister, C., et al., *Cellulose* 20(5): 2451(2013).

ABOUT THE AUTHORS

It seems possible that CNF can be applied in the papermaking industry in the near future. However, to the best of our knowledge, there has not been a reported method that is feasible and effective for measuring the retention rate of CNF in paper sheets formed.

In others' previous research, the white water was centrifuged to weigh the solid. In our work, the retention rate values were detected using the spectrum method. The spectrum method is faster, simpler, and more economical than the weighing method.

The characterization of CNF in water is difficult. We addressed this difficulty by dye labeling. Using dye-labelled CNF as an additive, we developed a feasible and effective method to determine the retention rate and distributions of CNF in paper sheets. We were surprised to observe that with the addition of CNF, the CNF initially fill the porous configuration of the paper sheets and subsequently evenly deposit on the paper sheet surface.

The benefit of this paper is that it provides a basis for measuring the retention rate and distribution state of CNF in paper sheets. The next step is to explore the effect of CNF on internal structure of the paper sheets.

S. Wang is a Ph.D. student; Gao, Xu, and B. Wang are associate professors; Chen is an academician; and Zeng is a professor at State Key Laboratory of Pulp and Paper Engineering, South China University of Technology, Guangzhou, China. Email Gao at segaowenhua@scut.edu.cn.


S.Wang


Gao


Xu


B. Wang


Chen


Zeng

23. Merayo, N., Balea, A., Fuente, E., et al., *Cellulose* 24(2): 677(2017).
24. Lin, T., Yin, X., Retulainen, E., et al., *Appita J.* 60(6): 469(2007).
25. Wang, S.D., Chen, J.C., Yang, G.H., et al., *BioResources* 12(1): 1031(2016).
26. Missoum, K., Martoïa, F., Belgacem, M.N., et al., *Ind. Crops Prod.* 48: 98(2013).
27. Oz, F., *J. Food Process. Preserv.* 38(3): 1356(2014).
28. Lee, Y.H., and Patterson, D., *Color. Technol.* 101(10): 314(1985).
29. Fang, Z., Zhu, H., Preston, C., et al., *J. Mater. Chem. C* 1(39): 6191(2013).
30. Hubbe, M.A., Pawlak, J.J., and Koukoulas, A.A., *BioResources* 3(2): 627(2008).

ABOUT THIS PAPER

Cite this article as: Wang, S., Gao, W., Chen, K., et al. *TAPPI J.* 17(3):157(2018). https://doi.org/10.32964/TJ17.03.157

DOI: https://doi.org/10.32964/TJ17.03.157

ISSN: 0734-1415

Publisher: TAPPI Press

Copyright: ©TAPPI Press 2018

About this journal

Photo-catalytic degradation of gaseous pollutants in paper mills of southern China

XIN TONG, JIAO LI, JUN MA, XIAOQUAN CHEN, AND WENHAO SHEN

ABSTRACT: Studies were undertaken to evaluate gaseous pollutants in workplace air within pulp and paper mills and to consider the effectiveness of photo-catalytic treatment of this air. Ambient air at 30 sampling sites in five pulp and paper mills of southern China were sampled and analyzed. The results revealed that formaldehyde and various benzene-based molecules were the main gaseous pollutants at these five mills. A photo-catalytic reactor system with titanium dioxide (TiO_2) was developed and evaluated for degradation of formaldehyde, benzene and their mixtures. The experimental results demonstrated that both formaldehyde and benzene in their pure forms could be completely photo-catalytic degraded, though the degradation of benzene was much more difficult than that for formaldehyde. Study of the photo-catalytic degradation kinetics revealed that the degradation rate of formaldehyde increased with initial concentration fitting a first-order kinetics reaction. In contrast, the degradation rate of benzene had no relationship with initial concentration and degradation did not conform to first-order kinetics. The photo-catalytic degradation of formaldehyde-benzene mixtures indicated that formaldehyde behaved differently than when treated in its pure form. The degradation time was two times longer and the kinetics did not reflect a first-order reaction. The degradation of benzene was similar in both pure form and when mixed with formaldehyde.

Application: The developed photo-catalytic system had an excellent degradation performance on the gaseous pollutants in the paper mills. The findings from this work will be useful in the further development of workplace air conditioning devices.

Pulp and paper mills can be significant sources of liquid pollutants [1-4] and gaseous pollutants, such as volatile organic compounds (VOCs), nitrous oxide (NO_x), sulfur dioxide (SO_2), and formaldehyde (HCHO) [5,6], some of which may be associated with health risks [7,8]. While some work reporting gaseous constituents in paper mill workplace environments is available [9,10], the qualitative and quantitative analysis of gas compositions in these environments are scarce.

Treatment strategies for gaseous pollutants include condensation [11], solvent absorption [12], porous material adsorption [13], incineration [14], membrane separation [15], low temperature plasma [16], biological treatment [17], and photo-catalytic oxidation [18]. Among these techniques, photo-catalytic oxidation has attracted considerable attention for degrading organics, given its reaction conditions at room temperature and pressure and non-selective oxidation [18,19]. Numerous VOCs with small and large molecular weights can be successfully photo-catalytic degraded under various conditions [20-22]. However, application of this treatment technique to ambient air in paper mills is limited to only a few studies with methanol [23,24].

In this article, the ambient air at 30 sampling sites in five pulp and paper mills located in southern China was sampled and analyzed. Subsequently, photo-catalysis oxidation using nanometer-titanium dioxide (TiO_2) was evaluated to treat molecules identified in these ambient air samples. A photo-catalytic reactor was developed, optimized, and applied to degrade formaldehyde and benzene. The findings from this work will be useful in the further development of workplace air conditioning devices.

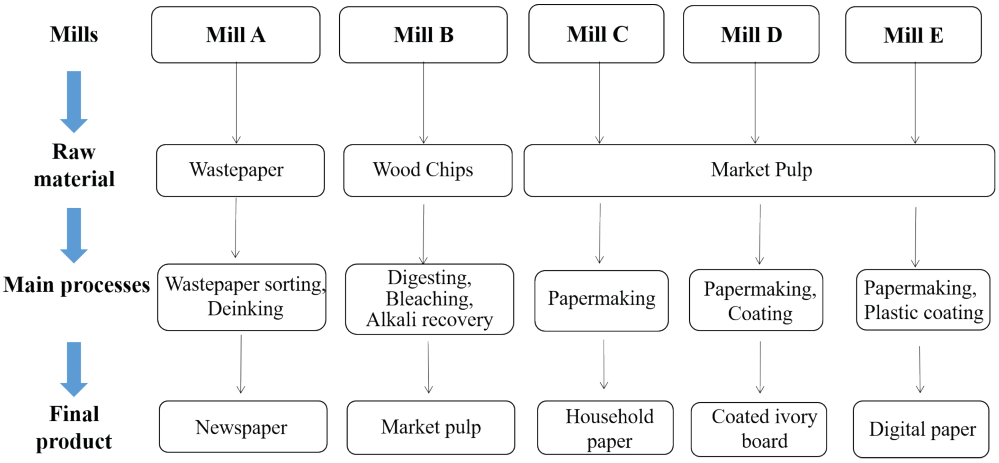
EXPERIMENTS AND METHODS

Sampling and analysis of ambient air samples

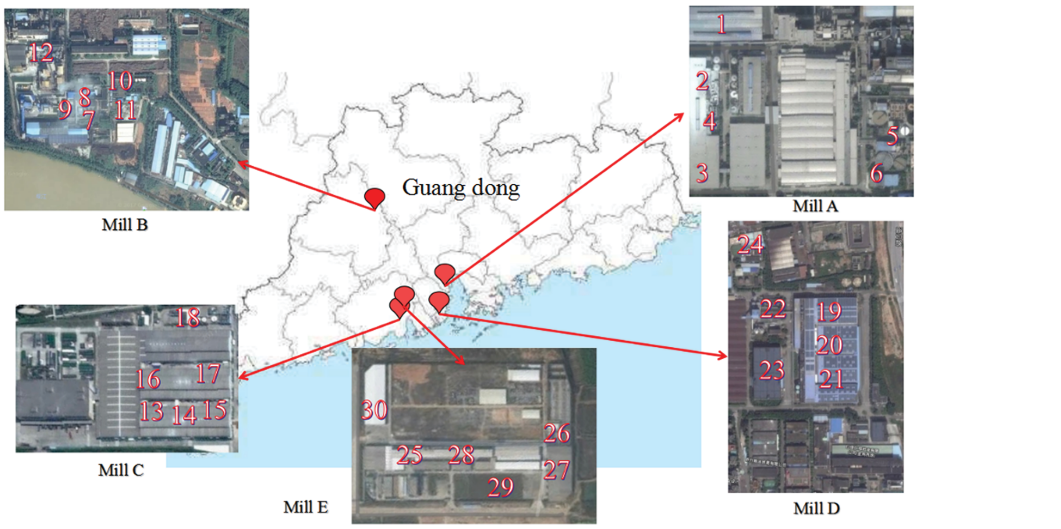
Five pulp and paper mills (Mills A-E) in southern China were selected to investigate their gaseous pollutants. Details regarding these facilities are presented in **Fig. 1**. Six ambient air samples from different sites in each mill were collected and analyzed (30 sites in total). The location of the five mills and the distribution of sampling sites at each mill are shown in **Fig. 2**.

Air samples were analyzed for total VOC (TVOC) and formaldehyde. The TVOC concentration was continuously measured in-situ by a portable gas detector for 15 min at a height of 1.5 m, with a resolution of 1 ppb, and at a flow rate of 220 mL/min (FirstCheck+ 5000, Ion Science Ltd.; Royston, UK). The composition of formaldehyde in the air sample was collected with an active air sampler (TWA-300Z, Tianyue Instrument Co.; Yancheng, China) at a height of 1.5 m from the ground and at a flow rate of 500 mL/min for 20 min. The formaldehyde content in the ambient air sample was analyzed by acetylacetone spectrophotometry. Further study on the composition of VOCs in paper mills was conducted with the gas chromatography-mass spectrometry (GC-MS) analysis method described fully in our previous work [7].

The calculation of the standard-exceeding multiple (SeM) of gaseous pollutants over the standards was given in Eq. 1.



1. Process schematics of five pulp and paper mills.



Mill A-1.Wet end of paper machine, 2.Wastepaper sorting room, 3.Deinking section, 4.Vacuum pump outlet, 5.Office area, 6.Wastewater treatment plant; Mill B-7.Pulping section office, 8.Digester outlet, 9.Bleachery outlet, 10.Black liquor evaporator outlet, 11.Alkali recovery section outlet, 12.Wastewater treatment plant; Mill C-13.Chemical join section of pulping area, 14.Wet end of paper machine, 15.Facial tissue workshop, 16.Product warehouse, 17.Raw material warehouse, 18.Wastewater treatment plant; Mill D-19.Wet end of paper machine, 20.Coatings preparation workshop, 21.Coating section, 22.Raw material warehouse, 23.Product warehouse, 24.Wastewater treatment plant; Mill E-25.Wet end of paper machine, 26.Coating material warehouse, 27.Coating plant, 28.Plastic coating workshop, 29.Product warehouse, 30.Wastewater treatment plant.

2. Overview of five mills in southern China and the sampling locations in each mill.

$$SeM = \frac{\text{detected value-standard value}}{\text{standard value}} \quad (1)$$

Degradation of gaseous pollutants by photo-catalytic oxidation

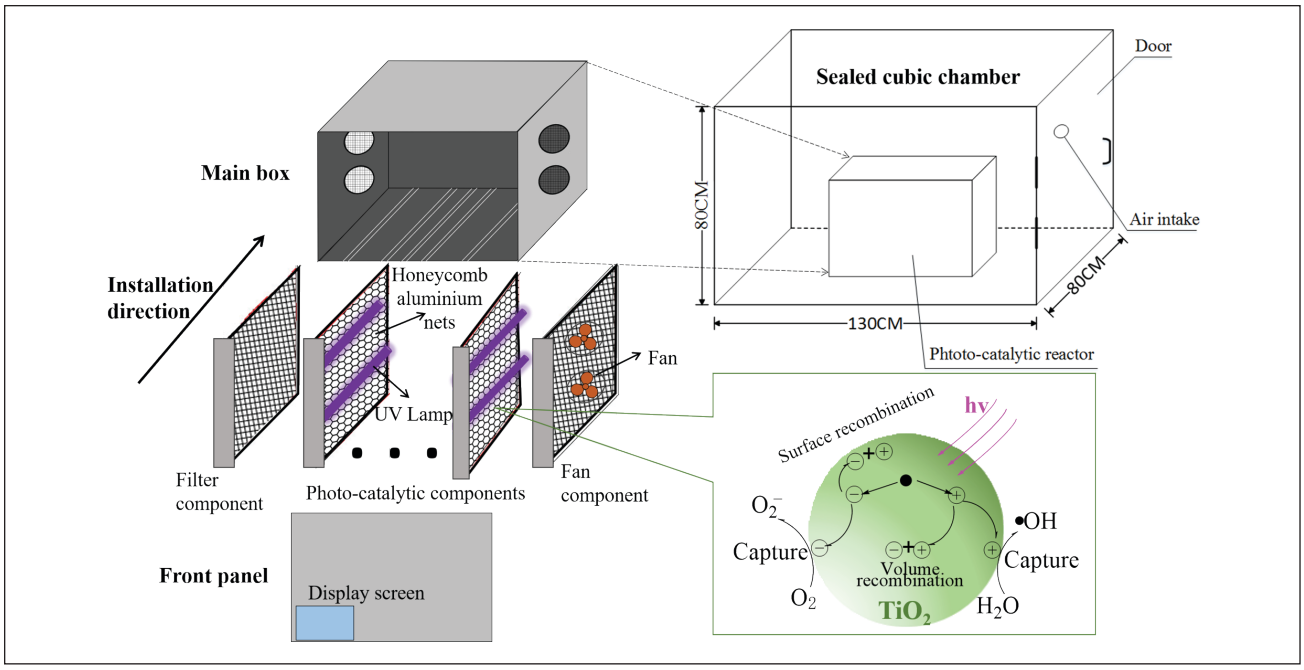
Photo-catalytic reactor system

A photo-catalytic reactor system was designed and studied for treatment of formaldehyde and benzene, as the latter was a parent molecule for a number of the VOCs detected in ambient air. The overall framework of the system is shown in **Fig. 3** and includes a front panel, multiple components, and a main box.

Combined with a microcontroller unit (MCU), the front panel with a liquid crystal display screen was used for real-time indications of gaseous pollutants concentrations, temperature/humidity, and gas flow rate during the photo-catalytic degradation. The gas flow rate could be adjusted from 0–324 m^3/h using the MCU.

Three types of components were included in the reactor: a filter component for the removal of the solid particles in gas, several sets of photo-catalytic components for the degradation of gaseous pollutants, and a fan for adjusting the gas flow rate in the reactor.

Formaldehyde and benzene were the two target gases treated. A formaldehyde sensor (EC803-CH_2O, Bluemoon



3. Schematic diagram of the photo-catalytic system.

Technology Co. Ltd.; Shenzhen, China), a portable benzene sensor (FirstCheck+ 5000, Ion Science Ltd.), and a digital temperature/humidity sensor (DHT11, Aosong Electronics Co. Ltd.; Guangzhou, China) were mounted on the filter component. The photo-catalytic components included three sets of honeycomb aluminium nets coated with nanometer-TiO_2 (30 wt%), which were subjected to the illumination using UVC lamps (254 nm, 15W). The morphology and surface element distribution of the honeycomb aluminum nets were studied by scanning electron microscopy (SEM) and energy dispersive spectrometer (EDS), respectively.

Two sets of small circular holes on two sides of the main box were designed for importing and exporting of gas.

As constructed, the system had two operational modes, manual and automatic, which could be controlled using the MCU to determine the optimal photo-catalytic conditions.

Photo-catalytic oxidation degradation experiments

The degradation experiments with the photo-catalytic reactor were conducted in the following sequence: blank experiments (BE) (**Table I**), optimization experiments (OE), and degradation experiments (DE). Formaldehyde was applied as the target pollutant in the BE and OE. Temperature and relative humidity were approximately 30°C and 48% in the study.

All the experiments were carried out in a sealed cubic chamber (top right corner of Fig. 3) made of polyvinyl chloride and polymethyl methacrylate, to simulate the gaseous environment of a paper mill. The reactor system was placed into the chamber, which had a working volume of 832 L. After the reactor system had operated for 5–10 min, all the sensor data became stable and the target gaseous pollutants were injected into the chamber using a 50 mL injector at the air intake on the chamber. The UV lamps were turned on to start the photo-catalytic DEs. During the degradation process, experimental data were recorded every 5 min. After finishing one DE, the chamber was opened by taking away the door (top right corner of Fig. 3) to discharge the residual gas and prepare for the next experiment.

Experiment No.	Experimental Conditions			Objective
	UV Lamp	Honeycomb Aluminum Nets	HCHO	
BE 1	√	√	×	Testing the zero pollution of the system.
BE 2	√	×	×	Testing if the illumination of UV lamps causes pollution.
BE 3	×	√	×	Testing if the honeycomb aluminum nets cause pollution.
BE 4	×	×	×	Testing if the cubic chamber causes pollution.
BE 5	√	×	√	Testing the effects of UV lamps on the degradation of formaldehyde.

I. Experimental conditions of blank experiments (BE): √ = yes, × = no.

Composition	Mills with Pulping Process		Mills without Pulping Process		
			Mill without Post-processing	Mills with Post-Processing	
	Mill A	Mill B	Mill C	Mill D	Mill E
TVOC	60.83	589.50	6.35	6.59	73.46
HCHO	0.28	1.75	1.30	0.00	0.03

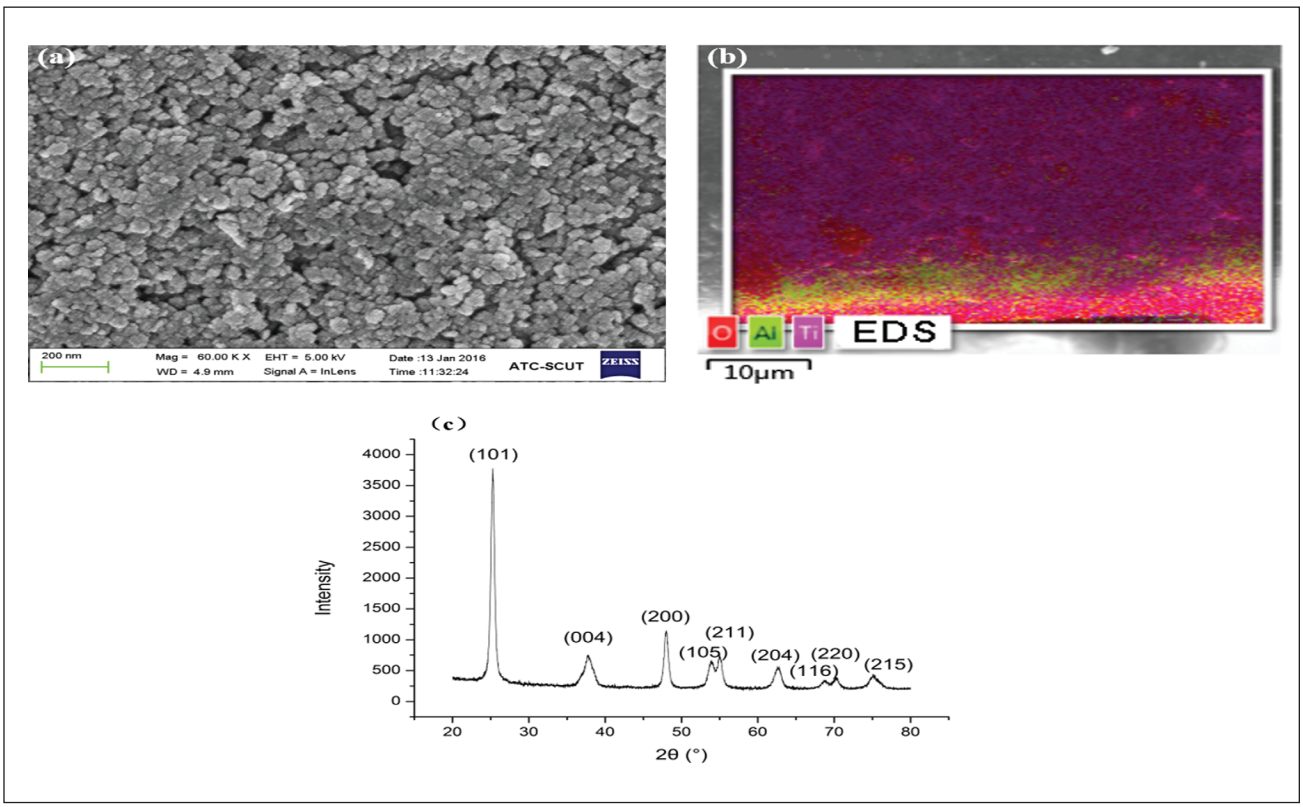
II. Average standard-exceeding multiples (SeMs) of total volatile organic compounds (TVOC) and formaldehyde (HCHO) in the ambient air of five mills.

In the photo-catalytic OEs, three parameters thought to influence photo-catalytic degradation were studied: gas flow rates (32.4, 97.2, 162, 259, and 324 m^3/h), number of photo-catalytic components (1, 2, and 3 sets), and the geometric size (2 and 3 mm) of the honeycomb aluminium mesh. Formaldehyde solution (36%–38%) and pure liquid benzene (analytical reagent, 99.5%) were used as the sources of the gaseous pollutants in the photo-catalytic experiments.

RESULTS AND DISCUSSION

Determination of ambient air in five pulp and paper mills

The TVOC and HCHO compositions of ambient air were collected and analyzed from 30 sites in five pulp and paper mills (Fig. 2). Published Chinese standards for TVOC and formaldehyde are 0.60 mg/m^3 and 0.10 mg/m^3, respectively [25,26]. Average SeMs for TVOC and formaldehyde at the six sites at each mill, calculated using Eq. 1, are listed in **Table II**. Most of the the SeM values were above zero, meaning that almost all the detected levels of TVOC and formaldehyde in the ambient air at the five pulp and paper mills exceeded the standards. In particular, the SeMs of TVOC were generally much higher than those of formaldehyde. As disclosed in our published work, the VOCs composition in the air samples of Mill A (a secondary fiber paper mill), desorbed with the non-polar and polar reagents, included benzene, alkane, phenols, esters, and other substances, in which the benzene homologues were the main hazardous substances [7].



4. Scanning electron miscroscopy (SEM), energy dispersive spectrometer (EDS), and X-ray diffraction (XRD) images of the surface of honeycomb aluminum mesh in the photo-catalytic reactor: (a) SEM image in the direction perpendicular to the gas flow; (b) EDS elemental mapping in the direction parallel to the gas flow: oxygen (red), aluminum (green), titanium (purple); and (c) XRD peaks of the titanium dioxide (TiO_2).

These ambient air results revealed that formaldehyde and benzene series were the main gaseous pollutants at the five pulp and paper mills studied. Due to its toxicity and resistance to degradation [27,28], benzene has often been used for evaluating the performance of photo-catalysts and photo-catalyst reactor systems. Therefore, in this study, formaldehyde, benzene, and mixtures of the two were selected to assess the performance of the photo-catalytic reactor system.

Degradation of gaseous pollutants by photo-catalytic oxidation

SEM and EDS analysis of honeycomb aluminum nets

The morphology and the surface element distribution of the honeycomb aluminum nets play an important role in photo-catalytic oxidation and these were characterized by SEM, EDS, and X-ray diffraction (XRD) analysis methods. Results are given in **Fig. 4**. The net surface was covered with the spherical particles whose average size was 15 nm (Fig. 4a) and the elements on the net surface contained oxygen, aluminum, and titanium (Fig. 4b). Moreover, as shown in Fig. 4c, the diffraction peaks at 2θ = 25.2°, 37.7°, 48.0°, 53.8°, 54.9°, 62.8°, 68.6°, 70.2°, and 75.1° were identified to be the (101), (004), (200), (105), (211), (204), (116), (220), and (215) crystal faces of TiO_2 with anatase phase (JCPDF No. 21-1272), respectively. In other words, the characterizations in Fig. 4 show that the honeycomb aluminum nets were covered with the spherical nanometer-TiO_2 wherein the large specific surface area and anatase phase were beneficial to the photo-catalytic degradation of gaseous pollutants.

To ensure the accuracy and reliability of the experimental results, prior to the degradation performance study of the photo-catalytic reactor system, the BEs and OEs were conducted as described in the previous "Photo-catalytic oxidation degradation experiments" section.

Blank experiments (BE) of photo-catalytic system

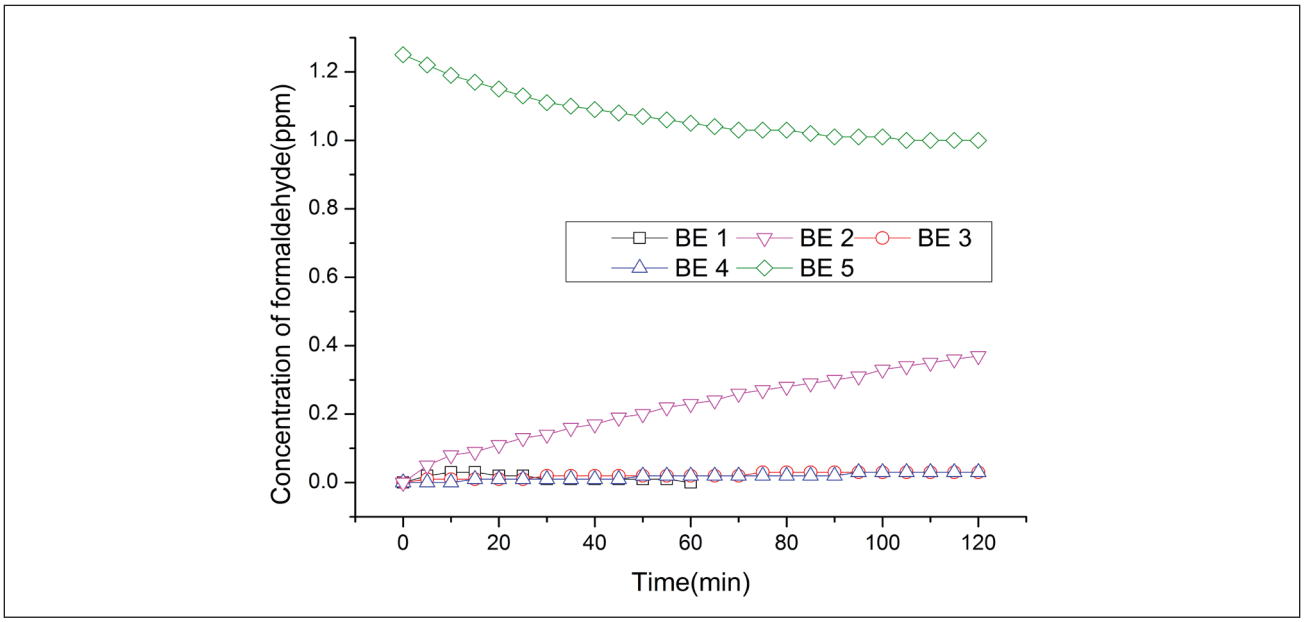
To achieve the objectives listed in Table I, five BEs were conducted. Results are given in **Fig. 5**. These BE results can be explained as follows:

1. BEs 1 and 2 revealed that the ozone produced by the UV lamps (wavelength of 253.7 nm) [29] influenced the formaldehyde sensor data, but formaldehyde could be degraded by the photo-catalytic components [30].
2. BEs 3 and 4 demonstrated that no formaldehyde was detected, which meant that the honeycomb aluminum nets and the cubic chamber did not introduce formaldehyde in the experiments.
3. BE 5 suggested that the UV lamps themselves could degrade formaldehyde about 20% in 120 min.

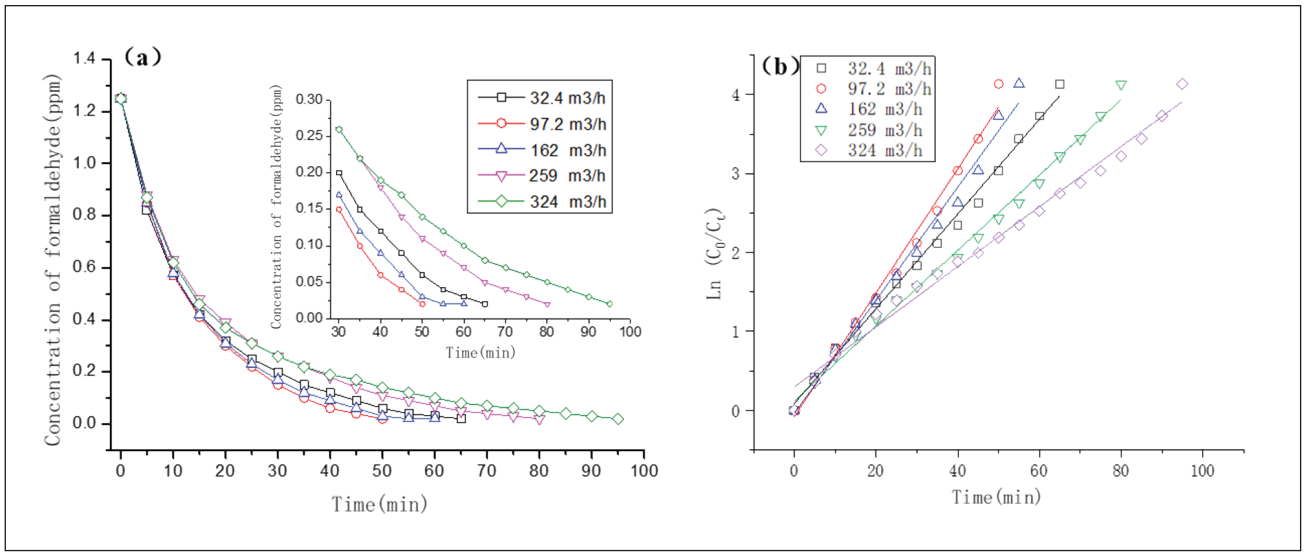
Optimization experiments (OE) of photo-catalytic system

A series of OEs were conducted to investigate the optimal conditions of the photo-catalytic reactor system.

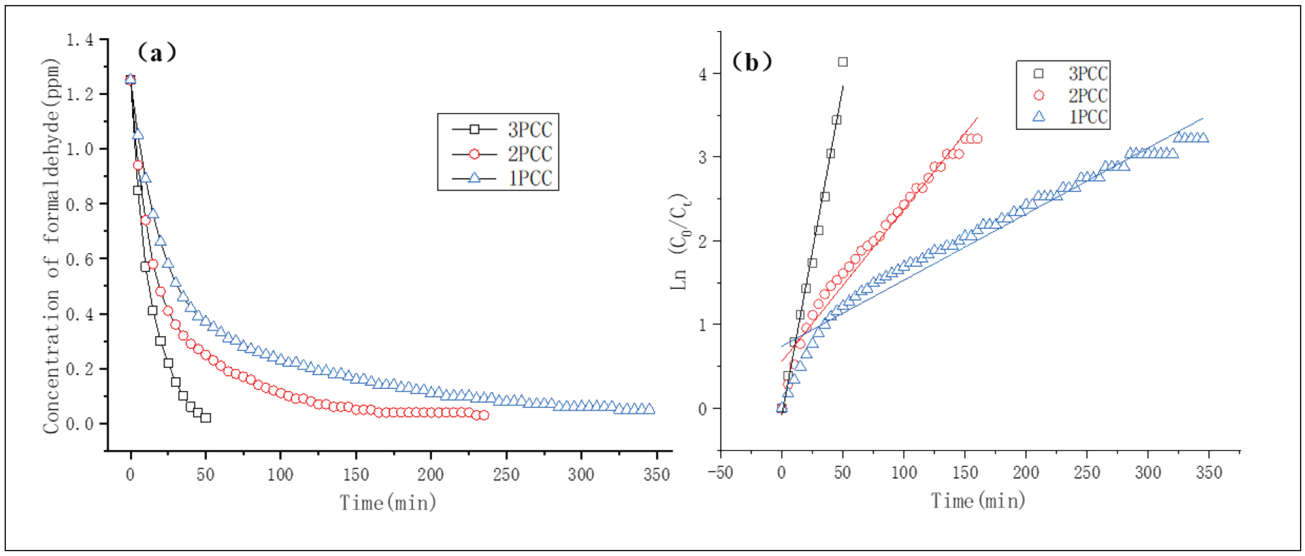
Gas flow rate. Since the gas flow rate indirectly implies the residence time of gas on the photo-catalyst in the range of 32.4 to 324 m^3/h (corresponding to the residence time range [92 to 9 s]), the influence of gas flow rate on the photo-catalytic degradation was studied. Results are shown in **Fig. 6** plots with the flow rates of 32.4, 97.2, 162, 259, and 324 m^3/h. Times for complete degradation were 65, 50, 60, 80, and 95 min (Fig. 6a), and the first order rate constants were 0.060, 0.078, 0.072, 0.048, and 0.038/min (Fig. 6b), respectively. The photo-catalytic degradation processes were slower at high flow rates (324 and 259 m^3/h) relative to low flow rates (162, 97.2, and 32.4 m^3/h). The photo-catalytic reaction rate could be expressed by the time needed to degrade the same amount of formaldehyde (Fig. 6a) or the first order rate constant cal-



5. Results of five blank experiments (BE) in the experimental photo-catalytic system.



6. Influence of gas flow rate on the photo-catalytic degradation process: (a) evolutions of formaldehyde concentration with time, and (b) correlations of Ln (C_0/C_t) *with time.*

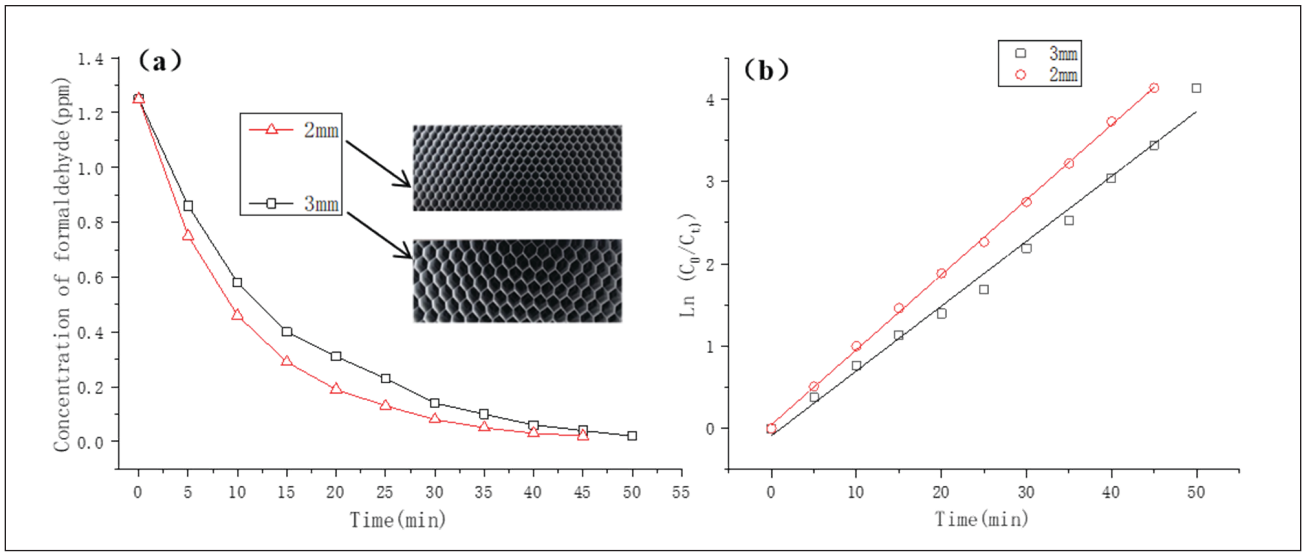


7. Influence of the number of photo-catalytic components (PCC) on the photo-catalytic degradation process: (a) evolutions of formaldehyde concentration with time, and (b) correlations of Ln (C_0/C_t) *with time.*

culated by fitting curve in Fig. 6b. From these results it was determined that the optimal gas flow rate was 97.2 m³/h (residence time of 31s).

It was evident from the results in Fig. 6 that suboptimal gas flow rates decreased the photo-catalytic degradation rate. This phenomenon is attributed to the effect of flow rate on photo-catalytic reaction, which is double antagonistic [29]. When the flow rates were low (in the range of 32.4 and 97.2 m³/h with residence times of 92 and 31 s, respectively), photo-catalytic oxidation was mainly a mass transfer in which the reaction rate increased with the increase of flow rate. When the flow rate became high (in the range of 162 and 324 m³/h with residence times of 18 and 9 s, respectively), the photo-catalytic reaction dominated the mass transfer reaction. In this case, lower flow rate with longer residence time on the photo-catalyst increased the reaction rate, which is in agreement with Monteiro et al. [31] and could explain why a medium gas flow rate (97.2 m³/h) performed best in the study.

Number of photo-catalytic components. Under the optimal gas flow rate of 97.2 m³/h, when the number of photo-catalytic components increased from 1 to 3, the necessary time for the complete degradation of formaldehyde was 345, 235, and 50 min (**Fig. 7a**), and the first order rate constant increased from 0.008 to 0.018 to 0.079/min (Fig. 7b), respectively. From the perspective of degradation time and rate constant, the photo-catalytic activity was remarkably enhanced with the use of three photo-catalytic components, allowing



8. Effect of the geometric size of honeycomb aluminum mesh on the photo-catalytic degradation process: (a) evolutions of formaldehyde concentration with time, and (b) correlations of* Ln (C_0/C_t) *with time.

greater catalyst surface area, more contact area between catalyst and pollutants, and a higher concentration of pollutants adsorbed on the photo-catalyst. More photo-catalytic components also meant higher UV light intensity, which could generate more photons and electron-hole pairs [29,32]. Therefore, the optimal number of photo-catalytic components was determined as three in the study.

Geometric size of honeycomb aluminum mesh. Functioning as the substrate of the photo-catalyst, geometric size of the honeycomb aluminum mesh can influence the contact area between the catalyst and the gaseous pollutants. With the optimal gas flow rate of 97.2 m³/h and 3 photo-catalytic components, two sizes of the honeycomb aluminum mesh, 2 mm and 3 mm, were applied and compared in the study. As displayed in **Fig. 8a**, the photo-catalytic degradation performance with 2 mm mesh was slightly better than that with 3 mm mesh. It took 45 and 50 min for the same amount of formaldehyde to be completely degraded with 2 mm mesh and 3 mm mesh, respectively. As shown in Fig. 8b, the photo-catalytic degradation with different geometric sizes of honeycomb aluminum mesh also accorded with the first order kinetics, and the rate constants were 0.091 and 0.079/min by 2 mm and 3 mm meshes, respectively. These results demonstrated that the smaller the mesh size performed slightly better due to the larger contact area with the catalyst.

The previously described OEs indicated that the optimal conditions for the photo-catalytic reactor system were as follows: gas flow rate 97.2 m³/h, 3 photo-catalytic components, and a 2 mm geometric size for the honeycomb aluminum mesh.

Degradation performance of the photo-catalytic reactor

After having performed the BEs and OEs of the photo-catalytic reactor system, degradation performance studies were conducted under the optimal conditions.

To study the kinetic behavior of photo-catalytic degradation of formaldehyde and benzene, the degradation rate equation of the simplified model of Langmuir-Hinshelwood (L-H) [33], which is a well-known kinetic model for describing the heterogeneous photo-catalytic oxidation, was applied in the study. The simplified L-H model can be expressed as:

$$\gamma = -\frac{dC}{dt} = kC \qquad (2)$$

where γ is the degradation rate, C is concentration of reactant, t is the reaction time, and k is the reaction rate constant. The integral form of Eq. 2 is:

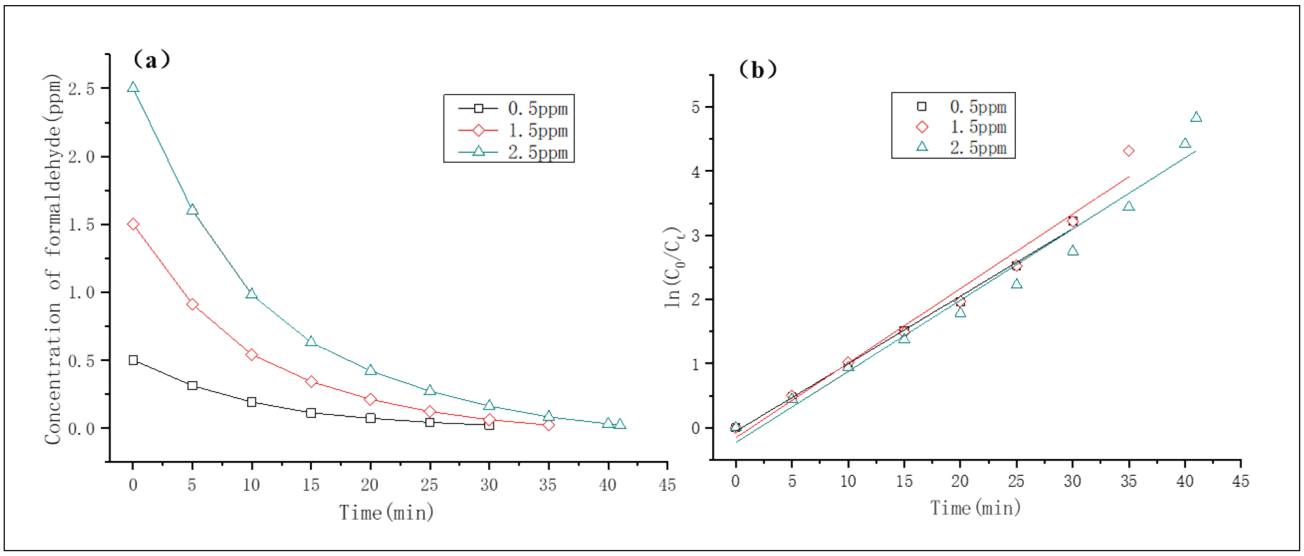
$$Ln\frac{C_0}{C_t} = kt \qquad (3)$$

where C_0 and C_t are the concentrations of reactant at the initial time and the reaction time, t.

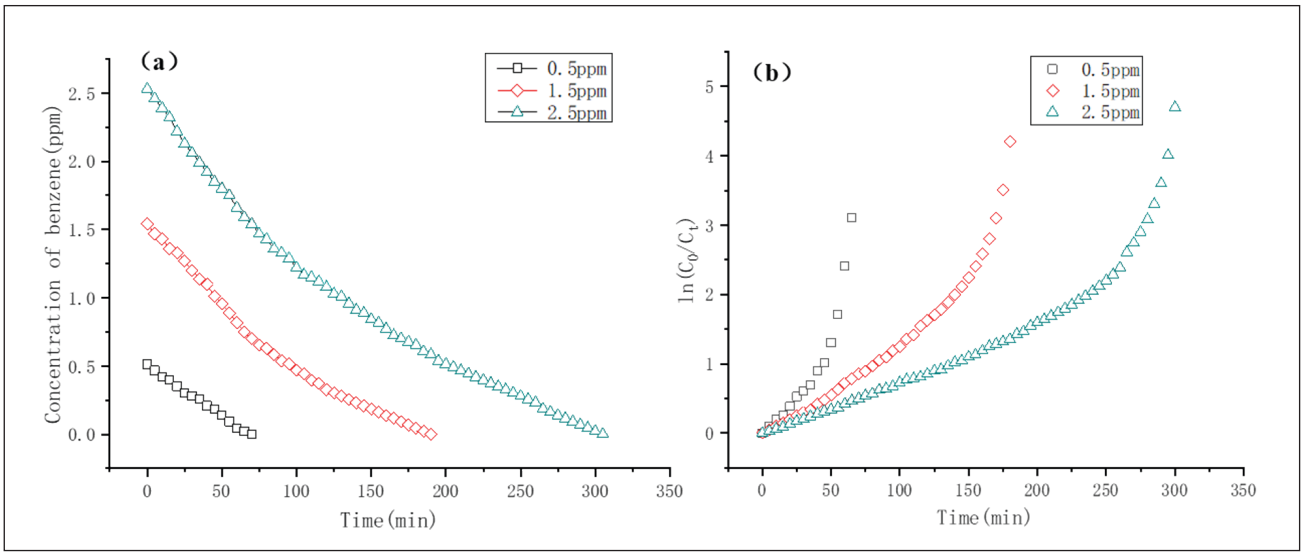
Formaldehyde as the target pollutant. The DEs results of formaldehyde with different initial concentrations are given in **Fig. 9**.

As indicated in Fig. 9a, regardless of what the initial levels of formaldehyde were, it could all be completely degraded by the photo-catalytic reactor, and the times needed for complete degradation were 41, 35, and 30 min for the 2.5, 1.5, and 0.5 ppm initial concentrations of formaldehyde, respectively. Moreover, according to Eq. (2), the degradation rate, γ, of formaldehyde increased with higher initial concentration, C_0.

Considering the kinetic behavior of the photo-catalytic degradations of formaldehyde, as shown in Fig. 9b, the coefficients of determination of linear fitting curves for 2.5, 1.5, and 0.5 ppm formaldehyde were 0.968, 0.975, and 0.996,



9. Influence of initial formaldehyde concentration on the photo-catalytic degradation under optimal conditions: (a) evolutions of formaldehyde concentration with time, and (b) correlations of Ln (C_0/C_t) *with time.*

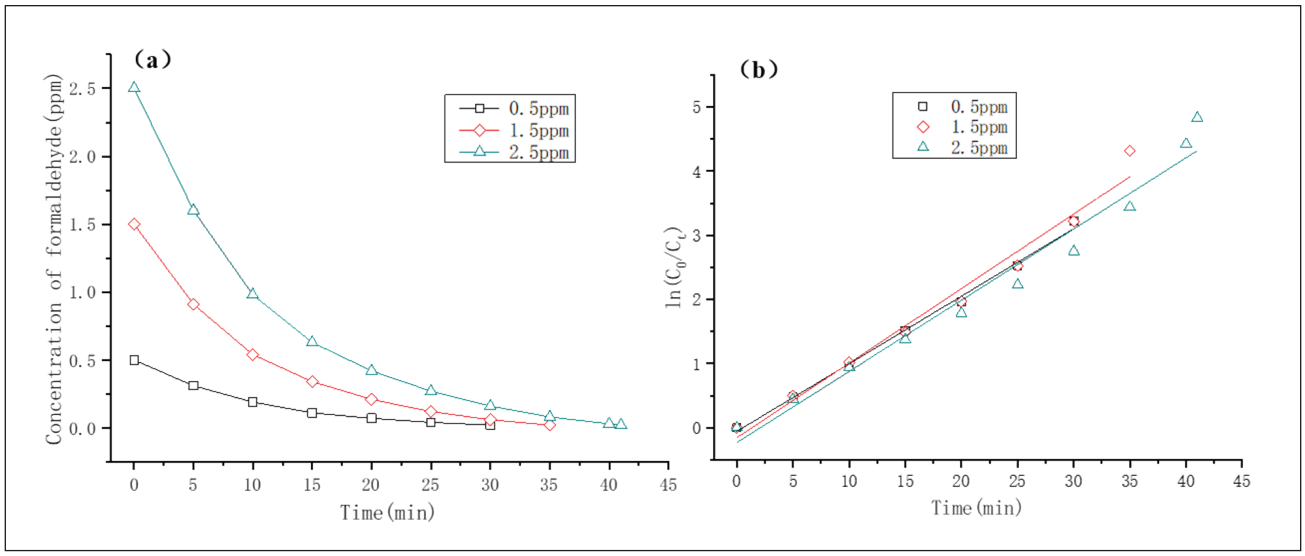


10. Influence of initial benzene concentration on the photo-catalytic degradation under the optimal conditions: (a) evolutions of benzene concentration with time, and b) correlations of Ln (C_0/C_t) *with time.*

respectively, which was close to 1. According to Eq. 3, these high linear correlations indicated that the photo-catalytic degradation process of formaldehyde fitted the first-order reaction, and the first-order reaction rate constants, *k*, for 2.5, 1.5, and 0.5 ppm formaldehyde were 0.111, 0.116, and 0.105 /min, which was similar and independent of the initial concentration.

Benzene as the target pollutant. Under the optimal conditions, the DE results of benzene with different initial concentrations are shown in **Fig. 10**. Compared with the results in Fig. 9, although the photo-catalytic reactor could completely degrade benzene in 310, 180, and 70 min for 2.5, 1.5, and 0.5 ppm initial concentrations of benzene, respectively, the degradation processes were considerably longer than those for formaldehyde degradation at the same initial concentrations. As shown in Fig. 10a, the degradation behavior was very different from that of formaldehyde (Fig. 9a). When the initial concentration of benzene increased, the time for total degradation increased linearly. Because of these differences, the kinetic behavior of the photo-catalytic degradation of benzene was studied further. As shown in Fig. 10b, no linear correlation between $Ln\frac{C_0}{C_t}$ and the reaction time, *t*, was observed, indicating that the degradation of benzene did not conform to the first-order kinetics.

To compare the degradation behaviors of formaldehyde and benzene, their degradation curves with the same initial concentrations of 1.25 ppm are plotted in **Fig. 11**. From Fig.



11. Comparison of the photo-catalytic degradation profiles of formaldehyde and benzene in pure forms with the same initial concentration: (a) evolutions of concentration with time, and (b) correlations of* Ln (C_0/C_t) *with time.

11a, it was evident that the necessary complete degradation time for benzene was almost four times longer than that for formaldehyde.

The possible reasons why the benzene was more difficult to degrade than formaldehyde are as follows:

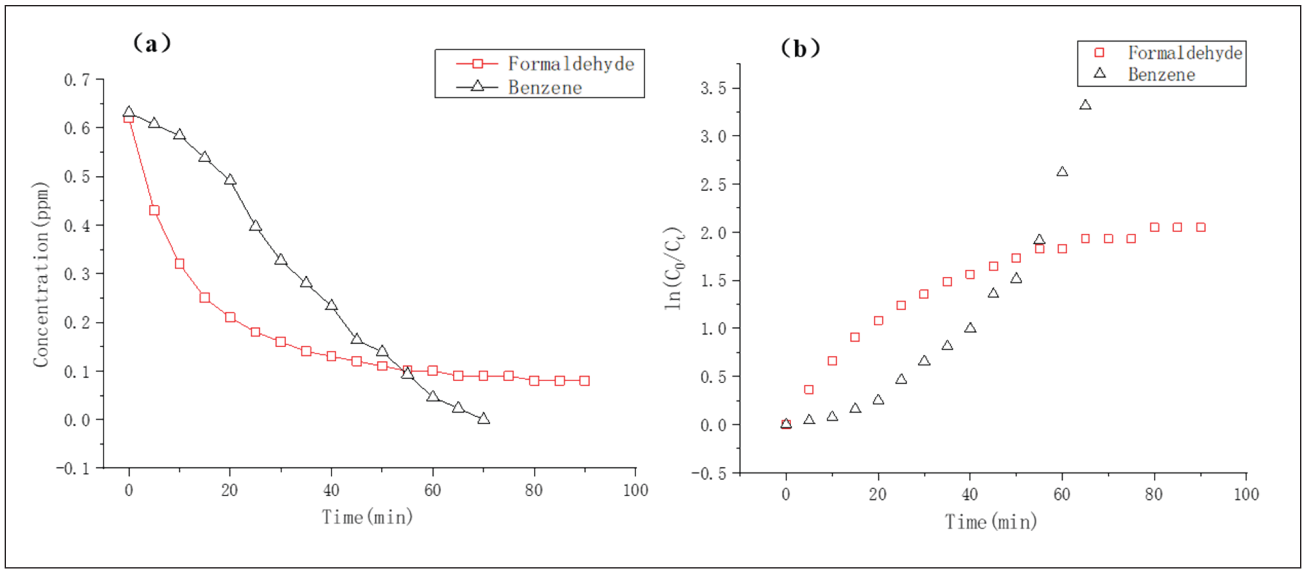
1. Owing to a lower bond energy than that of benzene [34], formaldehyde can be easily degraded to formic acid and then completely converted into carbon dioxide and water, displaying a short pathway for degradation [35]. However, the pathway of benzene for being photo-catalytically degraded is long and complex [36], which includes several intermediate processes, the direct reaction of benzene and electron hole pairs, the reaction of benzene and hydroxyl radical, and the polymerization of benzene.
2. The intermediate products of benzene vary and can be strongly adsorbed by the catalyst, leading them to be less reactive with the catalyst [36]. Thus, the competitive adsorptions of the intermediate products and the deactivated catalyst might be the main causes of the slow degradation of benzene [36,37]. Thus, as shown in Fig. 11b, the deactivation of TiO_2 in the photo-catalytic process may be the reason why the degradation of benzene did not fit the first-order reaction.
3. Another possible reason for the different kinetic degradation behaviors of formaldehyde and benzene might be that the optimal degradation conditions obtained with formaldehyde in the section on "Optimization experiments (OE) of photo-catalytic system" were not suitable for the degradation of benzene.

Mixture of formaldehyde and benzene as the target pollutant. In order to better simulate the actual gaseous conditions in paper mills, a mixture of formaldehyde and benzene was employed to evaluate the degradation performance of the photo-catalytic reactor. The initial concentrations of both formaldehyde and benzene were about 0.625 ppm and the initial total concentration of the mixture was 1.25 ppm. The photo-catalytic degradation results for the mixture are given in **Fig. 12**.

The degradation of formaldehyde in the mixture, as plotted in Fig. 12a, decreased rapidly in the initial phase, but the rate gradually slowed, and became even slower than that of benzene, without being degraded completely in the end. The benzene concentration decreased relatively slowly in the initial stage and then dropped to near zero. Compared with the results in their pure forms (Fig. 11a), the reaction process of formaldehyde in the mixture was different; it took about two times longer to be degraded, while the degradation of benzene in the mixture was similar to that in its pure form.

Furthermore, owing to the different degradation behavior of formaldehyde in the mixture, as shown in Fig. 12b, the previously observed linear correlation between $Ln\frac{C_0}{C_t}$ and the reaction time, t, for formaldehyde in its pure form (Fig. 11b) became nonlinear, which revealed that the photo-catalytic kinetics of formaldehyde in the mixture no longer belonged to the first-order reaction.

This degradation phenomena for the mixture could be explained as due to the presence of the hydroxyl group that is an electron-donor functional group in formaldehyde [38]. The adsorption ability of formaldehyde on the catalyst is greater than that of benzene. Hence, in the initial stage of the photo-catalytic oxidation, formaldehyde was adsorbed on the TiO_2 and degraded preferentially. With the formaldehyde concentration decreased, the adsorption and degradation of benzene gradually became dominant in the mixture, and the competitive adsorptions of the intermediate products of benzene impeded the further degradation of formaldehyde in the mixture. Another possible explanation may be that aldehyde substances, intermediate products of benzene [36,39], influenced the



12. Comparison of the photo-catalytic degradation profiles of formaldehyde and benzene in the mixed forms with the same initial concentration: (a) evolutions of concentration with time, and b) correlations of* Ln (C_0/C_t) *with time.

formaldehyde sensor and caused it to deliver a signal that might not represent the real concentration of formaldehyde.

The photo-catalytic experiment results in the "Degradation performance of the photo-catalytic reactor" section indicated that when employing formaldehyde, benzene, and their mixtures as representative gaseous pollutants in paper mills, the developed photo-catalytic reactor was capable of degrading the test gasses. These bench scale results suggest the possibility that a photo-catalytic reactor could be used to purify gaseous pollutants in the ambient air of paper mills.

CONCLUSION

Analytical results of ambient air in five pulp and paper mills showed formaldehyde and TVOC (including benzene series) to be the two main gaseous pollutants. A photo-catalytic reactor system with TiO_2 was developed and tested to degrade these gaseous pollutants. After having conducted blank and optimization studies on the reactor, studies were undertaken with the reactor by applying formaldehyde, benzene, and their mixtures as the target gasses. The following points were concluded from the study:

1. Both formaldehyde and benzene could be completely photo-catalytic degraded, but the complete degradation time for benzene was almost four times longer than that for formaldehyde, which revealed the difficult degradation of benzene.
2. The photo-catalytic degradation rate of formaldehyde increased with initial concentration, and its degradation could be modeled as a first-order reaction. Reaction rate constants were similar and independent of the initial concentration. On the contrary, the degradation rate of benzene had no relationship with initial concentration, and its photo-catalytic degradation did not conform to the first-order kinetics reaction.
3. The photo-catalytic reaction process of formaldehyde in the mixture was different; it took about two times longer to be degraded than in its pure form, and related kinetics were no longer first-order. However, the photo-catalytic degradation of benzene in the mixture was almost the same as in pure form.

These study results demonstrated that the photo-catalytic reactor could degrade formaldehyde and benzene. **TJ**

ACKNOWLEDGEMENTS

This research was supported by the Research Funds of the National Science Foundation of Guangdong, China (No. 2016A030313478), State Key Laboratory of Pulp and Paper Engineering (No. 2017ZD03), and Science and Technology Program of Guangzhou, China (No. 201607010050).

LITERATURE CITED

1. Chandra, R. and Sankhwar, M., *J. Environ. Biol.* 32(6): 739(2011).
2. Kamali, M. and Khodaparast, Z., *Ecotoxicol. Environ. Saf.* 114: 326(2015).
3. Wen, Z.G., Di, J.H., and Zhang, X.Y., *J. Environ. Manage.* 169: 67(2016).
4. Meyer, T. and Edwards, E.A., *Water Res.* 65: 321(2014).
5. Kiurski, J.S., Maric, B.B., Aksentijevic, S.M., et al., *Renewable Sustainable Energy Rev.* 28: 224(2013).
6. Lattuati-Derieux, A., Bonnassies-Termes, S., and Lavedrine, B., *J. Cultural Heritage* 7(3): 227(2006).
7. Tong, X., Zhang, Z.B., Chen, X.Q., et al., *BioResources* 10(4): 8487(2015).
8. Tong, X., Liu, Z., Chen, X.Q., et al., *J. Environ. Sci. Health, Part A: Toxic/Hazard. Subst. Environ. Eng.* 51(13): 1149(2016).

9. Nez Perce National Air Toxics Program, "Characterization of air toxics concentrations around a kraft pulp and paper mill facility, Lewiston, Idaho," Final Report, EPA Assistance ID No. XA-97079001-3, Nez Perce Tribe Environmental Restoration and Waste Management Division Air Quality Program, 30 September 2009.
10. U.S. Environmental Protection Agency, "Pulp, paper, and paperboard industry—Background information on proposed air emission standards," EPA Document ID No. EPA-453/R93-050a, U.S. Environmental Protection Agency Office of Air and Radiation, Research Triangle Park, NC, USA, October 1993.
11. Zheng, X., Li, H., Zhang, W., et al., *Cryogenics & Superconductivity* 43(02): 67(2015).
12. Heymes, F., Manno-Demoustier, P., Charbit, F., et al., *Chem. Eng. J.* 115(3): 225(2006).
13. Zhang, X.Y., Gao, B., Creamer, A.E., et al., *J. Hazard. Mater.* 338: 102(2017).
14. Lin, C., Da Chen, M., Hsieh, M.K., et al., *Abstr. Pap. Am. Chem. Soc.* 226: U535(2003).
15. Zhang, L., Weng, H.X., Chen, H.L., et al., *J. Environ. Sci. China* 14(2): 181(2002).
16. Schmidt, M., Jogi, I., Holub, M., et al., *Int. J. Environ. Sci. Technol.* 12(12): 3745(2015).
17. Lu, Y., Liu, J., Lu, B.N., et al., *J. Hazard. Mater.* 182(1-3): 204(2010).
18. Ravelli, D., Dondi, D., Fagnoni, M., et al., *Chem. Soc. Rev.* 38(7): 1999(2009).
19. Wang, S.B., Ang, H.M., and Tade, M.O., *Environ. Int.* 33(5): 694(2007).
20. An, T.C., Sun, L., Li, G.Y., et al., *Appl. Catal., B* 102(1-2): 140(2011).
21. Sun, L., Li, G.Y., Wan, S.G., et al., *Chemosphere* 78(3): 313(2010).
22. Chen, J.Y., Li, G.Y., He, Z.G., et al., *J. Hazard. Mater.* 190(1-3): 416(2011).
23. Stokke, M.J., Mazyck, D.W., Wu, C.Y., et al., *Environ. Prog.* 25(4): 312(2006).
24. Tao, Y., Wu, C.Y., and Mazyck, D.W., *Chemosphere* 65(1): 35(2006).
25. People's Republic of China, *National Standards of People's Republic of China*, GB/50325-2010, 2010.
26. People's Republic of China, *National Standards of People's Republic of China*, GB/T18883-2002, 2002.
27. Tasbihi, M., Bendyna, J.K., Notten, P.H.L., et al., *J. Nanosci. Nanotechnol.* 15(9): 6386(2015).
28. Xu, Y.J., Zhuang, Y.B., and Fu, X.Z., *J. Phys. Chem. C* 114(6): 2669(2010).

ABOUT THE AUTHORS

We chose to research this topic because analysis of gaseous pollutants in paper mills has been scarce for some time, and few studies have dealt with degrading treatment of gaseous pollutants in mills. In the past few years, we have performed systematic research on the main composition of gaseous pollutants from paper mills. This work introduces a photo-catalytic degradation system for dealing with these pollutants.

The most difficult aspect of this research was finding a way to conduct the degradation experiments for the papermaking gaseous pollutants in the laboratory. Therefore, we developed feasible photo-catalytic degradation equipment so we could degrade and observe the evolution of the main types of polluted gas. When we applied formaldehyde, benzene, and their mixtures as the target pollutants, the photo-catalytic reactor system we developed had excellent degradation performance for these pollutants. It was interesting to find that the degradation behaviors of formaldehyde and benzene are different in their pure forms and that they may affect each other in their mixing form during the degradation process.

This study will raise awareness around the serious gaseous pollution in the paper industry, and the photo-catalytic degradation technology introduced here can help paper mills control the emission of polluting gases. Our subsequent research will study the photo-catalytic degradations of other gaseous pollutants and realize their practical application in paper mills.

Tong is a post-doctoral student, Li is a doctoral student, Chen is associate professor, and Shen is professor at the State Key Laboratory of Pulp and Paper Engineering, South China University of Technology, Guangzhou, China. Email Shen at ppwhshen@scut.edu.cn.


Tong


Li


Chen


Shen


Ma

29. Mamaghani, A.H., Haghighat, F., and Lee, C.S., *Appl. Catal., B* 203: 247(2017).
30. Lu, Y.W., Zhao, X.H., Wang, M.Y., et al., *Build. Environ.* 81: 42(2014).
31. Monteiro, R.A.R., Silva, A.M.T., Angelo, J.R.M., et al., *J. Photochem. Photobiol., A* 311: 41(2015).
32. Alonso-Tellez, A., Masson, R., Robert, D., et al., *J. Photochem. Photobiol., A* 250: 58(2012).
33. Deng, X.Q., Liu, J.L., Li, X.S., et al., *Catal. Today* 281: 630(2017).
34. Luo, Y.R., *Handbook of Bond Dissociation Energies in Organic Compounds*, CRC Press, Boca Raton, FL, USA, 2003, pp. 45-45.
35. Liang, W.J., Li, J., and Jin, Y.Q., *Build. Environ.* 51: 345(2012).
36. Dhada, I., Nagar, P.K., and Sharma, M., *Ind. Eng. Chem. Res.* 54(20): 5381(2015).
37. Zhang, Q.C., Zhang, F.B., and Zhang, G.L., *Chin. J. Catal.* 25(1): 39(2004).
38. Geng, Q., Wang, Q., and Zhang, B., *Ind. Eng. Chem. Res.* 51(47): 15360(2012).
39. Wang, X.Q., Zhang, G.L., Zhang, F.B., et al., *Chem. Res. Appl.* 18(4): 344(2006).

ABOUT THIS PAPER

Cite this article as: Tong, X., Li, Jiao, Ma, J., et al. *TAPPI J.* 17(3):167(2018). https://doi.org/10.32964/TJ17.03.167

DOI: https://doi.org/10.32964/TJ17.03.167

ISSN: 0734-1415

Publisher: TAPPI Press

Copyright: ©TAPPI Press 2018

About this journal

Removal of phthalate from papermaking wastewater by MIL-101(Fe) in the presence of persulfate

XUEMING LIN, ZEYU GUAN, JINQUAN WAN, YONGWEN MA, AND YAN WANG

ABSTRACT: Phthalates are found in most papermaking wastewater, as are various other pollutants. Phthalates such as diethyl phthalate (DEP) and dibutyl phthalate (DBP) are endocrine-disrupting compounds (EDCs). The objective of this research was to use metal organic frameworks (MOFs) MIL-101(Fe) as a new-style adsorbing material and persulfate (PS) activator for removing DEP and DBP from artificial aqueous model solutions. We used X-ray diffractometer, scanning electron microscope, and Fourier transform infrared spectroscopy technologies to characterize the MIL-101(Fe). More than 80% of the DEP and DBP were removed with a MIL-101(Fe)/PS system over a 5 h period when the initial concentrations of the pollutants (DEP or DBP) were around 3 ppm. MIL-101(Fe) was able to absorb the pollutants and activate persulfate, which together contributed to phthalate removal. As the amount of MIL-101 and PS was increased, the percentage of removed phthalate increased gradually. We concluded that the MIL-101(Fe)/PS system removed phthalate effectively from papermaking wastewater.

Application: Metal organic frameworks MIL-101(Fe) could be applied to activate persulfate for phthalate removal, which would reduce the risk for exposure to EDCs from papermaking wastewater.

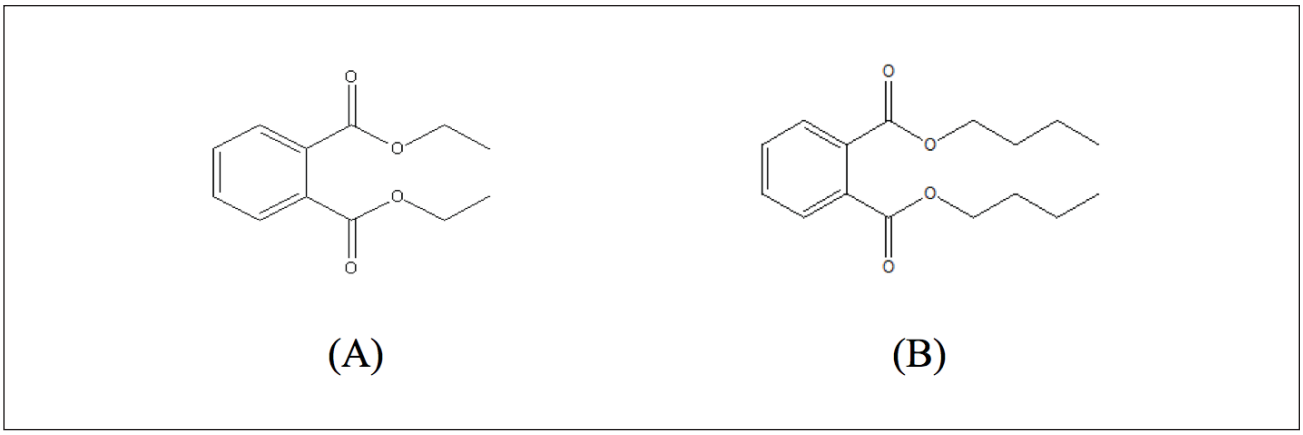
Pulp and paper mills discharge various pollutants in wastewater. Of increasing concern are the endocrine-disrupting compounds (EDCs) among the various pollutants from wastewater of paper mills. EDCs include mainly phthalates (phthalic acid esters [PAEs]), such as dimethyl phthalate, diethyl phthalate (DEP), dibutyl phthalate (DBP), benzyl butyl phthalate, etc. [1]. Additives in the papermaking process, bleaching process, and recyclable paper can be sources of phthalates in wastewater. Different articles have investigated the presence of PAEs in papermaking wastewater [2-4].

We chose to investigate compounds identified in requirements of the European Union Water Framework Directive (2000/60/EC and 2008/105EC) and the laws of certain countries. Chinese laws limit specific levels of only some typical PAEs. The integrated wastewater discharge standard (GB8978-1996), for example, sets the specific levels of dibutyl phthalate (DBP), one kind of PAE, as 0.2 mg/L, 0.4 mg/L, and 2.0 mg/L for grade I, grade II, and grade III, respectively. Although the amounts of these pollutants are not so large, they could cause great disruption to endocrine and greatly affect the development of wildlife, and even human beings. PAEs have been found in aqueous effluents of paper mills even after aerobic or aerobic-anaerobic treatment [1]. Incomplete degradation of EDCs by biological treatment results in significant levels of EDCs that might still affect human life. Scientists and engineers have developed various technologies to further remove these pollutants. Particularly, filtration technology and advanced oxidation processes (AOPs) are methods for removing pollutants that are hard to remove by biological methods [5].

Traditional AOPs are mainly based on hydroxyl radicals (HO·), which can effectively degrade various pollutants. In addition to the traditional AOPs, sulfate radical ($SO_4^{\cdot-}$)-based AOPs have attracted increasing attention in recent years [6-8]. Sulfate radicals are produced mainly by activation of persulfate. Sulfate radicals have oxidation-reduction potential similar to that of hydroxyl radicals and can be used to degrade various pollutants. Sulfate radicals also have longer effective half-lives than do hydroxyl radicals [9-11]. This advantage makes it possible to break down trace amounts of EDCs pollutants in the papermaking wastewater.

Metal organic frameworks (MOFs) have drawn more and more attention. Their porous character resembles activated carbon or molecular sieves. One way that MOFs could help to remove pollutants is by adsorption. In addition, the active transition metal center could behave as the effective heterogeneous activator for AOPs. MOFs have been investigated for many applications, including absorption or catalysis in aqueous solution [12-14]. However, most of the reported works on MOFs so far are mainly for dye removal [15-17]. Some researchers found that MOFs could effectively absorb certain dyes, such as methyl orange, methylene blue, and so on. Moreover, some researchers showed that ferrous (Fe)-based MOFs, including MIL-53(Fe), MIL-101(Fe), and MIL-88(Fe), effectively activate water or persulfate for dye removal [18,19]. However, these works mainly focus on discoloration of dye-containing pollutants with iron-based MOFs and activated PS.

MIL-101(Fe) was one kind of MOF with comparable stabil-



1. Structure of (A) diethyl phthalate and (B) dibutyl phthalate.

ity in water and good performance in absorbing pollutant or activating oxidants for pollutant removal [20,21]. This work focused on MIL-101(Fe) developed for absorbing and degrading PAEs. DEP and DBP were used as the model for PAEs found in papermaking wastewater treated by traditional methods.

To our knowledge, ours is the first work about MOF/PS systems for PAEs removal. As mentioned, DEP and DBP could be found in papermaking wastewater. Even after traditional treatment, the level of PAEs in effluents still could be harmful to human beings. Therefore, we applied MIL-101(Fe) to activate PS for DEP and DBP removal. **Figure 1** shows the structures of DEP and DBP. In the traditional paper mills, the concentration of PAEs was less than 1 mg L^{-1} before and after water treatment. However, the model concentration of PAEs in our works was about 3 mg L^{-1}, which could help to tell the ability of MOF/PS systems for PAEs removal [3]. The concentration of PAEs might vary in different kinds of paper mill streams because of specific papermaking techniques, thus it is hard to provide one typical concentration of PAEs in paper mill streams. However, the concentration of 3 mg/L in our model system was based on our measurement in some paper mill streams collected in Zhongshan and Dongguan in China, so that the PAE concentrations of 3 mg/L in our model system is relevant.

EXPERIMENTAL

Chemical

Iron (III) chloride hexahydrate ($FeCl_3 \cdot 6H_2O$) and dimethylformamide (DMF) were bought from Sinopharm Chemical Reagent Co. Ltd. (Beijing, China). DEP, peroxydisulfate, and terephthalic acid (H_2BDC) were obtained from Aladdin Chemistry Co. Ltd. (Shanghai, China). The chemicals were used without purification.

Sample preparation

Fe-MIL-101 was prepared to match other studies [22,23], with some modifications. In a typical procedure, 2.7 g of $FeCl_3 \cdot 6H_2O$, 0.824 g of H_2BDC, and 60 mL of DMF were mixed together and heated at 110°C for 20 h in a Teflon-lined stainless steel reactor. The raw product was filtered off and washed twice with hot ethanol at 60°C for 3 h each time. Finally, the purified product was dried in a vacuum drying oven (70°C) overnight.

Synthetic aqueous solution of DEP or DBP were prepared to be 3 ppm after being stirred for 2 days.

Characterization

Technologies including X-ray diffractometer (XRD) (Bruker; Ettlingen, Germany), Fourier transform infrared spectroscopy (FTIR) (Bruker), thermal field-emission scanning electron microscope (FESEM) (Quanta 200, FEI Co.; Eindhoven, The Netherlands) were used to characterize the morphology and crystallographic structures and so on.

Evaluation of catalytic activity

To investigate the ability of pollutants removal, batch tests were carried out in glass conical flasks. The flasks were shaken in a Zhicheng (Shanghai, China) ZHWY-20102C rotary shaker at 180 rpm at room temperature (25±0.5°C). A certain amount of solution sample was withdrawn at specified intervals, then immediately the same amount of ethanol was added for detection by high performance liquid chromatography (HPLC) using a Shimadzu (Kyoto, Japan) LC-20A with an InertSustain C18 column. For detection of DEP, the mobile liquid was water and methanol mixed at a rate of 65:35 (V/V) at a wavelength of 236 nm and temperature of 40°C. But for detection of DBP, the mobile liquid was water and methanol mixed at a rate of 90:10 (V/V) at a wavelength of 225 nm and temperature of 30°C.The HPLC technique was applied to detect the residual PAEs in water, which could tell the amount removed by MIL-101(Fe)/PS system.

RESULTS AND DISCUSSION

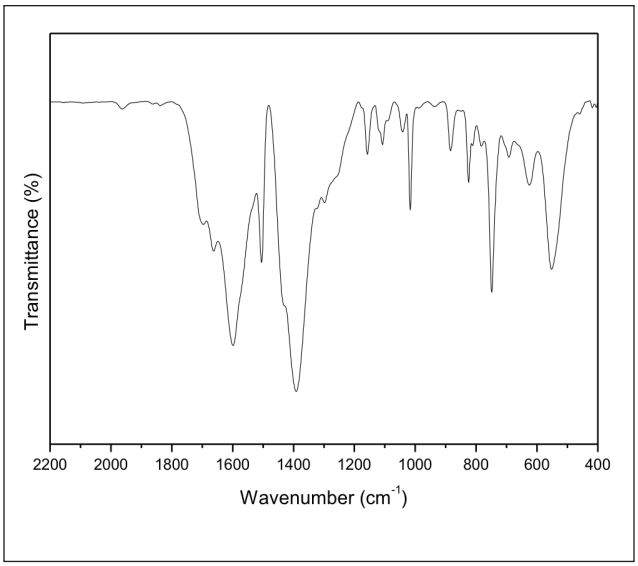
The objective of this research was to study whether MIL-101(Fe)/PS systems could remove PAEs and thereby reduce the environmental impact of papermaking wastewater. The character of MIL-101(Fe) and the ability of MIL-101(Fe)/PS were studied.

Characterization of MIL-101(Fe)

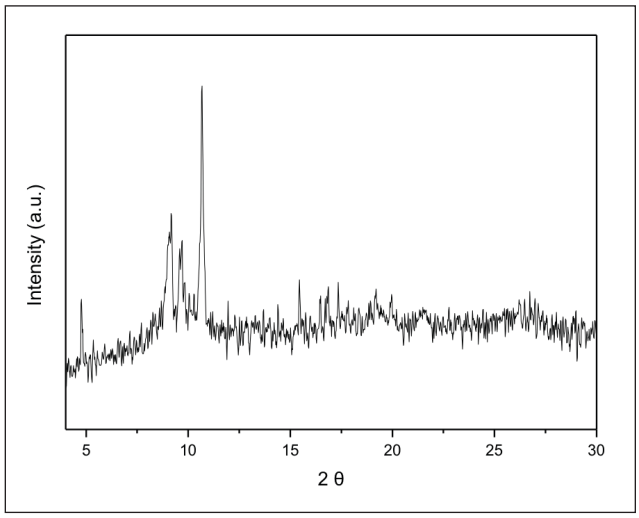
Figure 2 shows the XRD pattern of MIL101 (Fe) before activation. The fresh samples presented the typical peaks near 2θ of 5° and 10°, which agreed well with the previous reports [20,23].

Figure 3 shows the morphology of MIL-101(Fe) that can be observed by SEM. It shows that MIL-101(Fe) has octahedral morphology and is about 0.5 μm to 1.0 μm in diameter. The morphology agreed well with that described in related articles [20,24]. The SEM and XRD patterns together proved the successful preparation of MIL-101(Fe).

FTIR spectroscopy is a sensitive method to detect the vibrations of bonds between different elements, such as metal-oxygen and carbon-oxygen. FTIR was applied to further investigate bonding changes of MIL-101 (Fe). As shown in **Fig. 4**, all peaks of fresh samples were similar to those reported in previous articles [19,20,23]. According to the images, MIL-101(Fe) are built from trivalent metal centers and carboxylate ligands. Typical peaks might result from the carboxylate or Fe-O vibrations. Peaks between 1300 cm^{-1} and 1750 cm^{-1} could be indexed to v_{as}(COO), v_s(COO), and v(C-C) vibrations, which implied that MIL-101 had a dicarboxylate linker. In addition, peaks at about 1110 and 748 cm^{-1} could be indexed to σ(C–H) and γ(C–H) vibrations of aromatic rings. The band at 1659 cm^{-1} could be attributed to the C=O vibration. The peak at about 549 cm^{-1} could be assigned to the Fe-O vibration. All in all, testing showed that MIL-101(Fe) was prepared successfully.



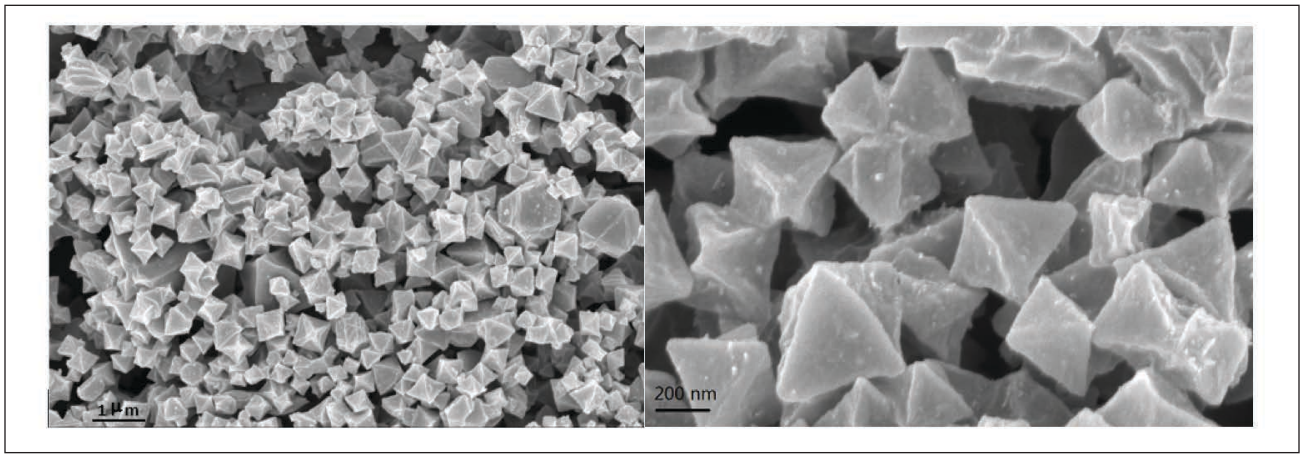
4. Fourier transform infrared (FTIR) spectroscopy spectrum of MIL-101(Fe).



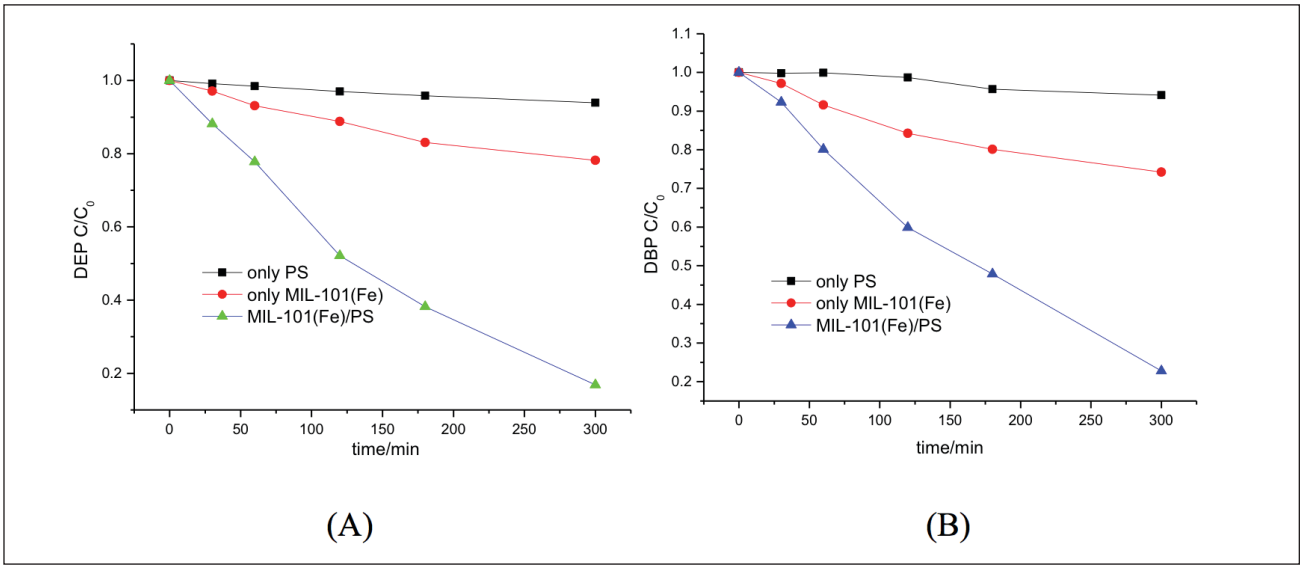
2. X-ray diffractometer (XRD) patterns of MIL-101(Fe).

Removal efficiency of PAEs by MIL-101(Fe)/PS

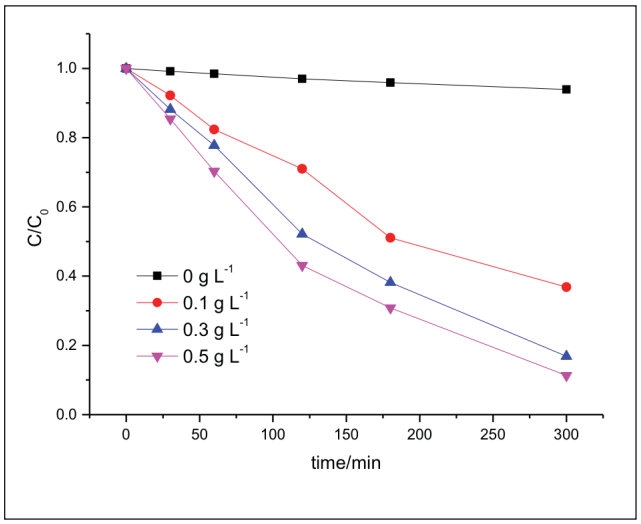
Degradation tests of DEP and DBP were used to study whether a MIL-101(Fe) system could be applied to PAE removal in papermaking wastewater. As **Fig. 5** shows, more than 80% of DEP and DBP could be removed by a MIL-101(Fe)/PS system in a 5 h period. However, only a little of the PAEs could be removed when PS only was added. This might be because the reduction potential of persulfate was not high enough to degrade PAEs. However, when MIL-101(Fe) was added without PS, around 21% of DEP and 26% of DBP could be removed



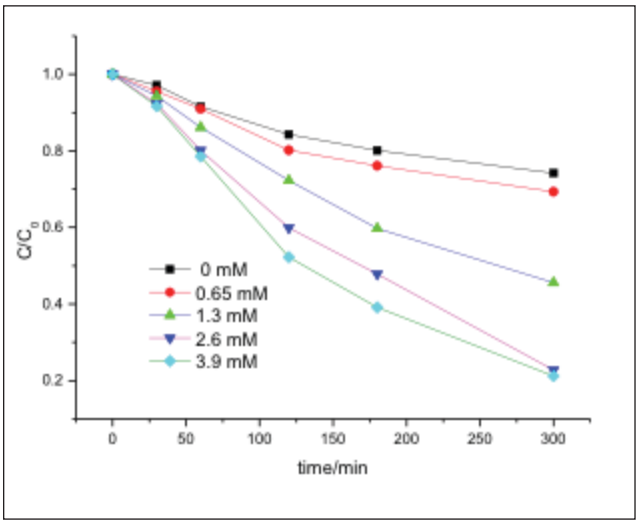
3. Scanning electron microscope (SEM) images of MIL-101(Fe).



5. Removal of diethyl phthalate (DEP) and dibutyl phthalate (DBP) in different conditions. Conditions: DEP or DBP = 3 mg L^{-1}, persulfate (PS) = 2.6 mM, MIL-101(Fe) = 0.3 g L^{-1}.



6. Removal of DBP in different amount of MIL-101(Fe). Conditions: DEP = 3 mg L^{-1}, PS = 2.6 mM.



7. Removal of DBT in different amount of PS. Conditions: DEP = 3 mg L^{-1}, MIL-101(Fe) = 0.3 g L^{-1}.

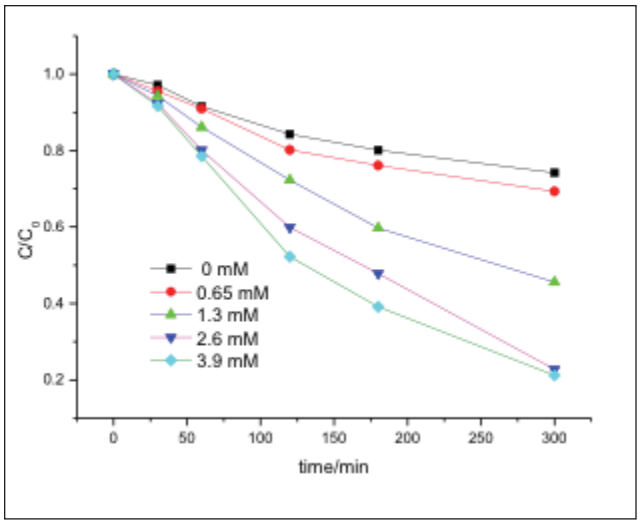
in 5 h. Thus, the MIL-101(Fe) could absorb PAEs. This absorption ability could contribute to PAE removal. According to BET measurement and other studies, the BET surface area could be more than 1000 m^3 g^{-1}. Such a large area offers effective absorption of PAEs. We know that adding MIL-101(Fe) and PS together greatly increases the efficiency of DBP and DEP removal. This phenomenon indicated that the transition metal center of iron could activate PS, which can produce radicals for removing pollutants. The phenomenon of absorption and PS activation occurred at the same time, and these two pathways together promoted PAEs degradation.

Effect of reaction parameters PAEs removal

Our analysis indicated that MIL-101(Fe) could absorb DEP and DBP, and also help activate PS for further DEP and DBP removal. To study the effect of the MIL-101(Fe) and PS dosing more easily, DBP was chosen as the target pollutant in the following research.

Figure 6 shows the effect of MIL-101(Fe). The efficiency increased as the amount of MIL-101(Fe) increased. That might be because the increased amount of MIL-101(Fe) offered more sites for PS activation. Removal efficiency did not increase significantly when the amount of MIL-101(Fe) was more than 0.3 g L^{-1}.

Because PS has a great effect on the treatment process and operational costs, it is important to investigate the effects of using differing amounts of PS. As **Fig. 7** shows, the efficiency of degradation gradually increased as the amount of PS increased. More persulfate could offer more opportunities to contact MIL-101(Fe) to produce more radicals for PAEs degra-



8. Removal of DBT in different initial pHs. Conditions: DEP = 3 mg L^{-1}, MIL-101(Fe) = 0.3 g L^{-1}, PS = 2.6 mM.

dation. However, the removal efficiency did not increase obviously as the PS was more than 2.6 mM. Thus, the material and PS amounts must be controlled when applying a MIL-101(Fe)/PS system for PAEs removal.

The initial pH of traditional Fenton system based on H_2O_2/Fe^{2+} is below 3.5. However, the range of initial pH for persulfate based reaction is larger. As shown in **Fig. 8**, as initial pH changed from 3.0 to 7.5, the reaction ratio changed little. This is because persulfate is an acid oxidant, which can make the pH of wastewater acid and keep the reaction process.

CONCLUSION

Pulp and papermaking industries make important contributions to the development of society. However, raw wastewater and effluents contain various pollutants, which do harm to human health and affect sustainable development. PAEs, including DEP and DBP, which could be potential endocrine-disrupting compounds (EDCs), were still detected after biological treatment. This research tried to apply metal organic frameworks MIL-101(Fe) to activate persulfate for PAEs removal. We found that a MIL-101(Fe)/PS system could remove DEP and DBP. The method we describe provides a feasible way to remove phthalates from papermaking wastewater. **TJ**

ACKNOWLEDGEMENTS

This study was funded by the National Natural Science Foundation of China (No. 31570568, 31670585), China Postdoctoral Science Foundation (2017M622711), High-level Personnel Foundation of Guangdong Higher Education Institutions (201339), Science and Technology Planning Project of Guangzhou City, China (No. 201607010079, 201607020007), State Key Laboratory of Pulp and Paper Engineering in China (No.201535), and the Science and Technology Planning Project of Guangdong Province, China (No. 2016A020221005). The authors thank all the anonymous reviewers for their insightful comments and suggestions.

ABOUT THE AUTHORS

We chose this research topic because it is meaningful to study the removal of phthalates from papermaking wastewater by MIL-101(Fe) in the presence of persulfate. This is the first step in further studies.

The most difficult aspect of this study was that it needed more effort for this technique in the actual application. We learned that advanced oxidation processes based on persulfate activation could degrade phthalates in water. We found it interesting that phthalates in the model system could be effectively degraded.

The results of our study could help mills find more methods for wastewater treatment and pay more attention to phthalates pollution from mills. The next step is to improve the effect of the technique.

Lin is post-doctoral researcher, College of Natural Resources and Environment, South China Agricultural University, Guangzhou, China. Guan is research assistant, Wan is professor, Ma is professor, and Wang is associate professor, South China University of Technology, Guangzhou, China. Email Guan at guanzeyu1@126.com.


Lin


Guan


Wan


Ma


Wang

LITERATURE CITED

1. Balabanic, D., Hermosilla, D., Merayo, N., et al., *J. Environ. Sci. Health, Part A: Environ. Sci. Eng. Toxic Hazard. Subst. Control* 47(10): 1350(2012).
2. Balabanic, D., Filipic, M., Krivograd Klemencic, A., et al., *Sci. Total Environ.* 574: 78(2017).
3. Damjan Balabanič , A.K.K., *Fresenius Environ. Bull.* 20(1): 86(2011).
4. Yu, R. and Wan, J., *Paper and Papermaking* 28: 47(2009).
5. Begum, J.A., Menezes, G.B., and Moo-Young, H.K., *Water Environ. Res.* 84(10): 1502(2012).
6. Lin, X.-M., Ma, Y.-W., Wang, Y., et al., *RSC Adv.* 5(115): 94694(2015).
7. Oh, S.-Y., Kang, S.-G., and Chiu, P.C., *Sci. Total Environ.* 408(16): 3464(2010).
8. Lin, X., Ma, Y., Wan, J., et al., *Chem. Eng. J.* 315: 304(2017).
9. Lutze, H.V., Kerlin, N., and Schmidt, T.C., *Water Res.* 72: 349(2015).
10. Olmez-Hanci, T. and Arslan-Alaton, I., *Chem. Eng. J.* 224: 10(2013).
11. Yang, Y., Pignatello, J.J., Ma, J., et al., *Environ. Sci. Technol.* 48(4): 2344(2014).
12. Du, J.J., Yuan, Y.P., Sun, J.X., et al., *J. Hazard. Mater.* 190(1-3): 945(2011).
13. Janiak, C. and Vieth, J.K., *New J. Chem.* 34(11): 2366(2010).
14. Hasan, Z. and Jhung, S.H., *J. Hazard. Mater.* 283: 329(2015).
15. Lin, S., Song, Z., Che, G., et al., *Microporous Mesoporous Mater.* 193: 27(2014).
16. Haque, E., Jun, J.W., and Jhung, S.H., *J. Hazard. Mater.* 185(1): 507(2011).
17. Haque, E., Lee, J.E., Jang, I.T., et al., *J. Hazard. Mater.* 181(1-3): 535(2010).
18. Lv, H., Zhao, H., Cao, T., et al., *J. Mol. Catal. A: Chem.* 400: 81(2015).
19. Vu, T.A., Le, G.H., Dao, C.D., et al., *RSC Adv.* 4(78): 41185(2014).
20. Li, X., Guo, W., Liu, Z., et al., *Appl. Surf. Sci.* 369: 130(2016).
21. Yue, X., Guo, W., Li, X., et al., *Environ. Sci. Pollut. Res. Int.* 23(15): 15218(2016).
22. Oller, I., Malato, S., and Sanchez-Perez, J.A., *Sci. Total Environ.* 409(20): 4141(2011).
23. Skobelev, I.Y., Sorokin, A.B., Kovalenko, K.A., et al., *J. Catal.* 298: 61(2013).
24. Balu, A.M., Lin, C.S.K., Liu, H., et al., *Appl. Catal., A* 455: 261(2013).

ABOUT THIS PAPER

Cite this article as: Lin, X., Guan, Z., Wan, J., et al. *TAPPI J.* 17(3):181(2018). https://doi.org/10.32964/TJ17.03.181

DOI: https://doi.org/10.32964/TJ17.03.181

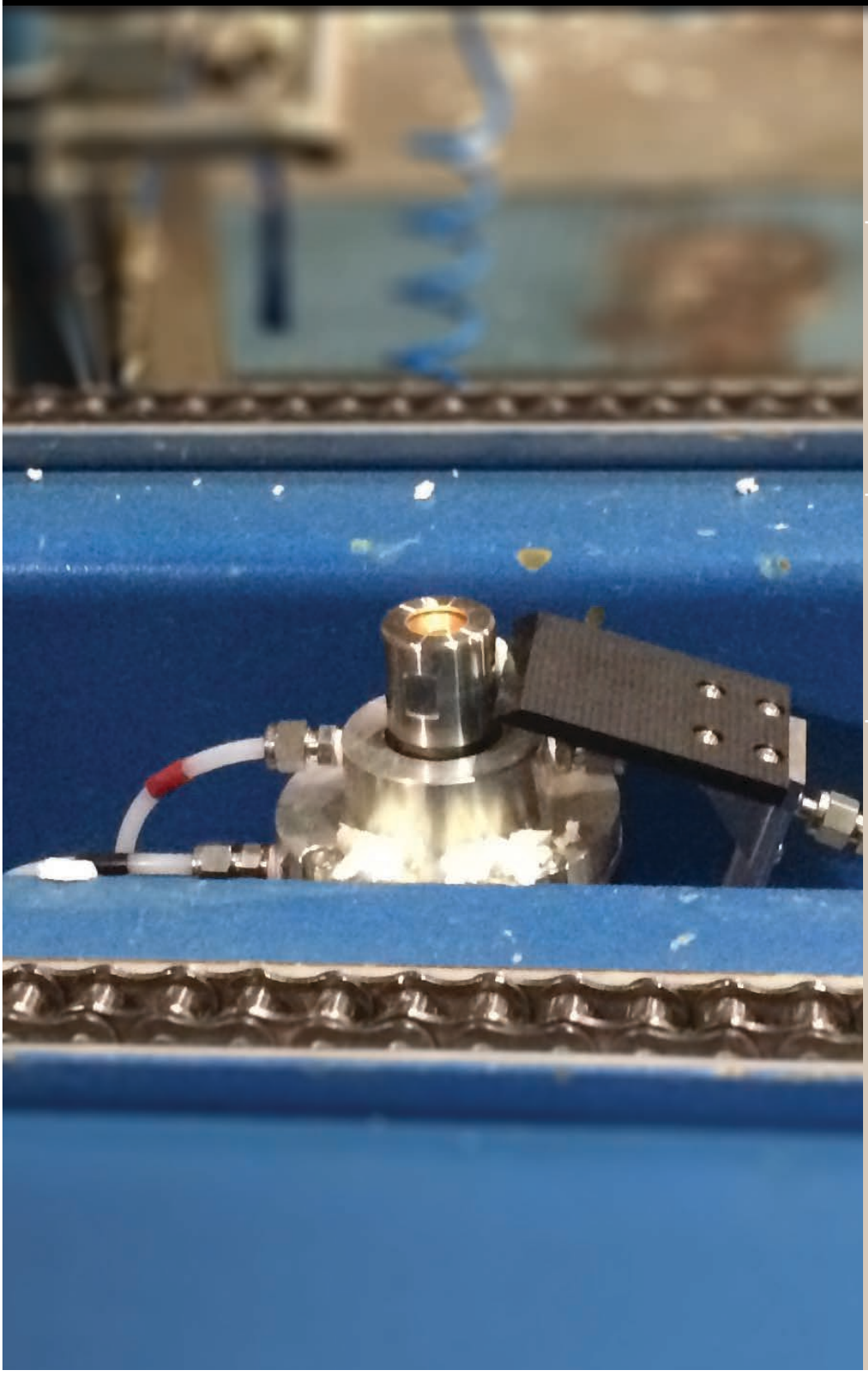
ISSN: 0734-1415

Publisher: TAPPI Press

Copyright: ©TAPPI Press 2018

About this journal

TAPPI JOURNAL
WWW.TAPPI.ORG
THE PAPER AND PACKAGING INDUSTRIES' TECHNICAL RESOURCE
APRIL 2018 | VOL. 17 NO. 4



RECOVERY CYCLE 197
Monitoring the free lime content in lime mud using zeta potential
Wei Ren and Honghi Tran

PULPING 207
Online measurement of bulk, tensile, brightness, and ovendry content of bleached chemi-thermomechanical pulp using visible and near infrared spectroscopy
Matthew R. Tomkins, Wesley Gilbert, and Thanh Trung

CORRUGATED CONTAINERS 219
Importance of specimen preparation for edgewise compressive strength (ECT) testing
Jerry Loza, Doug Cash, and Benjamin Frank

PAPERBOARD 231
On the nominal transverse shear strain to characterize the severity of creasing
Douglas W. Coffin and Joel C. Panek

April 2018

TABLE OF CONTENTS VOL. 17 NO. 4

193 EDITORIAL
Shifts and gains in research funding
Monica Shaw

197 RECOVERY CYCLE
Monitoring the free lime content in lime mud using zeta potential
Wei Ren and Honghi Tran

207 PULPING
Online measurement of bulk, tensile, brightness, and ovendry content of bleached chemithermomechanical pulp using visible and near infrared spectroscopy
Matthew R. Tomkins, Wesley Gilbert, and Thanh Trung

219 CORRUGATED CONTAINERS
Importance of specimen preparation for edgewise compressive strength (ECT) testing
Jerry Loza, Doug Cash, and Benjamin Frank

231 PAPERBOARD
On the nominal transverse shear strain to characterize the severity of creasing
Douglas W. Coffin and Joel C. Panek

»COVER CREDIT: To provide real-time data on pulp properties as a complement to handsheet testing, researchers Tomkins, Gilbert, and Trung (p. 207) developed and trialed a prototype online visible and near infrared (Vis-NIR) sensor. The system consists of a cabinet located near a probe (shown) on a conveyor belt so that when the pulp bale stops on it, the probe rises and contacts the bale to take a spectral measurement for predicting its properties.

TAPPI JOURNAL
WWW.TAPPI.ORG

Editor-in-Chief
Brian N. Brogdon brian.brogdon@gmail.com
+1 678 581-9114

Associate Editor
Peter W. Hart peter.hart@westrock.com
+1 409 276-3465

Editorial Director
Monica Shaw mshaw@tappi.org
+1 770 367-9534

PRESS Manager
Jana Jensen jjensen@tappi.org
+1 770 209-7242

Webmaster
Trina Heath theath@tappi.org
+1 770 209-7416

***TJ* EDITORIAL BOARD**

Randy Branston, BASF
randy.branston@basf.com, +1 704 819-4251

Brian N. Brogdon, FutureBridge Consulting & Training LLC
brian.brogdon@gmail.com, +1 678 581-9114

David A. Carlson, Carlson Consulting
dacarlson39@aol.com, +1 847 323-2685

Mahendra Doshi, Doshi and Associates
mahen@aol.com, +1 920 832-9101

Marc Foulger, GL&V USA Inc.
Marc.foulger@glv.com +1 315 767-2920

Peter W. Hart, WestRock
peter.hart@westrock.com, +1 409 276-3465

Carl J. Houtman, USDA Forest Products Laboratory
choutman@fs.fed.us, + 1 608 231-9445

Lucian Lucia, North Carolina State University
lucian.lucia@gmail.com, +1 919 889-7059

John A. Neun, John A. Neun LLC
john.neun@gmail.com, +1 518 275-8139

Jim Niemiec, Verso Corporation
jim.niemiec@versoco.com, +1 715 422-7404

Steven P. Ottone, Omya
steven.ottone@omya.com, +1 919 641-7854

Gaurav Pranami, Imbed Biosciences
gpranami@imbedbio.com, +1 515 230-7005

Arthur Ragauskas, Oak Ridge National Laboratory
aragausk@utk.edu

Gerard J.F. Ring, University of Wisconsin—Stevens Point
gerrryring@wi-net.com, +1 715 592-3732

Scott Rosencrance, Kemira Chemicals
scott.rosencrance@kemira.com, +1 770 429-2753

Paul Wiegand, NCASI
pwiegand@ncasi.org, +1 919 941-6417

Junyong Zhu, USDA Forest Products Laboratory
jzhu@fs.fed.us, +1 608 231-9520

Join TAPPI *today!*

TAPPI JOURNAL is a free benefit of TAPPI membership, and is only available to members. To join TAPPI, to renew your TAPPI Membership, or to learn about other valuable benefits, visit www.tappi.org.

TAPPI, 15 Technology Parkway S., Suite 115, Peachtree Corners, GA 30092, publishes *TAPPI JOURNAL* monthly.

ATTENTION PROSPECTIVE AUTHORS: All papers published are subject to *TAPPI JOURNAL's* peer-review process. Not all papers accepted for review will be published. Before submitting, check complete author guidelines at http://www.tappi.org/s_tappi/doc.asp?CID=100&DID=552877.

Statements of fact and opinions expressed are those of individual authors. TAPPI assumes no responsibility for such statements and opinions. TAPPI does not intend such statements and opinions or construe them as a solicitation of or suggestion for any agreed-upon course of conduct or concerted action of any sort.

Copyright 2018 by TAPPI, all rights reserved. For copyright permission to photocopy pages from this publication for internal or personal use, contact Copyright Clearance Center, Inc. (CCC) via their website: www.copyright.com. If you have questions about the copyright permission request process, please contact CCC by phone at +1 978 750-8400. To obtain copyright permission to use excerpts from this publication in another published work, send your specific request in writing to Editor, TAPPI JOURNAL, 15 Technology Parkway S., Suite 115, Peachtree Corners, GA 30092, USA; or by fax to +1 770 446-6947. Send address changes to TAPPI, 15 Technology Parkway S., Suite 115, Peachtree Corners, GA 30092, USA; Telephone +1 770 446-1400, or FAX +1 770 446-6947. www.tappi.org

Editorial

MONICA SHAW | EDITORIAL DIRECTOR
mshaw@tappi.org



Shifts and gains in research funding

A Pew Research Center survey of U.S. citizens in 2015 highlighted interesting opinions regarding science and its funding. Among other findings, the survey showed that around 70% of adults felt government investments in engineering and technology, as well as basic scientific research, will pay off in the long term [1]. It also revealed that 61% of respondents considered government investment as essential for scientific progress, with just 34% saying private investment is enough to make sure science evolves.

The Pew findings are especially interesting given that, in the U.S., the government's funding of basic research at companies dropped to just 44% of the $86 billion spent in 2015, according to the National Science Foundation (NSF) [2]. This is after topping 70% in the 1960s and 1970s and holding around 60% in 2004. However, basic research makes up only about one-sixth of the total research and development (R&D) spending at U.S. companies, with applied research taking up another one-sixth and development taking the bulk of funding at $316 billion.

The NSF data also showed creeping growth in basic research by universities and private foundations in 2015, making up 25% of the total. In this column, we'll take a look at the shifts in university R&D funding in the U.S.

Federal funding at universities grows, but share drops

Notably, federal funding for higher education research did increase between FY 2015 and FY 2016 after falling for four straight years, according to the National Center for Science and Engineering Statistics (NCSES) [3]. Of the 640 universities in the NCSES Higher Education Research and Development (HERD) Survey that reported $1 million or more in R&D, federal funding for R&D increased 2.5% to $38.8 billion, but a closer look at the data showed that government's funding share had actually dropped to 54% from about 63% in 2011.

Where did the growth in federal funding from 2015 to 2016 occur? While NSF funding remained the same, dollars from NASA and the Departments of Agriculture, Defense, Energy, and Health and Human Services saw increases ranging from 2% to 5%. Funds from other federal agencies, however, dropped around 5%.

About 65% of R&D for higher education is spent in three areas. At the top are health sciences at $22.4 billion, followed by biological and biomedical sciences ($13 billion) and engineering ($11.4 billion).

Non-federal sources of funding see largest gains

While government funding of university R&D grew more moderately, non-federal sources saw larger increases, according to NCSES [3]. The total rose 7.6% in 2016 over the previous year to $33 billion.

The non-federal source that grew the most was from nonprofit organizations, which rose over 9% to $4.6 billion. Other sources like foreign governments and donors grew almost 9%.

Following closely behind in terms of funding outside the government was university funding of R&D, which grew 8.2% to about $18 billion. Most of this growth came from direct funding from universities for R&D, which has grown almost 50% since 2012.

Hope amid uncertainty

Given the value the public places on scientific research, the hope is that funding continues to increase for U.S. universities, including those with programs in pulp, paper, bioenergy, and biomaterials, so that these industries are sustained and prepared for growth by evolving science. With many economic, political, and shifts in funding focus at play, this evolution will be compelling to watch, as will the reported spending data from organizations like NSF. **TJ**

References

1. Funk, C. and Rainie, L., "Public and Scientists' views on science and society," Pew Research Center, January 2015.
2. Mervis, J., "Data check: U.S. government share of basic research funding falls below 50%," Science, March 2017.
3. Britt, R., "Universities report increased federal R&D funding after 4-year decline; R&D fields revised for FY 2016," NSF/NCSES, November 2017.

Monitoring the free lime content in lime mud using zeta potential

WEI REN AND HONGHI TRAN

ABSTRACT: The presence of unreacted lime (free lime) in the lime mud can cause many problems in the chemical recovery operation of kraft pulp mills. There are currently no standards for free lime determination. Conventional methods used in mill laboratories require extensive preparations and give inconsistent and sometime erroneous results.

A systematic study was performed to determine if zeta potential, a dispersion characteristic of the lime mud and liquor slurry, can be used to indirectly indicate the amount of free lime in the lime mud. Lime mud with different free lime contents was produced in the laboratory by causticizing green liquors with lime at different liming ratios. The results show that zeta potential changes from negative to positive when the free lime in lime mud exceeds a critical value. This unique characteristic enables a rapid detection of free lime.

Application: This research can help mills take appropriate actions to avoid problems associated with "overliming" in the recovery process.

In the causticizing plant of kraft pulp mills, lime (CaO) is used to convert sodium carbonate (Na_2CO_3) in green liquor into sodium hydroxide (NaOH) in white liquor. The causticizing process is carried out by two main reactions:

$$CaO + H_2O \rightarrow Ca(OH)_2 \quad \text{(Reaction 1)}$$

$$Na_2CO_3 + Ca(OH)_2 \rightarrow 2NaOH + CaCO_3 \quad \text{(Reaction 2)}$$

Reaction 1 is the slaking reaction, which occurs rapidly in the slaker to form calcium hydroxide ($Ca(OH)_2$). Reaction 2 is the causticizing reaction, which is much slower and occurs in both the slaker and the causticizers. The resulting slurry is a mixture of white liquor that is mostly NaOH, sodium sulfide (Na_2S) and unreacted Na_2CO_3, and lime mud that is mostly calcium carbonate ($CaCO_3$) and unreacted $Ca(OH)_2$. The slurry is sent through a clarifier or a pressure filter to separate the white liquor and lime mud. The mud is washed to remove residue white liquor and dewatered with precoat drum filters before being fed into a lime kiln where it is calcined into reburned lime (CaO) for reuse in the slaker.

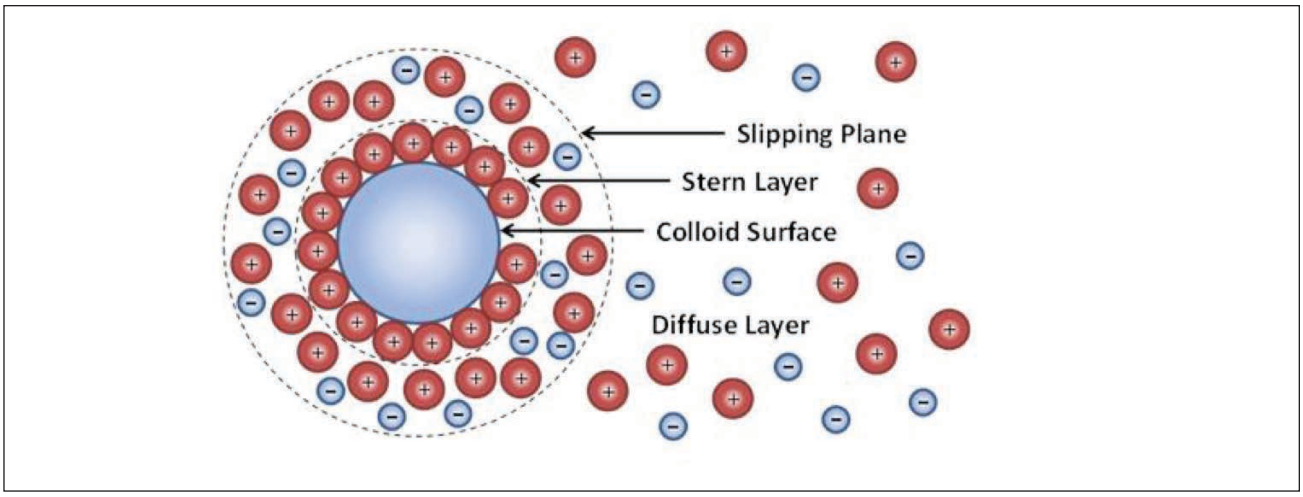
The causticizing reaction is an equilibrium reaction. Under a given operating condition, the reaction proceeds to the right only when the hydroxyl ion concentration in the liquor is below the equilibrium concentration of the system. When hydroxyl ion exceeds the equilibrium concentration, the reaction reverses, producing $Ca(OH)_2$ and Na_2CO_3 until a new equilibrium is reached. The degree of completion for the causticizing reaction can be expressed as the causticizing efficiency (CE), which is defined in the following equation:

$$CE\ (\%) = \frac{[OH]}{[OH] + [CO_3]} \times 100 \quad (1)$$

where [OH] and [CO_3] are the hydroxide and carbonate concentration, respectively, expressed in g/L Na_2O.

Under a given operating condition, the highest degree of completion the causticizing reaction can reach is known as equilibrium CE. The correlations between equilibrium CE, total titratable alkali (TTA), and sulfidity of the liquor are known as the Goodwin curves [1-3]. Theoretically, equilibrium CE is equivalent to the maximum liming ratio (or CaO/Na_2CO_3 molar ratio) [4]. For example, if an equilibrium CE of 85% is desired, the amount of lime added into the slaker should be adjusted so that the liming ratio is equal to 0.85. Exceeding this ratio would cause the system to be "overlimed" and the resulting lime mud would contain unreacted $Ca(OH)_2$ or "free lime". Similarly, if the amount of lime added to the slaker is insufficient, the system is said to be "underlimed". In practice, because the exact amount of lime added to the slaker is often not known, many mills have to set their target CE at about 5% below the equilibrium CE to avoid free lime [5] by controlling their lime addition, either manually or automatically through various control systems. However, if the reburned lime quality is low or if the residence time for the causticizing reaction is short, the resulting lime mud can still contain free lime.

The presence of free lime can cause many problems in causticizing plants and lime kilns, including "dirty" white liquor, poor mud settling, pressure filter clogging, low mud solids, and high sodium content in lime mud [6]. These prob-



1. Double layer model for zeta potential [9].

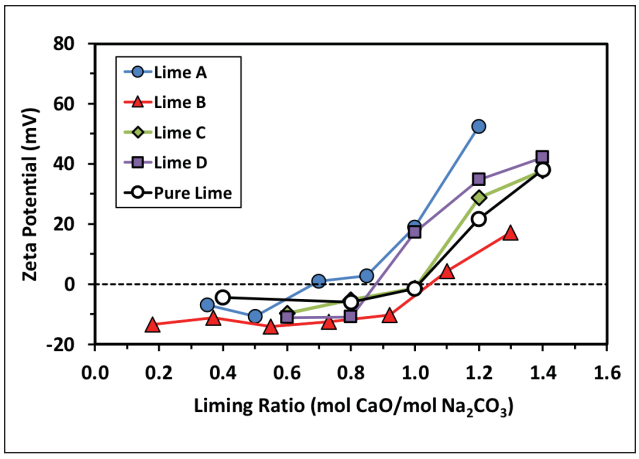
lems could lead to ring formation in the lime kiln, increased total reduced sulfur (TRS) emissions, and reduced kiln thermal efficiency [7]. Even though free lime in lime mud can be used as an indication for overliming, many mills do not regularly monitor the free lime content due to difficulties associated with the measurement methodology and varying consistency with the result.

A previous study was conducted to understand why the measured free lime was consistently low at mills with problems associated with free lime [8]. Since a standard method for free lime measurement does not exist, the study examined the validity of two main analytical methods that are often used to determine free lime. The ammonium chloride (NH_4Cl) method uses NH_4Cl to dissolve $Ca(OH)_2$ and separate it from the mud, as well as titration to determine the amount of dissolved free lime. The other method is the thermal decomposition (TD) method where a sample is heated in a muffle furnace at up to 400°C, and the weight loss due to $Ca(OH)_2$ decomposition is used to estimate the amount of free lime. The study concluded that the NH_4Cl method is not suitable for free lime measurement and the TD method is more accurate as long as error associated with the presence of $Mg(OH)_2$

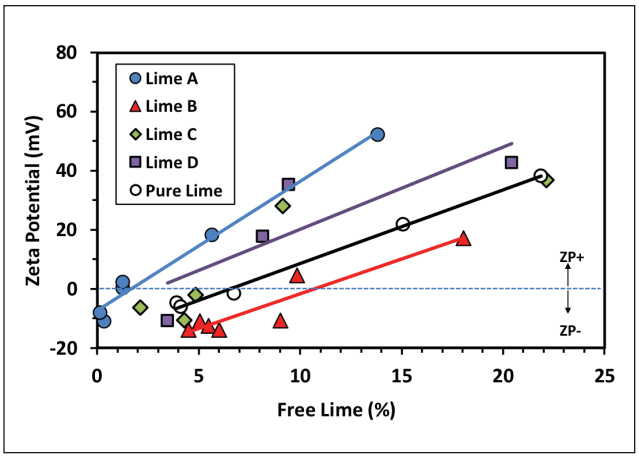
Physical Properties	**Lime A**	**Lime B**	**Lime C**	**Lime D**
Mean number diameter, μm	7.4	30.9	14.2	10.3
Specific surface area, m^2/g	0.8	0.3	0.4	0.6
Zeta Potential, mV	+36.6	+32.2	+34.3	+31.6
Chemical Composition, wt%				
CaO	88.1	91.7	86.2	89.3
MgO	5.5	4.3	1.9	2.6
Na_2O	1.4	0.7	1.5	1.4
P_2O_5	1.5	1.6	2.5	2.0
MnO	0.9	0.01	n/a	0.02
SO_3	0.7	1.0	0.9	1.5
Fe_2O_3	0.5	0.1	n/a	0.1
SiO_2	0.2	0.3	0.4	0.4
Al_2O_3	0.2	0.1	0.3	0.1
LOI	0.8	0.2	6.3	2.6

CaO = lime; MgO = magnesium oxide; Na_2O = sodium oxide; P_2O_5 = phosphorus pentoxide; MnO = manganese(II) oxide; SO_3 = sulfur trioxide; Fe_2O_3 = ferric oxide; SiO_2 = silicon dioxide; Al_2O_3 = aluminum oxide; LOI = Loss on Ignition, mostly CO_2 and H_2O.

I. Physical and chemical characteristics of reburned lime [11]



2. Effect of liming ratio on zeta potential [11].



3. Zeta potential as a function of free lime content as measured by thermal decomposition method [11].

is taken into account. The study also concluded that mud washing significantly lowers free lime content, and lime mud samples need to be taken before the pre-coat filters to obtain an accurate measurement of free lime. Finally, the study calls for a new method that can effectively and quickly determine free lime content.

ZETA POTENTIAL

Zeta potential is a dispersion characteristic of the lime mud slurry. It is a measure of the difference in electrical potential between the particle surface and the solution. Zeta potential of a system can be affected by its chemical composition and concentration, i.e., free lime content. Zeta potential is most often used to indicate the stability of the colloidal system. In general, dispersion systems with a higher absolute zeta potential will cause particles to repel one another, leading to a more stable system. On the other hand, dispersion systems with a lower absolute zeta potential will cause particle agglomeration, resulting in a faster settling rate [9].

As schematically shown in **Fig. 1**, zeta potential is a measure of the double layer force [10]. Charges build up at the colloid surface, forming an electrostatic field that affects other ions in the solution. The negatively charged colloid experiences attraction forces from the positively charged ions and repulsion forces from the negatively charged ions. Ions that are absorbed to the colloid surface form an inner stationary layer known as the "Stern layer". Ions on the outer surface form the free flowing dispersion medium called the "diffuse layer". The slipping plane is an imaginary boundary that sets apart the Stern and the diffuse layer [9]. Theoretically, zeta potential is the potential difference between the particle surface and the slipping plane.

Azgomi measured zeta potential of lime mud slurries using a micro-electrophoretic apparatus based on laser light-scattering theories [11]. The lime mud was prepared by causticizing synthetic green liquor made of pure Na_2CO_3 solution with both pure lime (CaO) and reburned lime from four kraft pulp mills (**Table I**) at different liming ratios. She showed that zeta potential is relatively constant and negative at liming ratios below 1.0, but it drastically increases and becomes positive as liming ratios exceed 1.0 (**Fig. 2**). When zeta potential is plotted against the free lime content of the lime mud samples, the correlations are clearly linear, as shown in **Fig. 3**.

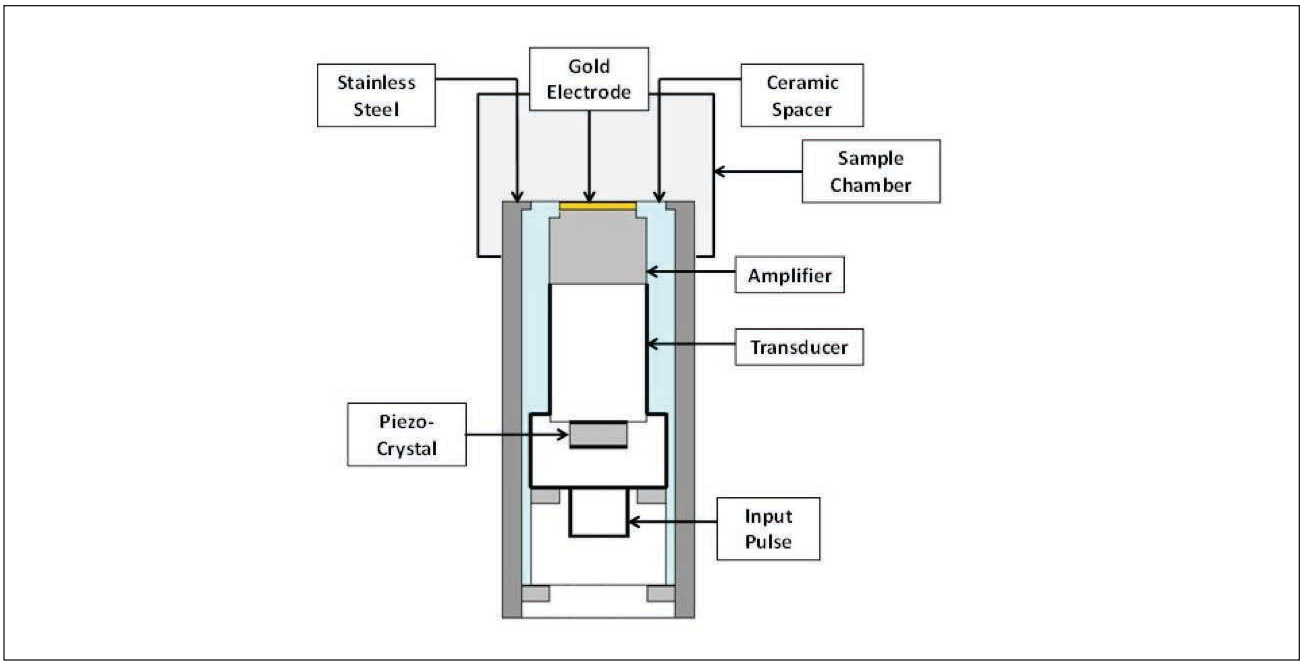
A systematic study was further conducted on lime mud slurries prepared directly from mill green liquor and reburned lime to: 1) verify Azgomi's finding that a correlation exist between zeta potential and liming ratio (or free lime), and 2) determine the effect of various parameters (e.g., lime reactivity) on zeta potential. This paper discusses the methodology used to conduct the experiments, the main results, and their implications.

METHODOLOGY

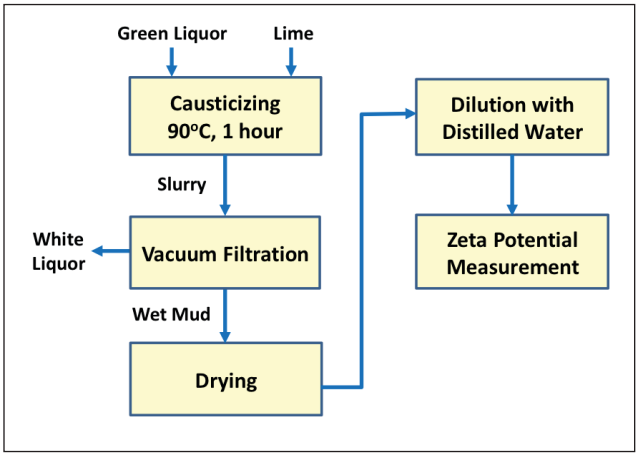
The relationship between zeta potential and liming ratio was studied using both pure chemicals and mill samples. The zeta potential of lime mud slurries produced with different liming ratios was measured using an acoustic and electroacoustic spectrometer (Model DT-1202, Dispersion Technology Inc.; Bedford Hills, NY, USA). This acoustic-based instrument allowed tests to be performed at a higher slurry concentration than the previously used laser light scattering-based instrument [11]. Thermogravimetric analysis (TGA) was used to determine the free lime content in the lime mud.

Figure 4 shows the schematic diagram of the DT-1202 measurement probe. A sample chamber is attached to a measurement probe. The piezo-crystal at the bottom of the probe receives an input pulse and produces ultrasound waves that reach the sample in the sample chamber through the gold electrode. The transducer and amplifier adjust the transmission of ultrasound waves according to the sample composition. The ultrasound waves, in turn, produce particle motion within the sample and set up an oscillating potential on the gold electrode. This potential is then used in combination with sample concentration to calculate the zeta potential.

Synthetic lime mud and liquor samples were prepared using analytical grade chemicals with purity of >99.9%. For mill green liquor samples, the TAPPI Standard Test Method



4. Zeta potential measurement probe used in DT-1202.



5. Experimental procedure flowchart.

624 cm-00 "Analysis of soda and sulfate white and green liquors" was used to determine the carbonate (CO_3) concentration so that appropriate amounts of lime could be added to obtain a wide range of liming ratios. The DT-1202 instrument was calibrated daily using a standard slurry of 10 wt% silica in 0.01 M potassium chloride (KCl).

Figure 5 shows simplified sample preparation and measurement procedures used in this study. Tightly sealed plastic bottles containing pure Na_2CO_3 solution or mill green liquor were heated in a well-agitated water bath controlled at 90°C. Various amount of pure CaO or mill reburned lime were then added to produce a wide range of liming ratios. The causticizing reactions were carried out for 1 h in order for the system to reach equilibrium. The resulting white liquor slurry was filtered and the separated wet lime mud slurry was dried for 90 min in an oven controlled at 120°C. The lime mud was diluted to 1 wt% concentration and zeta potential was measured at room temperature.

The zeta potential measurement probe took into account the effect of pH of the sample slurry. For each measurement, the instrument required the sample pH value was input to its proprietary software program before it could provide a calibrated zeta potential value. However, since the pH of the lime mud produced from various reburned lime samples at different liming ratios were all about the same, around 12, it had little effect on zeta potential measurement.

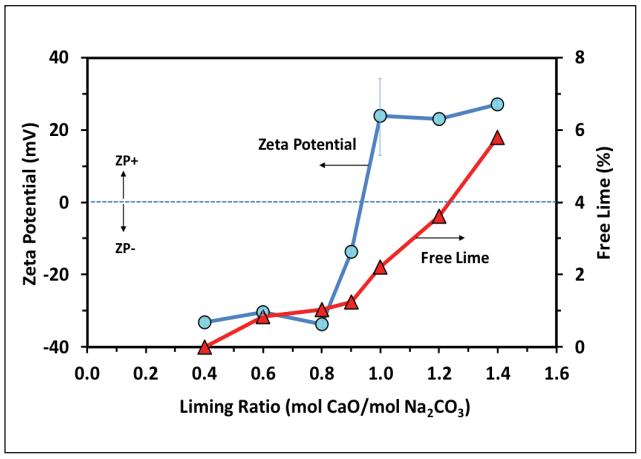
RESULTS AND DISCUSSION

Effects of liming ratio and free lime on zeta potential

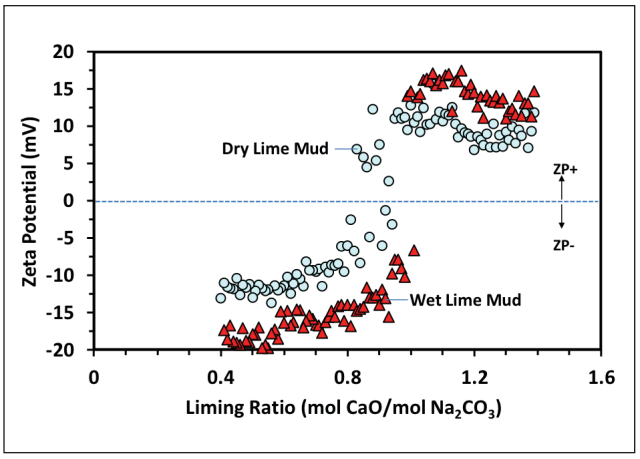
Measurements of zeta potential were first made on lime mud samples produced using pure CaO and Na_2CO_3 using procedures outlined in the previous section. Experiments were repeated up to 20 times, and each lime mud sample was measured 3 times to determine the reproducibility of the results.

Figure 6 shows the effects of liming ratio and free lime on zeta potential. The zeta potential is expressed as millivolts (mV), liming ratio as CaO/Na_2CO_3 molar ratio, and free lime contents as wt% $Ca(OH)_2$ in lime mud. When the liming ratio is equal to or below 0.8, the average zeta potential is negative. However, when the liming ratio exceeds 0.8, the zeta potential becomes positive. The results are more inconsistent at the liming ratio = 1.0.

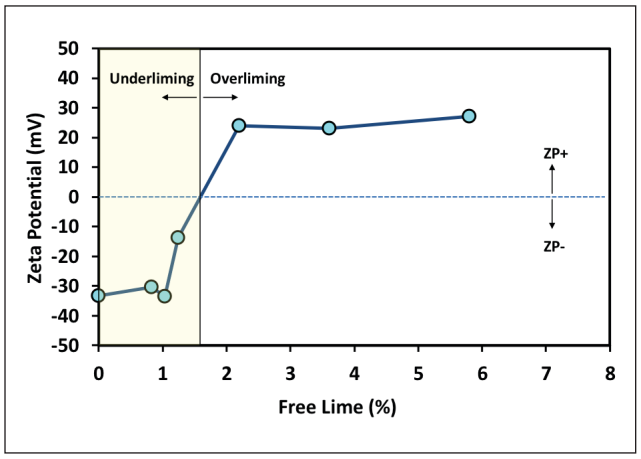
These results are consistent with the previous study showing that underliming and overliming systems had negative and positive zeta potential values, respectively [11]. The high variation in zeta potential measurements at the liming ratio of 1.0



6. Zeta potential and free lime content of lime mud as a function of liming ratio between 0.4 and 1.4 (pure chemicals, 1 h reaction, 90°C reaction temperature, oven dried).



8. Zeta potential of lime mud as a function of liming ratio between 0.4 and 1.4. Samples were prepared from mill green liquor and reburned lime at 90°C for 1 h. Both wet and dried lime mud samples were tested.



7. Zeta potential of lime mud as a function of free lime. Samples were prepared from pure chemicals at 90°C for 1 h and oven dried.

is expected since the system was either slightly underlimed or overlimed. The region between liming ratios of 0.8 and 1.0 is thus referred to as the "transition zone". Figure 6 also shows zeta potential versus free lime content of lime mud prepared at different liming ratios. Since pure chemicals are used and the reactions are well controlled, free lime contents are expected to be low for liming ratios below 1.0. As the system becomes overlimed, the free lime content increases to almost 6 wt%.

Figure 7 plots zeta potential against free lime content. When the free lime content is below 2 wt%, the average zeta potential is negative, and when the free lime content is above 2 wt%, the average zeta potential becomes positive. This means that zeta potential can be used to represent free lime concentration in lime mud within the typical range of liming ratio observed under normal causticizing plant operations. A positive zeta potential can be used to quickly indicate an overlimed system.

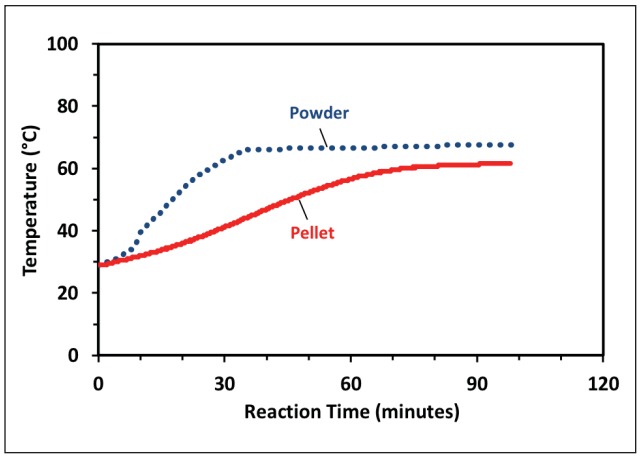
The zeta potential values of numerous lime mud samples, both wet and dry, produced with mill green liquor and reburned lime are shown in **Fig. 8**. The samples were prepared and measured at 0.01 liming ratio increments in order to observe how zeta potential changes in the transition zone where liming ratios range from 0.8 to 1.0.

The overall trend of zeta potential is similar between wet and dried lime mud. An abrupt increase in zeta potential occurs at a liming ratio of about 0.9 and becomes relatively constant at a higher liming ratio. The main difference between wet and dried lime mud measurements is that the dried mud samples have a smaller change in zeta potential from a negative value to a positive value in the transition phase. This difference may be caused by impurities that are present in the residual liquor remaining in the wet lime mud samples, since polyvalent ions such as aluminum (Al^{3+}) and silicon (Si^{4+}) can have an impact on zeta potential values [9].

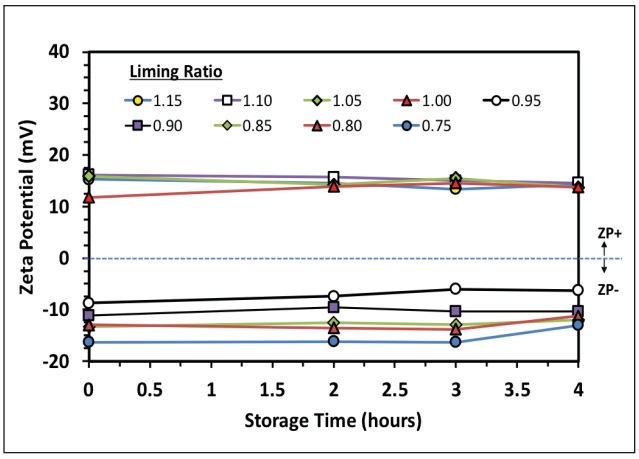
Since wet lime mud samples have a more abrupt/clear change in zeta potential values at a liming ratio of about 0.9, they are more advantageous for use in the development of a free lime monitoring system. Furthermore, wet lime mud samples are easier to prepare than dried mud samples, making it possible for mills to quickly detect a rapid rise in free lime and respond to an overliming situation in a more timely and appropriate manner. The bigger difference in zeta potential between underlimed and overlimed systems also allows more flexibility when setting a threshold for free lime detection.

Effect of lime properties on zeta potential

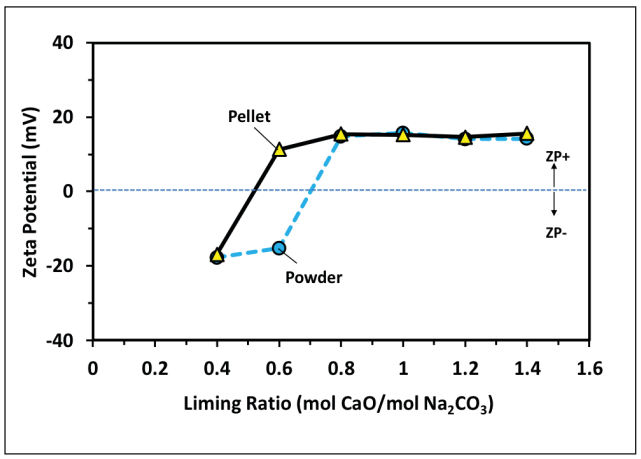
Since poor lime quality can adversely affect the causticizing reaction and increase the residence time required to reach maximum CE, the sensitivity of zeta potential was tested using limes at various sizes to simulate a change in lime reactivity. Lime reactivity was tested in an isotherm cylindrical Dewar container with a laboratory stirrer. Powdered lime and pelleted lime (ranging from 1 mm to 2 mm in diameter) were used and their reactivity is shown in **Fig. 9**. Compared to pel-



9. Change in water temperature during slaking tests of a reburned lime sample in both pellet and powder forms.



11. Zeta potential of lime mud as a function of storage time (1 h reaction, 90°C reaction temperature).



10. Zeta potential of lime mud slurry as a function of liming ratio between 0.4 and 1.4. Lime mud samples prepared by causticizing mill green liquor with reburned lime pellets and pulverized lime at 90°C for 1 h.

leted lime, powdered lime reaches a higher steady state temperature and also reaches that temperature in a shorter period of time.

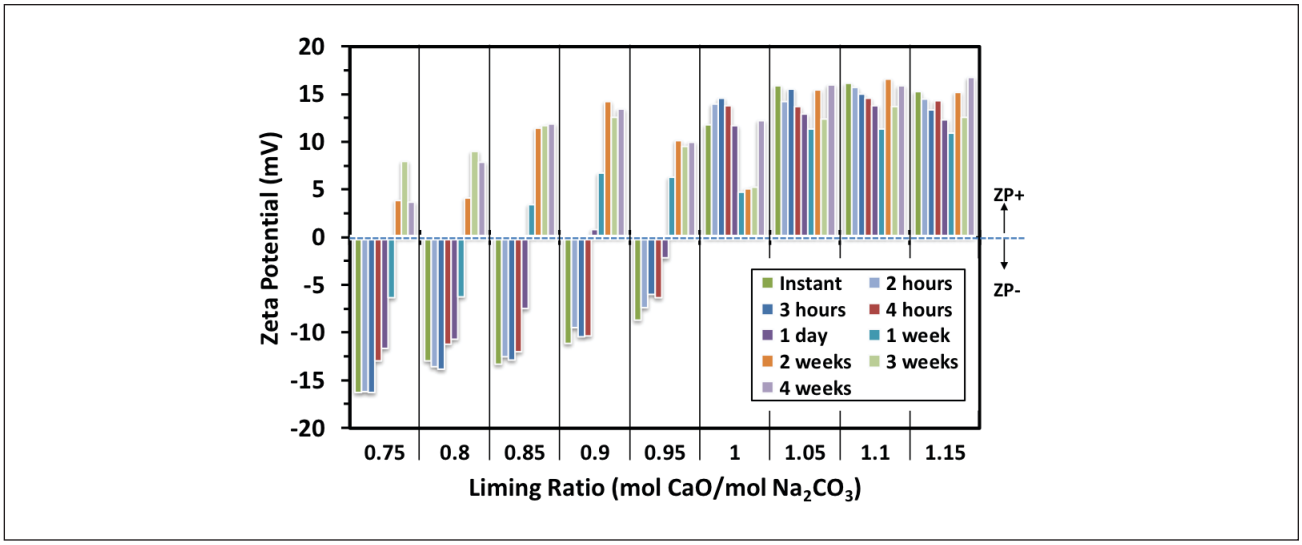
Figure 10 shows the zeta potential of lime mud samples prepared using both powdered and pelleted lime at various liming ratios. When the liming ratio is equal to 0.6 (i.e., underlimed system), samples prepared using pelleted lime show a positive zeta potential, which is an indication of overliming. Due to the larger sizes of pelleted lime, it could not completely react with Na_2CO_3 in the green liquor, which means $Ca(OH)_2$ in the inner core ends up in the lime mud sample, resulting in a positive zeta potential value. These results suggest that a decrease in lime reactivity can result in an increase in free lime content, even when the lime dosage is correct.

Effect of lime mud storage time on zeta potential

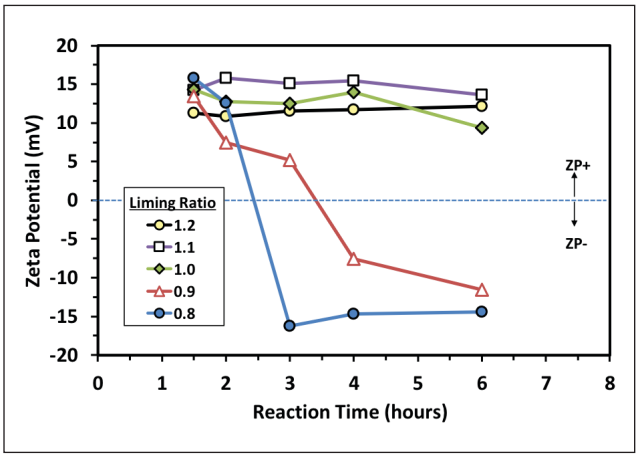
Since most mills are not equipped with instruments to measure zeta potential on site, they must send lime mud samples to commercial laboratories to get tests done. The samples may therefore be subjected to different storage times before they can be tested. In this study, the effect of storage time on zeta potential was examined. Lime mud samples, prepared at various liming ratios, were first stored up to 4 h before testing. The results confirm that systems with a liming ratio equal or greater than 1 have a positive zeta potential, while systems with a liming ratio less than 1 have a negative zeta potential (**Fig. 11**). The results remain unchanged at up to 4 h of storage time. This implies that short term storage (up to 4 h) does not affect zeta potential measurements.

The storage time was then extended up to 1 month, and the result is plotted in **Fig. 12**. In this case, the zeta potential remained positive for overlimed systems, regardless of storage time. However, for underlimed systems, the zeta potential changed to positive after samples had been stored for some time. After two weeks of storage, the zeta potential for all samples became positive. One possible explanation for this phenomenon is that the $CaCO_3$ coating formed on the outer surface of the lime particle may break down or crack after an extended storage time, allowing the $Ca(OH)_2$ (free lime) in the inner layer to diffuse out and become measurable. Since overlimed systems are saturated with $Ca(OH)_2$, no changes in zeta potential are detected.

To test the hypothesis that $Ca(OH)_2$ in the inner core was exposed during storage and caused a change in zeta potential, the causticizing reaction was extended for longer periods of time. **Figure 13** shows measurements made on samples at different liming ratios reacted for different amounts of time, with all stored for 1 month. Similar to previous results, when the reaction time is less than 3 h, zeta potential for all samples is positive after 1 month of storage time, regardless of the liming ratio. However, when the reaction times are longer, zeta potentials stay negative, even after 1 month of storage. This is likely due to more $Ca(OH)_2$ completely reacting to form $CaCO_3$ and no free lime is "hidden" within the inner core.



12. Effect of extended storage time on lime mud zeta potential (1 h reaction, 90°C reaction temperature).



13. Effect of reaction time on zeta potential – 1 month storage (1 h reaction, 90°C reaction temperature).

PRACTICAL IMPLICATIONS

This study confirmed that a correlation exists between free lime and zeta potential and explored the possibility of using zeta potential to quickly detect the presence of free lime in the lime mud. More specifically, the abrupt change in zeta potential from a negative value to a positive value as free lime content increases can be used to determine if the causticizing system is overlimed or not. It is also possible to develop an online monitoring system that can quickly identify the extent of liming. For example, if the process is underlimed, it would have a zeta potential of -20 mV. If the zeta potential subsequently increases to -10 mV, this means an increase in free lime content in the mud, which may be indicated by the monitoring system as a "warning" for a potential overliming situation. Similarly, if zeta potential becomes positive, the monitoring system can immediately provide the mill with an overliming alarm.

The benefit of using zeta potential over the conventional free lime measurement methods is that it is much faster and simpler, allowing a measurement to be done in approximately 30 s on diluted lime mud slurries. It may complement other control strategies at the slaker to ensure they are working properly. The disadvantage is, however, that the equipment may be expensive. In addition, the zeta potential of lime mud slurry might be mill-dependent, varying with the amount and type of impurities in the liquor cycle. Further research is required to standardize the testing procedure for measuring zeta potential.

CONCLUSIONS

A systematic study was conducted to investigate the feasibility of using zeta potential to detect free lime content in lime mud slurries in the causticizing plant. Lime mud samples were prepared from pure analytical chemicals (CaO and Na_2CO_3 solution) and from actual green liquor and reburned lime at different liming ratios. The zeta potential of the prepared lime mud samples was measured using an electroacoustic spectrometer. The results showed that:

1. Repeated measurements of lime mud samples produced with analytical chemicals gave consistent zeta potential values. As liming ratio increases, zeta potential changed from negative to positive. At liming ratios between 0.8 and 1.0, both positive and negative zeta potential were observed, indicating a "transition zone".
2. Compared to dried lime mud, wet lime mud showed more acute changes in zeta potential during the transition zone and had a larger difference between positive and negative values. This suggests that measurements on wet lime muds are better suited for fast free lime detection.
3. Samples prepared using pelleted lime gave positive zeta potential, even when the liming ratio was low. This implies that changes in lime reactivity may result in overliming system conditions, even when the lime dosage is correct. **TJ**

ACKNOWLEDEMENTS

This work was conducted as part of the research program on "Increasing Energy and Chemical Recovery Efficiency in the Kraft Process - III", jointly supported by the Natural Sciences and Engineering Research Council of Canada (NSERC) and a consortium of the following companies: Andritz, AV Nackawic, Babcock & Wilcox, Boise, Canadian Kraft Pulp, Carter Holt Harvey, Celulose Nipo-Brasileira, Clyde-Bergemann, DMI Peace River Pulp, Eldorado, ERCO Worldwide, Fibria, FP Innovations, International Paper, Irving Pulp & Paper, Kiln Flame Systems, Klabin, WestRock, StoraEnso Research, Suzano, Tembec, and Valmet.

LITERATURE CITED

1. Grace, T.M., in *Pulp and Paper Manufacture, Volume 5, Alkaline Pulping* (T.M. Grace and E.W. Malcolm, Eds.) 3rd edn., Canadian Pulp and Paper Association, Montreal, 1989, Chap. XXI, pp. 566-573.
2. Cornell, C.F., in *Chemical Recovery in the Alkaline Pulping Processes* (R.P. Green and G. Hough, Eds.) 3rd edn., TAPPI Press, Atlanta, GA, USA, 1987, Chap. 7, pp. 119-152.
3. Saiedi, S., Tran, H., and Papangelakis, V.G., *TAPPI J.* 8(3): 21(2009).
4. Azgomi, F., Farnood, R., and Tran, H.N., "Effects of liming ratio on lime mud settling and filterability," *PEERS Conf.*, TAPPI Press, Atlanta, 2010.
5. Sanchez, D.R., "Recausticizing – Principles and practice," *TAPPI Kraft Recovery Short Course*, TAPPI Press, Atlanta, Section 2.1, 2013.
6. Dorris, G.M., and Allen, L.H., *J. Pulp Pap. Sci.* 3(3): J99(1987).
7. Tran, H.N., "Lime kiln chemistry and effects on kiln operations," *TAPPI Kraft Recovery Short Course*, TAPPI Press, Atlanta, Section 2.3, 2010.
8. Mao, X., Ren, W., and Tran, H.N., *TAPPI J.* 14(7): 481(2015).
9. Weiner, B.B., Tscharnuter, W.W., and Fairhurst, D., "Zeta potential: A new approach," *Canadian Mineral Analysts Meet., 25th,* Canadian Mineral Industry, Kirkland Lake, ON, Canada, 1993.
10. Lyklema, J., *Fundamentals of Interface and Colloid Science: Volume 1 - Fundamentals*, 2nd edn., Academic Press, San Diego, CA, USA, 1993.
11. Azgomi, F., "Impact of liming ratio on lime mud settling and filterability in the kraft recovery process," Ph.D. dissertation, University of Toronto, Toronto, ON, Canada, 2013.

ABOUT THIS PAPER

Cite this article as: Ren, W., Tran, H. *TAPPI J.* 17(4):197(2018).

https://doi.org/10.32964/TJ17.04.197

DOI: https://doi.org/10.32964/TJ17.04.197

ISSN: 0734-1415

Publisher: TAPPI Press

Copyright: ©TAPPI Press 2018

About this journal

ABOUT THE AUTHORS

We chose to study this topic because there are presently no reliable methods for rapidly determining the free lime content in lime mud. Such information is needed for preventing problems caused by overliming in causticizing plants. This research complements previous research in our laboratory, but the focus was mainly placed on the use of zeta potential technology to rapidly determine the free lime content.

Since this research was the first of its kind, it was difficult to know where to start and how to develop a proper procedure for sample preparation. We addressed the problem by conducting numerous exploratory experiments.

This study demonstrated how old and seemingly unsolvable problems in our industry can be solved with technologies that are available in other industries. The most interesting and surprising finding was getting consistent and repeatable correlations between zeta potential and free lime content.

Mills can see from this research that conventional free lime measurement methods do not provide reliable results and that zeta potential measurement can be a good alternative. Our next step is to work with equipment suppliers and kraft pulp mills to develop a rapid and reliable online free lime monitoring system.



Ren



Tran

Ren is research engineer with FPInnovations in Vancouver, BC, Canada. Tran is Frank Dottori Professor of Pulp & Paper Engineering, Department of Chemical Engineering and Applied Chemistry, at the University of Toronto, Toronto, ON, Canada. Email Tran at honghi.tran@utoronto.ca.

Online measurement of bulk, tensile, brightness, and ovendry content of bleached chemithermomechanical pulp using visible and near infrared spectroscopy

MATTHEW R. TOMKINS, WESLEY GILBERT, AND THANH TRUNG

ABSTRACT: Current pulp mill practice to determine the pulp properties of bleached chemithermomechanical pulp (BCTMP) is to prepare and test handsheets for properties of interest. While the use of handsheets is well established, tests require well trained technical staff and introduce a significant lag before test results can be acted upon. In this report, a prototype online visible and near infrared (Vis-NIR) sensor that complements handsheet testing was trialed for 16 months at a BCTMP mill. The system consists of a cabinet located near a probe installed on a conveyor belt between a slab press and a bale press. When a bale stops on the conveyor belt, the probe rises and comes into contact with the bale, taking a spectral measurement and predicting its bulk, tensile strength, brightness, and ovendry (o.d.) content. The data presented here covers a period of 100 days of real-time measurements that correlated with laboratory tests with an R^2 of 0.88 for bulk, 0.87 for tensile, and 0.92 for brightness. Bulk, tensile strength, and brightness measurements had root mean square error of prediction (RMSEP) values of 0.19 cm^3/g, 3.994 Nm/g, and 0.96 brightness points, respectively. Ovendry content measurements trended with the mill's existing online moisture measurement system and had an R^2 of 0.36 and an RMSEP value of 1.04%. The quality of the correlation for o.d. content was substantially impacted because of difficulties with synchronizing the time stamps between the mill's existing online measurements and the online system reported here.

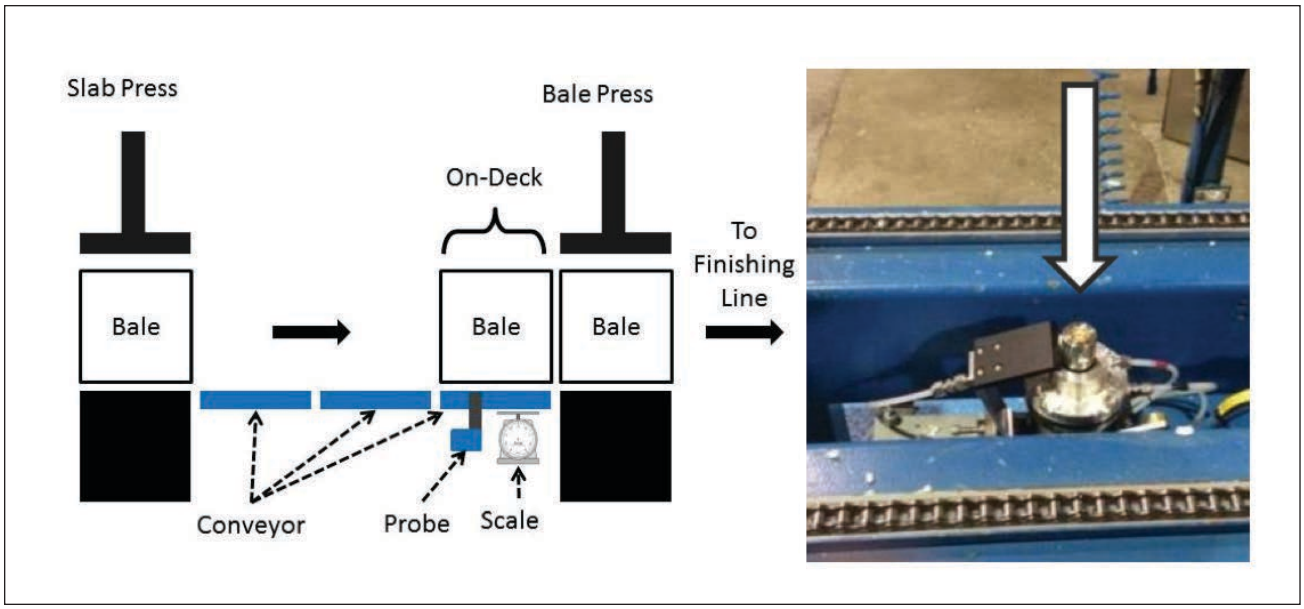
The online Vis-NIR sensor provides information in real time and has the potential to be used to reach target grade properties more quickly, assist in the identification of inefficient chemical dousing, reduce the effect of operator bias during testing, allow for the prioritizing of laboratory tests, and improve segregation of final products according to customer needs. However, further development would be necessary to use these measurements as part of a process control strategy.

Application: New Vis-NIR sensor technology can provide mills with more information about pulp properties.

The attributes of mechanical pulp are determined by the species of the wood supply as well as the conditions under which it is processed. For bleached chemithermomechanical pulp (BCTMP), mills attempt to influence the pulp properties by the amount of energy applied during refining as well as the conditions and length of time the pulp undergoes bleaching [1]. Of particular interest to the industry is controlling a pulp's freeness, brightness, bulk, tensile strength, and ovendry (o.d.) content. To measure brightness, bulk, and tensile strength, the pulp is formed into handsheets and conditioned at a set temperature and humidity for a minimum of 24 h (TAPPI Standard Test Methdod T 402 sp-13 "Standard conditioning and testing atmospheres for paper, board, pulp handsheets, and related products"). In the author's experience, pulp mills typically will only condition for 4–6 h. Anecdotal experience included in the test standard suggests that shorter times may be suitable. Regardless, the need to condition creates a significant lag between the manufacturing and identification of off-grade product.

Visible and near infrared spectroscopy (Vis-NIR) is an optical-based measurement that has wide ranging applications in industries such as pulp and paper, mining, agriculture, and pharmaceuticals [2–5] and is particularly sensitive to brightness, water, organic bonds and particle size (TAPPI T 452 om-08 "Brightness of pulp, paper and paperboard [directional reflectance at 457 nm]"). In brief, NIR shines a light on a sample and, by measuring the diffusely reflected spectra, one can infer its composition and properties. Correlating the spectra to the property of interest requires the use of multivariate mathematics [3].

Wallbäcks et al. [6] first reported the successful prediction of some pulp properties with NIR, but initial studies suggested that unbeaten pulps did not show a relationship between



1. (Left) schematic of bale movement in relation to the location of the presses and the probe; (right) pneumatic probe in scanning position.

their spectra and their physical properties [7]. A commercial unit for predicting pulp properties on a paperboard machine was developed [8]. However, articles relating to the development and application of this commercial unit suggest that samples did not have their moisture content varied when creating calibrations [9–11]. Given water's significant effect on the NIR spectrum, calibrations should either exclude all regions influenced by water or include samples with a variety of moisture contents (TAPPI T 452 om-08).

The objective of this work is to develop a rapid and accurate sensor based on Vis-NIR spectroscopy for measuring the key attributes of high yield bleached pulp with varying moisture content. This report will present the results of a trial for an online system that uses Vis-NIR to measure the bulk, tensile, brightness, and o.d. content of unbeaten BCTMP hardwood pulp.

PROCESS DESCRIPTION

At the tail end of the flash drying stage in a BCTMP mill, dried pulp is formed into bales on a slab press. These bales are then transported, typically by conveyors, to a bale press before being passed to the finishing line. At the mill where this trial was undertaken, bales stop briefly at the conveyor immediately before the bale press to be weighed, even if the bale press is not occupied. This conveyor also is the waiting position for a bale before it enters the bale press during periods of backed up production. The online Vis-NIR sensor was installed on this conveyor and wired into the mill's distributed control system (DCS). A schematic of the process between the slab press and bale press is shown in **Fig. 1**, with a bale shown waiting on the weigh conveyor before the bale press. A bale waiting in this position is subsequently referred to as the on-deck bale.

Normal operation

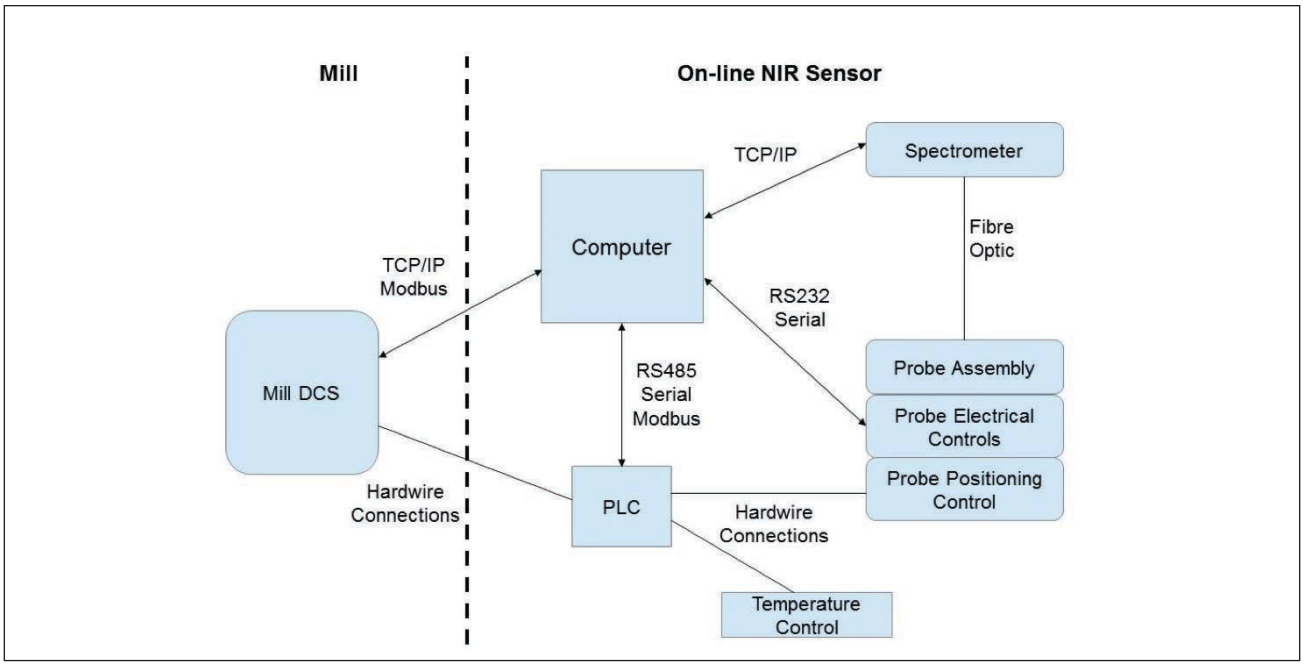
Before the installation of the online sensor, bales did not usually stay for longer than necessary in the on-deck position and would move directly into the bale press after the weighing was completed. To facilitate the time needed to scan a bale, the mill arranged for a bale to always be waiting in the on-deck position. To allow for normal variability in bale movement through the line, the decision was taken to only measure every third bale. This allowed for the Vis-NIR sensor to provide a new set of real-time bale property measurements roughly every 2.5 min. Furthermore, the mill was given the ability to deactivate the Vis-NIR sensor for any reason. At no time during the trial did the time required for scanning cause a slowdown in production. The operation of the Vis-NIR sensor was fast enough to process backlogs and did not require further modification to the mill's standard procedures. However, the mill adopted the practice of deactivating the sensor during upsets.

ONLINE VIS-NIR SENSOR

Hardware setup

The online Vis-NIR sensor consists of five main components: spectrometer, computer, programmable logic controller (PLC), pneumatic cylinder, and probe. The spectrometer is able to scan the visible and NIR spectrum (350–2500 nm). The spectrometer, computer, and PLC are housed in a cooled, temperature controlled cabinet with wiring to the mill's DCS and intranet. The pneumatic cylinder and probe are assembled into a custom built probe base that can be welded or bolted onto a metal structure. Finally, a fiber optic cable connects the probe to the spectrometer.

The probe base is designed to sit in an industrial conveyor, between two beams as shown in Fig. 1 (right). During the



2. Hardware and software relationships. Arrows indicate directional communication.

scan, the probe extends upward until it contacts the bottom of the target bale, performs a scan, and then retracts when complete. The probe's action is activated pneumatically with an air pressure of approximately 70 psi. When the probe is in a dormant position, an opaque plastic door covers the window to prevent contamination. Because of tight clearances, the door's displacement was minimized so there is no contact between the door and the bale. The pneumatic cylinder is outfitted with two position sensors to identify when it is in the raised and lowered positions. Low pressure air lines are passed through an oil filter and fed into the top of the pneumatic cylinder to provide constant cleaning of the sapphire window surface, reducing the need for maintenance.

The computer acts as the communications hub for the online Vis-NIR sensor while the PLC controls the mechanical operation of the system and receives commands from the mill. A simplified hardware and software relationship diagram is shown in **Fig. 2**. Interlocking logic was included so that the unit would not rise without active input from the mill's DCS signalling that a bale is ready to be scanned and would retract immediately if the input was deactivated. The states of the unit, along with the outputted predictions, were communicated to the mill's DCS so that the operators could quickly see the current state of the system. A user can access similar information through a graphical user interface when connecting directly to the computer. The PLC regulates the temperature of the cabinet via a vortex cooler and operates the valve controlling the pneumatic cylinder. The computer has its own user interface to load calibration data, set probe electrical controls, communicate with the spectrometer, and record data into a local database. It also communicates with the PLC and the mill's DCS to provide state information. While the computer could be programmed to control all functions of the cabinet and probe, in the event of a computer error or delay, commands might not be processed quickly enough. Therefore, for robustness and safety reasons, a PLC was chosen to control critical functions.

Model development

Pulp samples were acquired from a BCTMP hardwood mill in eastern Canada. More than 190 pulp samples were scanned in a prototype benchtop system designed to mimic the Vis-NIR sensor. An additional 40 pulp samples cut from the bottoms of pulp bales were scanned using the Vis-NIR sensor before the unit being commissioned. Of the approximately 230 unique samples, 117 samples had their moisture content modified by being placed either in a humidity chamber, or dried in an oven. This resulted in the accumulation of more than 600 unique Vis-NIR spectra for a calibration model. The physical properties of interest for the pulp samples were determined by the mill in advance of the sample being shipped. Ovendry content was determined by taking <5 g of a pulp sample and measuring the change in weight after a 24-h period in an oven at 105°C. **Table I** lists the range of properties for the pulps investigated in this report.

Calibration model

The calibration for this system was prepared using GRAMS IQ v. 9.1 (Thermo Fischer Scientific; Waltham, MA, USA), a multivariate chemometrics package designed to build calibration models. Models were built using a PLS-1 partial least squares model with cross-validation. For PLS-1, the eigenvectors and scores obtained through partial least squares were individually calculated for each constituent. Data preprocess-

Hardwood Pulps	Bulk, cm^3/g	Tensile Index, nm/g	Ovendry Content, %	Brightness, ISO
Minimum	1.6	7.4	80.3	69.9
Maximum	3.9	59.5	93.3	87.1
Estimated laboratory error	0.13	2.1	1	0.4

I. Ranges of physical properties investigated.

Property	Spectral Regions, nm	Number of Principal Components	Linearity, R^2	RMSECV
Bulk, cm^3/g	800–902	6	0.71	0.22
	1081–1825			
	1859–2160			
Tensile index, nm/g	799–903	5	0.60	5.93
	1076–1727			
	1966–2276			
Ovendry content, %	538–689	2	0.86	1.03
	821–969			
	1150–2200			
Brightness, ISO	453–926	6	0.73	1.01
	1105–1230			
	1385–1479			
	1561–1687			
	1899–2007			

II. Calibration model parameters (RMSECV = root mean squared error of cross-validation).

ing involved mean centering and a Savitsky-Golay second derivative with 143 smoothing points. Spectral regions were chosen to maximize correlation between the spectral variation and the property of interest. A summary of the number of principal components used in each model is presented in **Table II** along with the root mean squared error of cross-validation (RMSECV) and Pearson's r squared (R^2). Pulp samples were scanned under laboratory conditions and combined to create a set of calibration spectra. These brightness, bulk, and tensile index models were augmented with an additional 100 scans taken at the mill using the online Vis-NIR sensor.

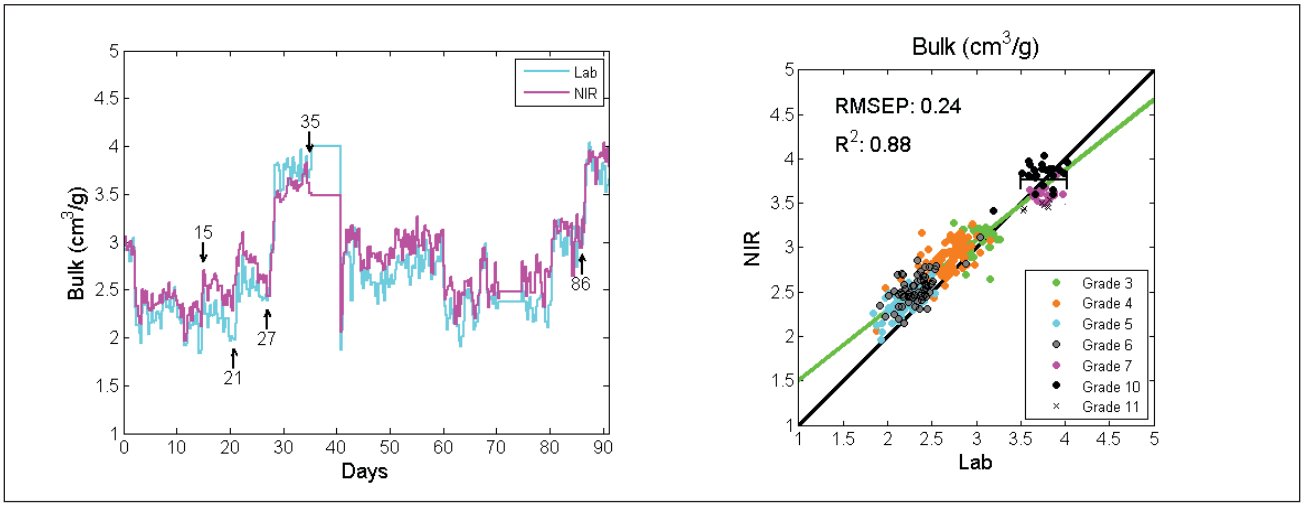
RESULTS AND DISCUSSION

The online Vis-NIR sensor was installed in the same BCTMP mill where the samples were acquired and ran uninterrupted for a 9-month period starting in early 2014. Because of wear failure in the lower bushing of the pneumatic piston, the piston seized and was removed from the line for repair. The piston was evaluated and a new design was constructed with a self-lubricating bushing to prevent this type of failure from occurring in the future. The system was then reinstalled in spring 2015 and operated uninterrupted for another 7 months until decommissioned in fall 2015. For the purposes of maintenance, the probe assembly and surrounding area were cleaned daily and the lightbulb was replaced yearly.

Property	τ, min	τ_{settle}, min
Bulk	20.2	80.4
Tensile	25	100
Ovendry content	7.9	31.6
Brightness	16.1	64.4

III. Values of τ used for the first-order filter and the settling times.

Filtering was used to better hone in on the true mean value of the pulp properties. Filtering was accomplished using a discrete-time first-order filter (also known as an exponentially weighted moving average) [12]. The filter time constants (τ) were determined by performing time series analysis on raw data collected over an 8-day period of normal operation. A summary of filter time constants and asymptotic settling times (τ_{settle}) for the various signals are presented in **Table III**. A potentially negative effect of filtering is that an additional lag is added to the filtered data. The settling time is a measure of this lag as it indicates how long it would take



3. Bulk (cm³/g) near infrared (NIR) and laboratory measurements. (Left) NIR and laboratory measured values overlaid in time. Arrows indicate specific days; (right) NIR and laboratory measured values presented independently of time. The horizontal bar is the 95% confidence interval of the laboratory tests.

a step in the mean value of the raw signal to be fully registered in the filtered value.

Sensor validation

Validation of the sensor was done against the mill's regular tests. These consisted of taking hand-grab samples from bales once per hour over a 6-h period. The samples were subsequently mixed, formed into handsheets, and tested. This resulted in four composite sample tests per day. To validate the Vis-NIR sensor data using this composite handsheet data, the sensor predictions were averaged over the 6-h period coinciding with the collection of the hand-grabbed samples.

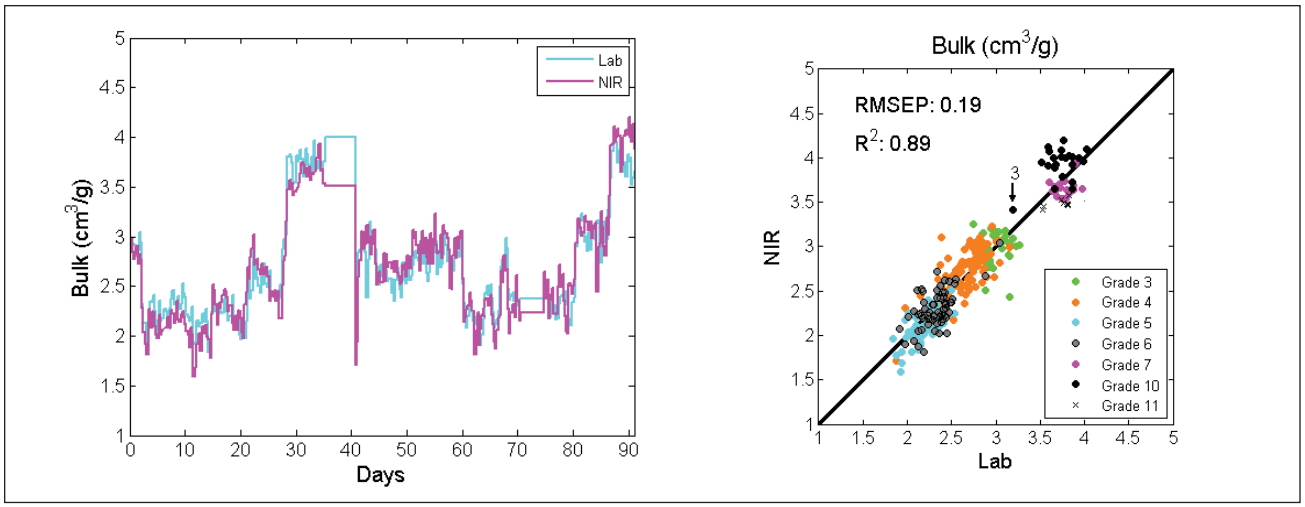
A summary of the data during a 3-month period in 2014 comparing the predicted and measured values for bulk is presented in **Fig. 3**. During this period, seven different grades were produced by the mill. Figure 3 (left) shows how the NIR predictions from the online Vis-NIR sensor closely track the corresponding laboratory measurements. For example, starting from day 15, both measured and predicted bulk values decrease by approximately 0.3 cm³/g over a period of 3 days. The bulk abruptly increases because of a grade change on day 21 and, once again, decreases over a period of 4 days before two grade changes occur on day 27. The mill produces that same grade until a mill shutdown starts on day 35. While gradual changes in predicted bulk occur within a grade, abrupt changes in bulk correspond to grade changes. For example, a substantial grade change occurred on day 86 when production went from grade 4 (bulk approximately 3.2 cm³/g) to grade 10 (bulk approximately 3.9 cm³/g).

The averaged NIR predictions are plotted against laboratory tests independent of time in Fig. 3 (right). The solid green line is the least squares fit of all of the data points and serves as a visual guide to show how closely the entire set of points approaches the y = x line. Overall, the trend is promising and demonstrates the validity of the online Vis-NIR sensor. Grade 5 is the grade with the lowest observed bulk and forms an ellipsoidal cluster with a major axis along the green line. Similar shapes are observed with grades 4 and 6 and, to a lesser extent, grades 3 and 11. In contrast, grades 7 and 10, while close to the line of best fit, tend to form wide and short ellipsoidal clusters with a major axis not in alignment with the green line. This could be a limitation of the laboratory based testing. An error bar has been placed at the center of the data around grades 7 and 10. The width of the error bar is equal to the 95% confidence interval (CI) of the laboratory's testing error. Because all of the data points for grades 7 and 10 lie within the 95% CI of laboratory testing, the accuracy of the online Vis-NIR sensor cannot be proved or disproved for these grades with the data provided here.

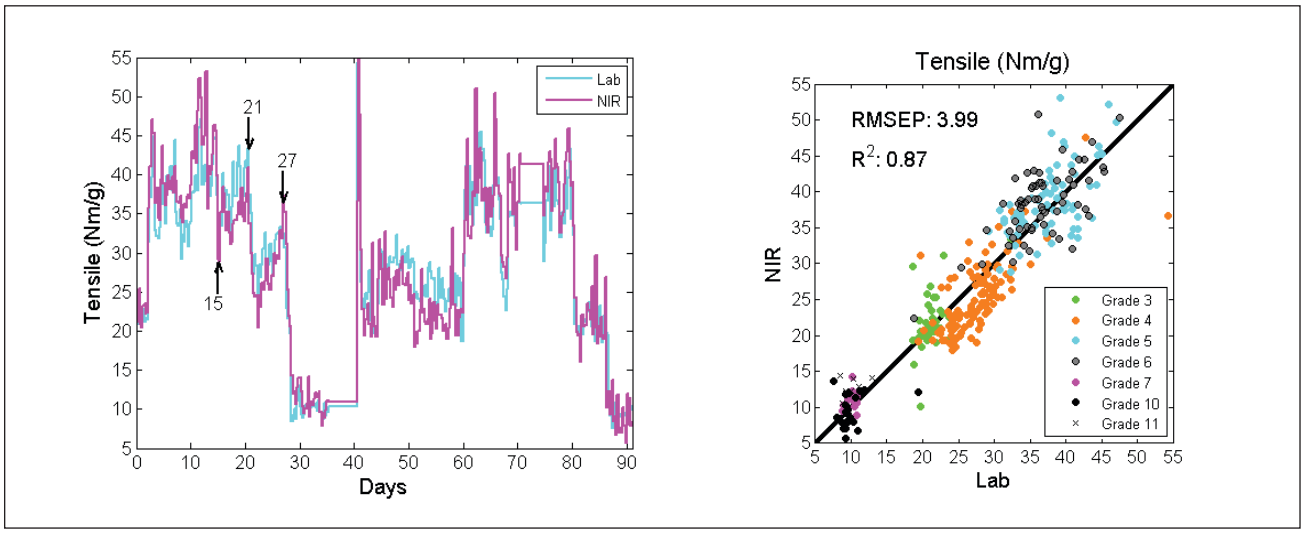
The root mean squared error of prediction (RMSEP) was 0.24 cm³/g. Presenting the data after slope and intercept correction will reduce the bias error to zero [13]. Because validation relies on laboratory testing to calculate the RMSEP, even if NIR measurements result in less error than laboratory testing, the practical limit of the apparent RMSEP is equal to the validating laboratory's error, shown in Table I [14].

The line of best fit shown in Fig. 3 has a slope of 0.7173 and an intercept of 0.6525. These values can be used as factors to modify the calibration resulting in more accurate predictions. Slope and intercept corrected data for bulk is presented in **Fig. 4**. In contrast with Fig. 3 (left), the prediction and laboratory measurement trends in Fig. 4 (left) overlap more closely, with the exception of the high bulk grades 7 and 10, for reasons discussed earlier. A consequence of using factors to correct predictions is that while predictions are centered on the y = x line and bias is eliminated, the data become more spread out. As an alternative to using factors to correct NIR measurements, the calibration could be rebuilt with the addition of validated spectra. This was not attempted here.

The slope and intercept corrected tensile data are shown



4. Bulk (cm³/g) NIR measurements from Fig. 3 with slope and intercept corrected plotted with laboratory measurements. (Left) NIR and laboratory measured values overlaid in time; (right) NIR and laboratory measured values presented independently of time. The arrow in the upper right figure indicates a point that is an outlier from its grade due to averaging during a grade change. The number indicates the preceding grade.

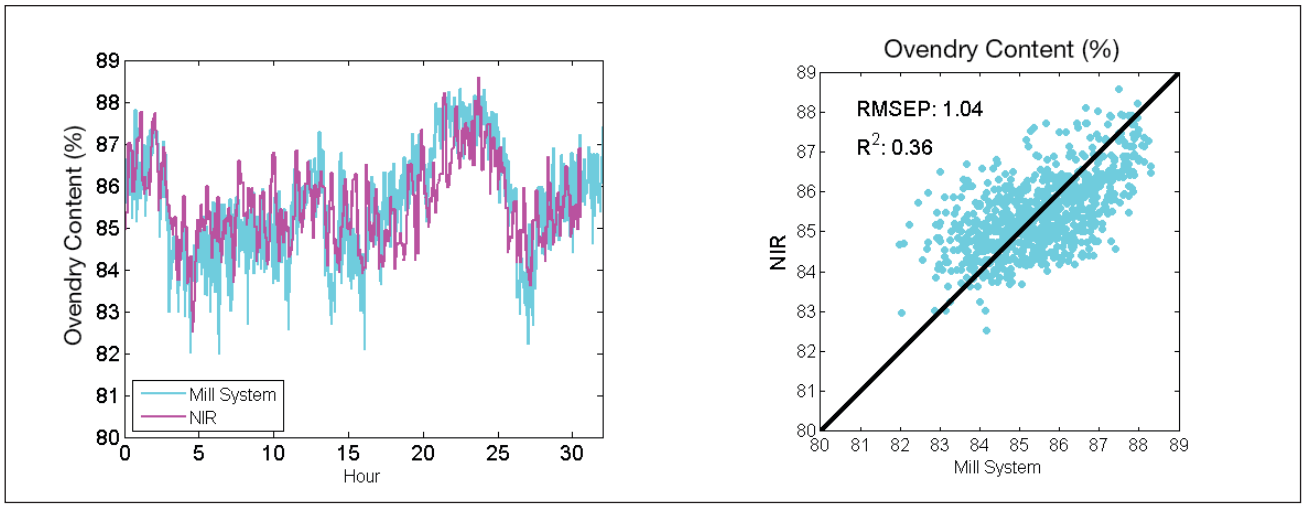


5. Tensile strength (nm/g) corrected NIR and laboratory measurements. (Left) NIR and laboratory measured values overlaid in time; (right) NIR and laboratory measured values presented independently of time.

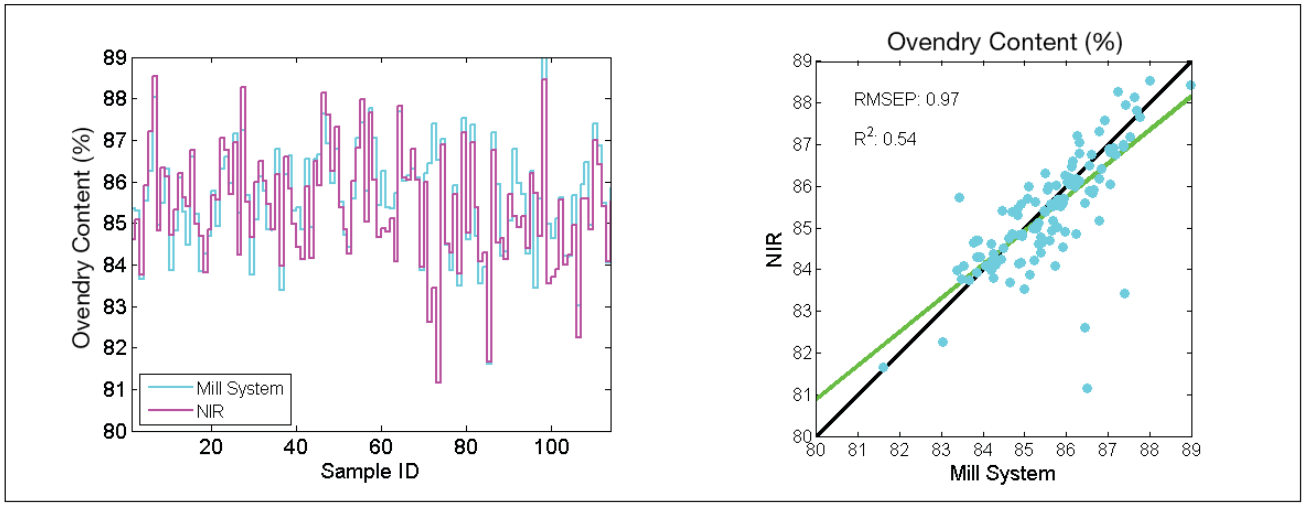
in **Fig. 5**. The ability of the online Vis-NIR sensor to track changes in tensile strength is best seen in the period starting from day 15 where tensile rises by approximately 5 nm/g over a period of 3 days, at which point it abruptly decreases because of a grade change on day 21 and, once again, increases over a period of 4 days before two grade changes on day 27. Because bulk and tensile tend to be inversely correlated, one would expect that tensile will increase as bulk decreases, as is being observed [15]. Grades 3–6 form roughly ellipsoidal groupings whose major axes are aligned with the y = x line. Similar to what was seen with bulk, laboratory tests for grades 7 and 10 have less variability than the 95% CI of the laboratory's error (not shown) and the accuracy of the online Vis-NIR sensor cannot be proved or disproved for these grades.

Typically, a mill relies on an automated moisture measurement system for determining the o.d. content of its pulp and does not perform routine independent determinations. **Figure 6** shows a comparison of the Vis-NIR sensor's (filtered) real-time measurements against the mill's system over a 32-h period starting on day 51. In Fig. 6 (left), the o.d. content measured by the mill and the online Vis-NIR sensor appear to trend well. For example, both experience peak moisture measurements near hours 12 and 23. When these data sets are plotted independently of time, in Fig. 6 (right), a weaker correlation than was observed for bulk and tensile is seen resulting in an R^2 of 0.36 and an RMSEP of 1.04 %. However, this is likely because the data have not been averaged and it was not always possible to properly synchronize the NIR and the mill's measurements.

Over a period of 1 year, the mill took samples from bales



6. Ovendry content measured over a 32-h period starting on day 51. (Left) NIR and the mill's moisture measurement overlaid in time; (right) NIR and the mill's moisture measurement presented independently of time.

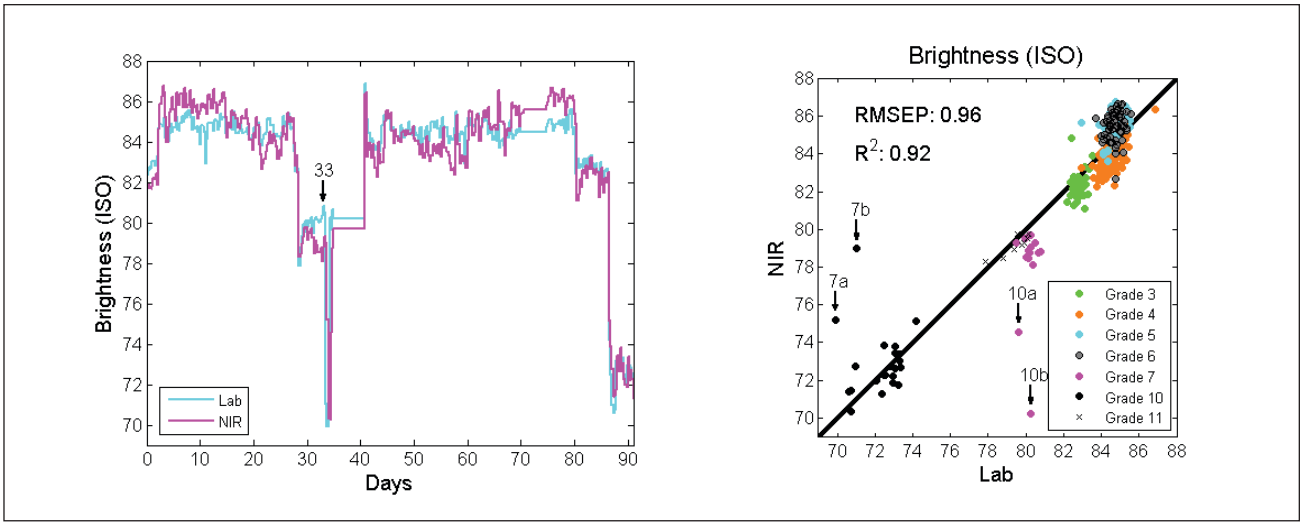


7. Ovendry content measured for specific bales. (Left) NIR and the mill's moisture measurements overlaid in time; (right) NIR and the mill's moisture measurements presented independently of time.

that were scanned by the online Vis-NIR sensor and determined their o.d. content in the laboratory. No correlation was found between the laboratory measurements and either online measurement. However, this created a data set (**Fig. 7**), where both the mill's moisture measurement system and the Vis-NIR sensor could be compared on a bale-by-bale basis. The correlation between these data sets improved the R^2 to 0.54, but the RMSEP only decreased to 0.97 (Fig. 6).

Measuring brightness requires good control over multiple factors (T 452-om 08). Factors that can affect brightness measurements include light source, angle of measurement, and angle of reflection. While the spectrometer used in this system contains a visible detector with the appropriate range for conducting brightness measurements, the tightly controlled conditions for accurate brightness determination could not be incorporated into the system. Therefore, the values for brightness are predicted from full spectrum NIR measurements in the same way as other properties. As the brightness values are measured using composite samples, they are also compared against the 6-h averaged NIR measurements.

Figure 8 (left) shows how brightness measurements from the Vis-NIR sensor and laboratory measurements correlate during grade changes. The data independent of time in Fig. 8 (right) allow for the examination of how well brightness is tracked within individual grades. Grade 3 samples appear near the y = x line, but their groupings are more vertical than diagonal. A possible explanation for this lack of correlation could be attributed to short-term variations in bale brightness. Bleaching towers with high residence times and low flow rates tend to exhibit plug flow behavior. Therefore, short-term mass flow variations might show up as short-term quality variations at the end of the process. Over the 6-h period where the NIR brightness measurements are averaged, any variation would affect the brightness of specific bales and hence the average brightness. Furthermore, one would not expect these variations to be captured during a mill's regular tests. An ad-



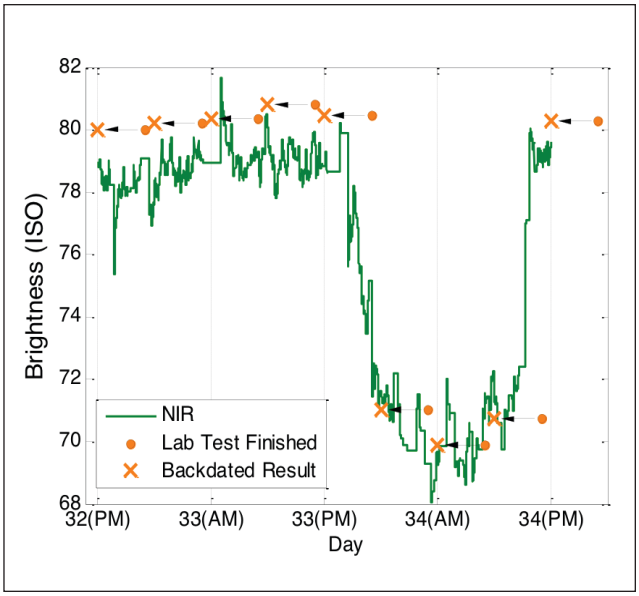
8. Brightness (ISO) corrected NIR and laboratory measurements. (Left) NIR and laboratory measured values overlaid in time; (right) NIR and laboratory measured values presented independently of time.

vantage of the online Vis-NIR sensor is that these short-term variations in brightness might be captured.

Another example of the effects of using a 6-h averaged brightness measurement is presented in Fig. 8 (right), where four distinct points are indicated that are well off the y = x line. These points were generated on day 33 in 2014 when the mill went from producing grade 7 to grade 10 and then back to grade 7 within a period of about 24 h. The identified points are between-grade for the NIR brightness but on-grade for the laboratory values. A similar observation can be made with the physical properties, for example, as with the indicated point in Fig. 4. The NIR values are the arithmetic average of up to 145 individual bale measurements roughly equally spaced in time, and thus are representative of the time-weighted average brightness during a grade change when a step change in brightness occurs. The laboratory measurements, on the other hand, are harder to explain. Some possibilities are that they might be the result of poor mixing of grab samples or the intentional timing of samples to correspond with on-grade production.

Advantage of real-time measurements

Each laboratory test requires collecting samples over a 6-h period and approximately 4–6 h of conditioning before results are known. Furthermore, the handsheet testing standard suggests using the average of five handsheets for bulk or strength tests (TAPPI T 220 sp-10 "Physical testing of pulp handsheets"). Over the same 6 h, the online Vis-NIR sensor can provide up to 145 measurements with real-time results provided throughout. **Figure 9** shows how the real-time NIR measured brightness compares against the laboratory measured brightness from the composite handsheet during a grade change. The data period in Fig. 9 corresponds with the four points that appear as outliers in Fig. 8 (right). The mill prepares handsheets every 6 h. Once



9. Brightness (ISO) corrected NIR (solid line) and laboratory measurements (discrete points). Laboratory measurements are presented as circles (time when laboratory results become available) and crosses (backdated values stored in mill's historian).

the laboratory results are finalized, the values are backdated into the mill's historian. Because the actual time when these test results become available was not recorded, Fig. 9 assumes that results are available 5 h after the last hand-grab sample is taken. On day 33 (p.m.) the last sample of grade 7 is taken and a handsheet is prepared. At the same time, the mill begins a grade change. Six hours later, the pregrade change handsheet results have been recorded and another composite sample is ready for processing, but the mill still does not have confirmation of what has happened as a result of the grade change. It will be another 6 h before the mill knows whether

the grade change is successful. By comparison, the online Vis-NIR sensor has been outputting data to the mill in real time and is already reporting that brightness has reached the target of 70. For the next 5 h, the NIR sensor measures further decreases in brightness. Just before day 34 (a.m.), at about the same time that the laboratory brightness results are being entered, an increase of four brightness points is recorded by the online Vis-NIR sensor over the next hour, followed by a correction back to 70 brightness. By relying on handsheet testing, which provides lagged values only once every 6 h, the mill is only able to document the fact that step changes in brightness occur and has limited ability to deal with process upsets or slow drifts in properties that occur between test results. During the production of this 70 brightness grade, mill personnel are reliant on only three handsheet tests. With the Vis-NIR sensor providing real-time measurements, one can observe and infer more details about the process and have access to information that could be used to better control process variability. However, further development would be necessary to use these measurements as part of a process control strategy.

CONCLUSIONS

An online Vis-NIR sensor has been developed to measure the bulk, tensile, brightness, and o.d. content of BCTMP in real time. This sensor consists of a probe to scan the NIR spectra of bales and a cabinet that houses the hardware to interpret the resulting spectra. This system has the necessary safety interlocks and communications needed to operate in a mill environment and has demonstrated its robustness through 16 months of mill trials. The data presented here for the online Vis-NIR sensor provided real-time measurements that correlated with laboratory tests with an R^2 of 0.88 for bulk, 0.87 for tensile, and 0.92 for brightness for more than 100 days. Ovendry content measurements correlated poorly with the mill's existing moisture measurement system having an R^2 of 0.36, but was improved when comparing specific samples ($R^2 = 0.54$). Bulk, tensile strength, o.d. content, and brightness measurements had RMSEP values of 0.19 cm^3/g, 3.994 nm/g, 1.04%, and 0.96 brightness points, respectively. Two identified sources of error are the laboratory's testing error and the need to average the online measurements over a 6-h period to validate the sensor against the mill's regular testing. Even though this technology is not yet sufficiently developed to be used as part of a process control strategy, having access to continuous real-time information of bale properties has the potential to enable the mill to reach on-grade targets more quickly, assist in the identification of inefficient chemical dousing, reduce the effect of operator bias during testing, allow for the prioritizing of laboratory tests, and improve segregation of final products according to customer needs. **TJ**

LITERATURE CITED

1. Kocurek, M.J. (Ed.), *Pulp and Paper Manufacture, Vol. 2*, 3rd edn., Joint Textbook Committee of the Paper Industry, Montreal, 1987.
2. Workman, J.J., *Appl. Spectrosc. Rev.* 36(2-3): 139(2001).
3. Burns, D.A. and Ciurczak, E.W. (Eds.), *Handbook of Near-Infrared Analysis*, 2nd rev. edn., Marcel Dekker, New York, 2001.
4. Furumoto, H., Lampe, U., Meixner, H., et al., *TAPPI J.* 83(10): 1(2000).
5. Demera, A.-M., Gosselin, R., Simard, J.-S., et al., *Can. J. Chem. Eng.* 90(2): 299(2012).

ABOUT THE AUTHORS

This research topic was chosen because of a need in the industry for rapid feedback of pulp properties. Currently, this technology is lacking. This research complements earlier work by applying multivariate analysis to the near-infrared spectra of BCTMP to predict the physical properties of a handsheet made from that pulp. It differs from previous work by demonstrating the technology in an industrial setting.

The most difficult aspect of this work was to demonstrate a working prototype and gather sufficient data for this validation. The most interesting aspect of the findings was how well the NIR-based measurements correlated with the laboratory measurements over the long term.

Mills would benefit from the awareness that modernizing their technology could bring exponentially more information about pulp properties. The information we present also addresses the limitations surrounding NIR technology. The next steps are to more closely study how NIR spectroscopy provides such accurate predictions and attempt to commercialize this technology.



Tomkins



Gilbert



Trung

Tomkins is an engineer, Sensor Development and Applications, and Gilbert is a senior control engineer, FP Innovations, Vancouver, BC, Canada. Trung is vice president of technology, FITNIR Analyzers Inc., Vancouver, BC, Canada. Email Tomkins at matthew.tomkins@fpinnovations.ca

6. Wallbäcks, L., Edlund, E., Nordén, B., et al., *Nord. Pulp Pap. Res. J.* 6(2): 74(1991).
7. Wallbäcks, L., Edlund, E., Nordén, B., et al., *Nord. Pulp Pap. Res. J.* 6(3): 104(1991).
8. Skoglund, A. and Brundin, A., *Nord. Pulp Pap. Res. J.* 15(3): 183(2000).
9. Sjoeberg, K., Bjoerklund, C., Karlsson, M., et al., "Spectrophotometric method to measure quality and strength parameters in trees, lumber, timber, chips, saw dust, pulp and paper," WO9531710 (A1) (Nov. 23, 1995).
10. Malmstrom, E., *Sven. Papperstidn.* 102(9): 38(1999).
11. Karlsson, M. and Stahl, C.W., *Pap. Technol.* 41(1): 25(2000).
12. Hunter, J.S., *J. Qual. Technol.* 18(4): 203(1986).
13. Davies, A.M.C. and Fearn, T., *Spectrosc. Eur.* 18(2): 31(2006).
14. DiFoggio, R., *Appl. Spectrosc.* 49(1): 67(1995).
15. Dence, C.W. and Reeve, D.W. (Eds.), *Pulp Bleaching: Principles and Practice*, 1st edn., TAPPI Press, Atlanta, 1996.

ABOUT THIS PAPER

Cite this article as: Tomkins, M., Gilbert, W., Trung, T. *TAPPI J.* 17(4):207(2018). https://doi.org/10.32964/TJ17.04.207

DOI: https://doi.org/10.32964/TJ17.04.207

ISSN: 0734-1415

Publisher: TAPPI Press

Copyright: ©TAPPI Press 2018

About this journal

Importance of specimen preparation for edgewise compressive strength (ECT) testing

JERRY LOZA, DOUG CASH, AND BENJAMIN FRANK

ABSTRACT: While more than 50 years of published studies recognize the importance of rectangular, parallel edgewise compressive strength (ECT) specimens, none of the existing test methods address the degree to which a sample specimen is defined as sufficiently parallel. We present a detailed exploration of ECT results for specimens whose edges deviate from parallel with varying severity. We work to identify causes of variation in dimensional measurements and the corresponding ECT values across several industry standard cutters. These variations present a significant challenge to the industry in satisfying customer expectations for performance-based packaging, as well as to the development of improved predictive models for packaging performance.

Application: This work serves as an early step for identifying or developing more optimal test methodologies to measure the inherent compressive strength of corrugated materials.

Although box compression strength (box compression test [BCT]) of corrugated containers is the primary end-use performance criteria for many boxes, the edgewise compressive strength (ECT) of the material remains the most common parameter specified by customers. ECT measures the force required to cause a vertically-oriented specimen of corrugated fiberboard to crush, with measured values providing an assessment of a fundamental material property. The ECT value can be related to the ultimate stacking performance of the container, and has been used in predictive modeling for over 50 years [1-3]. As well, many box plants measure ECT to control or optimize their processes and assure they are meeting customers' performance requirements. ECT is also codified in the most common certification process for boxes, the conforming (circular) box manufacturer's certificate (BMC). The BMC is a guarantee by the box maker that the box meets certain standards set in the National Motor Freight Classification (NMFC), so that the carrier in a less-than-truck-load shipping environment will agree to accept the shipment for carriage. The rules outlined in National Motor Freight Traffic Association Item 222 [4] specify TAPPI Standard Test Method T 811 "Edgewise compressive strength of corrugated fiberboard (short column test)" as the referee method for determining the ECT of boxes used for shipping.

ECT testing strives to capture the strength of the bulk composite structure formed by the linerboard and fluted medium, an intrinsic material property. Various factors can affect the measurement of ECT. These include failure at the specimen's loading edges, specimen buckling, and structural damage sustained during the production and handling of specimens, all of which can reduce the measured value from a true reflection of the material strength. Several different specimen preparation approaches, including waxing edges (TAPPI T 811), necking down (TAPPI T 838 "Edge crush test using neckdown"), clamping (TAPPI T 839 "Edgewise compressive strength of corrugated fiberboard using the clamp method [short column test]"), and testing geometrically short columns (ISO 3037 "Corrugated fiberboard — determination of edgewise crush resistance [unwaxed edge method]"), attempt to mitigate the effect of these factors. As the literature consistently demonstrates [5-13], these differing approaches do not produce similar results. For samples loaded directly on their edges (TAPPI T 811, TAPPI T 838, and ISO 3037), Eriksson's exploration of test factors [14] highlights specimen parallelism in particular as an important consideration, as do McClain and Boltnott [15] and Ernst and Graf [16].

The TAPPI standards have generally incorporated the learnings from these and similar studies in their equipment specifications. The tolerance on the compression equipment, used consistently throughout all tests on containerboard materials (see, for example, TAPPI T 822 "Ring crush of paperboard [rigid support method]" and TAPPI T 809 "Flat crush of corrugating medium [CMT test]"), is designed to prevent artificially low values due to one part of the material under load failing before the entire specimen is loaded. For example, the specification for parallelism of the compression tester in TAPPI T 811 (section 3.1.1) states, "Within the specimen contact area, each platen shall be flat within 0.0025 mm (0.0001 in.) of the mean platen surface, and the platens shall remain parallel to each other within 1 part in 2000 throughout the test." What seems an arbitrarily tight tolerance (0.05%) becomes less capricious when one considers that paper materials fail at strains on the order of 0.5%–1%.

The initial development of the ECT test required the use of a table saw to prepare specimens [17]. In that work, the authors observe that a slightly tilted saw blade, which would produce trapezoidal specimens (from an end-on perspective), "can cause a very severe reduction in compression results because of the bevel incurred in the loading edges of the specimens. Every effort should be made to ensure that the blade is as perpendicular as possible." (Note: Throughout this paper, we use the word "trapezoidal" to describe ways in which the samples are not pure rectangular parallelepipeds. Trapezoids are planar figures; the description of samples as trapezoidal actually refers to a given face of a sample, not to the entire piece. For example, if one examines the ECT specimen from the side of the doubleback liner, the piece is rectangular if the opposite edges are the same size and parallel with the corners forming right angles, and it is trapezoidal if the top edge of the liner is parallel to but not the same length as the bottom edge.)

As the industry moved to safer and cleaner cutting methods, including the single knife and double knife systems described in the next section, we continued to observe that test specimens should "be cut with the loading edges exactly perpendicular to the flutes" [8] and that "lack of parallelism in the loading edges across the board width or along the thickness… will result in lower ECT values." Nowhere, however, does the literature provide actionable guidance on how much lower, for a given amount of deviation from perfect parallelism, nor any scale of the effect of trapezoidal specimens.

As Eriksson noted, the parallelism requirement for the equipment is more than an order of magnitude greater than the typical accuracy in cutting a test specimen. TAPPI T 811 provides only that "opposite edges shall be parallel to each other and perpendicular to adjacent edges," with no quantification. The interior alignment of the clamping text fixture in TAPPI T 839 uses similar language of "held exactly perpendicular to the base," with no quantification of how parallel or perpendicular, nor any obvious means of measuring or checking such alignment. Given the dimensions of a typical C-flute ECT specimen for TAPPI T 811 (2 in. [50.8 mm] wide specimen, ~0.160 in. [~4.1 mm] thick), a 0.5% difference across the length would be 0.01 in. (0.254 mm). Higher levels of deviation from "true parallel" were observed in Eriksson's work. More critically, in the thickness direction, one part in 2000 from the TAPPI T 811 parallelism requirement is ~0.00008 in. (~0.0020 mm). This provides a sense of the scale over which parallelism may matter.

This paper does not solve the challenge of cutting a specimen parallel. By presenting a detailed exploration of the issue, we hope to spur the industry to develop better cutting methods and perhaps better test methods to help reduce the level of variation present in our current test results. This variation presents challenges to the industry as we attempt to satisfy customer expectations for performance-based packaging and develop better models to predict package performance. The deviations inherent in specimen preparation limit our ability to quantify the inherent material strength, and to optimize our materials.

Because of its effective codification in U.S. Carrier Rules and its primary use by customers as a specification for combined board strength, in this paper we focus on the effect of parallelism on specimens prepared for TAPPI T 811, where the specimen is loaded directly on the cut edge after the edge has been supported by waxing. After a discussion of several styles of specimen preparation equipment, we explore parallelism measurement. We will then be equipped to discuss deviation from "parallel" observed on typical specimens and to measure the impact those shifts have on ECT values.

CUTTING DEVICES

Several cutters are used across the industry, all with distinguishing features that add to the diversity of the data. While some conform to the TAPPI T 811 requirement to use single beveled blades, others do not. We examined five in detail in this study, and divide them into two general categories: dual blade and single blade.

- Single blade cutters always require two cuts to produce the loading edges, potentially allowing for the sample material to twist or shift between cuts. This could affect the parallelism of the specimen loading edges. Given that cutting blades are typically beveled on at least one side, these types of cutters tend not to allow full conformance with the requirements of the TAPPI T 811 test method, as at least one edge (depending on cutter configuration) typically ends up being cut against the beveled side of the blade.
- Dual blade cutters attempt to assure parallelism in the two specimen loading edges by cutting the specimens to size in one stroke using a pair of parallel blades. Specimens cut with a single pass have parallelism defined by the accuracy of the blades and cutting instrument. Specimens that might need to be cut to a smaller size than the blade spacing (for example, a 1.5 in. [38.1 mm] C-flute specimen prepared on a dual blade cutter with a 2 in. [50.8 mm] spacing) require a second cut of one edge. This two-step process potentially allows for some twisting or lifting of the specimen during cutting that might cause deviation from perfectly parallel, similar to a single blade cutter.

For all cutters, samples are held against a backstop nominally perpendicular to the travel of the blades so that the resulting specimen's loading edges are cut orthogonal to the vertical edges. Out of deference to the various cutter suppliers, we will refer by number to the five cutters we examined. Challenges with parallelism can apply to all the cutting approaches explored.

Cutter 1 has two single-bevel blades that run along the inner wall of parallel channels, with the unbeveled blade side facing the inside of the channel. Setting the blades so that they rest along the inner wall limits the movement of the blades during cutting. This configuration reduces potential deviation from a parallel specimen by preventing inward movement of the



1. Images of the measurement of a sample specimen. Note that the jaws of the caliper, resting on a level surface, are elevated above the surface and so measure just the area of the upper facing at one edge.

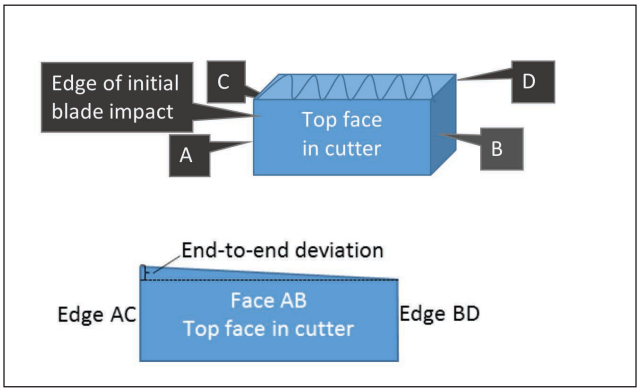
blades and providing some support to restrict blade bowing. Specimens cut with both blades have a nominal height and parallelism defined by the channel width, 2 in. (50.8 mm) for our version of the equipment. A mountable guide bar running parallel to the blade channel can be installed to prevent the right-most blade from affecting the material being cut, allowing a second cut on the specimen to trim it to a smaller height.

Cutter 2 is similar, a dual blade device with blades that are at a 2 in. (50.8 mm) fixed separation. These blades are installed with some pressure against the inside edge of their guiding channels, potentially causing the guide to wear over time, thus leading to deviations from parallel in the shape of the specimen in the initial cut. The right-most blade can be removed, allowing a metal guide block to be mounted to set a new specimen height with a second cut.

For cutter 3, also a dual blade cutter with single bevel blades, the blades rest in the center of their guiding channel, preventing wear on the channel itself. However, this allows some movement of the blades during cutting, potentially causing the specimens to exhibit a variation in edge measurements from blade flexing. For this cutter, the blade carriage itself is adjustable, allowing the distance between the two blades to be shifted to cut ECT specimens of any height with a single pass. This avoids any effects from the specimen twisting in a second cut and maintains the parallelism levels achievable by the spacing and rigidity of the instrument and blades.

Cutter 4 is a single blade cutter, using a blade beveled on both sides that runs in the center of its guide channel. An adjustable guide bar parallel to the blade channel enables specimen preparation to any desired size. Because the blade is beveled, there is no need, nor option, for non-beveled edges on the specimen to be maintained. In many operations, this common cutter may be used for the machine direction cuts of the board before cross directional cuts performed on other cutters to create the loading edges, but some may also use it for cutting the loading edges despite its inability to support conformance with TAPPI T 811.

Cutter 5 is also a single blade cutter, with the blade running along the center of a channel and the sample resting against a guide stop to determine specimen size. Uniquely, this cutter's blade is circular, with a much less significant bevel on both sides. However, the existing bevel still means this cutter does not strictly follow TAPPI T 811 standards for specimen preparation.



2. Definition of the four vertical sample edges used to define sample geometry. End-to-end variation is the difference in the averages of A with C (defining sample edge AC) and B with D. Face-to-face variation is the difference in the averages of A with B (defining face AB) and C with D.

Cut specimens were examined as produced, with the cutting blades changed at the first sign of wear, when specimen edges diverged from clean and crisp. This varied by cutter, blade system, and sample material, but was typically at least daily.

MEASURING PARALLELISM

Quantifying the parallelism of an ECT specimen presented some unique challenges. We needed a method that was relatively robust, repeatable, and easily executed. For this work, we used a standard digital caliper with a resolution of 0.0005 in. (0.0127 mm) and an accuracy of ±0.001 in. (0.0254 mm) to measure each vertical edge of the test specimens (**Fig. 1**). By measuring each facing at each end of the specimen, we get four measurements. This allowed us to calculate an average change across the specimen, both along the length of the specimen (end-to-end) and front to back (face-to-face) (**Fig. 2**). Note that the accuracy of our measurement is the same as the specified tolerance for the parallelism of the crush

Cutter No.	Blade Thickness, in.	Impact Angle, °	Impact Depth, in.	Bevel Depth, in.
1	0.0257	40	0.315	0.130
2	0.0177	35	0.301	0.073
3	0.0241	26	0.284	0.109
4	0.0237	40	0.237	0.083 (double)
5	0.0118	~40 (circular)	0.282	0.038 (double)

I. Blade dimensions for the blades used in each cutter. The impact angle and depth are fixed by the geometry of the structure holding the blade in place for most cutters. Note that for cutters 4 and 5, the beveled area rises up along each side of the blade. For cutter 5, the angle of impact is estimated at the top of a typical C-flute specimen, and changes based on the thickness of the specimen to be cut, given the curvature of the blade itself.

tester platens themselves, as stated in the TAPPI T 811 ECT method.

Each ECT specimen has a specific orientation in the cutting process. For all the cutters, a sample strip is placed flat on a support surface and the cutting blade travels across the sample. Given the blade angle, the blade first impacts the top surface of one edge of the specimen (edge A). We call the edge immediately below that, on the same end of the specimen, edge C. The average of our caliper measurements on edge A and edge C define for us the height of the specimen on that end. On the other end, edge B is on the top face in the cutter and edge D is on the bottom face, with the average of measurements B and D defining the height of the specimen on the other end. The difference in the averages on each end defines the edge-to-edge or end-to-end deviation from parallel along the length of the specimen. This mimics the measurements made by Eriksson [14]. Similarly, the difference between the average of A and B (defining the size of face AB, facing up in the cutter) and the average of C and D (defining the face CD, facing down) provides an assessment of the average face-to-face deviation from one side of the specimen to the other. This quantifies the deformation to one liner/facing, which would occur before the other liner picks up any load.

Given these definitions, all cutters showed some challenges maintaining parallelism. This might have resulted from strips moving vertically or twisting during the cutting process. It also might have resulted from individual specimens shifting in the cutter for cases where a second cut is necessary. The blade(s) might also be flexing as they pass through the sample. Each cutter uses a different blade, impacting the specimens at different angles, with bevels of different sizes (**Table I**). The one common factor for all cutters is that the top liner receives the initial impact before the rest of the specimen. This can cause a slight roll at the edge (**Fig. 3**), which we observed for many specimens.



3. Three specimens from the same material cut with cutter 5. The left side of each specimen was face up in the cutter, and the blade impinged first on the leftmost surface. Note that both liners are curled in the same direction because of the force of the blade pressing down during cutting. The left specimen is unwaxed and appears as cut. The middle specimen is after edge waxing. The rightmost specimen has been tested, with a clear edge bias following the initial edge curl. Specimens were identically sized and are offset one from another in the image for visual clarity. Few samples have this dramatic an edge curl, but many samples cut with the various cutters have some observable edge impact.

TYPICAL SPECIMEN PARALLELISM

From the literature, we would expect specimen parallelism, both end-to-end and face-to-face, to affect measured ECT values. To understand how much variation might exist, we can look at a subset of randomly sampled materials cut on a range of cutters at laboratories across the industry. We find that a set of specimens can have an average deviation from parallel of several mils (0.001 in.; 0.0254 mm), both along their length and, more critically, through their thickness (**Table II**). The majority of these values are statistically different from zero, indicating a meaningful deviation from parallel across each set of specimens. The most parallel "face-to-face" specimens came from fixed distance dual blade cutters using single bevel blades, despite the requirements of a second cut when the specimen size requirement was smaller than the blade separation distance. The most parallel "end to end" specimens came from single blade cutters. Effectively, independent of labora-

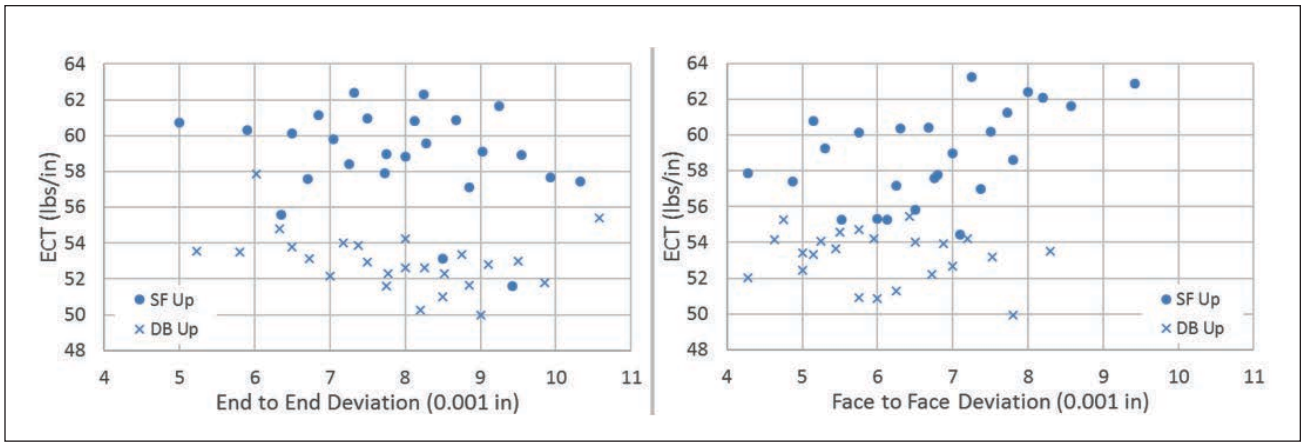
		Nominal Height		Absolute Variation			
				End-to-End		Face-to-Face	
Lab	Cutter	in.	mm	mil	mm	mil	mm
B	4	1.25	31.75	6.08	0.154	1.58	0.040
A	1	1.50	38.10	3.31	0.084	0.07	0.002
C	2	1.50	38.10	3.08	0.078	0.46	0.012
G	2	1.50	38.10	6.17	0.157	0.17	0.004
G	2	1.50	38.10	8.46	0.215	0.63	0.016
A	4	1.50	38.10	0.42	0.011	1.17	0.030
B	4	1.50	38.10	4.73	0.120	0.35	0.009
A	5	1.50	38.10	0.10	0.003	2.60	0.066
E	5	1.50	38.10	2.60	0.066	1.20	0.030
E	5	1.50	38.10	2.95	0.075	1.83	0.046
E	5	1.50	38.10	2.50	0.064	0.60	0.015
E	5	1.50	38.10	2.75	0.070	2.65	0.067
E	5	1.50	38.10	2.75	0.070	1.55	0.039
E	2	2.00	50.80	3.10	0.079	0.50	0.013
E	2	2.00	50.80	4.75	0.121	0.25	0.006
E	2	2.00	50.80	5.37	0.136	0.27	0.007
E	2	2.00	50.80	6.40	0.163	0.50	0.013
E	2	2.00	50.80	5.70	0.145	0.40	0.010
D	4	2.00	50.80	0. 92	0.023	2.67	0.068
D	4	2.00	50.80	1.23	0.031	0.77	0.020
F	4	2.00	50.80	2.29	0.058	4.86	0.123
F	4	2.00	50.80	3.79	0.096	0.64	0.016

II. Parallelism measurements on specimens of different sample materials supplied by various industry laboratories. The first sample (1.25 in.) was B-flute. All other samples were C-flute. Samples were cut to different heights by the supplying laboratories, in line with their needs. We find meaningful deviation of nearly all specimens from true parallel in at least one direction, independent of laboratory, cutter type, blade used, or nominal specimen height (ECT = edgewise compressive strength).

tory or preparation equipment, typical specimens produced for ECT testing are not truly rectangular.

At its extreme, deviations from parallel along the length of the specimen can result in a significantly trapezoidal specimen, end-to-end, causing one end of the specimen to load to failure before the other end supports any load. Based on the literature discussed previously [14-16,18], that might occur if the size difference end-to-end was on the order of 0.5%-1% of the height of the sample specimen. Few, if any, of the ECT specimens measured here appear to have variations large enough to lead to that effect explicitly. However, it is reasonable to expect a continuum of impact from a specimen where one end loads to failure (and the test stops) before the other end loads at all, up to the point where the specimen truly is perfectly parallel and the entire specimen loads uniformly and fails as such. These samples collected from across the industry are all somewhere along that continuum, with an unknown reduction from the true inherent compression strength of the material in each case.

Similarly, deviations from parallel along the thickness of the specimen, from one face to the other, can cause one liner to carry proportionally more load than the other. We can imagine that a perfect compression failure would have both the singleface and doubleback liners reaching their maximum carrying capacity simultaneously. If, however, the specimen is cut so that one facing is slightly larger than the other, it might cause that facing to reach its failure strain first, thus ending the test at a lower measured strength than if both of the liners failed together. (Conceptually, this is not unlike a load-sharing situation with a corrugated box and divider — the system reaches its highest peak strength when the box and divider reach their maximum carrying capacity at the



4. The effect of end-to-end and face-to-face variation, averaging sets of 10 specimens cut from a single lot of material using cutter 3. The orientation in the cutter dominates the data, even above the relatively high variability arising from this cutter. (Standard deviations on each point are on the order of 8%–10%.)

same overall deformation.) As with end-to-end deviations, the samples in Table II are all somewhere along the continuum between simultaneous failure of all structural components and loading of one component to failure before the other picks up any load. We have the ability to begin to identify the effect of those deviations.

EFFECT OF TRAPEZOIDAL SPECIMENS

ECT is conceived as a bulk material property with uniform failure throughout the material. However, from our observations, total specimen failure actually occurs only a small fraction of the time. We commonly find that a group of sample specimens cut from a single lot of material in a consistent manner exhibits a failure bias, collapsing predominantly on one side of the specimens. While at first glance this implies that the structure is unbalanced, we find the size of this bias depends not only on the board structure but also on the equipment used to cut the specimen. Thus, the cutting equipment can force failure to one face or the other, with the potential to shift the ECT value.

Unbalanced material

In an attempt to more clearly quantify the effect to ECT values, we cut 500 ECT specimens from an individual singlewall C-flute board sample (nominal combination 42-23-69), using cutter 3. Likely because of the flexibility of the blades during the cutting process and their freedom to move in their tracks, this cutter produced some of the more significantly trapezoidal specimens in our explorations, both end-to-end and face-to-face. Half the specimens were cut with the singleface side oriented face up during cutting and the other half with the singleface oriented down, creating specimens with one or the other liner slightly larger. We measured the edges (A-D) on each specimen and compressed them individually. We then sorted the samples in order of deviation from parallel, and grouped them in sets of 10 to form ECT averages with average deviations from parallel.

Plotting these average ECT values against either the average end-to-end or face-to-face deviations for each set shows that the dominant factor governing the ECT measured is which side of the board was face up in the cutter (**Fig. 4**). When the doubleback side of the board was facing up, all the specimens exhibited failure at maximum load on the doubleback side and not on the singleface side. When the singleface side was up, more than 75% of the specimens exhibited failure only on the singleface side. While we might expect the weaker doubleback liner to reach collapse first, it is clearly the orientation of the sample strip in the cutter, not the strength of

Cutter	Average Variation		Doubleback (DB) up ECT			Singleface (SF) up ECT			ECT	
	End-to-End	Face-to-Face	Fail on SF	Average ±STD		Fail on SF	Average ±STD		Difference	
	mil	mil		lbs/in.	N/mm		lbs/in.	N/mm	lbs/in	N/mm
1	4.7	0.4	25%	61.4±1.8	10.8±0.3	83%	63.4±2.2	11.1±0.4	2.0	0.3
3	7.9	6.3	0%	52.9±5.3	9.3±0.9	75%	58.9±6.8	10.3±1.2	6.0	1.0
4	0.5	3.1	Edge	54.8±2.9	9.6±0.5	Edge	58.2±2.0	10.2±0.4	3.4	0.6
5	1.4	2.5	0%	57.8±2.2	10.1±0.4	100%	60.1±5.4	10.5±0.9	2.3	0.4

III. Side of failure and TAPPI Standard Test Method T 811 ECT values for a single material (42-23-69) across multiple cutters.

the papers, that governs the failure and controls the ultimate ECT measured. The average ECT when the failure occurs on the stronger singleface liner was more than 10% higher than when the failure occurs on the doubleback liner. Beyond this primary factor, we also find end-to-end variation to be statistically significant (p=0.006) over the level of testing variation when we run an analysis of variance on the entire 500 data point set. (Face-to-face variation is overpowered by the orientation in the cutter and noise in the data, and is not independently resolved.)

This behavior on unbalanced material from our designed experiment persists across cutters. The difference in cutting orientation can lead to an ECT difference of 5%-10% or more (**Table III**). The larger the face-to-face difference in size, the larger the ECT difference. Importantly, no cutter we examined was entirely free from sidedness bias. Although cutter 1 appeared to give the least bias, none seem capable of consistently producing truly parallel samples. We can hypothesize that the edge curl discussed previously (Fig. 3) arising from the blades impacting one side of the sample material first during cutting might be influencing the distribution of load on the loading surfaces of each specimen, potentially explaining the edge failure bias connected with cutting orientation.

Designed experiment, balanced and unbalanced

We can further clarify how cutting affects ECT by analyzing test results from a separately designed experiment. In one production run we produced four C-flute board combinations with either light or heavy liners on each side of the board, then sampled across the corrugator at five positions for each combination. Using cutters 1 and 5, we prepared ECT specimens for each combination at each corrugator position, cutting specimens with the singleface side up or the doubleback side up. We then tested the specimens in two orientations in our test equipment (singleface side oriented to the right or left). In the full factorial experiment ($4 \times 5 \times 2 \times 2 \times 2 = 160$ sets of ECT) we recorded not just the average ECT of 10 specimens for each combination of conditions, but also identified explicitly which side failed on each specimen during testing. We later repeated a subset of this testing on the same material, producing samples using cutter 3.

Analysis of the ECT values and the typical side of failure (failure mode) found no dependence on either the orientation of the specimen in the test equipment (the crush tester, during compression) or the sampling position across the corrugator, neither as individual factors nor as significant factors in combination with others. This is good; our conclusions are robust to variation from the compression equipment and corrugator. Board combination was the primary contributor to ECT, as would be expected. Stronger papers should lead to higher ECT values, and the heavier papers had about twice the ring crush of the lighter papers.

We again expect that for a balanced combination, where the two liners have very similar strength and the specimen was cut squarely (with the two sample faces parallel and of the same size), that the ECT specimens should fail on the singleface side about as often as on the doubleback side. The specimen should reach critical strain first on one side or the other based on random variation in the materials. Instead, we found a sidedness dependence to the failure for cutters 3 and 5, notably less so for cutter 1 (**Table IV**), similar to our observations for the 500 specimens of unbalanced board produced on cutter 3 discussed previously. Despite this sidedness bias, ECT values were statistically independent of the failure side in these balanced materials, regardless of the cutter used, as would be expected given the similar strength of the faces for each specimen. The values measured do have some dependence on the cutter, which might arise from the propensity of each cutter to produce samples trapezoidal in the end-to-

Doubleback (DB)/ Singleface (SF)	Orientation	% Fail SF			ECT (Average ±STD)					
					Cutter 1 (n=100)		Cutter 5 (n=100)		Cutter 3 (n=10)	
		Cutter 1 (n=100)	Cutter 5 (n=100)	Cutter 3 (n=10)	lbs/in.	N/mm	lbs/in.	N/mm	lbs/in.	N/mm
Light/Light	DB up	63.5	6.5	0.0	38.1±1.2	6.7±0.2	36.3±1.3	6.4±0.2	32.1±2.6	5.6±0.5
	SF up	61.0	88.5	90.0	37.9±1.4	6.6±0.2	36.8±1.4	6.4±0.2	33.9±1.9	5.9±0.3
Heavy/Heavy	DB up	58.8	15.5	0.0	58.0±2.0	10.2±0.4	55.7±3.3	9.8±0.6	55.9±2.7	9.8±0.5
	SF up	72.0	98.0	90.0	57.3±2.2	10.0±0.4	55.0±2.9	9.6±0.5	55.1±0.9	9.6±0.2
Light/Heavy	DB up	1.5	1.0	0.0	44.7±1.5	7.8±0.3	41.3±1.6	7.2±0.3	38.9±2.6	6.8±0.5
	SF up	3.0	57.5	65.0	45.5±1.8	8.0±0.3	48.2±1.8	8.4±0.3	44.6±4.9	7.8±0.9
Heavy/Light	DB up	99.0	70.5	90.0	41.9±1.4	7.3±0.2	48.8±1.7	8.5±0.3	47.3±2.2	8.3±0.4
	SF up	98.5	100.0	100.0	44.6±1.4	7.8±0.2	44.1±2.1	7.7±0.4	40.4±2.1	7.1±0.4

IV. Results of a designed experiment exploring cutting orientation, cutter, and failure mode on ECT values. The initial rounds of testing included just cutter 1 and cutter 5. Cutter 3 was added in at a later time, on a small subset of the material.

Cutter	Average Variation		Doubleback (DB) up ECT			Singleface (SF) up ECT			ECT	
	End-to-End	Face-to-Face	Fail on SF	Average ±STD		Fail on SF	Average ±STD		Absolute Difference	
	mil	mil		lbs/in	N/mm		lbs/in	N/mm	lbs/in	N/mm
1	4.1	0.3	55%	50.3±1.7	8.8±0.3	55%	48.5±1.6	8.5±0.3	1.7	0.3
2	4.0	0.2	45%	54.6±0.9	9.6±0.2	50%	52.8±1.0	9.2±0.2	1.8	0.4
4	0.4	1.7	45%	50.3±1.7	8.8±0.3	45%	48.5±1.6	8.5±0.3	1.7	0.3
5	1.5	2.7	35%	50.4±3.0	8.8±0.5	35%	50.8±1.3	8.9±0.2	0.4	0.1
1	5.4	1.0	55%	66.6±1.7	11.7±0.3	55%	66.6±4.9	11.7±0.9	0.0	0.0
3	8.6	7.7	35%	64.1±1.4	11.2±0.2	65%	63.7±1.4	11.2±0.2	0.4	0.0
4	0.1	3.1	50%	63.3±2.2	11.1±0.4	45%	66.7±1.9	11.7±0.3	3.4	0.6
5	1.8	2.1	25%	63.1±3.5	11.1±0.6	80%	64.8±2.7	11.3±0.5	1.7	0.2

V. Side of failure and TAPPI T 839 ECT values for two materials across multiple cutters. Ten specimens were cut with each cutter. ECT values are statistically independent of which side was cut facing up for all cutters except cutter 4. The first set of data is from the "heavy/light" materials in Table IV, with the heavier liner on the DB side. The second set is from the same set of materials as Table III, with the heavier liner on the SF side. For both materials, the ECT value tends to be higher when the heavier liner is impacted first by the cutting blades, though the difference is generally smaller than for the TAPPI T 811 ECT test (Tables III and IV).

end direction. Cutter 1, with less sidedness bias, produced higher ECT values, indicating an area for future study in the development of optimal cutting methodology.

For the unbalanced combinations in this experiment, we found that orientation in the cutting apparatus shifted the failure mode from the weaker paper for two of the three cutters. When the singleface side was oriented up in the cutter, a significant fraction of the specimens failed on the singleface side for those two cutters, regardless of which liner was stronger (Table IV). Similarly, cutting with the doubleback side up increases the propensity of specimens to fail on the doubleback side, and again appears to shift the ECT values. Specimens could be influenced to fail on whichever side was oriented up in the cutting process, to different degrees, depending on the cutter used. This had a notable effect on the measured ECT value, with higher measured values occurring when the stronger liner failed first under load.

Although the previously mentioned data has focused primarily on the waxed ECT test, we can repeat these types of measurements with other ECT methods. With the clamp method (TAPPI T 839), for example, we find that the effect of cutting bias is reduced, but not necessarily eliminated, especially for dual blade cutters designed to cut 2 in. specimens with a single cut (Table II and **Table V**). In this method, ECT values are generally independent of cutting orientation. This observation might also support the development of a test method that, along with adjustments to our cutting, can help us dramatically reduce the potential for bias and variation in ECT values.

A TEMPORARY PATH FORWARD

Together, these observations provide a standard that a new cutting process must reach to truly meet the criteria of "parallel" test specimens presented in TAPPI T 811. We must clearly find a cutting method that avoids influencing the side on which the specimens fail.

The literature is replete with ECT data, with dozens of papers [18] discussing ECT measurements, modeling, and utility. The many models for estimating ECT from paper strength [19] provide similar functional forms, but fundamentally different constants. The same issue arises with box compression estimations that rely on ECT. Few of these studies mention the cutters used, or make mention of end-to-end or face-to-face size variations. The differences discussed here apparently provide a hidden contribution to the variations measured, and might well account for some or perhaps even all of the differences between models. Furthermore, these differences might also account for a meaningful fraction of between-laboratory differences, as in the industry collaborative round-robin testing program [20].

We clearly need a more detailed and extensive study that includes finished boxes to determine what effect these differences might have on estimation equations for BCT. Without revising any of the existing equations, simply shifting the ECT values by changing cutting preparation methods might shift our estimate of BCT by as much as 10% or more. Clearly, the box strength is whatever it is, and this shift in estimation is not inherently helpful. A more consistent ECT method might lead to estimation equations with less variability, and it might help us more accurately predict performance of boxes in the field.

To make the methodology more robust and reduce the effect of variation, our industry's technical committees will have to explore how to specify and measure parallelism, and at what accuracy. Until we have a better specimen preparation method, we might mimic the instructions for some of our paper tests. For example, the ring crush test (TAPPI T 822) specifies alternating specimen orientation in the test fixture to minimize the issue of edge influence. By the same token,

we may choose to specify alternating sample orientation in today's cutting equipment to at least average out the cutting bias arising from cutting blades impacting the top of the material first. That would not eliminate the effect of end-to-end bias, but it might help address the specimen edge curl challenge and establish a clearer comparison, avoiding face-to-face bias from cutting. Additional work exploring this issue for the standard referee method (TAPPI T 811) and other ECT methods would be extremely valuable.

The underlying physics and mechanics are robust; paper strength contributes to combined board strength, and the inherent compression strength of the combined board contributes to box performance. Our challenge is in measuring that strength as accurately as possible. Although our current level of ECT test variation might have been acceptable historically, as our industry moves toward true performance packaging, we must do more to reduce the variation in our testing methodology so that we can improve and optimize the boxes we provide to our customers. **TJ**

ACKNOWLEDGEMENTS

We thank our industry colleagues for sending us sets of samples for measurement, which were cut in their facilities, to corroborate and support the work done in our laboratory.

LITERATURE CITED

1. McKee, R.C., Gander, J.W., and Wachuta, J.R., *Paperboard Packag.* 48(8): 149(1963)
2. Urbanik, T.J. and Frank, B., *Wood Fiber Sci.* 38(3): 399(2006)
3. Frank, B., *Packag. Technol. Sci.* 27(2): 105(2014).
4. National Motor Freight Traffic Association, "Packaging," National Motor Freight Traffic Association, Alexandria, VA, USA. Available [Online] http://www.nmfta.org/pages/NMFCPackaging.
5. Institute of Paper Chemistry, "An investigation of testing methods for determination of the ultimate edgewise compression behavior of corrugated board. Part VI. A comparison of various test methods on commercially-made corrugated board," IPC Project 1940-4, Institute of Paper Chemistry, Appleton, WI, USA, June 1962.
6. Stott, R.A., *Appita J.* 29(1): 29(1975).
7. Schrampfer, K.E. and Whitsitt, W.J., *Tappi J.* 71(10): 65(1988).
8. Kroeschell, W.O., *Tappi J.* 75(1): 79(1992).
9. Urbanik, T.J., Catlin, A.H., Friedman, D.R., et al., *J. Test Eval.* 21(1): 62(1993).
10. Markstrom, H., *Testing Methods and Instruments for Corrugated Boards*, Lorentzen & Wettre, Kista, Sweden, 1999.
11. Frank, B., "Which ECT?" *Corrugating International*, August 2003, pp. 34-38.
12. Frank, B., *Corrugated Today* 2(3): 52(2006).
13. Popil, R.E., *BioResources* 7(2): 2553(2012).
14. Eriksson, L., *Boxboard Containers*, March 1979.
15. McLain, T.E. and Boltnott, R.L., *TAPPI J.* 65(3): 148(1982).
16. Ernst, U. and Graf, E., *Papier* 45(9): 549(1991).
17. Institute of Paper Chemistry, "An investigation of testing methods for determination of the ultimate edgewise compression behavior of corrugated board. Part V. A study of dipped-end columns and description of methods of column preparation," Container Research Progress Reports to the Fourdrinier Kraft Board Institute, IPC Project 1940-4, Institute of Paper Chemistry, Appleton, WI, USA, September 1960.
18. Popil, R., "An annotated bibliography of ECT," Georgia Institute of Technology, Atlanta, GA, USA, 2005. Available [Online] http://www.rbi.gatech.edu/sites/default/files/documents/Annotated%20Bibiography%20of%20ECT.pdf.
19. Fibre Box Association, *Edge Crush Test*, Fibre Box Association, Itasca, IL, USA, 2008.
20. Collaborative Testing Services, Inc., *Containerboard*, Collaborative Testing Services Inc., Sterling, VA, USA, 2018. Available [Online] http://www.collaborativetesting.com/store/main.aspx?DepartmentId=42.

ABOUT THIS PAPER

Cite this article as: Loza, J., Cash, D., Frank, B. *TAPPI J.* 17(4):219(2018).

https://doi.org/10.32964/TJ17.04.219

DOI: https://doi.org/10.32964/TJ17.04.219

ISSN: 0734-1415

Publisher: TAPPI Press

Copyright: ©TAPPI Press 2018

About this journal

ABOUT THE AUTHORS

We chose this topic to research because we were intrigued by variations in our ECT data. We believe this is the first work of this type to examine parallelism in detail. Perhaps the most difficult aspect of the study was the sheer quantity of test materials required to build a statistically robust signal from the noise. The results show that we have a lot of work to do to improve standard test methods.

Frank is senior manager, Technical Operations and Resources, Loza is senior technician, and Cash is contract technician, Packaging Corporation of America, Mundelein, IL, USA. Email Frank at bfrank@packagingcorp.com.



Frank



Loza



Cash

On the nominal transverse shear strain to characterize the severity of creasing

DOUGLAS W. COFFIN AND JOEL C. PANEK

ABSTRACT: A transverse shear strain was utilized to characterize the severity of creasing for a wide range of tooling configurations. An analytic expression of transverse shear strain, which accounts for tooling geometry, correlated well with relative crease strength and springback as determined from 90° fold tests. The experimental results show a minimum strain (elastic limit) that needs to be exceeded for the relative crease strength to be reduced. The theory predicts a maximum achievable transverse shear strain, which is further limited if the tooling clearance is negative. The elastic limit and maximum strain thus describe the range of interest for effective creasing. In this range, cross direction (CD)-creased samples were more sensitive to creasing than machine direction (MD)-creased samples, but the differences were reduced as the shear strain approached the maximum. The presented development provides the foundation for a quantitative engineering approach to creasing and folding operations.

Application: The provided equation characterizing the shear experienced by the paperboard increasing can be used to determine multiple crease tool configurations that yield the same effect on creasing (relative crease strength or springback). The range of interest in shear strain is identified for practical evaluation and further studies of creasing and folding. The differences between MD and CD creasing is further illuminated.

In order to form a defect-free and aesthetically pleasing edge on a box, Shelton [1], in an 1876 U.S. patent, specified that the paperboard first be creased and then folded such that a smooth and straight inner bead developed along the inside edge. In a 1912 U.S. patent, Bird [2] illustrated the importance of delamination to the creased zone. These two aspects, (1) forming the crease geometry and (2) preparing the paper for ease of delamination, are essential for a successful creasing operation. A recent literature review pertaining to creasing and folding [3] concluded that using a measure of a nominal transverse shear-strain induced during creasing would be fruitful to characterize the behavior of a paperboard under various creasing tool geometries. In fact, as early as 1939, Halladay and Ulm [4] captured this concept with what they termed "angle of break". Nagasawa et al. [5,6] defined a shear strain measure for a rounded rule and characterized various aspects of creased board such as folding resistance, tensile strength, and the presence of cracks. Coffin and Nygårds [3] followed the same reasoning of reference [5] and presented a transverse shear strain equation valid for a square-tipped rule. Coffin and Panek [7] presented a more general measure for shear strain for generic rules and channels with rounded corners. The latter expression allows one to characterize the effects of tooling that span the spectrum from fully rounded rules to square-tipped rules. The objective of the following study is to establish that the transverse shear equation, presented by Coffin and Panek [7], provides a robust measure that can normalize creasing data for a wide range of tool geometries.

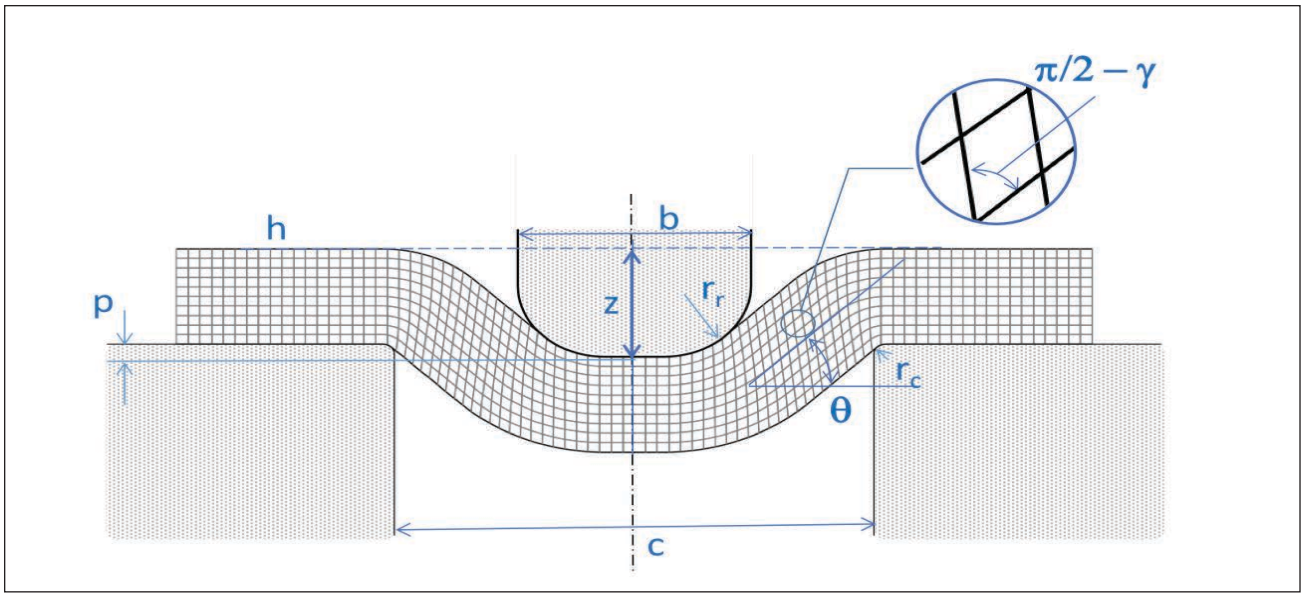
THEORY

Figure 1 provides the geometry for a generic creasing operation. Note, that the penetration, p, is the maximum distance the tip of the rule travels relative to the top surface of the channel. The crease depth, z, is the penetration plus the board thickness, h. The uncreased sample corresponds with $z=0$ or $p=-h$. The lines on the creased material shown in Fig. 1 illustrate a permissible deformation the board might undergo during the creasing. For the undeformed paperboard, the lines formed a square gird, and the deformation shown results from simple transverse shearing of the paperboard. In other words, z direction (ZD) compression and machine direction (MD) or cross direction (CD) (in-plane) elongation are ignored. This assumption attributes all the deformation to direct transverse shear and is approximately correct as borne out by inspection of micrographs presented by Coffin and Nygårds [3] and Halladay and Ulm [4]. The measure of shear, γ, is defined as the change in angle of the originally square lines as illustrated in the insert of Fig. 1.

With the assumptions outlined above, the angle, θ, that forms in the free-span region is derived in the Appendix and the final expression is written as:

$$\tan(\theta) = \frac{\sqrt{(1-\kappa)^2+\lambda(2+\lambda)}-(1-\kappa)(1+\lambda)}{\lambda(2+\lambda)}, \quad \text{which} = \frac{\kappa(2-\kappa)}{2(1-\kappa)} \text{ for } \lambda = 0 \tag{1}$$

where $\kappa=z/(r_c+r_r+t)$ and $\lambda=\frac{(c-b-2t)}{2(r_c+r_r+t)}$ are the dimensionless



1. Crease geometry.

crease displacement and crease clearance, respectively. The shear strain in the free-span region is then determined as:

$$\tan(\gamma) = \theta = tan^{-1}\left(\frac{\sqrt{(1-\kappa)^2+\lambda(2+\lambda)}-(1-\kappa)(1+\lambda)}{\lambda(2+\lambda)}\right) \quad (2)$$

Eq. 1 and Eq. 2 reveal that this shear measure is only a function of two dimensionless parameters, κ and λ. The crease-clearance, λ, is significant because it determines the free-span of the paper between the rule and the channel. Note that the dimensionless parameters only depend on the sum of the tooling radii and the caliper. Increasing this sum decreases λ and κ and the resulting shear strain, γ.

For the case of no clearance, λ=0 (second part of Eq. 1), there is a maximum depth of draw at which point θ=90°. After this point, the paperboard will be drawn (or extended) in to the tooling, but the extent of shear remains the same. The maximum value of the shear, γ_{max} = 57.20°, is when λ=0 and κ =1.

For the case where the clearance is less than zero, λ<0, there is a maximum depth of draw, where further creasing must be accompanied with a compression of the thickness. Using just shearing strain to characterize the severity of the crease beyond this point is not justified. This critical draw occurs when the quantity within the square-root symbol of Eq. 1 is zero. That translates to:

$$z_{cr} = (r_c + r_r + t)\left(1 - \sqrt{|\lambda|(2+\lambda}\right) \quad (3)$$
$$\tan(\gamma_{cr}) = sin^{-1}(1+\lambda)$$

If the rule and channel radii approach zero and the corners are sharp, a nominal shear strain could be expressed simply as previously stated in [3] as:

$$\tan(\gamma_{square}) = \frac{2z}{c-b} \quad (4)$$

For the case where the rule radius is half the rule width and the channel radius approaches zero, the shear strain could be expressed as previously given in [5] as:

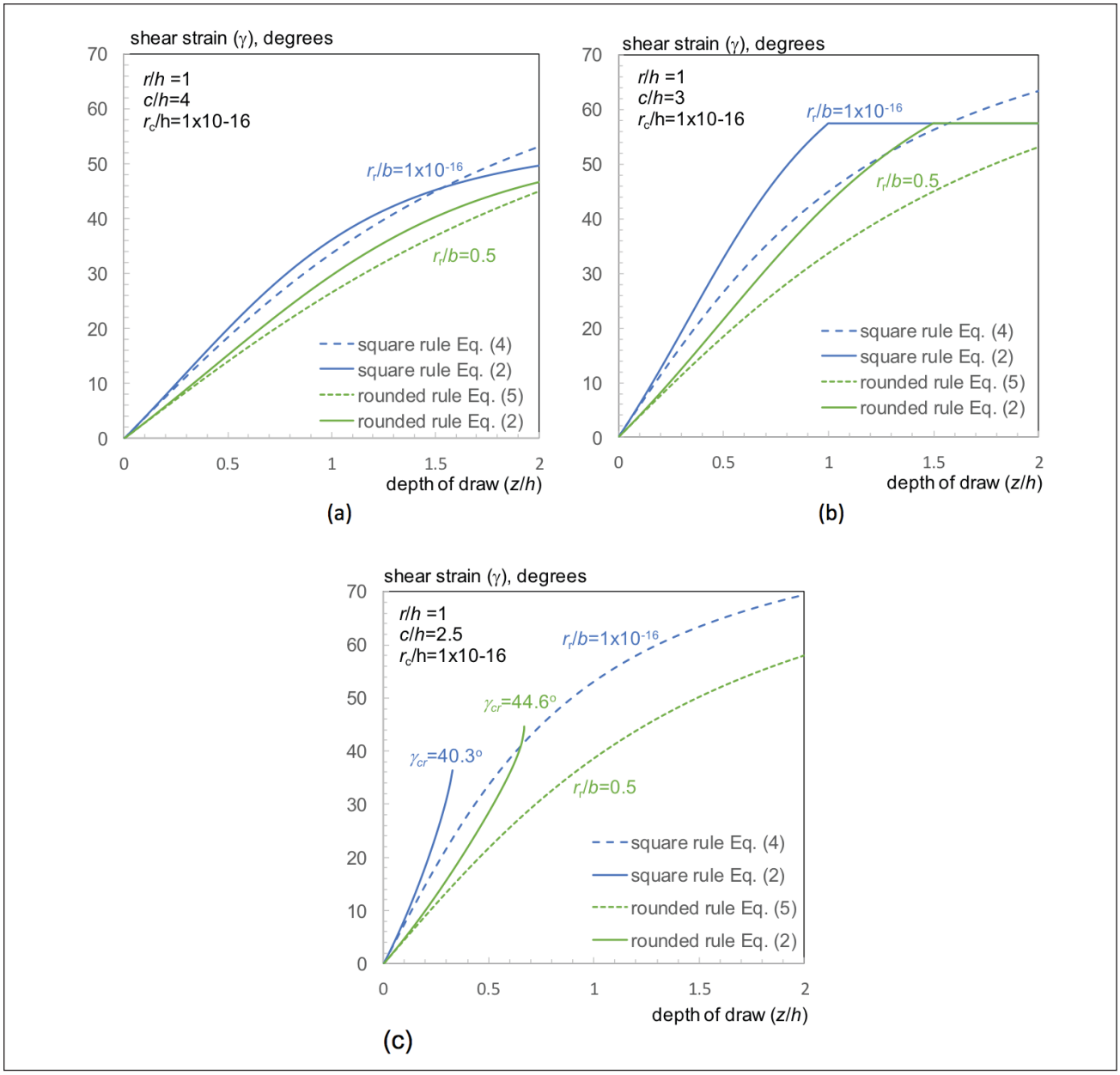
$$\tan(\gamma_{rounded}) = \frac{2z}{c} \quad (5)$$

Eqs. 4 and 5 represent alternative representations of the shear strain compared to Eq. 2. The curves of **Fig. 2** provide comparisons of these predictions for three cases: (a) λ>0, (b) λ=0, and (c) λ<0. For small depth of draws, Eq. 2 reasonably matches both Eqs. 4 and 5. The match is best for the case of λ>0, but as the creasing operating parameters produce more severe shearing deformation, the various shear measures deviate. The advantage of Eq. 2 over Eqs. 5 and 6 is that it applies to a full range of tool geometries. In addition, Eq. 2 highlights that for the case of $\lambda \leq 0$, maximum shear strain occurs for a finite draw, and further creasing beyond this point would introduce ZD compression and possibly MD-CD extension. The advantage of Eqs. 5 and 6 are that they are simpler and provide a measure for all values of crease draw.

METHODS & MATERIALS

A series of creasing and folding tests were completed on a commercially produced coated solid bleached sulfate (SBS) board (309 g/m²; h=0.401 mm; TAPPI Standard Test Methods T 410 "Grammage of paper and paperboard [weight per unit area]" and T 411 "Thickness [caliper] of paper, paperboard, and combined board," respectively).

Paperboard samples were creased with a custom laboratory creasing device. The channel segment was mounted to the base structure and the rule segment was mounted to a

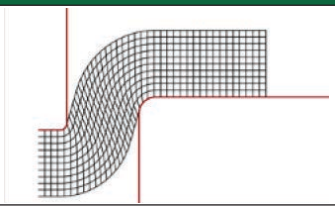
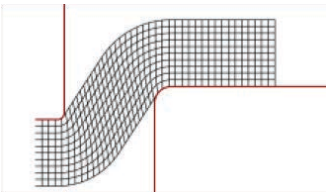
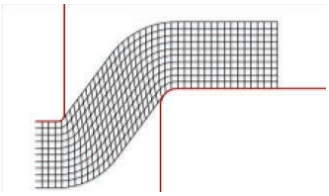
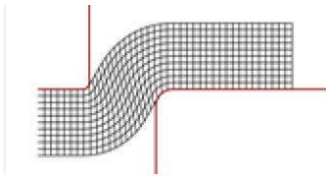
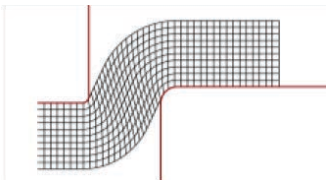
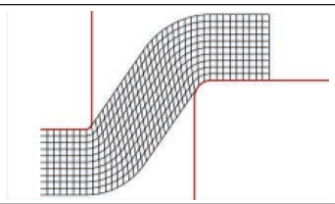
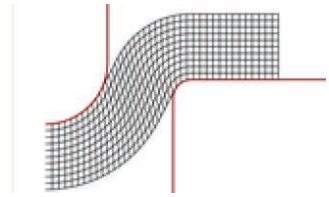
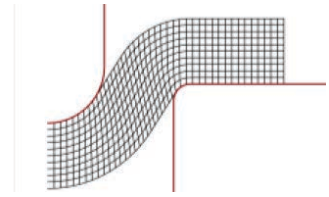


2. Comparison of shear values from Eqs. 2, 5, and 6 for example cases of (a) λ>0, (b) λ=0, and (c) λ<0.

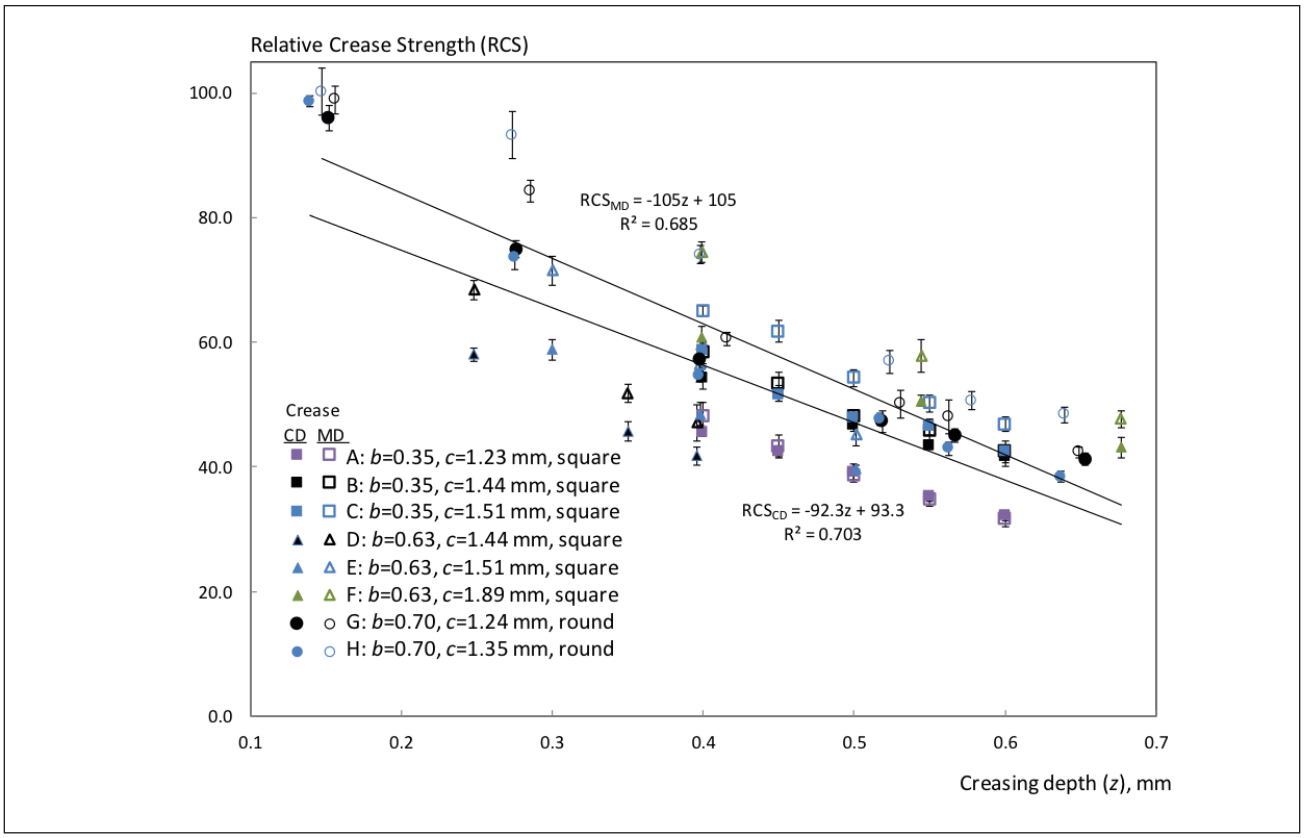
linear motor. The linear motor controlled the motion of the rule to a target penetration depth, *p*, (+/- 0.005 mm) as reported in **Table I**. The velocity of the rule tip was 160 mm/s at point of contact with the paperboard. At this velocity, the total contact time of the rule with the paperboard was ~10 ms.

The tool segments (14 mm x 20 mm x 85 mm) are made of hardened steel, with a dimension tolerance of +/-0.02 mm. For the tooling used in this study, the rule width, *b*, and channel width, *c*, are given in Table I. The rules (A-F) were 50.8 mm long and 1.5 mm high, with either a flat tip profile having a 45° chamfered edge (A-F) or a rounded tip (G and H). The channels were 51.4 mm long and 1.0 mm deep with a 45° chamfered edge. Table I also provides a sketch of the crease at maximum penetration for each set of tooling geometry, as well as the dimensionless clearance and crease depth.

Paperboard samples (100 mm x 300 mm) were clamped on the narrow ends, with one clamp fixed to the base and the other clamp mounted on a slide. The sample was held under a tension of 1.1 kN/m using weights (11 kg) attached to the slide clamp. The rule and channel were oriented so that they were parallel to the short dimension of the sample. In this configuration, the applied tension is perpendicular to the crease. Strips were creased in both the MD and the CD and aligned with the creasing tools. Creases where the axis was aligned in the MD of the paperboard were designated as MD creases, and creases aligned in the CD of the paperboard were designated as CD creases. Four creases were produced on

Set	Crease Shape at Maximum Penetration	Tooling Geometry, mm	Range of Penetration Depths (p), mm	Crease Clearance (λ)	Range of Crease Depth (κ)
A		b= 0.35, c = 1.23 r_r = 0.04, r_c = 0.1	0.00 to 0.20	0.074	0.74 to 1.11
B		b= 0.35, c = 1.44 r_r = 0.04, r_c = 0.1	0.00 to 0.20	0.269	0.74 to 1.11
C		b= 0.35, c = 1.51 r_r = 0.04, r_c = 0.1	0.00 to 0.20	0.333	0.74 to 1.11
D		b= 0.63, c = 1.44 r_r = 0.04, r_c = 0.1	-0.15 to 0.00	0.009	0.46 to 0.73
E		b= 0.63, c = 1.51 r_r = 0.04, r_c = 0.1	-0.10 to 0.10	0.074	0.56 to 0.93
F		b= 0.63, c = 1.89 r_r = 0.04, r_c = 0.1	0.00 to 0.30	0.426	0.74 to 1.25
G		b= 0.70, c = 1.24 r_r = 0.35, r_c = 0.1	-0.24 to 0.25	-0.153	0.30 to 1.31
H		b= 0.70, c = 1.35 r_r = 0.35, r_c = 0.1	-0.26 to 0.24	-0.088	0.13 to 1.13

I. Creasing settings.



3. Relative crease strength (RCS) versus depth of crease.

each strip and evenly spaced along the longer direction of the sample. Samples were then cut to provide one crease per specimen. The height and width of each crease was measured.

The creased specimens were folded to 90° using a Lorentzen & Wettre (Kista, Sweden) bending tester, code 160. Test pieces were 38-mm wide, the bending length was 10 mm, and the crease was aligned to within 1.0 mm of the clamp. The sample was folded to 90° (45°/s) and then back to 0°. The bending moment [mNm] versus angle of bend was recorded for the full curve. Eight replicates were measured for each case given in Table I.

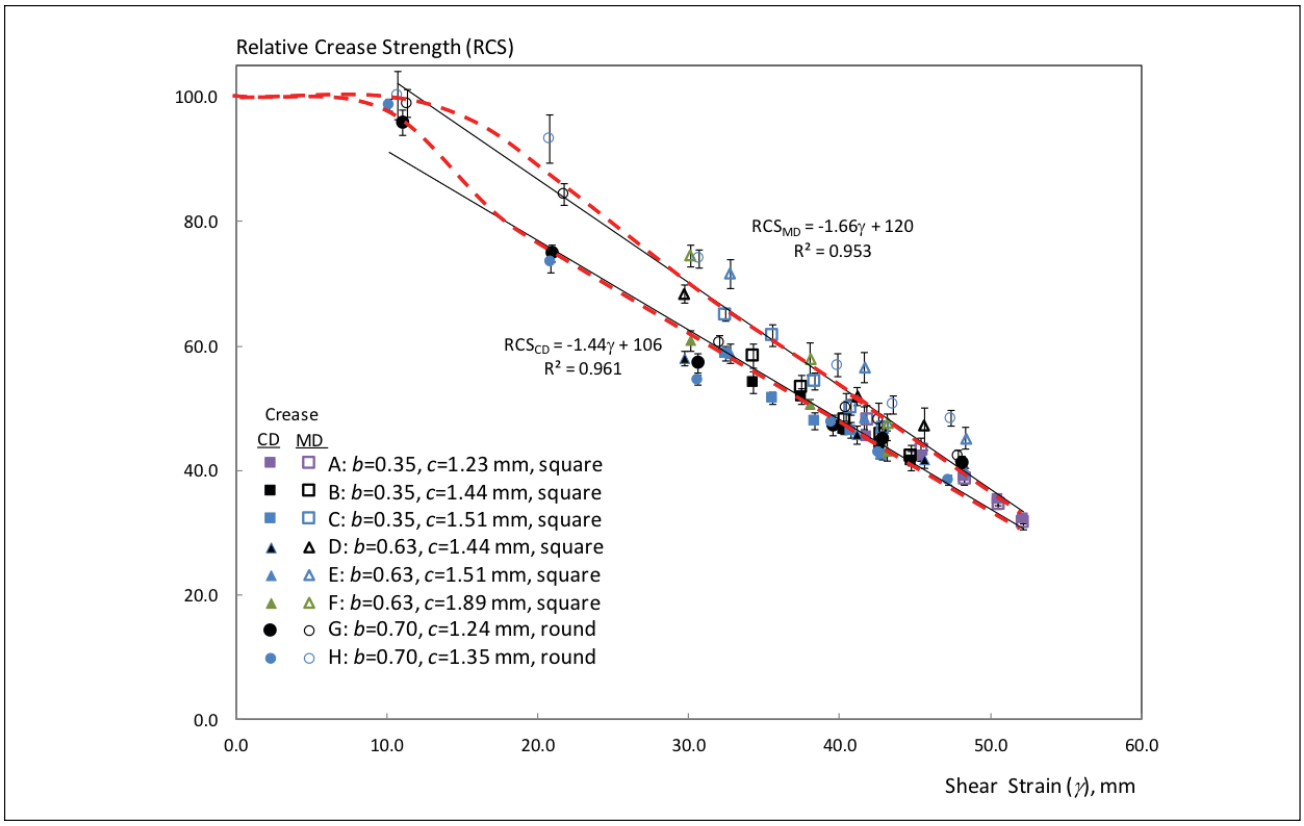
The relative crease strength (RCS) was calculated as the ratio of the uncreased peak moment divided by the creased peak moment, using the peak bending moments less than an angle of 30°. The springback ratio was calculated as the ratio of the uncreased peak moment divided by the creased peak moment, using the bending moments at 90° after 15 s of relaxation.

RESULTS

The testing produced sets of data for eight different creasing-tool configurations and up to six penetration depths, in both MD and CD. The shear strains for each creasing configuration were calculated using Eqs. 1 and 2. **Figures 3** and **4** provide respective graphs of RCS versus penetration depth and shear strain for each tooling set. In general, Fig. 3 demonstrates that as crease penetration increased, the RCS decreased, but each tooling configuration resulted in a unique curve. When RCS was plotted against shear strain, Fig. 4, the curves converged to produce one MD and one CD curve. The linear lines demonstrate the improvement gained by describing RCS as a function of shear strain (R^2>0.95) instead of crease depth, and the red-lines suggest the diminishing effect of creasing on RCS for low creasing angles. Below a shear strain of approximately 10°, the creasing had negligible effect on RCS, but as shear strain increased, RCS decreased. The CD crease required a higher peak moment (33% increase on average) than an MD crease for all levels of creasing. As indicated in Fig. 4, the CD crease showed a larger drop in RCS for intermediate levels of strain, but the difference diminished as the shear-strain increased.

Springback ratio versus shear strain, **Fig. 5**, shows that the various tooling configurations formed unique MD and CD curves. The bi-linearity of the CD curve is more pronounced for springback compared to RCS. This suggests that the response to folding for this paperboard is most sensitive for CD creasing between 10° and 20° shear strain.

Strong linear correlations were found between measured MD and CD properties, as indicated in **Table II**. Only the crease width was independent of crease direction, and as one would expect, slightly larger and strongly correlated to channel width (width =1.025 c, R^2=0.88). The crease height for CD creases was on average 79% of the height for MD creases, while the RCS for a CD crease was on average 90% that of an MD crease. Note that the intercept of the correlation of MD and CD



4. RCS versus transverse shear strain. Error bars are 95% confidence limits of mean.

Property	Slope CD vs. MD	Intercept	Coefficient of Determination, R^2
Crease width	0.989	0.008	0.980
Crease height	0.760	0.003	0.981
RCS	0.836	3.57	0.917
RCS, γ>20°	0.679	11.53	0.921

II. Correlations between machine direction (MD) and cross direction (CD) measured crease characteristics (RCS = relative crease strength).

RCS does not pass through zero, reflecting a more complex response of RCS to creasing as demonstrated in Fig. 4.

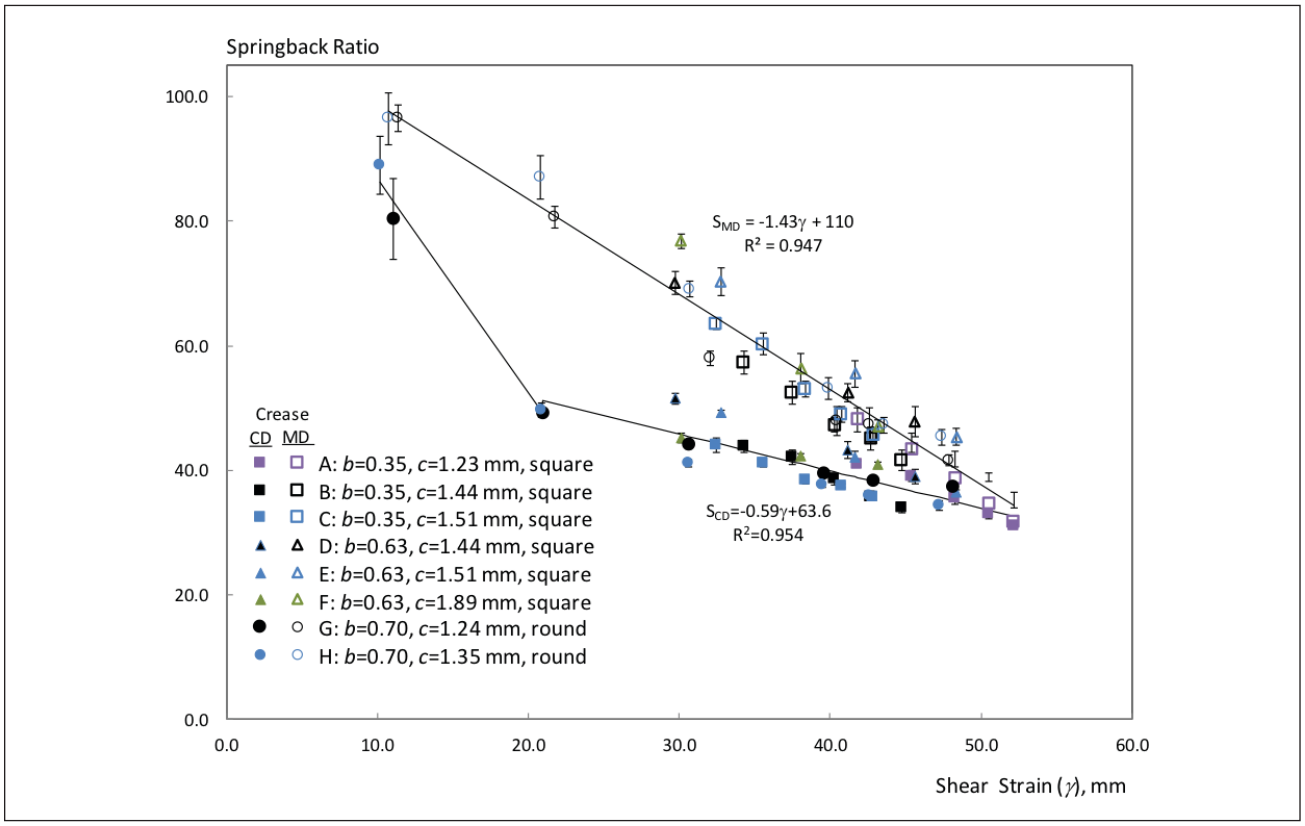
Figure 6 shows the bending moment versus bending angle for select creasing configurations. These represent average curves that were normalized to the peak moment (less than 30°) of the uncreased sample yielding that the peaks in the curves are RCS values. The shear values given to three significant figures were calculated for the respective curve. The shear values reported to two significant figures are a nominal value for the group of similarly colored curves. The solid lines are for the square-tipped rules, and the dashed lines are for the rounded rules.

DISCUSSION

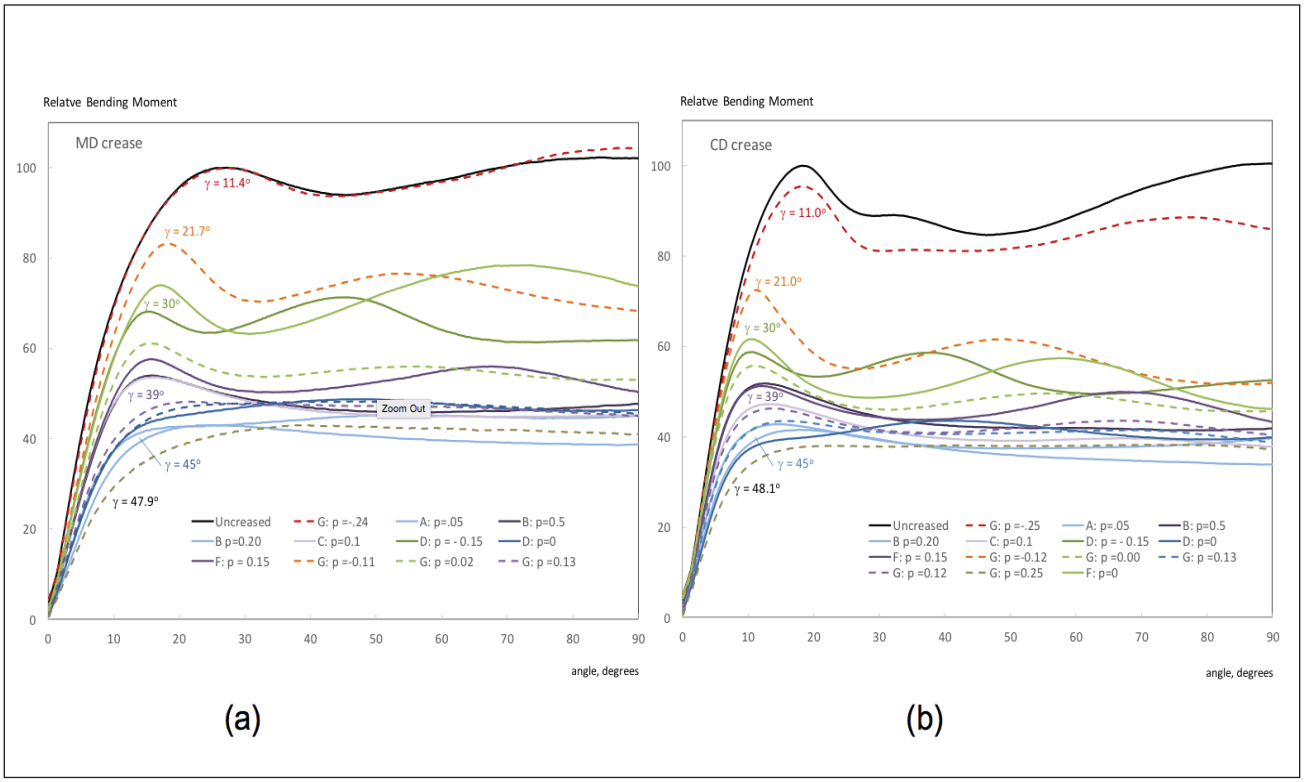
The convergence of the data into MD and CD curves (Figs. 4 and 5) demonstrates that the transverse shear strain (Eq. 2) is a meaningful measure to characterize crease severity for a wide range of tooling configurations. This validates the hypothesis that transverse shear dominates creasing and that a nominal measure of the shear strain provides a means to quantify creasing behavior. For the paperboard tested, RCS versus shear strain was linear in the range of strain from 20° to 55°. Therefore, only two calibration points are needed to apply Eqs. 1 and 2 to determine a range of tooling parameters that yield the same shear strain and thus the same RCS.

Creasing at shear strains less than 10° did not appear to decrease the force required to fold the board. The peak moment in an uncreased board marks the onset where the bending initiates a delamination and buckling of the inner plies and the start of an uncontrolled bead formation. Once the creasing creates enough shear damage, the delamination initiates at lower load and the crease shape provides for a controlled bead formation, which manifests in a reduction of peak moment. Figures 4 and 6 show that for shear angles near 10°, the RCS is close to 100%, and the bending moment versus angle curves are quite similar to the uncreased samples, indicating that the creasing operation at this level was essentially an elastic deformation.

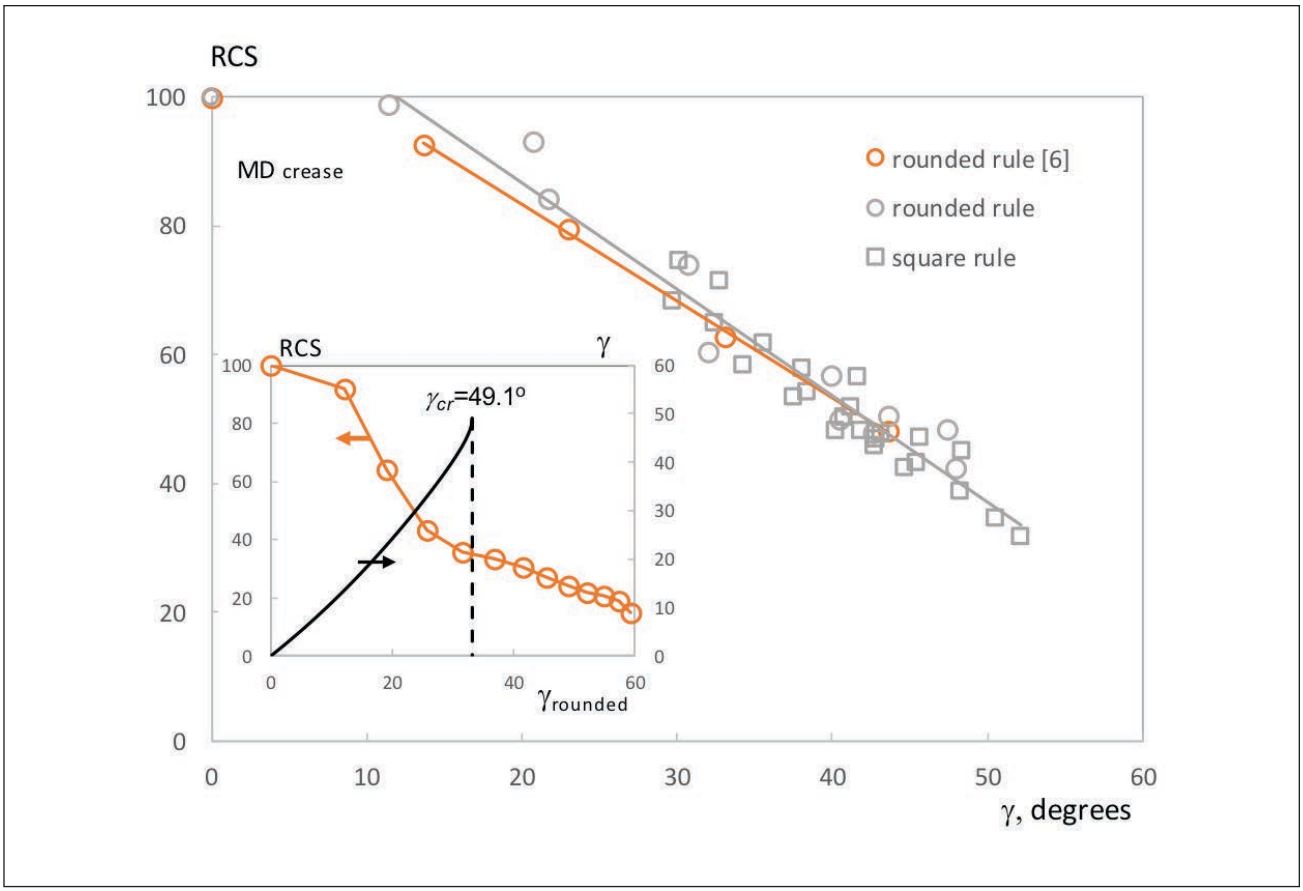
Because a CD crease engages the MD properties, the response should be more brittle in nature (more damage at



5. Springback ratio versus transverse shear strain. Error bars are 95% confidence limits of mean.



6. Sample moment versus angle of bend for (a) machine direction (MD) creases and (b) cross direction (CD) creases.



7. Comparison to results in literature [6].

lower strains) compared to MD creases. This is observed in the greater reduction of both RCS and springback ratio in the range of 10° to 20° shear strain. In addition, the bending moment versus angle curves of Fig. 6 exhibit a sharper decrease in post-peak response. The major reduction in springback ratio for a CD creased sample indicates more severe damage from creasing. The lower CD crease height compared to the MD crease height for the same strain suggests more plastic flow for the MD crease, yet the relative decrease in strength is lower, suggesting that the plastic deformation in an MD crease does not improve the ability to delaminate in folding compared to the CD crease.

The theory predicted a maximum shear angle of γ_{max} = 57.20°, beyond which shear would be constant. In Fig. 4, the MD and CD curves intersect at γ = 63.6°, and in Fig. 5 the intersection is at γ = 55.2°. This gives an average of γ = 59.4°. Therefore, at the maximum strain, the relative change in MD and CD are the same and the shear strain has reached a maximum level. For the paperboard tested, the RCS is less than 30% in this region and below desired levels sought in practice.

Figure 7 compares the current MD crease data along with that from [6], plotted against γ, but only up to the critical strain (γ=49.1°, because clearance was negative [6]). Figure 7 shows that both sets of data produced essentially the same RCS versus strain curve. Greater creasing depths were evaluated in [6] beyond the range of validity of Eq. 2. Therefore, Eq. 5 was used to plot the RCS data from [6], as shown in the inset graph of Fig. 7. The equivalent shear strain, γ, is also shown on the secondary ordinate up to the critical strain. This graph reveals that after the critical strain, the slope of the RCS curve is greatly reduced. This is presumably because the shear strain remains almost constant, but additional ZD compression and CD tension are added. This further suggests that RCS is mainly controlled by the extent of transverse shear deformation created in the creasing operation. The region of interest for practical creasing operations should be in the range of 20° to 50°, and the data in the inset Fig. 7, which represents creasing past the critical shear, is in a regime beyond typical industrial practice.

CONCLUSIONS

A two-parameter transverse shear measurement, Eq. 2, was shown to provide a robust characterization of creasing severity. By including corner radii of the tooling, the expression is applicable to a wide range of configurations and can provide more guidance than current industrial strategies. The equation predicts that the magnitude of the transverse shear strain reaches a maximum of 57.2°, which is further reduced for cases of negative clearance. Ninety-degree fold tests showed

that the relative crease strength and springback correlated well with the transverse shear strain. For a given paperboard, minimal tests could be completed to determine the shear strains that reduce the relative crease strength to the desired level (say 60%), and Eq. 2 can be used subsequently to determine a family of tooling geometries that will produce the desired reduction.

The folding tests revealed that initial creasing penetrations are elastic; followed by an inelastic region where damage reduces peak bending moment. The CD creased samples were more sensitive to creasing in the mid-range of shear strains (10°–20°), but as the shear strain approached the maximum, the differences in relative crease strength for MD and CD creased samples was negligible. Comparison to creasing data from the literature showed that the CD creased behavior of two papers was essentially the same, and that creasing beyond the critical strain denoted a decrease in the effectiveness of the creasing.

The presented approach to creasing offers a quantitative engineering-based approach to creasing and folding that should allow industry to move beyond the current practice of applying heuristic guidelines. **TJ**

LITERATURE CITED

1. Shelton, E. De. F., U.S. pat. 183423 (Oct. 17, 1876).
2. Bird, C.S., U.S. pat. 1,022,923 (April 9, 1912).
3. Coffin, D.W. and Nygårds, M., "Creasing and folding of paper," *Trans. Fundam. Res. Symp., 16th,* 69: 136(2017).
4. Halladay, J.F. and Ulm, R.W.K., "Creasing and bending of folding boxboard," *Pap. Trade J., Tappi Section*, 108(5): 36(Feb. 2., 1939).
5. Nagasawa, S., Fukuzawa, Y., Yamaguchi, D., et al., "Deformation characteristics of creasing on paperboard under shallow indentation," *Adv. Fract. Res., Proc. Int. Conf. Fract., 10th*, ICF10-0202OR, Elsevier Science, New York, 2001.
6. Nagasawa, S., Fukuzawa, Y., Yamaguchi, D., et al., *J. Mater. Process. Technol.* 140(1-3): 157(2003).
7. Coffin, D.W. and Panek, J.C., in *Progress in Paper Physics Seminar 2016 Conference Proceedings* (S. Schabel and H.-J. Schaffrath, Eds.), Technische Universität Darmstadt, Darmstadt, Germany, 2016, p. 132.

APPENDIX

Consider a Cartesian coordinate system (X,Y) with origin aligned with the center of the rule and the top surface of the channel. The position vector for any point (X,Y) located in

ABOUT THE AUTHORS

Several years ago, we began working on creasing and folding issues, starting with a critical review of the literature and then examining the mechanics of creasing and folding. There appeared to be a gap in the literature dealing with how to characterize the severity of creasing in terms of some fundamental measure of shear. The authors then sought to develop a robust measure that can normalize creasing data for a wide range of tool geometries.

The research here complements prior work using shear strain expressions to characterize the behavior of a paperboard under various creasing tool geometries. It adds a more robust equation that is valid over a range of realistic results. This research extends previous literature in terms of using a transverse shear measurement to characterize creasing severity. The new expression accounts for tooling geometry and multiple data sets collapsed to the same curve.

Although we initially set up the model and developed expressions rather quickly, it took time and retrospection to realize we needed to invert the expressions to make them usable and choose the best expression for shear strain. Once we did this, everything seemed to fall into place, but it did take discipline to stick with the research over a period of years.

Rediscovering the 19th century patents and the work of Halladay and Ulm from 1939 provided new perspectives and insights that are missing from more recent literature. A most interesting aspect was the development of a critical shear strain and how one can interpret previous data in light of this knowledge (Fig. 7).



Coffin



Panek

Those that produce paperboard, convert it, or design packaging can use the shear measurement as an indication of creasability. This can help tie relative crease strength to board properties and tooling geometry. Results from one set of tooling can be transferred to different tooling. This research also provides knowledge that can shift the way people working in the field look at creasing and folding. The next step is to apply the approach in practical situations. Also, there is an operating window for the creasing operation that will lead to successful creasing and folding for a given paperboard, and we need to better define that window for converters.

Coffin is professor in the Department of Chemical, Paper, and Biomedical Engineering at Miami University in Oxford, OH, USA. Panek is research scientist with WestRock in Richmond, VA, USA. Email Coffin at coffindw@miamioh.edu.

the free-span region is made of up three components: the flat portion of the rule, the arc of the wrap around the rule radius, and the angle (θ) free span section. This position vector $\hat{R}$ can be written as:

$$\hat{R}(X,Y) = \left[\frac{b}{2} - r_r + (r_r + h - Y)\sin(\theta) + \left(X - \frac{b}{2} + r_r - (r_r + h - Y)\theta\right)\cos(\theta)\right]\hat{\imath} + \left[-z - h + Y + (r_r + h - Y)(1 - \cos(\theta)) + \left(X - \frac{b}{2} + r_r - (r_r + h - Y)\theta\right)\sin(\theta)\right]\hat{\jmath}$$

Assuming that lines of constant Y remain parallel and maintain the same spacing such that the thickness, h, is preserved (as shown in Fig. 1), then the deformation can be described as the change in the unit vectors ($\hat{\imath}, \hat{\jmath}$), which formed a right angle on the undeformed material: $\frac{\pi}{2} - \gamma$. The magnitude of these two vectors can be written as stretches (Λ_1, Λ_2), which equal:

$$\Lambda_1 = \left\|\partial \hat{R}(X,Y)/\partial X\right\| = 1 \text{ and } \Lambda_2 = \left\|\partial \hat{R}(X,Y)/\partial Y\right\| = 1 + \theta^2$$

The dot product of the two partial derivatives of the position vector yields:

$$\Lambda_1 \Lambda_2 \cos\left(\frac{\pi}{2} - \gamma\right) = \sqrt{1 + \theta^2}\sin(\gamma) = \partial \hat{R}(X,Y)/\partial X \cdot \partial \hat{R}(X,Y)/\partial Y = 0$$

This expression is equivalent to:

$$\tan(\gamma) = \theta$$

For completeness, the stretches indicate inextensibility along the length of the paper, and a stretch through the thickness to maintain constant thickness, h. This is analogous to a case of direct shear.

ABOUT THIS PAPER

Cite this article as: Coffin, D., Panek, J. *TAPPI J.* 17(4):231(2018).

https://doi.org/10.32964/TJ17.04.231

DOI: https://doi.org/10.32964/TJ17.04.231

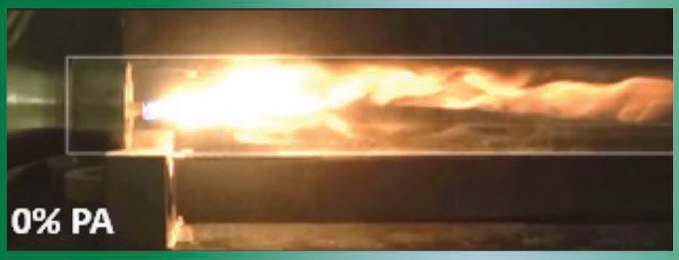
ISSN: 0734-1415

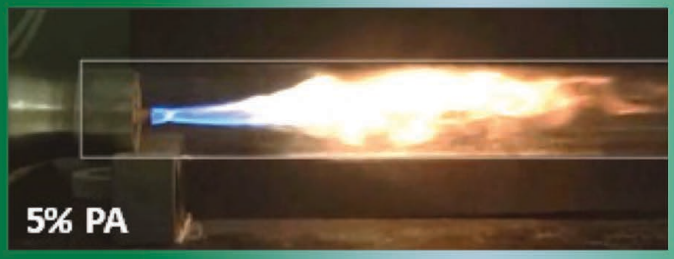
Publisher: TAPPI Press

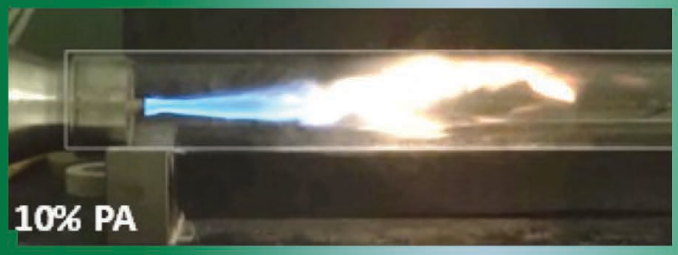
Copyright: ©TAPPI Press 2018

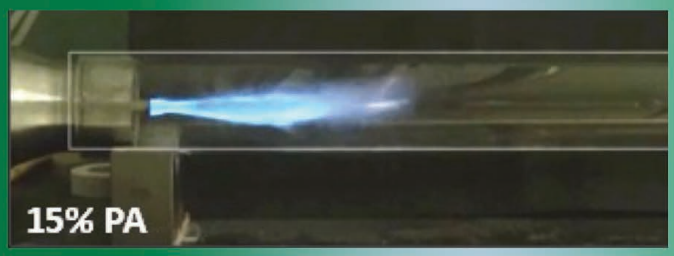
About this journal

TAPPI JOURNAL
WWW.TAPPI.ORG
THE PAPER AND PACKAGING INDUSTRIES' TECHNICAL RESOURCE
MAY 2018 | VOL. 17 NO. 5

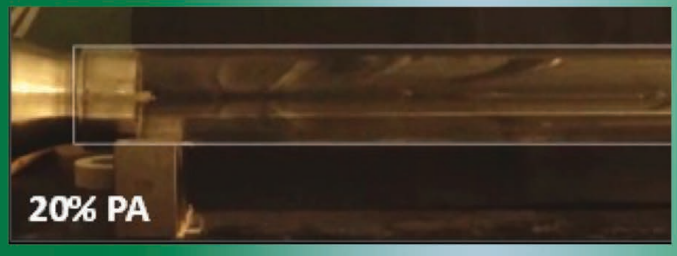












CORROSION 253
A hundred years of corrosion in the pulp and paper industry
Max Moskal

RECOVERY CYCLE 261
Use of vent stack temperature as a feedforward variable for dissolver total titratable alkali (TTA) control
Wei Ren, Brennan Dubord, Jason Johnson, and Bruce Allison

EMISSIONS 273
Factors affecting particulate removal efficiency of kraft recovery boiler electrostatic precipitators: a technical review
Ezzat Jaroudi, Ivan Sretenovic, Greg Evans, and Honghi Tran

RECOVERY CYCLE 285
Effect of ring formation on burner flame stability in lime kilns
Girish Mohanan, Honghi Tran, Markus Bussmann, and Richard Manning

PULPING 295
Dry chip feedrate control using online chip moisture
Wesley Gilbert, Ivan Trush, Bruce Allison, Randy Reimer, and Howard Mason

FEATURING SPECIAL CONTENT FROM THE:
2017 PEERS Conference

May 2018

TABLE OF CONTENTS VOL. 17 NO. 5

249 EDITORIAL
2017 PEERS Conference: Maximizing success through innovation
Brian N. Brogdon and Peter W. Hart

253 CORROSION
A hundred years of corrosion in the pulp and paper industry
Max Moskal

261 RECOVERY CYCLE
Use of vent stack temperature as a feedforward variable for dissolver total titratable alkali (TTA) control
Wei Ren, Brennan Dubord, Jason Johnson, and Bruce Allison

273 EMISSIONS
Factors affecting particulate removal efficiency of kraft recovery boiler electrostatic precipitators: a technical review
Ezzat Jaroudi, Ivan Sretenovic, Greg Evans, and Honghi Tran

285 RECOVERY CYCLE
Effect of ring formation on burner flame stability in lime kilns
Girish Mohanan, Honghi Tran, Markus Bussmann, and Richard Manning

295 PULPING
Dry chip feedrate control using online chip moisture
Wesley Gilbert, Ivan Trush, Bruce Allison, Randy Reimer, and Howard Mason

»COVER CREDIT: Using a laboratory mock lime kiln, researchers Mohanan et al. examined the effect of rings on burner operation as a function of primary air (PA) and ring characteristics (p. 285). The results showed that PA greatly affects the burner flame pattern and stability. Without a ring, the flame is brighter and shorter, with an increase in PA up to 17%, and it blows out at 20% PA or higher. In the presence of a ring, the flame becomes unstable and blows out when the ring is placed near the burner, but it is more stable when the ring is placed away from the burner.

TAPPI JOURNAL
WWW.TAPPI.ORG

Editor-in-Chief
Brian N. Brogdon brian.brogdon@gmail.com
+1 678 581-9114

Associate Editor
Peter W. Hart peter.hart@westrock.com
+1 409 276-3465

Editorial Director
Monica Shaw mshaw@tappi.org
+1 770 367-9534

PRESS Manager
Jana Jensen jjensen@tappi.org
+1 770 209-7242

Webmaster
Trina Heath theath@tappi.org
+1 770 209-7416

***TJ* EDITORIAL BOARD**

Randy Branston, BASF
randy.branston@basf.com, +1 704 819-4251

Brian N. Brogdon, FutureBridge Consulting & Training LLC
brian.brogdon@gmail.com, +1 678 581-9114

David A. Carlson, Carlson Consulting
dacarlson39@aol.com, +1 847 323-2685

Douglas W. Coffin, Miami University
dacarlson39@aol.com, +1 847 323-2685

Mahendra Doshi, Doshi and Associates
mahen@aol.com, +1 920 832-9101

Marc Foulger, GL&V USA Inc.
Marc.foulger@glv.com +1 315 767-2920

Peter W. Hart, WestRock
peter.hart@westrock.com, +1 409 276-3465

Carl J. Houtman, USDA Forest Products Laboratory
choutman@fs.fed.us, + 1 608 231-9445

Lucian Lucia, North Carolina State University
lucian.lucia@gmail.com, +1 919 889-7059

John A. Neun, John A. Neun LLC
john.neun@gmail.com, +1 518 275-8139

Jim Niemiec, Verso Corporation
jim.niemiec@versoco.com, +1 715 422-7404

Steven P. Ottone, Omya
steven.ottone@omya.com, +1 919 641-7854

Gaurav Pranami, Imbed Biosciences
gpranami@imbedbio.com, +1 515 230-7005

Arthur Ragauskas, Oak Ridge National Laboratory
aragausk@utk.edu

Gerard J.F. Ring, University of Wisconsin—Stevens Point
gerrryring@wi-net.com, +1 715 592-3732

Scott Rosencrance, Kemira Chemicals
scott.rosencrance@kemira.com, +1 770 429-2753

Paul Wiegand, NCASI
pwiegand@ncasi.org, +1 919 941-6417

Junyong Zhu, USDA Forest Products Laboratory
jzhu@fs.fed.us, +1 608 231-9520

Join TAPPI *today!*

TAPPI JOURNAL is a free benefit of TAPPI membership, and is only available to members. To join TAPPI, to renew your TAPPI Membership, or to learn about other valuable benefits, visit www.tappi.org.

TAPPI, 15 Technology Parkway S., Suite 115, Peachtree Corners, GA 30092, publishes *TAPPI JOURNAL* monthly.

ATTENTION PROSPECTIVE AUTHORS: All papers published are subject to *TAPPI JOURNAL's* peer-review process. Not all papers accepted for review will be published. Before submitting, check complete author guidelines at http://www.tappi.org/s_tappi/doc.asp?CID=100&DID=552877.

Statements of fact and opinions expressed are those of individual authors. TAPPI assumes no responsibility for such statements and opinions. TAPPI does not intend such statements and opinions or construe them as a solicitation of or suggestion for any agreed-upon course of conduct or concerted action of any sort.

Copyright 2018 by TAPPI, all rights reserved. For copyright permission to photocopy pages from this publication for internal or personal use, contact Copyright Clearance Center, Inc. (CCC) via their website: www.copyright.com. If you have questions about the copyright permission request process, please contact CCC by phone at +1 978 750-8400. To obtain copyright permission to use excerpts from this publication in another published work, send your specific request in writing to Editor, TAPPI JOURNAL, 15 Technology Parkway S., Suite 115, Peachtree Corners, GA 30092, USA; or by fax to +1 770 446-6947. Send address changes to TAPPI, 15 Technology Parkway S., Suite 115, Peachtree Corners, GA 30092, USA; Telephone +1 770 446-1400, or FAX +1 770 446-6947. www.tappi.org

Editorial





BRIAN N. BROGDON
Editor-in-Chief
TAPPI Journal

PETER W. HART
Associate Editor
TAPPI Journal

2017 PEERS Conference: Maximizing success through innovation

Norfolk, Virginia, hosted close to 350 participants at the 2017 Pulping, Engineering, Environmental, Recycling and Sustainability (PEERS) Conference this past November. Industry professionals met and discussed the newest technologies and best practices related to pulp manufacture, chemical recovery, power & steam, corrosion mitigation, environmental issues, regulatory compliance, sustainability, and biorefining.

The 2017 PEERS Conference showcased ten technical tracks that contained more than thirty-eight sessions covering a variety of topics. Some of the sessions were:

- Chip quality management tutorial
- Kraft pulping & brownstock washing
- Bleaching optimization
- Digester corrosion
- Recovery boiler operations & control
- Chemical byproducts recovery

Keynote focused on innovation

Robert C. Tiede, Executive Vice President and Chief Operations Officer of Sonoco Products Company, gave the conference keynote address, titled "Disrupter or Disrupted? How Innovation Defines your Destiny." In his speech, Tiede noted that we are in the midst of a new business revolution—e-Commerce—that is redefining how goods are bought, sold, and distributed. Buying items at brick-and-mortar stores will decline in the future and will shift towards online purchases with deliveries made directly to the end user. This will affect our industry by increasing the need for paper and paperboard packaging, which has the desirable attributes of biodegradablity, recyclability, and sustainability over other forms of packaging.

Tiede also noted that innovation is a key component in making disruptive discoveries and technologies in our industry. The innovation process is based on the building blocks of "curiosity, associating, questioning and insights."



Robert C. Tiede, Executive Vice President and Chief Operations Officer at Sonoco Products Company, gave the PEERS 2017 keynote address about the importance of innovation.

Curiosity is the key to making new discoveries, and is the foundation to innovating. Another factor is being able to associate and connect unrelated items or ideas from different fields. The next item is questioning, which is determining which ideas to support and scale while balancing risks and rewards. The final block of innovation is insights; it relates to how innovations can excite your customers and create new markets.

Awards recognized industry leaders

The Conference's opening session recognized National TAPPI and Division award winners, including:

- Adriaan van Heiningen for Research and Development Technical Award and William Aiken Prize
- John A. Neun for Engineering Division Technical Award with Beloit Prize
- Scott B. Pantaleo for Engineering Division Leadership & Service Award with AMEC Foster Wheeler Prize
- Paul S. Wiegand for Environmental Technical Award with Roy F. Weston Prize

- Garnet L. Bremner for Pulp Manufacturing Division Leadership & Service Award with Joseph K. Perkins Prize
- Brian N. Brogdon for Outgoing Pulp Manufacturing Division Chair

The High Impact Paper Award from the 2016 PEERS Conference was "Recovery Boiler Inspection Strategy," which was written and presented by W.B.A. "Sandy" Sharp.

Special PEERS content in *TAPPI Journal*

As members of the *TAPPI Journal* Editorial Board, we solicited papers from the 2017 TAPPI PEERS Conference for peer review. Some of these papers are brought to you in this month's special PEERS issue of *TAPPI Journal*. Additionally, we will bring to you several other papers accepted from these conferences in future issues later this year. We would like to thank all the authors who offered their work for publication in this issue and returned their revised papers in a timely manner, as well as all the peer reviewers who critiqued and provided their valued comments and improvements to the authors' work.

Mark your calendars for the 2018 TAPPI PEERS Conference, which will be held in Portland, Oregon, on October 28-31, and will be co-located with the 2018 TAPPI International Bioenergy & Bioproducts Conference (IBBC). This year's PEERS theme will be "Technical Solutions for Today and Beyond." The conference will host four training workshops on Sunday, such as Brownstock Washing, Bleach Plant Operations, Lime Kiln & Recaust: Process & Mechanical Overview, and Process Simulations. **TJ**

Brian N. Brogdon, Ph.D., is the Editor-in-Chief for TAPPI Journal*, and is the owner of Future Bridge Consulting Services LLC, Marietta, GA, USA.*

Peter W. Hart, Ph.D., is Associate Editor and past Editor-in-Chief for TAPPI Journal*. He is Director, Fiber Technology and Innovation, for WestRock, Atlanta, GA, USA.*

A hundred years of corrosion in the pulp and paper industry

MAX MOSKAL

ABSTRACT: Through the decades, the pulp and paper industry greatly expanded production capacity to meet increasing demands. Correspondingly, the cost of corrosion damage soared. The most serious corrosion control challenges were researched and met by university and governmental researchers, and by task groups within the TAPPI Engineering Division's Corrosion and Materials Engineering Committee. Today, thanks to material and process advances, mills encounter less corrosion than in the past. This overview takes a historical look back, covering many decades, at how corrosion problems have been managed in the pulp and paper industry. Yet, corrosion keeps on going, and today mills appear less able to manage corrosion problems for which known solutions are available. This paper also addresses the significant yet underrated task of optimizing corrosion control management in the present and into the future. Discussion is provided on best practices needed to mitigate new and ongoing corrosion problems.

Application: This review should help mills better realize the importance and benefits of systematic corrosion management.

Along with documenting notable corrosion events, this historical look at corrosion problems reveals how changes in paper and paperboard processing methods have influenced corrosion and its related costs. Additionally, advances over the years in materials technology, fabrication methods, and testing and analysis techniques have shaped what is perceived today as corrosion control in the industry. Past lessons can provide insights toward ways to anticipate and control corrosion events of the future. Aside from documenting the most notable events over the decades, this paper also addresses current advances in corrosion management technology that are being adopted by other corrosion-intensive industries, and why similar approaches have been so difficult to implement in the pulp and paper industry.

THE COST OF CORROSION

According to the 2016 NACE International IMPACT study, the global direct cost of corrosion across all industries is estimated to be 3.4% of gross domestic product [1]. Other studies have shown that within the pulp and paper industry, which is among the highest of capital intensive industries, the cost of corrosion is estimated to be near that in petroleum refining and chemical industries combined; between 1.2% and 6% of pulp and paper sales, depending on product and process [2]. Today, there are about 500 paper mills in the United States, with production capacity of about 79,000,000 metric tons/year of paper and paperboard [3]. Thus, the annual cost of corrosion to the paper industry is estimated to be 2.7 to 4.7 million metric tons of paper and paperboard.

Pulp and paper manufacturers can benefit from better corrosion control practices because in most cases the paths to good control are already known. By using best practices in corrosion control, and avoiding actions that involve doing things wrong, 50% or more of all corrosion costs might be avoided [2].

THE EARLY YEARS — 1900 TO THE 1950s

From 1900 to the 1950s, the U.S. paper industry expanded production from 2 million tons/year to near 34 million tons/year [4]. Interestingly, growth in production was not made by building more paper machines, but rather by speeding up existing machines, and replacing machines with wider ones that produced more tonnage. From 1914 to 1940, the total papermaking capacity doubled, but the number of paper machines in the United States remained nearly constant at about 1500 machines. Thus, the average machine capacity also doubled during that time. Along the way, the most significant factors influencing corrosion were process changes, such as the type of paper produced. Because of the increased demand for stronger paper, kraft production surpassed sulfite after 1939. From a corrosion viewpoint, this change was more favorable because the kraft process has proved to be less costly from a corrosion standpoint than sulfite.

Corrosion control was not a priority from 1900 up to 1930 or 1940. Rather, the industry considered corrosion to be more of a maintenance issue, and mill management focused on increasing paper production rather than on corrosion control.

Equipment and materials

Until the 1920s, the materials generally available for equipment manufacture were cast iron, wrought iron, steel, brass, bronze, some Monel nickel alloys, and aluminum. Acid-resistant brick and mortar were used to line towers, tanks, and

chests. Paper machine frames were made from gray cast iron, and suction rolls were made from either cast iron or bronze. Nickel and chromium plating were also used to protect steel from corrosion and wear. Because copper, bronze, and brass were used for sulfite pulping, frequent replacement was required, at considerable cost. Lead lining was effective for acid production in the sulfite process. Wood was widely used for corrosion resistant tanks and pipes. Batch digesters were made from riveted carbon steel with brick lining; a few of these early digesters were still in use 100 years later.

In just 15 years, from 1915 to 1930, design engineers found a wider choice of materials for corrosion control. Stainless steels became available, and so did 14%–30% nickel cast iron (Ni-Resist). Some applications for Ni-Resist castings during this period included paper machine fourdrinier frames, dryer rolls, pumps, and pipe fittings. By 1930, carbon steel welding was much better developed and welding was included in the pressure vessel code. However, weldability of the new stainless steels was poor because better gas shielding was still needed to control porosity and embrittlement problems. Carbon control in the production of early stainless steels also was difficult. Nevertheless, by the mid-1930s, 18-8 chromium-nickel with 3% molybdenum (similar to Type 316), and 27Cr-4.5Ni-1.5Mo duplex stainless steels (similar to Type 329 duplex stainless steel) were becoming widely used [5].

In the 1930s, the Tomlinson recovery boiler for kraft paper production was invented, and so was the Kamyr continuous digester. However, the continuous digester did not become fully developed and used until about 1950. Paper machine speeds were increasing – up to 1500 ft/min – double that from just a few years earlier. Multi-stage bleaching with direct treatment with chlorine was well developed by the 1940s.

During World War II, gas-tungsten arc-welding was developed, and welding of stainless steel could be reliably performed. After the war, a wide variety of materials for resisting corrosion became more readily available. These included high alloy stainless steels, and wider ranges of nickel-based and copper-based alloys. Flame spraying of corrosion resistant coatings, although available for decades, became more prominent, but plasma and high velocity oxyfuel coatings would not be available until the 1960s. Better materials testing methods also became widely available, such as ultrasonic testing for thickness and flaw detection.

The first high pressure recovery boilers, 1200 psi and above, introduced to increase energy efficiency, were built during the 1950s.

Associations and research

The Technical Association of the Pulp and Paper Industry (TAPPI) was founded in 1915, and the Institute of Paper Chemistry (now the Renewable Bioproducts Institute at Georgia Institute of Technology) was established in 1920. The Pulp and Paper Research Institute of Canada (PAPRICAN, now FPInovations) was established in 1925, and the National Society of Corrosion Engineers (now NACE International) was founded in 1943. During the 1930s, a TAPPI Materials of Construction Committee set up specifications for stainless steel casting alloys [5]. The first field and laboratory studies on the metallurgical and electrochemical aspects of kraft liquor corrosion were made in the 1950s by Walter Mueller at PAPRICAN [6]. The TAPPI Digester Corrosion Subcommittee (later becoming the Corrosion Committee) was started in about 1950, and its first major task was to survey the extent of corrosion in kraft digesters. The committee published reports on digester corrosion every year for 10 years. From the 1950s on, corrosion became a far more important and costly burden to the paper industry.

Notable corrosion events in the early years

During 1930, a kraft digester catastrophically failed at Berlin, NH, USA. Until that time, carbon steel kraft digesters were not expected to corrode because they operated in an alkaline environment. Digester corrosion surveys during the 1930s into the 1950s showed wide variations in the corrosivity of liquors. Ultimately, study of the effects of varying liquor sulfidity on corrosion rates in carbon steel was published by Wensley et al. [7].

Significant corrosion pitting of stainless steel bleach washers, winding wire, and cloth was reported during the 1930s, and nickel-based materials such as Hastelloy-C, Hastelloy-A, and Monel were tested to resist corrosion from free chlorine in the pulp [5].

Probably the most important process change contributing to corrosion for decades to come was during the 1950s when water reuse began. Recycled water contributed to a buildup of chemicals in water systems, especially chlorides and potassium. Water temperatures also were boosted. All of this increased the corrosivity of water and process systems.

A process change contributing to corrosivity of paper machine whitewater was the use of hydrosulfite as a brightening agent. Unknown at the time (1940s), hydrosulfite would break down and produce thiosulfate ions in whitewater, which would be found to pit Type 304 stainless steel. The cause for the thiosulfate corrosion would not be discovered until 1978 [8].

High-pressure recovery boilers were introduced during the 1950s, with design pressures increasing from about 700–800 psig up to 1250–1650 psig. The higher temperatures resulted in unacceptable corrosion rates in carbon steel tubes, and a decades-long search for optimum tube materials began [9,10].

CORROSION EVENTS OF THE 1960s–1970s

The paper industry was in full swing in the 1960s, and the period into the 1970s was considered the "wave of the good times." In just five years, from 1965 to 1970, more than a 100 continuous Kamyr digesters were built and put into production in dozens of mills across North America [11]. During the 1970s, 70 new recovery boilers were built in the United States, and most were of the high pressure type, averaging above 950 psi in steam pressure [12]. Larger and faster paper machines were built, including the so-called 10 m (390+ in.) width machines.

On the debit side, cast CA-15 and austenitic stainless steel suction rolls had poor corrosion fatigue strength and a terrible lifespan, some failing in less than a year. The first cast duplex stainless steel (DSS) suction roll material (1963), Alloy 63, had good strength and excellent corrosion resistance, but still cracked prematurely and unpredictably. In the following years, more than 30 different stainless steel alloys were developed and put in service in suction rolls, some at the cost of more than a million dollars per roll. Respectable suction roll life was eventually achieved when machine builders recognized the need to design the rolls more conservatively, and shell producers developed stainless alloys with a compromise of good corrosion fatigue strength and low residual stresses. Low residual stress in suction roll shells could only be obtained by slower and more uniform cooling during heat treatment, but at the same time, the stainless metal chemistry had to be formulated to avoid precipitation of undesirable intermetallic phases during the slow cooling process.

Another problem of the times was recovery boiler explosions; first a few explosions, then many. The Black Liquor Recover Boiler Advisory Committee (BLRBAC) was established in 1961 for the purpose of sharing knowledge and generating and maintaining guidelines to facilitate the safe, reliable operation of recovery boilers. In the 20-year period ending in 1980, BLRBAC documented 99 recovery boiler explosions, an average of five per year. Lower furnace waterwall tube corrosion and cracking was a contributor to boiler smelt water explosions, particularly in boilers with operational pressure over about 900 psi. To address the problem, the first composite stainless steel boiler tubes were installed in a new recovery boiler in Scandinavia in 1971, but the first composite tube recovery boiler built in North America was at Continental Can Company, Hopewell, VA, USA, in 1980.

During this period, and into the 1990s, recovery boilers were fired with changes in air distribution and increasing black liquor solids to increase boiler efficiency and reduce total reduced sulfur (TRS), nitrogen oxides (NOx), and carbon monoxide emissions, resulting in greater corrosion of mid-furnace and upper furnace tubes [13].

Bleach plant corrosion also became a serious problem during the 1960s and 1970s, largely because of the combination of bleach filtrate recycling, higher temperatures, and difficulties in controlling carryover of unused chlorine and chlorine dioxide. Where Types 316L and 317L stainless steels were previously resistant to pitting corrosion, the stronger bleach environments of C and C/D stages required the use of higher molybdenum stainless steel alloys or titanium. In the late 1970s, into the 1980s, a TAPPI task group, headed by Arthur Tuthill, conducted numerous plant tests on the performance of stainless steels (including welded coupons) used for piping in bleach plants [14,15]. Ultimately, 6% molybdenum stainless steel alloys became standard in the most severe bleach stage environments. Fiber-reinforced plastics (FRP), although used for bleach plants since the 1950s, got a boost in bleach plant equipment during this period. The year 1978 also marked the first successful operation of electrochemical protection in a bleach washer in Canada, and there were about 100 installations by 1989 [16].

Associations and research

The greatly increased cost of corrosion during the period from 1961 to 1980 prompted several companies, consultants, institutions, and researchers to increase efforts to combat corrosion problems. TAPPI's Corrosion Committee (changed to the Corrosion and Materials Engineering Committee during the 1970s) greatly increased its activity and projects, beginning in around 1972. A series of 11 pulp and paper corrosion forums, sponsored by TAPPI, the Canadian Pulp and Paper Association (CPPA), the Swedish Corrosion Institute, the Finnish Paper Engineer's Association, and NACE were held at 3-year intervals between 1974 and 2004. The Institute of Paper Chemistry established a corrosion department about 1975. Likewise, PAPRICAN increased research on corrosion problems.

CORROSION EVENTS OF THE 1980s TO 2000

SA 210/304L composite tubes were first installed in a recovery boiler in 1980, and in many more high pressure boilers in the United States and Canada afterward. In just a few years, problems with corrosion and cracking of these tubes emerged [17]. During the period from 1983 to 1984, localized corrosion of the outer layer of 304L at air ports was reported. The problem persisted for years until better-designed, well-sealed casting inserts helped to minimize the air port problem [18]. During the early 1990s, cracking of the 304L stainless steel layer of composite tubes was found at air ports and on the boiler floor [19]. During this period, mills experimented with the use of nickel alloy composite tubes and weld overlaid tubes (Alloys 825 and 625). Causes of the composite tube cracking mechanisms were not well defined until 1999 and later [20,21].

Another dilemma in recovery boilers during the 1980s was near-drum corrosion of generating tubes resulting from increased throughput [22]. A mechanism of waterside cracking was identified in 1987 as stress-assisted corrosion (SAC), also known as waterside corrosion fatigue cracking [23]. The SAC damage mechanism was later found to be widespread, up to about 50%, in boilers older than 15 years [24].

In 1980, a Kamyr continuous digester ruptured at Pine Hill, AL, USA. Analysis showed the damage mechanism to be hydroxide stress-corrosion cracking (SCC). After the event, many continuous digesters were found to have similar cracking. Research on the causes of SCC and methods to mitigate cracking were initiated by a TAPPI task group chaired by David Bennett [25].

In 1983 a catastrophic explosion of a feedwater deaerator storage tank occurred, also at the Pine Hill, AL, paper mill. A NACE task group (T-7H-7) was established to study causes and provide recommendations for mitigation of deaerator cracking [26]. Ultimately, 38% to 46% of operating deaerators and deaerator storage tanks were found to have corrosion fatigue cracking severe enough to require weld repairs.

During the early 1990s, elemental chlorine bleaching was completely phased out to reduce toxic dioxins. Substitution with near-neutral chlorine dioxide became the norm. With the combination of recycled filtrate and higher temperatures, the bleach environment continued to be highly corrosive. "Superaustenitic" stainless steel alloys (6% molybdenum) and titanium were largely specified for areas subject to the most aggressive corrosion, including chlorine dioxide washer vats, drums, and piping. Alternate bleaching processes of the 1990s, such as substituting oxygen and peroxide for chlorine and chlorine dioxide, allowed use of lesser alloys, such as 316L and 317L, for washer equipment.

Another notable event during the 1990s was the introduction to North America of second-generation DSS for digesters and liquor tanks. DSS alloys had already been used for years in pulp and paper mills in New Zealand, Australia, and Scandinavia, but the alloys were slow to be adopted by U.S. mills. The first DSS batch digester built in North America was installed at Abitibi Consolidated, Fort Frances, ON, Canada, in 1997 [27]. The motivation for movement into DSS for batch digesters was prompted in part by a catastrophic carbon steel digester explosion in Panama City, FL, USA, in April 1994.

CORROSION — 2001 TO PRESENT

Process stream effects

There seems to have been little change in mill processes that have caused or accelerated corrosion in nearly two decades. Bleaching processes have gradually become less corrosive and lower cost materials have been used for washers, vats, and piping. Pulping and papermaking processes have remained similar to pre-2000 times, although uncontrolled oxidant carryover, such as chlorine dioxide from bleaching, has increased corrosivity affecting paper machine wet-end rolls and exhaust equipment. Recovery processes and the Tomlinson recovery boiler have not changed significantly. The benefits of raising the temperature of superheated steam has been limited by poor resistance of available superheater tube alloys to corrosion in molten salt deposits.

Materials

DSS alloys have gradually been accepted for use in digesters and liquor tanks. However, the economical use of DSS grades throughout the mill has continued to be vexed by spotty availability of lean, more economical DSS grades and volatility of nickel prices and surcharges. Fabricators also have introduced up-charges for DSS weld fabrication.

Fitness-for-service and risk-based inspection

Risk-based inspection methodology was introduced as API 580 and API 581 from 1996 to 2002. The purpose was to use risk-based concepts for optimizing examination of pressure vessels and tanks.

During 2007, the Joint American Society of Mechanical Engineers (ASME)/American Petroleum Institute (API) Committee published the first API 579-1/ASME FFS-1 Fitness-for-Service Code for post-construction of pressure equipment that contained flaws and corrosion damage. The risk-based codes can potentially extend the life of critical equipment. However, as with risk-based examination, the FFS analysis technology seems to be only minimally used by pulp and paper manufacturers.

LESSONS FROM PAST EXPERIENCES

Research and engineering analysis after the events identified almost all of the major corrosion failures, catastrophic events, and their damage mechanisms. In almost every case, the events were triggered by changes in process methods, local chemistry changes, or the rush to apply new construction materials. Notable observations include the following:

- Carbon steel rapidly corroded in kraft (alkaline) cooking – 1930s-1940s
- Hydrosulfite brightening agent contributed to corrosion by thiosulfate ions in whitewater – 1950s
- Water reuse contributed to corrosivity of water process streams – 1950s-2000s
- High pressure recovery boilers suffered excessive sulfidation corrosion of carbon steel tubes – 1950s
- Increased paper machine width caused excessive stresses and corrosion fatigue failure of press rolls – 1970s
- Increased load on chlorine bleach plants and carryover of oxidants caused rapid pitting failures – 1960s-1980s
- Introduction of carbon steel continuous digesters without stress relieving caused stress corrosion cracking – 1960s-1970s
- High solids firing of recovery boilers resulted in tube corrosion higher in the furnace – 1980s-2000s
- Type 304L/SA210 composite tubing in recovery boilers is susceptible to stress corrosion and thermal fatigue cracking – 1980s-1990s
- Older boilers are susceptible to waterside SAC – 1980s
- Near-drum tube corrosion of recovery boilers – 1980s

FUTURE CHALLENGES

Corrosion engineering resources

In 2009, Sandy Sharp gave an informal presentation to the TAPPI Corrosion and Materials Engineering Committee titled "The rise and fall of corrosion engineering in the pulp and paper industry" [28]. Sharp stated that the increase in corrosion engineers employed by pulp and paper companies started in the late 1970s, and that it continued for about two decades. At the same time, the number of corrosion research projects grew in North American institutions (Oak Ridge National Laboratory, PAPRICAN, IPST), with project funding mainly by industry consortiums and the U.S. Department of Energy. The approximate number of full-time corrosion personnel working in pulp and paper in the 1980s and 1990s was a maximum of about 35 in paper companies and 12 in research institutions, totaling some 47 full-time people. Within 10 years, by 2009, this number was reduced to only about five corrosion personnel employed by pulp and paper companies, and five at North American research institutions.

Sharp said that the fall in numbers of corrosion engineers and scientists probably occurred because research solutions had largely eliminated catastrophic failures, and that processes had not changed much, so the value of corrosion engineering was not convincing. He also stated that much of the corrosion expertise had not been transferred to corrosion specialists in pulp and paper mills and that many mill technical positions were eliminated by profitability pressures in the low-profit years. This expertise in the industry also declined through attrition as experts and knowledgeable mill personnel retired.

Overall, current corrosion management in North American pulp and paper is considered by the author to be poor, at best, partly because there are far fewer corrosion engineers working in the industry today than in decades past. Most attempts at corrosion control within organizations have been reactive and "firefighting" by corrosion specialists or reliability engineers, supplemented by a few aging corrosion consultants. In-mill project management by systematic means, such as risk-based inspection and fitness-for-service methodologies, is generally beyond the capability of reliability engineers. Corrosion management methods are unfamiliar to decision makers within pulp and paper mills and their central organizations (higher-level management). Thus, the pulp and paper industry is bypassing the potential for significant savings that is being realized through systematic corrosion management strategies used by other equipment intensive industries, such as the chemical and petroleum industries.

Systematic corrosion management

Notable in the 2016 NACE IMPACT study are the benefits of reducing corrosion: (1) maintenance costs are reduced; (2) inspection costs are reduced and intervals are extended; (3) fewer failures occur, with less production loss and interruption; (4) environmental impact, injuries, property damage are reduced; and (5) the useful life of the asset is extended and capital expenditures are reduced.

As stated in the 2016 NACE IMPACT report, the largest impediment to systematic corrosion control is that cost savings are difficult to measure, because benefits are extended into the future. Corrosion control is generally viewed as a cost, rather than an investment in better practice with future savings. Instead of considering total cost, most design and construction of pulp and paper equipment is directed toward bringing new equipment into operation in the shortest period and at lowest cost, almost always with disregard for maintaining fitness-for-service over its lifetime. Further, capital equipment design and manufacture is invariably performed by equipment suppliers who are less interested in lifecycle cost. Another impediment in the pulp and paper industry is that corrosion control is most often handled by local operations, usually at the maintenance or reliability engineering level, and any systematic means to improve on the life-cycle cost for an equipment asset is bypassed.

On the positive side, there have been relatively few operational changes in the pulp and papermaking for the past two to three decades. Serious and catastrophic events over the decades have already been studied; causes and their solutions to most serious corrosion problems are already known. New or unknown corrosion problems might not surface until significant changes in operation are introduced.

The 2016 NACE IMPACT study also provides models for incorporation of corrosion management systems throughout the asset lifecycles. The study conclusions are that total buy-in from the top down is essential for effective corrosion control strategies to be realized. All levels of the organization—design, construction, operations, and maintenance—must have a level of involvement when planning equipment replacements and upgrades.

To be successful in recovering some of the annual costs of corrosion, higher management in the industry must recognize that significant cost recovery and return on investment can be achieved through establishment of a corrosion management system within the organization. The potential reward for better corrosion management could be up to 6% of total product sales. **TJ**

LITERATURE CITED

1. Koch, G., Varney, J., Thompson, N., et al., *International Measures of Prevention, Application, and Economics of Corrosion Technologies Study*, NACE International, Houston, TX, USA, 2016. Available [Online] http://impact.nace.org/documents/Nace-International-Report.pdf.
2. Goodman, L. and Singh, P.M., "Stress corrosion cracking in pulp and paper systems," Institute of Paper Science and Technology, Georgia Institute of Technology, Atlanta, GA, USA, 2012. Available [Online] http://www.ipst.gatech.edu/meeting/2012/2012_presentations/06-Goodman%20--%20Stress%20Corrosion%20Cracking%20in%20Pulp%20and%20Paper%20Systems_Goodman%202012.pdf.
3. Neun, J.A., *Paper 360°* 12(3): 16(2017).
4. Ince, P.J., "Industrial wood productivity in the United States, 1900-1998," United States Department of Agriculture, Madison, WI, USA, 2000. Available [Online] https://www.fpl.fs.fed.us/documnts/fplrn/fplrn272.pdf.
5. Miller, J.D., *Ind. Eng. Chem.* 28(12): 1363(1936).
6. Mueller, W.A., "Mechanism and prevention of corrosion of steels exposed to kraft liquors," *Proceedings of the Pulp and Paper Industry Corrosion Problems Symp.*, NACE International, Houston, 1974, p. 109.
7. Wensley, A., "The effect of sulfidity on the corrosivity of white, green and black liquors," *NACE CORROSION/99 Conf.*, NACE International, Houston, 1999.
8. Garner, A., "Thiosulphate and paper machine corrosion: is the problem solved?" *Pulp & Paper Canada*, 31 January 2005. Available [Online] https://www.pulpandpapercanada.com/innovation/thiosulphate-and-paper-machinecorrosion-is-the-problem-solved-1000193563.
9. Tran, H. and Vakkalainnen, E.K., "The kraft chemical recovery process," *TAPPI Kraft Recovery Boiler Course*, TAPPI Press, Atlanta, GA, USA, 2008.
10. Sharp, W.B.A.,"Corrosion and cracking in recovery boilers," *TAPPI Recovery Boiler Course*, TAPPI Press, Atlanta, 2008.

11. Laakso, S., "Modeling of chip bed packing in a continuous kraft cooking digester," Ph.D. dissertation, Helsinki University of Technology, Helsinki, Finland, 2008. Available [Online] http://lib.tkk.fi/Diss/2008/isbn9789512296781/isbn9789512296781.pdf.
12. Black Liquor Recovery Boiler Advisory Committee, "Recovery boilers in service – United States," 2015. Available [Online] http://www.blrbac.org/recovery_boilers_in_service.
13. Singh, P.M., "Capital equipment preservation – corrosion control," *Institute of Paper Science and Technology 2011 Executive Conf.*, Institute of Paper Science and Technology, Georgia Institute of Technology, Atlanta, 2011.
14. Tuthill, A., "Progress report: corrosion test results – phase I bleach plant C, D, & H stages," *The Proceedings of the Third International Symposium on Corrosion in the Pulp & Paper Industry*, NACE International, Houston, 1980, vol. 3, p. 7685.
15. Tuthill, A., "TAPPI phase II corrosion test program – part I, aggressive C, D, & H stage bleach plant environments," *The Proceedings of the Fourth International Symposium on Corrosion in the Pulp and Paper Industry*, Swedish Corrosion Institute, Stockholm, 1983, p. 133.
16. Singbeil, D.L. and Munro, I.J., "Papritection for the bleach plant of the 90's," *Can. Pulp Pap. Assoc. Conf.*, CPPA/PAPTAC, Montreal, 1990. Available [Online] https://www.researchgate.net/publication/239533244_PapritectionR_for_the_Bleach_Plant_of_the_90's.
17. Barna, J.L. and Rivers, K.B., "Improving recovery boiler furnace reliability with advanced materials and application methods," Canadian Pulp & Paper Association, Montreal, 1999.
18. Kish, J.R., Singbeil, D.L., Keiser, J.R., et al., "Assessment of molten Na_2SxH_20/NaOH solutions as a cause of composite tube corrosion in kraft recovery boilers," *NACE CORROSION 2006 Conf.*, NACE International, Houston, 2006.
19. Sharp, W.B.A., "Breakthroughs in corrosion control and materials engineering in the pulp and paper industry – lessons from history," *NACE CORROSION 2011 Conf. Expo*, NACE International, Houston, 2011.
20. Keiser, J.R., Singbeil, D.L., Sarma, G.B., et al., "Status report on studies of recovery boiler floor tube cracking," *TAPPI Engineering/Process and Product Quality Conf.*, TAPPI PRESS, Atlanta, 1999, p. 1099.
21. Keiser, J.R, Singbeil, D.L., Sarma, G.B., et al., "Causes and solutions for recovery boiler primary air port composite tube cracking," *11th Int. Symp. Corros. Pulp Pap. Ind.*, TAPPI PRESS, Atlanta, 2004.
22. Singbeil, D.L., Kish, J.R., and Keiser, J.R., "Process changes and corrosion of materials in recovery boilers," *Black Liquor Combustion Colloq.*, Pulp and Paper Research Institute of Canada, 2003. Available [Online] http://www.eng.utah.edu/~whitty/black-liquor/colloquium2003/pdfs_handouts/2.1.Singbeil-Corrosion_Handout.pdf.
23. Sylvester, W.R. and Sidla, G., "Waterside stress-assisted corrosion cracking in boilers," *TAPPI Eng. Conf.*, TAPPI PRESS, Atlanta, 1989, p. 269.
24. Moskal, M.D., "Waterside stress-assisted corrosion cracking," *Joint AF&PA-BLRBAC Corrosion Seminar*, American Forest & Paper Association/Black Liquor Recovery Boiler Advisory Committee, Washington D.C./Atlanta, 1996.
25. Bennett, D.C., "Cracking of continuous digesters: review of history, corrosion engineering aspects and factors affecting cracking," *The Proceedings of the Fourth International Symposium on Corrosion in the Pulp and Paper Industry*, Swedish Corrosion Institute, Stockholm, 1983, p. 2.
26. NACE International, *Prevention, detection, and correction of deaerator cracking*, NACE RP0590-96, NACE International, Houston, 1996.
27. Moskal, M.D., Cheetham, G., Paultre, J., et al., "Quality requirements for duplex stainless steel digester fabrication," *9th Int. Symp. Corros. Pulp Pap. Ind.*, Canadian Pulp & Paper Association, Toronto, 1998, p. 67.
28. Sharp, W.B.A., "The rise and fall of corrosion engineering in the pulp and paper industry," *TAPPI PEERS Conf.*, TAPPI Press, Atlanta, 2009.

ABOUT THIS PAPER

Cite this article as: Moskal, M. *TAPPIJ.* 17(5):253(2018).

https://doi.org/10.32964/TJ17.05.253

DOI: https://doi.org/10.32964/TJ17.05.253

ISSN:0734-1415

Publisher: TAPPI PRESS

Copyright: © TAPPI Press 2018

About this journal

ABOUT THE AUTHOR

Corrosion costs have soared over the decades be-cause of changes in pulp and paper industry pro-cesses. This paper draws attention to how even small process changes have time and again resulted in catastrophic corrosion failures. Notable corrosion events have been well docu-mented by TAPPI work groups and researchers. This is a systematic overview of the work of others, with conclusions on how process changes over decades have influenced corrosion. Literature searches on combating pulp and paper mill corrosion problems in early years, before the 1950s, were difficult because so little documentation exists. Instead, early emphasis was on production, not corrosion.



Moskal

In preparing this review, I learned that researching historical corrosion events can be very interesting. It was surprising that the petroleum and chemical process industries have found systematic corrosion management to be important and profitable, whereas emphasis on corrosion control is generally minimal in the pulp and paper industry.

Mills might better realize the importance and benefits of systematic corrosion management by reading the NACE 2016 IMPACT study on corrosion, available online at http://impact.nace.org/documents/Nace-International-Report.pdf.

The next step is to continue to promote the use of systematic corrosion management methods in the pulp and paper industry.

Moskal is principal engineer, M&M Engineering Associates, Division of Acuren Inspection Inc., Indian Head Park, IL, USA. Email Moskal at max_moskal@ mmengineering.com.

Use of vent stack temperature as a feedforward variable for dissolver total titratable alkali (TTA) control

WEI REN, BRENNAN DUBORD, JASON JOHNSON, AND BRUCE ALLISON

ABSTRACT: Tight control of raw green liquor total titratable alkali (TTA) may be considered an important first step towards improving the overall economic performance of the causticizing process. Dissolving tank control is made difficult by the fact that the unknown smelt flow is highly variable and subject to runoff. High TTA variability negatively impacts operational costs through increased scaling in the dissolver and transfer lines, increased deadload in the liquor cycle, under- and over-liming, increased energy consumption, and increased maintenance. Current practice is to use feedback control to regulate the TTA to a target value through manipulation of weak wash flow while simultaneously keeping dissolver density within acceptable limits. Unfortunately, the amount of variability reduction that can be achieved by feedback control alone is fundamentally limited by the process dynamics. One way to improve upon the situation would be to measure the smelt flow and use it as a feedforward control variable. Direct measurement of smelt flow is not yet possible.

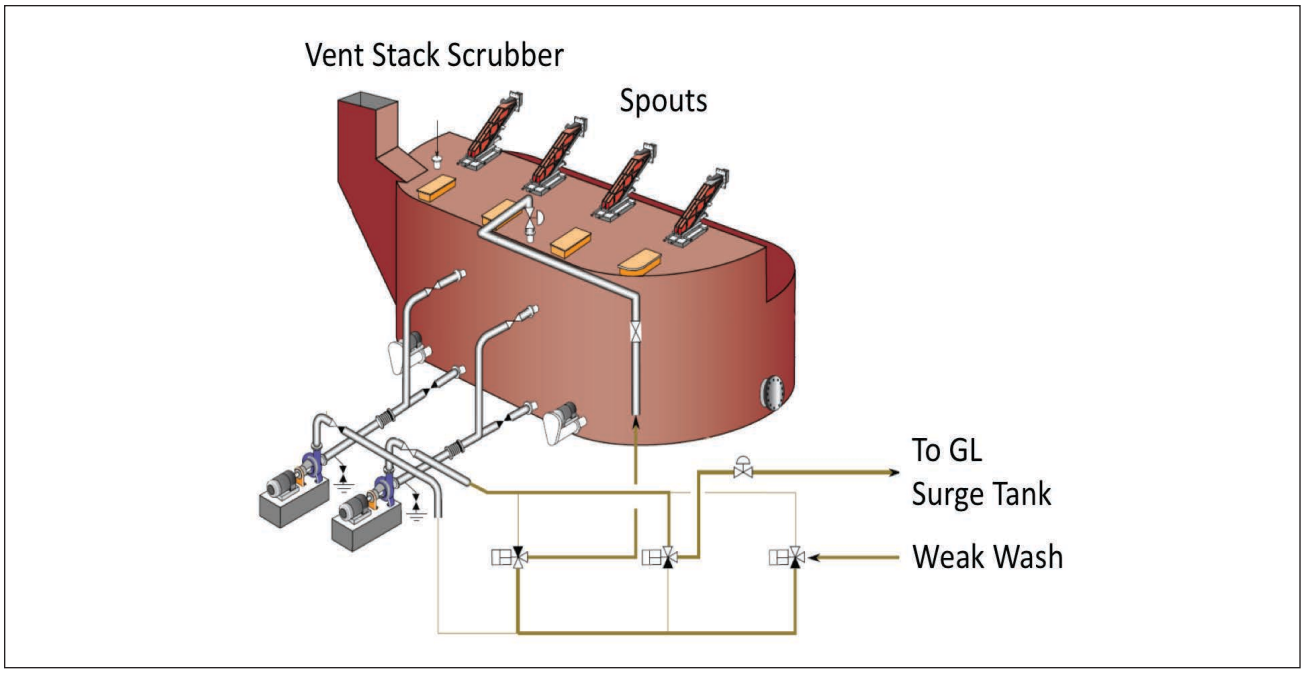
The use of an indirect measurement, the dissolver vent stack temperature, is investigated in this paper as a surrogate feedforward variable for dissolving tank TTA control. Mill trials indicate that significant variability reduction in the raw green liquor TTA is possible and that the control improvements carry through to the downstream processes.

Application: Implementing feedforward control at the dissolving tank can reduce raw green liquor TTA variability, which leads to improved operation at the slaker. Feedforward control can also minimize the impact of smelt runoffs and improve safety at the dissolving tank.

The main purpose of the causticizing process is to maximize the conversion of sodium carbonate to sodium hydroxide while simultaneously producing a strong, uniform white liquor, as well as lime mud particles that are easily separated. Costs in the recovery cycle are minimized when both the effective alkali (EA) and the causticizing efficiency (CE) of the white liquor are as high as possible [1,2]. Unfortunately, it is not possible to simultaneously control both the EA and the CE of the white liquor when the green liquor total titratable alkali (TTA) varies [3,4]. High TTA variability negatively impacts operational costs through increased scaling in the dissolver and transfer lines [5], increased deadload in the liquor cycle, under- and over-liming, increased energy consumption, and increased maintenance. Thus, tight control of green liquor TTA may be considered an important first step toward improving the overall economic performance of the causticizing process.

The role of the smelt dissolving tank (SDT) is to safely dissolve molten smelt from the recovery boiler in weak wash such that the density of the resulting raw green liquor is kept within desirable limits. Dissolving tank control is made difficult by the fact that smelt flow is highly variable and, in severe cases, subject to runoff [6,7]. Density meters react to all the constituents in the liquor, not just those associated with TTA. Therefore, constant density does not necessarily result in constant TTA. Ideally, the dissolving tank control strategy should regulate the TTA to a target value while simultaneously ensuring that density stays within acceptable limits. A cascaded feedback control strategy that achieves this has been reported [8]. A potential shortcoming of this strategy is that the amount of variability reduction that can be achieved by feedback control alone is fundamentally limited. That is, changes in density and TTA significantly lag smelt flow disturbances because the tank volume is large relative to the nominal liquor flow rate, and this large hydraulic time constant limits the efficacy of the control.

One way to improve the situation would be to measure the smelt flow and use it as a feedforward control variable. Direct measurement of smelt flow is not yet possible. The use of an indirect variable, the dissolver vent stack temperature, is investigated in this paper as a surrogate feedforward variable for dissolving tank TTA control. Theliander and Aksnes [6] considered using vent stack temperature for dissolver control, but as a feedback control variable only. The key idea in this work came from a mill observation that density and TTA disturbances were almost always preceded by a disturbance in the vent stack temperature. The obvious question was: could this be used for feedforward control? To answer this question, a two-part approach was taken: (i) attempt to establish a relationship between the stack temperature and the unknown smelt flow; and (ii) quantify the information in the temperature signal such that a feedforward controller could be designed and implemented. The remainder of this paper is orga-



1. Process diagram for dissolving tank operation (GL = green liquor).

nized as follows. The SDT process where the new controls were trialed is explained. A process model that was used for data analysis and to determine the required feedforward gain is also presented. The control strategy, which includes a TTA soft sensor, the TTA to density cascaded feedback and the new feedforward controls, is described. Finally, this paper presents and discusses the results of a mill trial, as well as practical benefits for the mill that participated in this study.

PROCESS DESCRIPTION

Cariboo Pulp & Paper in Quesnel, BC, Canada, is a joint venture between West Fraser and Daishowa-Marubeni. It is a single line northern bleached softwood kraft (NBSK) mill with a digester production of approximately 1140 a.d. metric tons/day. The mill is equipped with a five-effect evaporator train and a single concentrator that raises the as-fired black liquor solids to approximately 65%. The black liquor solids firing rate is approximately 4.3 x 10^6 lb/day (1950 metric tons/day).

As shown in **Fig. 1**, the molten smelt that forms in the recovery boiler is discharged to the dissolving tank via four smelt spouts. Weak wash and fresh water enter the dissolving tank from several sources:

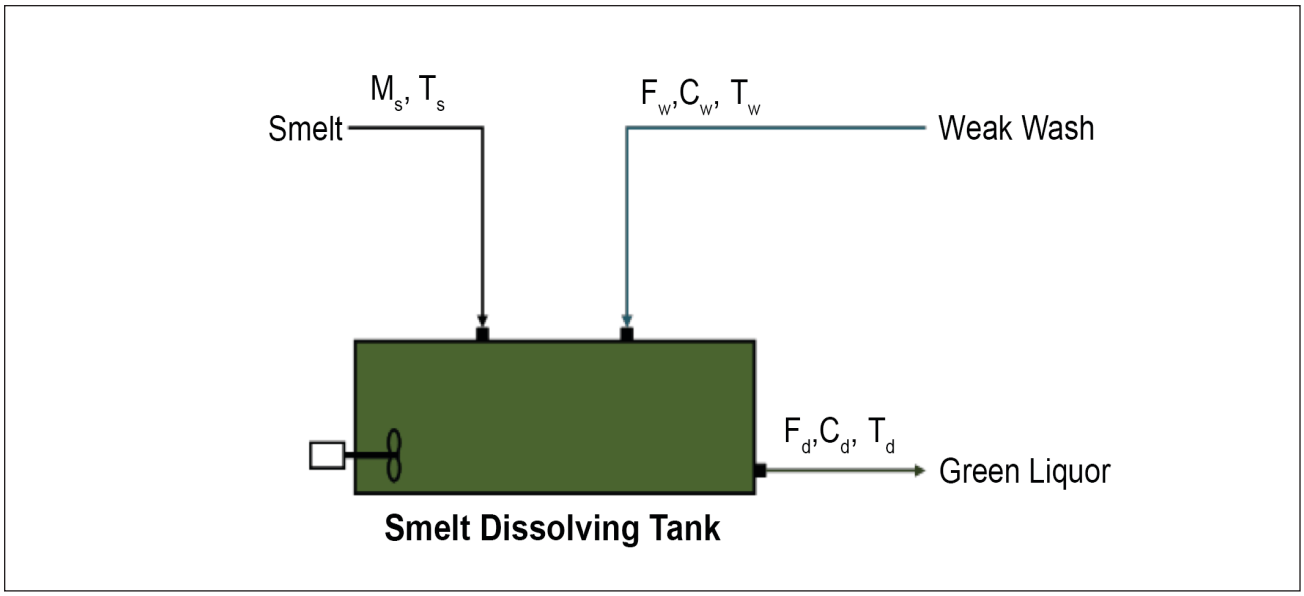
1. Weak wash main addition line – approximately 70% of the total weak wash/mill water flow
2. Dissolver scrubber nozzles – fresh water and weak wash
3. Dissolver wall washers – fresh mill water and weak wash
4. Weak wash through the offline transfer pump

The smelt dissolves in the weak wash to make raw green liquor and the tank is agitated to help promote the dissolution process. Weak wash from the main addition line is manipulated to control the density and TTA of the green liquor. There are two transfer lines, A and B, each equipped with a pump. One line removes the green liquor from the tank and transfers it to the green liquor clarifier, while the other line is soaking in weak wash to help reduce scale buildup.

The dissolving tank has two overflows (roughly at 83% level) that feed a standpipe to the green liquor transfer pumps. The level in the standpipe is controlled through a variable speed pump, which in turn maintains the level in the dissolving tank. The operating volume of the dissolver is roughly 30000 U.S. gallons (113 m^3). In 2011, Cariboo converted the density measurement from an in-line nuclear device on the tank outlet to a differential pressure measurement to alleviate the scaling issues that would cause erratic and drifting indication. The differential pressure is measured on both sides of the tank and the overall raw green liquor density is the average of the two measurements.

A Fourier transform near-infrared (FT-NIR) liquor analyzer was installed in 2012 with the purpose of improving causticizing process control. The analyzer has four sample points: raw green liquor, clarified green liquor, #1 causticizer, and #4 causticizer. Liquor constituents measured for each sample include: sodium carbonate, sodium sulfide, sodium hydroxide, sodium sulfate, and sodium thiosulfate. The sample locations are as follows:

1. Raw green liquor (RGL) – downstream of the dissolving tank green liquor transfer pumps
2. Clarified green liquor (CGL) – discharge of green liquor pump to slaker
3. #1 causticizer – overflow from the #1 to the #2 causticizer
4. #4 causticizer – discharge of the #4 causticizer liquor pump to the white liquor clarifier



2. Simplified process schematic showing variables used for modeling.

For the raw green liquor sample point, a sample line comes off each of the green liquor transfer lines in order to divert a small amount of liquor to the analyzer. The analyzer samples and measures the liquor constituents, including TTA, every 35–40 min. The results from this analysis provide the information needed for feedback control of the raw green liquor TTA. Additional details on raw green liquor measurements using FT-NIR liquor analyzer technology are available [9].

PROCESS MODEL

A dynamic model of the smelt dissolving tank was previously developed by one of the authors [10], and the work reported here is based on that model. **Figure 2** shows a simplified schematic diagram of the smelt dissolving tank. The dissolver is assumed to be a continuously stirred tank reactor (CSTR). The molten smelt from the recovery boiler, which enters the dissolver at mass flow rate M_s, is assumed to contain only those chemical species which, when dissolved into solution, contribute to the TTA of the resultant green liquor. This assumption is reasonable since other green liquor constituents, such as sodium sulfate, sodium thiosulfate and sodium chloride, are typically present in relatively small concentrations (0-10 g/L). Thus, the units of M_s are kg/min as Na_2O. The smelt dissolves in weak wash, which enters the dissolver at volumetric flow rate F_w and TTA concentration C_w (kg/m^3 as Na_2O), to form raw green liquor that exits the tank at TTA concentration C_d (also kg/m^3 as Na_2O). The volume of the tank is equal to V_d. Combining volumetric and material balances [10] give the following nonlinear ordinary differential equation for the raw green liquor TTA:

$$V_d \frac{dC_d}{dt} = M_s + F_w(C_w - C_d) \quad (1)$$

The relationship between green liquor TTA and density may be approximated by the following static linear relationship:

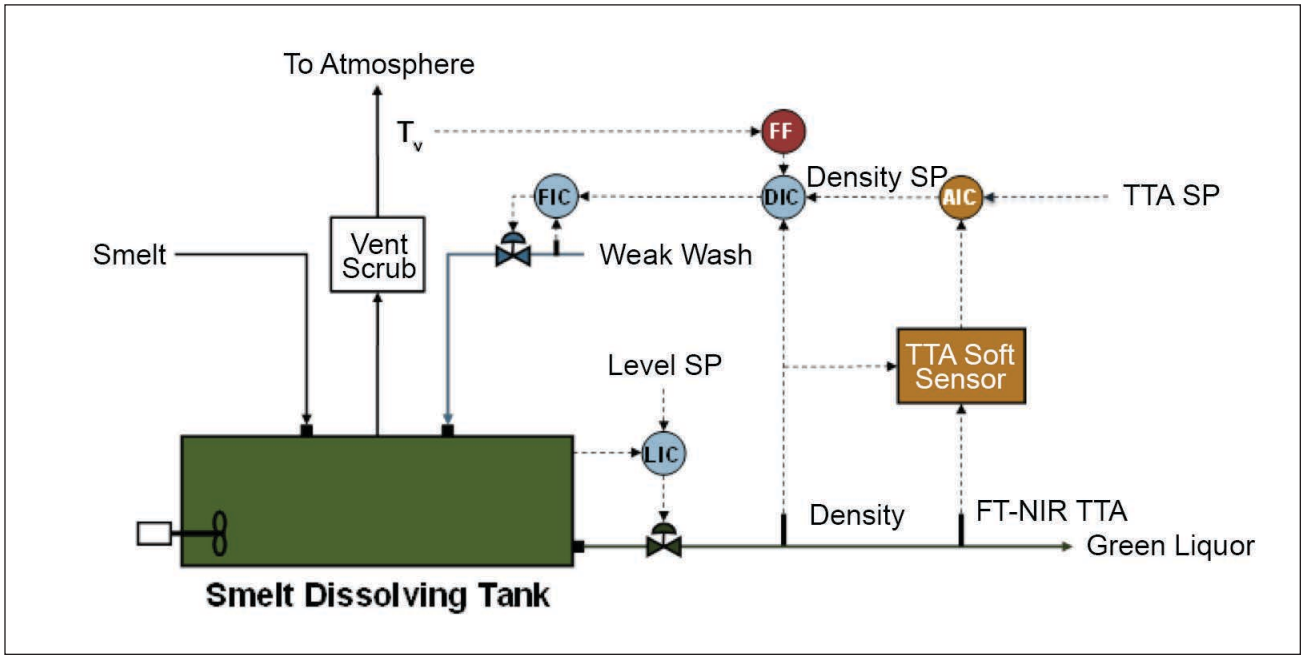
$$C_d = aD_d + b \quad (2)$$

where D_d is dissolver density and parameters a and b were determined for a typical green liquor, assuming a fixed liquor temperature of 95°C [10]. Although the actual relationship is nonlinear and depends on liquor composition and temperature, a sensitivity analysis indicates that it is sufficient to use a single regression line to represent a mill's green liquor, provided the temperature is well controlled.

CONTROL STRATEGY

The control scheme that was in place prior to this work is indicated by the blue-colored symbols in **Fig. 3**. As indicated earlier, the dissolver overflows to a standpipe (not shown) and the standpipe level controller manipulates the green liquor flow out of the system. In addition, the dissolver density is controlled by manipulating the setpoint to the weak wash flow controller.

The TTA controls, which are indicated by the brown-colored symbols, consist of a TTA soft sensor and a TTA feedback controller that regulates the TTA to a target value through manipulation of the density setpoint. Safe operation is achieved by limiting the density to an allowable range through overrides. The role of the soft sensor is to use the density measurement to predict the TTA between the discrete FT-NIR sample times. The soft sensor uses a static linear (gain and offset) model, i.e., Eq. 2, to relate TTA to density. The gain is a fixed value, but the offset is estimated, i.e., when a new FT-NIR measurement is made, the offset is adjusted based on the error between the TTA measurement and the predicted value from the soft sensor. In this way, the soft sensor can adjust for



3. Simplified process schematic showing total titratable alkali (TTA) control strategy (SP = setpoint; FT-NIR = Fourier transform near-infrared).

drift in the density signal. When the soft sensor is working well, it is a good predictor of incoming TTA measurements.

The new feedforward control from vent stack temperature is indicated in red. Changes in stack temperature are multiplied by a gain and act in a direct feedthrough manner to adjust the weak wash flow setpoint through the density controller. A model-based approach to calculating this feedforward gain is discussed in the next section. All the functionality described here was implemented in the mill's Emerson DeltaV DCS.

RESULTS

This section is divided into two parts. In the first part, the dissolver process model is used to establish the relationship between the vent stack temperature and the unknown smelt flow and to calculate the feedforward gain used for control. In the second part, a performance assessment of dissolver control with and without feedforward compensation is presented.

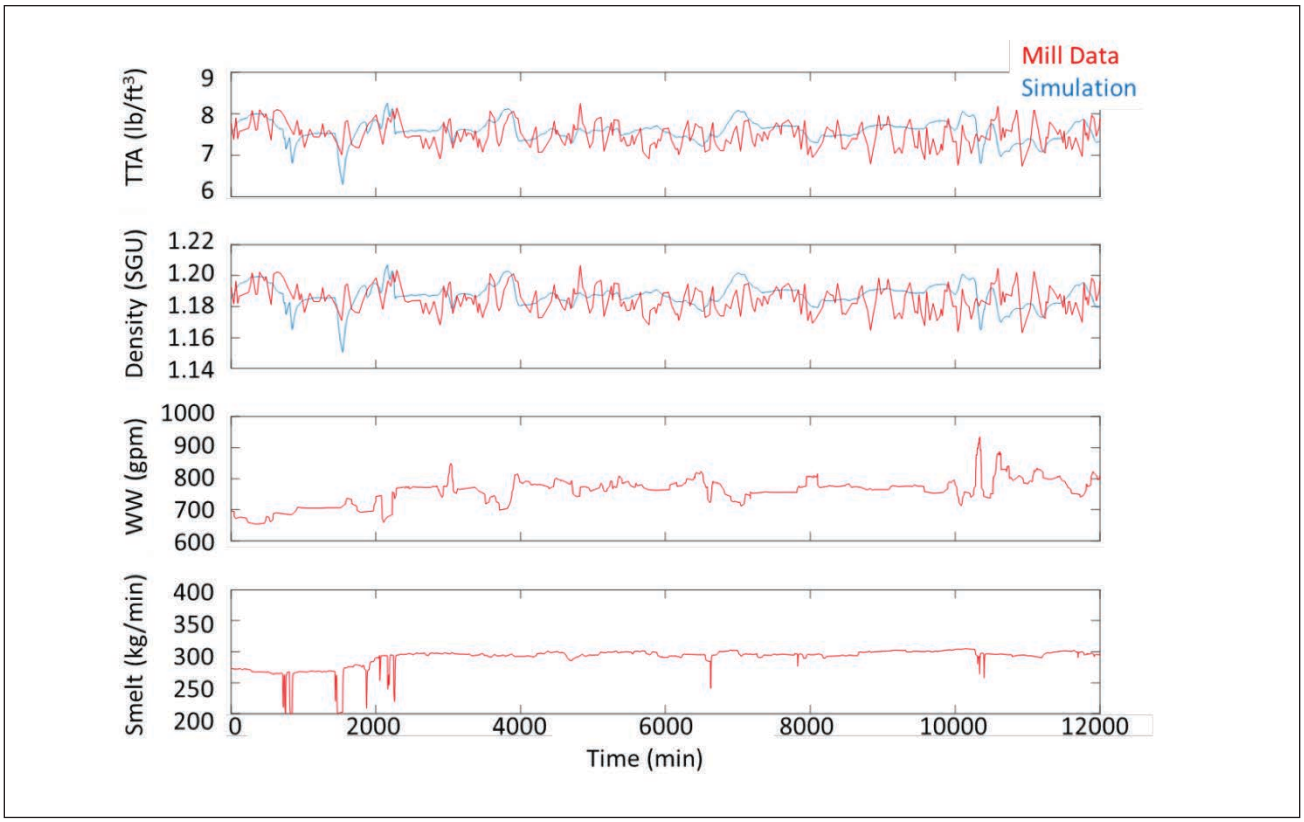
Modeling of feedforward gain

All of the variables in the model (Eqs. 1 and 2) are either known or may be measured on line, except for the smelt mass flow rate (M_s). One approach to estimate the smelt mass flow rate, or at least its steady-state value, is to base it on the black liquor solids firing rate and to assume 1 kg of black liquor solids produces 0.4 kg of smelt. **Figure 4** shows a simulation of the dissolving tank TTA and density that results when the weak wash flow and the estimated steady-state smelt flow are inputs to the model. The model outputs are compared to the mill data over a period of approximately eight days. Figure 4 shows that the mill data contains significantly more short-term variability in TTA and density than the simulated values. Not surprisingly, the most likely explanation is that the actual smelt flow is significantly more variable than that calculated from the black liquor solids firing rate; i.e., a constant black liquor solids firing rate does not generally result in a constant smelt flow rate.

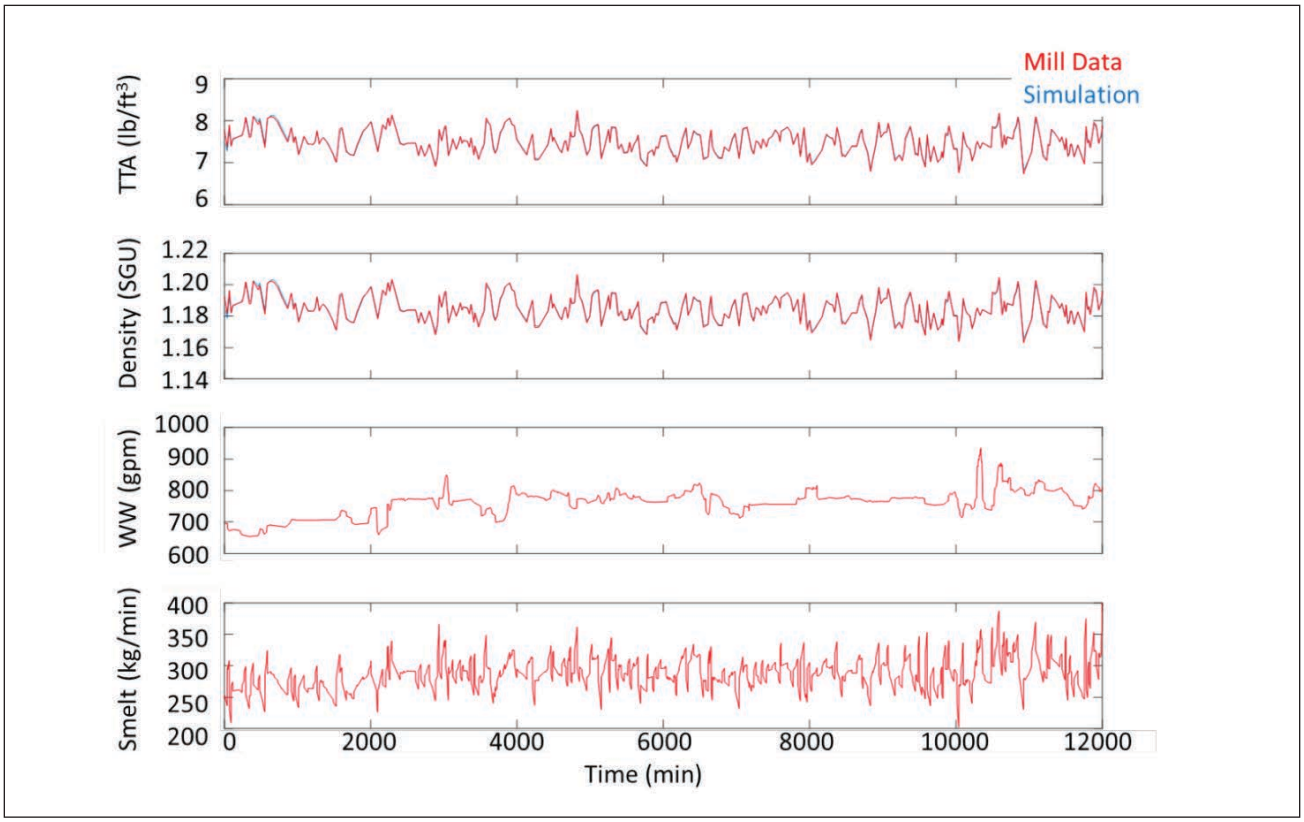
A better approach is to estimate the unknown smelt flow directly from the model (Eq. 1). For this analysis, the dissolver TTA and weak wash data were discretized at a 1-min sampling interval. The data was then filtered and resampled at a lower rate. The TTA of the weak wash was assumed constant at 20 kg/m^3, and a finite difference approximation was used for the derivative term. Note that an analysis such as this is only possible with off-line data, as future outputs are required to properly estimate the derivative term. Once the smelt flow was estimated, the simulation was rerun using the new estimates. The simulation results based on this approach are shown in **Fig. 5**. Note that the simulated TTA and density now essentially overlap the mill data, and that the estimated smelt flow has the anticipated short-term variability with this modification to the model.

The next step was to establish the relationship between the vent stack temperature and the estimated smelt flow rate. **Figure 6** shows the estimated smelt flow plotted against the dissolving tank stack temperature. A linear correlation exists between the two variables, and the gain (slope) of the relationship is shown in Eq. 3:

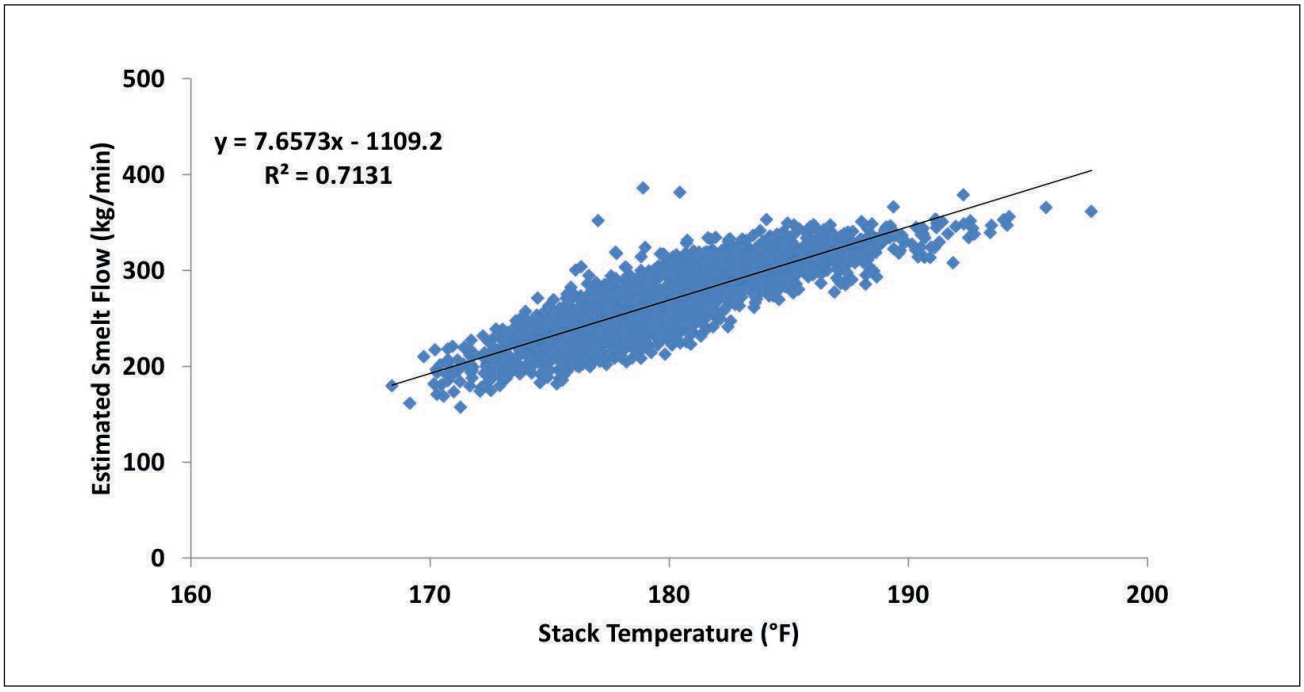
$$M_s = 7.6573T_v \quad (3)$$



4. Simulation of dissolver TTA and density using estimated smelt flow based on black liquor solids firing rate (WW = weak wash).



5. Simulation of dissolver TTA and density using estimated smelt flow from process model (WW = weak wash).



6. Estimated smelt flow plotted against dissolving tank stack temperature.

where T_v is the dissolving tank vent stack temperature (°F).

As a visual check, **Fig. 7** shows one day of operation where the stack temperature and the estimated smelt flow are plotted versus time. Note that the stack temperature was in no way involved in the estimation of the smelt flow, so the close temporal relationship between the two variables effectively proves that vent stack temperature changes are caused by changes in smelt flow. This is not an unreasonable proposition, since an increase in smelt flow would be expected to generate more steam and thereby increase the temperature of gaseous emissions from the dissolver.

The final step was to calculate the feedforward gain from vent stack temperature to weak wash flow. As discussed in the "Control Strategy" section, the feedforward gain is used to adjust the weak wash flow rate when changes in stack temperature occur. The feedforward gain (K_{FF}) was calculated by combining the gain (slope) information from Fig. 6 with the steady state relationship between weak wash and smelt flow (Eq. 1) to give

$$K_{FF} = \frac{F_w}{T_v} = \frac{M_s}{T_v}\frac{F_w}{M_s} = \frac{M_s}{T_v}\frac{1}{C_d - C_w} \quad (4)$$

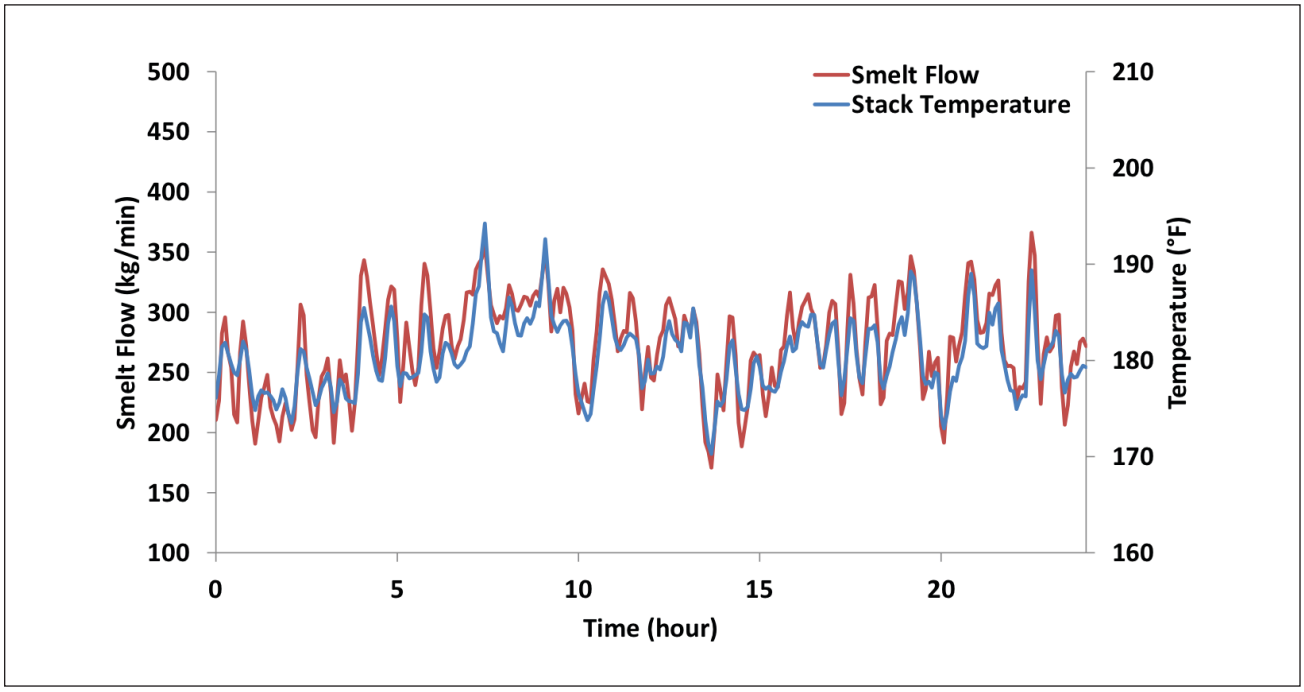
Combining Eqs. 3 and 4, and substituting nominal values of 20 kg/m³ and 120 kg/m³ for C_w and C_d, respectively, as well as converting from cubic meters to gallons per minute (264 gpm/m³), the feedforward gain equals to 20.2 gpm/°F. This value was rounded to 20 gpm/°F when feedforward control was implemented at the mill.

Assessment of control performance

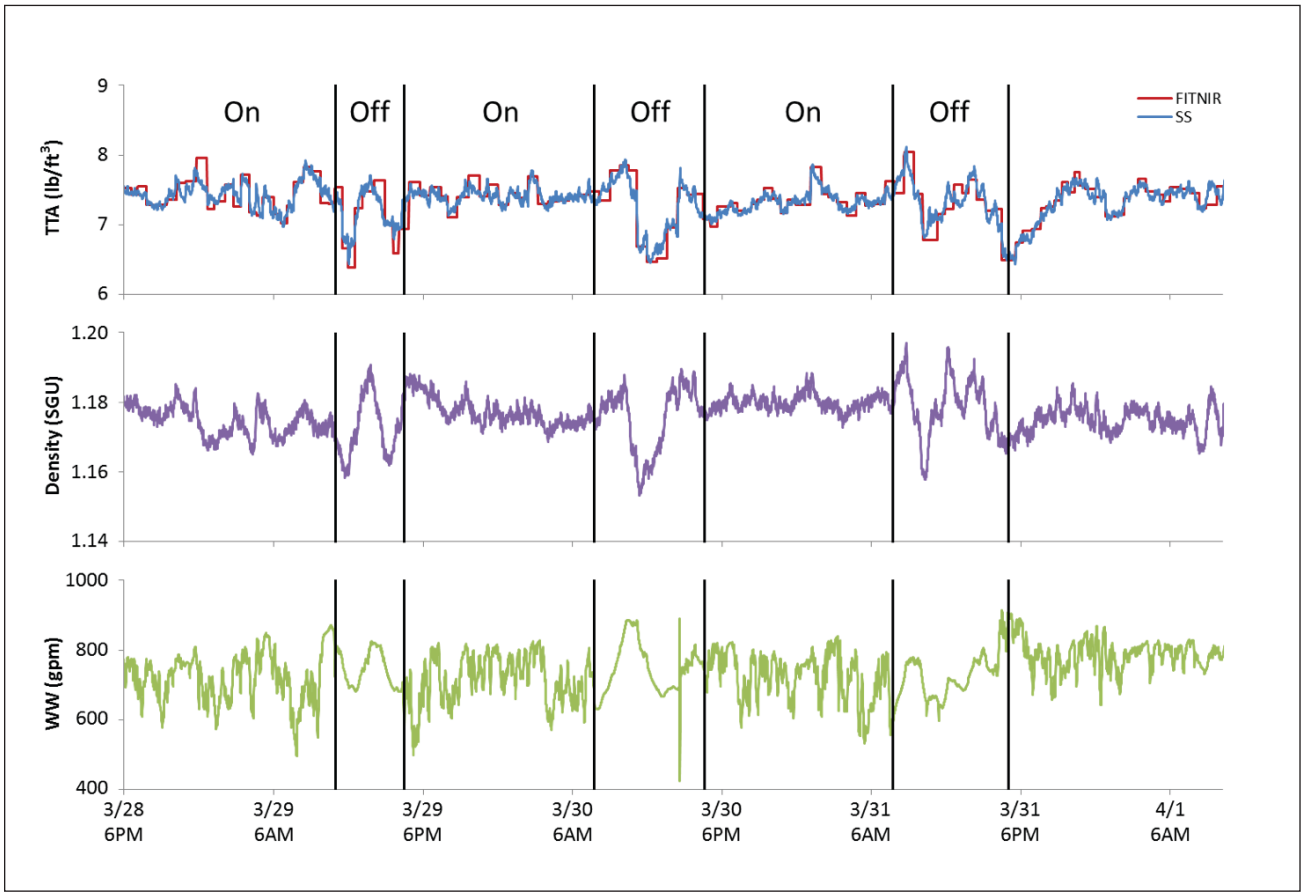
In order to demonstrate the improvement provided by the combination of feedforward and feedback control as com-

	On	Off	On	Off	On	Off
Tank level, %	**0.54**	0.70	**0.47**	0.80	**0.50**	0.83
Tank T, °F	**1.03**	1.98	**0.82**	1.77	**0.90**	2.13
WW flow, gpm	**73.2**	52.4	**69.5**	72.5	**68.2**	62.1
Density, SGU	**0.0042**	0.0085	**0.0040**	0.0091	**0.0024**	0.0085
RGL TTA, lb/ft³	**0.18**	0.43	**0.16**	0.48	**0.18**	0.38

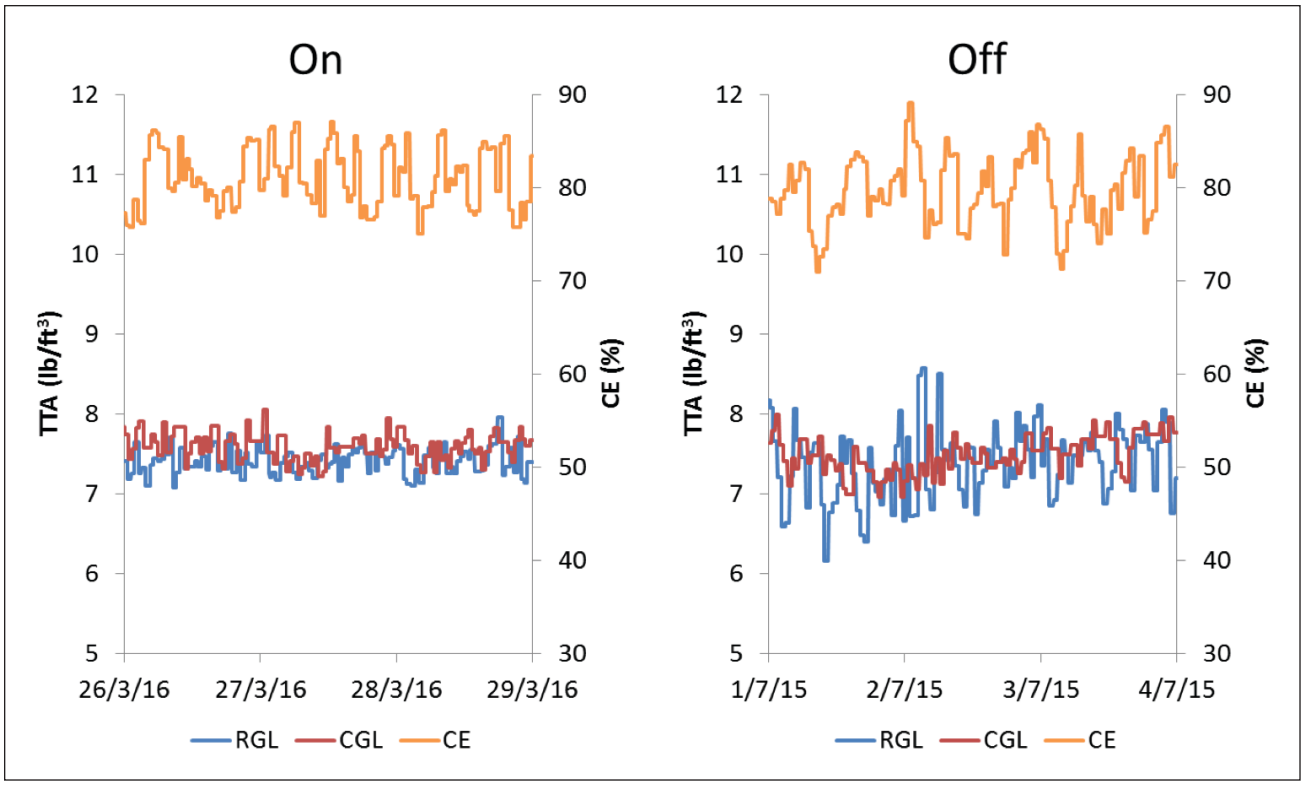
I. Standard deviations when cycling feedforward gain between 20 gpm/°F and zero (WW = weak wash; SGU = specific gravity units; RGL = raw green liquor; TTA = total titratable alkali).



7. Smelt flow and stack temperature during typical operation for a 24-h period.



8. Variability for TTA, density and weak wash (WW) when cycling feedforward gain between on and off.



9. Variability for raw green liquor (RGL), clarified green liquor (CGL), and causticizing efficiency (CE) when cycling feedforward gain between on and off.

pared to feedback control alone, a one-week trial was conducted. In the trial, the feedforward gain was cycled between its nominal value of 20 gpm/°F and zero. The results are shown in **Fig. 8** and **Table I**. The reduction in variability with feedforward (FF) control is clearly seen in Fig. 8. The variability in TTA and density with FF control is less than half of that with feedback (FB) control alone (Table I). Furthermore, this is achieved without a substantial increase in the overall variability of the weak wash flow, although there is more short-term weak wash (WW) flow variability with FF control as one might expect.

One would expect that reduced variability in the RGL TTA should translate into improved uniformity in the CGL TTA and even the white liquor causticity (CE), since TTA variability is a disturbance to the causticizing process. **Figure 9** compares two 3-day periods, one in 2015 under manual RGL TTA operation and the other in 2016 under FB + FF RGL TTA control. The graph shows that the improved performance (i.e., variability reduction) carries through the system. The CGL standard deviation improves from 0.28 lb/ft³ (4.5 g/L) with manual operation to 0.18 lb/ft³ (2.9 g/L) with automatic control, while the standard deviation of the 4th causticizer CE decreases from 4.5% to 3.2%.

A reduction in raw green liquor TTA excursions has resulted in less time running the dissolving tank with TTAs exceeding the pirssonite solubility limit of approximately 8.0 lb/ft³ (128 g/L), as shown in **Table II**. Consequently, the raw green liquor TTA set point has been raised from 7.2 lb/ft³ (115 g/L) to 7.5 lb/ft³ (120 g/L) to reduce energy costs in the liquor cycle. It is estimated that the resulting energy savings, mainly steam savings in the evaporators, will amount to approximately CAD $250,000/year. Limited pirssonite scaling was observed in green liquor piping during the 2017 annual maintenance outage compared to previous years.

Date	% Time that RGL TTA Exceeded 8.0 lb/ft³
2014	4.7%
2015	5.2%
2016	0.6%

II. Percentage of time that dissolver TTA exceeded 8.0 lb/ft3 each year.

CONCLUSIONS

Dissolving tank control is difficult because the main disturbance—the smelt flow from the recovery boiler—is unknown and highly variable. Control based on feedback alone from raw green liquor measurements is fundamentally limited, because changes in density and TTA significantly lag smelt flow disturbances. In this report, it was shown that dissolving tank vent stack temperature may be used as a feedforward variable

for improved control of raw green liquor TTA. A process model was used to demonstrate that the stack temperature is correlated with the estimated smelt flow and to calculate the required feedforward gain from stack temperature disturbances to weak wash flow adjustments. The improvement in raw green liquor density and TTA control was clearly demonstrated in an on-off control trial. Significant variability reduction was also achieved in the clarified green liquor TTA and even the white liquor causticity values. Raw green liquor TTA control improvements were used to increase the TTA target value to reduce energy costs (approximately CAD $250,000/year) in the liquor cycle. **TJ**

LITERATURE CITED

1. Kojo, M., *Pulp Pap. Can.* 54(11): 174(1980).
2. Axelsson, O., Gustafsson, E., Wiklander, G., *Pulp Pap. Can.* 84(2): 55(1983).
3. Dorris, G.M., "Equilibrium of the causticizing reaction and its effect on slaker control strategies," *TAPPI Pulping Conf.*, TAPPI Press, Atlanta, GA, USA, 1990.
4. Swanda, A.P., Seborg, D.E., Holman, K.L., et al., *TAPPI J.* 83(4): 73(2000).
5. Frederick, W.J., Krishnan, R., and Ayers, R.J., *Tappi J.* 73(2): 135(1990).
6. Theliander, H. and Aksnes, O., *Nord. Pulp Pap. Res. J.* 4(4): 263(1989).
7. Tran, H., Jones, A.K., Grace, T.M., *TAPPI J.* 14(1): 41(2015).
8. Coyle, I., Russell, S., Rajbhandari, V., et al., "Improving smelt dissolving tank TTA control at Zellstoff-Celgar", *PACWEST Conf.*, PAPTAC, Montreal, 2013.
9. Trung, T.P., Betts, S., Pouw, D., et al., "On-line determination of green liquor reduction efficiency using infrared spectrometry," *Int. Chem. Recovery Conf.*, TAPPI Press, Atlanta, 2007.
10. Allison, B.J., "A dynamic model for monitoring and control of the smelt dissolving tank," *International Control Systems Program 2010*, SPCI & INNVENTIA, Stockholm/Gothenburg, 2010.

ABOUT THIS PAPER

Cite this article as: Ren, W., Dubord, B., Johnson, J., Allison, B. *TAPPI J.* 17(5): 261(2018). https://doi.org/10.32964/TJ17.05.261

DOI: https://doi.org/10.32964/TJ17.05.261

ISSN: 0734-1415

Publisher: TAPPI Press

Copyright: © TAPPI Press 2018

About this journal

ABOUT THE AUTHORS

We studied this topic because a partner mill, Cariboo Pulp & Paper, was interested in improving raw green liquor TTA control. This work complements previous work on feedback control at the dissolving tank.

The most difficult part of this research was estimating smelt flow, which was solved by using a dynamic dissolving tank model. In the course of this study, we found that observations made by mill process engineers are an important part of research. Also, to our surprise, there was excellent correlation between the dissolver vent stack temperature and estimated smelt flow.

Cariboo Pulp & Paper has already seen improvements and savings in their recovery cycle operation.



Ren



Allison



Dubord



Johnson

Our next step is to implement the feedforward strategy at more mills.

Ren is research engineer and Allison is principal research engineer and research leader at FPInnovations in Vancouver, BC, Canada. Dubord is process engineer and Johnson is control systems coordinator, Steam & Recovery, at Cariboo Pulp & Paper in Quesnel, BC, Canada. Email Ren at wei.ren@fpinnovations.ca.

Factors affecting particulate removal efficiency of kraft recovery boiler electrostatic precipitators: a technical review

EZZAT JAROUDI, IVAN SRETENOVIC, GREG EVANS, AND HONGHI TRAN

ABSTRACT: Electrostatic precipitators (ESPs) are used in most pulp mills to remove particulate from recovery boilers, power boilers, and lime kilns. As environmental regulations have become increasingly stringent in recent years, maintaining high ESP performance is of vital importance in mill operation. This paper discusses results of a literature review of the ESP technology used in industrial combustion units, including recovery boilers, as well as results of a parametric study using the well-known Deutsch-Anderson equation to correlate recovery boiler operating conditions with ESP collection efficiency. The results show that for particles up to about 0.3 μm, the ESP collection efficiency decreases drastically with increased particle size and with decreased temperature. For particles larger than 0.5 μm, however, the trend reverses; the collection efficiency increases with increased particle size and decreased temperature. The results also suggest that the particle concentration (or loading) in the flue gas has no effect on collection efficiency and that sodium chloride particles are more readily captured than sodium sulfate particles. The latter prediction, however, appears to be in contradiction with mill experience that sodium chloride particles are more difficult to capture.

Application: Mills can maximize their boiler throughputs by better understanding key operating factors that affect electrostatic precipitator performance.

While air quality standards have become increasingly stringent over the past few decades, the removal of particulate matter (PM) entrained in flue gases from various industrial combustion processes have been the concern of engineers and scientists for much longer. Devices used to remove PM from boiler flue gases can be either mechanical or electrical. Cyclones and filters are the main devices that rely on mechanical principles to remove particles, while the electrostatic precipitator (ESP) is the most common device that relies on electrical principles. Electrostatic precipitators are preferred over their mechanical counterparts because of their ability to treat larger volumes of gas at higher removal efficiency (up to 99.9%) and with lower pressure drop.

This paper discusses the development history of ESP technology, the operating principles, and results of a sensitivity analysis to examine the effects of temperature, ash composition, and concentration on the collection efficiency of ESP.

HISTORY OF ESP TECHNOLOGY

The Greeks were believed to be the first to make use of electrostatic phenomena to attract and remove fine particles [1], but it was not until the eighteenth century that the science behind this concept was explained as a result of advances in the fields of electricity and magnetism. The first application of electrostatic precipitation was the equipment commercialized in 1907 for collecting condensed sulfuric acid fumes [1]. The technology was then adopted by the mining industry in 1910 and the cement industry in 1911. It was not until 1916 that an electrostatic precipitator (ESP) was first used by the pulp and paper industry to collect alkali salts from evaporators and later, in the 1930s, on recovery boilers. The motive behind using an ESP in the pulp and paper industry at the time was mainly economical; the intent was to recover valuable alkali salts rather than to reduce particulate emissions [2]. The rapid increase in coal-fired boilers for power production in the early 1920s spurred the use of ESPs as a means of capturing fly ash particulates from coal combustion and established ESP as the most common particle capturing technology to clean flue gases.

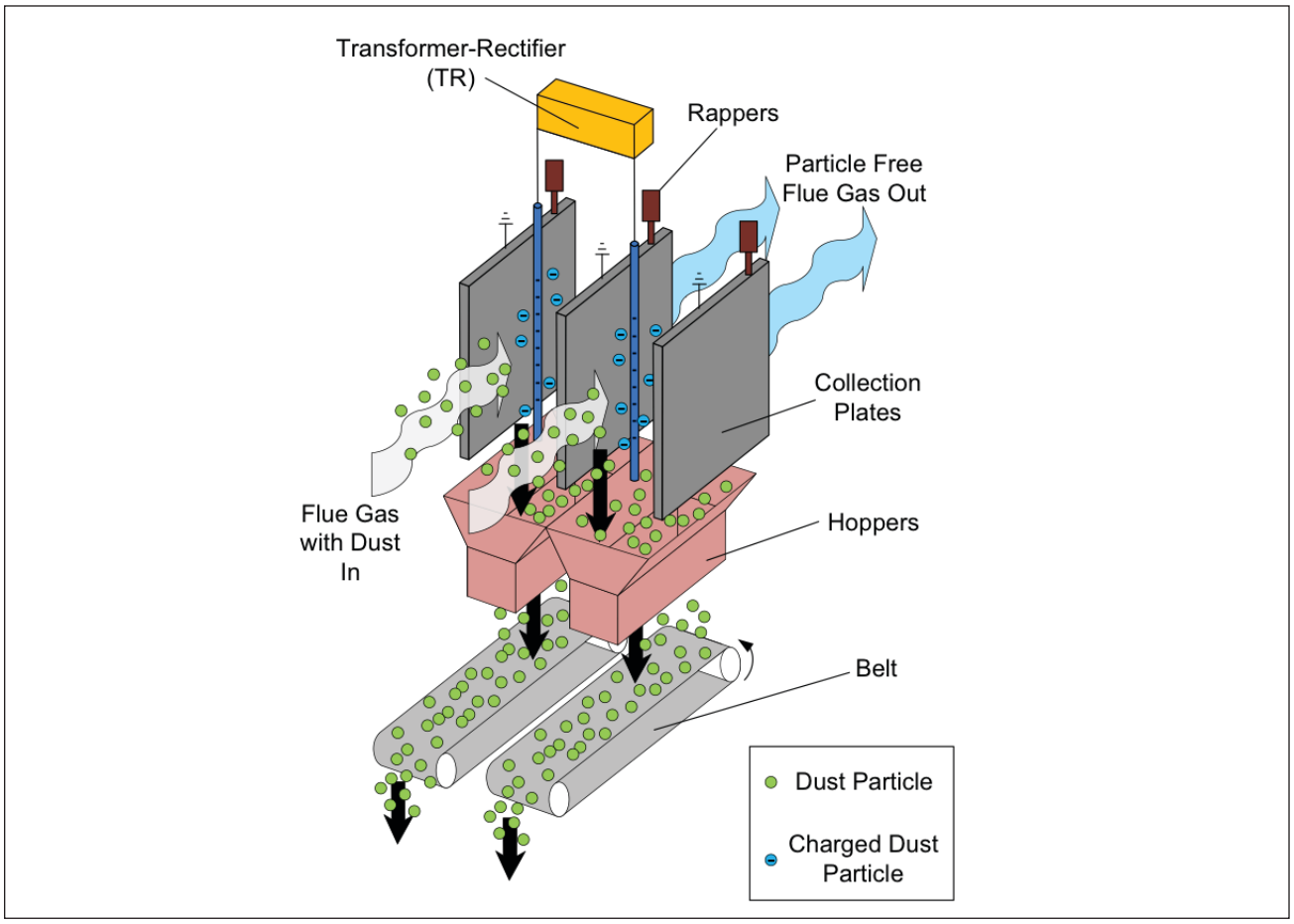
As ESPs became increasingly accepted as an effective method for removing particulates from flue gases, advances in ESP technology initially aimed at increasing the collection efficiency. As the removal efficiency approaches 100%, the focus of improvements shifted toward making the ESP more compact and able to handle changes in boiler operation, which lead to wide variation in dust load, as well as increasing the equipment life. These improvements were possible thanks to various research programs on ESP technology. Some research focused on improving the mechanical components of the ESP, mainly the high voltage electric circuit, and the mechanics of deposit removal from the collection surface.

Advances in computational power have also helped researchers to develop models to simulate flows in the ESP and predict its performance under different conditions. Numerical models have been used in various ways; some simulated particle charging [3,4] and others attempted to understand the overall particle removal process and how it is affected by different ESP parameters [5,6]. Other models have been used to simulate full-scale ESPs, either to simulate the gas flow through the ESP and determine how that could affect particle collection [7] or to simulate the particle collection mechanisms inside an ESP to determine its collection efficiency [8]. Tests have also been performed to examine the impact of ash composition and flue gas conditions on the performance of either full-scale ESPs [9-11] or laboratory-scale ESPs [12-14].

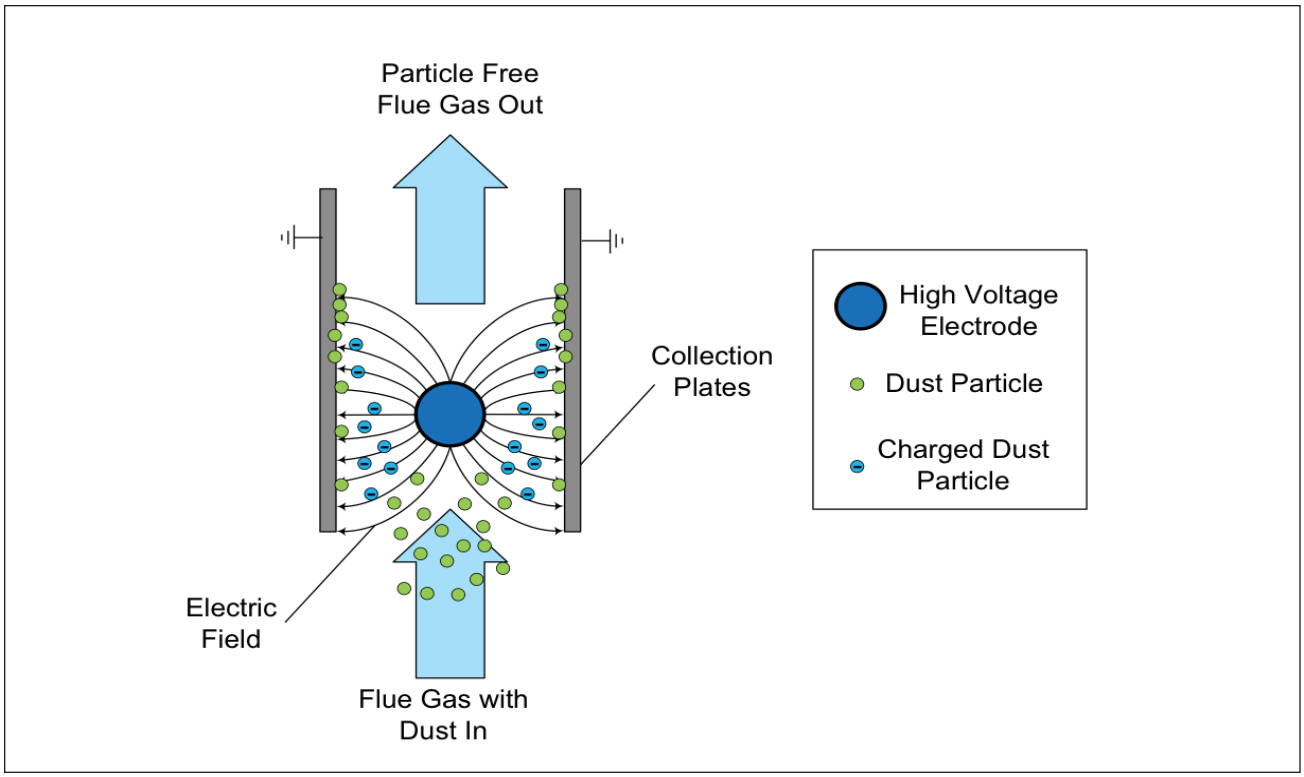
An important factor affecting the ESP performance is the electrical resistivity of the fly ash. The fly ash resistivity has an optimal range where it is easiest to capture and discharge from the ESP. Any increase or decrease from that optimal value results in a decrease in collection efficiency. A common belief is that high-resistivity ash particles are more difficult to charge and therefore cannot be collected well [15,16]. Once charged, high-resistivity ash particles are less likely to lose their charge. This means that once the particles have deposited on a collection plate, they cannot lose their charge readily and so would tend to be more tenacious and keep buildup on the collection plate due to the electrostatic attraction between the charged deposited dust and the plate. This, in turn, would reduce the voltage difference between the collection plate and discharge electrode, lower the electric field strength, and negatively affect the collection efficiency. Low-resistivity ash particles, on the other hand, can be collected more efficiently but also can be discharged more readily. As a result, they may fall off the plate and become re-entrained in the flue gas [17].

While there has been extensive research done on the performance of ESP in coal-fired boilers, little attention has been given to date to ESP in recovery boilers. Research to understand the behavior of ash in the recovery boiler ESP is limited to a review of ESP application to recovery boilers [18], a comparison between the performance of two ESPs from two different recovery boilers [11], and a study on factors affecting the resistivity of fly ash in recovery boilers [19].

Ash particles entrained in the flue gas at the inlet of a recovery boiler ESP are mainly condensed alkali fume that con-



1. Electrostatic precipitator (ESP) operating principle and main components (Adapted from "Conceptual diagram of an electrostatic precipitator" by E. Mason, Wikimedia Commons licensed under CC BY-SA 3.0).



2. Three-step process of particle collection in an ESP.

sists of sodium sulfate (Na_2SO_4) and sodium carbonate (Na_2CO_3) with a small amount of sodium chloride (NaCl) and potassium salts. Such ash composition differs substantially from that of coal-fired boiler ash, which is made of mainly silicates, oxide minerals, and unburned carbon [20]. Recovery boiler ash also has a much smaller and more uniform particle size (typically 0.3–0.6 μm). These differences likely make recovery boiler ash particles behave differently in the ESP than coal-fired boiler ash particles.

ESP DESIGN AND OPERATING PRINCIPLES

As shown in **Fig. 1**, the two main components that make up an ESP are a high-voltage discharge electrode system and a series of neutral grounded collection plates. The high voltage between the discharge electrodes and collecting plates is provided by a transformer-rectifier (TR) set. There are two basic dust removal mechanisms required in an ESP application. The first is a rapping mechanism that dislodges deposits from the surface of the collection plate and the second is a discharge mechanism (typically a hopper and a chain conveyor) that transports the collected particles out of the ESP.

Particles are removed from the flue gas by mean of electrostatic force. The high voltage between the electrode and the collection surface is needed not only to charge the particles, but also to set up an electric field in the space between the electrode and the neutral collection plate. The combination of an electrode and collection plate arrangement is referred to as a field. In a typical ESP design, there are multiple fields in series. The flue gas flow through each field is usually split in parallel chambers to allow for maintenance of one chamber at a time without shutdown of the other chamber.

The removal of a particle in an ESP is a three-step process as shown in **Fig. 2**. In the first step, the particles entering the space between the electrode and the collection plate collect ions generated at the high voltage electrode. There are two main mechanisms through which a particle acquires the charge: diffusion charging and field charging. Diffusion charging is a result of the collision of charges undergoing Brownian motion with the particle. Field charging is a result of charges being driven toward the particles by an electric field created between the electrode and the uncharged particles. Diffusion charging is known to be the dominant charging mechanism for small particles (<0.3 μm) while field charging is dominant in larger particles (>1 μm). Particles in the size range between 0.3 μm and 1 μm are subject to both mechanisms.

In the second step, a force is created by the electric field on the charged particle. This electrostatic force results in the particle accelerating towards the collection plate. As the particle accelerates and gains velocity, an opposing increasing drag force is generated on the particle. The two opposing forces rapidly balance out as the particle reaches its terminal velocity. This terminal velocity is also known as the migration velocity.

In the third step, the charged particle impacts the collection surface where it sticks and loses its charges. As more and more particles impact the collection surface with time, an ash layer is formed, causing the collection efficiency to decrease. For the ESP to perform as designed, the ash layer must be periodically removed from the collection plates.

There are a variety of ESP designs. Geometry is one feature that defines the type of ESP used. The two most common geometries are the rigid tube-and-plate design and the rigid tube-and-cylinder design. Another feature that defines the type of ESP is the number of stages in which the charging and removal processes are carried out. In a single-stage ESP, the charging of the particles and the collection take place in the same stage. In a two-stage ESP, the particles are charged in one stage and collected in another stage. Another feature that distinguishes one type of ESP from the other is the way in which ash build-up is removed from the collection plates. One type of ESP is known as dry ESP and the other type as wet ESP. A dry ESP or wet ESP is used depending on the application whereas wet ESPs are more commonly used to recover liquids. In dry ESPs, which are more commonly used, the removal of particles from the collection plates is carried out by means of mechanical rappers. The impact of the rappers on the collection plates results in vibrations that cause the deposit layer to fall off. In wet ESPs, a liquid (typically water) is sprayed on the collection plate to wash off deposits that build up.

The three design parameters often used to estimate the capture efficiency of an ESP are the particle migration velocity, the gas flow rate, and the collection area. The particle migration velocity is affected by the field strength, the particle size, the particle electric properties, and the viscosity of the gas. By setting a desired collection efficiency and using an estimate of the ash properties and the flue gas flow rate, the required collection area can be determined to size the ESP. A commonly used parameter in ESP design is the specific collection area, which is obtained by dividing the precipitator collection area by the flowrate.

The simplest equation that can be used to estimate the collection efficiency of an ESP is known as the Deutsch-Anderson equation (Eq. 1) [21,22]:

$$\text{Eff} = (1\text{-}e^{-\omega\left(\frac{A}{Q}\right)})\times 100 \quad (1)$$

where ω (m/sec) is the particle migration velocity, Q (m^3/sec) is the flue gas flow rate, and A (m^2) the effective collection area. The migration velocity, as explained earlier, is the velocity at which the electric force applied on the particle is in balance with the drag force. As such, it is expressed as Eq. 2:

$$\omega = \frac{n\, e\, E\, C_c}{3\pi\, \mu\, d_p} \quad (2)$$

where n is the number of charges acquired by the particle, e (C) is the elementary charge, E (V/m) is the electric field strength, C_c is the Cunningham slip correction factor, μ (Pa·s) is the viscosity of the gas, and d_p (m) is the particle diameter.

There are several approaches to determine the number of charges acquired by a particle [4], the simplest of which is using the constant charge model. This model assumes that particles instantaneously achieve their saturation charge as a result of field and diffusion charging, and the number of charges is given by Eq. 3:

$$n = \left[(1+\frac{2\lambda}{d_p})^2+\frac{2(\varepsilon-1)}{(1+\frac{2\lambda}{d_p})(\varepsilon+2)}\right]\pi\varepsilon_0 E d_p^2 \quad (3)$$

where λ (m) is the ionic mean free path of the gas, ε is the dielectric constant of the particle, and ε_0 (F/m) is the permittivity of air.

The Deutsch-Anderson equation is theoretical and derived from fundamental physical principles. It well describes the charging and collection of the particles. However, when applying it to estimate the collection efficiency of an ESP system, the equation is known to have several deficiencies that prevent it from accurately predicting the actual ESP efficiency. First, the equation can only be applied to particles of uniform size while in reality particles entering the ESP are known to have a nonuniform size distribution. Second, the equation does not consider the re-entrainment of particles after they have been collected. Finally, the equation takes into account the dielectric constant of the particles, but not the resistivity which is the most common factor considered when designing an ESP.

A deviation to the Deutsch-Anderson equation that is more commonly used for ESP design is the Matts-Öhnfeldt equation (Eq. 4) [23]:

$$\text{Eff} = (1\text{-}e^{-\omega_k\left(\frac{A}{Q}\right)^k})\times 100 \quad (4)$$

The Matts-Öhnfeldt equation takes a more practical approach to ESP design. As with the Deutsch-Anderson equation, Q represents the flue gas flow rate and A the effective collection area. The migration velocity ω_k uses the subscript to distinguish it from the calculated migration velocity in the Deutsch-Anderson equation. The dimensionless parameter k in the equation varies between 0.4 and 0.6 depending on the dust properties and standard deviation of the particle size distribution. The values for variables in this equation, mainly the migration velocity and the dimensionless k, are based on empirical values obtained from historical data of full installations, and they vary for different ESP manufacturers. The values are determined on the basis of fly ash resistivity and the application.

PROBLEMS IN ESP OPERATION

Despite the wide use of ESPs in recovery boiler operation, there are still problems in operation and maintenance that can affect the ESP efficiency. It is often difficult to fine-tune the ESP operation to respond to large changes in boiler operation, such as increased boiler firing loads, combustion air flowrate changes, and high solids firing. These changes result in changes in flue gas flow rate, temperature, moisture content, particle loading, composition, size, and size distribution. These changes in process conditions inevitably affect the ESP efficiency.

Under normal conditions, the collection efficiency of an ESP is typically >99.5%. This high collection efficiency means, however, that a slight decrease in efficiency can cause particulate emissions to increase several fold, as shown in **Fig. 3**. For example, a 1% decrease in efficiency from 99.5% (point A in Fig. 3) to 98.5% (point B in Fig. 3) results in three times as much particulate emissions. Such a large increase in particulate emissions can cause mills to be out of regulatory compliance. When this happens, mills must lower the black liquor firing load (and hence the pulp production capacity) to keep their particulate emissions under control.

For a given ESP, the collection area and the gap between plates are fixed. The only way to maintain the high efficiency without extensive ESP equipment modifications is to change either the ash cleaning frequency or TR controller settings. Therefore, it is important to consider potential future changes in boiler operation in the design and installation of the ESP.

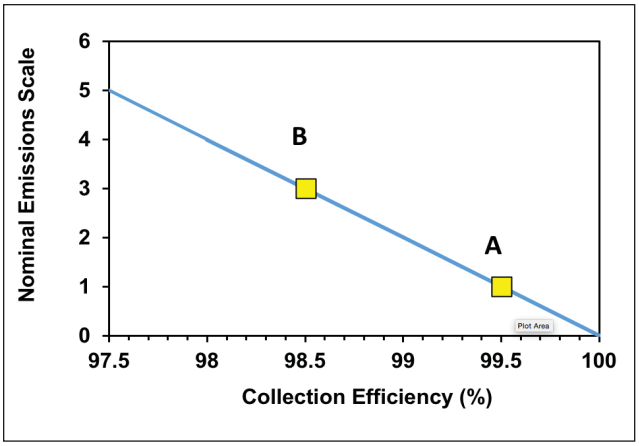
Another common problem in ESP operation is the heavy buildup of ash deposits on the collection plates and flue gas distribution media. This can lead to premature sparking, grounded electrical sections, and flue gas channeling caused by massive ash buildup. All of these can deteriorate ESP performance. Recovery boiler ESPs typically are designed with safeguards such as a larger than theoretically required collecting surface area to achieve emission compliance with one or more TR sets out of service or multiple ESP compartments (usually two), each of which can be isolated from gas flow, allowing safe personnel entry. Typically, each chamber is sized to handle 70% of the full rated gas flow to be able to maintain a high boiler load with flue gas passing through only one chamber while maintenance is performed on the adjacent chamber.

Although the previously mentioned measures are usually sufficient to help mills meet particulate emission requirements, a better understanding of key operating factors that affect ESP performance can help mills to maximize their boiler throughputs.

SENSITIVITY ANALYSIS

Using the Deutsch-Anderson equation (Eq. 1) and other equations needed to calculate its parameters (Eqs. 2 and 3), a sensitivity analysis was performed on a typical recovery boiler ESP to determine the effects of particle composition and flue gas temperature on the collection efficiency. The Deutsch-Anderson equation is used instead of the Matts-Öhnfeldt equation for several reasons, mainly because the purpose of this analysis is to study the collection efficiency without considering the effect of deposit formation or re-entrainment. Also, the Deutsch-Anderson equation does not require the use of any empirical values for the analysis.

A typical ESP requires the specific collection area of 200–600 ft² per 1000 ft³/min (or 656–1968 m² per 1000 m³/min) of flue gas. The voltage applied ranges from 55 to 70 kV, depending on the distance between the discharge electrode and the collection plate. The gap between the two adjacent plates is 6–12 in. (15–30 cm). The ash particle size varies between 0.3 μm and 0.6 μm. In this parametric analysis, the values used in the calculations are as follows: specific collection area (400 ft²/1000 ft³/min [1312 m²/1000 m³/min]), voltage (60 kV), plate spacing (12 in. [30 cm]), and particle size (0.01–10 μm).



3. Effect of ESP collection efficiency on particulate emissions.

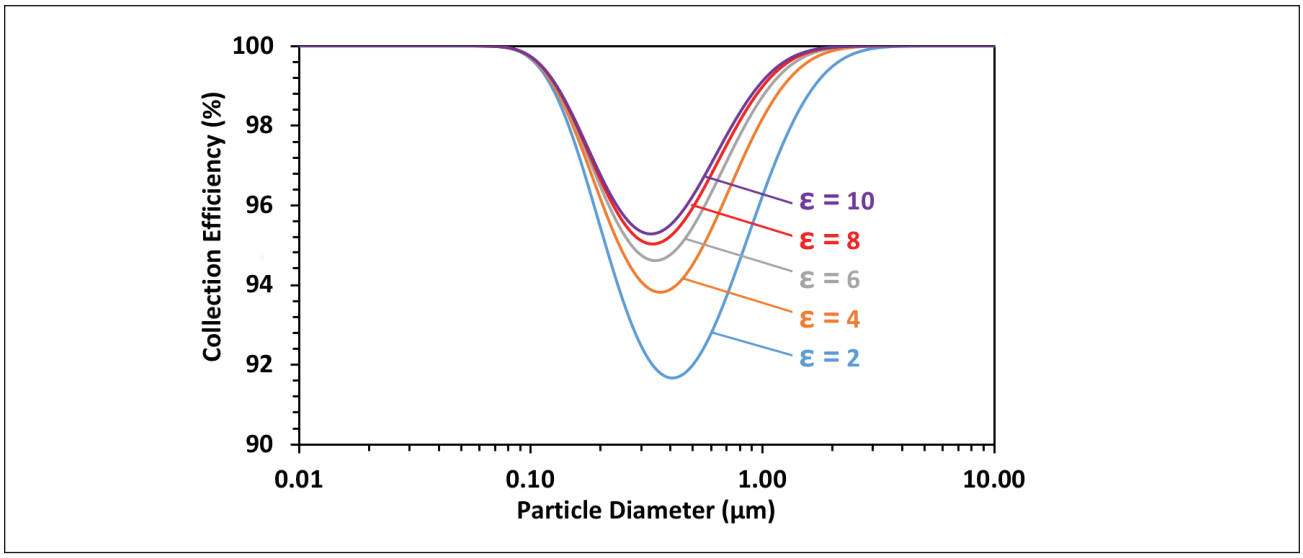
Compound	Dielectric Constant
Sodium sulfate (Na_2SO_4)	2.7
Sodium carbonate (Na_2CO_3)	8.4
Sodium chloride (NaCl)	3.2
Potassium sulfate (K_2SO_4)	5.9
Potassium carbonate (K_2CO_3)	5.6
Potassium chloride (KCl)	5.0

I. Dielectric constants for compounds found in recovery boiler ash.

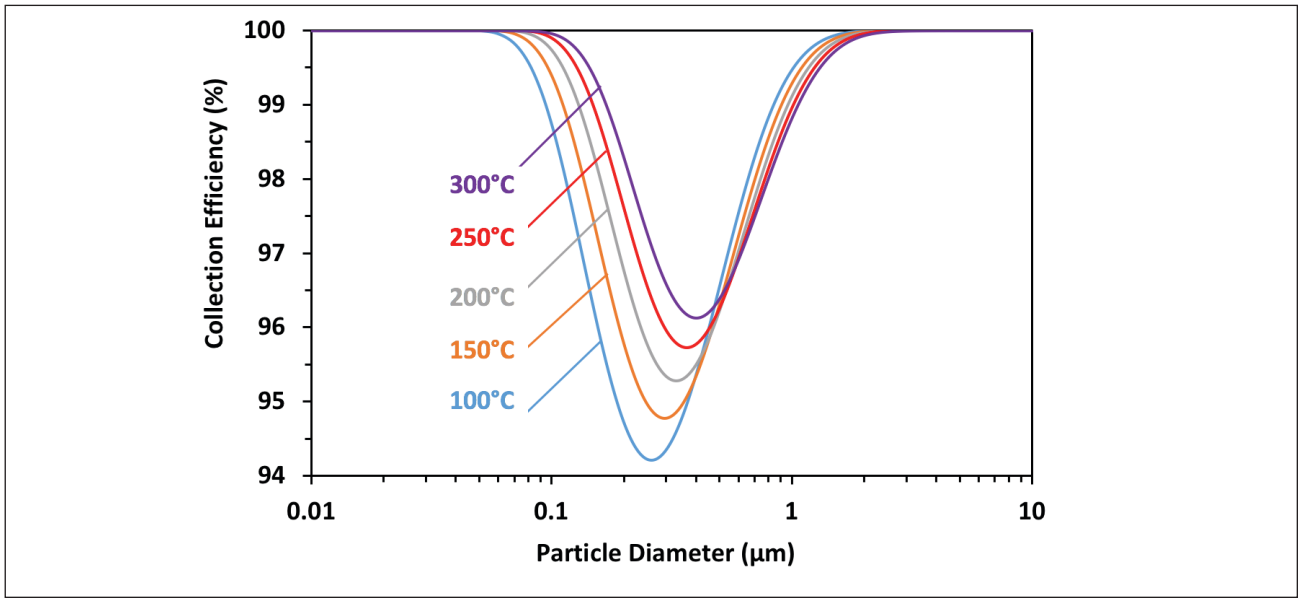
Effect of chemical composition

To determine the effect chemical composition has on the collection efficiency using the Deutsch-Anderson equation, information regarding the dielectric constant is needed. Recovery boiler ash is made up of a mixture of compounds whose dielectric constants are summarized in **Table I**. The dielectric constants for fly ash compounds vary between 2.7 and 8.4. The analysis is therefore done for a dielectric constant between 2 and 10 to cover this range, and the results are shown in **Fig. 4**.

The results show that the collection efficiency is lowest for particles around 0.4 μm. As particle size increases, the collection efficiency decreases for particles less than 0.4 μm, where it reaches a minimum and then increases beyond that point. This is consistent with the charging modes of particles explained earlier. Small particles are dominated by diffusion charging, while big particles are dominated by field charging. The particles in the middle range, even though subject to



4. Effect of the particle dielectric constant ε on calculated ESP collection efficiency.

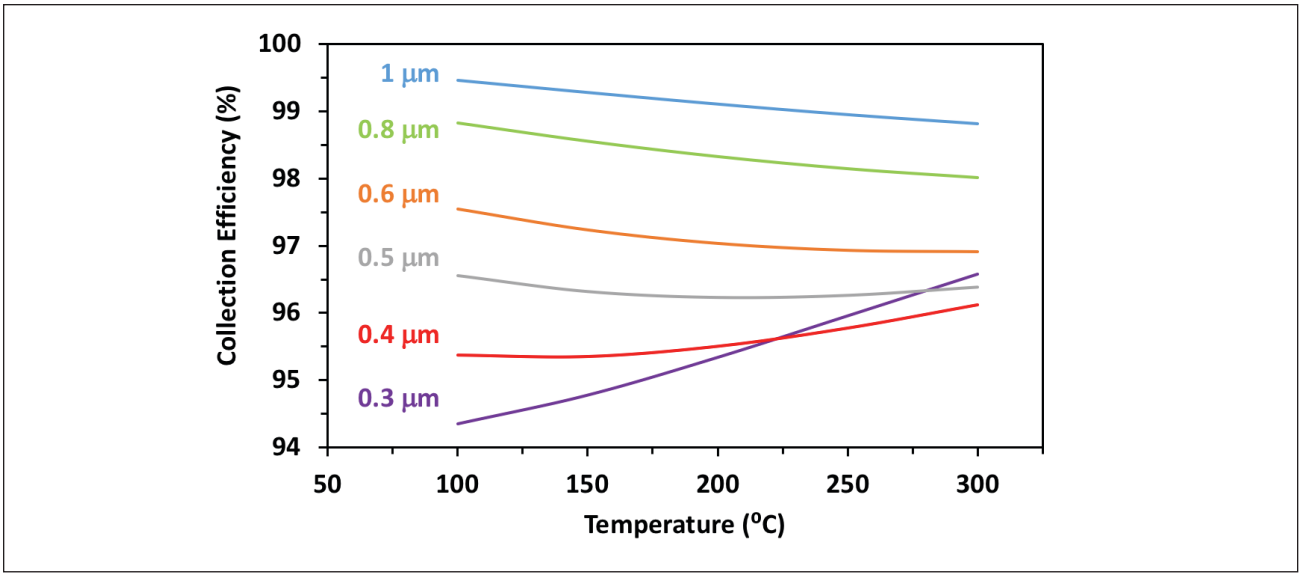


5. Effect of temperature on ESP collection efficiency.

both modes, carry the least charges and therefore are harder to collect.

The Deutsch-Anderson equation predicts that for an increase in dielectric constant, the collection efficiency increases for all particle sizes. A higher dielectric constant means that particles can carry a higher charge leading to a higher migration velocity and ultimately to a higher capture efficiency. This implies that Na_2SO_4, which has a dielectric constant of 2.7, is harder to capture than NaCl, which has a dielectric constant of 3.2. The graph also shows that for the same increase in dielectric value, the difference in collection efficiency is higher for smaller values of the dielectric constant.

The prediction, however, is not consistent with actual experience where ash with a higher NaCl content tends to be more difficult to capture. The discrepancy between the Deutsch-Anderson equation prediction and the actual experience can be attributed to a combination of two distinct factors: Particle composition, and particle size. In the model used previously, the particles are assumed to be pure compounds to determine the extreme scenarios. In reality, recovery boiler ash is mostly made up of Na_2SO_4, and the difference between high chloride content and low chloride content is around 10% by mass. Because of that assumption, the variations in efficiency presented in Fig. 4 as a result of change in dielectric constants are inflated and smaller variation would be expected for the same particle sizes in reality. With that in



6. Effect of temperature on ESP collection efficiency for different particle sizes.

mind, particle size explains why ash with high chloride content exhibits lower collection. Ash with high chloride content typically has smaller particle sizes than ash with low chloride content [24]. That particle size difference is the main cause of the observed decrease in collection efficiency.

An explanation for the discrepancy can be attributed to the fact that NaCl has higher resistivity than Na_2CO_3 and Na_2SO_4 [19,25]. When high chloride ash deposits on the collection plate, its higher resistivity prevents it from losing its charge and being removed, thus causing a reduction in the voltage difference between the high voltage electrode and the plate. The decrease in voltage difference translates into a lower electric field. This, in turn, results in particles carrying lower charge, lower electric force, and eventually lower collection efficiency, as previously explained. Thus, the particle dielectric constant alone may not be enough to determine how the composition of the fly ash affects the collection efficiency.

Effect of temperature

Using the Deutsch-Anderson equation, the collection efficiency for different particle sizes at different temperatures was calculated as shown in **Fig. 5**.

The calculation results also show a shift in the size of particles that have the lowest collection efficiency. At 100°C, 0.25 µm particles have the lowest efficiency, while at 300°C, 0.4 µm particles have the lowest efficiency. For particles between 0.1 µm and 0.4 µm, increasing the gas temperature from 100°C and 300°C can result in an increase of up to 4% in efficiency. However, for particles larger than 0.6 µm, increasing the gas temperature decreases the collection efficiency, but only by about 1%. This change in behavior takes place in the particle size range between 0.3 µm and 0.6 µm. In **Fig. 6**, the effect of the temperature between 100°C and 300°C is shown for different particle sizes according to the Deutsch-Anderson equation. Particles smaller than 0.5 µm show an increase in collection efficiency with increasing temperature, whereas particles 0.6 µm and larger show a decrease in collection efficiency with increasing temperature. Particles around 0.5 µm show a nonuniform trend. The collection efficiency for 0.5 µm particles shows a minimum around 200°C. Before that point, the collection efficiency decreases slightly with increasing temperature, and changes trend after. From field experience, increasing temperature is known to reduce ESP performance, which is consistent with the prediction for a given particle size.

Effect of particle concentration

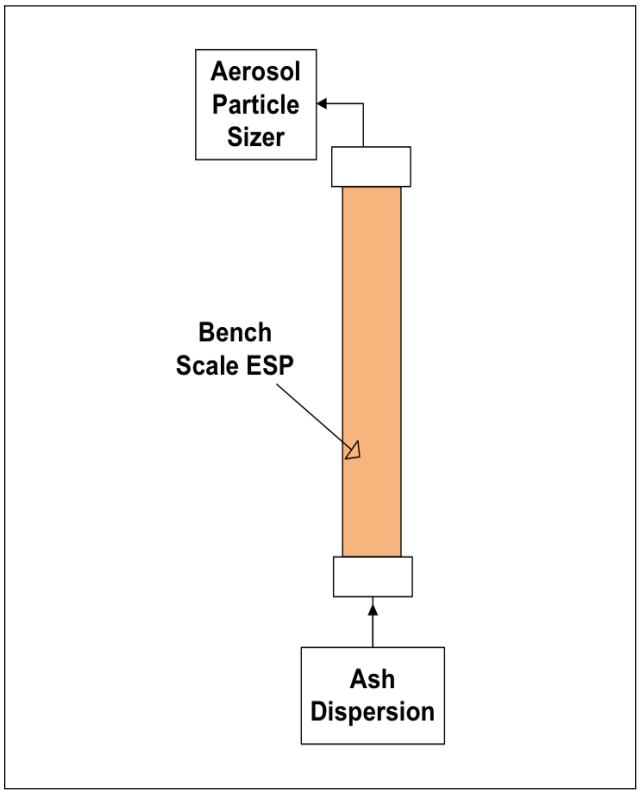
When taking into consideration all the variables used in the Deutsch-Anderson equation to determine collection efficiency, the particle concentration or loading in the flue gas does not alter any terms of Eq. 1 or complementary equations (Eqs. 2 and 3). On that basis, the Deutsch-Anderson equation predicts that particle concentration does not affect the collection efficiency. Similarly, the Matts-Öhnfeldt equation predicts that the particle concentration does not affect the collection efficiency. The only result of increasing particulate concentrations at the inlet is an increase by an equal fraction at the exit of the ESP. There have been previous studies that have considered the effect of particle concentration on the collection efficiency using numerical simulations; however, the predictions obtained were contradictory from one study to another. One study found that the collection efficiency decreases with increasing particle concentration [26], whereas another study found that an increase in particle concentration results in a slight increase in efficiency [27]. The ideal way to investigate the effect of particle concentration on collection efficiency would be through controlled laboratory experiments.

BENCH-SCALE ESP

While the temperature results from the sensitivity analysis performed agree with the common knowledge of ESP performance, other results regarding other factors in the analysis differed. The prediction of the Deutch-Anderson equation regarding the effect of ash composition contradicts experience, and the effect of ash loading also contradicted predictions by other mathematical models. To further explore the effect of the parameters discussed in the previous section, an experimental setup was designed and built in our laboratory at the University of Toronto. As shown in **Fig. 7**, the setup consists of three parts. The first part is an ash dispersion system that uses compressed air to disperse a recovery boiler precipitator ash sample into a cloud of dust particles. The second part is the bench-scale ESP, and the third part is an aerosol particle sizer (APS) that is used to count the number of particles in the gas stream.

The ash dispersion system, shown in detail in **Fig. 8**, uses a shaker to agitate a container that houses a precipitator ash sample collected from a recovery boiler. Compressed air is injected into the container near the sample surface to disperse the ash into a fine particle cloud. This ash cloud is then directed to the bench-scale ESP. Hot filtered air is used to dilute the sample and heat it to the desired temperature before entering the bench-scale ESP. The two control valves at the compressed air inlet and dilution air inlet are used to control total flow rate and dilution.

The detailed design of the bench-scale ESP is shown in **Fig. 9**. It consists of a 2-in. (5-cm) inside diameter by 1-in. (30-cm) long copper cylinder, a copper wire, Teflon caps, and a variable high-voltage power supply. The copper wire runs parallel to the copper cylinder at its center and is connected to the high-voltage supply. The copper cylinder acts as the collection plate of the bench-scale ESP and the copper wire acts as the discharge electrode. Teflon caps are used to enclose the ESP, isolate the copper wire from the copper cylinder, and allow for the sample to flow in from the ash dispersion system and out to the APS.



7. Components of setup for laboratory experiments.

The APS at the exit of the bench-scale ESP is an instrument typically used for ambient air particulate concentration measurements. It provides total particle number count as well as particle size distribution every second for particles in the size range between 0.3 μm and 20 μm.

To determine the collection efficiency at a certain voltage, the particle concentrations measurements are done with the voltage switched off and then with the voltage switched on. The recorded concentrations are then used to calculate the collection efficiency. The copper cylinder is cleaned frequently to prevent any ash buildup that could affect the performance.

To test the performance of the bench-scale ESP and ensure its performance is consistent with theory, experiments are run at different voltages. A curve fit is applied to the data obtained to test how well the data correlate with the theory. The form of the curve fit applied is shown in Eq. 5:

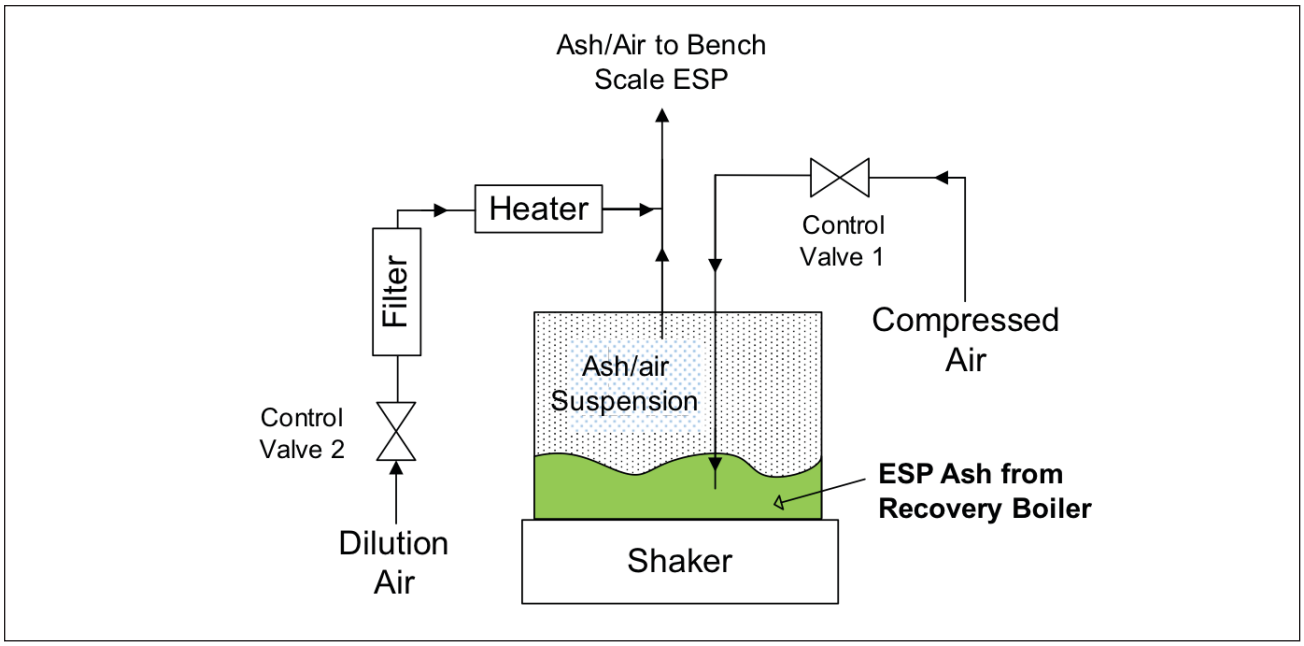
$$\text{Eff} = [1 - c_1 \exp(-c_2 * \text{voltage}^2)] \times 100 \quad (5)$$

The form used for the curve fit is obtained when the Deutsch-Anderson equation is rearranged to separate voltage as the only variable and take into consideration the fact that ash particles in the sample do not have a uniform size. The results are shown in **Fig. 10**. The experimental data correlate well with the curve fit. This indicates that the performance of the bench-scale ESP is consistent with that described by the Deutsch-Anderson equation.

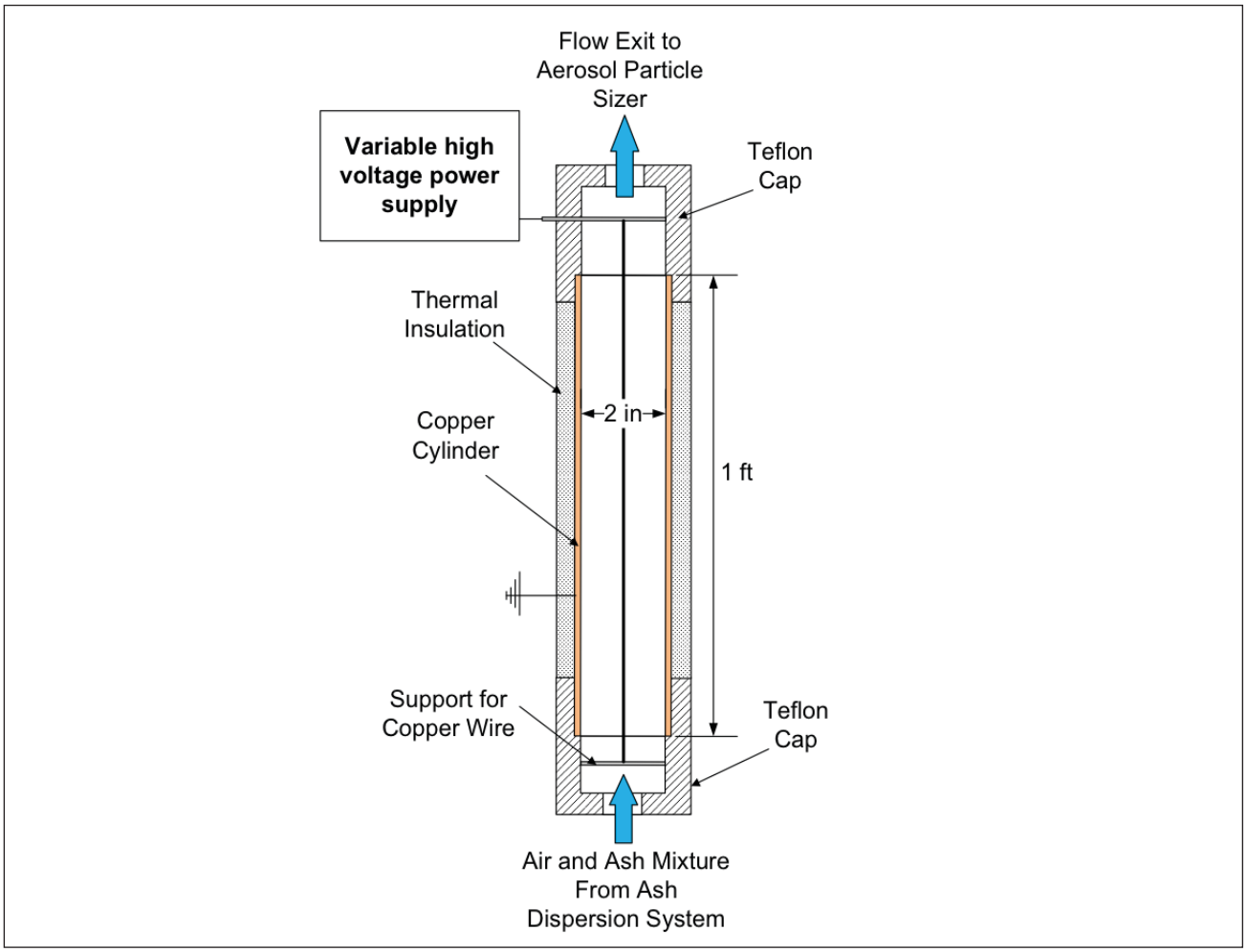
These results show that bench-scale ESP can be used as a reliable experimental setup. The next steps are to use the setup to test the effect of various parameters on collection efficiency. These include the parameters considered in the sensitivity analysis (composition, temperature, and concentration), as well as other potential factors such as applied voltage, moisture content, and sulfur dioxide content.

SUMMARY

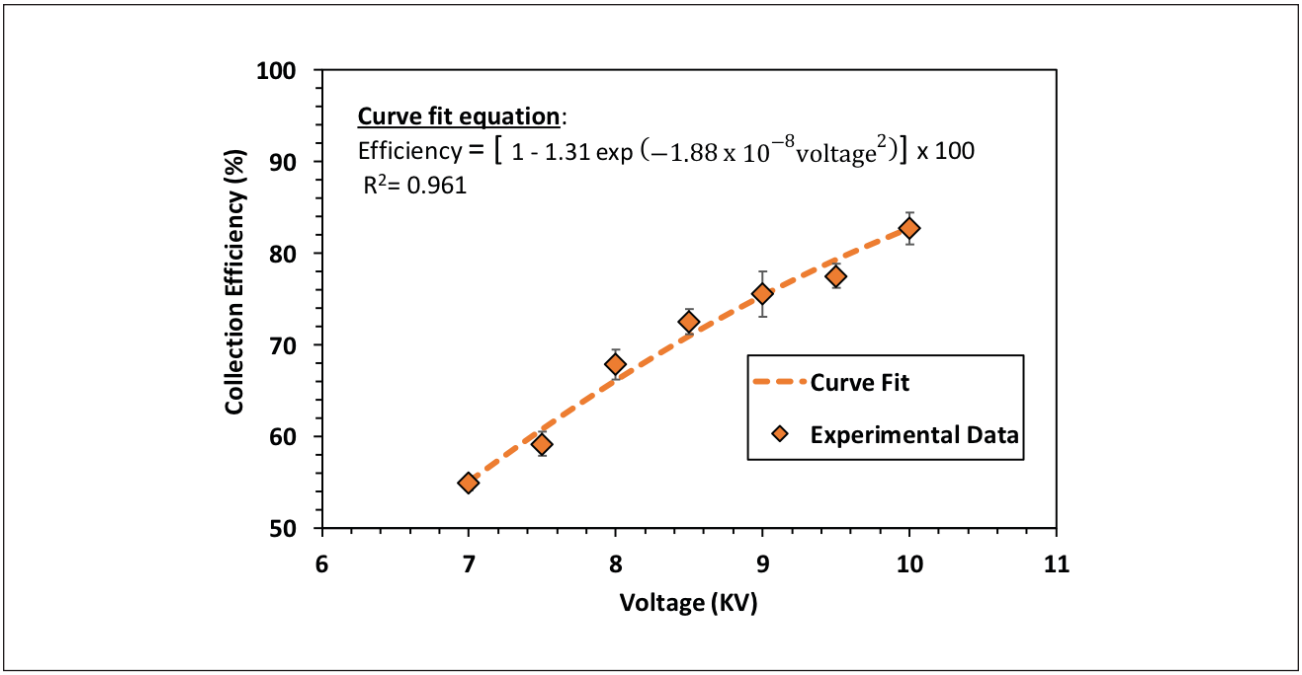
This work involved a literature review of the ESP technology used in industrial combustion units, including recovery boilers, and a parametric study using the Deutsch-Anderson equation to correlate recovery boiler operating conditions with ESP collection efficiency. The results suggest that up to about 0.3 μm, the ESP collection efficiency decreases drastically with increased particle size and with decreased temperature. For



8. Details of ash dispersion system.



9. Detailed design of bench-scale ESP.



10. Experimental data and curve fit of bench-scale ESP.

particles larger than 0.5 µm, however, the trend reverses; the collection efficiency increases with increased particle size and decreased temperature.

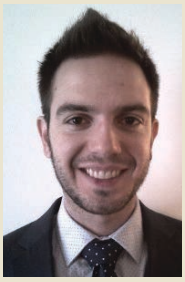
Particle concentration (or loading) in the flue gas in theory should have little effect on the collection efficiency; however, no experimental evidence exists to support that. Sodium chloride particles in the flue gas are more readily captured than Na_2SO_4 particles. This, however, appears to contradict mill experience that NaCl particles are more difficult to capture. A bench-scale experimental apparatus is being built to further investigate the effects of particle composition concentration and various ESP operating conditions on ESP collection efficiency. **TJ**

LITERATURE CITED

1. White, H.J., *Industrial Electrostatic Precipitation*, Addison-Wesley, Reading, MA, USA, 1965.
2. White, H.J., *J. Air Pollut. Control Assoc.* 7(3): 166(1957).
3. Arif, S., Branken, D.J., Everson, R.C., et al., *J. Electrost.* 84: 10(2016).
4. Long, Z. and Yao, Q., *J. Aerosol Sci.* 41(7): 702(2010).
5. Skodras, G., Kaldis, S.P., Sofialidis, D., et al., *Fuel Process. Technol.* 87(7): 623(2006).
6. Ning, Z., Podlinski, J., Shen, X., et al., *J. Electrost.* 80: 76(2016).
7. Haque, S.M.E., Rasul, M.G., Deev, A.V., et al., *Appl. Therm. Eng.* 29(10): 2037(2009).
8. Varonos, A.A., Anagnostopoulos, J.S., and Bergeles, G.C., *J. Electrost.* 55(2): 111(2002).
9. McCain, J.D., Gooch, J.P., Smith, W.B., *J. Air Pollut. Control Assoc.* 25(2): 117(1975).
10. Jedrusik, M., Jedrusik, J., and Sarna, M., "Industrial Scale study of a retrofitted electrostatic precipitator," *Proc. Int. Conf. Electrost. Precip., 7th*, International Society for Electrostatic Precipitation, Atlanta, 1998.
11. Lind, T., Hokkinen, J., Jokiniemi, J.K., et al., *J. Environ. Sci. Technol.* 40(2): 584(2006).
12. Noda, N. and Makino, H. *Adv. Powder Technol.* 21(4): 495(2010).
13. Jedrusik, M. and Świerczok, A. in *Air Pollution—Monitoring, Modelling, Health and Control* (D.M. Khare, Ed.), InTech, London, 2012, pp. 197–220.
14. Nouri, H., Zouzou, N., Dascalescu, L., et al., *Process Saf. Environ. Prot.* 104: 225(2016).
15. Adamiak, K., *IEEE Trans. Ind. Appl.* 38(4): 1001(2002).
16. Yu, D., Castle, G.S.P., and Adamiak, K., *IEEE Trans. Ind. Appl.* 46(3): 1159(2010).
17. Tomei, G.L., *Steam: Its Generation and Use*, 42nd edn., Babcock & Wilcox, Charlotte, NC, USA, 2015, pp. 32–38.
18. Nichols, G.B., *IEEE Trans. Ind. Appl.* IA–13(1): 74(1977).
19. Sretenovic, I., Farkhondehkavaki, M., Kortschot, M., et al., *TAPPI J.* 13(7): 31(2014).
20. Tran, H.N., *Tappi J.* 82(1): 212(1999).
21. Deutsch, W., *Ann. Phys. (Berlin, Ger.)* 373(12): 335(1922).
22. Anderson, E., *Chem. Metall. Eng.* 26: 151(1922).
23. Matts, S. and Öhnfeldt, P.-O., *Flakten Rev.* 6–7: 105(1964).
24. Duhamel, M., Tran, H., and Frederick, W.J. Jr., *TAPPI J.* 3(10): 25(2004).
25. Samuelsson, I.L., "Effect of salt cake properties on precipitator performance," *Prepr.—PAPTAC Annu. Meet., 86th*, Pulp and Paper Technical Association of Canada, Montreal, 2000.
26. Al-Hamouz, Z., *Energy Convers. Manage.* 79: 487(2014).
27. Xu, X., Gao, X., Yan, P., et al., *Sep. Purif. Technol.* 143: 184(2015).

ABOUT THE AUTHORS


Jaroudi


Sretenovic


Evans


Tran

We chose this topic to research because little work has been done to date on the effect of ash properties on recovery boiler electrostatic precipitator (ESP) performance. This is complementary to previous research that measured the recovery boiler ash resistivity and speculated how it might affect ESP efficiency.

The current research investigated theoretically and experimentally how various ash properties might affect the efficiency.

The most difficult aspect of this research was to build a bench-scale ESP that could simulate a full-scale ESP. We addressed it by conducting an extended literature review and consulting with ESP experts. We discovered that it is possible to predict the effects of various ash properties and operating conditions on ESP performance using a simple equation. The findings were not surprising as most were expected.

This information can help mills identify the main causes of their high-particulate emission problems. Our next step is to conduct experiments using the bench-scale ESP under controlled conditions to determine the effects of flue gas conditions and fly ash properties.

Jaroudi is a graduate student, Evans is a professor, and Tran is Frank Dottori Professor of Pulp and Paper Engineering in the Department of Chemical Engineering and Applied Chemistry, University of Toronto, Toronto, ON, Canada. Sretenovic is product manager-ESP, Air Pollution Control Product Division, Clyde Bergemann Power Group Americas Inc., Hanover, MD, USA. Email Tran at honghi.tran@utoronto.ca.

ABOUT THIS PAPER

Cite this article as: Jaroudi, E., Sretenovic, I., Evans, G., Tran, H. *TAPPI J.* 17(5):273(2018). https://doi.org/10.32964/TJ17.05.273

DOI: https://doi.org/10.32964/TJ17.05.273

ISSN: 0734-1415

Publisher: TAPPI Press

Copyright: © TAPPI Press 2018

About this journal

Effect of ring formation on burner flame stability in lime kilns

GIRISH MOHANAN, HONGHI TRAN, MARKUS BUSSMANN, AND RICHARD MANNING

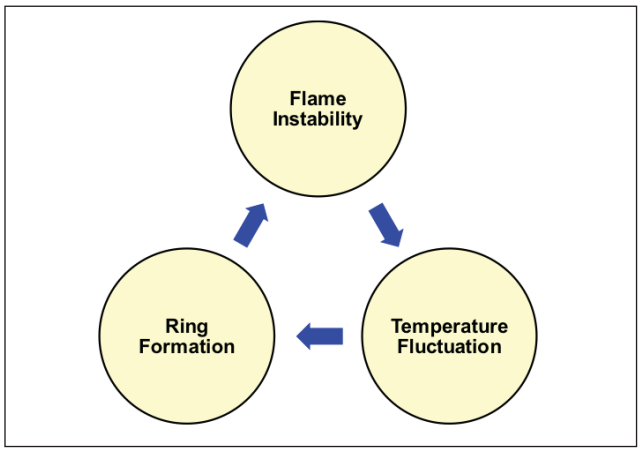
ABSTRACT: Ring formation in lime kilns is a common problem in pulp mills. Unstable burner operation that causes wide temperature variations within the kiln has been shown to be a main contributor. As rings grow thicker and longer, they are expected to affect the burner flame pattern, alter the temperature distribution, and further aggravate the problem. This study systematically examines the effect of rings on burner operation as a function of primary air and ring characteristics, using a laboratory mock kiln. The results show that primary air greatly affects the burner flame pattern and stability. Without a ring, the flame is brighter and shorter, with an increase in primary air (PA) up to 17%, and blows out at 20% PA or higher. In the presence of a ring, the flame becomes unstable and blows out when the ring is placed near the burner, but it is more stable when the ring is placed away from the burner. Thick and long rings destabilize the flame more than thin and short rings.

Application: Pulp mill engineers may use the information in this study to help stabilize the lime kiln burner flame.

Ring formation in lime kilns is a persistent problem in many pulp mills, limiting the kiln production capacity, and in severe cases, resulting in unscheduled kiln shutdown for ring removal. As lime mud/lime solids slide and tumble through the kiln, they cover the refractory brick surface with a layer of dust. The deposited dust layer grows thicker with time and has a cross-section that resembles a ring. It has been postulated that in order for rings to form, particles must first adhere to the refractory surface to form deposits. The deposits must subsequently become hard to withstand the abrasiveness of the sliding and tumbling motion of the solids bed [1,2].

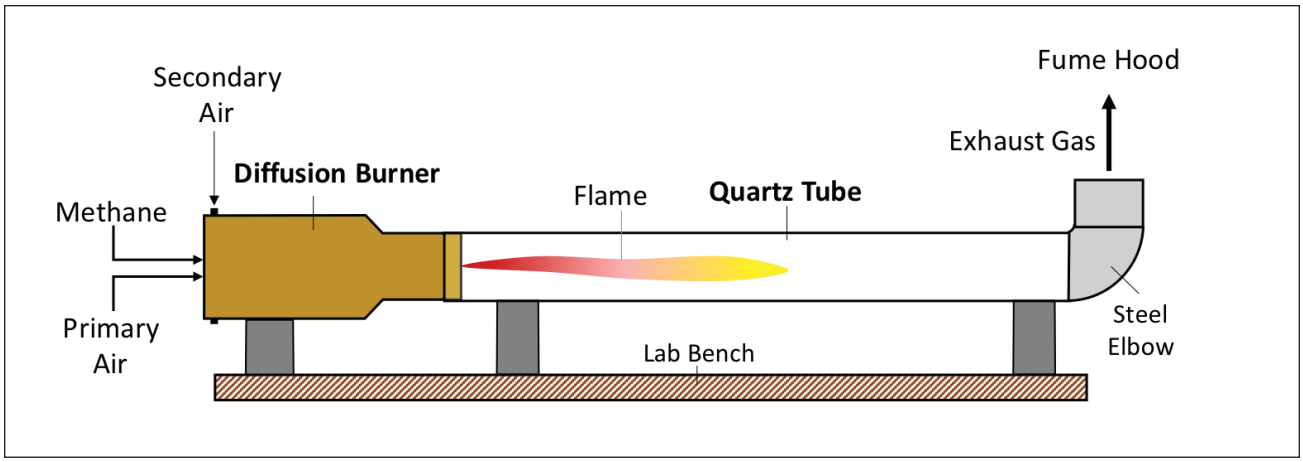
There are three distinct types of rings that are commonly observed. *Mud rings* typically form right after the chain section, due mainly to the high moisture and sodium contents of the lime mud. Mud rings are usually soft, but they can grow rapidly, completely blocking the kiln in a few hours. *Mid-kiln rings* form in the calcination zone, starting from the middle of the kiln to about 20 m (66 ft) from the kiln front end. The main hardening mechanism of mid-kiln rings is believed to be "recarbonation", the reaction between the lime (CaO) particles deposited on the refractory surface and carbon dioxide (CO_2) in the kiln gas that occurs when the temperature of the particles drops below 750°C (1382°F) [2]. *Front-end rings* typically form near the kiln burner, particularly when the temperature in this area is excessively high, causing the deposited lime on the refractory brick surface to rapidly sinter. For kilns that burn high sulfur-containing fuels such as crude oil, non-condensable gases, petroleum coke, etc., the ringing problem can be further aggravated due to the formation of hard calcium sulfate ($CaSO_4$) deposits [3].

Of these types of rings, mid-kiln rings are the most common and also the most difficult type to tackle, due primarily to their inaccessibility from the outside during operation. Stabilizing kiln operation (particularly the burner flame) is key to minimizing temperature fluctuations, recarbonation, and hence ring formation.

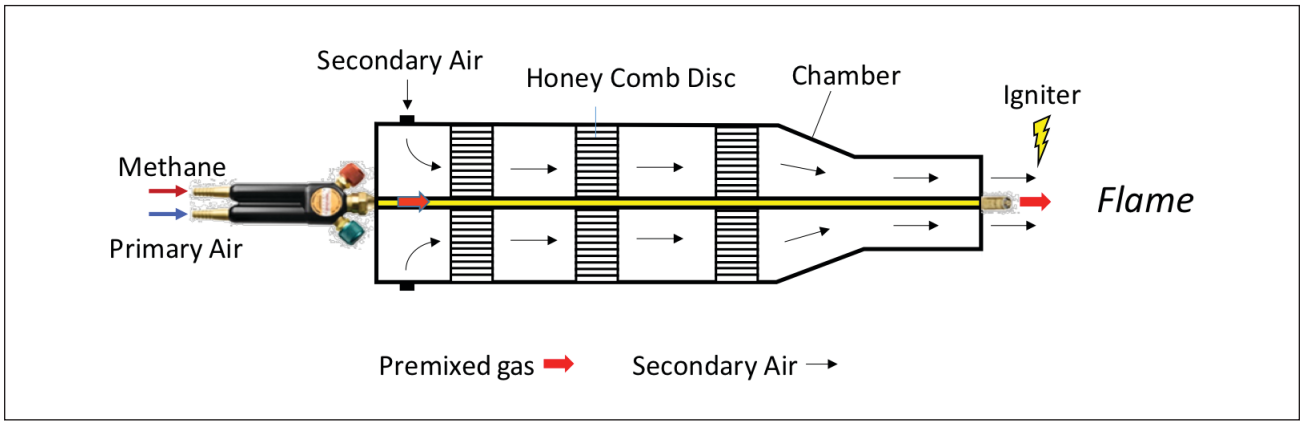


1. Vicious cycle of flame instability, temperature fluctuation, and ring formation.

Since the burner is the main (in most cases, the only) source of heat supplied to the kiln, any disturbance in the burner flame can quickly change the temperature profile further down the kiln [4]. Depending on where they are formed in the kiln, rings may obstruct the gas flow, affecting the flame pattern as they grow larger and longer along the kiln. This means that an unstable burner flame could result in wide gas temperature fluctuations and cause rings to form. Once formed, however, rings could further alter the burner flame pattern, causing more temperature fluctuations and more rings to form. The vicious cycle of flame instability → temperature fluctuation → ring formation → flame instability is conceptually shown **Fig. 1**. Understanding how ring formation destabilizes the burner flame and alters the temperature



2. Experimental setup.



3. Miniature diffusion burner assembly.

profile in the kiln may help mills develop viable strategies to "break up" the cycle and minimize ring growth.

The objective of this study is to systematically investigate how ring formation affects the flame pattern and stability. In this paper, we will first describe the experimental setup and procedures used in the study, and then discuss the results obtained and the practical implications of the results.

EXPERIMENTAL SETUP AND PROCEDURES

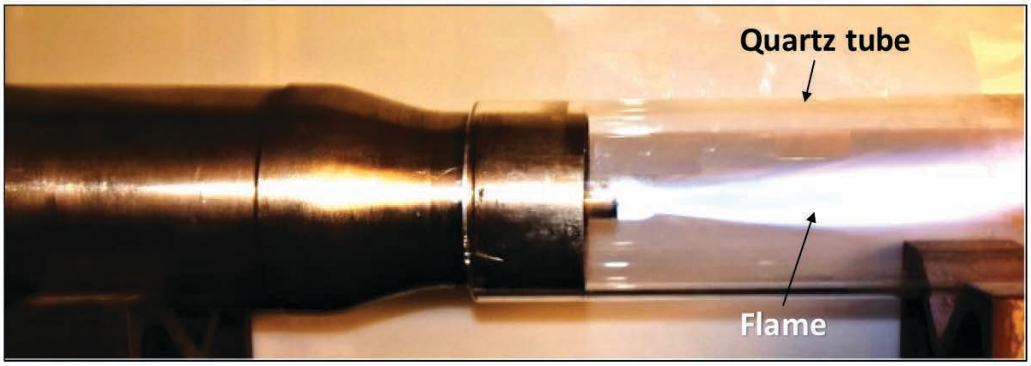
Figure 2 shows the setup for a mock kiln used in this study. It consists of a miniature diffusion gas burner, a quartz glass tube, and an exhaust gas system. The entire assembly, 2.15 m (7 ft) long, is laid horizontally on three supporting bricks on a laboratory bench.

The miniature diffusion burner simulates actual burners used in lime kilns, although methane is used as fuel instead of natural gas. As shown in **Fig. 3**, the burner consists of a methane and primary air (PA) pre-mixed burner embedded concentrically in a chamber that mimics an actual kiln hood. Secondary air (SA) from a compressed air cylinder (not shown here) enters the chamber and passes through a series of 3 honeycomb flow straighteners. As it emerges from the chamber, the secondary air diffuses into the methane/PA mixture. The combustion is subsequently initiated using an electric igniter.

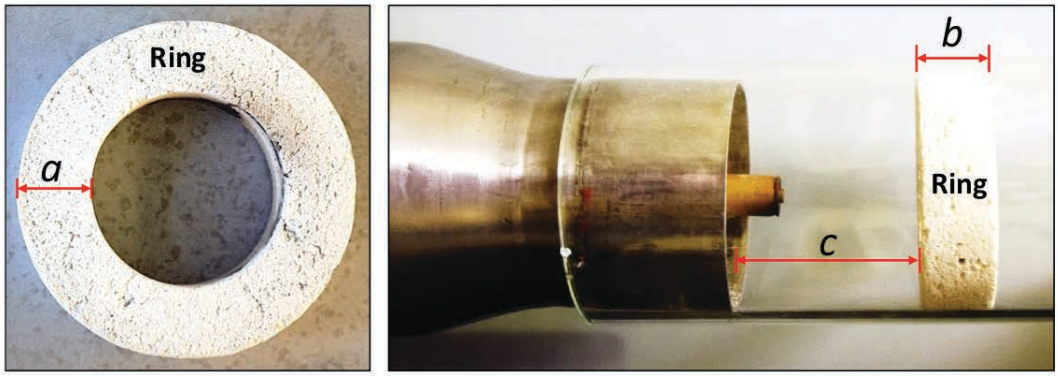
The quartz tube, 89 mm (3.5 ft) inner diameter (ID) x 1.83 m (6 ft) long, is connected to the diffusion burner at one end and the exhaust system at the other end. Quartz glass is used not only because it can withstand high temperatures, but also because it allows the burner flame inside to be visualized and documented with a high-resolution video camera (**Fig. 4**). The exhaust gas system is made of a simple 90° steel elbow connected to the quartz tube to direct the combustion gas to a laboratory fume hood located directly above. The exhaust gas can be readily purged from the system due to the high gas pressure in the mock kiln and the negative draft pulled by the fume hood.

The ring formation is simulated by placing a refractory cylinder in the quartz tube. The "ring" (the refractory cylinder) is carved from a piece of refractory brick and placed at various positions in the quartz tube by sliding it along the tube wall. The ring thickness, length, and position are defined as shown in **Fig. 5**.

The problem with this setup is that because the ring is made of refractory brick, it blocks the view of the burner flame. The setup is good only for short rings since the burner



4. Burner flame clearly visible through the quartz glass tube.



5. a=Ring thickness, b=Ring Length and c= Ring position

flame is still visible. For long rings, however, the setup does not work well, as the burner flame cannot be seen once it goes inside the ring. In order to make the burner flame visible inside the ring, the long ring is made by inserting both ends of a smaller quartz tube concentrically into two short refractory cylinders, as shown in **Fig. 6a**. While the approach is not perfect, it does provide reasonably good insights on how a long ring may affect the burner flame (Fig. 6b).

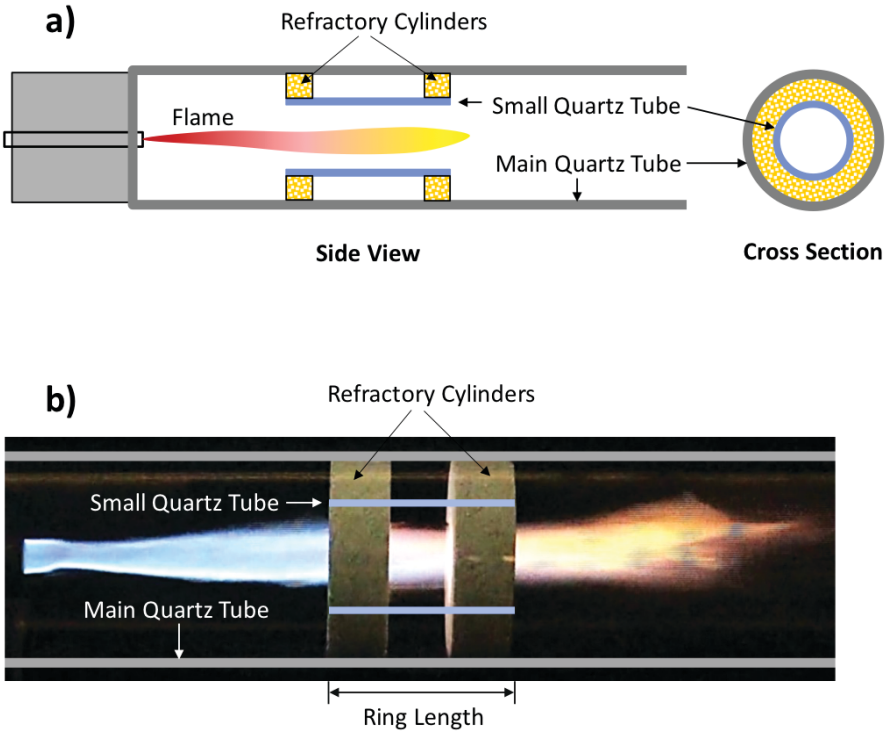
In this study, methane was supplied through the fuel port of the premix burner at a flow rate of 6 liters per minute (L/min). The PA was fed to the burner through the air port of the premix burner at a flow rate varying between 10% and 25% of the total air. The SA was added into the air chamber through two opposing air ports. Both PA and SA flow rates were automatically controlled by means of two separate mass flow controllers. The methane flow rate was monitored and manually controlled using a rotameter.

The total air was the sum of the stoichiometrically required air and excess air (EA). Numerous trial runs showed that the optimum EA required for a stable burner flame operation of the mock kiln was about 10%. Depending on the goal of a specific test, the primary air was changed while keeping the total air constant at 10% EA. In other words, for tests where the primary air was increased (or decreased), the secondary air was automatically decreased (or increased) by the same amount so that the total air was the same, and the system was maintained at 10% EA. The three main ring characteristics examined were position, thickness, and length.

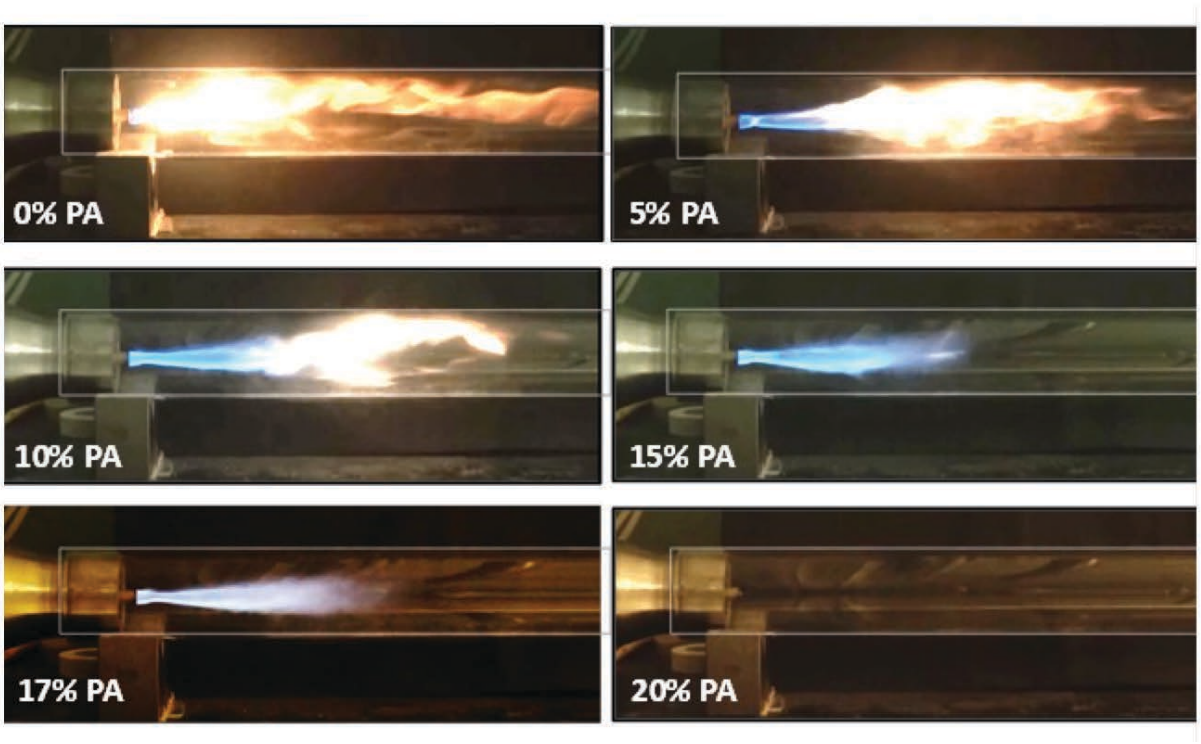
RESULTS AND DISCUSSION

Effect of primary air

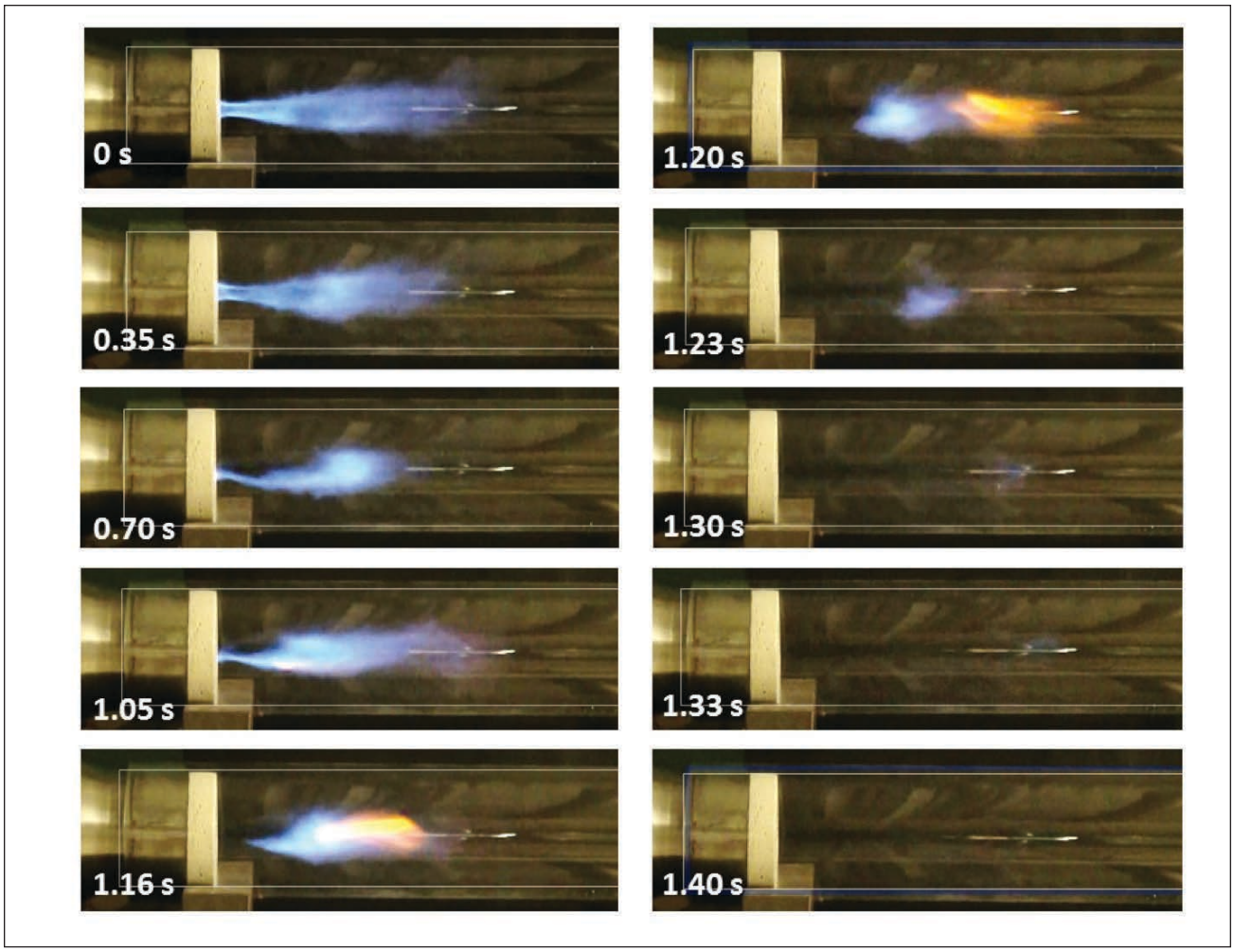
Figure 7 shows the change in appearance of the burner flame with increasing primary air (expressed as % of total air) while burning 6 L/min of methane with 10% EA in the absence of a ring. At 0% PA (no primary air), the flame was yellow and long and appeared to be "lazy". As the primary air was increased to 17% PA, the flame became increasingly brighter, shorter, bushier, and more intense. It eventually blew out at 20% PA. Tests were also carried out at 22% and 25% PA, and blowout occurred in both cases. This change in flame pattern with increased primary air resembles that of a Bunsen burner (or a propane welding torch) when more air is added to it, and it is consistent with that observed in a previous study using a pilot scale kiln [5] and that described by Adams [6].



6. Experimental setup for investigating the effect of a long ring on burner flame pattern: a) setup schematic, and b) image of a burner flame passing through the ring.



7. Change in burner flame pattern with increasing primary air (methane flowrate = 6 L/min; excess air [EA] = 10%). Note: No flame (or blowout) at 20% primary air (PA) and higher.



8. Photos of a burner flame when a 2 cm-thick, 2.5 cm-long ring was placed right in front of the burner (methane flowrate = 6 L/m, 15% PA, 10% EA). Note that blowout occurred in less than 1.3 s.

Effect of ring position

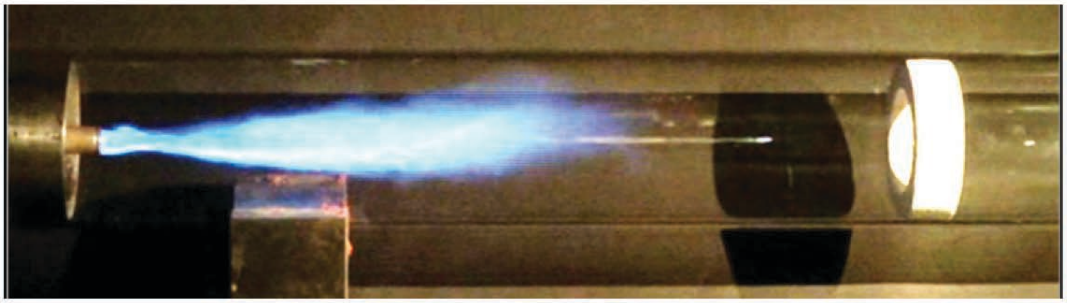
Figure 8 shows how the burner flame, produced by burning 6 L/min methane at 15% PA and 10% EA, changed when a 2 cm thick, 2.5 cm long ring was placed in front of the burner. The flame immediately broke away from the burner tip and blew out in less than 1.3 s. The blowout was likely caused by the sudden blockage of the secondary air by the ring, which literally starved off the burner flame.

Under the same burning condition (6 L/min methane, 15% PA, and 10% EA), the flame was stable with no blowout when there was no ring (Fig. 7) or when the very same ring was placed at 50 cm away from the burner (**Fig. 9**).

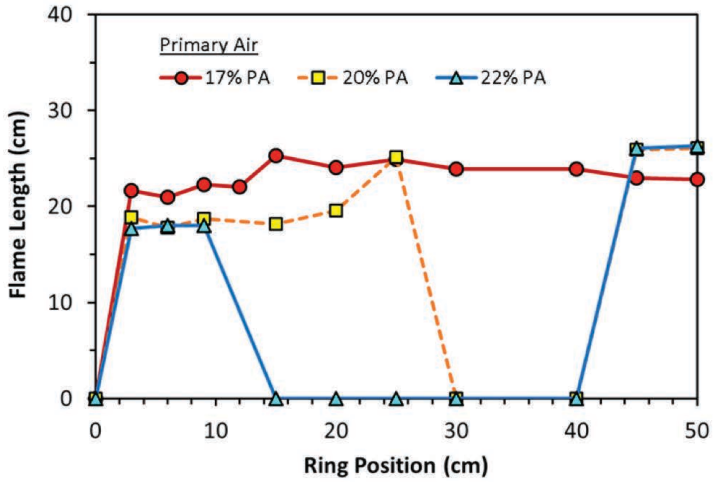
Figure 10 summarizes results of a series of tests in which the effect of ring position on the burner flame was examined at different primary air flow rates between 17% and 22% PA. During each test, the burner flame was videoed for 60 s after it had stabilized. The video was divided into six 10 s-long clips; each clip contained 360 frames or images. The frames were then analyzed using an open image processing software, ImageJ, to determine the flame length. Since each data point shown in this figure was derived from 2160 frames, the error was small, about ±2.5% with a confidence of 95%.

In all cases, the flame length was zero (i.e., no flame or flame blowout) when the ring was placed right at the burner tip. At 17% PA, the flame was consistently 22 to 25 cm long when the ring was farther than 3 cm from the burner, suggesting that under such test conditions, ring position had no impact on flame stability. At 20% PA, the flame was somewhat shorter and stable when the ring was placed at 3 to 30 cm from the burner. It was less stable and blew out when the ring was placed at 30 to 40 cm, but became stable again when the ring was placed at 45 cm or farther from the burner. Similar results were obtained at 22% PA, except that in this case, the ring position where the flame blew out was only 15 to 40 cm to the burner—much closer than that at 20% PA.

Note from Fig. 7 that at 20% PA and higher, the flame blew out when there was no ring in the quartz tube. However, when there was a ring and it was placed at a right position, the flame was stabilized with no blowout, as shown in Fig. 10. One possible explanation for this observation is that at high



9. A ring at 50 cm away from the burner had no visible effect on flame stability (methane flowrate = 6 L/m, 15% PA, 10% EA).



10. Destabilizing effect of ring at higher primary air.

PA, the momentum of the methane/PA mixture is so great that it creates a significant low-pressure (vacuum) region that rapidly draws or recirculates the surrounding gas, mostly SA and combustion products (CO_2 and H_2O vapor) into the root of the flame. This, in turn, can cause the flame to extinguish. The presence of a ring can disturb the recirculation flow, making it harder for the combustion products to recirculate back to the root of the burner flame. This helps prevent the flame from extinguishing. Furthermore, since flame impingement on the ring can rapidly elevate the ring surface temperature, the extinguished flame can be reignited by the hot surface and stabilized. These burner flame characteristics are consistent with the so-called "flame puffing" phenomenon that is occasionally observed on a kiln platform when the flame suddenly blows out and rapidly relights.

Effect of ring thickness

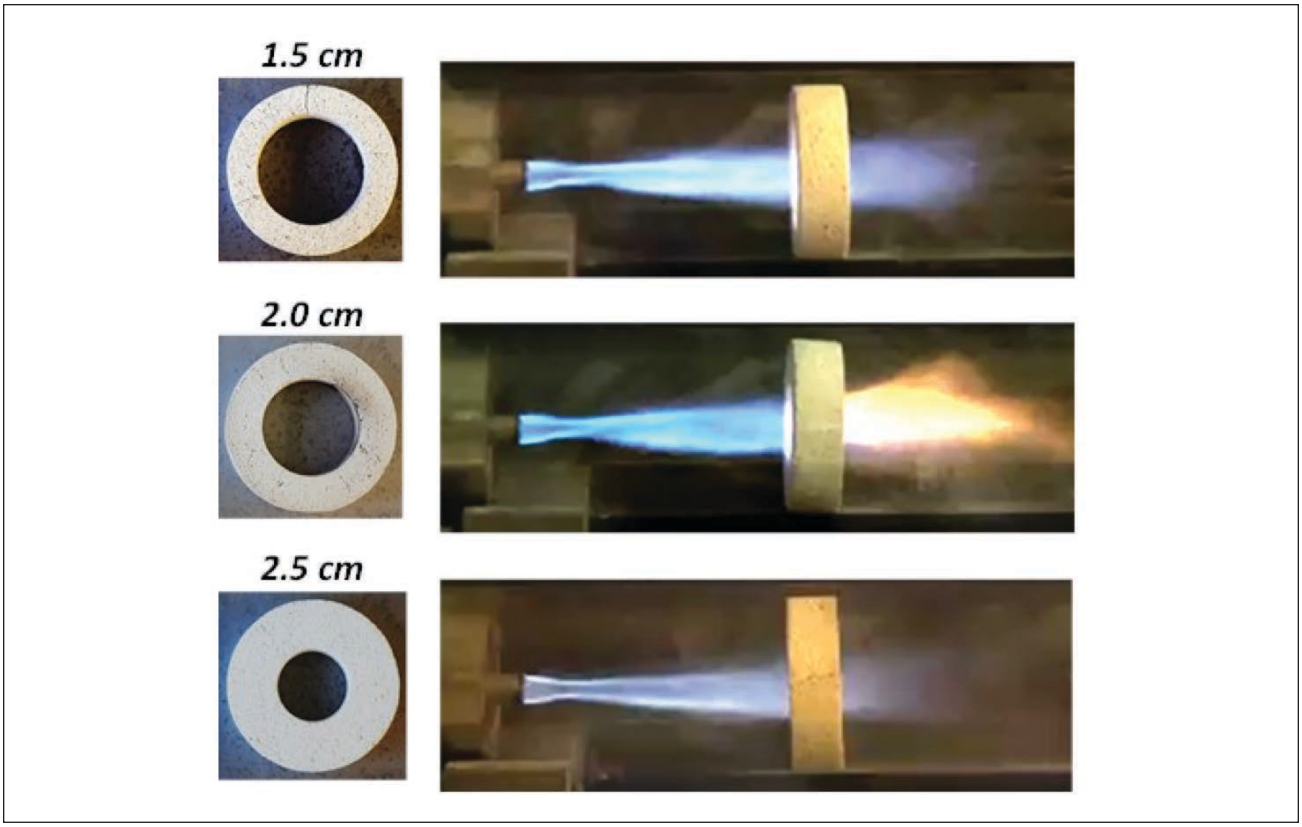
In lime kilns, rings become radially thicker and axially longer with time. They are therefore expected to have a different effect on the burner flame. In this series of tests, the effect of ring thickness on flame stability was examined using rings of three different thicknesses: 1.5 cm, 2 cm, and 2.5 cm. The burner was operated at 6 L/min methane, 10% EA, and at a constant PA flow rate.

Figure 11 shows photos of the burner flame at 15% PA with different ring thicknesses placed at 15 cm from the burner. In all three cases, the flame appeared to be stable with no significant difference in flame characteristics.

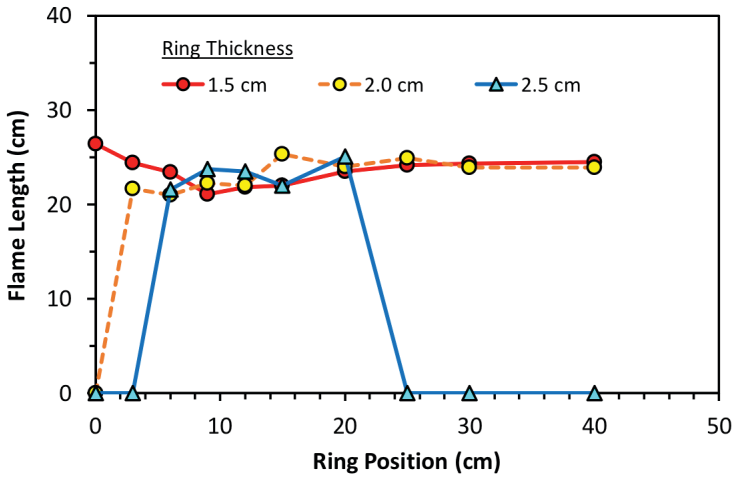
Figure 12 plots burner flame lengths at 15% PA versus ring positions for different ring thicknesses. Both 1.5 cm and 2 cm thick rings appeared to have no significant effect on the flame length, except that the 2 cm thick ring stabilized the flame when it was placed at 3 cm away from the burner. For the 2.5 cm thick ring, the flame was stable only when the ring was placed between 6 and 20 cm from the burner. These results suggest that while rings can help stabilize the burner flame, thick rings are not as effective as thin rings. This is understandable because thick rings have a smaller area through which the SA can pass, so they affect the flame stability more than thin rings.

Effect of ring length

In this series of tests, 2 cm-thick rings of three different lengths were used: 2.5 cm, 5.0 cm, and 7.5 cm. As with the



11. Effect of ring thickness on flame stability (methane flowrate = 6 L/m, 22% PA, 10% EA, ring position = 15 cm).

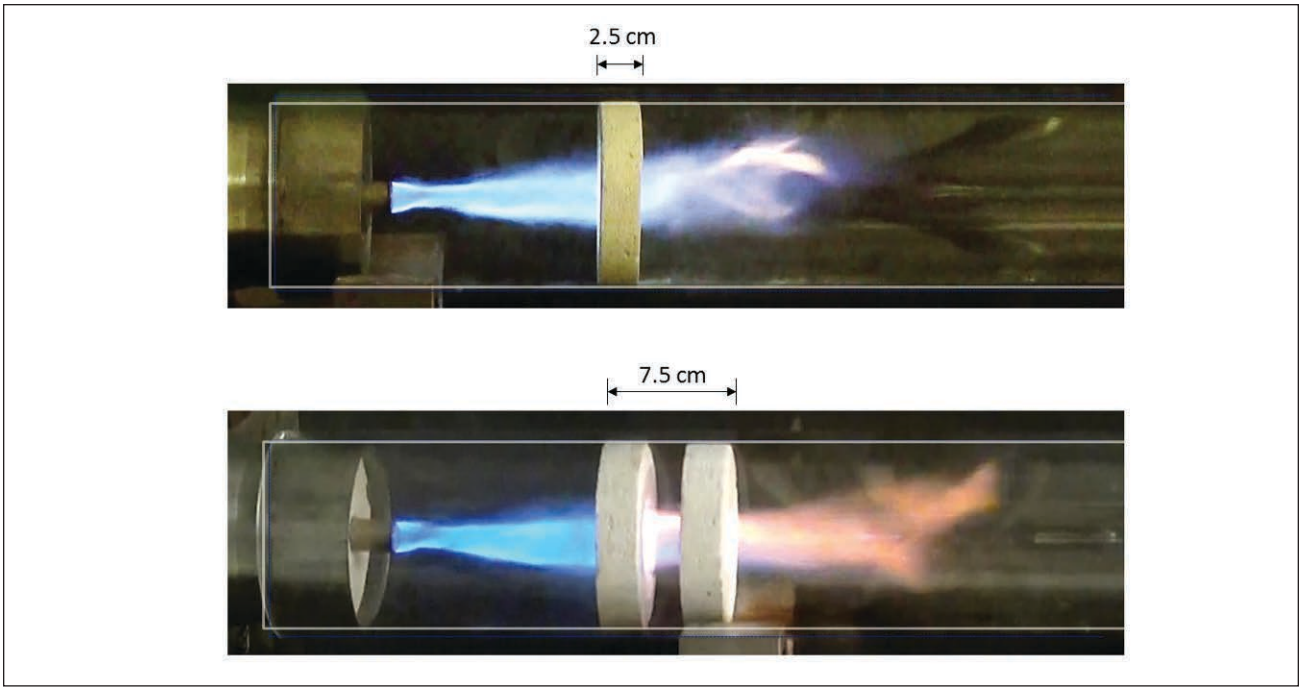


12. Effect of ring thickness on flame stability (6 L/min methane, 15% PA, 10% EA)

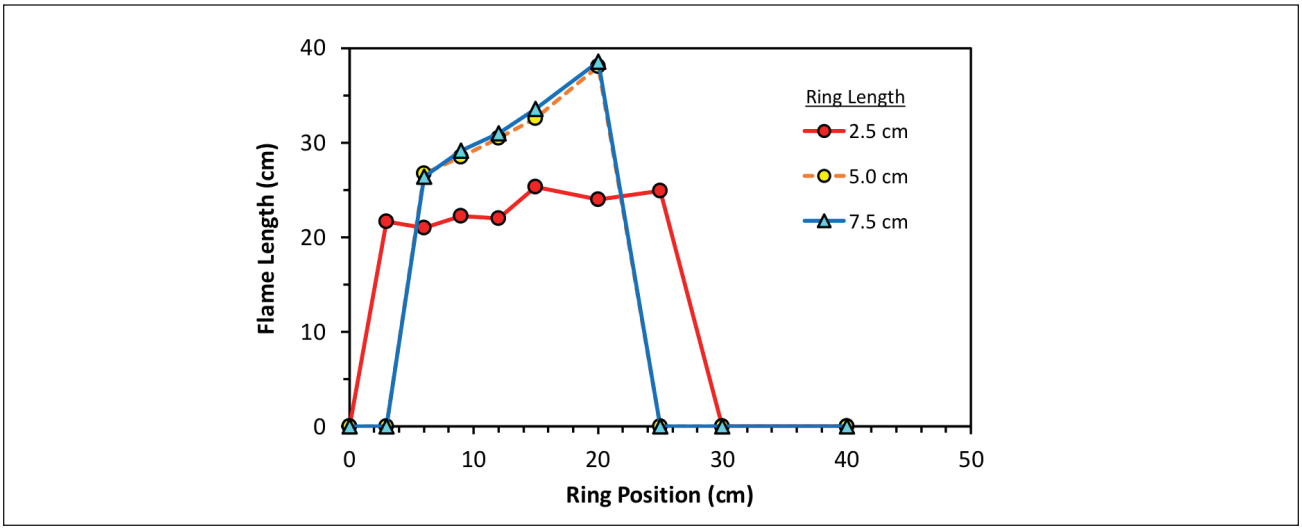
previous test series, the rings were placed at different positions inside the quartz tube and the burner flame characteristics at each position were recorded and analyzed. **Figure 13** compares the interaction between the burner flame and the short (2.5 cm) ring and that between the burner flame and the long (7.5 cm) ring. The longer ring appeared to make the burner flame longer.

Figure 14 plots burner flame lengths at 15% PA versus ring positions for different ring lengths. The short ring (2.5 cm) had no significant effect on the flame length, which was stabilized when it was placed at 3 cm and 25 cm away from the burner. For longer rings (5 cm and 7.5 cm), the flame was longer and stable only when the ring was placed between 6 cm and 20 cm from the burner.

The possible explanation for this finding is that in the case of short rings, although the flame is initially disturbed, it can recover quickly once it has passed through the ring. In the case of long rings, however, it is more difficult for the flame



13. Longer rings elongate the flame by reducing the volume available for combustion reaction (6 L/min methane, 15% PA, 10% EA).



14. Effect of ring length on flame stability (methane flowrate = 6 L/m, 15% PA, 10% EA).

to pass, causing the flame pressure inside the ring to increase, and this likely results in an elongated flame.

SUMMARY

A laboratory study was conducted using a mock kiln to systematically investigate the effect of ring formation on the burner flame stability. Experiments were carried out by burning 6 L/min of methane mixed with various amounts of PA while keeping the total air constant at 10% EA. The ring characteristics investigated were position, thickness, and length. The results show that:

- PA is the main parameter that affects flame stability. In the absence of a ring, the flame becomes brighter, shorter and more intense with an increase in PA up to 17%, and blows out at 20% PA or higher.
- In the presence of a ring, the flame is not stable when the ring is placed too close to the burner, but becomes stabilized when the ring is placed away from the burner.
- Thick rings are more susceptible to flame destabilization than thin rings. The effect of ring thickness on flame stability varies with ring position.
- Long rings destabilize and elongate the flame more than short rings.

This study clearly shows that ring formation can have a great effect on the flame shape and length. However, how it affects the gas and ring surface temperatures and the temperature distribution in the kiln is not clear. This is an interesting and important subject for future research. **TJ**

ACKNOWLEDGEMENTS

This work was conducted as part of the research program on "Increasing Energy and Chemical Recovery Efficiency in the Kraft Process - III", jointly supported by the Natural Sciences and Engineering Research Council of Canada (NSERC) and a consortium of the following companies: Andritz, Arauco, AV Group, Canadian Kraft Pulp, Celulose Nipo-Brasileira, Clyde-Bergemann, Domtar, DMI Peace River Pulp, Eldorado, ERCO Worldwide, Georgia Pacific, Fibria, FPInnovations, International Paper, Irving Pulp & Paper, KFS, Klabin, Stora Enso, Suzano, Tembec, Valmet, and WestRock.

LITERATURE CITED

1. Tran, H.N., "Lime kiln chemistry and effects on kiln operations," *TAPPI Kraft Recovery Course*, TAPPI Press, Atlanta, GA, USA, 2010.
2. Tran, H.N., Mao, X., and Barham, D., *J. Pulp Pap. Sci.* 19(4): 167(1993).
3. Tran, H.N., Griffiths, J., and Budge, M., *Pulp Pap. Can.* 92(1): 78(1991).
4. Gorog, J.P. and Adams, T.N., "Design and performance of rotary kilns in the pulp and paper industry – Part 3 – How flame characteristics and product coolers affect lime kiln performance," *TAPPI Kraft Recovery Operations Seminar*, TAPPI Press, Atlanta, 1986.
5. Alyaser, A.H., "Fluid flow and combustion in rotary kilns," Ph.D. dissertation, University of British Columbia, Vancouver, BC, Canada, 1998.
6. Adams, T. N., "Lime reburning," *TAPPI Kraft Recovery Course*, TAPPI Press, Atlanta, 1992.

ABOUT THIS PAPER

Cite this article as: Mohanan, G., Tran, H., Bussman, M., Manning, R. *TAPPI J.* 17(5):285(2018). https://doi.org/10.32964/TJ17.05.285

DOI: https://doi.org/10.32964/TJ17.05.285

ISSN: 0734-1415

Publisher: TAPPI Press

Copyright: © TAPPI Press 2018

About this journal

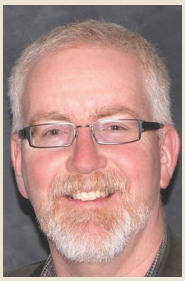
ABOUT THE AUTHORS



Mohanan



Tran



Bussmann



Manning

We chose this topic to research to see if we could prove that as rings grow thicker and more massive with time, they can destabilize the burner flame and alter the temperature profile in the lime kiln. This study complements our previous research that showed how flame instability can lead to ring formation. This research is the other way around, investigating how ring formation may lead to flame instability.

The most difficult part of this study was how to characterize the burner performance under various operating conditions in the model kiln. We address the problem by clearly defining the flame length using an imaging computer program. It was interesting to discover that ring formation is a self-promoting process; once formed, it will likely get worse with time. It was also surprising to find that a minor change in burning conditions in the model kiln could abruptly change burner flame behavior.

Mills may use the information here to address the importance of stable process operation as a means to minimize the ringing problem. Our next step is to investigate how growth of rings may affect the temperature profile, both experimentally and with computational fluid dynamic modeling.

Mohanan is a graduate student and Tran is Frank Dottori Professor of Pulp & Paper Engineering in the Department of Chemical Engineering and Applied Chemistry at the University of Toronto, Toronto, ON, Canada. Bussmann is professor in the Department of Mechanical and Industrial Engineering at the University of Toronto, Toronto, ON, Canada. Manning is director and chief technology officer at KFS in High Wycombe, U.K. Email Tran at honghi.tran@utoronto.ca.

Dry chip feedrate control using online chip moisture

WESLEY GILBERT, IVAN TRUSH, BRUCE ALLISON, RANDY REIMER, AND HOWARD MASON

ABSTRACT: Normal practice in continuous digester operation is to set the production rate through the chip meter speed. This speed is seldom, if ever, adjusted except to change production, and most of the other digester inputs are ratioed to it. The inherent assumption is that constant chip meter speed equates to constant dry mass flow of chips. This is seldom, if ever, true. As a result, the actual production rate, effective alkali (EA)-to-wood and liquor-to-wood ratios may vary substantially from assumed values. This increases process variability and decreases profits. In this report, a new continuous digester production rate control strategy is developed that addresses this shortcoming. A new noncontacting near infrared–based chip moisture sensor is combined with the existing weightometer signal to estimate the actual dry chip mass feedrate entering the digester. The estimated feedrate is then used to implement a novel feedback control strategy that adjusts the chip meter speed to maintain the dry chip feedrate at the target value. The report details the results of applying the new measurements and control strategy to a dual vessel continuous digester.

Application: A new method of dry chip feedrate control could help mills stabilize and potentially increase production rates and achieve better production quality when combined with existing liquor dosing controls.

In kraft pulping, the primary goals are to manufacture uniform, high quality pulp, maximize production, and minimize costs. This is a substantial challenge given that the raw material (i.e., wood chips) is a heterogeneous material with high inherent variability. Normal practice in continuous digester operation is to set the production rate through the chip meter speed. The chip meter is effectively either a screw feeder of known volume or a rotating wheel with pockets designed to deliver a uniform volume of chips per revolution. The speed is seldom, if ever, adjusted except to change production. The dry wood mass feedrate is estimated by applying factors for the chip dry bulk density and the pocket fill factor. An estimate of the pulp production rate is then obtained by applying a yield factor. Most of the other inputs to the digester are ratioed to the assumed dry wood feedrate. Of particular importance are the white and black liquor flow rates, which are set through the effective alkali (EA)-to-wood and liquor-to-wood ratios. The inherent assumption here is that constant chip meter speed equates to constant dry mass flow of chips. This is seldom true.

Variability in chip shape, size distribution, moisture content, and temperature (thawed or frozen chips) affects the packing of chips (bulk density) in the pockets. Moreover, the pockets are not always full. The degree of pocket filling may be time-varying, or it may vary with chip meter speed. The end result is that the actual production rate, EA-to-wood ratio, and liquor-to-wood ratio may vary substantially from the assumed values. The actual production rate will almost always be less than expected as the production rate calculation typically assumes full pockets. Variability in EA-to-wood and liquor-to-wood ratios causes disturbances in the EA profile and chip residence time in the digester, resulting in pulp quality variability, most notably in the kappa number. For a 1000 tons/day mill, a 1% loss of production reduces revenues by approximately US$1 million/year, assuming a marginal profit of US$300/ton. Simulation results indicate that undetected variability in the dry mass flow of chips to a continuous digester of ±5% causes the EA-to-wood ratio to vary ±1.5% and the kappa number to vary ±8 units when pulping softwood to kappa no. 30 at an EA-to-wood ratio of 15%. Similar observations have been reported elsewhere [1-3].

One way to compensate for variability in the wood chip feed entering a continuous digester is through feedback control via a liquor analyzer [2,4]. Feedback control of the residual effective alkali is, however, limited in its effectiveness by the extremely long process dynamics. Residual effective alkali control also fails to address variability in the liquor-to-wood ratio. A better approach is to measure the wood chip mass flow and moisture content before the chips enter the digester and use this for feedforward control to the other inputs. Various devices have been proposed to achieve this [1,5], but most of these require a chip sampling system and are, therefore, difficult to maintain. Furthermore, the measurements are most often made on the chip belt upstream of the chip bin so proper compensation must be made for variability caused by the chip bin level controller. This aspect of the problem has received little attention in the literature.

In this report, a new continuous digester production rate control strategy is proposed that addresses these shortcom-

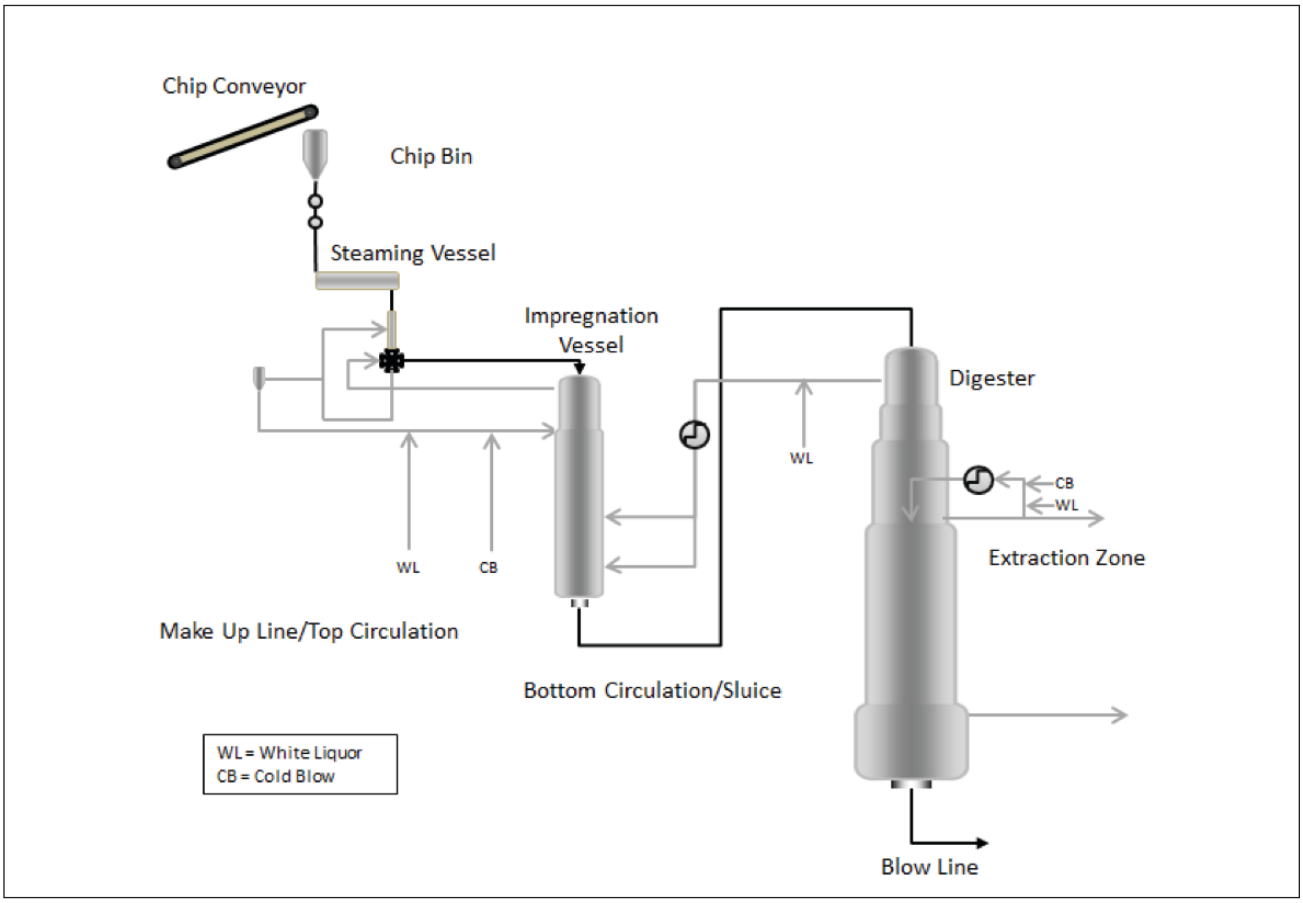
ings. A new noncontacting near infrared (NIR)-based chip moisture sensor [6] is combined with a weightometer to measure the actual dry wood mass feedrate entering the digester. In addition to using the new measurement for feedforward control as has been proposed in the past, a novel feedback control strategy is developed that adjusts the chip meter speed to maintain the feedrate at the target value.

Chircoski et al. [7] trialed a dry chip feedrate control strategy, but their implementation required a chip volume measurement in addition to chip weight and moisture, and no details were given on how compensation for variability caused by the chip bin level controller was achieved. One difficulty faced during development of the feedback control strategy is that the chip weight and moisture sensors are located on the chip belt on the inlet side of the chip bin. The flow of chips is highly variable in this location, and therefore inappropriate as a basis for control, because of the actions taken by the chip bin level controller. What was needed was a measurement of the dry wood flowrate through the chip meter, on the outlet side of the chip bin. Because this quantity is unmeasured, a chip bin mass balance was used to devise a state estimator for this purpose. The chip bin model, state estimator, and feedrate control strategy are described and the results of applying the new measurements and control strategy to a dual vessel continuous digester are discussed.

PROCESS DESCRIPTION

A dual vessel hydraulic digester is depicted in **Fig. 1**. Chips are fed via a conveyor system to the chip bin, where saturated steam at atmospheric pressure is added to heat the chips and remove entrained air. The level in the chip bin is controlled by manipulating the volume of chips feeding the bin. The chips are metered and then enter the steaming vessel where steam at a higher pressure further increases temperature. Chips are then mixed with cooking liquors in the chip chute and fed to a high-pressure feeder. The high-pressure feeder exposes the mixture to the higher operating pressures required for liquor impregnation and to a high-velocity liquor flow to transfer the chips to the impregnation vessel. Most of the white liquor addition occurs at the feed to the impregnation vessel, and the high pressure drives penetration of the liquor into the wood chip. Proper impregnation ensures cooking liquor fills all internal void spaces inside the chip, resulting in a uniformly cooked chip.

The next vessel is the digester, which is divided into different zones. The purpose of the digester is to remove the lignin from the wood chips, leaving behind the hemicellulose and cellulose fibers. The reaction is driven by pressure, temperature, and cooking chemicals. The top of the digester is called the bottom circulation zone, which circulates liquor from the



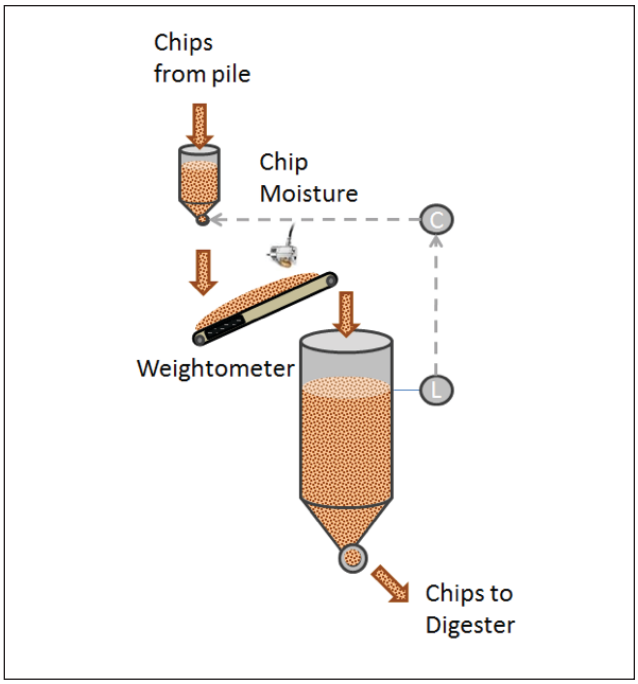
1. Continuous dual vessel hydraulic digester.

top of the digester to the bottom of the impregnation vessel. The circulated liquor is heated to the cooking temperature and is used to help sluice the chips out of the bottom of the impregnation vessel to the top of the digester. A small amount of liquor is added to the bottom circulation zone to ensure the specified amount of effective alkali for the cooking process. The chips and liquor flow concurrently down to the next set of liquor extractions screens, which is called the modified cooking zone. This zone removes a portion of the cooking liquor and replaces it with fresh white liquor and some extracted wash liquor. The fresh liquor and wash liquor are heated before being introduced into the digester to keep the digester temperature at the desired target. The chips then continue down to the digester wash zone, where more liquor is extracted and cooled black liquor filtrate from brownstock washing, called cold blow, is added to cool the bottom of the digester. The chips then pass out the blowline where the chips become pulp fibers as the pressure drops across the blowline valves.

The amount of liquor and temperature in the digester are controlled to ensure a uniform cook of the chips. The cooking reduces the kappa number and hemicellulose content of the chips, while retaining the cellulose. The amount of white liquor at the different zones is added to maintain a desired alkali residual profile in the digester. A too high residual can lead to yield loss as cellulose could also be damaged, while a too low residual can lead to lignin precipitation. A temperature profile is also maintained in the digester for similar reasons. The amount of cooking in the digester is measured by the kappa number.

Figure 2 is a detailed diagram of the chip feed system. Wood chips reclaimed from chip piles are transported to the chip bin via a belt conveyor. The rate of chip removal from the bin is determined by the chip meter, which is a pocket or screw feeder equipped with a variable speed drive. The chip meter ultimately controls the chip feedrate to the digester. The mill is equipped with a Kistler-Morse 1700 weightometer (Kistler-Morse; Spartanburg, SC, USA) and a chip moisture sensor [5]. Both sensors are located on the chip belt upstream of the chip bin.

As mentioned previously, the mass flow of chips on the belt is highly variable due to the chip bin level controller, which manipulates the rate at which chips are reclaimed and placed on the belt. This is illustrated in **Fig. 3**, which shows the chip bin level and its setpoint in the upper plot, the chip bin level controller output in the middle plot, and the mass flow rate of bone dry chips on the belt (moisture corrected weightometer signal) in the lower plot over an 8-h period. The output of the level controller is inversely correlated with the level, as expected, and positively correlated with the dry chip mass flow rate. This short-term variability in dry chip mass flow, which is 60 tons/hour peak to peak or roughly 40% of the nominal value, is only present to correct the level. More to the point, it is not indicative of the dry chip feedrate to the digester through the chip meter and, therefore, is an inappropriate signal for control.



2. Chip feed handling system.

DEVELOPMENT OF CONTROL STRATEGY

What is needed to properly control the digester production rate is a measurement of the dry wood flowrate through the chip meter, on the outlet side of the chip bin. Because this quantity is unmeasured, a chip bin mass balance was used, together with the available measurements, to devise a state estimator (extended Kalman filter or EKF [8]) for this purpose. This section begins with the development of a nonlinear process model for the chip bin level, required for state estimation.

Nonlinear dynamic model for chip bin level

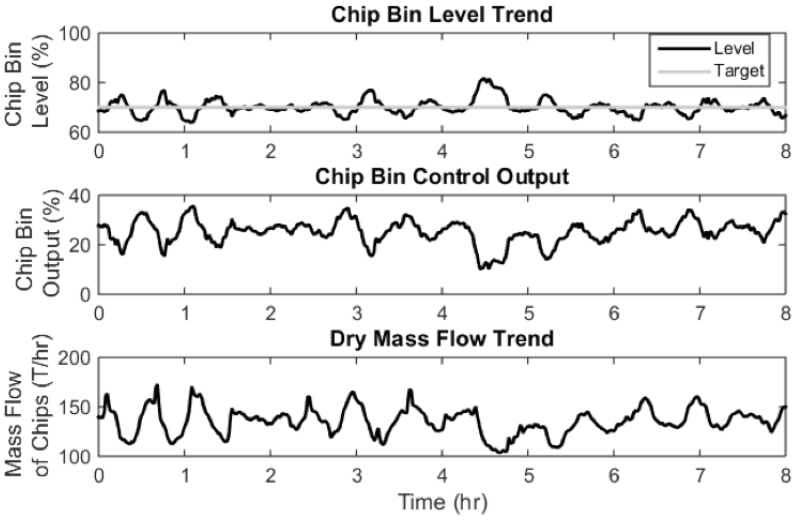
A level model for the chip bin is derived from the material balance of a vessel with fixed cross-sectional area and constant material density (Eq.1):

$$\frac{dL}{dt} = \frac{1}{\rho A}(\dot{m}_{in} - \dot{m}_{out}) \quad (1)$$

where ρ is the density of the material, A is the fixed cross-sectional area, and $\dot{m}_{in}$ and $\dot{m}_{out}$ are the mass flows in and out, respectively. The dry mass flow of chips into the bin is a combination of the chip mass flow measurement (weightometer) and chip moisture (chip sensor), as in Eq. 2:

$$\dot{m}_{in} = (1 - x_w)\dot{m}_c \quad (2)$$

where x_w is the mass fraction of water in the chips and $\dot{m}_c$ is the mass flow of wet chips. As mentioned previously, both variables are measured on the belt leading to the chip bin.



3. Response of weightometer to chip bin level controller.

Here it is assumed that the small transport delay between the locations of the weightometer and the chip sensor is small compared with the dynamics of the chip bin level controller. At the exit of the vessel, only the chip meter speed is known. An additional unknown parameter is required for the conversion to mass flow (Eq. 3):

$$\dot{m}_{out} = \theta S \tag{3}$$

Here S represents the chip meter speed in revolutions per time. The unknown parameter θ represents the amount of dry chip mass per revolution; it is the product of the chip meter volume per revolution, its fill factor, and the chip dry bulk density. Finally, combining Eqs. 1–3 gives the chip bin level model (Eq. 4):

$$\frac{dL}{dt} = \frac{1}{\rho_{bd} A}\left((1 - x_w)\dot{m}_c - \theta S\right) \tag{4}$$

The constants of Eq. 4 include the dry bulk density of the chips ρ_{bd} and the chip bin cross-sectional area A. While the area of the bin is accurately known, the dry bulk density is known to vary as stated earlier. A steady-state analysis of Eq. 4 implies that errors in the bulk density only affect the dynamic component of the model (i.e., unsteady-state level deviations). Therefore, no persistent biasing of the unknown parameter θ is to be expected when using Eq. 4 for estimation.

Extended Kalman filter

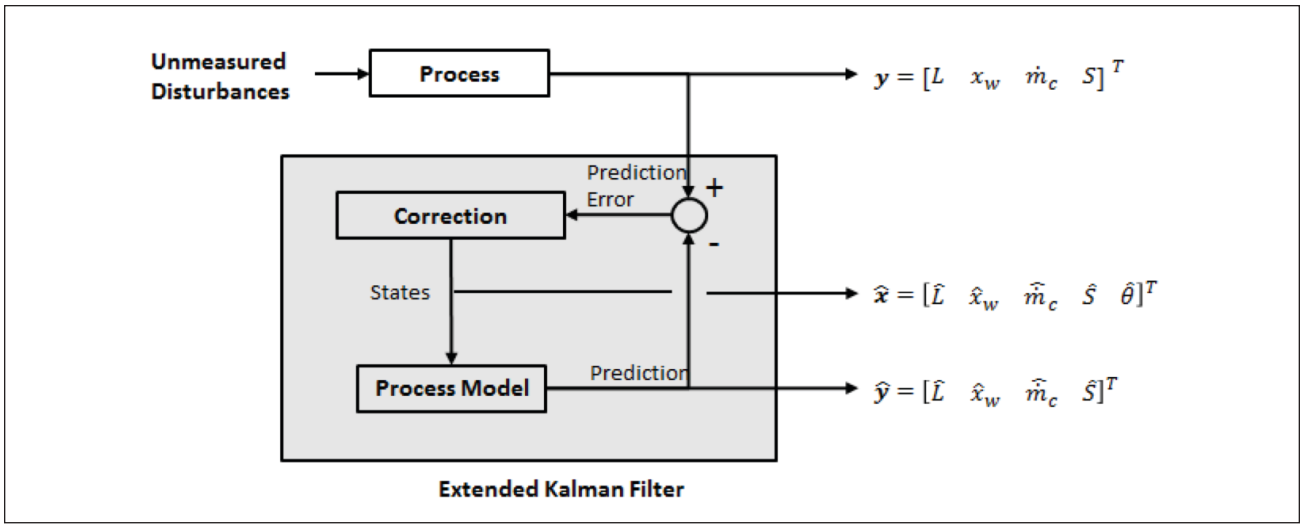
The EKF provides a mechanism to determine an estimate of the unknown parameter θ and to filter noisy measurements. Details of the EKF are provided in the Appendix. **Figure 4** is a schematic block diagram of the EKF showing the flow of information. In this implementation there are no inputs to the process model. Instead, the inputs are included as states so that the EKF can be used to filter those variables. The model runs in parallel with the process and is used to predict the outputs $\hat{y}$. At the sample times, the measured process outputs y are fed back to the EKF and are compared to the predicted outputs, which results in a prediction error. This error is then used to apply a correction to the state estimates that reduces the magnitude of future prediction errors. This prediction-correction process is repeated on an interval T_s.

Determination of covariance matrices

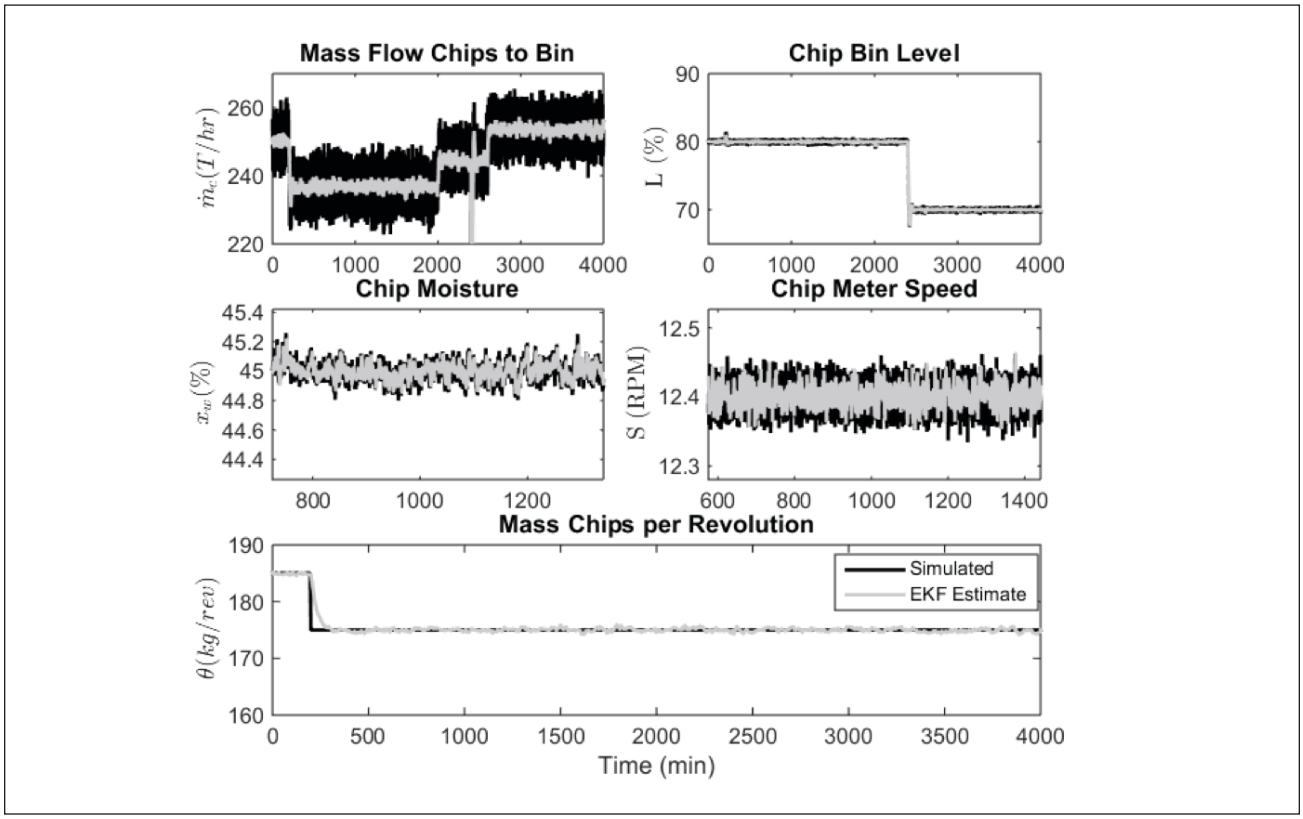
The filtered estimate from the EKF is influenced by two factors: (1) the model contribution (Eq. A8) and (2) the data contribution (Eq. A11). As the measurement error R_v is increased relative to the model error R_w, the EKF will weight the model more and the measurement less. Likewise, if R_v is decreased relative to R_w, the EKF will weight the model less and the measurement more. Thus, the elements of R_v and R_w are the tuning parameters of the EKF. Generally speaking, the covariance matrices are usually taken to be diagonal, both for convenience and for lack of information regarding covariances. Usually, R_v is easily obtained from knowledge of the measurement sensors or from measurement data. The diagonal elements of R_w (variances) are chosen to reflect the total error in predicting the state over the time interval t to $t + T_s$.

To estimate R_v, raw (unfiltered) time series data was obtained from the mill's data historian at a 1-min sampling interval. These values were subsequently fixed and the diagonal elements of R_w were then chosen via simulation to achieve the desired EKF response.

As shown in the following section, the parameter estimate $\hat{\theta}$ is used directly in the dry chip feedrate control calculation



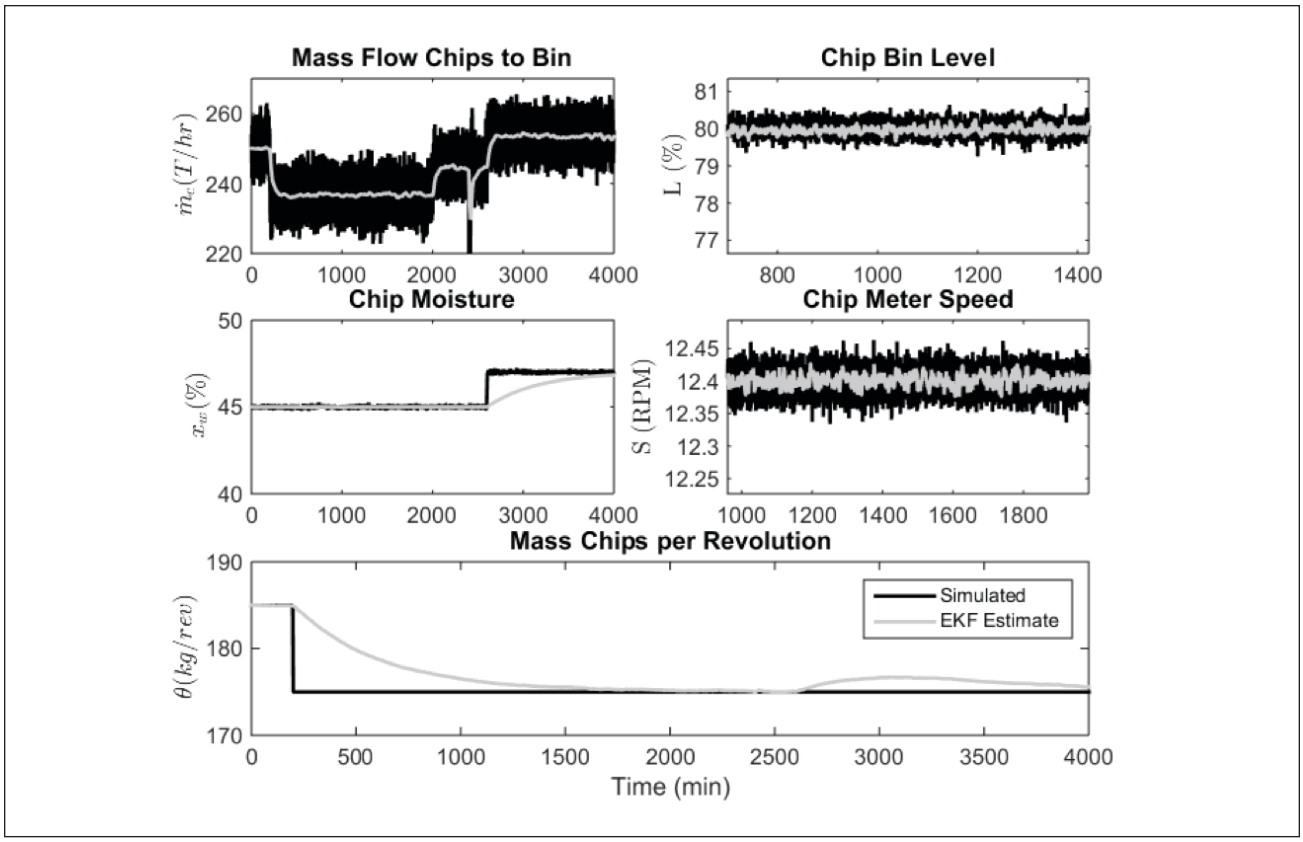
4. Block diagram of extended Kalman filter showing flow of information.



5. Extended Kalman filter response with nominal tuning to step changes in (1) θ, (2) chip meter speed, (3) chip bin level, and (4) chip moisture.

(Eq. 5). Therefore, the tracking error ($\theta - \hat{\theta}$) was of primary importance during tuning of the EKF. In addition, it was anticipated that the filtered state associated with the chip moisture $\hat{x}_w$, together with θ, would be needed for future EA-to-wood and liquor-to-wood control modifications. Finally, it was desirable that the filtered states be insensitive to chip level variability. The following three-step procedure was established to tune the EKF through the choice of R_w diagonal elements: (1) choose a nominal set of tuning criteria, (2) design a test sequence to evaluate the design against the criteria, and (3) fine-tune the design until the criteria are met.

Initial estimates of the state error variances, R_w, were taken as 1% of the nominal operating value. **Figure 5** shows the nominal response of each of the state estimates against the



6. Extended Kalman filter response with refined tuning to step changes in (1) θ, (2) chip meter speed, (3) chip bin level, and (4) chip moisture.

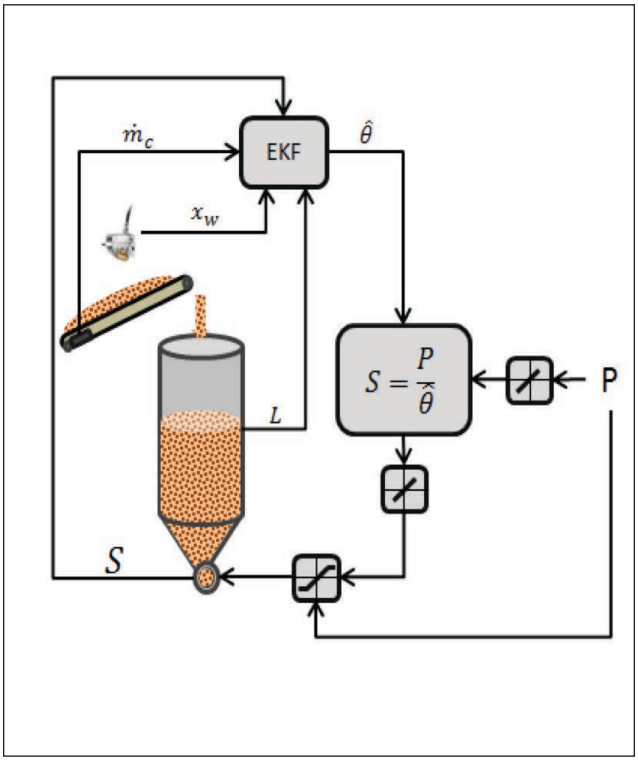
simulated values for step changes in θ, chip meter speed, chip bin level target, and chip moisture. In simulation, the EKF is able to completely remove the effects of changes to the chip meter speed, chip bin level target, and moisture, and it has a 1-h response to a step in unknown θ. However, the response of $\hat{\theta}$ and $\hat{x}_w$ was deemed too fast and it was determined that more filtering was required for practical application.

The desired response time of the estimator was based on the specified maximum allowable chip meter rate of change. To ensure compliance the rate was further reduced by 50%. The EKF was then tuned by trial and error until the desired performance was achieved.

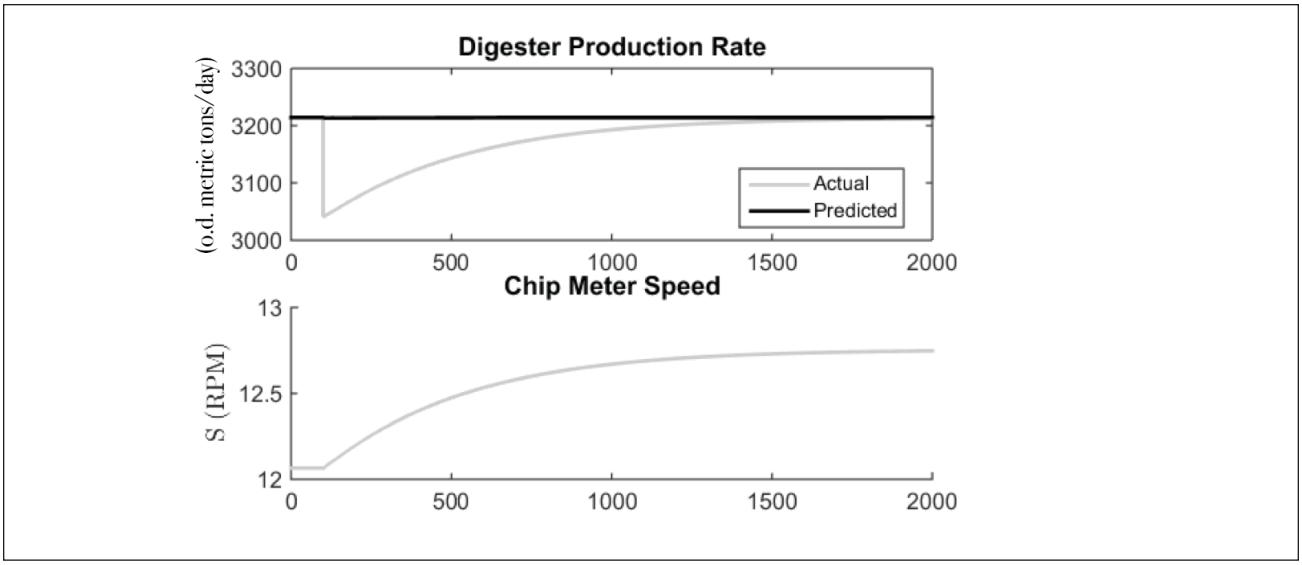
Figure 6 shows the response with the modified tuning to the same changes. No noticeable loss in performance for chip meter and level changes is noticed, and the desired response time in $\hat{\theta}$ is achieved. The step change in moisture affects the estimate of $\hat{\theta}$, as deviation from the actual value, x_w, is temporarily accounted for in the unmeasured state. The implications of this deviation and likelihood of a step disturbance are low. Typical disturbances in chip moisture occur over a similar time frame to the estimator response.

Dry chip feedrate control

The new dry chip feedrate control strategy is shown in **Fig. 7**. The output of the EKF is fed into the following static calculation (Eq. 5):



7. Online extended Kalman filter-based feedrate control.



8. Dry feed rate control response to 10 kg/rev step.

$$S = \frac{P}{\hat{\theta}} \tag{5}$$

where P is the desired chip feedrate in kg/min and is computed from the target pulp production rate through a yield factor. While the calculation of the chip meter speed itself seems trivial, (Eq. 5) effectively closes the loop.

Figure 8 shows the response of the controller to a 10 kg/rev step in θ. Note that the closed loop settling time of the control response is identical to the asymptotic tracking time of the EKF (compared with Fig. 6).

Practical implementation required that the control algorithm fit into the mills pre-existing digester control system, provide onsite tuning capabilities, and protect against unexpected events. Tuning of the EKF alone cannot guarantee prevention of excessive output manipulation. To alleviate this problem, the control algorithm was modified to include an output rate limiter, which allows for mill adjustment to the final control action. In addition, production rate changes traditionally are done using ramping on the digester. Ramping provides time for the digester and its operation to adapt. The production is tied to all the key flowrate and temperature targets of the digester via a multitude of ratio controllers. To ensure similar behavior, the new controller's target was tied to the existing one to ensure seamless integration with the digester control system. Finally, accuracy of the estimator is tied to the accuracy of the chip moisture and wet mass flow measurements. While short-term variation from the mean is inherently handled by the EKF, deviation from the true mean will bias the EKF estimates. Examples of this include instrument drift and failure. To help mitigate this risk, limits were added to the output of the controller. Linear limit constraints as a function of the current production target ensured that chip meter speed manipulations stay in an acceptable range for all operational regimes.

ONLINE APPLICATION RESULTS

The new dry chip feedrate controller was implemented on the digester of a 2000 a.d. metric tons/day Canadian hardwood kraft mill. Both the EKF and controller were implemented in the mill's distributed control system.

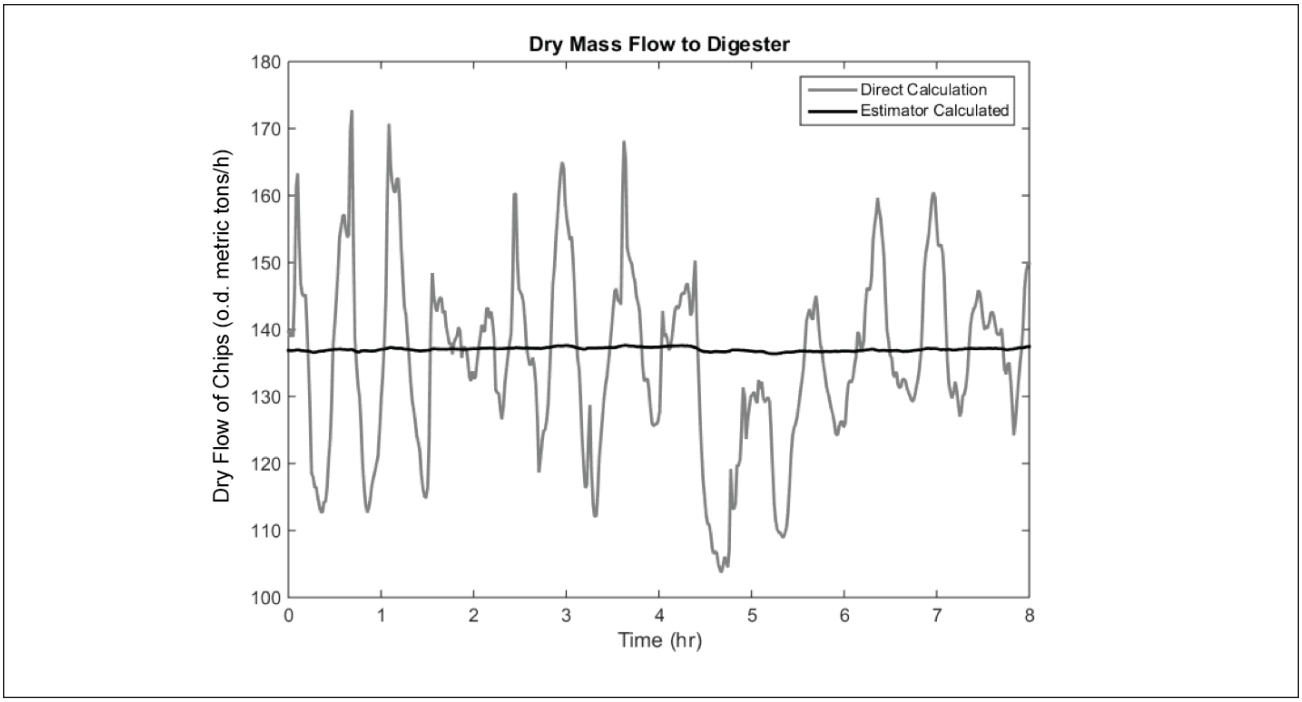
Estimator implementation

The key purpose of the estimator is to remove the short-term variability imposed on the wet chip mass flow measurement from the action of the chip bin level controller. Simulation results showed that the EKF performed very well, both with nominal and final tuning, to disturbances directly affecting the level. **Figure 9** shows an 8-h trend that compares the chip bin dry mass inlet (Fig. 3) and outlet flows. The outlet flow is estimated via the product $\hat{\theta}S$, from Eq. 3. The impact of the level control is effectively removed, providing better representation of the dry mass flow of chips fed to the digester.

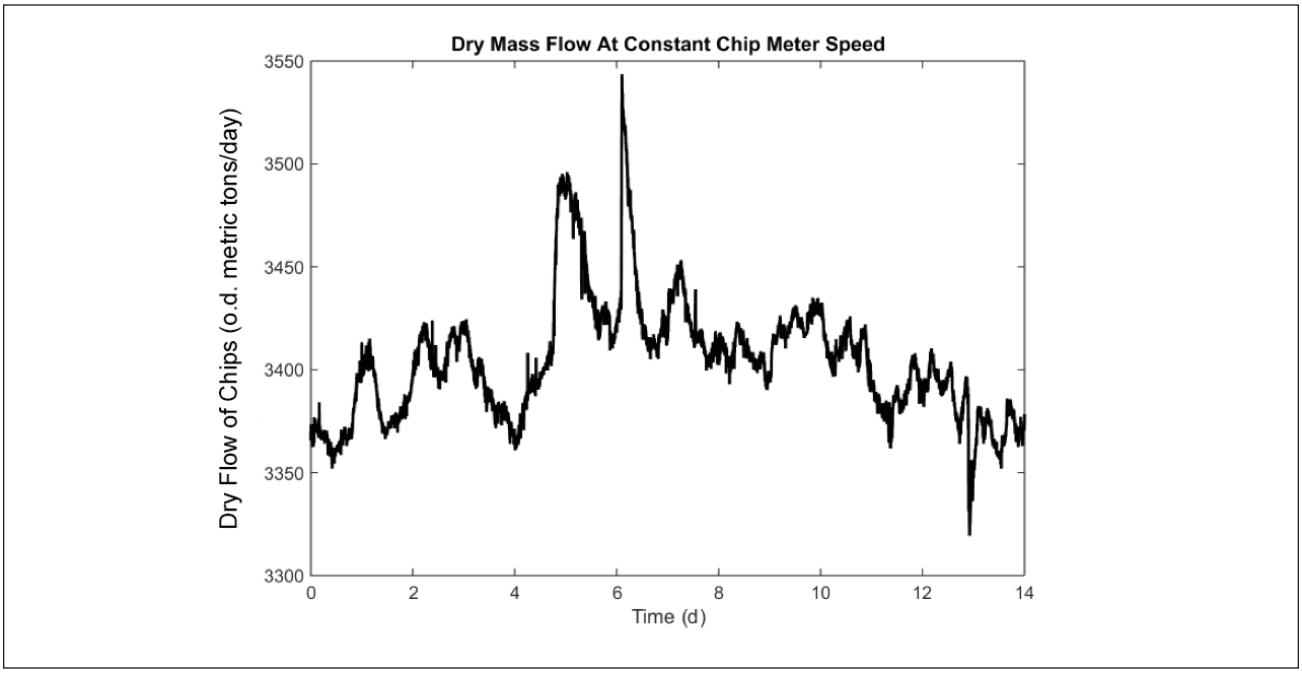
Data from the EKF output over a longer time frame, as shown in **Fig. 10**, reveal significant variation in the overall dry mass flow even though chip meter speed is constant. This demonstrates the weakness of the constant production to chip meter speed relationship traditionally used in the industry.

Control implementation

A 60-day trial was conducted with the final implementation of the chip feedrate controller shown in Fig. 7. The controller performance is evaluated against a 50-day period from the previous year. The results, shown in **Fig. 11**, are normalized by the feedrate target. For the period prior to the implementation of the EKF, the control feedrate was found to vary substantially during the period and typically resulted in an actual feedrate lower than targeted. Production rates greater than

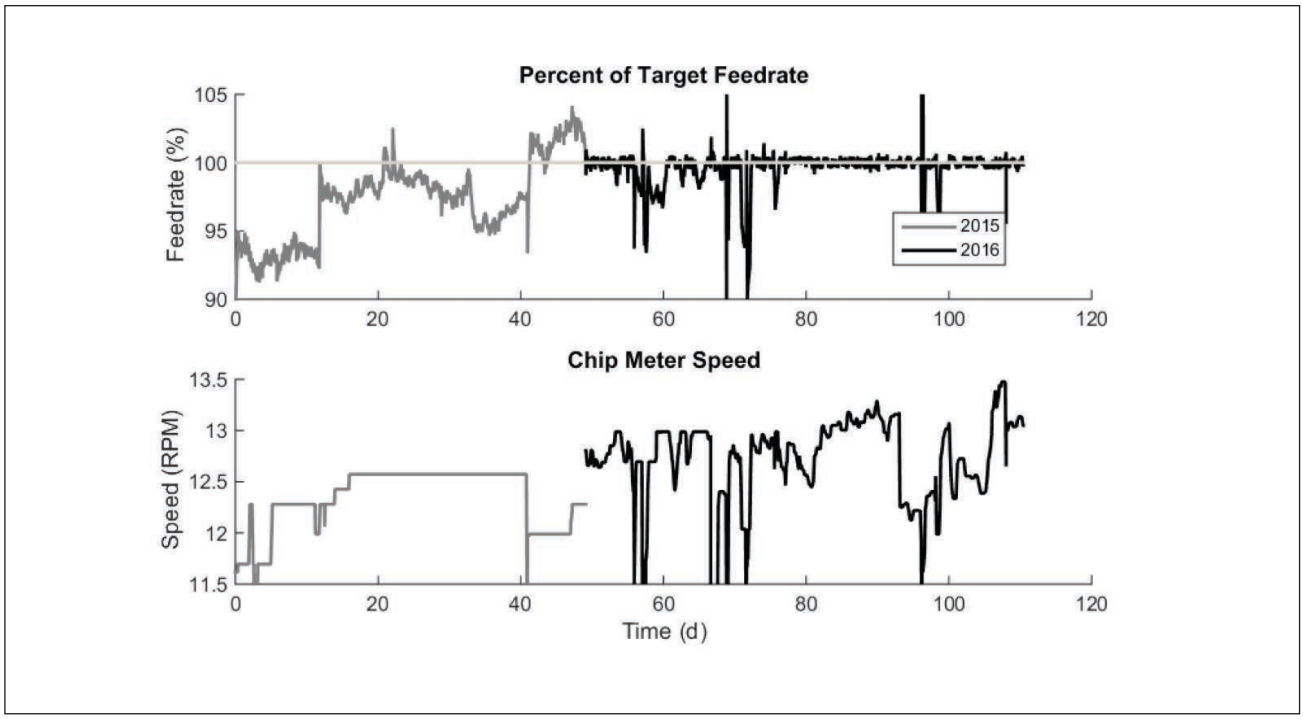


9. Eight-hour trend of dry mass inlet and estimated outlet flow.



10. Long-term trend of estimated dry mass flow at constant chip meter speed.

the target are still possible. After implementation the feedrate holds the target. Short periods of deviation from the target are the result of chip meter saturation. Comparison of the datasets suggests an overall increase in production of 2.5%. It is difficult to extrapolate these results on the basis of the relatively short run time to date, but if we assume that a 1% increase in production is sustainable, then for the February 2017 hardwood spot price of US$500/ton from the RISI database [9], this improvement would be worth US$3.5 million/year in increased revenue to the mill. Also, the feedrate to the digester is stabilized. Better control of the feedrate ensures cooking chemicals are consistently dosed (EA to wood). The liquid/solid or hydraulic balance of the vessel (liquor to wood) also becomes more consistent. This reduction in operational variation is expected to reduce pulp quality variation and alleviate operational issues.



11. Comparison of feedrate for constant chip meter versus extended Kalman filter control.

CONCLUSIONS

A new continuous digester dry chip feedrate control strategy was designed and implemented on a dual vessel digester. The new strategy uses a noncontacting NIR-based chip moisture sensor and a weightometer. One difficulty faced during the development is that the chip weight and moisture sensors are located on the chip belt on the inlet side of the chip bin, whereas what was needed was a measurement of the dry chip flowrate through the chip meter, on the outlet side of the bin. Because this quantity is unmeasured, a chip bin mass balance was used to devise an estimate of the dry mass per chip meter revolution θ via an extended Kalman filter. The new dry chip feedrate controller, based on this estimate, was implemented on the digester of a 2000 a.d. metric tons/day Canadian hardwood kraft mill. The results indicate that, under constant chip meter speed, the actual digester dry chip feedrate can be anywhere between -8% and +3% of the target value and, on average, is 2.5% below the target. Under the new control strategy, the actual dry chip mass flow was able to hold the target value and only showed deviations when the chip meter was saturated or when the digester was upset. Comparison of the datasets suggests an overall increase in production of 2.5%. This improvement is estimated to be worth roughly US$3.5 million/year in increased revenue to the mill. In addition, the removal of large swings in the dry chip feedrate is expected to improve overall digester operation and reduce pulp quality variability by providing more consistent control of chemical dosing and vessel hydraulic loading. **TJ**

LITERATURE CITED

1. Latos, P.J., *Pulp Pap.* 53(2): 160(1979).
2. Tikka, P.O., Kuusela, M.J., and Saarenpaa, M.S., "New methods to master continuous digesters," *Control Syst. Conf., Prepr.*, Pulp and Paper Technical Association of Canada, Montreal, 1988.
3. Smith, D. and Bourdeau, D., "Practical aspects of on-line chip moisture measurement," *TAPPI Pulping Conf.*, TAPPI Press, Atlanta, GA, USA, 1998.
4. Pelletier, S., Evans, R., and Wesslen, T., *Pulp Pap.* 75(5): 79(2000).
5. Langrande, R., *Pap. Trade J.* 170(2): 42(1986).
6. Hans, G., Allison, B.J., and Gilbert, W., *J. Sci. Technol. For. Prod. Processes* 6(3): 6(2017).
7. Chircoski, J., Leclerc, M., and Morissette, L., "Improved continuous digester controls using wood chip analyzer at Zellstoff-Celgar," *PACWEST Conf.,* PACWEST Conference, North Vancouver, BC, Canada, 2013.
8. Jazwinski, A.H., *Stochastic Processes and Filtering Theory*, Academic Press, New York, 1970.
9. RISI, *RISI Database*, RISI, Bedford, MA, USA. Available [Online] https://www.risiinfo.com.

APPENDIX

Extended Kalman filter

State space representation of the model.

The EKF is used to estimate the unknown parameter θ and to filter noisy measurements in the model [4]. The model must first be converted into state space representation. All variables in the model, with the exception of θ, are measured. The state

vector for the model is defined as:

$$x = [L \quad x_w \quad \dot{m}_c \quad S \quad \theta]^T \tag{A1}$$

Then, Eq. 4 can be rewritten as:

$$\dot{x}_1 = \frac{1}{\rho_{bd} A}\left((1 - x_2)x_3 - x_4 x_5\right) \tag{A2}$$

The remaining states are assumed to contain an unknown stochastic behavior. The time derivatives for these states are assumed equal to zero:

$$\dot{x}_i = 0, \quad i = 2,3,4,5 \tag{A3}$$

While states 2–4 could just as easily have been considered as inputs to the model, the decision to incorporate them as states was done to allow for filtering of the values in the EKF directly. The filtering employed helped to remove noise from the measurements, while also reducing responsiveness to short-term process upsets.

The measurements available for state estimation consist of states 1–4:

$$y = [L \quad x_w \quad \dot{m}_c \quad S]^T \tag{A4}$$

This leads to the linear observation matrix C:

$$y = \underbrace{\begin{bmatrix} 1 & 0 & 0 & 0 & 0 \\ 0 & 1 & 0 & 0 & 0 \\ 0 & 0 & 1 & 0 & 0 \\ 0 & 0 & 0 & 1 & 0 \end{bmatrix}}_{C} \begin{bmatrix} x_1 \\ x_2 \\ x_3 \\ x_4 \\ x_5 \end{bmatrix} \tag{A5}$$

The state space model is defined by Eqs. A2, A3, and A5.

State estimation via an extended Kalman filter

Consider the general nonlinear model for the process dynamics arising from unsteady-state material balances:

$$\begin{aligned} \dot{\boldsymbol{x}}(t) &= \boldsymbol{g}\big(\boldsymbol{x}(t), \boldsymbol{u}(t)\big) \\ \boldsymbol{y}(t) &= \boldsymbol{h}\big(\boldsymbol{x}(t), \boldsymbol{u}(t)\big) \end{aligned} \tag{A6}$$

where g and h are vectors of nonlinear functions. The idea behind EKF [8] is to extend linear Kalman filter theory to nonlinear systems. This is achieved by linearization of the system about the current state estimate, and by application of the Kalman filter to the resulting time-varying linear process. The nonlinear functions in Eq. A6 are linearized about the current conditions, $x(t)$ and $u(t)$, and discretized to yield a linear, discrete-time model of the form:

$$\begin{aligned} \boldsymbol{x}(k+1) &= \boldsymbol{A}\boldsymbol{x}(k) + \boldsymbol{B}\boldsymbol{u}(k) \\ \boldsymbol{y}(k) &= \boldsymbol{C}\boldsymbol{x}(k) + \boldsymbol{v}(k) \end{aligned} \tag{A7}$$

Here, the time argument k refers to the current discrete-time sampling instant corresponding to time tk and $k + 1$ refers to a time t_{k+1} one sampling instant into the future where $t_{k+1} = t_k + T_s$ and T_s is the sampling interval. The matrices A, B, and C are generally functions of the states $x(k)$ and controls $u(k)$. Vectors $w(k)$ and $v(k)$ are independent, normally distributed white noise vectors with covariance matrices $R_w = cov\{w(k)\}$ and $Rv = cov\{v(k)\}$, respectively, where $w(k)$ is introduced to account for errors in the one-step-ahead prediction of the state arising from modeling errors and errors due to linearization and $v(k)$ is measurement error.

At the k[th] sampling interval, the current estimate of the state vector, using all the available information at that time, is $\hat{x}(k|k)$, $\hat{x}(k|k)$, and the errors associated with this estimate have a covariance matrix $P(k|k)$. The EKF uses the linearized model to make a one-step-ahead prediction of the state estimate using the available information:

$$\begin{aligned} \boldsymbol{x}(k+1|k) = \boldsymbol{A}\big(\hat{\boldsymbol{x}}(k|k), \boldsymbol{u}(k)\big)\hat{\boldsymbol{x}}(k|k) + \\ \boldsymbol{B}\big(\hat{\boldsymbol{x}}(k|k), \boldsymbol{u}(k)\big)\boldsymbol{u}(k) \end{aligned} \tag{A8}$$

The errors associated with this prediction have a covariance matrix $P(k+1|k)$, that is given by:

$$\begin{aligned} \boldsymbol{P}(k+1|k) = \\ \boldsymbol{A}\big(\hat{\boldsymbol{x}}(k|k), \boldsymbol{u}(k)\big)\boldsymbol{P}(\boldsymbol{k}|\boldsymbol{k})\boldsymbol{A}\big(\hat{\boldsymbol{x}}(k|k), \boldsymbol{u}(k)\big)^T + \boldsymbol{R}_{\boldsymbol{w}} \end{aligned} \tag{A9}$$

The observation functions are then linearized about this prediction to yield the linearized observation matrix, and this is used in the calculation of the Kalman gain matrix for correction of the one-step-ahead prediction:

$$\begin{aligned} \boldsymbol{K}(k+1) \\ = \boldsymbol{P}(k+1|k)\boldsymbol{C}\big(\hat{\boldsymbol{x}}(k+1|k), \boldsymbol{u}(k)\big)^T \times \Big[\boldsymbol{C}\big(\hat{\boldsymbol{x}}(k+1|k), \\ \boldsymbol{u}(k)\big)^T + \boldsymbol{R}_{\boldsymbol{v}}\Big]^{-1} \end{aligned} \tag{A10}$$

When the new measurement $y(k+1)$ becomes available, the prediction is corrected (filtered) using this new information and the Kalman gains:

$$\begin{aligned} \hat{\boldsymbol{x}}(k+1|k+1) = \hat{\boldsymbol{x}}(k+1|k) + \boldsymbol{K}(k+1)\big[\boldsymbol{y}(k+1) - \\ \boldsymbol{C}\big(\hat{\boldsymbol{x}}(k+1|k), \boldsymbol{u}(k)\big)\hat{\boldsymbol{x}}(k+1|k)\big] \end{aligned} \tag{A11}$$

The covariance matrix, $P(k+1|k+1)$, of this one-step-ahead filtered estimate is then computed:

$$\begin{aligned} \boldsymbol{P}(k+1|k+1) = \boldsymbol{P}(k+1|k) - \\ \boldsymbol{K}(k+1)\boldsymbol{C}\big(\hat{\boldsymbol{x}}(k+1|k), \boldsymbol{u}(k)\big)\boldsymbol{P}(k+1|k) \end{aligned} \tag{A12}$$

and both $\hat{x}(k+1|k+1)$ and $P(k+1|k+1)$ are stored for the next interval. The EKF is defined by Eqs. A8–A12.

ABOUT THE AUTHORS

This particular work was part of an overall program to increase digester yield. Inside this program, a new chip moisture measurement shed light into an opportunity for better control of production rate. This work helps improve overall chip management in a continuous digester. It can be used to supplement traditional digester control strategies.

Overcoming the impact of the chip bin level controller on the weightometer was the most difficult part of the work. We overcame this challenge using estimation/modeling techniques to transform the information to something more readily used for control.

Our research was the first application using extended Kalman filtering techniques and their use as part of a control algorithm. An interesting finding was the sheer size of the variability caused by the assumptions made using a constant chip meter speed for production rate control.

This information could be used to improve the overall feed of chips to the mill for control purposes. Benefits to mills could include stabilized and potentially increased production rates and better production quality when combined with existing liquor dosing controls.

The next step is to apply the method at a number of different mills to identify any differences about how it might be implemented in their control systems.

Gilbert is senior control engineer and Allison is research leader at FPInnovations, Vancouver, BC, Canada. Trush is process control specialist, Reimer is business unit leader for fiberline/pulp finishing, and Mason is fiberline area specialist at Alberta Pacific, Boyle, AB, Canada. Email Gilbert at Wesley.gilbert@fpinnovations.ca.


Gilbert


Allison


Trush


Reimer


Mason

ABOUT THIS PAPER

Cite this article as: Gilbert *TAPPI J.* 17(5): 285(2018). https://doi.org/10.32964/TJ17.05.285

DOI: https://doi.org/10.32964/TJ17.05.285

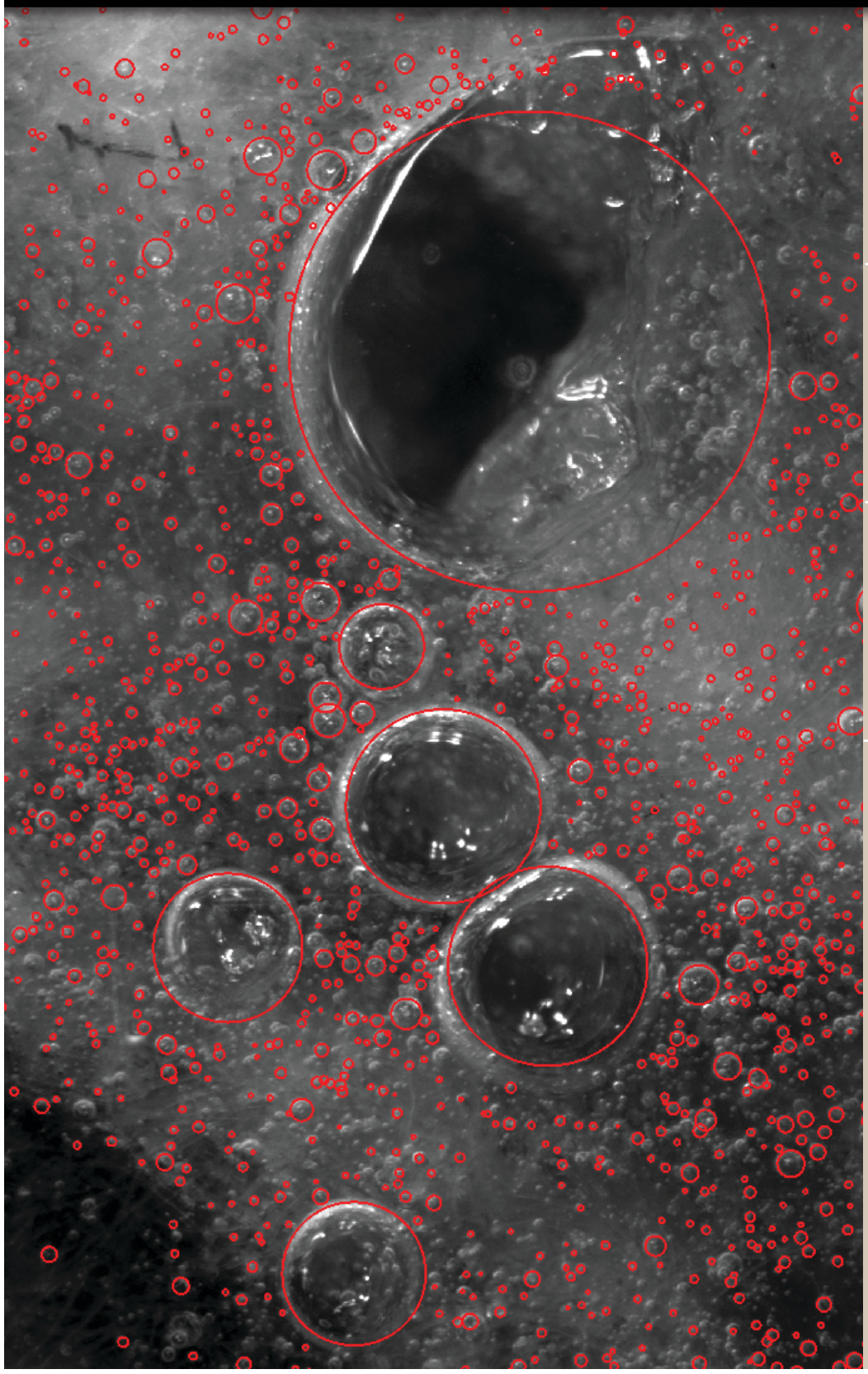
ISSN: 0734-1415

Publisher: TAPPI Press

Copyright: © TAPPI Press 2018

About this journal

TAPPI JOURNAL
WWW.TAPPI.ORG
THE PAPER AND PACKAGING INDUSTRIES' TECHNICAL RESOURCE
JUNE 2018 | VOL. 17 NO. 6



PAPERMAKING 317
Factors affecting the free shrinkage of handsheets: apparent density, fines content, water retention value, and grammage
Nader Mayeli

PAPER PHYSICS 329
Evaluation of the out-of-plane response of fiber networks with a representative volume element model
Yujun Li, Zengzhi Yu, Stefanie Reese, and Jaan-Willem Simon

DELIGNIFICATION 343
Using online bubble size and total dissolved solids measurements to investigate the performance of oxygen delignification
Riku Kopra, Heikki Mutikainen, and Olli Dahl

BLEACHING 353
Decreased water usage in a softwood ECF bleaching sequence—full mill simulations
Pia Jour, Karin Lindgren, Katarina Gutke, and Johan Wallinder

June 2018

TABLE OF CONTENTS VOL. 17 NO. 6

313 EDITORIAL
TAPPI Journal 2017 Best Research Paper Award recognizes recycling technology
Monica Shaw

317 PAPERMAKING
Factors affecting the free shrinkage of handsheets: apparent density, fines content, water retention value, and grammage
Nader Mayeli

329 PAPER PHYSICS
Evaluation of the out-of-plane response of fiber networks with a representative volume element model
Yujun Li, Zengzhi Yu, Stefanie Reese, and Jaan-Willem Simon

343 DELIGNIFICATION
Using online bubble size and total dissolved solids measurements to investigate the performance of oxygen delignification
Riku Kopra, Heikki Mutikainen, and Olli Dahl

353 BLEACHING
Decreased water usage in a softwood ECF bleaching sequence—full mill simulations
Pia Jour, Karin Lindgren, Katarina Gutke, and Johan Wallinder

»COVER CREDIT: As part of their study on the performance of oxygen delignification, researchers Kopra, Mutikainen, and Dahl employed a bubble size imaging system to monitor gas dispersion (p. 343).

TAPPI JOURNAL
WWW.TAPPI.ORG

Editor-in-Chief
Brian N. Brogdon brian.brogdon@gmail.com
+1 678 581-9114

Associate Editor
Peter W. Hart peter.hart@westrock.com
+1 409 276-3465

Editorial Director
Monica Shaw mshaw@tappi.org
+1 770 367-9534

PRESS Manager
Jana Jensen jjensen@tappi.org
+1 770 209-7242

Webmaster
Trina Heath theath@tappi.org
+1 770 209-7416

***TJ* EDITORIAL BOARD**
Randy Branston, BASF
randy.branston@basf.com, +1 704 819-4251

Brian N. Brogdon, FutureBridge Consulting & Training LLC
brian.brogdon@gmail.com, +1 678 581-9114

David A. Carlson, Carlson Consulting
dacarlson39@aol.com, +1 847 323-2685

Douglas W. Coffin, Miami University
dacarlson39@aol.com, +1 847 323-2685

Mahendra Doshi, Doshi and Associates
mahen@aol.com, +1 920 832-9101

Marc Foulger, GL&V USA Inc.
Marc.foulger@glv.com +1 315 767-2920

Peter W. Hart, WestRock
peter.hart@westrock.com, +1 409 276-3465

Carl J. Houtman, USDA Forest Products Laboratory
choutman@fs.fed.us, + 1 608 231-9445

Lucian Lucia, North Carolina State University
lucian.lucia@gmail.com, +1 919 889-7059

John A. Neun, John A. Neun LLC
john.neun@gmail.com, +1 518 275-8139

Jim Niemiec, Verso Corporation
jim.niemiec@versoco.com, +1 715 422-7404

Steven P. Ottone, Omya
steven.ottone@omya.com, +1 919 641-7854

Gaurav Pranami, Imbed Biosciences
gpranami@imbedbio.com, +1 515 230-7005

Arthur Ragauskas, Oak Ridge National Laboratory
aragausk@utk.edu

Gerard J.F. Ring, University of Wisconsin—Stevens Point
gerrryring@wi-net.com, +1 715 592-3732

Scott Rosencrance, Kemira Chemicals
scott.rosencrance@kemira.com, +1 770 429-2753

Paul Wiegand, NCASI
pwiegand@ncasi.org, +1 919 941-6417

Junyong Zhu, USDA Forest Products Laboratory
jzhu@fs.fed.us, +1 608 231-9520

Join TAPPI *today!*
TAPPI JOURNAL is a free benefit of TAPPI membership, and is only available to members. To join TAPPI, to renew your TAPPI Membership, or to learn about other valuable benefits, visit www.tappi.org.

TAPPI, 15 Technology Parkway S., Suite 115, Peachtree Corners, GA 30092, publishes *TAPPI JOURNAL* monthly.

ATTENTION PROSPECTIVE AUTHORS: All papers published are subject to *TAPPI JOURNAL's* peer-review process. Not all papers accepted for review will be published. Before submitting, check complete author guidelines at http://www.tappi.org/s_tappi/doc.asp?CID=100&DID=552877.

Statements of fact and opinions expressed are those of individual authors. TAPPI assumes no responsibility for such statements and opinions. TAPPI does not intend such statements and opinions or construe them as a solicitation of or suggestion for any agreed-upon course of conduct or concerted action of any sort.

Copyright 2018 by TAPPI, all rights reserved. For copyright permission to photocopy pages from this publication for internal or personal use, contact Copyright Clearance Center, Inc. (CCC) via their website: www.copyright.com. If you have questions about the copyright permission request process, please contact CCC by phone at +1 978 750-8400. To obtain copyright permission to use excerpts from this publication in another published work, send your specific request in writing to Editor, TAPPI JOURNAL, 15 Technology Parkway S., Suite 115, Peachtree Corners, GA 30092, USA; or by fax to +1 770 446-6947. Send address changes to TAPPI, 15 Technology Parkway S., Suite 115, Peachtree Corners, GA 30092, USA; Telephone +1 770 446-1400, or FAX +1 770 446-6947. www.tappi.org

Editorial



MONICA SHAW | EDITORIAL DIRECTOR
mshaw@tappi.org

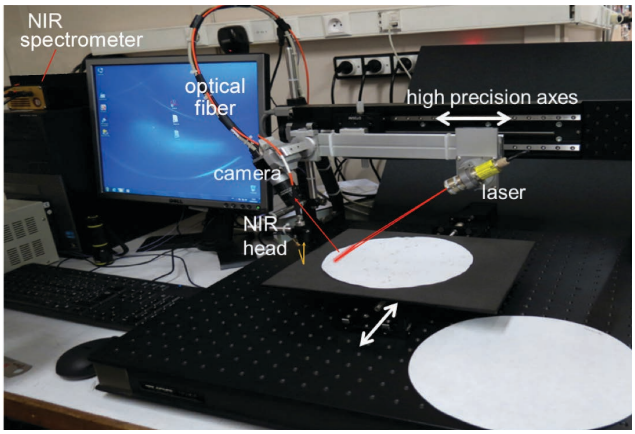
TAPPI Journal 2017 Best Research Paper Award recognizes recycling technology

TAPPI and the *TAPPI Journal* (*TJ*) Editorial Board would like congratulate the authors of the 2017 *TAPPI Journal* Best Research Paper Award: Sylvie Ossard, Patrick Huber, Pascal Borel, Davy Soysouvanh, and Thierry Delagoutte, who developed the paper's concept and its implementation at the Centre Technique du Papier (CTP) in Grenoble, France. Their paper, "New automated method for macrocontaminant analysis: Industrial applications," appeared on p. 623 of the November 2017 issue. In addition to winning the *TJ* Best Research Paper Award for 2017, the paper also received the 2016 Wayne Carr Award from TAPPI's Recycling Committee.

First author Ossard, a former project engineer at CTP, now studies management at Grenoble École de Management. Co-authors Huber, Borel, and Delagoutte are continuing the work as project engineers at CTP, where co-author Soysouvanh is team leader. Recently, *TJ* spoke with Ossard about the work leading to the award-winning paper.



Sylvie Ossard



Ossard says that one mill told her that the online version of the 3D-Stick device provided more data on stickies in 10 days than it had collected in five years.

How did the development of the 3D-Stick measurement method transpire?

We conceived the 3D-Stick method after noticing during mill visits that there was a definite lack of methods for qualitatively classifying macrostickies, which vary in their chemical nature. Because of this, there was a definite knowledge gap as to which kind of glues made up those stickies and how those could be specifically removed. Both the INGEDE #4 Method and TAPPI Standard Test Method T 277 pm-99, "Macro stickies content in pulp: The 'pick-up' method," provide valuable information about the particle count and size of stickies, but they are manual tests, provide only a two-dimensional (2D) view, and don't provide a breakdown by contaminant classes, such as hot melt, various glues, and plastics.

What led CTP to apply near infrared (NIR) spectroscopy for this issue?

My colleagues and I at CTP discussed how to address this lack of information about stickies composition, and after a year of trying different approaches, we decided to carry on with NIR spectroscopy. From literature searches and knowledge of how other teams used NIR, we could see that it applied well in flow processes like sorting a recycled paper stream and assessing raw material quality. So, we decided to try it because it can see differences between very similar chemicals, and it is quite fast and efficient. In addition, we also decided to take a three-dimensional (3D) look at the morphology of stickies using a laser triangulation approach that was developed at CTP a few years before, but for very different applications.

There was a great deal of teamwork involved with de-

veloping the 3D-Stick method. My input began with identifying the issue itself at mills, and then with team discussions and project management. Patrick Huber and Thierry Delagoutte provided a great deal of conceptual ideas as to the approach. Davy Soysouvanh and Pascal Borel did a lot of work on the development of the device itself, and its electronic and data analysis capabilities.

How does the 3D-Stick method determine details about stickies?

Using the laser triangulation, it first determines the 3D morphology of the particles, as well as the x-y axis positions of the particles on the filter paper. The laser moves across the sheet so you can reconstruct an image in three dimensions and know the location and size of each particle. Next, using NIR spectroscopy, the particles are analyzed and classified as to their chemical composition.

CTP actually developed two devices. The first device analyzes contaminants in the laboratory after they have been separated, which was what mostly described in our *TAPPI Journal* paper. As part of a long-term project, an online sensor based on the lab 3D-Stick device was developed in conjunction with TechPap in Grenoble, who are very good with online device development and automation. Several online mill trials were conducted where the device was connected to the pulp flow and automatically sampled and analyzed the contaminants in the pulp. This allows us to know onsite where to remove the stickies to quantify them at different points of the circuit.

How did the mills receive the online 3D-Stick device?

They liked it a great deal. The first trial was definitely more complicated because the device wasn't yet perfected. However, in subsequent trials, we improved a lot and ran the online 3D-stick device for days, with five automatic samplers giving results. This worked out well, because the mill could change process parameters and see what the impact was on stickies removal. With some mills, we also worked on the raw material modification, according to what they wanted to produce, so it's a great tool for controlling the stickies and knowing what you should do about stickies in the process.

Compared with the TAPPI and the INGEDE methods, how does the 3D-Stick device perform?

For one, the laser triangulation method doesn't deform the sample because it scans the filter paper rather than pressing it. This scan also reconstructs the altitude profile of stickies in 3D, giving length, width and thickness distributions, instead of 2D.

You still have to wait around two hours to get the measurement itself because you have to screen contaminants. However, you get a *lot* of results and that's the advantage. One mill told me that the online device provided more data in 10 days than it had collected in five years! This is because the device runs 24 hours a day because it's automated and not manual with a person performing the test, and you have a measurement every 30 minutes. So, if you change some parameters or some raw material, so you will see it in the results.

What do think of the future for the 3D-Stick device?

I really hope the online 3D-Stick device will be a success, because stickies are still a huge problem for recycling mills. I think this method and device will help them understand how the different types of stickies behave. It will be interesting for it to help mills perform deeper analysis and truly sort out their stickies issues. **TJ**

Ossard currently studies at Grenoble École de Management and can be reached at sylvieossard@free.fr. Co-authors Patrick Huber and Thierry Delagoutte can be reached at Patrick.Huber@webCTP.com and Thierry.Delagoutte@webCTP.com at CTP in Grenoble, along with the other co-authors of the award-winning paper.

Factors affecting the free shrinkage of handsheets: apparent density, fines content, water retention value, and grammage

NADER MAYELI

ABSTRACT: Industrial papermaking is a high-speed process during which a suspension of cellulosic fibers is formed into a continuous web via dewatering followed by drying. Dewatering in the paper machine occurs mechanically in the forming and pressing sections; however, most of the remaining water, whose removal requires applying high temperatures, evaporates in the dryer section. As a result, the paper web shrinks, due to the shrinkage of individual fibers in the paper web. On the paper machine, the paper web is under restraint in the machine direction (MD), whereas it can shrink in the cross-machine direction (CD). The edges of the web shrink more than the center of the web. A shrinkage profile is therefore created in the CD of the web. All machine-made papers exhibit a CD shrinkage profile. The CD shrinkage profile is significant because it affects the final product quality and manufacturing efficiency. The prime cause of the CD shrinkage profile during drying is free shrinkage. The effects of several wood pulp fibers on the free shrinkage of handsheets were investigated to obtain deeper understanding of the mechanism of paper shrinkage during drying processes.

Application: Mills can better understand the role of different fiber types, density, fines content, water retention value, and grammage on the free shrinkage of handsheets formed from a selection of softwood and hardwood pulps.

After initial stock preparation processes, papermaking is essentially a process of water removal. In the first stage of manufacture, fibers are deposited as a dilute suspension via a filtration process to form a mat with solids content around 20%. In the second stage, the wet web is pressed, increasing the solids content between 40% and 50% and consolidating the web, which increases the amount of interfiber contact [1]. In what is typically the final stage, the web is dried, such that the equilibrium moisture content is around 8% [2,3]. During this drying process, the web shrinks [4] and this shrinkage affects the mechanical and printing properties of the sheet [5-7], which are specified by customers. Paper sheet shrinkage is not the direct consequence of water evaporation. However, it is a result of structural modification of individual fibers during drying, in particular by considerable transverse shrinkage that causes contraction of the fiber network and creates internal stresses in the paper. Cross-machine direction (CD) shrinkage exhibits a profile that it is greater at the edges of the web and minimal at the center, where the web is much more restrained compared with the edges [8-10]. A nonuniform mechanical property profile in the CD is a consequence of the shrinkage profile [7,11]. Drying tension builds up in the paper when paper is restrained from shrinking by the application of drying restraints. This drying tension is larger in the machine direction (MD) than in the CD because more fibers are oriented in the MD and fibers have higher longitudinal stiffness than transverse ones.

Several studies [11-13] have shown that the use of drying restraint for the purpose of reducing shrinkage affects the development of the paper sheet's mechanical properties. Increase in modulus of elasticity, decrease in stretch, and increase in tensile strength can be achieved by increasing drying restraint [12]. Wahlström [13] reported that an 8% strain increase, from -4% (shrinkage) to +4% (stretch), can give a relative increase in tensile stiffness of as much as 500%. It is now established that the shape of the shrinkage profile depends on length and width of the free draws in the dryer section [7,14]. The total amount of free shrinkage depends on the unrestrained shrinkage of the web in the CD and MD. Wahlström and Lif [7] showed that the geometric mean shrinkage was equal to the free shrinkage of an isotropic handsheet.

SHRINKAGE EVENT

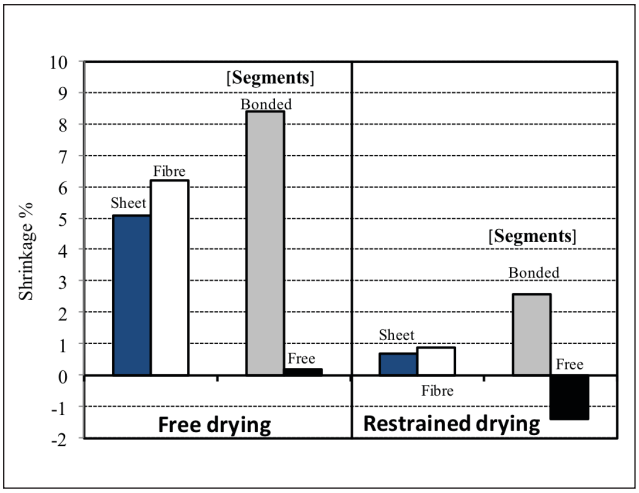
As water is removed during drying, the attractive forces associated with the surface tension of water pull fibers sufficiently close so that hydrogen bonds can form between the fibers [15,16]. If the web is not restrained, these forces cause contraction of the web during drying. This shrinkage is the prime cause of deformations in the plane of paper at this stage. If the web is restrained during drying to prevent or reduce shrink-

age, dried-in stresses are developed in the web [17,18]. Htun and de Ruvo [17] showed that the drying stress of restrained paper increases drastically after the solids content of the sheet reaches 80%, which was later proved by Nanko et al. [19]. Htun and de Ruvo concluded that the type of pulp and the degree of beating usually determine the starting point of the drying stress built up in the paper. They discussed that as solids content increases surface tension, drying forces and free shrinkage also increase [17]. In agreement with Htun and de Ruvo, Hansson et al. [20] stated that the greater part of the shrinkage happens in the solids content range of 60% to 80%. The magnitude of the shrinkage depends on the degree of swelling of the fibers and on the fiber orientation in the paper. Nanko et al. reported that the solids content from which this shrinkage starts is the fiber collapse point (FCP) and it is in the range of 85%–88% [19]. Fiber collapse point is the point at which the solids content is such that fibers are transformed from cylindrical tubes into flat ribbons to allow extended bonding area. At the FCP, the fibers shrink rapidly in the transverse direction, introducing microcompressions in the crossing fibers. Nanko et al. argued that the water remaining in the fiber wall at the FCP coincided with the value of bound water and stated that the evaporation of bound water, which has strong interaction with cellulose, caused the shrinkage of the fiber [19]. Later, Hoole et al. [10] proved that the profile is not caused by the press section and showed that shrinkage profile is set by the FCP.

FREE SHRINKAGE

Drying a paper without applying any external forces results in paper exhibiting shrinkage due to the hygroscopic nature of its constituent fibers as its moisture content reduces. It is accepted that fibers shrink by only 1%–2% along their length and by around 35% in width [20]. Shrinking of a single fiber in the direction of fiber width depends on the swelling capability of wood fiber components [21-23]. Accordingly, the classical interpretation of the mechanism of sheet shrinkage is that transverse shrinkage of fibers results in longitudinal contraction of contacting fibers in bonded regions [20,24]. Nanko and Wu [24] reported that the longitudinal shrinkage of the fibers is 30%–80% greater than that of the sheet, depending on the degree of beating. This finding was contrary to the results reported by Page and Tydeman [20], who found that the longitudinal shortening of the fibers was the same as the shrinkage of the sheet. What Nanko and Wu reported as the longitudinal shrinkage of the fibers is more likely to be the longitudinal contraction of crossing fibers at the bond, because they measured the shrinkage of the fibers in the sheet. According to Nanko and Wu, the longitudinal shrinkage of the fibers often happens at the bonded area in the freely dried sheet, which had been proved by Page and Tydeman.

Figure 1 shows the average longitudinal shrinkage of a sheet, an individual fiber in the sheet, and the segments (bonding sites and free segments) of a fiber in a fiber network [24]. In a freely dried sheet, the bonded segments shrink more than



1. Average fiber shrinkage during free and restrained drying.

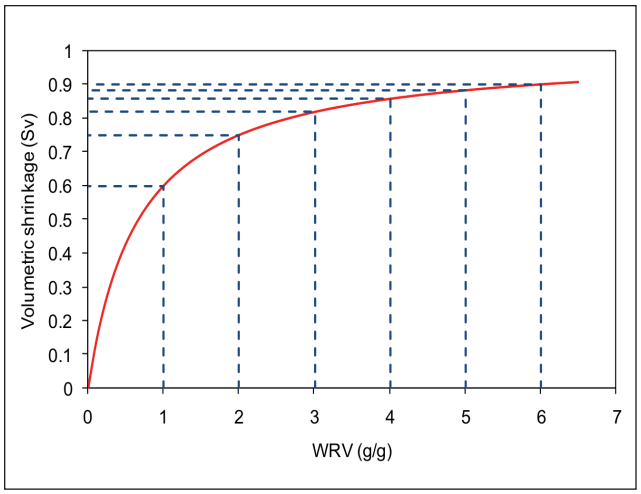
the bonded segments in the restrained dried sheet case. The shrinkage rate of the bonded segments is larger than that of fiber. Nanko and Wu observed no significant dimensional change in free segments of freely dried paper and found that the free shrinkage of the sheet was somewhat less than the longitudinal contraction of fibers. They noticed that during restrained drying, contraction of bonded segments causes stretching of free segments that are situated between two bonded segments (Fig. 1). As mentioned earlier, water elimination from a swollen fiber during drying results in considerable fiber shrinkage; that is, as water is removed from the cell wall, the fiber begins to decrease in cross-section as surface tension forces draw the fibrous components together [16,23,25]. Hansson et al. [21] reported that if no external forces are applied on paper during drying, the magnitude of the free shrinkage depends on the degree of fiber swelling in the paper.

Sampson and Yamamoto [26] investigated the influence of water retention value (WRV) on the free shrinkage of handsheets. Assuming the density of the fiber wall to be 1.5 g/cm^3, a simple mass balance can be used to show that the total volumetric shrinkage of a fiber on complete drying from a moisture content, m, is (Eq. 1) [26]:

$$S_v \approx \frac{3m}{3m+2} \quad (1)$$

This volumetric shrinkage of fibers provides the driving force for the shrinkage of paper (**Fig. 2**). Sampso and Yamamoto reported that although free shrinkage was directly proportional to WRV, an analysis based on volumetric shrinkage of fiber, S_v, revealed that this dependence is not influenced significantly by WRV, which is greater for fines than it is for fibers (WRV substitutes for parameter m in [Eq. 1]).

Several studies have shown that fines have a strong influence on the structure and properties of the fiber network [15,25,27-30]. The primary effect of fines is an increase in



2. Volumetric shrinkage plotted against water retention value (WRV).

Fiber Type	Pulp Type	SR Value (No Beating)
Softwoods		
BP	Bleached Lapponia pine*	7
BS1	Bleached Mercer spruce**	8
BS2	Bleached star spruce***	14
UBSP	Unbleached spruce/pine (70:30 blend)*	9
Hardwoods		
BB1	Bleached Eno birch*	10
BB2	Bleached Södra gold birch*	13
BE	Bleached eucalyptus*	11
Notes: *Kraft; **sulfite; ***chemithermomechanical.		

I. Pulping procedures.

density, which results in an increased number of interfiber bonds and improved tensile-strength properties of the sheet [25,27-29]. Fines act as a bridge between fibers, contributing to the formation of a coherent paper network. Uesaka and Moss [29] showed that the fines considerably increase shrinkage; in particular the chemical pulp (low-yield sulfite) fines gave a greater increase than the mechanical pulp (groundwood) fines. Sampson and Yamamoto showed that the free shrinkage of handsheets is strongly influenced by the fraction of fines retained in the sheet. They stated that in the absence of fines, the increased density due to beating has only a small influence on free shrinkage. They also provided experimental evidence confirming that the shrinkage should increase with sheet grammage [26]. The proposed mechanism for this grammage dependance is that fibers located at the sheet surfaces are less efficient at transferring shrinkage forces to other fibers because they can induce longitudinal contraction with other fibers on one side only, and the fraction of all fibers that are located in the surfaces of the sheet diminishes with increasing grammage. They reported that when fines were removed from the sheet, no grammage dependence of free shrinkage was observed.

The purpose of this paper is to better understand the mechanism of free shrinkage during drying by investigating the influence of several softwood (SW) and hardwood (HW) pulp fibers on the free shrinkage of handsheets and the factors that can affect it.

EXPERIMENTAL

Seven commercial once-dried pulps were investigated in this study (**Table I**). Pulps were soaked for 24 h and beaten in a Valley beater according to TAPPI T-200 "Laboratory beating of pulp (Valley beater method)"; samples were taken at regular intervals. Schopper Riegler (SR) freeness of all pulp samples was measured according to TAPPI T-227 "Freeness of pulp (Canadian standard method)". Measurements of fiber geometry of the pulps are summarized in **Table II**. The fines content was obtained using a Somerville fractionator fitted with

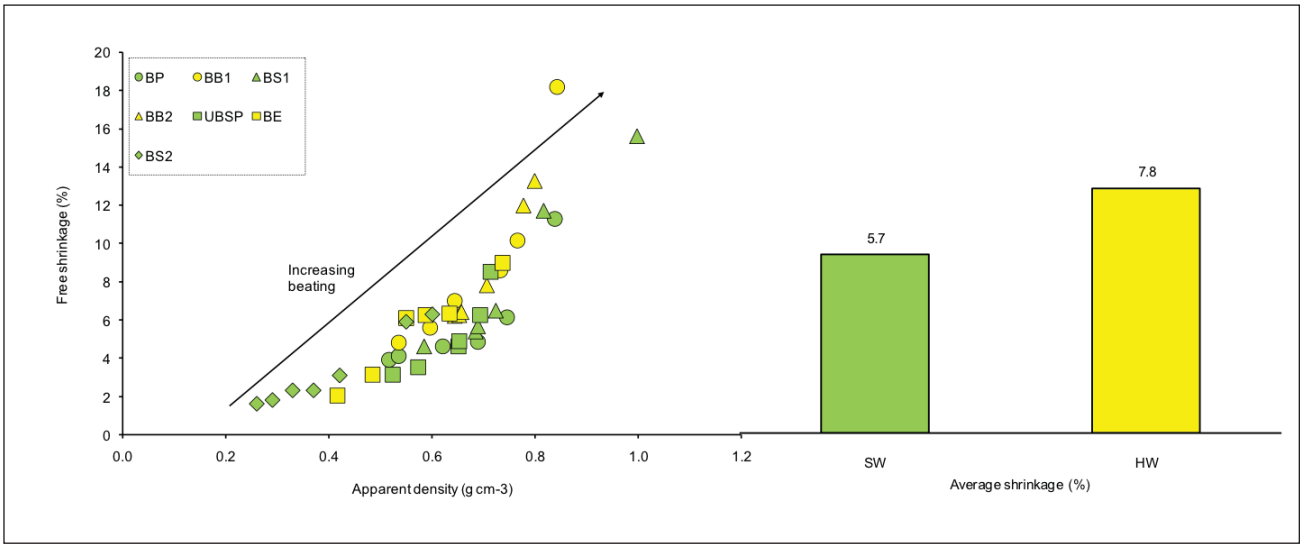
Pulp Samples	Mean Length, mm	Standard Deviation (δ)	Coefficient of Variation (CV)	Mean Width, µm	Standard Deviation (δ)	Coefficient of Variation (CV)	Mean Wall Thickness, µm	Standard Deviation (δ)	Coefficient of Variation (CV)
BP	3.79	0.39	0.10	32.90	6.00	0.18	6.81	0.96	0.14
BS1	4.13	0.59	0.14	32.30	6.76	0.21	4.17	0.54	0.13
BS2	3.63	0.45	0.12	35.70	4.58	0.13	4.46	0.76	0.17
UBSP	4.36	0.57	0.13	47.50	5.55	0.12	8.03	0.30	0.04
BB1	1.02	0.18	0.18	16.20	4.38	0.27	2.19	0.46	0.21
BB2	1.04	0.17	0.17	13.11	2.89	0.22	3.13	0.50	0.16
BE	1.37	0.30	0.22	20.90	3.87	0.19	6.27	0.38	0.06

II. Pulp fiber geometry measurements.

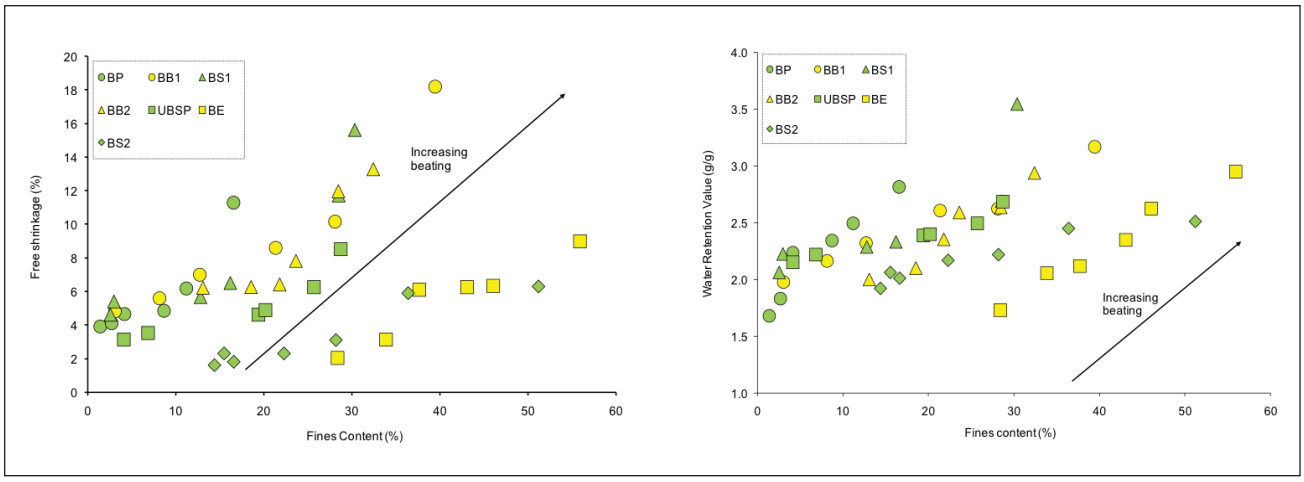
200 mesh screen according to TAPPI UM 242 "Shive content of mechanical pulp (Somerville fractionator)". The WRV of the pulps was determined by centrifugation. Sets of standard handsheets (60 g/m^2) were made from the whole pulp samples in a standard handsheet former and press according to TAPPI T-205 "Forming handsheets for physical tests of pulp". They were then dried and conditioned under controlled temperature and humidity 23 ± 1°C and 50% ± 2% RH for a minimum of 24 h before testing for grammage and thickness. To investigate the influence of grammage on free shrinkage, handsheets were formed with grammage between 20 and 120 g/m^2 for each pulp for three beating times. Their free shrinkage was determined by measuring the distance after free drying between a pair of marks made on a wet sheet after pressing according to TAPPI T-205. For the sheets formed with a range of grammages, the intrinsic density was computed from the gradient of a plot of grammage against thickness. In all cases a linear regression on the data exhibited a coefficient of determination greater than 0.96, confirming that there was no significant effect of grammage on the density of sheets, and hence on the extent of contact between fibers.

RESULTS AND DISCUSSION

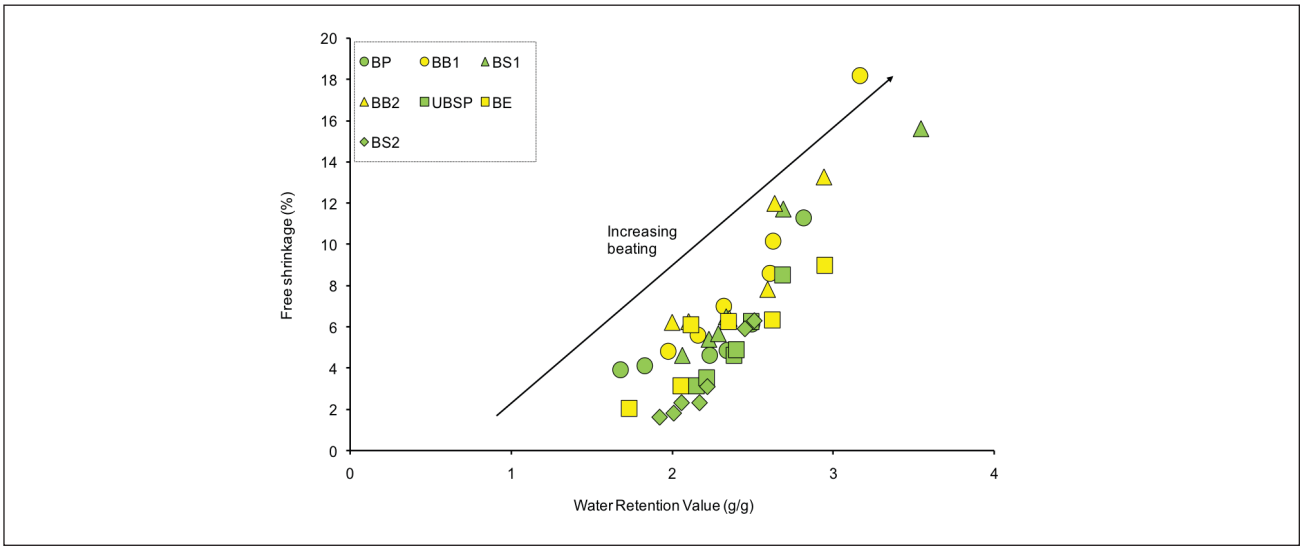
The free shrinkage of 60 g/m^2 handsheets is plotted against apparent density in **Fig. 3**. As anticipated, the free shrinkage increases with apparent density for all pulps. The free shrinkage of Mercer spruce, eucalyptus, and star spruce pulps increases linearly with density, which yields a coefficient of determination greater than 0.942, while the free shrinkage of Lapponia pine, Eno birch, Södra gold birch, and spruce/pine blend pulps increases exponentially with density, which yields a coefficient of determination greater than 0.912. Further, the free shrinkage of HW pulps is a few percent higher than that of SW pulps at a given density (Fig. 3). It is clear that free shrinkage of all pulps gradually increases, about 4%, by increasing apparent density from 0.5 to 0.7 g/cm^3. The Mercer spruce and Eno birch pulps exhibited the highest free shrinkage, 15.6% and 18.2%, respectively, whereas the spruce/pine blend, eucalyptus, and Star spruce pulps exhibited the lowest free shrinkage among other pulps. From fiber geometry measurements, both Mercer spruce and Eno birch pulps have the lowest cell wall thickness, 4.17 and 2.19 µm, respectively. On the other hand, the spruce/pine blend, eucalyptus, and Star spruce pulps have the highest cell wall thickness at 8.03, 6.27, and 4.46 µm, respectively. It is well accepted that fiber wall thickness directly influences fiber flexibility (deformability) [29,31-35], and thereby indirectly influences the development of interfiber bonding. Paavilainen [32] reported that increase in cell wall thickness can decrease fiber collapsibility. Increases in cell wall thickness can affect free shrinkage negatively by reducing the total surface area of the fibers for bonding, as shrinkage forces less transmitted in the sheet. This is in agreement with Nanko and Wu [24], who reported that thick-walled fibers shrank less than thin-walled fibers when the sheet is freely dried. However, when the sheet restrained, the longitudinal shrinkage of thick-walled fibers was more than thin-walled fibers. Also, no meaningful influence of length and width of pulp fibers on the free shrinkage of handsheets is observed. However, it can be stated that the Lapponia pine pulp fiber with the fiber length of 3.79 mm, which is more than triple that of Eno birch pulp fiber length of 1.02 mm, exhibits lower shrinkage, about 7% at the same density of 0.84 g/cm^3 (the last data point in **Fig. 3**). As shown in Fig. 3, there is a very rapid increase in free shrinkage at higher densities for the Eno birch and Mercer spruce pulps. The free shrinkage of the handsheet formed from the Eno birch pulp increases from 10.2% to 18.2%, while the apparent density changes from 0.77 to 0.84 g/cm^3. The SR value changes from 41 to 76.



3. Free shrinkage plotted against apparent density (left); average free shrinkages of softwood (SW) and hardwood (HW) pulps (right). BP = bleached Lapponia pine; BB1 = bleached Eno birch; BS1 = bleached Mercer spruce; BB2 = bleached Södra gold birch; UBSP = unbleached spruce/pine; BE = bleached eucalyptus; BS2 = bleached Star spruce.



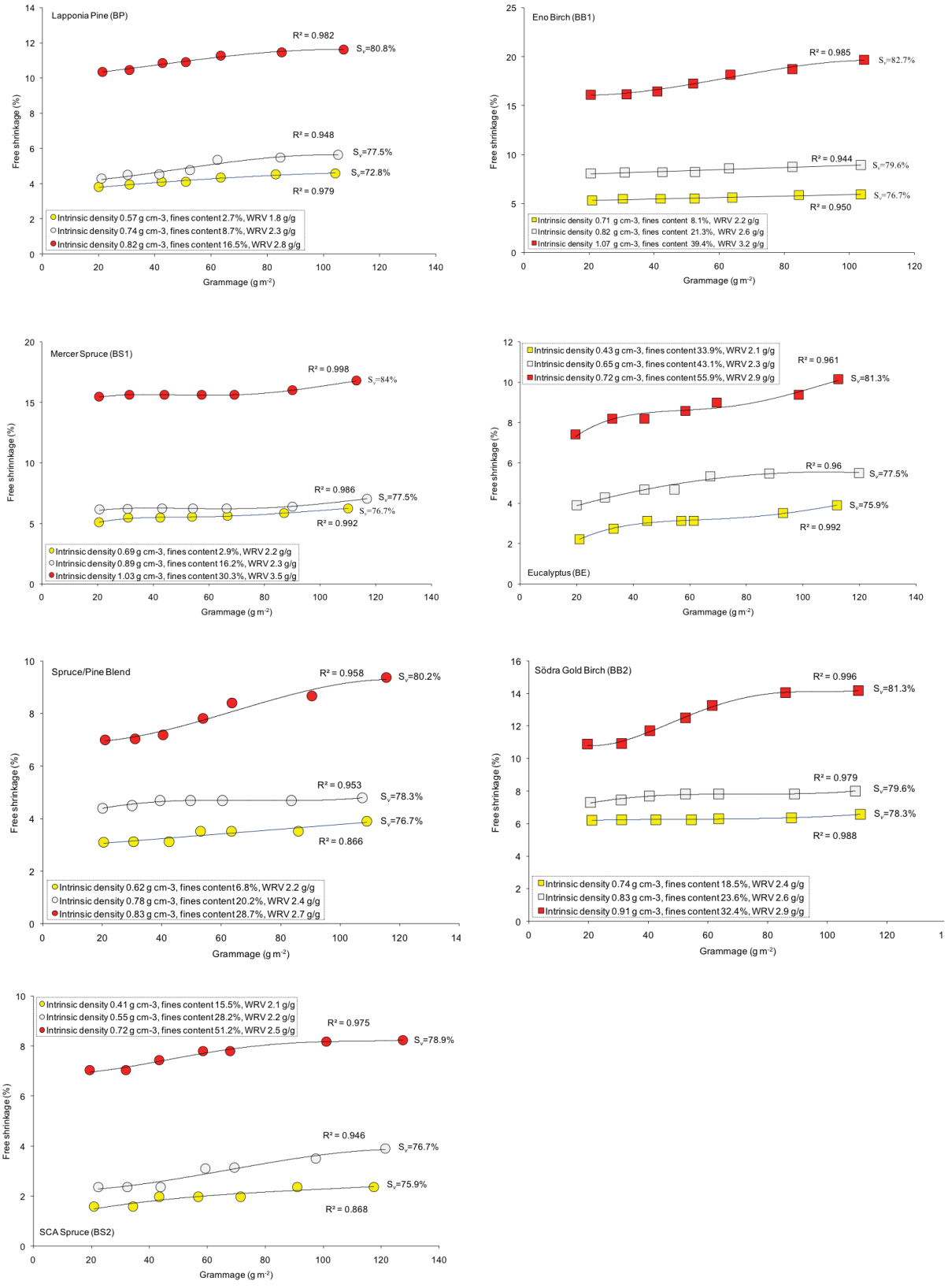
4. Free shrinkage plotted against fines content (left); WRV plotted against fines content (right).



5. Free shrinkage plotted against WRV.

The free shrinkage of the handsheet formed from the Mercer spruce pulp increases from 11.7% to 15.6%, whereas the apparent density changes from 0.82 to 1.00 g/cm^3. The SR value changes from 77 to 86.

Free shrinkage is plotted against fines content in **Fig. 4**. As anticipated, for a given pulp free shrinkage increases with fines content. There are, however, marked differences among the different pulps. For example, the eucalyptus and Star spruce pulps have high fines content, but not particularly high free shrinkage. The Star spruce and Eno birch pulps with the same fines content, 28%, exhibited different free shrinkage, 3.1% and 10.2%, respectively. It can be noted that the high fines content of these pulps has not resulted in particularly high apparent densities. The free shrinkages of the Lapponia pine and Mercer spruce pulps are influenced significantly by the amount of fines retained in the sheet. For the Lapponia pine pulp, for the last two data points in Fig. 4, the free shrinkage increases from 6.2% to 11.3% by increasing the fine contents from 11.2% to 16.5%, whereas for the Mercer spruce pulp the free shrinkage increases from 11.7% to 15.6% by increasing the fines content from 28.5% to 30.3%. It is clear the fines content of the last data point for the Mercer spruce pulp is almost double that of the Lapponia pine. However, the Star spruce pulp with the largest increase in the amount of fines, from 36.4% to 51.2%, which is more than triple that of the Lapponia pulp fines content, exhibits the smallest increase in free shrinkage, from 5.9% to 6.3%. It is the same for the HW pulps. For the last two data points in Fig. 4, the free shrinkage for the Eno birch pulp increases from 10.2% to 18.2%, whereas the fines content changes from 28.1% to 39.4%. For the Södra gold birch pulp, the free shrinkage increases from 12.0% to 13.3%, whereas the fines content changes from 28.4% to 32.4%. On the basis of the last data point in Fig. 4, the Eno birch pulp exhibits 4.9% higher shrinkage compared with that of the Södra gold birch pulp as a result of an increase in fines content, which is 11.3%. However, for the eucalyptus pulp with



6. Free shrinkage plotted against grammage for the handsheets formed from all pulps.

the largest increase in the amount of fines, from 46.0% to 55.9%, the free shrinkage changes from 6.3% to 9.0%.

Figure 4 also shows WRV plotted against fines content. As expected, for all pulps the WRV increases with fines content. Further, there is a good linear relationship between the WRV and fines content of the all pulps ($R^2 = 0.95$), except the Mercer spruce pulp. Because fines can absorb more water, they swell more than fibers. Salmén et al. [30] reported that WRV of fines is greater than that of fibers; this was in agreement with Sampson and Yamamoto [26], who later showed that the WRV of fines is about double that of the fines-free pulp. The dependence of free shrinkage on WRV is shown in **Fig. 5**, which exhibits a strong positive correlation. It is clear that by increasing the WRV from 2.0 to 2.5 g/g, the free shrinkage of all pulps increases around 6%. The Star spruce pulp exhibited the lowest WRV among all pulps. Sampson and Yamamoto reported that the influence of fines on free shrinkage is not attributable to their greater WRV; at most, this is likely to be a second-order effect [26]. Substituting WRV for parameter m in (Eq. 1), a value is obtained for the volumetric shrinkage of a fiber, S_v, of 72% at the lower end of the observed range (i.e., $m = 1.5$, and a value of $S_v = 84\%$ at the higher end of the observed range, $m = 3.5$). So, the relative change in S_v across the range of samples is around 12%, which is insufficient to induce the observed relative change in free shrinkage, which is around 900%. This is in disagreement with the conclusion made by Salmén et al. [30] who reported that the higher shrinkage of sheets containing fines is a consequence of the greater WRV of fines compared to that of fibers.

From Figs. 3 and 4, it is clear that the general dependence of free shrinkage on density and fines content is the same for each pulp, but there is a difference in the absolute values. The effect of grammage on free shrinkage is now considered. Typical data are shown in **Fig. 6**; data were obtained for all pulps. There is little difference between the free shrinkages over the range of grammages at low densities, whereas by increasing the density, a significant difference is observed and it is consistent for all pulps. However, some pulps exhibited very strong grammage dependence, such as the eucalyptus, spruce/pine blend, and Södra gold birch pulps, especially at higher densities. For most of the pulps, the free shrinkage remains almost constant by increasing grammage up to 40 g/m², but when grammage goes higher than this, the free shrinkage increases meaningfully. Further, some pulp samples with different densities and grammages exhibited the same free shrinkage. The Lapponia pine pulp with intrinsic density of 0.57 g/cm³, which corresponds to grammage of 83.1 g/m², has the same free shrinkage, 4.5%, as a sample with intrinsic density of 0.74 g/cm³ and grammage of 30.4 g/m². Another example is the eucalyptus pulp with intrinsic density of 0.43 g/cm³, which corresponds to grammage of 112.1 g/m², that has the same free shrinkage, 3.9%, as a sample with intrinsic density of 0.65 g/cm³ and grammage of 20 g/m².

Comparing the Lapponia pine and Södra gold birch pulps, it is clear that there is little difference between the free shrinkages over the range of grammages for the handsheets formed from the Lapponia pine pulp. The volumetric shrinkages (S_v) of the samples with different intrinsic densities are estimated by substituting WRV for parameter m in Eq. 1. At low intrinsic densities of 0.57 and 0.74 g/cm³, the difference in volumetric shrinkage is 4.7%; however, the difference in free shrinkage is 0.5% at low grammages and 1.1% at higher grammages. For the two samples with intrinsic densities of 0.74 and 0.82 g/cm³, the difference in their volumetric shrinkage is 3.2%, whereas the difference in their free shrinkage is about 6.2%. The difference in free shrinkage in handsheets with densities of 0.57 and 0.8 g/cm³ and 0.74 and 0.82 g/cm³ is almost the same, 6.1% and 6.2%, respectively. The difference in volumetric shrinkage of handsheets with intrinsic densities of 0.57 and 0.82 g/cm³ and 0.74 and 0.82 g/cm³ is different, 7.9% and 3.2%, respectively. Therefore, the influence of WRV is limited. For the handsheets formed from the Södra gold birch pulp, at low densities, there is little or no influence of grammage on free shrinkage, though as density increases, a significant dependence is seen. This is consistent with the findings of Sampson and Yamamoto [26] for pulp with and without fines. Interestingly, for the handsheets with low intrinsic densities, 0.74 and 0.83 g/cm³, the difference in free shrinkage and volumetric shrinkage is almost the same, 1.41 ± 1%.

CONCLUSIONS

Overall, the role of different fiber types on the free shrinkage of handsheets is explored within this paper. The influence of density, fines content, WRV, and grammage on the free shrinkage of handsheets formed from several SW and HW pulps are presented. A nonlinear dependence of free shrinkage on apparent density is observed, though in general the free shrinkage of HW pulps is a few percent higher than that of SW pulps at the same density. Both fines content and WRV have a positive influence on the free shrinkage of handsheets. In spite of the fact that free shrinkage increases with fines content for a given pulp, from volumetirc shrinkage of a fiber, this dependence is not influenced significantly by WRV, which is reported to be greater for fines than it is for fibers. In addition, a high fines content does not imply high shrinkage, as evidenced by the eucalyptus and Star spruce pulps studied here. Considering the fiber geometry measurements, fiber wall thickness is the most influential factor because free shrinkage is strongly affected by it. According to the results, pulp fibers with a thicker cell wall are more resistant to sheet shrinkage, as pulp fibers with a thinner cell wall exhibit higher shrinkage over the range of grammages compared with pulp fibers with a thicker cell wall. The free shrinkage of the handsheets formed from HW pulps at low densities is almost equal to the volumetric shrinkage of that fiber over the range of grammages. This is not consistent for the SW pulps. Finally, free shrinkage of handsheets formed from all pulps is sensitive to sheet grammage. There is a little differ-

ence between free shrinkages over the range of grammages at low densities, whereas by increasing the density, a significant difference is observed and it is consistent for all pulps. It is also found that free shrinkage of handsheets formed from HW pulps is more sensitive to sheet grammage compared with that of SW pulps. In agreement with Sampson and Yamamoto [26], it is observed that the plots of shrinkage against grammage do not pass through the origin. The preliminary understanding is that the longitudinal shrinkage of fibers represents a lower boundary on the shrinkage of the network. Future work is in hand to investigate this hypothesis. It is also found that some of the pulp samples with the same intrinsic density and WRV exhibit different free shrinkage over the range of grammages, which needs to be investigated further. **TJ**

LITERATURE CITED

1. Sampson, W.W., *Int. Mater. Rev.* 54(3): 134(2009).
2. Biermann, C.J., *Handbook of Pulping and Papermaking*, Academic Press, 1996, p. 13.
3. Smook, G.A., *Handbook for Pulp and Paper Technologists*, 2nd edn., Angus Wilde, 1992, p. 264.
4. Keränen, J., Myllys, M., and Kiiskinen, H., *Appita J.* 62(2):146(2009).
5. Lindem, E., *TAPPI Int. Pap. Phys. Conf., Proc.*, TAPPI Press, Atlanta, GA, USA, 1991, p. 327.
6. Niskanen, K., *Paper Physics*, TAPPI Press, Atlanta, 1998, p. 222.
7. Wahlström, T. and Lif, J.O., *TAPPI Int. Pap. Phys. Conf., Proc.,* TAPPI Press, Atlanta, 2003, p. 169.
8. Wadhams, K.R., I'Anson, S.J., James, D.M., et al., *Pap. Technol.* 32(1): 36(1991).
9. Viitaharju, P.H. and Niskanen, K.J., *Tappi J.* 76(8): 129(1993).
10. Hoole, S.M., I'Anson, S.J., Ora, M., et al., *Pap. Technol.* 40(10): 63(1999).
11. Wedel, G.L., *TAPPI Annu. Meet. Proc.*, TAPPI Press, Atlanta, 1989, p. 23.
12. Pulkowski, J.H., *Pulp Pap. Can.* 94(6): 48(1993).
13. Wahlström, T., *TAPPI J.* 31(5): 31(1999).
14. Constantino, R.P.A., I'Anson, S.J., and Sampson, W.W., in *Adv. Pap. Sci. Technol., Trans. Fundam. Res. Symp.,13th*, Pira International, Leatherhead, U.K., 2005, p. 283.
15. Nanko, H. and Oshawa, O., in *Fundam. Papermaking Mater., Trans. Fundam. Res. Symp., 9th*, Pira International, Leatherhead, U.K., 1989, p. 783.
16. Silvy, J., *Paper Technol.* 12(5): 377(1971).
17. Htun, M. and Ruvo, A., in *Fiber-Water Interactions in Papermaking, Trans. Fund. Res. Symp., 6th*, Pira International, Leatherhead, U.K., 1977, p. 477.
18. Htun, M. and Ruvo, A., in *The Role of Fundamental Research in Papermaking, Trans. Fund. Res. Symp., 7th*, Pira International, Leatherhead, U.K., 1981, p. 385.
19. Nanko, H., Asano, S., and Oshawa, J., *TAPPI Int. Pap. Phys. Conf., Proc.*, TAPPI Press, Atlanta, 1991, p. 365.
20. Page, D.H. and Tydeman, P.A., in *The Formation and Structure of Paper, Trans. Fund. Res. Symp., 2nd*, Pira International, Leatherhead, U.K., 1961, p. 397.
21. Hansson, T., Fellers, C., and Htun, M., in *Fundam. Papermaking Mater., Trans. Fundam. Res. Symp., 9th*, Pira International, Leatherhead, U.K., 1989, p. 743.
22. Karlsson, M., *Papermaking Part 2: Drying*, Fapet Oy, Helsinki, 2000, p. 16.
23. Baum, G.A., in *Prod. Papermaking, Trans. Fund. Res. Symp., 10th*, Pira International, Leatherhead, U.K., 1993, p. 1.
24. Nanko, H. and Wu, J., *TAPPI Int. Pap. Phys. Conf., Proc.*, TAPPI Press, Atlanta, 1995, p. 103.

ABOUT THE AUTHOR

I chose this topic to research because free shrinkage is a fundamental property of any paper web. A better understanding of this property of a furnish can lead to a better understanding of the factors affecting cross-machine direction (CD) shrinkage. By investigating the influence of several softwood and hardwood pulp fibers on the free shrinkage of handsheets, this work contributes to a wider understanding of the mechanism of free shrinkage during the drying process.

Obtaining a stable temperature was the key for gaining reliable results from examining the handsheets, which dried freely. To achieve this, I followed the necessary procedures, such as using temperature control devices and making sure air flow was controlled during the drying process in the laboratory environment.

One of the findings was that a high fines content does not imply high shrinkage, as evidenced by the eucalyptus and Star spruce pulp studied. Interestingly, fines content has a positive influence on the free shrinkage of handsheets. However, this is not significantly influenced by their greater water retention value. Free shrinkage of handsheets formed from hardwood pulps is more sensitive to sheet grammage.



Mayeli

This work benefits the industry by providing wider and deeper knowledge about free shrinkage of isotropic paper sheets, which is the main cause of the CD shrinkage profile. The next step is the investigation of the longitudinal shrinkage of fiber on the shrinkage of the network.

Mayeli was a Ph.D. researcher at the University of Manchester, Manchester, UK. Email Mayeli at nader.mayeli@hotmail.com.

25. Salmén, L. and Berthold. J., in *Fundam. Papermaking Mater., Trans. Fundam. Res. Symp., 11th*, Pira International, Leatherhead, U.K., 1997, p. 683.
26. Sampson, W.W. and Yamamoto, J., *Appita J.* 64(1): 76(2011).
27. Nanri, Y. and Uesaka, T., *Tappi J.* 76(6): 62(1993).
28. Vainio, A., Kangas, J., and Paulapuro, H., *J. Pulp Pap. Sci.* 33(1): 29(2007).
29. Uesaka, T., and Moss, C., in *Fundam. Papermaking Mater., Trans. Fundam. Res. Symp., 11th*, Pira International, Leatherhead, U.K., 1997, p. 663.
30. Salmén, L., Boman, R., Fellers, C., et al., *Nord. Pulp Pap. Res. J.* 2(4): 127(1987).
31. Steadman, R. and Luner, P., in *Papermaking Raw Mater., Trans. Fund. Res. Symp., 8th*, Pira International, Leatherhead, U.K., 1985, p 311.
32. Paavilainen, L., *Pap. Puu* 72(9): 689(1993).
33. Broderick, G., Paris, J., Valade, J.L., et al., *Tappi J.* 79(1): 161(1996).
34. Wimmer, R., Downes, G.M., Evans, R., et al., *Holzforschung* 56(3): 244(2002).
35. Pulkinnen, I., Fiskari, J., and Alopaeus, V., *BioResources* 4(1): 126(2009).

ABOUT THIS PAPER

Cite this article as: Mayeli, N. *TAPPI J.* 17(6):317(2018). https://doi.org/10.32964/TJ17.06.317

DOI: https://doi.org/10.32964/TJ17.06.317

ISSN: 0734-1415

Publisher: TAPPI Press

Copyright: ©TAPPI Press 2018

About this journal

Evaluation of the out-of-plane response of fiber networks with a representative volume element model

YUJUN LI, ZENGZHI YU, STEFANIE REESE, AND JAAN-WILLEM SIMON

ABSTRACT: Many natural and synthetic materials have fibrous microstructures, including nonwoven fabrics, paper, and fiberboard. Experimentally evaluating their out-of-plane mechanical behavior can be difficult because of the small thickness compared with the in-plane dimension. To properly predict such properties, network-scale models are required to obtain homogenized material mechanics by considering fiber-scale mechanisms. We demonstrate a three-dimensional representative volume element (RVE) for fiber networks using the finite element method. We first adopted the classical deposition procedure to generate fiber networks with random or preferential fiber orientations and then an artificial compression to achieve the practical fiber volume fraction. The hollow fibers, described with elastic-plastic brick elements, were joined by interface-based cohesive zone elements introduced in all fiber-fiber contact areas. Thereafter, the fiber networks were subjected to displacement boundary conditions, and their apparent mechanical response was evaluated by a homogenized stress. To determine the RVE dimension, we further conducted an RVE size convergence study for the out-of-plane compression and tension (varying specimen length while keeping the specimen thickness constant). Finally, we evaluated the apparent out-of-plane response of the obtained RVE for four loading cases: out-of-plane compression, tension, simple shear, and pure shear. The results show a quite different mechanical behavior of fiber networks between all these out-of-plane loading cases, particularly between tension and compression.

Application: Virtual fiber networks can be generated to evaluate the out-of-plane mechanical properties.

Many biological and synthetic materials have fibrous microstructures, in which natural or artificial fibers are randomly or directionally aligned and bonded together by starch or adhesive material. These materials, such as nonwoven fabrics, fiber mats, paper, and fiberboard, form the structural foundations for various engineering applications. Their mechanical properties essentially depend upon the spatial and mechanical properties of the single fibers and the connectivity of the network referring to fiber-fiber bonds.

There have been extensive investigations on modeling fiber networks, which can be classified into two main categories: phenomenological models and micromechanical ones. Phenomenological models are based on fitting mathematical equations to the observed experimental stress-strain curves. However, these models do not reveal the effect of fiber and bond property variation on the effective stiffness and strength of fiber networks. Additionally, it is usually difficult to experimentally evaluate the out-of-plane mechanical behavior, particularly tension and shear, because the material is so thin. This difficulty is overcome by commonly used micromechanical models. In micromechanical models, geometrical and physical properties are modeled for fibers and bonds separately, which increases the computational cost. The effective material response is then predicted by homogenization of the generated virtual network.

Existing network models are generally reliable to predict the effective mechanical properties of fiber networks qualitatively in the elastic, the visco-elastic, and the elastic-plastic ranges. Within this framework, it is convenient to evaluate the effect of fiber and bond strength variations on the effective stiffness and strength. This kind of network model also provides insight into the detailed deformation at the microscale level, such as strain localization behavior and strength statistics. Accurate estimation of microscale deformation is necessary to increase understanding of the fracture mechanisms, but it also leads to high computational cost. Nowadays, with the increase of the characterization capability of fiber [1-3] and bond [4-8], and increased computing power, micromechanical models have become more and more popular.

Many researchers have adopted this category of methods to study fiber networks in two-dimensional and three-dimensional spaces. They developed different methods to generate the artificial fiber network [9-12]. These methods explicitly took into account the statistical distribution of the fiber orientation and geometry. Here, the fibrous microstructure can be built as a two-dimensional [13-17] or three-dimensional fiber network [9,18,19]. Because two-dimensional network models are relatively easy to build and to analyze, they have been successfully used to predict the in-plane properties. However, several issues lead to the prediction of questionable values for fibrous materials with a two-dimensional model. For instance,

it is impossible to evaluate three-dimensional properties, such as the practical thickness and fiber density of the virtual network. Hence, more realistic fiber networks are generated with three-dimensional models, which also provide a better insight into local deformation fields. Each fiber is represented as a series of beam or solid elements with either solid or hollow cross-section, while the fiber-fiber bonds are considered to be either rigid or flexible.

An alternative approach to predicting the effective mechanical properties of fiber networks is based on the orientation averaging scheme [20-22]. The basic framework to address this problem is first to describe the microgeometries by use of the orientation distribution function (ODF) of the fibers [23], whose parameters can be determined experimentally. Thereafter, orientated averaging of the appropriate tensors is performed, which, in general, can be done via direct analytical or numerical integrations. This orientation averaging method has also been adopted to analyze the hygro-expansive behavior of paper sheets [24] and compressive behavior of nonwoven fabrics [20].

To date, numerous investigations have mainly focused on understanding the in-plane tension and out-of-plane compression behavior of fiber networks. In this work, we have attempted to directly simulate all the out-of-plane loading cases, including tension, compression, and shear. We outline a three-dimensional representative volume element (RVE) for fiber networks, along with the models of fibers and bonds. We then assess RVE size convergence characteristics of the model to determine how many fibers must be considered to obtain statistically relevant results. We also analyze the out-of-plane tension, compression, simple shear, and pure shear.

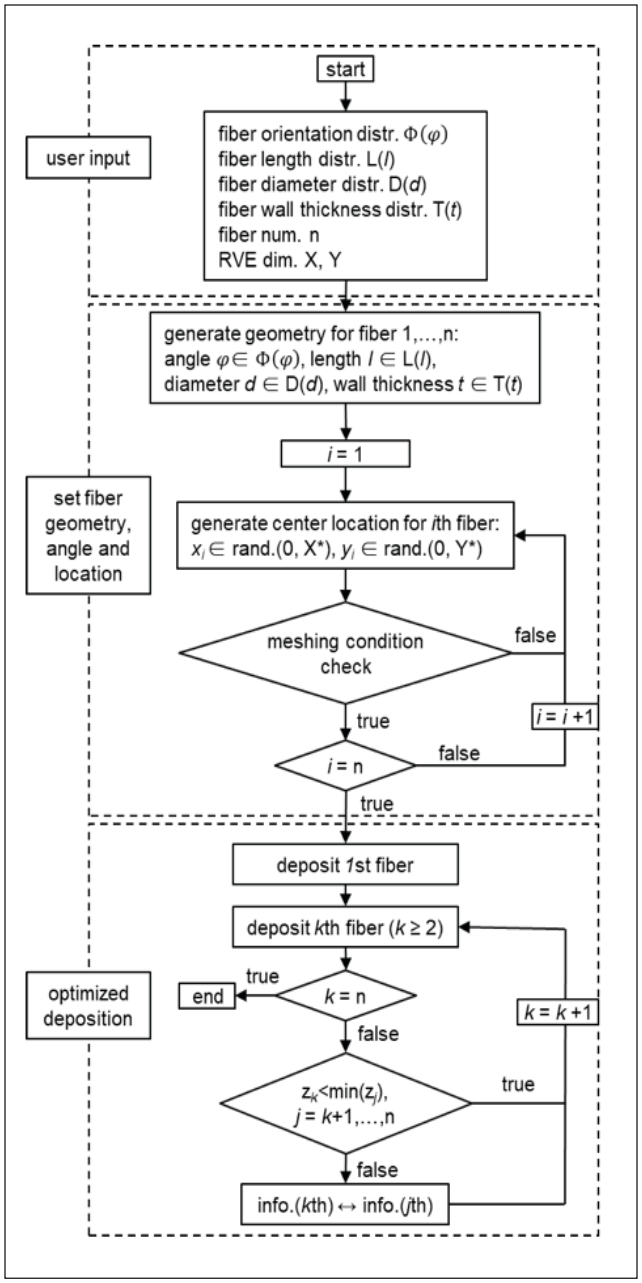
MODEL

To create a link between network-scale parameters and effective mechanical behavior, we created an RVE model. This section presents the method for generating RVE for fiber networks, the implementation of homogenization, and the constitutive models of fibers and fiber-fiber bonds. Finally, we introduce the numerical studies to determine the RVE size convergence characteristics and the parameters we used.

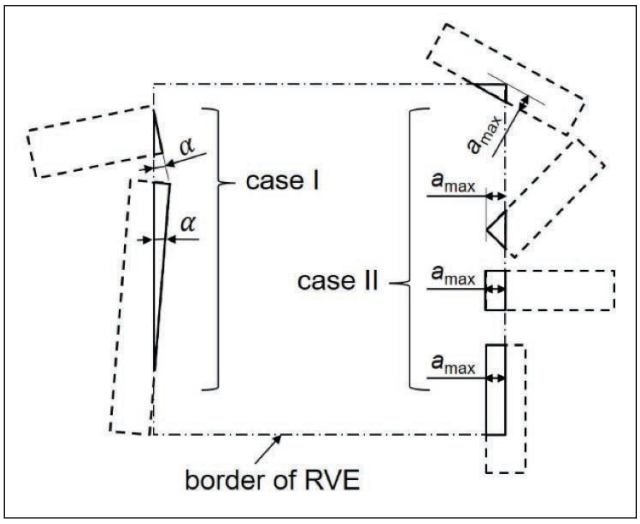
Generation of fiber networks

The thickness of practical fiber networks is typically small compared with their in-plane dimensions. As a consequence, we select the RVE to be large enough along the in-plane directions to represent effective characteristics in a representative manner, but to have the actual layer thickness. The procedure to generate fiber networks includes two steps. At the first step, a generation tool creates a stack of straight fibers with given dimensions and orientation distributions. This tool adopts the classical deposition technique, as shown in the flow chart (**Fig. 1**). Initially, all fibers are constructed according to the statistics provided by the user. These inputs include the fiber orientation distribution, $\Phi(\phi)$; the fiber length distribution, $L(l)$; the fiber diameter distribution, $D(d)$; the fiber wall thickness distribution, $T(t)$ (for hollow fibers); RVE dimensions X and Y; and the desired number of fibers, n. Usually, a Gaussian distribution with a zero mean value is sufficient to describe the orientation information. Then, the in-plane centroid of fiber i (i = 1, …, n) is generated with a uniform probability distribution on a rectangular domain [0, X*] × [0, Y*]. The values of X* and Y* are selected to be larger than the target size of the RVE network at each side. The difference is set to the mean length of fibers:

$$X^* = X + \text{mean}(l_i) \text{ and } Y^* = Y + \text{mean}(l_i) \quad (1)$$



1. Flow chart of the fiber stacking algorithm according to the input data (RVE = representative volume element).



2. Tiny and slim pieces of fiber cut by the RVE border.

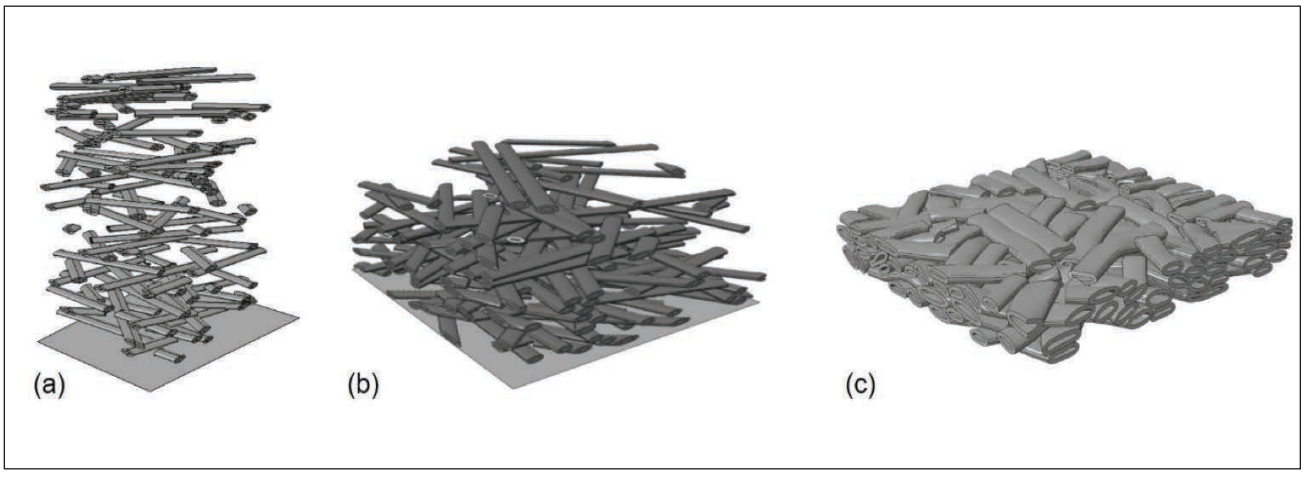
Here, a meshing condition is checked as to whether any tiny pieces of fiber *i* cut by the RVE borders lie within the RVE domain. In this study, the check criterion includes two cases, as shown in **Fig. 2**:

- Case I: a too sharp angle between the fiber and the boundary of RVE ($\alpha < 15°$).
- Case II: a very small part of the fiber (the maximum distance $\alpha_{max} < 0.25d$).

If fiber *i* belongs to one of the cases above, an iterative process works to generate a new random location of the fiber centroid. This relocation procedure is attempted to avoid meshing problems later. It might reduce the fiber volume fraction in the border region, which will be solved by a compression step. Thereafter, we follow a common deposition technique [25] to create the artificial fiber network. During this procedure, the fibers are deposited one by one on a flat surface. Initially, all fibers are parallel to the *x*-*y* surface and positioned randomly in *z*-direction above it. As deposition starts, the fiber *i* lands flat until it contacts the surface or other deposited fibers. The surface gradually becomes covered with fibers.

The aforementioned procedure consists of a geometrical description of fiber, a planar projection, and a crossing search algorithm. To increase the fiber volume fraction of RVE, the fiber deposition sequence is optimized. As shown in Fig. 1, all the possible *z* coordinates of the remaining fibers are detected, and the fiber with minimum value is always selected to deposit first. **Figure 3** (a and b) shows the comparison of generated fiber networks with and without optimization for the same number of fibers. The optimization procedure leads to a significant increase of fiber volume fraction. After deposition, the RVE of target size is trimmed from the larger network. This process eliminates all the fiber pieces out of the boundaries, which admittedly might lead to change of the fiber length distribution within the RVE domain. However, the length distribution within RVE is not the concern of this study; we intend to generate a representative fiber network in the mechanical viewpoint, but not in the geometric viewpoint.

The generated fiber networks still have too low of a volume fraction to represent realistic microstructures. At the second step, the fiber stack is compressed by two rigid shell elements using an explicit finite element (FE) simulation in Abaqus 2017 (Dassault Systèmes Simulia; Providence, RI, USA) until the desired fiber volume fraction is achieved. Here, each fiber gets discretized with a C3D8R element. To retain the RVE planar borders, all the in-plane degrees of freedom of nodes located in the border are constrained. The contact condition with a high friction coefficient is applied between fibers to ensure that the fiber orientation distribution almost remains unchanged. Friction-free contact is used between fibers and rigid shells. In addition, during this visual compression, the final network structure can be handled by assigning an artificial Young's modulus and Poisson's ratio to fibers. Usually, the higher the Young's modulus, the straighter the fiber becomes after compression. The values of 200 GPa and 0.3 are used for these two parameters in the current study.



3. The generated fiber network without (a) and with (b) optimized deposition sequence, and after compression (c).

After compression, all the state variables are set to zero and only the deformed mesh is exported to a second FE model for further deformation analysis. Therefore, no residual stress presents at the beginning of the FE simulation on the obtained RVE. Figure 3c shows an obtained fiber network. Some fibers appear to have a collapsed cross section. Finally, the bonds are created at all fiber-fiber contact areas and the friction contact condition is used for the interaction between internal surfaces of fibers.

Models of fiber and bond

In the current work, for simplicity, the cross section of hollow fibers is described as two concentric ellipses. Depending on the morphology of investigated materials, it can be easily changed to other profiles, such as a solid rectangle for collapsed wood fibers or solid circle for synthetic fibers. In addition, we have to define an appropriate constitutive law for each individual fiber. The actual fibers are usually anisotropic and their deformation is considerably complex, such as wood fiber [26]. However, for an initial numerical study, the applied material model is assumed to be elastic-plastic with isotropic strain hardening. Although the elastic behavior is linear and isotropic, the von-Mises yield criterion is used to describe the onset of yield. The post-yield behavior is characterized by linear hardening. This simplification has also been adopted in some numerical studies on fiber networks[11,12,18].

Furthermore, the damage of fiber-fiber bonds can occur from normal stress and shear stress. To characterize fiber-fiber bonds, the interaction between fibers is described by interface-based cohesive zone elements (CZE) introduced at all fiber-fiber contact areas. The cohesive model is represented by constitutive equations that relate the applied traction to the separation at the interface. As shown in **Fig. 4**, the traction-separation (τ-δ) law is assumed to be linear before damage onset, whereas a linear function also describes the softening region after damage initiation. The irreversible, bilinear single mode is expressed as:

$$\tau_i = \begin{cases} K_i\delta_i & \text{if } \max(\delta_i) \le \delta_i^0 \\ (1-D_i)K_i\delta_i & \text{if } \delta_i^0 \le \max(\delta_i) \le \delta_i^f \\ 0 & \text{if } \max(\delta_i) \ge \delta_i^f \end{cases} \quad (2)$$

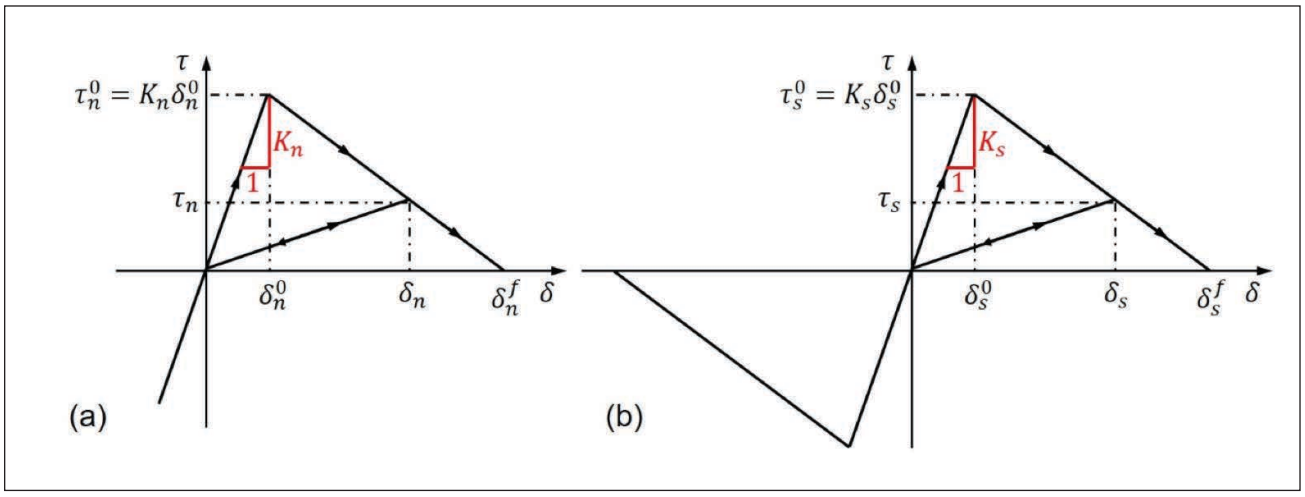
$$D_i = \frac{\delta_i^f(\delta_i - \delta_i^0)}{\delta_i\left(\delta_i^f - \delta_i^0\right)}, i = n, s;\ D_i \in [0,1] \quad (3)$$

where K_i is the penalty stiffness, δ_i^0 is the critical separation corresponding to the maximum traction τ_i^0, δ_i^f is the final separation at complete failure, and D_i is the scalar damage variable representing the overall damage at the interface. The index i can stand for either n (normal direction) or s (in-plane shear direction). Figure 4 also shows the parameters. The value of K_i needs to be high enough to avoid interpenetration of fiber surfaces. D_i has a value varying from 0 to 1 with damage evolution. Figure 4 also includes the linear unloading-reloading paths. The properties required to define the bond behavior are the penalty stiffness, K_n and K_s; the critical separation, δ_n^0 and δ_s^0; and the final separation, δ_n^f and δ_s^f. The critical single mode energy release rates G_{Ic} and G_{IIc} are used in the following:

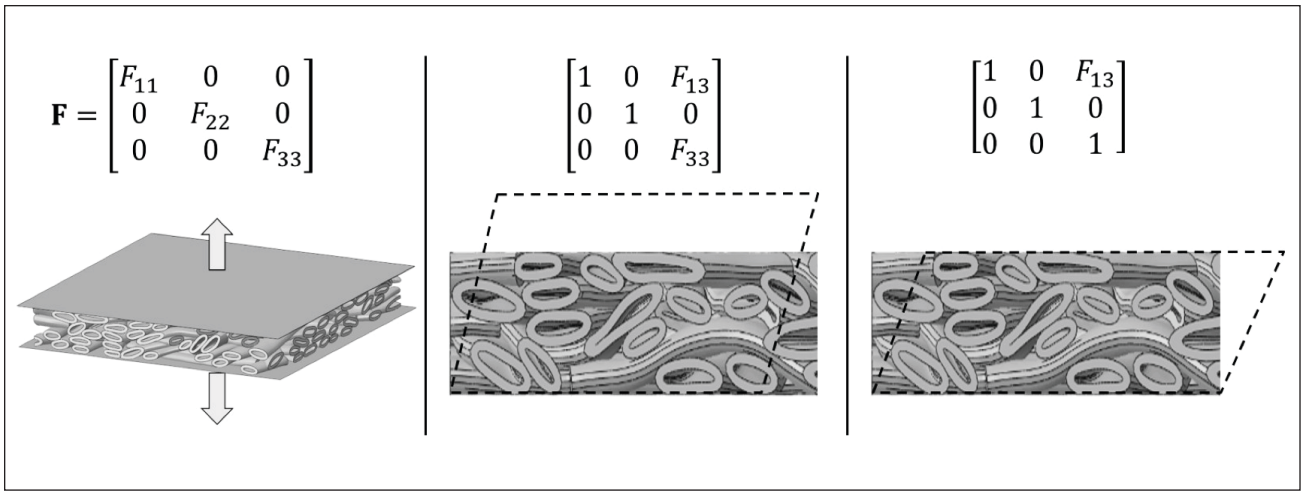
$$G_{Ic} = \frac{1}{2}K_n\delta_n^0\delta_n^f \text{ and } G_{IIc} = \frac{1}{2}K_s\delta_s^0\delta_s^f \quad (4)$$

The upper limit of the critical separation, $\delta_i^0 \to \infty$, renders the model to exclude the following damage behavior at fiber-fiber bonds. In this case, the RVE can mimic the microstructure with perfect bonded fiber networks.

During the deformation of networks, the damage growth at fiber-fiber bond is very likely to occur under mixed-mode loading. Therefore, a general formulation for interface ele-



4. Cohesive zone elements (CZE) traction-separation response: mode I (a) and mode II (b).



5. Three out-of-plane loading cases: uniaxial tension or compression, pure shear, and simple shear.

ments must deal with mixed-mode I/II delamination cases. To take in the interaction between mode I and mode II, a mode mixity is introduced as follows:

$$\beta = \frac{\delta_s}{\delta_n} \text{ for } \delta_n > 0 \tag{5}$$

In addition, the total mixed-mode separation $\bar{\delta}$ is defined as:

$$\bar{\delta} = \sqrt{\delta_n^2 + \delta_s^2} = \delta_n\sqrt{1+\beta^2} \tag{6}$$

By analogy to the single mode, we have the similar traction-separation ($\bar{\tau}$ - $\bar{\delta}$) and mixed-mode damage variable D relations for the mixed-mode I/II delamination:

$$\bar{\tau} = \begin{cases} \bar{K}\bar{\delta} & \text{if } \max(\bar{\delta}) \le \bar{\delta}^0 \\ (1-D)\bar{K}\bar{\delta} & \text{if } \bar{\delta}^0 \le \max(\bar{\delta}) \le \bar{\delta}^f \\ 0 & \text{if } \max(\bar{\delta}) \ge \bar{\delta}^f \end{cases} \tag{7}$$

$$D = \frac{\bar{\delta}^f(\bar{\delta} - \bar{\delta}^0)}{\bar{\delta}(\bar{\delta}^f - \bar{\delta}^0)};\ D \in [0,1] \tag{8}$$

where $\bar{\delta}^0$ and $\bar{\delta}^f$ denote the mixed-mode separation at damage onset and complete failure, respectively, and $\bar{K}$ denotes the mixed-mode penalty stiffness. We assumed that the onset of damage can be predicted using the quadratic failure criterion. Considering that compressive normal tractions do not affect delamination onset, $\bar{\delta}^0$ is given as

$$\bar{\delta}^0 = \begin{cases} \delta_n^0\delta_s^0\sqrt{\dfrac{1+\beta^2}{(\delta_s^0)^2 + \beta^2(\delta_n^0)^2}} & \text{if } \delta_n > 0 \\ \delta_s^0 & \text{if } \delta_n \le 0 \end{cases} \tag{9}$$

For the prediction of total failure in the mixed-mode case, the widely used BK-criterion[27] is adopted. Consequently, $\bar{\delta}^f$ is obtained as:

$$\bar{\delta}^f = \begin{cases} \dfrac{2}{\bar{\tau}^0}\left[G_{Ic} + (G_{IIc} - G_{Ic})\left(\dfrac{\alpha\beta^2}{1+\alpha\beta^2}\right)^\eta\right] & \text{if } \delta_n > 0 \\ \delta_s^f & \text{if } \delta_n \le 0 \end{cases} \tag{10}$$

where η is a mixed-mode parameter. The introduced maximum mixed-mode traction, $\bar{\tau}^0$, is determined as follows:

$$\bar{\tau}^0 = \tau_n^0\tau_s^0\sqrt{\frac{1+\alpha^2\beta^2}{(\tau_s^0)^2 + \alpha^2\beta^2(\tau_n^0)^2}}, \text{ where: } \alpha = \frac{K_s}{K_n} \tag{11}$$

In regard to the derivation on the damage onset and propagation criterions previously mentioned, the reader is referred to detailed discussion published elsewhere [28,29]. In summary, the mixed-mode delamination is treated like single mode damage, which involves only one state variable, the mixed-mode separation variable $\bar{\delta}$. In addition to six material parameters for single modes, one more parameter is introduced to define the mixed mode formula, the parameter η.

After complete failure, the Coulomb's law of friction turns to dominate the interaction between fibers. The friction law is also applied to describe the interface between fibers, which are initially not in contact.

Numerical examples

To illustrate the behavior of the model, several different loading cases were analyzed (**Fig. 5**). A picture of the loading along with the applied deformation gradient tensor, F, are shown for each loading case. Tension and compression loading cases were chosen to determine the minimum RVE size required, because they were able to represent the typical deformation mechanism, i.e., the bond failure and the fiber-fiber contact. This made the convergence more representative for

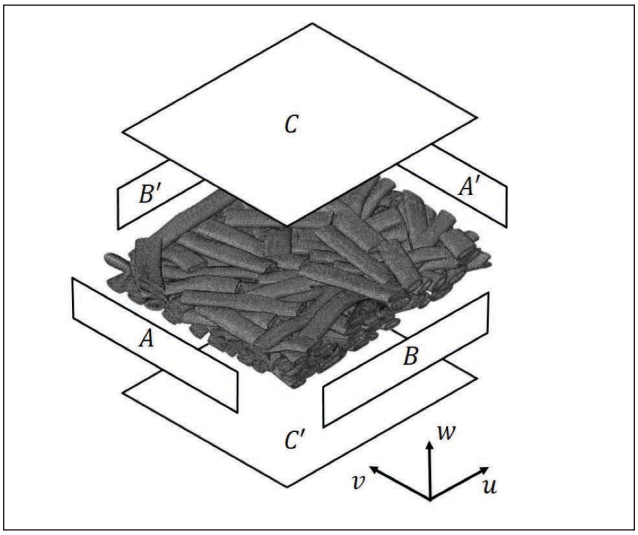
	Compression	Tension	Pure shear	Simple shear
RVE size, X (= Y) [μm]	250, 300, 325, 350, 410, 490		350	350
RVE mean thickness, Z [μm]	54.5, 55.1, 56.5, 54.0, 54.9, 55.1		54.0	54.0
Number of fibers, n	100, 130, 150, 160, 200, 250		160	160
Repetitions per RVE size	5			
Applied deformation	F_{33}		F_{13}	F_{13} and F_{33}
Boundary conditions	$u_A = u_{A,1} = \cdots = u_{A,m_A}$ $u_{A'} = u_{A',1} = \cdots = u_{A',m_{A'}}$ $v_B = v_{B,1} = \cdots = v_{B,m_B}$ $v_{B'} = v_{B',1} = \cdots = v_{B',m_{B'}}$		$v_B = v_{B,1} = \cdots = v_{B,m_B}$ $v_{B'} = v_{B',1} = \cdots = v_{B',m_{B'}}$ $u_C = u_{C,1} = \cdots = u_{C,m_C}$ $u_{C'} = u_{C',1} = \cdots = u_{C',m_{C'}}$ $= 0$	
		$w_C = w_{C,1} = \cdots = w_{C,m_C}$		$w_C = w_{C,1} = \cdots = w_{C,m_C} = 0$

I. Summary of all the simulations (RVE = representative volume element).

different deformation phenomena. These two loading cases were run for six different RVE sizes, with five repetitions for each RVE size. The relative deviation of normal stress was chosen for this work to explore the convergence behavior of the model. In addition, pure shear and simple shear loading cases were tested to investigate the dilation phenomenon and the internal friction effect found in experiments [30].

These two tests were conducted with the converged RVE. All the loadings were tested with one initial fiber volume fraction of 50% because the volume change during loading resulted in a range of volume fractions. **Table I** summarizes the simulations performed with Abaqus 2017 Explicit solver. One related point to consider is the RVE size used. As discussed previously, we aimed to find an appropriate in-plane dimension to be representative while taking the actual thickness of the material. Consequently, the change of RVE size was achieved by varying the number of fibers in this study. The mean thickness of RVE can remain almost unchanged, as listed in Table I. Furthermore, mass scaling was introduced to reduce the computational cost of the explicit model. Careful attention must be paid to the amount of mass scaling used to increase the critical stable time step, but without causing undesired dynamic effects. Its value was set to 50 in the current study.

Because of the high number of contact pairs, the widely used periodic boundary conditions (BCs) probably led to an excessive computational effort in the explicit simulation. Thus, displacement BCs were directly applied to each node at the RVE borders (**Fig. 6**). Here, u, v, and w denote three displacements in the Cartesian coordinate system. Table I shows



6. RVE meshes and notations of RVE boundary (A, A′, B, B′, C and C′ denote the node set at the respective border).

Parameters	Value	Unit
Young's modulus	50000	MPa
Poisson's ratio	0.3	-
Yield stress	150	MPa
Hardening modulus	50000	MPa
Fiber length (mean, std)	(150, 200)	μm
Fiber diameter—major axis (mean, std)	(20, 6)	μm
Fiber cross aspect ratio	2.78	-
Fiber wall thickness	1.2	μm
Penalty stiffness, K_n and K_s	375000	MPa/μm
Critical separation, δ_n^0 and δ_s^0,	4×10^{-4}	μm
Final separation, δ_n^f and δ_s^f	0.4	μm
Mixed-mode parameter, η	1.73	-
Friction coefficient	0.2	-

II. Parameters for fibers and bonds.

the BCs for all the loading cases. In the loading case of compression, the RVE was compressed by two rigid shells while constraining transversal surfaces planar. Therefore, it was possible to detect the lateral expansion from the relative movement between one side (*A* or *B*) and the opposite side (*A'* or *B'*). The friction-free condition was used for the contact between fibers and rigid shells.

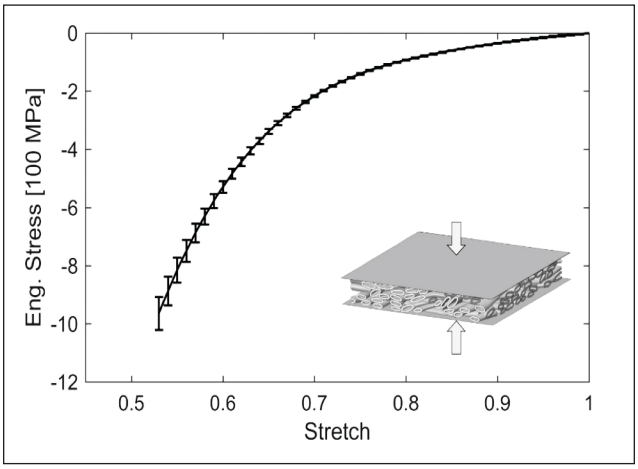
Finally, the homogenized stress was determined by dividing the reaction force on the rigid shell by the initial cross-section area. In the other loading cases, the reaction force used was the sum of nodal reaction forces at the RVE border. **Table II** shows the elastic-plastic fiber properties and geometry, as well as the bonding properties. Because of a lack of experimental data, the fibers were assumed to be isotropic and the remainder of the parameters were set for numerical convenience. Most of experiments indicated different fracture properties of fiber-fiber bonds between the normal direction and the shear direction [7,31]. However, for an initial simulation such as this, the identical values were taken for mode I and mode II.

RESULTS AND DISCUSSION

To determine the minimum RVE size required for accurate results, an RVE size convergence study was conducted for fiber networks under out-of-plane compression and tension. The results of each loading case are shown in individual sections. Each section shows the average response of specimens with $X = Y = 350$ μm and n = 160 fibers, which was chosen because it displayed a response generally representative of the converged response.

Out-of-plane compression

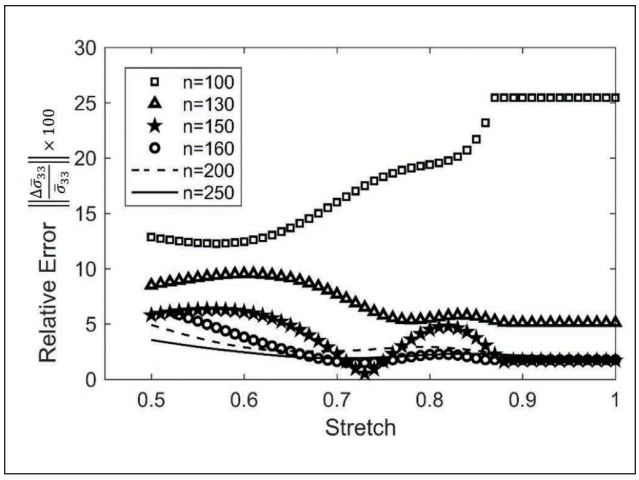
First, the RVE was loaded in compression along the thickness direction. The average homogenized stress, $\bar{\sigma}_{33}$, was the variable used to compare RVEs. **Figure 7** shows a typical response along with standard deviation for specimens under out-of-plane compression. One general observation was that



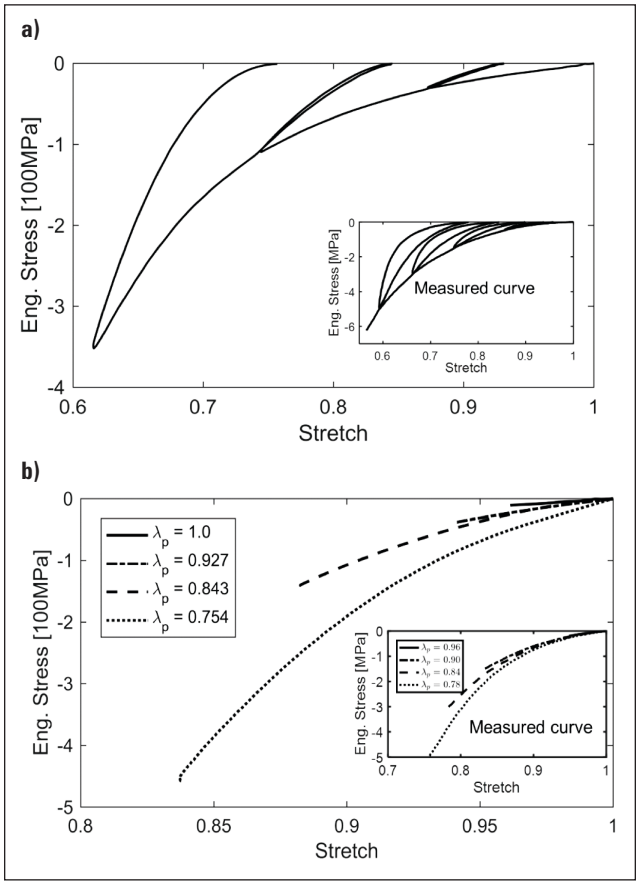
7. Average homogenized stress–deformation ($\bar{\sigma}_{33}$ – F_{33}) curve with error bars of RVE with n = 160 under compressive loading.

the stress rapidly increased with compressive loading, which was associated with the material densification process. **Figure 8** shows the relative standard deviation of the homogenized stress as a function of stretch for different RVE sizes. It appears that the average of the five specimens converges at about n = 160, with the relative error lower than 5%. Larger RVE sizes did not result in any better convergence because of the intrinsic disorder of microstructure.

To further investigate the material densification effect, the RVE was subjected to progressive compressive loading-unloading-reloading sequences. As shown in **Fig. 9a**, pronounced permanent deformation was present after unloading, indicating a typical elastic-plastic behavior. The slope of the stress-stretch curve was relatively high at the beginning of unloading, but decreased rapidly when the stress approached zero. To further study the pure elastic response, the respective plastic deformation was subtracted from the three unloading paths. Figure 9b shows the resulting pure elastic response. Also in-

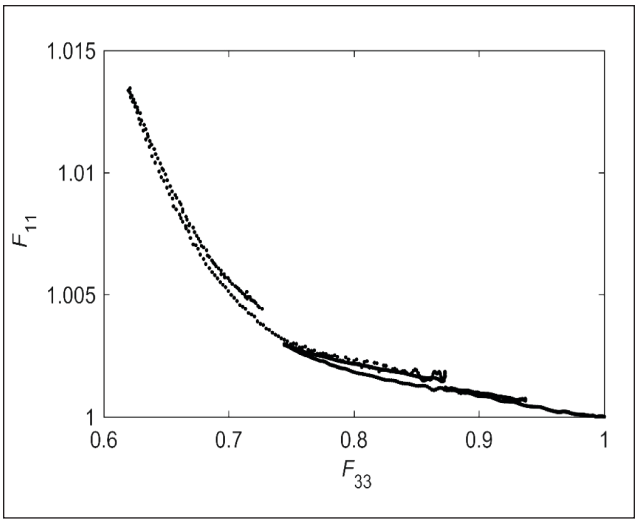


8. RVE size convergence in compression test ($\Delta\bar{\sigma}_{33}$ – standard deviation).



9. Cyclic compression of an RVE with n = 160 along the thickness direction: (a) Stress-deformation ($\bar{\sigma}_{33} - F_{33}$) response upon progressive cyclic compression, and (b) Corresponding elastic stress-deformation ($\bar{\sigma}_{33} - F^e_{33}$) curves after removing plastic deformation.

cluded is the initial loading path of the whole cyclic loading for the convenience of comparison. The elastic response appeared to evolve exponentially because of the densification effect of the network. Figure 9b also indicates the dependence



10. Lateral deformation during compression.

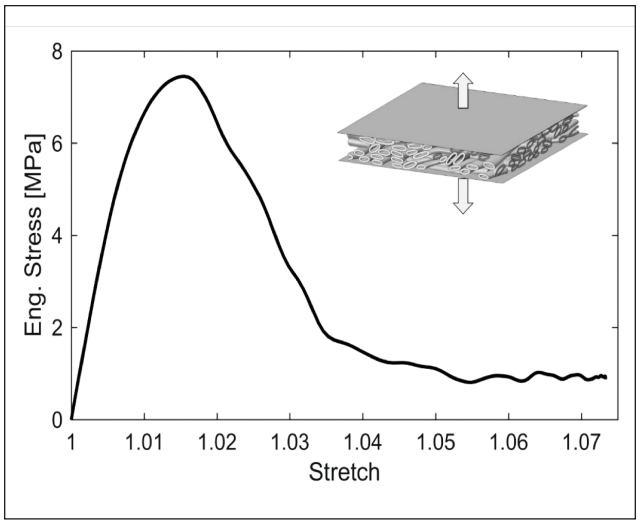
of the elastic response on the permanent densification. With the accumulation of plastic deformation, the elastic stiffness increased greatly. All these plotted stress-stretch curves agree qualitatively with experimental data on paper (Fig. 9) [30,32]. However, the current work has not taken into account the rate-dependent behavior and the kinematic hardening found in wood fiber networks [33,34]. Thus, it failed to predict the observed discrepancies between unloading and reloading paths in experiments (Fig. 9a).

Figure 10 was generated to investigate the lateral expansion during the cyclic compression process. This figure shows a rather small Poisson effect during the elastic deformation range and also a negligible amount of plastic expansion. In other words, the out-of-plane normal stress does not contribute to the in-plane deformation much, which is also supported by the out-of-plane tension. Additionally, it is not necessary to differentiate the engineering stress and the Cauchy stress.

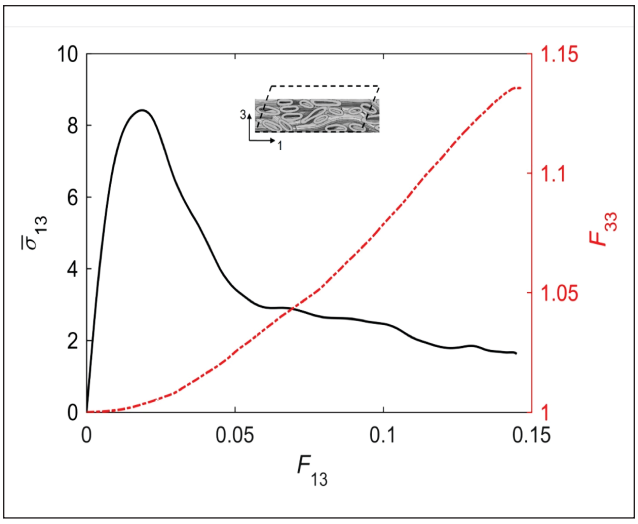
Out-of-plane tension

The second loading case tested was out-of-plane tension. **Figure 11** shows the response typical for this loading case. It shows an initial nearly linear increase of stress followed by a hardening before the peak value, and afterwards a significant softening region up to complete failure at the end of the fiber bridging length. In contrast with compression, this loading case induced the softening range, dominated by the fiber-fiber debonding.

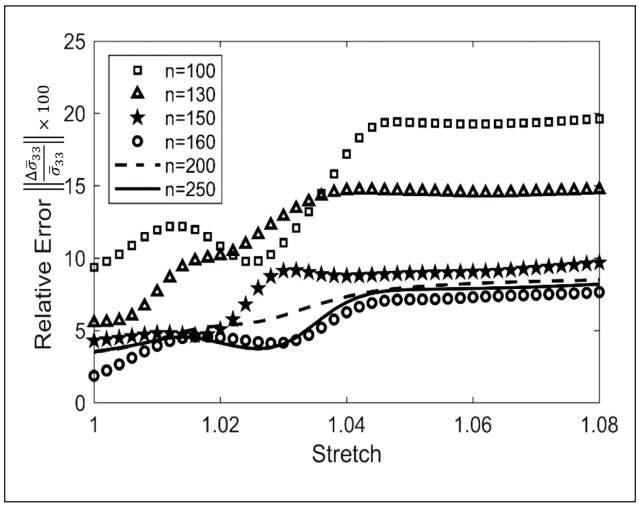
Figure 12 shows the relative standard deviation of the average stress for all RVE sizes. Similar to compression, it appears that the average of the five specimens converges at about n = 160. The relative deviation gradually reaches a local maximum value at the stage of peak load. This might imply that the tensile strength of networks is susceptible to the structure disorder. Furthermore, all RVE sizes show a pronounced fluctuation in average stress at the final stage before complete failure. This is the result of the discrete breaks of fiber-fiber bonds.



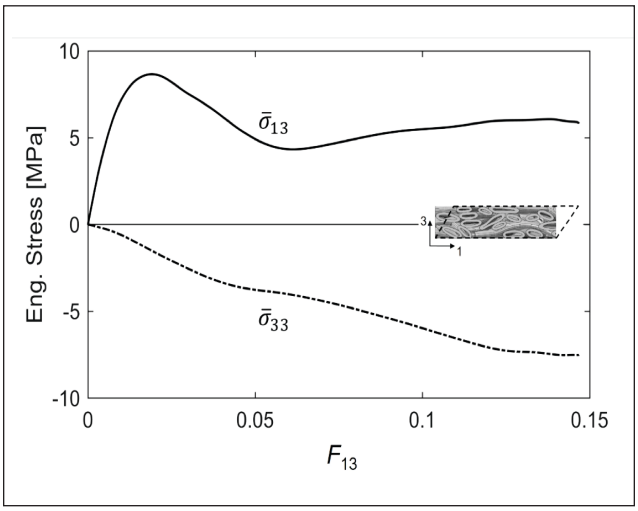
11. Average homogenized stress-deformation ($\bar{\sigma}_{33} - F_{33}$) curve of RVEs with n = 160 under tensile loading.



13. Average homogenized stress-deformation ($\bar{\sigma}_{13} - F_{33}$) curve and average thickness change of RVEs with n = 160 under pure shear loading.



12. RVE size convergence in tension test ($\Delta\bar{\sigma}_{33}$ – standard deviation).



14. Average homogenized stress-deformation ($\bar{\sigma}_{13} - F_{13}$, $\bar{\sigma}_{33} - F_{13}$) curve of RVEs with n = 160 under simple shear loading.

Pure shear and simple shear

Another loading case tested was to apply pure shear in the 1-3-direction. For this loading case, the typical response of RVEs with n = 160 is plotted in **Fig. 13**. The stress-stretch curve shared a similar trend to the previous tensile test. However, maximum average stress and released energy were higher than in tensile loading, although parameters in mode I and mode II took the same values on the fiber scale. This corresponds to the well-known properties of composites, where the fracture toughness is usually higher in shear than in normal opening. One more interesting phenomenon is dilatation along the thickness direction during shear loading, as depicted by the red curve in Fig. 13. Because the fiber-fiber bonds break, fiber networks loosened gradually.

The final loading tested was simple shear in the 1-3 direction. As shown in **Fig. 14**, induced normal stress resulted from the constraint to the dilatation. Furthermore, the stress appeared to increase again after the softening region. This is a combined effect of fiber bridging and internal friction. So the stabilized value of stress greatly depends on the friction coefficient between fibers.

SUMMARY AND CONCLUSIONS

The current study demonstrates a model for fiber networks in which an RVE approach was used to find a response of an equivalent homogeneous continuum. The model was built using finite element methods, where the hollow fibers, described with elastic-plastic brick elements, were joined by interface-based cohesive zone elements introduced in all fiber-fiber contact areas. Furthermore, a deposition procedure was presented to generate fiber networks with any prescribed fiber orientations. A following artificial compression helped to achieve the desired fiber volume fraction.

To explore the size convergence characteristics and the mechanical behavior of RVEs, four out-of-plane loading cases were applied for four RVE sizes with five specimens for each size. The RVE size was varied by changing the number of fibers while keeping the thickness constant. The considered four loading cases included tension, compression, pure shear, and simple shear. In tension and compression, the relative error of average stress was used to judge convergence. The testing showed that the smallest RVE that represented a reasonable response was n = 160.

The current study establishes the framework for a model that can be used for numerous kinds of fiber networks at the individual fiber level and pass the information up to the macro-scale for further analysis. This model is suitable to analyze the out-of-plane deformation, where a model with beam elements shows difficulty. Experimental studies of fiber networks are needed for future validation and characterization of RVE models. One of the major areas of future work is to evaluate the contribution of single fiber and fiber-fiber bond to the effective mechanical response during out-of-plane loading cases. **TJ**

ACKNOWLEDGEMENTS

The author gratefully acknowledges the financial support of the China Scholarship Council (CSC), the Fundamental Research Funds for the Central Universities, and the Ministry of Innovation, Science, and Research of the State of North Rhine-Westphalia, Germany.

LITERATURE CITED

1. Miettinen, A., Ojala, A., Wikstrom, L., et al., *Composites, Part A* 77: 188(2015).
2. Shah, D.U., Schubel, P.J., Clifford, M.J., et al., *Polym. Comp.* 33(9): 1494(2012).
3. Pai, C.-L., Boyce, M.C., and Rutledge, G.C., *Polymer* 52(10): 2295(2011).
4. Fischer, W.J., Zankel, A., Ganser, C., et al., *Cellulose* 21(1): 251(2014).
5. Magnusson, M.S., *Nord. Pulp Pap. Res. J.* 31(1): 109(2016).
6. Hirn, U. and Schennach, R., *Sci. Rep.* 5: 10503(2015), DOI: 10.1038/srep10503.
7. Magnusson, M.S. and Ostlund, S., *Cellulose* 20(4): 1691(2013).
8. Borodulina, S., Wernersson, E., Kulachenko, A., et al., *Nord. Pulp Pap. Res. J.* 31(3): 469(2016).
9. Karakoç, A., Hiltunen, E., and Paltakari, *J., Compos. Struct.* 168: 335(2017).
10. Sliseris, J., Andrä, H., Kabel, M., et al., *Mech. Mater.* 79: 73(2014).
11. Lavrykov, S., Lindstrom, S.B., Singh, K.M., et al., *Nord. Pulp Pap. Res. J.* 27(2): 256(2012).
12. Kulachenko, A. and Uesaka, T., *Mech. Mater.* 51: 1(2012).
13. Lee, Y. and Jasiuk, I., *Comput. Mater. Sci.* 79: 715(2013).
14. Liu, J.X., Chen, Z.T., Wang, H., et al., *Theor. Appl. Fract. Mech.* 55(2): 131(2011).
15. Bronkhorst, C.A., *Int. J. Solids Struct.* 40(20): 5441(2003).
16. Shahsavari, A S. and Picu, R.C., *Int. J. Solids Struct.* 50(20): 3332(2013).

ABOUT THE AUTHORS



Li



Yu



Reese



Simon

The out-of-plane properties of fiber networks are very important in some industry applications. We developed a macro-constitutive model previously, which required the current study to obtain the material parameters.

It is difficult to describe the failure behavior of fiber-fiber bonds. We adopted the interface-based cohesive model to all the interactions between fibers. We developed the network model, which can be used to evaluate the out-of-plane properties.

An interesting finding from this study is that maximum average stress and released energy in shear were both higher than in tensile loading, although parameters in mode I and mode II took the same values on the fiber scale.

Mills can use this method to study the influence of single fiber and bonds on the effective out-of-plane properties of fiber networks.

The next steps in this project are to 1) bring this network model together with our previous macro constitutive model, and 2) take paper as an example to validate this multi-scale method.

Li is assistant professor, School of Mechanical Engineering, Northwestern Polytechnical University, Xi'an, China. Yu is engineer, Schlaich Bergermann Partner GmbH, Shanghai, China. Reese is professor and head of institute, and Simon is composite materials and structures group leader, Institute of Applied Mechanics, RWTH Aachen University, Aachen, Germany. Email Li at li.yujun@hotmail.com.

17. Mao, R., Goutianos, S., Tu, W., et al., *Mater. Des.* 126(Suppl C): 183(2017).
18. Borodulina, S., Motamedian, H.R., and Kulachenko, A., *Int. J. Solids Struct.*, in press.
19. Sliseris, J., Andrä, H., Kabel, M., et al., *Eur. J. Wood Wood Prod.* 75(3): 397(2017).
20. Kumar, V. and Rawal, A., *Mech. Mater.* 78: 66(2014).
21. Bosco, E., Peerlings, R.H.J., Lomans, B.A.G., et al., *Int. J. Solids Struct.,* in press.
22. Bosco, E., Peerlings, R.H.J., and Geers, M.G.D., *Int. J. Solids Struct.* 115–116: 180(2017).
23. Li, Y., Stier, B., Bednarcyk, B., et al., *Mech. Mater.* 92: 261(2016).
24. Bosco, E., Peerlings, R.H.J., and Geers, M.G.D., *Mech. Mater.* 108: 11(2017).
25. Niskanen, K. and Alava, M.J., *Phys. Rev. Lett.* 73(25): 3475(1994).
26. Borodulina, S., Kulachenko, A., and Tjahjanto, D.D., *Comput. Mater. Sci.* 110: 227(2015).
27. Benzeggagh, M.L. and Kenane, M., *Compos. Sci. Technol.* 56(4): 439(1996).
28. Simon, J.W., Höwer, D., Stier, B., et al., *Compos. Struct.* 122(Suppl C): 477(2015).
29. Camanho, P.P., Davila, C.G., and de Moura, M.F., *J. Compos. Mater.* 37(16): 1415(2003).
30. Li, Y., Stapleton, S.E., Reese, S., et al., *Int. J. Solids Struct.* 130-131: 172(2018).
31. Borodulina, S., Kulachenko, A., Galland, S., et al., *Nord. Pulp Pap. Res. J.* 27(2): 318(2012).
32. Girlanda, O., Tjahjanto, D.D., Östlund, S., et al., *J. Mater. Sci.* 51(17): 8131(2016).
33. Alava, M. and Niskanen, K., *Rep. Prog. Phys.* 69(3): 669(2006).
34. Tjahjanto, D.D., Girlanda, O., and Östlund, S., *J. Mech. Phys. Solids* 84: 1(2015).

ABOUT THIS PAPER

Cite this article as: Li, Y., Yu, Z., Reese, S., et al. *TAPPI J.* 17(6): 329(2018). https://doi.org/10.32964/TJ17.06.329

DOI: https://doi.org/10.32964/TJ17.06.329

ISSN: 0734-1415

Publisher: TAPPI Press

Copyright: ©TAPPI Press 2018

About this journal

Using online bubble size and total dissolved solids measurements to investigate the performance of oxygen delignification

RIKU KOPRA, HEIKKI MUTIKAINEN, AND OLLI DAHL

ABSTRACT: The main target of oxygen delignification is to continue delignification that started in cooking in a more selective manner than occurs in the digester (i.e., remove a substantial fraction of the residual lignin using oxygen and alkali at a moderate temperature). Delignification with oxygen is a gentler way of reducing the kappa number than extended cooking. Lowering inlet kappa to bleaching also decreases bleaching chemicals consumption and, because of this, reduces organic wastewater load from bleaching.

We studied the performance of oxygen delignification by installing bubble size imaging systems and refractometers, which measure dissolved dry solids in the oxygen stage feed. Based on these measurements, we gathered information about gas dispersion (bubble size distribution) and the behavior of dissolved matter in the hardwood mill's oxygen delignification stage. Our goal was to investigate the effects of different variables on the oxygen stage's gas dispersion, kappa reduction, yield, and pulp quality. Gas dispersion improved (i.e., average bubble size decreased) when the chemical mixer speed increased. Increasing the mixer speed and the amount of oxygen yielded higher kappa number reductions and increased the amount of dissolved organic matter.

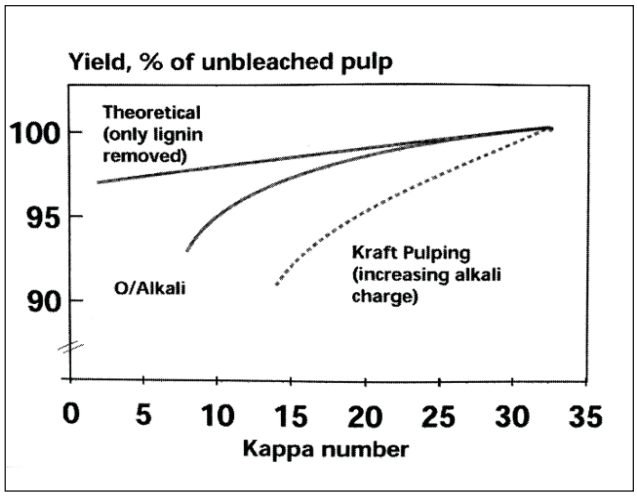
Application: Methods described here could help mills adjust the oxygen charge and gas dispersion in delignification processes and allow for future monitoring and controlling of the oxygen process.

In the late 1970s, medium-consistency mixing technology became available and the new high-shear mixing devices made it possible to efficiently disperse oxygen as very small bubbles in 10%–14% consistency pulp. Thus, most of the oxygen delignification systems installed today are medium-consistency ones. The main reasons for the interest in medium-consistency applications are lower capital costs, greater ease of stock handling with medium-consistency mixing and pumping technology, and improved selectivity in the presence of appreciable amounts of black liquor solids [1].

The process is very flexible, and is best viewed as a "bridging strategy" between cooking and final bleaching. The method and degree to which oxygen delignification is applied involves a comprehensive optimization of the fiber line process, considering total cost, pulp quality, and environmental impacts.

Process variables, such as the consistency of pulp, temperature, pressure, amount of alkali, amount of oxygen, and washer losses, and inhibitors, such as magnesium salts, influence the performance of oxygen delignification. Agarwal et al. in 1999 [2] stated that consistency has no major effect on kappa reduction if mixing is sufficient. However, in an industrial environment, neither mixing nor mass transfer is perfect. Elton et al. in 1980 [3] showed that higher consistency results in lower diffusion distance and higher alkali concentration at a given alkali charge.

Alkalinity and temperature are the most important factors affecting delignification during the oxygen delignification process. Although molecular oxygen has high electronegativity, it is a mild oxidizing agent for lignin because of its normal electronic configuration (i.e., its triplet state). Therefore, the reactivity of oxygen for delignification is intensified by increasing the reaction temperature or the alkali dosage. The limitation of oxygen is actually a diffusion limitation from the gas into the fiber. In addition, decreasing bubble size actually increases the surface area available for diffusion. The oxygen charge has a less important role than the alkali charge and temperature. Even so, a sufficient amount of oxygen must be present during the process to achieve a decent degree of delignification. However, increasing the oxygen charge too much can provoke the formation of larger gas bubbles and channeling through the tower, which again decreases the effectiveness of the oxygen delignification. Higher pressure helps diffuse the oxygen, and only the dissolved oxygen can react with the phenol groups of the lignin. The organic substances dissolved in cooking create side reactions during the oxygen stage. This causes additional oxygen consumption and degra-



1. Comparison of yield selectivity between extended cooking and oxygen delignification [4].

dation of cellulose chains. An increase in washing loss before the oxygen stage causes reductions in pulp viscosity, strength, and yield. Correspondingly, efficient post-oxygen washing is the key for low-cost bleaching. Magnesium salts in the softwood process improve the selectivity of the oxygen delignification and result in higher viscosity at a given kappa number.

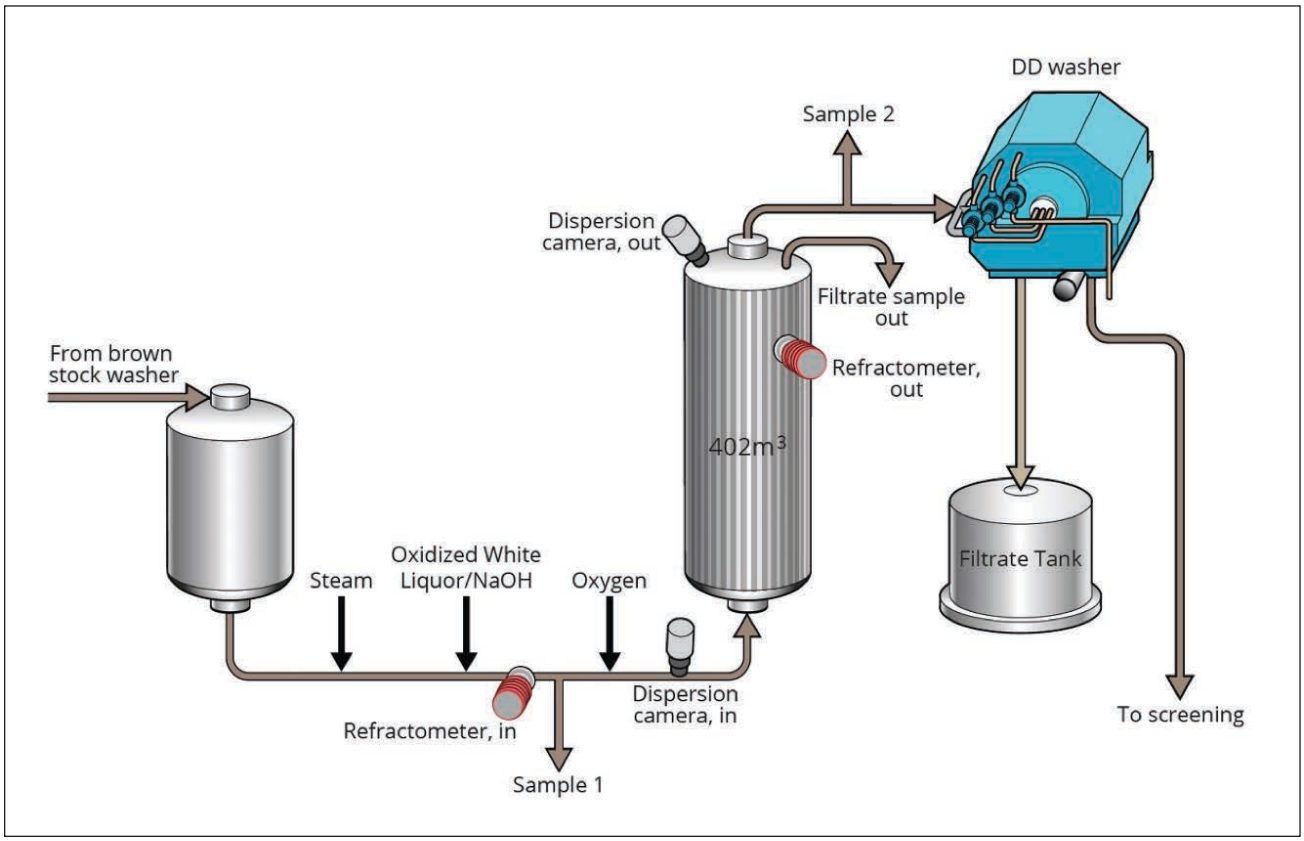
The effectiveness and potential of a powerful oxygen stage is obvious when comparing it with cooking and bleaching using a yield vs. kappa number curve, as can be seen from **Fig. 1** [4]. According to Gullichsen et al. 1992 [5], removing 1 kappa unit in cooking, decreases the yield by 0.16%, whereas removing 1 kappa unit in oxygen delignification decreases the yield by 0.12%.

The purpose of this work was to study the effects of process conditions on the dissolved solids, kappa, and pulp quality, and to quantify the state of gas dispersion in the process and the effects of oxygen bubble size on different factors.

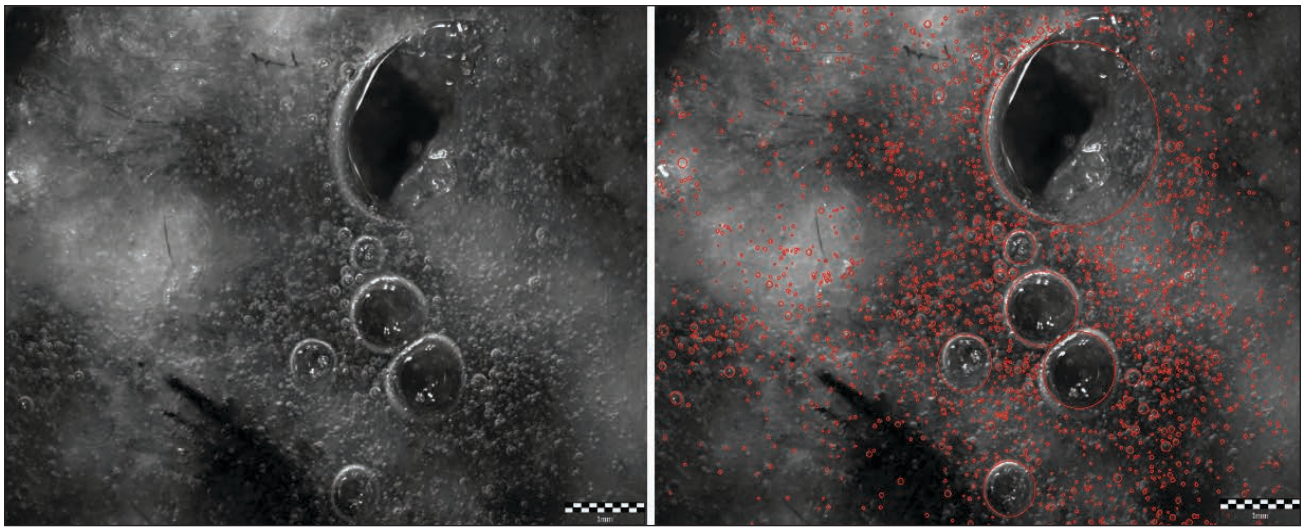
MATERIALS AND METHODS

The study was carried out by installing two continuous refractometers that measured the concentration levels (i.e., total dissolved solids [TDS]) of filtrates in the oxygen stage feed and at the top of the reactor in a Finnish hardwood kraft pulp mill (**Fig. 2**). Data from these two measurements allow us to calculate the reactor's residence time and oxygen stage's pulp yield. Simultaneously, gas dispersion was monitored in real time using a continuous Pixact Bubble Monitoring (PBM) system (Pixact Ltd.; Tampere, Finland). PBM was used to evaluate the oxygen gas dispersion, which is connected to the mixing efficiency of used oxygen charge into pulp suspension. The principle behind the PBM system was presented in detail in an earlier study [6].

A complete 2-week mill trial was performed. The alkali



2. Installation sites of the refractometers and Pixact Bubble Monitoring (PBM) systems in the pulp mill's oxygen delignification (NaOH = sodium hydroxide; DD = drum displacer).



3. a) Original image of bubble flow illuminated with ring light, and b) the detected bubbles are circled with red outlines on top of the image [6].

used in the first test week was oxidized white liquor. During the second week of testing, fresh caustic (14% sodium hydroxide) was used. Three oxygen dosages were used (5 kg/a.d. metric ton, 6.5 kg/a.d. metric ton, and 8 kg/a.d. metric ton) at three different mixer rotation speeds (1000 rpm, 1088 rpm, and 1175 rpm), three operating pressures (280 kPa, 330 kPa, and 380 kPa), and three reactor temperatures (90°C, 92.5°C, and 95°C). Consistency was quite stable, at about 11%, and the alkali dosages were controlled so that the pH was about 10.5 in the discharge of the reactor. In test week 1, we had 10 test points and in week 2, we had 15 points.

Pulp samples were taken from the oxygen stage feed pulp (sample 1) and after the oxygen reactor (sample 2), as denoted in Fig 1. The kappa number was measured from the pulp samples. The filtrate sample was also extruded from the pulp through wire gauze after sampling. The pH, conductivity, and chemical oxygen demand (COD) were measured from the filtrates. The samples were analyzed using the following methods:

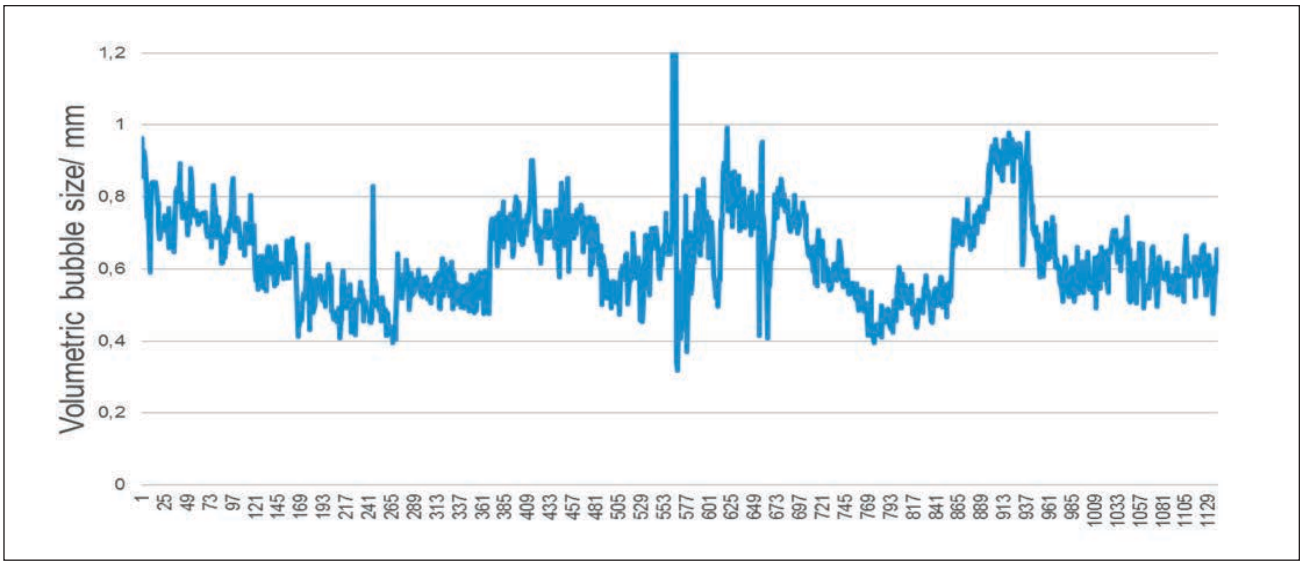
- Determination of dry matter content (analytical) (ISO 638 "Paper, board and pulps — Determination of dry matter content — Oven-drying method")
- Determination of dry matter content (on-site), refractometer
- Conductivity (on-site), Mettler Toledo conductivity meter (Columbus, OH, USA)
- pH (on-site), Mettler Toledo conductivity meter
- COD liquor, samples filtrated using 1.6 μm grade GF/A paper and then analyzed in a COD analyzer (ISO 15705 " Water quality — Determination of the chemical oxygen demand index [ST-COD] — Small-scale sealed-tube method")
- Pulps, determination of kappa number (ISO 302 "Pulps — Determination of Kappa number")

RESULTS AND DISCUSSION

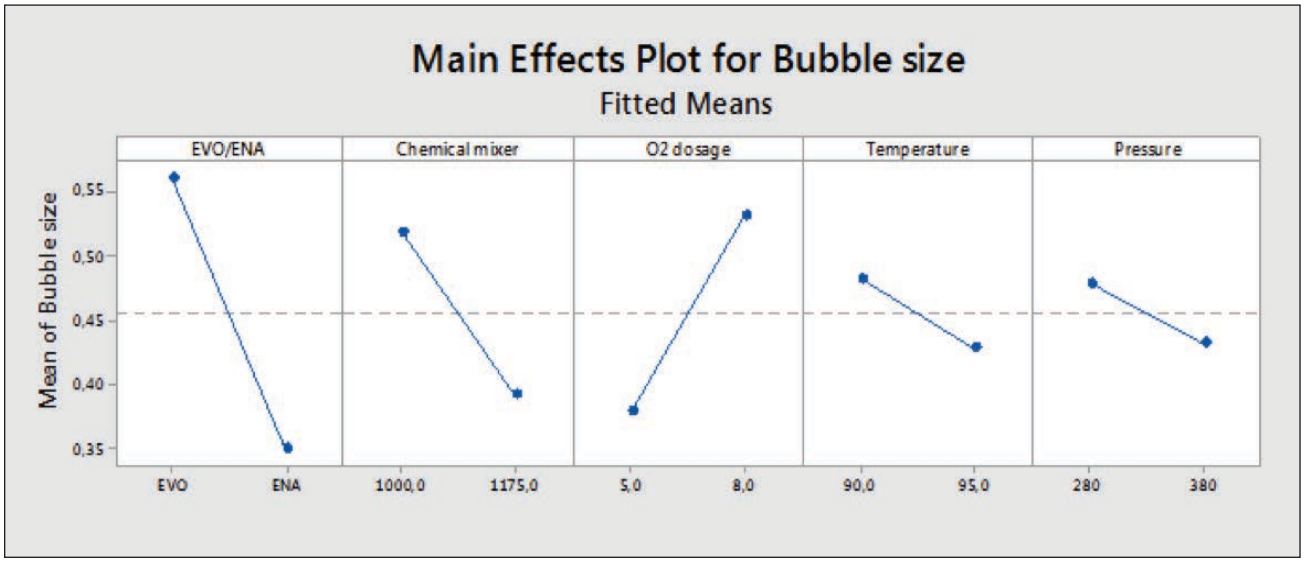
Continuous PBM system

We used an image analysis algorithm developed by Pixact Ltd. to detect gas bubbles and measure their diameters. **Figure 3a** shows an original image of the bubble flow [6]. Figure 3b shows the detected bubbles. The bubble size data produced by PBM are averaged over 60 s and reported every 30 s to the mill's data collection and as a row in an Excel file. The data include numerical, Sauter diameter, and volumetric distributions of bubble size and other relevant statistical values, such as mean and standard deviation values; percentiles of D10, D50, and D90 of the distributions; and number of bubbles per image. This makes it possible to calculate and monitor different bubble size fractions under different process conditions.

Figure 4 [6] shows the volumetric bubble size measured over the 1.5-month period. The measurements and pictures obtained (Fig. 3) indicate that gas distribution in this hardwood pulp suspension was not as homogeneous as in the softwood pulp suspension observed earlier [7]. There happened to be several very large bubbles, which were also irregularly shaped and could not be measured accurately. However, the average arithmetic bubble diameter was 48 μm under typical process conditions and the average volumetric bubble diameter was around 500 μm. The arithmetic bubble diameter is approximately equal, but the volumetric average diameter is 10 times higher than the measurements made on the softwood pulp line [7]. Figure 4 also displays the short-term and long-term variation in the average volumetric bubble size, ranging from 0.4 mm to 1 mm. This means that the surface area of the bubbles enabling the dissolution of oxygen changes in the same ratio. The existence of large bubbles also might promote the coalescence and uneven distribution of oxygen in the pulp. The mill has been in a normal production state, including typical process variations: production, chemical dosage, pulp consistency, etc.



4. Volumetric bubble size after the oxygen mixer on a Finnish hardwood pulp fiber line during a measuring period of 1.5 months [6].



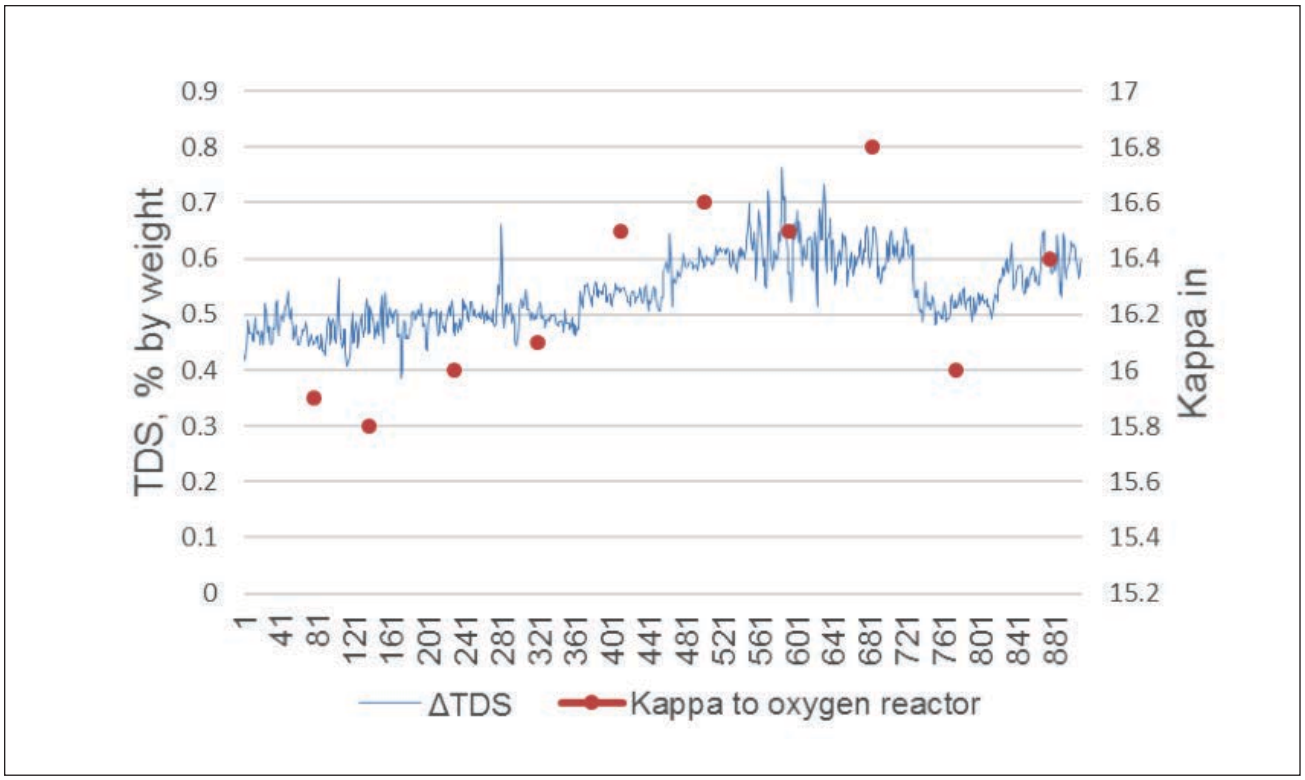
5. Results from the factorial analysis, main effects plot for bubble size (EVO = oxidized white liquor; ENA = sodium hydroxide) [6].

The results from the factorial analysis (**Fig. 5**) [6] confirmed that all the trial factors had a statistically significant effect on the bubble size. The effect of the alkali form (EVO = oxidized white liquor and ENA = sodium hydroxide) was the most significant, but the rotor speed of the chemical mixer also had a remarkable effect, even with a small increase from 1000 rpm to 1175 rpm. The results from the factorial analysis also confirm the assumption that the measuring method is able to measure the effect of mixing efficiency and other process parameters on the state of dispersion.

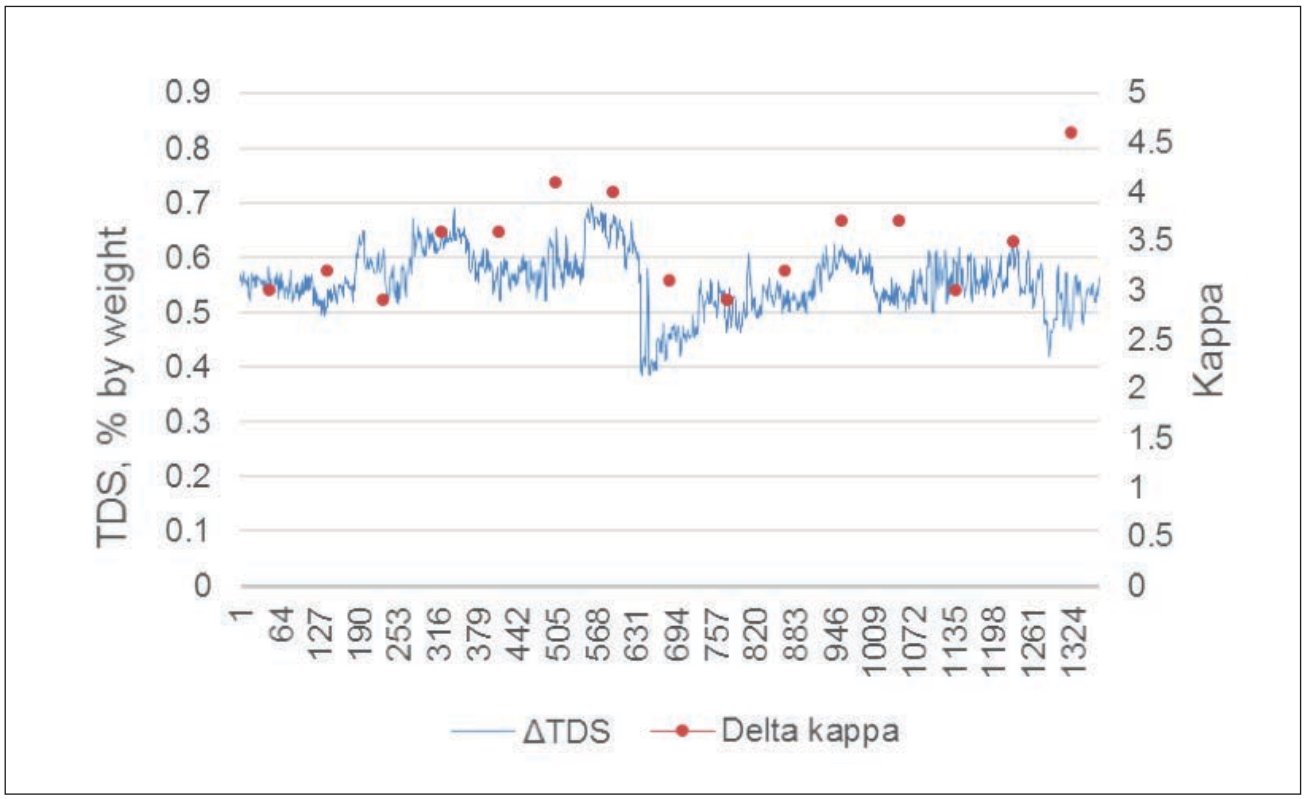
Total dissolved solids (TDS) measurement by process refractometer

The refractometer measurements allowed us to calculate the change in the dissolved solids within the oxygen reactor. As the figures illustrate, this correlated clearly with the oxygen delignification feed kappa (**Fig. 6**) [8] and changes in kappa (**Fig. 7**) [8]. Changes in temperature also clearly affected the behavior of dissolved solids (**Fig. 8**) [8].

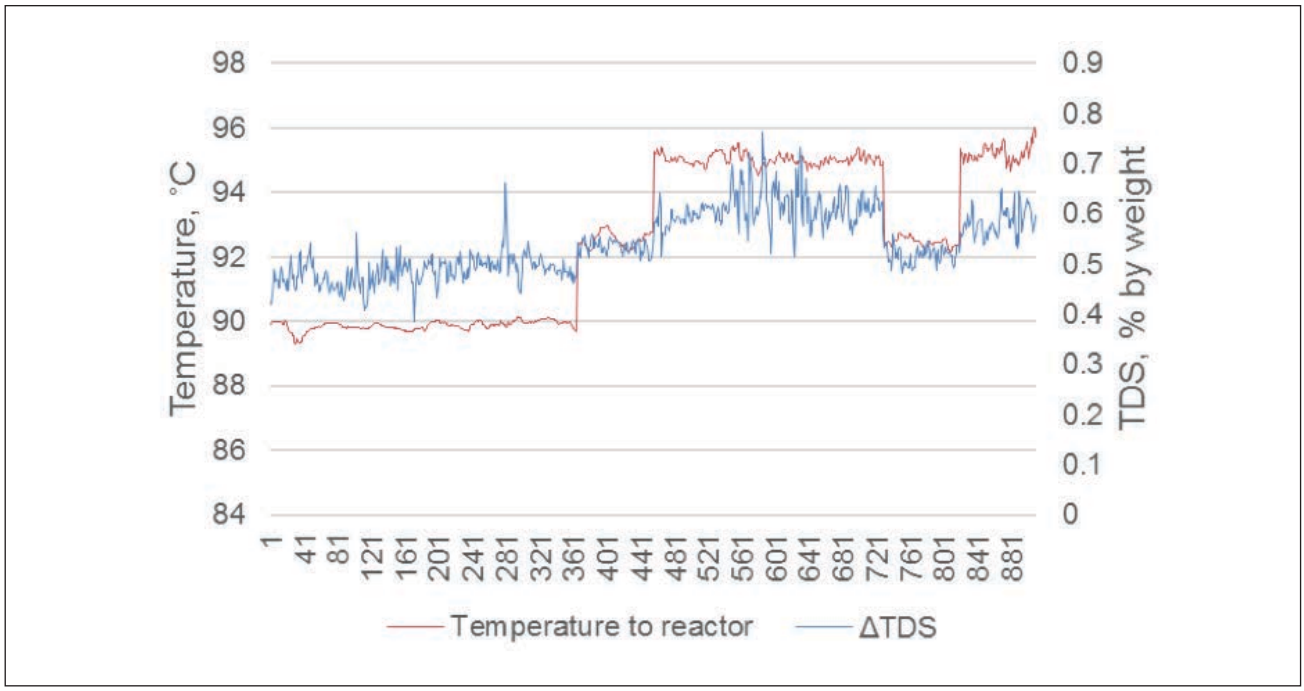
As expected, the medium consistency (MC) mass flows were plug flow in the oxygen reactor. Gas flows, however, might find an easier passage for themselves, which leads to their channeling. Dissolved solids in the liquid phase will also be seen to pass in a plug-flow like way. Measuring the TDS before and after the oxygen stage and aligning these two measurements allows us to calculate the reactor's residence time. **Figure 9** [8] shows how the residence time calculation was carried out using TDS measurements. The average residence time, when pulp goes from measurement point 1 to point 2, was 36 min. The larger differences in the graphs



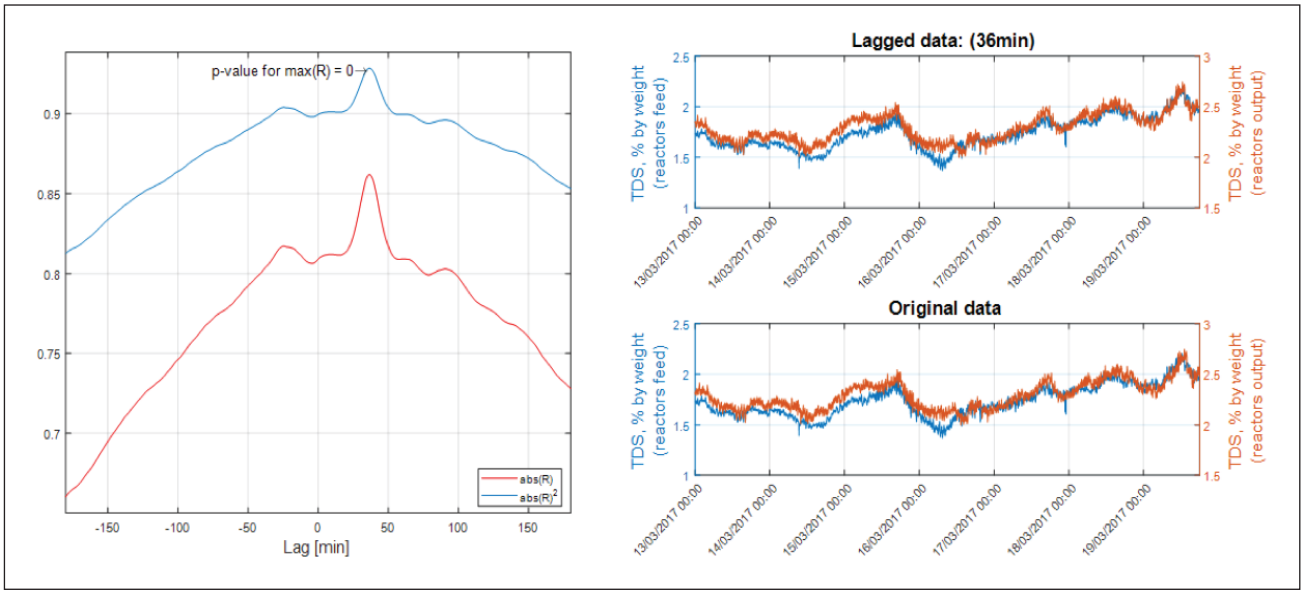
6. ΔTDS (total dissolved solids) and kappa$_{in}$ to oxygen reactor (test week 1) [8].



7. ΔTDS (total dissolved solids) and Δkappa$_{in}$ to oxygen reactor (test week 2) [8].



8. Temperature and ΔTDS to oxygen reactor (test week 1) [8].



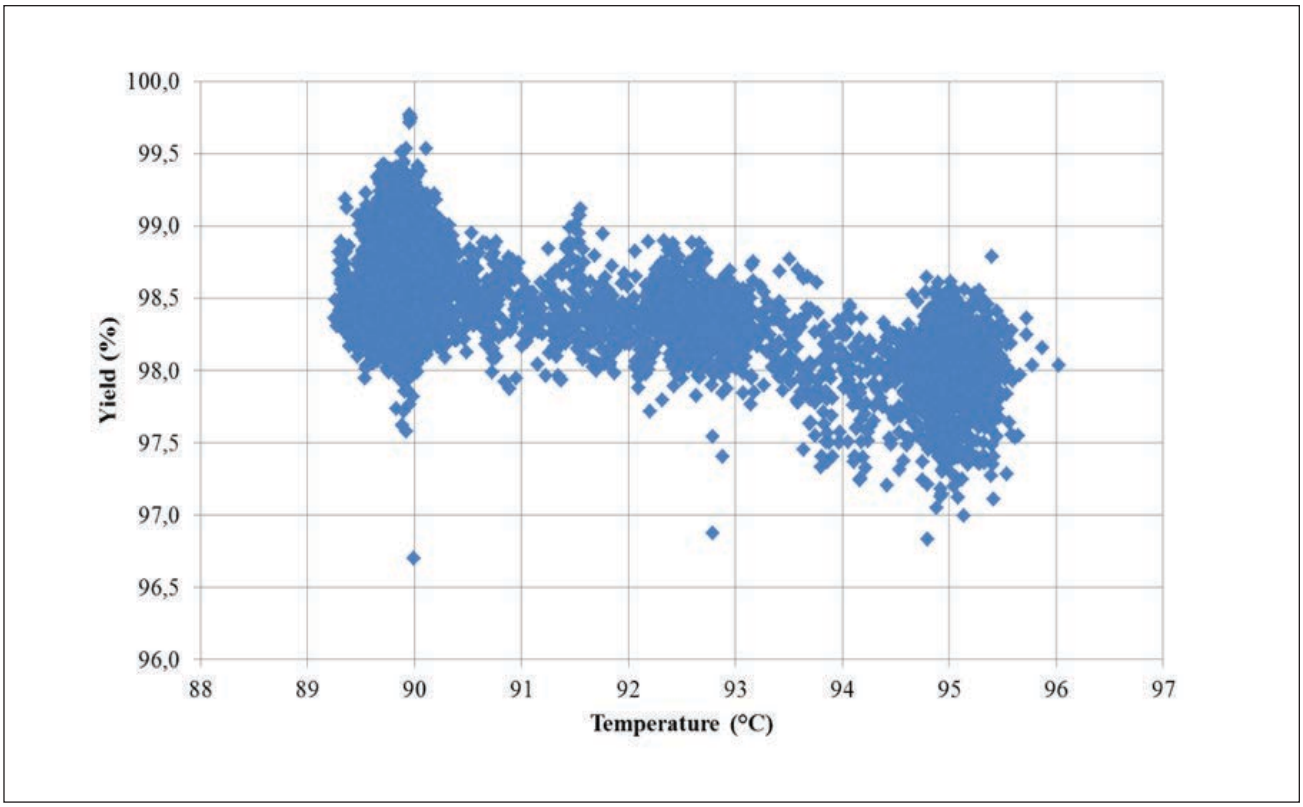
9. Calculation of the oxygen stage time delay [8].

represent changes in production levels and times when the delay deviated from the average delay of 36 min. The results were consistent with the delays calculated from the oxygen stage feed.

The measurements, alongside additional measurements and calculation, allow us to calculate the oxygen stage pulp yield. **Figure 10** [8] shows the yield as a function of reactor temperature. The pulp yield seems to decrease when the reactor temperature increases. We did not observe an increased kappa drop as a function of temperature. A lower temperature leads to an increased pulp yield in oxygen delignification, which leads to lower wood consumption. The level of the pulp yield is lower, which would be expected based on the literature [5].

CONCLUSIONS

The PBM system can be used for continuous monitoring of gas dispersion in oxygen delignification. In addition to the improvement of general knowledge related to the process, this method could form the basis for adjusting the oxygen



10. Oxygen stage pulp yield calculation as a function of temperature [8].

charge and gas dispersion in delignification processes.

TDS measurements at the oxygen stage feed and at the oxygen reactor outlet allow us to calculate the changes in dissolved solids within the oxygen reactor (delta concentration) and provide a new way of calculating the residence time in the oxygen reactor, as well as pulp yield. Measurements at the oxygen stage feed also indicate the amount of washable dissolved material coming through to the oxygen stage. These TDS measurements, together with other measurements, allow for future monitoring and controlling of the oxygen process. **TJ**

ACKNOWLEDGMENTS

This study was initiated under a contract between the South-Eastern Finland University of Applied Sciences, K-Patents OY, Andritz Oyj, and Stora Enso Oyj. This work was financed partially by the European Regional Development Fund via South Savo Center for Economic Development, Transport and the Environment (ELY Center). The authors thank Liz Dexter for editing the manuscript and thank Anu Pihlajaniemi for helping with the data analysis. The authors are grateful to all participants involved in this study.

LITERATURE CITED

1. McDonough, T.J., in *Pulp Bleaching: Principles and Practice* (C.W. Dence and D.W. Reeve, Eds.), TAPPI Press, Atlanta, GA, USA, 1996, pp. 213-239.
2. Agarwal, S., *J. Pulp Pap. Sci.* 25(10): 361(1999).
3. Elton, E., Magnotta, V., Markham, L., et al., *Tappi* 63(11): 79(1980).
4. Pikka, O., Vesala R., Vilpponen, A., et al., in *Chemical Pulping*, Finnish Paper Engineers' Association, Jyväskylä, Finland, 2000, pp. 616-664.
5. Gullichsen, J., Kolehmainen, H., and Sundqvist, H., *Pap. Puu* 74(6): 486(1992).
6. Mutikainen, H., Kopra, R., Pesonen, A., et al., "Measurement, state, and effect of the gas dispersion on the oxygen delignification," *Int. Pulp Bleaching Conf.*, ABTCP, São Paulo, SP, Brazil, 2017.
7. Mutikainen, H., Peltonen, K., Pikka, O., et al., "Characterization of oxygen dispersion in delignification process," *Int. Pulp Bleaching Conf.*, INP Pagora, Grenoble, France, 2014.
8. Kopra, R., Mutikainen, H., Pesonen, A., et al., "Using online total dissolved solids (TDS) measurements for investigating the performance of oxygen delignification," *Int. Pulp Bleaching Conf.*, ABTCP, São Paulo, SP, Brazil, 2017.

ABOUT THE AUTHORS

Oxygen delignification continues the delignification that starts in the cooking process in a more selective manner than occurs in the digester. It can achieve economic savings by optimizing the oxygen stage. It affects the quality and yield of the pulp and also the consumption of energy and chemicals.

We have been the pioneers of oxygen dispersion research and have been studying the behavior of dissolved solids during brownstock washing and oxygen stages for approximately 10 years. We have also published our findings in several journals and presented our results at various conferences.

The most challenging aspect for us has been to ensure that our measurement technology is reliable enough to allow us to obtain accurate data on the dispersion in challenging processing conditions. We have cooperated in this field for several years now with bubble imaging device manufacturers. The durability and accuracy of imaging is finally at a level where it can be used in the process for months without maintenance. The total dissolved solids (TDS) measurements have succeeded very well because of our extensive experience.

The most important finding of this study is most likely that we have managed to prove that it is natural for the bubble size to vary widely and that we can also affect this by changing the process conditions. The TDS measurement, on the other hand, has provided a new point of view from which to measure the change in dissolved solids during the oxygen stage. This change correlates on some level with kappa reduction.

Previously, we studied the performance and bubble size of a softwood line's oxygen stage. To our surprise, the dispersion of the bubble size was very different on the hardwood line in comparison with the softwood line. The TDS measurements enabled us to calculate the reactor's residence time and pulp yield. The results seem to indicate that temperature changes have a rather significant effect on the yield in the oxygen stage.



Kopra



Mutikainen



Dahl

The measurements provide mills with an opportunity to monitor the oxygen stage in a completely new way. This information will also provide tools to optimize the process parameters.

The next objective is to get references from other mills, especially from those that produce eucalyptus pulp. Our long-term goal is to start using these measurements when making adjustments to the oxygen stage.

Kopra is RDI scientist, Fiber Laboratory, Southeastern Finland University of Applied Sciences, Savonlinna, Finland. Mutikainen is R&D engineer, Fiber Technologies Division, Andritz Ltd., Kotka, Finland. Dahl is professor, Clean Technologies Group, Department of Bioproducts and Biosystems, School of Chemical Engineering, Aalto University, Espoo, Finland. Email Kopra at riku.kopra@xamk.fi.

ABOUT THIS PAPER

Cite this article as: Kopra, R., Mutikainen, H., Dahl, O. *TAPPI J.* 17(6):343(2018). https://doi.org/10.32964/TJ17.06.343

DOI: https://doi.org/10.32964/TJ17.06.343

ISSN: 0734-1415

Publisher: TAPPI Press

Copyright: ©TAPPI Press 2018

About this journal

Decreased water usage in a softwood ECF bleaching sequence—full mill simulations

PIA JOUR, KARIN LINDGREN, KATARINA GUTKE, AND JOHAN WALLINDER

ABSTRACT: In this study, an elemental chlorine free (ECF) bleach plant with a $D_0(EOP)D_1(EP)D_2$ sequence was studied with the aim of identifying options for significantly decreasing (fresh) water usage in the bleach plant and decreasing the effluent volume. A base-case simulation model for a softwood kraft market pulp mill was made based on a reference model representing the best available techniques as well as data produced in an extensive laboratory pulp bleaching study. This model was used to evaluate increased closure within the bleach plant and the recirculation of bleach plant effluent to the brownstock system and their effects on both the bleach plant and the recovery cycle. The results indicate that it is possible to reduce the fresh water consumption from 15 metric tons/a.d. metric ton in the base case to about 2 metric tons/a.d. metric ton, without increasing the carryover of chemical oxygen demand (COD) to the pulp machine.

Nonprocess elements in wood contribute to the levels of metals found in the bleach plant and thus to the risk of precipitates such as calcium oxalate, barium sulfate, and calcium carbonate. The risk of precipitates forming is a key factor determining the possible degree of closure. In addition, chloride concentration in the black liquor is another important factor that is affected by recirculating bleach plant filtrate to the brownstock washer and by the grade of the sodium hydroxide used in the mill.

Application: The intention of this work is to give input for possible steps than can be taken in order to reduce the water use in a pulp mill applying ECF bleaching technology.

Water is an important natural resource and reducing water consumption in the pulp industry is a key factor in achieving sustainable pulp production. With a growing world population and the increasing scarcity of fresh water in certain parts of the world, the need for the industry to reduce its "water footprint" is accentuated. In this study, an elemental chlorine free (ECF) bleach plant with a $D_0(EOP)D_1(EP)D_2$ sequence was studied with the aim of identifying options for significantly decreasing (fresh) water usage in the bleach plant and thereby decreasing the volume of effluent emitted to the recipient.

During the mid-1990s, pulp mill closure was already an area of focus, both among researchers as well as in the industry. In general, the work was targeting reduced effluent volumes and chemical oxygen demand (COD) discharge from the pulp mill, including partial closure solutions. This work builds on previous work and adds information about scale deposits [1-3].

EXPERIMENTAL

A base-case simulation model for a softwood kraft pulp mill was developed in the WinGEMS process simulator (Valmet; Espoo, Finland) based on a reference model representing the best available technology for a softwood kraft pulp mill developed by RISE Bioeconomy, formerly Innventia [4]. The simulation program was equipped with an extension tool that handles the chemical model used for determining the equilibrium composition in the fiber line. The chemical equilibrium calculations were based on minimizing Gibbs free energy and include the metal interactions with the pulp as well as with the dissolved organic material.

Some of the chemical formation constants of the main chemical species formed can be found in the chemical literature, but in many cases, the chemical conditions found in a pulp mill and a bleach plant are highly specific, with no applicable data being available in the literature. Accordingly, an extensive series of measurements were performed at RISE Bioeconomy [5-9] to determine these formation constants and to formulate the chemical model describing the system under the technical conditions found in a kraft pulp mill. This makes it possible to predict the formation of scaling—calcium oxalate, barium sulfate, and calcium carbonate—at different positions in the fiber line.

The model mill with the $D_0(EOP)D_1(EP)D_2$ bleaching sequence was equipped with vacuum filters in both the brownstock and the bleach plant. The last washer before the bleach plant was a wash press. The dilution factor for the washers used in the bleach plant was 2.4–2.5 metric tons/a.d. metric ton.

Supplementary data produced in a laboratory bleaching study was also included in the model. The bleaching experiments were carried out on an industrial oxygen delignified softwood kraft pulp, from a southern U.S. mill, with a kappa

number of 12.4 and brightness of 39% ISO. The bleaching stages were performed in polyethylene bags in water baths, and the pressurized stages were performed in steel autoclaves. The metal content was measured in the washed pulps before entering each bleaching stage in the sequence. The content of metals was also, together with chlorides (Cl^-), measured in the softwood (southern pine) raw material used in this study. The COD, carbonate, and oxalate contents were analyzed in the filtrates from the individual bleaching stages.

ISO brightness and kappa number were analyzed according to ISO 2470-1:2016 "Paper, board and pulps—Measurement of diffuse blue reflectance factor—Part 1: Indoor daylight conditions (ISO brightness)" and ISO 302:2015 "Pulps—Determination of Kappa number", respectively. The COD was analyzed according to the Dr. Lange Cuvette Test Method with a Hach Lange DR 2800 instrument (Hach Lange; Berlin, Germany). Ion chromatography was used to analyze oxalate after pre-treating the sample with nitric acid and heat. Carbonate was analyzed as inorganic carbon using a Shimadzu TOC-VCPH instrument (Shimadzu; Kyoto, Japan); metal content was determined following acid digestion using nitric acid, hydrogen peroxide (H_2O_2), and hydrochloric acid with an inductively coupled plasma instrument (iCAP 6500 Duo, Thermo; Cambridge, U.K.); and chloride was analyzed by capillary ion electrophoresis with a Model 7100 Capillary Electrophoresis (CE) System (Agilent Technologies; Santa Clara, CA, USA) after combustion in an oxygen bomb (Model 1108 Oxygen Combustion Bomb, Parr Instrument Company; Moline, IL, USA).

RESULTS AND DISCUSSION

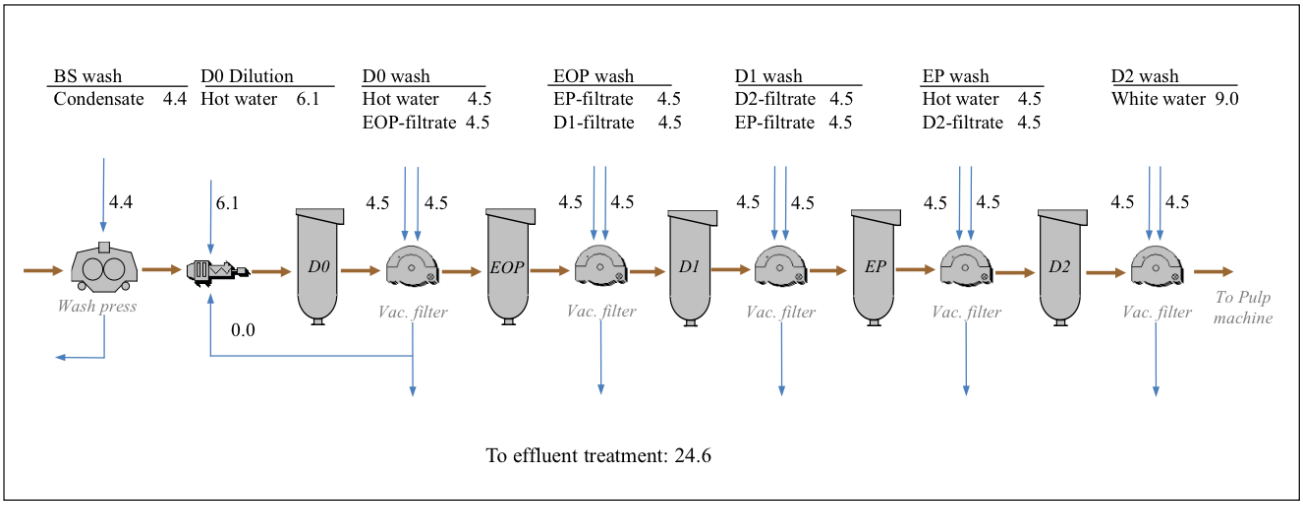
Nonprocess elements (NPEs) content in wood significantly affects the levels in the pulp entering the bleach plant. The calcium and barium content contribute to the risk of formation of precipitates such as calcium oxalate, barium sulfate, and calcium carbonate. Chloride content is important for levels present in the recovery area. Nonprocess elements content (mg/kg dry solids) in the wood used in the simulations were: barium (Ba), 6.9; calcium (Ca), 646; potassium (K), 388; magnesium (Mg), 182; manganese (Mn), 75; and chlorine (Cl), 42. The formation of COD, carbonate and oxalate used in the model are based on the results from the laboratory study and presented in **Table I**.

Base case (case A1)

The base case, A1, adopts a fairly open washing strategy with no bleach plant filtrate being recycled to the brownstock washer. The washing strategy used in the bleach plant can be seen in **Fig. 1**. White water from the drying machine was used on the vacuum filter after the D_2 stage. D_2 filtrate was used in equal shares for washing on the (EP) and D_1 filters. Hot water was used together with the D_2 filtrate for washing

	D_0	(EOP)	D_1	(EP)	D_2	Total
COD, kg/a.d. metric ton	7.7	11.3	3.1	2.3	1.0	25.4
Carbonate, kg/a.d. metric ton	0	2.19	0	0.60	0	2.79
Oxalate, kg/a.d. metric ton	0.49	0.27	0.15	0.06	0.04	1.01

I. Chemical oxygen demand (COD), carbonate, and oxalate formed in the different stages in the D_0(EOP)D_1(EP)D_2 bleaching sequence used in the WinGEMS simulation.



1. Washing strategy used for the base case, A1. The flows are given as metric tons/a.d. metric ton. The total effluent consists of D_0 filtrate 11.9, (EOP) filtrate 4.6, D1 filtrate 5.4, condensate 0.4, and white water 2.3 metric tons/a.d. metric ton (BS = brownstock).

	D_0	(EOP)	D_1	(EP)	D_2	Total
Chlorine dioxide, kg aCl/a.d. metric ton	27.1	-	15.4	-	3.6	46.1
Hydrogen peroxide, kg/a.d. metric ton	-	1.8	-	0.9	-	2.7
Sulfuric acid, kg/a.d. metric ton	2.8	-	-	-	0.1	2.9
Sodium hydroxide, kg/a.d. metric ton	-	6.5	1.8	2.7	-	11.0
Temp, °C	70	80	70	80	70	-
pH	2.5	~ 11	3.3	~ 11	4.2	-

II. Conditions and chemical charges used in the base case.

	A1
Total effluent volume, metric tons/a.d. metric ton	24.6
White water to effluent, metric tons/a.d. metric ton	2.3
Condensate to effluent, metric tons/a.d. metric ton	0.4
Fresh water to bleach plant, metric tons/a.d. metric ton	15.2
COD to effluent, kg/a.d. metric ton	31.4
COD to pulp machine, kg/a.d. metric ton	1.3
Sodium hydroxide makeup, kg/a.d. metric ton	15.0
Chlorides in black liquor as fired, %	0.26
Total charge of chlorine dioxide, kg aCl/a.d. metric ton	46.1

III. Key data for the base case, A1.

on the (EP) filter. (EP) filtrate was used in equal shares for washing on the D_1 and (EOP) filters. Half of the D_1 filtrate was used for washing on the (EOP) filter and the rest was sent to effluent treatment. A mix of (EOP) filtrate and hot water was used on the vacuum filter after the D_0 stage. The dilution of the pulp prior to the D_0 tower was accomplished using hot water. The dilution of pulp in the other bleaching stages was accomplished through internal dilution. Black liquor condensate was used for washing the pulp on the press prior to the bleach plant (the press is denoted BS [brownstock] wash in **Figs. 1-4**). The remaining condensate was used in the white liquor preparation and a small share was sent to the effluent treatment. The total effluent from the base case consists of D_0 filtrate 11.9, (EOP) filtrate 4.6, D_1 filtrate 5.4, condensate 0.4, and white water 2.3 metric tons/a.d. metric ton.

Apart from the effluent shown in the flow sheet, there was also a minor effluent flow from the pulp machine with reject, corresponding to 0.15 metric ton/a.d. metric ton. This amount was the same in all cases and will henceforth be excluded from all of the effluent figures presented. Apart from the specified D_2 filtrate, there were small amounts available for washing (0.1 metric ton/a.d. metric ton). In the model, these amounts were used in different positions. However, to simplify Figs. 1-4, these amounts have been included in the amount of D_1 filtrate used.

The conditions and charges used in the bleach plant for the base case are listed in **Table II**. The final brightness after bleaching was 89.5%–90% ISO and the carryover of COD to the bleach plant was 9 kg/a.d. metric ton. The total charge of bleaching chemicals used in this case was 46 kg active chlorine (aCl)/a.d. metric ton and 2.7 kg H_2O_2/a.d. metric ton. The chlorine dioxide (ClO_2) charges in the D_0 and D_1 stages were increased due to increased carryover of COD in order to reach the same final brightness in all of the cases compared; a factor of 0.3 kg aCl/kg COD was used. The peroxide charges have been the same regardless of the carryover of COD. The temperature and pH used in the D_0 stage was 70°C and 2.5, respectively, resulting in no calcium oxalate formation being predicted. All conditions except for the charge of chlorine dioxide were kept constant in all of the cases compared.

Calcium carbonate can be formed around the alkaline stages in the bleach plant and is known to require a high degree of supersaturation before it starts to precipitate. If precipitation does occur, this is often on the pulp, and might not therefore impact the runnability of the mill. The levels of calcium carbonate predicted in the base case simulations

	A1	A2	B1	B2	B3	B4	C1
Total effluent volume, metric tons/a.d. metric ton	24.6	21.9	12.9	10.5	10.5	9.8	11.4
White water to effluent, metric tons/a.d. metric ton	2.3	0	0	0	0	0	0
Condensate to effluent, metric tons/a.d. metric ton	0.4	0	0	0	0	0	0
Fresh water to bleach plant, metric tons/a.d. metric ton	15.2	12.5	3.5	1.1	1.1	0.4	2.1
COD to effluent, kg/a.d. metric ton	31.4	31.5	30.3	25.6	25.6	24.6	26.0
COD to pulp machine, kg/a.d. metric ton	1.3	1.3	2.2	2.2	2.2	2.2	1.4
Sodium hydroxide makeup, kg/a.d. metric ton	15.0	15.0	15.0	13.2	13.2	12.7	13.0
Chlorides in black liquor as fired, %	0.26	0.26	0.26	1.03	0.82	1.02	1.01
Total charge of chlorine dioxide, kg aCl/a.d. metric ton	46.1	46.1	46.4	47.5	47.5	47.8	47.7

IV. Key parameters for the simulated cases evaluated. Diaphragm sodium hydroxide was used in case A1, A2 , B1 and B2 and membrane sodium hydroxide was used in cases B3, B4 and C1.

were considered to be low and not to cause any problems. Barium sulfate formation was indicated only in the D_0 stage, although the amount modelled was also considered low and not to cause any precipitation problems. If a wood source with another composition of NPEs had been used, the risk for precipitation would have been different.

Some key data for the base case can be found in **Table III**. With this fairly open system and sodium hydroxide (NaOH) produced with the diaphragm method, the levels of chloride in the white and black liquors were maintained at acceptable levels, 0.77 g/l and 0.26%, respectively. The fresh water used in the bleach plant, 15.2 metric tons/a.d. metric ton, does not include the water used for diluting chemicals, which ranges from 1.8–1.9 metric tons/a.d. metric ton in all cases compared in this study. The amount of fresh water used on the pulp machine was kept constant at 4.9 metric tons/a.d. metric ton. The purge of precipitator dust in the base case was 14.9 kg/a.d. metric ton. The total effluent flow was 24.6 metric tons/a.d. metric ton containing 31.4 kg COD/a.d. metric ton.

Closure strategies

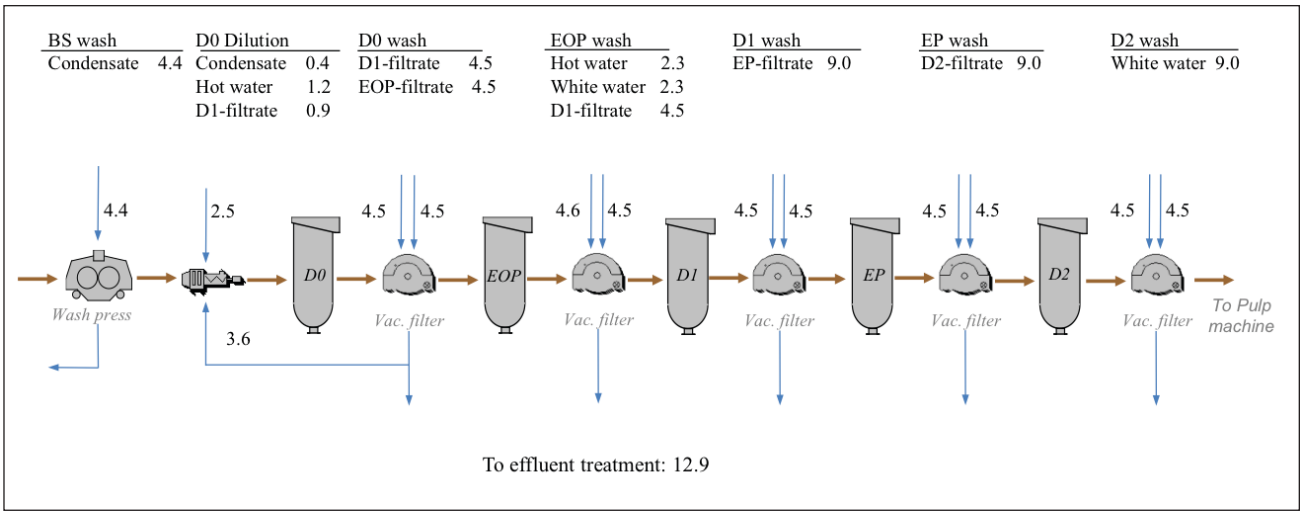
In this study, three concepts were studied:

- The first step towards increased closure was to increase the use of white water and condensate (case A2).
- The second concept, denoted B (cases B1-B4), was to use countercurrent washing on the last three washers in the bleach plant (D_1, (EP) and D_2). That is, white water was used for washing after the D_2 stage, D_2 filtrate was used for washing after the (EP) stage, etc.
- The third concept, denoted C (case C1), was to use a semi-countercurrent washing strategy for the washers in the bleach plant. The last filtrate used for washing is from the following bleaching stage. For example, for the D_1 washer, half of the washing liquor used was D_2 filtrate and the other half was (EP) filtrate.

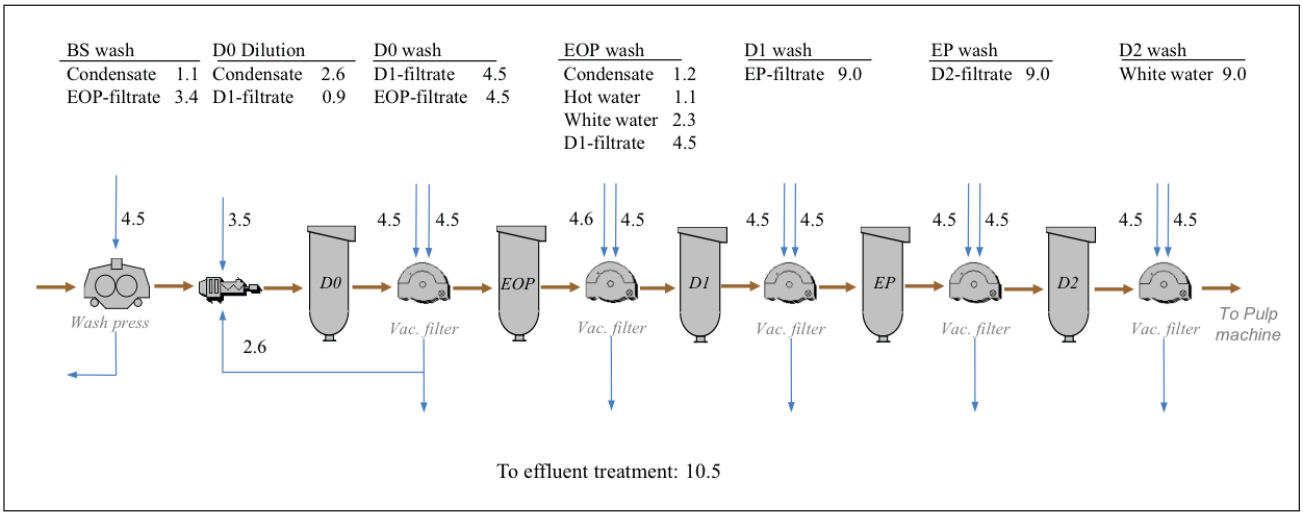
The purpose of the concepts B and C was to increase the use of D_0 and (EOP) filtrates until the limitations for calcium oxalate precipitation and/or chloride content in the black liquor were reached. The D_0 filtrate was used in the D_0 dilution and the (EOP) filtrate was recirculated to the brownstock. This applies for all cases except for case B1 where only the use of D_0 filtrate was maximized. In the studied cases, we have not considered the possible changes in the need for additional charges of acid and alkali in order to reach the pH targets in the bleach plant.

Increased usage of white water and condensate (case A2)

The first step towards increased closure of the base case was to use the remaining white water and condensate, which in the base case was sent to effluent treatment, in the dilution/mixing before the D_0 stage, case A2. This did not impact the risk of scaling or the amounts of chlorides in the white and black liquor since the content of NPEs are low in both streams. The fresh water used in the bleach plant was reduced by 2.7 metric tons/a.d. metric ton and the total effluent was reduced from 24.6 metric tons/a.d. metric ton in the base case to 21.9 metric tons/a.d. metric ton. The key data for case A2 can be found in **Table IV**.



2. Washing strategy for countercurrent concept, B1. The flows are given as metric tons/a.d. metric ton. The total effluent consists of D_0 filtrate 8.1 and (EOP) filtrate of 4.8 metric tons/a.d. metric ton (BS = brownstock).



3. Washing strategy for the countercurrent concept, B2. The flows are given as metric tons/a.d. metric ton. The total effluent consists of D_0 filtrate 9.1 and (EOP) filtrate of 1.4 metric tons/a.d. metric ton (BS = brownstock).

Countercurrent washing (cases B1–B4)

The washing strategy for the first countercurrent case, B1, described in more detail in **Fig. 2**, utilizes D_0 filtrate to the point where calcium oxalate precipitation is about to form in the D_0 tower. The fresh water used in the D_0 dilution for the base case was replaced with a mix of D_0 filtrate, hot water, condensate, and D_1 filtrate. This washing strategy decreases the fresh water used in the bleach plant to 3.5 metric tons/a.d. metric ton and the total effluent to 12.9 metric tons/a.d. metric ton containing 25.6 kg COD/a.d. metric ton.

The next case, B2, utilizes both the (EOP) and D_0 filtrates to the point where calcium oxalate precipitation is about to form and the level of chloride in the black liquor was about 1%. The washing strategy for this case, B2, is described in more detail in **Fig. 3**. In this case it was possible to use 3.4 metric tons of (EOP) filtrate/a.d. metric ton on the last washer before the bleach plant. In the D_0 dilution, a mix of D_0 filtrate, condensate, and D_1 filtrate is used. This washing strategy decreases the fresh water used in the bleach plant to 1.1 metric tons/a.d. metric ton and the total effluent to 10.5 metric tons/a.d. metric ton containing 25.6 kg COD/a.d. metric ton.

One possibility for further closing up the bleach plant and increasing the use of (EOP) filtrate on the brownstock washer was to improve the quality of the sodium hydroxide used in the mill (makeup to white liquor, oxygen delignification, and bleach plant). The sodium hydroxide produced with the membrane technology has a lower content of chlorides compared to sodium hydroxide produced using the diaphragm method, 0.0064 wt% compared to 0.75 wt%, respectively. This measure reduces the chloride content in the black liquor from 1.04 wt% to 0.82 wt%, case B3, and makes it possible to increase the use of (EOP) filtrate somewhat. Maximizing the use of both D_0 filtrate and the use of (EOP) filtrate makes it

possible to reach a total fresh water consumption in the bleach plant of 0.4 metric tons/a.d. metric ton and a total effluent volume of 9.8 metric tons/a.d. metric ton, case B4. The key data for cases B1–B4 can be found in Table IV. One drawback using this concept was the increased carryover of COD to the pulp machine, from 1.3 kg COD/a.d. metric ton in the base case to 2.2 kg COD/a.d. metric ton, which might have a negative effect on the final pulp produced. Therefore, another washing concept—semi-countercurrent washing—was also evaluated.

Semi-countercurrent washing (case C1)

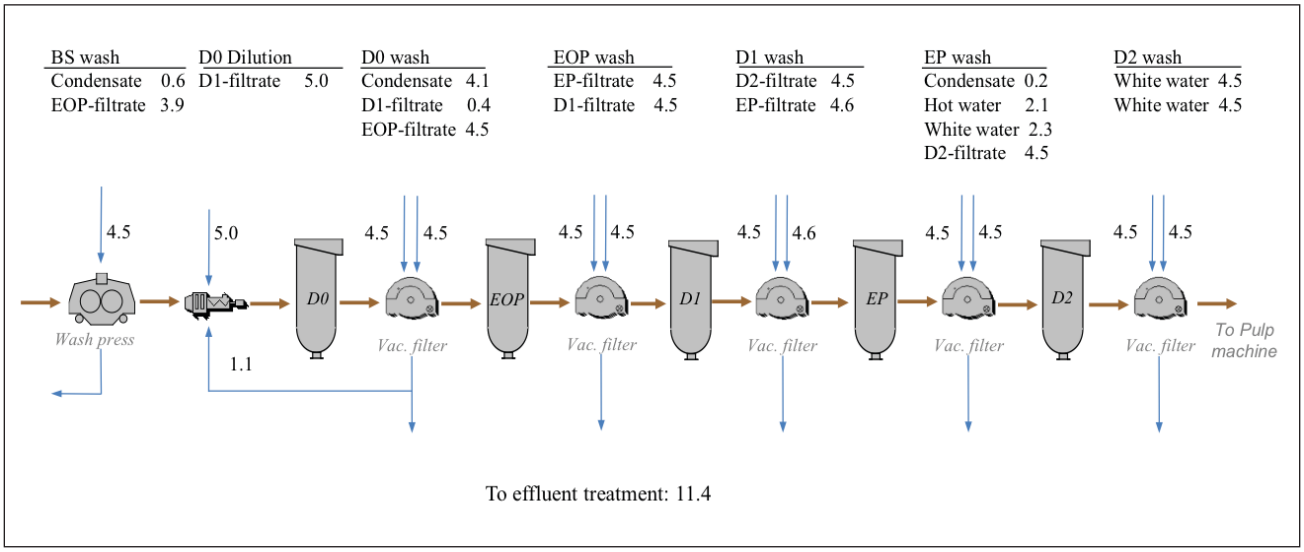
A description of the case where the semi-countercurrent washing strategy has been adopted, case C1, can be seen in **Fig. 4**. The filtrates from the D_2 and (EP) stages are divided and used in equal amounts on the two preceding washers. Membrane sodium hydroxide was used in this case and the use of D_0 and (EOP) filtrates was again maximized to the limit for calcium oxalate precipitation in the D_0 stage and the level of chloride in the black liquor to about 1 wt%. The amount of fresh water used in this case was 2.1 metric tons/a.d. metric ton on the (EP) filter. The total effluent was 11.4 metric tons/a.d. metric ton, containing 26.0 kg COD/a.d. metric ton. Using this concept results in a similar carryover of COD to the pulp machine as in the base case. The key data for this case is presented in Table IV.

Comparison of the different cases

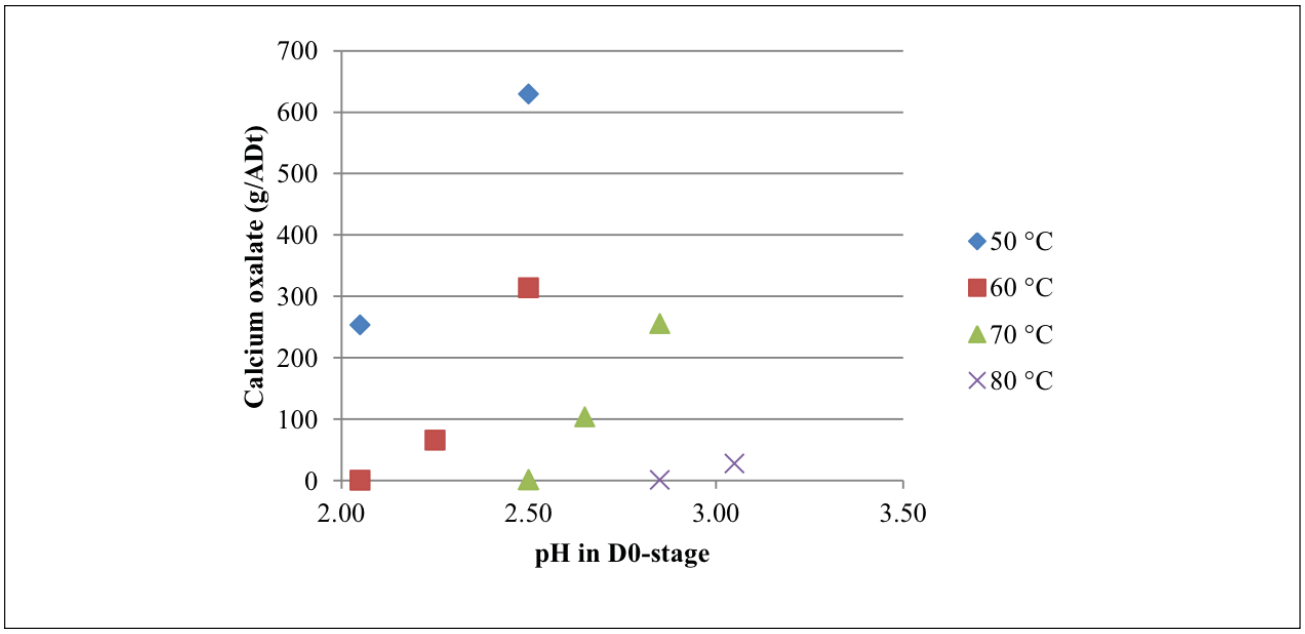
The key data for all of the cases included in this study are summarized and presented in Table IV. The use of fresh water in the bleach plant could be reduced from 15.2 metric tons/a.d. metric ton in the base case, A1, to 0.4 metric tons/a.d. metric ton, case B4, using the countercurrent washing concept, also including the use of sodium hydroxide produced with the membrane method, with a low content of chlorides. In this case, B4, a total effluent volume of 9.8 metric tons/a.d. metric ton including 24.6 kg COD/a.d. metric ton, could be attained. The drawback of using this concept was the increased carryover of COD to the pulp machine. For case C1, using the semi-countercurrent washing concept, it was possible to keep the carryover of COD to the pulp machine at the same level as in the base case. However, this concept resulted in a need for somewhat higher fresh water use in the bleach plant, 2.1 metric tons/a.d. metric ton, and a total effluent flow of 11.4 metric tons/a.d. metric ton, containing 26.0 kg COD/a.d. metric ton. The net wash loss decreased when more (EOP) filtrate was used for brownstock washing, resulting in a decreased need for sodium hydroxide makeup when closing up the bleach plant.

In all of the cases compared, fresh water to the pulp machine and fresh water for the dilution of chemicals was kept constant at 4.9 metric tons/a.d. metric ton and 1.8–1.9 metric tons/a.d. metric ton, respectively. The potassium content in the black liquor as fired was relatively unaffected by the increased closure, between 1.43%–1.49% for all of the cases evaluated. The sulfidity in the white liquor was kept constant at 35%. The purge of precipitator dust increased somewhat due to the increased closure, from 14.9 kg/a.d. metric ton in the base case, A1, to between 16.2–16.7 kg/a.d. metric ton for the B1–B4 and C1 cases.

In all cases, the degree of closure has been pushed to be on, or just below, the limit for the formation of calcium oxalate. Formation of barium sulfate is predicted in all cases around the D_0 stage, although the levels are low and not expected to cause problems. Calcium carbonate formation is predicted in the alkaline stages, both in the tower and in the filtrate tank, with the highest levels being found in the (EOP) tower. However, since the degree of supersaturation is low in all cases, calcium carbonate precipitation is not expected to have an impact on the runnability of the bleach plant.



4. Washing strategy for the semi-countercurrent washing strategy, C1. The flows are given as metric tons/a.d. metric ton. The total effluent consists of D_0 filtrate 10.6 and (EOP) filtrate of 0.8 metric ton/a.d. metric ton (BS = brownstock).



5. Formation of calcium oxalate in the D_0 stage, at different temperatures and final pH levels.

Effect of temperature and pH in the D_0 stage on formation of calcium oxalate using the semi-countercurrent concept (case C1)

It is well known that increased temperature and/or decreased pH could be applied to decrease the risk of formation of calcium oxalate [7,9]. In this work, the closure has been taken to the limit for when precipitation of calcium oxalate was predicted by the model. The position most sensitive to this was around the D_0 stage, in the bleach tower and filtrate tank.

Using a wood source with a calcium content of 646 mg/kg dry solids and the conditions applied in the D_0 stage in case C1 using the semi-countercurrent washing concept, at 70°C and a final pH of 2.5, it was possible to run the simulation without predicting calcium oxalate formation. A study was performed in order to evaluate different combinations of temperature and pH that could be used in the D_0 stage in order to avoid calcium oxalate formation being predicted when using this concept. The results are presented in **Fig. 5**. As can be seen in the figure, the model indicates that it would be possible to avoid calcium oxalate formation by using either a temperature of 60°C and a final pH of 2.05, a temperature of 70°C and a pH of 2.5, or a temperature of 80°C and a pH of 2.85.

CONCLUSIONS

The WinGEMS simulation of a mill producing ECF bleached softwood kraft pulp indicates that it is possible to significantly reduce the amount of fresh water used in the bleach plant. In this work, three main concepts were studied to reduce the use of fresh water. The first step towards increased closure was to use all available white water and condensate in the bleach plant. The next step was to introduce countercurrent washing and increase the internal use of D_0 filtrate, resulting in a fresh water consumption of 3.5 metric tons/a.d. metric ton and an effluent flow of 12.9 metric tons/a.d. metric ton.

By using a countercurrent washing strategy and sodium hydroxide produced by the membrane process, it was possible to achieve a fresh water consumption in the bleach plant of 0.4 metric tons/a.d. metric ton and an effluent flow of 9.8 metric tons/a.d. metric ton, containing 24.6 kg COD/a.d. metric ton. However, the carryover of COD to the pulp machine increased compared to the open base case. The other concept, based on semi-countercurrent washing, made it possible to reach an effluent flow of 11.4 metric tons/a.d. metric ton, containing 26 kg COD/a.d. metric ton and fresh water usage of 2.1 metric tons/a.d. metric ton. In this case, the carryover of COD to the pulp machine was comparable with the base case.

Two parameters of importance are the NPEs in wood and pulp and the purity of the sodium hydroxide makeup. In particular, the calcium and barium content in wood and pulp are crucial for the degree of closure that can be attained. The highest risk of calcium oxalate precipitation is around the D_0 stage. The risk can be reduced by decreasing the pH and/or increasing the temperature in the D_0 stage. By using sodium hydroxide produced by the membrane technology, with a low chloride content, it is possible to further increase the recirculation of the alkaline filtrates to the brownstock washer.

This work is based on the assumption that the process is in steady state. In a real mill, this is seldom the case; warm and cold areas exist in the process and there could be variations in the process conditions. With significant changes in the conditions, severe scaling could occur. It is therefore important to keep in mind that the implementation of the outcome of this study in a real mill must be done with care and in a stepwise manner. The indicated positions for precipitations could serve as a guideline for manual inspections during a maintenance stop. **TJ**

ACKNOWLEDGEMENTS

The authors wish to thank Doug Reid, Scott Carmichael, and Eva Wackerberg at AkzoNobel Pulp and Performance Chemicals for valuable input and discussions throughout the work.

LITERATURE CITED

1. STFI, "Ecocyclic pulp mill. Final report from the KAM program 1996-2002," KAM Report A100, STFI, Stockholm, 2003.
2. Reid, D.W., Johansson, N.G., Petre, K.L., et al., "Evaluation of bleach plant partial closure for an operating North American ECF market kraft pulp mill," *1997 Minimum Effluent Mills Symp.*, TAPPI Press, Atlanta, GA, USA, 1997.
3. Reid, D.W., Hicks, A.G., Clark, F.M., et al., "Evaluation of bleach plant partial closure, part two: a North American ECF kraft mill with oxygen delignification," *TAPPI Pulping Conf.*, TAPPI Press, Atlanta, 1998.
4. Berglin, N., Lovell, A., Delin, L., et al., "The 2010 reference mill for kraft market pulp," *TAPPI PEERS Conf.*, TAPPI Press, Atlanta, 2011.
5. Ulmgren, P. and Rådeström, R., *Nord. Pulp Pap. Res. J.* 14(3): 214(1999).
6. Ulmgren, P. and Rådeström, R., *Nord. Pulp Pap. Res. J.* 14(4): 330(1999).
7. Ulmgren, P. and Rådeström, R., *Nord. Pulp Pap. Res. J.* 16(4): 389(2001).
8. Ulmgren, P. and Rådeström, R., *J. Pulp Pap. Sci.* 27(11): 391(2001).
9. Wadsborn, R., Samuelsson, Å., Rådeström, R., et al., "Metal profiles in the bleach plant: Modelling and mill validation," *Int. Pulp Bleaching Conf.*, SPCI/STFI-Packforsk, Stockholm, 2005.

ABOUT THIS PAPER

Cite this article as: Jour, P., Lundgren, K., Gutke, K., et al. TAPPI J. 17(6): 353(2018). https://doi.org/10.32964/TJ17.06.353

DOI: https://doi.org/10.32964/TJ17.06.353

ISSN: 0734-1415

Publisher: TAPPI Press

Copyright: ©TAPPI Press 2018

About this journal

ABOUT THE AUTHORS



Jour



Lindgren



Gutke



Wallinder

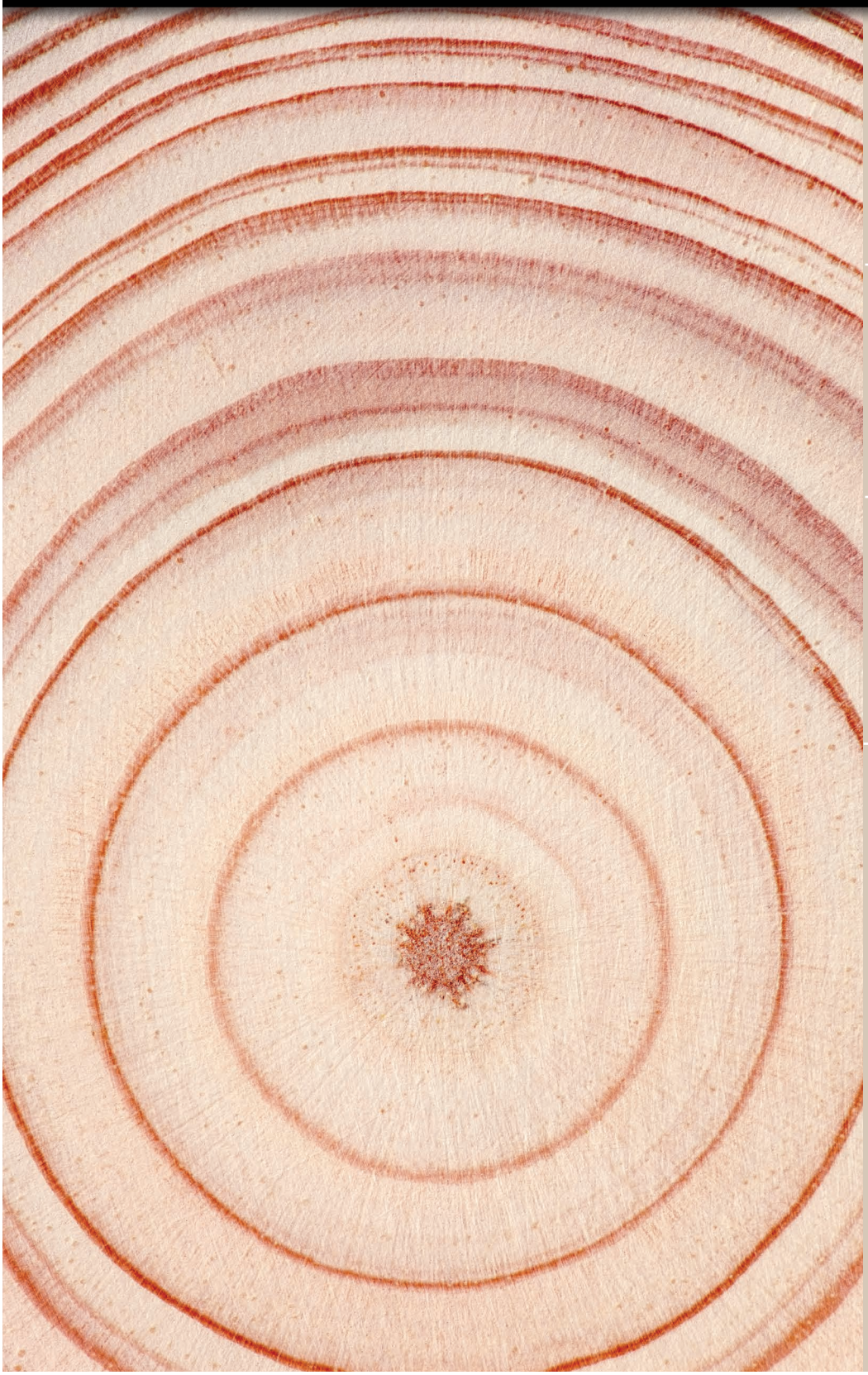
The growing global population and the increasing scarcity of freshwater in the world accentuate the need for the pulp and paper industry to lower its water footprint. Efficient water use is an important factor in achieving more sustainable pulp production. In this study, we wanted to identify options for significantly decreasing (fresh) water usage in an ECF bleach plant, thereby decreasing the volume of effluent emitted to the recipient.

Earlier, we studied a generic pulp mill producing eucalyptus pulp with typical Brazilian conditions. In this study, we were interested in also evaluating the possibilities to reduce the water usage in a mill producing softwood pulp using conditions more "typical" for North America. The most difficult aspect of this work was to design a general simulation model representing a "typical" North American mill.

Our most interesting finding in this study was the importance of using a sodium hydroxide quality with a low content of chlorides. For mills, the method used in this study can be applied in a specific mill case in order to evaluate different closure strategies and find ways to further reduce the freshwater use in the bleach plant. Our next step is to verify the simulation results in a real mill situation and to develop solutions for the potential limitations identified to make it possible to reach a lower water usage.

Jour is a scientist and Gutke is a research engineer with AkzoNobel Pulp and Performance Chemicals, Bohus, Sweden. Lindgren is a senior research associate and Wallinder is a research engineer with RISE Bioeconomy, Stockholm, Sweden. Email Jour at pia.jour@akzonobel.com.

TAPPI JOURNAL
WWW.TAPPI.ORG
THE PAPER AND PACKAGING INDUSTRIES' TECHNICAL RESOURCE
JULY 2018 | VOL. 17 NO. 7



DELIGNIFICATION **373**
Effects of lignin chemistry on oxygen delignification performance
Valeria Juste Gomes, Hasan Jameel, Hou-Min Chang, Robert Narron, Jorge Colodette, and Peter W. Hart

PULP PROPERTIES **383**
Influence of tensile straining and fibril angle on the stiffness and strength of previously dried kraft pulp fibers
John M. Long and Warren J. Batchelor

NANOTECHNOLOGY **395**
Wet-end addition of nanofibrillated cellulose pretreated with cationic starch to achieve paper strength with less refining and higher bulk
Matthew C. Rice, Lokendra Pal, Ronalds Gonzalez, and Martin A. Hubbe

RECYCLING **407**
Effect of pH and enzymes on strength of recycled fibers during refining
Ashok Ghosh, Breland Thornton, and Peter W. Hart

July 2018

TABLE OF CONTENTS VOL. 17 NO. 7

369 EDITORIAL
Remembering Phil Clark: A Coating "Master Man"
Monica Shaw

373 DELIGNIFICATION
Effects of lignin chemistry on oxygen delignification performance
Valeria Juste Gomes, Hasan Jameel, Hou-Min Chang, Robert Narron, Jorge Colodette, and Peter W. Hart

383 PULP PROPERTIES
Influence of tensile straining and fibril angle on the stiffness and strength of previously dried kraft pulp fibers
John M. Long and Warren J. Batchelor

395 NANOTECHNOLOGY
Wet-end addition of nanofibrillated cellulose pretreated with cationic starch to achieve paper strength with less refining and higher bulk
Matthew C. Rice, Lokendra Pal, Ronalds Gonzalez, and Martin A. Hubbe

407 RECYCLING
Effect of pH and enzymes on strength of recycled fibers during refining
Ashok Ghosh, Breland Thornton, and Peter W. Hart

»COVER CREDIT: Researchers Long and Batchelor studied the tensile mechanical properties of single fibers of radiata pine as a function of fibril angle (p. 383), selecting two samples from sections in a core to give a wide range of fibril angles.

TAPPI JOURNAL
WWW.TAPPI.ORG

Editor-in-Chief
Brian N. Brogdon brian.brogdon@gmail.com
+1 678 581-9114

Associate Editor
Peter W. Hart peter.hart@westrock.com
+1 409 276-3465

Editorial Director
Monica Shaw mshaw@tappi.org
+1 770 367-9534

PRESS Manager
Jana Jensen jjensen@tappi.org
+1 770 209-7242

Webmaster
Trina Heath theath@tappi.org
+1 770 209-7416

***TJ* EDITORIAL BOARD**

Randy Branston, BASF
randy.branston@basf.com, +1 704 819-4251

Brian N. Brogdon, FutureBridge Consulting & Training LLC
brian.brogdon@gmail.com, +1 678 581-9114

David A. Carlson, Carlson Consulting
dacarlson39@aol.com, +1 847 323-2685

Douglas W. Coffin, Miami University
dacarlson39@aol.com, +1 847 323-2685

Mahendra Doshi, Doshi and Associates
mahen@aol.com, +1 920 832-9101

Marc Foulger, GL&V USA Inc.
Marc.foulger@glv.com +1 315 767-2920

Peter W. Hart, WestRock
peter.hart@westrock.com, +1 409 276-3465

Carl J. Houtman, USDA Forest Products Laboratory
choutman@fs.fed.us, + 1 608 231-9445

Lucian Lucia, North Carolina State University
lucian.lucia@gmail.com, +1 919 889-7059

John A. Neun, John A. Neun LLC
john.neun@gmail.com, +1 518 275-8139

Jim Niemiec, Verso Corporation
jim.niemiec@versoco.com, +1 715 422-7404

Steven P. Ottone, Omya
steven.ottone@omya.com, +1 919 641-7854

Gaurav Pranami, Imbed Biosciences
gpranami@imbedbio.com, +1 515 230-7005

Arthur Ragauskas, Oak Ridge National Laboratory
aragausk@utk.edu

Gerard J.F. Ring, University of Wisconsin—Stevens Point
gerrryring@wi-net.com, +1 715 592-3732

Scott Rosencrance, Kemira Chemicals
scott.rosencrance@kemira.com, +1 770 429-2753

Paul Wiegand, NCASI
pwiegand@ncasi.org, +1 919 941-6417

Junyong Zhu, USDA Forest Products Laboratory
jzhu@fs.fed.us, +1 608 231-9520

Join TAPPI *today!*

TAPPI JOURNAL is a free benefit of TAPPI membership, and is only available to members. To join TAPPI, to renew your TAPPI Membership, or to learn about other valuable benefits, visit www.tappi.org.

TAPPI, 15 Technology Parkway S., Suite 115, Peachtree Corners, GA 30092, publishes *TAPPI JOURNAL* monthly.

ATTENTION PROSPECTIVE AUTHORS: All papers published are subject to *TAPPI JOURNAL's* peer-review process. Not all papers accepted for review will be published. Before submitting, check complete author guidelines at http://www.tappi.org/s_tappi/doc.asp?CID=100&DID=552877.

Statements of fact and opinions expressed are those of individual authors. TAPPI assumes no responsibility for such statements and opinions. TAPPI does not intend such statements and opinions or construe them as a solicitation of or suggestion for any agreed-upon course of conduct or concerted action of any sort.

Copyright 2018 by TAPPI, all rights reserved. For copyright permission to photocopy pages from this publication for internal or personal use, contact Copyright Clearance Center, Inc. (CCC) via their website: www.copyright.com. If you have questions about the copyright permission request process, please contact CCC by phone at +1 978 750-8400. To obtain copyright permission to use excerpts from this publication in another published work, send your specific request in writing to Editor, TAPPI JOURNAL, 15 Technology Parkway S., Suite 115, Peachtree Corners, GA 30092, USA; or by fax to +1 770 446-6947. Send address changes to TAPPI, 15 Technology Parkway S., Suite 115, Peachtree Corners, GA 30092, USA; Telephone +1 770 446-1400, or FAX +1 770 446-6947. www.tappi.org

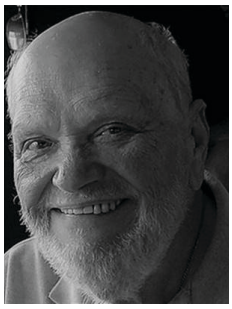
Editorial



MONICA SHAW | EDITORIAL DIRECTOR
mshaw@tappi.org

Remembering Phil Clark: A Coating "Master Man"

A pillar of the Coating and Graphic Arts (C&GA) community, Philip Charles (Phil) Clark, passed away this June. Phil spent most of his career managing the Potlatch Paper Coating Division, a part of the company's research department in Cloquet, MN. His technical contributions to the industry include development and introduction of precipitated calcium carbonate (PCC) coating pigments to the industry and invention and commercialization of high-solids coating formulations. Born in Syracuse, NY, in 1933, Phil received both his B.A. and M.S. degrees in Paper Chemistry from Syracuse University.



Phil Clark (1933-2018), "a pillar of TAPPI and the coating industry."

Phil was also an avid, involved member of TAPPI and served as an officer in TAPPI's C&GA Division from 1996 to 2005. He also served as the C&GA editor for *TAPPI Journal* from 1992 to 2001. Phil was involved in the Lake States Local Section for 15 years and a participant in the Coating Materials Common Interest Group from 2000 to 2010. Phil was recognized for his work with TAPPI in 1997 by receiving the C&GA Division's Leadership and Service Award.

Despite his many technical accomplishments in coating, perhaps his greatest was that of being a mentor, both within the industry and life in general, as suggested by the comments below from the CG&A community. As he approached retirement from Potlatch, Phil was also ordained as an Episcopal priest, serving St. Andrew's in Cloquet. Upon his passing of cancer, he willed his body to the University of Minnesota Medical School.

"I was deeply saddened to hear of the passing of Phil Clark, one of the pillars of the C&GA community. As a C&GA leader, he always promoted TAPPI and encouraged many young students to get involved with the organization and C&GA committees.

"Phil was also one of the early C&GA technical editors for *TAPPI Journal*. During his tenure at the Journal, numerous seminal advances in coating and printing technologies were published, like advanced coating binders, plastic pigments, high-solids coatings, and most importantly, the genesis of studies on critical issues, like the physics of blade/air knife/roll/size press coatings, coating rheology, and gloss development. He passed the editorial baton to me in 2001.

"Besides his contributions to PCC applications, he championed development of high-solids coatings for beneficial property development, where he was co-inventor of one of the important patents on the subject.

"Phil was indeed a pillar of TAPPI and the coating industry, and a mentor to many young professionals. I loved engaging him in arguments for the grandness of understanding—an Aristotelean trait."
— Nick Triantafillopoulos, former member of TAPPI Journal *Editorial Board.*

"Phil Clark was what we would call here in the U.K. a 'Master Man'. Just like a master craftsman who had learned his trade through many years of apprenticeship and experience, Phil had the experience in his craft, as well as the rare gift of empathy. While he was an excellent debater and challenger, he would do it with humor and caring. In addition, he had a passion for TAPPI and saw the value in how everyone had an opportunity to share and learn while building the expertise of our industry. Yes, without a doubt, he was a 'Master Man', and will be missed sorely."
— Phil Jones, TAPPI Board Member (retired), and Principal, PhylloSci LLC.

"Phil was a diligent researcher who mentored the development of a generation of coating research professionals. He was a person who would answer a question with a question and help the questioner to think through things.

"Prior to working at Potlatch, Phil worked for Wyandotte Chemical before and after its acquisition by Pfizer. He was there at the same time as Bob Hagemeyer, and the two of them were the pioneers in application of PCC in papermaking and coating. At Potlatch, Phil, Gerry Hein, and Bob Hershey pioneered and developed high-solids coating, which eliminated a lot of coating quality problems and became a key to ultra-high quality coated freesheet papers. I had the pleasure of working with all of them as a supplier of chemicals and coating equipment and later as a consultant."
— *Charles P. (Chuck) Klass, Principal, Klass Associates.*

"Phil was very influential in my work on *TAPPI Journal*. He had a passion for coating and the skill to explain things to me (not a coater) in simple terms. He will be missed."
— *Mary Beth Cornell, Membership and Global Development Director, TAPPI.*

"For many who knew Phil as both a coworker and a friend, he was 'Father Phil'. Outside of his tremendous experience and knowledge, he was always a welcoming sounding board for whatever you wanted to talk about. He will be sorely missed."
— *Randy Branston,* TAPPI Journal *Editorial Board Member, and Technical Specialist, Coatings, BASF.*

"I can remember working with Phil on a number of TAPPI Journal submissions. As a young participant in the paper industry at the time, the thing that struck me as he asked for my help reviewing works was the great respect he gave me as a scientist. I'll never forget the opportunity to work with such a fine contributor to our industry."
— *Steven Ottone,* TAPPI Journal *Editorial Board Member, and Technical Service Manager, Omya Inc.*

"I hold fond memories of Phil. One of the most moving moments was when I was receiving the C&GA Division's Technical Award and Phil was receiving the Leadership and Service Award. He made the first speech and became emotional over his attachment to TAPPI. The audience was so warm and supportive of him. Then, it was my turn, and what could I add? Phil stole the show, and rightly so. He shall do so also in our memories."
— *Patrick Gane, Vice President Special Projects, Omya International AG* **TJ**

Effects of lignin chemistry on oxygen delignification performance

VALERIA JUSTE GOMES, HASAN JAMEEL, HOU-MIN CHANG, ROBERT NARRON, JORGE COLODETTE, AND PETER W. HART

ABSTRACT: The present work focused on characterizing the chemical and structural properties of isolated lignin from six hardwoods and their kraft pulps in an attempt to better understand the relationship between lignin's chemical properties and resultant oxygen delignification performance. Several hardwood samples were cooked under the same conditions with varying alkali charges to obtain unbleached pulps with kappa numbers between 19 and 20. These pulps were then subjected to an oxygen delignification stage. Both processes were evaluated for pulp quality, residual lignin, and O-stage delignification efficiency. The oxygen delignification stage was carried out under fixed conditions and evaluated with regards to kappa number, which was corrected for hexenuronic acid (HexA) contributions. Results revealed that different hardwood species exhibited differing oxygen delignification efficiencies. A high correlation was found between the O-stage delignification efficiency and the content of phenolic groups in the unbleached lignin, which confirmed that free phenolic groups are the reactive site for molecular oxygen attack. When different hardwood species were compared, the HexA contents were not found to affect O-stage delignification efficiencies.

Application: The authors are attempting to understand how the structure of different hardwood species impacts oxygen delignification performance. If they can develop this understanding, the performance of the oxygen stage can be tailored to specific seasonal changes in the wood hardwood species being harvested.

Oxygen delignification stage (O-stage) is a well-established technology with environmental, technical and economic benefits. This stage allows kraft cooking to end at a higher kappa number than normal, thus minimizing pulping yield losses since the reactions during the oxygen delignification are more selective than kraft pulping when cooking to low lignin contents. Furthermore, oxygen delignification helps to decrease bleach consumption in subsequent bleaching stages [1]. With the aim to preserve selectivity (i.e., maximizing lignin removal while simultaneously minimizing cellulose degradation), lignin reduction in hardwood and softwood using oxygen delignification is limited to approximately 40% and 50%, respectively [2]. Further reductions beyond these limits will result in a significant increase in cellulose degradation [3]. Another reason postulated as to why kappa number reduction is limited to less than 50% is related to the presence of hexenuronic acid (HexA) groups, which contributes to the measured kappa number of the pulp [4]. These functional groups on the xylans are non-reactive towards oxygen, and they cause the pulp to appear to have a higher lignin content when based on its measured kappa number [4,5].

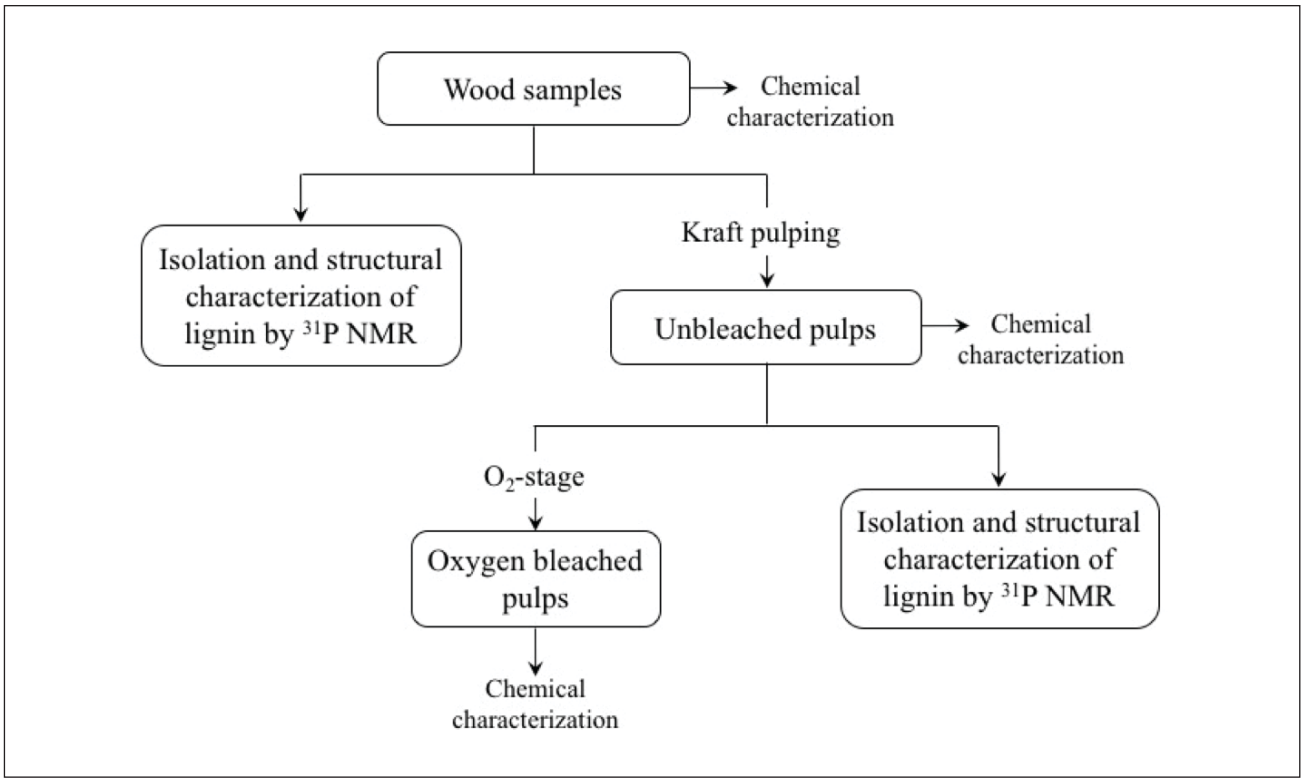
Several studies have demonstrated that phenolic functional groups of lignin are one of the most reactive sites for oxygen delignification. The primary interaction of alkali with these structures generates anions, which are attacked by oxygen and its intermediate species [6,7]. The chemical characteristics of lignin are among the most important features for understanding the mechanism of its removal from the cell wall during chemical pulping and O-stage delignification processes [8]. To understand and improve O-stage delignification, the chemistry involved in delignification must be studied carefully [9]. Some studies [7,10,11] have indicated that the structure of the residual lignin is not greatly altered by the O-stage. These authors have observed some changes to residual lignin, such as the loss of non-condensed phenolic units; the authors also observed that C5 condensed units, such as 5,5'-biphenyl moieties, are 50% less reactive towards oxygen delignification when compared to non-condensed phenolic units.

The presented work is focused on the chemical and molecular characterization of isolated lignin from wood and kraft pulp produced from several hardwoods species. The goal is to understand what structural features exist in pulp prior to oxygen delignification in order to make informed comparisons between unbleached and oxygen-delignified pulps, as well as overall O-stage delignification efficiency. Several hardwood samples were cooked under the same time-temperature conditions with varying alkali charges in order to obtain unbleached pulps with kappa numbers between 19 and 20. These pulps were then oxygen-delignified. The resulting pulps were evaluated for pulp quality, residual lignin content, and O-stage delignification efficiency.

EXPERIMENTAL

Analytical scheme

The flowchart presented in **Fig. 1** depicts the work plan. Six hardwood samples were subjected to kraft cooking with the goal of producing unbleached pulps for oxygen delignifica-



1. Flowchart for pulp production and oxygen delignification stage (O-stage) (^{31}P NMR = phosphorus-31 nuclear magnetic resonance).

tion performance studies. Woods, brownstocks, and oxygen-delignified pulps were chemically characterized. Isolated lignins from hardwoods and unbleached pulps were also chemically characterized, including hydroxyl group characterization using a phosphorus-31 nuclear magnetic resonance (^{31}P NMR) method [12].

Material

Wood samples of sweet gum (*Liquidambar styraciflua*), red oak (*Quercus rubra*), white oak (*Quercus alba*), and *Eucalyptus benthamii* were received as single species logs selected by forestry personnel from a paper company. The sweet gum and both oak species were obtained from the low country area of South Carolina. The eucalypt was obtained from a plantation in Southeast Texas. The specific trees harvested were picked by professional foresters as typical species that are representative for bleached paper production. Logs of yellow birch (*Betula alleghaniensis*) and white birch (*Betula papyrifera*) where obtained from a forest in northern New Hampshire. It was important to maintain the diameter of each log to 4–6 in. in order to fit it into the lab chipper. Each of the single species logs was shipped to North Carolina State University (NCSU) in Raleigh, NC, USA, and then manually debarked and chipped in a laboratory rotary chipper. All visible knots were manually removed from the chips. The chips, with bark and knots removed, were ground in a Wiley mill and sieved, and then the meal fraction that passed between 40 and 60 mesh screens was collected. The wood meals were extracted in a Soxhlet extractor for 24 h with benzene-ethanol 2:1 (v/v) (TAPPI Standard Test Method T 264 om-88 "Preparation of wood for chemical analysis"), dried, and later used either for pulping or for lignin isolation.

Methods

Chemical composition

Approximately 100 mg of the extracted wood meal was hydrolyzed with 1.5 mL of 72% sulfuric acid (H_2SO_4) at room temperature for 120 min. The mixture was then diluted to 3% H_2SO_4 using deionized water, transferred to a vial, sealed, and autoclaved at 121°C for 90 min. Klason (acid-insoluble) lignin and acid-soluble lignin (ASL) [13] were determined for each of the different hardwoods through the use of gravimetric and spectrophotometric techniques, respectively. The Klason and acid soluble methods followed TAPPI Standard Test Method 222 OM-15 "Acid-insoluble lignin in wood and pulp" and TAPPI Useful Method UM 250 "Acid-soluble lignin in wood and pulp," respectively. The sum of Klason and acid-soluble lignin is reported as the total lignin content.

The hydroliyzed monosaccarides (monomeric sugar content) were determined by injecting 2.5 ml samples into a high-performance anion-exchange chromatography with pulsed amperometric detection (HPAE-PAD) on a Dionex IC-3000 chromatography system (Thermo Fisher Scientific; Waltham, MA, USA). Sugars were separated using a Carbo-Pac PA1 guard and analytical columns (Thermo Fisher Scientific) connected in series. Water was used as an eluent at a flow rate of 1.0 mL/min.

The column temperature was 18°C. A post-column base 40 mM sodium hydroxide (NaOH) was added to improve detection by pulsed amperometry. The post-column flow rate was 1.0 mL/min as reported elsewhere [14].

Chemical characterization

Alkaline nitrobenzene oxidations of the solvent-extracted wood meals were performed in accordance to the method of Chen [15], Chang [16], and Min et al. [17]. The oxidation roughly approximates the proportion of syringyl and guaiacyl units in the lignin from their corresponding nitrobenzene oxidation products, syringaldehyde (S) and vanillin (V), respectively, which is expressed as the S/V ratio. Approximately 200 mg of the meal was reacted with 7 ml of 2N NaOH and 0.4 ml of nitrobenzene at 170°C for 2.5 h in a stainless steel bomb. After the reaction was completed, the hot bomb was immediately cooled down with cold water. Then, 1 ml of 5-iodovanillin (80 mg/ml in 5 mL 1,4-dioxane) was added to the solution as an internal standard. The mixture was extracted with methylene dichloride (CH_2Cl_2) four times (around 30 ml each time), and the organic phase was discarded. The aqueous phase was acidified to approximately 2.5 pH with 2N hydrogen chloride (HCl). The acidified mixture was further extracted with CH_2Cl_2 three times (around 30 ml each time), and the organic phase was collected, combined, and dried over anhydrous Na_2SO_4 overnight. One milliliter of the solution was dried by rotary evaporator at 30°C and then derivatized by adding 50 µl of pyridine and 50 µl of *N*,O-bis(trimethylsilyl)trifluoroacetamide (BSTFA) to the dried sample. The solution was shaken for 15 min at 50°C. The derivatized solution was analyzed by gas chromatography on a HP 6890 GC equipped with a flame ionization detector and HP-1 column (30 m × 0.32 mm × 0.25 µm) (GenTech Scientific; Arcade, NY, USA). Specific details for the conditions used for the GC analysis are reported by Mi et al. (2015) [17].

Hexenuronic acid content was measured according to the method of Vuorinem et al. [5] and Tenkanen et al. [18]. Intrinsic viscosity of the pulp was measured by ISO 5358 "Pulps – Determination of limiting viscosity numbers in cupriethylenediamine (CED) solution." Kappa number of the pulp was measured by TAPPI Standard Test Method T 236 om-85 "Kappa number of pulp."

Kraft pulping

The kraft pulping of the hardwoods was carried out using an M/K digester (M/K Systems Inc., Peabody, MA, USA) with capacity of 7.0 liters equipped with temperature controller and recirculation heater system. The following conditions were used for pulping: liquor/wood ratio of 4:1; temperature 160°C; H-factor 800; sulfidity 25%; and active alkali (AA) charge adjusted to obtain a kappa number between 19 and 20.

Oxygen delignification stage

The resulting unbleached kraft pulps were subjected to oxygen delignification (O-stage). The O-stage was carried out in a pressurized cylindrical vessel. The vessel was preheated to 70°C–80°C and charged with 200 oven dry (o.d.) g of unbleached pulp. The consistency was adjusted to 10% with distilled water and 2% NaOH on o.d. pulp was added. Additional O-stage conditions are listed in the accompanying table in the "Results and Discussion" section (Table III).

Lignin isolation

Cellulolytic enzyme lignin (CEL) was isolated from selected samples by adapting reported literature procedures for milled wood and for pulp [12,16,19]. The CEL was prepared by enzymatic hydrolysis of the sample using 20 filter paper units (FPU) of cellulase enzyme (from *Trichoderma viride*, 9.1 U/mg solid, purchased from Sigma-Aldrich; St. Louis, MO, USA) per gram of substrate in an acetate buffer solution (pH 4.5) at 45°C for 72 h [20]. After enzymatic hydrolysis, the solid material was separated by centrifugation, washed with the buffer solution followed by deionized water, and then freeze-dried. The dried material was extracted with 96% 1,4-dioxane. The solvent was then evaporated under vacuum at 35°C. To remove traces of 1,4-dioxane, a few drops of H_2O were added to the solid matter and evaporated again. This procedure was repeated three times. Finally, the solid matter was dried in a vacuum oven at 35°C to obtain CEL preparations.

^{31}P NMR spectra

Approximately 40 mg vacuum-dried lignin that was obtained from the cellulolytic enzyme treatment of a wood or pulp sample [12,21] was placed into an NMR tube, which was followed by the addition of 500 µl deuterated chloroform ($CDCl_3$)/pyridine solution (1:1.6 v:v). After the lignin was dissolved with continuous shaking, 200 µl internal standard solution (9.23 mg/ml endo-N-hydroxy-5-norbornene-2,3-dicarboximide solution) and 50 µl relaxation reagent solution (5.6 mg/ml chromium (III) acetylacetonate solution) was added to the tube. The solvent used for the dissolution of internal standard and relaxation reagent was a $CDCl_3$/pyridine solution (1:1.6 v:v). Afterwards, 100 µl phosphitylating reagent (2-chloro-4,4,5,5-tetramethyl-1,3,2-dioxaphospholane) was added to the NMR tube and thoroughly mixed prior to ^{31}P NMR analysis. The ^{31}P NMR spectra were recorded using a Bruker 300 MHz spectrometer (Bruker; Villerica, MA, USA) with a quad probe. The contents of various types of hydroxyl groups were determined in accordance to the ^{31}P NMR experimental method described by Granata and Argyropoulous [22].

RESULTS AND DISCUSSION

Wood chemical composition

Chemical characterizations of all wood samples were performed, and the results are presented in **Table I**.

The main functional groups on the lignin polymer include the hydroxyl, methoxyl, carbonyl, and carboxyl. The proportion of these groups depends on the genetic origin of the hardwood and isolation processes applied [23-29]. Lignins were

Samples	Sugars, %			Lignin, %			Uronic acid, %	S/V
	Glc	Xyl	Others	ASL	Klason	Total		
Sweet gum	42.1	14.8	4.6	2.2	20.6	22.8	5.5	2.70
Red oak	42.7	15.8	4.6	2.3	20.5	22.8	4.4	2.50
White oak	38.1	15.1	5.1	2.2	20.9	23.1	5.3	2.42
E. benthamii	40.0	11.3	3.7	1.6	27.3	28.9	5.8	2.63
Yellow birch	43.3	21.9	3.9	1.8	18.2	20.1	4.5	2.39
White birch	46.0	24.2	4.1	2.1	19.4	21.5	4.4	3.00
Glc = glucomannan; Xyl = xylan; ASL = acid soluble lignin.								

I. Wood chemical characterization: sugar composition, lignin content, uronic acid content, and syringaldehyde/vanillin (S/V) ratio of lignin.

Samples	mmol/g lignin				
	Aliphatic OH	Phenolic OH groups			Carboxylic OH
		5-substituted	5-free	Total	
Sweet gum	7.4	0.6	0.7	1.4	0.1
Red oak	7.0	0.5	0.7	1.2	0.0
White oak	7.2	0.9	0.9	1.7	0.2
E. benthamii	7.7	0.9	1.1	2.0	0.1
Yellow birch	7.7	0.5	0.6	1.2	0.0
White birch	8.2	0.5	0.5	1.0	0.0

II. Aliphatic, phenolic, and carboxylic hydroxyl groups (OH) content (mmol/g of lignin) determined by quantitative phosphorus-31 nuclear magnetic resonance (^{31}P NMR) analysis of cellulolytic enzyme lignin (CEL) isolated from wood samples.

Samples	AA, % Na_2O on O.D. Wood	Screened Yield, %	Rejects, %	Kappa	HexA, mmols/kg	Viscosity, dm^3/kg
Sweet gum	15.0	42.6	5.54	20.0	47.5	1314
Red oak	13.5	42.9	7.28	20.0	36.7	1485
White oak	16.0	47.9	2.88	25.3	47.4	1286
E. benthamii	15.0	46.6	1.77	19.4	46.2	1304
Yellow birch	15.4	46.7	6.21	20.0	52.3	1400
White birch	16.0	48.7	1.52	19.8	49.2	1280
*H-factor, sulfidity, and temperature were 800, 25%, and 160°C, respectively. (AA = active alkali; O.D. = oven dry; HexA = hexenuronic acid.)						

III. Kraft pulping conditions* and results

isolated from wood and pulp samples using the CEL method described earlier. Functional group analyses can be used to characterize lignin structure and reactivity [12,28]. Hydroxyl derivatization and analysis by ^{31}P NMR is often used for the quantitation of different hydroxyl group types in lignin [21]. The ^{31}P NMR spectra were acquired from CEL preparations to quantify the different types of phenolic (PhOH) groups. In the phenolic hydroxyl region, the signals in the range of 144.3 to 140.3 ppm are attributed to 5-substituted units (which included condensed 5,5'-biphenyl moieties), and those in the range of 140.3 to 137.2 ppm are assigned to non-condensed units (free C5 position). The contents of aliphatic, phenolic, and carboxylic hydroxyl moieties in the CEL preparations obtained from wood samples are shown in **Table II**.

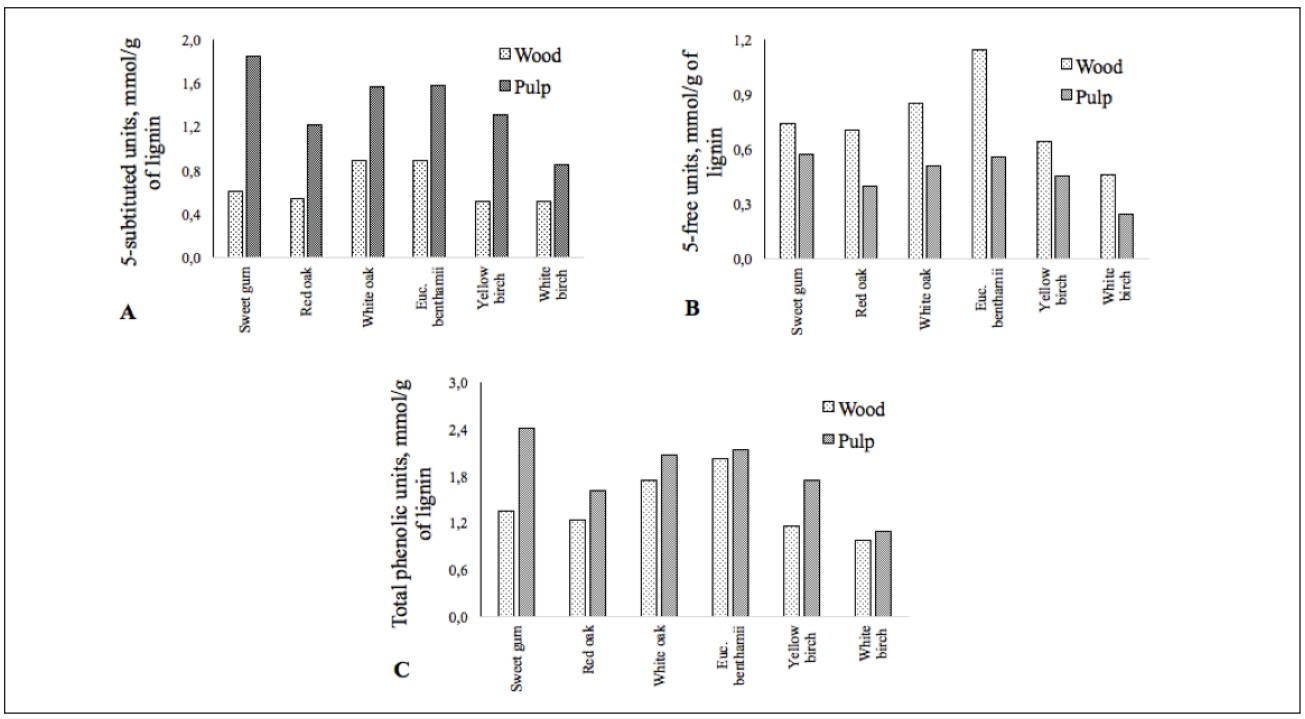
Samples	mmol/g lignin				
	AliphaticOH	Phenolic OH groups			Carboxylic OH
		5-substituted	5-free	Total	
Sweet gum	12.8	1.8	0.6	2.4	0.4
Red oak	15.1	1.2	0.4	1.6	0.2
White oak	14.2	1.6	0.5	2.1	0.7
E. benthamii	12.7	1.6	0.6	2.1	0.3
Yellow birch	15.5	1.3	0.5	1.7	0.3
White birch	8.72	0.9	0.2	1.1	0.3

IV. Aliphatic, phenolic, and carboxylic hydroxyl groups (OH) content (mmol/g of lignin) determined by quantitative ^{31}P NMR analysis of CEL isolated from unbleached pulp samples.

Kraft cooking of hardwood samples

Kraft cooking of the wood samples was performed under fixed conditions, except for the alkali charge, in order to produce brownstocks with similar degrees of delignification (kappa number between 19 and 20). **Table III** shows the pulping results, which includes the active alkali (% AA) charge needed to reach the desired kappa number.

This study characterized the amounts and types of free phenolic hydroxyl groups in the unbleached lignin since it has been documented in the literature that these groups are reactive towards molecular oxygen during oxygen delignification [7,30]. The contents of aliphatic, phenolic, and carboxylic hydroxyl moieties in CEL preparations isolated from the unbleached pulp samples are listed in **Table IV**. Carboxylic hydroxyl groups varied from 0.17 (red oak) to 0.68 mmol/g of lignin (white oak). The values for the unbleached pulps are much higher than what was found in the raw hardwoods (0.01–0.18 mmol/g, Table II). This is attributed to the hydrolysis of lactones and esters present in wood, which afforded carboxylic acid functional groups [20,31]. The same observation was noted by Prinsen et al. [32], who investigated the hydroxyl groups in milled wood lignin (MWL) of a eucalypt hybrid before and after kraft pulping. The data from the various phenolic groups) in the raw hardwoods (Table II) and unbleached kraft pulp (Table IV) are graphically summarized in **Fig. 2**.



2. 5-Substituted phenolic (A), 5-free phenolic (B), and total phenolic units (C) of isolated cellulolytic enzyme lignin (CEL) in the wood and unbleached pulps samples.

	Sweet gum	Red oak	White oak	*E. benthamii*	Yellow birch	White birch
Kappa number	10.5	10.3	12.2	10.7	11.2	12.2
HexA, mmol/kg	43.1	31.0	39.2	43.2	44.7	45.0
Viscosity, dm^3/kg	1105	1300	1200	950	1178	1108
Kappa drop, %	47.5	48.5	48.1	44.8	44.0	38.4
Viscosity drop, dm^3/kg	209	185	86	354	222	172
Selectivity**	0.44	0.31	1.19	0.29	0.31	0.45
O-stage delignification efficiency*, %	59.4	55.9	59.7	56.8	54.4	48.3

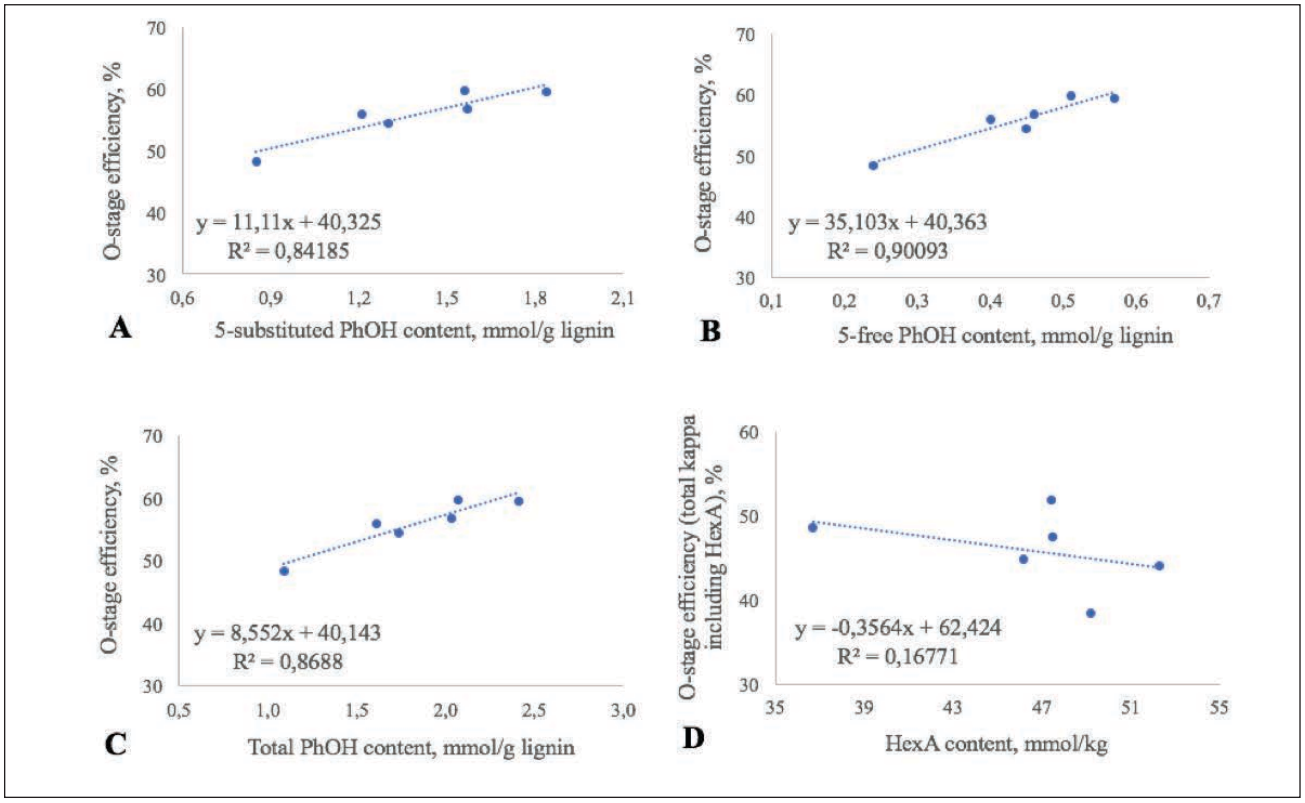
O-stage conditions: 2.0% NaOH on o.d. pulp, temperature of 100°C, time-to-temperature of 45 min, time-at-temperature of 30 min, O_2 pressure of 100 psig, and consistency 10%. *Based on true lignin kappa number removal (excluding HexA), assuming that 10 mmol HexA/kg of pulp are equivalent to 1 kappa unit (according to Vuorinen et al. [5]);**Δ kappa no./ Δ viscosity (dm^3/kg). In retrospect, it might have been better to use the approximation of ~10 mmol HexA/kg of pulp is equivalent to 0.86 kappa units reported by Li and Gellerstedt [35], who eliminated interferences from lignin.

V. Oxygen delignification results and performance

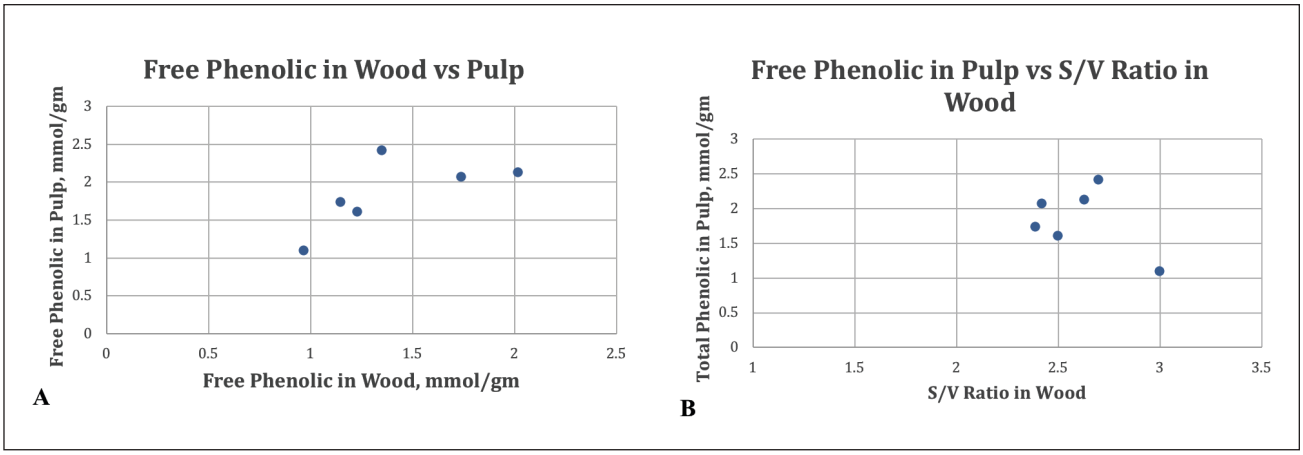
Oxygen stage delignification

All unbleached pulp samples were subjected to an oxygen delignification stage under fixed conditions, and the results from this treatment are presented in **Table V**. High delignification efficiencies, ranging from 48.3% for white birch to 59.7% for white oak, were observed.

According to Gellerstedt and Lindsfors [33] and Gellerstedt et al. [10], two factors govern lignin solubilization during oxygen delignification. The first factor is the amount of hydrophilic functional groups on the otherwise hydrophobic residual lignin. The second factor is the cleavage of the residual lignin into smaller molecular weight fragments, which improves its transport out of the fiber wall and into the bulk solution. From a reactivity point of view, free phenolics are the most important functional



3. O-stage delignification efficiency versus 5-substituted (A), 5-free (B), and total phenolic hydroxyl groups (C) and O-stage delignification efficiency (based on total kappa number, including HexA) versus HexA content in unbleached pulps (D).



4. Free phenolic content in pulp versus free phenolic content in wood (A), and versus syringaldehyde/vanillin (S/V) ratio in wood (B).

group that is contained in unbleached lignin as these groups are preferentially oxidized by oxygen [10,34].

O-stage delignification efficiency (based on the HexA-corrected kappa number) versus 5-substituted, 5-free and total phenolic hydroxyl groups in the residual lignin of the unbleached pulp is presented in **Figs. 3A-C**. As expected, unbleached pulp samples with higher PhOH quantities demonstrated higher O-stage delignification efficiency. A strong and positive correlation was found to exist between PhOH contents and O-stage delignification efficiency, especially when only 5-free moieties are considered (Fig. 3B). Some researchers have indicated that condensed structures tend to lower lignin reactivity during oxygen delignification [36]. It is important to emphasize that 5-substituted moieties in hardwood samples include syringyl lignin (S-type) and C_5-C_5' condensed lignin (i.e., condensed guaiacyl units [G-type lignin]). The observations in this study reinforce the understanding that free phenolic hydroxyl groups are the primary reactive sites for oxygen delignification, with their abundance effectively governing O-stage delignification efficiency. O-stage delignification efficiency based on the uncorrected kappa number (which included HexA contributions) versus HexA content in unbleached pulps is presented in Fig. 3D; there was no correlation found for these two parameters ($R^2 = 0.17$). This observation indicates that HexA content was not a governing factor affecting oxygen delignification efficiency for the various hardwoods investigated.

Since the oxygen delignification efficiency is affected by the free phenolic content in pulp, it is important to understand which factors affect free phenolic content. Nitrobenzene oxidation provides the information of non-condensed syringaldehyde (i.e., S-type lignin) and vanillin units (i.e., G-type lignin) in the raw hardwoods. The ratio of syringaldehyde-to-vanillin (S/V ratio) may affect pulping delignification, which in turn affects the amounts of free phenolic groups in the unbleached pulp. **Figure 4** shows no correlation between the S/V ratio of the raw hardwoods and the amount of free phenolics in the unbleached pulps. The free phenolic content was mostly dependent on the initial free phenolic content in raw hardwood. This is an important observation to consider when maximizing delignification efficiency (while minimizing cellulose loss). Future research work should focus on how kraft pulping conditions affect the free phenolic content of the pulp prior to oxygen delignification.

CONCLUSIONS

The six hardwood species examined in this study were shown to differ widely regarding their chemical composition, but their individual syringaldehyde/vanillin (S/V) ratio values did not vary appreciably. Hydroxyl quantification of CEL obtained from raw hardwoods and unbleached pulps showed an increase in aliphatic, 5-substituted and carboxylic hydroxyl groups after pulping. A decrease in 5-free phenolic hydroxyl groups was also observed. Kraft pulping afforded different pulp yields for the same kappa number range. This observation can best be explained by the variance of chemical constituents in the six hardwood species examined. The oxygen delignification stage, carried out under fixed conditions, displayed high delignification efficiency. A strong correlation was observed between O-stage delignification efficiency and phenolic hydroxyl group content of the lignin; this observation corroborated that free phenolic hydroxyl groups are the reactive sites for molecular oxygen reactions with lignin. Finally, the efficiency of oxygen delignification of the six hardwood pulps was found not to correlate to the HexA content.**TJ**

LITERATURE CITED

1. McDonough, T.J., *Tappi J.* 69(6): 46(1986).
2. Ji, Y., Vanska, E., and Heiningen, A.V., *Holzforschung* 63(3): 264(2009).
3. Argyropoulos, D.S., *J. Pulp Pap. Sci.* 29(9): 308(2003).
4. Vuorinen, T., Fagerstrom, P., Buchert, J., et al., *J. Pulp Pap. Sci.* 25(5): 155(1999).
5. Suess, H.U., *Pulp Bleaching Today*, Walter de Gruyter, Berlin, Germany, 2010, Chap. 4, p. 64.

6. Gierer, J., *Wood Sci. Technol.* 20(1): 1(1986).
7. Asgari, F. and Argyropoulos, D.S., *Can. J. Chem.* 76(11): 1606(1998).
8. Aguayo, M.G., Ruiz, J., Norambuena, M., et al., *Maderas: Cienc. Tecnol.* 17(3): 625(2015).
9. Yang, R., Lucia, L., Ragauskas, A.J., et al., *J. Wood Chem. Technol.* 23(1): 13(2003).
10. Gellerstedt, G.L., Heuts, L., and Robert, D., *J. Pulp Pap. Sci.* 25(4): 111(1999).
11. Moe, S.T. and Ragauskas, A.J., *Holzforschung* 53(4): 416(1999).
12. Mansouri, N.E.E. and Salvadó, J., *Ind. Crops Prod.* 26(2): 116(2007).
13. Dence, C.W., in *Methods in Lignin Chemistry* (S.Y. Lin and C.W. Dence, Eds.), Springer-Verlag, Berlin, 1992, pp. 33-61.
14. Santos, R.B and Hart, P.W., *TAPPI J.* 15(11): 707(2016).
15. Chen, C-L., in *Methods in Lignin Chemistry* (S.Y. Lin and C.W. Dence, Eds.), Springer-Verlag, Berlin, 1992, pp. 301-321.
16. Chang, H.-m., in *Methods in Lignin Chemistry* (S.Y. Lin and C.W. Dence, Eds.), Springer-Verlag, Berlin, 1992, pp. 71-74.
17. Min, D., Xiang, Z., Liu, J., et al., *J. Wood Chem. Technol.* 35(1): 52(2015).
18. Tenkanen, M., Gellerstedt, G., Vuorinen, T., et al., *J. Pulp Pap. Sci.* 25(9): 306(1999).
19. Lupoi, J.S., Singh, S., Parthasarathi, R., et al., *Renewable Sustainable Energy Rev.* 49(Sept.): 871(2015).
20. Chang, H.-M., Cowling, E.B., Brown, W., et al., *Holzforschung* 29: 153(1975).
21. Lupoi, J.S., Singh, S., Parthasarathi, R., et al., *Renewable Sustainable Energy Rev.* 49: 871(2015).
22. Granata, A. and Argyropoulos, D.S., *J. Agric. Food Chem.* 43(6): 1538(1995).
23. Argyropoulos, D.S., Sun, Y., and Palus, E., *J. Pulp Pap. Sci.* 28(2): 50(2002).
24. Balakshin, M.Y., Capanema, E.A., and Chang, H.-m., in *Characterization of Lignocellulosics* (T. Hu, Ed.), Blackwell Publishing Ltd., Oxford, UK, 2008, pp. 148-166.
25. Jääskeläinen, A.S., Sun, Y., and Argyropoulos, D.S., *Wood Sci. Technol.* 37(2): 91(2003).
26. Morais, P.H.D., "Effect of age of eucalyptus wood on its chemistry and pulpability, and bleachability and physical properties of pulp," M.S. thesis, Federal University of Viçosa, Viçosa, MG, Brazil, 2008.

ABOUT THE AUTHORS

Over the course of several years of operating a hardwood oxygen stage, it was observed that different species of hardwoods behaved differently with respect to degree of delignification. The current work was a first step in attempting to understand what caused some of these behaviorial differences. Other efforts have shown that free phenolic groups are the main structural lignin feature that correlates with delignification during oxygen treatment. The current work examined a plethora of structures and confirmed that free phenolics is indeed the largest single contributor towards the degree of delignification.

In this study, the isolation of the hardwood lignin was exceptionally difficult, especially for the pulps being treated by oxygen delignification. Low yields were obtained when standard procedures typically employed for softwoods were used on these pulps. A tremendous amount of experimental work is required to elucidate the structures of lignin. The extraction and analysis methods require multiple steps and take a long time to perform. One small mistake or misstep results in weeks of work being lost.

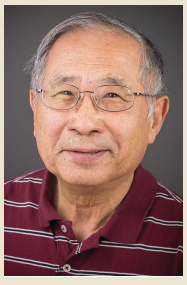
Interestingly, hexenuronic acid content had little to no impact on the degree of oxygen delignification. Of the multiple structures examined, it appeared that only the free phenolic group content has a significant impact.

Better understanding of the lignin structures that correlate with delignification may allow mills to alter their cooking conditions to render specific pulps more prone towards oxygen deligification. The next step is to obtain a variety of hardwood species with a larger spread of S/G ratios and repeat some of this work. Also, we want to develop an improved method of lignin isolation specifically for hardwoods.

Juste Gomes is visiting scholar, Jameel is professor, Chang is professor, and Narron is a Ph.D. candidate at North Carolina State University in Raleigh, NC, USA. Colodette is professor at University Federal de Viçosa, in Viçosa, MG, Brazil. Hart is director, Fiber Science and Innovation at WestRock in Richmond, VA, USA. Email Hart at peter.hart@westrock.com.


Gomes


Jameel


Chang


Narron


Colodette


Hart

27. Wallis, A.F.A., Wearne, R.H., and Wright, P.J., *Appita J.* 49(4): 258(1996).

28. Hu, Z., Yeh, T.F., Chang, H.-m., et al., *Holzforschung* 60(4): 389(2006).

29. Sjöström, E., *Wood Chemistry: Fundamentals and Applications*, 2nd edn., Academic Press, San Diego, CA, USA, 1993.

30. Pinto, P.C., Evtuguin, D.V., and Neto, C.P., *Ind. Eng. Chem. Res.* 44(26): 9777(2005).

31. Zhang, Dongcheng, "Characterization and enhancement of carboxyl groups in softwood kraft pulps during oxygen delignification," Ph.D. dissertation, Georgia Institute of Technology, Atlanta, GA, USA, 2006.

32. Prinsen, P., Rencoret, J., Gutierrez, A., et al., *Ind. Eng. Chem. Res.* 52(45): 15702(2013).

33. Gellerstedt, G.L. and Lindsfors, E.L., *Tappi J.* 70(6): 119(1987).

34. Toven, K. and Gellerstedt, G., "Structural changes of softwood kraft lignin in oxygen delignification and prebleaching," *Int. Symp. Wood Pulping Chem., 10th*, Japan TAPPI, Tokyo, 1999, p. 340.

35. Li, J. and Gellerstedt, G., *Carbohydr. Res.* 302: 213(1997).

36. Lucia, L.A., Ragauskas, A.J., and Chakar, F.S., *Ind. Eng. Chem. Res.* 41(21): 5171(2002).

ABOUT THIS PAPER

Cite this article as: Gomes, V., Jameel, H., Chang, H., et al. *TAPPI J.* 17(7):373(2018). https://doi.org/10.32964/TJ17.07.373

DOI: https://doi.org/10.32964/TJ17.07.373

ISSN: 0734-1415

Publisher: TAPPI Press

Copyright: ©TAPPI Press 2018

About this journal

Influence of tensile straining and fibril angle on the stiffness and strength of previously dried kraft pulp fibers

JOHN M. LONG AND WARREN J. BATCHELOR

ABSTRACT: It has long been known that in individual wood fibers, the tensile mechanical properties are heavily determined by the nature of the cellulose chains in the fibers. Both elastic tensile modulus and strength are directly related to the fibril angle, which is the steepness with which the cellulose chains wind their way around the fiber in the secondary wall of the middle layer, named the S_2 layer. Classic work from the 1970s measured modulus and strength in wood fibers as a function of the fibril angle and compared the results with theoretical models. The measurements were hampered by the presence of defects in the fibers, some which occurred naturally and others which resulted from pulp processing. In this study, we performed more accurate measurements of strength and modulus in single fibers of radiata pine by loading the fibers in cycles, gradually pulling some of the defects out of the fibers in an attempt to obtain defect-free values of modulus and strength. We then plotted these properties against measured fibril angle and compared our results with theoretical models. The results show that even when the fiber had reached maximum load before fracture, at a given value of fibril angle, it still had a measured modulus that is around half the theoretically expected value. The results suggest that the load required to fully remove defects from the fibers may be larger than the fibers can bear before fracturing.

Application: Information contained in this investigation will help paper researchers and engineers better understand the relationship between processing defects and mechanical properties of single wood fibers.

In single wood fibers, longitudinal mechanical properties, such as strength, stiffness, and breaking strain, play a large role in determining mechanical properties in the paper manufactured from these fibers. In a wood fiber, the thickest component is the secondary wall of the middle layer, named the S_2 layer [1,2]. Because the S_2 layer is the thickest, the mechanical properties of this layer determine the overall properties of the fiber. The cellulose microfibrils wind their way around the fiber in a helix. The steepness of this helix determines the fibril angle. This angle influences the fiber's properties: density, strength, and tensile elastic modulus, as well as expansion and shrinkage from fiber processing [3-8]. The main factors that control fiber mechanical properties are the fibril angle of the S_2 layer [9,10], any defects in the fiber [11], and the amount of shrinkage of the fiber as it dries [12]. Fibers that are held under restraint as they are dried are stiffer and stronger than those that have been allowed to freely dry. Similar microstructural and mechanical behavior can be found in the fibers of some plants, such as flax [13].

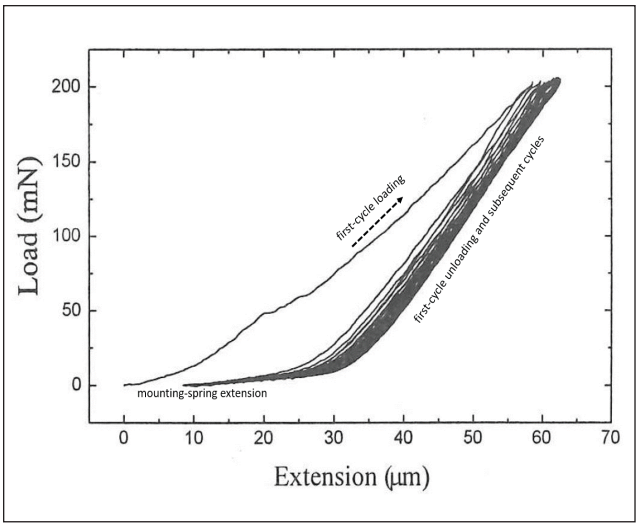
The fibril angle strongly influences the longitudinal mechanical properties, because the bonds along the cellulose chains are much stronger than the bonding between the chains. Despite the importance of fiber mechanical properties to paper properties, there are few sets of data in the literature in which stiffness of single fibers has been measured as a function of fibril angle. The lack of data is probably because such measurements are quite difficult to obtain. In addition to measuring the fibril angle, the fiber cross-sectional area must also be measured in order to convert the measured loads into stresses. Perhaps the most well known of these is the pioneering work by Page, El-Hosseiny, and their colleagues [9,10]. This one full set of measurements was made over 40 years ago, and only fibers from white and black spruce trees were tested. Their data showed that while the elastic modulus and strength of fibers are approximately constant at very low fibril angles (cellulose chains aligned with the fiber longitudinal direction), they fall rapidly for fibril angles beyond 5° or 10°. At fibril angles of 40°, the modulus is reduced to about a fifth [9] compared to fibers with fibril angles between 0 and 10°. More recent investigations on single fibers are consistent with the results presented by Page, but the data sets only contained very small numbers of fibers, such as work on Chinese fir [14] and yew [15]. Other studies have measured mechanical properties of single-fiber southern pine and related the measurements to the position in the trees from which the fibers were collected, noting a relationship between the fibers' strength and stiffness and fibril angle [16-18], but not making an explicit correlation between the two.

Defects can be introduced when the fibers are grown in the wood [19], or more commonly during the pulping process. Defects also become set into chemically pulped fibers when they are dried for the first time. The fibers irreversibly shrink and collapse, a process known as hornification [20-22].

It is known that refining can reverse hornification and can remove defects in previously-dried, chemically-pulped fibers [23]. The forces applied to the fibers in the refiner can straighten fibers and increase the pore volume in the cell wall. Defects in a fiber can cause deterioration of the fiber's mechanical properties. This is especially evident in the work on modulus versus fibril angle in samples of spruce by Page and colleagues, where their data clearly can be seen lying below the theoretical curve for defect-free fibers [9].

Previous work has suggested that it is possible to remove defects in wood fibers by subjecting them to a tensile strain. Experiments on white and radiata pine fibers have shown that repeated cyclic loading in tension can increase their stiffness [24,25]. As an example, **Fig. 1** (taken from Conn and Batchelor [25]) shows how applying cyclic forces to a fiber can change its mechanical properties. The figure shows a single-fiber tensile fatigue test conducted on a radiata pine fiber, conducted in a custom-made tensile test rig designed to eliminate sideways movement and thus ensure uniaxial tension forces. The fiber had been allowed to freely dry before testing. In the test, ten loading cycles of 0–200 mN were performed. Figure 1 shows a very large difference between the initial and subsequent loading cycles. The loading curve for the first cycle has a substantially lower slope than the unloading curve, resulting in substantial plastic strain in the fiber. In the second and subsequent cycles, the loading and unloading curves have similar slopes to the unloading curve of the first cycle, indicating little change in the elastic modulus and no further plastic deformation during these loading cycles. Thus, the initial cyclic load had substantially stretched the fiber (a plastic strain of around 3% for the fiber shown here), possibly removing a defect, such as that of the shrinkage that occurred during the drying process, and thus increasing its stiffness in subsequent cycles. The data shows that at each point on the initial loading curve, the fiber is being stretched. At around 50 mN, there is a sudden increase in extension with little increase in force, 1–1.5 μm. One possible explanation for this effect is that a large defect has been pulled out, such as a kink. Similar load-extension curves to that shown in Fig. 1 have also been observed for white-pine TMP fibers [24]. For a single fiber test of the type shown in Fig. 1, the difference between the modulus in the initial and subsequent cycles is controlled by the degree of restraint under which the fiber is dried, with the largest differences occurring when the fibers are dried unrestrained. Sheets that are restrained as they dry tend to be stiffer and have higher failure loads, because the fibers have not been allowed to shrink as much as unrestrained sheets [26].

In the studies previously cited, where strength and stiffness were related to the fibril angle, all the mechanical tests employed by the respective research groups used single-cycle tensile tests, where the fiber was pulled in tension once, and load and elongation were measured until the fiber fractured. Apart from the study by Wild and colleagues [24], one other study investigated cyclic loading in fibers of ginkgo, juniper, and Norway spruce [27]. The authors presented a model of



1. Typical dry radiata pine fiber load-extension curves, 10 cycles, taken from Conn and Batchelor [25]. During the first 10–20 μm of extension, the rig's mounting springs stretch slightly before the fiber takes up the load.

the fibers' "work hardening" through dynamic chemical effects at the molecular level. The investigation presented in this paper is more on the microscopic rather than on the nanoscale level. Our aim is twofold: using radiata pine rather than spruce fibers, we wish to repeat the work of Page and co-workers by measuring the elastic modulus and strength as a function of fibril angle for different species. It is also the goal of this work to examine how loading these fibers in cycles changes their mechanical properties. We hoped to see whether cyclic loading has reversed the shrinkage and defects produced during drying.

EXPERIMENTAL METHOD

The method chosen was to apply a cyclic tensile load to a single fiber, with the maximum load in a cycle increased in each successive cycle. This methodology was chosen because an increase in elastic modulus produced by stretching the fiber in one cycle can only be measured in a subsequent loading cycle. Thus, by gradually increasing the maximum load, the change in modulus can be measured as a function of the maximum load applied. These measured moduli were then compared with the theoretical modulus calculated from the measured fibril angle for the fiber to determine how much of the strength potential of the fiber has been recovered by the tensile loading applied to the fiber.

To give a wide range of fibril angles, two radiata pine wood samples were selected from sections in a core. The bulk fibril angle along a radiata pine core was measured by means of X-ray diffraction [28]. The two wood samples were then pulped in a conventional kraft process by using a solution of sodium sulfide and sodium hydroxide and then cooking at 140°C for 2 h. Prior to pulping, each piece of wood was wrapped in fine wire mesh that held the samples together during pulping. Upon completion of the pulping, six small



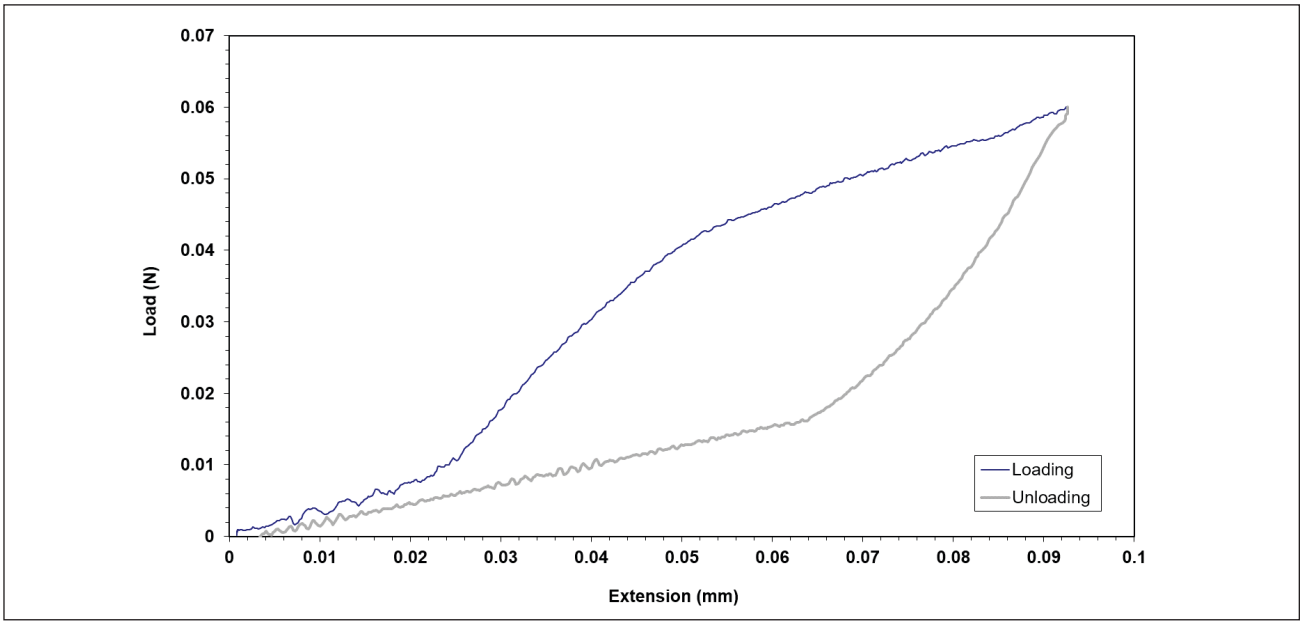
2. Confocal images of one typical fiber's cross section, determined by the method of Xu et al. [29]. From three measurements, the average wall thickness was determined to be 3.1 µm ± 10%, an equivalent diameter of 25 µm, and a cross-sectional area of 190 µm².

clumps of pulp were taken from various sections of the samples. To remove most of the hemicellulose from the fibers, each clump was separately bleached in a chlorine dioxide (ClO_2) solution (6.85g ClO_2/L) for 3 h at 70°C. The clumps were then dispersed in water to separate the fibers, and then they were allowed to freely dry on a glass microscope slide. Between 15 and 20 fibers from each clump were randomly selected and mounted between small aluminum tabs using an epoxy cement that was allowed to set over three days. After mounting, the cross-sectional areas of the fibers were determined by means of confocal light microscopy [29]. **Figure 2** shows a sample cross section from one fiber.

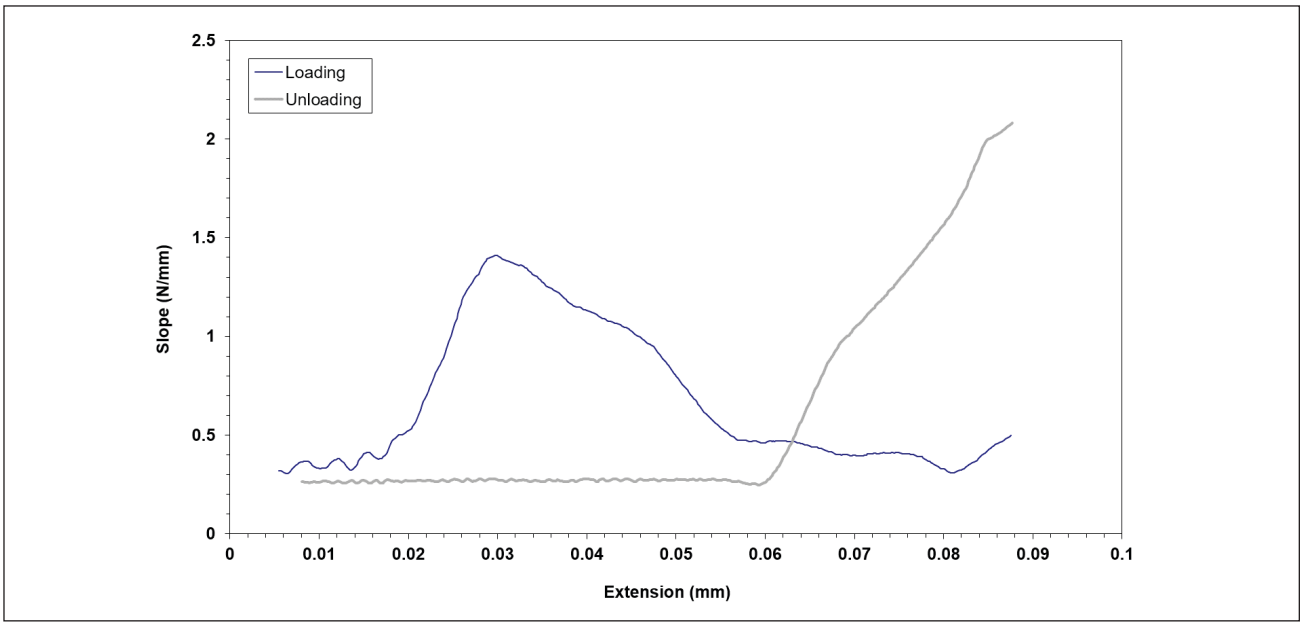
The fibril angles of the same fibers were then determined by means of a confocal microscope and an analyzer crossed with polarization of the incident laser light [30]. The fibril angle was determined by the angular position of the microscope stage when the image of fiber rotating on the microscope stage reached optical extinction. A few fibers showed little or no optical extinction. One reason that we considered for this was that perhaps some of the mounting epoxy wicked up the fiber and thus interfered with the optical effects. Such a condition would interfere with the mechanical tests and lead to dubious results. We discounted this possibility firstly because the mounted fibers were directly examined with a microscope to make sure this did not happen. Secondly, in the development of the test method, the action of epoxy as a mounting glue was investigated very carefully and no ill effects were observed [25]. Thirdly, other research groups have also used epoxy for mounting fibers and reported no wicking or other ill effects [14,24,31]. Perhaps, as cautioned by El-Hosseiny and Page [32], there were further, intrinsic anomalies in those fibers that interfered with optical extinction from the cellulose in the S_2 layers. Regardless of the reason, those fibers where optical extinction was difficult to obtain were deleted from the analysis. The comparison between the bulk fibril angles in the wood core measured by X-ray diffraction and those measured by confocal microscopy on individual fibers was published previously [33] and showed excellent agreement. Near the surface of the trunk, less than 20 mm from the bark, the average bulk fibril angle was 6°. The bulk fibril angle increased with distance into the tree to about 30° at a depth of 80 mm. Compression wood had an average fibril angle of 37°.

To ensure that environmental effects would not influence the properties of the fibers, the testing laboratory was held constant at 23°C and 50% relative humidity. The tensile testing of the single fibers was done using an attachment for an Instron universal tester (Instron; Norwood, MA, USA), which was designed to ensure that the load was only applied uniaxially along the fiber. The details of the apparatus and analysis method are described by Conn and Batchelor [25]. Once the test sample was mounted, the gauge length was measured via a travelling microscope. Typical gauge lengths were between 0.4 and 1.0 mm. Using a 1 N load cell, each fiber was tested under cyclic loading conditions with the maximum load in the first cycle set to 0.02 N. Thereafter, the maximum load was incremented for each successive cycle by 0.02 N until the fiber failed. The raw data for each tensile test were a succession of load-extension curves. For each cycle in a test, the slope of the load-extension curve as a function of extension was calculated by means of numerical differentiation. The slope-extension data for each cycle was then corrected for the test rig's mounting spring by subtracting the internal spring constant, which gives each plot of slope versus extension a small vertical offset. Then, the maximum slopes for loading and unloading were determined from the corrected data. The maximum slopes were combined with the measured gauge length and cross-sectional area to calculate the elastic modulus for the fiber in the loading case and for the unloading case. Finally, the breaking load was noted and the breaking stress was calculated. For each successfully tested fiber, the elastic modulus in the first cycle, the elastic modulus in the final complete cycle, the breaking load of the fiber, and the degree of plastic deformation at the commencement of the final cycle were extracted from the test data.

As an example of our technique, **Fig. 3** shows the raw load-extension data for the third cycle of a fiber with a fibril angle of 24° after tensile testing. This sample was taken from a piece of compression wood, and it was expected to have a relatively high fibril angle. Beforehand, this fiber had a mea-



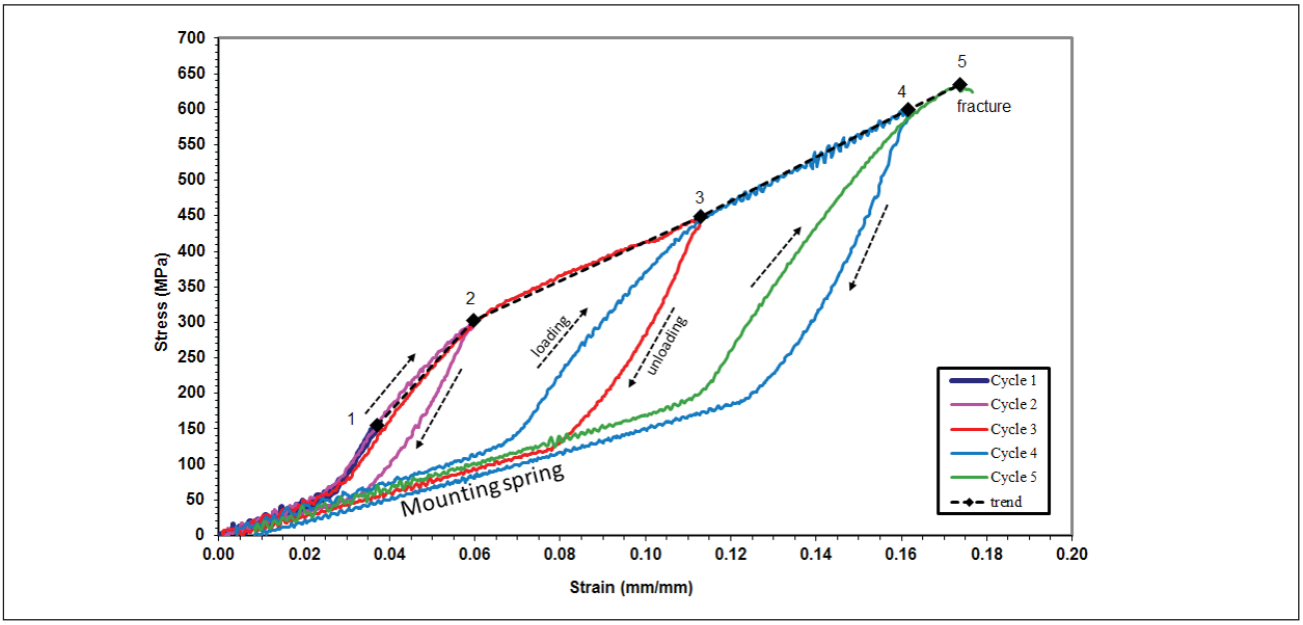
3. Load-extension curve of the third cycle of a single radiata pine fiber.



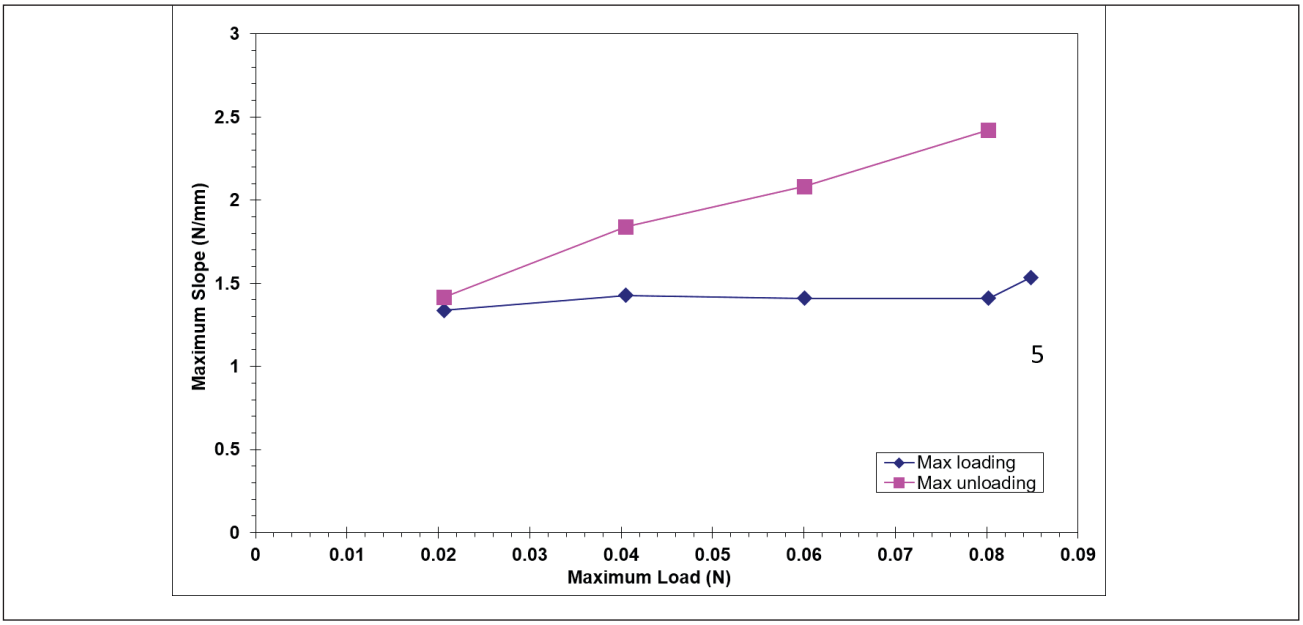
4. Slope of the load-extension curve of Fig. 3's fiber. The presence of the mounting spring is visible in the vertical offset of 0.3 N/mm.

sured fibril angle of 43°. At first, the load was absorbed by the mounting spring in the test apparatus. The mounting spring, shown in Fig. 1 of reference [25], ensure that there is no lateral movement in the loading of the fiber. At an extension of about 0.025 mm, the fiber begins to bear the load. In this cycle, the load was increased to 0.06 N, and then decreased back to zero. The fiber shows yielding at an extension of 0.045 mm. Plastic deformation is evident from the large hysteresis in the curves. The slope of the load-extension curve is related to the stiffness of the fiber (**Fig. 4**). On loading, the fiber shows the maximum slope at an extension of around 0.03 mm. However, the slope is larger still at the beginning of the unloading part of the test. The effect of the test rig's mounting spring was subtracted out from the slope data by averaging the slope data at the start of the test before the slope begins to rise (about 0.3 N/mm in this case) and subtracting this vertical offset from the data set. Of the 80 fibers that were initially mounted, 21 were successfully strained to fracture, and the fibril angle on these fibers was remeasured after completion of the cyclic tensile tests.

According to our theory, and as suggested by Page and colleagues [9], before mechanical testing, a given fiber contains kinks, knots, pores, and other defects. Placing the fiber gradually under tension pulls the defects associated with fiber



5. Stress-strain curve of a single radiata pine fiber in cyclic loading. The maximum load has been increased in 0.02 N increments, until the fifth cycle, where the sample has fractured. The fibril angle decreased from 43 ±2° before cyclic loading to 24 ±1° after loading. The numbers indicate cycle number, the squares indicate the overall trend, and the arrows indicate loading or unloading.

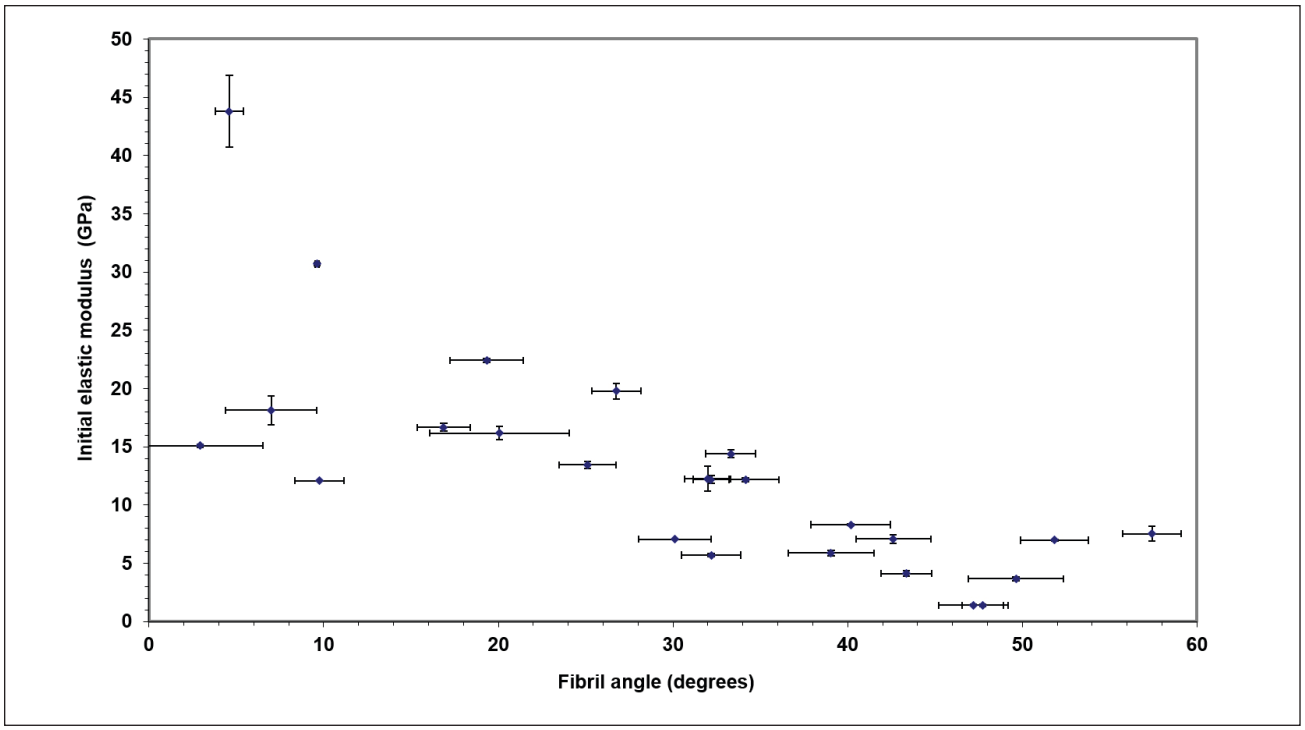


6. Slope of the load-extension curves for Fig. 5's fiber. A greater stiffness is shown in the unloading cycles, which suggests that with plastic deformation, the fiber modulus is increasing.

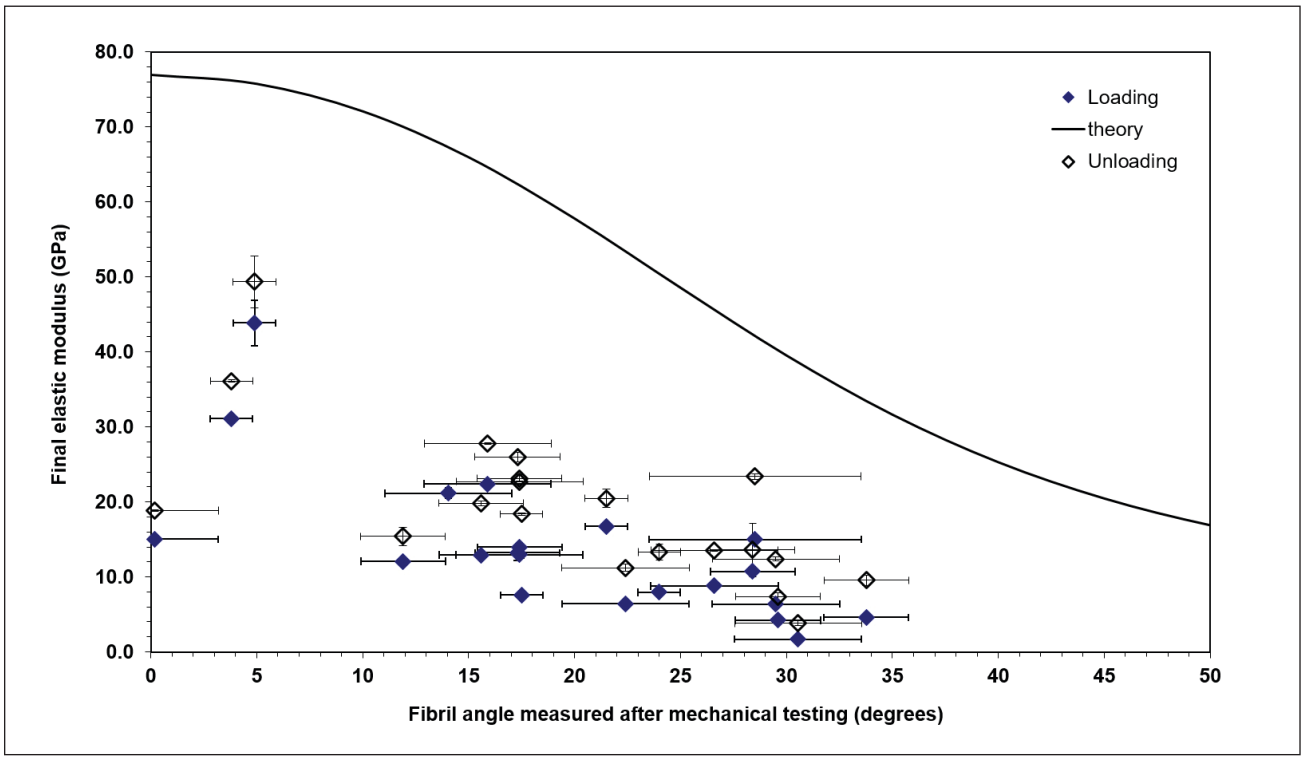
processing out of the fiber. As the defects are removed, we expect to see the fiber becoming stiffer (increased modulus) from cycle to cycle. Also, we expect the fibril angle to decrease as the number of cycles increase because the tensile loads tend to pull the cellulose chains more parallel with the length of the fiber. Thus, to determine the properties of "defect-free" fibers, we used fibril-angle measurements after cyclic loading was complete. We also compared modulus (slope of a stress-strain curve) in both loading and unloading cases.

RESULTS

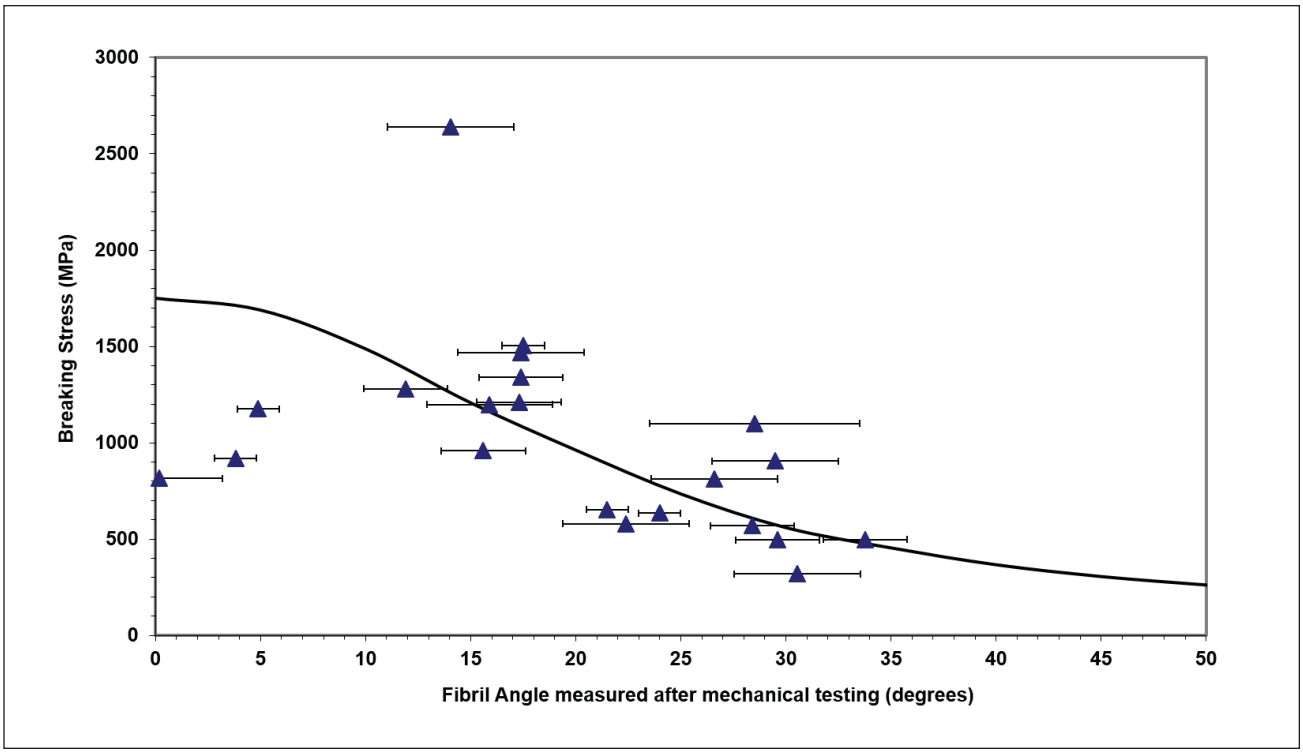
Figure 5 shows an example of the results obtained from the representative fiber of Figs. 3 and 4. Prior to mechanical testing, the fibril angle of this fiber was measured to be 43 ±2°. The gauge length of this particular fiber was 0.82 mm, and its measured cross-sectional area was 134 μm². The second loading cycle shows similar behavior to that seen in the first loading cycle of Fig. 1. The slopes of the loading curves are lower than the corresponding slopes of the unloading curves



7. Initial elastic modulus determined from the slope of the stress-strain curve in the initial loading cycle, as a function of the fibril angle measured before the commencement of mechanical testing.



8. Elastic modulus measured in the final cycles before fracture as a function of the fibril angle measured after fracture. Closed symbol is for loading in the final cycle, and open symbol is for final unloading. The solid line is the maximum attainable modulus, calculated from the theoretical work of Page et al. [9, p. 116].



9. Breaking stress achieved in the final cycle before fracture versus fibril angle. The curve represents the theoretical limit for spruce as calculated by El-Hosseiny and Page [34].

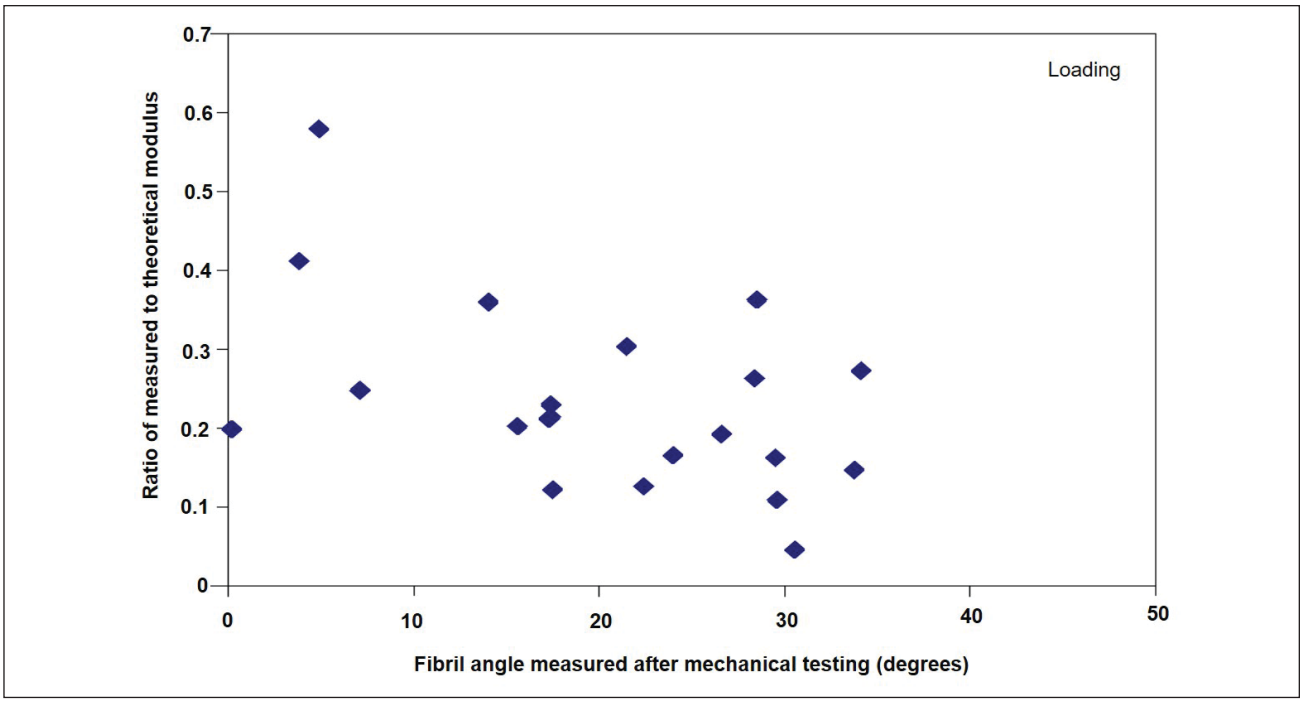
(**Fig. 6**), as expected, and the sample has undergone substantial plastic deformation during loading. In many cases, we observed that the loading curve of the next cycle shows a similar modulus to the unloading while the sample is being loaded to the maximum load attained in the previous cycle. The sample then begins to plastically deform again once the maximum load from the previous cycle is exceeded. The process was repeated until the sample fractured. This fiber completed four cycles and broke in the fifth. The slope of the load-extension data was a maximum in the fifth cycle for loading and in the fourth for unloading. The data show that the stiffness of the fiber increases with the amount of plastic deformation, with the biggest change occurring between the first and second cycles. From the maximum slope values, the elastic modulus for this fiber was determined to be 8.0 ±0.4 GPa while loading the fiber, and 13 ±1 GPa while unloading. One can call the elastic modulus determined in the loading case the initial modulus and that in the unloading case the final modulus. Strength of a fiber was determined by the maximum stress on the fiber prior to fracture. In the case of the sample fiber discussed here, the strength was 634 MPa. After mechanical testing, the fibril angle was remeasured and found to have decreased to 24 ±1°. Some of the fibers tested broke after only three cycles. Many fibers passed 10 cycles, and one fiber completed 20 cycles before fracture. We observed the general behavior of stiffening with successive cycles repeatedly in all the fibers that we tested.

Elastic modulus results

We observed that for most, but not all, fibers, the measured fibril angle before tensile testing was greater than that after tensile testing, ranging from near 0 to 58°. **Figure 7** shows the initial elastic modulus obtained in the initial loading cycle for all fibers. We use caution in calling these values "moduli" because as the previous discussion has indicated, the initial loading data had no measurable elastic region, and plastic deformation occurs continuously throughout the loading cycle. In further analysis here, we use the fibril-angle data measured after tensile testing. Replotting these results as a function of fibril angle measured after tensile testing yields **Fig. 8**. Also plotted on this graph is the theoretical curve for radiata pine as calculated from Page's analysis [9]. The unloading values are significantly higher than the loading values, especially at higher fibril angles. This confirms the hypothesis that the fibers become stiffer as cyclic loading proceeds and reach a maximum with the final unloading cycle.

Strength results

Figure 9 shows our results for breaking stress versus fibril angle. El-Hosseiny and Page [34] calculated a theoretical limit for similar data in spruce fibers, and this curve is included in the plot. Between 10° and 35°, the curve fits the data rather well. However, strengths for fibril angles lower than 10° are much lower than what one might expect from the theory. Further experiments may shed more light on this surprising result.



10. Ratio of modulus measured in the last loading cycle to the theoretical modulus.

DISCUSSION

We observed significant plastic deformation in many of the fibers, and that of Fig. 5 is typical. After bleaching, these fibers were allowed to dry without restraint and we suggest that the plastic deformation is due to several sources. First, some of the shrinkage and defects, which had been introduced into the fiber as it was dried, have been pulled out. Second, the fibril angle of the fiber tends to decrease as the fiber is loaded. The reduction in the pitch at which the fibrils are helically wound will reduce the cross-sectional dimensions of the fiber and increase the length. It is interesting that for the fiber of Fig. 5, the plastic deformation seems to increase continuously with increasing load. While an approximate yield point is visible in cycles 3 and 4, this apparent yield stress increases with each cycle.

Figure 8 shows the elastic-modulus results. In this figure, the elastic modulus in the final loading cycle is plotted against the fibril angle after testing—that is, after the fiber has fractured. In comparison to the results in Fig. 7, several interesting trends can be seen. The first trend is that the mechanical loading has, in general, reduced the fibril angle, with the average fibril angle falling from 29° to 19°. Furthermore, the largest reductions in fibril angle occur for fibers that had the highest initial fibril angle. These figures further show the large increase in elastic modulus of the final cycle before fracture compared to the slope of the stress-strain curve in the initial cycle. However, despite the increase in modulus as the sample is stretched out, it can be seen that the measured modulus before failure is still much less than the theoretical value. The ratio of the measured to the theoretical modulus was plotted in **Fig. 10**. The data shows a general upward trend with decreasing fibril angle, with the fibers with lowest fibril angles tending to attain the highest percentage of the theoretical maximum. The average ratio over the whole set of data is only 22%. The results show that even when the fibers have reached the maximum load before fracture, they still have values of elastic modulus that are around half that predicted by theory, given the fibril angle of the fiber. From this result, we conclude that the load required to fully remove all defects from the fibers may be larger than what the fibers can bear before breaking. There are certainly some defects that would not be removed by cyclic straining, such as pits in a side wall. What interests us here are those defects that result from processing and shrinkage as the fibers dry.

The information that comes from performing the experiments this way is much more than could be obtained with conventional single-cycle testing. The mechanical properties of the fibers after drying can be measured and compared with the modulus obtained after the fiber has been stretched again. The cyclic loading method allows for these changes to be monitored at different levels of stress, given that the sample is periodically unloaded. Deformation of wood fibers during cyclic loading warrants further study. For instance, these experiments could be performed on another species of wood. Furthermore, the fibers could also be subjected to detailed microscopic analysis to observe processing defects directly before and after cyclic loading. Finally, the stiffening of the fibers during cyclic loading may be a combination of both reducing defects through cyclic strain and any resulting reduction of the fibril angle. Theoretical modelling of the mechanical behavior of loaded fibers with defects and a simultaneous change in the fibril angle may shed some light on this.

CONCLUSIONS

The tensile mechanical properties of single fibers of radiata pine were studied as a function of fibril angle (the steepness with which cellulose molecules wind their way around the S_2 layer of the fiber). In an attempt to determine the elastic modulus and strength of defect-free fibers, single fibers were loaded in cycles of increasing load, noting the slope of the stress-strain curve while loading and unloading in each cycle. The fibers had varying values of fibril angle ranging from near 0 to 35°. For each fiber, the maximum slope of the stress-strain curves was taken to be the elastic modulus. Strength was taken as the breaking stress. The measured elastic moduli of the fibers were observed to increase from that measured in the first cycle to that measured in the final cycle, confirming the hypothesis that fibers can be stiffened by means of cyclic straining. At the same time, the measured values of fibril angle tended to decrease from before mechanical testing to after mechanical testing, especially in the case of fibers with higher initial fibril angles. Plots of elastic modulus versus fibril angle and strength versus fibril angle were similar in shape to previously published plots taken from data obtained from spruce fibers. Our measured values of modulus were well below classic theoretical predictions, while our measurements of strength showed slightly better agreement with the classic theoretical model. We conclude from these results that due to strength limitations, cyclic loading was insufficient to remove all the defects from the fibers and thus obtain the "true" value of elastic modulus. Nonetheless, the results are quite interesting and worthy of further study with different species of wood. **TJ**

ACKNOWLEDGEMENTS

The financial support of the Commonwealth Government of Australia through the Australian Research Council is gratefully acknowledged. JML acknowledges support from a Deakin-University research fellowship while this work was being performed. We also thank A.B. Conn and Y. Filonenko for their valuable assistance during this project.

LITERATURE CITED

1. Barnett, J.R. and Bonham, V.A., *Biol. Rev.* 79(2): 461(2004).
2. Mark, R. and Gillas, P., in *Handbook of Physical and Mechanical Testing of Paper and Paperboard* (R. Mark, Ed.), Marcel Dekker, New York, 1983, vol. 1, chap. 10.
3. Donaldson, L., *IAWA J.* 29(4): 345(2008).
4. Courchene, C.E., Peter, G.F., and Litvay, J., *Wood Fiber Sci.* 38(1): 112(2006).
5. Farber, J., Lichtenegger, H.C., Reiterer, A., et al., *J. Mater. Sci.* 36(21): 5087(2001).
6. Fang, S.Z., Yang, W.Z., and Fu, X.X., *J. For. Res.* 15(4): 261(2004).
7. Reiterer, A., Lichtenegger, H., Tschegg, S., et al., *Philos. Mag. A* 79(9): 2173(1999).
8. Burgert, I., Frühmann, K., Keckes, J., et al., *Trees* 18(4): 480(2004).
9. Page, D.H., El-Hosseiny, F., Winkler, K., et al., *Tappi* 60(4): 114(1977).
10. Page, D.H., El-Hosseiny, F., Winkler, K., et al., *Pulp Pap. Mag. Can.* 73(8): 72(1972).
11. Mohlin, U.B., Dahlbom, J., and Hornatowska, J., *TAPPI J.* 79(6): 105(1996).
12. Jentzen, C.A., *Tappi* 47(7): 412(1964).

ABOUT THE AUTHORS

An opportunity for a collaborative research project arose between Deakin and Monash Universities, and this research enhances the field of paper research in that it attempts to extend previous work on mechanical properties of wood fibers in an enhanced way that has not been tried before.

The preparation of individual fibers for tensile testing was the most difficult aspect of this work. The second most difficult aspect was the lengthy data analysis that was required. Personally, I (Long) discovered new ways of testing single fibers, both mechanically and microstructurally, and I expanded my personal expertise in the general field of materials analysis. I also clearly observed the correlation between fibril angle in wood fibers and their tensile properties.

The most interesting aspect of this work was repeating classic research on fibers, confirming the original results on another species of wood, and then extending the investigation. Surprisingly, even straining the fibers in cycles did not result in the fibers having measurable stiffnesses and strengths matching the theoretical predictions.

Through this research, mills may gain further insight into fiber properties of softwoods and their relationship to the fibril angle. The next step is to repeat the theoretical strength and stiffness calculations for radiata pine fibers by means of modern finite element modeling.



Long



Batchelor

Long is senior lecturer in the School of Engineering, Deakin University, Geelong, Victoria, Australia. Batchelor is associate professor in the Department of Chemical Engineering, Monash University, Clayton, Victoria, Australia. Email Long at john.long@deakin.edu.au.

13. Bourmaud, A., Morvan, C., Bouali, A., et al., *Ind. Crops Prod.* 44: 343(2013).
14. Wang, G., Yu, Y., Shi, S.Q., et al., *Wood Fiber Sci.* 43(3): 251(2011).
15. Keunecke, D., Eder, M., Burgert, I., et al., *J. Wood Sci.* 54: 420(2008).
16. Groom, L., Mott, L., and Shaler, S., *Wood Fiber Sci.* 34(1): 14(2002).
17. Mott, L., Groom, L., and Shaler, S., *Wood Fiber Sci.* 34(2): 221(2002).
18. Groom, L., Shaler, S., and Mott, L., *Wood Fiber Sci.* 34(2): 238(2002).
19. Eder, M., Jungnikl, K., and Bugert, I., *Trees* 23(1): 79(2009).
20. Laivins, G.V. and Scallan, A.M., "The mechanism of hornification of wood pulps," *Transactions of the Tenth Fundamental Research Symposium*, PIRA International, Leatherhead, UK, 1993.
21. Fernandes-Diniz, J.M.B., Gil, M.H., and Castro, J.A.A.M., *Wood Sci. Technol.* 37(6): 489(2004).
22. Page, D.H., *Sven. Papperstidn.* 88(5): R30(1985).
23. Page, D.H., in *Fundamentals of Papermaking Transactions of the Ninth Fundamental Research Symposium* (C.F. Baker and V.W. Punton, Eds.), Mechanical Engineering Publications, London, 1989, Vol. 1, pp. 1-38.
24. Wild, P.M., Provan, J.W., Guin, R., et al., *TAPPI J.* 82(4): 209(1999).
25. Conn, A.B. and Batchelor, W.J., *Appita J.* 52(4): 290(1999).
26. Kiiskinen, H., Paltakari, J., and Pakarinen, P., "Drying and paper quality," in *Papermaking Part 2: Drying* (M. Karlsson, Ed.), Fapet Oy, Helsinki, 2000.
27. Keckes, J., Burgert, I., Frühmann, K., et al., *Nat. Mater.* 2: 810(2003).
28. Evans, R., Stuart, S.A., and Van der Touw, J., *Appita J.* 49(6): 411(1996).
29. Xu, L., Filonenko, Y., Li, M., et al., *Appita J.* 50(6): 501(1997).
30. Batchelor, W.J., Conn, A.B., and Parker, I.H., *Appita J.* 50(5): 377(1997).
31. Mott, L., Shaler, S.M., and Groom, L.H., *Wood Fiber Sci.* 28(4): 429(1996).
32. El-Hosseiny, F. and Page D.H., *Wood Fiber* 5(3): 208(1973).
33. Long, J.M., Conn, A.B., Batchelor, W.J., et al., *Appita J.* 53(3): 206(2000).
34. El-Hosseiny, F. and Page, D.H., *Fibre Sci. Technol.* 8(1): 21(1975).

ABOUT THIS PAPER

Cite this article as: Long, J., Batchelor, W. *TAPPI J.* 17(7): 383(2018). https://doi.org/10.32964/TJ17.07.383

DOI: https://doi.org/10.32964/TJ17.07.383

ISSN: 0734-1415

Publisher: TAPPI Press

Copyright: ©TAPPI Press 2018

About this journal

Wet-end addition of nanofibrillated cellulose pretreated with cationic starch to achieve paper strength with less refining and higher bulk

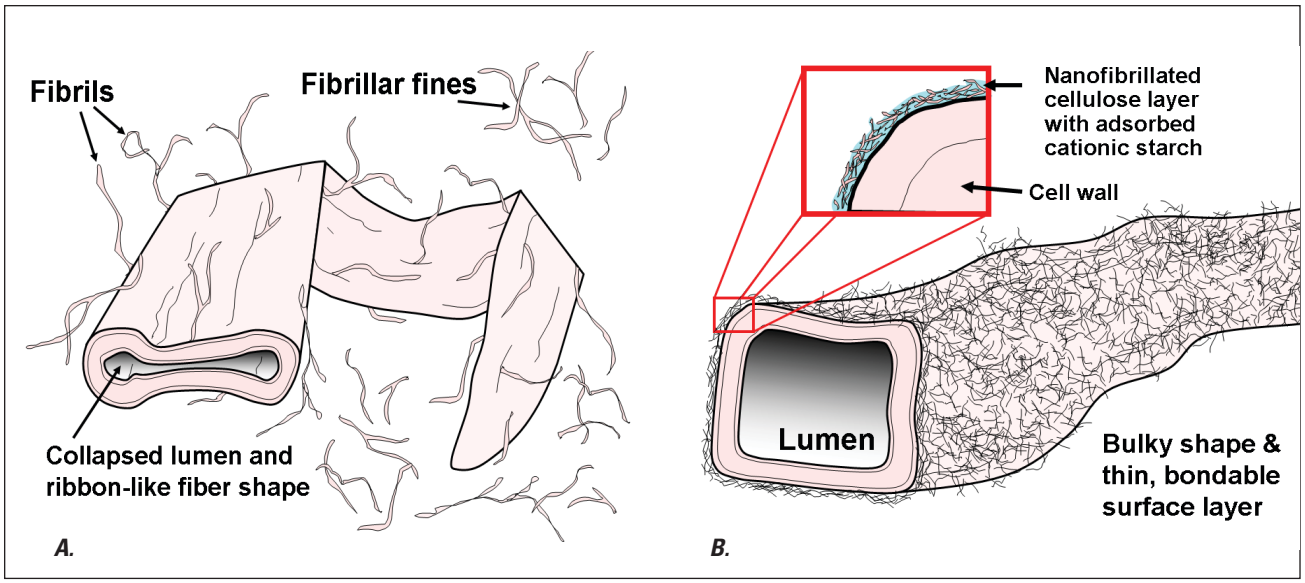
MATTHEW C. RICE, LOKENDRA PAL, RONALDS GONZALEZ, AND MARTIN A. HUBBE

ABSTRACT: Nanofibrillated cellulose (NFC) treated with cationic starch was evaluated as a bonding system to permit lower degrees of refining and lower apparent density of high-mass handsheets made from bleached kraft pulp. Mixed pulp (70% hardwood, 30% softwood) was formed into sheets with the optional addition of 5% by dry mass of NFC. The default addition of NFC was compared with a system in which the NFC had been pretreated either with cationic starch (at various levels) or optionally followed by colloidal silica. Comparative tests also were carried out with separate addition of cationic starch to the main furnish. Unrefined fibers (514 mL CSF) were compared with low-refined (473 mL CSF) and high-refined (283 mL CSF) pulp mixtures. The NFC that had been pretreated with cationic starch at a high level was especially effective at boosting the tensile strength and stiffness of sheets prepared from pulp that had been refined at a low level, thus achieving improved strength at relatively low apparent density (high bulk) of the handsheets. The results support a strategy, for applicable grades of paper, of using cationic starch-pretreated NFC in place of refining energy applied to the main fiber furnish. It was further established that colloidal silica can be employed as a further pretreatment of the cationic starch–treated NFC as a means of promoting dewatering in the combined system.

Application: Higher caliper at a defined basis weight, while maintaining tensile strength and stiffness, can be achieved by use of cationic starch–pretreated nanofibrillated cellulose, while decreasing the main refining of kraft fibers. Mills can consider this technology for paper and board grades for which low apparent density and maintaining stiffness are primary goals.

In the manufacture of paper and paperboard, it can be difficult to maintain specified strength levels while minimizing fiber costs and meeting specified targets for caliper [1,2]. Refining of the pulp is generally regarded as a primary tool by which to enhance bonding within paper. However, excessive refining tends to slow the dewatering rate during the paper forming process, and the resulting paper tends to be denser [3,4]. If substantially increased bonding could be achieved without as much refining of the main furnish, then it might be possible to achieve paper property targets—including caliper and stiffness targets—at lower basis weights. Also, a wet web composed of less-refined fibers can be expected to exhibit greater recovery of its thickness (caliper) when exiting from a wet-press nip [5,6]. Thus, the combination of lower-refined fibers, possibly a lower amount of fibers per a given area of product, and enhanced bonding has the potential to decrease the amount of evaporative energy needed to dry paper as it is being made. Such technology would also be of great interest to papermakers who rely strongly on the use of recycled fibers, which often have less capacity to be improved by refining. For instance, Delgado-Aguilar et al. [7] demonstrated that highly fibrillated cellulose can be effective as a bonding agent in furnish composed of recycled fibers. Paper grades that are likely to benefit from the ability to achieve strength properties at lower apparent density would include return postcard stock, book paper, paper towel, folding boxboard, and various specialty products.

Micro- and nanofibrillated cellulose (MNFC) has been considered in past studies as a papermaking wet-end additive [8–12]. Though such addition of nanocellulose to papermaking furnish has been shown to increase paper strength, it also tends to slow the rate of dewatering [13], which is often a key factor affecting the speed of production. However, most such studies have not involved the usage of cationic starch or other cationic polymers. An exception was the work of Ahola et al. [14]. Those authors pretreated the main cellulosic pulp fibers with a high-mass, high-charge wet-strength polymer, polyamidoamine-epichlorohydrin, followed by the addition of NFC. A dense layer of NFC was collected onto the fiber surfaces by that approach. When the cationic polymer was instead used



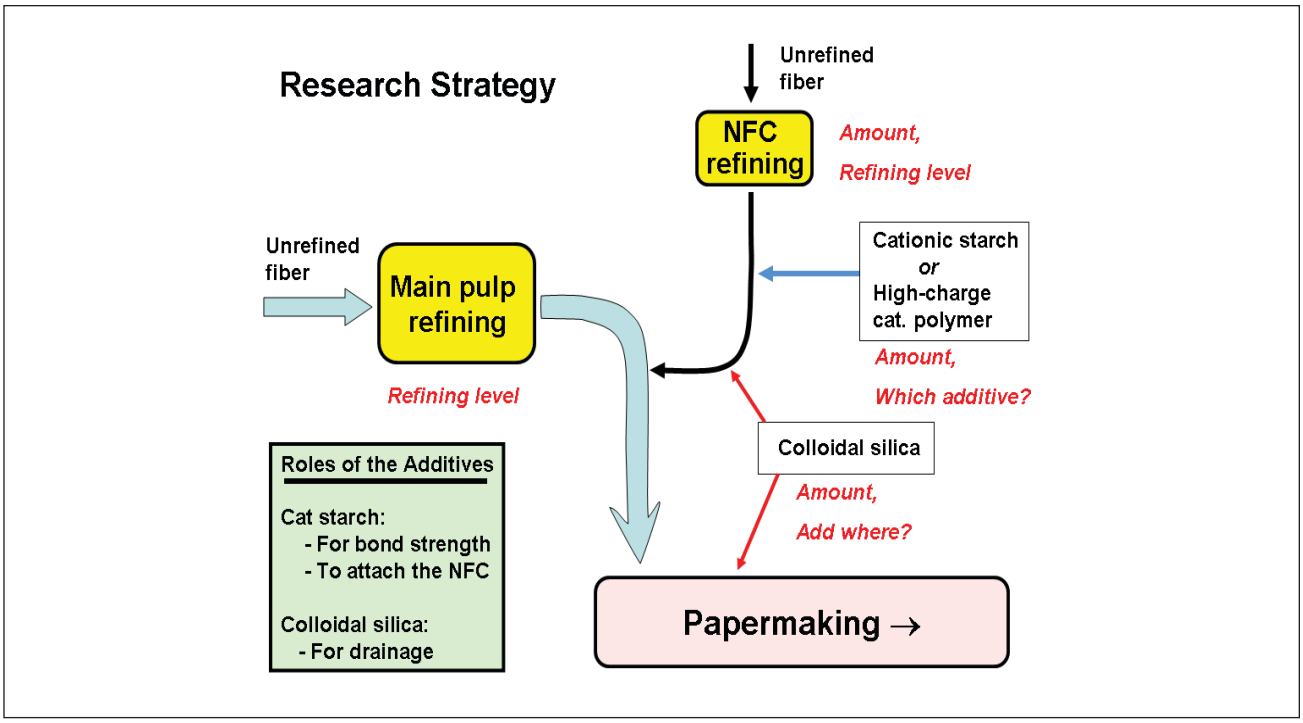
1. Illustration of a contrast in fiber cross-sectional shape (ribbonlike versus tubelike) and fines content when comparing (A) conventional refining and (B) placement of pretreated nanofibrillated cellulose (NFC) at the surfaces of lower-refined fibers.

to pretreat the NFC, excessive agglomeration occurred, which may have been a result of the high molecular mass and charge density. Increases in paper strength were observed, especially when sequentially adding the cationic polymer and NFC to the furnish. More recently, Merayo et al. [15] found synergistic relationships between the use of NFC and certain cationic polymers. Likewise, Hollertz et al. [16] showed that favorable strength benefits were achieved when certain NFC preparations were added together with polyvinyl amine, a strongly cationic polymer.

The main hypothesis underlying this work can be understood from the diagrams in **Fig. 1**. The image at the left represents a conventionally well-refined kraft pulp fiber in the wet state. As is well known [17], sufficiently high levels of refining promote internal delamination in the fiber walls, such that the fiber lumens are able to collapse, giving rise to a ribbonlike fiber shape. The ribbonlike, conformable fibers resulting from extensive refining enable development of strong interfiber bonding, relatively high tensile strength of the paper, but relatively low caliper (lower bulk) at a given basis weight. By contrast, at the other extreme, a completely unrefined fiber will have a greater tendency to regain its three-dimensional character even after such processes as wet pressing [5,6]. Ordinarily, such unrefined fiber would have poor interfiber bonding ability due to having a low relative bonded area with adjacent fibers in a sheet [18]. Part B of Fig. 1 shows the proposed system in which NFC, after having been treated with cationic starch, preferentially becomes attached to the surfaces of the negatively charged fiber surfaces, thus providing a highly bondable layer. It is proposed that the combined system with NFC pretreated with cationic starch can provide synergistic benefits of added strength, beyond what would be achieved by either NFC or cationic starch alone. At the same time it is proposed that a bulkier sheet structure can be achieved.

The hypothesis just introduced offers a potential way to achieve paper strength at lower apparent density, at least before calendering, but there still is a need to address concerns regarding the rate of water removal during sheet formation. Past studies have shown that the presence of highly fibrillated cellulose in papermaking furnish has the potential to greatly slow the drainage rates [10,13]—and potentially decrease production rates—on a paper machine. To address this concern, the present research considers two approaches. First, the fact that the NFC becomes treated with a cationic polymer makes it more likely that the NFC will become attached to fiber surfaces; it follows that such bound NFC would not have as much of an adverse effect on dewatering in comparison with unattached fine cellulosic matter [19]. Further, the addition of a suitable dosage of colloidal silica to a mixture of NFC and cationic starch may be able to increase the dewatering rates without interfering with the system's ability to contribute to paper strength. The effect of the silica additive on dewatering has been well demonstrated [20–22], but not in the case of NFC that has been treated by cationic starch, then treated by colloidal silica, then added to papermaking furnish. While the use of cellulosic micro- and nanofibrillated materials have been associated with being very costly, our group recently has conducted the most extensive manufacturing cost analysis for MNFC, determining values as low as US$1200 per dry ton equivalent of MNFC. This means that a 1% MNFC charge would cost approximately US$12 per finished ton of paper [23] in addition to the cost of the cationic polymer additive. This application cost should be compensated by savings in energy cost (related to refining) and potentially fiber reduction.

Figure 2 provides a schematic view of how the proposed system might be later optimized, depending on the process and product requirements of a given paper mill. Key variables in control of the papermaking team would include the degree



2. Schematic view of the proposed process, in which the level of refining of the main fiber furnish is dialed back, and NFC is pretreated with either a high-charge polymer (just to make it cationic) or with cationic starch (in an effort to achieve a synergistic strengthening effect), followed by optional colloidal silica treatment (either to the treated NFC or to the whole furnish) for tuning of drainage and water retention value effects.

of refining of the main furnish, the amount and refining level of highly fibrillated cellulose (NFC in the present research), the amount of cationic starch or other cationic polymer used to treat the highly fibrillated cellulose, and the amount and addition point of an optional drainage-promoting additive such as colloidal silica. As shown, there are two purposes for the addition of cationic starch. One is to contribute bonding strength to the paper structure. The other is to hold the NFC effectively on the fiber surfaces in the course of the process described in the figure.

Because the present work was designed to evaluate a concept, the conditions selected do not necessarily correspond to a specific grade of paper. Meaningful characterization of the apparent density of the material was a main concern in the present work; therefore, an intentionally high basis weight condition was selected. Preliminary work showed that good formation uniformity could be achieved and pressing operations could be carried out effectively with a basis weight of 350 g/m^2. By working at a very high basis weight, the effect of differences in surface smoothness, relative to the evaluation of density, is greatly reduced. The selection of bleached hardwood kraft as the major furnish type was based on the widespread use of hardwood fibers in some bulky grades of paper, such as book paper and tissue, as well as the excellent formation uniformity that can be achieved in handsheet evaluations. It made sense to include some softwood fiber as well because papermakers often employ a blend to achieve tear strength objectives and efficient paper machine operations.

EXPERIMENTAL

Chemicals and materials

A mixture of 70% bleached hardwood kraft pulp and 30% bleached softwood kraft pulp (southern U.S. fibers) was either unrefined or corefined using a laboratory Hollander beater to the following CSF levels: 514 mL (unrefined), 473 mL (lightly refined), and 283 mL (heavily refined). The NFC, of the spray-dried form (lot no. U38, grade cellulose nanofibrils [CNF]), was provided by the University of Maine, Process Development Center. Properties of the NFC material have been presented [24]. Tap water was added to achieve a solids content of 0.5%, and sodium sulfate was added to reach an electrical conductivity of 1000 µS/cm at room temperature (approximately 22°C [71.6°F]) before further testing. Sodium bicarbonate was added at the 1.0 mM level as a means of achieving approximately neutral pH.

The cationic starch used in this work was Chargemaster L340 (Grain Processing Corp.; Muscatine, IA, USA), a cationic starch paste of the pregelatinized type. It was prepared for use by dilution in water at least 1 h before usage. The colloidal silica was NP 320 (Kemira; Helsinki, Finland). This product is known to be of the gel type; it consists of irregular fused chains of approximately 2 nm primary silica particles and is designed to promote both fine-particle retention and increased rates of dewatering when used in combination with a high-mass, low-charge cationic polymer such as cationic starch. The no. 40,901-4 poly-diallyldimethylammonium chloride (poly-DADMAC) (Sigma-Aldrich; St. Louis, MO, USA) is a

linear homopolymer with one positive (quaternary nitrogen) charge per repeat unit with a molecular mass range 100000–200000 g/mol).

Pretreatments and blending

Pretreatments of the NFC were carried out at 1000 µS/cm electrical conductivity. The cationic starch solution (diluted to 1% solids solution before addition) was added with agitation, to achieve the selected addition level (10% or 50% starch solids on the basis of NFC solids). The colloidal silica was added, after addition of cationic starch to NFC, at levels of either 5%, 10%, or 20% on the basis of NFC solids. Solids were adjusted so that the overall percentage solids were constant during experimentation.

Sheet forming, pressing, and drying

To enable reliable evaluation of caliper and apparent density, the sheets were prepared with a high basis weight. On the basis of preliminary tests, a basis weight of 350 g/m^2 was selected. Sheets were prepared using a procedure that was otherwise consistent with TAPPI Standard Test Method T 205 "Forming handsheets for physical tests of pulp". As described, a roller was used to initially press the damp sheets. Each sheet was subsequently passed through the nip of an Atlas laboratory wringer at the automated feed rate (2.8 cm/s) and an applied load equivalent to 50 lb (22.68 kg) applied to a 12-in. (30.48 cm) wide nip between 2-in. (5.08 cm) diameter rubber rollers, giving a nip load of 0.742 kg/cm. Sheets were dried under restraint, using the standard TAPPI rings to hold the circular sheets. Sheets were equilibrated to TAPPI test conditions (50% RH, 23°C [73.4°F]) TAPPI T 402 "Standard conditioning and testing atmospheres for paper, board, pulp handsheets, and related products" at least overnight before physical testing.

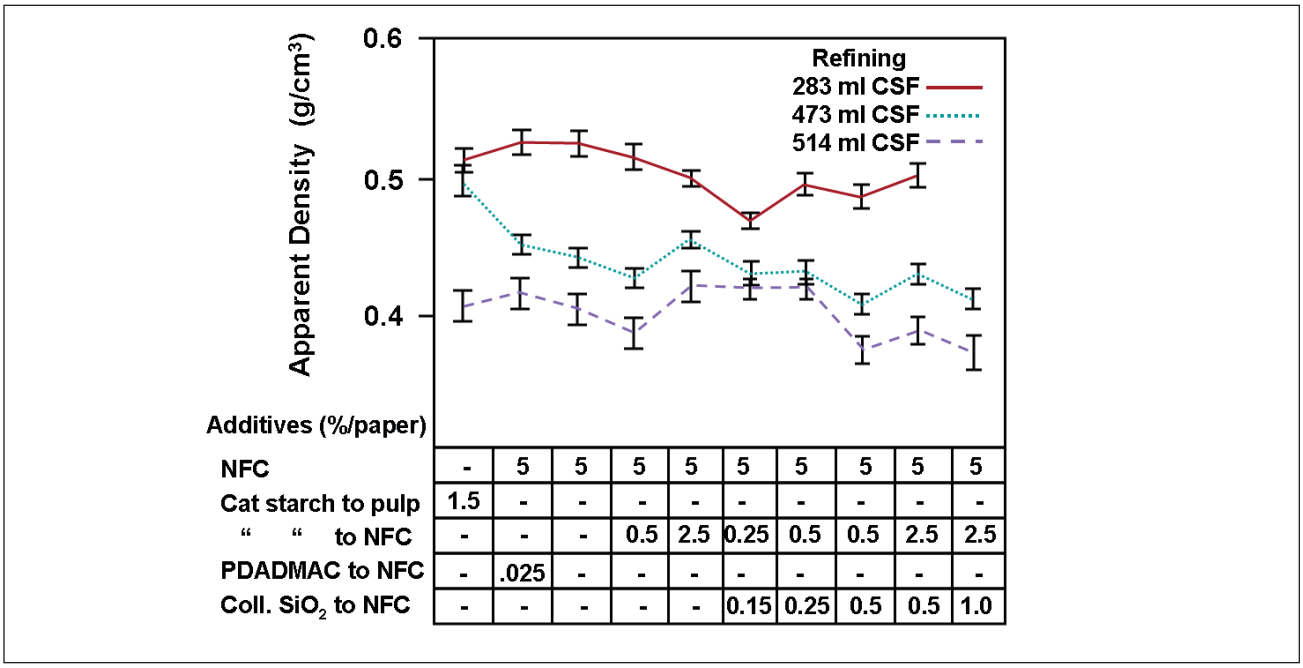
Process-related tests

Dewatering rate tests were carried out using a modified Schopper-Riegler method [25]. Briefly stated, 1000 mL of 0.5% solids suspension, prepared in just the same way as for the other experiments, was placed in the device above a closed sealing ring. A stopwatch was started simultaneously with the opening up of the ring to permit drainage, and the mass of filtrate was evaluated with a tared pan balance after passage of 20 s.

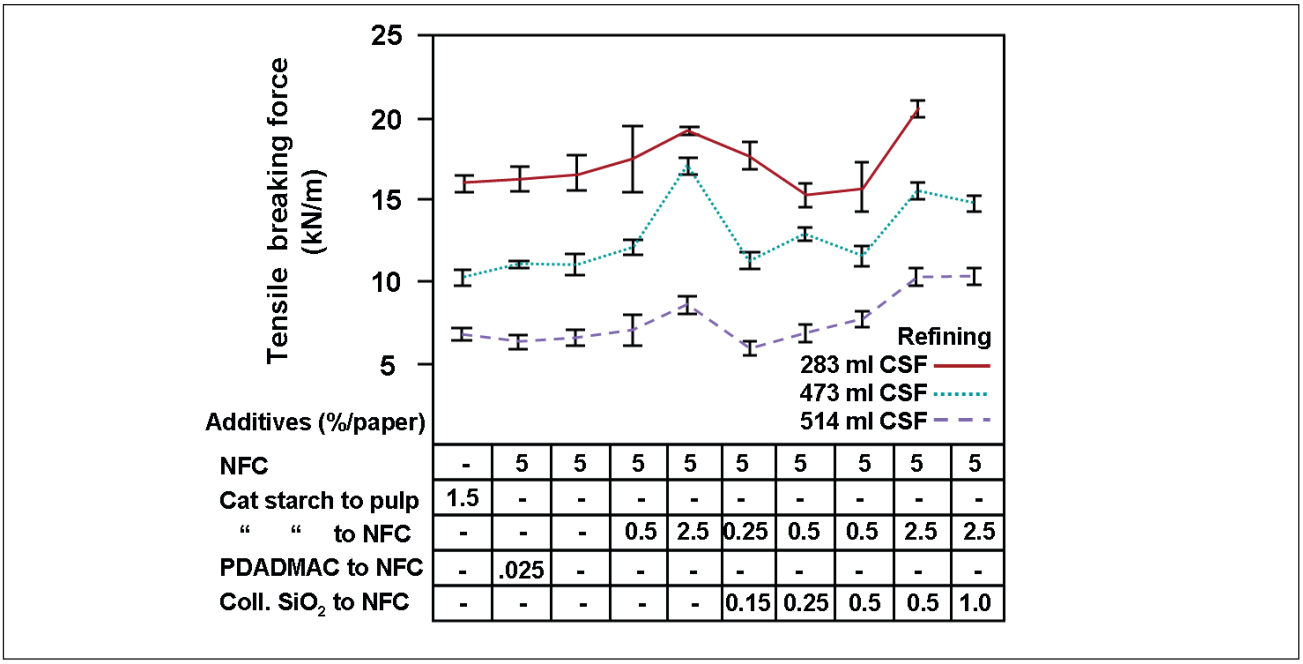
Streaming potential values were obtained using a simple apparatus consisting of a Buchner funnel fitted with a 200-mesh stainless steel screen having two welding-wire probes, one in contact with the aqueous phase on each side of the screen. The difference in voltage readings when applying either about 90 kPa or zero differential pressure across the pad of fibers (using house vacuum) was recorded for each test. The sensing unit of the device was the same as what is described in [26], except that the pressure difference was applied by vacuum rather than by compression and the device was operated manually.

Physical tests

Caliper tests were conducted according to TAPPI T 411 "Thickness (caliper of paper, paperboard, and combined board)". Tensile strength was based on TAPPI T 494 om-96 "Tensile



3. Effects of refining level of the main furnish, as well as effects of nanofibrillated cellulose (NFC), cationic (Cat) starch, and colloidal silica (Coll. SiO_2) treatments on the apparent density of the pressed handsheets. Error bars give 95% confidence intervals for the mean values. See Experimental section for further explanation of the conditions. (PDADMAC = polydiallyldimethylammonium chloride.)



Additives (%/paper)										
NFC	-	5	5	5	5	5	5	5	5	5
Cat starch to pulp	1.5	-	-	-	-	-	-	-	-	-
" " to NFC	-	-	-	0.5	2.5	0.25	0.5	0.5	2.5	2.5
PDADMAC to NFC	-	.025	-	-	-	-	-	-	-	-
Coll. SiO_2 to NFC	-	-	-	-	-	0.15	0.25	0.5	0.5	1.0

4. Tensile breaking force of the pressed handsheets as a function of refining level of the main furnish, as well as effects of nanofibrillated cellulose (NFC), cationic (Cat) starch, and colloidal silica (Coll. SiO_2) treatments. Error bars give 95% confidence intervals for the mean values. (PDADMAC = polydiallyldimethylammonium chloride.)

properties of paper and paperboard (using constant rate of elongation apparatus)". Taber stiffness was measured using TAPPI T 489 om-04 "Bending resistance (stiffness) of paper and paperboard (Taber-type tester in basic configuration)". The weight corresponded to "+1000 stiffness units" and the degrees were 15 on each side. Gurley densometer (Gurley Precision Instruments; Troy, NY, USA) values (resistance to air permeation) were evaluated as in TAPPI T 460 om-96 "Air resistance of paper (Gurley method)".

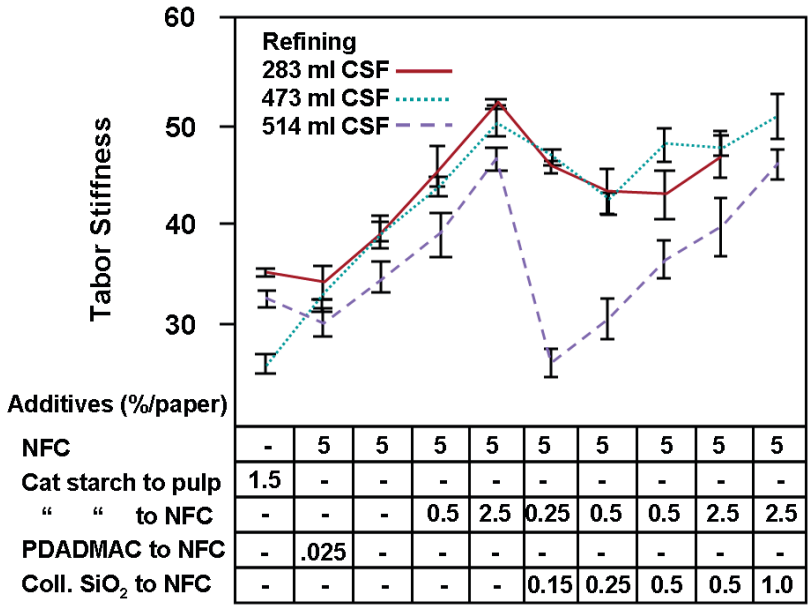
RESULTS

Apparent density

As shown in **Fig. 3**, the extent of refining of the main kraft furnish had a major effect on the apparent density of the resulting handsheets. Note that the first column of data corresponds to a system in which there was no NFC, and instead a relatively high level of cationic starch was added for purposes of strength enhancement. The labels of the other columns correspond to conditions as described in the Experimental section. Results of preliminary tests showed that in the absence of cationic polymer, the added NFC did not significantly increase the strength of the resulting sheets; therefore the third column titled "Default" can be regarded as a reference point that would not be very different from the main furnish with no additives of any kind. This finding is consistent with the observations of Campano et al. [27], who showed that some kind of retention additive may be needed to achieve important benefits of NFC addition. The label "Fixative" means that the high-change cationic polymer was employed as a means of electrostatically attracting the NFC to fiber surfaces in the absence of the cationic starch dry-strength additive. The remaining columns correspond to different treatment levels of cationic starch (the first additive) and colloidal silica (the second additive). The highly refined pulp yielded the densest sheets, and the unrefined fibers yielded the lowest-density sheets. The most interesting finding was that the apparent density achieved with the lightly refined pulp was strongly dependent on the addition of NFC, as well as its pretreatment. The presence of NFC tended to yield less-dense paper in comparison with the blank that had no NFC. These results are tentatively attributed to the highly flexible nature of NFC, which might allow greater recovery of caliper of the paper sheet after the press nip while still maintaining interfiber bonding.

Paper strength

Figure 4 gives corresponding results for paper tensile strength. As would be expected [17], tensile strength generally increased as a function of increasing level of refining. However, significantly increased tensile strength was also achieved when adding NFC (at the 5% level) that had been treated by a high level of cationic starch (equivalent to 2.5% addition on a product basis). The increase was especially notable in the case of the lightly refined pulp. Also of note, greatly increased strength was achieved when NFC had been treated not only with a high level of cationic starch, but also with colloidal silica. These results suggest that NFC that has been pretreated with a high level of cationic starch, either with or without subsequent treatment with colloidal silica, can achieve substantially increased strength. In particular, the strength levels as-



Additives (%/paper)										
NFC	-	5	5	5	5	5	5	5	5	5
Cat starch to pulp	1.5	-	-	-	-	-	-	-	-	-
" " to NFC	-	-	-	0.5	2.5	0.25	0.5	0.5	2.5	2.5
PDADMAC to NFC	-	.025	-	-	-	-	-	-	-	-
Coll. SiO_2 to NFC	-	-	-	-	-	0.15	0.25	0.5	0.5	1.0

5. Taber stiffness of the pressed handsheets as a function of refining level of the main furnish, as well as effects of nanofibrillated cellulose (NFC), cationic (Cat) starch, and colloidal silica (Coll. SiO_2) treatments. Error bars give 95% confidence intervals for the mean values. (PDADMAC = polydiallyldimethylammonium chloride.)

sociated with the high level of refining could be approached by adding the pretreated NFC to the lightly refined pulp. The results achieved when adding the cationic starch–pretreated NFC (with a high starch level of 2.5% on the basis of sheet solids) greatly exceeded the results achieved when adding either NFC by itself or when adding a high level of cationic starch (1.5% by mass) separately in the absence of NFC. Though the levels of starch were different (1.5% versus 2.5% on the basis of sheet solids) in this comparison, it is well known that cationic starch tends to reach a point of diminishing returns when it is added at high levels to ordinary papermaking furnish [28]. A wide range of positive effects on tensile strength have been reported when highly fibrillated cellulose has been added to papermaking furnish, of which the following reports are representative [7,8,13,14,27,29]. The diversity of results from the various studies can be rationalized on the basis of different properties and refining of the main fibers, unknown efficiencies of retention of the highly fibrillated cellulose in most reported cases, and the inclusion or exclusion of polymers contributing to bonding or fiber agglomeration.

Figure 5 shows corresponding results for Taber stiffness. As shown, although NFC by itself could increase paper stiffness, much greater increases were achieved when using NFC that had been pretreated by increasing levels of cationic starch. Remarkably, the stiffness of sheets prepared with lightly refined fibers with cationic starch-pretreated NFC were in the same range of stiffness (e.g., sometimes higher, sometimes lower) compared with those prepared without NFC and a high level of cationic starch at the high level of refining of the main furnish (281 mL CSF) (first set of data at the left of the plot). Another aspect worth noting is that high levels of stiffness were achieved whether or not colloidal silica had been added after the cationic starch.

Paper air permeability and smoothness

Gurley densometer tests revealed that the level of refining of the main furnish was the most important factor governing air permeability. The readings were generally in the ranges shown in **Table I**, regardless of the addition of NFC, cationic starch, or colloidal silica in different combinations. Pretreatment with high levels of cationic starch, especially when followed by colloidal silica, increased the resistance to air permeation, but such effects were minor in comparison with that of the level of refining of the main kraft fibers.

Other investigators who have evaluated effects of adding highly fibrillated cellulose (micro- or nanofibrillated cellulose) to fiber slurries before paper formation have reported increases in Gurley densometer and related test values in the range of 16%–460% [7,8,10,15,27,29,30]. A possible explanation for the different behavior in the present work, where no significant effect of NFC on air permeability was found, is that the pretreatment system allowed the NFC to deposit efficiently onto the surfaces of the main fibers in the paper rather than occluding pores within the paper and thus impeding dewatering [31]. Of course, such a hypothesis would need to be evaluated in future work.

Tests carried out with a Parker Print Surf apparatus showed only minor differences in smoothness among the samples, regardless of refining level of the main furnish and treatments with cationic starch.

Refining Level	Gurley Densometer Value, s/100 cm³	Parker Print Surf Roughness, µm
Unrefined	3.4–5.3	10.2–10.4
Lightly refined	7.3–10.8	10.3–11.1
Heavily refined	21.1–29.9	11.5

I. Gurley densometer results for the 350 g/m² sheets.

Results of process-related tests

Table II shows the results of tests to evaluate the dewatering rate and the zeta potential for certain test conditions that were selected on the basis of their strongly contrasting effects relative to paper strength. As shown in the table, the treatment of the NFC with a high level of cationic starch (2.5% cationic starch solids on the basis of the mass of solids in the paper) resulted in an apparent increase in the mean value of filtrate that had drained within 20 s in the modified Schopper-Reigler test device; however the change was not significant at a 95% confidence level. Greater increases in dewatering rate were obtained in two cases where the cationic starch treatment of NFC was followed by colloidal silica. Both such treatments yielded significant increases in dewatering rate relative to treatment of the NFC with starch alone. Such findings are consistent with the reported effects of sequential treatment with cationic starch and colloidal silica, when this is done under ordinary papermaking conditions [21]. However, this is the first time such an effect has been reported when the additives were used to pretreat NFC.

Although freeness tests are widely used as a means to assess the drainability, and hence the refining levels of pulps, such results do not necessarily correlate with drainage rates observed on paper machines. In particular, as shown by Gess [32], filtration tests with high basis weight sheets—which is essentially the situation employed during standard freeness tests—tend to exagerate the effects of furnish conditions such as the level of fines on the rate of dewatering. Thus, it would be reasonable in future work to confirm the present findings with pilot-scale or commercial-scale forming equipment.

Results of zeta-potential tests, based on the streaming potential method [26], showed that the treated stock suspension had a negative zeta potential for all of the conditions considered. Of note, the addition of colloidal silica, which has a negative surface charge, resulted in less negative values of zeta potential. This change is tentatively attributed to a greater adsorption of the cationic starch onto cellulose surfaces in the presence of colloidal silica [33].

DISCUSSION

The processing sequence considered in this work, which may substantially decrease the need to refine papermaking fibers, has the potential to extend the life cycle of pulp resources. Though it is well known that fibers from recovered paper can be used multiple times in new paper products, excessive mechanical refining of a fiber, in the course of multiple cycles of usage, is to be avoided. By applying most of the refining energy to a minor component of the cellulose, which becomes microfibrillated or nanofibrillated, the degree of mechanical degradation of the main fibers can, in principle, be minimized.

While the strategy described in this work shows promise in terms of reducing the refining of the main furnish, achieving lower apparent density, and maintaining key strength properties, it is important to keep in mind that some other properties will not match those of paper made under the default conditions with higher levels of refining. The paper will tend to be rougher and more porous. In some paper grades, where surface smoothness or porosity are critical, this might be a deal breaker. In other cases the resulting surface either may be suitable relative to the target performance of the paper, or it might be overcome by subsequent processing steps (e.g., calendering or coating). Whether a production

Condition*	3 Default	5 High Starch	9 with Silicon Dioxide	10 with Silicon Dioxide
NFC level, %	5	5	5	5
Cationic starch to NFC, % based on paper mass	0	2.5	2.5	2.5
Colloidal SiO_2 to NFC, % based on paper mass	0	0	0.5	1
Filtrate mass after 20 s, g				
Mean	511.5	530.4	552.1	583.3
Upper 95% Confidence limit	532.0	545.7	559.0	597.4
Lower 95% Confidence limit	491.0	515.2	545.2	569.1
Mean zeta potential, mV	-92	-93	-62	-55

NFC = nanofibrillated cellulose; SiO_2 = silicon dioxide.
* Conditions correspond to the third, fifth, ninth, and 10th columns of data in Figs. 3, 4, and 5.

II. Drainage rate and zeta potential of selected stock suspensions.

scheme as outlined in this study can achieve lower wet-web solids after the wet presses, while still providing lower apparent density, will need to be established through experiments that simulate realistic production speeds for modern paper machines and a variety of fiber types. If the answer is yes, then pretreatment of NFC with cationic starch (and optional colloidal silica), together with reductions in the refining level of the main furnish, has the potential to save energy because there will be less water to evaporate from the paper web after the wet presses. A further question that needs to be addressed in subsequent work is the extent to which the apparent advantages, especially in terms of stiffness and apparent density, might be obscured in cases where calendering (to achieve a smoothenss target) is a necessary part of the production scheme.

It needs to be emphasized that certain process options cosidered in this work showed much lower benefits. In particular, as has been noted in a review of earlier work [27], addition of cationic starch directly to papermaking furnish usually can provide only modest gains in paper's strength. Likewise, just adding NFC to the furnish did not achieve important gains in dry strength. Rather, the results of this work suggest a synergistic effect when cationic starch and highly fibrillated cellulose are used in combination. One way to view this synergism is that the NFC may be acting as an extender for the cationic starch, allowing the dry strength agent to form bonds between surfaces that could not be spanned by individual starch molecules. Seen another way, the cationic starch may be providing a mechanism of retention, as well as enhanced hydrogen bonding ability, to the NFC. In either case, the treated NFC holds promise as a papermaking wet-end additive, and it merits further research.

While the results shown in this study demonstrate some interesting points, many questions remain to be considered. For example, the present work does not shed any light on whether the pretreatment of NFC can contribute meaningful benefits in the case of paper grades that require relatively high values of apparent density. In such cases it might be hypothesized that interfiber joints comprising NFC might prove to be structurally inferior to what can be achieved by more direct bonding between long fibers within the paper structure. Another limitation is that the present work considered only one type of NFC, ignoring whether similar benefits can be achieved when using coarser, more easily obtained materials, such as fibrillar cellulosic fines [34] or microfibrillated cellulose [35]. Also, there are many more optional sequences in which the chemical additives can be combined—for instance, adding the colloidal silica to the combined furnish rather than as part of the pretreatment of the NFC. Finally, different basis weights and furnish types can be considered, possibly at the pilot papermaking scale, to establish the findings under more realistic conditions for certain paper and paperboard grades.

It was proposed that a sharp decrease in refining of papermaking fibers can be expected to result in reduced moisture in the wet web after pressing, while at the same time yielding lower apparent density of the resulting sheet. Only the last part of this hypothesis has been evaluated and shown to be valid by the present work; indeed, the strategy of using unrefined or less-refined fibers, together with an NFC-based bonding strategy, yielded low apparent density at favorable levels of tensile strength and stiffness. There has been little published research regarding the effects of wet-end parameters relative to the dewatering effectiveness of wet pressing [36], and there is a need for follow-up in that area for the present work. There are theoretical reasons, however, to support an assumption that increased refining will tend to inhibit release of water during wet pressing. According to Zhao and Kerekes [37], the main resistance to compression of the paper web in a wet-press nip is always hydrostatic in nature. It follows that resistance to compression will be dominated by factors that block the passage of water (i.e., the ability of highly conformable and high-surface area matter to act as hydraulic seals, as well as water retention within the fiber cell wall) [31]. By contrast, the cell walls of the fibers themselves are always much too weak, if the lumen is not filled with water, to make a major contribution to avoiding compressing within the wet-press nip [37]. Research is being planned to address such questions under conditions of interest for grades of paper.

CONCLUSIONS

Tests carried out in the laboratory support a new strategy for achieving lower apparent density in paper products, while maintaining tensile strength, stiffness, and rates of dewatering during the formation of paper. Such goals can be achieved by decreased refining of the main fiber furnish, which ordinarily would result in a sharp decrease in strength attributes of the paper. Addition of either untreated NFC or cationic starch were relatively ineffective in boosting the strength of the paper made from the under-refined fibers. But by pretreating the nanocellulose with high levels of cationic starch, the resulting paper strength was comparable to what ordinarily would have been achieved at a higher level of refining. Though NFC is known to be unfavorable for the rates of drainage from papermaking furnish, test results showed that such issues can be addressed in a new way—pretreatment of nanocellulose first with cationic starch, then with colloidal silica before addition to the main pulp suspension. Bulkier paper, prepared by use of the described strategy, can be expected to save materials and energy when producing certain paper grades, such as return postcard stock, some grades of boxboard, book paper, and paper towels. **TJ**

ACKNOWLEDGEMENT

This work was funded by the Buckman endowment, which as established as a gift from Robert Buckman and his wife to North Carolina State University for the support of a faculty position, education, and research in the area of papermaking chemistry.

LITERATURE CITED

1. Sampson, W.W. and Wilde, R., *Appita J.* 54(6): 547(2001).
2. Kouko, J., Salminen, K., and Kurki, M., *Pap. Puu* 89(7): 424(2007).
3. Wang, X.S., Paulapuro, H., and Maloney, T.C., *Nord. Pulp Pap. Res. J.* 20(4): 442(2005).
4. Anjos, O., Garcia-Gonzalo, E., Santos, A.J.A., et al., *BioResources* 10(3): 5920(2015).
5. Pikulik, I.I., McDonald, J.D., and Mentele, C.J., *TAPPI J.* 81(6): 122(1998).
6. Nordstrom, B., *Nord. Pulp Pap. Res. J.* 31(3): 422(2016).
7. Delgado-Aguilar, M., González, I., Pèlach, M.A., et al., *Cellulose* 22(1): 789(2014).
8. Eriksen, O., Syverud, K., and Gregersen, O., *Nord. Pulp Pap. Res. J.* 23: 299(2008)
9. Guimond, R., Chabot, B., Law, K.N., et al., *J. Pulp Pap. Sci.* 36(1–2): 55(2010).
10. Taipale, T., Österberg, M., Nykanen, A., et al., *Cellulose* 17(5): 1005(2010).
11. Gao, W.-H., Chen, K.-F., Yang, R.-D., et al., *BioResources* 6(1): 144(2011).
12. González, I., Boufi, S., Pèlach, M.A., et al., *BioResources* 7(4): 5167(2012).
13. He, M., Yang, G., Cho, B.-U., et al., *Cellulose* 24(12): 5657(2017).
14. Ahola, S., Österberg, M., and Laine, J., *Cellulose* 15(2): 303(2008).
15. Merayo, N., Balea, A., de la Fuente, E., et al., *Cellulose* 24(2): 2987(2017).
16. Hollerz, R., Durán, V.L., Larson, P.A., et al., *Cellulose* 24(9): 3883(2017).
17. Brandstrom, J., Joseleau, J.P., Cochaux, A., et al., *Holzforschung* 59(6): 675(2005).
18. Page, D.H., *Tappi* 52(4): 674(1969).
19. Cole, C.A., Hubbe, M.A., and Heitmann, J.A., *TAPPI J.* 7(7): 15(2008).
20. Andersson, K. and Lindgren, E., *Nord. Pulp Pap. Res. J.* 11(1): 15(1996).
21. Hubbe, M.A. in *Micro and Nanoparticles in Papermaking* (J.M. Rodriguez, Ed.), TAPPI Press, Atlanta, GA, USA, 2005, pp. 1–36.
22. Lenze, C.J., Peksa, C.A., Sun, W.M., et al., *Cellulose* 23(6): 3951(2016).
23. Abbati de Assis, C., Iglesias, M.C., Bilodeau, M., et al., *Biofuels, Bioprod. Biorefin.* 12: 251(2017).
24. Kumar, A., Singh, S.P., and Singh, A.K., *Cellulose* 23(4): 2663(2016).
25. Sampson, W.W. and Kropholler, H.W., *Tappi J.* 78(12): 145(1995).
26. Wang, F. and Hubbe, M.A., *Colloids Surf., A* 194: 221(2001).
27. Campano, C., Merayo, N., Balea, A., et al., *Cellulose* 25(1): 269(2018).
28. Glittenberg, D., Tippett, R.J., and Leonhardt, P., *Pap. Technol.* 45(6): 27(2004).
29. González, I., Vilaseca, F., Alcalá, M., et al., *Cellulose* 20(3): 1425(2013).
30. Ottesen, V., Syverud, K., and Gregersen, Ø.W., *Nord. Pulp Pap. Res. J.* 31(3): 441(2016).
31. Hubbe, M.A. and Heitmann, J.A., *BioResources* 2(3): 500(2007).
32. Gess, J., *TAPPI Retention Drain. Semin. Notes*, TAPPI Press, Atlanta, 1989, p. 49.
33. Hubbe, M.A., *BioResources* 9(1): 1634(2014).
34. Nurminen, I, Saharinen, E., and Siviö, J., *BioResources* 13(3): 5032(2018).
35. Lavoine, N., Desloges, I., Dufresne, A., et al., *Carbohydr. Polym.* 90: 735(2012).
36. Wegner, T., *Tappi J.* 70(7): 107(1987).
37. Zhao, J. and Kerekes, R., *BioResources* 12(1): 2125(2017).

ABOUT THIS PAPER

Cite this article as: Mayeli, N. *TAPPI J.* 17(7):403(2018). https://doi.org/10.32964/TJ17.07.403

DOI: https://doi.org/10.32964/TJ17.07.403

ISSN: 0734-1415

Publisher: TAPPI Press

Copyright: ©TAPPI Press 2018

About this journal

ABOUT THE AUTHORS

We chose to undertake this re-search because we had a prom-ising idea and wanted to test it. We had never actually tried such an approach with reduced refin-ing levels, cationic starch, and silicon dioxide.

To address the difficult aspects of this research, we had to try different settings of the wetpress device to establish a procedure. We were surprised to learn that only a combination of both nanocelluse and cationic starch was effective. An interesting finding was that colloidal silica made it possible to improve drainage, while still get-ting a big strength gain. Mills that make low-density products want to achieve higher caliper, or use recycled fiber can benefit from this work. The next step is to investigate other grade applications, such as dense grades.



Rice



Pal



Gonzalez



Hubbe

Rice is a student, Pal and Gonzalez are associate pro-fessors, and Hubbe is a professor in the Department of Forest Biomaterials, North Carolina State University, Raleigh, NC, USA. Email Hubbe at hubbe@ncsu.edu.

Effect of pH and enzymes on strength of recycled fibers during refining

ASHOK GHOSH, BRELAND THORNTON, AND PETER W. HART

ABSTRACT: Recycled fiber-based papermaking in America is experiencing a persistent reduction in the strength of the incoming fiber. To maintain paper strength properties, paper mills respond by increasing basis weight, dry strength, etc. On average, the fiber cost component in recycled paper is approximately 40% of the total manufacturing cost. Increased fiber weight results in higher operating cost and has a negative effect on production rate, especially on dryer-limited paper machines. Increased pH and use of certain enzymes can improve strength during subsequent refining. The ProLab refiner was used to generate laboratory refining curves to evaluate changes in fiber bonding. The effect of pH and enzymes pretreatment on the strength development and change in drainage of recycled fibers with refining was evaluated.

Application: This study can demonstrates potential uses and net positive effects of enzyme treatments of recycled fiber.

Papermaking fibers can either be sourced from the trees and nonwood species or recovered from existing paper products. The recovery of fiber from existing paper products involves collecting used paper materials and processing these materials in a pulp mill. Paper collection involves gathering used paper products from end users into centralized facilities. The paper in the collection centers is separated from extraneous materials, such as metals, plastic, and food. The paper products are then sorted by fiber type and quality and sent to mills in bale form where the recycled paper is mechanically defibrated in a hydropulper. The resulting pulp slurry is sent through coarse screens to remove plastic and other foreign materials. Fine screens and hydrocyclones may be used to remove fiber clumps, flakes, coating pieces, etc. This equipment also may be used to fractionate fibers by length. The strength of the resulting fibers may be augmented by mechanical treatment in refiners and by strength aids such as starch and other dry strength polymers.

Refining involves passing the fibers through a narrow gap between rotating discs that have metal bars and grooves on the surface of each disc. The refining action produces fibrils on the surface of the fibers, which significantly increases the total fiber surface area and, thereby, the inter-fiber bonding. The increase in strength from higher inter-fiber bonding is limited by fiber damage and cutting during refining. Paper strength is reduced each time paper is reused [1]. A potential cause for the strength reduction with reuse of paper has been attributed to fiber hornification [2-5]. When chemical pulp fibers are dried, either in sheet or pulp form, the internal fiber volume shrinks. If the fibers are rewetted in water, the original water-swollen state is not regained. The physical change manifested by this inhibited reswelling is termed "hornification" [6]. The potential mechanisms for hornification tend to fall into two categories; either some of the hydrogen bonds are stabilized and are retained after rewetting [7] or some of the fibrils and fibers are covalently bonded, and the bond cannot be broken when water is added to the dried pulp [5]. Refining may be used to promote fiber swelling; however, refining tends to generate fines, which inhibit drainage. Refining might also result in fiber damage, which reduces the strength potential of the pulp and ultimately that of the resulting paper.

Certain classes of enzymes are used to improve fiber swelling, which can increase OCC strength. Fibril separation may be aided by breaking the inter-fibril bonds with cellulases and hemicellulases [8]. Within cellulases are three broad families of enzymes: 1) endocellulases, 2) exocellulases, and 3) beta-glucosidases. The endocellulases react with cellulose in amorphous regions. The exocellulases react with cellulose chain ends and cleave mono and dimeric groups. The beta-glucosidases are significantly smaller enzymes and can only hydrolyze mono and dimers to glucose [9]. Generally, endocellulases and exocellulases tend to be used in enzymatic strengthening of pulp. Depending on the mechanism of the enzyme reaction, some of the charge end groups also might be destroyed, which results in a net reduction in fiber charge, fines, colloidal material, and dissolved organics, all of which help improve the efficacy of wet end chemicals.

Certain oxidases are used to create aldehyde end groups in lignin, which can then bond with cellulose and other polymers [10].

Recycled pulp contains hydrophobic materials. Sources of hydrophobic content include wood extractives (fatty acids, fatty acid esters) and defoamers present in the pulp slurry or binders and glues added to paper (e.g., PVAc, styrene, acrylate components) [11]. If the pulp has significant hydrophobic

Parameter	Value
Rotor diameter, mm	184
Pulp consistency, %	3.5
Pulp flow, cc/s	1500
Rotational speed, rpm	2200
Filling gap, mm	0.2
Specific refining energy rate, kW.h/ton per min	12.2

I. Technical specifications of the ProLab laboratory refiner

loading, this might interfere with the formation of hydrogen bonds. Certain lipases may be used to break down the hydrophobic materials in pulp [12].

Changes in certain process variables tend to promote fiber fibrillation with minimum fiber damage. These include a reduction in refining intensity by an increase in the number of bars on the refiner plate, an increase in pulp consistency during refining; an increase in temperature and/or pH to increase fiber swelling and flexibility, and the treatment of the fibers with certain enzymes before refining.

EXPERIMENTAL METHODS

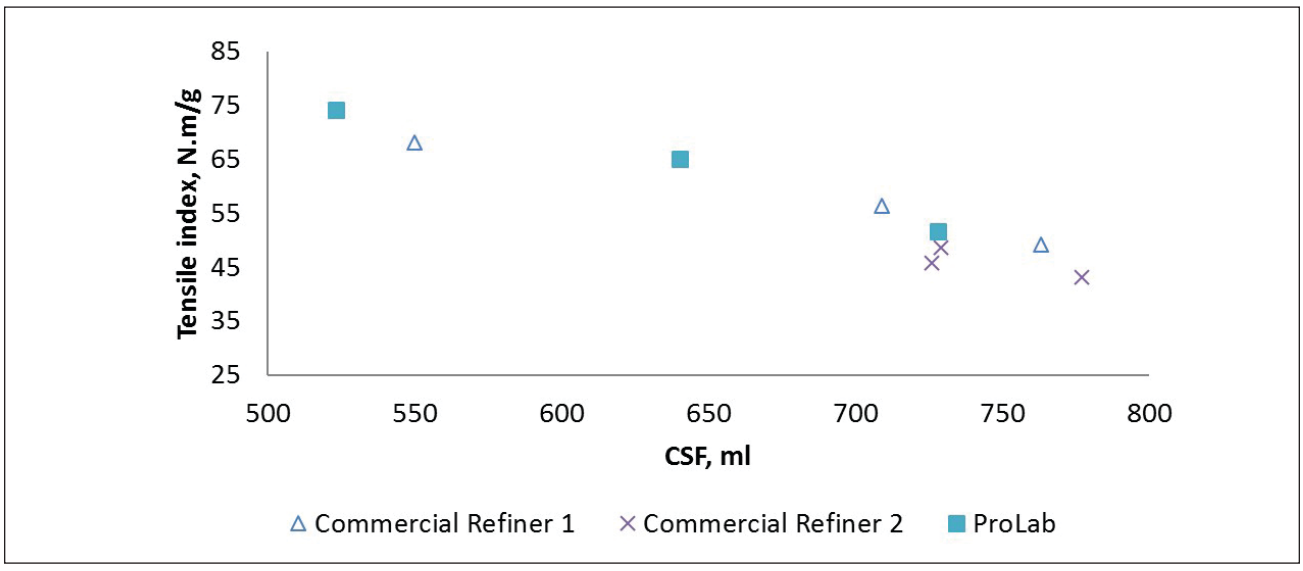
The ProLab refiner (Valmet; Espoo, Finland) [13] used in this study is located at the WestRock R&D Laboratory (Richmond, VA, USA). **Table I** shows some of the technical specifications of the refiner. The disc refiner plates used in this study were supplied by AFT (Sherbrooke, QC, Canada) and were designed to simulate the refiner plates at one of the company's recycle mills. This laboratory refiner is able to closely match the performance of commercial scale refiners (**Figs. 1 and 2**) [14].

The laboratory refiner's rotor is moved axially to adjust the refiner plate gap, and the stator plate axial position is fixed. The axial position of the rotor plate is determined by an inductive position sensor. The axial position for zero gap is determined with the refiner running dry at 1500 rpm; a vibration sensor is used to indicate plate clashing. The gap between the refiner disc fillings is calculated by the relative axial distance of the rotor from the zero position. All the refining runs for this work were done at a fixed plate gap of 0.2 mm.

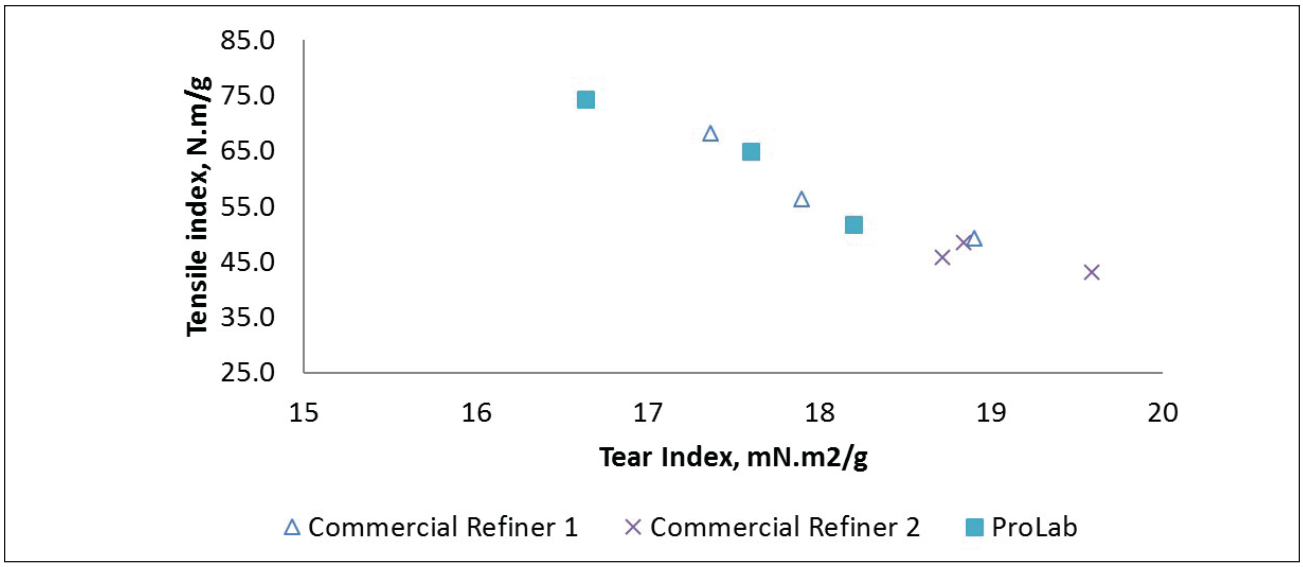
This study used old corrugated container (OCC) pulp obtained from a WestRock pulp mill at about 25% consistency. The pulping process included coarse screening, fine screening, hydrocyclone treatment, and thickening. The pulp was diluted to 3.5% consistency before pretreatments for pH and enzyme application. Treatment for each process was applied at 120°F for 1 h. For this study, the same set of refining conditions (refiner plates, revolutions per minute, and flow) were used to maintain similar refining intensity and specific refining energy. The refiner has a 40 L feed tank. The pulp was recirculated through the refiner back to the feed tank. The specific refining energy was increased about 0.62 horsepower days/ton (hp-d/ton) per minute of refining. The pulp was sampled at different times, which corresponded to a range of 0 to 3 hp-d/ton at 0.5 hp-d/ton increments.

Canadian standard freeness (CSF) and fiber length properties were measured for all samples. The fiber length, fines, and kink measurements were done with an FQA-360 fiber quality analyzer (OpTest Equipment Inc.; Hawkesbury, ON, Canada) [15]. Handsheets of 120 g/m² basis weight were made for pulp samples above 300 mL CSF. The handsheets were tested for physical properties, which included density, porosity, tensile, burst, short span compression, and z-direction tensile (ZDT). The testing procedures were done according to the TAPPI Standard Test Methods (**Table II**).

The enzyme treatments for this study were done at pH 7.5 and 120°F for 1 h using a commercial enzyme formulation, referred to as "Enzyme A," obtained from Enzymatic Deinking



1. Comparison of commercial and ProLab refining of softwood: drainage versus tensile.



2. Comparison of commercial and ProLab refining of softwood: tear-tensile.

TAPPI Standard Test Methods
T-205 — Forming handsheets for physical tests of pulp
T-220 — Physical testing of pulp handsheets (basis weight, caliper, density)
T-227 — Freeness of pulp (Canadian standard method)
T-403 — Bursting strength of paper
T-460 — Air resistance of paper (Gurley method)
T-494 — Tensile properties of paper and paperboard (using constant rate of elongation apparatus)
T-541 — Internal bond strength of paperboard (z-direction tensile)
T-826 — Short span compressive strength of containerboard

II. TAPPI Test Methods used in the study

Technologies (EDT) (Norcross, GA, USA). The enzyme selection was based on an unpublished internal study in which several commercial EDT "cellulase-based" enzyme formulations were evaluated on OCC refining.

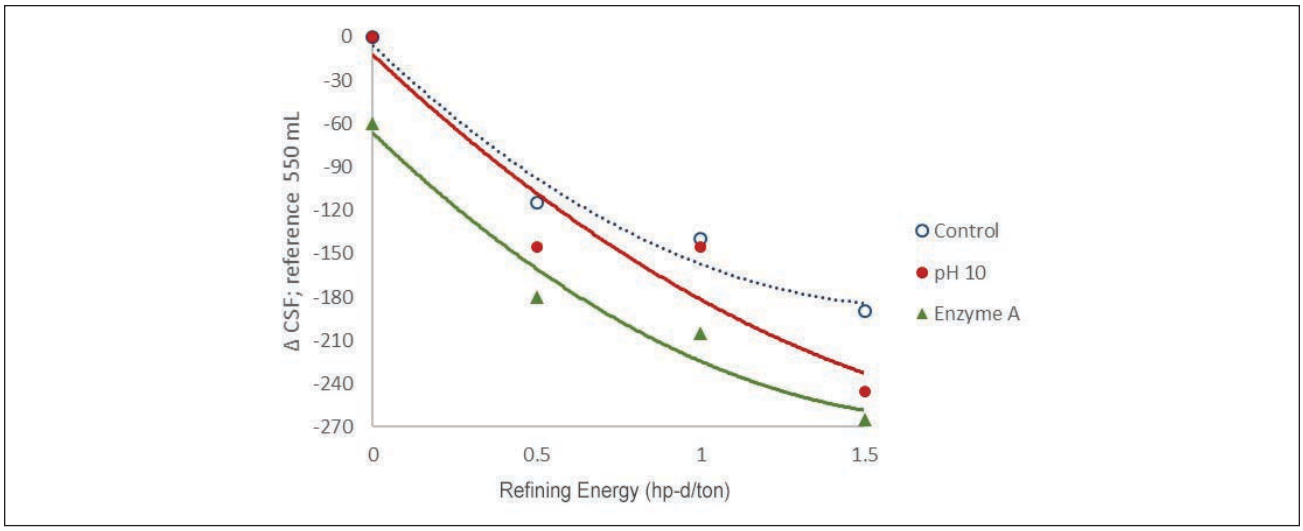
RESULTS AND DISCUSSIONS

OCC pulp has a relatively short storage life before going rancid. Therefore, the pH and enzyme studies were done with fresh OCC samples that were produced at different times at the recycle mill. Although the sample location was the same, the pulp samples had significantly different properties, which highlights the variability inherent with OCC pulps. Because the controls for each of the trials were different, the test results have been graphed as a difference from the respective control values. The handsheet strength data were normalized for basis weight.

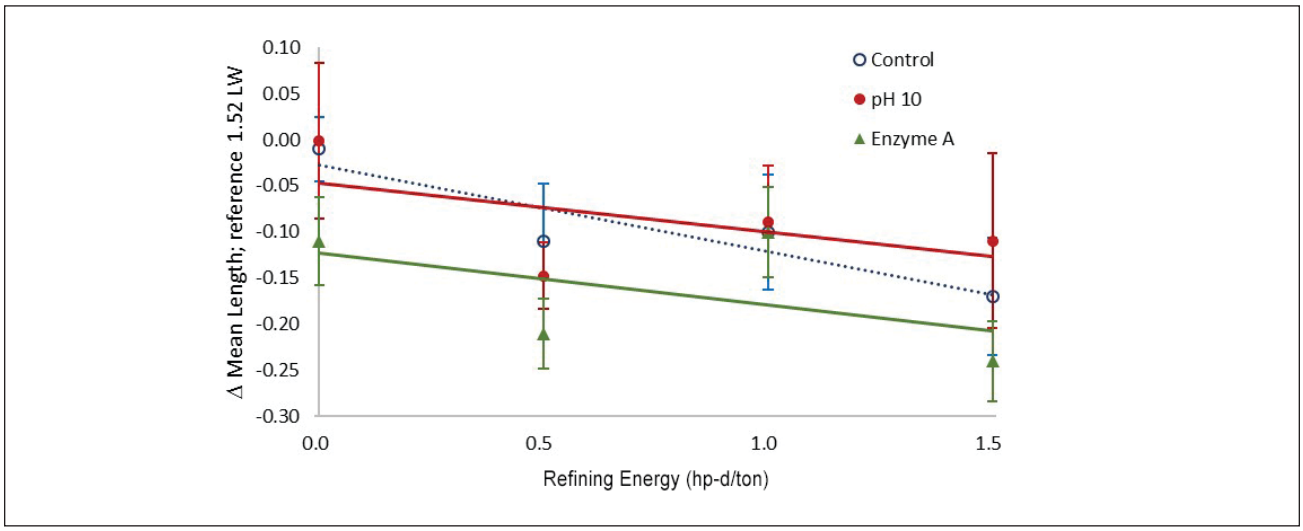
The freeness reduction as a function of specific refining energy was similar when pulp pH was increased from 7.5 to 10 (**Fig. 3**). The energy required to achieve the target desired freeness was significantly lower with Enzyme A than for the control (Fig. 3).

Figures 4-6 show, respectively, the length-weighted average fiber length, percent fines, and kinks resulting during refining. Each time paper is recycled, fiber damage occurs and is expressed as fiber length reduction and increased fines content. Fines have a significantly higher surface area for a given weight than do whole fibers. The fines compete with whole fibers for chemicals added at the wet end. Fines that are retained in the sheet clog the pores in the sheet and reduce dewatering. The fines that are not retained in the sheet end up in the white water and add to the dirt and organic load of the wet end system. The data showed no distinctive difference in any of the three variables (fiber length, percent fines, and kinks), which suggests that none of the pretreatments reduced measurable fiber damage during refining.

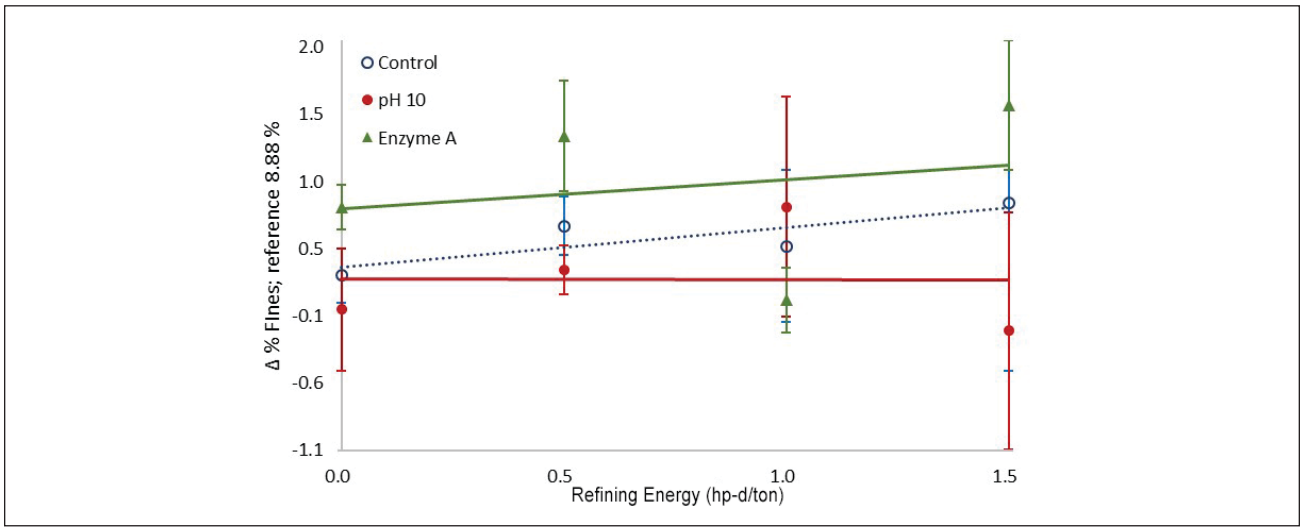
Significant changes in paper properties were apparent with enzyme treatment. An increase in pH from 7.5 to 10 had little effect on STFI strength (i.e., the short span compression



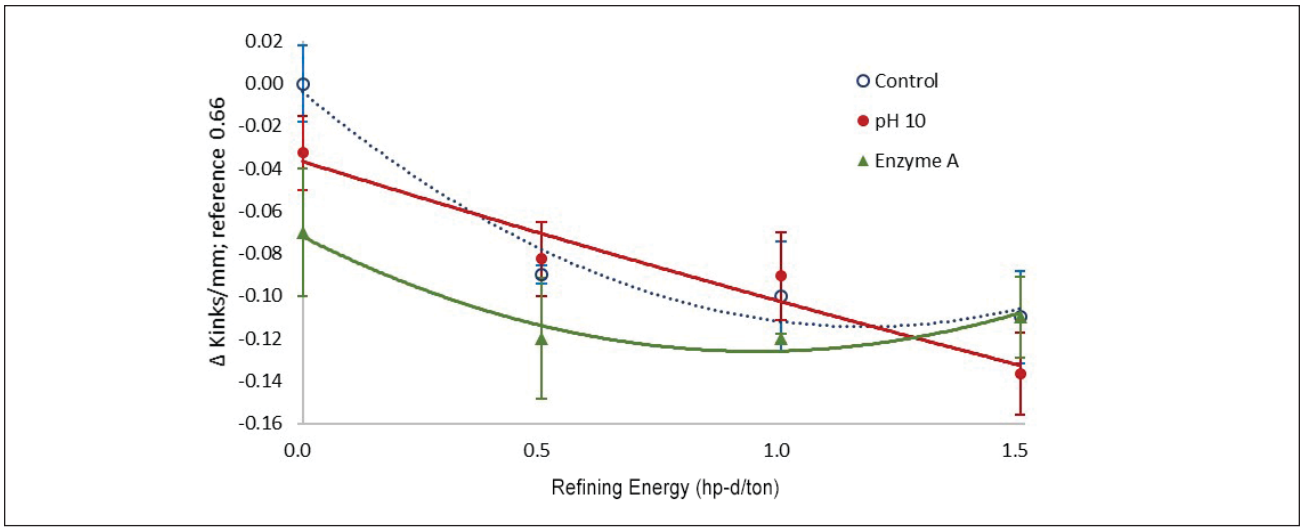
3. Pulp freeness as function of specific refining energy.



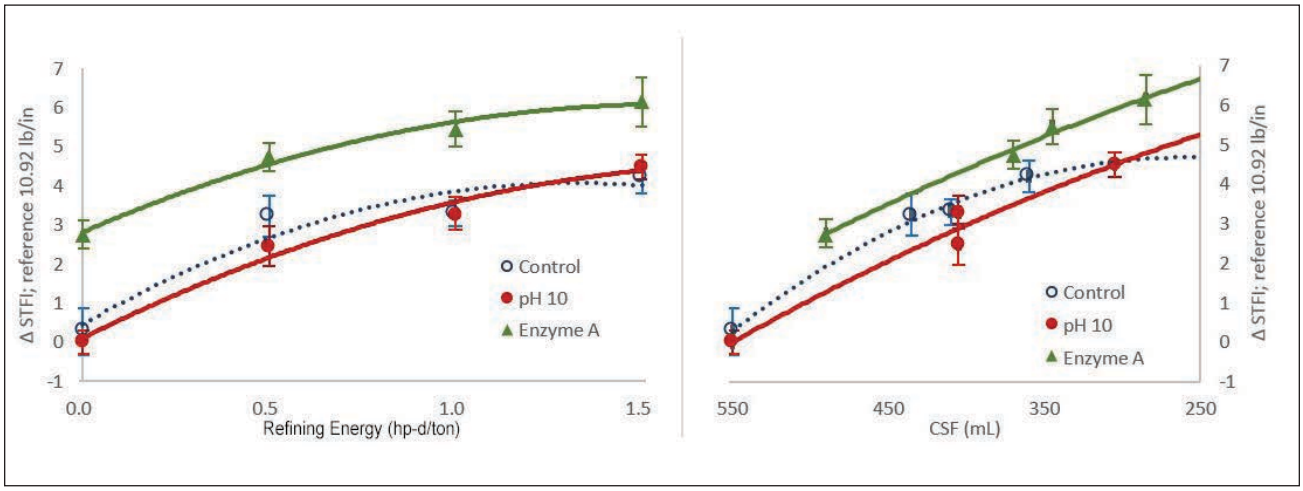
4. Effect of refining on fiber length of old corrugated container (OCC).



5. Effect of refining on fines content of OCC.



6. Effect of refining on fiber damage of OCC.



7. Short span compression (STFI) as function of refining energy and CSF.

test [SCT]) (**Fig. 7**). At similar refining energy, the Enzyme A treatment resulted in 1.5 points higher SCT than did the control. When compared at the same SCT, the freeness was significantly higher for the Enzyme A treated pulp than for the control pulp. For the papermaker, the flexibility of optimizing the process for either increased strength or increased drainage, and maintaining strength properties, is a significant advantage.

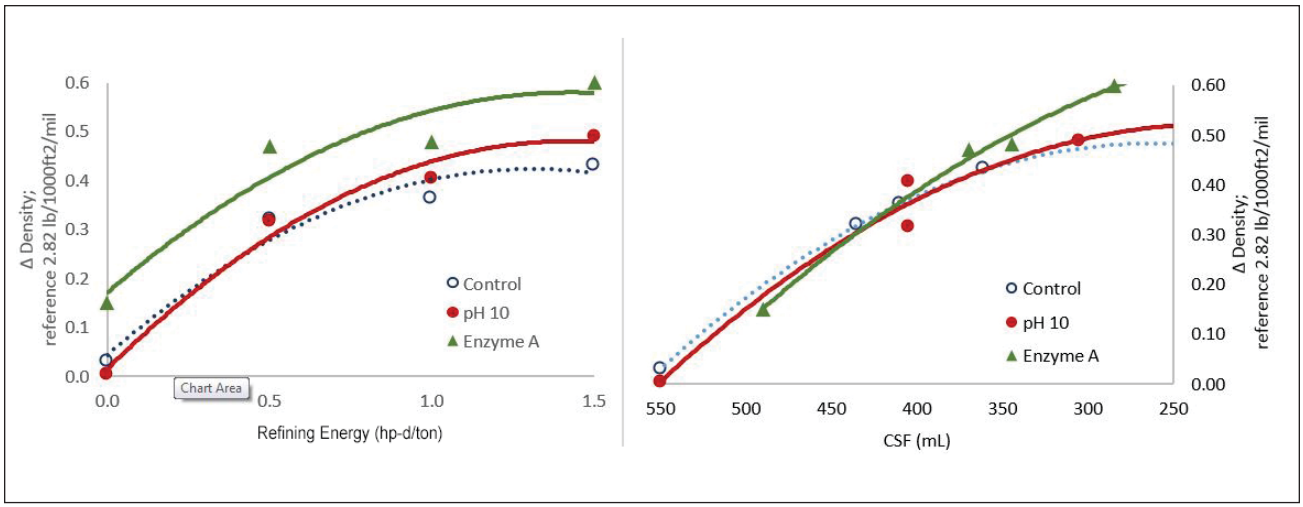
Enzyme-treated pulp exhibited higher density compared with control at similar refining energy, while the density at pH 10 was similar to that of the control (**Fig. 8**). We saw no significant differences in freeness vs. density (Fig. 8). The effect on density (bonding), with no effect on drainage, suggests that the enzymatic treatment might make it easier for the fibrils to separate during the refining process, without increasing the fines content.

Handsheet porosity at pH 10 was generally similar to that of the control, except for the sample at the highest refining energy (1.5 hp-d/ton) (**Fig. 9**). Enzyme A treatment resulted in significantly higher porosity compared with control at any given refining energy (Fig. 9). Less refining energy would be required with enzymatic treatment. Sheet porosity was similar when compared at a given pulp freeness (Fig. 9).

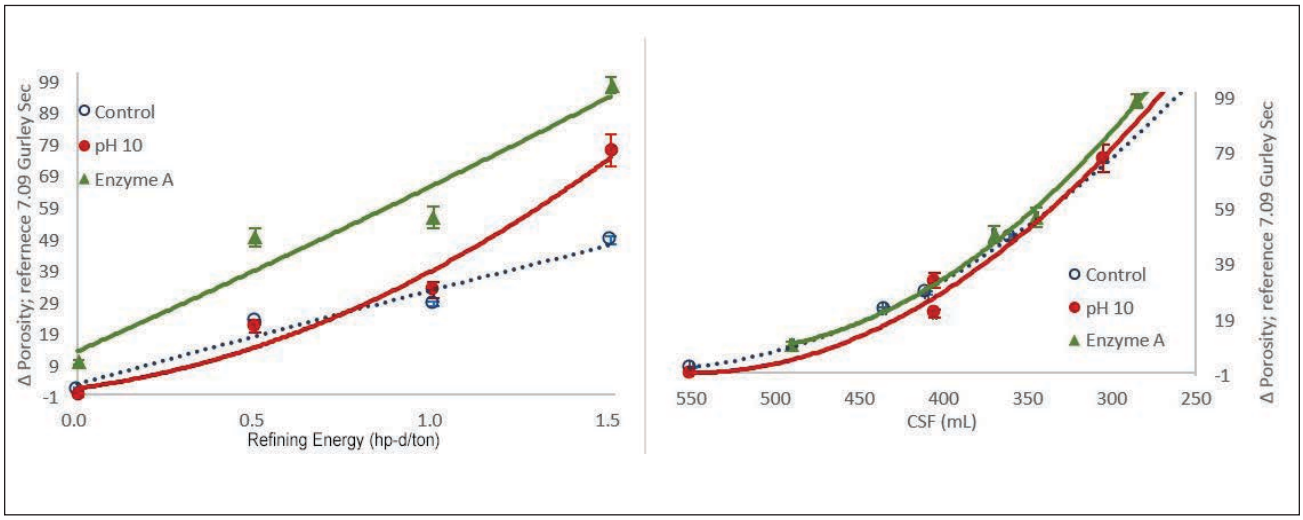
Handsheet ZDT analysis showed no relevant difference in results between pH 10 and control samples (**Fig. 10**). The ZDT values with Enzyme A were significantly higher than with control at the same refiner energy (Fig. 10). Significant energy savings could be achieved using enzyme treatment to influence ZDT.

Burst strength showed negligible difference between the pH 10 and control samples for a given refining energy (**Fig. 11**). The enzyme treatment resulted in significant burst increase (Fig. 11) for a given energy input. At a given freeness, the enzyme treated samples had higher burst strength than the control. Results for the pH 10 samples closely matched those of the control (Fig. 11).

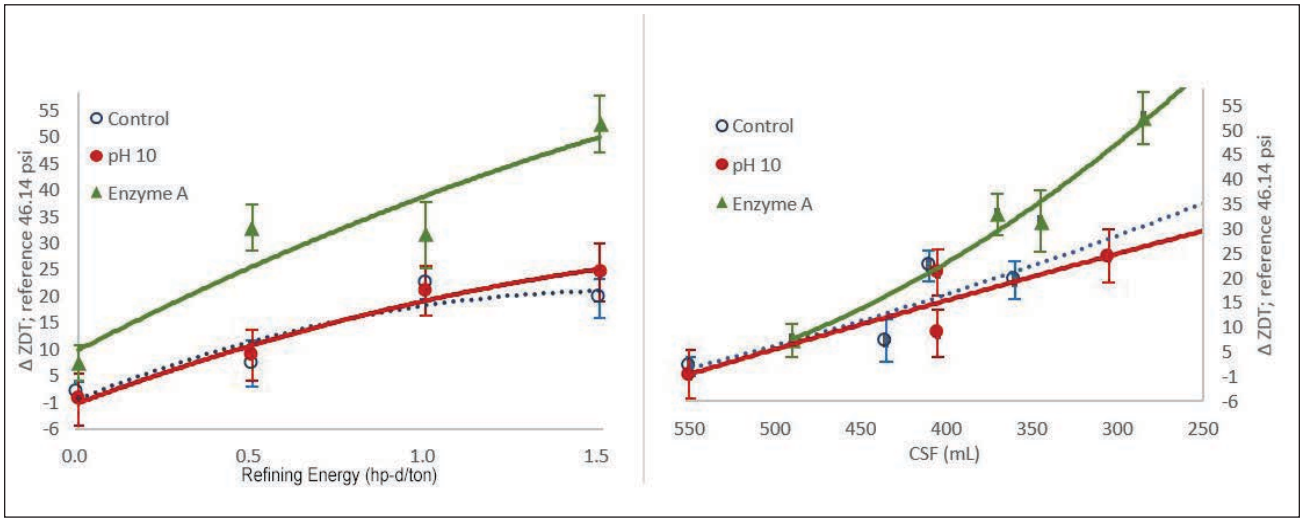
Several researchers have investigated the effect of high pH on strength development during refining of recycled fibers;



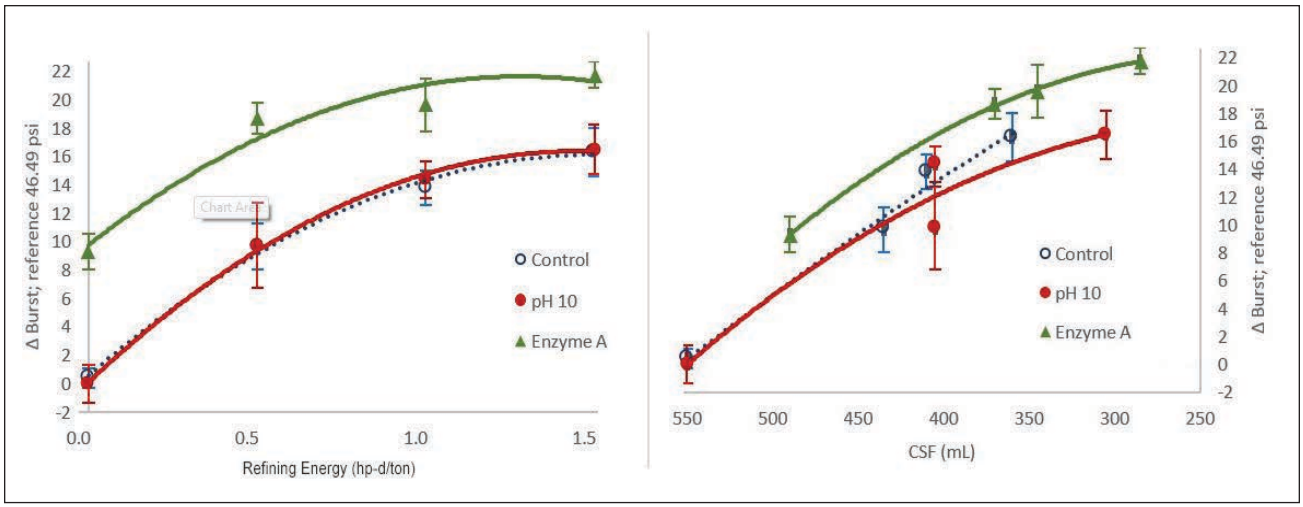
8. Density as function of refining energy and CSF.



9. Porosity as function of refining energy and CSF.



10. Z-direction tensile (ZDT) as function of refining energy and CSF.



11. Burst as function of refining energy and CSF.

some found net positive effects [16-20], others saw no significant effect [21]. Several investigators have used caustic dosages in excess of 2% on pulp [16-19], which is very high and might require additional capital costs to capture and reuse the residual caustic to be efficient. Additionally, there may be extra costs to neutralize the caustic carryover in the pulp. The present work was done at pH 10 using about 0.4% caustic on dry pulp, which are more realistic conditions to evaluate the effect of caustic addition to an existing recycle plant.

Several authors have reported using a PFI mill for refining OCC in the laboratory. This could be an issue because a PFI mill has a very low refining intensity, whereas commercial pulp refiners have significantly higher refining intensity, which results in more fiber damage [16,19].

Some of the earlier studies were done with OCC that contained significant quantities of wet strength resins [16]. Wet strength resins, such as polyamide-epichlorohydrin (PAE), generally require a pH of 12 or higher to degrade [1]. In the absence of high pH and temperature, the repulping of OCC containing wet-strength resin tends to be incomplete, which results in high screen rejects and low repulper yields. Additionally, increasing the repulper time to break apart the fiber bundles caused by the wet strength resin also increases the chances that the fibers will be damaged during defiberation, which lowers overall pulp strength. Hence, recycling paper that contains significant quantities of wet strength resin might confound the results, because increasing the pH can improve defibration of the wet strength paper.

The enzyme-treated pulp samples did not show any significant change in particle charge demand (PCD), streaming zeta potential (SZP), conductivity, and turbidity (**Table III**). These observations suggested that the enzymatic reactions with the dissolved and colloidal materials were unlikely to be a major factor in the increase of pulp strength. PCD is a measure of the anionic trash in the system. The anionic trash might interfere with the fiber-fiber bonding. Because the charge levels did not significantly change, we can assume that there were no significant changes in the anionic trash content. In this study, the laboratory handsheets were made without any dry strength polymers. If chemical strength adjuncts are added to the pulp, the efficacy of the polymers to enhance pulp strength might improve with reduction in dis-

Enzyme Dosage, lb/ton	Turbidity, NTU	SZP, mV	Conductivity, µS/cm	PCD, µeq/L
0	191	-34.4	581	-574
0	190	-35.5	574	-539
0	200	-33.4	588	-583
1.5	202	-33.4	571	-550
1.5	219	-33.4	560	-571
1.5	227	-33.6	575	-602

III. Effect of Enzyme A on particle charge demand (PCD), streaming zeta potential (SZP), and other characteristics of old corrugated container (OCC) slurries with mill white water.

solved/colloidal anionic trash in the pulp slurry going to the paper machine.

The addition of Enzyme A to the OCC aided strength improvement during subsequent refining. The energy required to achieve a targeted freeness value was less with the enzyme application. In addition, the strength achieved at a given freeness was higher for the enzyme-treated pulp. Additionally, enzyme treatment alone caused a reduction in pulp freeness and an increase in pulp strength properties, without subsequent refining. Some earlier studies have reported increased fibrillation during the refining of pulps when treated with enzymes [23,24]. Other studies have reported that enzyme treatment alone did not increase freeness [22]. This discrepancy might be a result of the choice of enzymes in the formulation, as well as the pulp and white water characteristics. Indeed, in some cases, certain cellulases and hemicellulases have caused reductions in strength with improvements in drainage [25].

CONCLUSIONS

Various paper properties made with OCC pulp can be improved with an enzyme treatment, whereas a high pH treatment (pH 10) is relatively ineffective. Enzyme treatment helped to improve fiber reswelling, which resulted in increased fiber strength properties at a given refining energy. The improved pulp drainage could be used to increase paper machine production, which would depend on machine configuration and dryer steam availability. Potential next steps in future investigations will include the evaluation of the effect of certain specific cellulase and lipase strains on the strength of the paper made with recycled fibers. **TJ**

LITERATURE CITED

1. Bajpai, P., *Recycling and Deinking of Recovered Paper*, Elsevier Science Publishing Co., Burlington, MA, USA, 2014, pp. 183-184.
2. Weise, U., *Pap. Puu* 80(2): 110(1998).
3. Klungness, J.H. and Caulfield, D.F., *Tappi J.* 65(12): 94(1982).
4. Carlsson, G. and Lindström, T., *Sven. Papperstidn.* 87(15): R119(1984).
5. Diniz, J.M.B.F., Gil, M.H, and Castro, J.A.A.M., *Wood Sci. Technol.* 37(6): 489(2004).
6. Minor, J.L., *Prog. Pap. Recycl.* 3(2): 93(1994).
7. Laivins, G.V. and Scallan, A.M., "The mechanism of hornification of wood pulps," *10th Fundamental Research Symposium*, Pira, Oxford, UK, 1993, pp. 1235-1260.

ABOUT THE AUTHORS

The fiber cost component in recycled paper is approximately 40% of the total manufacturing cost. The overall recycled fiber quality has been deteriorating. To maintain paper strength properties, paper mills respond by increasing basis weight, dry strength, etc.

The methods used in this study (increased pH and enzymes) previously have been evaluated in recycled paper. Several authors have found the effect of pH 10 to be net positive, while others found it to not have any effect. This study evaluated the effect of raising pH on recycled paper furnish that does not contain wet strength paper. We also did a head-to-head comparison between pH and enzymes. In addition, the work was done on a disc refiner, which is known to provide more realistic results than a Valley beater or other laboratory refiners.

OCC pulp has a relatively short storage life before going rancid. Therefore, the pH and enzyme studies were done with OCC samples that were produced at different times at the recycle mill. Although the sample location was the same, the pulp samples had significantly different properties, which highlight the variability inherent with OCC pulps. Because the controls for each of the trials were different, the test results have been graphed as a difference from the respective control values.

The enzyme formulations can be a bit "black-box" when it comes to applying the work to the various production sites. The effect of certain enzymes can provide significant gains; however, the effect varies significantly depending on fiber type.

Some mills are hesitant in using enzymes, either because it's "new," or they had bad experience in the past. The authors hope this work will add to the body of evidence in the net positive effect of enzyme treatments.

Our next step is to evaluate individual enzyme strains to build better understanding of the enzyme action on various substrates.



Ghosh



Hart



Thornton

Ghosh is senior R&D engineer and Hart is director, Fiber Technology and Innovation, WestRock Company, Richmond, VA, USA. Thornton is a chemical engineering student at Virginia Commons University, Richmond, VA, USA. Email Ghosh at ashok.ghosh@westrock.com.

8. Strey, E.G., "Enzymatic modification of woody cell walls for improved stability of pulp fibres," Ph.D. thesis, University of Pretoria, Pretoria, South Africa, 2009, Sec. 1, pp. 17-20.
9. Pere, J., Siika-Aho, M., Buchert, J., et al., *Tappi J.* 78(6): 71(1995).
10. Lange, H., Decina, S., and Crestini, C., *Eur. Polym. J.* 49(6): 1151(2013).
11. Delagoutte, T. and Brun, J., "Drying section deposits: origin, identification, and influence of the recycling processes: deinking and packaging line operations," *TAPPI Eng., Pulping, Environ. Conf.*, TAPPI Press, Atlanta, GA, USA, 2005.
12. Herington, B.L., *J. Dairy Sci.* 37(7): 775(1954).
13. Lundin, T., Lönnberg, B., Soini, P., et al., "LC-refining by modified hydraulic volume designs," *Pira Int. Refin. Conf., 6th*, Pira International, Leatherhead, UK, 2001.
14. Ghosh, A.K., unpublished data from a refining study on southern pine kraft pulp.
15. OpTest Equipment Inc., "Fiber Quality Analyzer–360," OpTest Equipment Inc., Hawkesbury, ON, Canada, 2017. Available [Online] http://www.optest.com/LDA12.htm.
16. Freeland, S., "Caustic soaking: a pilot plant study," *TAPPI Recycl. Symp.*, TAPPI PRESS, Atlanta, 1995.
17. Freeland, S. and Hrutfiord, B., "Caustic treatment of OCC for strength improvement during recycling," *TAPPI Pulping Conf.*, TAPPI PRESS, Atlanta, 1993.
18. Nazhad, M., "Optimizing OCC pulp process and quality using caustic soda and refining," *TAPPI Corrugating Conf.*, TAPPI Press, Atlanta, 2001.
19. Phuong, D. and Nazhad, M., "Effect of swelling or surface agents on OCC," *Appita Annu. Conf. Proc., 60th, Appita*, MacLeod, VIC, Australia, 2006.
20. Zanuttini, M.A., Marzocchi, V.A., and Mocchiutti, P., *Cellul. Chem. Technol.* 43(1-3): 65(2009).
21. Wistara, N. and Young, R.A., *Cellulose* 6(4): 291(1999).
22. Siqueira, E., Naoui, W., Marlin, N., et. al., *Nord. Pulp Pap. Res. J.* 28(4): 529(2013).
23. Przybysz Buzala, K., Przybysz, P., Kalinowska, H., et. al., *PLoS One* 11(8): e0161575(2016).
24. Maximino, M.G., Taleb, M.C., Adell, A.M., et. al., *Cellul. Chem. Technol.* 45(5-6): 397(2011).
25. Stork, G. and Wood, T.W., *Tappi J.* 78(2): 79(1995).

ABOUT THIS PAPER

Cite this article as: Ghosh, A., Thornton, B., Hart, P. *TAPPI J.* 17(7):407(2018). https://doi.org/10.32964/TJ17.07.407

DOI: https://doi.org/10.32964/TJ17.07.407

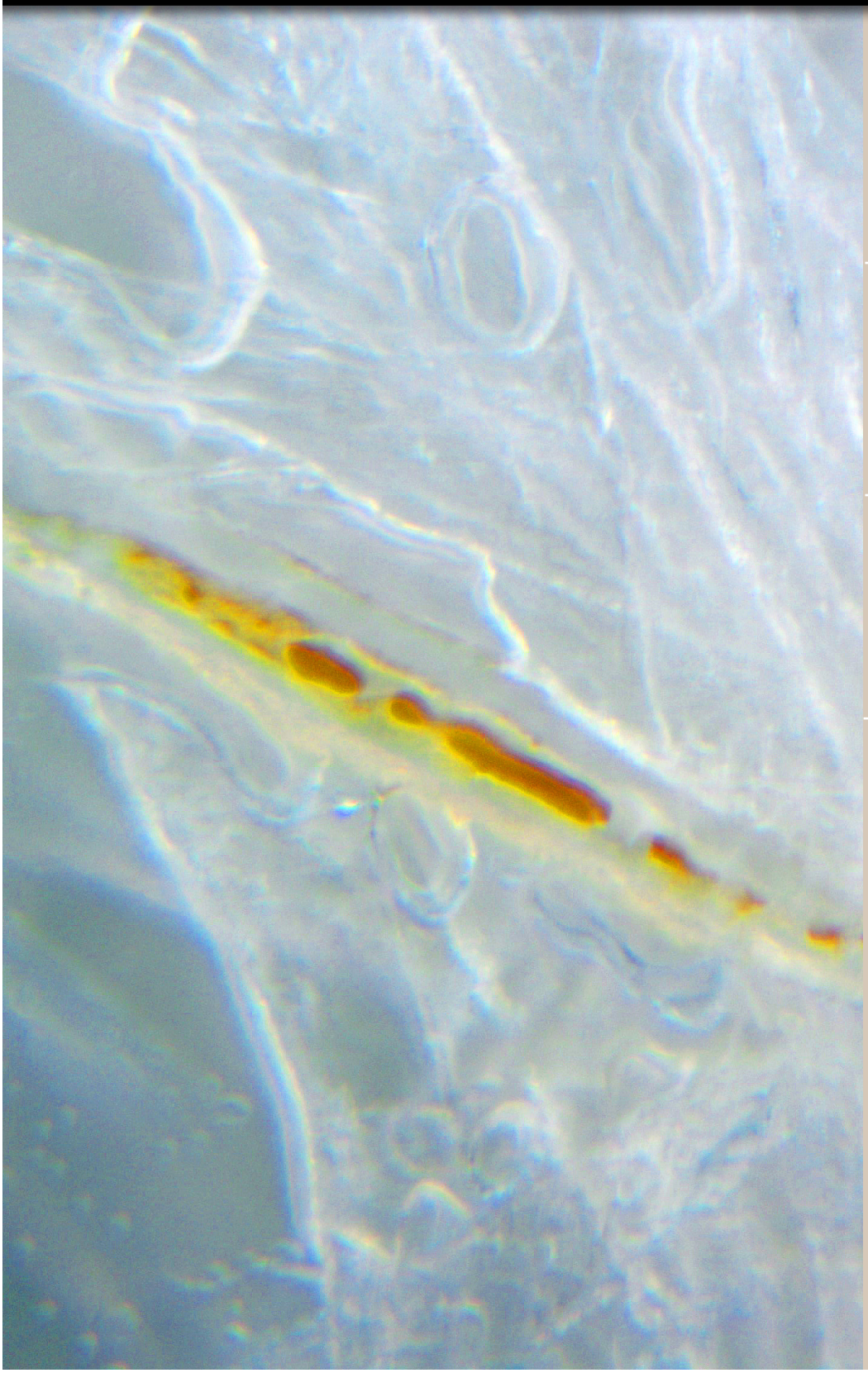
ISSN: 0734-1415

Publisher: TAPPI Press

Copyright: ©TAPPI Press 2018

About this journal

TAPPI JOURNAL
WWW.TAPPI.ORG
THE PAPER AND PACKAGING INDUSTRIES' TECHNICAL RESOURCE
AUGUST 2018 | VOL. 17 NO. 8



PAPER PHYSICS 429
Prediction of box failure from paper data for asymmetric corrugated board
Heinz Joachim Schaffrath, Felix Reichenbach, and Samuel Schabel

PAPERMAKING 437
Impact of fiber structure on edge-wicking of highly-sized paperboard
Lebo Xu, Jeremy Meyers, and Peter W. Hart

FIBER PROPERTIES 447
Enzymatic treated viscose fibers functionalized by chitosan
Urška Vrabič Brodnjak, Diana Gregor-Svetec, and Maja Klančnik

Progress in Paper Recycling

RECYCLING 461
Effect of pulper consistency on stickies size distribution
Mahendra Doshi, Salman Aziz, Robert De Jong, and Carl Houtman

August 2018

TABLE OF CONTENTS VOL. 17 NO. 8

425 EDITORIAL
Douglas Coffin: Paper Physics Guru
Monica Shaw

429 DELIGNIFICATION
Prediction of box failure from paper data for asymmetric corrugated board
Heinz Joachim Schaffrath, Felix Reichenbach, and Samuel Schabel

437 PAPERMAKING
Impact of fiber structure on edge-wicking of highly-sized paperboard
Lebo Xu, Jeremy Meyers, and Peter W. Hart

447 FIBER PRIORITIES
Enzymatic treated viscose fibers functionalized by chitosan
Urška Vrabič Brodnjak, Diana Gregor-Svetec, and Maja Klančnik

Featuring Exclusive Content from
Progress in Paper Recycling

461 RECYCLING
Effect of pulper consistency on stickies size distribution
Mahendra Doshi, Salman Aziz, Robert De Jong, and Carl Houtman

»COVER CREDIT: Coffee trapped within a single fiber in a handsheet shows that fiber walls and lumens are a major pathway for edge-wicking in highly-sized paper (p. 437).

TAPPI JOURNAL
WWW.TAPPI.ORG

Editor-in-Chief
Brian N. Brogdon brian.brogdon@gmail.com
+1 678 581-9114

Associate Editor
Peter W. Hart peter.hart@westrock.com
+1 409 276-3465

Editorial Director
Monica Shaw mshaw@tappi.org
+1 770 367-9534

PRESS Manager
Jana Jensen jjensen@tappi.org
+1 770 209-7242

Webmaster
Trina Heath theath@tappi.org
+1 770 209-7416

***TJ* EDITORIAL BOARD**

Randy Branston, BASF
randy.branston@basf.com, +1 704 819-4251

Brian N. Brogdon, FutureBridge Consulting & Training LLC
brian.brogdon@gmail.com, +1 678 581-9114

David A. Carlson, Carlson Consulting
dacarlson39@aol.com, +1 847 323-2685

Douglas W. Coffin, Miami University
dacarlson39@aol.com, +1 847 323-2685

Mahendra Doshi, Doshi and Associates
mahen@aol.com, +1 920 832-9101

Marc Foulger, GL&V USA Inc.
Marc.foulger@glv.com +1 315 767-2920

Peter W. Hart, WestRock
peter.hart@westrock.com, +1 409 276-3465

Carl J. Houtman, USDA Forest Products Laboratory
choutman@fs.fed.us, + 1 608 231-9445

Lucian Lucia, North Carolina State University
lucian.lucia@gmail.com, +1 919 889-7059

John A. Neun, John A. Neun LLC
john.neun@gmail.com, +1 518 275-8139

Jim Niemiec, Verso Corporation
jim.niemiec@versoco.com, +1 715 422-7404

Steven P. Ottone, Omya
steven.ottone@omya.com, +1 919 641-7854

Gaurav Pranami, Imbed Biosciences
gpranami@imbedbio.com, +1 515 230-7005

Arthur Ragauskas, Oak Ridge National Laboratory
aragausk@utk.edu

Gerard J.F. Ring, University of Wisconsin—Stevens Point
gerrryring@wi-net.com, +1 715 592-3732

Scott Rosencrance, Kemira Chemicals
scott.rosencrance@kemira.com, +1 770 429-2753

Paul Wiegand, NCASI
pwiegand@ncasi.org, +1 919 941-6417

Junyong Zhu, USDA Forest Products Laboratory
jzhu@fs.fed.us, +1 608 231-9520

Join TAPPI *today!*

TAPPI JOURNAL is a free benefit of TAPPI membership, and is only available to members. To join TAPPI, to renew your TAPPI Membership, or to learn about other valuable benefits, visit www.tappi.org.

TAPPI, 15 Technology Parkway S., Suite 115, Peachtree Corners, GA 30092, publishes *TAPPI JOURNAL* monthly.

ATTENTION PROSPECTIVE AUTHORS: All papers published are subject to *TAPPI JOURNAL's* peer-review process. Not all papers accepted for review will be published. Before submitting, check complete author guidelines at http://www.tappi.org/s_tappi/doc.asp?CID=100&DID=552877.

Statements of fact and opinions expressed are those of individual authors. TAPPI assumes no responsibility for such statements and opinions. TAPPI does not intend such statements and opinions or construe them as a solicitation of or suggestion for any agreed-upon course of conduct or concerted action of any sort.

Copyright 2018 by TAPPI, all rights reserved. For copyright permission to photocopy pages from this publication for internal or personal use, contact Copyright Clearance Center, Inc. (CCC) via their website: www.copyright.com. If you have questions about the copyright permission request process, please contact CCC by phone at +1 978 750-8400. To obtain copyright permission to use excerpts from this publication in another published work, send your specific request in writing to Editor, TAPPI JOURNAL, 15 Technology Parkway S., Suite 115, Peachtree Corners, GA 30092, USA; or by fax to +1 770 446-6947. Send address changes to TAPPI, 15 Technology Parkway S., Suite 115, Peachtree Corners, GA 30092, USA; Telephone +1 770 446-1400, or FAX +1 770 446-6947. www.tappi.org

Editorial



MONICA SHAW | EDITORIAL DIRECTOR
mshaw@tappi.org

Douglas Coffin: Paper Physics Guru

Editor's Note: This month, we continue our series of columns profiling the background and expertise of TJ*'s editorial board members. These volunteer members spend long hours overseeing the peer review process and contributing to* TJ*. TAPPI would like to express its gratitude to the editorial board members for their hard work and willingness to share their expertise with the forest products community.*

– Monica Shaw, Editorial Director

TAPPI and the *TAPPI JOURNAL* (*TJ*) editorial staff would like to welcome a new member to the *TJ* Editorial Board, Douglas W. (Doug) Coffin, a professor in the Department of Chemical, Paper, and Biomedical Engineering at Miami University in Oxford, OH. A member of TAPPI since 1994, Doug has been recognized numerous times for his contributions to the field of Paper Physics, including with the Van den Akker Prize in Paper Physics in 2001 and the TAPPI Corrugated Division Award and Bettendorf Prize in 2011.



Douglas W. (Doug) Coffin,* TJ *Editorial Board

A native of Lancaster, PA, Doug received his Bachelor's (1987) and Master's degrees (1989) in Civil Engineering from the University of Delaware, where he also received his Ph.D. in Mechanical Engineering in 1993, with a focus on mechanics of composite materials. From 1989 to 1994, he was a structural engineer with the Electric Boat Division of General Dynamics, after which he became faculty member at the Institute of Paper Science and Technology (IPST) in Atlanta Georgia. He joined Miami University in 2002 and was promoted to professor in 2008. At the university, he teaches courses in Paper Physics, Statics and Mechanics, Thermodynamics, and Chemical Process Safety, in addition to his research in Paper Physics.

Doug has completed extensive work in the mechanics of paper materials and in the creep behavior of paper. He has developed robust nonlinear viscoelastic-plastic constitutive equations for paper and expanded on the role of bonding in sheet efficiency and tensile behavior. An active researcher, his projects have ranged from tissue and corrugated board to nanofibers and converted boxes. He has also overseen a number of studies and papers by his students, from undergraduate to post-graduate.

Doug's publication experience includes a book and book chapters, as well as numerous journal and presentation papers. As a member of the *TJ* Editorial Board, which he has previously assisted as a reviewer, he looks to "help facilitate the connection between author and reader to bring relevant and high-quality technical information in the areas of paper physics and corrugated board that will be useful to readers."

TAPPI involvement and industry perspective

Doug first joined TAPPI when he became a faculty member at IPST in 1994. He is a member and past Chair (along with holding other positions) of the TAPPI Paper Physics Committee. He was also the TAPPI representative at the 2007 International Paper Physics Conference and is the TAPPI representative on the Fundamental Research Committee of the Pulp and Paper Fundamental Research Society. Doug says that "connections to people" have been TAPPI's greatest benefit to his career.

From the industry angle, Doug says that the biggest change he has seen as an academician is the "loss of sponsored research and very few researchers in the U.S. that still focus on pulp and paper." This, he feels, will result in "a lack of people that understand the fundamentals of the behavior of pulp and paper as a material and know the previous work that was completed. Information not found online will be lost to those in the future, and time will be spend rediscovering that knowledge."

As a professor of young engineering students, one of Doug's top teaching philosophies is "learn to learn," with the belief that "the most important mindset to instill in students is that they are lifetime learners." He says that "many students begin their college career with the expectation that all answers can be found in a book, and that they will not be asked to perform tasks that they have not had prerequisite study," but understands that "it's impossible to teach engineers everything that they will need in their careers." He goes on to say:

"My experiences as an engineer are that we rarely use the exact information that we learned in undergraduate education. We do apply the skills we developed. Teaching students that to be successful they must develop skills of learning is an important component of every course."

On a personal note, Doug enjoys spending time outdoors and with his wife of 31 years, Susan, and their three older sons (ages 24, 23, and 21), along with their seven-year-old son who keeps them "young at heart." He also enjoys woodworking but finds it a challenge to create time for it in recent years. **TJ**

TAPPI's Int'l Research Management Committee to Visit Andritz, SAPPI, BASF and Merck

TAPPI's International Research Management Committee has organized it's fall meeting to include visits to several important research centers in Europe. Scheduled for the week of October 22-26, the trip is a stimulating experience of research, discovery, and networking among pulp, paper and tissue R&D leaders.

The committee will visit paper research facilities at Andritz in Graz, Austria, and at BASF and Merck near Frankfurt, Germany. They will also enjoy a tour of Sappi's Gratkorn Mill and the EU's FAIR Particle Accelerator, which is currently under construction.

The program includes plenty of time for sightseeing and networking. Members of the committee are encouraged to register by **September 14**. More information is available on the website. If you are interested in being a part of the ***TAPPI International Research Management Committee***, please contact Scott Springmier at sspringmier@tappi.org. Nominations will be considered by the Membership Working Group.

Prediction of box failure from paper data for asymmetric corrugated board

HEINZ JOACHIM SCHAFFRATH, FELIX REICHENBACH, AND SAMUEL SCHABEL

ABSTRACT: The well-known McKee formula was derived in 1963 for symmetric fluting constructions. This paper presents investigations showing the influence of asymmetric properties, either geometric or concerning the elastic moduli. Paper properties of the base papers used are taken to calculate the panel properties of corrugated boards. From these results, the box failure is predicted. To do this, a model approximating the corrugated medium by triangles is presented. With this assumption, the bending stiffness of corrugated board, no matter how many flutes, can be predicted from paper data. Machine direction and cross direction are treated separately. The theoretical considerations are verified by measuring paper parameters such as short compression test (SCT), thickness, and bending stiffness, as well as edge compression test (ECT) and bending stiffness of corrugated board and box compression test (BCT) of the boxes. It can be stated that the prediction of using paper data instead of corrugated board data may lead to even better prediction results, as the measuring of bending stiffness at the board may sometimes be influenced by sampling inconveniences. Finally, thickness of the used base papers, as well as thickness of the manufactured board, appear to be the main influencing parameters. The McKee formula is robust enough to be applied for asymmetric corrugated board as well.

Application: The results here help to predict the BCT values from paper data.

Since 1963, when McKee et al. [1] published a formula to predict box compression strength (BCT) from edge compression strength (ECT) and bending stiffness (S) of corrugated board, the manufacturers of corrugated boxes have used this equation as a simple, practical, and quite stable estimation of the quality of their end product. The formula was enhanced by Jonson and Ponton [2] in 1985 and Müller [3] in 2002 in order to be able to use paper data to predict box quality. Both proposed the short span compression strength (SCT value) to estimate the ECT value, which can further be used to calculate the BCT value.

In 1965, Shick [4] used the McKee formula for double-fluted board, but he had to state other fitting parameters. Pommier et al. [5] emphasize the importance of bending stiffness and discuss the ECT as too poor to be useful for BCT prediction, as ECT is highly dependent on grammage of the base papers. The authors point out that the McKee formula with the published constants is only applicable for symmetric board structure. They underline their comments with finite element calculations.

However, the McKee formula is subject to some restrictions. First, the connection of the flute to the liner is regarded to be ideal. Second, the ratio between box perimeter and box height must be higher than 7. The formulas have been derived from panels. In 1993, Batelka and Smith [6] indicated that they are most applicable to square boxes where all the panels are the same. Therefore, length and width of a box should not differ more than by a factor of 3. Finally, the corrugated board plate has to be assumed as symmetric in thickness (see also Pommier et al. [5]). This last restriction needs to be eliminated, as more and more board with two different flutes are produced. In Germany, the amount of corrugated board with more than one flute increased from 26% in 2000 to almost 33% in 2015. In addition, the grammage range of the papers used to produce corrugated boxes has changed to a higher variety since 1963. The corrugated base material may only have 80 g/m² or even less in manufacturing today. If coated liner is used, 180 g/m² is a common grammage in the upper range. A common grammage in 1963 was 120 g/m²; coated liner or white top liner was unknown at that time. To save material and costs, total mass of corrugated board declined from 531 g/m² in 2000 to 515 g/m² in 2015 [7].

In 1985, Carlsson et al. [8] published their work concerning the prediction of bending stiffness for asymmetric corrugated boards consisting of several layers. The way to estimate the contribution of flat layers to bending stiffness is the same as described later in this paper, which means that the same fundamental equations of mechanics are used. However, the contribution of the corrugated layers is calculated in a different manner. Finally, the authors do not extend the analytics to predict box failure.

Therefore, it is necessary to evaluate whether the McKee formula can also be used for low grammage corrugated papers, and whether the formula has to be enhanced to asymmetric corrugated boards with two or three flutes.

THE MCKEE FORMULA AND SOME THEORY

McKee used the theory of buckling plates. The critical load

P_{crit} causes buckling. The material can withstand the applied pressure until P_{max} (which means either break under pressure or total failure by buckling) is achieved. This leads to [1]:

$$\frac{P_{max}}{P_{crit}} = c \cdot \left(\frac{P_{Mat}}{P_{crit}}\right)^{b}$$
$$\text{respectively:} \quad P_{max} = c \cdot P_{Mat}^{b} \cdot P_{crit}^{1-b} \tag{1}$$

where P_{Mat} is a material property and will equal edge crush test (ECT) in this case, as well as P_{max} equals box compression test (BCT). The perimeter of the box Z and the bending stiffness S in machine direction (MD) and cross direction (CD) can be used to replace the critical load P_{crit} and leads to:

$$BCT = 2{,}028 \cdot ECT^{0{,}746} \cdot \sqrt{S_{MD} \cdot S_{CD}}^{0{,}254} \cdot Z^{0{,}492} \tag{2}$$

which is known as the original McKee formula. A second version uses ECT values and thickness of the board instead of bending stiffness. As thickness is much easier to measure than bending stiffness, this version is more often used in the corrugated board industries. However, Mühlenbein [9] and Maltenfort [10] discussed this approach in their publications. Mühlenbein recommended the four-point method for determination of bending stiffness, as described in ISO 5628:2012 "Paper and board — Determination of bending stiffness— General principles for two-point, three-point and four-point methods." He refused the use of thickness as an alternative, as he could not confirm the correlation between board thickness and BCT, as published by McKee et al. [1]. Maltenfort disagreed and showed that Mühlenbein had a mistake in his calculations. Maltenfort emphasised the correctness of the McKee approach, but it has to be mentioned that taking the bending stiffness to predict BCT, 80% of the tested boxes are in a range ± 10% around the calculated value but only 75% if the thickness is taken instead [1]. The numbers of the parameters have been derived from experiments with more than 100 boxes.

As bending stiffness seems to be the better parameter to predict BCT, some work dealing with this subject will be mentioned. Fellers and Carlsson [11] referred to the importance of bending stiffness for packaging board and summarized methods and theories for stiffness evaluation. It is important to know that the four point method delivers the possibility to calculate bending stiffness without regarding shear effects. Fellers, in his ongoing work [12], carried out a round robin study in 1997. He stated that variance of results increases with decreasing grammage.

Creeping and influence of climate changes on corrugated board and its bending stiffness have been subject of investigation as well (e.g., [13-14]), but this is not the focus of this paper.

Besides the semi-empirical approach to predict box strength offered by McKee, some authors published statistical, analytical, and numerical studies to predict paper and board properties. As an example, Lu and Carlsson in 1986 [15] used the Monte Carlo method to calculate paper formation and paper structure as a starting point to predict paper strength and stiffness properties and its variations. Biancoli and Brutti published a paper in 2003 dealing with the investigation of buckling by means of finite element analysis [16]. They found an excellent agreement of calculated values with experimental results for ECT as well as for BCT. This work was carried out for a single C-flute, and the results were also found to be in accordance with the prediction done by the McKee formula. Part of their approach is to replace the corrugated structure by a homogeneous layer. In 2013, Aboura et al. [17] presented an analytical model of single flute board. The approach is comparable to Carlsson et al. [8], as the shape of the flute is taken as a sine. Experimental results fit well to analytical predictions; however, the investigation is done in the elastic range of deformation. In 2014, Åslund et al. [18] did a numerical analysis of a single flute board plate regarded as a sandwich structure. They succeeded in getting insights not only about panel buckling, but also about local face buckling.

Despite many efforts to get a better prediction of BCT values, the McKee formula is still the favorite means of estimating the strength of a box from paper parameters. The main reason is probably its easy use for industrial requirements. Nevertheless, Coffin [19] addressed in his 2015 paper the necessity to decrease the number of boxes with unsatisfactory predictions of BCT. He suggested including independent investigations of material properties, edge restraints, and geometrical effect in the focus of research.

Concerning multilayered, asymmetric corrugated board constructions, an attempt is proposed in this paper to use different material properties of the base papers, as well as given geometric conditions, to calculate a box strength.

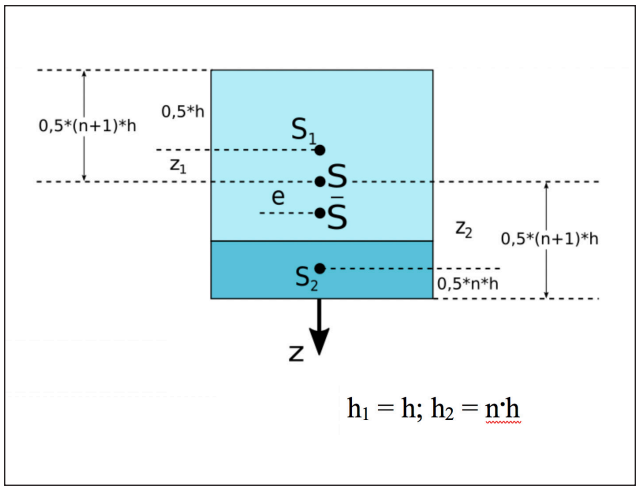
To start, a look back to the Euler theory of beams is helpful [20]. Although the McKee formulas have been derived by using plate theory, the beam theory is sufficient to understand the influence of asymmetry. In the Euler theory, the bending stiffness is given by multiplying the E-modulus of the material with the area moment of inertia, depending on the cross-section of the beam.

Bending stiffness in cross direction (CD)

The area moment of inertia is easy to calculate for symmetric, rectangular structures. However, for example, a combination of B- and C-flute or even B- and E-flute will lead to a structure comparable to **Fig. 1**.

Layer 1 and layer 2 have different heights, h_1 and h_2, as well as different E-moduli, E_1 and E_2. The ratio of h_2 to h_1 is n. S_1 is the position of the neutral axis of layer 1, S_2 of layer 2, S the middle axis and $\overline{S}$ the neutral axis of the whole structure. With the parallel axis theorem, the area moment of inertia of the two layers can be calculated. Therefore, the distance between the neutral axis of each layer to the neutral axis of the whole structure has to be calculated with the help of z_1, z_2, and eccentricity e.

The values of z_1 and z_2 may be derived from geometric con-



1. Asymmetrical structures [21].

ditions. The eccentricity is influenced by the elastic moduli E_1 and E_2 of the layers. Letting m be the relation of E_2 to E_1, eccentricity e results in:

$$e = \frac{n \cdot h_1 \cdot (m-1)}{2 \cdot (n \cdot m+1)} \tag{3}$$

Using this and applying the parallel axis theorem leads to:

$$\overline{E \cdot I} = E_1 \left\{ \frac{b h_1^3}{12} + b h_1 \cdot \left[\frac{1}{2} n h_1 + e \right]^2 + m \cdot \left(\frac{b h_1^3}{12} n^3 + n b h_1 \cdot \left[\frac{1}{2} h_1 - e \right]^2 \right) \right\} \tag{4}$$

as the bending stiffness of the whole structure. The width of the corrugated plate is *b*. These steps may be carried out for more than two layers as well and will lead to bigger formulas. With two different liners and one fluting medium, three layers are already given [21].

The next step is to calculate a substitutional E-modulus for the flute. Sine shapes cannot be calculated analytically; therefore the sine flute is approximated by a triangular shape (**Fig 2**). This appears to be reasonable, as the flute-shape very often is not an exact sine in the industrial corrugators.

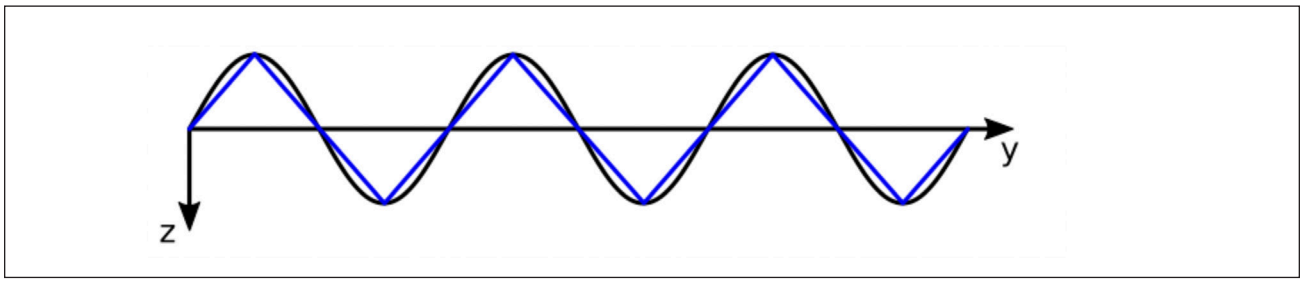
Assuming that the width of a corrugated board is much larger than the pitch of the flute, the triangles may be displaced in a manner shown in **Fig. 3**. This will still lead to the same bending stiffness across the y-axis as the structure in Fig. 2.

Now, the bending stiffness of the flute-layer is easy to calculate knowing the E-modulus of the fluting paper in cross direction ($E_{CD,fl}$) and the geometry (height of the flute h_{fl}, pitch p, width of the flute-strip w and thickness of the fluting-paper δ_{fl}):

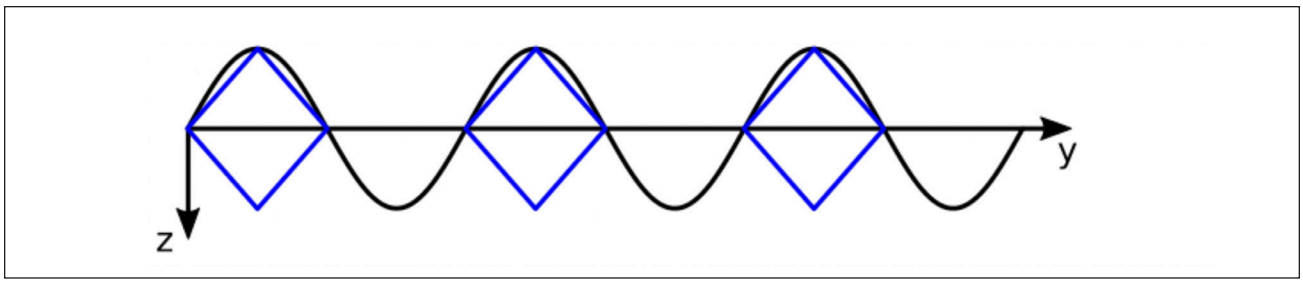
$$\overline{E_{CD,fl} \cdot I_{fl}} = E_{CD,fl} \cdot \frac{w}{p} \cdot \frac{1}{6} \delta_{fl} \cdot h_{fl}^2 \cdot \sqrt{\frac{1}{4} p^2 + h_{fl}^2} \tag{5}$$

This bending stiffness can be used to derive a substitutional E-modulus in CD, $E_{CD,sub}$. Therefore, imagine to substitute the flute-layer by a homogeneous layer with the height h_{fl} and the width w (which may be measured). The moment of inertia $I_{CD,sub}$ can then be calculated as:

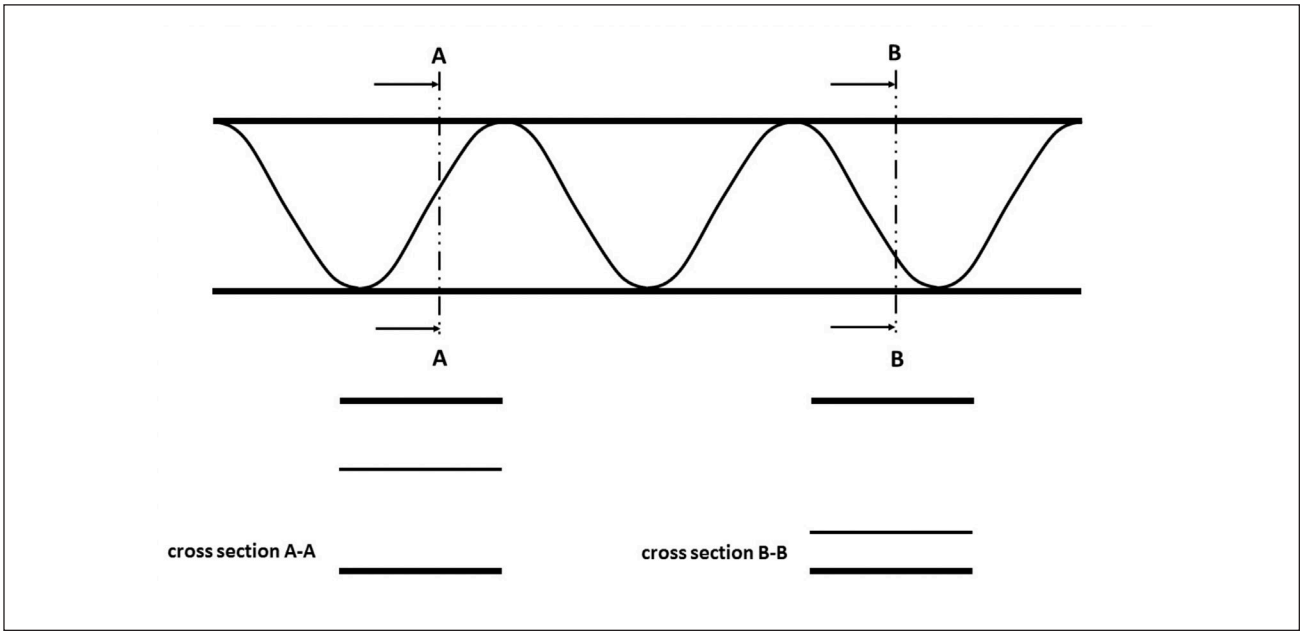
$$I_{CD,sub} = \frac{w \cdot h_{fl}^3}{12} \tag{6}$$



2. Approximation of a sine-shape flute by triangles.



3. Displacing the triangles.



4. Contribution of fluting paper, depending on cutting position.

As the imaginary homogeneous layer shall have the same bending stiffness as the real layer, the substitutional E-modulus can now be calculated as well [21]:

$$E_{CD,sub} = E_{CD,fl} \cdot \frac{2 \cdot \delta_{fl}}{p \cdot h_{fl}} \cdot \sqrt{\frac{1}{4} p^2 + h_{fl}^2} \qquad (7)$$

The layer of liner paper is characterized by the thickness of the liner δ_{lin}, which equals the height of the liner layer h_{lin}, and the liner E-modulus in cross direction, $E_{CD,lin}$. Going back to Eq. 4, E_1 may be taken as E_{sub}, h_1 as h_{fl}, in consequence E_2 equals E_{lin} and h_2 equals h_{lin}. So, one liner layer connected to one flute is described.

The results may be taken, and analogous to the described procedure, a second liner layer can be added. Therefore, the obtained E of the liner fluting combination will be regarded as a new E_1 for Eq. 4, and the new h_1 will be $h_{lin} + h_{fl}$. The other E_2 is given by the E-modulus of the second liner layer, and the other h_2 by the thickness of the second liner layer. Now, a complete corrugated board consisting of two liners and one flute is described.

This result can be enhanced by adding the next fluting layer, calculated in the proposed way with a substitutional E-modulus, and so on. By this, it is possible to calculate the bending stiffness of multilayer corrugated boards in CD just by knowing the flute type and by measuring the thicknesses and the E-moduli of the papers used.

Bending stiffness in machine direction (MD)

The same procedure for the CD has to be carried out in the MD. However, the contribution of the fluting paper to the bending stiffness is dependent on the position where the cross section is selected (**Fig. 4**).

Paper Grade Applied for Indicated Corrugated Board	δ, mm	E_{MD}, N/mm²	E_{CD}, N/mm²
Liner 1 (used for B-flute)	0.172	3477	1188
Liner 2 (used for B-flute)	0.172	3458	1150
Flute (used for B-flute)	0.139	3503	1151
Liner 1 (used for C-flute)	0.175	3001	1164
Liner 2 (used for C-flute)	0.151	3700	1271
Flute (used for C-flute)	0.142	3157	1449
Liner 1 (used for BC-flute)	0.280	3824	1267
Liner 2 (used for BC-flute)	0.151	3681	1383
Liner 3 (used for BC-flute)	0.248	3699	1613
Flute C (used for BC-flute)	0.153	3359	1096
Flute B (used for BC-flute)	0.145	3798	1625
Liner 1 (used for EB-flute)	0.156	6109	1847
Liner 2 (used for EB-flute)	0.154	3954	1224
Liner 3 (used for EB-flute)	0.149	3919	1556
Flute E (used for EB-flute)	0.144	4104	1379
Flute B (used for EB-flute)	0.151	3522	1467

I. Paper data.

To overcome the problem resulting from the unknown position of the flute, the influence is estimated by using the thickness of the paper and the width of the strip. This covers the situation when the fluting paper is in the center between the two liners. The fluting layer is used to create a distance between the liner papers; its contribution to bending resis-

tance is low. So, the mistake made by this assumption is expected to be low, as well.

$$I_{MD,fl} = \frac{w \cdot \delta_{fl}^3}{12} \quad (8)$$

Analogue to cross direction, a substitutional E-modulus $E_{MD,sub}$ can be calculated in MD:

$$E_{MD,sub} = E_{MD,fl} \cdot \left(\frac{\delta_{fl}}{h_{fl}}\right)^3 \quad (9)$$

Now, the same procedure applies as described in cross direction. With help of Eq. 4, the resulting bending stiffness of a liner flute combination can be calculated, and the next liner layer may be added and so on.

The goal of this calculation is to take the obtained bending stiffness of the whole, asymmetric structure in MD and CD and use it in Eq. 2, the McKee formula. The calculated BCT should match to the measured one.

EXPERIMENTS

Prediction of bending stiffness of corrugated board from paper quality

During the production of corrugated board, samples were taken in a board mill. They include paper as well as board. E-moduli E of the papers (**Table I**) were derived using bending tests according to ISO 2493-1:2010 "Paper and board—Determination of bending resistance—Part 1: Constant rate of deflection."

In addition, the bending stiffness divided by the width of the tested stripes (called S) of the corrugated board was measured according to ISO 5628. With the derived equations, the bending stiffness S (related to width) of the board was calculated from the E-moduli of the papers. The results are demonstrated in **Table II**.

The height of the B-flute was 2.43 mm, pitch was 6.09 mm, and take-up factor was 1.3 mm. The C-flute was 3.21 mm high, pitch was 7.92 mm, and take-up factor was 1.34 mm. The values of the E-flute were: height 1.27 mm, pitch 3.23 mm, and take-up factor 1.32 mm. As documented in Table II, the results for calculated and measured bending stiffness of the board fit quite well for the BC- and EB-combination, but less well for the single flutes. It has to be mentioned that a slight curl could be observed with the single flutes. This is assumed to be the reason of the high difference. Box I and box II made with C-flute are different in dimension. Due to this, no sample in CD could be cut from box II, because it was too small. For further calculations, CD values of S are taken from box I.

Prediction of BCT from paper quality and from ECT

According to Jonson and Ponton [2], the SCT values of different papers were measured and used to calculate the ECT value of the corresponding corrugated board. As described in the "Prediction of bending stiffness of corrugated board from paper quality" section, the bending stiffness in MD and CD of the papers were calculated and used to derive the bending stiffness of the board. From this board, boxes were manufactured, and the BCT value was measured and calculated both according to the McKee formula (Eq. 2), with ECT-values and

Board Type	S_{MD} Board Calculated, Nmm	S_{MD} Board Measured, Nmm	Difference, %	S_{CD} Board Calculated, Nmm	S_{CD} Board Measured, Nmm	Difference, %
B-flute	2023	3260	-37.9	844	1330	-36.5
C-flute (box I)	3073	4350	-29.4	1430	2040	-29.9
C-flute (box II)	3073	4620	-33.5	./.	./.	./.
BC-flute	30487	28180	8.2	14578	13100	11.3
EB-flute	8373	7930	+ 5.6	4083	3900	+ 4.7

II. Calculated board stiffness and measured board stiffness, S, from paper data for machine direction (S_{MD}) and cross direction (S_{CD}).

Board	BC-Flute, kN	EB-Flute, kN	C-Flute I, kN	C-Flute II, kN	B-Flute, kN
BCT measured	5.47	2.69	1.08	1.85	1.28
McKee results with measured ECT (old method)	5.22	2.49	1.74	1.76	1.14
McKee results with new method	5.34	2.73	1.44	1.44	1.51
BCT = board compression test; ECT = edge compression test.					

III. Comparison of measured BCT using McKee formula to calculated BCT [20].

stiffness values S measured from samples cut from the box, and according to the theory demonstrated in the previous sections of this paper (**Table III**). Again, the double flute boards fit better than the single flute boards. The McKee formula was least applicable to the C-flutes (box I: Z/h >7; box II: Z/h < 7). This may be regarded as an outlier, as it is well known that the McKee formula fits well to single layer, symmetric boards. On the other hand, these results show that more data is necessary and that better fits for single-flute boards may be found.

CONCLUSIONS

Both theory and the experiments lead to the result that asymmetric board structures, caused by the papers used or due to double flute structures, do not influence the mechanics so much that the McKee formula becomes invalid. Predictions are still expected in the range of ± 10%.

The thicknesses of the papers used, and even more significantly the thicknesses of the different flute-layers, are the main influencing parameters of the total stiffness and the final box strength. Hence, the McKee formula is robust enough to be applied when using low grammage papers, as well as multilayer board constructions. **TJ**

LITERATURE CITED

1. McKee, R.C., Gander, J.W., and Wachuta, J., *Paperboard Packag.* 38(8): 149(1963).
2. Jonson, G. and Ponton, S., *Boxboard Containers* 93(11): 23(1985).
3. Müller, G., "Die erweiterte McKee-Formel," *Papier + Folien.* 37(5): 22(2002).
4. Shick, P.E. and Chari, N.C.S., *Tappi* 48(7): 423(1965).
5. Pommier, J.C., Poustis, J., Fourcade, E., et al., *Int. Pap. Phys. Conf., Proc.*, TAPPI Press, Atlanta, GA, USA, 1991, p. 437.
6. Batelka, J.J. and Smith, C.N., "Package Compression Model," Project 3746, Final Report to the Containerboard and Kraft Paper Group of the American Forest and Paper Association, AF&PA, Washington, DC, USA, 1993.
7. Verband der Wellpappen-Industrie, "Zahlen und Fakten – Daten für die Wellpappenindustrie," Verband der Wellpappen-Industrie e.V., Darmstadt, Germany, Ausgabe 2016.
8. Carlsson, L., Fellers, C., and Jonsson, P., *Das Papier* 39(4): 149(1985).
9. Mühlenbein, K.-J., *Verpack.-Rundsch.* 17(10): 1406(1966).
10. Maltenfort, G., *Verpack.-Rundsch.* 19(1): 38(1968).
11. Fellers, C. and Carlsson, L., in *Handbook of Physical and Mechanical Testing of Paper and Paperboard* (R.E. Mark, Ed.) Vol. 1, Marcel Dekker, New York, 1983, pp. 323-347.
12. Fellers, C., *Nord. Pulp Pap. Res. J.* 12(1): 42(1997).
13. Söremark, C. and Fellers, C., *J. Pulp Pap. Sci.* 19(1): J19(1993).
14. Fellers, C. (Ed.) *Proc.—Moisture-Induced Creep Behaviour of Paper and Board*, STFI, Stockholm, 1994.
15. Lu, W. and Carlsson, L.A., *Tappi J.* 79(1): 203(1996).
16. Biancoli, M.E. and Brutti, C., *Packag. Technol. Sci.* 16(2): 47(2003).
17. Aboura, Z., Talbi, N., Allaoui, S., et al., *Compos. Struct.* 63(1): 53(2004).
18. Åslund, P.E., Hägglund, R., Carlsson, L.A., et al., *J. Sandwich Struct. Mater.* 16(3): 272(2014).
19. Coffin, D.W., *TAPPI J.* 14(8): 537(2015).
20. Gross, D., Hauger, W., Schröder, J., et al., *Technische Mechanik 2*, Springer Verlag, Heidelberg, Germany, 2012.
21. Reichenbach, F., "Erweiterung der Formel nach McKee zur Vorhersage des Stapelstauchdrucks von Wellkisten aus Rohpapiereigenschaften und Überprüfung der theoretischen Ergebnisse an Wellpappen und Wellkisten," Bachelor's thesis, Technische Universität Darmstadt, Darmstadt, 2016.

ABOUT THIS PAPER

Cite this article as: Schaffrath, H., Reichenbach, F., Schabel, S. *TAPPI J.* 17(8):429(2018). https://doi.org/10.32964/TJ17.08.429

DOI: https://doi.org/10.32964/TJ17.08.429

ISSN: 0734-1415

Publisher: TAPPI Press

Copyright: ©TAPPI Press 2018

About this journal

ABOUT THE AUTHORS

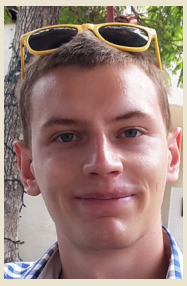
Research on the topic of box failure is necessary for the packaging industry. The work here comple-ments previous research in that it considers asym-metric paper and board properties.

The most difficult aspect of this research was the analytical derivation of usable equations, which we addressed as a team. It was interesting to dis-cover that lightweight packaging papers still corre-spond to the McKee equations. Surprisingly, as long as the thickness of the board is high, bending stiffness may be predicted quite well from paper stiffness.

The information here may help corrugated board mills better select the necessary paper quality. Our next step is to gather more data on a wider range of furnishes.



Schaffrath



Reichenbach



Schabel

Schaffrath is senior researcher, Reichenbach is a Master's student, and Schabel is professor in the Department of Mechanical Engineering at the Technical University of Darmstadt, Darmstadt, Germany. Email Schaffrath at schaffrath@papier.tu-darmstadt.de.

Impact of fiber structure on edge-wicking of highly-sized paperboard

LEBO XU, JEREMY MEYERS, AND PETER W. HART

ABSTRACT: Coffee edge-wicking testing was conducted on two groups of highly-sized paperboard manufactured at two mills with similar manufacturing processes, but with vastly different local fiber sources. Although the Hercules size test (HST) indicated similar internal size levels between the two types of board, the edge-wicking behavior was noticeably different. Analysis of fiber structure revealed that the board with more edge-wicking had fibers with thicker fiber walls, which kept the fiber lumen more open after pressing and drying on a paper machine. It was demonstrated that liquid penetration through voids between fibers in highly-sized paperboard was limited, because the fiber surface was well protected by the presence of sufficient sizing agent. Nevertheless, freshly exposed fiber walls and lumens at the cut edge of the sheet were not protected by sizing material, which facilitated edge-wicking. The correlation between fiber structure and edge-wicking behavior was highlighted in this work to inspire development of novel sizing strategies that protect the freshly cut edge of the sheet from edge-wicking.

Application: The current work shows the contribution of fiber structure to the edge-wicking process for highly-sized paperboard after all the surfaces are protected with size. Understanding the impact of fiber structure on edge-wicking should inspire the development of novel sizing strategies to further reduce edge-wicking.

Paper is easily wet by solvents similar to water due to the intrinsic hydrophilicity of cellulose fibers. With treatment of hydrophobic material, known as size, wetting can be delayed, which makes the manipulation of the wetting behavior possible during the papermaking process. The desired level of water resistance is governed by the end use of the paper product, which may include high moisture environments or direct water contact.

Previous research has suggested four major mechanisms for water transport in paper [1-3]:

1. Capillary penetration in the void between fibers.
2. Diffusion on the fiber surface.
3. Diffusion through fibers.
4. Vapor phase transport.

For applications such as printing and general packaging, liquid penetration perpendicular to the paper surface is a major concern. In this case, capillary penetration in the void spaces between fibers is the most important wetting mechanism.

Capillary penetration in paper voids is well described by the Lucas-Washburn equation, which is widely used to describe liquid penetration in a porous substrate [4-5]. Originally, the equation was developed to describe capillary flow in an array of parallel cylindrical pores, as shown in **Fig. 1**. The Lucas-Washburn equation can be expressed as follows:

$$l = \sqrt{\frac{\gamma \cdot R \cdot \cos\theta}{2\eta}} \cdot \sqrt{t} \qquad (1)$$



1. Scheme of capillary flow in an array of parallel cylindrical pores.

where l (m) is penetration depth, γ (dyne/cm) is liquid surface tension, R (m) is radius of cylindrical pore, θ (°) is contact angle, η (cp) is liquid viscosity, and t (s) is penetration time. One can see that the properties of both the liquid (γ,η) and the substrate (R,θ) have an impact on liquid penetration. To make paper more resistant to water penetration, many sizing materials (such as rosin, alkenyl succinic anhydride [ASA], alkylketene dimer [AKD], etc.) were developed to modify the surface of fibers to reduce the surface tension. The modified surface gives a larger water contact angle, which translates to a smaller $cos\ \theta$ value in the Lucas-Washburn equation, and therefore less water penetration (smaller l value). The pores in the scheme represent voids between fibers, not the fiber lumen. Liquid flow through the fiber (inside the fiber wall and in the lumen) is not considered by the Lucas-Washburn equation.

Edge-wicking is liquid penetration into the paper sheet from the in-plane direction rather than the cross direction. It is a concern for certain paper packaging applications where a cut paper edge is exposed to a liquid, such as with paper cups and juice or milk cartons. Edge-wicking can vary from a minor cosmetic problem, such as stained or discolored raw edges of a paper cup, to more serious package failures around seams. The current industrial trend is towards packaging applications that are considerably more challenging with respect to edge-wicking; for example, liquid packaging manufacturing additives may contain aggressive surfactants. Harsh processing conditions (peroxide or steam treatment) may be employed to sterilize paper packages in filling lines. Factors such as these adversely affect edge-wicking and can potentially lead to package failure. In many cases, plastic laminate, such as polyethylene, is used as a popular approach in addition to a sizing program for enhanced water resistance in the perpendicular direction to the paper surface. However, lamination does not address the edge-wicking issue, as lamination material does not cover the fiber at the cut edge of a sheet of paperboard.

Over the last fifty years, substantial efforts have been made to reduce edge-wicking [6-13]. Most of these efforts have focused on chemical modification of the fiber surface via sizing programs. With sufficient sizing, capillary penetration of water into the voids between fibers is significantly reduced and may no longer be the dominant contribution to overall liquid transport into the paper sheet. In fact, some studies have indicated that liquid diffusion within the fiber wall and in fiber lumens is the major mechanism of liquid transport in highly-sized paper [14-18]. Based on these findings, fiber structure, rather than chemical surface modification, should have a major impact on edge-wicking in highly-sized paper, in which the fiber surface has been well protected by sizing material. However, to our knowledge, no work has been done to reveal the effect of fiber structure on edge-wicking of highly-sized paper.

For the current work, several highly-sized paper samples were obtained from two North American mills with vastly different fiber sources. These samples were produced to meet the same grade specification. Even though these samples were made with a similar sizing program and achieved the same Hercules size test (HST) targets, the samples exhibited significantly different edge-wicking behavior. These samples were compared to each other to help understand how the physical fiber structure contributes to edge-wicking. The mechanism of edge-wicking in highly-sized paper was also investigated. By understanding the impact of fiber and sheet structure on edge-wicking behavior, we hope to find ways to mitigate edge-wicking and develop new sizing strategies beyond the internal size program currently employed in mills.

EXPERIMENTAL

All paper samples were conditioned at TAPPI standard temperature and humidity (TAPPI T 402 sp-08 "Standard conditioning and testing atmospheres for paper, board, pulp handsheets, and related products") prior to being tested. General paper property tests, such as grammage and caliper, were measured with TAPPI T 410 om-13 "Grammage of paper and paperboard (weight per unit area)" and TAPPI T 411 om-15 "Thickness (caliper of paper, paperboard, and combined board)," respectively. Sizing of paperboard was evaluated by HST. The test was conducted at room temperature with reflectance of 80%. Green dye ink with 20% (by weight) formic acid was used in the test.

Edge-wicking of paperboard was evaluated by a hot coffee test. A sample paperboard was laminated with plastic film (Scotch thermal laminating pouch, 3M; Maplewood, MN, USA) on both surfaces. The laminated board was cut into strips of 1 in. x 5 in. Freshly brewed coffee with a powdered creamer (creamer concentration 3.6 v/v%) was used as the testing liquid, and the temperature of the coffee/creamer mixture was maintained at 90°C. The test strip was inserted 3 in. into the hot coffee/creamer mixture for a specified amount of time. When the specified time was reached, the strip was removed from the solution and wiped dry for evaluation. Tested strips were scanned to form color images (TIFF format). The color images were converted to binary images with ImageJ software (1.50i) (National Institutes of Health; Bethesda, MD, USA). The black pixel of a binary image represents coffee stain. Coffee penetration depth was measured on each binary image with the ImageJ software. The total number of black pixels counted by the ImageJ software represents the total amount of absorbed coffee. This value is referred to as the absorption index of the sample.

The amount of hydrophobic material within each of the paper samples was determined by extraction from the different samples obtained from different mills. The total amount of extracted hydrophobic organic compounds was compared to determine the efficiency of various internal sizing programs. Paper samples of identical weight were extracted with chloroform using an Accelerated Solvent Extractor (ASE100, Thermo Fisher Scientific; Waltham, MA, USA). The extraction was conducted at 100°C for 1 h. After evaporation of the solvent, residues were weighed to determine the amount of hydrophobic organic compounds in each sample.

Sample	Grammage, g/m²	Caliper, mils	Density, grammage/caliper	HST, s	Extracted Hydrophobic Material
Sample N	306	17.9	17.1	896	1.12 eq.
Sample S	333	18.0	18.5	842	1.00 eq.

I. Characterization of samples from mill N and S (HST = Hercules size test).

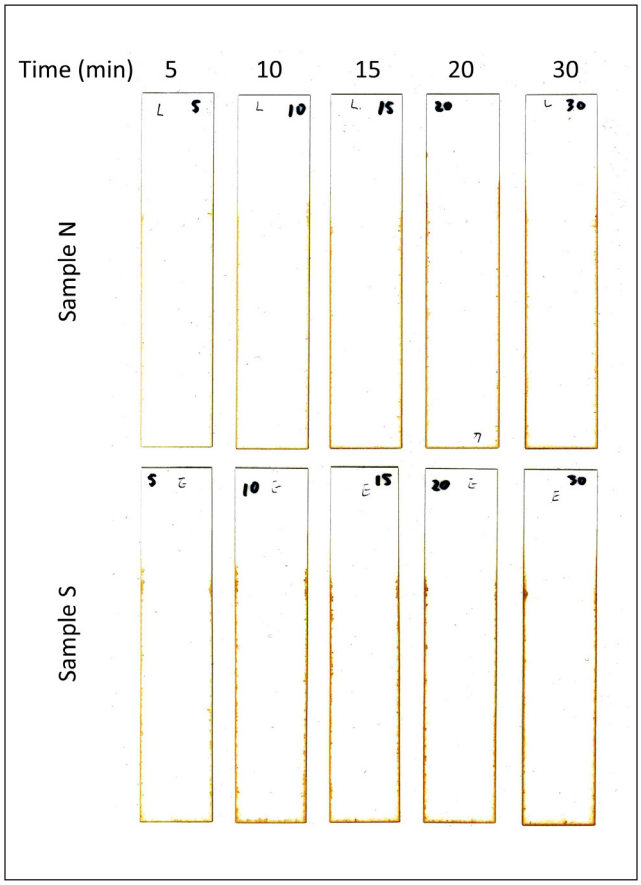
Scanning electron microscope (SEM) images were collected with a Cryo microtome without embedding medium to maintain the void spacing between fibers. Optical microscope images were collected on a Leitz Ergolux microscope with Olympus Stream Essentials software (Olympus; Tokyo, Japan). Fiber dimensions were determined with an OpTest Fiber Quality Analyzer (FQA) (OpTest Equipment; Hawkesbury, ON, Canada) via standard methods.

RESULTS AND DISCUSSION

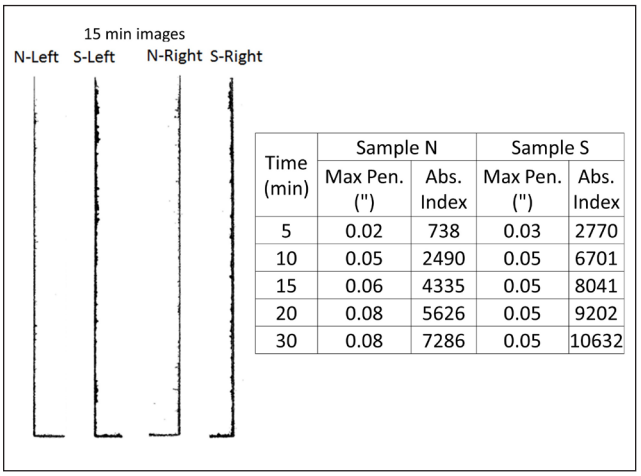
Paper samples of the same manufacturing grade were collected from two North American mills with significantly different fiber species. Both mills used essentially the same internal sizing program and other wet end additive programs. Samples from both mills met the same product specifications for a specific grade of cup stock. Both mills were integrated pulp and paper facilities that used local wood species to make pulp for papermaking. The wood species employed in pulp production was one of the major differences between the two sets of paper samples obtained from these two mills.

The physical and internal sizing characteristics of both sets of samples were determined. The results are presented in **Table I**. The two groups of cup stock had similar grammage, caliper, and bulk density. Sample N had a slightly longer HST time than that of sample S. The solvent extraction test showed that sample N contained slightly more hydrophobic material than sample S, which could explain the longer HST time of sample N. In general, internal sizing levels of the two groups of samples were approximately the same.

The coffee edge-wicking test was performed on both paper samples. Images of the tested samples are shown in **Fig. 2**. Visually, sample S had more edge-wicking. For quantitative analysis, samples from both sets were scanned to collect digital images for image analysis. Maximum penetration depth, absorption amount (abs. index) and a working binary image sample of 15 min samples were given in **Fig. 3**. The two groups of samples had similar maximum penetration depth at a certain testing time. Sample S had a much higher coffee absorption amount (total dark area calculated through image analysis) than sample N across all testing time ranges. The data suggested that the visual edge-wicking difference was due to a higher amount of adsorbed coffee rather than the penetration depth. Even though internal sizing levels were similar for the two sets of samples (based on HST value), the edge-wicking behavior was quite different. The HST test, a perpendicular penetration test, did not predict edge-wicking (in-plane

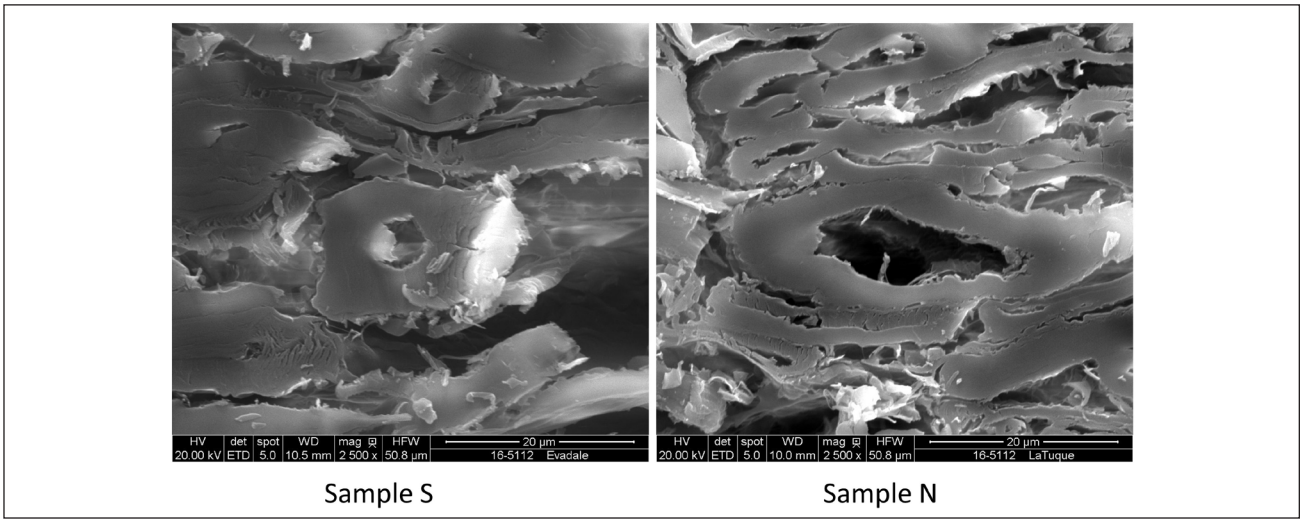


2. Optical images of tested samples from coffee edge-wicking test.



Time (min)	Sample N		Sample S	
	Max Pen. (")	Abs. Index	Max Pen. (")	Abs. Index
5	0.02	738	0.03	2770
10	0.05	2490	0.05	6701
15	0.06	4335	0.05	8041
20	0.08	5626	0.05	9202
30	0.08	7286	0.05	10632

3. Sample working binary image of 15 min samples and image analysis results of the samples.



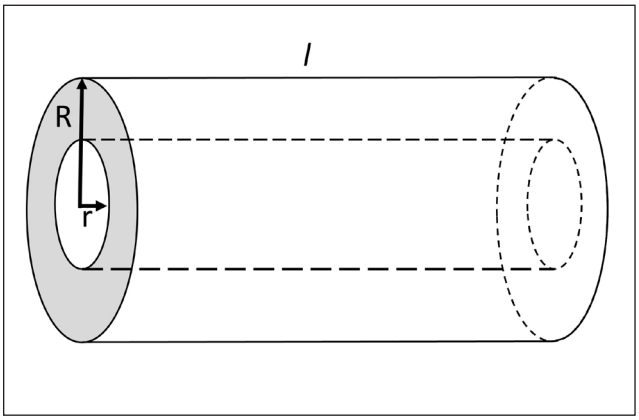
4. Cross-section images of fibers in sample S and N.

penetration) very well in the case of highly-sized paper grades. The results suggest that edge-wicking of highly-sized paper is affected by something other than internal size levels.

As previously mentioned, the fiber source (wood species) was a major difference between the two groups of samples. To assess the fiber structure of these sheets, cross-section SEM images were collected from both sample groups. Fiber cross-section images, **Fig. 4**, showed different fiber characteristics in the two types of paperboard. Fibers in paper sample S had thicker fiber walls, and most of the fiber lumens remained open after pressing and drying on the paper machine. Paper sample N had fibers with thin fiber walls, and those fibers were more flexible and collapsible than the thick-walled fibers found in sample S. Most of the fibers in sample N collapsed during the papermaking process, which resulted in relatively closed lumens.

Though clear structural differences were highlighted in the SEM images, the number of observed fibers was limited due to the complexity of SEM analysis. To confirm the fiber structural difference between the two types of samples, the samples were repulped and subjected to FQA testing. The average fiber wall thickness for each set of samples was estimated based on FQA data. Considerably more fibers were measured with the FQA compared to the SEM fiber measurements, which provided a more representative analysis of the structural differences in the fibers from sample S versus sample N.

The fiber structure can be simplified by assuming the fibers exist as straight tubes, **Fig. 5**, and the mass of a fiber



5. Scheme of simplified fiber structure.

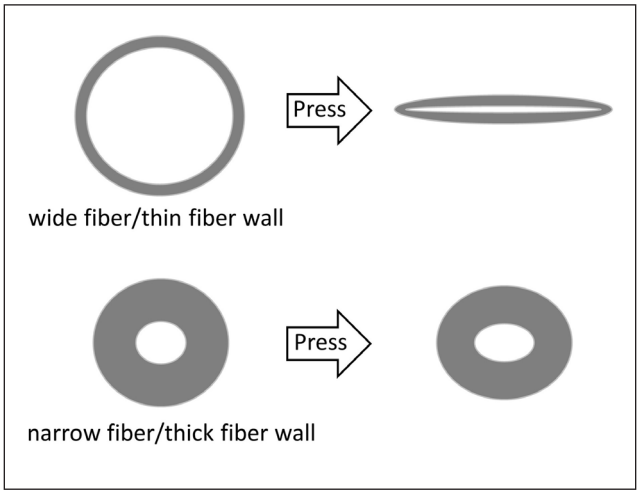
can then be expressed by Eq. 2, where R (μm) is radius of fiber, r (μm) is radius of lumen, ρ (g/cm^3) is cellulose density in the fiber wall, l (mm) is fiber length, and C (mg/m) is coarseness (mass of fiber with unit length):

$$(\pi R^2 - \pi r^2) \times \rho \times l = C \times l \quad (2)$$

The fiber radius (R) and coarseness (C) can be obtained from FQA testing, and a cellulose density of 1.5 g/cm^3 can be assumed; one can then solve the equation for lumen radius (r), with results shown in **Table II**. Fiber wall thickness is the difference between the fiber radius (R) and lumen radius (r). Based on this analysis, fibers from mill S have thicker walls

Fiber Source	*R*, μm	Coarseness, mg/m	*r*, μm	Fiber Wall Thickness, μm	(*R*-*r*)/*R*
Mill N	12.835	0.111	11.882	0.95	0.07
Mill S	9.235	0.111	7.857	1.38	0.15

III. Fiber structure parameters based on fiber quality analyzer (FQA).



6. Scheme of fiber's cross-section and its ability to collapse.

(1.38 µm) compared to fibers from mill N (0.95 µm), which is in agreement with the SEM analysis.

If the cellulose material of different fibers has a similar Young's modulus, a wider fiber with thinner fiber walls would be easier to collapse during pressing and drying, as depicted in **Fig. 6**. The ratio between fiber wall thickness (*R-r*) and fiber radius (*R*) can be used as a parameter to evaluate a fiber's ability to collapse. The smaller the value of this ratio, the easier for a fiber to collapse. The value of (*R-r*)/*R* for fibers from both mills is also shown in Table II. The fibers of mill N have about half the value of (*R-r*)/*R* versus the fibers of mill S; therefore, fibers of mill N are more easily collapsed and would tend to have closed lumens because of the fiber structure. This characterization is also consistent with the SEM observations.

Different fiber characteristics lead to different sheet structure as well. Cross-section SEM images of paper sample S and N are shown in **Fig. 7**, in which the white area is fibers and the black area is the voids between the fibers. It is clear that sample S has more fiber cross-sectional area than sample N.

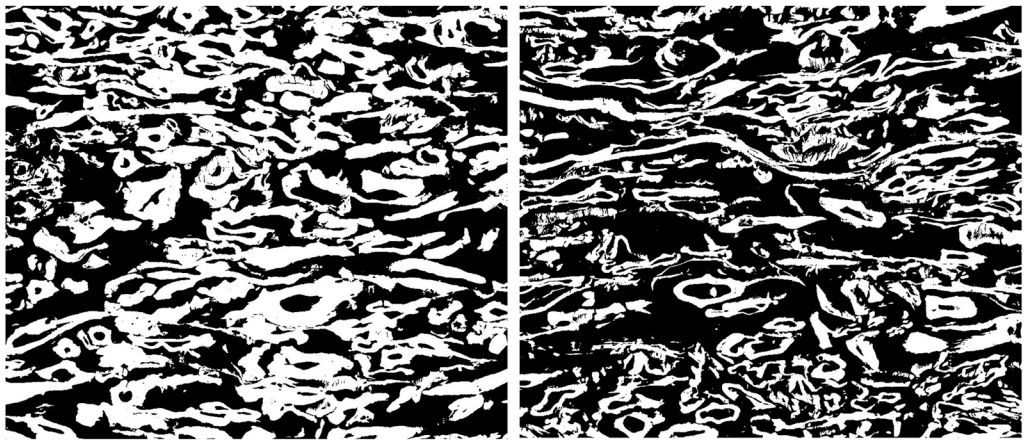
[Creamer] in HST Ink, v/v%	HST, s
5	>600
10	>600
20	>600

III. Hercules size test (HST) time with different amounts of coffee creamer in the ink.

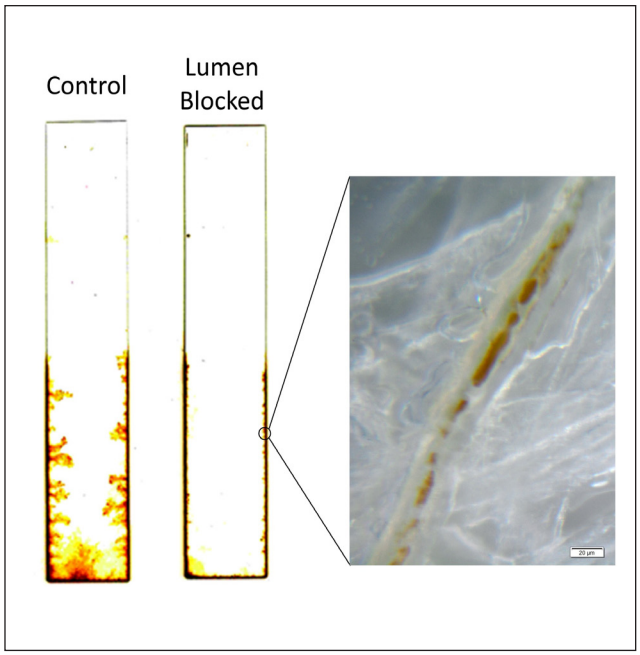
When cut (in the converting process, for example), the raw edge of sample S would have a significantly larger exposed hydrophilic fiber wall and lumen area with no sizing protection compared to sample N. Therefore, an aqueous solution would tend to edge-wick considerably more in sample S than sample N.

The creamer used in the hot coffee test is known to contain a certain amount of surfactant, which reduces liquid surface tension and makes coffee easier to wet heavily-sized fiber surfaces. To check whether creamer dosage in the edge-wicking test helped wet-sized fiber surfaces, we ran the HST test with additional creamer in the ink on sample S. The results are listed in **Table III**. The data indicate that the critical creamer concentration was between 20 v/v% and 30 v/v%. When creamer concentration was below 20 v/v%, internal size material was sufficient to lower the fiber surface energy enough to protect against wetting, which minimized liquid transport through the voids between the fibers. The coffee penetration into voids (black area in Fig. 7) was limited during the edge-wicking test with 3.6 v/v% creamer because the surfactant concentration was less than the critical concentration; therefore, new exposed fiber wall area and lumens (white area in Fig. 7) were likely the major pathway for liquid to wick into the paperboard.

A lumen "blocking" test was done by making handsheets with Bersize AEW (Bercen; Denham Springs, LA, USA), a



7. Sheet cross-section images of sample S and N.



8. Handsheet coffee edge-wicking samples. Note trapped coffee within a single fiber in the photo at right.

polymer dispersion with very small particle size that can enter and size the fiber lumens. To test the hypothesis that fiber wall area and lumens are the path for coffee edge-wicking in highly-sized paperboard, pulps from mill S with the same internal size dosage were used in the handsheet study. The hot coffee test was used to compare handsheets made with and without the blocking agent; the use of the blocking agent significantly reduced edge-wicking, as shown in **Fig. 8** (left). Further microscopic observations of the sample with the lumen blocking agent found that coffee was trapped in some fibers. The image in Fig. 8 (right) clearly showed that the fiber walls and lumens were a major pathway for edge-wicking in highly-sized paper.

CONCLUSIONS

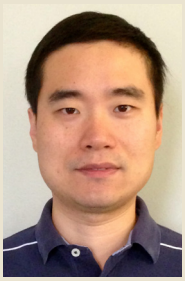
An internal sizing program, as typically applied under mill operating conditions, protects the fiber's outer surface to reduce liquid penetration between fibers. Such a sizing program typically reduces liquid penetration perpendicular to the surface of the paperboard. At low size levels, internal size is also an efficient way to reduce edge-wicking. At high size levels, the fiber's outer surface is well protected and liquid transport through voids between fibers is minimized; however, fiber cross-sectional area at cut edges is not protected by sizing material. The raw, cut fiber edges become an entry point, which results in increased edge-wicking. Transport of liquid through the fiber wall and lumen has been demonstrated to be a major pathway for edge-wicking in highly-sized paper. When internal size level is high enough to cover all the fiber surfaces, the HST test shows lower correlation with edge-wicking behavior than at lower size levels. In addition, further increases in the internal size level offer limited benefit towards the mitigation of edge-wicking in highly-sized paper. In this case, some new sizing strategies are desired for high performance liquid packaging grades, once a traditional internal sizing program provides full coverage of the surface of the fibers. In addition to new sizing technology, it may be possible to address the issue, at least in part, through either enzymatic fiber modification or decreasing the void volume by addressing the fiber cell wall. **TJ**

ABOUT THE AUTHORS

Edge-wick is an aesthetic and functional performance feature important to cup producers. Improving our understanding of the edge-wicking phenomenon can assist in the development of improved methods to control edge-wicking in our products. Our efforts here have developed an improved understanding of the cause of edge-wicking.

Developing a theory that explained the edge-wicking performance of similar products produced at multiple mills was difficult. An interesting finding was that similar amounts of material wicking into the cut edge of the sheet could result in a passing test for one sheet structure, while another structure wicking a similar amount of material would fail the test. Surprisingly, the role of fiber structure upon edge-wicking was found to be greater than expected.

Hopefully, this work will lead to suppliers and papermakers developing enhanced methods to control edge-wicking. The next step is to share our enhanced understanding of edge-wick with suppliers to help develop improved solution methods.


Xu


Meyers


Hart

Xu is senior research chemist and Hart is director, Fiber Science and Innovation, for WestRock, Richmond, VA, USA. Meyers is assistant papermill superintendent, WestRock, Evadale, TX, USA. Email Hart at peter.hart@westrock.com.

ACKNOWLEDGEMENTS

The efforts of John Dejarnette (senior R&D researcher, WestRock), Nichole Kilgore (R&D researcher, WestRock) and Adele Panek (R&D researcher, WestRock) are appreciated for sample characterization, handsheet making, and FQA testing. The authors also appreciate support from the WestRock R&D Analytical Group, led by Paul Giusti (R&D manager, WestRock). SEM analysis was conducted by William Mallory (lead R&D researcher, WestRock). Solvent extraction analysis was conducted by Vitaly Khazan (R&D scientist/engineer, WestRock).

Bersize AEW was kindly provided by Bercen to support this research.

LITERATURE CITED

1. Salminen, P., "Studies of water transport in paper during short contact times," Ph.D. thesis, Åbo Akademi University, Turku, Finland, 1988.
2. Swanson, J.W., *The Sizing of Paper* (W.F. Reynolds, Ed.) 2nd edn., TAPPI Press, Atlanta GA, USA, 1989, p. 133.
3. Eklund, D. and Lindström, T., *Paper Chemistry: An Introduction*, DT Paper Science Publications, Grankulla, Finland, 1991, p. 192.
4. Washburn, E.W., *Phys. Rev.* 17(3): 273(1921).
5. Lucas, R., "Ueber das Zeitgesetz des Kapillaren Aufstiegs von Flüssigkeiten," *Kolloid-Z.* 23: 15(1918).
6. Hintz, H.L. and Webb, J.T., U.S. pat. 3,849,224 (Nov. 19, 1974).
7. Floyd, J.M., U.S. pat. 4,859,244 (Aug. 22, 1989).
8. Kern, N.T., U.S. pat. 5,308,441 (May 3, 1994).
9. Camden, R. and Claytor, P., U.S. pat. 5,766,732 (June 16, 1998).
10. Larsson, J., Aksberg, R., and Tufvesson, H., U.S. pat. 2012/0114959 A1 (May 10, 2012).
11. Propst, C.W. and Jones, J.C., U.S. pat. 8,333,872 B2 (Dec. 18, 2012).
12. Theisen, J.T., Unruh, B.C., Feit, S.L., et al., U.S. pat. 8,337,919 B2 (Dec. 25, 2012).
13. Meyers, J., U.S. pat. 20160186381 (June 30, 2016).
14. Verhoeff, J., Hart, J.A., and Gallay, W., *Pulp Pap. Mag. Can.* 64(12): P509(1963).
15. Van den Akker, J.A. and Windle, W.A., *Tappi* 52(12): 2406(1969).
16. Bristow, J.A., *Sven. Papperstidn.* 74(20): 645(1971).
17. Bristow, J.A., *Sven. Papperstidn.* 75(21): 847(1972).
18. Wedin, P., Senden, T., and Knackstedt, M., *Int. Pap. Coat. Chem. Symp., 6th*, SPCI, Stockholm, Sweden, 2006, Book of Abstracts, p. 127.

ABOUT THIS PAPER

Cite this article as: Xu, L., Meyers, J., Hart, P. *TAPPI J.* 17(8): 437(2018). https://doi.org/10.32964/TJ17.08.437

DOI: https://doi.org/10.32964/TJ17.08.437

ISSN: 0734-1415

Publisher: TAPPI Press

Copyright: ©TAPPI Press 2018

About this journal

Enzymatic treated viscose fibers functionalized by chitosan

URŠKA VRABIČ BRODNJAK, DIANA GREGOR-SVETEC, AND MAJA KLANČNIK

ABSTRACT: Our research focused on the sorption properties of enzymatically treated viscose/chitosan and viscose fibers treated with enzymes and chitosan. To improve sorption properties of viscose fibers and to obtain the characteristics similar to viscose/chitosan fibers, we performed two different treatments. First, we treated both fibers with enzyme cellulase for 60 min and afterwards treated viscose fibers with the chitosan in an ultrasonic bath. In our research, structural characteristics and the accessibility of free adsorption places were investigated. We noted a noticeable change in the structure (degree of polymerization, crystallinity, and molecular orientation) of treated viscose and viscose/chitosan fibers. Changes that occurred in the morphology and in the structural properties of both types of tested fibers were also reflected in their physical and chemical properties. Research showed that the sorption properties of enzymatic treated fibers were improved.

Application: This study provides structure and sorption properties of viscose/chitosan fibers and viscose fibers treated with chitosan and analyzes the improvement of sorption properties of fibers, based on enzymatic treatment. Such treated fibers could be used in paper, packaging, hygiene towels, pads, and other applications.

Viscose fiber is regenerated cellulose fiber, made from wood pulp, usually from pine, spruce, or hemlock trees and cotton linters. It is biodegradable, produced from renewable source, with the properties similar to those of natural fibers. It has good moisture regain property, is hydrophilic and absorbent, feels soft and silky, has moderate dry strength and abrasion resistance, and is mechanically and chemically stable [1]. Viscose fibers can be modified in different ways, which indicates potential benefits of the fibers. Beside physical modifications, chemical modification to meet specific functionality is possible. A soft, smooth and also highly absorbent fiber is ideal for a wide range of very different applications, from apparel textiles to nonwoven materials for hygiene applications as well as special technical papers. [1] The addition of viscose fibers to wood pulp gives a sheet with improved dewatering ability, decreased density, and increased tear strength, but decreased tensile strength because of low interfiber bonding [2,3]. If instead of standard, round viscose fibers, very thin, flat fibers are used, a very high flatness of fiber, surface smoothness and good bendability give sufficient bonding area for the formation of strong paper [1]. As the bond strength is affected by the surface chemical composition and the swelling behavior, a chemical modification is another way to improve properties of viscose fiber. Bernt showed that fine-tuning of paper characteristics can be done with modification of the physical shape of viscose fibers or functionalization by anionic chemical modification [4]. Today, the surface modification of fibers is considered as the best route to obtain modern treated fibers [5]. Surface and bulk properties have an important role in paper products like hygiene towels and packaging applications.

Chitin derivatives have great adsorption characteristics and low cost, compared with other biopolymers used in the industry. Chitosan is the main derivative form of chitin. Chitosan, a commonly used biopolymer, has unique chemical and physical properties. It is produced by deacetylation of chitin, which is a biodegradable, nontoxic polysaccharide, soluble in acid, etc. There are many applications in pharmacy, biotechnology, and cosmetic industries [6]. Cellulose and chitosan have similar molecular structures, with the same β-glycoside linkages. The main difference is the presence of primary amino groups at the C-2 positions in chitosan, where cellulose has hydroxyl groups. The presence of active groups in chitosan molecular structure allows for easy chemical modification [7]. The presence of amino groups is responsible for the solubility in a diluted aqueous acid solution as a polycationic polymer [8]. In recent years, a lot of studies were done regarding different applications of chitosan, especially on cellulose functionalized by chitosan [9-15].

Chitosan treatments offer many advantages to regenerated cellulose fibers, such as biodegradability, non-toxicity, improved absorption ability, etc. Many techniques are available for introducing chitosan into cellulose fibers, such as treatments of cellulose fiber with cross-linking agents, soaking fiber in chitosan solution, and wet-spinning from blend [16]. In Japan, the representative commercial fiber derived from cellulose and chitosan is named Crabyon (Omikenshi Co.; Osaka, Japan) [17]. It is a fiber composed from a chitosan,

N,O-carboxymethylated chitosan, and viscose [18]. It is prepared by wet-spinning from a mixed solution of chitin viscose and cellulose viscose [19]. Along with improved antimicrobial activity, Crabyon fiber shows higher absorption ability and good mechanical properties, compared with regenerated cellulose fibers.

In response to environmental concerns about other treatments, enzymes have been widely used in many fields of industry. Many of the latest development studies on the enzyme treatments have been focused to improve the characteristics of fibers, among them regenerated cellulose fibers with cellulase treatment. There has been a considerable process in elucidating the mechanisms of the cellulolytic degradation. Better understanding is improving and extending the scope of finishing processes that use cellulase [20]. Enzymatic surface modification of cellulose fibers in textiles is a way to address issues of surface smoothness, pilling, and softness, all without the need to treat fabrics with traditional chemical methods [21].

Enzymes accelerate the rate of chemical reactions that occur with lower activation energy [22]. The result is formation of an intermediate enzyme substrate. Enzymes bind with the substrate by hydrogen, hydrophobic, and ionic bonds and also Van der Waals interactions. Cellulases are enzymes produced by microorganisms and plants, which have a great role in biodegradation of cellulose. Cellulase enzymes perform specific catalytic action on the 1,4-β-glucosidic bonds of the cellulose molecule [23]. The hydrolysis of this bond cleaves the molecule to smaller parts. These are not single enzymes, but complicated enzyme complexes composed of active subunits that cooperate synergistically. Cellulase enzymes are generally considered environmentally friendly and are usually dosed at low concentrations.

In recent decades, many studies have been conducted to determine the sorption properties of viscose and other regenerated cellulose fibers [16-21]. Viscose/chitosan fiber has great sorption properties, but is quite expensive. It can be used in many different products for single use, such as paper, packaging, hygiene towels, pads, etc., which is the same as viscose fibers. The aim of this research was to compare the structure and sorption properties of viscose/chitosan fibers to viscose fibers treated with chitosan, to then improve sorption properties of fibers based on enzymatic treatment.

EXPERIMENTAL

Materials

Viscose fibers (Lenzing Viscose) from Lenzing AG (Lenzing, Austria) were used throughout this work. The declared value of the linear density and the length of the fibers are 3.0 dtex and 29 mm, respectively. Viscose/chitosan fibers were obtained from Omikenshi Co. Ltd. The declared value of the linear density is 2.8 dtex and the length of the fibers is 28 mm. Both types of tested fibers have irregular cross sections.

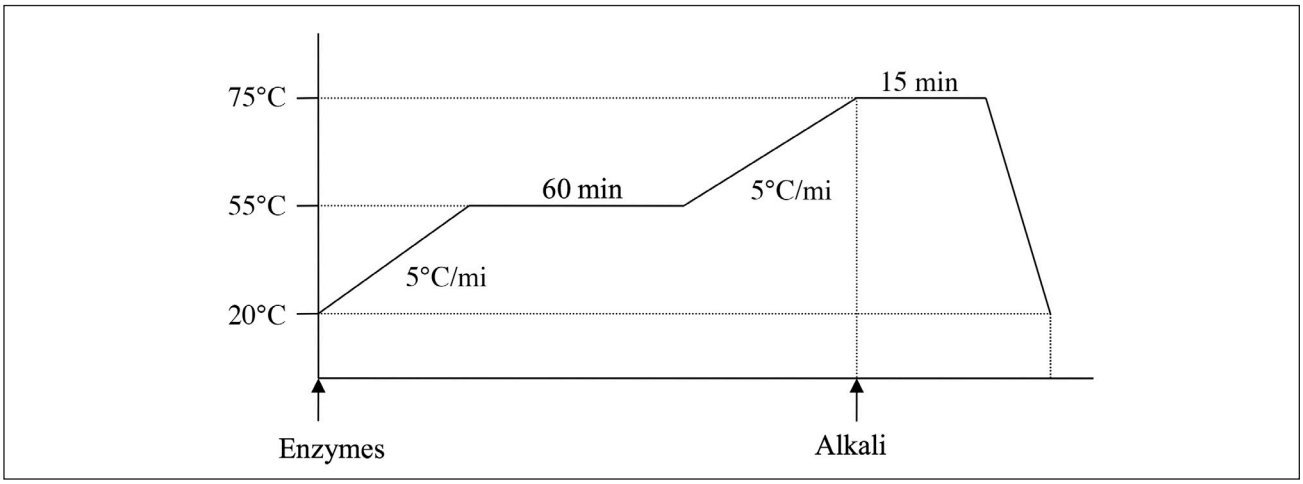
The enzyme cellulase used was Primasoft 100 from DuPont (Wilmington, DE, USA). Chitosan (low molecular weight, acetylation degree 85%) was purchased from Sigma-Aldrich (St. Louis, MO, USA). Chitosan solution was prepared by dissolving the chitosan in 2% aqueous acid solution. The acetic acid (99.8% assays) used was Honeywell Fluka (Honeywell; Morris Plains, NJ, USA).

Treatments

All tested fibers were first washed for 60 min in a bath containing 1 g/L of non-ionic surfactant with a liquor ratio 1:20. After washing, viscose/chitosan fibers were dried for 4 h at 105ºC in a laboratory oven, then treated with the enzymes. The viscose fibers were first treated with the enzymes and afterwards with the chitosan.

Enzymatic treatment of viscose and viscose/chitosan fibers

The enzymatic treatment of fibers was performed with the enzymes cellulase in a launder-o-meter laboratory unit. Fibers of 2.5 g were treated for 60 min at 55ºC in acetic acid buffer of pH 4.8 and liquor ratio of 20:1. The enzymes were deactivated by addition of soda (Na_2CO_3) and by increasing the temperature to 75ºC for 15 min. **Figure 1** shows the enzymatic



1. Procedure of enzymatic treatment of tested fibers.

Sample	Treatment of Fibers
V	Untreated viscose fibers
V/C	Untreated viscose/chitosan fibers
$V_{-en.tr.}$	Enzymatic treated viscose fibers
$V/C_{-en.tr.}$	Enzymatic treated viscose/chitosan fibers
$V_{-en+ch.tr.}$	Viscose fibers treated first with enzymes and then with chitosan

I. Shows sample of the notation for untreated and treated viscose and viscose/chitosan fibers.

treatment procedure. After enzymatic treatment, samples were washed in distilled water to achieve the neutral pH of the fibers. Finally, fibers were dried in the laboratory oven for 4 h at 105°C.

Treatment of viscose fibers with the chitosan

A chitosan solution was prepared by dissolving 3.0 g of chitosan in 2% aqueous acetic acid at 60°C. Viscose fibers were immersed in the chitosan solution in the ultrasound bath for 120 min under constant frequency of 40 kHz and then washed with distilled water (20 mL × 100 mL) to remove the unreacted chitosan. The chitosan treated viscose fibers were first dried in the air for 12 h and then in the laboratory oven for 1 h at 50°C. **Table I** shows characteristics of the analyzed and treated samples.

METHODS

Determination of surface topography

To see the effects of different treatments on the surface of fibers, we used a JEOL (Tokyo, Japan) JSM-6060LV scanning electron microscope (SEM). The instrument was operated at 10 kV and magnifications of 5500× and 6000×.

Determination of the degree of polymerization

The degree of polymerization was determined using the viscosimetric method, according to the Schulz-Blaschke equation [24]. The degree of polymerization of the samples dissolved in cuoxam was determined using an Oswald shear dilution viscosimeter. In the research, four parallel measurements were done for each type of tested fibers.

Determination of crystallinity

We used the Schwertassek method to determine the crystallinity of the fibers from iodine sorption [24]. The fibers were first treated with KI_3 solution, after which the concentration of non-absorbed iodine was determined by titration. With this method, we took four parallel measurements for each type of tested fibers.

Iodine sorption value (IS) is the amount of iodine adsorbed by 1 gm of cellulose substrate. It was calculated by following equation:

$$IS = (a - b \cdot 1.33) \cdot F \cdot 2.5384/m \quad (1)$$

where a is volume [mL] of sodium thiosulfate ($Na_2S_2O_3$) solution (c = 0.01 mol/L) for a liquor of blank potassium iodide solution; b is volume (mL) of $Na_2S_2O_3$ solution (c = 0.01 mol/L) for a liquor of sample solution; F is a liquor factor of $Na_2S_2O_3$ solution, determined by potassium permanganate ($KMnO_4$) (0.02 mol/L); and m is weight of absolutely dry fiber sample [g].

From the given values of iodine sorption for amorphous cellulose (IS = 412 mg/g) the proportion of amorphous (x_a) and crystalline (x_c) phase was calculated [24].

Determination of molecular orientation

The average molecular orientation was determined from the birefringence measurement. The birefringence of the fibers was determined using a Meopta polarizing light microscope (Meopta; Prerov, Czech Republic)and an Ehringhaus compensator. The relative phase shift between the orthogonal wave fronts depends on the refractive index and thickness of specimen. The high relative standard variation of average molecular orientation obtained (**Table II**) is the consequence of irregular cross-sections of fiber, which has a big influence on the determined diameter under the microscope, resulting in high standard deviation of thickness. In the research, 50 measurements were done for each type of tested fibers.

Sample	DP, /	RSD, %	IS, /	RSD, %	X_c, %	RSD, %	f_{or}, /	RSD, %
V	510.58	0.05	100.95	0.99	75.50	1.29	0.4457	8.70
V/C	458.40	0.19	106.85	0.94	74.07	0.65	0.4603	31.42
$V_{-en.tr.}$	475.51	0.19	107.60	0.98	73.88	1.31	0.3890	13.11
$V/C_{-en.tr.}$	402.04	0.16	75.75	1.17	72.62	1.36	0.4979	21.13
$V_{-en+ch.tr.}$	439.76	0.08	104.13	1.08	62.59	0.45	0.3781	16.06

II. Degree of polymerization (DP), number for iodine sorption (IS), degree of crystalline part of the fibers (X_c), and factor of average molecular orientation (f_{or}) of untreated and treated viscose and viscose/chitosan fibers; RSD = relative standard variation.

Determination of the presence of carboxyl groups

The methylene blue method is a classic method for determining the presence of carboxyl groups in cellulose fibers. The methylene blue dye binds to acid carboxylic groups of fibers according to the principle of ion exchange. The share of carboxyl groups in the mass of the absolutely dry cellulose sample was calculated from the part of the unbound methylene blue dye, as follows [25]:

$$-COOH(absolutely\ dry\ sample) = {(7.5 - A) \cdot 0.00313}/{m} \quad (2)$$

where A is free, total amount of unbound methylene blue dye [mg] and m is mass of absolutely dry sample [g].

The amount of the dye in the dye bath was determined using the Perkin Elmer Lambda 2 UV/VIS spectrophotometer (PerkinElmer; Waltham, MA, USA) and the amount of dye concentration was calculated on the basis of the calibration curve. For each individual sample, three parallel measurements were taken.

Determination of contact angle and surface free energy

The wettability of fibers was determined by contact angle measurement. The measurement was carried out at room temperature, with Krüss apparatus using two different test liquids, water and heptane. The samples' mass changes, as a function of time during the water adsorption phase, were monitored. The initial slope of the function $m^2 = f(t)$ is known as the capillary velocity, from which the contact angle between the solid (polymer sample) and the water was calculated using a modified Washburn equation [26-28]:

$$cos\varphi = \left({m^2}/{t}\right) \cdot \left({\eta}/{\rho^2 \cdot \sigma \cdot c}\right) \quad (3)$$

where φ is the contact angle between the solid and liquid phase, m is the mass of the sample [kg], t is the time [s], η is the liquid's viscosity [mPa·s], ρ is the liquid's density [g/cm^3], σ is the surface tension of the liquid [mN/m], and c is a material constant or c factor. The constant c was determined for each sample from contact angle measurements using n-heptane, for which the contact angle on the nonwoven was zero, η = 0.4 mPa·s, ρ = 0.6836 g/cm^3, and σ = 20.4 mN/m [27].

Surface free energy can be determined from the measured contact angles with different liquids.

It is possible to determine the solid surface free energy (γ_s) as the sum of the polar (γ_s^p) and dispersive (γ_s^d) contribution [28]. Surface free energy was determined using the Zissman, Owens-Wendt-Raeble-Kaeble method.

Determination of zeta potential

The influence of different fiber composition on zeta potential value was investigated. An electrokinetic analyzer (EKA) (Anton Paar KG; Graz, Austria) was used to take streaming potential measurements. The detailed description of the method applied has been described by many researchers [26-31]. Potential measurements of fibers were always performed in the fiber cell using 0.001 n potassium chloride (KCl) as the electrolyte solution. The pH was adjusted using 0.1 n sodium hydroxide and 0.1 n hydrogen chloride. Zeta potential ζ was calculated from the streaming potential data using the Smoluchowski equation and the approach of Fairbrother and Mastin [21]. Surface conductivity was not taken into account.

We used the following equation for determining zeta potential [27]:

$$\zeta = {U_s \cdot \eta \cdot R_{0.1(KCl)} \cdot \chi_{0.1(KCl)}}/{\Delta p \cdot \varepsilon \cdot \varepsilon_0 \cdot R} \quad (4)$$

where ζ is zeta potential [mV], U_s is the streaming potential, η the liquid viscosity (mPa·s), $R_{0.1(KCl)}$ is the electrical resistance of the plug when the measurement cell is filled with KCl, whose specific conductance $\chi_{0.1(KCl)}$ is accurately known, Δp is the hydrodynamic pressure difference across the plug, ε is the liquid permittivity, ε_0 is the permittivity of free space, and R the electrical resistance across the plug.

Measurement was carried out by a computer program, where it was necessary to set the known parameters as follows: KCl (0.001 mol/L), concentration of the electrolyte (2.108 E^{-03}), fluid viscosity (0.826 mPa·s) and dielectric constant (77.335) [27].

Determination of adsorption capacity for dyes

For determination of the amount of dye adsorbed on fibers, methylene blue dye (Kemika; Ras el Khaimah, UAE) and bemacid yellow GR 200% (CHT Bezema; Tübingen, Germany) acid dye were selected. With adsorption of basic dye, the bonding on anionic groups of viscose fibers was evaluated. With acid dye, the adsorption on cationic amino groups of chitosan was determined.

Adsorption experiments were carried out with 2 g of fibers in 200 mL dye solution prepared with a dye concentration of 0.01 g/L at 25°C. In experiments of adsorption of basic dye on fibers, the dye alkaline solution of pH 9.5 (adjusted with solution of 2 g/L Na_2CO_3) was used. In experiments of adsorption of acid dye on fibers, dye solution of pH 5 (adjusted with solution of 3 mL/L acetic acid 30%) was applied. The adsorption was conducted at 25°C until the adsorption equilibrium was reached, which was in basic dye solution in 4 days and in acid dye solution in 3 days for all fibers.

By absorbance measurements of dye solutions and the calibration curve made on spectrophotometer Cary 1E UV-VIS (Varian; Palo Alto, CA, USA) at a wavelength of maximum absorbance (664 nm for basic dye and 401 nm for acid dye), the concentration of remaining dye in solution after adsorption was determined.

The percentage of adsorbed dye by the fiber was calculated using the following equation:

$$(\%) of\ dye\ adsorbed = {}^{C_o - C}/_{C_o} \cdot 100 \quad (5)$$

where C_o and C are the initial dye concentration and the remaining dye concentration in solution at adsorption equilibrium, respectively.

The adsorption capacity of fibers (q) for selected dyes was calculated by following equation:

$$q = {}^{(C_o - C) \cdot V}/_{m} \quad (6)$$

where C_o is the initial dye concentration (mg/L) and C is remaining dye concentration in solution at adsorption equilibrium (mg/L), V is the volume of solution (L), and m is the mass of fiber (g).

Determination of mechanical properties

Mechanical properties of fibers were determined in the standard atmosphere using an Instron 6022 (Instron; Norwood, MA, USA) tensile testing machine. The cross-head speed was 0.15 mm/s, pre-loading 0.5 cN/dtex and the gauge length 2.5 mm, respectively. The tensile data presented in this article are the average of 50 fibers.

RESULTS AND DISCUSSION

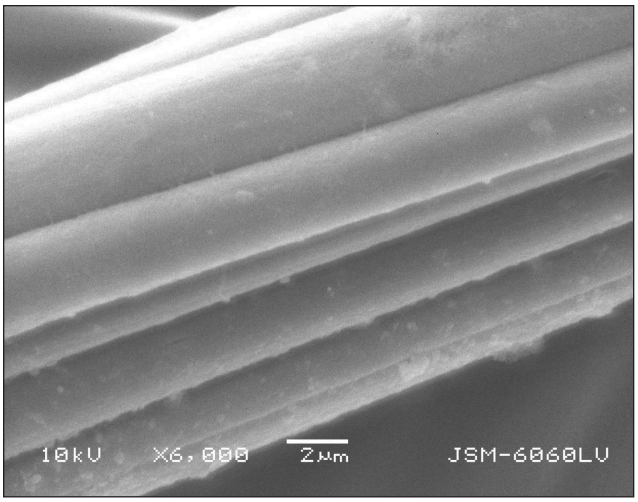
Surface topography

In our research, the effect of enzymatic treatment on the surface of the fibers was determined using SEM techniques. As seen from the SEM images in **Figs. 2-6**, the surface of enzymatically treated fibers (Figs. 4-5) was less even than the surface of untreated fibers (Figs. 2-3). There were some surface damages and irregularities, such as small holes and grooves along the fibers detected as the consequence of enzymatic treatment. Surface damages (e.g., longer holes) were more pronounced at viscose/chitosan than at viscose fibers. As seen from the micrograph (Fig. 6), chitosan that is bound on the surface of viscose fibers is clearly seen.

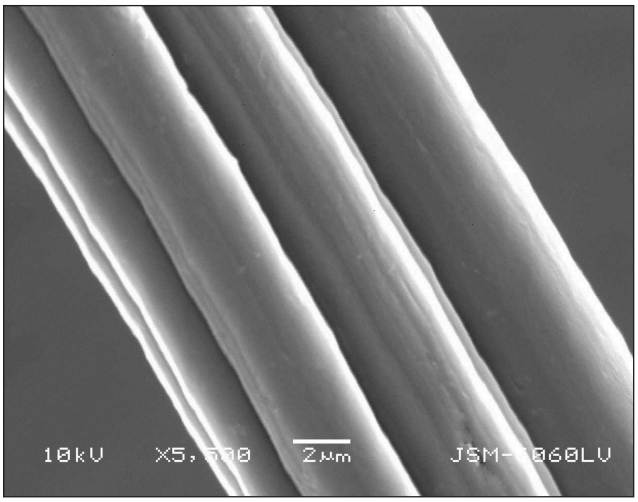
Structural characteristics

Generally, the structure of viscose/chitosan fibers is less ordered than that of viscose fibers. On average, viscose/chitosan fibers have shorter macromolecules, which result in a lower degree of polymerization, are less oriented, and have lower degree of crystallinity than viscose fibers (Table II). Because of the presence of α-cellulose and chitosan in viscose/chitosan fibers, the alignment and bonding of macromolecules in crystalline lattice is more difficult compared to pure cellulose molecules in viscose fibers.

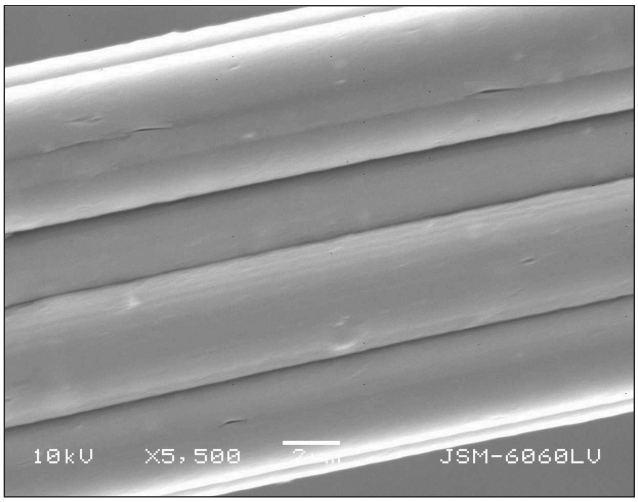
Treatment with the enzymes affects the orientation of macromolecules, and primarily tends to lower the orientation in



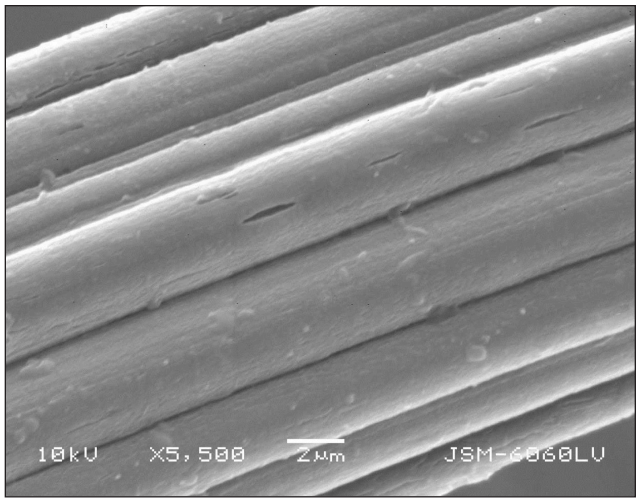
2. Untreated viscose fibers.



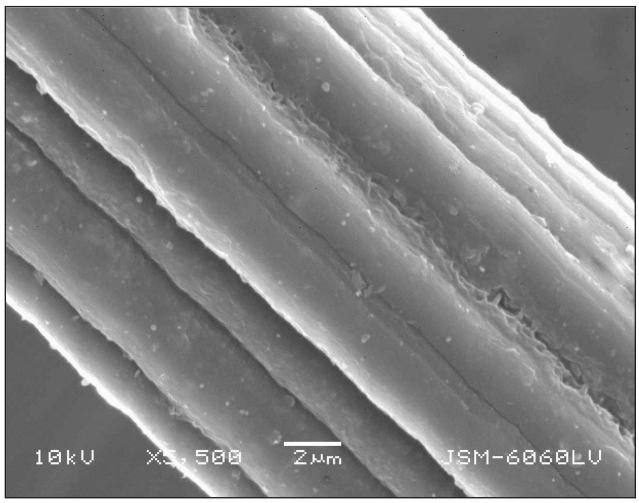
3. Untreated viscose/chitosan fibers.



4. Enzymatic treated viscose fibers.



5. Enzymatic treated viscose/chitosan fibers.



6. Viscose fibers treated with chitosan.

amorphous regions [21,22]. The average length of macromolecules is reduced, and cleavage of macromolecules occurs, particularly collapse of shorter molecules. In amorphous regions, arranged parts of macromolecules, long binding molecules and several shorter, accessible parts of the molecules (which can bind water) are present. Enzymes remove shorter molecules from the surface and cause rearrangement in amorphous and partly in crystalline areas, which leads to only a small lowering of the degree of crystallinity in the fibers. After 60 min of enzymatic treatment, the degree of polymerization of viscose fibers decreased by 6.9% and of viscose/chitosan fibers by 12.3%. The crystallinity of both fibers deceased by about 2%. The degree of polymerization of viscose fibers treated with chitosan also decreased, by 13.9%. The additional treatment of viscose fibers with the chitosan decreased the level of crystallinity and molecular orientation by more than 15%, suggesting that chitosan is bound not only on the surface of the fibers, but also interferes with the structure of viscose fibers.

Viscose fibers treated with the chitosan are less oriented and have a lower degree of polymerization and crystallinity than viscose/chitosan fibers. The reason lies in the different manufacturing routes. Viscose/chitosan fibers are manufactured from chitosan and cellulose pulp solutions, and the structure is formed by removing the solvent. The already formed structure of viscose fibers was treated with the chitosan that changed and partly destroyed the original structure of viscose fibers.

Results of structural measurements of viscose fibers treated with enzyme and chitosan show that macromolecules are shorter on average, which also indicates that the amount of ordered crystalline areas in fibers should be smaller. We assumed that the cleavage of cellulose molecules starts in the amorphous regions, releasing cellulose fragments, and then proceeds with the cleavage of the accessible cellulose molecule on the crystalline surface, leading to a lower degree of polymerization and lower orientation of molecules in amorphous regions.

Sorption characteristics

The results of the methylene blue dye method show that all fibers, untreated and treated, possess a considerable part of the carboxyl group. The higher the content of -COOH groups, the greater the amount of methylene blue dye is bound to the fibers. However, in addition to monovalent binding of dye cations to the carboxyl groups of cellulosic fibers, binding of the hydroxyl groups also occurs. Therefore, the ion-exchange interactions depend on the content of -COOH groups.

As expected, and seen in **Table III**, untreated viscose and viscose/chitosan fibers have fewer carboxyl groups. Likewise, enzymatic treatment causes an increase of carboxyl groups and free functional groups, which leads to lower zeta potential and higher values of surface free energy, resulting in a higher hydrophilic character of the fibers. Methylene blue dye is also adsorbed at other accessible places in the amorphous regions of fibers, not only by the carboxyl groups.

The results of the methylene blue dye method confirm the changes of structural characteristics of fibers determined

	V	V/C	$V_{-en.tr.}$	$V/C_{-en.tr.}$	$V_{-en+ch.tr.}$
-COOH, mmol/kg	46.43	46.66	48.91	47.36	47.28
RSD, %	0.39	0.73	0.72	0.23	2.05

III. Carboxyl content (-COOH) of untreated and treated viscose and viscose/chitosan fibers, determined using methylene blue dye method; RSD is relative standard variation.

Solvent	Sample									
	V		V/C		$V_{-en.tr.}$		$V/C_{-en.tr.}$		$V_{-en+ch.tr.}$	
	φ, °	RSD, %	φ, °	RSD, %	φ, °	RSD, %	φ, °	RSD, %	φ, °	RSD, %
Water	84.43	0.85	81.79	1.10	82.33	1.26	81.44	1.08	83.45	1.09
Heptane	88.09	1.93	83.06	1.09	85.76	0.87	82.76	1.49	86.11	0.39

IV. Values of contact angles (φ) of water and heptane on untreated and treated viscose and viscose/chitosan fibers; RSD = relative standard variation.

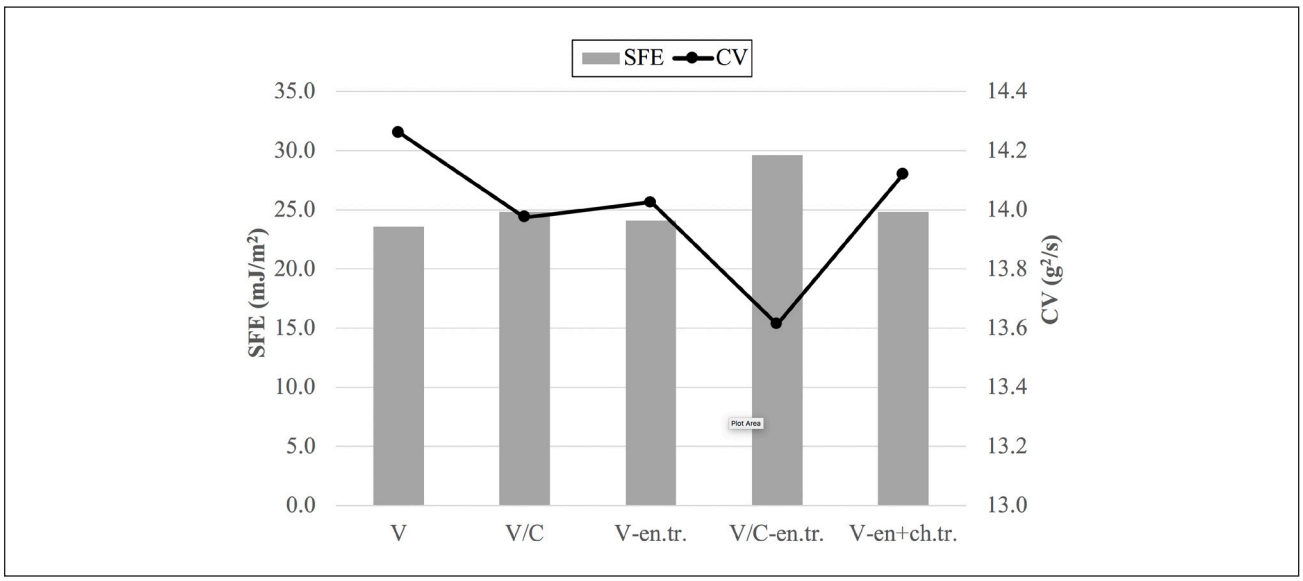
after enzymatic treatment and treatment of viscose fibers with chitosan.

The hydrophilic/hydrophobic character of fibers was determined using tensiometry. **Table IV** presents the contact angles of two different solvents with untreated and treated fibers. Contact angles were determined from the measured sorption velocities using the Washburn equation. The results represent the ability to determine the wetting behavior of fibers with two different reagents. The lowest contact angle with water was obtained at untreated viscose/chitosan fiber, which is 3.1% lower than untreated viscose fibers. The same trend is detected with heptane solvent. As expected, the enzymatic treatment of fibers lowers the contact angles for both solvents used. Lowering of the contact angle with the water of enzymatic treated viscose and viscose/chitosan fibers is the consequence of the structural changes, which resulted in more hydrophilic character of fibers. The differences are not significant, but still detected. Fibers tested in water have contact angles lower than tested with the heptane. The reason for this is the polar contribution of surface tension of each solvent, which reacts with the polar contribution of surface tension of the fibers.

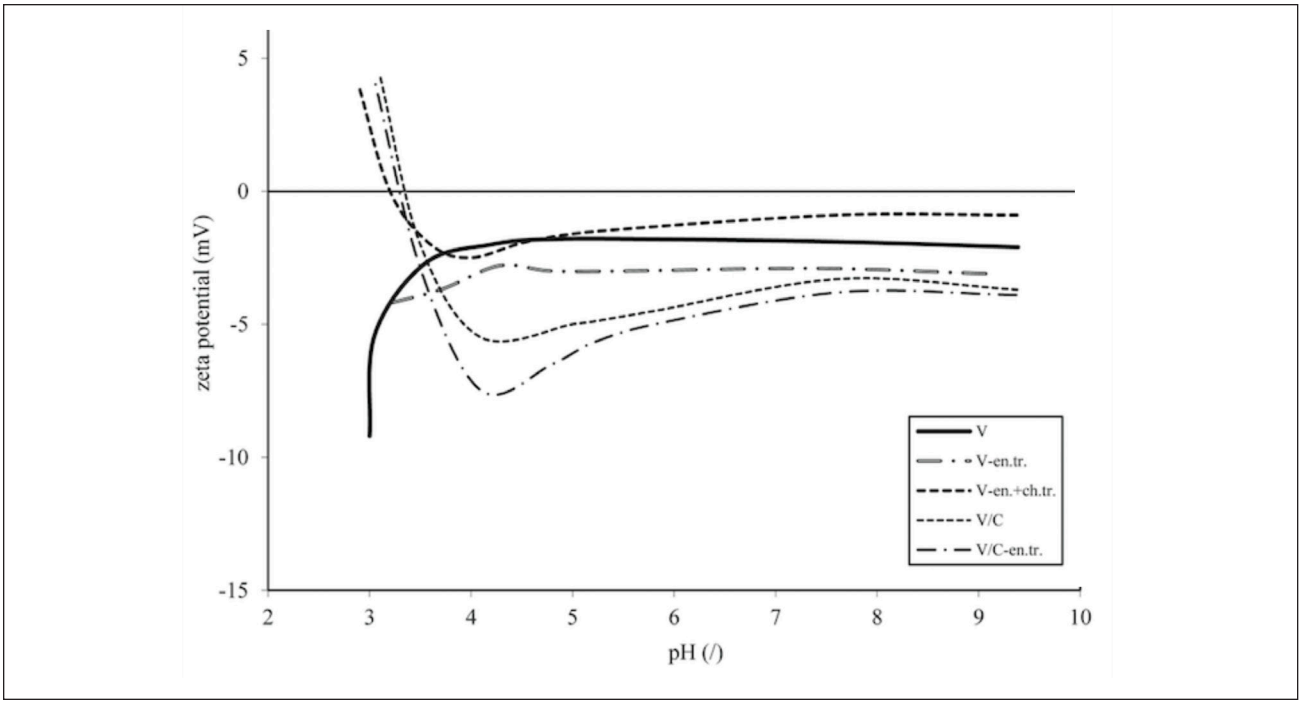
Surface free energy was determined on the basis of the Wendt Owens approximation procedure used for determining the interaction between the surface of the substrate and the liquid phase. As seen from **Fig. 7**, there are no significant differences among fibers. It appears that untreated viscose/chitosan fibers have a higher value of surface free energy (24.825 mJ/m²) than untreated viscose fibers (23.582 mJ/m²). The same trend is shown for enzymatic treated viscose/chitosan fibers, which reached the highest value among all treated samples (29.672 mJ/m²).

Capillary velocity for untreated and treated viscose fibers is higher in comparison with untreated and enzymatic treated viscose/chitosan fibers. Among all viscose fibers, the untreated sample achieved the highest value (14.26 g²/s). That correlates with structural characteristics; viscose fibers have the highest degree of polymerization and crystallinity among tested fibers, resulting in reduced absorption and wettability. Treatment with enzymes and chitosan changed the availability and amount of functional groups, as well as the mechanism of interaction. The lowest value of capillary viscosity (13.61 g²/s) was seen in the viscose/chitosan fibers treated with enzymes.

Zeta potential depends on the chemical structure, surface



7. Surface energy (SFE) and capillary velocity (CV) determination of untreated and treated viscose and viscose/chitosan fibers.



8. Zeta potential as function of pH of untreated and treated viscose and viscose/chitosan fibers.

polarity, fiber diameter, porosity, and specific surface interactions with water and swelling in water [30]. Low zeta potential is the result of adsorption of water and anions, with a simultaneous potential drop in the surface layer. In our research, measurements showed the lowest zeta potential in the alkaline pH region for viscose/chitosan fibers (**Fig. 8**). Adsorption of water and electrolyte solution causes swelling of the surface, thereby reducing the activity area. Negative charge of viscose/chitosan and viscose fibers is caused by the presence of -COOH and -OH groups.

Higher values of zeta potential indicates less hydrophilic character of the fibers. Because of the presence of chitosan in viscose/chitosan fibers and viscose fibers treated with chitosan, a positive zeta potential occurs at a pH between 3 and 4, which decreases at a higher pH. Figure 8 shows that the untreated viscose/chitosan fibers are more hydrophilic and have more anionic groups (mostly OH groups) than do untreated viscose fibers. Because of that, untreated fibers have a lower zeta potential. Enzymatic treatment of viscose increases the number of anionic groups (OH and COOH), which is noticed from lower zeta potential in the alkaline region. After enzymatic treatment of viscose/chitosan fibers, the zeta potential is slightly lower, mostly because of a slightly higher number of COOH groups. The number of anionic groups of viscose fibers treated with enzyme and chitosan is very similar as in enzyme-treated viscose fibers. At the lowest pH levels, all fibers with chitosan have positive zeta potential because of protonated ammonia groups.

The adsorption of basic (cationic) dye in alkaline pH is carried out on anionic dissociated hydroxyl in carboxyl groups of fibers. Although the differences in the adsorption of the basic dye between the fibers are very small, the highest adsorption capacity has viscose/chitosan fibers with 81.1% of adsorbed dye (**Table V**). These fibers are more hydrophilic and, according to zeta potential measurements (Fig. 8), have more anionic groups and are 3% more adsorptive for

Parameter	Sample				
	V	V/C	$V_{-en.tr.}$	$V/C_{-en.tr.}$	$V_{-en+ch.tr.}$
q, mg/g RSD, %	0.7834	0.8065	0.7976	0.7996	0.7759
	0.15	0.13	0.14	0.33	0.15
% of adsorbed dye RSD, %	78.81	81.14	80.24	80.44	78.06
	0.15	0.13	0.04	0.26	0.14

V. Adsorption capacity of fibers (q) and percentage of adsorption of basic dye (methylene blue); RSD is relative standard deviation.

Parameter	Sample				
	V	V/C	$V_{-en.tr.}$	$V/C_{-en.tr.}$	$V_{-en+ch.tr.}$
q, mg/g RSD, %	0.0089 /	0.8301 0.09	0.0345 /	0.7242 0.11	0.7994 0.16
% of adsorbed dye RSD, %	0.89 /	83.04 0.08	3.48 /	72.45 0.17	79.97 0.14

VI. Adsorption capacity of fibers (q) and percentages of adsorption of acid dye (Bemacid yellow GR 200%); RSD = relative standard variation.

Sample	σ, (cN/dtex)	ε, (%)	A_{sp}, J/g	σ_y, (cN/dtex)	E_o, GPa
V	2.51	33.20	64.99	0.80	4.59
V/C	2.15	36.71	65.01	0.81	4.60
$V_{-en.tr.}$	2.59	42.00	67.00	0.37	4.14
$V/C_{-en.tr.}$	2.12	38.55	64.87	0.75	4.55
$V_{-en+ch.tr.}$	2.68	37.44	54.55	0.78	4.39

VII. Mechanical properties: stress at break (σ), strain at break (ε), specific work at break (Asp) yield stress (σ_y), and elastic modulus (E_0) of fibers.

basic dye than viscose fiber. Enzymatic treatment of viscose/chitosan fiber practically has no effect on the adsorption of dye. Measurements (Table V) show only a slight (less than 0.9%) decrease in the adsorption capacity. After enzymatic treatment of viscose fiber, the adsorption on viscose is a little bit higher, with 80.2% of adsorbed dye, as on untreated viscose with 78.8% of adsorbed dye, because of having a more open and hydrophilic structure of enzymatically treated fiber with a higher number of anionic groups. The viscose treated with enzyme and chitosan has the same adsorption capacity for basic dye as viscose fiber. It has higher numbers of carboxylic groups (Table III). However, according to zeta potential (Fig. 8), the number of anionic groups (-OH) at alkaline pH is lower than in viscose.

The anionic acid dye of a small molecule adsorbs in acid medium on the cationic ammonium groups of chitosan in fibers. Adsorption does not occur on viscose, which does not have amino groups, although enzymatically treated viscose, which is more wettable, takes slightly more dye than does untreated viscose (**Table VI**).

The viscose/chitosan has the highest adsorption capacity for acid dye among all fibers with chitosan; it adsorbed 83% of dye. Enzymatically treated viscose/chitosan has 13% lower adsorption capacity for acid dye than does untreated viscose/chitosan fiber, suggesting a lower number of amino groups in viscose/chitosan treated with enzyme, which is also seen from zeta potential measurements (Fig. 8). The adsorption of acid dye on viscose treated with enzyme and chitosan is a little bit lower (3.7%) than on viscose/chitosan fiber.

Mechanical properties

Table VII shows tensile properties of the fibers. Tensile properties depend on the degree of crystallinity, degree of polymerization, and molecular orientation. In general, the influence of enzymatic treatment on the tensile properties of fibers is quite small, the changes in stress at break and specific work at break are below 5%. Depolymerization of macromolecules first occurs in amorphous regions. The influence on the strength of fibers is small, as strength is mainly determined from the crystalline regions. Shorter macromolecules and less ordered structure has more influence on the stretchability of fibers, resulting in an increase in the strain at break and decrease of yield stress and elastic modulus for both fibers treated with the enzyme. These changes are more evident in enzymatically treated viscose fibers. The treatment of viscose fiber with the enzyme and chitosan had no influence on fiber strength. Even a small increase in stress at break was noted. The treatment influenced the deformability, the strain at break increased, and the resistance to deformation, elastic modulus, and work at break were lowered.

CONCLUSIONS

In this study, we compared the sorption properties of viscose and viscose/chitosan fibers, first on untreated and afterwards on enzymatic treated fibers. Because of the higher zeta potential, capillary velocity, and contact angle with water, the untreated viscose fibers had lower wettability and were less adsorptive for basic dye than were untreated viscose/chitosan fibers.

Viscose fibers treated with enzyme cellulase have im-

proved sorption properties because the enzymes caused changes not only on the surface, but also in the amorphous parts of fibers. Enzymatic treatment reduced the orientation of macromolecules, the degree of crystallinity, and the degree of polymerization. More functional groups became available, which in turn resulted in a greater absorbency. Similarly, viscose/chitosan fibers treated with enzymes were less crystalline, had a lower degree of polymerization and a higher amount of carboxylic groups, lower zeta potential, and a higher value of surface free energy than did untreated fibers.

Viscose fibers treated with chitosan after enzymatic treatment had the improved sorption properties of enzyme-treated viscose fibers. The research has shown that treatment with enzymes and chitosan improved sorption properties, without significant damage to the fibers. Fibers showed sorption behavior similar to that of viscose/chitosan fibers; therefore, chitosan-treated viscose fibers could be a good substitute for viscose/chitosan fibers. **TJ**

ACKNOWLEDGEMENTS

The authors gratefully acknowledge the financial support received from the Slovenian Research Agency.

LITERATURE CITED

1. Roggenstein, W., *Lenzinger Ber.* 89: 72(2011).
2. El-Shinnawy, N.A. and Heikal, S.O., *Cellul. Chem. Technol.* 14(6): 919(1980).
3. Niskanen, K., Yu, Y., and Kettunen, H., *J. Pulp Pap. Sci.* 25(11): 398(1999).
4. Bernt, I., *Lenzinger Ber.* 89: 78(2011).
5. Jocic, D., Vilches, S., Topalovic, T., et al., *Carbohydr. Polym.* 60(1): 51(2005).
6. Monteiro, O.A.C. and Airoldi, Jr. C., *J. Colloid Interface Sci.* 212(2): 212(1999).
7. El-Nagar, E.K., Nagy, N.M., and Elgamal, M.A., *Int. J. Chem.* 4(2): 79(2012).
8. Kitkulnumchai, K., Ajavakom, A., and Sukwattanasinitt, M., *Cellulose* 15(4): 599(2008).
9. Vrabic Brodnjak, U. and Gregor-Svetec, D., *J. Coat. Technol. Res.* 10(2): 247(2013).
10. Wu, Y.B., Yu, S.H, Mi, F.L., et al., *Carbohydr. Polym.* 57(4): 435(2004).
11. Abdul Khalil, H.P.S, Saurabh, C.K., Adnan A.S., et al., *Carbohydr. Polym.* 150: 216(2012).
12. Shen, S.S., Yang, J.J., Liu, C.X., et al., *RCS Advances* 7(17): 10424(2017).
13. Ristić, T., Zabret, A., Fras-Zemljič, L., et al., *Cellulose* 24(2): 739(2017).
14. Fras-Zemljič, L., Ristić, T., and Tkavc, T., *J. Eng. Fibers Fabr.* 7(1): 50(2012).
15. Rahman Bhuiyan, M.A., Hossain, M.A., Zakaria, M., et al., *J. Polym. Environ.* 25(2): 334(2017).
16. Zemljič Fras, L., Strnad, S., Šauperl, O., et al., *Text. Res. J.* 79(3): 219(2009).
17. Shimizu, Y., Dohmyou, M., Yoshikawa, M., et al., *Text. Res. J.* 74(1): 34(2004).
18. Li, Z., Liu, X., Zhuang, X., et al., *J. Appl. Polym. Sci.* 84(11): 2049(2002).
19. Yoshikawa, M., *Kagaku/Chemistry* 54(3): 34(1999).
20. Cavaco-Paulo, A., Almeida, L., and Bishop, D., *Text. Res. J.* 68(4): 273(1998).
21. Carrilo, F., Colom, X., Lopez-Mesa, S.M., et al., *Process Biochem.* 39(2): 257(2003).
22. Cavaco-Paulo, A. and Gübitz, G.M., *Textile Processing with Enzymes*, Woodhead Publishing, Cambridge, UK, 2003, pp. 124-168.
23. Pedersen, G.L., Screws, G.A., and Cedroni, D.M., *Can. Text. J.* 109(10): 31(1992).
24. Scholz, C. and Flath, H.J., *Textilveredlung* 26(6): 188(1991).
25. Fras, L., Stana-Kleinschek, K., Ribitsch, V., et al., *Mater. Res. Innovations* 8(3): 145(2004).
26. Stana-Kleinschek, K., Peršin, Z., and Maver, T., *Mater. Tehnol.* 45(3): 253(2011).

ABOUT THE AUTHORS

We chose this topic to research because of our interest in biobased materials. Our research is focused on fibers, paper, packaging, and textiles and the characterization of these materials. The most challenging aspect of the study was the functionalization process.

One lesson we learned from this study was that a literature review gives you the starting point for the experimental work, which then has to be done with a lot of trials. We were surprised to be able to obtain better fiber characteristics than expected.

Mills might benefit from this functionalization of regenerated cellulose fibers, which could lead to new products with added value. Our next step is to try different treatments and functionalizations of various substrates and optimization of processes.



Brodnjak



Gregor-Svetec



Klančnik

Brodnjak is assistant professor, Gregor-Svetec is professor, and Klančnik is assistant professor,University of Ljubljana, Faculty of Natural Sciences and Engineering, Department of Textiles, Ljubljana, Slovenia. Email Gregor-Svetec at diana.gregor@ntf.uni-lj-si.

27. Stana-Kleinschek, K., Ribitsch, V., Kreže, T., et al., *Mater. Res. Innovations* 6(1): 13(2002).

28. Pandiyaraj, K.N., and Selvarajan, V., *J. Mater. Process. Tech.* 199(1-3): 130(2008).

29. Klemm D., Philipp B., and Heinze T., *Comprehensive Cellulose Chemistry: Fundamentals and Analytical Methods*, Vol. 1, Wiley-VCH Verlag GmbH & Co. KGaA, Weinheim, Germany, 1998.

30. Schoff, C.K., in *Polymer Handbook* (J. Brandrup, E.H. Immergut, and E.A. Grulke, Eds.) 4th edn., John Wiley and Sons, New York, 1999, Sect. VII, pp. 265-290.

ABOUT THIS PAPER

Cite this article as: Brodnjak, U., Gregor-Svetec, D., Klancnik, M. *TAPPI J.* 17(8):447(2018). https://doi.org/10.32964/TJ17.08.447

DOI: https://doi.org/10.32964/TJ17.08.447

ISSN: 0734-1415

Publisher: TAPPI Press

Copyright: ©TAPPI Press 2018

About this journal

Effect of pulper consistency on stickies size distribution

MAHENDRA DOSHI, SALMAN AZIZ, ROBERT DE JONG, AND CARL HOUTMAN

ABSTRACT: Pulper consistency affects production capacity, defibering efficiency, and particle size distribution of contaminants, and in particular, stickies and inks. The effect of pulper consistency on stickies size distribution, though important, has not been studied in detail.

In this project, pressure-sensitive adhesive (PSA)-containing furnish was pulped in a laboratory at 5%, 10% and 15% consistency. Results show that 15% consistency pulp produced many more small-sized stickies compared to pulps produced at 5% and 10% consistency. This is contrary to the generally accepted hypothesis and needs further investigation.

Calcium carbonate, usually present in varying proportions in many recovered paper grades, is known to have some pacifying effect on stickies. A new pacifying agent prepared from silicone release liner, called desiliconized pulp (DSP), behaves like bleached virgin hardwood kraft pulp. DSP seems to have a pacifying effect similar to that of calcium carbonate. Thus, DSP may potentially replace a small amount of bleached virgin hardwood kraft pulp, with a bonus stickies-pacifying effect.

Application: Stickies size distribution is important for paper recycling mills. The goal is to keep stickies particles large enough for easy removal by screens, cleaners, and flotation. Small-sized stickies or microstickies may be pacified by the new additive—desiliconized pulp (DSP).

Adhesives and glues, called stickies, entering the paper recycling process through recovered papers pose significant problems, as they affect paper machine productivity and/or product quality. Effective removal of stickies is, therefore, of paramount importance to the overall economic health of a recycling mill.

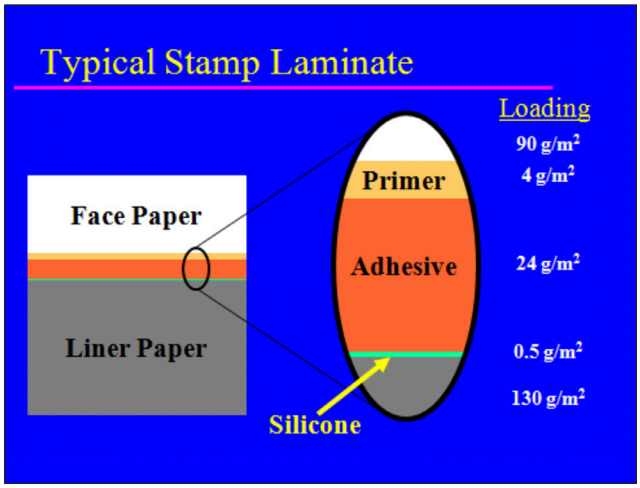
One of the first steps in recycle paper processing is pulping. One of the objectives of pulping is to defiber recovered papers without disintegrating stickies [1]. Stickies removal becomes relatively easy by existing well-developed screens, cleaners, and flotation cells, as long as stickies are kept in a relatively large size and not fragmented into particles smaller than 0.5-mm diameter during pulping [2,3].

Delagoutte et al. and Fabry et al. [2,3] evaluated stickies size distribution and removal in eleven deinking mills. They concluded that stickies with equivalent diameter greater than 1.52 mm or with area greater than 1.81 mm^2 are removed with efficiency close to 100%, whereas stickies smaller than equivalent diameter 0.575 mm (0.26 mm^2 area) are removed with efficiency close to 0%. This is surprising due to the fact that many modern deinking mills use fine screens with slot width 0.10–0.15 mm. One reason for this apparent anomaly is that some of the stickies are not globular but are a flat or fibril shape that may squeeze through the slot opening under the pressure differential across the screen. Another possible explanation is the way stickies size distribution is measured. Delagoutte et al. and Fabry et al. [2,3] point out that during measurement, stickies are "flattened out," altering the original 3-D structure. Nevertheless, it is clear from this study that the larger the stickies size, the higher the removal efficiency.

The effect of pulping temperature is well summarized in an editorial [4]. In general, there are many examples showing fragmentation of stickies at higher temperature that results in lower screening efficiency [2,3,5,6,7,8,9]. Additionally, stickies become more flexible at higher temperature, allowing somewhat easier passage through the screen opening. Pulping pH also affects stickies size distribution. For example, under alkaline conditions, stickies distribution shifts toward smaller size [3,8,10]. In short, higher temperature, increased pulping time, and alkaline pH each lead to difficult-to-remove, small-sized stickies.

To the best of our knowledge, systematic studies on the effect of pulper consistency on stickies size distribution have not been published. A generally accepted hypothesis is that higher consistency in the range of 12% to 16% will not fragment stickies as much as pulp produced at lower pulping consistency of 5% to 8% [1]. Schabel and Respondek [11] have shown that higher shear forces in medium consistency screening (3% to 6%) may lead to stickies disintegration compared to lower consistency screening (less than 2.5%) where shear forces are generally lower.

After pulping, stickies, inks, and other contaminants are removed by the use of screens, hydrocyclones, flotation, and other operations. However, in most mill operations, relatively small-sized stickies are not effectively removed. These stickies accumulate and agglomerate in the paper machine white



1. General loading of various layers in a postage stamp [14].

water system and eventually deposit on wires, felts, and dryer surfaces. Pacifying additives like talc, enzymes, cationic polymers, or surfactants are used to stabilize or pacify small-sized stickies and reduce their tendency to agglomerate.

Venditti et al. [12] and Hubbe et al. [13] observed that the presence of silicone release liner alters the stickies characteristics and reduces the tendency for stickies to agglomerate. The structure of release liner used in postage stamp laminate is shown in **Fig. 1** [14]. The liner consists of a thin layer of silicone for easy removal of the stamp. A major portion of the liner material consists of well-refined virgin kraft fibers with basis weight of 130 g/m². Currently, most of the liner material with silicone layer is not reused.

Pulp made solely from release liner, called desiliconized pulp (DSP), has a potential as a pacifying agent [15]. DSP has properties very similar to that of bleached virgin hardwood kraft pulp, as shown in **Table I** [15]. Pacifying properties of DSP and calcium carbonate ($CaCO_3$) are further explored in this project.

OBJECTIVE

The primary objective of this project is to evaluate the effect of pulper consistency on stickies size distribution. A secondary objective is to compare the efficacy of desiliconized pulp (DSP) to that of $CaCO_3$ in pacifying stickies.

MATERIALS AND METHODS

Three sets of experiments were planned, as shown in **Fig. 2**. Set I was designed to evaluate the effect of consistency on stickies size distribution. The impact of pacifying agents DSP and $CaCO_3$ on stickies size distribution during pulping was planned in Set II. The effectiveness of DSP and $CaCO_3$ to pacify stickies was compared in Set III.

For the purpose of this study, a standard PSA sheet specifically made for U.S. Postal Service (USPS) work from the U.S. Department of Agriculture Forest Products Laboratory (FPL) was used. This sheet contained 10% PSA. The shredded pre-sheets were pulped at high consistency (HC), medium consistency (MC), and low consistency (LC) at 45°C for 8 min in a Formax 450H Laboratory Pulper by Adirondack Machine Corp. (Hudson Fall, NY, USA). The batch pulper and the rotor are shown in **Fig. 3**. After each run, consistency was measured and handsheets were prepared for measuring stickies by blue dye method [16]. Results are shown in **Table II**.

The measured consistencies were: HC 15.6%; MC 11.5%; and LC 6.1% (Set I).

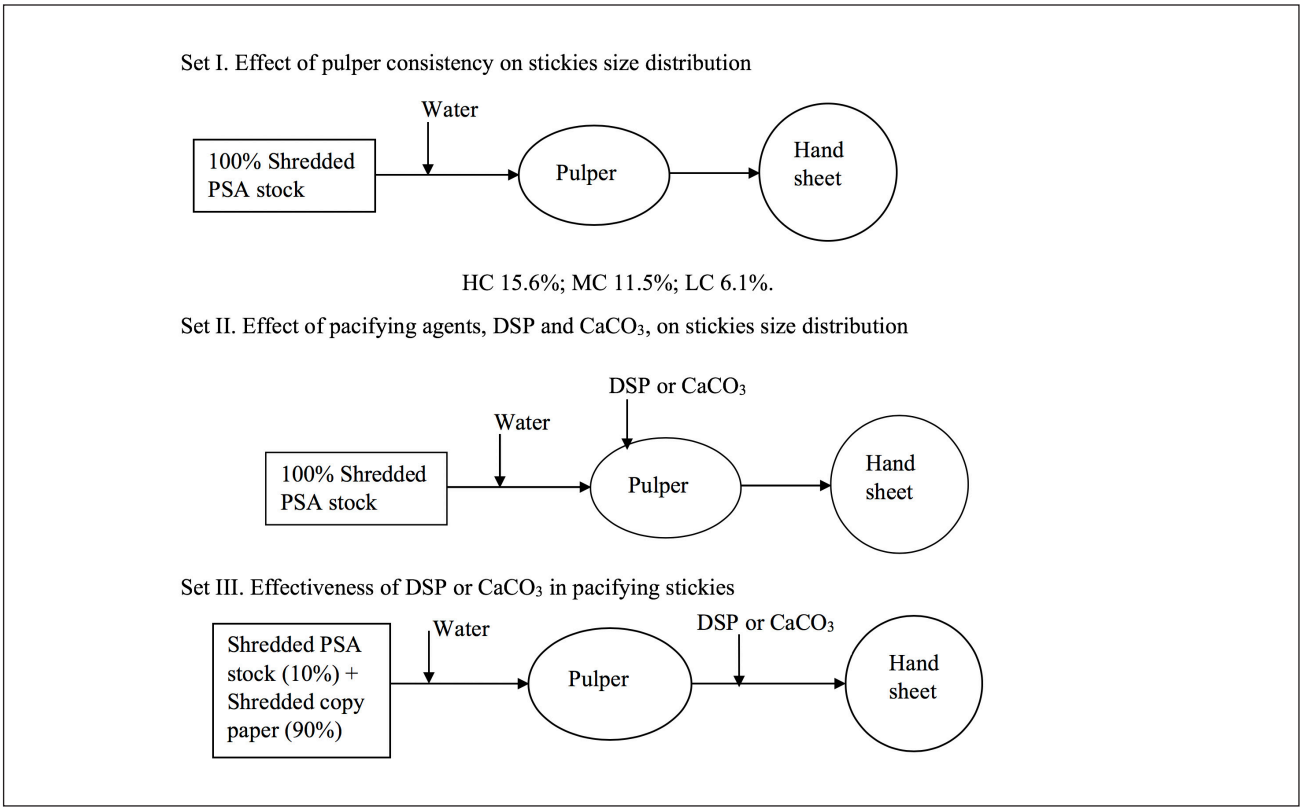
Stickies size distribution and handsheets are shown in **Fig. 4** and **Fig. 5**, respectively.

Set II experiments were conducted to evaluate the effect of consistency and the impact of two pacifying agents, DSP

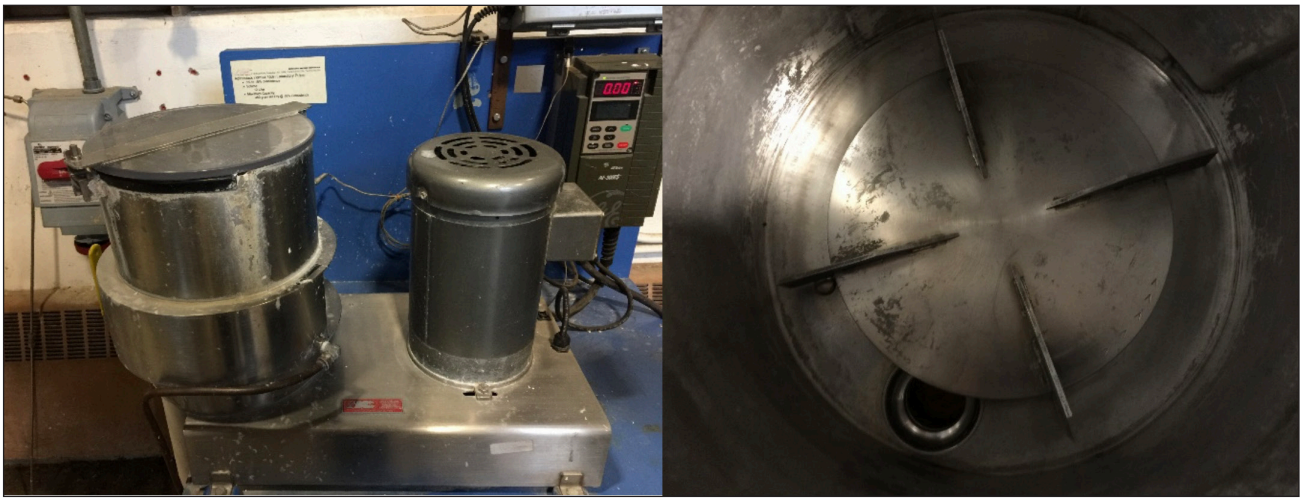
Parameter	DSP	BHKP	BSKP	DIP
CSF, Ml	290	500–550	500–550	425
Brightness, %	87	88–90	88–90	85
Ash content, %	0.2	< 0.5	< 0.5	1.0–5.0
Tensile index, Nm/g	42	50	80	45
Tear index, mN m²/g	11.0	7.0	12.0	8.0
Density, kg/m³	667	700	750	750
Dirt count, mm²/kg	< 20	< 20	< 20	< 100
Ink residuals	No	No	No	Yes
Fiber length, mm	1.0	1.1–1.4	1.7–2.0	0.9

DSP and DIP not refined. BHKP and BSKP refined to CSF 500–550 ml.
DSP = desiliconized pulp; BHKP = bleached hardwood kraft pulp (from birch); BSKP = bleached softwood kraft pulp (from pine/spruce); DIP = deinked pulp (from sorted office paper [SOP]).

I. Properties of DSP compared to other market pulps [14].



2. Experimental plan (PSA = pressure sensitive adhesive; HC = high consistency; MC = medium consistency; LC = low consistency; DSP = desiliconized pulp; $CaCO_3$ = calcium carbonate).



3. Formax 450H laboratory pulper and rotor.

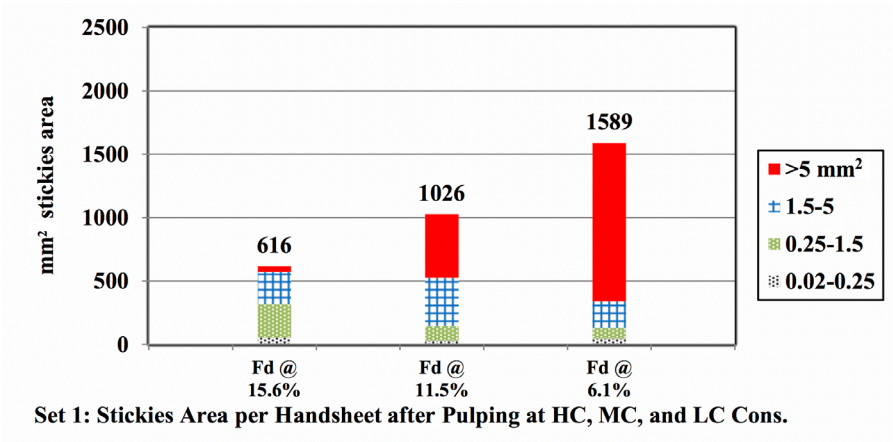
and $CaCO_3$, on stickies size distribution. The following runs were carried out:

- Run P1: 450 g PSA stock + 50 g DSP + 2.7 L water (45°C, pH 7). Pulp for 8 min.
- Run P2: 135 g PSA stock + 15 g DSP + 2.7 L water (45°C, pH 7). Pulp for 8 min.
- Run P3: 450 g PSA stock + 50 g $CaCO_3$ + 2.7 L water (45°C, pH 7). Pulp for 8 min.
- Run P4: 135 g PSA stock + 15 g $CaCO_3$ + 2.7 L water (45°C, pH 7). Pulp for 8 min.

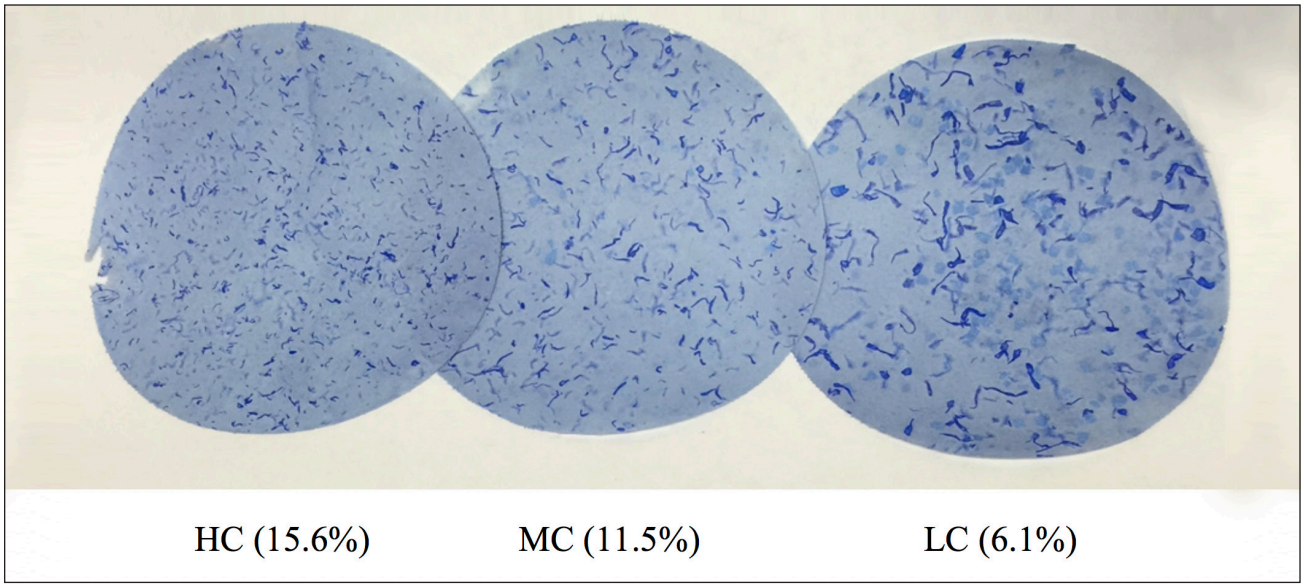
Runs P1 and P3 produced pulp with consistency of 12% to 14%, while runs P2 and P4 produced pulp with consistency of about 5%. Two handsheets were made from each pulp sample after mixing in a Waring blender for 30 s on low setting. Results of the blue dye measurement method are reported in **Table III** and **Fig. 6**.

Run	Consistency, %	ppm	Stickies per Handsheet		Mean Area, mm²
			mm²	count	
High consistency	15.6	37019	1589	980	0.63
Medium consistency	11.5	61697	1026	664	1.59
Low consistency	6.1	95507	616	772	2.06

II. Effect of pulper consistency on stickies size distribution.



4. Stickies distribution per class size after pulping at (left-to-right) high, medium, and low consistencies.



5. Handsheets after pulping at three consistencies. Left: high consistency, 15.6%; Middle: medium consistency, 11.5%; and Right: low consistency, 6.1%.

So far, all experiments were conducted using 100% PSA stock. A study was carried out by mixing standard 10% PSA sheet with 90% of plain copy paper sheets. The sheets were shredded before pulping. Pulping was conducted as before at high consistency.

Handsheets with no additives, with DSP, and with $CaCO_3$ were prepared to evaluate the extent of stickies pacification (Set III):

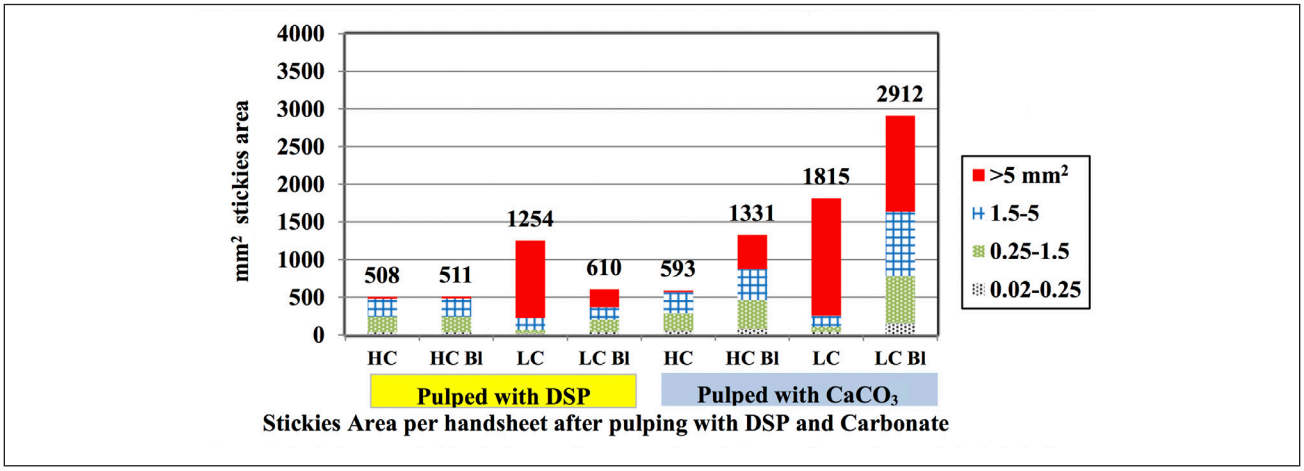
- Pulp P5: Blended 10 g of pulp in a Waring blender for 30 s on low setting.
- Pulp P5 + DSP: Blended 10 g of pulp + 2 g DSP in a Waring blender for 30 s on low setting.
- Pulp P5 + Car: Blended 10 g of pulp + 3 g $CaCO_3$ in a Waring blender for 30 s on low setting.

After blending, each pulp was placed in a beaker, diluted

Run No.	Additive	Consistency, %	ppm	Stickies per Handsheet		Mean Area, mm²
				mm²	count	
P1.1	DSP	12.1	30558	508	761	0.668
P1.2	DSP	12.1	30709	511	775	0.659
P2.1	DSP	5.2	75383	1254	463	2.71
P2.2	DSP	5.2	36637	610	684	0.891
P3.1	$CaCO_3$	14.3	35639	593	1,011	0.586
P3.2	$CaCO_3$	14.3	80024	1331	1,550	0.859
P4.1	$CaCO_3$	5.1	109118	1815	715	2.54
P4.2	$CaCO_3$	5.1	193784	2912	2,899	1.11

DSP = desiliconized pulp; $CaCO_3$ = calcium carbonate.

III. Effect of pulper consistency and pacifying additives on stickies.



6. Effect of DSP and $CaCO_3$ addition on stickies size distribution without blending and with blending (Bl) in a mixer after pulping at high and low consistencies.

with water, and mixed for 15 min using a magnetic stirrer.

All handsheets (1.2 g each) were made using the TAPPI sheet mold. Handsheets were dried and then dyed with a blue dye (Morplas Blue 1003, Sunbelt; Rock Hill, SC, USA). Dyed handsheets were scanned and analyzed for stickies size distribution using Verity IA software (Verity IA; Brookfield, WI, USA). This protocol was developed for the USPS work by FPL [16].

RESULTS AND DISCUSSION

The effect of consistency on stickies size distribution using 100% PSA stock is reported in Table II and Fig. 4. Blue dyed handsheets are displayed in Fig. 5. Results show that low consistency (6.1 %) pulp has average stickies area of 2.06 mm² (1.62 mm equivalent diameter) compared to stickies area of 0.628 mm² (0.89 mm equivalent diameter) for the high consistency (15.6%) pulp. Thus, based on the study of Delagoutte et al. and Fabry et al. [2,3], stickies from low consistency pulp should have higher screening efficiency (close to 100%) compared to those from high consistency pulp. This is contrary to the generally accepted hypothesis and needs to be further investigated in much detail with different types of adhesives, pulping time, pulper rotors, temperature, etc.

Results from Set II experiments are shown in Table III and Fig. 6. The purpose of these experiments was to study the change in stickies size distribution due to the addition of pacifying agent in the pulper.

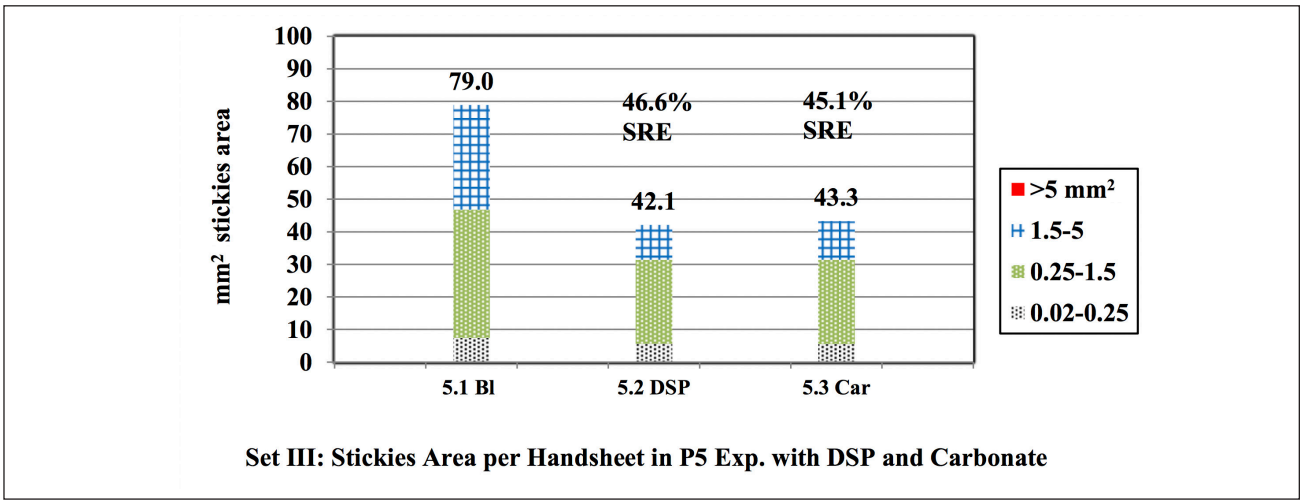
Duplicate handsheet measurements, labeled as P1.1, P1.2, etc., are presented in Table III. Most results show significant variation, except for Runs P1.1 and P1.2. The addition of DSP did not have any material effect on stickies area or ppm as can be seen by comparing HC results from Table II and P1.1, P1.2 results from Table III. Other duplicate results in Table III show significant variation, making it difficult to draw any meaningful conclusion.

Set III experiments were conducted to evaluate the effectiveness of DSP and $CaCO_3$ in pacifying stickies. The average results of 3 to 4 handsheets from the blended sample, with or

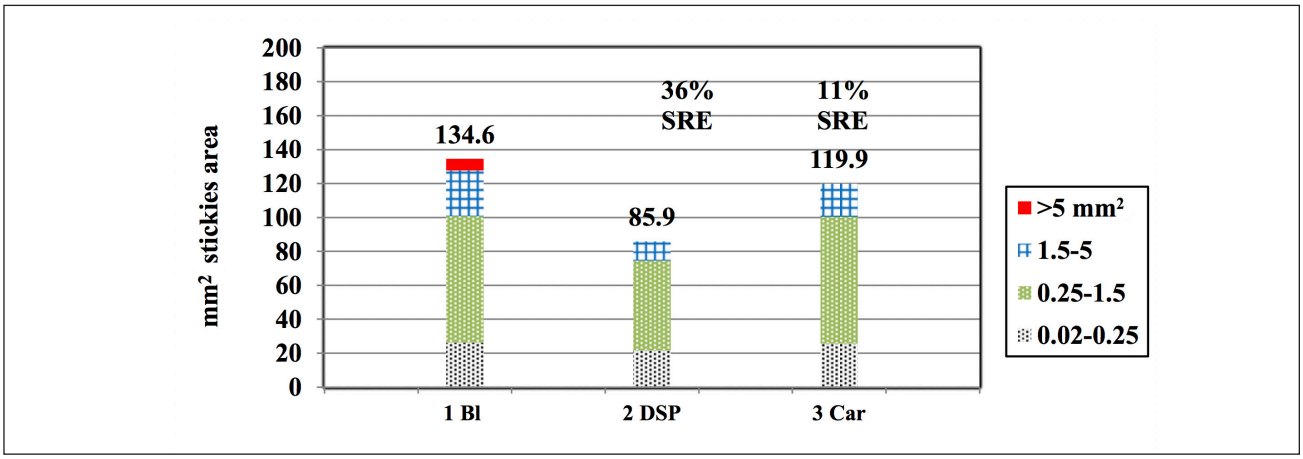
Sample Description	Stickies Area, mm² per handsheet per class size				Total
	0.02–0.25 mm²	0.25–1.5 mm²	1.5–5 mm²	>5 mm²	
Blended	7.5	39.3	32.1	0	79.0
With DSP	5.6	25.8	10.7	0	42.1
With $CaCO_3$	5.5	26.0	11.9	0	43.3

DSP = desiliconized pulp; $CaCO_3$ = calcium carbonate.

IV. Effect of adding DSP and $CaCO_3$ on stickies size distribution.



7. Effect of DSP and $CaCO_3$ on stickies size distribution compared to the blended sample without any additive.



8. Preliminary deinking line experiments adding DSP and $CaCO_3$.

without pacifying agents, are shown in **Table IV** and **Fig. 7**.

The reduction in stickies area was 46.6% for the DSP sample and 45.1% for the $CaCO_3$ sample compared to the blended sample without addition of DSP or $CaCO_3$. Results from Table IV and Fig. 7 indicate that areas of large size stickies (1.5–5 mm²) are much more affected by DSP or $CaCO_3$ compared to that of small-sized stickies. For example, comparing results with and without DSP in Table IV, pacifying effects of small-, medium-, and large-sized stickies are 25%, 34%, and 67%, respectively. Pacifying effect of $CaCO_3$ is quite similar.

The pacifying effect of DSP and $CaCO_3$ was evaluated on stickies from tertiary fine screen rejects from a deinking mill. Preliminary results displayed in **Fig. 8** show promise with DSP; however, the stock already contained considerable amounts of $CaCO_3$ so that the effect of additional carbonate was reduced.

CONCLUSION

Experiments were conducted to evaluate the effect of consistency on stickies size distribution. Results from using the same pulper and the same 100% PSA stock reveal that low consistency (6.1%) pulp has average stickies area of 2.06 mm² (1.62 mm equivalent diameter) compared to average stickies area of 0.628 mm² (0.89 mm equivalent diameter) for the high consistency (15.6%) pulp. In other words, the higher the consistency, the greater the stickies fragmentation. This is contrary to the accepted hypothesis that lower pulper consistency leads to more stickies fragmentation. This needs to be investigated further using a variety of stickies and pulper rotors.

The pacifying effect of desiliconized pulp (DSP) and $CaCO_3$ is about the same—about 45% to 47%. Carbonate is generally present in varying amounts in most recovered paper grades and is known to have a pacifying effect on stickies when present in relatively large amounts. DSP seems to be as effective also. The addition of DSP is like adding bleached hardwood kraft pulp with a bonus stickies-pacifying effect. Therefore, DSP may be worth considering in some special application by replacing a small percentage of bleached virgin hardwood kraft pulp.

INDUSTRIAL APPLICATION

A high consistency pulper could potentially fragment stickies. Therefore, it is very important to control pulping time carefully so as to achieve defibering without significant disintegration of contaminants.

The addition of desiliconized pulp (DSP) that has properties similar to bleached hardwood kraft pulp should be considered for stickies pacification. **TJ**

LITERATURE CITED

1. Doshi, M.R. and Dyer, J.M., in *Recent Advances in Paper Recycling* (M.R. Doshi, Ed.), Doshi & Associates Inc., Appleton, WI, USA, 2002, p. 35.
2. Delagoutte, T., Fabry, B., Guyard, A., et al., "Mini-stickies: A family of macro-stickies difficult to control," *TAPPI PEERS Conf.*, TAPPI Press, Atlanta, GA, USA, 2010.
3. Fabry, B., Delagoutte, T., Guyard, A., et al., "Benchmarking of macrostickies contamination along several deinking lines," *PTS-CTP Deinking Symp.*, Papiertechnische Stiftung/Centre Technique du Papier, Heidenau, Germany/Grenoble, France, 2010.
4. Doshi, M.R., *Prog. Pap. Recycl.* 11(2): 5(2002).
5. Houtman, C., Scallon, K., Guo, J., et al., "Controlling adhesive behavior during recycling," *Res. Forum Recycl., 7th*, PAPTAC, Montreal, 2004.
6. Huo, X., Venditti, R.A., and Chang, H., *Prog. Pap. Recycl.* 10(2): 15(2001).
7. Venditti, R.A., Lucas, B.E., and Jameel, H., "Breakage and extrusion of pressure sensitive adhesives in industrial and laboratory processes," *TAPPI Pulping Conf.*, TAPPI Press, Atlanta, 2001.
8. Abraham, S. in *Paper Recycling Challenge, Vol. 1, Stickies* (M.R. Doshi and J.M. Dyer, Eds.), Doshi & Associates Inc., Appleton, 1997, pp. 22-27.
9. Carre, B., Fabry, B., and Beneventi, D., "Interface mechanisms in deinking processes," *PTS Deinking Symp.* (R. Grenz, and J. Weigl, Eds.), Papiertechnische Stiftung, Heidenau, 2001.
10. Haynes, R.D., Banerjee, S., and Koskinen, J.T., "Effective measurement of microstickies accumulation potential from pulper to the paper machine," *Res. Forum Recycl., 7th*, PAPTAC, Montreal, 2004.
11. Schabel, S. and Respondek, P., *Wochenbl. Papierfabr.* 125(16): 736(1997).

ABOUT THE AUTHORS

We needed to produce pulp containing a significant quantity of microstickies. We thought pulping at 5% consistency would accomplish this, but to our surprise, we found more microstickies while pulping at 15% consistency. This was confirmed by one mill representative at the 2016 TAPPI PEERS Conference.

Our next step is to explore the validity of present observations to other types of pulpers or pulping conditions, such as temperature, pH, pulping time, and pulper rotor.

The second part of the project is the extension of our earlier work on the use of desiliconized pulp (DSP) to pacify microstickies [15]. Mills may benefit from the use of DSP as it behaves like hardwood pulp with a microstickies-pacifying effect as a bonus.


Doshi


Aziz


DeJong


Houtman

Doshi is president, Doshi & Associates Inc., Appleton, WI, USA. Aziz is ex-president and founder, Integrated Paper Services Inc., Appleton, WI, USA. De Jong is president, 2 Fiber Consulting, Appleton, WI, USA. Houtman is research chemical engineer, U.S. Department of Agriculture Forest Products Laboratory, Madison, WI, USA. Email Doshi at mahen@aol.com.

12. Venditti, R., Gilbert, R., Zhang, A., et al., "The effect of release liner materials on adhesive contaminants, paper recycling and recycled paper properties," *TAPPI Recycl. Symp.*, TAPPI Press, Atlanta, 2000.
13. Hubbe, M.A., Rojas, O.J., and Venditti, R.A., *Nord. Pulp Pap. Res. J.* 21(2): 154(2006).
14. Houtman, C., Seiter, D.F., Donermeyer D., et al., "Using laboratory and pilot results to predict behavior of adhesives in recycling mills," *Recycl. Technol. Conf., 7th,* Pira International, Leatherhead, UK, 2002.
15. Doshi, M.R., de Jong, R., Aziz, S., et al., *INPAPER Int.* 17(2): 14(2015).
16. Houtman, C. and Tan, F., "Determination of the factors that affect image analysis quantification of adhesive materials," *TAPPI Pulping/Process Prod. Qual. Conf.*, TAPPI Press, Atlanta, 2002.

ABOUT THIS PAPER

Cite this article as: Doshi, M., Aziz, S., De Jong, R., Houtman, C. *TAPPI J.* 17(8):461(2018). https://doi.org/10.32964/TJ17.08.461

DOI: https://doi.org/10.32964/TJ17.08.461

ISSN: 0734-1415

Publisher: TAPPI Press

Copyright: ©TAPPI Press 2018

About this journal

TAPPI JOURNAL
WWW.TAPPI.ORG
THE PAPER AND PACKAGING INDUSTRIES' TECHNICAL RESOURCE **SEPTEMBER 2018** | VOL. 17 NO. 9



PAPERMAKING **479**
Rewet in wet pressing of paper
J. David McDonald and Richard J. Kerekes

DRYING **489**
Boosting the elongation potential of paper by mechanical refining and additives
Anders Strand, Jarmo Kouko, Antti Oksanen, Kristian Salminen, Annika Ketola, Elias Retulainen, and Anna Sundberg

PAPER TESTING **501**
Dielectric spectroscopic studies of biological material evolution and application to paper
Mary Kombolias, Jan Obrzut, Karl Montgomery, Michael T. Postek, Dianne L. Poster, and Yaw S. Obeng

MICROFIBRILLATED CELLULOSE **507**
Mineral/microfibrillated cellulose composite materials: High performance products, applications, and product forms
David Skuse, Mark Windebank, Tafadzwa Motsi, and Guillaume Tellier

SUSTAINABILITY **519**
Regulatory and sustainability initiatives lead to improved polyaminopolyamide-epichlorohydrin (PAE) wet-strength resins and paper products
Mark T. Crisp and Richard J. Riehle

September 2018

TABLE OF CONTENTS VOL. 17 NO. 9

475 EDITORIAL
PaperCon: A ten-year journey of papermaking excellence
Gerard J.F. Ring, Scott Rosencrance, and Frank Sutman

479 PAPERMAKING
Rewet in wet pressing of paper
J. David McDonald and Richard J. Kerekes

489 DRYING
Boosting the elongation potential of paper by mechanical refining and additives
Anders Strand, Jarmo Kouko, Antti Oksanen, Kristian Salminen, Annika Ketola, Elias Retulainen, and Anna Sundberg

501 PAPER TESTING
Dielectric spectroscopic studies of biological material evolution and application to paper
Mary Kombolias, Jan Obrzut, Karl Montgomery, Michael T. Postek, Dianne L. Poster, and Yaw S. Obeng

507 MICROFIBRILLATED CELLULOSE
Mineral/microfibrillated cellulose composite materials: High performance products, applications, and product forms
David Skuse, Mark Windebank, Tafadzwa Motsi, and Guillaume Tellier

519 SUSTAINABILITY
Regulatory and sustainability initiatives lead to improved polyaminopolyamide-epichlorohydrin (PAE) wet-strength resins and paper products
Mark T. Crisp and Richard J. Riehle

»COVER CREDIT: Photograph (foreground) and SEM image of mineral/microfibrillated cellulose (MFC) composite showing its high viscosity and high surface area hydrophilic fibrils, as discussed by researchers Skuse et al. (p. 507).

TAPPI JOURNAL
WWW.TAPPI.ORG

Editor-in-Chief
Brian N. Brogdon brian.brogdon@gmail.com
+1 678 581-9114

Associate Editor
Peter W. Hart peter.hart@westrock.com
+1 409 276-3465

Editorial Director
Monica Shaw mshaw@tappi.org
+1 770 367-9534

PRESS Manager
Jana Jensen jjensen@tappi.org
+1 770 209-7242

Webmaster
Trina Heath theath@tappi.org
+1 770 209-7416

***TJ* EDITORIAL BOARD**
Randy Branston, BASF
randy.branston@basf.com, +1 704 819-4251

Brian N. Brogdon, FutureBridge Consulting & Training LLC
brian.brogdon@gmail.com, +1 678 581-9114

David A. Carlson, Carlson Consulting
dacarlson39@aol.com, +1 847 323-2685

Douglas W. Coffin, Miami University
dacarlson39@aol.com, +1 847 323-2685

Mahendra Doshi, Doshi and Associates
mahen@aol.com, +1 920 832-9101

Marc Foulger, GL&V USA Inc.
Marc.foulger@glv.com +1 315 767-2920

Peter W. Hart, WestRock
peter.hart@westrock.com, +1 409 276-3465

Carl J. Houtman, USDA Forest Products Laboratory
choutman@fs.fed.us, + 1 608 231-9445

Lucian Lucia, North Carolina State University
lucian.lucia@gmail.com, +1 919 889-7059

John A. Neun, John A. Neun LLC
john.neun@gmail.com, +1 518 275-8139

Jim Niemiec, Verso Corporation
jim.niemiec@versoco.com, +1 715 422-7404

Steven P. Ottone, Omya
steven.ottone@omya.com, +1 919 641-7854

Gaurav Pranami, Imbed Biosciences
gpranami@imbedbio.com, +1 515 230-7005

Arthur Ragauskas, Oak Ridge National Laboratory
aragausk@utk.edu

Gerard J.F. Ring, University of Wisconsin—Stevens Point
gerrryring@wi-net.com, +1 715 592-3732

Scott Rosencrance, Kemira Chemicals
scott.rosencrance@kemira.com, +1 770 429-2753

Paul Wiegand, NCASI
pwiegand@ncasi.org, +1 919 941-6417

Junyong Zhu, USDA Forest Products Laboratory
jzhu@fs.fed.us, +1 608 231-9520

Join TAPPI *today!*
TAPPI JOURNAL is a free benefit of TAPPI membership, and is only available to members. To join TAPPI, to renew your TAPPI Membership, or to learn about other valuable benefits, visit www.tappi.org.

TAPPI, 15 Technology Parkway S., Suite 115, Peachtree Corners, GA 30092, publishes *TAPPI JOURNAL* monthly.

ATTENTION PROSPECTIVE AUTHORS: All papers published are subject to *TAPPI JOURNAL's* peer-review process. Not all papers accepted for review will be published. Before submitting, check complete author guidelines at http://www.tappi.org/s_tappi/doc.asp?CID=100&DID=552877.

Statements of fact and opinions expressed are those of individual authors. TAPPI assumes no responsibility for such statements and opinions. TAPPI does not intend such statements and opinions or construe them as a solicitation of or suggestion for any agreed-upon course of conduct or concerted action of any sort.

Copyright 2018 by TAPPI, all rights reserved. For copyright permission to photocopy pages from this publication for internal or personal use, contact Copyright Clearance Center, Inc. (CCC) via their website: www.copyright.com. If you have questions about the copyright permission request process, please contact CCC by phone at +1 978 750-8400. To obtain copyright permission to use excerpts from this publication in another published work, send your specific request in writing to Editor, TAPPI JOURNAL, 15 Technology Parkway S., Suite 115, Peachtree Corners, GA 30092, USA; or by fax to +1 770 446-6947. Send address changes to TAPPI, 15 Technology Parkway S., Suite 115, Peachtree Corners, GA 30092, USA; Telephone +1 770 446-1400, or FAX +1 770 446-6947. www.tappi.org

Editorial



GERARD J.F. RING
TAPPI Journal
Editorial Board



SCOTT ROSENCRANCE
TAPPI Journal
Editorial Board



FRANK SUTMAN
TAPPI Journal
Guest Editor

PaperCon: A ten-year journey of papermaking excellence

TAPPI's PaperCon was "born" May, 2008, in Dallas, TX, by combining the technical contributions and meetings of the former Papermakers, Coating, and PIMA conferences. Fast forward ten years, and PaperCon has become TAPPI's largest and arguably most successful event.

PaperCon 2018 in Charlotte, NC—attended by 2,000-plus industry professionals from around the world— featured up to nine concurrent technical sessions. This issue of *TAPPI Journal* highlights the breadth and depth of the excellent contributions to the Papermaker's Technical Program—just one portion of this exciting megaconference. In this issue, you'll find research from PaperCon 2018, peer reviewed for TAPPI Journal, on these topics:



J. David McDonald (center), an author in this issue of* TAPPI Journal*, receives the Gunnar Nicholson Gold Medal Award at PaperCon 2018 from Paul R. Durocher, TAPPI Board of Directors Chair (left) and TAPPI President and CEO Larry N. Montague (right).

- **McDonald** and **Kerekes** present a mechanistic model of the press section rewet phenomenon that can guide work to minimize it through operational changes and press and fabric design (p. 479). It's an honor for TAPPI Journal to publish work co-authored by McDonald, the current Gunnar Nicholson Gold Medal Award winner (TAPPI's top honor), and Kerekes, his 2010 predecessor for the same award.
- Plastic pollution of our waterways is increasingly in the headlines, and it opens the door for recyclable, compostable paper alternatives. **Strand** and co-authors (p. 489) present a study on the ability to increase paper stretch—a critical property required for certain packaging applications so that paper competes with plastic on a functional basis.
- **Kombolias** and co-authors (p. 501) consider advances in analytical chemistry to improve upon the age-old headache and limited skill set of manual fiber species identification via microscopy.
- Microfibrillated cellulose has advanced from a laboratory concept to commercial practice over the past several years. **Skuse** and co-authors (p. 507) review advances in production techniques and materials via coprocessing the fiber with mineral fillers.
- The environmental and regulatory space for paper chemicals is ever more complex. Consumers demand more environmentally sustainable products. **Crisp** and **Riehle** (p. 519) review advances in wet strength resin chemistry that allow products with lower residual contaminant levels and cleaner environmental, safety, and health profiles.

Hopefully, reading this issue of *TAPPI Journal* will whet your appetite, and you'll look forward to joining us for more groundbreaking technical content at PaperCon 2019, to be held in Indianapolis, IN, from May 5-8, 2019. Enjoy! It's a great time to be a Papermaker! **TJ**

Ring is professor emeritus, University of Wisconsin—Stevens Point; Rosencrance is senior manager, marketing and technical applications, for Kemira; and Sutman is senior group leader, global technology, for Solenis.

Rewet in wet pressing of paper

J. DAVID MCDONALD AND RICHARD J. KEREKES

ABSTRACT: Wet pressing in papermaking removes water by pressure applied over time, but some of the expelled water may return to the web in an action called "rewet." This water, and the other remaining water, must be removed by drying. To understand the underlying factors of rewet, we have developed a mathematical model of it comprised of a time-dependent term that accounts for water flow from the felt to paper and a time-independent term that accounts for splitting of interfacial water between the felt and paper. Our model is consistent with measurements from the literature and can be used to understand how paper properties, press operation, and felt design can minimize rewet.

Application: This paper provides a physical model that can describe and quantify rewet. This model can be used to guide work to minimize rewet by means of operational changes and through press and fabric design.

Wet pressing in papermaking removes water by pressure acting over time, but some of the expelled water may return to the web in an action called "rewet." At present, there is no method to directly measure rewet; therefore, its size has been estimated indirectly from laboratory and pilot machine experiments. In a previous paper [1], we summarized these estimates. For lightweight grades (≤100 g/m²), rewet was estimated to be as high as 35 g/m² in pilot machine studies and 72 g/m² in laboratory experiments. Rewet of 55 g/m² was measured after the couch on a pilot paper machine [2] and exceeded 1000 g/m² in a double-wire pulp machine [3]. Given these large values, there is a clear need to better understand and quantify rewet to guide strategies to minimize its effect.

For lightweight grades, rewet is a constant that depends on furnish and felt design, independent of basis weight. This can be expressed as follows [4,5]:

$$m = m_m + \frac{R}{W} \quad (1)$$

where:
m = moisture ratio after the press
m_m = minimum moisture ratio within the nip
R = rewet, kg/m²
W = basis weight, kg/m²

We propose that rewet proceeds by two mechanisms [6,7]: water flow from the felt back into the paper (flow rewet) and water remaining with paper surface during separation of the felt and paper (separation rewet). Wrist [6] concluded that capillary forces would cause in-nip rewet and that flow-rewet would be proportional to the relative difference in pore size between the felt and paper [8]. Noting that the film of water pressed from the paper is typically the same thickness as the pulp and felt fibers (at that time wool), he suspected that rewetting caused by film splitting between the two surfaces would dominate the capillary flow rewet in the expanding nip [6]. We now consider how these mechanisms can be modeled.

ANALYSIS

General

In previous work [1,9-11], we defined rewet as water that is expelled from the web by pressure but remains with paper on leaving the press. This concept was modelled in the decreasing permeability model equation, which can be used for single and double-felted nips [1,9-12]:

$$m = (m_o - m_e)\left(1 + \frac{An(m_o - m_e)^n I}{\nu W^2}\right)^{\frac{-1}{n}} + m_e + \frac{R}{W} \quad (2)$$

where:
m = pressed moisture ratio defined as mass of water divided by mass of fiber
m_0 = incoming moisture ratio
A = specific permeability, g/m
n = compressibility factor
I = press impulse = press nip load divided by machine speed P_l/V, kPa.s
W = basis weight, kg/m²
ν = kinematic viscosity, m²/s
R = rewet, kg/m²
m_e = equilibrium moisture ratio defined as the moisture attained when the peak pressure (P_p) is applied for infinite time:

$$m_e = \delta P_p^{-d} \quad (3)$$

where δ and d are obtained by fitting Eq. 3 to experimental platen pressing data [10].

The operational parameters (impulse, basis weight, and temperature) can be easily measured. The furnish-dependent coefficients A and n in Eq. 2 can be determined by fitting the model equation to pilot or commercial pressing data [1,10-13]. The equilibrium moisture, which also depends on furnish, can be determined by fitting Eq. 3 to laboratory platen press data. Rewet can be determined for specific conditions on pilot

machines [1,9] or pilot presses [9,11], but a procedure does not exist to apply these results to commercial machines. A more fundamental understanding of rewet is required to accomplish this. A number of publications have speculated on the mechanism for rewet, but as yet, there is no consensus [1,6,7,9,11]. In this paper, we propose a mechanism for rewet based on previous experimental observations.

Postulated mechanism

In the converging side of the press nip, increasing pressure expels air and water from the paper. This water flows into the felt and from the felt into the cavities in the backing roll. After the point of peak nip pressure, pressure decreases in the expanding nip, causing air to enter the paper and felt. This creates surface tension, which at some point exceeds the diminishing hydraulic pressure, causing water to flow from the felt back into the paper, a process called "in-nip rewet." If the felt and paper remain in contact beyond the nip, where external pressure is no longer applied, this flow might continue. This is called "post-nip rewet." When the felt and paper separate, the water at their interface splits, leaving some of this water on the paper. This is called "separation rewet."

Mathematical model of rewet

In-nip flow rewet

Our in-nip flow rewet model is based on a force balance on a water column perpendicular to the plane of web/ felt (**Appendix A**). The difference in surface tension on each end of the column acts to overcome viscous resistance to flow from the pore structure. The net force causing flow arises from differing pores size and surface tension properties between the felt and paper. Under some circumstances, centripetal force becomes important and is included in the force balance. This force is expressed as a limiting condition (Appendix A).

Separation rewet

Our model for separation rewet assumes that water at the interface between felt and paper splits in proportion to the surface tension forces exerted by each material, which in turn depends on their pore size and surface tension (**Appendix B**). The amount of "interfacial water" available to be split is deemed to be water that does not face hydraulic resistance in order to move between felt and paper. We assume this depth to be the sum of the pore sizes in the felt and paper surfaces.

Total rewet

The total rewet, R, is the sum of flow rewet R_f and separation rewet R_s. From the appendices, this is given by:

$$R = R_f + R_s = a(m_m - m_e)^{1/2} t^{1/2} + bD \qquad (4)$$

where:

t = contact time between the felt and paper starting in the expanding nip, s

D = diameter of the batt fibers, μm

b = empirical factor related to the felt structure obtained by a fit to experimental data, Gg/m

m_m = minimum moisture ratio achieved inside the press nip (see Appendix A, Eq. 11A):

$$m_m = (m_0 - m_e)\left[1 + \frac{An(m_0 - m_e)^n I}{\mu W^2}\right]^{-1/n} + m_e \qquad (5)$$

a is a furnish dependent constant, defined as:

$$a = \left(\frac{2\sigma_p r_{p,0}}{\mu}\right)^{1/2} \qquad (6)$$

where:

σ_p = surface tension of the water in the paper, N/m

$r_{p,0}$ = a constant representative of the paper, $(kg/m^2)^2$

μ = viscosity of water, Ns/m

The constant "a" is determined by a fit to laboratory or pilot machine data.

COMPARISONS TO EXPERIMENTAL DATA

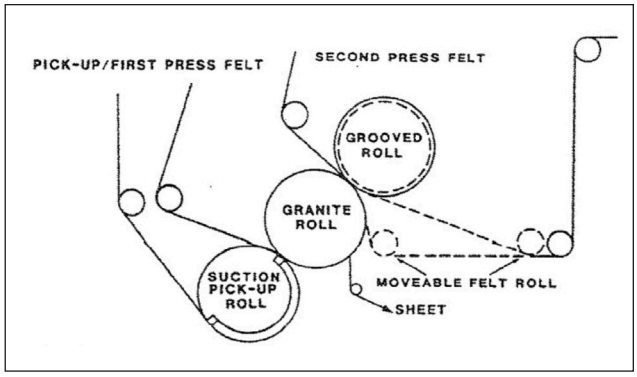
We now compare various aspects of our rewet model to experimental findings reported in the literature.

In-nip rewet

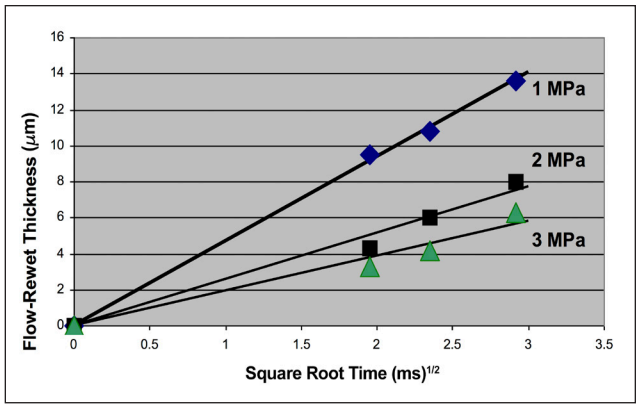
Bliesner and MacGregor [14] estimated in-nip rewet from measurements of post-nip rewet obtained by sampling paper for differing felt-paper contact distances using a press configuration similar to that in **Fig. 1** [15]. By extrapolating their post-nip rewet measurements to the center point of the nip, they obtained an in-nip rewet value of 7 g/m^2.

Post-nip rewet

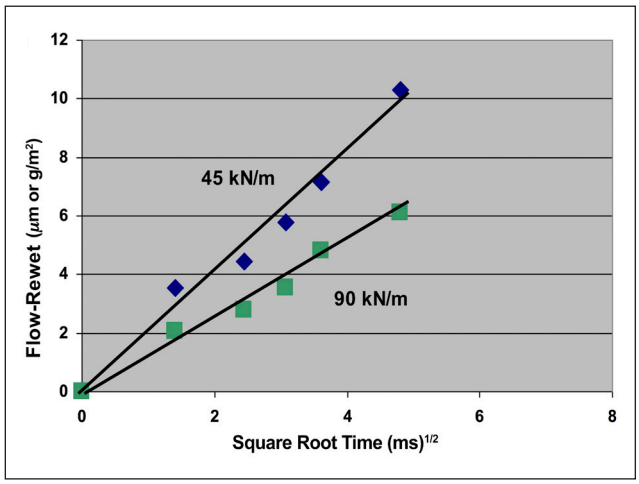
Post-nip flow rewet was determined by taking the difference between the paper moisture after a given post-nip paper-felt contact time and the paper moisture immediately after the nip. The first term of Eq. 4 includes in-nip and post-nip flow rewet. To isolate post-nip rewet, the flow rewet term is mod-



1. Pilot machine press configuration to measure post-nip rewet by changing the felt-paper contact distance with a moveable roll [15].



2. Post-nip (flow) rewet is proportional to the square root of paper-felt contact time for measurements at 380 m/min. The rate of post-nip rewet (slope of the lines) was reduced as the nip pressure was increased from 1 MPa to 2 MPa to 3 MPa [14].



3. Post-nip flow rewet is proportional to the square root of paper-felt contact time for measurements at 800 m/min [15]. The web with a higher moisture content (nip load 45 kN/m) rewets at a greater rate than does the dryer web (nip load 90 kN/m). A water layer thickness of 1 µm is equal to 1 g/m² when the density of water is 1 g/cm³.

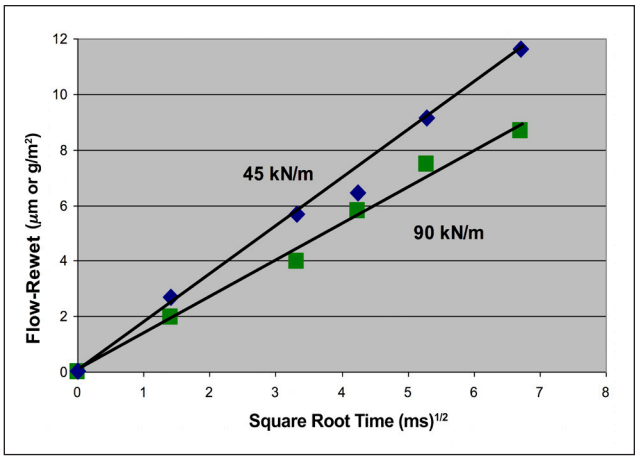
ified as follows (see Appendix A, Eqs. 17A and 18A):

$$R_f = a(m_p - m_e)^{1/2} t^{1/2} \quad (7)$$

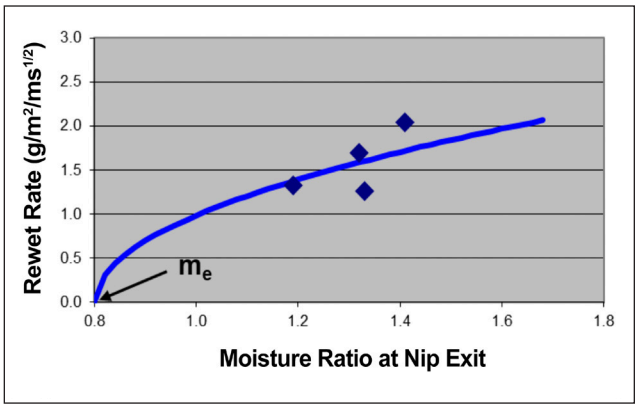
where m_p is the moisture measured immediately after the nip.

As shown in **Fig. 2**, Bliesner's and MacGregor's [14] measurements of post-nip rewet are proportional to the square root of time, which is consistent with Eq. 7. Increasing nip pressure was found to diminish rewet (Fig. 2) because increased pressure has a larger effect on pressed moisture through press impulse and peak pressure than it does on equilibrium moisture through peak pressure alone. The increased pressure reduces the coefficient a, defined by Eq. 6, by reducing the average pore size of the paper r_p (Eq. 10A).

In other work, McDonald and Pikulik [15] measured the solids content of webs after pressing for different web-felt



4. Post-nip flow rewet is proportional to the square root of paper-felt contact time for measurements at 400 m/min [15]. The web with a higher moisture content (nip load 45 kN/m) rewets at a greater rate than does the dryer web (nip load 90 kN/m.) A water layer thickness of 1 µm is equal to 1 g/m² when the density of water is 1 g/cm³.

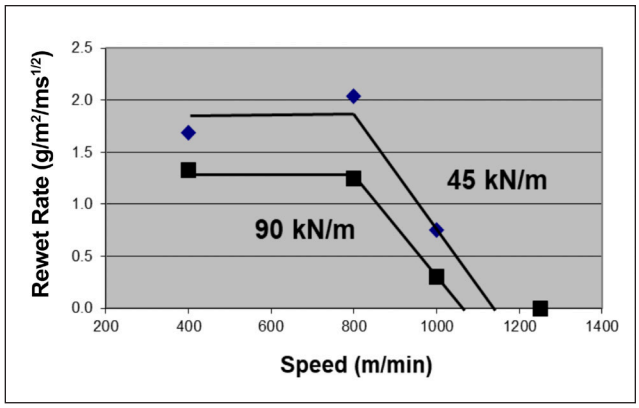


5. Rewet rate (rewet/square root of time) is greater for wetter sheets at the nip exit. The fitted line is proportional to $m_p^{1/2}$. Data are from reference [15].

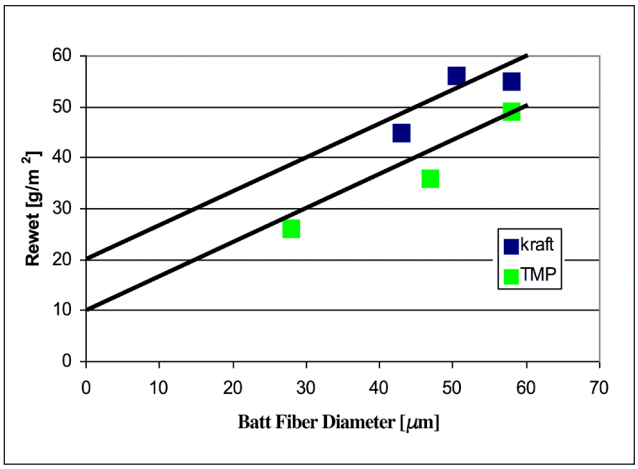
contact distances at several nip loads and speeds (**Fig. 3**). Using the pilot paper machine press configuration shown in Fig. 1 [15], they found that post-nip rewet increased with contact time and was larger for webs that leave the nip at lower solids contents (higher moisture ratio) produced by lower nip load (45 kN/m vs. 90 kN/m).

Plotting the data from McDonald and Pikulik [15] as the amount of rewet in micrometers (or g/m²) versus the square root of paper-felt contact time gives a straight-line relationship (Fig. 3 and **Fig. 4**), consistent with Eq. 7. In addition, higher nip loads (higher pressure) lowered the rate of rewet, likely due to diminished paper pore size as previously discussed.

The slopes of the lines in Figs. 3 and 4 reflect the rate of rewet. These rates increase with moisture ratio after pressing (**Fig. 5**), which is consistent with previous pilot press experiments that measured total rewet. In these experiments, we found that total rewet was proportional to $(m_o\text{-}m_e)^q$. The exponent q had an average value of 0.38, with a maximum



6. In pilot machine experiments using the press section configuration shown in Fig. 1, centripetal force limited rewet rate (rewet/square root of time) at speeds above 800 m/min for two different second press nip loads [15].



7. Rewet versus batt fiber diameter for an ingoing moisture ratio (m_o) of 4 [11].

0.44 [11]. This compares favorably to the theoretical value of 0.5 predicted in Eq. 7. The value of q depends on the felt design, generally decreasing with increasing batt fiber diameter [11].

Previous pilot machine experiments for lightweight paper showed that pressed solids (and rewet) were independent of felt moisture content [16], indicating that most of the water carried by the felt into the nip is not available for rewet. This suggests that the water pressed from the web resides in a region of the felt adjacent to the paper and is available for rewet. A similar conclusion was reached for laboratory platen press experiments using a porous plate in place of a felt [17] and a felted laboratory shoe-press [18].

Lastly, McDonald and Pikulik [15] examined the effect of speed on rewet. Above a certain speed, depending on roll diameter (defined by Eq. 1A in Appendix A), centripetal force becomes important. In these experiments, because the paper was between the roll and felt, centripetal force was directed from the paper toward the felt, in effect diminishing rewet caused by surface tension forces (**Fig. 6**). We note here that the roll diameters on this pilot machine were 0.75 m, which are much smaller than typical rolls on commercial machines. Accordingly, the speed at which centripetal force will inhibit rewet is larger for commercial machines.

In summary, when the felt wraps the solid press roll and centripetal force equals or exceeds the net force from surface tension in the paper, there is no post-nip flow rewet.

Separation rewet

As described earlier, separation rewet is the portion of water at the felt/paper interface that stays with paper upon separation. The analysis in Appendix B shows that this component of rewet, R_s, is linearly dependent on felt pore size, r_f. Assuming that felt pore size is proportional to the batt filament diameter, and that b reflects the amount of available interfacial water, this gives:

$$R_s = bD \qquad (8)$$

The average thickness of the available interstitial water has been estimated to be between 10 and 40 μm for press felts constructed with batt fibers ranging from 22 μm to 78 μm in diameter [19]. Measurements of rewet for different felt designs have shown that rewet is greater for larger diameter batt fibers [11,18,20-23], which is consistent with Eq. 8.

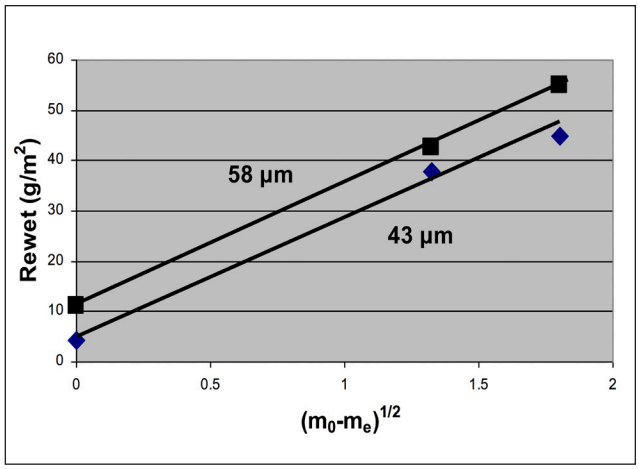
Total rewet calculated using the decreasing permeability model from pilot press experiments [11] is plotted against batt fiber diameter in **Fig. 7**. In these experiments, 60 g/m² papers made from kraft and thermomechanical pulp (TMP) were pressed using six different felts. The slopes of the lines are the coefficient b in Eqs. 4 and 7 and have the same value of 0.67 for both furnishes. Coefficient b, which is derived in Appendix B, relates the amount of interfacial water to the felt and paper pore sizes. The value of 0.67 is similar to the ratio of the depth of interstitial water at paper/felt interface to batt fiber diameter measured by Axelsson et al. [19].

Extrapolating to zero batt fiber diameter, Eq. 4 gives the sum of in-nip and post-nip flow rewets. As shown in Fig. 7, the zero diameter intercept for kraft is larger than for TMP. This can be explained by the longer contact time in the expanding nip (press speed was 72 m/min for kraft experiments and 120 m/min for TMP). In addition, TMP had a larger equilibrium moisture ratio than kraft (0.95 vs. 0.75). For the conditions used, Fig. 7 shows that for the kraft paper in-nip "flow rewet" was 20 g/m² and separation rewet was 25–35 g/m², depending on felt design. Similarly, in-nip "flow" rewet for the TMP paper was 10 g/m², with separation rewet of 15–40 g/m².

Substituting approximate times and equilibrium moisture ratios for TMP and kraft in the flow rewet Eq. 7, gives the ratio of the a furnish coefficients:

$$a_K = 1.5\ a_T \qquad (9)$$

where a_K and a_T are the furnish dependent coefficients for the kraft and TMP furnishes.



8. Plotting rewet data from reference [11] versus $(m_0-m_e)^{1/2}$ shows that rewet decreases as ingoing moisture, m_0, is reduced to equilibrium value (0.8). At this value, there is only separation rewet, which is about 10 g/m² for the felt with 58 µm batt fibers and 6 g/m² for 43 µm batt fibers.

The consequence of this ratio in Eq. 6 is:

$$r_K = 1.5\frac{\sigma_T}{\sigma_K} r_T \tag{10}$$

where the subscripts denote the surface tension and average pore size of the kraft and TMP papers.

This result is in accord with pore size distribution measurements, which have shown that kraft papers have larger internal pores than newsprint [24] largely because of the presence of fines in the mechanical furnish.

Total rewet

We can now summarize total rewet as:

$$R = R_f + R_s = a(m_m - m_e)^{1/2} t^{1/2} + bD \tag{11}$$

where:

$$m_m - m_e = (m_0 - m_e)\left[1 + \frac{An(m_0 - m_e)^n I}{\mu W^2}\right]^{-1/n} \tag{12}$$

Simplifications to Eq. 12 are possible, as follows:

If $\left[1 >> \frac{An(m_0 - m_e)^n I}{\mu W^2}\right]$ in Eq. (5), then $m_m = m_o$ (Appendix A, Eq. 13A).

So that:

$$R = a(m_0 - m_e)^{1/2} t^{1/2} + bD \tag{13}$$

Total rewet increases with the square root of initial moisture less equilibrium moisture ratio. When m_0 approaches the equilibrium moisture ratio, flow rewet (the first term in Eq. 13) disappears. Thus, water expelled from the web by pressure only fills the surface cavities of the paper and does not reach the felt. Separation rewet (the second term in Eq. 13) is now proportional to the surface pores of the paper so that $R_s = br_p$, giving:

$$m = m_e + \frac{br_p}{W} \tag{14}$$

Equation 14 has been confirmed in experiments in which a web was passed through a press nip many times until there is no further change on pressed moisture [11]. When the paper and felt separate, this water remains with the paper (**Fig. 8**). For the conditions of these experiments, equilibrium moisture ratio was about 0.8, and consequent separation rewet in the limit as m_o approaches m_e was 6-10 g/m², as given by Eq. 14.

STRATEGIES TO REDUCE REWET

Equations 3 and 4 can be used to evaluate strategies to reduce rewetting such as the following:

- Using felts with smaller pore size to reduce separation rewet, recognizing that this could lead to more plugging and shorter felt life
- Pressing to low web moisture content
- Minimizing felt-web contact time by:
  - Minimizing post nip contact
  - Maintaining high pressure until abrupt decrease at nip exit [18]
- Increasing surface energy of felt material

SUMMARY AND CONCLUSIONS

We have developed a theoretical model of rewet in wet pressing that is consistent with experimental observations from various sources. The model has two components. One is a time-dependent flow term governed by the web-felt contact time in the expanding nip and post-nip if the paper and felt remain in contact. The other component is a separation rewet term that is strongly related to the surface structure of the felt.

Our results are in line with Wrist's [6] and Norman's [7] conjectures that separation rewet dominates flow rewet in the expanding nip under commercial pressing conditions.

The model can be used with the decreasing permeability model to assess the effect of various factors on moisture content leaving press sections, such as pressure, press impulse, and paper and felt properties. However, a direct measurement of rewet is still needed. Determining this measurement is a topic worthy of further study, given the importance of rewet in reducing energy in papermaking. **TJ**

APPENDIX A – MODEL OF FLOW REWET

We model flow rewet by a force balance in which a net surface tension force imposed by the felt and paper causes a laminar flow through the connected pores from the felt to the paper. Variables r_p and r_f are the respective pores sizes of paper and felt and there are n paper pores for each felt pore [24,25]. We assume the walls bounding the pores to be infinitely thin. Thus, $nr^2_p = r^2_f$. We consider the connected lengths of pores in paper and felt to be l_p and l_f. The force balance gives:

$$2\pi(nr_p\sigma_p - r_f\sigma_f) = \mu(n\frac{2\pi r_p V_p}{r_p}l_p + \frac{2\pi r_f V_f l_f}{r_f}) \quad (1A)$$

where:
σ_f = surface tension for water and felt
σ_p = surface tension for water and paper
V_p, V_f = speed of water movement in paper and felt
μ = water viscosity

We note here that it is common in the expanding portion of a roll nip for the paper to follow the roll and the felt to pass straight out from the nip. Consequently, there is a centripetal force acting on the water in the paper. Equation 2A assumes this force to be negligible, i.e., it assumes:

$$nr_p\sigma_p - r_f\sigma_f >> nr_p^2 l_p \rho\frac{V_R^2}{R} \quad (2A)$$

Calculation using representative values shows Eq. 2A to be the typical case. If it is not, the centripetal force, $nr_p^2 l_p \rho\frac{V_R^2}{R}$, must be included as one of the driving forces in the left-hand side of Eq. 1A.

The assumption of infinitely thin walls implies that $V_p = V_f$. Assuming that the felt is fully saturated over length $l_{f,o}$ and that at $t = 0$, $l = l_{fo}$ and $l_p = 0$, Eq. 1A reduces to:

$$nr_p\sigma_p - r_f\sigma_f = \mu V_p(l_p(n-1) + l_{fo}) \quad (3A)$$

Substituting $n = \frac{r_f^2}{r_p^2}$, gives:

$$r_p\sigma_p - \frac{r_f\sigma_f}{n} = \mu V_p(l_p + \frac{r_p^2}{r_f^2}(l_{fo} - l_p)) \quad (4A)$$

Assuming $r_p << r_f$, and $V_p = \frac{dl_p}{dt}$, Eq. 4A reduces to:

$$r_p\sigma_p - \frac{r_f\sigma_f}{n} = \mu V_p l_p = \mu l_p\frac{dl_p}{dt} \quad (5A)$$

Only water that has been pressed from the paper is available for rewet, which means there is an upper limit given by:

$$l_{p,\max} = \frac{W}{\rho}(m_o - m_e) \quad (6A)$$

Integrating Eq. 5A gives the rewet l_p at time t;

$$\int_0^t (r_p\sigma_p - \frac{r_f\sigma_f}{n})dt = \int_0^{(l_{p,\max})} \mu l_p dl_p \quad (7A)$$

Substituting $n = \frac{r_f^2}{r_p^2}$ gives:

$$l_p = (\frac{2r_p t}{\mu})^{\frac{1}{2}}(\sigma_p - \frac{r_p\sigma_f}{r_f})^{\frac{1}{2}}$$

for

$$0 \le l_p \le l_{po} \quad (8A)$$

We note that for the case of drawing water into pores of radius r_p from an infinite reservoir ($r_f \to \infty$), Eq. (8A) reduces to Eq. 9A below. This is similar to the Washburn equation derived from Poiseuille's equation, which assumes water penetration from a reservoir into cylinders of radius r_p [26]:

$$l_p = (\frac{\sigma_p r_p 2t}{\mu})^{\frac{1}{2}} \quad (9A)$$

When $\sigma_p \approx \sigma_f$ and $r_p << r_f$, we may use Eq. 9A as an approximation of rewet.

The extent of rewet clearly depends on the relative pore sizes of the felt and paper. Pore size is a material property, but in the case of paper, it is also a function of the degree to which paper has been compressed. The relationship between pore size and moisture ratio is the basis of the decreasing permeability model, and similarly we can relate pore size in the nip to the minimum moisture in the nip, m_m. This minimum will occur when the applied pressure in the expanding nip becomes less than pressure from surface tension causing rewet. Thus, we assume that the "openness" of the paper to receive water is proportional to the moisture ratio of the paper, m_m, less the equilibrium moisture, m_e, which gives:

$$r_p = r_{p,o}(m_m - m_e) \quad (10A)$$

where $r_{p,0}$ is a constant that is representative of the paper.

The minimum moisture reached in the press nip (m_m) is given by the first two terms on the right-hand side of the decreasing permeability model equation (Eq. 1):

$$m_m = (m_0 - m_e)\left[1 + \frac{An(m_0 - m_e)^n I}{\mu W^2}\right]^{-1/n} + m_e \quad (11A)$$

So that:

$$r_p = r_{p,0}(m_m - m_e) = r_{p,0}(m_0 - m_e)\left[1 + \frac{An(m_0 - m_e)^n I}{\mu W^2}\right]^{-1/n} \quad (12A)$$

When the ingoing moisture equals the equilibrium moisture, no water is pressed out because the pores are closed off. Consequently, no rewet can take place.

For light pressing, when the impulse I is small, such that:

$$\left[1 >> \frac{An(m_0 - m_e)^n I}{\mu W^2}\right], \text{ then } m_m = m_0 \quad (13A)$$

and

$$r_p = r_{p,o}(m_0 - m_e). \quad (14A)$$

When the press impulse I is large, such that:

$$\left[1 << \frac{An(m_0 - m_e)^n I}{\mu W^2}\right] \text{ then } m_m = \left(\frac{\mu W^2}{AnI}\right)^{1/n} + m_e \quad (15A)$$

$$m_m - m_e = \left(\frac{\mu W^2}{AnI}\right)^{1/n} \text{ and } r_p = r_{p,0}\left(\frac{\mu W^2}{AnI}\right)^{1/n} \quad (16A)$$

There is no simple or direct way to measure the position or the size of the minimum moisture, m_m, inside the press nip. Values for m_m were calculated by Bliesner and MacGregor [14] by extrapolating post-nip rewet measurements into the nip and by Beck [27], who measured the distance between press rolls online to infer the thickness of water and fiber in the nip. Both results are calculations that have limited accuracy. Thus, in the absence of better measurements, our best estimate of m_m at present comes from Eqs. 11A, 13A, and 15A.

On the other hand, post-nip flow rewet can be measured when moisture immediately after the press nip, m_p, is known. The following equation gives the additional rewet flow as a function of paper/felt contact time outside the nip:

$$l_p = \left(\frac{\sigma_p r_p 2t}{\mu}\right)^{\frac{1}{2}} = \left(\frac{2\sigma_p r_{p,o}(m_p - m_e)t}{\mu}\right)^{\frac{1}{2}} \quad (17A)$$

Equation 17A implies that post-nip rewet is proportional to the square root of time t and $(m_p - m_e)$. Thus, post-nip flow rewet can be represented by:

$$R_f = a(m_p - m_0)^{1/2} t^{1/2} \quad (18A)$$

where:

$$a = \left(\frac{2\sigma_p r_{p,o}}{\mu}\right)^{\frac{1}{2}} \quad (19A)$$

Given that m_m is difficult to determine and in-nip rewet should be accounted for in a useable rewet model, we must make approximations to obtain predictive equations for rewet. We do so by considering in-nip and post-nip rewet together as different phases of flow rewet starting from moisture m_m and extending in time from the point of peak pressure in the nip, which in the case of rolls is mid-nip.

We note here that this is an approximation of the starting moisture and time of rewet. In reality, in-nip rewet will commence in the expanding part of the nip where applied pressure is decreasing from peak pressure and, consequently, time of rewet will be shorter. Improving the model to account for these factors must await improved knowledge of nip mechanics in wet pressing.

In summary, the flow rewet equation may be expressed as follows:

$$R_f = a(m_0 - m_e)^{1/2}\left[1 + \frac{An(m_0 - m_e)^n I}{\mu W^2}\right]^{-1/2n} t^{1/2} \quad (20A)$$

APPENDIX B – MODEL OF SEPARATION REWET

As described earlier, separation rewet is water that stays with the paper upon separation of the paper and felt. The mechanism is film splitting of water located in the interstitial zone between the felt and paper. The depth of water available in this zone is not precise, but it can be considered to be water that requires no flow to stay with either the felt or paper upon their separation.

We consider the amount of water available for splitting to be Q_T and this to split into water on paper, Q_p, and water on felt, Q_f. Thus:

$$Q_t = Q_p + Q_f \quad (1B)$$

As above, we consider paper to have n pores of size r_p facing one pore of size r_f on the felt. We assume that water Q_t will split in proportion to the surface tensions acting on water from the felt and paper. This gives:

$$\frac{Q_p}{Q_f} = \frac{nr_p\sigma_p}{r_f\sigma_f} \quad (2B)$$

Further, we note that:

$$nr_p^2 = r_f^2 \quad (3B)$$

Substituting Eqs. 2B and 3B into Eq. 1B, we obtain:

$$Q_p = \frac{Q_t}{(1+\frac{\sigma_f r_p}{\sigma_p r_f})} \quad (4B)$$

We note that if $\sigma_f = \sigma_p$, then:

$$Q_p = \frac{r_f}{r_f + r_p} Q_t \quad (5B)$$

We further note that if $r_f = r_p$ (and $\sigma_f = \sigma_p$), rewet splits evenly, i.e., $Q_p = 0.5Q_t$.

If the available water for film splitting is proportional to the combined depth of the fabric and paper pore sizes, i.e., $Q_t = k(r_p + r_f)$, then:

$$Q_p = kr_f \quad (6B)$$

In short, for the assumptions made, felt pore size determines the amount of water that splits onto paper.

There is little information on the pore size of felts, but some on the filament sizes, D. If we assume that $r_f \propto D$, then:

$$Q_p \propto D \quad (7B)$$

or when expressed as separation rewet,

$$R_s = bD \quad (8B)$$

This result is valid when the amount of water in the felt available for rewet exceeds bD. If this is not the case, then rewet is dominated by the paper pore size:

$$R_s = br_p \quad (9B)$$

LITERATURE CITED

1. McDonald, J.D. and Kerekes, R.J., *Tappi J.* 78(11): 107(1995).
2. McDonald, D., *TAPPI Eng./Process and Product Quality Conf.*, TAPPI PRESS, Atlanta, GA, USA, 1999, p. 597.
3. Luotonen, A. and Sampi, J., "Dewatering in a double-wire pulp machine – press theory and test results," *TAPPI Eng. Conf.*, TAPPI PRESS, Atlanta, 1995.
4. Sweet, J.S., *Pulp Pap. Mag. Can.* 62(8): T367(1961).
5. Wahlstrom, P.B., *Pulp Pap. Mag. Can.* 70(19): 76(1969).
6. Wrist, P.E., *Pulp Pap. Mag. Can.* 65(7): T284(1964).
7. Norman, B., *Nord. Pulp Pap. Res. J.* 75(8): 39(1987).
8. Wilder, J.E., *Tappi* 51(2): 104(1968).
9. McDonald, J.D., Hamel, J., and Kerekes, R.J., *J. Pulp Pap. Sci.* 26(11): 401(2000). 10. Kerekes, R.J., McDonald, E.M., and McDonald, J.D., *J-FOR* 3(2): 46(2014).
11. McDonald, J.D., McDonald, E.M., and Kerekes, R.J., *J-FOR* 3(2): 53(2014).
12. McDonald, J.D. and Kerekes, R.J., *BioResources* 12(4): 9520(2017).
13. McDonald, J.D. and Kerekes, R.J., *Tappi J.* 74(12): 142(1991).
14. Bliesner, W.C. and MacGregor, M.A., *Tappi* 59(6): 114(1976).
15. McDonald, J.D. and Pikulik, I.I., *Nord. Pulp Pap. Res. J.* 3(3): 115(1988).

ABOUT THE AUTHORS

Rewet in wet pressing lowers the solids content of the web entering dryers, leading to higher energy use. It is a controversial subject, and there are many speculations about its mechanism and magnitude. Through modelling, we thought that we could identify the important factors and devise strategies to minimize rewet.

Previously, we developed the decreasing permeability model to predict dewatering in a press nip and used an empirical constant to account for rewet. This research provides a mechanistic explanation of rewet and equations to predict its magnitude under different conditions.

Rewet is a combination of in-nip and separation rewet. The most difficult aspect of this research was devising the means to quantify each contribution separately.

Rewet in the expanding press nip depends on the properties of the paper. Separation rewet, which occurs when the felt and paper separate, is a function of the surface structure of the felt.

One of the most interesting findings from this study is that the model predictions agreed extremely well with experimental data from a number of different sources.



McDonald



Kerekes

Mills could use the results of this study to reduce energy in the dryers by minimizing press rewet.

A better understanding of the effect of felt construction on rewet could lead to further improvements in dryness after the press.

McDonald is president, JDMcD Consulting Inc., Vaudreuil-Dorion, QC, Canada, and Kerekes is professor emeritus, University of British Columbia, Pulp and Paper Centre, Vancouver, BC, Canada. Email McDonald at mcdonald.jdavid@gmail.com.

16. McDonald, J.D. and Pikulik, I.I., *Tappi J.* 70(2): 77(1987).
17. Jaavidaan Y., Ceckler, W.H., and Thompson, E.V., *Tappi J.* 71(3): 151(1988).
18. Ahlman, A., "Development of a laboratory shoe press and a study of separation rewet," Licentiate thesis, Royal Institute of Technology, Stockholm, Sweden, 1997.
19. Axelsson, M., Östlund, C., Vomhoff, H., et al., *Nord. Pulp Pap. Res. J.* 21(3): 395(2006).
20. Hansson, K.F., *Pap. Technol. Ind.* 18(3): 206(1972).
21. Smart, J.S., *Pap. Technol. Ind.* 16(3): T112(1975).
22. Jackson, G.W., *Tappi J.* 72(9): 103(1989).
23. Xu, J., Phillip, R., and Hedou, D., "The effect of press felt non-uniformity on sheet smoothness and dewatering," *TAPPI PaperCon*, TAPPI PRESS, Atlanta, 2011.
24. Gorres, J.H., Amiri, R., and McDonald, J.D., "The specific pore volume of multi-planar webs: the role of the short and long fiber fractions," *The Science of Papermaking: Transactions of the 12th Fundamental Research Symposium*, Pulp and Paper Fundamental Research Society, Bury, UK, 2001, p. 1371-1383.
25. Thibault, X., Bloch, J.-F., and Boller, E., *Appita J.* 55(2): 145(2002).
26. Washburn, E.W., *Phys. Rev.* 17(3): 273(1921).
27. Beck, D.A., *TAPPI Eng. Conf.*, TAPPI PRESS, Atlanta, 1986, p. 105.

ABOUT THIS PAPER

Cite this article as: Mayeli, N. *TAPPI J.* 17(9):479(2018). https://doi.org/10.32964/TJ17.09.479

DOI: https://doi.org/10.32964/TJ17.09.479

ISSN: 0734-1415

Publisher: TAPPI Press

Copyright: ©TAPPI Press 2018

About this journal

Boosting the elongation potential of paper by mechanical refining and additives

ANDERS STRAND, JARMO KOUKO, ANTTI OKSANEN, KRISTIAN SALMINEN, ANNIKA KETOLA, ELIAS RETULAINEN, AND ANNA SUNDBERG

ABSTRACT: The procedures used in restraining the web during drying will severely affect paper properties. In this work, the main differences between restrained drying and unrestrained drying on paper properties were identified. The mechanical properties of paper were studied as a function of low-consistency mechanical refining energy; wet-end additions of carboxymethyl cellulose (CMC) with cationic starches; as well as spray addition of alginate, chitosan, and cationic guar gum. After restrained drying, the tensile index and tensile stiffness increased with increasing refining energy, but the elongation at break was severely limited. After unrestrained drying, the elongation at break increased linearly with increasing refining energy. However, unrestrained drying also resulted in significantly lower tensile index and tensile stiffness values. After restrained drying, the largest increases in tensile index and stiffness were obtained by sequential wet-end addition of CMC and cationic starches. Certain combinations could mitigate all of the decrease in tensile index from unrestrained drying, while maintaining the distinctively high elongation potential of the paper. Wet-end addition of CMC and cationic starches could mitigate some of the decrease in tensile stiffness, but not completely. Spray addition of alginate, chitosan, or cationic guar gum increased the tensile index after both restrained and unrestrained drying. Spray addition of alginate resulted in significant increases in elongation at break and two-dimensional formability of the handsheets after unrestrained drying. After restrained drying, the tensile stiffness increased after spray addition of all of the different polysaccharides. After unrestrained drying, however, stiffness was unaffected by all of the tested polysaccharide spray additions. The same pulp treatment/additives will increase either stiffness or stretch, depending on the drying technique, but both properties could not be maximized simultaneously.

Application: Increased elongation of paper could lead to new packaging products. Altering the drying technique increases elongation but also affects other paper properties. Mills can benefit from understanding the effects of different treatments after unrestrained and restrained drying.

The role of the fiber properties and the fiber-fiber interaction is known to have an important role in the deformability and extensibility of the fiber network [1]. Recently published studies have shown the possibilities of creating highly extensible networks from wood fibers that can be molded by available forming techniques into three-dimensional (3D) shapes [1-8]. Mechanical treatment of pulp, wet-end additives, and sprayed additives have been previously used to modify paper properties. Mechanical refining of the pulp is known to reverse adverse effects of pulp drying, increase fiber flexibility, expand the microfibrillar structure of the pulp, and enhance the entanglement between fibrils and fibers in suspension [9-13]. Addition of hydrophilic polymers or polyelectrolytes improves the adhesion between cellulosic fibers and improves fiber-fiber bonding [14,15]. Additives that successfully enhance strength should be of sufficiently high molar mass to remain on the fiber surface, be hydrophilic, be retainable to the fiber network, and be able to form hydrogen bonds [14-16]. Spray application of such polymeric additives can be an effective way to circumvent the difficulties with polymer or polyelectrolyte retention to the fiber network that wet-end additions may result in.

Unrestrained drying greatly increases the elongation potential of paper [17]. It has been suggested that formation of microcompressions in the longitudinal direction of fibers caused by fiber shrinkage in transversal direction is the mechanism behind paper shrinkage during unrestrained drying.

The aim of this study was to identify the main impacts of unrestrained drying on paper properties in a broad and systematic fashion. The impact of unrestrained drying was studied as a function of low-consistency mechanical refining of pulp; as a function of wet-end additions of carboxymethyl cellulose (CMC) and cationic starches; and as a function of spray additions of alginate, chitosan, and cationic guar gum onto wet paper sheets. An additional aim of the study was to improve the mechanical properties of paper while maintaining the distinctively high elongation potential of papers after unrestrained drying.

EXPERIMENTAL

Materials

Elemental chlorine free-bleached, once-dried softwood kraft pulp was obtained from a Finnish pulp mill. Sodium CMC (DS

0.80-0.95, Mw 700 kDa) was obtained from Sigma-Aldrich (St. Louis, MO, USA). The CMC was dissolved in pH-adjusted, distilled water with aid of boiling and agitation. Four different cationic starches—Classic 135 (starch A), Raifix 01015 SW (starch B), Raifix 25035 (starch C), and Raisabond 15 (starch D)—were obtained from Chemigate (Lapua, Finland) as preboiled slurries or in dry form [18]. The dry starch was dissolved in pH-adjusted distilled water with aid of boiling and agitation, while the preboiled slurries were diluted with pH-adjusted distilled water. Alginic acid sodium salt from brown algae (alginate) was obtained from Sigma-Aldrich. The alginate powder was directly dissolved in distilled water to a concentration of 1 wt% with the aid of boiling and agitation. Chitosan (medium molar mass) was obtained from Sigma-Aldrich. The chitosan powder was dissolved in 1.5% acetic acid to a concentration of 1 wt% with the aid of boiling and agitation. Cationic guar gum was obtained from MakingCosmetics (Redmond, WA, USA). The content of nitrogen was +772 µmol/g obtained by titration. The cationic guar gum powder was dissolved in distilled water to a concentration of 0.5 wt% with the aid of boiling and agitation. Sorbitol was obtained from Sigma-Aldrich and directly dissolved in distilled water to a concentration of 20 wt%.

Methods

Refining

The refining of the kraft pulp was performed with a trademarked ProLab refining station (Valmet; Espoo, Finland) at Åbo Akademi University in Turku, Finland, according to the previously published procedure [18]. Samples of the pulp were taken at refining energy values of 50, 100, 150, 200, 250, and 300 kW·h/metric ton. A sample of disintegrated kraft pulp was included as reference (0 kW·h/metric ton). The Schopper-Riegler (°SR) values of the pulp samples were measured according to ISO 5267-1 "Pulps—determination of drainability—part 1: Schopper-Riegler method," and the refined pulp was characterized using a Valmet Kajaani Fiberlab optical fiber analyzer.

Papermaking

Handsheets were formed on a 125-mesh wire in a 165 x 165 mm laboratory sheet former. Handsheets for the wet-end addition study with CMC and cationic starches were prepared with recirculation of water [18], while the rest of the handsheets were prepared without recirculation of water. The consistency of the pulp suspension was 0.3% and the consistency during sheetmaking was 0.03%. The aimed grammage of all of the handsheets was 100 g/m². Wet-end addition of CMC and cationic starches were added to the pulp suspension and allowed to interact under constant low-shear agitation for 20 min before sheet forming [18]. The CMC was always added before the starches. For the spray study, base handsheets were formed and stored wet (26%–28% dry content) in sealed plastic bags between wet blotters until further use. The polysaccharide solutions, 1% solids content for chitosan and alginate and 0.5% for cationic guar gum, were sprayed onto the top of the wet sheets using a commercial, high-volume, low-pressure (HVLP) gravity feed air spray gun. For spraying, a wet sheet was placed on a rigid plastic plate that was on a gravimetric scale. The targeted amount of solution was adjusted by controlling the wet weight of the sheet after spraying according to the known consistency of the dispersion. Reference sheets were sprayed with an equivalent amount of pure water. The sprayed samples were set on a vacuum table covered with a fabric wire, and a vacuum level of approximately 5–10 kPa was applied below the sample. The aim of the vacuum treatment was to remove excess water from the sheets and impregnate the polymers into the wet fiber network.

Restrained drying. The formed sheets were dried between blotters on a 60°C drying cylinder, or on a drying plate with a blotter, strapped into a drying frame at paper testing conditions overnight. None of the sheets were wet pressed before drying.

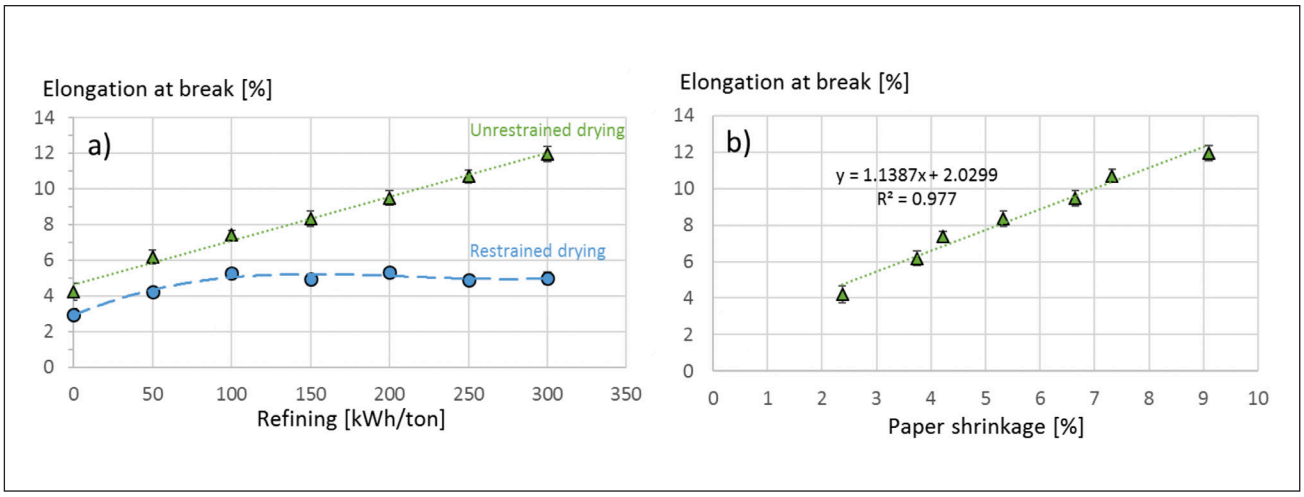
Unrestrained drying. The formed handsheets were dried between two pieces of 280-mesh polyamide fabric, or in specially built drying frames in between two polymer wires with a gap of approximately 3 mm, to allow for paper shrinkage during drying while simultaneously preventing severe cockling and curling of the sheets. None of the sheets were wet pressed before drying, to amplify the shrinking potential, especially for unrestrained dried papers.

Paper testing

The basis weight of the paper samples was determined according to ISO 536:1995 "Paper and board—determination of grammage." The thickness was determined according to ISO 534:1998 "Paper and board—determination of thickness and apparent bulk density or apparent sheet density," and the density was determined based on the measured values of the basis weight and thickness. The mechanical properties (tensile index, stretch, work, and tensile stiffness) of the paper sheets were determined with a Lorentzen & Wettre tensile strength tester (AB Lorentzen & Wettre; Kista, Sweden) or a Lloyd tensile strength tester (Ametek; Berwyn, PA, USA), in accordance with ISO 5270:1998 "Pulps—laboratory sheets—determination of physical properties." The straining speed was 12 mm/min and 100 mm/min in the tensile measurements, respectively. Paper samples were conditioned and all testing of the samples took place at a temperature of 23°C and at 50% RH. The decrease in handsheet area during unrestrained drying was measured and recalculated into one-dimensional shrinkage using Eq. 1:

$$1D\ shrinkage\ (\%) = \left(1 - \sqrt{1 - \frac{2D\ shrinkage\ (\%)}{100}}\right) \times 100\% \qquad (1)$$

Two-dimensional formability tests. The formability strain and force of the paper samples were measured using a 2D-formability tester at VTT Technical Research Centre of Finland. A detailed description of the measurement procedure



1. (a) The elongation at break (%) of handsheets made from kraft pulp subjected to different refining energy values (kW·h/metric ton). The handsheets were dried with or without restraint. (b) The elongation at break (%) of handsheets plotted against paper shrinkage (%) during drying.

and setup is available in literature [19]. In this investigation, the velocity of the forming press was 1 mm/s and the width of the paper sample was 20 mm. The paper samples were set in the tester so that the sprayed surface was not in contact with the heated press.

RESULTS AND DISCUSSION

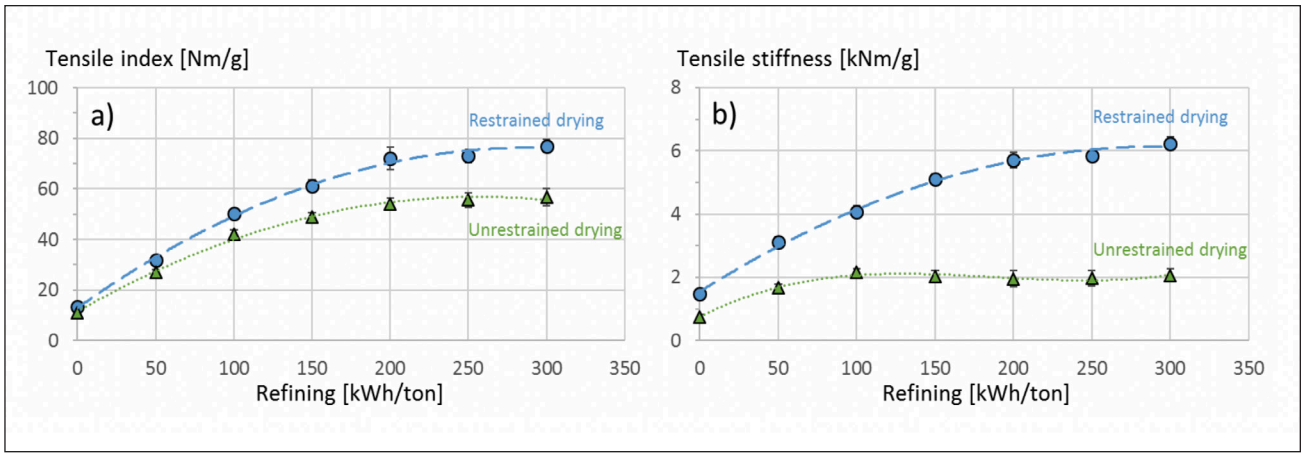
Effect of low-consistency mechanical refining on paper properties

Low-consistency refining of the kraft pulp resulted in increased elongation at break of the handsheets from the initial values of 2.7% and 4.2%, both after restrained and unrestrained drying (**Fig. 1a**). After restrained drying, the elongation at break leveled off at around 5% at 100 kW·h/metric ton of refining. After unrestrained drying, however, the elongation potential of the handsheets increased with increasing refining energy in an almost linear fashion, and no plateau was visible between 0 and 300 kW·h/metric ton of refining. When plotting the elongation at break as a function of paper shrinkage during unrestrained drying, a linear correlation was discovered (**Fig. 1b**). A somewhat linear correlation between strain at break and paper shrinkage has also previously been reported; a linear correlation was seen in both machine-direction and cross-direction of the paper after negative strain (i.e., shrinkage) [20].

The results indicated that prolonged refining causes additional paper shrinkage during unrestrained drying, which increases the elongation potential of the formed fiber network. It has been suggested that formation of microcompressions in the longitudinal direction of fibers caused by fiber shrinkage in the transversal direction is the mechanism behind paper shrinkage during unrestrained drying [17]. Stretching a shrunken fiber network is to a certain extent a reversal of shrinkage, as the applied forces tend to pull out the kinks and microcompressions, both between and within the bonds. As hydrogen bonds gradually break, the microcompressions are released, allowing for a greater extension of the fiber network before it breaks due to localization of stress and failure of fiber-fiber bonds. Paper shrinkage during drying is required to reach high elongation at break values, as the plateau around 5% after restrained drying persisted between at least 100 and 300 kW·h/metric ton of refining.

Low-consistency refining increased the tensile index of the handsheets from the initial values of 13.5 and 11.2 Nm/g after restrained and unrestrained drying (**Fig. 2a**). After restrained drying, the increase in tensile index became less noticeable after 200 kW·h/metric ton. The highest determined tensile index, 77 Nm/g, was a result of the highest refining energy. It has previously been reported that refining of pulp increases the strength of individual fiber-fiber joints [9]. The authors attributed most of the increase in paper strength from refining to flexibility and conformability of fibers, which increased the number of fiber contacts per unit fiber length. Unrestrained drying resulted in sheets with categorically lower tensile index than restrained drying (Fig. 2a). The decrease in tensile index became more noticeable at higher refining energy values; the difference was 4.8 Nm/g at 50 kW·h/metric ton, while the difference at 300 kW·h/metric ton was 20.3 Nm/g. It was noted that the density of handsheets after unrestrained drying was categorically lower due to paper shrinkage, and decreased with increased refining energy, than after restrained drying. This fact could partly explain the observed decrease in tensile index.

Low-consistency refining increased the tensile stiffness of handsheets from the initial values of 1.5 and 0.7 kNm/g after restrained and unrestrained drying (**Fig. 2b**). After restrained drying, the increase in tensile stiffness became less noticeable after 200 kW·h/metric ton, in a very similar fashion as the observed tensile index (Fig. 2a). The tensile stiffness after restrained drying reached its maximum around 6 kNm/g. After unrestrained drying, however, the tensile stiffness of the handsheets reached its maximum value at much lower refin-



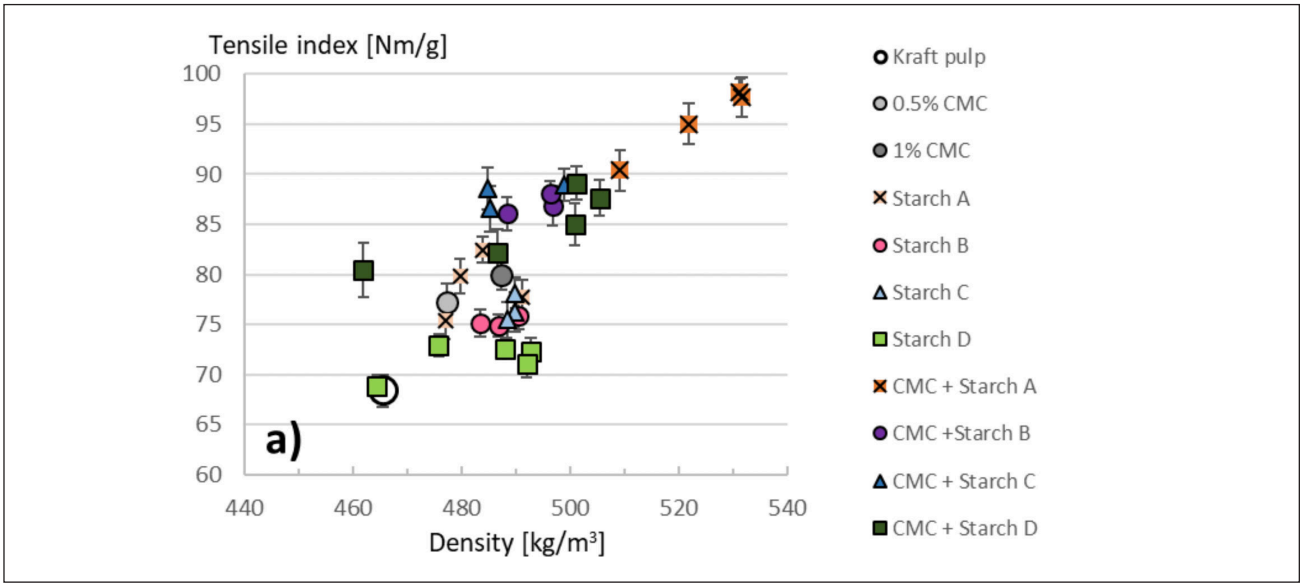
2. (a) The tensile index (Nm/g) and (b) the tensile stiffness (kNm/g) of handsheets made from kraft pulp subjected to different refining energy values (kW·h/metric ton). The handsheets were dried with or without restraint.

ing energy, and remained unchanged between 100 and 300 kW·h/metric ton (Fig. 2b). The tensile stiffness reached its plateau at a value of about 2 kNm/g, and further refining had no impact on this value. The difference in tensile stiffness between handsheets after restrained and unrestrained drying increased with refining energy; the difference was 1.5 kNm/g at 50 kW·h/metric ton, whereas the difference at 300 kW·h/metric ton was 4.2 kNm/g.

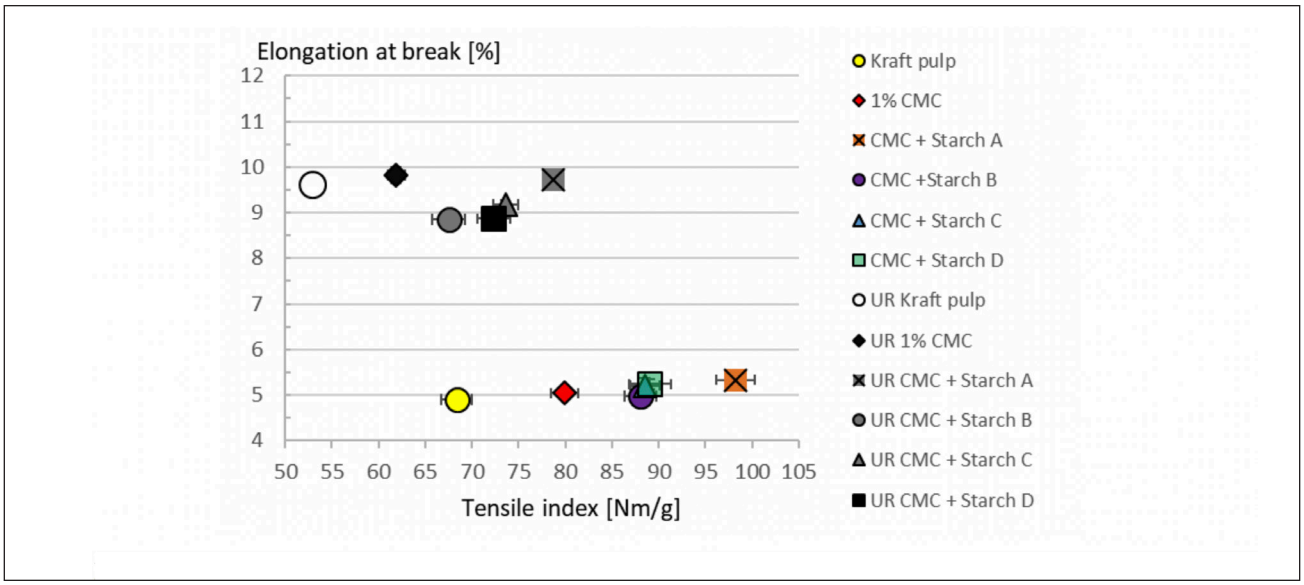
It has been previously reported that drying under limited restraint lowers the tensile stiffness of paper and increases the elongation potential [20,21]. Unrestrained drying of paper sheets lowers their tensile stiffness quite significantly, and reported stiffness values are therefore usually quite low [5,27,20]. Because of the severe and obvious limitations in tensile stiffness, it was decided that the tensile stiffness alongside the elongation at break should be the properties in focus for additional improvements. For the continued experiments, the refining level of 135 kW·h/metric ton (°SR 25) was chosen to ensure that the tensile stiffness had reached its plateau during unrestrained drying.

Effect of chemical additives on strength, stiffness, and elongation potential

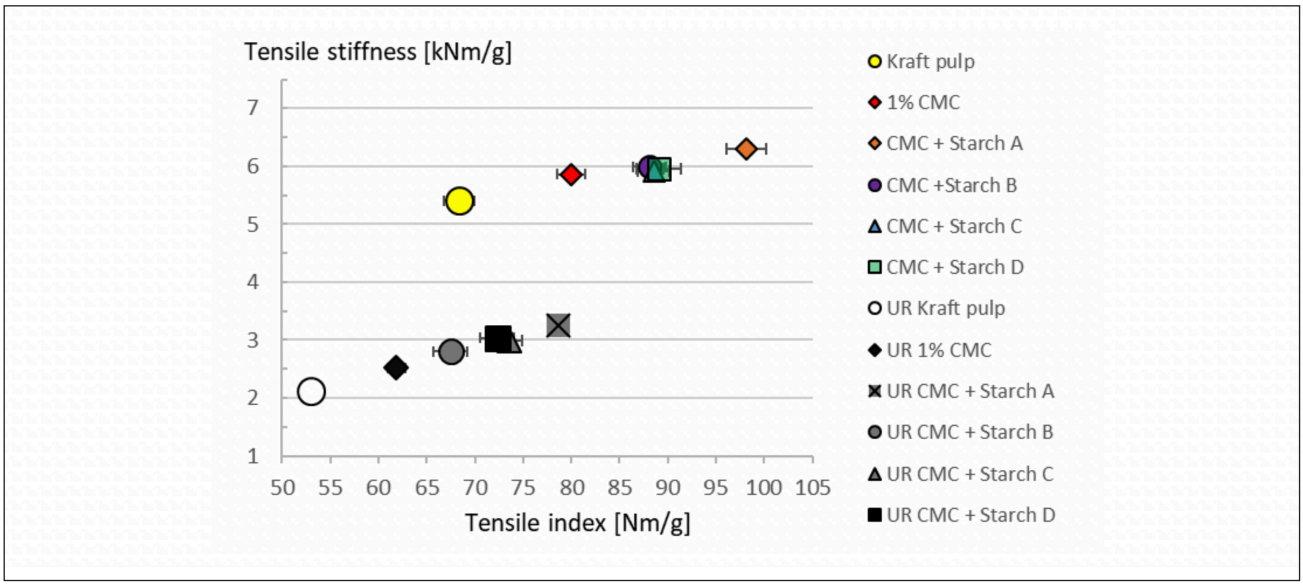
Laboratory handsheets were prepared from °SR 25 kraft pulp. The sheets were prepared with wet-end additions of CMC and/or different dosages of four different commercially available cationic starches [18]. The measured tensile indexes of the paper sheets were plotted against their measured densities after restrained drying (**Fig. 3a**). All of the tested additives increased the tensile index of handsheets above the



3. (a) The tensile index (Nm/g) versus the density (kg/m³) and b) the tensile stiffness (kNm/g) versus density (kg/m³) of paper sheets made with different wet-end additions of 0.5% or 1% carboxymethyl cellulose (CMC), 1%–5% cationic starches, or 1% CMC and 1%–5% cationic starches. The sheets were dried under restraint. The average values with their 95% confidence level intervals are shown.



4a. The elongation at break (%) versus the tensile index (Nm/g) of handsheets made with wet-end additions of 1% CMC and 4% cationic starch after restrained drying (grey legends) and unrestrained drying (UR, colored legends). The average values with their 95% confidence level intervals are shown.



4b. The tensile stiffness (kNm/g) versus the tensile index (Nm/g) of handsheets made with wet-end additions of CMC, cationic starches, or both after restrained drying and unrestrained drying (UR). The average values with their 95% confidence level intervals are shown.

reference value of 68 Nm/g when added as single components at different dosages. It was noted that wet-end addition of 1% CMC according to solids increased the tensile index significantly compared with addition of up to 4%–5% of the cationic starches. When used alone, CMC acts as a bonding agent and reduces the flocculation tendency of pulp; increases the water retention value of pulp; and increases the tensile strength, tear strength, and surface strength of paper [14,22,23]. Adsorbed CMC is believed to extend outward from the fiber surfaces due to repulsion between the anionic charges in its chain, and this may facilitate more efficient interdiffusion of macromolecules at the fiber surfaces [14,24].

Combinations of 1% CMC with 1%–5% cationic starches resulted in tensile indexes surpassing the values of the individual components after restrained drying (Fig. 3a) [18]. The CMC was added to the pulp suspension before the cationic starches in this study, as this should improve the formation of the paper sheets [25]. These results supported the conclusion that sequential addition of oppositely charged polyelectrolytes is an effective way to improve paper properties [14]. The highest tensile index, 98.2 Nm/g, was achieved by combination of the cationic starch with the highest molar mass and the lowest

charge density, starch A, with 1% CMC [18]. The fiber-fiber bonds are usually the limiting factor for the strength of paper, and the highest recorded tensile strengths of paper are far below the values obtained for single fibers [26,27]. To form strong contact between fibers, it is important to have a large molecular contact area between the fibers [28]. The softness of the surface layer will have a large influence on the joint strength between fibers, while the bulk properties will affect the possibility for fibers to form contact points with other fibers. Therefore, the properties of the different adsorbed CMC–starch layers were also studied with quartz crystal microbalance with dissipation monitoring (QCM-D) and surface plasmon resonance (SPR) adsorption techniques [18].

The measured tensile stiffness of the paper sheets were plotted against their measured densities after restrained drying (Fig. 3b). It was seen that wet-end addition of the different cationic starches resulted in very low increases, or even decreases, in the tensile stiffness of the handsheets. The highest tensile stiffness by any starch dosage was 5.6 kNm/g compared with the reference value of 5.4 kNm/g [18]. The results indicated that addition of cationic starch does not increase the tensile stiffness of paper significantly on its own, which was in agreement with previous findings [29]. However, wet-end addition of 1% CMC by itself increased the tensile stiffness to 5.9 kNm/g (i.e., significantly compared with the different cationic starches). Adsorption of CMC onto fibers has been previously shown to increase the stiffness, or sheet modulus, of paper [23,29]. The tensile stiffness of the paper was increased even higher by combining CMC with the different cationic starches. The highest tensile stiffness, 6.4 kNm/g, was achieved by combination of the cationic starch with the highest molar mass and the lowest charge density, starch A, with 1% CMC [18]. By using these additives, and combinations of them in various ratios, the papers obtained a broad range in tensile index, 68–98 Nm/g, and in tensile stiffness, 5.3–6.4 kNm/g, after restrained drying.

The cationic starch-to-CMC ratio 4:1 was chosen for further testing on the basis of the initial results [18]. In Fig. 4, results from both restrained drying (grey legends) and unrestrained drying (colored legends) are included. After restrained drying, the tensile index of the paper was significantly increased, while the elongation at break was limited to values around 5% (**Fig. 4a**). These results, as well as the refining experiments discussed earlier, showed that the maximum elongation at break value after restrained drying was about 5%, and this limit cannot be increased even by significant increases in paper strength. Enhanced fiber-fiber bonding by addition of cationic starch or CMC has been previously reported to allow for greater use of the elongation potential of the fiber network before it breaks [4]. In these experiments, however, the mechanical refining already had increased the fiber-fiber bonding of the pulp to its plateau value after restrained drying.

Unrestrained drying

The elongation at break of the handsheets was significantly increased. With wet-end addition of 1% CMC, it was possible to increase the tensile index while maintaining a high elongation at break. When combining CMC with the different cationic starches, it was possible to increase the tensile index of the handsheets further, and the maximum tensile index after unrestrained drying was 78.7 Nm/g. However, certain combinations of CMC and cationic starch seemed to slightly decrease the elongation at break of the paper. Only one of the tested cationic starches could maintain the same level of elongation at break while increasing the tensile index (i.e., starch A). Adsorption experiments with quartz crystal microbalance with dissipation monitoring (QCM-D) and SPR techniques showed that this particular CMC and starch combination contained the highest amount of coupled water and resulted in the thickest and softest surface layer [18]. It was therefore suggested that a soft layer, containing a large amount of coupled water, might act as a plasticizer during unrestrained drying. This mechanism has also been suggested earlier [16]. During drying, the fiber web continuously loses water until it reaches a dry content where the hydrogel surfaces of the fibers begin to adhere to each other, and bonds start to vigorously develop [15].

Restrained drying

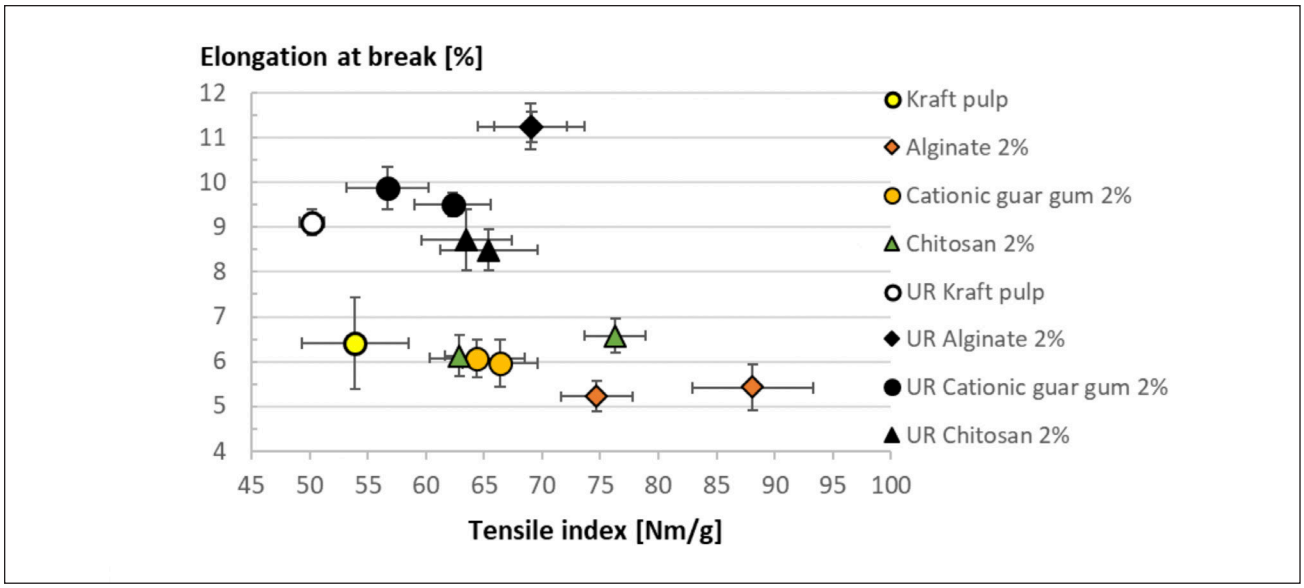
The tensile stiffness of the handsheets was significantly increased by the wet-end addition of 1% CMC and combinations of 1% CMC and 4% of the cationic starches (**Fig. 4b**). Unrestrained drying caused a decrease in tensile stiffness from 5.4 to 2.1 kNm/g for the reference sample. Wet-end addition of 1% CMC could increase the tensile stiffness to 2.5 kNm/g on its own, whereas the increases were more significant with combinations of 1% CMC and 4% of the cationic starches. The largest tensile stiffness value after unrestrained drying was obtained when combining CMC with starch A (i.e., 3.2 kNm/g). Even with the most efficient additives, the tensile stiffness value was still 2.2 kNm/g below the reference sample after restrained drying.

Enhanced strength, stiffness, and elongation potential of paper by spray addition of polysaccharides

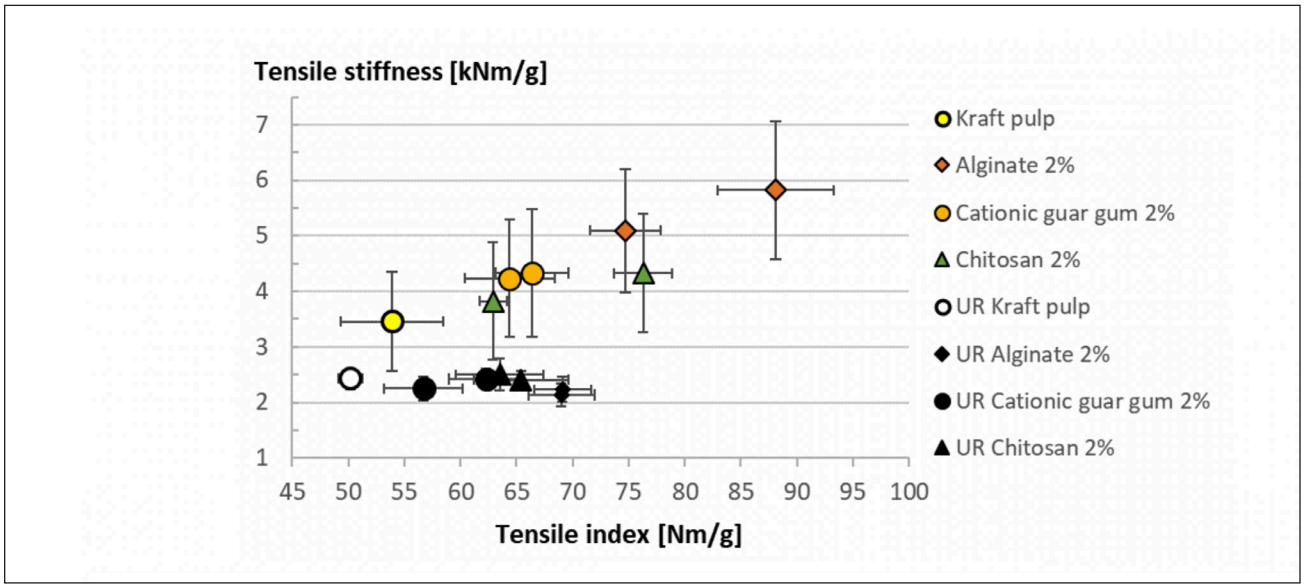
Laboratory handsheets were prepared from °SR 25 kraft pulp and stored wet until further use. The wet sheets were sprayed with the different polysaccharide solutions, to a dosage level of 2 wt%. The chosen polysaccharides for the investigation were alginate, chitosan, and cationic guar gum, based on a wide preliminary study of model film properties of different polysaccharides. In the preliminary study, a softener, sorbitol, was required to effectively prepare model films from polysaccharides. Therefore, 20% and 30% sorbitol, calculated on polysaccharide dry weight, was added to the solutions before spraying.

Restrained drying

The measured elongation at break of the paper sheets was plotted against tensile index (**Fig. 5a**). After restrained dry-



5a. The elongation at break (%) versus the tensile index (Nm/g) of handsheets sprayed with different polysaccharide solutions, with 20% or 30% sorbitol, after restrained drying and unrestrained drying (UR). The average values with their standard deviations are shown.

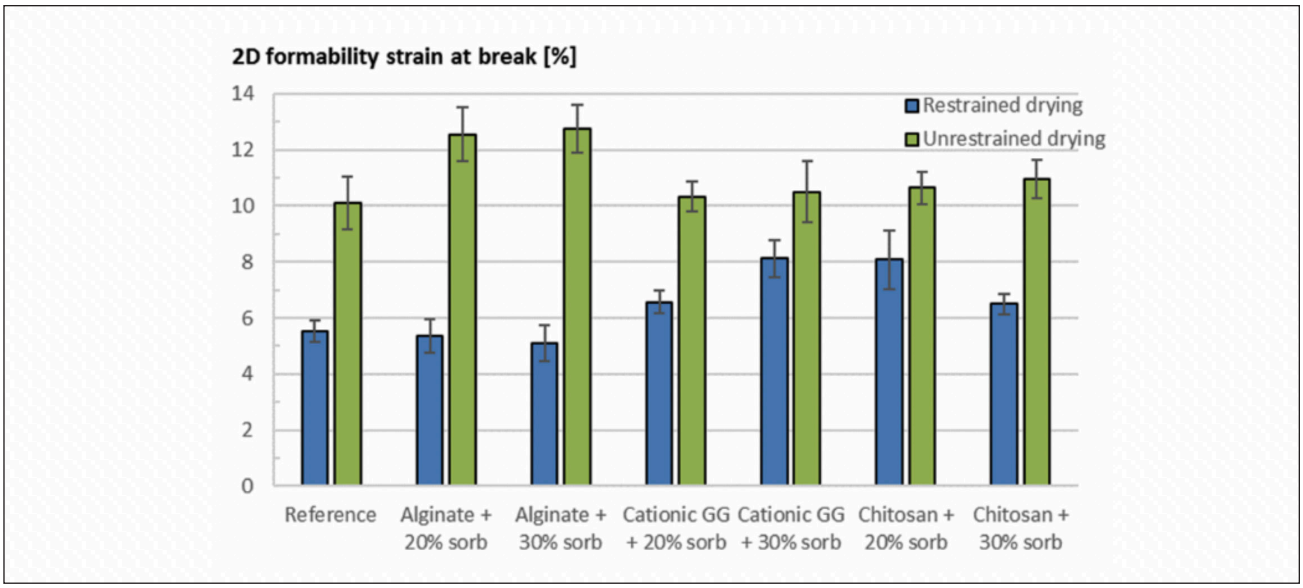


5b. The tensile stiffness (kNm/g) versus the tensile index (Nm/g) of handsheets sprayed with different polysaccharide solutions after restrained drying and unrestrained drying (UR). The average values with their standard deviations are shown.

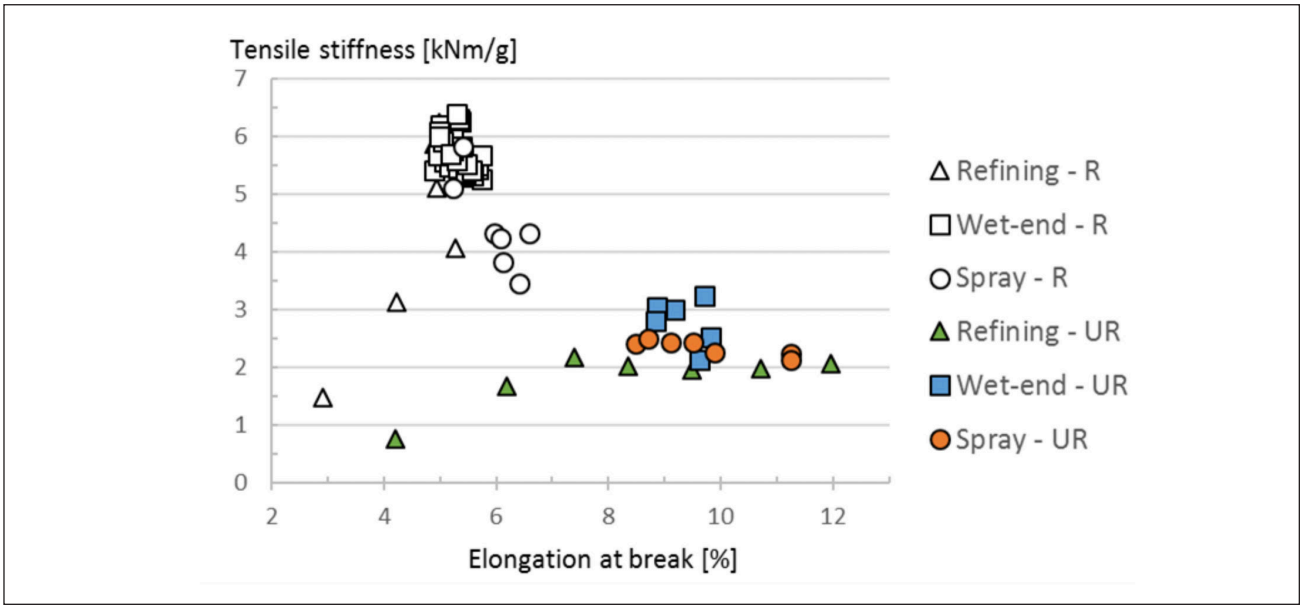
ing, all of the sprayed additives increased the tensile index of handsheets above the reference value of 53.9 Nm/g. Spraying the handsheets with cationic guar gum containing 20% sorbitol as softener resulted in a tensile index of 66.4 Nm/g after restrained drying. Spray addition of chitosan with 20% sorbitol resulted in 76.3 Nm/g, whereas increasing the amount of softener to 30% decreased the tensile index to 62.9 Nm/g. The highest tensile index, 88.1 Nm/g, was seen after spray addition of alginate containing 30% sorbitol. Decreasing the amount of softener lowered the tensile index to 74.7 Nm/g. After restrained drying, the elongation at break was not increased by the spray addition of polysaccharides. The elongation potential of the handsheets was similar to, or lower than, the level of the reference sheets.

Unrestrained drying

All of the different spray additions resulted in increased values of tensile index (Fig. 5a). Once again, the largest increase was seen with spray addition of alginate solution, from the reference value at 50.2 Nm/g to 69.1 Nm/g. After unrestrained drying, the elongation at break was significantly increased by spray addition of alginate (from 9.1% to 11.3%) and slightly by



6. The two-dimensional (2D) strain at break (%) of handsheets sprayed with different polysaccharide solutions after restrained drying and unrestrained drying. The average values with their standard deviations are shown.



7. The tensile stiffness (kNm/g) versus the elongation at break (%) of handsheets from kraft pulp. The handsheets were prepared from kraft pulp after different refining energy values; wet-end additions of carboxymethyl cellulose, cationic starches, or both; and handsheets sprayed with different polysaccharide solutions. The handsheets were dried with restraint (R) or without restraint (UR).

spray addition of cationic guar gum (9.1% to 9.9%). The increased elongation potential after spray addition with alginate was an effect of additional shrinkage during drying, whereas this was not the case with cationic guar gum.

The measured tensile stiffness of the paper sheets was plotted against tensile index (**Fig. 5b**). After restrained drying, all of the sprayed additives increased the tensile stiffness of handsheets above the reference value of 3.5 kNm/g. Of the tested polysaccharides, alginate was the only component that resulted in stiffness values exceeding 5 kNm/g (i.e., 5.8 kNm/g with 30% sorbitol and 5.1 kNm/g with 20% sorbitol). After unrestrained drying, all of the stiffness values of the sprayed sheets were similar to the reference value at 2.4 kNm/g. Spray addition of 2% alginate, chitosan, or cationic guar gum had no significant effect on the stiffness of handsheets after unrestrained drying, even though noticeable changes were seen in elongation at break and tensile index.

The 2D formability results showed similar trends as the elongation at break values. After restrained drying, the 2D formability of the handsheets increased from 5.5% to 8.1% after

spray addition of cationic guar gum (30% sorbitol) and to 8.1% after spray addition of chitosan (20% sorbitol) (**Fig. 6**). After unrestrained drying, the 2D formability of handsheets increased significantly, from 10.1% to 12.8%, by spray addition of alginate (30% sorbitol). Spray addition of chitosan and cationic guar gum only resulted in slight improvements in 2D formability. Alginate was the only tested polysaccharide that caused a significant increase in 2D formability and elongation at break. It had also been previously reported that gelatin and agar can be sprayed onto wet paper to improve the elongation potential of paper [8]. After spray addition of alginate, the air permeability of the handsheets dramatically decreased, whereas chitosan and cationic guar gum did not have this effect. This indicated that the alginate formed a film on the top of the paper, much like spray addition of agar, which is another viable polysaccharide for spray addition [19].

Combining the tensile stiffness and elongation at break values from these three studies into one single graph highlights the main differences between restrained and unrestrained drying. Restrained drying results in very stiff paper after prolonged refining, with certain wet-end additives, or with spray additions of polysaccharides, but the elongation potential of the fiber network is limited to a maximum of about 6% (**Fig. 7**). Unrestrained drying results in high elongation at break values as a result of prolonged refining, with certain wet-end additions or with spray addition of polysaccharides, but the tensile stiffness is limited to a maximum of about 3 kNm/g.

CONCLUSIONS

The main differences between the effects of restrained drying and unrestrained drying on paper properties were identified. The mechanical properties of paper were studied as a function of low-consistency mechanical refining energy (0–300 kW·h/metric ton); wet-end additions of CMC with cationic starches; and spray addition of alginate, chitosan, and cationic guar gum.

After restrained drying, the tensile index and tensile stiffness increased with increasing refining energy, but the elongation at break reached its plateau around 5% already at 100 kW·h/metric ton. After unrestrained drying, the elongation at break increased linearly with increasing refining energy, and no plateau was seen between 0 and 300 kW·h/metric ton. However, the tensile stiffness after unrestrained drying already reached its plateau value, 2 kNm/g, after 100 kW·h/metric ton of refining.

Sequential wet-end addition of CMC and cationic starches resulted in stronger and stiffer paper compared with wet-end addition of single components. Wet-end addition of CMC resulted in both increased tensile index and stiffness of the paper, whereas addition of cationic starch only resulted in increased tensile index. Certain combinations of CMC and cationic starch could mitigate all of the decrease in tensile index from unrestrained drying while maintaining the distinctively high elongation potential of the paper. Wet-end addition of CMC and cationic starches could mitigate some of the decrease in tensile stiffness from unrestrained drying, but not completely.

Spray addition of alginate, chitosan, or cationic guar gum increased the tensile index after both restrained and unrestrained drying. Spray addition of alginate resulted in significant increases in elongation at break and 2D formability of the handsheets after unrestrained drying. After restrained drying, the tensile stiffness was increased by spray addition of all tested polysaccharides. After unrestrained drying, however, the tensile stiffness was unaffected by all of the tested polysaccharide spray additions and resulted in values close to the reference value of 2.4 kNm/g.

Restrained drying resulted in very stiff paper after prolonged refining, with certain wet-end additions, or with spray additions of polysaccharides, but the elongation potential of the fiber network was quite limited. Unrestrained drying resulted in high elongation at break values as a result of prolonged refining, with certain wet-end additions or spray addition of polysaccharides, but the tensile stiffness was very limited. It was concluded that the same pulp treatment/additives will cause either stiffness or stretch depending on the drying technique, but both properties could not be maximized simultaneously.

Future biobased materials must have a stronger and more deformable structure to compete with oil-based materials in such areas as packaging, construction, composites, and furniture. Highly extensible fiber networks will have the potential to improve the properties of current products but also to create a new product sector in packaging materials. This will make it possible to design new types of packages and packaging lines that use continuous webs and combine several process phases into one continuous line. **TJ**

ACKNOWLEDGEMENTS

This work is a part of the project ExtBioNet, appointed by the Academy of Finland and of the activities of the Process Chemistry Centre (PCC) at Åbo Akademi University, Turku, Finland. Special thanks to Mattias Strandberg and Richard Sundberg for their enthusiastic and relentless laboratory work.

LITERATURE CITED

1. Vishtal, A. and Retulainen, E., *BioResources* 9(4): 7951(2014).
2. Svensson, A., Lindström, T., Ankerfors, M., et al., *Nord. Pulp Pap. Res. J.* 28(4): 602(2013).
3. Vishtal, A., Hauptmann, M., Zelm, R., et al., *Packag. Technol. Sci.* 27(9): 677(2014).
4. Seth, R., *Pulp Pap. Can.* 106(2): 33(2005).
5. Zeng, X., Vishtal, A., Retulainen, E., et al., *BioResources* 8(1): 472 (2013).
6. Khakalo, A., Filpponen, I., Johansson, L.-S., et al., *React. Funct. Polym.* 85: 175(2014).
7. Khakalo, A., Vishtal, A., Retulainen, E., et al., *Cellulose* 24(1): 191(2017).

DRYING

8. Vishtal, A., Khakalo, A., Rojas, O.J., et al., *Nord. Pulp Pap. Res. J.* 30(3): 452(2015).
9. Mayhood, C.H., Kallmes, O.J., and Cauley, M., *Pulp Pap. Mag. Can.* 62(11): T479(1961).
10. Kibblewhite, R., *Appita* 26(5): 341(1973).
11. Scallan, A. and Tigerström, A., *J. Pulp Pap. Sci.* 18(5): J188(1992).
12. Koskenhely, K., in *Papermaking Part 1, Stock Preparation and Wet End* (H. Paulapuro, Ed.), Finnish Paper Engineers' Association, Jyväskylä, Finland, 2008, p. 94.
13. Belle, J., Kleemann, S., Odermatt, J., et al., *Nord. Pulp Pap. Res. J.* 31(2): 205(2016).
14. Hubbe, M.A., *BioResources* 1(2): 281(2006).
15. Fornue, E., Allan, G., Quinones, H., et al., *Papel* 72(9): 85(2011).
16. Pelton, R., *Appita J.* 57(3): 181(2004).
17. Page, D. and Tydeman, P., in *Formation and Structure of Paper Vol. 1*, (F. Bolam, Ed.), Technical Section, British Paper and Board Makers' Association, London, 1962, p. 397.
18. Strand, A., Khakalo, A., Kouko, J., et al., *Nord. Pulp Pap. Res. J.* 32(2): 324(2017).
19. Vishtal, A. and Retulainen, E., *Nord. Pulp Pap. Res. J.* 29(3): 434(2014).
20. Wahlström, T., "Influence of shrinkage and stretch during drying on paper properties," Licentiate thesis, Royal Institute of Technology, Stockholm, Sweden, 1999.
21. McKenzie, A. and Higgins, H., *Aust. J. Appl. Sci.* 6: 208(1955).
22. Beghello, L., Long, L.Y., and Eklund, D., *Pap. Puu* 79(1): 55(1997).
23. Laine, J., Lindström, T., Nordmark, G.G., et al., *Nord. Pulp Pap. Res. J.* 17(1): 50(2002).
24. Duker, E. and Lindström, T., *Nord. Pulp Pap. Res. J.* 23(1): 57(2008).
25. Ankerfors, C. and Wågberg, L., in *Polyelectrolyte Complexes in the Dispersed and Solid State II* (M. Müller, Ed.), Springer, Berlin/Heidelberg, 2013, p. 1.
26. Page, D., *Tappi* 52(4): 674(1969).
27. Davison, R., *Tappi* 55(4): 567(1972).
28. Torgnysdotter, A. and Wågberg, L., *Nord. Pulp Pap. Res. J.* 19(4): 440(2004).
29. Myllytie, P., Yin, J., Holappa, S., et al., *Nord. Pulp Pap. Res. J.* 24(4): 469(2009).

ABOUT THIS PAPER

Cite this article as: Strand, A., Kouko, J., Oksanen, A., et al. *TAPPI J.* 17(9):489(2018). https://doi.org/10.32964/TJ17.09.489

DOI: https://doi.org/10.32964/TJ17.09.489

ISSN: 0734-1415

Publisher: TAPPI Press

Copyright: ©TAPPI Press 2018

About this journal

ABOUT THE AUTHORS

Packaging is a growing sector. Paper is an excellent packaging material but it has some disadvantages, and low elongation is one. We chose this topic to research because we wanted to boost the elongation potential of paper. Research at Åbo Akademi University has dealt with paper chemistry and at VTT with paperphysics. By joining our strengths we were able to get some nice results.



Strand

A difficulty we encountered was to understand how the gel-like layer on the hydrated fibers will af-fect fiber bonding and the fiber network. We used refining, wet-end additives, and spray addition of additives to approach this from different angles.

We discovered that elongation is linear to shrinkage during drying. We were surprised to find that additives or treatments will increase stiffness or elongation, depending on the drying procedure.

For mills, this research might lead to opening up a new product sector, if drying can be performed without restraint. The next step is to test other bio-based additives that could allow the paper to shrink during drying.



Kouko



Oksanen



Salminen



Ketola



Retulainen



Sundberg

Turku, Finland. Kouko and Oksanen are senior scientists and Ketola is a research scientist at VTT Technical Research Centre of Finland, Jyväskylä, Finland. Salminen is a senior scientist at VTT, Tampere, Finland. Retulainen is principle scientist at VTT and adjunct professor at South China University of Technology, Jyväskylä, Finland. Email Sundberg at anna.sundberg@abo.fi

Sundberg is a university lecturer and docent and Strand is a postdoctoral researcher at the Laboratory of Wood and Paper Chemistry, Åbo Akademi University,

Dielectric spectroscopic studies of biological material evolution and application to paper

MARY KOMBOLIAS, JAN OBRZUT, KARL MONTGOMERY, MICHAEL T. POSTEK, DIANNE L. POSTER, AND YAW S. OBENG

ABSTRACT: Current product composition and quality test methods for the paper and pulp industry are mainly based on manual ex-situ wet-bench chemistry techniques. For example, the standard method for determining the furnish of paper, TAPPI T 401 "Fiber analysis of paper and paperboard," relies on the experience and visual acuity of a specially trained analyst to determine the individual plant species present and to quantify the amount of each constituent fiber type in a sheet of paper. Thus, there is a need for a fast, nondestructive analytical technique that leverages intrinsic attributes of the analytes.

In this paper, we demonstrate an application of dielectric spectroscopy (DS) as a potential metrology to differentiate between nonwood pulp and wood pulp fibers. This in-situ, noncontact and nondestructive assessment method has inherent forensic capabilities and is also amiable to quality assurance techniques such as gauge capability studies and real-time statistical process control (SPC).

Application: The dielectric spectroscopy results presented in this paper can nondestructively determine the amount of lignin in paper products and are in principle comparable to the performance specifications of the TAPPI Standard Test Method T 401. This DS method should enable the sources of printing substrates to be both authenticated and validated in real time in a paper testing laboratory environment.

TAPPI Standard Test Method T 401 om-88, "Fiber analysis of paper and paperboard," is currently the most commonly used method to determine the fiber types and their ratios within a paper sample [1]. For example, the TAPPI T 401 Test Method is used to distinguish between the type of pulping process used, i.e., kraft fibers versus sulfite or groundwood processes. The test method is also utilized in applications such as secure credentials manufacturing, law enforcement, custom inspections, archeology, and art conservation. However, the TAPPI T 401 test has many inherent limitations, such as being a manual, colorimetric technique that relies upon the visual acuity and level of experience of an analyst viewing chemically-stained fiber samples mounted onto glass slides via an optical microscope [1]. Sample preparation for the T 401 test is physically laborious and time consuming, requiring boiling, maceration, and acid/base treatments to liberate constituent fibers from a sheet. Finally, the T 401 test results are fraught with multiple sources of imprecision and inaccuracies [2], and liberated fiber samples are also often subject to the effects of atmospheric oxidation once a reagent stain has been applied, making it difficult to archive samples for preservation or specimen banking.

Dielectric spectroscopy (DS) probes the relaxation dynamics of dipoles and mobile charge carriers in response to an alternating electric field and provides information on the molecular fluctuations of dipoles within a matrix in response to rapidly changing electromagnetic fields [3]. This molecular polarization involves rotational reorientation in rapidly changing electromagnetic fields, making DS particularly well suited to examine the dynamics of molecules in confined spaces, such as in paper products. In this work, we leverage water as a probe molecule. The water molecule is hydrogen-bonded to the various polar polymers, such as cellulose and lignin, confined within a sheet of paper. Hydrogen bonding, especially with the adsorbed water molecules, influences the level of cross-linking within the cellulose structure and the level of polarizability [4]. In DS, the dielectric loss profile is a measure of the polarization relaxation, and the magnitude of the polarization is related to the length scale of the displacement. It depends on the electronic polarizability of the polar molecules and can be obtained by summarizing the characteristic polarizabilities, $\alpha 0$, of its covalent bonds. Cellulose is a syndiotactic polymer with many sites available for water to bind via hydrogen bonding, while lignin is a polarizable heteropolymer containing polar and polarizable conjugated bonds, all of which contribute to the dielectric loss function. The value of the dielectric function is also dependent on the density and on moisture content [5]. The total dielectric response of a material results from a vector sum of all the dipole moments of the system in its present orientation; thus, DS is able to distinguish different molecular units of a polymeric system,

like cellulose, in relation to the rate of their orientational dynamics [6].

While there is a significant body of work that uses DS techniques to study cellulose, wood, pulp, and paper, these studies have typically been focused on moisture content determination in the prediction of the mechanical properties based upon the dielectric anisotropy [7-12]. In this paper, we demonstrate the application of DS to test paper beyond moisture and mechanical properties to distinguish and understand the relationships between the various types of fiber present in an analyte [13]. This in-situ, nondestructive assessment method is also amiable to quality assurance techniques such as gauge capability studies and real-time statistical process control (SPC).

Resonant microwave cavity measurement was chosen for this initial work because it is noncontact, nondestructive, and experimentally simple in comparison to other methods of DS analysis. It is also particularly suited to characterize thin, sheeted materials, such as paper, as it eliminates the need for duplicate sets of measurements to account for the two sides of a sample sheet [14]. Resonant microwave cavity measurements have the advantage of being sensitive to both the surface and bulk conductivity, and the surface conductance of a sample material is determined by monitoring a change in the quality factor (Q-factor) of the cavity as a specimen is progressively inserted into the cavity in quantitative correlation with the specimen's surface area and volume [14-16]. In a thin, sheeted material, the surface conductance is a good proxy for the dielectric profile of a material under test (MUT), as it is directly proportional to the dielectric loss,ε'', of the MUT [14-16]. Dielectric loss is an indication of how much heat is dissipated by a dielectric material when an electric field is applied across it; more conductive materials will have a higher dielectric loss value than less conductive materials.

The dielectric loss, ε'', associated with the specimen, is represented as the slope of the line given by Eq. 1 as follows:

$$(Q_s^{-1} - Q_0^{-1}) = \varepsilon'' \frac{4V_X}{V_0} - 2b'' \quad (1)$$

where (Q_s^{-1} – Q_0^{-1}) represents the difference of the reciprocal of the Q-factor of the specimen from the Q-factor of the empty cavity, and $\frac{V_X}{V_0}$ is the ratio of the volume of the inserted specimen to the volume of the empty cavity [15].

MATERIALS AND METHODS

Sample preparation

Paper strips were cut using a rotary cutter. Strip angles were measured using a student's protractor with the basis of the machine direction set to 90°, while the cross direction is set to 0°. Paper strips of width 0.5 cm were cut roughly to 8 cm in length to accommodate the sample holder of the resonant cavity device setup. Sample strips were placed between glass microscope slides and stored in a nitrogen-filled dry box. The samples were re-equilibrated with ambient conditions for several hours before the microwave measurements. The reported thickness of the paper was determined through an average of ten caliper measurements.

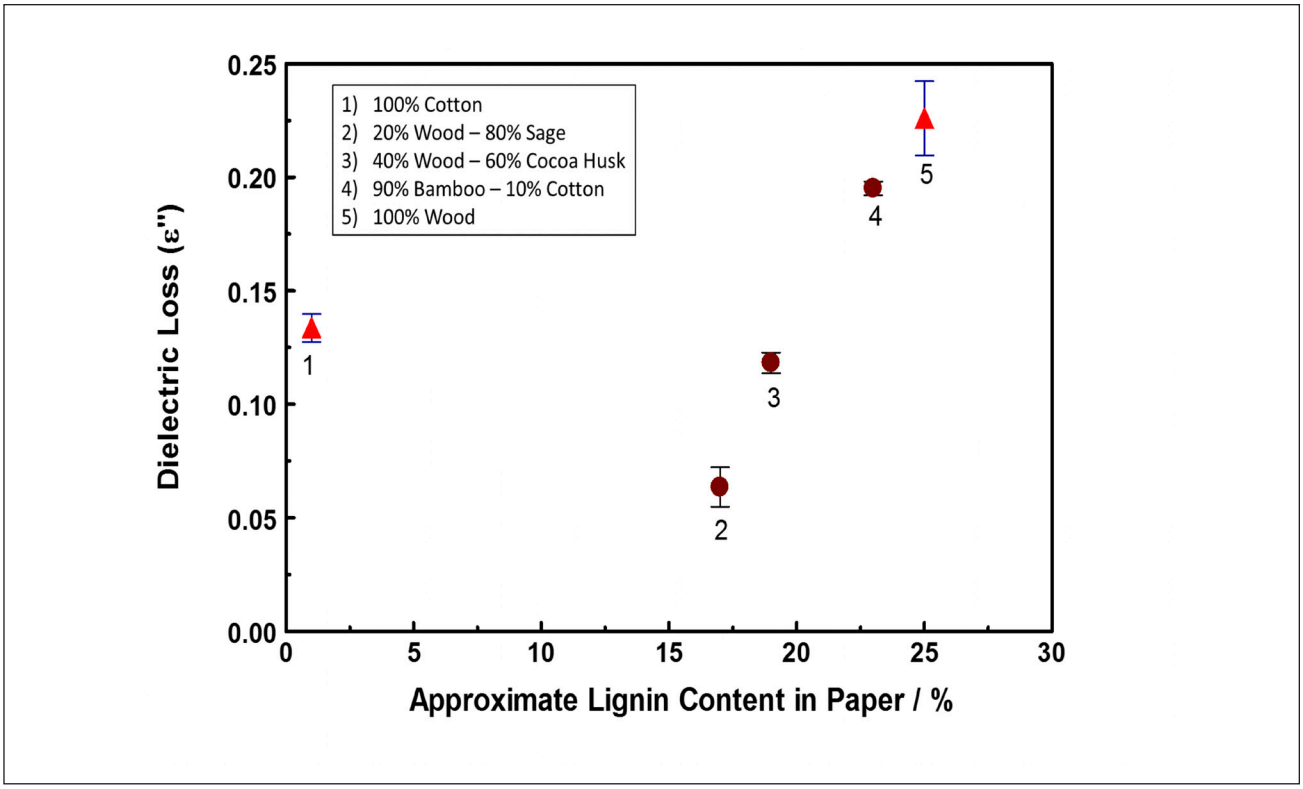
Resonant cavity

The resonant cavity fixture used in this work consists of an air-filled standard R100 rectangular waveguide (Agilent Technologies, Santa Clara, CA, USA; a = 10.16 mm, b = 22.86 mm, l_z =127.0mm), with an operating microwave frequency range of 6.700–13.000 GHz. The cavity is connected to an Agilent N5225A network analyzer with semirigid coaxial cables and coaxial to R100 coupling adapters. The coupling adapters are nearly cross polarized in respect to the waveguide polarization angle, which makes sharp impedance discontinuities at both waveguide ends and consequently the cavity walls. The polarization angle is about 87°, which results from the standard dimensions of the R100 flange and is sufficient to achieve optimal power loading into cavity while maximizing the quality factor. The specimen is inserted into the cavity through a slot machined in the center of the cavity, where the electric field, E_x, attains a maximum value at each odd TE_{10n} mode.

The quality factor, Q_0, and the resonant frequency, f_0, of the empty cavity at the third odd resonant mode TE_{103} at which we make the measurements are 3.200 and 7.435 GHz, respectively. During measurements, the specimen is partially inserted into cavity in steps to a certain volume, V_x, while the quality factor, Q_x, and the resonant frequency, f_x, is recorded. Dielectric permittivity of the paper samples was obtained by plotting the measured V_x, f_x, and Q_x data and solving the two linear perturbation equations for complex permittivity as described in references [14-16]. The measurements were performed in ambient laboratory conditions. The storage history of the samples did not appear to impact the measurements.

RESULTS AND DISCUSSION

Nonwood fibers serve as a source of low environmental impact pulp that is quicker to bring to market than wood-based pulps. Historically, documents of interest to archeologists and historians have often been produced on papers manufactured from nonwood fibers [17]. In the modern era, cotton is the most common nonwood fiber used in papermaking for secure and nonsecure high-value printing papers. Cotton fiber is easily distinguishable from wood fiber via optical microscopy by its dimensions and morphology, as well as its reaction to iodine-based stains, such as Graff's C-Stain [12,13,15]. However, the quantitative determination of cotton content in paper is still a lengthy and onerous task if one relies upon an optical microscope and the TAPPI T 401 procedure. This is because the determination of the cotton content depends upon the correct identification and calculation of the ratios of hardwood and softwood fibers in cotton-blend papers, via optical microscopy. By examining papers with varying proportions of wood to nonwood fiber, we hope to show that resonant cavity dielectric spectroscopy can dis-



1. Dependence of dielectric loss profiles (slope, see Eq. 1) on estimated weighted lignin fraction in the analyte. The weighted lignin fraction was calculated from the average literature values of lignin content in each fiber source weighted for the advertised composition.

cern between wood and nonwood fibers. The discriminating metric, the dielectric loss profile, is presented as the slope of the change in the Q-factor of the cavity as the specimen volume is varied.

Chemically, a typical plant-based paper product is comprised of cellulose (40%–50%), hemicellulose (15%–35%), and lignin (20%–40%). Functionally, lignin combines with the hemicellulose to impart mechanical strength to the composite raw materials. However, lignins are generally undesirable contaminants in paper products, as they age poorly, turn brown, and become acidic, resulting in paper embrittlement with time. While lignins make up 20% to 30% of wood-based paper products, they are only about 1% in cotton-based bond paper. Figure 1 compares the dependence of the observed dielectric loss profile of papers of varying furnishes based on the estimated weight fraction of lignin in each analyte. For this work, test strips cut at 60° relative to the paper's cross direction were used. Inspection of the figure shows that two paper types that were nominally advertised as containing no wood fiber, namely, 100% cotton bond paper and bamboo blend paper (90% bamboo, 10% cotton), showed different dielectric loss responses. The presence of the bamboo fiber significantly elevated the average dielectric loss profile in comparison to the pure cotton bond paper. This disparity in response is attributed to the high lignin content in bamboo [18]. In fact, the lignin content in bamboo (20%–26%) is substantially higher than the normal range of lignin in nonwoody biomass (11%–27%), and closely resembles the ranges reported for softwoods (24%–37%) and hardwoods (17%–30%) [19]. Thus, based on lignin content, the 90% bamboo paper is in fact more chemically like 100% wood paper products. It must be emphasized that in these comparisons the precise chemical structure of the lignins was not considered, although there are many different types of lignins.

The increasing ε'' values with the lignin content are evident in Fig. 1. The effect represents the extent of polarization of water molecules with the paper sample; the more polarized the environment around the water molecule, the larger ε''. Thus, Fig. 1 suggests that the relaxation time of water changes with increasing lignin content of the paper analyte. This is reasonably consistent with the current understanding of the physicochemical impact of lignin in wood. Water molecules in paper may be bound within the fiber wall or adsorb to the surface as free water [20]. Nuclear magnetic resonance (NMR) studies show that the molecular motions of sorbed water in paper depend upon the physical state and crystallinity of the cellulose polymer. The water molecules that are tightly bound to cellulose will exhibit restricted motion as compared to free water [21,22]. Lignins modulate the water mobility in paper by cooperatively binding with hydrophilic polysaccharides to displace the bound water within the fibril network [23]. The lignins also form slightly hydrophobic domains, and water molecules in these channels have higher mobility than tightly bound ones [24]. The presence of less hydrophilic lignin, how-

ever, reduces some of the opportunities for water to associate with the more hydrophilic cellulose polymer but does not necessarily generate unbound water. The mobility of water molecules associated with the lignin hydroxyl regions is significantly reduced due to hydrogen bond formation, but the mobility of the water associated with the bulky methoxyl groups is only slightly restricted, due to steric and hydrophobic effects [25,26]. This restricted motion translates into a lower dielectric loss response. The limited lignin content puts pure cotton paper in a physicochemically distinct class that is different from wood-containing paper in terms of the structure of water in paper.

With this understanding, the DS results clearly illustrate the impact of the chemical composition of the paper analyte on the dielectric loss response, and are consistent with investigations of wood species and cotton using other dielectric spectroscopy techniques [3]. The results suggest that resonant cavity DS could be a useful tool for discriminating between paper of different compositions.

CONCLUSIONS

We have successfully applied resonant cavity DS to nondestructively determine the amount of lignin in paper products. The DS results presented in this paper are in principle comparable to the performance specifications of the TAPPI Standard Test Method T 401 and should enable the sources of printing substrates to be both authenticated and validated in real time. Moreover, DS offers an objective metrology approach that does not rely on the qualitative judgments of an analyst and can be adapted as a means of inline quantifying the amount of lignin present during the manufacturing of paper products. The technique can also be automated and easily integrated into a paper testing laboratory setting to increase the throughput of quality assurance/quality control (QA/QC) acceptance testing and can be extended to disciplines beyond the paper, pulp, and printing industries.

Further studies under tightly controlled test environments will be necessary to assess the technique's robustness and reliability. A proper evaluation of the DS technique must include studies to understand the impact of such product variables as lignin chemistry, filler type and percentage, and pulping process type, at a minimum.

ABOUT THE AUTHORS

We chose to study this topic because the paper and pulp industry needs fast, objective, and nondestructive metrologies for material analyses and quality control. The most challenging aspect of this research was that traditional paper testing angles (i.e., the machine and cross directions) provided poor resolution. This required trying nonorthogonal angles, which are not normally selected when performing physical testing of paper.

In contrast to the traditional TAPPI Standard Test Method T 401, we found there are nondestructive ways to perform fiber analysis without a specially trained human analyst. Also, we observed that nonorthogonal sample angles can yield better information and should be investigated while performing other testing of the physical properties of paper. Measuring samples from a nonorthogonal angle (60°) provided better resolution between paper analytes than measurements taken along the machine and cross directions.

The approach here could ultimately help mills authenticate and validate fiber content of printing substrates in real time, and this technique can be automated and integrated into a paper testing laboratory setting to increase the throughput of QA/QC acceptance testing.

In the future, further studies under tightly controlled test environments will be necessary to assess this technique's robustness and reliability. A proper evaluation of the technique must include studies to understand the impact of such product variables as lignin chemistry, filler type and percentage, and pulping process type, at a minimum.

Kombolias is senior chemist in Testing and Technical Services, Plant Operations, at the United States Government Publishing Office, Washington, DC, USA. Obrzut is materials research engineer and Poster is research chemist in the Materials Measurement Laboratory, National Institute of Standards and Technology, Gaithersburg, MD, USA. Montgomery is engineering student trainee, Postek is senior scientist, and Obeng is research chemist in the Physical Measurement Laboratory, National Institute of Standards and Technology, Gaithersburg, MD, USA. Email Kombolias at mary.kombolias@nist.gov.


Kombolias


Obrzut


Montgomery


Poster


Postek


Obeng

clude studies to understand the impact of such product variables as lignin chemistry, filler type and percentage, and pulping process type, at a minimum. Such studies should be carried out at the handsheet level rather than at the commercial product level. It is our hope that other researchers will contribute to the further development of the measurement technique.

PUBLICATION NOTES

This paper is a contribution of the National Institute of Standards and Technology, not subject to copyright. Certain commercial equipment, instruments, or materials are identified in this report to specify the experimental procedure adequately. Such identification is not intended to imply recommendation or endorsement by the National Institute of Standards and Technology or the United States Government Publishing Office, nor is it intended to imply that the materials or equipment identified are necessarily the best available for the purpose. **TJ**

LITERATURE CITED

1. Woodward, J.H., *Microscopy and Microanlaysis* 8(Suppl. 2): 196(2002).
2. Jablonsky, M., Dubinyova, L., Varga, S., et al., *BioResources* 10(3): 5845(2015).
3. Roig, F., Ramanantsizehena, G., and Lahatra Razafindramisa, F., et al., *Wood Sci. Technol.* 51(6): 1389(2017).
4. Sahin, H.T. and Arslan, M.B., *Int. J. Mol. Sci.* 9(1): 78(2008).
5. Hollertz, R., Arwin, H., Faure, B., et al., *Cellulose* 20(4): 1639(2013).
6. Einfeldt, J. and Kwasniewski, A., *Cellulose* 9(3-4): 225(2002).
7. Driscoll, J.L., *Pap. Technol. Ind.* 17(2): 71(1976).
8. Metaxas, C. and Driscoll, J.L., *J. Microwave Power* 9(2): 79(1974).
9. Morgan, V.T., *IEEE Trans. Dielectr. Electr. Insul.* 5(1): 125(1998).
10. Simula, S., Ikäläinen, S., Niskanen, K., et al., *J. Imaging Sci. Technol.* 43(5): 472(1999).
11. Sundara-Rajan, K., Byrd, L., and Mamishev, A.V., *TAPPI J.* 4(2): 23(2005).
12. Williams, N.H., *J. Microwave Power* 1(3): 73(1966).
13. Kombolias, M., Obeng, Y., Obrzut, J., et al., "Non-destructive analysis of printing substrates via resonant cavity broadband dielectric spectroscopy," *254th Am. Chem. Soc. Natl. Meet.*, American Chemical Society, Washington, DC, 2017.
14. Orloff, N.D., Obrzut, J., Long, C.J., et al., *IEEE Trans. Microwave Theory Tech.* 62(9): 2149(2014).
15. Obrzut, J., Emiroglu, C., Kirilov, O., et al., *Measurement* 87: 146(2016).
16. IEC, "Nanomanufacturing - Key control characteristics - Part 6-4: Graphene - Surface conductance measurement using resonant cavity," IEC TS 62607-6-4:2016, International Electrotechnical Commission, Geneva, Switzerland, 2016.
17. Durkin-Meisterernst, D., Friedrich, M., Hahn, O., et al., *J. Cultural Heritage* 17: 7(2015).
18. Banik, N., Dey, V., and Sastry, G.R.K., *Materials Today: Proceedings* 4(2): 3222(2017).
19. Li, X., "Physical, chemical, and mechanical properties of bamboo and its utilization potential for fiberboard manufacturing," Master's thesis, Louisiana State University, Baton Rouge, LA, USA, 2004.
20. Perkins, E.L. and Batchelor, W.J., *Carbohydr. Polym.* 87(1): 361(2012).
21. Froix, M.F. and Nelson, R., *Macromolecules* 8(6): 726(1975).
22. Natarajan, B., Emiroglu, C., Obrzut, J., et al., *ACS Appl. Mater. Interfaces* 9(16): 14222(2017).
23. Perkins, E.L. and Batchelor, W.J., *Carbohydr. Polym.* 87(1): 361(2012).
24. Glasser, W.G., Northey, R.A., and Schultz, T.P., Eds., *Lignin: Historical, Biological and Materials Perspectives, Vol. 742, ACS Symp. Ser.*, American Chemical Society, Washington, DC, 2000.
25. Hatakeyama, H. and Hatakeyama, T., *Adv. Polym. Sci.* 232: 1(2010).
26. Vu, T., Chafee, A., and Yarocsky, I., *Mol. Simul.* 28(10-11): 981(2002).

ABOUT THIS PAPER

Cite this article as: Kombolias, M., Obrzut, J., Montgomery, K., Postek, M., et al. *TAPPI J.* 17(9):501(2018). https://doi.org/10.32964/TJ17.09.501

DOI: https://doi.org/10.32964/TJ17.09.501

ISSN: 0734-1415

Publisher: TAPPI Press

Copyright: ©TAPPI Press 2018

About this journal

Mineral/microfibrillated cellulose composite materials: High performance products, applications, and product forms

DAVID SKUSE, MARK WINDEBANK, TAFADZWA MOTSI, AND GUILLAUME TELLIER

ABSTRACT: When pulp and minerals are co-processed in aqueous suspension, the mineral acts as a grinding aid, facilitating the cost-effective production of fibrils. Furthermore, this processing allows the utilization of robust industrial milling equipment. There are 40000 dry metric tons of mineral/microfbrillated (MFC) cellulose composite production capacity in operation across three continents. These mineral/MFC products have been cleared by the FDA for use as a dry and wet strength agent in coated and uncoated food contact paper and paperboard applications.

We have previously reported that use of these mineral/MFC composite materials in fiber-based applications allows generally improved wet and dry mechanical properties with concomitant opportunities for cost savings, property improvements, or grade developments and that the materials can be prepared using a range of fibers and minerals.

Here, we: (1) report the development of new products that offer improved performance, (2) compare the performance of these new materials with that of a range of other nanocellulosic material types, (3) illustrate the performance of these new materials in reinforcement (paper and board) and viscosification applications, and (4) discuss product form requirements for different applications.

Application: The benefits of using mineral/MFC composite materials can include cost savings by filler increase; optical and print quality improvements; coating holdout improvements; improvements in many mechanical properties; and improved wet strength and runnability. In addition, these materials offer opportunities for grade development.

Microfibrillated cellulose (MFC) has been known to the paper and packaging industry for many years [1]. However, its commercial use has been limited due, at least in part, to the high energy consumption during production and the relatively complex equipment requirements [2].

We have previously reported a new cost-effective grinding-based method for the production of MFC from minerals and cellulose pulp [3-8]. There are two key aspects to this development: (1) the cellulose fibers are co-processed with mineral particles that act as micro-grinding media, thus reducing the energy requirements, and (2) the process can be accomplished using robust, industrially proven grinding equipment. There are 40000 dry metric tons of mineral/MFC composite production capacity in operation across three continents, with further capacity under construction.

Performance observations

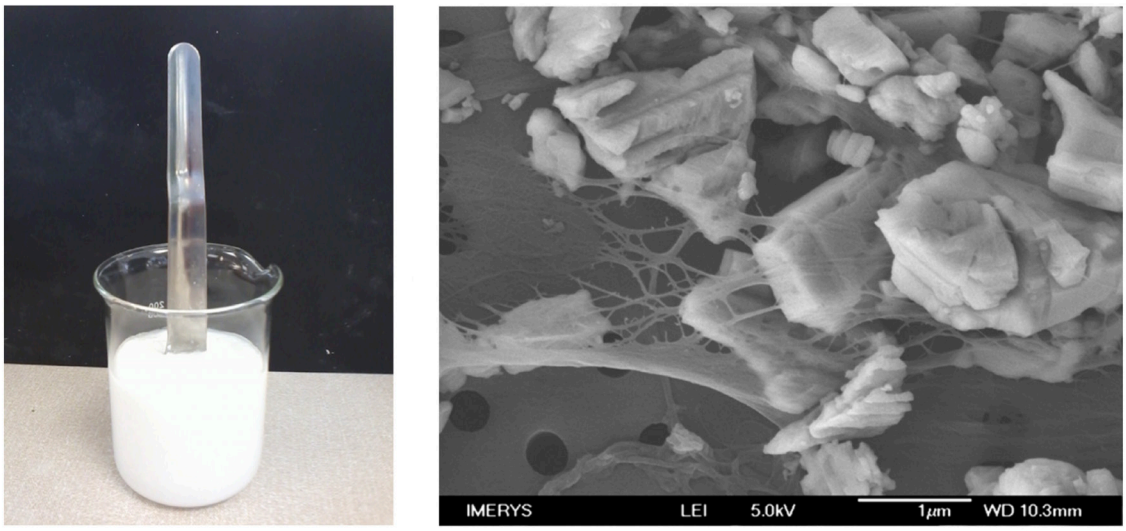
Mineral/MFC composites have been shown to improve both the wet and dry mechanical properties of paper webs, presumably because of increased hydrogen bonding associated with the increased surface area and, hence, bonding area of the MFC component. Typically, use of mineral/MFC composites with a concomitant filler increase is associated with the following: excellent performance stability; increased initial wet web strength; minimal impact on wet end chemistry; overall positive impact on drainage; improved dry mechanical properties; improved opacity; a much tighter sheet (reduced porosity); improved coating holdout; and improved smoothness. Maintaining bulk when fiber is replaced by higher specific gravity filler is a challenge, but it can be managed [3-8].

MATERIALS AND METHODS

Product characterization and test methods

The processing and handling of mineral/MFC composites are dominated by the high viscosity of the MFC, which limits the solids content to ~2.5% fiber solids, depending on the fiber source. This high viscosity is thought to arise from the presence of high surface area hydrophilic fibrils (**Fig. 1**).

Product characterization is relatively straightforward. The total solids and percentage of the solids that are fiber can be conventionally determined. Viscosity at a constant fiber content is a useful performance indicator and can be determined



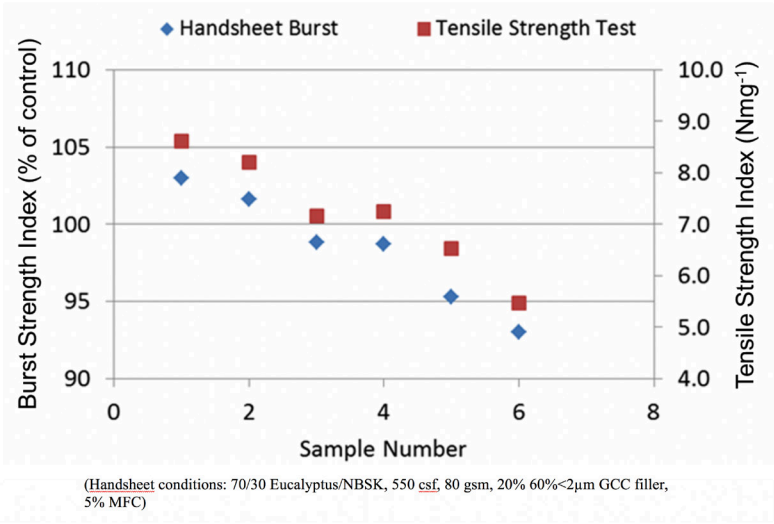
1. Photograph (a) and scanning electron micrograph (b) of mineral/microfibrillated cellulose (MFC) composite showing the high viscosity and fibrillar structure.

using a Brookfield viscometer equipped with a vane geometry spindle. We use an in-house tensile test for characterizing the performance of mineral/MFC composites. In this test, an 80 wt% mineral, 20 wt% MFC sheet is formed using the test mineral/MFC composite, with the sheet mineral content adjusted by addition of further fresh filler as required. This method gives fast, precise results and correlates well with handsheet and full-scale papermaking observations. **Figure 2** shows a comparison between performance data measured using our tensile strength test and conventional handsheets for a series of samples prepared under different processing conditions. The correlation between the tensile test data and the handsheet data can be seen.

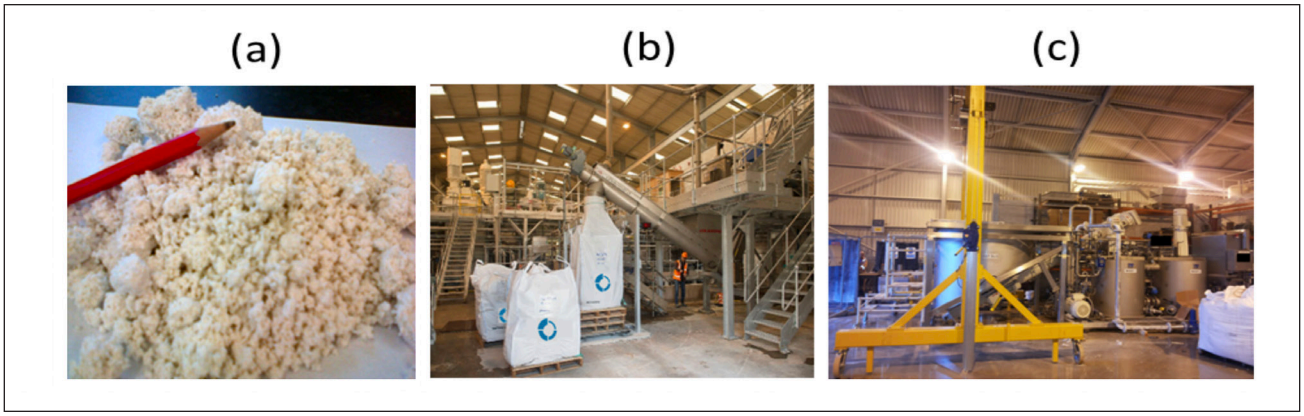
Running full scale trials with low solids products

One of the biggest challenges in the development of mineral/MFC composites has been running full scale trials with potential customers. It is not practical to build an onsite plant for each trial, and it is cost-prohibitive to ship low solids product from remote production locations.

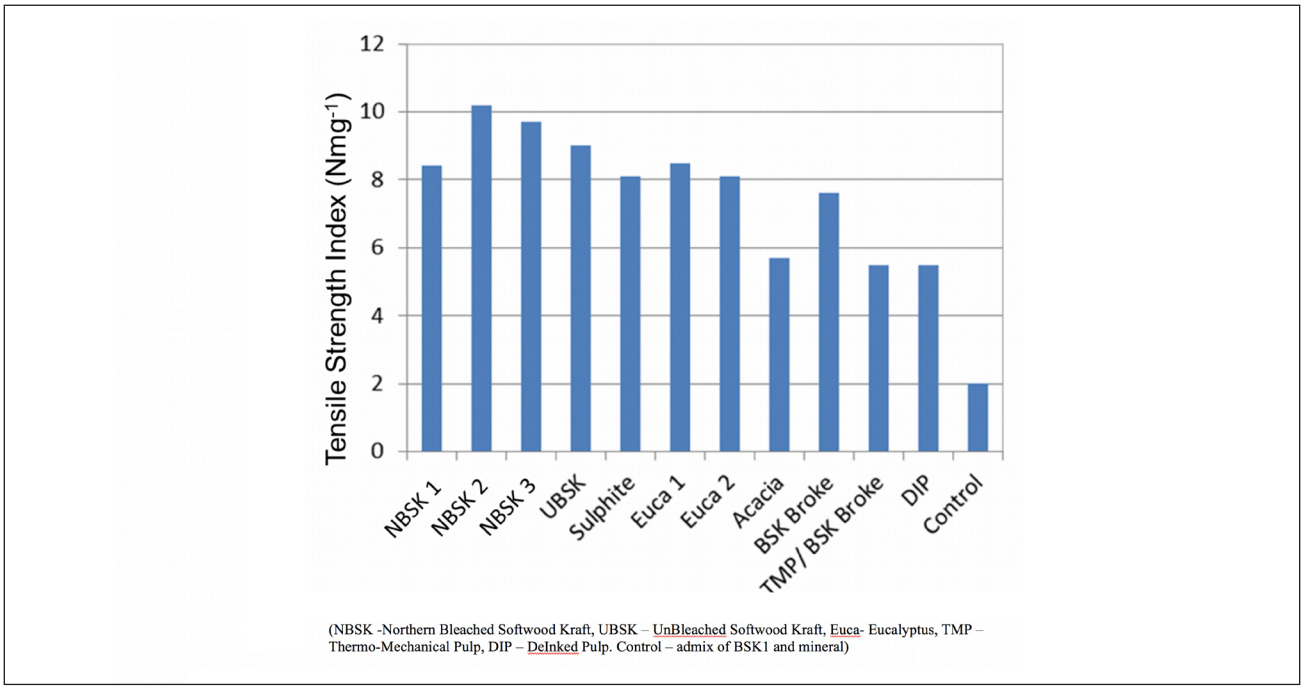
Our solution has been to build a production facility adjacent to our technical resource in Cornwall, UK, along with product dewatering capability. The mineral/MFC composite product is produced using mineral and pulp sources that are relevant for the potential customer location. Once made, the viscous slurry is dewatered to a filter cake product form. Typically, MFC fiber contents of 10–15 wt% can be achieved



2. Comparison of tensile test and handsheet data for a range of mineral/MFC composites samples prepared with varying processing conditions. (Handsheet conditions: 70/30 eucalyptus/northern bleached softwood kraft [NBSK] pulp; 550 csf; 80 gsm; 20% 60%<2μm ground calcium carbonate [GCC] filler; 5% MFC.)



3. Mineral/MFC composite filter cake product form (a), the mineral/ MFC composite production plant in the UK (b), and the mineral/ MFC composite filter cake make-down unit (c).



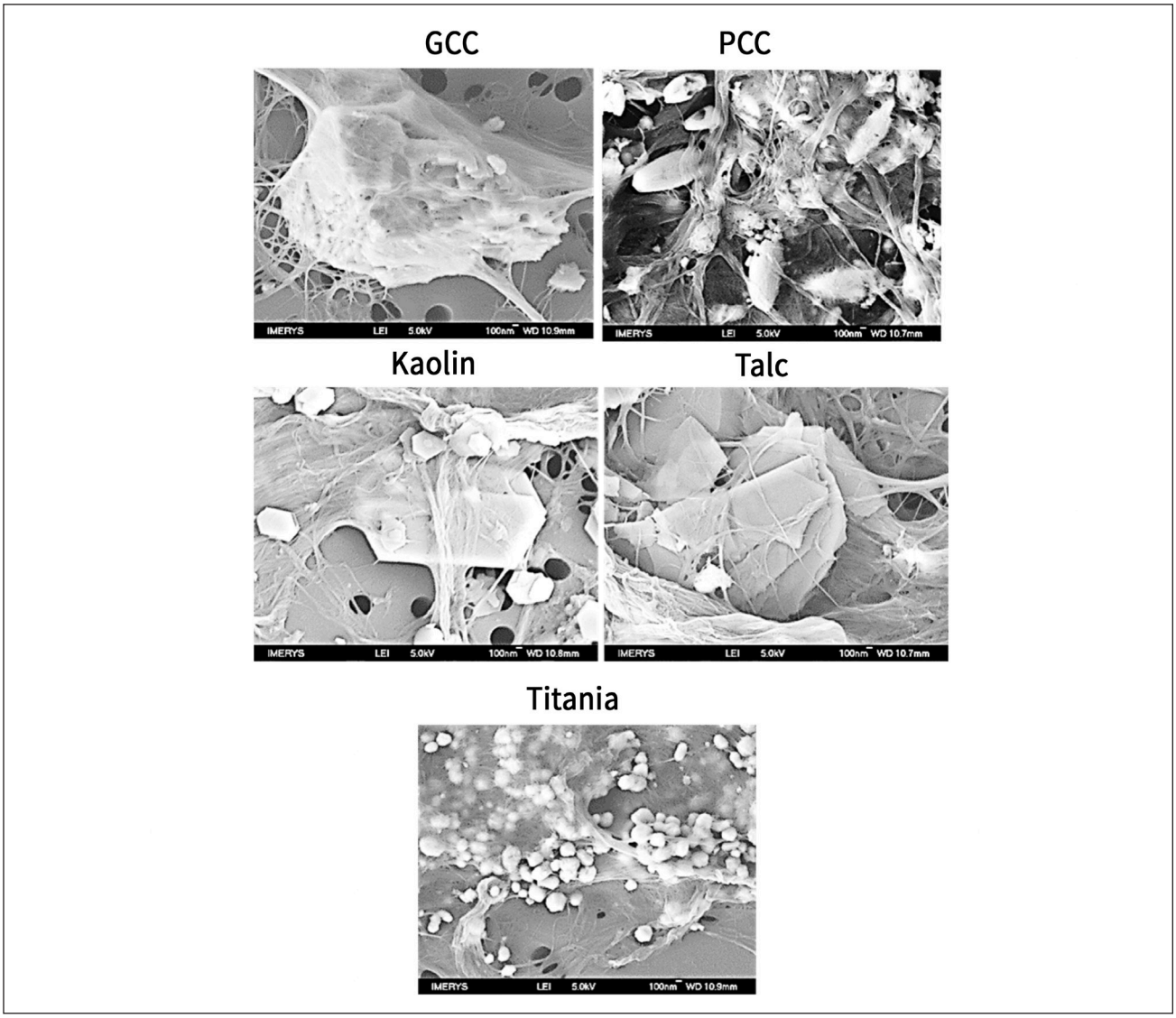
4. Tensile test data for mineral/MFC composites samples prepared with a range of different fibers (80:20; 60%<2µm GCC/fiber; mineral/MFC composite). (NBSK = northern bleached softwood kraft pulp; UBSK = unbleached softwood kraft pulp; Euca = eucalyptus pulp; TMP = thermomechanical pulp; DIP = deinked pulp; Control = mix of bleached softwood kraft pulp 1 [BSK1] and mineral.)

in the cake form (for example, a 20% fiber/80% mineral content product would typically be at 50% total solids). The filter cake product can then be treated with biocide if required prior to shipment in big bags. Once the product has arrived at the trial location, the filter cake is made-down to its original slurry product form using a make-down mixer. The make-down mixer is sized such that product make-down can keep up with an approximately 300000 metric tons/year paper machine running with a 2 wt% MFC dose. The filter cake product form, production plant in the UK, and the make-down unit are shown in **Fig. 3**. Typically, the mineral/MFC composite is produced such that either 50% or 20% of the product dry weight is MFC.

Mineral/MFC composites with a range of fibers

Figure 4 shows the tensile test data for a series of mineral/MFC composites prepared at laboratory scale using the same mineral, a 60%<2µm GCC, and a wide range of different fibers. In each case the process conditions were optimized to give the best performance for the particular mineral/fiber combination.

These data show that it is possible to prepare effective mineral/MFC composites from: (1) a wide range of pulp types, including bleached and unbleached softwood and hardwood kraft pulps and sulfite pulps; and (2) from broke and recycled streams.



5. Scanning electron micrographs of mineral/MFC composites samples prepared with a range of different minerals (80:20; mineral/NBSK; mineral/MFC composite).

Mineral/MFC composites with a range of minerals

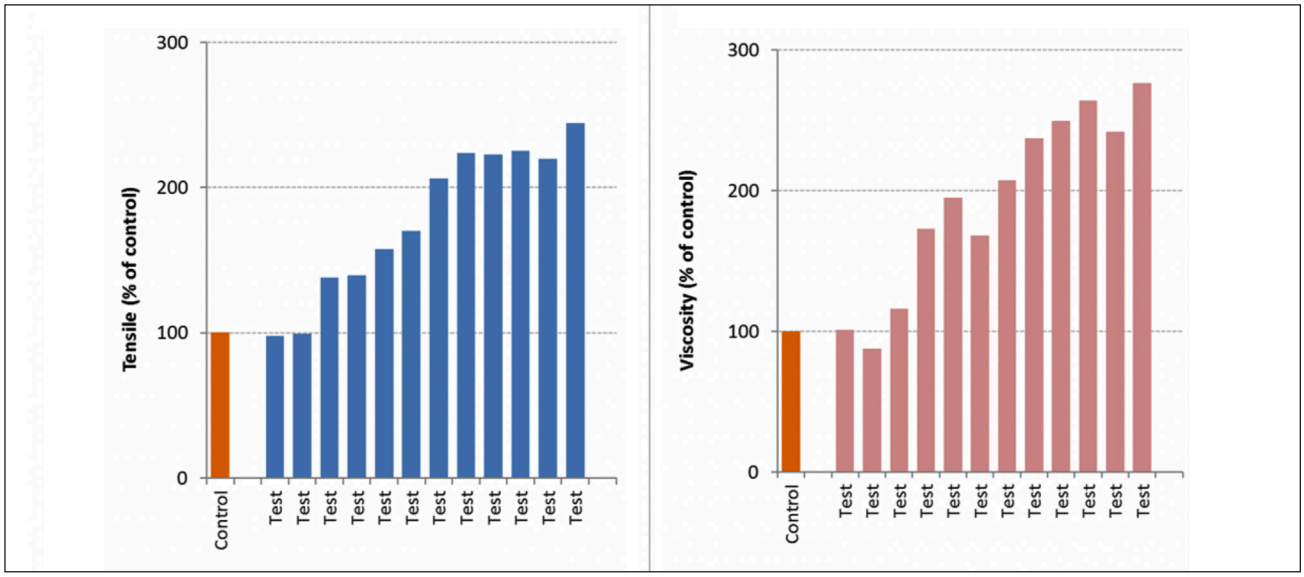
Figure 5 shows scanning electron micrographs of mineral/MFC composites prepared at laboratory scale using the same fiber, an NBSK pulp, but with GCC, PCC, kaolin, talc, and titania as the mineral components. The common fibril structure between the samples and the differing mineralogy are evident.

HEALTH AND SAFETY

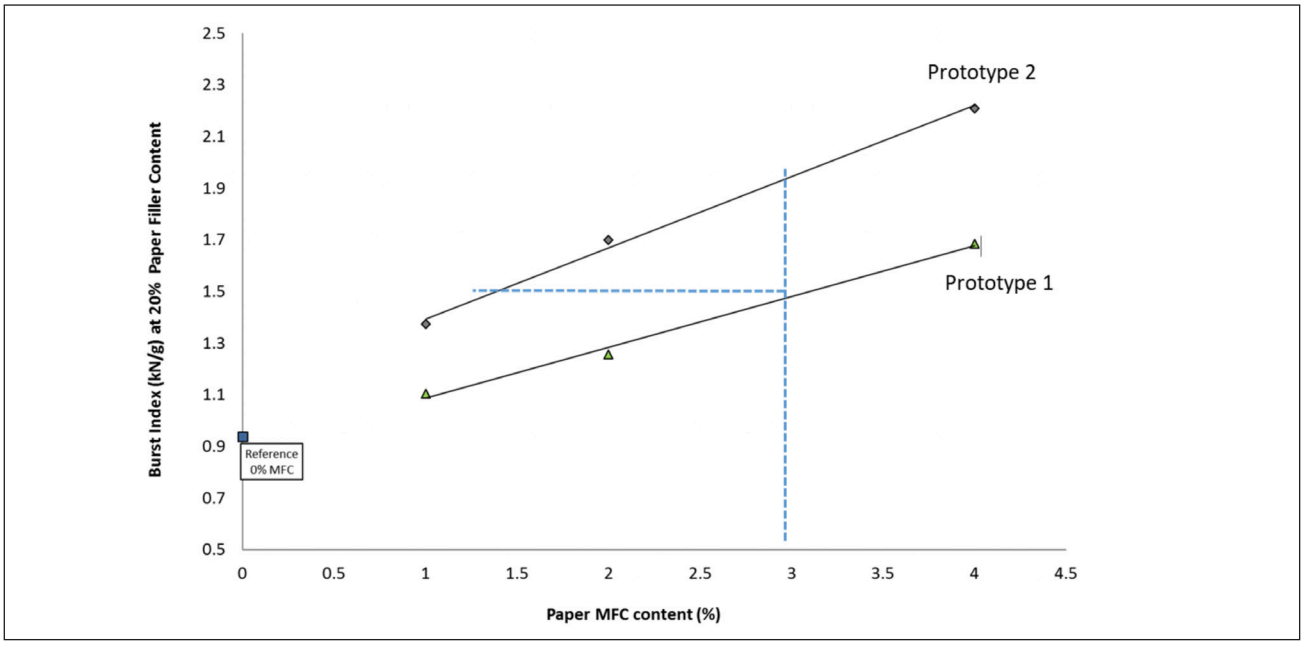
In the United States and Canada, the components of the trademarked FiberLean MFC and grinding minerals calcium carbonate and kaolin have been determined to be existing substances under the Toxic Substances Control Act (TSCA) [9], as well as the Canadian Environmental Protection Act (CEPA) [10], and therefore do not require new substance notifications. As existing substances, there are no restrictions on their manufacture or use in articles in the United States and Canada.

For food packaging applications, the manufacture of FiberLean MFC is cleared according to the specifications in FCN 1582, effective November 6, 2015 [11]. With regard to food contact uses in Canada, no regulatory authorization is required; however, in a voluntary review, Health Canada issued an opinion in January 2016 stating that "…we see no reason to object…" to the use of FiberLean in food contact packaging, under conditions as described in the FCN.

In Europe, cellulose pulp, kaolin and calcium carbonate are exempt from the chemicals legislation Registration, Evaluation, Authorization and Restriction of Chemicals (REACH), including registration. For food contact uses, MFC must be separately authorized in Europe due to the size dimensions, which meet the current European Commission definition of a nanomaterial. We are currently pursuing regulatory authorization for MFC in food use paper and board packaging in Germany and Netherlands. European Union (EU) countries



6. Tensile and viscosity performance of a series of laboratory and pilot scale prototype mineral/MFC composite products (80:20; mineral/MFC composite).



7. Paper sheet burst index at 20 wt% filler content versus MFC content for two mineral/MFC composite product prototypes (30% pine, 70% eucalyptus, 550 csf, 80 gsm handsheets, [80:20, 60%<2um GCC/ NBSK, mineral/MFC composite]).

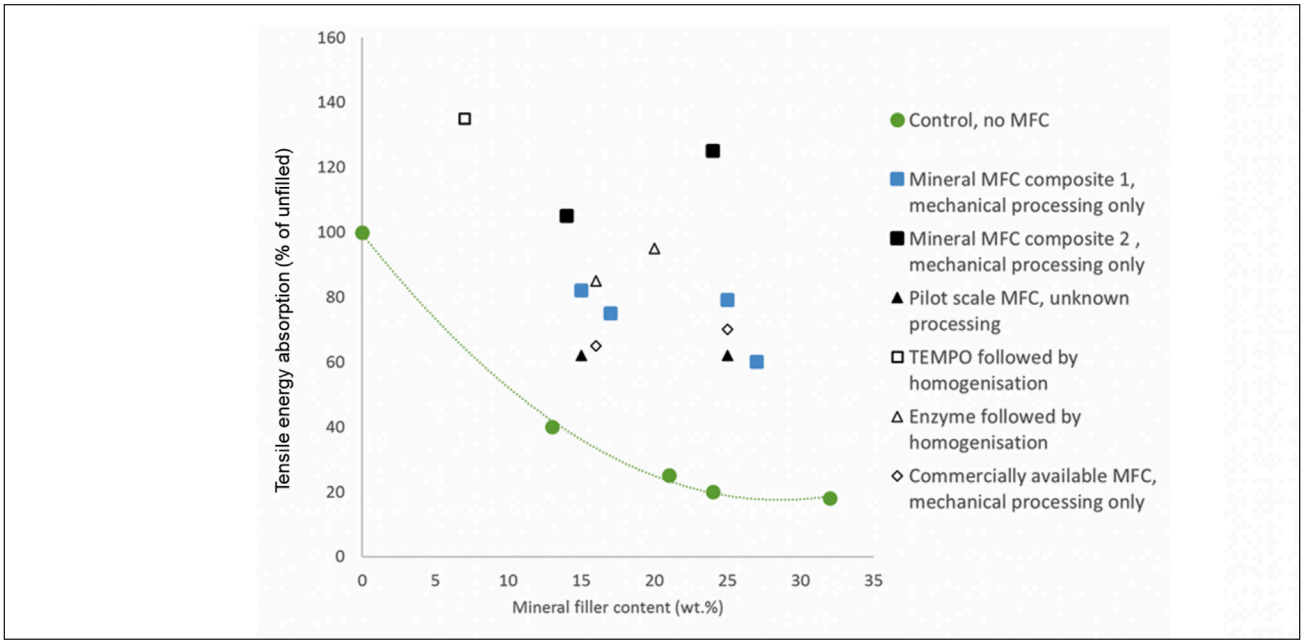
have a mutual recognition of individual country authorization, whereby approval from the German BfR and Dutch RIVM will also be accepted in other EU countries.

MINERAL/MFC COMPOSITE PRODUCTS AND PERFORMANCE

Since our initial launch of mineral/MFC composite products in 2015 [4], we have further developed our products giving improved tensile properties and higher viscosities [8], broadened the MFC contents [6], and increased solids contents [8]. In particular, high solids content products have been a focus, as these open the possibility to have merchant, in addition to satellite, sales models.

Figure 6 shows the tensile and viscosity performance of a series of laboratory and pilot scale prototype mineral/MFC composite products. The increases in tensile and viscosity performance have been achieved by optimization of pulp type and fibrillation environment.

Figure 7 shows representative application data, in this case burst index, that illustrates how these product improvements can affect the performance of mineral/MFC products in paper applications. The data show increased burst index



8. Tensile energy absorption versus mineral filler content for two mineral/MFC composite products and other MFCs (30% pine, 70% eucalyptus, 550 csf, 80 gsm handsheets, [80:20, 60%<2um GCC/NBSK, mineral/MFC composite]).

	Product Dried Solids, wt%	Tensile, % of control	Total Nib Surface Area, mm^2g^{-1}
Feed	30	100	1
High solids product 1	51	130	0
High solids product 2	58	120	1
High solids product 3	70	100	0
High solids product 4	86	100	0

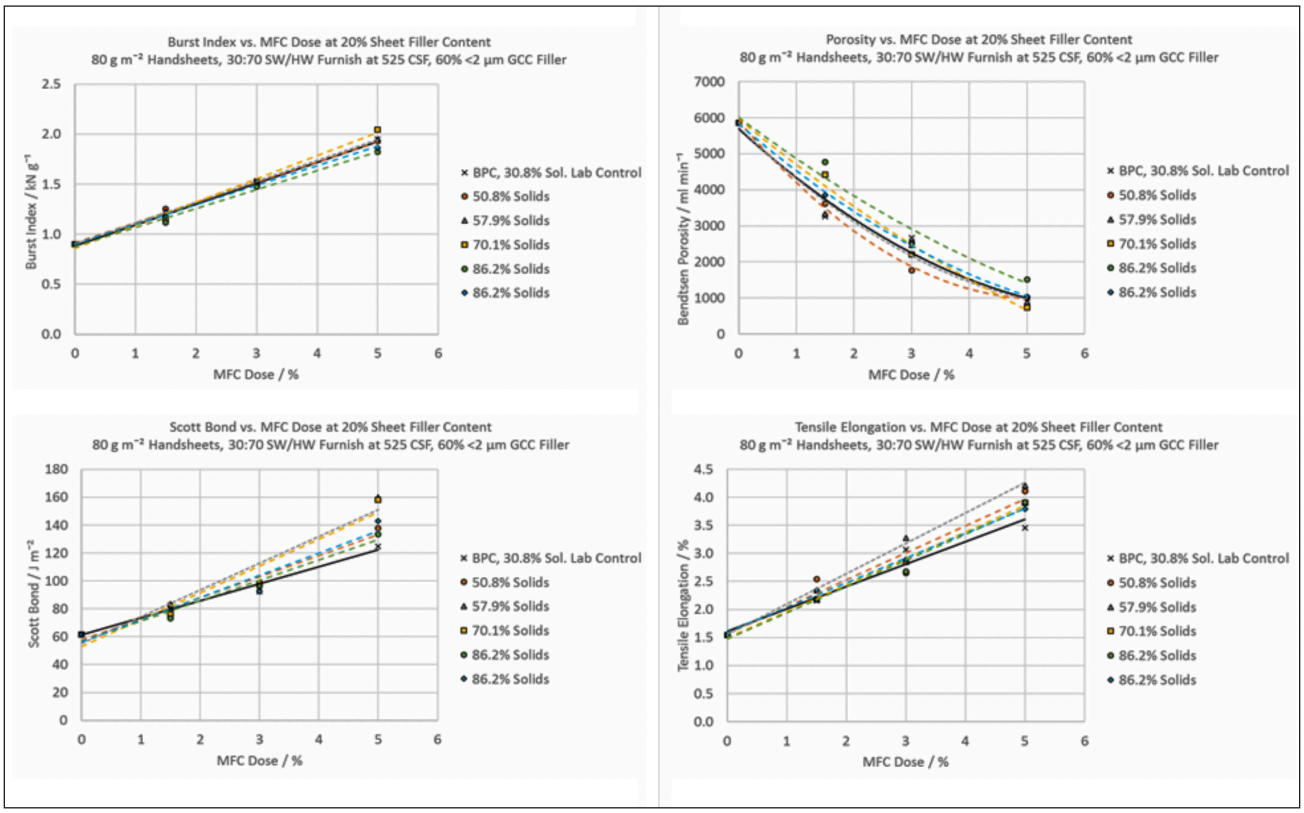
I. Redispersion behavior of high solids mineral/MFC composite products (50:50, 60%<2um GCC/NBSK mineral/MFC composite).



9. High solids mineral/MFC composite product form ([50:50, 60%<2um GCC/NBSK mineral/MFC composite, 51% solids)).

	T=0		T=90 days		T=120 days		T=150 days	
	Tensile Control, %	Viscosity Control, %	Tensile, % of control	Viscosity, % of control	Tensile, % of control	Viscosity, % of control	Tensile, % of control	Viscosity, % of control
Test 1	100	100	105	118	105	112	102	130
Test 2	100	100	104	120	108	113	101	130
Test 3	100	100	102	112	107	120	100	128

II. Redispersion behavior of high solids mineral/MFC composite products (50:50, 60%<2um GCC/NBSK mineral/MFC composite at 51% solids) stored for 90, 120, and 150 days.



10. Paper properties of high solids mineral/MFC composites (50:50, 60%<2um GCC/NBSK mineral/MFC composite feed material dried to 51%, 58%, 70%, and 86% solids and redispersed).

with increased MFC content and enhanced performance with an improved prototype.

Comparison of mineral/MFC composites with other MFCs **Figure 8** shows how two mineral/ MFC composite prototypes compare in performance with MFCs prepared by other process routes in a paper application. The data show that the mineral/MFC composites give at least equivalent performance to that obtained with other MFCs.

Mineral/MFC composites product forms

The availability of a high solids MFC product form is highly desirable, as this opens the opportunity for merchant sales. It is straightforward to dry MFC, but the challenge lies in the redispersion of the dried material in water at the customer location. Mineral/MFC composites can be dried to high solids and then easily redispersed with low energy input in water so that the original properties are recovered. **Table I** shows data for a series of high solids mineral/MFC product prototypes. The 50:50, 60%<2um GCC/northern bleached softwood kraft (NBSK) mineral/MFC composite feed material was dried from the feed presscake solids of 30% to 51%, 58%, 70%, and 86% solids, respectively. These high solids materials were then stored for several months before being redispersed in water, and the tensile behavior and aggregate (nib) content of the redispersed materials characterized. The data show that the original tensile behavior was recovered for all the samples and all the aggregate contents were equivalent to the feed.

Figure 9 shows images of the high solids products. These

products were prepared at full production scale. The pelletized product form gives a higher packed density. A biocide suitable for the end use application can be added during the process.

Table II shows the redispersed tensile and viscosity behavior of high solids mineral/MFC composite materials that have been stored for up 150 days. The data show no loss in tensile or viscosity behavior during storage.

Performance of high solids mineral/MFC product forms

Figure 10 shows data from a handsheet study that used 50:50, 60%<2um GCC/ NBSK mineral/ MFC composite material that had been dried to 51%, 58%, 70%, and 86% solids prior to redispersion. The data show that the burst index, porosity, Scott bond, and tensile elongation behavior of sheets containing the dried and redispersed mineral/MFC composite materials was the same as the undried control.

Testing of the high solids dried mineral/MFC composite materials indicated that the made-down product had no lumpy texture in standard matt paint and could be screened through standard paint industry screens. The made-down high solids product could also be extruded through fine capillaries in a nonwovens test.

CONCLUSIONS

In this paper, after an initial introduction to mineral/MFC composite materials we have: (1) shown that the tensile and viscosification behavior of the materials has developed since the initial concept was introduced in 2015; (2) shown that mineral/MFC composite behavior is comparable to that of other MFCs; and (3) introduced high solids product forms of mineral/MFC composites and illustrated their application behavior.

Given the robust process, the cost-effective nature of these products, their proven full-scale availability and the imminent availability of high solids product forms we believe that mineral/MFC composite materials are an important additive for both paper and packaging applications. **TJ**

ACKNOWLEDEMENTS

The authors are grateful to TAPPI for the opportunity to publish and present this work.

LITERATURE CITED

1. Syverud, K., Xhanari, K., Chinga-Carrasco, G., et al., *J. Nanopart. Res.* 13: 772(2011).
2. Fukuzumi, H., Saito, T., Iwata, T., et al., *Biomacromolecules* 10(1): 162(2009).
3. Svending, P., "Commercial break-through in MFC processing," *TAPPI Nanotechnol. Conf.*, TAPPI Press, Atlanta, GA, USA, 2014.
4. Skuse, D.R., Phipps, J.S., and Svending, P., "Development, scale-up and production of mineral/microfibrillated cellulose composite materials for paper and board applications," *TAPPI PaperCon*, TAPPI Press, Atlanta, 2015.
5. Skuse, D.R., Phipps, J.S., and Svending, P., "Development, scale-up and production of mineral/microfibrillated cellulose composite materials for paper and board applications," *TAPPI Int. Conf. Nanotechnol. Renewable Mater.*, TAPPI Press, Atlanta, 2015.

ABOUT THE AUTHORS


Skuse


Windebank


Motsi


Tellier

The availability of MFC in industrially relevant quantities and at practical costs opens a wealth of opportunities for the improvement of paper and board grades, with some opportunities for new product types and many opportunities in other types of engineered materials. This paper builds on previous publications from our group and details developments in the technology since our last report.

The principle difference between this work and others is that of scale. Most of the materials described are routinely produced in multi-metric ton quantities.

Through our work, we discovered how impressive cellulose is as material, and that there is a wide breadth of possible applications where MFC composites may have value. For mills, the benefits can include cost savings by filler increase; optical and print quality improvements; coating holdout improvements; improvements in many mechanical properties; and improved wet strength and runnability.

Our next steps are the rollout of improved products and high solids products, as well as grade developments in the printing and writing and packaging areas.

Skuse is vice president of Technology, Windebank is senior research engineer, Motsi is senior research engineer, and Tellier is vice president of Manufacturing at FiberLean Technologies Ltd., Cornwall, UK. Email Skuse at david.skuse@fiberlean.com.

6. Skuse, D.R., Svending, P., Phipps, J.S., et al., "New commercial process for production of mineral/microfibrillated cellulose composite materials exhibits great flexibility," *TAPPI PaperCon*, TAPPI Press, Atlanta, 2016.

7. Skuse, D.R., Svending, P., Phipps, J.S., et al., "New commercial process for production of mineral/microfibrillated cellulose composite materials exhibits great flexibility," *TAPPI Int. Conf. Nanotechnol. Renewable Mater.*, TAPPI Press, Atlanta, 2016.

8. Skuse, D.R., Svending, P., Phipps, J.S., et al., "Mineral/microfibrillated cellulose composite materials: Next generation products, applications and product forms," *TAPPI Int. Conf. Nanotechnol. Renewable Mater.*, TAPPI Press, Atlanta, 2017.

9. U.S. EPA, Toxic Substances Control Act (15 U.S.C. §2601 et seq. (1976)), Chemical Substances Control Inventory, U.S. Environmental Protection Agency, Washington, DC, 2016.

10. Government of Canada, "Lists of substances: Canadian Environmental Protection Act, 1999." Available [Online] *https://www.canada.ca/en/environment-climate-change/services/canadian-environmental-protection-act-registry/substances-list.html*.

11. U.S. FDA, "Inventory of Effective Food Contact Substance Notifications," FCN No. 1582. Americarb Inc., U.S. Food and Drug Administration, Silver Spring, MD, USA. Available [Online] *https://www.accessdata.fda.gov/scripts/fdcc/?set=FCN&id=1582&sort=FCN_No&order=DESC&startrow=1&type=basic&search=1582* <25Sept2018>.

ABOUT THIS PAPER

Cite this article as: Skuse, D., Windebank, M., Motsi, T., Teller, G. *TAPPI J.* 17(9):507(2018). https://doi.org/10.32964/TJ17.09.507

DOI: https://doi.org/10.32964/TJ17.09.507

ISSN: 0734-1415

Publisher: TAPPI Press

Copyright: ©TAPPI Press 2018

About this journal

Regulatory and sustainability initiatives lead to improved polyaminopolyamide-epichlorohydrin (PAE) wet-strength resins and paper products

MARK T. CRISP AND RICHARD J. RIEHLE

ABSTRACT: Polyaminopolyamide-epichlorohydrin (PAE) resins are the predominant commercial products used to manufacture wet-strengthened paper products for grades requiring wet-strength permanence. Since their development in the late 1950s, the first generation (G1) resins have proven to be one of the most cost-effective technologies available to provide wet strength to paper. Throughout the past three decades, regulatory directives and sustainability initiatives from various organizations have driven the development of cleaner and safer PAE resins and paper products. Early efforts in this area focused on improving worker safety and reducing the impact of PAE resins on the environment. These efforts led to the development of resins containing significantly reduced levels of 1,3-dichloro-2-propanol (1,3-DCP) and 3-monochloropropane-1,2-diol (3-MCPD), potentially carcinogenic byproducts formed during the manufacturing process of PAE resins. As the levels of these byproducts decreased, the environmental, health, and safety (EH&S) profile of PAE resins and paper products improved. Recent initiatives from major retailers are focusing on product ingredient transparency and quality, thus encouraging the development of safer product formulations while maintaining performance.

PAE resin research over the past 20 years has been directed toward regulatory requirements to improve consumer safety and minimize exposure to potentially carcinogenic materials found in various paper products. One of the best known regulatory requirements is the recommendations of the German Federal Institute for Risk Assessment (BfR), which defines the levels of 1,3-DCP and 3-MCPD that can be extracted by water from various food contact grades of paper. These criteria led to the development of third generation (G3) products that contain very low levels of 1,3-DCP (typically <10 parts per million in the as-received/delivered resin). This paper outlines the PAE resin chemical contributors to adsorbable organic halogens and 3-MCPD in paper and provides recommendations for the use of each PAE resin product generation (G1, G1.5, G2, G2.5, and G3).

Application: Paper manufacturers and their customers have key information needed for the proper choice of PAE resin to meet regulatory and sustainability initiatives.

Polyaminopolyamide-epichlorohydrin (PAE) resins are the predominant chemistry used to wet strengthen a diverse range of paper industry products for grades requiring wet strength permanence. First developed and marketed in 1957 [1,2], the early PAE resins quickly displaced urea-formaldehyde (UF) technology for wet strengthening tissue and towel products. Today, they are also used to provide wet strength to grades such as liquid packaging board (for milk and juice), board (beverage carriers), tea bag and coffee filter paper, and specialty grades such as currency. These paper products are designed to retain a portion of their dry strength, typically 20%–35%, under aqueous conditions to fulfill the consumer need.

Following the initial development of PAE resins 60 years ago, resin manufacturers continued to conduct research and innovate. The innovation focus has been on development of products with (1) an improved environmental, health and safety (EH&S) profile and (2) higher solids to reduce freight costs. Although products containing higher solids typically were less efficient, G1 products recently closed that gap [3]. The effort to improve the EH&S profile resulted in less efficient and more expensive PAE resin products. Innovative concepts and advances in process chemistry and engineering improved the cost efficiency of G2 products and closed the efficiency gap between G2 and G3 product offerings.

In the past 30 years, greater awareness of the hazards posed to human health and the environment by some of the processes and chemicals used to manufacture paper products has resulted in various regulatory measures being imposed on the industry. To ensure business sustainability, papermakers must comply with these regulatory measures, typically through operational changes. In addition, these same regulatory concerns have motivated chemical suppliers to develop new products and technologies to help papermakers meet these ever-changing demands.

As these regulatory measures evolved, newer generations of PAE resins were developed. Typically, these regulatory measures are specific to a region; therefore, the development of a global solution will not meet the current manufacturer and consumer needs in all regions. However, paper manufacturers who produce for the global market must ensure that regulatory compliance for both grade and region are met [4].

In addition to the external regulatory measures imposed on the industry, major producers of wet-strengthened paper products maintain corporate sustainability programs to ensure the long-term viability of their businesses. These programs often include a commitment to environmental sustainability by reducing the impact of their overall manufacturing footprint.

PAE resin manufacturers have focused their product improvement and development efforts on the paper manufacturers' improved health and sustainability objectives. These objectives have varied widely due to market and regional differences. Regulatory directives are the main catalyst for cleaner products with much lower levels of epichlorohydrin byproducts and adsorbable organic halogens (AOX). Higher solids and higher efficiency PAE resins positively influence sustainability. The types of sustainability directives and initiatives that need to be considered are summarized in Table I.

BACKGROUND

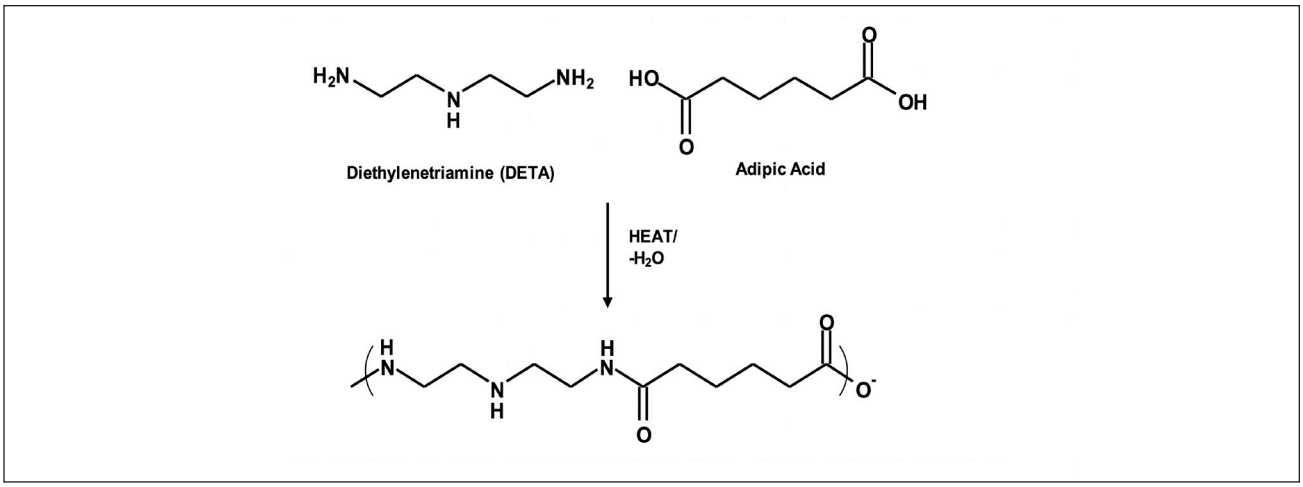
The basic underlying chemistry for the manufacture of a PAE resin has not changed in nearly 60 years [5,6]. A polyaminopolyamide with low molecular weight, known as a prepolymer, is initially formed by polycondensation of adipic acid and diethylenetriamine (DETA), but alternative dibasic acids (and acid derivatives) and polyalkylenepolyamines have been used (Fig. 1). The ratio of the adipic acid and DETA monomers can be varied to provide a prepolymer with higher amine functionality. This prepolymer allows for PAE resins with lower levels of 1,3-dichloropropanol (1,3-DCP) and 3-monochloropropane-1,2-diol (3-MCPD), which are byproducts resulting from side reactions involving the epichlorohydrin (epi) monomer [7,8]. An aqueous mixture of the prepolymer is alkylated with epichlorohydrin at typically 20°C–40°C to initially form tertiary aminochlorohydrin (ACH) functionality. Good temperature control is required to minimize epichlorohydrin hydrolysis and to minimize chloride ion formation [9,10]. After the initial alkylation step, the reaction mixture is typically heated to 60°C–80°C. This step results in further conversion of ACH functionality to azetidinium (AZE) functionality (Fig. 2) and further crosslinking to build a PAE resin of the desired molecular weight. The reaction is quenched with acid (typically sulfuric acid) at the target viscosity and cooled to typically < 25°C before pumping to storage.

DISCUSSION

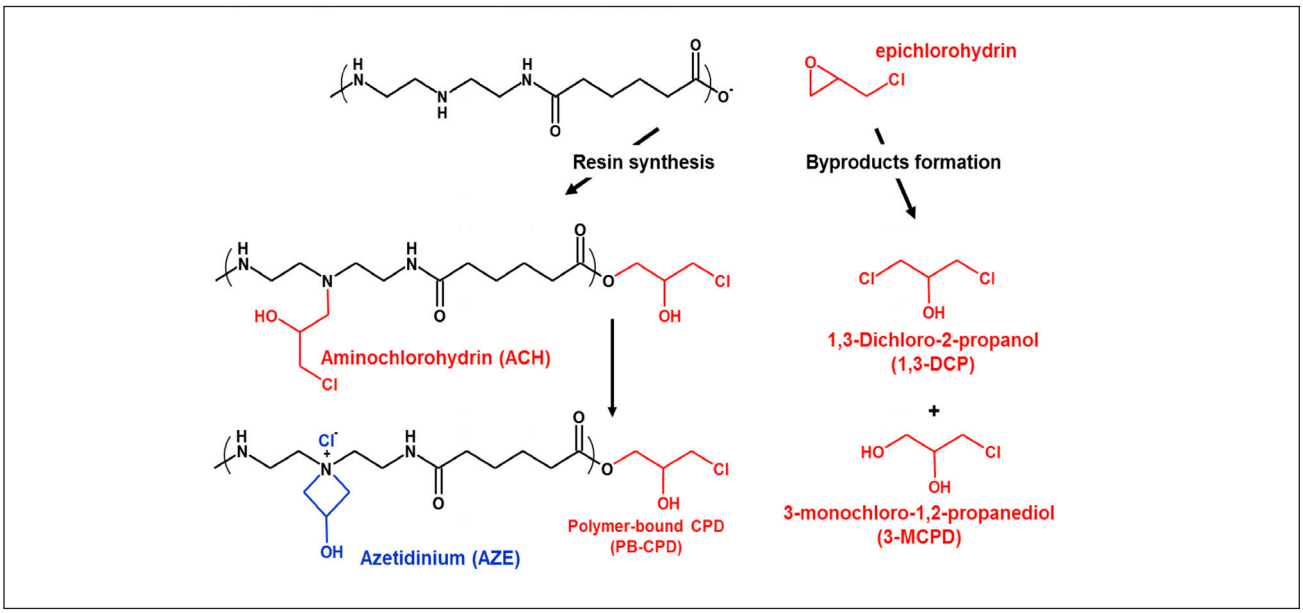
To confirm compliance with governmental directives and nongovernmental organizations' guidelines, the chemistry that affects each directive and guideline must be considered. In PAE wet-strength resins, two types of organic chlorine species exist (Fig. 2): (1) free epichlorohydrin byproducts (1,3-DCP and 3-MCPD) and epichlorohydrin (typically at very low levels) and (2) polymer-bound organic chlorine (PBOX) species. These PBOX species are ACH, the principle species

Governmental Regulations	Nongovernmental Organization Guidelines	Cost and Performance
Worker safety (e.g., Globally Harmonized System [GHS] safety data sheets [SDSs], Occupational Safety and Health Administration [OSHA], California Proposition 65, volatile organic compounds [VOCs]) using polyaminopolyamide-epichlorohydrin (PAE) resins	Guidelines for product and environment (e.g., European Union Ecolabel, Blue Angel, Nordic Ecolabel, and Green Seal, paper manufacturers, and major retailers)	Maximize solids to minimize transportation (e.g., reduce freight cost, carbon dioxide, and pollutants), "fewer trucks on the road"
Consumer safety (e.g., U.S. Food and Drug Administration [FDA], German Federal Institute for Risk Assessment [BfR], Brazil National Health Surveillance Agency [ANVISA]) using paper products made with PAE resins		Resin efficiency at time of customer usage; more efficient resin allows lower dosage, higher retention of PAE (less PAE resin in effluent)
Environmental safety (e.g., GHS; U.S. Environmental Protection Agency [EPA]; Registration, Evaluation, Authorization and Restriction of Chemicals [REACH]) using PAE resins (adsorbable organic halogens [AOX] in effluent, aquatic toxicity, VOC)		

I. Types of sustainability directives and initiatives.



1. Typical manufacture of polyaminopolyamide intermediate to polyaminopolyamide-epichlorohydrin (PAE) resin.



2. Typical PAE resin manufacture and formation of epichlorohydrin byproducts.

formed from the initial reaction between epichlorohydrin and the amine groups of the poly(adipic acid-co-diethylenetriamine) prepolymer and PB-CPD, the species formed from the reaction between epichlorohydrin and the acid end groups of the prepolymer. An additional free epichlorohydrin byproduct is 2,3-dichloropropanol (2,3-DCP), which, except for its AOX content, is not regulated. This byproduct is typically at very low levels but can be significant when low-quality epichlorohydrin is used in the PAE resin manufacturing process.

The free epichlorohydrin byproducts and the PBOX species in the PAE resin are interrelated regarding regulations and guidelines, which can result in confusion. In an effort to clarify, the following sections will be presented; (1) global governmental regulatory directives and nongovernmental organizations' guidelines, (2) worker safety with PAE resins and epichlorohydrin byproducts, (3) consumer safety with paper products treated with PAE resins, (4) environmental effects of PAE resins and AOX and (5) PAE resins' effects on the total organic chlorine content of paper. As PAE resins evolved, the product definitions regarding AOX and epichlorohydrin byproducts became inconsistent across product generations [11]. These definitions are not arbitrary but are based on key customer needs.

Global governmental regulatory directives and guidelines by nongovernmental organizations

All PAE resins sold as wet-strength resins in the United States, including recently commercialized resins, comply with the U.S. Food and Drug Administration (FDA) 21 CFR 176.170. The food contact notification (FCN) process for new food contact substances indicates only one instance (FCN 276) of a new PAE resin chemistry, but this product is not currently available

commercially [12]. For the foreseeable future, no new FDA (i.e., no new legal regulatory) requirements are expected in the United States.

However, in the decades since FDA approval of PAE resins, several global governmental directives and nongovernmental initiatives have affected the levels of 1,3-DCP, 3-MCPD, and AOX in PAE resins and in the final paper consumer product. Best known are the recommendations of the German Federal Institute for Risk Assessment (BfR), which are relevant to food contact paper products manufactured or sold in the European Union (EU). In the future, other regions likely will implement BfR-type regulations. For example, Brazil's National Health Surveillance Agency (ANVISA) has implemented new regulations that took effect on June 29, 2018, and are similar to the BfR recommendations [13]. Before implementation, PAE resin manufacturers and paper manufacturers in Brazil prepared for these changes.

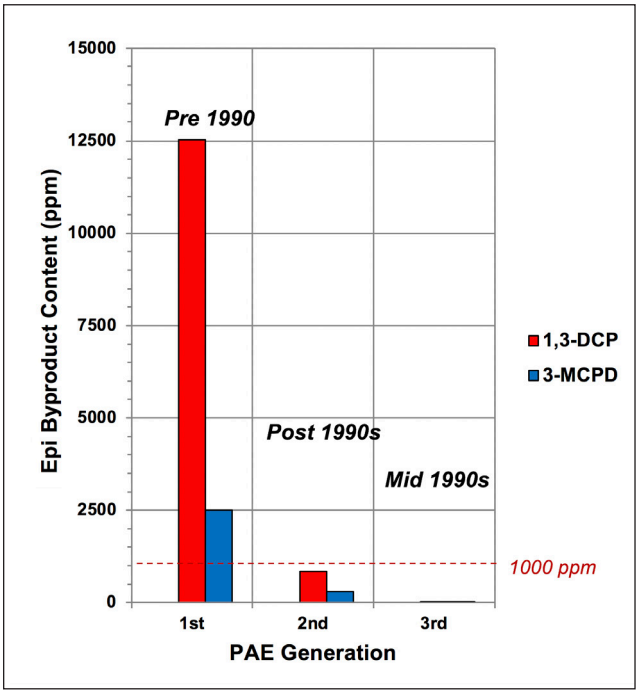
In addition to governmental regulatory directives, guidelines by nongovernmental organizations (i.e., not legally binding) are globally active and can affect PAE resins. The well-known Nordic Ecolabel and EU Ecolabel guidelines restrict the levels of 1,3-DCP and 3-MCPD in PAE resins. Even in the United States, major retailers have announced recent initiatives that could affect the levels of 1,3-DCP and 3-MCPD in food contact packaging [14,15]. Recently, PAE resin manufacturers and paper manufacturers have addressed the impact of California Proposition 65. Furthermore, in North America, towel, paper, and paperboard manufacturers typically have internal sustainability initiatives to address the levels of 1,3-DCP and 3-MCPD in their products.

In addition, before June 1, 2015, PAE resin manufacturers addressed the hazard communication changes mandated by the legal requirement to implement the Globally Harmonized System (GHS). In North America, these changes resulted in some customer concerns with the new hazard statements that have to be addressed. Moreover, a comparison of GHS safety data sheets (SDSs) shows clear differences between manufacturers. For example, some PAE resin products containing >0.1% (1000 parts per million [ppm]) of 3-MCPD indicate category 1B reproductive toxicity and include the H360 statement "may damage fertility or the unborn child" on the SDS.

PAE resins, epichlorohydrin byproducts, and their impact on worker safety

While epichlorohydrin is used to generate the key reactive functionality (AZE) and structure (molecular weight) for PAE resins, side reactions with epichlorohydrin result in the formation of 1,3-DCP and 3-MCPD. The formation of 3-MCPD is the result of hydrolysis of epichlorohydrin. The formation of 1,3-DCP results from the reaction between epichlorohydrin and chloride ion. The chloride ion is generated from the cross-linking reaction and from the formation of AZE species.

One of the concerns of users of PAE resins is the level of 1,3-DCP and 3-MCPD and very low levels of residual epichlorohydrin present in the wet-strength resin. All three substances are considered to be carcinogenic [16-23]. When first developed, PAE resins had high levels of 1,3-DCP and 3-MCPD (Fig. 3). Freshly produced resins have detectable quantities of residual epichlorohydrin. The level of residual epichlorohydrin rapidly decreases to nondetectable levels (<1 ppm) with all modern PAE resins.



3. The reduction of epichlorohydrin byproducts (12.5% active basis) and the historical definitions of generations 1, 2, and 3 resins.

As the carcinogenic nature of these organochloride species became understood, European (and similar North American) legislation was introduced that necessitated that containers of PAE resin containing 1000 ppm or more of 1,3-DCP (in the as delivered/received product) would have to be labeled with "may cause cancer" and either a skull-and-crossbones (under older European legislation) or the newer health hazard symbol (mandatory after June 1, 2015, in Europe and the United States). R&D efforts by the major chemical suppliers to reduce the levels of the epichlorohydrin byproducts resulted in what are now known as generation 2 (G2) PAE resins. These resins were developed through a combination of revised formulations and greater process control (to improve the efficiency of functionalizing the polymer with epichlorohydrin). The resulting resins contained <1000 ppm of 1,3-DCP in the as-received/delivered product [9,10].

With some paper producers looking for resins with levels of epichlorohydrin byproducts significantly lower than 1000 ppm, the R&D efforts of suppliers continued. These efforts resulted in a number of postreaction cleaning techniques that could be applied to G1 or G2 wet-strength resins to reduce the level of epichlorohydrin byproducts to <10 ppm in the as-received/delivered PAE resin products and still provide an acceptable wet-strength response. Post-treatment technologies

include microbial dehalogenation [24-27], membrane filtration [28], and carbon absorption [29–32]. It was discovered that technologies that only removed 1,3-DCP and free 3-MCPD still contributed to 3-MCPD in paper. The evidence indicated that this 3-MCPD contribution to paper was due to polymer-bound CPD (PB-CPD). This PB-CPD is believed to be due to CPD-ester functionality, with the main CPD-ester functionality shown in Fig. 2. Both free 3-MCPD and PB-CPD in PAE resins contribute to 3-MCPD in paper. Therefore, processes were developed and commercialized to provide G2.5 and G3 PAE resins with greatly reduced levels of PB-CPD [33-40]. These processes essentially destroy the CPD-ester functionality. A basic ion exchange process can also be used to destroy 1,3-DCP, 3-MCPD, PB-CPD, and AOX, but it is costly and produces a significant industrial waste stream [41,42]. An on-site base activation process was developed to remove 1,3-DCP, 3-MCPD, PB-CPD, and AOX [43,44].

For a PAE technology to be classified as generation 2.5 (G2.5) or generation 3 (G3), it is proposed that the PB-CPD must be reduced to a very low level. The level of PB-CPD can be easily determined by using the so-called acid test [33-40] or more sophisticated analyses. The acid test is relatively simple: the PAE resin is acidified to pH 1.0 with sulfuric acid and held at 50°C for 24 h. The 3-MCPD level of the PAE resin before the acid test is subtracted from the 3-MCPD level after the acid test. For G2.5 and G3 resins, the difference is <5 ppm, typically <1 ppm. For G1–G2.5 resins, the accuracy of the PB-CPD determination is greatly improved by removing 1,3-DCP and free 3-MCPD to a low level using membrane filtration or other technology on a sample of the PAE resin before the acid test.

To further define the generations of PAE resins, G1 products are those that contain >1000 ppm of 1,3-DCP in the as-received/delivered product. The SDSs for these products must disclose the presence of 1,3-DCP, and they must include a warning regarding the carcinogen hazard of 1,3-DCP. Further, the U.S. hazard communication legislation requires that the SDS indicate that 1,3-DCP is listed as a potential carcinogen by the International Agency for Research on Cancer. G1 wet-strength resin SDSs and labels prepared according to the GHS of Classification and Labeling of Chemicals (mandatory in the Europe and the United States as of June 1, 2015), contains the following hazard identifications (typically in section 2 of the SDS):

- GHS classification:
  - Hazardous classification: carcinogenicity, category 1B or 2; chronic aquatic toxicity, category 3
- GHS labeling:
  - Symbol(s): Health hazard pictogram
  - Signal word: Danger or warning
  - Hazard statements: H350 or H351 "may cause cancer" or "suspected of causing cancer"; H412 "harmful to aquatic life with long lasting effects"

For G2 wet-strength resins, which contain <1000 ppm of 1,3-DCP, classification and labeling for carcinogenicity, including the health hazard pictogram, is not required. Under the European regulation on Registration, Evaluation, Authorization and Restriction of Chemicals (REACH), 1,3-DCP is considered to be a substance of very high concern (SVHC). As such, wet-strength resins that contain >1000 ppm of 1,3-DCP typically are not manufactured or imported into the European Union.

The epichlorohydrin byproducts, 1,3-DCP and 3-MCPD, also are potential contributors to the volatile organic compound (VOC) content of the resin. Therefore, the total amount of these species present in the product must be considered for mills and customers that have limitations on VOC levels in their local operating environment.

Certain ecolabels place limitations on the total sum of 1,3-DCP, 3-MCPD and epichlorohydrin that is present in the wet-strength resin. For producers of tissue paper (e.g., kitchen towel) seeking an accreditation from Nordic Ecolabel or EU Ecolabel, the total sum of 1,3-DCP, 3-MCPD and epichlorohydrin in the wet-strength resin cannot exceed 7,000 ppm (expressed on a dry basis) [45–47]. This approach, coupled with the limitation of 1,3-DCP on the delivered product for the purposes of SDS and labeling, indirectly defines the amount of 3-MCPD that can be present in the resin. Additional provisions also limit the amount of any residual starting monomer (i.e., adipic acid, DETA and epi) to 100 ppm. In practice, residual epichlorohydrin is at nondetectable levels (<1 ppm) at the time of customer receipt of the PAE resin.

Epichlorohydrin byproducts in paper and consumer safety

Initial concerns about epichlorohydrin byproducts in PAE technology were related to the potential hazard to human health when handling the product and the impact they had on the environment. The focus in recent years has been the potential for these epichlorohydrin byproducts to enter the food chain by migration from various food contact paper grades. After much review and assessment of such risks, the BfR provides a series of recommendations (XXXVI) for the levels of 1,3-DCP and 3-MCPD that may be extracted with water from a paper sample or product manufactured for different types of food contact grades of paper.

For all food contact paper grades, the recommendation states that "the 1,3-dichloro-2-propanol must not be detectable in water extract of the finished product (detection limit 2 µg/L). The transfer of 3-monochloro-1,2-propanediol into the water extract of the finished product must be as low as technically achievable, a limit of 12 µg/L must not be exceeded in any case" [48].

While the BfR recommendation for the water extract is the same for all the different types of paper grades, the sample size and the method of aqueous extraction must be considered to appreciate what this means in terms of the levels of the allowable 1,3-DCP and 3-MCPD in paper (Table II).

Considering the sample size and the test methodology, kitchen towel grades are permitted higher levels of 1,3-DCP and 3-MCPD in the final paper product. For all other food con-

Recommended Sample Size and Extraction Method for the Determination of 1,3-DCP and 3-MCPD in Paper Samples							
Sample Type	Sample Weight	Extraction Method*	Hot/Cold Extraction	BfR Limit in Water Extract		BfR Limit Calculated Back to Paper	
				1,3-DCP	3-MCPD	1,3-DCP	3-MCPD
Teabag/coffee filter	40 g/L (10 g/250 mL)	EN647	Hot	2 µg/L	12 µg/L	50 ppb	300 ppb
Kitchen towel	4 g/L (1 g/250 mL)	EN645	Cold	2 µg/L	12 µg/L	500 ppb	3,000 ppb
Wipes	40 g/L (10 g/250 mL)	EN645	Cold	2 µg/L	12 µg/L	50 ppb	300 ppb
Other grades	40 g/L (10 g/250 mL)	EN645	Cold	2 µg/L	12 µg/L	50 ppb	300 ppb

* British Standards EN 647 "Paper and board intended to come into contact with foodstuffs: preparation of a hot water extract" and EN 645 "Paper and board intended to come into contact with foodstuffs: preparation of a cold water extract."

II. Summary of German Federal Institute for Risk Assessment (BfR) XXXVI recommendations.

tact grades, the levels permitted in the paper are one order of magnitude lower.

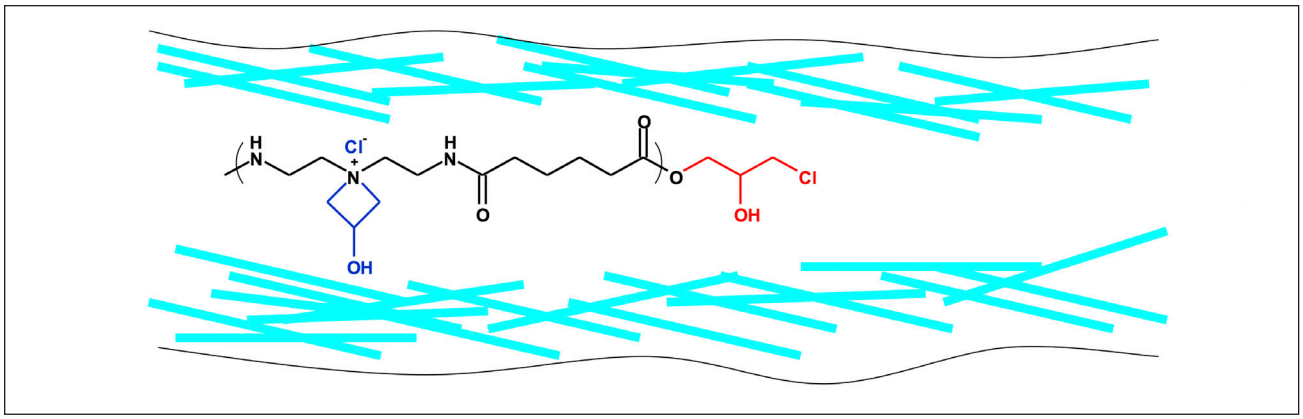
While the recommendations originate from Germany, they have been adopted by the different European countries and European Union institutions (e.g., the 2004 policy statement from the Council of Europe concerning tissue paper, kitchen towels, and napkins) [49]. The recommendations apply to food contact grades used in Europe, regardless of whether the paper is manufactured in or imported to the region. Therefore, to be active in the European market, producers worldwide need to ensure that their products comply with these recommendations.

The amount of 1,3-DCP and 3-MCPD in paper manufactured from PAE resins is dependent on a number of papermaking factors, including the amount of 1,3-DCP, 3-MCPD, and PB-CPD in the PAE resin; the PAE resin dosage; cycle-up of 1,3-DCP and free 3-MCPD (which is dependent on the water closure level); amount of broke or recycled paper used (especially if the recycled paper used a G1 resin); solids before the dryer section; and drying conditions. In practice, 1,3-DCP and free 3-MCPD are poorly retained by pulp fibers. The amount of 1,3-DCP and free 3-MCPD in the PAE resin is an inaccurate predictor for the amount of 1,3-DCP and 3-MCPD that will be in the paper (e.g., 1 ppm of 3-MCPD in the PAE resin is not likely to result in 1 part per billion [ppb] of 3-MCPD measured in the paper). Paper testing is needed to ensure compliance.

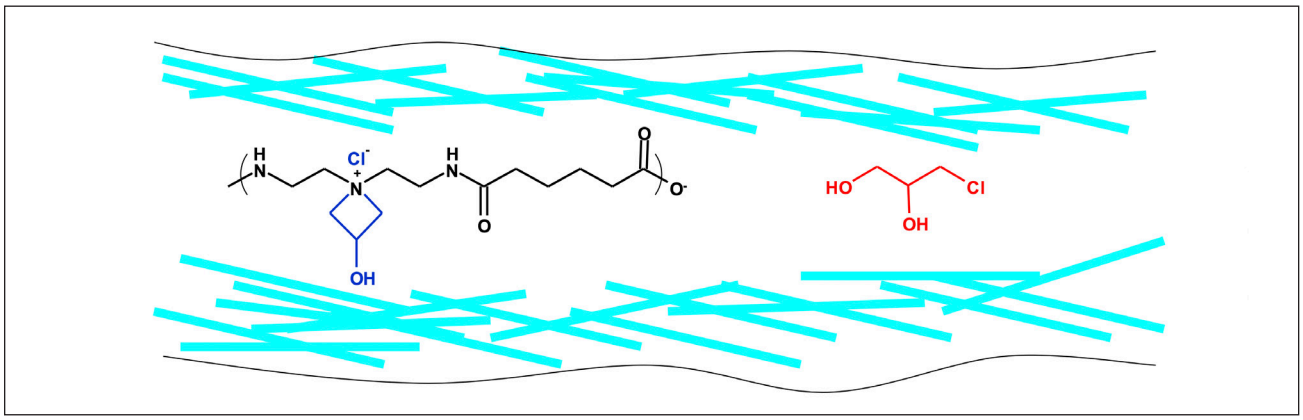
With current PAE resins, an examination of paper test results reveals that the 3-MCPD levels are much higher than the 1,3-DCP levels, even when much more 1,3-DCP is present in the wet-strength resin product. Usually, papermakers struggle to meet the limits for the level of 3-MCPD, whereas the 1,3-DCP level is typically well below the BfR limits. Differences in the partition coefficients with the pulp fibers and the differences in volatility between 1,3-DCP and 3-MCPD are two causes for the higher 3-MCPD level measured in paper.

However, the principle cause of high levels of 3-MCPD found in (and extracted from) paper is the generation of 3-MCPD in the papermaking process. G1 and G2 wet-strength resins contain a significant amount of PB-CPD species produced from the reaction of epichlorohydrin and acid end groups in the prepolymer (Fig. 2). The PB-CPD species (also known as CPD-esters) are part of the polymer that is adsorbed and retained by pulp fibers and fines in the wet end, which are formed into the wet paper web in the wire and press sections of the paper machine (Fig. 4). In the dryer section, the action of heat causes hydrolysis of the ester bond, thereby generating an acid end group on the polymer and freed 3-MCPD, both of which remain in the dried paper sheet (Fig. 5). During paper testing, the total of the initial free 3-MCPD before the dryer section and the freed 3-MCPD is measured to determine compliance with the recommendations of the BfR.

In kitchen towel grades (in paper machines that do not have a high water closure level), resins that contain lower levels of PB-CPD (e.g., G2 resins) typically allow papermakers to manufacture products that comply with the BfR XXXVI recommendations due to the lower paper sample size for the BfR test method permitting higher levels of 1,3-DCP and 3-MCPD to be present in the paper. However, for other grades (e.g., napkins, tea bag paper, coffee filters, and liquid packaging board), the paper sample size used in the test method is high-



4. PAE resin polymer retained on fiber and fines in the wet web. 1,3-dichloro-2-propanol (1,3-DCP) and free 3-monochloropropane-1,2-diol (3-MCPD) are poorly retained but will cycle up in the water component of the wet web.



5. Hydrolysis of the CPD-ester on PAE resin polymer in the dryer section. Both the PAE resin and the freed 3-MCPD are retained in the dry web and in the paper sheet.

er, thereby resulting in lower limits for 1,3-DCP and 3-MCPD to be present in the paper. PAE resins that contain PB-CPD species may result in levels of 3-MCPD that are not compliant with the BfR XXXVI/1, XXXVI/2, and XXXVI/3 recommendations. A PAE resin with very low or even nondetectable levels of free 3-MCPD could result in a paper with high levels of 3-MCPD if the PAE resin has a significant level of PB-CPD.

Formulation and process conditions for PAE resins can minimize the formation of PB-CPD. However, to achieve the very low levels of PB-CPD needed for G2.5 and G3 resins, post-manufacturing processes are needed. While initial products were based on acidic or enzymatic treatment to hydrolyze PB-CPD, basic treatment is currently the most cost-effective process resulting in the highest efficiency PAE resins. The basic treatment destroys much of the 1,3-DCP. During the basic treatment process, most of the initial 1,3-DCP, free 3-MCPD, and PB-CPD are ultimately removed from the PAE resin due to further reaction with amine functionality on the polymer and due to further hydrolysis to glycerol. This destruction of 1,3-DCP, free 3-MCPD, and PB-CPD reduces the environmental impact and potential hazard to human health when handling these products.

While hydrolysis processes can increase the overall free 3-MCPD in a resin (e.g., a G2.5 resin), the low substantivity of 3-MCPD to paper fibers (relative to PB-CPD on the cationic polymer) typically results in an overall lower level of 3-MCPD in the paper product. These hydrolysis processes allow post-treatment processes (e.g., microbial dehalogenation or membrane separation) to eliminate the PAE resin contribution to 3-MCPD in paper, resulting in a G3 resin. G3 resins have <10 ppm of 1,3-DCP and free 3-MCPD, but most importantly, they exhibit no potential to generate 3-MCPD due to having very low levels of PB-CPD. Use of G3 resins allows papermakers to manufacture products that meet all the recommendations of the BfR and to meet all of Brazil's ANVISA regulations.

PAE resin effect on AOX and the environment

The epichlorohydrin byproducts, 1,3-DCP and 3-MCPD, are the focus of worker safety and food contact paper regulations. Because of their AOX contribution, 1,3-DCP, 3-MCPD, PB-CPD, and ACH in PAE resins also affect environmentally driven regulations and guidelines. Legislation, such as the German Waste Water Act, imposes financial penalties on papermakers based on the level of AOX in their effluent stream. Adsorbable organic halogens is a blanket term that quantifies the amount of organochloride-containing compounds that can be ad-

sorbed onto activated charcoal from water. The term, and methodology used to determine amount, do not distinguish the chemical nature of different organochloride-containing species. It is a sum parameter for quantifying the total organic halogen load in water and often is used as a surrogate measure of persistent organic pollutants in the environment.

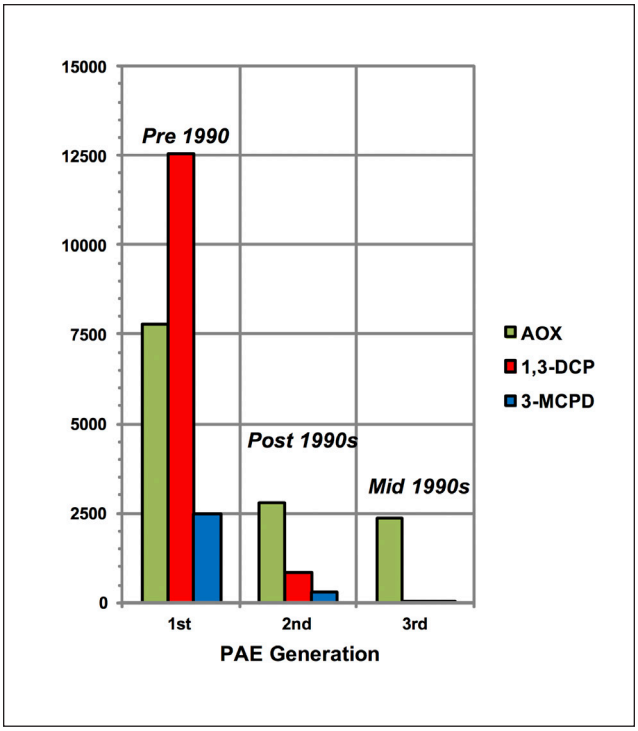
The methods for determining AOX have been standardized worldwide. A number of methods exist, such as U.S. Environmental Protection Agency (EPA) Method 1650C "Adsorbable organic halides by adsorption and coulometric titration," German Institute for Standardisation (DIN) EN 1485 "Water quality—determination of adsorbable organically bound halogens (AOX)," and International Standards Organization (ISO) 9562 "Water quality—determination of adsorbable organically bound halogens (AOX)." All of these methods follow the same basic principles: (1) a known quantity of aqueous sample is mixed with activated charcoal, (2) the charcoal is carefully washed with nitric acid to displace and remove any ionic halides (usually chloride ions) from the matrix, and (3) the total halide content is determined.

In the mid-1980s, a large amount of paper was produced using pulps bleached with chlorine gas. The organochloride compounds present in these pulps were the major contributor to the AOX content of a papermaker's effluent stream. The AOX contribution from the bleaching of pulp has been addressed by the use of alternative bleaching techniques: (1) chlorine dioxide for elemental chlorine free (ECF) bleaching, and (2) ozone/hydrogen peroxide for totally chlorine free (TCF) bleaching.

After bleaching of papermaking pulps, the next major contributor to the AOX content of a papermaker's effluent stream was PAE resins. The development of G2 wet-strength products to address worker safety regulations by reducing the levels of 1,3-DCP and free 3-MCPD also reduced the AOX content. The high levels of 1,3-DCP found in G1 products are a significant contributor to a papermaker's effluent stream.

However, 1,3-DCP and free 3-MCPD are not the only sources of organochloride species that can be determined by the AOX methodology and contribute to a papermaker's effluent stream. Resins containing low 1,3-DCP are sometimes referred to as low AOX. However, with G2, G2.5, and G3 resins, PBOX is the primary contributor to AOX in the effluent stream, not the free species 1,3-DCP and 3-MCPD. In the manufacture of a PAE resin, epichlorohydrin reacts with the secondary amine groups of the prepolymer to form ACH. This ACH species then converts to AZE functionality (Fig. 2). Epichlorohydrin also reacts with the acidic end groups of the prepolymer to generate PB-CPD. Both ACH and PB-CPD are examples of PBOX species. In the AOX methodology, the polymeric component of the PAE resin is retained on the activated charcoal and contributes significantly to the measured AOX.

Theoretically, the AOX content is the sum of the chloride content from the 1,3-DCP, 3-MCPD, PB-CPD, and polymeric ACH in the PAE resin. The chloride content of 1,3-DCP is 55 wt% and the chloride content of 3-MCPD is 32 wt%. The contribution of 3-MCPD to the AOX content of a resin is lower than theoretical because 3-MCPD is not completely adsorbed and retained by activated charcoal in the AOX methodology. Whereas 90%–95% of 1,3-DCP can be retained by activated charcoal, typically only 25% of 3-MCPD is retained under the same conditions. This is because of the greater hydrophilic nature of the 3-MCPD molecule.



6. Adsorbable organic halogens (AOX) content relative to the 1,3-DCP and 3-MCPD content (12.5% active basis), demonstrating the contribution from PBOX species (polymeric aminochlorohydrin [ACH] and PB-CPD).

The polymeric component of the PAE resin is considered to be well retained by the activated charcoal in the AOX methodology, so an abridged version of the equation (AOX = PBOX + 0.55xDCP) has been found to provide a good description of the AOX content of the PAE. Before 1990, G1 PAE resins had high levels of AOX, mainly because of the high levels of 1,3-DCP present. The development of G2 wet-strength resins resulted in a reduction not only of 1,3-DCP, by about one order of magnitude, but also in the AOX content of the PAE resin.

An analysis of the relative contributions of the free species (1,3-DCP and 3-MCPD) compared with the PBOX in a G2 PAE resin shows a much higher contribution of PBOX species to the AOX value. This is further exemplified by the application of a postreaction cleaning technique to a G2 resin to remove only the 1,3-DCP and the 3-MCPD (Fig. 6). To emphasize the fact that AOX, 1,3-DCP and 3-MCPD are not necessarily directly correlated and that PBOX is a primary contributor to AOX, note that a G1 resin can be designed to have an AOX level that is higher or lower than the 1,3-DCP level.

While the PBOX content decreases from G1 to G2 to G2.5 to G3, the high PBOX content of G2 resins, relative to the 1,3-

DCP and the 3-MCPD content, clearly shows that PBOX species are the major contributors to AOX in G2, G2.5, and G3 resins. In practice, most of the polymeric component of the PAE resin is retained in the paper product. This retained PBOX does not contribute to the AOX in a mill's effluent discharge. A high level of retained PAE resin (and therefore a lower AOX in effluent contribution) can be achieved by using best practice application techniques (e.g., optimum dosing points and anionic cofactors).

High-efficiency PAE resins with a high AZE level and therefore a high cationic charge are better retained than resins with a low AZE level when best application practices are employed. As an example, for grades using high PAE resin dosages, the use of an anionic dry-strength agent or an anionic retention polymer is an important factor. Resins with a high AZE level typically have a low level of ACH species, further minimizing the PBOX contribution to AOX. With high-efficiency PAE resins, the conversion of ACH to AZE during manufacture is maximized and the conversion of AZE to ACH during aging is minimized, resulting in lower PBOX at the time of papermaker use and, therefore, lower AOX in effluent.

In G2 resins, PB-CPD and especially polymeric ACH remain the major source of AOX in PAE resins. With G2.5 and G3 resins, the PBOX content of PAE resins is further reduced by greatly reducing the level of PB-CPD. With G3 resins, polymeric ACH is the only significant contributor to AOX. When considering how much a PAE resin contributes to the AOX content of an effluent stream, papermakers need to consider the actual/total AOX content of the resin and not just the level of epichlorohydrin byproducts present in a product.

PAE resin effect on total organic chlorine content of paper and consumer preference

Some manufacturers produce grades of paper considered to be TCF. For such grades, the total organic halogen content is <30 mg/kg of dry paper. These grades use TCF pulps, which are produced using oxygen-based bleaching agents (such as ozone, hydrogen peroxide, or both). Methods such as ISO 11480 "Pulp, paper and board—determination of total chlorine and organically bound chlorine" can be used to determine the (total) organic chlorine of pulp and paper. The principles of these methods are similar to those used for the determination of AOX content of aqueous samples, except that the paper sample is mixed with activated charcoal. The measured value typically is called organic halogen (OX) in paper. As with AOX in aqueous samples, the OX in paper is a sum parameter and does not differentiate between the different species present in the paper that contribute to the final value.

As with AOX in aqueous samples, all the organic chlorine species present in the PAE resin contribute to the OX content of the final paper product. The OX content in paper is primarily driven by the PBOX content and not by free epichlorohydrin byproducts (1,3-DCP and 3-MCPD) for G2, G2.5, and G3 resins. To illustrate this concept, when considering the maximum BfR limits for epichlorohydrin byproducts in paper (kitchen towel), 500 ppb of 1,3-DCP = 0.28 mg/kg of OX in the paper and 3000 ppb of 3-MCPD = 0.98 mg/kg of OX in the paper.

Even at the limits recommended by BfR, free epichlorohydrin byproducts are not significant contributors to the OX content of paper. The PBOX species of the resin are the main contributors to the OX content of paper.

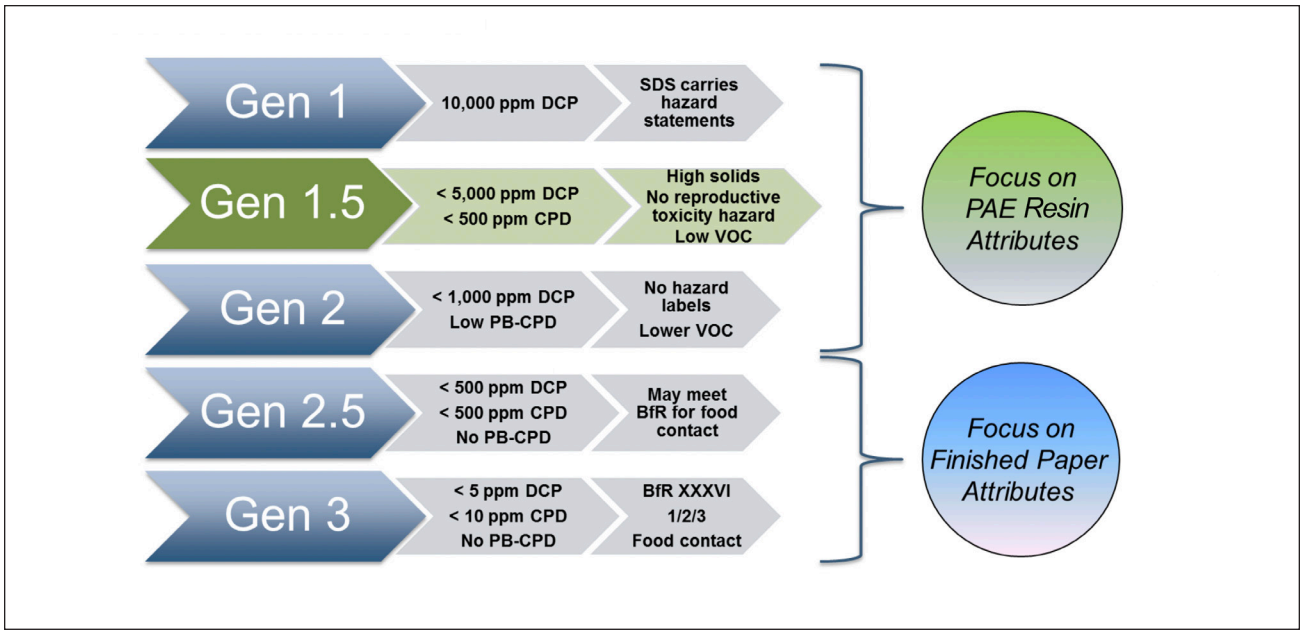
Of the two PBOX species present in the resin, polymeric ACH is the principle source of organic chlorine. The proprietary manufacturing processes for G2.5 and G3 wet-strength resins, which were developed to eliminate PB-CPD species from the final product, also reduce the level of ACH, thereby reducing the total AOX and PBOX content of the resin. Therefore, the same G2.5 and G3 resins that allow papermakers to minimize mill effluent AOX content also allow manufacturers to produce TCF grades of paper.

The evolution of cleaner PAE resin technology to help papermakers meet regulatory measures to address environmental and health concerns related to organochloride species has resulted in a better understanding of the PAE resin technology. Improved process control in the basic resin manufacturing process and the development of novel postreaction techniques were needed to address these concerns. This improved knowledge of PAE resins has been used across all the different generations of PAE technology to generate products with better performance characteristics that can be shipped at higher solids.

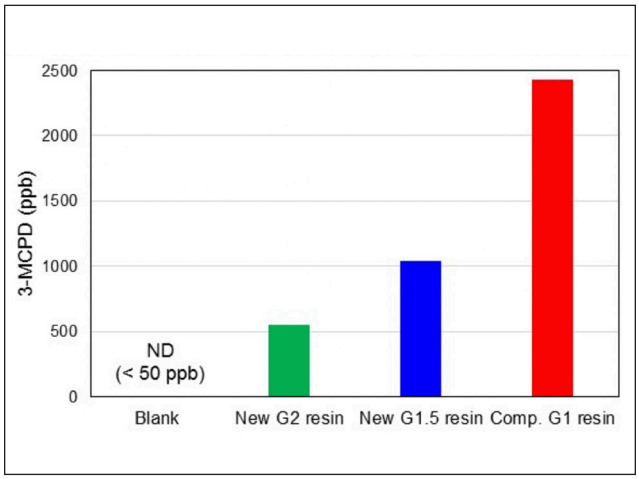
Development of a new class (G1.5) of high-solids, high-efficiency, wet-strength resin products

Resin products with higher wet-strengthening performance and higher solids present minimize the impact on the environment. More efficient PAE resins result in lower PAE resin usage to provide the required level of wet strength for a grade. In addition to the benefit of using less chemistry, the overall presence and contribution of organochloride sources in a papermaking system is reduced. Higher-solids versions of PAE resins contribute to a smaller environmental impact in terms of transportation of the resin from the supplier to the papermaker. Fewer tanker trucks are needed on the road; thus, in addition to a freight cost savings, the overall emissions associated with transporting PAE resins are reduced. These attributes align with the corporate environmental sustainability programs of major papermakers and their customers.

PAE resin manufacturers have focused significant effort to develop higher-solids and high-efficiency resins. Previously discussed research efforts [3] resulted in a breakthrough in G1 resin design such that resins with 12.5%–30% solids can be manufactured without compromising performance or gelation stability. Most recently, a new 26% solids, high-efficiency, PAE resin was developed with much lower 1,3-DCP, 3-MCPD, and VOC than traditional G1 resins. Because the 1,3-DCP level is not low enough to be a G2 resin, this resin is in a new class termed generation 1.5 (G1.5) due to its much improved EH&S profile. Notably, G1.5 resins have <0.1% (1000 ppm) of 3-MCPD, do not indicate category 1B reproductive



7. PAE resin environment, health, and safety class summary.



8. 3-MCPD in paper for generations (G) 2 and 1.5 and competitive G1 resins due to PB-CPD.

toxicity, and do not include the H360 statement "may damage fertility or the unborn child" on the SDS. Figure 7 summarizes the attributes of the different generations of PAE resins.

Figure 8 shows 3-MCPD determined in paper, which is dependent on the level of PB-CPD present in a new G2 resin, the new 26% G1.5 resin, and a typical competitive G1 resin. The dosage was 1.0% (dry resin on dry fiber), the furnish was 70:30 hardwood:softwood, and the papermaking was at pH 7.5. The extraction method was British Standards Institute EN645 "Paper and board intended to come into contact with foodstuffs: preparation of a cold water extract" using 1 g of paper for 250 mL of water (i.e., the kitchen towel method). In this evaluation and at equal dry dosage, the new G2 resin has about half the 3-MCPD in paper relative to the new G1.5 resin, and the new G1.5 resin has less than half the 3-MCPD in paper relative to a competitive G1 resin. With handsheet evaluation using a "Noble and Wood" handsheet device (FORMAX 8 in. x 8 in. stainless steel sheet mold, Adirondack Machine Corp.; Hudson Falls, NY, USA), the pulp furnish is very dilute, thus the free 3-MCPD does not significantly contribute to the 3-MCPD in paper (i.e., the 3-MCPD in paper with this evaluation is almost solely due to PB-CPD). With typical commercial papermaking (much less dilute furnish, cycle up of free 3-MCPD), the difference between the competitive G1 resin and the new G1.5 resin would be greater.

CASE HISTORIES

The following case studies illustrate how improved PAE technology has helped papermakers meet their objectives.

G1.5 PAE resin improves runnability, performance, and VOC

Using a conventional competitive G1 PAE resin, a southern U.S. tissue mill observed product efficiency decreases of 12%–28% during mill storage relative to freshly delivered material. This mill was further challenged by having a very high level of fines due to poor fiber quality and low retention. Switching from the conventional G1 PAE resin to the new G1.5 PAE resin resulted in a 14% decrease in resin dosage on a dry basis and provided an average US$256,000/year savings and an estimated 30 tons in reduction of VOC.

Using a conventional, competitive G1 PAE resin, a northern U.S. mill manufactures a specialty wet crepe grade with 95% softwood kraft and 5% broke. Improved performance was needed to achieve the corporate sustainability goal for reduced air pollution emissions. Switching from the conventional G1 PAE resin to the new G1.5 PAE resin resulted in a 60% improvement in the efficiency factor (wet tensile per

Attribute	Generation 1	Generation 1.5	Generation 2	Generation 2.5	Generation 3
1,3-DCP level (wet product basis)	~10000 ppm	5000 ppm	<1000 ppm	<700 ppm	<10 ppm
3-MCPD level (wet product basis)	>1000 ppm	<1000 ppm	<1000 ppm	<700 ppm	<10 ppm
PB-CPD present in the resin	Yes	Yes	Yes	No	No
% AOX level (20% basis)	>0.80 wt%	<0.80 wt%	<0.60 wt%	<0.25 wt%	<0.20 wt%
Customer need	Lowest cost	Not labeled as reproductive toxicant, VOC	No carcinogen warning label	AOX, OX in paper, BfR	BfR, AOX, OX in paper

Abbreviations: 1,3-DCP =1,3-dichloro-2-propanol; 3-MCPD = 3-monochloropropane-1,2-diol; PB-CPD = polymer-bound CPD; AOX = adsorbable organic halogens; VOC = volatile organic compound; OX = organic halogen; BfR = German Federal Institute for Risk Assessment; ppm = parts per million.

III. Recommended generation definitions based on customer needs.

dosage), a 17% increase in dry tensile, and a 47% increase in wet tensile, which yielded a 7% increase in wet/dry performance. The turbidity in the dissolved air flotation clarifier improved dramatically (turbidity decreased from >40 NTU to <2 NTU). The excellent machine runnability led to a several months' long extended trial.

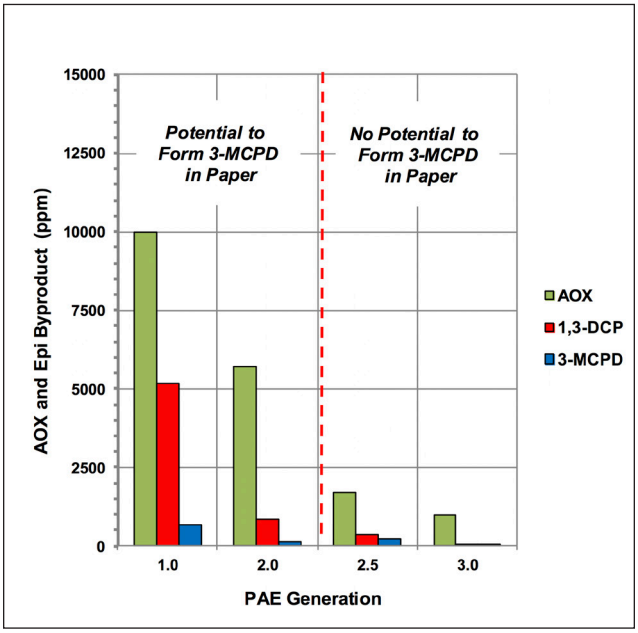
G2.5 PAE resin contributes to lower OX in high wet-strength towels for mills using TCF furnish

Using a G2 PAE resin, a European tissue producer was meeting BfR XXXVI requirements for kitchen towels. However, for high wet-strength grades, a key additional parameter to satisfy the specific supermarket customer's requirement was to achieve the TCF target of <30 mg/kg of OX in the finished paper product. Using the G2 PAE resin, the mill was unable to achieve this TCF target.

The towel manufacturer conducted trials using a proprietary G2.5 PAE product. The trial results indicated that the efficiency of the G2.5 resin was improved compared with incumbent G2 resin, achieving the 25% wet/dry tensile target with a 19 g/m² basis weight product. Analyses at an independent laboratory (ISEGA) of towel samples from the trial indicated much lower OX, 1,3-DCP and 3-MCPD than those obtained with the previous G2 resin program. These results were comfortably within the OX limits set by the Blue Angel ecolabel. These results were achieved for the same cost as the previous G2 PAE resin. The proprietary G2.5 resin product contained higher solids, thereby reducing order and delivery frequencies and truck fuel emissions into the environment.

New lower AOX G3 PAE resin product allows customer to achieve strict local AOX requirements

A German paper producer that has an effluent discharge close to a municipal water intake is required to meet very strict regulatory limits on AOX in the mill's effluent (500 µg/L). The mill typically achieved the AOX limits using the incumbent G3 product, but the customer wanted to further reduce AOX

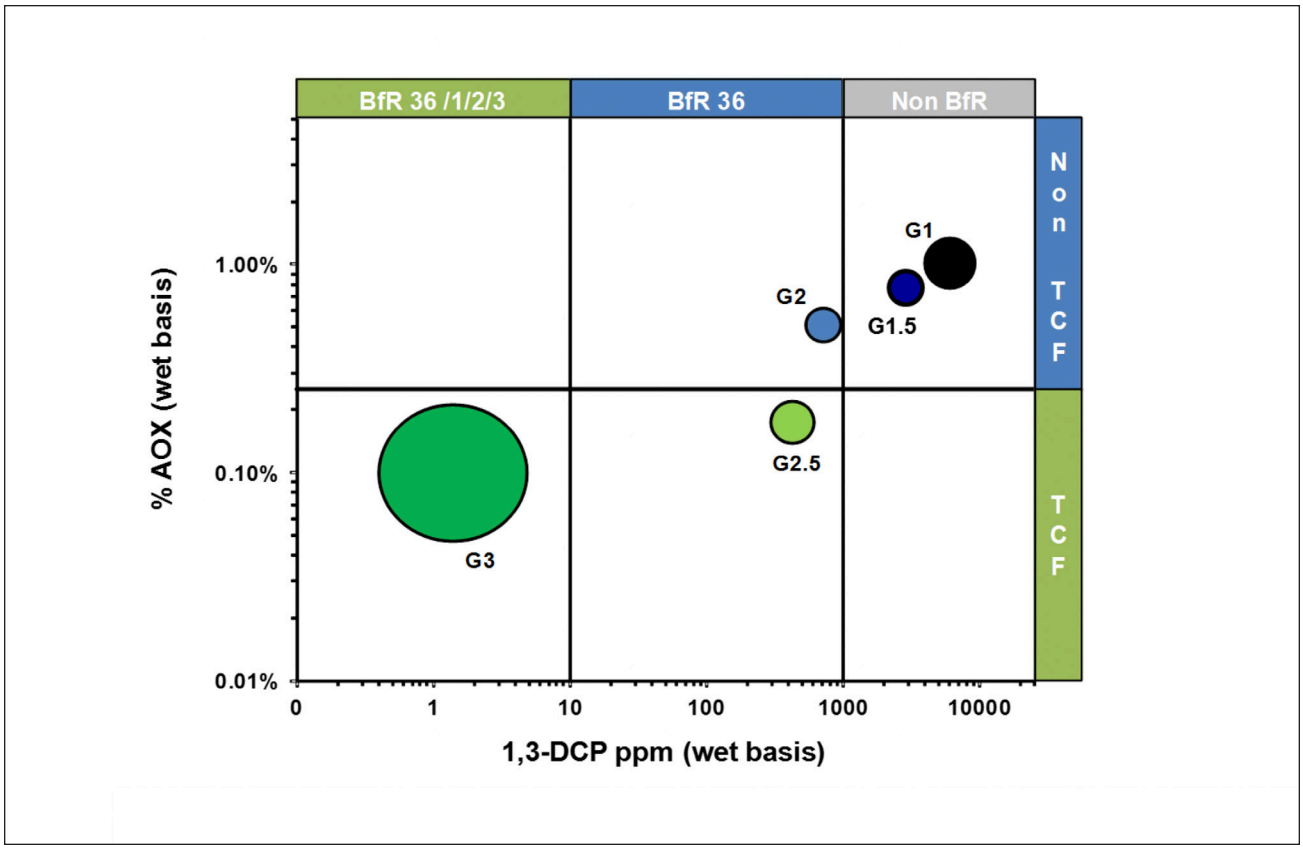


9. AOX and epichlorohydrin byproduct content for current PAE resins.

so that the AOX in effluent level would be comfortably below the limit even when disturbances to the papermaking system occurred. Additional research focused on reducing PBOX content, resulting in a new, proprietary G3 PAE resin that had a higher solids content, a higher AZE content, and a 60% reduction in PBOX and AOX content relative to the incumbent product. Customer trials confirmed a 7% increase in the average wet/dry strength and a 60% reduction of AOX in effluent.

SUMMARY

Regulatory drivers and sustainability efforts have resulted in step-change improvements in PAE resin technology. These improvements have dramatically lowered 1,3-DCP and 3-MCPD levels to reduce the potential hazard to worker and consumer health and lowered PBOX species to reduce the impact on the environment (AOX of mill effluent) and to allow



10. Paper compliance matrix for PAE resins with recommended generation definitions based on customer needs (TCF = totally chlorine free).

for the manufacture of TCF grades of paper. In gaining an understanding of mechanisms that produce undesired organochloride species, formulations and processes to reduce them were developed, which resulted in improvements in the wet-strengthening performance of PAE resins. High-solids, high-efficiency PAE resins contribute to a smaller environmental impact by allowing the use of less chemistry, less emissions from transportation, and less PAE resin (and AOX) in effluent. These attributes fit well with the corporate environmental sustainability programs of major papermakers.

Definitions of generations and AOX based on customer needs

As PAE resins evolved, the product definitions regarding AOX measurement and the epichlorohydrin byproduct definition became inconsistent regarding product generations [11]. Table III and Figs. 9 and 10 summarize the recommended definition for each product generation (G1, G1.5, G2, G2.5, and G3). These definitions are not arbitrary but are based on key customer needs.

When selecting which generation of technology to use, consideration of external regulatory directives, together with the papermaker's needs, is required to meet the guidelines of nongovernmental organizations and the papermaker's own corporate sustainability programs. **TJ**

LITERATURE CITED

1. Keim, G.I., U.S. pat. 2,926,116 (Feb. 23, 1960).
2. Keim, G.I., U.S. pat. 2,926,154 (Feb. 23, 1960).
3. Crisp, M.T. and Riehle, R.J., "Polyaminopolyamide-epichlorohydrin (PAE) wet strength resins for improved health and sustainability," *TAPPI PaperCon*, TAPPI Press, Atlanta, GA, USA, 2014.
4. Podd, B., "Global food contact regulations," *ChemCon The Americas*, ChemCon Conferences, Nijmegen, The Netherlands, 2012.
5. Espy, H.H., in *Wet-Strength Resins and Their Applications* (L.L. Chan, Ed.), TAPPI Press, Atlanta, 1994, Chap. 2.
6. Crisp, M.T. and Riehle, R.J., in *Application of Wet End Chemistry* (I. Thorn and C.O. Au, Eds.) 2nd edn., Springer, Dordrecht, 2009, Chap. 8.
7. Hasegawa, T., Takagishi, H., and Horiuchi, H., U.S. pat. 5,017,642 (May 21, 1991).
8. Maslanka, W.W., U.S. pat. 6,908,983 (June 21, 2005).
9. Miller, A.J. and Stubbs, B.M., U.S. pat. 5,171,795 (Dec. 15, 1992).
10. Bower, B.K., U.S. pat. 5,714,552 (Feb. 3, 1998).
11. Goldsberry, H., Luo, Y., and Chen, J., "New Approach for polyamidoamine-epichlorohydrin resin—a new low AOX wet-strength resin," *TAPPI PaperCon*, TAPPI Press, Atlanta, 2012.
12. U.S. FDA, "Inventory of effective food contact substance (FCS) notifications," U.S. Food and Drug Administration, Washington, DC. Available [Online] https://www.accessdata.fda.gov/scripts/fdcc/?set=FCN <22Sept2018>.

13. Brazilian Health Regulatory Agency, "ANVISA/DC Resolution No. 88 of 06/29/2016," ANVISA, Brasília. Available [Online] https://www.legisweb.com.br/legislacao/?id=325444 <24Sept2018>; Google translation: https://translate.google.com/translate?hl=en&sl=pt&u=https://www.legisweb.com.br/legislacao/%3Fid%3D325444&prev=search <24Sept2018>.
14. Walmart, "Sustainable packaging playbook," Walmart, Bentonville, AR, USA. Available [Online] https://www.resource-recycling.com/images/e-newsletterimages/Walmart_Sustainable_Packaging_Playbook.pdf <22Sept2018>.
15. Target, "Target announces new chemical strategy including policy and goals for its products and operations," Target, Minneapolis, MN, USA. Available [Online] https://corporate.target.com/article/2017/01/chemical-policy-and-goals <24Sept2018>.
16. California Environmental Protection Agency, Office of Environmental Health Hazard Assessment (OEHHA), "Chemicals considered or listed under Proposition 65," OEHHA, Sacramento, CA, USA. Available [Online] https://oehha.ca.gov/proposition-65/chemicals <24Sept2018>.
17. International Agency for Research on Cancer, "Epichlorohydrin," IARC Monographs vol. 71, World Health Organization, Geneva, Switzerland. Available [Online] http://monographs.iarc.fr/ENG/Monographs/vol71/mono71-26.pdf <22Sept2018>.
18. National Toxicology Program, "National Institutes of Health report on carcinogens," 14th edn., National Institutes of Health, U.S. Department of Health and Human Services, Washington, DC, 2016. Available [Online] https://ntp.niehs.nih.gov/ntp/roc/content/profiles/epichlorohydrin.pdf <24Sept2018>.
19. California Environmental Protection Agency, Office of Environmental Health Hazard Assessment (OEHHA), "Evidence on the carcinogenicity of 1,3-dichloro-2-propanol," OEHHA, Sacramento, June 2010. Available [Online] https://oehha.ca.gov/media/downloads/proposition-65/13-dcphida.pdf <24Sept2018>.
20. National Toxicology Program, "1,3-dichloro-2-propanol [CAS No. 96-23-1] review of toxicological literature," National Institutes of Health, U.S. Department of Health and Human Services, Washington, DC, January 2005. Available [Online] https://ntp.niehs.nih.gov/ntp/htdocs/chem_background/exsumpdf/dichloropropanol_508.pdf <22Sept2018>.
21. California Environmental Protection Agency, Office of Environmental Health Hazard Assessment (OEHHA), "Evidence on the carcinogenicity of 3-monochloropropane-1,2-diol," OEHHA, Sacramento, June 2010. Available [Online] https://oehha.ca.gov/media/downloads/proposition-65/3-mcpd_hida.pdf <24Sept2018>.
22. International Agency for Research on Cancer, "3-monochloro-1,2-propanediol," IARC Monographs vol. 101, World Health Organization, Geneva, pp. 349–374. Available [Online] http://monographs.iarc.fr/ENG/Monographs/vol101/mono101-010.pdf <22Sept2018>.
23. European Commission, "Opinion of the Scientific Committee on Food on 3-monochloropropane-1,2-diol (3-MCPD)," European Union, Brussels, 30 May 2001. Available [Online] https://ec.europa.eu/food/sites/food/files/safety/docs/cs_contaminants_catalogue_mcpd_out91_en.pdf <22Sept2018>.
24. Bull, A., Hardman, D.J., Stubbs, B.M., et al., U.S. pat. 5,470,742 (Nov. 28, 1995).
25. Bull, A., Hardman, D.J., Stubbs, B.M., et al., U.S. pat. 5,843,763 (Dec. 1, 1998).
26. Bull, A., Hardman, D.J., Stubbs, B.M., et al., U.S. pat. 5,871,616 (Feb. 16, 1999).
27. Fauzi, A.M., Hardman, D.J., and Bull, A.T., *Appl. Microbiol. Biotechnol.* 46(5-6): 660(1996).
28. Bigorra Llosas, J., Pinilla, J.-A., and Pi Subirana, R., Euro. Pat. EP 1 135 427 B1 (Sept. 26, 2001).
29. Amey, R.L., U.S. pat. 6,056,855 (May 2, 2000).
30. Amey, R.L., U.S. pat. 6,057,420 (May 2, 2000).

ABOUT THE AUTHORS

We chose this topic to provide an up-to-date resource to paper manufacturers and their customers regarding the proper choice of PAE resins to meet current regulatory requirements and their customers' specific sustainability initiatives. While this paper is more of a discussion, it is supported by previous patented research and commercial experience, much of which has not been published externally.

The chemistry and applications technology are relatively straightforward to scientific experts, but there are challenges and misunderstandings that act as barriers to proper commercial application. Our hope is that this paper will be a major step forward to address these barriers.

We have discovered the primary causes for 3-MCPD in paper, OX in paper, and AOX in mill effluent and how to address them using a science-based approach. A key finding is that polymer-bound CPD (PB-CPD) is a major cause of 3-MPCD in paper.

For mills, the proper choice of the correct generation of PAE wet-strength resins will allow them to meet their and their customers' needs. This is the guiding theme for this paper and for the definition of each generation.

As regulatory requirements and sustainability initiatives continue to evolve, research will continue into the development of new PAE wet-strength resins to meet these new goals.

Riehle is a Research Fellow at Solenis LLC, Wilmington, DE, USA. Crisp is a Research Fellow at Solenis Netherlands BV, Capelle aan den Ijessel, The Netherlands. Email Riehle at rjriehle@solenis.com.



Riehle



Crisp

31. Laurent, H., Dreyfus, T., Poulet, C., et al., U.S. pat. 6,342,580 B1 (Jan. 29, 2002).
32. Constantin, G., Fouquay, S., Poulet, C., et al., World pat. WO 01/18093 A1 (Mar. 15, 2001).
33. Riehle, R.J., Allen, A.J., Hoglen, J.J., et al., U.S. pat. 6,554,961 B1 (Apr. 29, 2003).
34. Allen, A.J., Hoglen, J.J., Busink, R., et al., World pat. WO 00/77076 A1 (Dec. 21, 2000).
35. Riehle, R.J., Busink, R., Berri, M., et al., U.S. pat. 7,303,652 B1 (Dec. 4, 2007).
36. Riehle, R.J., Allen, A.J., Hoglen, J.J., et al., U.S. pat. 7,175,740 B1 (Feb. 13, 2007).
37. Riehle, R.J., U.S. pat. 7,081,512 B1 (July 25, 2006).
38. Riehle, R.J. and Vinciguerra, S., U.S. pat. 7,932,349 B1 (Apr. 26, 2011).
39. Riehle, R.J. and Vinciguerra, S., U.S. pat. 8,101,710 B1 (Jan. 24, 2012).
40. Riehle, R.J., in *ACS Symposium Series 900* (H.N. Cheng and R.A. Gross, Eds.), American Chemical Society, Washington, DC, 2005, Chap. 21.
41. Gorzynski, M. and Pingel, A., U.S. pat. 5,516,885 (May 14, 1996).
42. Gorzynski, M. and Pingel, A., U.S. pat. 6,376,578 B1 (Apr. 23, 2002).
43. Riehle, R.J., U.S. pat. 6,429,267 (Aug. 6, 2002).
44. Crisp, M.T., Evans, M.A., Lewis, A.H., et al., U.S. pat. 9,719,212 (Aug. 1, 2017).
45. European Union, "The EU Ecolabel for tissue paper," European Union, Brussels, July 2009. Available [Online] *http://ec.europa.eu/environment/ecolabel/documents/tissue_paper.pdf* <22Sept2018>.
46. Nordic Ecolabelling, "Paper products – basic and chemical module," Version 2.5, Nordic Ecolabelling, Stockholm, 14 November 2017. Available [Online] *http://www.nordic-ecolabel.org/product-groups/group/?productGroupCode=005* <26Sep2018>.
47. Nordic Ecolabelling, "Nordic Ecolabelling of Tissue paper," Version 2.6, Nordic Ecolabelling, Stockholm, 14 December 2017. Available [Online] *http://www.nordic-ecolabel.org/product-groups/group/?productGroupCode=005* <26Sept2018>.
48. German Federal Institute of Risk Assessment, "XXXVI. Paper and board for food contact," (English translation), BfR, Berlin, pp. 1–7; fn 10. Available [Online] *https://bfr.ble.de/kse/faces/resources/pdf/360-english.pdf* <26Sept2018>.
49. Council of Europe, "Partial Agreement in the Social and Public Health Field," Council of Europe, Strasbourg, France, 22 September 2004. Available [Online] *https://www.edqm.eu/sites/default/files/policy_statement_concerning_tissue_paper_kitchen_towels_and_napkins_v1_september_2004.pdf* <26Sept2018>.

ABOUT THIS PAPER

Cite this article as: Crisp, M., Riehle, R. *TAPPI J.* 17(9): 519(2018). https://doi.org/10.32964/TJ17.09.519

DOI: https://doi.org/10.32964/TJ17.09.519

ISSN: 0734-1415

Publisher: TAPPI Press

Copyright: ©TAPPI Press 2018

About this journal

TAPPI JOURNAL
WWW.TAPPI.ORG
THE PAPER AND PACKAGING INDUSTRIES' TECHNICAL RESOURCE
OCTOBER 2018 | VOL. 17 NO. 10



BLEACHING **547**
Laboratory method for determining the source of brightness loss at a southern United States bleached paperboard mill
Aru Tiwari, Ashok Ghosh, and Peter W. Hart

PACKAGING **557**
Production of polyhydroxyalkanoates (PHA)-based renewable packaging materials using photonic energy: A bench and pilot-scale study
Michael Joyce, Lokendra Pal, and Tom Tran

RECOVERY CYCLE **571**
A review of green liquor scale information
Peter W. Hart

PAPER PHYSICS SPECIAL REPRINT **583**
A theory for the tensile strength of paper
D.H. Page

October 2018

TABLE OF CONTENTS VOL. 17 NO. 10

543 EDITORIAL
Looking back and looking forward: Paper physics and the paper industry
Douglas W. Coffin

547 BLEACHING
Laboratory method for determining the source of brightness loss at a southern United States bleached paperboard mill
Aru Tiwari, Ashok Ghosh, and Peter W. Hart

557 PACKAGING
Production of polyhydroxyalkanoates (PHA)-based renewable packaging materials using photonic energy: A bench and pilot-scale study
Michael Joyce, Lokendra Pal, and Tom Tran

571 RECOVERY CYCLE
A review of green liquor scale information
Peter W. Hart

583 PAPER PHYSICS - SPECIAL REPRINT
A theory of the tensile strength of paper
D.H. Page

»COVER CREDIT: Green liquor scale samples obtained from various kraft pulp mills. All samples are calcite, except for row 3-left and row 4-right, which are pirssonite. Author Hart provides a review of green liquor scale formation in this issue (p. 571). Photos courtesy of Honghi Tran, University of Toronto.

TAPPI JOURNAL
WWW.TAPPI.ORG

Editor-in-Chief
Brian N. Brogdon brian.brogdon@gmail.com
+1 678 581-9114

Associate Editor
Peter W. Hart peter.hart@westrock.com
+1 409 276-3465

Editorial Director
Monica Shaw mshaw@tappi.org
+1 770 367-9534

PRESS Manager
Jana Jensen jjensen@tappi.org
+1 770 209-7242

Webmaster
Trina Heath theath@tappi.org
+1 770 209-7416

***TJ* EDITORIAL BOARD**

Randy Branston, BASF
randy.branston@basf.com, +1 704 819-4251

Brian N. Brogdon, FutureBridge Consulting & Training LLC
brian.brogdon@gmail.com, +1 678 581-9114

David A. Carlson, Carlson Consulting
dacarlson39@aol.com, +1 847 323-2685

Douglas W. Coffin, Miami University
dacarlson39@aol.com, +1 847 323-2685

Mahendra Doshi, Doshi and Associates
mahen@aol.com, +1 920 832-9101

Marc Foulger, GL&V USA Inc.
Marc.foulger@glv.com +1 315 767-2920

Peter W. Hart, WestRock
peter.hart@westrock.com, +1 409 276-3465

Carl J. Houtman, USDA Forest Products Laboratory
choutman@fs.fed.us, + 1 608 231-9445

Lucian Lucia, North Carolina State University
lucian.lucia@gmail.com, +1 919 889-7059

John A. Neun, John A. Neun LLC
john.neun@gmail.com, +1 518 275-8139

Jim Niemiec, Verso Corporation
jim.niemiec@versoco.com, +1 715 422-7404

Steven P. Ottone, Omya
steven.ottone@omya.com, +1 919 641-7854

Gaurav Pranami, Imbed Biosciences
gpranami@imbedbio.com, +1 515 230-7005

Arthur Ragauskas, Oak Ridge National Laboratory
aragausk@utk.edu

Gerard J.F. Ring, University of Wisconsin—Stevens Point
gerrryring@wi-net.com, +1 715 592-3732

Scott Rosencrance, Kemira Chemicals
scott.rosencrance@kemira.com, +1 770 429-2753

Paul Wiegand, NCASI
pwiegand@ncasi.org, +1 919 941-6417

Junyong Zhu, USDA Forest Products Laboratory
jzhu@fs.fed.us, +1 608 231-9520

Join TAPPI *today!*

TAPPI JOURNAL is a free benefit of TAPPI membership, and is only available to members. To join TAPPI, to renew your TAPPI Membership, or to learn about other valuable benefits, visit www.tappi.org.

TAPPI, 15 Technology Parkway S., Suite 115, Peachtree Corners, GA 30092, publishes *TAPPI JOURNAL* monthly.

ATTENTION PROSPECTIVE AUTHORS: All papers published are subject to *TAPPI JOURNAL's* peer-review process. Not all papers accepted for review will be published. Before submitting, check complete author guidelines at http://www.tappi.org/s_tappi/doc.asp?CID=100&DID=552877.

Statements of fact and opinions expressed are those of individual authors. TAPPI assumes no responsibility for such statements and opinions. TAPPI does not intend such statements and opinions or construe them as a solicitation of or suggestion for any agreed-upon course of conduct or concerted action of any sort.

Copyright 2018 by TAPPI, all rights reserved. For copyright permission to photocopy pages from this publication for internal or personal use, contact Copyright Clearance Center, Inc. (CCC) via their website: www.copyright.com. If you have questions about the copyright permission request process, please contact CCC by phone at +1 978 750-8400. To obtain copyright permission to use excerpts from this publication in another published work, send your specific request in writing to Editor, TAPPI JOURNAL, 15 Technology Parkway S., Suite 115, Peachtree Corners, GA 30092, USA; or by fax to +1 770 446-6947. Send address changes to TAPPI, 15 Technology Parkway S., Suite 115, Peachtree Corners, GA 30092, USA; Telephone +1 770 446-1400, or FAX +1 770 446-6947. www.tappi.org

Editorial



DOUGLAS W. COFFIN
TAPPI Journal
Editorial Board

Looking back and looking forward: Paper physics and the paper industry

In 1937, E.W. Samson, a physicist for the Hammermill Paper Company, wrote an article titled "Physics in the paper industry" [1]. In his introduction, he wrote:

> *Without paper there would be few physicists and very little understood physics. Conversely, without physics there would be no paper, for paper making is fundamentally a physical process. And yet this great industry managed to wobble along for about two thousand years without the aid of the physicist, and without apparently missing him. It is a pointed question to ask, what can the physicist do for the paper industry?*



Derek Page's 1969* Tappi *paper is perhaps the single most important work from the heyday of the Paper Physics field.* TAPPI Journal *is excited to reprint the original paper as a starting point for those interested in the topic (p. 581).

It seems that this question is still relevant today, and maybe even more so than at any other point in the intervening 81 years. In the United States, Paper Physics started in 1935 when Johannes A. Van den Akker accepted the position of Chair of the Department of Physics for the fairly new Institute of Paper Chemistry in Appleton, WI, where he remained until 1970. During this time, the field of Paper Physics developed and grew. Samson stated that in 1937, he was only aware of 10 Ph.D. physicists in the entire U.S. paper industry. When I was a faculty member at the Institute of Paper Science and Technology (IPST) in Atlanta, GA, during the 1990s, we had 10 faculty in the Paper Physics group alone and a host of Ph.D. industrial advisors. In addition, all 14 paper programs in the United States at that time had staff involved in Paper Physics.

I was lucky to begin my career in the paper industry at such a place and time. Today, I think we can count the number of active paper physicists in the United States on one hand. I do not believe that this is because the physics of paper has become irrelevant, but rather the decline in activity was a consequence of the major consolidation of the industry and the poor economic times at the start of this century.

Renewed Emphasis on Paper Physics

I am starting to feel an excitement in the U.S. industry today surrounding Paper Physics. There is renewed interest in understanding and improving the performance of paper materials. Much of that excitement is geared toward packaging and tissue, but the fundamental physics remain unchanged. There is a wealth of information published in the literature from the 1930s to present just waiting to be exploited. In addition, there is an active international community of paper physicists continuing to make progress and provide knowledge and tools that could help the industry stay competitive.

Just this fall (September 23-27), the Progress in Paper Physics Seminar was held in Lodz, Poland. This conference generated much discussion and some wonderful worldwide developments in the area of paper physics were reported. In Lodz, the 2018 Van den Akker Prize, the highest award within the Paper Physics community, was presented

to Amanda Matson and Tetsu Uesaka of Mid Sweden University for their work on the statistical mechanics of creep and failure for paper [2]. Theirs is interesting work that forces us to look at an old problem from a different point of view.

New Research and the Page Equation

At the Progress in Paper Physics Seminar, there were two presentations that both related to the Page equation [3]. Part of the presented work of Dr. Joel Pawlak [4] of North Carolina State University was a model for the tensile strength of tissue. Pawlak and his co-authors developed a model based on the physics of tensile failure of tissue being dominated by fiber pullout. To me, this shows that we still have people in the United States that are willing to think critically and develop new insights into the response of paper. Interestingly, Pawlak found that the Page equation was equally valid as a predictive model, once again showing the robustness of this Page equation. I presented a model [5,6] at the seminar for approaching tensile and tear strength development from the standpoint of a characteristic length that captures the ability of the paper to concentrate stored energy; in other words, using fracture mechanics to predict tensile strength. I think this is important because it links peak tear strength to fiber length, and that characteristic length is not just a geometric parameter. I emphasized that my approach is not unsympathetic to the Page equation, but we need to think beyond it.

That said, one could argue that the development of the Page equation [3] is the single most important work that came out of the Paper Physics community in the heyday of the field—1950 to 2000. Its originator, Derek Page, joined the paper industry in 1955 in Britain. In 1964, he emigrated to Canada to work for Paprican, where he was until 1993. After that he spent winters at IPST in Atlanta, GA. In 1969, Derek published a paper in *Tappi* titled "A theory for the tensile strength of paper" [3]. In this paper, he presented what later become known as the Page equation. A most important lesson one can take away from this article and the Page equation is the following: the strength of paper is a result of how well the fibers are bonded into the paper. For a poorly bonded sheet, it does not require much force to pull fibers out and strength is dominated by this low "bond strength." As bonding is improved, the force to pull out a fiber exceeds the strength of the fibers until mostly fibers will break rather than pull out. The maximum possible strength is much closer to the fiber strength. This concept and the simple Page equation have withstood the test of time, and anyone interested in understanding of the physics of paper should read this paper by Derek Page. Thus, this month, *TAPPI Journal* is excited to reprint the original 1969 paper as a starting point for anyone interested in Paper Physics.

We hope TAPPI can foster the new resurgence of Paper Physics in the United States by bringing new articles on the topic in future issues of *TAPPI Journal*. We are very excited that the International Paper Physics Conference will be held as part of PaperCon 2019 in Indianapolis, IN, next May. The last time this conference was held in the United States was in 1999. Hope to see you in Indy!

Douglas W. Coffin is a member of the TAPPI Journal *Editorial Board and professor in the Department of Chemical, Paper, and Biomedical Engineering at Miami University in Oxford, OH, USA.*

References

1. Samson, E.W. "Physics in the paper industry," *J. Appl. Phys.* 8(7): 455(1937).
2. Mattsson, A. and Uesaka, T., "Characterisation of time-dependent, statistical failure of cellulose fibre networks," *Cellulose* 25(5): 2817(2018).
3. Page, D.H., "A theory for the tensile strength of paper," *Tappi* 52(4): 674(1969).
4. Wang Y., Pawlak J., and Gonzalez, R., "The effects of fiber selection on the physical property of bath tissue and paper," *Progress in Paper Physics Seminar*, Lodz University of Technology Press, Lodz, Poland, 2018, p. 64.
5. Coffin, D.W. "A fractured-based view of strength development in handsheets," *Progress in Paper Physics Seminar*, Lodz University of Technology Press, Lodz, Poland, 2018, p. 44.
6. Coffin, D.W., "A fracture-based description for the development of tensile and tear strength in paper," *J. Sci. Technol. For. Prod. Processes* 6(6): 29(2017).

Laboratory method for determining the source of brightness loss at a southern United States bleached paperboard mill

ARU TIWARI, ASHOK GHOSH, AND PETER W. HART

ABSTRACT: Bleached pulp is known to lose some brightness between the end of the bleach plant and the paper machine reel. An ISO brightness drop of 1–3 points is often experienced. There are many reasons for the brightness loss; however, the usual suspects tend to be water quality, metallurgy, and process chemicals.

One bleached paperboard mill in the southern United States had been experiencing brightness losses in the 6–8 point range for several years. A systematic study was conducted to determine the potential sources for this brightness loss. A laboratory simulation technique was developed to demonstrate the potential causes for the brightness loss along the process.

Application: This study examines how to define the relevant aspects of a pulp/papermaking process, followed by systematically modeling the effect of process chemicals on paper brightness. The concepts of this study may be used by process engineers to model their process in a laboratory, and to investigate the root cause for changes in many paper properties.

Brightness loss had been a substantial problem for a particular southern United States bleached paperboard mill over the past few decades. This reduction in brightness between the end of the bleach plant and the reel brightness of the paper machine had been reported as 6–7 ISO points. Several discussions had occurred between the paper mill and the pulp mill personnel regarding unacceptable levels of pulp brightness reversion. The mill had conducted several brightness reversion tests, and the results indicated the brightness reversion was about 0.5 ISO brightness points, which was significantly lower than the reported brightness loss of 6–7 ISO points. Nevertheless, pulp brightness targets were raised to help compensate for this brightness loss. The paper mill claimed the pulp brightness loss had considerably raised production costs due to increased use of bleaching chemicals, as well as papermaking additives and fillers, in order to meet the reel brightness target.

Over the years, several hypotheses were tested with projects by co-operative education (co-op) students to explain this brightness loss. Biocide activity, mill water treatment, and metallurgy issues were all individually investigated. None of these investigations produced an acceptable explanation for the discrepancy in brightness loss.

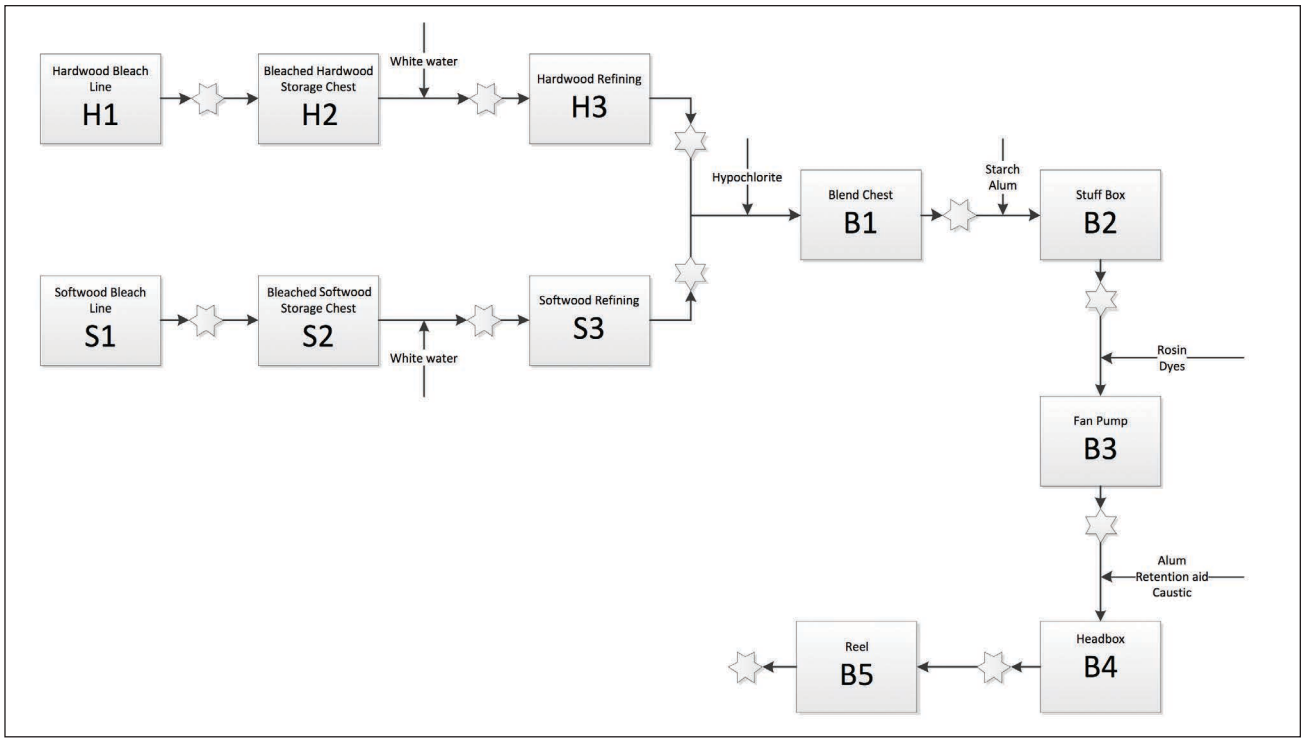
Instead of starting with a hypothesis and attempting to prove or disprove it, the current work takes a more holistic approach towards understanding the mill's brightness loss issue.

EXPERIMENTAL METHOD

Bleached hardwood and softwood pulps were separately sampled after the final bleach washer prior to dilution. A process flowsheet was prepared. Stock consistency, source of dilution water, and amount and type of chemical additive were recorded for each addition point (**Fig. 1**). Chemical additives used by the paper mill were sourced from the paper mill at the time of the pulp sampling.

The pulp mill's brightness method employed a quick dry test. A pulp "puck" of about 30% consistency was used. The quick dry test involves acquiring a small pulp sample and placing it into an air press to create a pulp disk ("puck"). Next, 25 ml of acetone was added to the disk prior to re-pressing in the air press. The disk was run through a wringer and dried for 4 min in an oven at 240°C. The mill's method was compared with brightness pads made in accordance with TAPPI Standard Test Method T 218 "Forming handsheets for reflectance testing of pulp (Büchner funnel procedure)." Brightness measurements were conducted on the dried pulp disks and TAPPI pulp pads using TAPPI Standard Test Method T 525 "Diffuse brightness of paper, paperboard and pulp (d/0)." After the initial comparison of the mill's method versus the TAPPI T 218 method for making brightness pads, the TAPPI T 218 method was used in rest of the study.

A stock slurry was created in a beaker with either distilled water or mill water. A separate stock slurry was prepared for each point where the pulp slurry was modified in the mill. These samples were heated to the mill process temperature



1. Block diagram of the process.

(55°C) and mixed with appropriate proportions of specific additives that would be added to the stock at the wet end of the paper machine. If several chemicals were added to the same sample, then each chemical was added 10 min apart to allow for adequate mixing/reaction with the pulp. Brightness pads were made in accordance with TAPPI T 218, and brightness was measured in accordance with TAPPI T 525.

Hardwood and softwood pulps were individually refined before being mixed at the blend chest. The major chemicals added to the process were added in the following order: (1) sodium hypochlorite (hypo) before the blend chest (hypochlorite is also added to raw mill water as a biocide); (2) starch and alum before the stuff box; (3) dispersed rosin and dyes before the fan pump; and (4) trim alum, retention aid, and caustic prior to the headbox. The effect of water quality was also investigated.

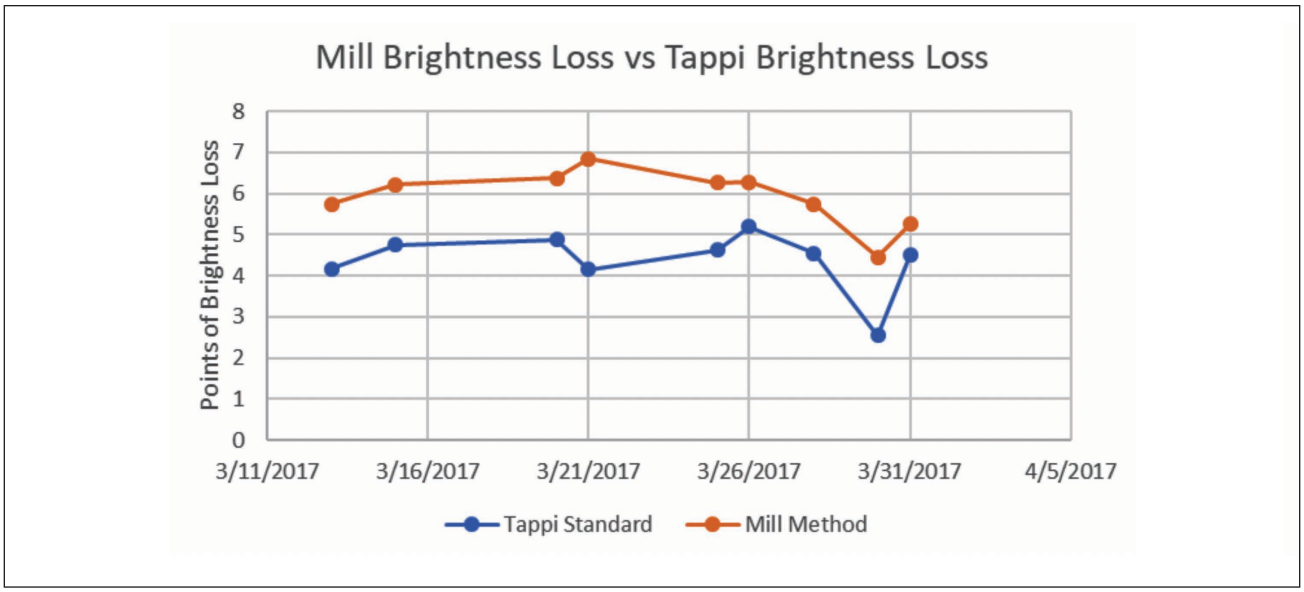
RESULTS AND DISCUSSION

The first step was to verify the amount of actual brightness reversion occurring in the pulp. Samples of fully bleached pulp were collected leaving the bleach plant and made into brightness pads. Brightness measurements were made on some of the pads. Others were placed in a 105°C oven overnight. The resulting loss in brightness due to heat reversion was about 0.4% ISO, which was similar to that determined in earlier internal mill studies.

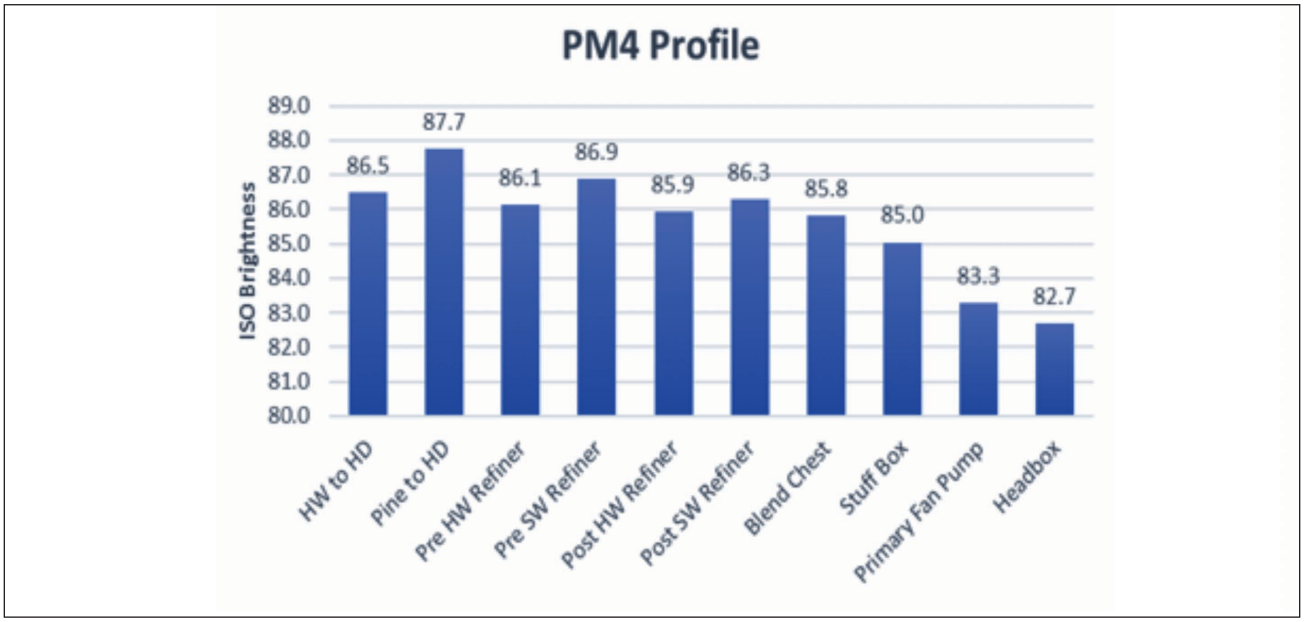
The next step consisted of verifying that the pulp mill and the paper mill were reporting the same values for the same sample. The pulp mill was found to be using an in-house developed test to obtain a quick brightness sample from wet pulp as detailed in the Experimental section ("puck" method), while the paper mill was using dry sheets off the reel. Twenty-two sets of brightness pads were made using the previously described mill method and using the TAPPI T 218 method. Brightness was measured by the TAPPI T 525 method. The brightness pads made with the mill method were about 1.5% ISO points higher than those made by TAPPI T 218 (**Fig. 2**). As the online paper machine reel brightness sensor was calibrated to absolute brightness scale, the actual brightness drop from bleach plant was about 5% ISO points instead of the originally reported 7% ISO points.

A comprehensive brightness profile was conducted in the paper mill to determine the change in brightness along the process (**Fig. 3**). The pre-refiner brightness dropped by 0.4 points for hardwood and by 0.8 points for softwood due to introduction of paper machine white water to the bleached pulps. The paper machine white water contains a mix of the various process chemicals, and small debris (fines), which may cause a reduction in brightness. The effect of fines was not evaluated as part of this study. Fines can negatively affect stock brightness, as they tend to have more chromophores than the pulp fibers. They also tend to adsorb pitch, dissolved lignin, transitional metal ions, etc., which make the fibers less bright. The fines may also affect the formed handsheet/brightness pad by changing the scattering coefficient (s) value of the pad. This in turn will affect the pulp brightness by the Kubelka-Munk relationship.

Refining the pulps reduced brightness of hardwood pulp by 0.2 points and reduced softwood by about 0.5 points (Fig. 3). Pulp refining changes the relative bonded area of the pulp



2. Comparison of mill method for making brightness measurement pads and the TAPPI Standard Test Method T 218 "Forming handsheets for reflectance testing of pulp (Büchner funnel procedure)."



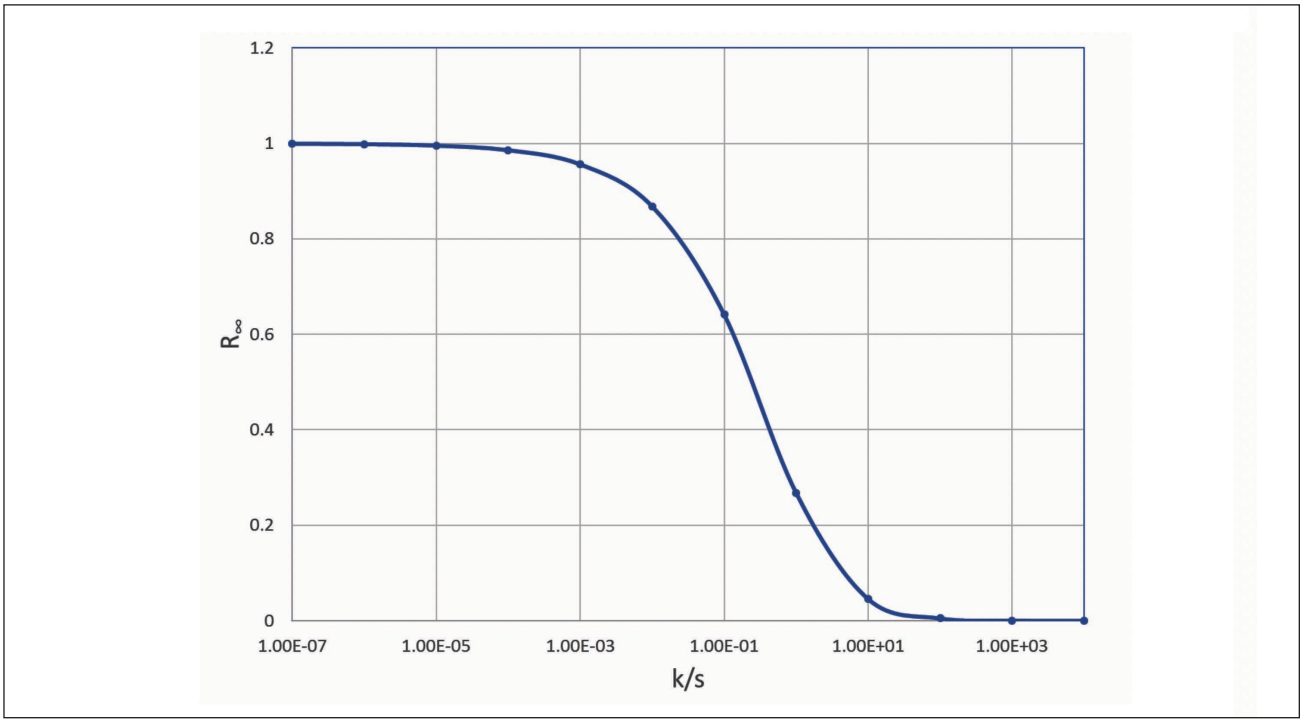
3. Change in brightness at paper mill (HW = hardwood; HD = high density storage chest; SW = softwood).

sheets, resulting in changes in scattering coefficient, which impacts brightness. Theoretical models have been developed to express the reflectance characteristics of the paper [1]. For an infinite thickness sheet, the Kubelka-Munk equation can be expressed as:

$$R_\infty = 1 + \frac{k}{s} - \sqrt{\left[\left(\frac{k}{s}\right)^2 + 2\left(\frac{k}{s}\right)\right]}$$

where R_∞ is the reflectance of an "infinitely" thick pad, k is the light absorption coefficient, and s is the light scattering coefficient. R_∞ is essentially a function of the ratio of absorption and scattering coefficient (k/s) and is graphically shown in **Fig. 4**. When measured at a light wavelength of 457 nm, the reflectance is equal to the brightness of the sheet when brightness is expressed in decimal form (not percentage). Pulp refining results in increased bonding, thereby reducing the possible number of fiber-air interfaces. The reduction of fiber-air interfaces will result in reduced light scattering, which in turn results in lower brightness.

The hardwood and softwood pulps, along with sodium hypochlorite, were mixed in the blend chest (location B1 in Fig. 1). The blend chest brightness was reduced by about 0.3



4. Change in reflectance versus* k/s *(Kubelka-Munk equation).

points based on the average of the hardwood and softwood post-refined pulp brightness.

After the blend chest, the next samples were taken from the stuff box (location B2 in Fig. 1), where starch and alum were added. The brightness loss from the blend chest to the stuff box was 0.8 points. In earlier internal studies, the starch was shown to have a minimal effect on brightness. Hence, the brightness loss in this instance was likely caused by the alum. Alum was found to have copious quantities of iron ions (**Table I**), which may explain the brightness loss [1].

The next samples were taken from the fan pump (location B3 in Fig. 1). Dispersed rosin and dyes were added between the stuff box and fan pump. The brightness loss from the stuff box to fan pump was 1.7 points. It should be noted that the dyes can affect the light absorption coefficient of the Kubelka-Munk relationship. If they absorb in the 452 nm wavelength, they will decrease brightness. If the dyes happen to fluoresce, they can possibly influence brightness, unless the brightness instrument corrects for fluorescence-induced brightness.

Rosin is generally colored, so it probably contributes some chromophores and increases the light absorption coefficient (*k*).

The final pulp sample was taken from the headbox (location B4 in Fig. 1), and the chemicals added between the headbox and fan pump were retention aid, alum, and caustic. The brightness loss from the fan pump to headbox was about 0.6 points.

There was a slight drop in brightness (about 0.2% ISO) from the headbox to the end of the paper machine reel (location B5 in Fig. 1). Past studies on newsprint machines [1] have shown that brightness loss during forming, pressing, and drying sections were primarily caused by a reduction in scattering coefficient due to fiber alignment and sheet consolidation during papermaking. A relatively smaller portion of the brightness loss was caused by the increase in absorption coefficient during sheet drying.

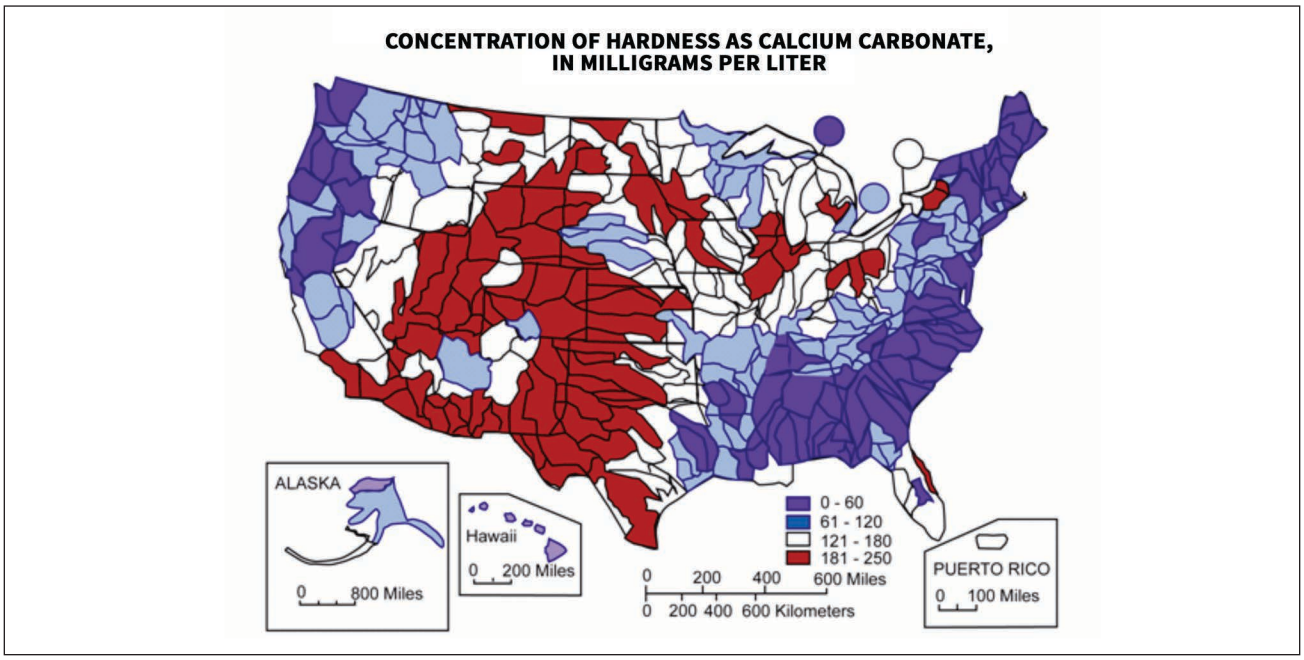
In summary, the previously described brightness profile (Fig. 3) showed that about 0.6 points of brightness loss was caused by refining and by the sheet forming/drying process. The remaining 4.5 points of brightness loss was caused by water and process chemicals. Contaminants, including fines, may also be responsible for some of the brightness loss; however, the contaminants (e.g., fines) were not considered in this study.

The next step was to develop and validate a laboratory method for determining the effect of chemicals on pulp brightness by comparing each laboratory step with the brightness profile determined in the paper mill. The hardwood and softwood bleached pulps after their respective final bleach plant washers were used in the laboratory simulation to eliminate the paper machine white water used for dilution. All the laboratory simulations were performed on unrefined pulp.

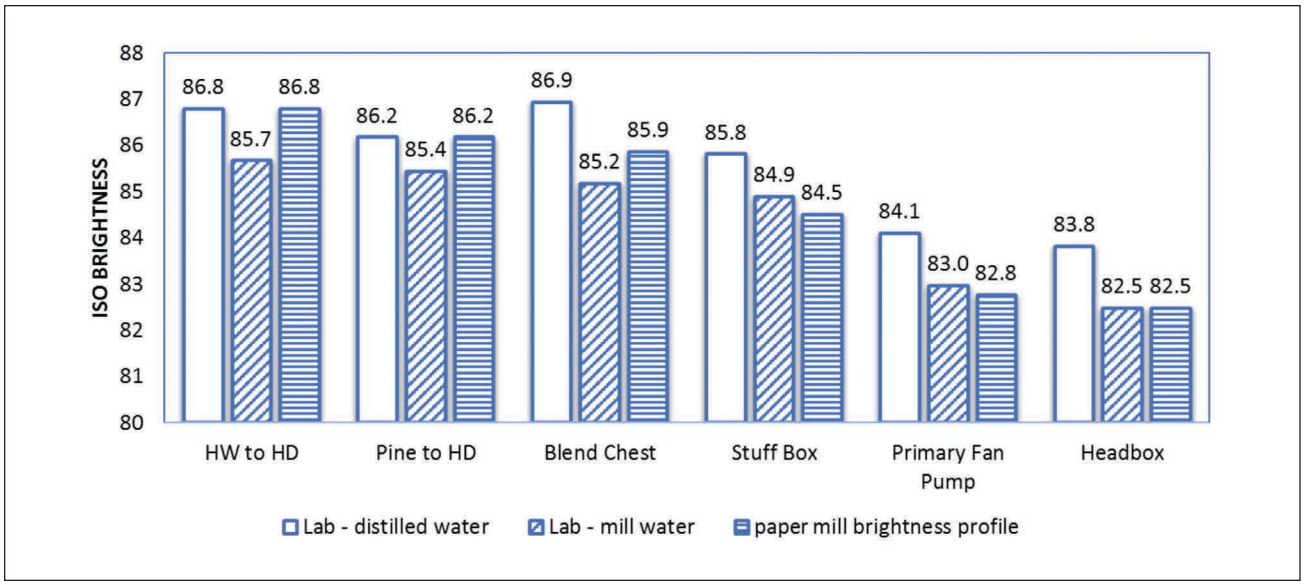
The mill draws its raw water supply from aquifers; the mill uses sodium hypochlorite for the control of biological growth. The chemical characteristics of the mill water are summarized in Table I. The mill does not have a water treatment plant to condition the incoming water from the aquifers; the raw water has a relatively low hardness of about 50 mg/l as calcium carbonate (**Fig. 5**).

	Mill Water	White Water	Hard-wood Filtrate	Soft-wood Filtrate	Rosin	Red Dye	Blue Dye	50% Alum	70% Sulfuric Acid	50% Caustic	Hard-wood Pulp	Soft-wood Pulp
Aluminum	< 0.02	8.2	0.06	0.02	2800	< 0.05	0.08	52,700	10	< 5.0	34	< 5.0
Barium	0.23	0.48	0.45	0.17	0.08	0.23	0.23	< 0.5	< 0.5	< 0.5	16	5.9
Calcium	16	54	0.31	14	30	17	18	< 50	< 50	< 50	930	440
Calcium hardness	40	134.8	77.4	35	74.9	42.4	44.9	< 125	< 100	< 100	2322	1099
Copper	< 0.002	0.011	0.011	0.007	0.27	< 0.005	42	5.6	0.7	< 0.5	< 0.5	< 0.5
Iron	0.02	0.17	0.08	0.05	1.5	0.12	0.13	1240	17	< 5.0	< 5.0	6.1
Total hardness	51	155	88	49	124	55	59	N/A	N/A	N/A	N/A	N/A
Potassium	1.7	2.4	3.6	2	8	1.7	2	< 20	< 20	140	< 20	< 20
Magnesium	2.6	4.9	2.5	3.4	12	3	3.3	< 20	< 20	< 20	67	79
Magnesium hardness	10.7	20.2	10.3	14	49.4	12.4	13.6	< 50	< 50	< 50	276	325
Manganese	0.02	0.47	0.43	0.079	1	0.021	0.02	1.2	< 0.5	< 0.5	13	2.8
Sodium	76	220	240	130	580	77	80	98	52	302,000	620	290
Strontium	0.29	0.49	0.24	0.25	0.15	0.29	0.28	0.6	< 0.2	< 0.2	7.1	6.4
Zinc	< 0.02	0.03	0.03	0.03	1	< 0.05	< 0.05	< 5.0	< 5.0	< 5.0	< 5.0	< 5.0

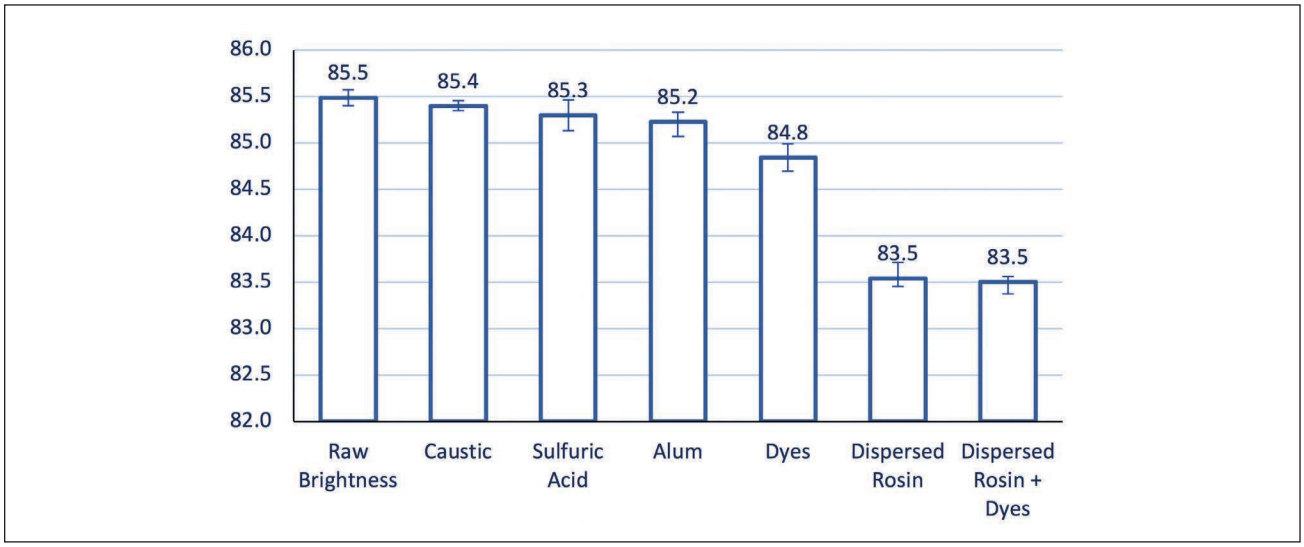
I. Metal analysis (mg metal/kg liquid or mg metal/kg pulp).



5. Patterns of water hardness in the United States during 1975 water year (i.e., Oct 1 – Sept 30) [1].



6. Laboratory method validation to match brightness loss in the paper mill (HW = hardwood; HD = high density storage chest; SW = softwood).



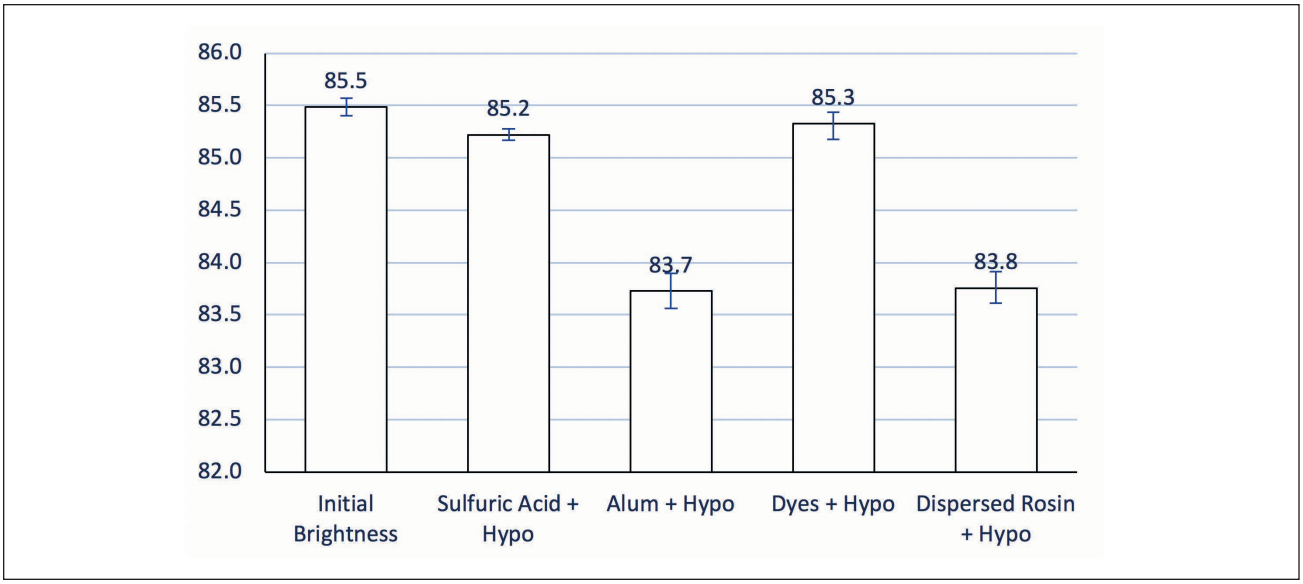
7. Effect of individual additives on brightness loss.

The mill had also expressed concern that the mill water was picking up metals, like iron and manganese, from the process, such as piping and equipment. These metal ions can be oxidized to higher valence by hypochlorite or chlorine to change their color. For example, Fe(II) is typically green in color whereas Fe(III) is generally yellow-orange to brown in color. This shift in color could intensify the loss in pulp brightness by making the pulp appear to have a yellow tint. Metal ions with higher valence states are generally more strongly adsorbed onto substrates that contain ligands (e.g., carboxylates and amines) than their lower valence state counterparts.

The chemical additions to the pulp samples were done with distilled water and fresh mill (hypo-treated) water to determine whether any chemicals such as dissolved minerals interact with components in mill water to further reduce brightness. The use of fresh mill water resulted in about a 1-point brightness loss as compared to using distilled water alone or when used in combination with process chemicals (**Fig. 6**).

The laboratory method matched the relative drop in brightness to that of the pulps sampled from the paper mill (Fig. 6). Thus, this laboratory investigation suggested that the largest brightness drop occurred due to the addition of rosin and dyes. This would correlate to the fan pump location in the paper mill. The second biggest drop in brightness occurred with the addition of retention aid, alum, and caustic. This would correlate to the headbox location in the paper mill.

Based on these previously described findings, some chem-



8. Effect of individual additives in presence of sodium hypochlorite on brightness.

icals were individually added with mill water to the hardwood-softwood pulp blend for evaluating their effect on brightness. The dispersed rosin reduced brightness by nearly 2 points, followed by the dyes, which caused about 0.7 points of brightness loss. When dyes and dispersed rosin were added together, the resulting brightness loss remained at about 2 points, indicating that the effect of the rosin was the dominant factor on brightness loss (**Fig. 7**). The brightness loss caused by the mill caustic, sulfuric acid, and alum were within 0.3 points from the starting brightness (Fig. 7). The results were somewhat surprising, as the brightness losses were generally higher during the earlier runs summarized in Fig. 6. A possible reason for the lower brightness caused by individual chemicals may be that hypochlorite was added in the previous run, which may interact with the additives and result in an additional brightness drop.

The individual chemicals were run again in combination with hypochlorite. The resulting brightness loss for alum in presence of paper mill water was 0.9 points (**Fig. 8**). A possible explanation may be related to the high iron content in alum, which is being oxidized by residual hypochlorite. Dyes, in the presence of residual hypochlorite, caused a brightness loss versus when hypochlorite was absent. It is possible that the residual hypochlorite oxidized the dyes and thereby affected its influence on pulp brightness. Further work is needed to substantiate this hypothesis.

CONCLUSIONS

A systematic investigation was performed on the cause for the reported 7-point brightness loss from the bleach plant to the paper machine. The brightness measurement procedures were checked, and the reported bleach plant brightness as measured using the mill's in-house method was determined to be about 1.5% ISO points higher than that measured by the TAPPI Standard T 218 method. Because the paper machine brightness measured at the online reel sensor was calibrated using TAPPI T 218 brightness method, this offset accounted for about 1.5 points of the reported brightness loss. The brightness reversion was determined to be about 0.4 points. Thus, the actual brightness loss from bleach plant to paper machine was about 5 points, which was still substantial. The hardwood lost less brightness (0.4 points) than softwood (0.8 points) when diluted with white water, likely due to the higher initial brightness for the bleached softwood (87.7% ISO) versus that of hardwood (86.5% ISO). Refining also caused a loss in brightness for hardwood (0.2 points) and softwood (0.5 points). The remaining brightness losses were caused by various process chemical additions.

A laboratory method was established to simulate the loss in brightness due to chemical addition. When individual chemicals were added, the most significant brightness loss was caused by the dispersed rosin (2 points) and dyes (0.7 points), and the remaining chemicals individually reduced brightness by less than 0.3 points each. Because some of the chemicals contain copious amounts of transition metal ions that are colored at a higher oxidation state, the chemicals were individually added in the presence of hypochlorite. The resulting brightness losses were about 1.8 points each for dispersed rosin and alum. However, the brightness loss due to dye addition in presence of hypochlorite was appreciably higher than in the absence of hypochlorite.

The technique described here may be used by paper mills to investigate the root cause for brightness loss and to determine which chemical additions could be replaced so that brightness losses are smaller. This could be accomplished by either using different chemical additives, or by using the same chemical additive with fewer impurities. **TJ**

LITERATURE CITED

1. Biermann, C.J., *Handbook of Pulping and Papermaking*, 2nd Edn., Academic Press, New York, 1996, pp. 487-505.
2. Ghosh, A. and Ni, Y., *J. Pulp Pap. Sci.* 24(1): 26(1998).
3. Poirier, N.A. and Pikulik, I., *Drying Technol.* 15(6-8): 1869(1997).
4. USGS, "Water Hardness and Alkalinity," U.S. Geological Survey, Reston, VA, USA, 2005. Available [Online] https://water.usgs.gov/owq/hardness-alkalinity.html <5Oct2018>.

ABOUT THIS PAPER

Cite this article as: Tiwari, A., Ghosh, A., Hart, P. *TAPPI J.* 17(10): 547(2018). https://doi.org/10.32964/TJ17.10.547

DOI: https://doi.org/10.32964/TJ17.10.547

ISSN: 0734-1415

Publisher: TAPPI Press

Copyright: ©TAPPI Press 2018

About this journal

ABOUT THE AUTHORS

We studied brightness loss at this bleached paperboard mill because it had resulted in increased production cost and the mill wanted to understand the effect of their process on brightness. In the past, we had successfully taken a holistic approach to solving a mill problem, but the difference here was in the sheer range of possible variables.

The most difficult aspect of this study was the number of process variables. The potential of interaction within chemicals was a challenge that had to be dealt with by carefully defining the variables that were going to be included in the study and then determining an appropriate experimental design to account for potential interaction. This was a challenging project for our co-operative education student and co-author of this paper, Aru Tiwari, and we appreciated his efforts in not only following directions but also working out some of the challenges by himself. The most interesting aspect of this work was being able to very successfully simulate the effect of so many process chemicals in the laboratory in matching the process response.



Tiwari



Ghosh



Hart

The mill in this study has used the information to evaluate its existing chemicals for minimizing brightness loss. It also plans to use this problem-solving concept for future issues.

Tiwari is a co-operative education student from Virginia Polytechnic Institute, Ghosh is research engineer, and Hart is director, Fiber Technology and Innovation, at WestRock, Richmond, VA, USA. Email Ghosh at ashok.ghosh@westorck.com.

Production of polyhydroxyalkanoates (PHA)-based renewable packaging materials using photonic energy: A bench and pilot-scale study

MICHAEL JOYCE, LOKENDRA PAL, AND TOM TRAN

ABSTRACT: This work describes the utilization of a new photonic heat treatment technology in combination with polyhydroxyalkanoates (PHA) materials for the development of biofriendly packaging and coated substrate materials. This technology advances the use of aqueous PHA coatings as a replacement for less environmentally friendly extruded plastic and fluorotreated packaging papers and boards. The new technology utilizes short burst photonic energy to heat PHA latex coatings. Utilizing a rapid pulse of photonic energy enables PHA particles to melt and form a film within milliseconds, as compared to conventional equilibrium drying that takes several minutes.

Coatings were applied to commercially produced papers in order to validate the combined use of photonic treatment technology with PHA materials for commercial applications. Photonic treatment for both bench-top and roll-to-roll pilot-scale studies resulted in kit values of 12, and 2 min Cobb values of <2 g/m^2. Repulpability studies showed the material to be completely repulpable, having 100% accepts after screening. The results demonstrate that the photonic treatment of PHA polymers could be used in current commercial settings to produce environmentally friendly packaging and coated products.

Application: By combining aqueous based PHA coating with photonic drying technology, it is now possible to implement PHA in commercial applications pertaining to environmentally friendly barrier coatings for the manufacture of functional paper and paperboard products, specifically for moisture vapor, moisture, and grease resistance. It presents an alternative to conventional non-renewable extruded polyethylene, petroleum-based latex coatings, and fluorochemical and chromium-containing coatings. Industry impacts for the introduction of this technology include: introduction of green chemistry formulations into coating processes, reduction of plastic waste in the recycle stream, increased utilization of renewable and sustainable product lines, and decreased carbon footprints.

Petroleum-based plastics present a major environmental and societal challenge. In 2013, approximately 32.5 million tons of plastic waste was generated in the United States, which accounted for approximately 12.8 percent of total municipal solid waste that same year [1]. Along with negative environmental impacts, conventional plastics are known to contain various additives that impact human health. These additives include bisphenol A (BPA), Di(2-ethylhexyl) phthalate (DEHP), and polyfluorinated compounds [2]. The substitution of plastics with biobased alternatives can help mitigate, if not eliminate, the negative consequences of petroleum-based plastic use. The use of polyhydroxyalkanoate (PHA) as a biodegradable plastic has been extensively studied and has shown great promise as a replacement for conventional plastics, including polyethylene (PE) and polypropylene (PP) [3-8]. It has also been shown that PHA improves the moisture resistance of paper [7] and its modification or blending of PHA with other natural materials provides similar barrier properties as plastic, such as water vapor transmission rate (WVTR) and oxygen transmission rate (OTR) [8].

In addition to the use of PHAs as a renewable and compostable barrier material, starch as a low-cost filler for bioplastic and petroleum-based polymers to improve the mechanical and thermal properties of films have been well studied. As a filler, it tends to reduce the tensile strength, elongation to break, and toughness of a blend, and tends to increase the blend's modulus. Starch has been blended with biodegradable polymers, such as aliphatic polyesters, to lower the cost and to enhance the biodegradability of the blends. For example, starch has been blended with polymers such as polycaprolactone (PCL) and poly-(hydroxybutyrate-co-3-hydroxyvalerate) (PHBV). Ramsay et al. [4] blended granular starch with PHBV. As the starch content increased from 0 to 50% (w/w), tensile strength decreased from 18 to 8 MPa, and Young's modulus increased from 1525 to 2498 MPa. The biodegradation rate was faster when starch was present in PHBV. Park et al. [9] blended granular cornstarch with poly(lactic acid) (PLA) and star-shaped PLA. Sun and Ke [10] blended PLA with granular cornstarch and talc to find starch effectively increased the crystallization rate of PLA. Reis et al. [11] found blends of

polyhydroxybutyrate-hydroxyvalerate (PHB-HV) with increasing waxy maize corn starch contents of 0%, 20%, 30%, 40%, and 50% to decrease the Young's modulus, strain to break, and puncture force. A lack of interfacial adhesion between starch and PHB-HV was also reported.

The use of PHA and its family of co-polymers with the addition of other natural materials for use in packaging has also been well studied. Shawaphun and Manangan [12] studied the possible use of PHA and PLA paper coatings for food packaging by dip coating papers with PHA and PLA resins dissolved in different solvents. The results showed PHB coated papers to have higher water resistance, but lower oil resistance in comparison to the PLA coated papers. Arrieta et al. [13] studied blends of PHB and PLA by preparing compression molded films from resin blends. Films were prepared with and without plasticizer and their properties compared. The addition of PHB greatly increased the film's oxygen barrier while decreasing wettability. The addition of poly(ethylene glycol) (PEG) and acetyl(tributyl citrate) (ATBC) showed the ATBC to be more effective than PEG in plasticizing the films. Modi et al. [14] used PHB with different polyhydroxyvalerate (PHV) contents (5%, 12%, and 20%) and varying molecular weights to obtain polymers with glass transition temperatures between 10°C and 20°C. The addition of PHBV enabled films with high elastic modulus, as well as flexural strength with low tensile strength and elongation at break, to be obtained. The WVTR of the films showed the PHBV polymers to be very hydrophilic. As a result, their WVTR in comparison to other thermoplastic polymers used for packaging were high. Bucci et al. [15] compared the dimensional and mechanical properties of PHB and polypropylene (PP). It was found that PHB packages had a different resistance to dynamic compression when compared to PP. The deformation value was about 50% lower than PP, due to the increased rigidity and lower flexibility of the PHB material. For freezing and refrigeration conditions, the PHB's performance was lower than that of PP. However, at higher temperatures, the PHB performed better than PP. Follain et al. [16] studied the structure and barrier properties of PHA films prepared by solvent cast and compression molding methods. It was found that the film-forming process used had a negligible influence on the thermal features displayed in the PHA films.

Much of the work that has been completed using PHA has focused on its use in thermoforming or hot melt extrusion applications; however; there is little research that has been done pertaining to its use in aqueous coatings. Since PHA particles are highly hydrophobic, additional steps are required to stabilize them in aqueous media. The ability to stabilize PHA particles in aqueous media was first reported by Showa in 2004 [17]. This work was furthered by Whitehouse in 2015, where a method for producing aqueous PHA emulsions with polymer dispersants was described [18]. Whitehouse's work was utilized by Metabolix (Cambridge, MA, USA) for the creation of barrier coatings.

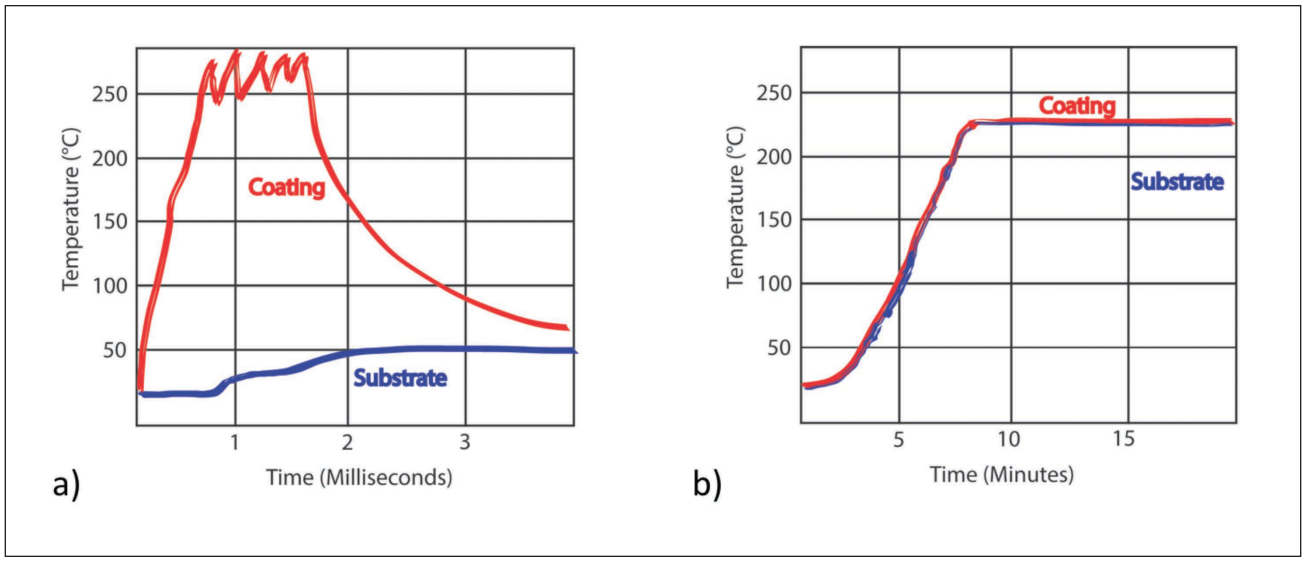
The ability of aqueous PHA latex to provide barrier properties makes it a viable candidate to replace holt melt extruded or fluoro treated papers and paperboards in applications such as food packaging. However, limiting factors such as high raw material costs [9] and loss in processing speed due to long dry time requirements still exist. Even if drying PHA materials using conventional techniques was not an issue, there would still be the issue of base substrate degradation due to the longer dwell time at high temperatures. As a result, the utilization of PHA materials for packaging has not been commercially adopted. Instead, extrusion or thermoforming processing methods that enable the high temperatures required to melt and form films from low cost petroleum-based plastics without detrimentally impacting the base substrate is practiced. However, as an off-machine process, its processing costs are higher than inline aqueous coating application methods.

Although advances in technology have improved the production yields of PHAs, at current manufacturing volumes the cost of PHA is not competitive with petroleum-based plastics. However, it is predicted that PHAs will be able to compete if manufacturing volumes increase. In order for manufacturing volumes to increase, a large-scale application is needed. Paper and paperboard coating applications could serve this need, if the process limitations noted previously could be overcome with the exposure of PHA latex coated papers to photonic energy.

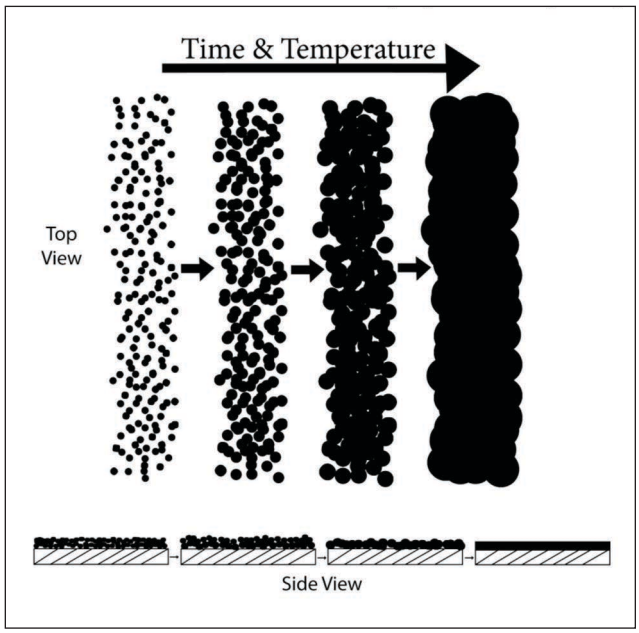
In this work, a high energy photonic surface treatment is explored due to its very specific advantage of rapidly heating a coated or printed surface to a high temperature without degrading the substrate. This is achieved by emitting a pulse of high intensity light from a xenon bulb. With this system, heat is transferred to the coating within milliseconds. The change-point for photonic vs. conventional drying is that photonic technology emits a light energy that is just intense enough to ensure thermal equilibrium between the particles and the substrate is never achieved (**Fig. 1**). The particles are treated and cooled before any substantial heat transfer to the base substrate occurs [19].

This drying technology differs from conventional equilibrium (oven) drying techniques where both the base substrate and coating material reach the ambient temperature within the drying system. The application of photonic energy enables the high-throughput film formation of (PHA) particles without damage to the base substrate. Melting of the PHA particles is required to create a continuous polymer film to achieve the desired barrier properties for packaging (**Fig. 2**).

The use of non-equilibrium drying methods will result in differences in the heating and cooling rates of the polymer throughout the coalescing and interdiffusion processes. Heating and cooling rates are known to impact the crystallinity of a polymer, which will subsequently impact functional barrier properties. The ability to tailor these heating and cooling rates may lead to the ability to further optimize functional coatings for application specific purposes. In this work, the main focus was on the feasibility of commercial implantation of this technology for drying of PHA materials. Future work could focus more on the optimization of barrier properties through a manipulation of heating and cooling rates via changes in photonic energy and/or pulse conditions.



1. Temperature of coating and substrate vs. time for a) equilibrium drying, and b) photonic drying.



2. Coalescing and interdiffusion of polyhydroxyalkanoates (PHA) particles with time and temperature.

EXPERIMENTAL

Materials

The PHA coating used was the trademarked Mirel 8000 latex supplied by Metabolix. Paper samples were supplied by two commercial paper manufacturers. The grade and basis weights of the substrates used are shown in **Table I**.

These basis weights are similar to the basis weights of products used in baking release and lightweight packaging applications. Having bleached and non-bleached samples was important to study the influence of color on photonic energy requirements.

Grade	Basis Weight, g/m²	Sample, #
Unbleached kraft	23	A
Bleached kraft	22	B
Bleached kraft	38	C
Unbleached kraft	90	D
Bleached kraft	95	E

I. Paper substrates.

Methods

Mirel 8000 latex was applied on selected papers using Meyer rods. Three different Meyer rods (#0, #10, and #22) were used to vary the coat weight applied. Sheeted samples were then treated using a photonic energy treatment system from Novacentrix (Austin, TX, USA). As a control, a set of samples was also dried using a hot air convection oven at 155°C for 10 min. The oven drying condition was selected based on the recommendation of the PHA latex supplier. After the initial lab screening to determine the photonic energy required to form a PHA film, studies were moved to pilot trials on a roll-to-roll coater equipped with a rod and gravure coating station, as well as photonic heat treatment units. For the application of PHA coating, an anilox roll with 9 billion cubic microns (bcm)/200 lines per inch (lpi) cells and Meyer rod #10 were used. **Table II** shows the pulse conditions used during the trial.

The determination of coat weight was completed using the ASTM F2217/F2217M-13 Standard Test Method "Standard practice for coating/adhesive weight determination." Coated samples were treated by one of two methods: infrared (IR) dried, and photonic energy treated. The pulse conditions varied based upon the coating application method used and the color of the substrate (white for bleached or brown for unbleached).

Condition #	Unbleached (Brown) Papers		Bleached (White) Papers
	1	2	3
Coating method	9 bcm Anilox	#10 Meyer rod	9 bcm Anilox and #10 Meyer rod
Power, V	275	320	400
Pulse length, us	5000	5600	5000
Number of pulses	1	1	1
Coating speed, ft/min	10 ft/min	10 ft/min	10 ft/min
Energy per unit area	3.35 J/cm^2	6.21 J/cm^2	10.38 J/cm^2

II. Pulse conditions used during pilot trial (bcm = billion cubic microns).

Name of Test	TAPPI Standard Test Method
Basis weight	T 410 "Grammage of paper and paperboard (weight per unit area)"
2-minute Cobb	T 441 "Water absorptiveness of sized (non-bibulous) paper, paperboard, and corrugated fiberboard (Cobb test)"
3M kit test	T 538 om-01 "Roughness of paper and paperboard (Sheffield method)"
Gurley porosity, HS, 10 mL/min	T 460 om-02 "Air resistance of paper (Gurley method)"
Water vapor transmission rate	TAPPI T 448 "Water vapor transmission rate of paper and paperboard at 23°C (73°F) and 50% RH"
Surface energy	T 558 "Surface wettability and absorbency of sheeted materials using an automated contact angle tester"

III. Standard TAPPI Methods for paper testing.

For unbleached papers, it was found that two different pulse conditions could be used: one for anilox coated samples and another for Meyer rod coated samples. The bleached substrates all utilized the same pulse condition regardless of the coating method utilized. The need for two different pulse conditions when using unbleached substrates is attributed to differences in coat weights obtained by both application methods. Less coating was transferred by the 9 bcm anilox. A larger anilox was not available. The higher energy required for bleached papers in comparison to the unbleached papers is attributed to the higher absorption of energy by the darker substrate. Also, because the color of the applied coating was white, differences in coat weight did not reduce the amount of energy absorbed. As a result, the pulse conditions required were the same regardless of the application method for the bleached papers.

When the #2 pulse condition was used for unbleached anilox coated samples, the substrate ashed. This problem did not occur with the bleached substrates as they absorbed much less energy. Higher energies were not used for the bleached substrates when using the Meyer rod due to lamp limits nearly being reached.

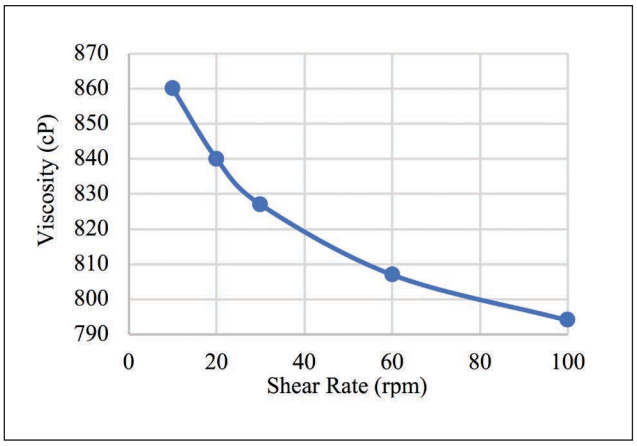
The particle size of PHA dispersion was measured with Malvern Panalytical 3600 Zetasizer particle size analyzer (Malvern Panalytical; Malvern, UK). Along with particle size, the viscosity of the coating at different shear rates was measured using a Brookfield DV-III Ultra viscometer (Ametek Brookfield; Middleboro, MA, USA) with a #3 spindle at 21°C. The thermal properties of the PHA coating were measured by thermal gravimetric analysis (TGA) with a TA Instruments Q500 TGA (New Castle, DE, USA), and differential scanning calorimetry (DSC) was used to purge the system using a TA Instruments Q2000 DSC (utilizing nitrogen gas). The TGA procedure was set to equilibrate at 30°C prior to ramping to 475°C at 10°C/min. TGA experiments were also run using air as a comparison to the nitrogen gas to determine if any oxidation reactions could be occurring that may affect the coating material structures. DSC measurements were run using a 10°C/min ramp to 100°C, where they were held for 10 min. They were then ramped to 190°C at 10°C/min. A purge gas flow rate to 20 psi was used for both TGA and DSC experiments.

The properties of uncoated and coated substrates measured and the test method used are shown in **Table III**. The 2-min Cobb test is a measure of water resistance, the 3M Kit test is a measure of oil and grease resistance. Gurley porosity is a measure of air permeability. Surface energy is a measure of printability (potential for anilox coating transfer), and level of internal sizing. The surface energy of the coated substrates was measured using an FDS OCA 15 EC goniometer (Future Digital Scientific; Garden City, NY, USA) with ultra-pure deion-

ized water and methylene iodide as the two testing fluids. Calculations were made using the Owens-Wendt method.

Scanning electron microscopy (SEM) images were obtained using a Hitachi S-3200N (Hitachi; Tokyo, Japan) variable pressure SEM system. Samples were sputter coated with 15 nm of Au/Pd (60/40) using a Hummer II sputter coating system (Anatech USA; Hayward, CA, USA) prior to imaging.

Repulpability testing was accomplished using the repulpability protocol established by the Fiber Box Association (Itasca, IL, USA). The two substrates tested were the #10 rod coated photonic treated and oven dried high basis weight unbleached paper, and the lowest basis weight bleached paper. These samples were tested because they represent the two different ends of the spectrum in regards to their properties and fiber types, with one being very bulky and porous (high basis weight unbleached grade) and the other having a very low grammage and low porosity (lowest basis weight bleached grade).

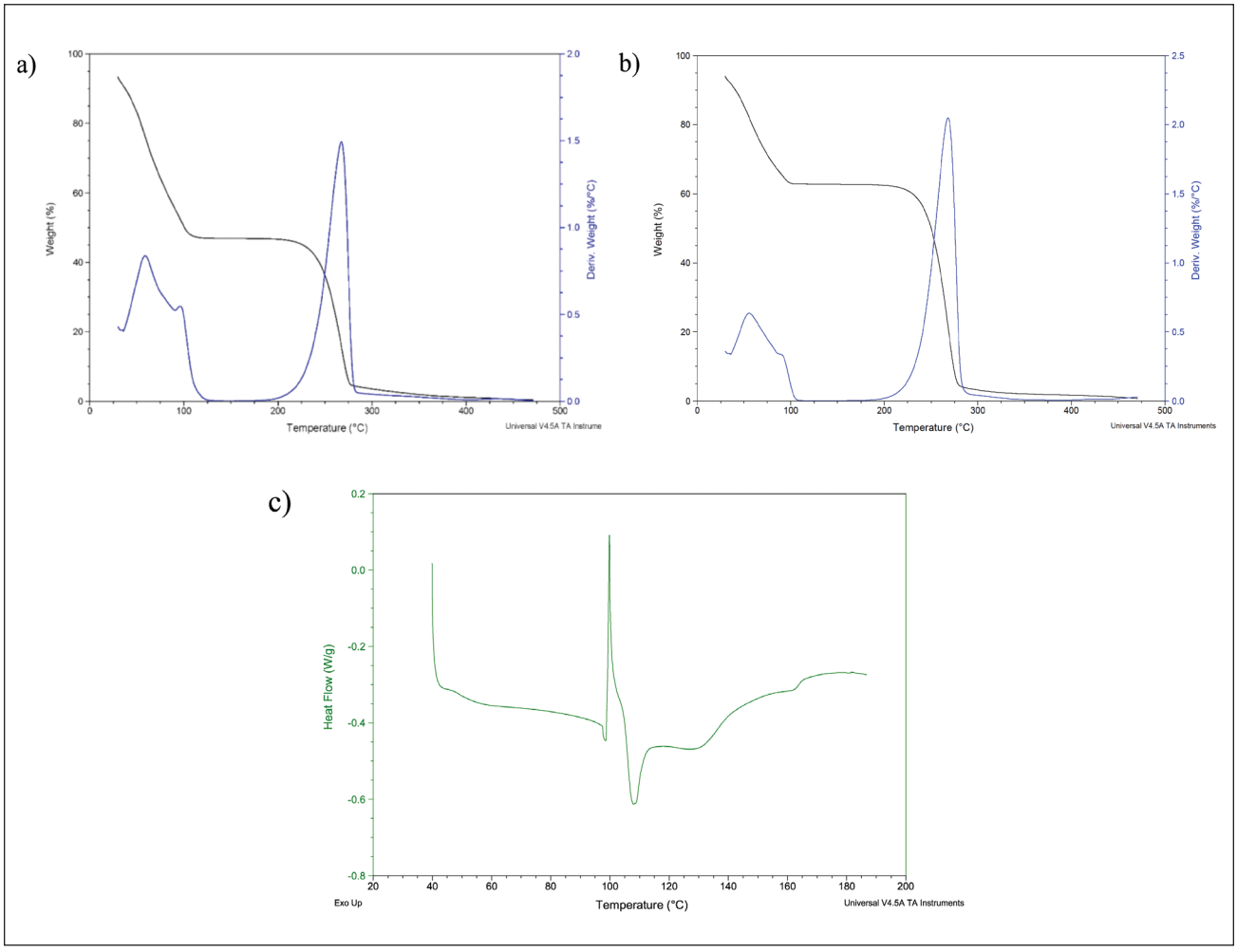


3. PHA Brookfield viscosity as a function of shear rate.

RESULTS

Aqueous PHA dispersion

The particle size was found to be 5 µm. The solids content and pH of the coating was measured and found to be 50.5% and 5.9, respectively. The Brookfield viscosities at different shear rates (rpm) is shown in **Fig. 3**. The density of the coating, measured using a pycnometer cup, was found to be 1.325 g/mL. The results of the TGA (left graph) and DSC (right graph) analysis are



4. PHA coating analysis using a) thermal gravimetric analysis (TGA; run with N_2), b) TGA (run with air), and c) differential scanning calorimetry (DSC).

Sample	Basis Weight, g/m²	2-min Cobb, g/m²	Porosity HP Gurley, s/10mL	Kit Value, #	Total Surface Energy, mN/m	Color
A	23	Fail	2.27	0	34.17	White (bleached)
B	23	15	0.84	0	41.03	Brown (unbleached)
C	36	18	4.08	0	17.33	White (bleached)
D	90	Fail	0.77	0	NA	Brown (unbleached)
E	97	30	0.96	0	35.33	White (bleached)

IV. Base sheet properties (HP = high pressure).

shown in **Fig. 4**. The results show the glass transition at 49.2°C, the crystallization at 99.8°C, and the product to have several melting points due to its multiple material constituents. Melting points are observed at 97°C, 108°C, 130°C, and 165°C.

From the TGA analysis seen in Fig. 4 (parts a and b), it can be seen that there are no oxidation reactions occurring that would impact the polymer performance. The relatively high T_g of this particular PHA material provides it with a unique plasticity that aids in film forming absent of excessive cracking. The ability to form a continuous film absent of cracking is necessary to provide optimal barrier performance, such as those of water vapor, oil, and grease. The melting temperature of this PHA is in line with previously published PHA/PHB materials [20,21].

Base substrate properties

The barrier properties of the uncoated substrates are shown in **Table IV**. Two of the base sheets failed the 2-min Cobb test. A failure of the Cobb test occurs when water penetrates through the test substrate and can be seen on the surface of the testing apparatus. The surface energy of one sample was unable to be obtained and is marked as ("NA") due to the test liquids penetrating into the substrate surface prior to the time to enable calculation of surface energetics.

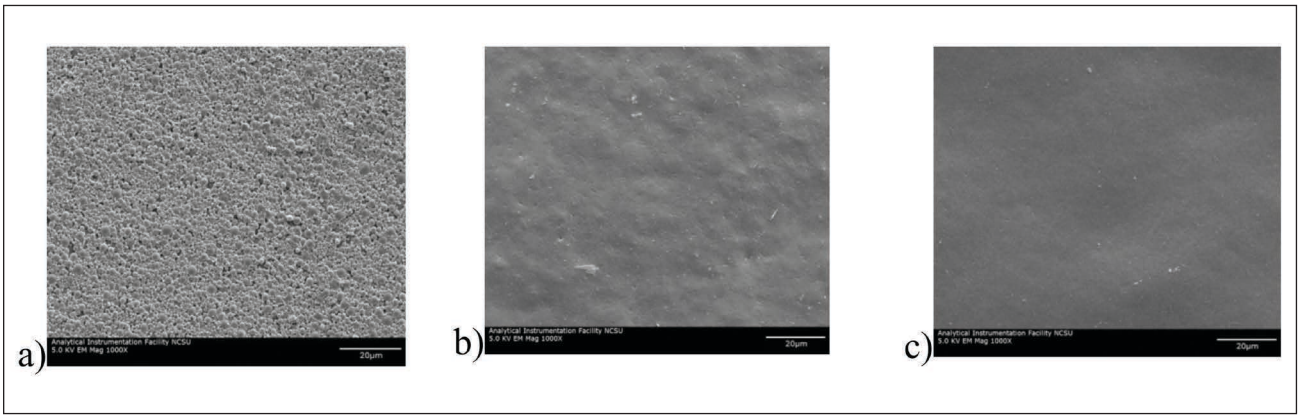
As expected, all samples showed little or no barrier to oil, grease, and water. Both Cobb and Gurley porosity are important because they influence coating holdout. Papers with greater coating holdout will tend to hold more coating on the surface (less coating penetration). Surface energy is a measure of surface wetting. The lower the surface energy, the less wetting on the surface.

Convection oven treated and pilot photonically treated samples

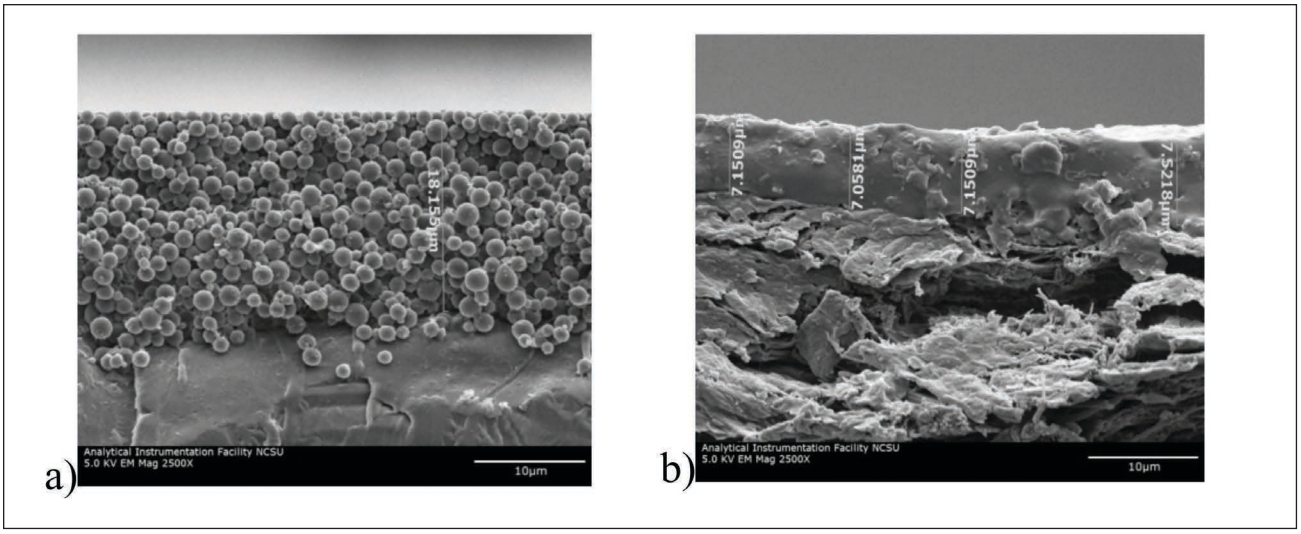
To determine the effect of photonic treatment on PHA film formation, SEM images were taken. **Figure 5a** shows the surface of the coating layer prior to heat treatment. Individual PHA particles are clearly present. Figures 5b and 5c show the surfaces after oven and photonic exposure. All images were taken at the same level of magnification. The differences show the effectiveness of heat treatment on film formation and that the two heat treatments are comparable.

It can be seen that the surfaces are significantly different, with discrete PHA particles clearly present on the surface of the uncured sample. The photonically cured surface shows a complete (continuous) film.

Cross-sectional images of the PHA coated samples both prior to and after curing (**Fig. 6**) were also taken. Prior to



5. Images of a) non-cured PHA coating, b) oven-cured PHA coating, and c) photonically treated PHA coating.



6. Cross section images of a) untreated, and b) treated PHA coating

Sample	Oven Treated			Photonic		
	2-min Cobb, g/m²	Kit, #	WVTR, g/m²/day	2-min Cobb, g/m²	Kit, #	WVTR, g/m²/day
A	2 (+/-) 1	8 (+/-) 1	70 (+/-) 8	3 (+/-) 1	9 (+/-) 1	84 (+/-) 7
B	2 (+/-) 1	8 (+/-) 1	102 (+/-) 20	5 (+/-) 1	8 (+/-) 1	115 (+/-) 35
C	2 (+/-) 1	9 (+/-) 1	70 (+/-) 6	10 (+/-) 1	10 (+/-) 2	90 (+/-) 7
D	Fail	2 (+/-) 2	70 (+/-) 4	Fail	3 (+/-) 1	95 (+/-) 4
E	4 (+/-) 1	6 (+/-) 1	86 (+/-) 9	7 (+/-) 1	6 (+/-) 1	81 (+/-) 5

V. Comparison of oven and photonic curing (WVTR = water vapor transmission rate).

Coat Weight, g/m²	Oven		Photonic	
	20-min Cobb, g/m²	Kit, #	20-min Cobb, g/m²	Kit, #
2.1	19.6	12	19.3	9
4.7	17.2	12	10.9	9
10.2	17.9	12	5.6	12

VI. Improvement of barrier properties due to elimination of pinholes.

curing, the sample had a thickness of approximately 18 µm. After curing, the sample had an approximate thickness of 7 µm. This difference in thickness before and after curing results from the PHA particles coalescing and melting.

Table V compares high coat weight samples (16+1 g/m²) treated in an oven (control) to those treated using photonic treatment. The results of the low coat weight samples (<13 g/m²) resulted in the failure of barrier property tests due to incomplete coverage of the base sheet. Incomplete coverage was verified by spraying the surface with an isopropyl alcohol (IPA) solution containing a blue dye. The immediate penetration of IPA into the coated surface was observed, indicating incomplete coverage. This test is also used to detect the presence of pinholes.

The comparison of the oven to photonic results show the photonic heat treatment to be effective. The kit and WVTR values for the photonic treatment were similar to all oven dried results, while the 2-min Cobb values are all higher. The higher Cobb values are attributed to pinholes, indicating further refinement of photonic treatment settings is needed.

From the results, it is evident that the presence of pinholes prevents the full benefits of PHA coating to be realized, espe-

cially at lower coat weights. To determine if property improvements could be obtained if pinholes could be eliminated, one additional study was performed with application of PHA coating with different Meyer rods onto substrate C after applying a 10 gsm precoat. The Kit values of the precoated base paper were 4 min and 20 min Cobb 21.0 gsm prior to applying the PHA coating. The pulse conditions used for treating these samples were 400V, 5000 µs, and 8 ft/min with an overlap factor of 2. As shown in **Table VI**, barrier properties were significantly improved by sealing and smoothing the base paper with a precoating. The barrier properties of the precoating itself are not as significant as those found for the PHA coating. This finding indicates that additional substrate development may be needed to obtain the full benefit of this technology.

Results of repulpability tests performed on oven and photonic treated samples showed 100% repulpability, with no rejects present (100% accepts).

CONCLUSIONS

The results of the trial show that photonic treatment is a commercially viable option for the solution-based processing of aqueous PHA coatings. The application of photonic energy enabled the complete film formation of PHA particles within microseconds, without degradation to the base substrate. While the coating speeds utilized during this trial are low in comparison to commercial coater and press speeds, the results are scalable. For higher speeds, additional lamps and capacitors can be added.

The use of photonic energy provides papermakers with a new material tool box for developing new products by enabling use of higher melting polymers. The ability to utilize this technology inline with a paper machine or printing press offers economic benefits over offline operations. The use of PHAs as a barrier material for paper packaging will mitigate the environmental and health issues caused by conventionally generated plastics having bisphenol A, Di(2-ethylhexyl) phthalate, fluorochemicals, or any number of other additives that are known to cause health and environmental issues. **TJ**

ACKNOWLEDGEMENTS

This work was funded by a collaborative funding grant from the North Carolina Biotechnology Center and Synthetic and Natural Polymers Inc. (SNP Inc.). We thank NovaCentrix for their contribution of equipment time and technical support.

LITERATURE CITED

1. U.S. EPA, "Advancing Sustainable Materials Management: 2015 Fact Sheet," U.S. Environmental Protection Agency, Washington, DC, 2018, p. 7. Available [Online] https://www.epa.gov/sites/production/files/2018-07/documents/2015_smm_msw_factsheet_07242018_fnl_508_002.pdf <15Oct2018>.
2. Halden, R.U., *Annu. Rev. Public Health* 31: 179(2010).
3. Scaffaro, R., Dintcheva, N. Tz., Marino, R., et al., *J. Polym. Environ.* 20(2): 267(2011).
4. Ramsay, B.A., Langlade, V., Carreau, P.J., et al., *Appl. Environ. Microbiol.* 59(4): 1242(1993).
5. Godbole, S., Gote, S., Latkar, M., et al., *Bioresour. Technol.* 86(1): 33(2003).
6. Garlotta, D., Doane, W., Shogren, R., et al., *J. Appl. Polym. Sci.* 88: (1775)2003.
7. Thellen, C., Andrews, M., Padwa, A., et al., "Biodegradable latex paper coatings based on polyhydroxyalkanoates for improved moisture resistance," *ANTEC 2015*, Society of Plastics Engineers, Bethel, CT, USA, 2015.
8. Bugnicourt, E., Cinelli, P., Lazzeri, A., et al., *eXPRESS Polym. Lett.* 8(11): 791(2014).
9. Park, J.W., Im, S.S., Kim, S.H., et al., *Polym. Eng. Sci.* 40(12): 2539(2000).
10. Ke, T. and Sun, X., *J. Appl. Polym. Sci.* 89: 1203(2003).
11. Reis, K.C., Pereira, J., Smith, A.C., et al., *J. Food Eng.* 89(4): 361(2008).
12. Shawaphun, S. and Manangan, T., *Science Journal Ubon Ratchanthani University* 1(1): 51(2010).
13. Arrieta, M.P., Samper Madrigal, M.D., López Martínez, J., et al., *J. Polym. Environ.* 22(4): 460(2014).
14. Modi, S., Koelling, K., and Vodovotz, Y., *Eur. Polym. J.* 47(2): 179(2011).
15. Bucci, D.Z., Tavares, L.B.B., and Sell, I., *Polym. Test.* 24(5): 564(2005).
16. Follain, N., Chappey, C., Dargent, E., et al., *J. Phys. Chem. C* 118(12): 6165(2014).

ABOUT THE AUTHORS

We chose this topic to research because there is a very significant need for alternatives to conventional plastics. It was interesting to discover how well PHA can perform as compared to conventional plastics. The most difficult aspect of this work was the energy requirements, which we discussed with industry experts.



Joyce

Mills may find benefit from this work from the standpoint of developing innovative products. The next step is to create a consumer product incorporating PHA.



Pal

Joyce is a post-doctoral student, Pal is associate professor, and Tran is director, Product Innovation, at North Carolina State University, Raleigh, NC, USA. Email Joyce at Michael@snpinc.com.

17. Doi, Y., Ishioka, R., Okino, Y., et al., U.S. pat. 6,716,911 B2 (Apr. 6, 2004).
18. Whitehouse, R.S., U.S. pat. 9,085,688 B2 (Jul. 21, 2015).
19. Schroder, K.A., McCool, S.C., and Furlan, W.R., "Broadcast photonic curing of metallic nanoparticle films," *NSTI Nanotech 2006, NSTI Nanotechnol. Conf. Trade Show*, Nano Science and Technology Institute, Austin, TX, USA, 2006.
20. Volova, T.G., Zhila, N.O., Shishatskaya, E.I., et al., *Polym. Sci., Ser. A* 55(7): 427(2013).
21. BPI, "Applications of PHA as bioplastic," Bio Plastics Info, Mumbai, India. Available [Online] http://bioplasticsinfo.com/polyhydroxyalkonates/applications-of-pha-as-bioplastic/ <11Oct2018>.

ABOUT THIS PAPER

Cite this article as: Joyce, M., Pal, L., Tran, T. *TAPPI J.* 17(10): 557(2018). https://doi.org/10.32964/TJ17.10.557

DOI: https://doi.org/10.32964/TJ17.10.557

ISSN: 0734-1415

Publisher: TAPPI Press

Copyright: ©TAPPI Press 2018

About this journal

A review of green liquor scale formation

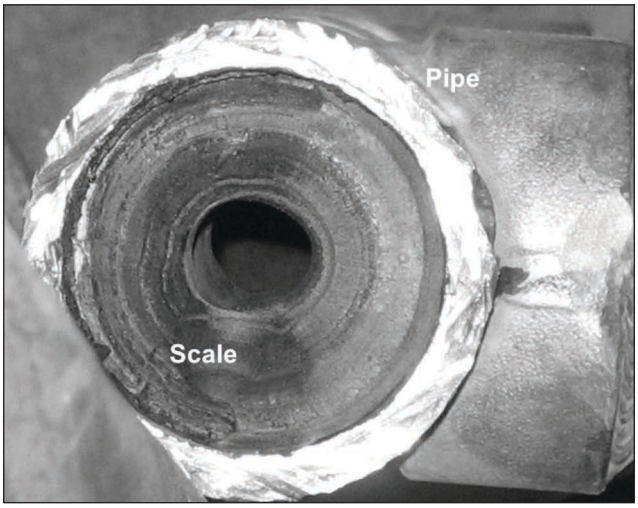
PETER W. HART

ABSTRACT: Green liquor scale is a recurring problem in most kraft mills. Several types of scale, e.g., pirssonite, calcite, sodium aluminosilicates, etc., have been identified in various green liquor scales. The mechanisms of formation and potential operational methods to control the formation of these scales is reviewed.

Application: For mills, understanding ways to prevent scale formation will benefit the process area.

Green liquor scale is a recurring problem in many pulp and paper mills around the world. A mill in Imatra, Finland, reported scale formation on its dissolving tank impeller blades so large that the amperage rating of the motor was exceeded in less than 3 months of operation. The mill was forced to take unscheduled downtime to remove the scale, ultimately resulting in a recovery boiler shutdown and significant production loss [1]. Scale issues reported from a mill in Springfield, OR, USA, suggested that 6-in. valve openings in raw green liquor lines were scaled to less than an inch of open area after just a few weeks of operation [2]. Significant and rapid green liquor scaling episodes have also been noted at mills in Brazil, Canada, and in various parts of the United States. Taylor and McGuffie found mixed scales containing both pirssonite ($Na_2CO_3 \cdot CaCO_3 \cdot 2H_2O$) and calcite ($CaCO_3$) in the green liquor system at the Elk Falls mill in British Columbia, Canada [3]. They found a dissolving tank scale sample was mainly composed of pirssonite, while a scale sample obtained from the green liquor clarifier was mainly calcite. Other researchers analyzed samples of green liquor dregs obtained from a mill in Brazil and reported scale formation from pirssonite, calcite, portlandite ($Ca[OH]_2$), larnite ($CaSiO_4$), and brucite ($Mg[OH]_2$) [4].

Deposits are frequently found on dissolving tank agitator blades, in the dog houses above the dissolving tank, in raw green liquor lines to the clarifiers, and in lines to the slakers [5,6]. Scale has been reported in the slaker screw conveyor as well. Intermittent deposition, characterized by alternating light and dark bands, suggests that scale formation is caused by temperature and/or strength (total titratable alkali [TTA]) variability. Scaling events can be quite difficult to manage under certain conditions. Sometimes, as suggested in the various mill experiences documented earlier, scaling is so severe that lines are plugged, and agitators are broken or damaged, resulting in unscheduled downtime and lost production. **Figure 1** shows a picture of a green liquor transfer line almost completely plugged with green liquor scale [5].



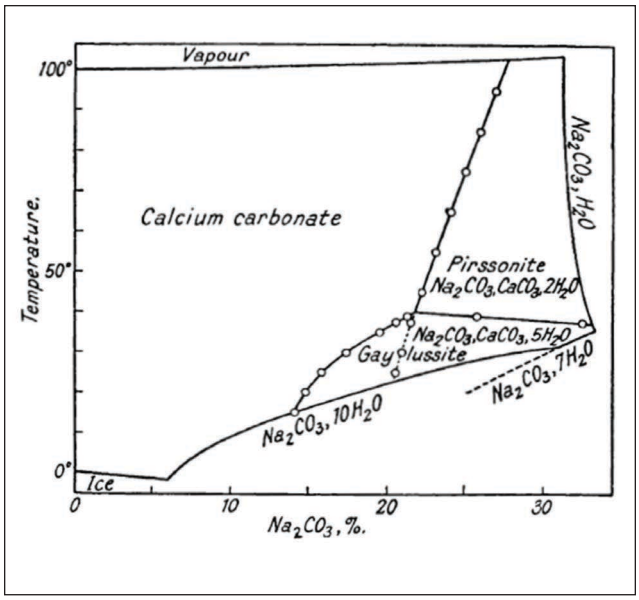
1. Green liquor scale formed inside a process pipeline. Note the reduction on available area for green liquor flow. Photo by Tran [5].

Types of scale formed

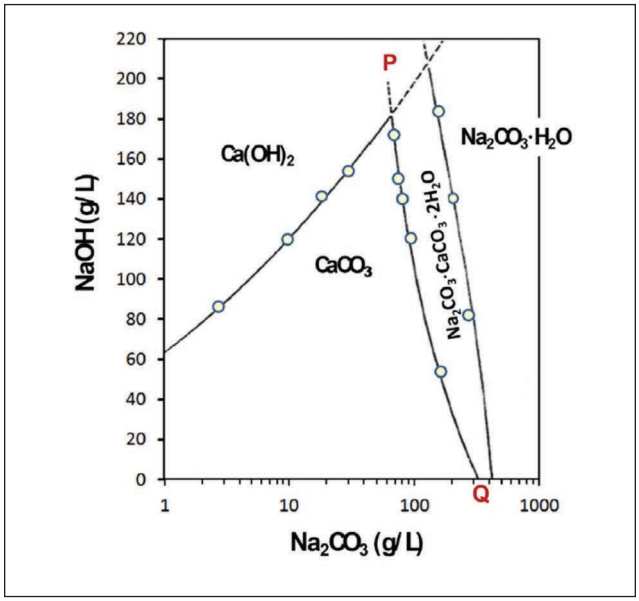
Initial work associated with green liquor scale analysis suggested the main type of scale formed in green liquor is pirssonite, a hydrated double salt of sodium and calcium carbonates ($Na_2CO_3 \cdot CaCO_3 \cdot 2H_2O$) [7,8]. More recent work has suggested that calcite, a form of calcium carbonate ($CaCO_3$), co-precipitates within the pirssonite and remains behind as the hard scale on pipe walls and agitators after the pirssonite re-dissolves into the green liquor [9]. To a lesser extent, calcium oxalate (CaC_2O_4) and sodium aluminosilicates ($AlNa_{12}SiO_5$) have also been identified as undesirable scale formations within the green liquor processing system [10].

PIRSSONITE ($Na_2CO_3 \cdot CaCO_3 \cdot 2H_2O$)

The sodium carbonate-calcium carbonate-water system was first studied in 1933 by Bury and Redd [7]. Pirssonite was found to form in concentrated sodium carbonate solutions of greater than 20 wt% in strength at temperatures of about



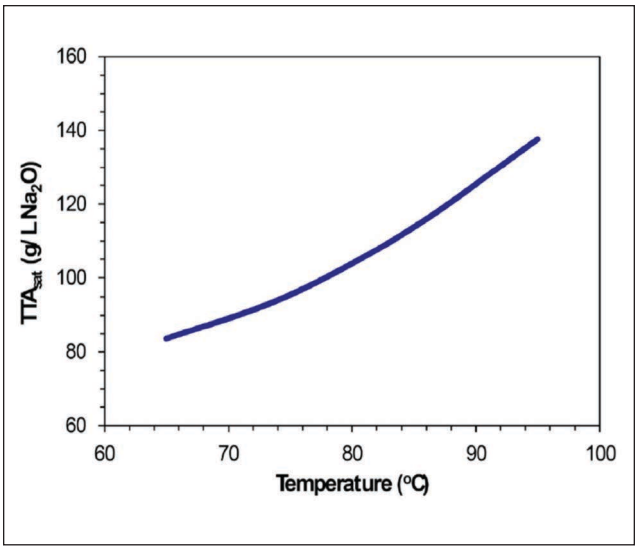
2. Phase diagram for the sodium carbonate-calcium carbonate-water system as developed by Bury and Redd [7].



3. Slaked lime-caustic-sodium carbonate-water system phase diagram at 95°C as developed by Littman and Gaspari [8,9].

40°C. Bury and Red completely investigated the three-component system at 15°C, 25°C, 35°C, 37.5°C, and 45°C. They partially investigated it at 20°C, 30°C, 39°C, 55°C, 65°C, 75°C, 85°C, and 95°C, performing sufficient work at these latter temperatures to fix the compositions of solutions at certain triple points. The phase diagram developed by Bury and Redd is shown in **Fig. 2** [7].

More than 20 years later, Littman and Gaspari studied the system using slaked lime ($Ca[OH]_2$), water and sodium carbonate [8]. As their system contained slaked lime and sodium carbonate, some amount of recaustizing was occurring, resulting in a significant amount of caustic (NaOH) being present in the system as well. They investigated the system at an industrially relevant temperature of 95°C. Their work developed the phase diagram shown in **Fig. 3** [8,9]. Littman and Gaspari's work clearly shows that pirssonite can only exist in a small concentration range of sodium carbonate and caustic in the reaction system solution. If the concentrations change significantly, the pirssonite will change form, likely re-dissolving or partially dissolving into solution.



4. Pirrsonite solubility as a function of temperature for a solution containing 30% sulfidity and 5% causticity [9].

Solubility

Pirssonite is a double salt of sodium and calcium carbonates. It is a semi-soluble scale that forms as deposits from precipitation events that occur when the sodium carbonate concentration exceeds the pirssonite solubility limit. Pirssonite solubility is highly temperature dependent. As green liquor cools, the solubility of pirssonite decreases by about 8 g/L as sodium oxide (Na_2O) for each 10°C decrease in liquor temperature [1]. Work by Frederick et al. determined that not only temperature but the total concentration of all the sodium salts (e.g., sodium sulfide, sodium chloride, sodium hydroxide, etc.) impacts pirssonite solubility. For example, the solubility of pirssonite decreases as the NaOH concentration increases. Therefore, solubility curves should be plotted versus the solution TTA instead of just the sodium carbonate concentration [1]. **Figure 4** shows the impact of temperature upon pirssonite solubility reported as the saturation TTA [9].

Of all the sodium salts contained in green liquor, pirssonite is the least soluble. Sodium carbonate (Na_2CO_3), sodium sulfate (Na_2SO_4), and Burkeite ($2Na_2SO_4 \cdot Na_2CO_3$) are all more soluble than pirssonite under green liquor processing conditions [1]. Work by Frederick et al. suggests that operating the mill TTA below 96% of the TTA saturation level is strongly advised to avoid pirssonite precipitation from occurring in green liquor systems [1].

Proposed formation mechanisms

It has been well demonstrated that pirssonite is formed by precipitation of the bi-salt of sodium carbonate and calcium carbonate in a hydrated form. The question is what is the exact mechanism of formation. As the process occurs in green liquor, the sodium carbonate concentration is always very high. Calcium carbonate has a low solubility in green liquor, and the calcium in the smelt resulting from the wood in the pulping process tends to rapidly form $CaCO_3$ in the dissolving tank. Pirssonite often forms in the dissolving tank where the smelt is dissolved into weak wash because the localized concentration of sodium and calcium carbonates are both quite high. It is possible that pirssonite forms from direct reaction between Na_2CO_3 in the solution and the surface of $CaCO_3$ (lime) particles either present in the weak wash or forming from the calcium obtained from the wood [1,5]. It is also possible that pirssonite forms via continuous dissolution of $CaCO_3$ particles to sustain a level of free Ca^{2+} ions in solution, which subsequently react with both Na+ and CO_3^{2-} ions to form and precipitate pirssonite scale. The continuous dissolution mechanism was first proposed by Bailik et al. [11].

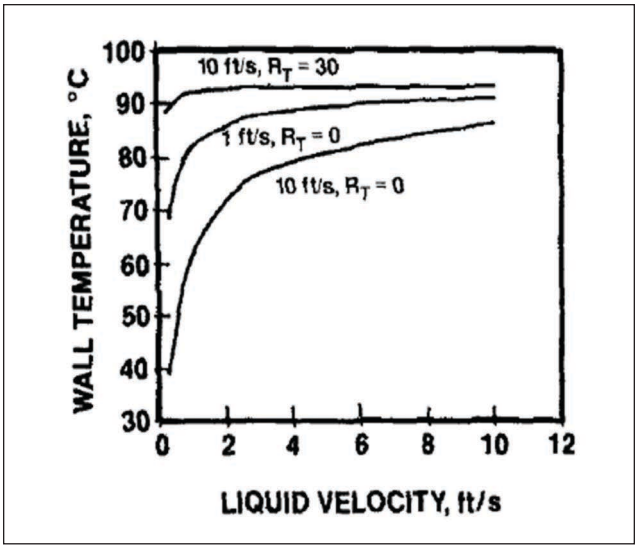
Due to the relatively high operating temperature and the Na_2CO_3 concentration dependence of pirssonite formation in green liquor as shown in the phase diagram in Fig. 4, the sodium phase of pirssonite will dissolve when the sodium carbonate concentration falls below the solubility limit of pirssonite. When this occurs, it is possible for the pirssonite to leave behind a porous skeleton of $CaCO_3$ scale on the pipes and impellors that can build up over time and cause its own scale problems in the form of calcite [5].

Guidelines to minimize pirssonite formation

Several guidelines have been developed to help minimize or prevent pirssonite deposition. These include, but should not be limited to, managing liquor temperature, swapping and cleaning liquor lines, and managing localized concentrations and operation of the green liquor system with a TTA target of 5%–10% below the saturation TTA.

Avoiding the death cycle

Typical saturation TTA for green liquor systems operating at 95°C is around 130 g/L as Na_2O. If a mill experiences significant scaling issues, they may experience unscheduled downtime for line cleaning or removal of scale from agitators. A mill will run a high TTA to ensure that it can supply sufficient green liquor to the slakers, but then the mill lines scale up and limit the green liquor flow because the green liquor TTA is higher than the saturation TTA. Many mills operate in this continual death cycle mode. To ensure they have green liquor to supply the recausticizing area, mills run the TTA as high as possible. This simply increases the rate and likelihood of scale formation, resulting in the mill having to shut down the green liquor system sooner than it normally would for scale removal. After cleaning lines, it is important that the mill lowers the TTA to less than 95% TTA_{sat} in order to break this cycle [12].



5. Wall temperature versus liquor velocity for an 8-in. green liquor line with a bulk fluid temperature of 93°C and an ambient air temperature of 0°C. The air velocity and level of insulation (as reported as thermal resistance, R_T) is indicated for each line [1].

Green liquor scale reduction methods.

Maintaining good mixing is critical to prevent weak wash from short circuiting the smelt dissolving tank and to avoid locally high concentrations of green liquor within the dissolving tank. As noted earlier, localized smelt dissolving concentrations should be maintained below the saturation concentration. Green liquor piping should be cleaned frequently to ensure that the weak wash supply is not limited. Finally, the dissolving tank agitators should be kept operating at all times and should receive a high priority for maintenance. The weak wash should maintain between 150–300 ppm suspended solids. This allows pirssonite to form onto the lime particles instead of on process equipment and piping.

Green liquor line management

All the green liquor lines should be well insulated. As green liquor cools near the pipe walls, the solubility of pirssonite decreases, so scale formation is more prevalent. Maintaining good liquor velocity through well-insulated pipes helps maintain high saturation concentrations. **Figure 5** shows the impact of insulation and liquor velocity on the temperature of liquor at the pipe wall. The conditions used in Fig. 5 are an 8-in. green liquor pipe with a bulk liquid temperature of 93°C and an ambient air temperature of 0°C [1]. Three different temperature lines are shown. One is for an outside air velocity of 10 ft/s, with an insulated line that has a thermal resistance (R_T) of 30 ft²h°F/BTU. The second line is for an uninsulated line with an outside air velocity of 1 ft/s. The third line is for an uninsulated line with an outside air velocity of 10 ft/s.

The results shown in Fig. 5 suggest that slowly moving to near stagnant liquor next to the pipe wall in an uninsulated line is always cool enough to promote pirssonite precipitation.

A reasonably well insulated line will prevent temperature drop-related scale formation if the liquor has some movement [1].

Several mills have installed parallel liquor lines to and from the dissolving tank. One line carries raw green liquor from the dissolving tank to the green liquor clarifier, while the second line carries weak wash from weak wash storage back to the dissolving tank. The mill should regularly switch raw green liquor and weak wash lines to and from the dissolving tank. The weak wash will dissolve sodium carbonate and partially clean the scale that has formed in the pipe. The slight abrasiveness of the suspended lime particles will also remove some of the porous calcium carbonate left behind once the sodium carbonate has dissolved. Hot water should be used to dissolve smelt when weak wash is unavailable. By routinely switching lines, the green liquor line can be cleaned when it is pressed into weak wash (or hot water) service while the other line is carrying green liquor so mill operations will not be interrupted [12]. If the lines are not cleaned enough to ensure an adequate flow of weak wash to the dissolving tank, excessively high levels of TTA are difficult to avoid, resulting in green liquor with extreme scaling tendency.

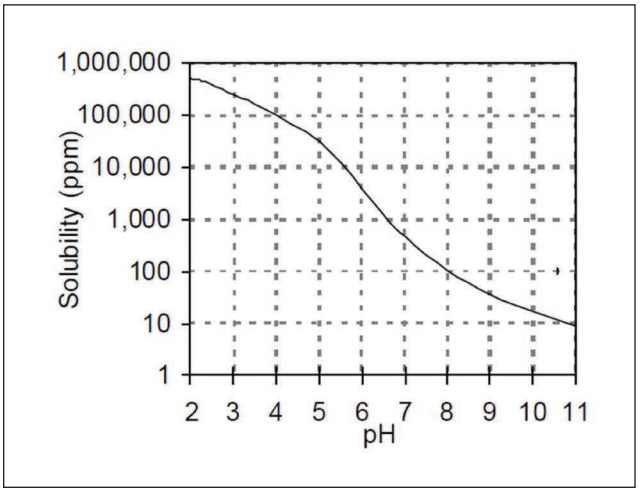
Daily operating practices

Several day-to-day operating practices can help minimize pirssonite formation. Dissolving tank density controllers should not be set on manual control. When the density controllers are on manual control, they are easy to ignore and allow the TTA to swing substantially. Automatic density control helps maintain nearly constant TTA strength in the green liquor system. The acid solution used for TTA titrations should be accurately standardized on a routine basis. Small changes in the titrating solution will result in swings in the actual TTA of the green liquor. When multi-tank systems are employed, tank-to-tank variability should be minimized. Pirssonite scale will form based on localized conditions, not on the average concentration of the multiple tanks.

CALCITE ($CACO_3$)

Besides pirssonite, the other scale commonly found in green liquor systems is calcium carbonate lime scale or calcite [4,5,10]. Calcite tends to be found more often in the green liquor clarifier and in the lines leading from the green liquor clarifier to the slaker. Pirssonite is more commonly found in the dissolving tank and in the lines leading to the green liquor stabilization tank and clarifier. Calcite is not particularly soluble in high pH solutions such as green liquor. As the pH increases, the likelihood of calcite crystallization increases. **Figure 6** shows the solubility of calcite as a function of pH [13].

In addition to pH, temperature and solution strength as measured by TTA also impact calcite solubility in green liquor solutions. Work by Giglio, Tran, and Papangelakis [14] has shown that liquor strength has a significant impact upon calcite solubility, with stronger liquors having significantly higher solubility limits than weaker liquors. At 80°C, Giglio determined the solubility of Ca^{2+} to be approximately 2.5 ppm in a 60 TTA green liquor solution, about 4.9 ppm in a 120 TTA green liquor solution, and about 8.5 ppm in a 180 TTA green liquor solution. The same work also showed that cooler operating temperatures decreased the solubility of calcite [14]. The green liquor causticity and sulfidity were determined to show no effect on calcium solubility.



6. Impact of pH upon calcite solubility [13].

Calcite formation mechanisms

Three hypotheses have been presented for calcite scale formation in green liquor systems. The first involves the formation of pirssonite and the re-dissolution of the sodium carbonate phase when the bulk solution concentration drops below the pirssonite solubility limit, leaving the calcite behind as scale. This hypothesis breaks down due to the prevalence of calcite scales found in lines between the green liquor clarifier and the slaker, where weak wash switching does not occur. As the TTA of the liquor in this line is fairly constant, there would be no driving force to dissolve the sodium carbonate and leave the calcium carbonate behind as scale.

The second hypothesis for calcite formation is related to the temperature solubility of calcite. It has been proposed that temperature gradients within the pipe will cause calcium to precipitate as calcite. The cooler temperatures at the pipe wall result in lower solubility, thus producing calcite scale.

The third hypothesis is that calcium is converted from a more soluble phase in the dissolving tank to a less soluble phase ($CaCO_3$) in the green liquor pipelines, resulting in precipitation as calcite. Work by Giglio et al. did show some kinetic basis for this hypothesis, as keeping raw green liquor at process temperatures for a period of time was found to decrease calcium solubility from about 15 ppm to about 5 ppm in 2.5 hours [14].

Calcite prevention

As green liquor cools or drops in TTA concentration due to various dilution and water infiltration streams, the solution

becomes supersaturated and calcium carbonate nuclei form. Calcite continues to grow in these nuclei until equilibrium conditions with the bulk fluid are obtained. The calcite precipitates onto pipe surfaces, clarifier walls, agitators, etc. Nucleation sites on these surfaces accelerate precipitation, resulting in significant amounts of scale formation that can restrict green liquor flow. Several methods, both physical and chemical, are available to help slow or eliminate calcite formations.

Physical prevention methods

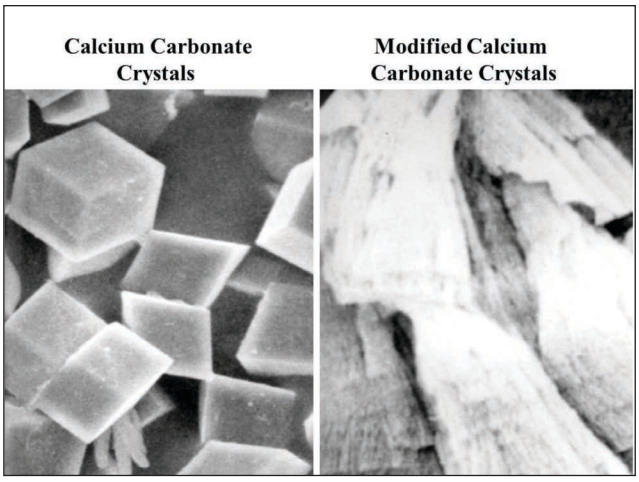
Mills have a limited number of tools available to prevent calcite scale from forming. Two methods are preventative, while the other two methods attempt to modify the crystalline structure of calcite to prevent severe scale build up. The preventative method relies upon TTA measurement and control to maintain the TTA of the green liquor leaving the dissolving tank at a constant and uniform level deemed by the mill to minimize scale formation [15,16]. As scale formation in green liquor lines tends to be episodic, corresponding to changing localized concentration and temperature conditions, maintaining a constant density or TTA out of the dissolving tank will help prevent supersaturation conditions resulting from swings in liquor strength and prevent scaling.

The second preventative method available to mills is to insulate the green liquor lines. As both calcite and pirssonite tend to precipitate at lower temperatures, insulating the green liquor pipes helps maintain the bulk fluid temperature and minimizes temperature gradients within the pipes. Figure 5 shows the impact of insulation and bulk liquor flow rate on the temperature gradients within pipes.

Polymer application

The next two available methods for preventing calcite scale attempt to modify the form or type of crystal growth that occurs. By modifying how the calcite crystal forms and grows, the resulting scale is soft and easily removed through attrition of the fluid and suspended solids moving in the bulk solution. A series of different polymers can be employed to achieve this end. The first way crystals may be modified is through the addition of processing chemicals known as crystal modifiers [13]. These polymers work by attaching themselves to the crystal growth sites, forcing the crystal to become irregular in shape. **Figure 7** shows a pair of high magnification pictures (both at the same magnification level) [13]. The photo on the left is of standard calcite crystals typically found in green liquor. Note the uniform, compact, cubic form of the crystals. The photo on the right is of calcite crystals treated with a polymeric crystal modifier. Note the non-uniform crystalline structure and the far less compact and less dense crystal formation.

Once the crystalline structure is disrupted, the growth rate of the crystal is reduced due to the incapacitation of the crystal growth sites. This effect results in slowing scale formation. Once the crystalline form is altered into non-uniform shapes, the resulting crystals cannot uniformly pack together and form a hard scale. Rather, the modified crystals form a soft scale that is typically removed by the abrasion of green liquor and suspended solids contained within the bulk flowing green liquor solution [17].



7. High magnification of calcite crystals formed with and without the addition of polymeric crystal modifiers [13].

Other polymers are sometimes used to break up the irregular crystals formed via application of the crystal modifiers so the material can be swept away more easily and not form an undesirable sludge at the bottom of the pipe or clarifier. Typically, these sludge conditioning or viscosity modifying materials consist of organic acids, which react with the modified crystal and fragment it into smaller pieces [17].

Finally, dispersion or antiscale polymers are anionic terpolymers that increase the surface charge of microcrystals in solution and prevent them from agglomerating into larger scale forming structures. By increasing the anion surface charge, a barrier is created that prevents further agglomeration [17,18].

External methodologies

Other than polymers, select mills have had some level of success with modification of the microcrystalline structure of calcite in the bulk green liquor through external treatment methods. These systems are typically mounted on the outside of the pipe and apply an external field that modulates rapidly. High frequency electric fields or radio frequencies modify the calcite crystalline structure at the micro level inside the bulk green liquor solution. The new crystalline form does not agglomerate and hence, does not form hard scales on the equipment surfaces [19-21]. Stora installed an electronic descaling system that was reported to have solved a long-term green liquor scaling problem at its mill in Point Tupper, Canada. The device used a frequency modulation technology that formed a pulse wave which changed direction several times a second, creating an induced electric field inside the pipe. The induced field also changed direction several thousand times a second. Crystal growth was thereby promoted, which remained suspended in the liquid and did not deposit onto the pipe walls

[19]. Responding to lower saturation levels, the existing scale deposits were softened, loosened, and reported to be removed in the water flow [19].

Work has continued on the development of these external devices. More recently, an electronic antifouling device has been reported in the literature that not only prevents calcite formation, but also removes existing scale in pipes, at insignificant energy consumption. Induction of a Radio-Frequency Alternating Electric Field (RFAEF) in water at a specific range of frequency and antenna voltage, along with its distinct sinewave waveform, has been reported to change the way minerals precipitate, minimizing hard calcite scale by instead producing a non-adherent mineral powder in the bulk water. Moreover, the unsaturated solution created by the formation of the mineral powder, along with enhanced carbon dioxide production, has been reported to gradually dissolve existing scale within the pipe [20].

Another form of external treatment has been the application of acoustic cavitation-generated erosion technology for the removal of calcite scale as it deposits onto surfaces [21]. As the scale forms, it is exposed to sonotrode-generated acoustic cavitation. The rate of scale removal was determined to be proportional to the pressure amplitude generated by the sonotrode. Descaling can also be intensified by reducing the substrate surface roughness. However, the scale destruction mechanism is largely dependent on the microstructure of the scale deposit, as local inhomogeneity may intensify the erosion rate. Scale deposits can, depending on the hardness of its surface and substrate surface finish, either be eroded layer-by-layer or by breakage of larger areas into chunks of scale [21].

SODIUM ALUMINISILICATES

Sodium aluminosilicates are occasionally found in green liquor scale [10] when there is a buildup of alumina or silica in the recovery cycle. Aluminosilicate scales are extremely hard and glassy in appearance. These scales are sparingly soluble and can precipitate in green, white, and black liquors. Once formed on pipes, tank walls, or agitators, these scales are quite difficult to remove. Aluminosilicates are typically eliminated from the liquor cycle as part of the green liquor dregs because their solubility is lower in green liquor than in white liquor [22-24]. Aluminum and silicon have been identified in dregs from the green liquor clarifier, primarily as the silicate diopside, $CaMgSi_2O_6$; the alummosilicates pargasite, $NaCa_2Mg_3Fe^{2+}Si_6Al_3O_{22}(OH)_2$; and as vermiculite, $Mg_{1.8}Fe^{2+}_{0.9}Al_{4.3}SiO_{10}(OH)_2 \cdot 4(H_2O)$ [3].

Aluminosilicates are typically controlled by limiting the amount of aluminum and silica that enters the liquor cycle. Typical sources of these materials include bark and dirt in the wood chips, alum from paper machine white water, lime makeup contamination, and excessive application of silicon-based defoamers. If a mill is having difficulties with aluminosilicate scale formation, efforts should be made to improve debarking of wood and to ensure that papermill white water is not being applied to the brownstock washing system. An analysis of the makeup lime should also be performed.

If aluminosilicate scale continues to be a problem, it is possible to purge these materials through the addition of magnesium sulfate to the green liquor [24]. Work by Ulmgren [24] has shown that treating a side stream of green liquor with sufficient Mg^{2+} to obtain a magnesium-aluminum ratio (Mg:Al) of greater than 3 to 1, and preferably 5 to 1, will result in the formation of $Mg_{1-x}Alx(OH)_2(CO_3)_{x/2} \cdot nH_2O$ with $0.1<x<0.34$. The resulting material will then precipitate out of solution, lowering the aluminum content of the liquor. Other conditions that favor aluminum precipitation are lower hydroxide concentration and lower temperature. Therefore, cooling the bleed stream prior to adding magnesium sulfate ($MgSO_4$) would be desirable to help maximize aluminum removal from the green liquor [10].

METALS REMOVED IN GREEN LIQUOR DREGS

The elemental composition of green liquor dregs samples found in the literature contain significant amounts on sodium and calcium, with the sodium content varying between 9% and 13% and the calcium content varying between 27% and 44%. A small but significant amount of magnesium between 0.5% and 3.2% has also been identified. For predominantly hardwood mills, the magnesium content may be higher. Iron, potassium, and manganese are also present in small amounts in all reported dregs samples. Some dregs samples have also contained lesser amounts of chlorine, zinc, silicon, aluminum, sulfur, and phosphorus. Other elements have been sporadically found in trace amounts [4]. Other studies have reported that sodium, sulfur, potassium, and boron may be found in green liquor dregs, along with aluminum, barium, calcium, cadmium, iron, magnesium, manganese, and zinc [25].

In general, most of the metals that enter the green liquor cycle originate with the wood and other raw materials used in the pulping and pulp washing process [26-28]. These metals come into the liquor cycle through the smelt, which is dissolved in the dissolving tank to make green liquor. When the smelt is dissolved in weak wash to form green liquor, the unburned carbon and several of the metals are only marginally soluble in the highly alkaline fluid. These metals tend to precipitate out of solution and join with the slightly soluble carbon materials to form dregs, which gravity then settles out of solution in the green liquor clarifier. Several mills will add some amount of polymer to the green liquor clarifier to help coagulate the dregs and improve the separation efficiency of the clarifier.

If the dreg settling in the clarifier is upset by thermal gradients, creating undesirable flow patterns or density variations in the clarifier, too high of liquor TTA, or other physical issues, dregs and undesirable metals will carry over into the clarified green liquor lines, slaker, and causticizers. Dregs carryover can result in some more uncommon scale formations, such as magnesium oxide or manganese dioxide. Typi-

cally, carrying a small number of suspended solids (mainly consisting of calcite particles) in the weak wash used for smelt dissolving helps improve dregs settling by providing nucleation sites for metals precipitation and increasing the density of the unburned carbon flocs so they have improved settling. This frequently enhances the performance of the green liquor clarifier and improves dregs removal efficiency. Carrying over too many suspended particles in the weak wash can have an undesirable impact on settling and hurt dregs separation, so it is important to monitor and control the quality of the weak wash being used in smelt dissolving.

SUMMARY

Green liquor scale is mainly composed of pirssonite and calcite. Both materials are formed as precipitation events that are somewhat dependent upon green liquor TTA (concentration) and temperature. Operating the TTA of the dissolving tank at about 95% of the saturation TTA is typically sufficient to prevent or at least significantly reduce pirssonite scaling. Insulating the green liquor transfer lines and clarifiers also reduce the likelihood of precipitation events forming thick scales within the system. Several other operational guidelines have been reviewed that also help mitigate scale formation events.

In addition to precipitation events, scale formation of aluminosilicate scales can result from a buildup of aluminum and silica in the liquor cycle. Typically, these undesirable materials are removed from the liquor cycles as part of the various heavy metals in the dregs. If the concentration of either of these materials gets high enough, they will precipitate onto equipment surfaces and form a very hard, difficult to remove glassy scale. Good debarking, white water segregation away from the liquor cycle, and judicious application of silicon-based defoamers all help maintain low levels of these contaminants and prevent scale formation.

Carryover of dregs from the green liquor clarifier is a source of less common scales, such as magnesium and manganese dioxide. These materials, like aluminum and silica, are only marginally soluble in the highly alkaline green liquor solutions and tend to scale onto equipment and piping when their concentration is increased due to poor dregs removal from the green liquor clarifier. **TJ**

ACKNOWLEDGEMENTS

This manuscript is part of the new *Lime Kiln and Recausticizing* textbook currently being prepared for publication through TAPPI Press.

LITERATURE CITED

1. Frederick, W.J., Jr., Krishnana, R., and Ayers, R.J., *Tappi J.* 73(2): 135(1990).
2. Slamenoja, K. and Kosonen, J., "Solving deposit problems in the smelt dissolving tank," *TAPPI Eng. Conf.*, TAPPI Press, Atlanta, GA, USA, 1996.
3. Taylor, K. and McGuffie, B., *Pulp Pap. Can.* 108(2): 27(2007).
4. Martins, F.M., Martins, J.M., Ferracin, L.C., et al., *J. Hazard. Mater.* 147: 610(2007).
5. Zakir, T., Tran, H., and Papangelakis, V.G., *TAPPI J.* 12(1): 55(2013).
6. Tran, H., "Scale formation in causticizing plants—An overview," *Annual Research Review Meet. Energy & Chemical Recovery*, University of Toronto, Toronto, ON, Canada, 2017.
7. Bury, C.R. and Redd, R., *J. Chem. Soc.* 272: 1160(1933).
8. Littmman, F.E. and Gaspari, H.J., *Ind. Eng. Chem.* 48(3): 408(1956).
9. Zakir, T., Tran, H., and Papangelakis, V.G., *TAPPI J.* 12(7): 33(2013).
10. DeMartini, N. and Frederick, W.J. Jr., "Review of sodium scaling in streams of the chemical recovery cycle of kraft pulp mills," *TAPPI Eng., Pulping, Environ. Conf.*, TAPPI Press, Atlanta, 2008.
11. Biakik, M., Wadsborn, R., Karlholm, I., et al., "Assessment of scaling risk in a pressurized black liquor gasification pilot plant," *Int. Chem. Recovery Conf.*, Vol. 1, TAPPI Press, Atlanta, 2010, p. 279.
12. Hart, P.W., "Green liquor scale – A guide towards minimization or elimination," *Frontline Focus*, TAPPI Press, Atlanta, 4(9): Sept. 2008.
13. Williamson, J., Adedire, A., and Baron, S.J., "Green liquor scale prevention," *TAPPI PEERS Conf.*, TAPPI Press, Atlanta, 2012, p. 2020.

ABOUT THE AUTHORS

This work is part of a text being prepared for the lime kiln and recausticizing areas of the mill. One troubling aspect of this process area is green liquor scale. Putting the current state of green liquor scale formation into one spot can only be of benefit to the industry. This work is a comprehensive review of the current state of the understanding of green liquor scale.

Finding the current work was somewhat difficult. Even though this is a problem area of the mill, there are not a lot of current research efforts in this area. Dr. Honghi Tran's group at the University of Toronto is doing most of the current work in this field. He received an award for detailing pirssonite scale then got an award the next year for determining it was not pirssonite but rather calcium carbonate.

For mills, understanding ways to prevent scale formation will benefit the process area. The next step is application of the technology in practice.



Hart

Hart is director, Fiber Science and Innovation, for WestRock, Richmond, VA, USA. Email Hart at peter.hart@westrock.com.

14. Giglio, A., Tran, H., and Papangelakis, V., "Calcite scale formation in green liquor handling systems," *Univ. Toronto Consortium Meet.*, University of Toronto, Toronto, ON, Canada, 31 October 2017.
15. Pyörälä, K., "Improved causticizing control by digital green liquor TTA measurement," *PAPTAC Annu. Meet., 85th,* Pulp and Paper Technical Association of Canada, Montreal, QC, Canada, Part A, 1999, Vol. B, p. B267.
16. Coyle, I., Russell, S., Rajbhandari, V., et al., "Improving smelt dissolving tank TTA control at Zellstoff-Celgar," PACWEST 2013 Technical Papers, Paper 5, Session 3A – Process Control, Pulp and Paper Technical Association of Canada, Montreal, 2013. Available [Online] http://www.texo-cc.com/images/files/Improving%20Smelt%20Dissolving%20Tank%20TTA%20Control%20at%20Zellstoff-Celgar%20-%20final.pdf.
17. ChemStone, "DSC metals management and scale control: How it works," *ChemStone Paper Training Presentatio*n, ChemStone Corporation, Greenville, SC, USA.
18. Hamalainen, H., Dutreix, J., and Jakara, J., "Calcium-derived scale control experiences in pulp mills," *Prepr.–PAPTAC Annu. Meet., 90th,* 2004, Vol. B, p. 129.
19. Horvath, R., *PIMA's North American Papermaker* 49(3): 38(1996).
20. Georgiou, D., Bendos, D., Kalis, M., et al., *J. Water Process Eng.* 22: 34(2018).
21. Pečnik, B., Hočevar, M., Širok, B., et al., *Wear* 356-357: 45(2016).
22. Gasteiger, H.A., Frederick, W.J., and Streisel, R.C., *Ind. Eng. Chem. Res.* 31(4): 1183(1992).
23. Wannenenmacher, N., Kimura, S., and Frederick, W.J., *Ind. Eng. Chem. Res.* 44(24): 9316(2005).
24. Ulmgren, P., *Nord. Pulp Pap. Res. J.* 2(1): 4(1987).
25. Golmaei, M., Kinnarinen, T., Jernström, E., et al., *Chem. Eng. J.* 317: 471(2017).
26. Lundqvist, F., Brelid, H., Saltberg, A., et al., *Appita J.* 59(6): 493(2006).
27. Doldán, J., Poukka, O., Salmenoja, K., et al., *O PAPEL* 72(7): 47(2011).
28. Santos, R.B., Gomide, J.L., and Hart, P.W., *BioResources* 10(4): 6538(2015).

ABOUT THIS PAPER

Cite this article as: Mayeli, N. *TAPPI J.* 17(10):571(2018).

https://doi.org/10.32964/TJ17.10.571

DOI: https://doi.org/10.32964/TJ17.10.571

ISSN: 0734-1415

Publisher: TAPPI Press

Copyright: ©TAPPI Press 2018

About this journal

D. H. PAGE

A Theory for the Tensile Strength of Paper

Theoretical consideration has been given to the mechanism of the tensile failure of paper in terms of the relative importance of fiber strength and bond strength. This has led to an explicit equation for the tensile strength of paper in terms of a few basic fiber and paper properties: $1/T = 9/8Z + 12A\rho g/bPL$(R.B.A.), where T is the finite-span tensile strength of paper (expressed as breaking length); Z is the zero-span tensile strength of paper (expressed as breaking length), a measure of the fiber strength; A is the mean fiber cross-sectional area; ρ is the density of the fibrous material; g is the acceleration due to gravity; b is the shear strength per unit area of the fiber-to-fiber bonds; P is the perimeter of the average fiber cross section; L is the mean fiber length; R.B.A. is the fraction of fiber surface that is bonded in the sheet. Qualitatively, this equation states that the strength of weakly bonded paper is controlled by factors associated with bonding strength, but for papers of progressively increasing strength, fiber strength becomes of importance. The equation has been tested from experimental evidence by verifying the linear relationships between $1/T$ and $1/L$ and $1/T$ and $1/$(R.B.A.). Indirect checks of the equation have been made from measurements of changes in paper strength due to humidity changes and heat treatment. In all cases, the equation fits the data excellently. It is concluded that, while the theory may not be rigorous, the derived equation provides a remarkably accurate description of the tensile strength of paper.

Keywords: Tensile strength · Zero-span tensile strength · Strength of materials · Mechanical properties · Paper · Fibers · Fiber dimensions · Fiber length · Fineness · Bonded area · Bonding strength · Theories · Humidity · Aging

PAPER is a bonded random network of natural cellulosic fibers, the tensile strength of which is appreciable, approaching that of hardened steel. During the drying of a paper sheet, the fibers mat together and adhere at regions where they cross because of the formation of intermolecular hydrogen bonds between adjacent fiber surfaces. It is clear that the strength of paper derives from both the tensile strength of individual fibers in the network and the strength of the forces that hold them to other fibers. If either one of these is zero, the paper has no strength. The relative importance of these two factors has been a matter of some controversy for a number of years. Formerly, it was believed that, for all papers, bond strength was the limiting and controlling factor. This view probably arose from a number of considerations. Polymeric chains of cellulose are oriented along the length of fibers so that fiber strength may be expected to originate from strong covalent linkages within the cellulose molecules, whereas fibers adhere to one another in paper by much weaker intermolecular hydrogen bonding. The highest tensile strengths recorded for paper, even when based on the cross-sectional area of the fibrous material, are only about one quarter of those obtained for the strength of single fibers. The strength of paper is always reduced by raising the humidity, which might be expected to reduce bond strength without changing the fiber strength appreciably. A casual study of the ruptured edge of paper shows that fibers have been pulled out rather than broken.

More recently, evidence has accumulated that has cast doubt on the view that bond strength is the overriding factor in controlling paper strength. It has been shown theoretically that the tensile strength of a random two-dimensional sheet does not exceed one third of the strength of individual component fibers (*1*) and, although this limit is never reached, it is certainly approached. Microscopical studies have revealed that paper is a closely bonded network, the average millimeter length of fiber being in bonded contact with as many as 20–40 other fibers (*2*). These fiber-to-fiber bonds are now known to have appreciable shear strength of the order of 1 g each (*3*), so that, acting in cooperation during straining of a sheet, they may frequently remain intact until the fiber failure stress is reached. Careful studies of the rupture process have shown that a considerable percentage of fibers are indeed broken during tensile failure, particularly in the strongest papers (*4*, *5*). A strong correlation has been found between fiber strength and paper strength (*6*) for pulps prepared from a range of wood species.

In this paper, an attempt is made to account for all these observations and to recognize the importance of both fiber strength and bond strength in controlling paper strength. The author freely admits at the outset the lack of rigor in the theory advanced, and the end result is thus a semi-empirical equation relating paper strength to a number of basic fiber and paper parameters.

D. H. PAGE, Pulp and Paper Research Institute of Canada, 570 St. John's Road, Pointe Claire, P. Q., Canada.

THEORY

First Premise

The first premise of the theory concerns the distribution of stress in a paper strip at the instant of tensile failure. Consider the state of the fibers crossing the line that will ultimately become the line of rupture. It is proposed that during the straining process the load is taken by progressively fewer fibers across this line due to the failure of bonds at the ends of fibers. It has been shown that this type of failure should occur (*7*) and it has been found in practice (*8*). As the point of failure is approached, more bonds fail in the rupture region and the remaining fibers take more of the sheet load, until the fibers lying in the direction of loading reach their rupture strain. At this point, catastrophic failure of the paper occurs. This premise may be written mathematically as follows:

$$T = n_f Z_e/(n_f + n_p) \qquad (1)$$

where

n_f = number of fibers crossing the rupture zone that take the load at failure and then break
n_p = number of fibers crossing the rupture zone that pull out intact due to prior bond breakage and hence carry no load at failure
T = tensile strength of the strip expressed as breaking length
Z_e = finite-span tensile strength of the strip expressed as breaking length if no bond breakage had occurred (this is a derived and not a measured quantity)

It is assumed that the formation of the sheet is good, so that the number of fibers crossing the rupture line is not appreciably lower than the number that cross any line traversing the strip, perpendicular to the direction of strain.

Z_e can now be obtained from the zero-span tensile test since in this test all fibers crossing the line of rupture fail. Z_e is not, however, equal to the zero-span tensile strength Z, because of the permitted

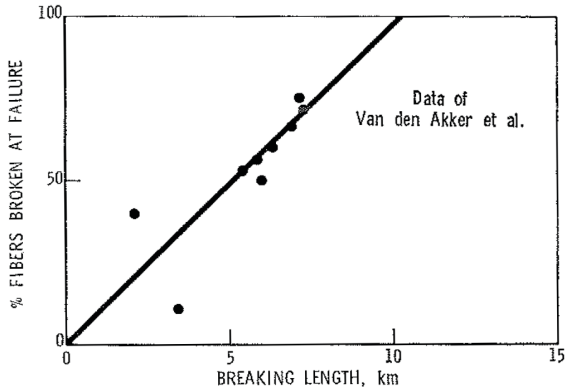


Fig. 1. Plot of percentage of fibers broken across line of tensile failure against breaking length for data of Van den Akker, Lathrop, Voelker, and Dearth (*4*).

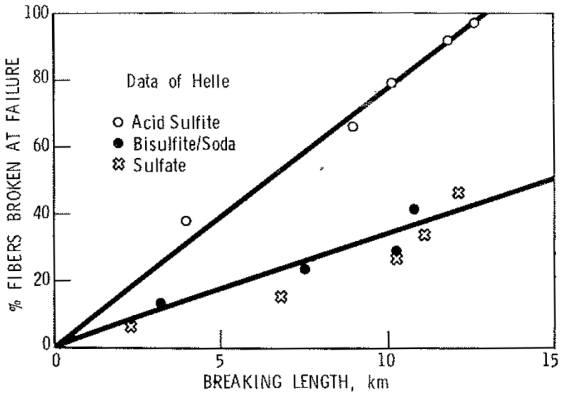


Fig. 2. Plot of percentage of fibers broken across line of tensile failure against breaking length for data of Helle (*5*).

lateral contraction in finite-span compared with zero-span conditions (*7*). Z and Z_c are related by the equation,

$$Z_c = Z(1 - \mu^2) \qquad (2)$$

where μ is Poisson's ratio. For random sheets, μ is theoretically one third (*1*), and this agrees reasonably with experimental values (*9*) so that,

$$T = 8n_fZ/9(n_f + n_p) \qquad (3)$$

Before proceeding with the theory it is proposed to test the validity of Eq. 3 by employing data taken from the literature. Van den Akker, Lathrop, Voelker, and Dearth (*4*) and Helle (*5*) have measured the tensile strength of handsheets at different beating degrees and recorded the percentage of fibers that have broken at failure. Equation 3 predicts a linear relationship between T and $n_f/(n_f + n_p)$ passing through $T = 0$, $n_f/(n_f + n_p) = 0$; $T = 8/9Z$, $n_f/(n_f + n_p) = 1.0$. The data of Van den Akker, Lathrop, Voelker, and Dearth (*4*) are shown in Fig. 1. Within the experimental error, the relationship is linear, passing through $T = 0$, $n_f/(n_f + n_p) = 0$. The intercept at $n_f/(n_f + n_p) = 1$ predicts a zero-span strength of 11.3 km, and this is reasonable although the measured value is not available for comparison. Helle's data shown in Fig. 2 also give linear plots passing through the origin. For his dried sulfite pulp at 48% yield, the predicted zero-span strength is 14.5 km and, for his sulfate and bisulfite-soda pulps, it is about 30 km. While this latter result is high, it is not entirely unreasonable for laboratory pulps of this type made from handcut chips. It is suggested that Eq. 3 provides a good description of the data.

Second Premise

The second premise of the theory relates the number of fibers that fail at the instant of rupture to the number that are pulled intact. It is proposed that each fiber that crosses the rupture line will fail or pull out, depending on the relative magnitude of the strength of the fiber and the forces that hold it in the sheet. This may be expressed as follows,

$$n_p/n_f = F(\phi, \beta) \qquad (4)$$

where

ϕ = mean fiber strength, dynes
β = mean force, in dynes, applied along the fiber axis and across the rupture line required to pull a fiber from the sheet

β thus depends on the relative bonded area of the sheet, the bond strength per unit area, and the fiber length.

From dimensional considerations this can further be written,

$$n_p/n_f = f(\phi/\beta) \qquad (5)$$

Combining Eqs. 3 and 5

$$\frac{1}{T} = \frac{9}{8}\left[\frac{1}{Z} + \frac{1}{Z}f\left(\frac{\phi}{\beta}\right)\right] \qquad (6)$$

This equation gives explicitly the tensile strength of the sheet but unfortunately contains an unknown function f. Further consideration can assist us in deriving its nature. When the fiber strength ϕ far exceeds the bond strength β, all the fibers are pulled intact and $f(\phi/\beta)$ must tend to infinity. When the bond strength far exceeds the fiber strength, all fibers fail and $f(\phi/\beta)$ must tend to zero. When the fiber strength ϕ is equal to the bond strength β, the fibers have equal chances of pulling or failing so that $f(\phi/\beta) = 1$. There is, of course, an infinite number of functions satisfying these three constraints, but the simplest is $f(\phi/\beta) = \phi/\beta$. It is proposed to use this function here and to comment subsequently on its use. This gives rise to the following equation,

$$\frac{1}{T} = \frac{9}{8}\left[\frac{1}{Z} + \frac{1}{Z}\cdot\frac{\phi}{\beta}\right] \qquad (7)$$

The fiber strength ϕ is given for random sheets of Hookean fibers, according to Van den Akker *et al.* (*4*), by the equation,

$$\phi = \frac{8}{3}A\rho gZ \qquad (8)$$

where

A = average fiber cross section
ρ = density of the fibrous material
g = acceleration due to gravity

If we assume that all fiber-to-fiber bonds act cooperatively along the length of a fiber, the bond strength β is given by,

$$\beta = bP\frac{L}{4}\text{(R.B.A.)} \qquad (9)$$

where

b = shear bond strength per unit bonded area
P = perimeter of the fiber cross section
L = fiber length (and hence $L/4$ is the mean pulled length)
R.B.A. = relative bonded area of the sheet

Combining Eqs. 7, 8, and 9, we arrive at final equations for the tensile strength of paper.

$$\frac{1}{T} = \frac{9}{8Z} + \frac{12A\rho g}{bPL\text{(R.B.A.)}} \qquad (10)$$

or

$$T = \frac{8ZbPL\text{(R.B.A.)}}{9bPL\text{(R.B.A.)} + 96A\rho gZ} \qquad (11)$$

This may be expressed further in a form that will not be used in this paper but may be of value elsewhere.

$$\frac{1}{T} = \frac{9}{8Z} + \frac{12g}{bL\alpha} \qquad (12)$$

where

α = the bonded area per gram of fibrous material

Equations 10, 11, and 12 are, of course, dimensionally correct provided that a consistent system of units, such as the centimeter-gram-second system, is used for each term. If T and Z are considered in units of stress, rather than breaking length, the term ρg should be omitted from Eq. 10.

The equation may be rewritten in a stylized form that may be helpful.

$$\frac{1}{T} = \frac{1}{F} + \frac{1}{B} \qquad (13)$$

where

F = an index that describes only the resistance of fibers to breakage
B = an index that describes only the resistance of bonds to breakage

It is instructive to examine the implications of Eq. 10 from a plot of T against the bonding index, bPL(R.B.A.)/$12A\rho g$, in Fig. 3. The breaking length T increases linearly with increasing bond strength per unit area, relative bonded area, and fiber length at low levels of bonding. It decreases as the ratio A/P increases. As T increases, a further improvement in the bonding parameters has progressively less effect. On the other hand, the fiber strength, measured by Z, has little effect on T at low bonding levels, but becomes more important at higher levels. It is clear that the equation is at any rate qualitatively in agreement with previous work and general experience. The equation will now be tested quantitatively from detailed data.

EXPERIMENTAL VERIFICATION

The theory relates the tensile strength of paper to six basic variables. Four of these are fiber properties—the fiber length, fiber density, the ratio of cross-sectional area to perimeter, and the fiber strength, as measured by the zero-span tensile test. One is a paper property—its relative bonded area. One is a property of fiber-to-fiber interaction—the shear strength per unit area of the adhesive bond.

A thorough test of the equation would involve the measurement of these six properties over a wide range of conditions of each variable. This would be a considerable undertaking and would be of limited value because of the lack of precise methods for measuring the bond strength per unit area and even the relative bonded area. Instead, experiments have been chosen in which certain of the variables

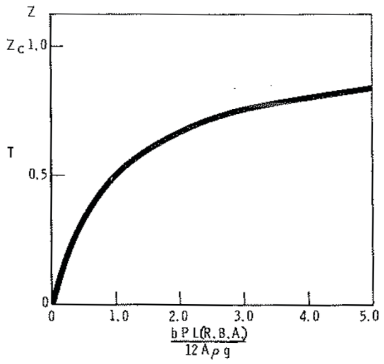


Fig. 3. Plot of theoretical Eq. 10 in arbitrary units relating the breaking length of paper, T, to the bonding index, bPL(R.B.A.)/$12A\rho g$.

have been maintained constant while others have been varied and measured.

Fiber Length

It is known that long-fibered pulps tend to have high tensile strengths and this is in agreement with the derived equation. For a rigorous test of the theory, tensile data must be obtained for which the fiber length is varied while maintaining all the other variables of Eq. 10 constant. Such a requirement presents experimental difficulties. Pulps of differing fiber length can be obtained by the use of different species, by beating, or by fractionation, but in all these cases changes in fiber length will be confounded with changes in other properties contained in Eq. 10. Three authors have published data obtained by methods that give a good chance of maintaining the constancy of the unmeasured variables and their data will be used to test the theory.

Arlov (*10*) used as his raw material a commercial bleached sulfite pulp in dry sheet form. A sample was beaten in the PFI mill and fractionated. The longest fraction was formed into sheets which were cut into narrow strips by guillotine while wet. After disintegration, the pulp was refractionated and sheets were made from the fractions. The mean fiber length of the fractions and stress-strain curves of the sheets were measured. For these and succeeding data in this section, the theory will be tested by a plot of $1/T$ against $1/L$. The theory predicts a linear relationship with a positive slope, the value of which depends on the other variables. It predicts an intercept at $1/L = 0$ such that $T = 8Z/9$. Arlov's data shown in Fig. 4, although sparse, are in excellent agreement with the theory. The value of r^2 for the fitted line shown is 0.991 and the residual error in T, ± 0.165 km, is within the experimental error. The predicted value of the zero-span tensile strength, obtained from the intercept at $1/L = 0$, is 11.80 ± 0.60 km. (In this and further cases the limits refer to the standard error.) The zero-span strength was not recorded, but this is a reasonable value for a dry bleached sulfite pulp.

Clark (*11*) prepared sheets from rayon filaments cut to various measured lengths. He added a proportion of highly beaten sulfite pulp and guar gum to provide adequate adhesion and obtained data for two levels of addition. His results are plotted in Fig. 5. Good linear relationships are again obtained with high values of r^2. The data plot as two lines of differing slope because of the change in relative bonded area and bond strengths that are given by the different levels of sulfite addition. The residual errors in T, ± 0.225 and ± 0.105 km for the two lines, are again within the experimental error. The values of zero-span strength from the intercepts are 5.36 ± 0.76 and 5.70 ± 0.14 km, and these are not significantly different. Zero-span data were not recorded, but this low value is to be expected in view of the much lower strength of rayon filaments, compared with natural fibers.

The data of Watson and Dadswell (*12*)

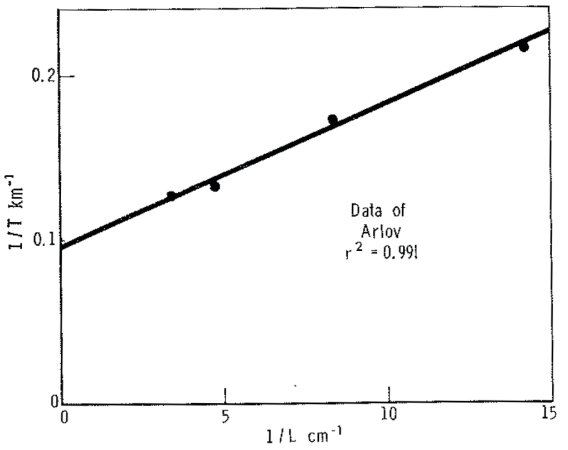


Fig. 4. Plot of $1/T$ against $1/L$ for the data of Arlov (*10*).

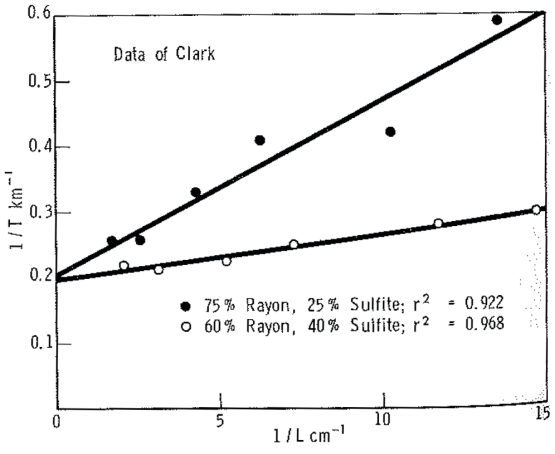


Fig. 5. Plot of $1/T$ against $1/L$ for the data of Clark (*11*).

are of particular value. These authors prepared four sulfate pulps of different mean fiber lengths from the long-fibered species *Araucaria klinkii* by cutting chips into different lengths prior to pulping. Fiber lengths were measured and tensile data obtained at four levels of beating in the Lampen Mill. The reduction in fiber length with beating was not recorded, but it may be expected to be small for a sulfate pulp and, in any case, provided the fractional reduction is independent of initial fiber length, it will not affect this verification of the theory. A plot of the data is given in Fig. 6. Lines have been fitted with the restriction that they should have a common intercept at $1/L = 0$. Again, the data plot as lines of differing slope indicating the increase in relative bonded area and bond strength with beating. The value of R^2 is 0.941 with a residual error in T of ± 0.525 km. The value of zero-span strength obtained from the common intercept is 12.30 km, and this is again a reasonable value.

Relative Bonded Area

No method has been perfected for the measurement of the relative bonded area in paper, but an estimate can be made from light scattering coefficient measurements according to Ingmanson and Thode (*13*). The plot of scattering coefficient S against tensile strength is extrapolated to zero strength and this is considered to give the scattering coefficient S_0 of the totally unbonded sheet. The relative bonded area is then $(S_0 - S)/S_0$. Ingmanson and Thode give tensile and relative bonded area data for a classified bleached sulfite wet-lap pulp beaten in a pebble mill to retain fiber length. They found that the relative bonded area-tensile strength relationship was independent of whether the strength was enhanced by beating or wet pressing. This indicates that, *for this pulp*, the bond strength per unit area is not appreciably changed by beating and, therefore, these data may be used for a study of the relationship between tensile strength and bonded area without fear of the variation of other properties. A plot of $1/T$ against 1/(R.B.A.) is shown in Fig. 7. The line has a value of $r^2 = 0.951$, with a residual error in T of 0.390 km. The intercept at 1/(R.B.A.) = 0 gives a value of $Z = 12.20 \pm 1.00$ km, and this is in excellent agreement with the value of 12.30 km obtained from a direct measurement of the zero-span tensile strength.

Fiber Dimensions in Cross Section

The term $A\rho/P$ appears in Eq. 10, A being the area and P the perimeter of the fiber cross section. This can be expressed as $D^{1/2}(A^{1/2}/P)\rho^{1/2}$ where D is the fiber coarseness in units of g/cm. For fibers of the same density ρ, the term depends therefore on the product of two factors; the first, $D^{1/2}$, is a function only of the fiber coarseness, while the second, $A^{1/2}/P$, is a function only of the cross-sectional shape of the fiber. For a solid circle this shape factor is 0.28, for a square 0.25, and for a long thin rectangle of aspect ratio 10:1 it is 0.14.

The test of Eq. 10 for various values of coarseness and cross-sectional shape presents an unusual difficulty in that both these variables have a large indirect effect on the relative bonded area. Coarseness will affect the rigidity of fibers and hence the number of fiber contacts, while cross-sectional shape will affect both the fiber rigidity and the area presented for bonded contact. Thus, although Clark (*11*) has carried out work using rayon filaments of varying coarseness, we are not able to use these data since we do not have a record of the relative bonded area at each coarseness value. The large change in specific volume with coarseness does indicate that the effect on relative bonded area would mask the direct effect of coarseness change discussed here.

Bond Strength per Unit Area

At present, only rough data can be obtained for the strength of bonds between fibers so that a direct test of Eq. 10 is impossible. An indirect test can be made from the effect of changing the bond strength by varying the test humidity. It is reasonable to suppose that the fractional increase in bond strength db/b for a given humidity change is independent of b. The zero-span strength may be assumed to be independent of humidity. Differentiating Eq. 10 we get,

$$\frac{dT}{T} = \frac{db}{b} \times (1 - T/Z) \qquad (14)$$

This states that the fractional increase in tensile strength of paper due to increasing bond strength is at a maximum for weak sheets and diminishes linearly with increasing tensile strength until it is zero for the zero-span test. To check this equa-

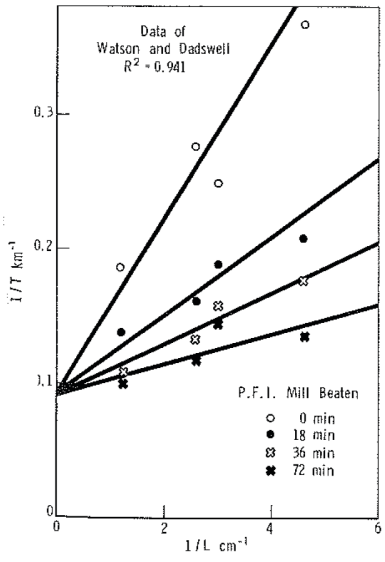


Fig. 6. Plot of $1/T$ against $1/L$ for the data of Watson and Dadswell (*12*).

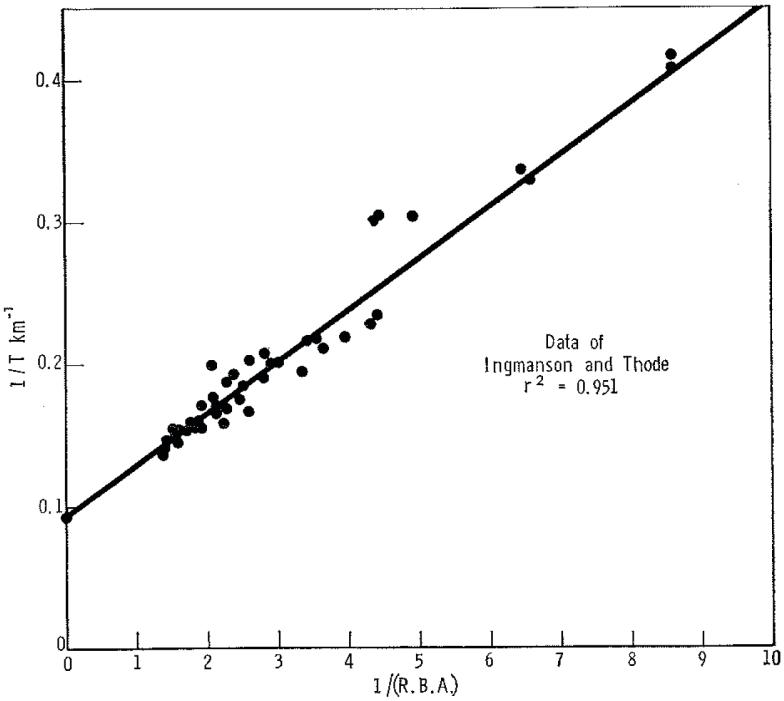


Fig. 7. Plot of $1/T$ against 1/(R.B.A.) for the data of Ingmanson and Thode (*13*).

tion, the data of Crook and Bennett (*14*) can be used. These authors measured machine direction tensile strengths of a series of commercial papers over a range of humidities. In Fig. 8, tensile strength is plotted against the fractional increase in tensile strength dT/T resulting from a change in the humidity from 65 to 20% RH. In spite of the fact that the 13 points refer to greatly different papers such as newsprint, kraft, and fine papers, the linear relationship is borne out. The value for r^2 is 0.892, and the intercept at $dT/T = 0$ indicates a zero-span strength of 14.90 ± 0.90 km, a reasonable average value for the machine direction of commercial papers.

The effect of additives on tensile strength is caused only in part by an increase in bond strength per unit area, since other factors such as a change in relative bonded area and an improvement in formation are known to be important (*15*). The theory does explain qualitatively, however, why additives show a greater improvement in strength for sheets whose strength is low compared with their zero-span tensile strength.

Effect of Heat Treatment

The properties of paper are changed by treatment at an elevated temperature. This aging process has two main effects of interest. It lowers the fiber strength by oxidation of the glucosidic bonds in the cellulose chain (*16*), and it increases the bond strength by an autocrosslinking reaction between adjacent cellulose chains (*17*). Since heat treatment can hardly be expected to change any of the other parameters contained in Eq. 10 it can be used as a tool to test the theory.

The results of heat treatment at 400°F on the tensile properties of a sulfate pulp at various beating degrees are shown as the plotted points in Fig. 9. The zero-span tensile strength decreases due to treatment, slowly at first, but more rapidly later. The tensile strength increases initially for all beating degrees, but, while for lightly beaten sheets it continues to rise, for highly beaten sheets it falls off. This is in agreement with preliminary work by Britt (*18*). Equation 10 can be recast as,

$$\frac{bPL(\text{R.B.A.})}{12A\rho g} = \frac{8ZT}{(8Z - 9T)} \qquad (15)$$

The right-hand side of Eq. 15 can be obtained from the measured values of zero-span and finite-span tensile strength and this is plotted against heat treatment in Fig. 10.

If the assumption is made that of the variables on the left-hand side of Eq. 15 only the bond strength per unit area b is affected by heat treatment, we would expect the curves of Fig. 10 to be similar, in the geometric sense, differing only by a factor in the ordinate scale that depends on the different values of fiber length and relative bonded area at different beating degrees. The lines of Fig. 10 are similar cubics fitted to the points, and it is evident that similar curves do indeed give a good fit to the data. From the curves of Fig. 10, the theoretical lines may be drawn on Fig. 9 and it is seen that they fit the experimental data well with a value of $r^2 = 0.998$ and a standard error in T of 0.170 km.

It is important to recognize what has been done here. The assumptions are that fiber strength and bond strength are the only relevant factors that are changed by heat treatment and that Eq. 10 holds. The theory then predicts that a family of lines may be drawn relating finite-span tensile strength to heat treatment. This family cannot be predicted since the theory can say nothing about the extent to which bond strength is affected by heat treatment. However, given the relationship between zero-span tensile strength and heat treatment and given the relationship between the tensile strength and heat treatment at any one level of beating, the equation enables us to predict the relationship between tensile strength and heat treatment at all other beating degrees.

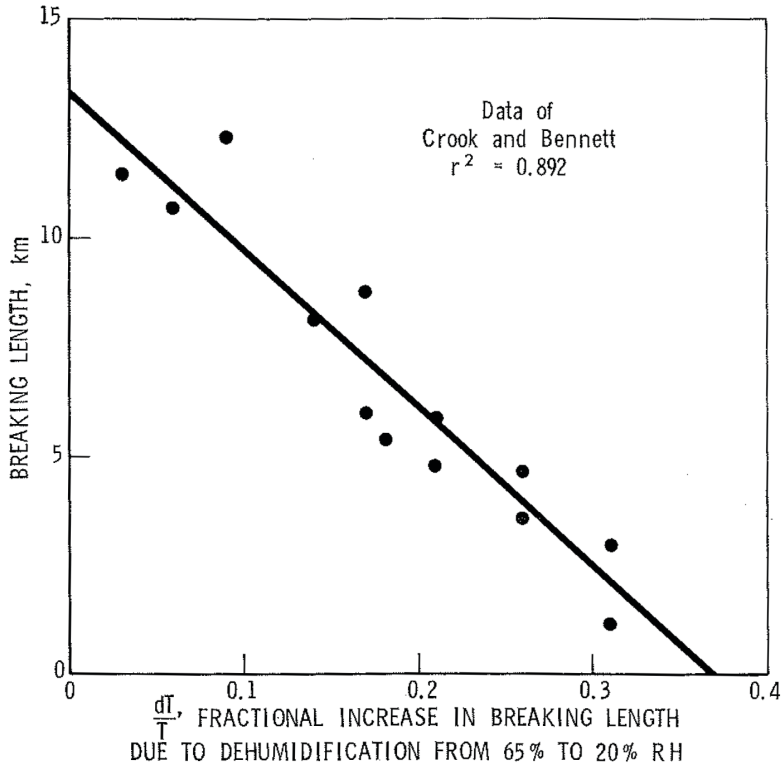


Fig. 8. Plot of breaking length T against dT/T, the fractional increase in breaking length due to dehumidification from 65 to 20% RH, for 13 commercial papers examined by Crook and Bennett (*14*).

Reasonable Values

The theoretical Eq. 10 has been derived without resort to arbitrary constants. The tensile strength of paper is related to seven variables which are all, in principle, measurable. While no experimental data exist for all these variables, it is instructive to check the validity of the equation by inserting probable values. Since the least known of the variables is bond strength, Eq. 10 is re-arranged to be explicit in this property.

$$b = \frac{96A\rho gZT}{(8Z - 9T)PL(\text{R.B.A.})}$$

Taking values for the classified sulfite pulp of Ingmanson and Thode (*13*):

Z = 12.30 km
T = 7.25 km
R.B.A. = 0.93

We may also take the following probable values:

L = 0.2 cm
$A = 2.4 \times 10^{-6}$ cm²
$P = 9.0 \times 10^{-3}$ cm
ρ = 1.56 gm/cm³

From this we obtain:

$$b = 5.9 \times 10^{7} \text{ dynes/cm}^2$$

Direct measurements from the strength of single fiber bonds (*3*, *19*, *20*) and from macroscopic data on adhesives (*21*, *22*) are given in Table I. The value obtained above is lower than that obtained from tests on commercial adhesives but is somewhat higher than the mean from single bond work. There are several

Table I. Experimental Values of Bond Strengths

Test	*Reference*	*Adherend*	*Adhesive*	*Bond strength, dynes/cm² × 10⁷*
Shear tests on single fiber bonds	Mayhood, Kallmes, and Cauley (*3*)	Spruce sulfite fibers	Natural adhesion	2.9
		Spruce sulfate fibers	Natural adhesion	3.6
	McIntosh (*19*)	Loblolly pine holocellulose summerwood	Natural adhesion	7.1
		Loblolly pine holocellulose springwood	Natural adhesion	2.7
	Schniewind, Nemeth, and Brink (*20*)	White fir	Natural adhesion	2.6 2.3 1.6
Shear tests on miscellaneous macroscopic specimens	De Bruyne and Houwink (*21*)	Glass	Cellulose nitrate	12.0
		Metal	Epoxy resin	25.0
		Glass	P.V. acetate	17.0
	Goring (*22*)	Regenerated cellulose	Natural adhesion	1.1
		Regenerated cellulose after corona discharge	Natural adhesion	7.5

factors such as damage during testing and failure by peeling rather than shear that would tend to reduce the single bond strength values from their strength in a tensioned sheet, so that the value of 5.9×10^7 dynes/cm² derived here is reasonable.

DISCUSSION

The original theory has two main premises. The first states that at the time of rupture the stress is borne in the sheet by only a fraction of the fibers crossing the rupture line, and that these fibers act cooperatively. This is not a new statement; it is contained in the theory of Kallmes and Perez (*23*). However, in this work it is less restrictive. It is an essential feature of Kallmes's theory that end-bond breakage should occur during straining, whereas in this theory, which does not comment on the shape of the stress-strain curve, it is only necessary that by the time catastrophic failure of the fibers occurs this state should have been reached. This theory allows, therefore,

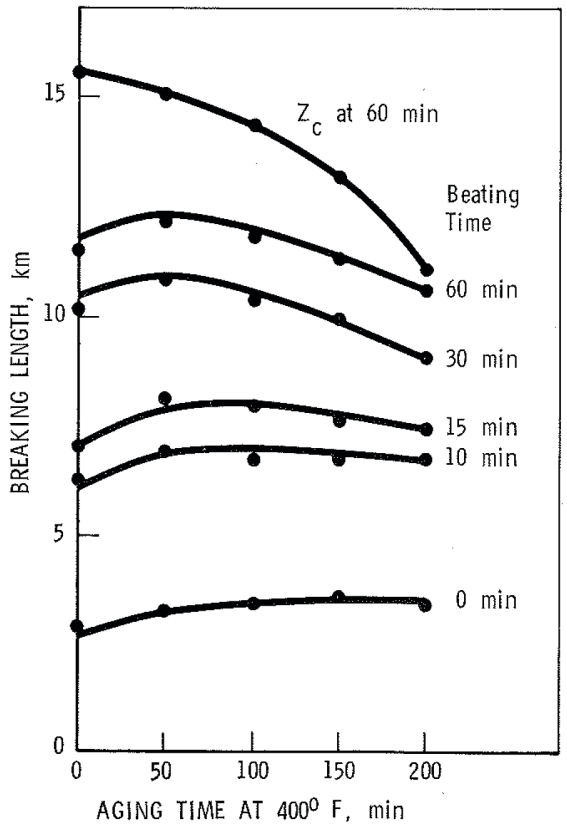


Fig. 9. Experimental data and theoretical lines for the breaking length of paper as a function of aging time at 400°F.

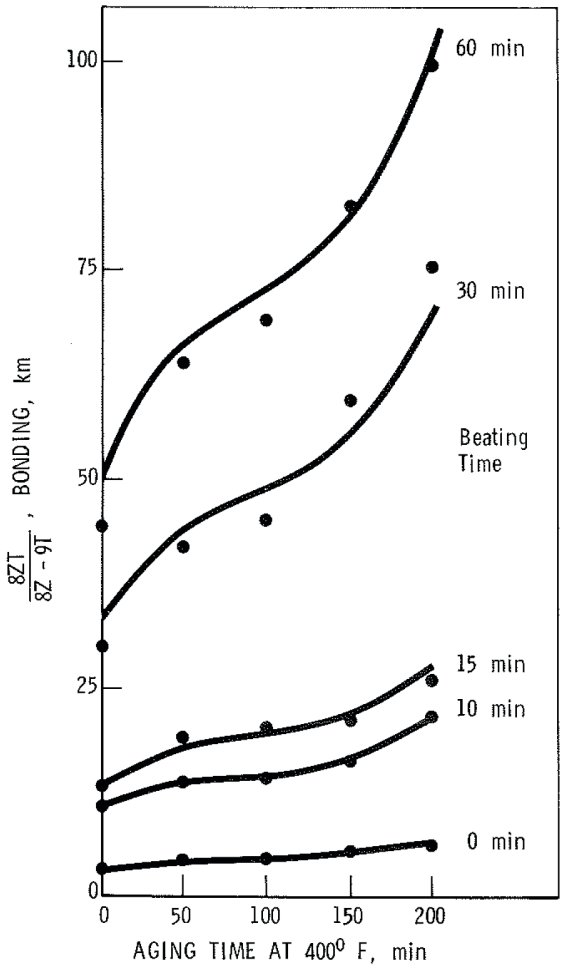


Fig. 10. Plot of $8ZT/(8Z - 9T)$, an index of bonding, against aging time.

the possibility of the rupture process occurring in two parts, firstly, a stage in which, due to bond breakage in the rupture zone, the stress is transferred from certain fibers to the remaining ones, and secondly a catastrophic failure of the load-bearing fibers.

The second premise relates to the competing effects of fiber strength and bond strength. When fibers are stronger than bonds, on the whole, bonds tend to break. When the bonds are stronger than the fibers, on the whole, the fibers break. The importance of the relationship between bond and fiber strength is contained in a general way in many previous publications but has never been expressed in this quantitative form. The statement $n_p/n_t = \phi/\beta$ is difficult to justify strictly. The ratio of the number of fibers that pull to those that fail is certainly a function of the ratio of a parameter of fiber strength to a parameter of bond strength, but there is no theoretical justification for the use of the mean as the parameter. Given the means and distributions of fiber strengths and bond strengths, and given their independence or the nature of their dependence, it would be possible to compute the percentage of fibers for which the fiber strength exceeds the bond strength and hence, obtain the ratio of the number of fibers that pull to those that fail. However, we do not know the distributions or their dependence. Bond strength is probably rectangularly distributed since the rupture line will cut the fibers into lengths of equal probability. The strength of fibers probably has a wide Gaussian distribution. We should not expect that these distributions will be independent though, since the strongest fibers have the thickest walls and will probably be the least bonded. We do not, therefore, have the information to obtain the ratio n_p/n_t, but it must be admitted that the use of independent distributions of the forms given above would not give Eq. 7. Assuming a narrow distribution of fiber strengths, Eq. 7 would be given if the distribution of bond strengths is of the form,

$$dn = \frac{\bar{\beta} d\beta}{(\bar{\beta} + \beta)^2}$$

where

dn = number of bond strengths lying between β and $\beta + d\beta$
$\bar{\beta}$ = mean bond strength

This would imply a frequency distribution biased towards weaker bonds, and the author has no justification for this.

Thus, the theory lacks rigor. Nevertheless, its success in explaining the tensile strength of paper is remarkable. A summary of the equations tested is listed in Table II. The values of r^2 are all high and, if one omits the uncontrolled data of Crook and Bennett (*14*), the residual standard error in T is on average about 0.25 km, which is within the confidence limits of the test methods. In the cases where linear plots are predicted from the theory, there is no indication of curvature in spite of the fact that all the tests have been made over a wide range of each of the variables.

Table II. Summary of Tests of the Theory

Variable	*Data*	r^2	*Standard error of residual T, km*
Fiber length	Arlov (*10*)	0.991	0.165
	Clark (*11*)	0.922	0.225
		0.968	0.105
	Watson and Dadswell (*12*)	0.941 (R^2)	0.525
Relative bonded area	Ingmanson and Thode (*13*)	0.951	0.390
Bond strength per unit area	Crook and Bennett (*14*)	0.892	1.170
Fiber strength and bond strength per unit area	Present work	0.998	0.170

This work is to an extent a vindication of the ideas of Clark (*24*), who has claimed for many years that paper properties result from a few well-defined, but difficult to measure, variables. He has particularly emphasized the importance of the following properties: fiber strength, fiber length, fiber coarseness, fiber wet flexibility (as measured by bulk), and fiber-to-fiber bond strength. The theory outlined here contains fiber strength, fiber length, and bond strength, but it is interesting to note that fiber coarseness is not a sufficient measure of the cross-sectional dimensions of fibers. A single parameter, the ratio of area to perimeter is sufficient, but, if coarseness is used, an additional shape factor must be included. In addition, relative bonded area is considered to be the basic relevant structural property of paper rather than bulk.

Clark has repeatedly claimed that the weight-biased fiber length, rather than the unbiased numerical length, is important in sheet properties, although he has given no theoretical justification. It would seem that, for tensile strength, the claim can be justified. The fibers crossing a rupture line are those that control the tensile strength. The chance of a fiber crossing a line is proportional to its length, so that the mean length of the fibers that control the rupture process is length-biased.

This theory has certain limitations. It does not apply to sheets of poor formation which will tend to fail under stress at regions of low basis weight (*25*). It does not apply without modification to sheets made from fibers that have been grossly kinked as in high consistency refining. In deriving Eq. 6 for the resisting force due to bonding, it is assumed that all the bonds act cooperatively along the fiber length and this is only possible in fibers that are straight. Kinked fibers have a reduced effective value of L in Eq. 10 and hence give a lower tensile strength. This is in good agreement with the experience that sheets containing kinked fibers are weaker than those with straight fibers. Curlation reduces sheet strength, but subsequent straightening of the fibers by low-consistency beating restores it (*26*). The work on latency of mechanical pulp shows the considerable increase in strength that can be obtained by thermally straightening kinked fibers (*27*). The theory is, in principle, applicable both to fiber-oriented and to shrunken sheets, although no tests have been made. It must be remembered that the term "relative bonded area" may have to be redefined for oriented sheets since it may itself be a directional property (*28*).

This work has some significant implications for pulp evaluation procedures. It becomes imperative, for a real understanding of the nature of pulps, that techniques be found for measuring the basic variables that have been introduced. Of the five that have been discussed, only two, the fiber length and the fiber strength (as measured by the zero-span test), are at all well defined. The others present difficulties.

Relative bonded area should be defined for the purpose of this work as the ratio of the area of load-bearing contacts between independent structural elements to the total area available for such contacts. It is not easy to devise a method for measuring a variable so defined. Indirect methods such as light scattering and gas absorption cannot distinguish between load-bearing and nonload-bearing surfaces. Fortunately, for low-yield chemical pulps, fiber lumens are substantially collapsed, and fine debris is sufficiently flexible to bond back to fiber surfaces, so that these methods do provide a reasonable assessment of the load-bearing contacts between crossing fibers. However, for high yield pulps and groundwood, such indirect methods are of doubtful value.

The ratio A/P may be measured by tedious microscopical methods. Alternatively, it is obtained by recognizing its identity to the ratio of the specific volume to the specific unbonded surface of the fibers. The specific volume of fibers is measurable and in any case is sensibly constant and the specific surface may again be derived from light scattering or gas absorption data on unbonded sheets.

There does not seem to be, at the

moment, any likelihood of a convenient method of measuring the shear strength per unit area of fiber-to-fiber bonds.

In spite of these drawbacks in measuring techniques, this theory should be of value, particularly for understanding the properties of new pulps and new species. As an example, let us consider the properties of high-yield pulps which are becoming of increasing economic importance. The effect of yield on tensile strength is, according to this theory, complex. It is known that for the usual pulping processes the fiber strength and hence the zero-span tensile strength of paper increases with decreasing yield. The cross-sectional area A decreases with decreasing yield. It seems likely that the bond strength should at first increase with decreasing yield since lignin-to-lignin bonds are likely to be weaker than those formed between hemicellulose molecules. At very low yield the bond strength may again decrease due to the absence of hemicelluloses. The relative bonded area of pulps under standard pressing conditions would also change with the yield and with the cooking process, since the rigidity of fibers is known to be a strong function of these factors. Thus, four of the major parameters controlling tensile strength will change with yield, and the effect of yield may be difficult to understand without understanding it in terms of the changes in these basic parameters.

If this theory is proved to be correct, it may provide an important method for determining the bond strength per unit area of pulps and the way in which this may be changed by various treatments. For example, by taking sheets of known fiber length and cross-sectional dimensions, the relative bonded area may be changed by pressing and, from a plot such as Fig. 7, the bond strength can be obtained from the slope of the line. Alternatively, the use of fibers of different length at the same relative bonded area could give the same information.

It is not claimed that sufficient work has been done on this theory to validate it totally. However, it seems unlikely that the ultimately accepted equation for the tensile strength of paper obtained perhaps by more sophisticated analyses will differ appreciably from the one presented here in view of the excellent corroboration that this has received from a variety of experimental data.

LITERATURE CITED

1. Cox, H. L., *Brit. J. Appl. Phys.* **3** (3): 72 (1952).
2. Page, D. H., Tydeman, P. A., and Hunt, M., Trans. Brit. Paper and Board Makers' Assoc. Sympos. Formation Struct. Paper, Oxford, 1961, pp. 171–193.
3. Mayhood, C. H., Jr., Kallmes, O. J., and Cauley, M. M., *Tappi* **45** (1): 69 (1962).
4. Van den Akker, J. A., Lathrop, A. L., Voelker, M. H., and Dearth, L. R., *Tappi* **41** (8): 416 (1958).
5. Helle, T., *Svensk Papperstid.* **66** (24): 1015 (1963).
6. Kellogg, R. M. and Wangaard, F. F., *Tappi* **47** (6): 361 (1964).
7. Van den Akker, J. A., Trans. Brit. Paper and Board Makers' Assoc. Sympos. Formation Struct. Paper, Oxford, 1961, pp. 205–241.
8. Page, D. H., Discussion Contribution, Trans. Brit. Paper and Board Makers' Assoc. Sympos. Formation Struct. Paper, Oxford, 1961, pp. 246–247.
9. Brecht, W. and Wanka, R., *Papier* **17** (4): 141 (1963).
10. Arlov, A. P., *Norsk Skogind.* **13** (10): 342 (1959).
11. Clark, J. d'A., *Tappi* **45** (8): 628 (1962).
12. Watson, A. J. and Dadswell, H. E., *APPITA* **14** (5): 168 (1961).
13. Ingmanson, W. L. and Thode, E. F., *Tappi* **42** (1): 83 (1959).
14. Crook, D. M. and Bennett, W. E., "The Effect of Humidity and Temperature on the Physical Properties of Paper," Brit. Paper and Board Ind. Res. Assoc. Confidential Report RA/T/90 (Feb. 1962). Data reproduced by kind permission of the Association.
15. Leech, H. J., *Tappi* **37** (8): 343 (1954).
16. Ott, E. and Spurlin, H. M., "Cellulose and Cellulose Derivatives," New York, Interscience, 1954.
17. Back, E. L., *Pulp Paper Mag. Can.* **68** (4): T165 (1967).
18. Britt, K. W. and Yiannos, P. N., *Tappi* **47** (7): 427 (1964).
19. McIntosh, D. C., *Tappi* **46** (5): 273 (1963).
20. Schniewind, A. P., Nemeth, L. J., and Brink, D. L., *Tappi* **47** (4): 244 (1964).
21. De Bruyne, N. A. and Houwink, R., "Adhesion and Adhesives," Amsterdam, Elsevier, 1951.
22. Goring, D. A. I., *Pulp Paper Mag. Can.* **68** (8): T372 (1967).
23. Kallmes, O. J. and Perez, M., Trans. Brit. Paper and Board Makers' Assoc. Sympos. Consol. Paper Web., Cambridge, 1965, pp. 779–800.
24. Clark, J. d'A., *Pulp Paper Mag. Can.* **59** (10): 134–137, 146 (1958).
25. Tydeman, P. A. and Hiron, A. M., Brit. Paper and Board Ind. Res. Assoc. Bull., Kenley, No. 35, pp. 9–21, 1964.
26. Hill, H. S., Edwards, J., and Beath, L. R., *Tappi* **33** (1): 36 (1950).
27. Jones, H. W. H., *Pulp Paper Mag. Can.* **67** (6); T283 (1966).
28. Kallmes, O. J. and Bernier, G. A., *Tappi* **47** (11): 694 (1964).

RECEIVED FOR REVIEW Aug. 8, 1968.

ACCEPTED Oct. 22, 1968.

Presented at the 54th Annual Meeting of the Technical Association of the Pulp and Paper Industry, held in New York, N. Y., Feb. 17–20, 1969.

TAPPI JOURNAL
WWW.TAPPI.ORG
THE PAPER AND PACKAGING INDUSTRIES' TECHNICAL RESOURCE **NOVEMBER 2018** | VOL. 17 NO. 11



BLEACHING **601**
Understanding the risks and rewards of using 50% vs. 10% strength peroxide in pulp bleach plants
Alan W. Rudie and Peter W. Hart

NONWOOD PULPING **611**
Does the kappa number method accurately reflect lignin content in nonwood pulps?
Sabrina Burkhardt

BLEACHING **621**
Using multistage models to evaluate how pulp washing after the first extraction stage impacts elemental chlorine-free bleach demand
Brian N. Brogdon and Lucian A. Lucia

BLEACHING **633**
Understanding the pulping and bleaching performances of eucalyptus woods affected by physiological disturbance
Juliana Marangon Jardim, Carolina Marangon Jardim, and Jorge Luiz Colodette

November 2018

TABLE OF CONTENTS VOL. 17 NO. 11

597 EDITORIAL
2018 *TAPPI Journal* features diverse content
Monica Shaw

601 BLEACHING
Understanding the risks and rewards of using 50% vs. 10% strength peroxide in pulp bleach plants
Alan W. Rudie and Peter W. Hart

611 NONWOOD PULPING
Does the kappa number method accurately reflect lignin content in nonwood pulps?
Sabrina Burkhardt

621 BLEACHING
Using multistage models to evaluate how pulp washing after the first extraction stage impacts elemental chlorine-free bleach demand
Brian N. Brogdon and Lucian A. Lucia

633 BLEACHING
Understanding the pulping and bleaching performances of eucalyptus woods affected by physiological disturbance
Juliana Marangon Jardim, Carolina Marangon Jardim, and Jorge Luiz Colodette

»COVER CREDIT: To determine how bleached pulp production is affected by wood quality, researchers Jardim et al. studied two hybrid clones of *Eucalyptus urophylla x Eucalyptus grandis*—one tolerant to disturbance and one sensitive—from sites where disturbance was present and absent. This photo of *Eucalyptus urophylla x Eucalyptus grandis* is courtesy of Roosevelt De Paula Almado, Development and Technology Manager at ArcelorMittal BioFlorestas in Belo Horizonte, Brazil. It was taken at a planting in the municipality of Juiz de Fora in Minas Gerais, Brazil.

TAPPI JOURNAL
WWW.TAPPI.ORG

Editor-in-Chief
Brian N. Brogdon brian.brogdon@gmail.com
+1 678 581-9114

Associate Editor
Peter W. Hart peter.hart@westrock.com
+1 409 276-3465

Editorial Director
Monica Shaw mshaw@tappi.org
+1 770 367-9534

PRESS Manager
Jana Jensen jjensen@tappi.org
+1 770 209-7242

Webmaster
Trina Heath theath@tappi.org
+1 770 209-7416

***TJ* EDITORIAL BOARD**
Randy Branston, BASF
randy.branston@basf.com, +1 704 819-4251

Brian N. Brogdon, FutureBridge Consulting & Training LLC
brian.brogdon@gmail.com, +1 678 581-9114

David A. Carlson, Carlson Consulting
dacarlson39@aol.com, +1 847 323-2685

Douglas W. Coffin, Miami University
coffindw@miamioh.edu, +1 513 529-0771

Mahendra Doshi, Doshi and Associates
mahen@aol.com, +1 920 832-9101

Marc Foulger, GL&V USA Inc.
Marc.foulger@glv.com +1 315 767-2920

Peter W. Hart, WestRock
peter.hart@westrock.com, +1 409 276-3465

Carl J. Houtman, USDA Forest Products Laboratory
choutman@fs.fed.us, + 1 608 231-9445

Lucian Lucia, North Carolina State University
lucian.lucia@gmail.com, +1 919 889-7059

John A. Neun, John A. Neun LLC
john.neun@gmail.com, +1 518 275-8139

Jim Niemiec, Verso Corporation
jim.niemiec@versoco.com, +1 715 422-7404

Steven P. Ottone, Omya
steven.ottone@omya.com, +1 919 641-7854

Gaurav Pranami, Imbed Biosciences
gpranami@imbedbio.com, +1 515 230-7005

Arthur Ragauskas, Oak Ridge National Laboratory
aragausk@utk.edu

Gerard J.F. Ring, University of Wisconsin—Stevens Point
gerrryring@wi-net.com, +1 715 592-3732

Scott Rosencrance, Kemira Chemicals
scott.rosencrance@kemira.com, +1 770 429-2753

Paul Wiegand, NCASI
pwiegand@ncasi.org, +1 919 941-6417

Junyong Zhu, USDA Forest Products Laboratory
jzhu@fs.fed.us, +1 608 231-9520

Join TAPPI *today!*
TAPPI JOURNAL is a free benefit of TAPPI membership, and is only available to members. To join TAPPI, to renew your TAPPI Membership, or to learn about other valuable benefits, visit www.tappi.org.

TAPPI, 15 Technology Parkway S., Suite 115, Peachtree Corners, GA 30092, publishes *TAPPI JOURNAL* monthly.

ATTENTION PROSPECTIVE AUTHORS: All papers published are subject to *TAPPI JOURNAL's* peer-review process. Not all papers accepted for review will be published. Before submitting, check complete author guidelines at http://www.tappi.org/s_tappi/doc.asp?CID=100&DID=552877.

Statements of fact and opinions expressed are those of individual authors. TAPPI assumes no responsibility for such statements and opinions. TAPPI does not intend such statements and opinions or construe them as a solicitation of or suggestion for any agreed-upon course of conduct or concerted action of any sort.

Copyright 2018 by TAPPI, all rights reserved. For copyright permission to photocopy pages from this publication for internal or personal use, contact Copyright Clearance Center, Inc. (CCC) via their website: www.copyright.com. If you have questions about the copyright permission request process, please contact CCC by phone at +1 978 750-8400. To obtain copyright permission to use excerpts from this publication in another published work, send your specific request in writing to Editor, TAPPI JOURNAL, 15 Technology Parkway S., Suite 115, Peachtree Corners, GA 30092, USA; or by fax to +1 770 446-6947. Send address changes to TAPPI, 15 Technology Parkway S., Suite 115, Peachtree Corners, GA 30092, USA; Telephone +1 770 446-1400, or FAX +1 770 446-6947. www.tappi.org

Editorial



MONICA SHAW | EDITORIAL DIRECTOR
mshaw@tappi.org

2018 *TAPPI Journal* features diverse content

As we wrap up our final issue of *TAPPI Journal* (*TJ*) for the year, it's interesting to look at the research topics that were covered in 2018. Once again, pulping-related topics dominated, with about one-third of the content. Members of the *TJ* editorial board organized diverse special issues on coating, lignocellulosics, pulping, and papermaking, which are discussed in the following sections.

Coating and Lignocellulosics



TAPPI Journal editorial board members Steve Ottone, Randy Branston, and Jim Niemiec organized special coating content for the January 2018 issue, with assistance from guest editor Gregory Welsh. Topics included slot die coating of nanocellulose on paperboard, prediction of coating failure, barrier coating, and print quality of flexographic printed paperboard.



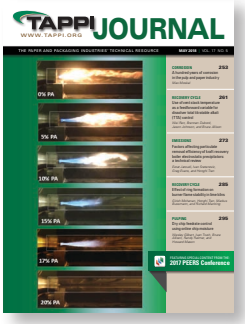
For February, editorial board member Art Ragauskas and guest editor Yunqiao Pu put together a special issue examining some of the challenges in lignocellulosics and highlighting new pathways available for research in the field. This issue covered lignin products, moisture sorption, hydrogels from lignocellulose, and functionalization of cellulose with nanomaterials.

Research from South China University of Technology

The March 2018 special issue featured content from South China University of Technology and the State Key Laboratory of Pulp and Paper Engineering in Guangzhou, China. Organized by J.Y. Zhu of the *TJ* editorial board and guest editor Fachuang Lu, the issue covered topics ranging from lignin products and nanocellulose to emissions and wastewater treatment.



Pulping, Bleaching and the Recovery Cycle



Much of the pulping-related coverage this year was coordinated by *TJ* editor-in-chief Brian Brogdon and assistant editor Peter Hart, with help from Lucian Lucia, who also serves on the editorial board. Brian and Peter organized special peer-reviewed content from the 2017 TAPPI PEERS Conference for the May 2018 issue, which covered corrosion and emissions in addition to pulping research.

Some of the pulping-related topics covered during the year were online measurement of bleached chemithermomechanical pulp properties, delignification, and kappa number as a questionable measure of lignin content in nonwood pulps. Recovery cycle content examined ring formation in lime kilns, vent stack temperature as a feedforward variable for total titratable alkali control, green liquor scale formation, and more. Bleaching topics included a risk/reward assessment of using 50% vs. 10% strength peroxide, multistage models for evaluating pulp washing impacts, and decreased water use in ECF bleaching.

Papermaking and Paper Physics

For September 2018, editorial board members Scott Rosencrance and Gerry Ring, with help from guest editor Frank Sutman, handled the peer review process for papers from PaperCon 2018 to create a special issue. Coverage included rewet in wet pressing of paper, boosting the

elongation potential of paper, paper testing, microfibrillated cellulose, and sustainability. For paper physics content, Gerry was assisted by the newest member of the *TJ* editorial board, Doug Coffin, who will also handle corrugated topics moving forward. In addition, Marc Foulger and John Neun handled a range of papermaking topics.



Other areas of research coverage

Recycling peer review was guided by Mahendra Doshi and Carl Houtman, while Dave Carlson offered expertise on corrugated topics. Paul Wiegand coordinated peer reviews for environmental and wastewater treatment coverage and Gaurav Pranami provided guidance on nonwovens and coatings.

A special thank you

TAPPI and the *TJ* staff would like to thank the editorial board for their tremendous help in providing expertise and handling the peer review process so *TJ* can provide readers with the most cutting-edge research in the forest products and related industries. We'd also like to thank all of the authors and peer reviewers who participate in this important process.

In 2019, *TJ* readers can expect to see more special content organized by our editorial board on foam forming, coating, nano-lignocellulose, pulping, and more. Stay tuned for exciting new developments coming for *TAPPI Journal* next year! **TJ**

For information on publishing in TAPPI Journal, *contact tjournal@tappi.org, mshaw@tappi.org, or an editorial board member in your field of expertise. You can submit your papers to our online peer review system at http://www.editorialmanager.com/tappi/.*

Understanding the risks and rewards of using 50% vs. 10% strength peroxide in pulp bleach plants

ALAN W. RUDIE AND PETER W. HART

ABSTRACT: The use of 50% concentration and 10% concentration hydrogen peroxide were evaluated for chemical and mechanical pulp bleach plants at storage and at point of use. Several dangerous occurrences have been documented when the supply of 50% peroxide going into the pulping process was not stopped during a process failure. Startup conditions and leaking block valves during maintenance outages have also contributed to explosions. Although hazardous events have occurred, 50% peroxide can be stored safely with proper precautions and engineering controls. For point of use in a chemical bleach plant, it is recommended to dilute the peroxide to 10% prior to application, because risk does not outweigh the benefit. For point of use in a mechanical bleach plant, it is recommended to use 50% peroxide going into a bleach liquor mixing system that includes the other chemicals used to maintain the brightening reaction rate. When 50% peroxide is used, it is critical that proper engineering controls are used to mitigate any risks.

Application: By understanding the risk/reward benefit, chemical pulp mills should realize there is no justification for using 50% peroxide in an extraction stage. If they lower the concentration of peroxide to 10%, their operation will be much safer.

Hydrogen peroxide has been used in the bleaching of both chemical and mechanical pulps for several decades. It is widely recognized as an environmentally friendly bleaching chemical with breakdown products of water and oxygen. Mechanical pulp mills typically use peroxide to obtain higher brightness pulps, with peroxide charges up to 4% on ovendry (o.d.) pulp used in some mills [1,2]. Chemical pulp mills typically employ smaller charges of peroxide (from 0.15%–1.0% on o.d. pulp), often as an oxidative reinforcement in the extraction stage to either reduce the amount of chlorine dioxide required in the first bleaching stage or to raise the brightness of the pulp entering the chlorine dioxide stage that follows [1,3].

Hydrogen peroxide can be and has been used safely for many years, but, like any strong oxidant, it must be handled with caution. Runaway decomposition of hydrogen peroxide has resulted in catastrophic events in pulp mills over the last few years. Several North American chemical pulp bleach plants have experienced catastrophic sudden pressure releases associated with the decomposition of 50 wt% peroxide, resulting in pieces of equipment, such as pump housings, being fragmented and propelled through bleaching towers, building walls, pipes, etc. [4-6]. Although plant personnel were badly injured in at least two of these instances, with the extent of damages, these mills were fortunate to have avoided fatalities in these accidents. Both bleach plants that had personnel injuries experienced a peroxide-induced pressure burst when peroxide and caustic were added to a medium consistency pump in which no pulp was flowing because of undetected operating problems. If pulp had been moving through the process, these explosions would not have occurred, as peroxide would not have been able to pool in the pump or line and decompose in this autocatalytic exothermic reaction. Other incidents, one in Europe and one in North America, resulted from rapid decomposition within a storage tank when an organic chelant was mistakenly mixed with hydrogen peroxide [6-8]. In these cases, the explosion was likely a combination of alkaline-catalyzed decomposition and rapid oxidation of an organic chemical.

Several people have told the authors that other peroxide decomposition incidents have occurred throughout Europe and southeast Asia, but have not been sufficiently documented in the literature to be cited here. Other industries also have experienced problems with rapid peroxide decomposition when using higher concentration applications. For instance, a well-known wine maker using 35% alkaline peroxide to sterilize corks also experienced a rapid decomposition that resulted in an unacceptable work hazard, but there were fortunately no recorded injuries. The Russian submarine Kursh sunk when the 70% peroxide used in the propulsion system of its torpedoes decomposed, with an explosion consequently rupturing the hull [8].

HAZARDS ASSOCIATED WITH THE USE OF HIGH CONCENTRATION PEROXIDE

Hydrogen peroxide is delivered to mills via either tank truck or railcar. Truck deliveries are near 50% concentration [8]. Railcar deliveries may be either at 50% or 70% concentration.

https://doi.org/10.32964/TJ17.11.601

If a mill receives hydrogen peroxide deliveries at 70% concentration, it is routinely diluted to 50% concentration as it is unloaded into storage. This is done to avoid the rigorous process safety management procedures required for 70% peroxide storage. Under proper storage conditions, hydrogen peroxide decomposes at a rate of about 1% per year [9-14]. Traces of transition metal ions (e.g., iron, copper, and manganese) increase the rate of hydrogen peroxide decomposition [15], and suppliers add stabilizers to sequester these metal ions. Physical contact with 50% concentration hydrogen peroxide solutions poses major safety hazards (e.g., skin burns, eye injuries). It also has the potential for rapid pressurization within tanks, pipes, pumps, and storage vessels. There is a potential for fire due to the formation of oxygen during the highly exothermic decomposition of hydrogen peroxide [9,16]. Despite these potential problems, a 50% peroxide bulk storage tank may be safely managed if proper engineering and administrative controls are employed to prevent contamination and the tank is routinely monitored for temperature rise. Note, however, that two of the serious explosions pulp mills have experienced were storage tanks and directly due to the failure to maintain proper vigilance in handling this chemical.

Chemical pulp bleach plants have routinely handled 50% peroxide without incident, but there is an inherent hazard at this concentration that makes it difficult to eliminate all risks of explosions and fires. If one accepts the "what can go wrong will go wrong" philosophy and that operations managers must eliminate risks to personnel and facilities from a worst-case scenario, it is hard to justify use of the chemical at 50% strength. Startup or shutdown failures, pump failures, blocked lines, or ruptured pipes or seals that could result in a small pool of 50% peroxide present potentially catastrophic conditions. Even when diluted to 10% strength, there is potential for personal injury from leaking pumps and piping. Although it cannot completely eliminate the risk of injuries, dilution of 50% peroxide to 10% significantly reduces the reaction rate, providing critical time to address exposure in the event of a spray from a leaking gasket or seal [9], and this will usually decrease the severity of injuries significantly

Storage tank hazards

A common hazard associated with 50% peroxide solutions is vessel rupture caused by peroxide decomposition. Vessel rupture occurs when the gas generation rate exceeds the venting capacity of the storage tank [9]. Catalytic decomposition of peroxide results in the liberation of oxygen and heat. One liter of 50% hydrogen peroxide can yield approximately 200 L of oxygen, in addition to steam. Under typical circumstances, hydrogen peroxide is stored at 50% concentration. This provides sufficient water to absorb any heat evolved due to normal slow (unaccelerated) peroxide disproportionation. The thermal mass also provides time to take actions to prevent catastrophic outcomes if the tank becomes contaminated and decomposition accelerates. In high concentrations, a catalytic decomposition can become self-accelerating because the rate of heat evolution exceeds the rate of heat loss to the surroundings [10]. Vaporization of water results in further concentration of the hydrogen peroxide solution, which results in faster decomposition. Vessel ruptures have occurred in both Europe and North American when an organic chelant was mistakenly unloaded into hydrogen peroxide storage tanks [6-8]. In these cases, the explosion was likely a combination of alkaline-catalyzed decomposition and rapid oxidation of an organic chemical.

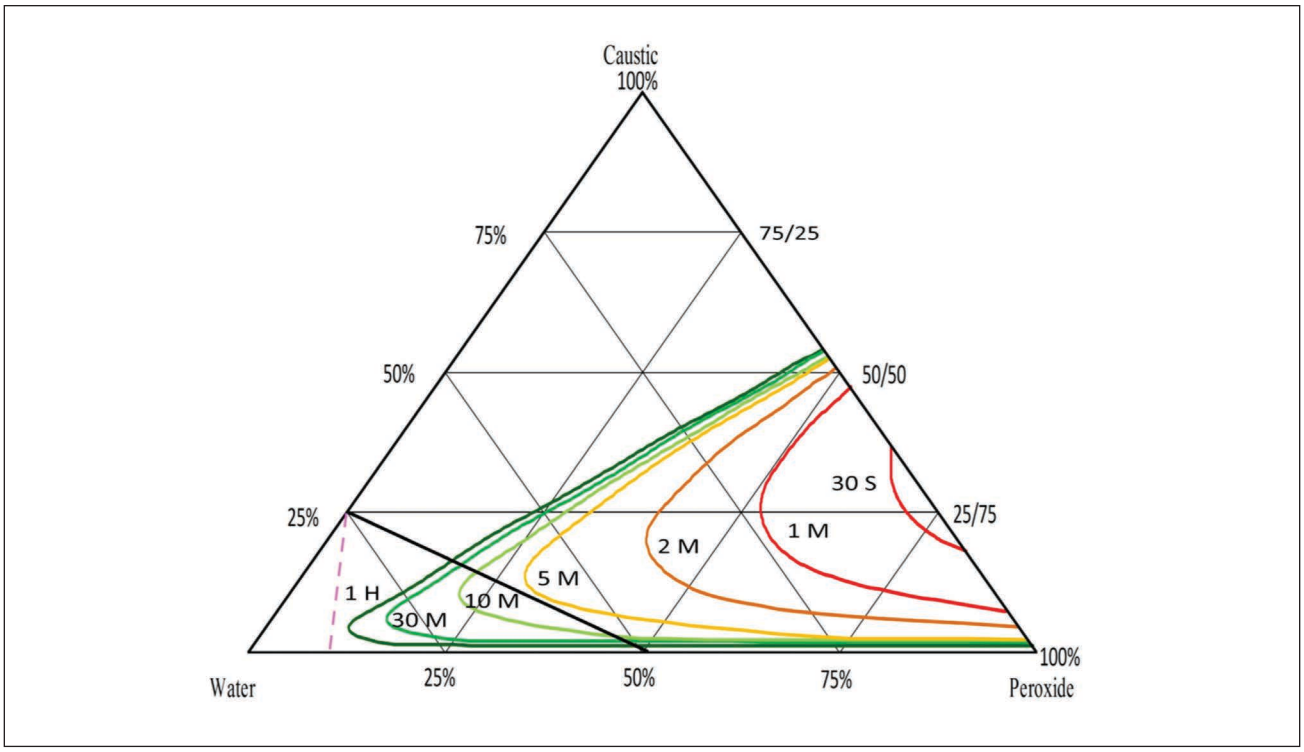
Hydrogen peroxide is typically stored at around 50% concentration in a mill. If it is shipped into the mill site via rail, it is possible to have it arrive at the mill at a higher concentration. The peroxide is diluted to about 50% at the point of unloading as it is being sent to storage. Mills generally store peroxide at 50% concentration to reduce capital costs, as considerably larger storage tanks would be needed to store peroxide at lower concentrations. Also, by storing at 50% concentration, the mill does not have to designate the storage tank and associated process piping as a process safety management (PSM) covered process. Fifty percent peroxide can be stored safely with proper precautions and engineering controls. Hydrogen peroxide storage tank temperature should be monitored. The decomposition process is typically slow at first and may take days or weeks to become "critical". A temperature increase of Δ1°C per hour, at 30°C–35°C, is indicative of a decomposition event. Decomposition reactions in storage can be quenched by external cooling or dilution.

Pressure burst hazards

Another failure mode for alkaline peroxide is a pressure burst occurring within processing equipment. At least two mill explosions have resulted from pressure bursts within the last several years [9]. Extensive kinetic modeling has been performed to predict pressure bursts from first principles models [10,11]. The initial modeling work used kinetic data for dilute peroxide developed by Makkonen [12] under laboratory conditions. A limitation of this work was that process model kinetics were extrapolated well beyond the experimental range of temperatures and concentrations from which the model was developed. Such large extrapolations have the potential to introduce substantial errors into the model predictions. To improve the kinetic modelling, additional experiments were conducted with chemicals, concentrations, and temperatures similar to bleach plant operating or startup conditions, and these results were used to reduce the extrapolation error [13].

DISCUSSION

The kinetics of decomposition were experimentally measured for mixtures of hydrogen peroxide and sodium hydroxide based on commercial diaphragm grade, membrane grade, and mercury cell grade sodium hydroxide and commercially available 50% hydrogen peroxide [13]. These results were used in a model to develop the three-component triangle diagram shown in **Fig. 1**. Decomposition rates when using membrane grade caustic were used to develop this diagram. The contour



1. Reaction model results for membrane grade caustic soda. For a mixture starting at 50°C, the contours represent the time required to reach 100°C. The blue line represents the operating line for typical mill operation with 50% peroxide. The pink line is the proposed safer operating line when 12% peroxide is employed.

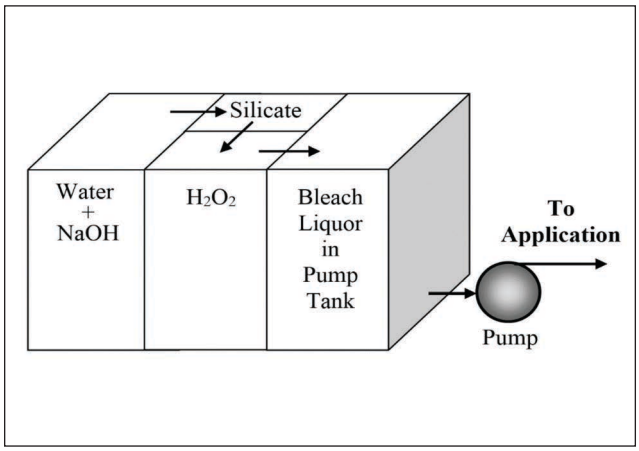
lines in the triangle diagram represent the time required for the reaction mixture to reach 100°C and enter a potentially explosive condition. Typical high concentration bleaching chemicals are 25 wt% caustic and 50 wt% peroxide. All mixtures of 25 wt% caustic soda and 50 wt% hydrogen peroxide will be somewhere on the thick line on the triangle diagram. This line represents the operating line when there is no pulp flowing in the system. Notably, the operating line enters the dangerous concentration range (arbitrarily chosen as 1 h), which suggests that an auto-accelerating reaction could occur in a mill using 50% peroxide if the stock flow that dilutes the chemicals were to be interrupted. Inspection of Fig. 1 shows that there is a region of inherent safety using hydrogen peroxide with a concentration below 12% (see the dotted fuchsia colored line representing 12% peroxide and 25% caustic). In order to account for process control fluctuations and provide a small safety factor, the authors are suggesting 10% concentration as the "relatively safe" concentration of peroxide for bleach plant application.

Startup condition modeling for chemical and mechanical pulps

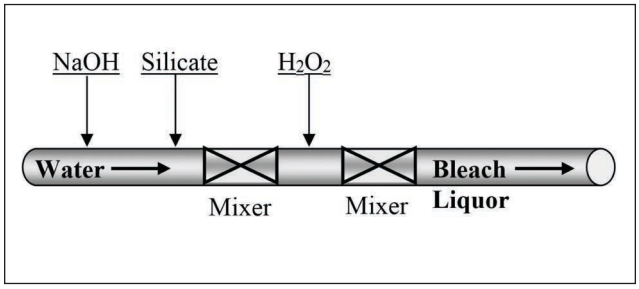
The alkali catalyzed peroxide decomposition reaction occurs when caustic is mixed with peroxide. This is a parasitic reaction that is always present in pulp bleaching but is typically a minor loss of reagent when bleaching proceeds normally. Without pulp present, alkaline catalyzed decomposition will consume the peroxide and generate considerable heat in the process. Catastrophic events appear to require a partially contained pool or supply of peroxide that can maintain the reaction long enough for the temperature and reaction rate to rise beyond the vent capacity of the system to release the steam and oxygen gas. Typically, this scenario—a pre-existing pool of peroxide—only occurs during non-standard operating conditions such as shutdowns, startups, or equipment failures.

Modeling was used to evaluate typical startup scenarios for both chemical and mechanical pulp bleaching processes. Chemical pulp mills usually employ direct injection of peroxide and caustic into a flowing pulp stream at the inlet of a pump; evaluation of this mixing system showed that one particular failure mode leads to an incredibly unstable situation. If caustic is added to a pre-existing pool of high concentration (50%) hydrogen peroxide—the autocatalytic reaction—can exceed the vent capacity of typical mixers and pumps causing the pressure to rise above atmospheric pressure. The kinetic model shows this as a runaway condition, and the predicted pressure buildup is quite sudden, very substantial and can exceed the ability of piping and pumps to contain the reaction. This model mimics at least one of the known explosions exceptionally well. When 10% peroxide is used, the water absorbs all the heat that is generated by the decomposition, and without the steam generation, the reaction does not build as much pressure and does not exceed the large vents of the suction and discharge of pumps or mixers [10,11,13].

High consistency peroxide bleaching in mechanical pulp mills has been used for nearly five decades. The key process

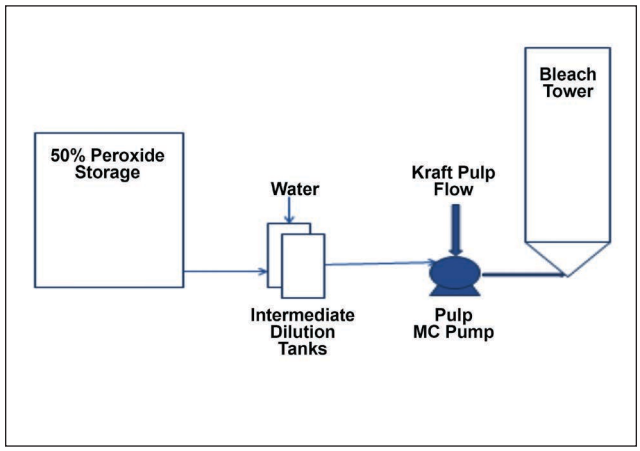


2. Addition of hydrogen peroxide prior to the bleach liquor tank [9]. Water and caustic, sometimes with Epsom salts, are combined. The resulting solution is blended with silicate. Peroxide is added to this stabilizing mixture and either sent to a day tank or pumped directly into the pulp being bleached.



3. In-line dilution of the hydrogen peroxide bleach liquor [9].

items are a press that can deliver a very high consistency pulp and a mixing system that works well at high consistency. Traditionally, this was a refiner or pulp fluffer that was mounted near the top of the tower and conveyed the pulp into the tower (with some air entrained with the pulp feed), and a chemical make-up system such as a cascade mixing tank system (**Fig. 2**). Water and Epsom salts were mixed in the first tank, which cascaded into a second tank where the sodium hydroxide was added. A third tank was used to add sodium silicate, and the final tank in the series was used to mix in the peroxide. The result was nominally a 10% peroxide solution that contained the other ingredients of the chemical cocktail to provide stability and the alkali to drive the bleaching reactions. These solutions are sufficiently stable that mills often include brief storage capacity (e.g., day tank), enough for several hours of operation. More modern installations pump these chemicals directly into the inlet of a pump using a series of inline mixers in the chemical addition line for the various chemicals; a typical in-line peroxide addition system used in mechanical pulp bleach plants is shown in **Fig. 3**. Hydrogen peroxide is typically added to the bleach liquor feed line just prior to the process application to reduce the loss of peroxide because of decomposition. The peroxide flow is typically interlocked to both pulp flow and bleach liquor flow, which provides a redundant control process so pools of undiluted peroxide should not accumulate within the process. As a comparison, a typical peroxide dilution system used to bring peroxide from nominally 50% concentration to about 10% concentration for chemical pulp bleaching systems is shown in **Fig. 4**.



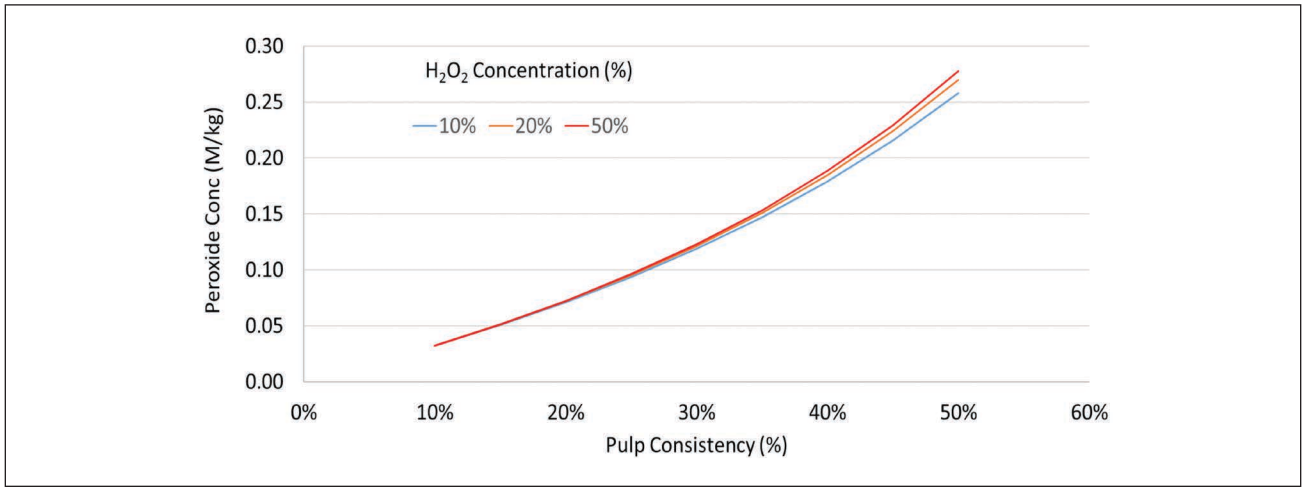
4. Typical dilution system to supply 10% peroxide from a 50% storage tank to a chemical pulp bleach tower

For the startup scenarios evaluated for the cascade type mixing systems used to prepare mechanical pulp bleaching solutions, failure of one part of the mixing process or supply system is predicted by the kinetic model to result in stable solutions or slow decomposition rates that can be readily managed even when 50% peroxide is being mixed with the other chemicals used in the bleaching system. Even when water flow fails, models of the addition of 50% peroxide to sodium hydroxide do not predict a significant pressure rise, partially because the gas is released in a steady stream as peroxide is added.

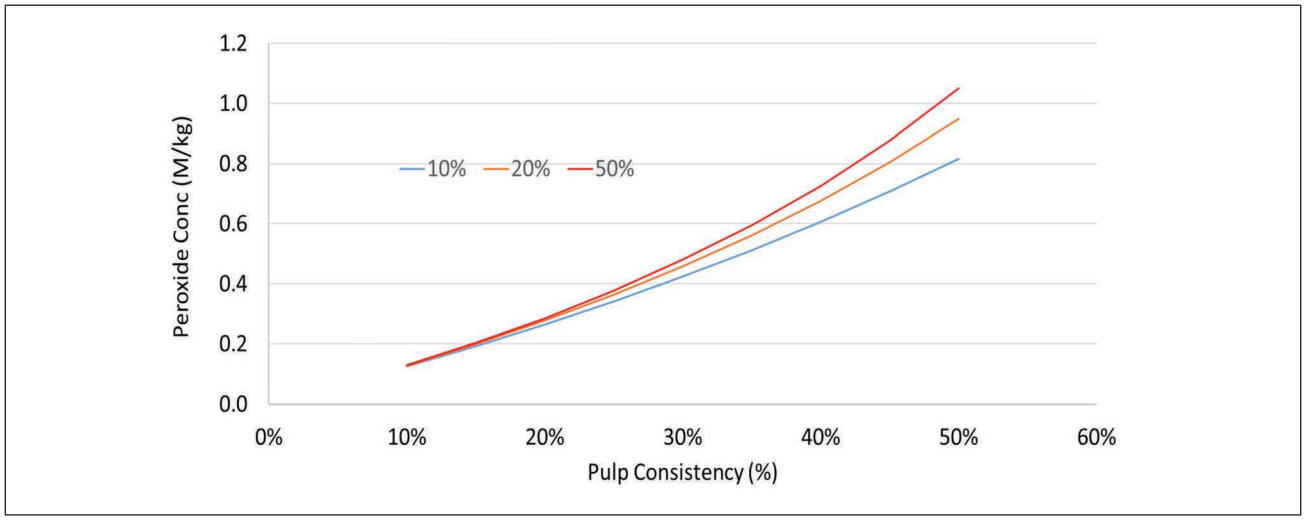
DIFFERENCES BETWEEN MECHANICAL AND CHEMICAL PEROXIDE BLEACHING

One of the main driving forces of medium consistency (MC) chemical pulp bleaching is the current ability to mix chemicals into pulp at 10%–15% pulp consistency. This is a desirable outcome of improved mixing technology because several bleaching chemicals, including hydrogen peroxide, have faster reaction rates at higher solution concentrations. One of the main tenets of MC bleaching is to keep as much water as possible out of the bleach plant by using stronger bleaching chemicals. Hence, some bleach plant suppliers now quote 50% peroxide as the required strength for their bleaching systems. Typical operating scenarios for both chemical pulp mills operating at MC conditions and mechanical pulp bleach plants operating at higher consistency have been evaluated to determine the impact of peroxide strength on the initial bleach tower peroxide concentration.

There are fundamental differences in peroxide bleaching for mechanical pulps and chemical pulps. Peroxide has limited effectiveness as a bleaching agent when used as an oxida-



5. Impact of pulp consistency on peroxide in chemical pulp bleaching solution for various strengths of hydrogen peroxide reagent at a 1% charge of peroxide on o.d. pulp.



6. Impact of pulp consistency on peroxide in mechanical pulp bleaching solution for various strengths of hydrogen peroxide reagent at a 4% charge of peroxide on o.d. pulp.

tive reinforcement of the extraction stage in chemical pulp bleaching and tends to be limited to about 1 wt% charge on o.d. pulp or less. Since most trace transition metal ions are removed in the first bleaching stage, peroxide stabilization is not typically a problem. When peroxide stabilization is required, it is usually accomplished with a chelating chemical (EDTA or DTPA) and sometimes with magnesium sulfate (Epsom salt). An increase in the concentration of the peroxide feed affects the concentration of the peroxide in the pulp, as shown in **Fig. 5**, as a function of the starting pulp consistency for a 1% peroxide charge on pulp. Note that peroxide concentration in the bleach tower is directly related to the reaction rate, and higher peroxide concentrations are best achieved with higher pulp consistency.

As is readily seen, at 1% charge on pulp, there is almost no increase in the solution concentration of peroxide during bleaching due to increases in peroxide concentration, even at very high peroxide concentrations of 50%. In comparison, raising pulp consistency before mixing is far more effective at increasing the peroxide concentration and reaction rates, but typical chemical pulp processing with MC pumps and towers limit the pulp consistency to 20% or less. At 20% pulp consistency before mixing, the impact of the as-delivered peroxide concentration is negligible, 0.072 moles/Kg for 50% strength peroxide compared to 0.071 moles/Kg at 10% peroxide strength. That represents about a 1.5% increase in solution concentration and reaction rate when using 50% peroxide compared to 10% peroxide. The safety concerns associated with the use of 50% peroxide far outweigh the value of the minimal enhancement in peroxide efficiency resulting from the use of 50% peroxide.

Peroxide stabilization is a challenge with mechanical pulps, which contain significant trace levels of manganese and iron. Stabilization usually starts with addition of a chelating chemical, followed by pressing to remove as much of the trace transition metal ions as possible; pressing results in a

pulp consistency of 25%–35%. A peroxide cocktail or bleach liquor that contains sodium silicate, magnesium sulfate, sodium hydroxide, and peroxide is then mixed with the pulp. The combination of chemicals required to stabilize the peroxide makes the use of peroxide for bleaching mechanical pulps more expensive. A typical peroxide charge under these conditions is 3 wt% or 4 wt% on o.d. pulp. The impacts of both the starting pulp consistency and peroxide strength when using a 4% peroxide charge on pulp are shown in **Fig. 6**.

As seen previously with the chemical pulp bleaching scenario, the starting pulp consistency in mechanical pulp bleaching has the larger impact on the peroxide concentration, relative to peroxide reagent concentration; hence, pulp consistency has the larger impact upon the peroxide bleaching reaction rate. At the high peroxide charge and high pulp consistency, the peroxide concentration can offer a marginal increase in concentration (and thus reaction rate). At 40% consistency for the pressed pulp (about the maximum that can be achieved with a twin wire press), the 10% peroxide strength provides a solution concentration of 0.606 moles/Kg, while the 50% peroxide solution increases this to 0.726 moles/Kg. Therefore, using 50% peroxide solution will result in about a 20% increase in reaction rate versus using a 10% strength peroxide solution.

CONCLUSIONS

An evaluation of the advantages and risks associated with storage and point of application of high versus low concentration hydrogen peroxide was performed. The major safety problems related to concentrated hydrogen peroxide use are the potential for rapid pressurization from catalyzed decomposition, fire due to oxygen formed in decomposition, and peroxide/organic vapor phase explosions. As peroxide is a strong oxidizing agent, 50% peroxide can cause severe burns when it contacts skin. Lowering the concentration of peroxide in storage will result in excessively sized storage tanks resulting in substantial increases in capital costs. **Table I** lists a series of recommendations for safer practices that balance capital costs, personnel and equipment risks, and bleaching performance.

Fundamental differences exist between mechanical pulp bleaching with peroxide and chemical pulp bleaching with peroxide. In general, mechanical pulp bleaching uses considerably higher charges of peroxide on o.d. pulp than chemical pulps and often uses higher consistencies than can be obtained with traditional chemical pulp washers, pumps, and mixers. The current work quantifies the benefit of using 50% peroxide in both bleaching processes compared to 10% peroxide. This work also reviewed the safety hazards associated with peroxide and how they differ for storage strength 50% versus diluted-strength 10% concentrations. In general, the use of 50% peroxide in mechanical pulp bleach liquors is considerably safer and provides a larger benefit than the use of 50% peroxide in chemical pulp mills.

For chemical pulp bleach plants, the benefit of operating with 50% peroxide instead of using the inherently safer 10% peroxide solution is very marginal. The boost in the reaction rate from the higher concentration is estimated at just 1.5%.

Process	Recommendation	Justification
Storage Tank	Store at about 50% concentration	Capital cost is too high vs. minimal risk as long as good controls are in place and followed
	Engineering controls – Temperature monitoring	Early warning of decomposition with enough lead time to mitigate issues
	Engineering Controls – Vents	Allow slow decomposition products to escape tank instead of gradually building pressure
	Administrative Controls – Unloading protocols	Signoff procedure as last line of defense from allowing wrong material to be unloaded into peroxide tank
Mechanical Pulp Bleaching	Use a mechanical device to make down a stabilized bleach liquor	Prevents rapid decomposition by stabilizing peroxide and dilutes high concentration peroxide to considerably lower concentrations
	Use 50% peroxide to free bleach liquor makedown system	Improves bleaching reaction by about 20% compared to using 10% peroxide. Bleach liquor is substantially diluted and stabilized prior to entering the pulp stream
Chemical Pulp Bleaching	Use 10% concentration peroxide	Very limited kinetic benefit as compared to using 50% peroxide. Enough water is present to prevent explosive decomposition reactions from occurring

I. Suggested conditions for balanced operation.

For mechanical pulp bleaching at 40% pulp consistency and 4% applied peroxide on pulp, the use of 50% peroxide resulted in about a 20% increase in reaction rate compared to the use of 10% peroxide. Mechanical pulp mills do not have the history of peroxide-based explosions that have occurred in chemical pulp peroxide bleach plants. This is due to a combination of differences in the processes: the use of a cocktail of chemicals needed to stabilize peroxide in mechanical pulp bleaching provides dilution and stabilization, and the use of high consistency refiner-like mixers that do not provide volume where a pool of peroxide is able to collect in during a process upset. **TJ**

LITERATURE CITED

1. Brogdon, B.N. and Hart, P.W., in *Bleaching of Pulp* (P.W. Hart and A.W. Rudie, Eds.) 5th Edn., TAPPI Press, Atlanta, GA, USA, 2012, Chap. 10.
2. Presley, J.R. and Hill, R.T., in *Pulp Bleaching, Principles and Practice* (C.W. Dense and D.W. Reeves, Eds.), TAPPI Press, Atlanta, 1996, Chap. 1, Sec. 5.
3. Hart, P.W. and Hsieh, J.S., *Tappi J.* 74(11): 117(1991).
4. Hoekstra, G., "Explosion rocks mill, two workers injured by blast," *Prince George Citizen*, Prince George, BC, Canada, 8 Feb. 2007.
5. Staff, "Ruptured pump may figure into Evadale mill explosion," *Beaumont Enterprise*, Beaumont, TX, USA, 18 Aug. 2001.
6. Mackenzie, J., *Chem. Eng.* 97(6): 1990(84).
7. Stora Enso, "Environmental Statement 2009," Skoghall mill, Stora Enso, Helsinki, Finland, 28 June 2010.
8. Hart, P.W. and Rudie, A.W., "Hydrogen peroxide—An environmentally friendly but dangerous bleaching chemical," *TAPPI Eng., Pulping Environ. Conf.*, TAPPI Press, Atlanta, 2007.
9. Hart, P.W., Houtman, C., Melenkevitz, G., et al., "Hydrogen peroxide (H_2O_2) safe storage and handling," TAPPI Technical Information Paper, TIP 0606-24, TAPPI, Atlanta, 2017.
10. Hart, P.W. and Rudie, A.W., *Chem. Eng. Educ.* 45(1): 15(2011).
11. Hart, P.W and Rudie, A.W., *Pulp Pap. Can.* 111(4): T60(2010).
12. Makkonen, H.P., "Decomposition of hydrogen-peroxide in dilute alkaline aqueous solutions," Ph.D. thesis, University of Washington, Seattle, WA, USA, 1971.
13. Hart, P.W., Houtman, C., and Hirth, K., *TAPPI J.* 12(7): 59(2013).
14. Schumb, W.C., Satterfield, C.N., and Wentworth, R.L., "Hydrogen peroxide," ACS Monograph No. 128, Reinhold Publishing, New York, 1955, p. 526.
15. Raines, J.C., Schmidt, J.P., Burelach, J.P., et al., *J. Therm. Anal. Calorim.* 85(1): 53(2006).
16. Solvay Chemicals, "Material safety data sheet," North American version, Solvay America, Houston, TX, USA, 9 Aug. 2013. Available [Online] http://www.h2o2.com/files/Solvay%2050%20H2O2%20SDS%20All%20Grades.pdf <8Nov2018>.

ABOUT THIS PAPER

Cite this article as: Mayeli, N. *TAPPI J.* 17(11):601(2018). https://doi.org/10.32964/TJ17.11.601

DOI: https://doi.org/10.32964/TJ17.11.601

ISSN: 0734-1415

Publisher: TAPPI Press

Copyright: ©TAPPI Press 2018

About this journal

ABOUT THE AUTHORS



Rudie



Hart

Vendors have been promoting the use of 50% peroxide in medium consistency (MC) bleach plants for many years due to the increase in reaction rate associated with higher concentration chemicals. It has been well documented that risk potential increases as the concentration of certain chemicals is increased. We decided to see what the actual risk/reward proposition was to determine if the use of 50% peroxide was truly justified.

Past research has looked at modeling the peroxide reaction and determining the conditions that result in an explosion. The impact of various industrial chemicals and operating conditions was also evaluated. This is the first study that determined the benefits of using the higher concentration peroxide and compared it with the associated elevated risk.

Deciding how to treat the differences between chemical and mechanical pulp bleaching was the most difficult aspect of this research. We reviewed and modified our approach a couple of times to make the paper concise and still convey the differences.

The impact of pulp consistency was surprising. Increasing the pulp consistency far overwhelmed the impact of chemical concentration.

By understanding the risk/reward benefit, chemical pulp mills should realize there is no justification for using 50% peroxide in an extraction stage. If they lower the concentration of peroxide to 10%, their operation will be much safer.

We have modeled the decomposition reaction using both ideal and industrial conditions. We also determined areas of safer operating conditions and described the differences between chemical and mechanical bleaching conditions. With this work, we developed the risk/reward associated with using 50% vs. 10% peroxide and have basically completely this line of research.

Rudie is assistant director, U.S. Department of Agriculture Forest Products Laboratory, Madison, WI, USA. Hart is director, Fiber Technology and Innovation, at WestRock, Richmond, VA, USA. Email Hart at peter.hart@westrock.com.

Does the kappa number method accurately reflect lignin content in nonwood pulps?

SABRINA BURKHARDT

ABSTRACT: The traditional kappa number method was developed in 1960 as a way to more quickly determine the level of lignin remaining in a completed or in-progress pulp. A significantly faster approach than the Klason lignin procedure, the kappa number method is based on the reaction of a strong oxidizing agent ($KMnO_4$) with lignin and small amounts of other organic functional groups present in the pulp, such as hexenuronic acid. While the usefulness of the kappa number for providing information about bleaching requirements and pulp properties has arguably transformed the pulp and paper industry, it has been mostly developed for kraft, sulfite, and soda wood pulps.

Nonwood species have a different chemical makeup than hardwood or softwood sources. These chemical differences can influence kappa and Klason measurements on the pulp and lead to wide ranges of error. Both original data from Sustainable Fiber Technologies' sulfur and chlorine-free pulping process and kappa and Klason data from various nonwood pulp literature sources will be presented to challenge the assumption that the kappa number accurately represents lignin content in nonwood pulps.

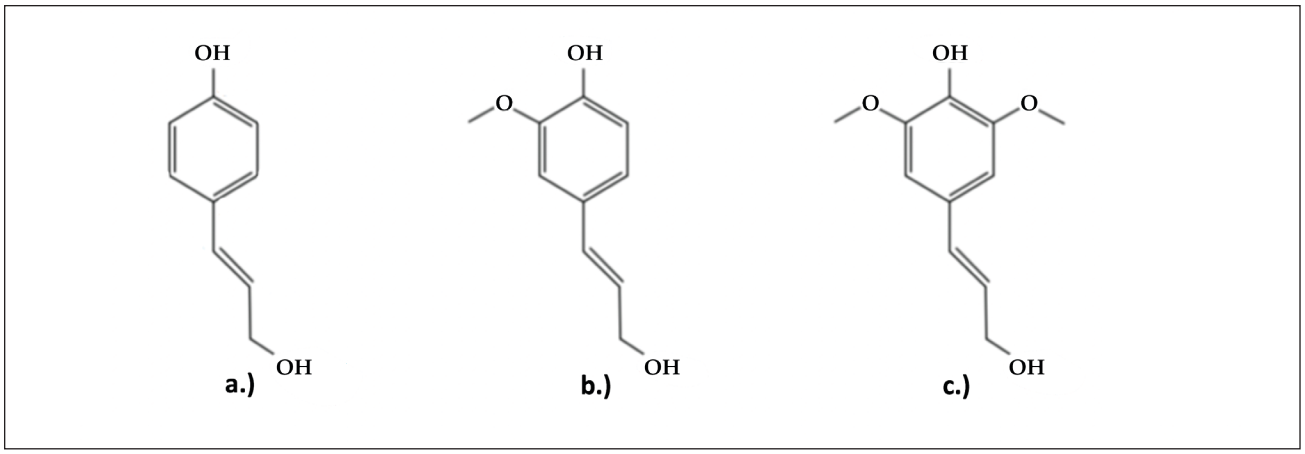
Application: The information provided in this study closely examines typical results of the analysis of lignin in nonwood pulps and encourages researchers in this area to measure both kappa number and Klason lignin separately to determine if a consistent correlation can be applied.

Lignin analysis of unbleached pulps is essential in the modern pulp mill for estimating the degree of delignification that occurs during pulping and subsequently the charge of bleaching chemicals needed to bleach the pulp. Pulp mills most often will use the kappa test to estimate lignin content, as the method is significantly faster than the Klason lignin test (a method that cannot be employed in an online measurement) (TAPPI Standard Test Method T 236-om85 "Kappa number of pulp") [1-5]. Both tests have a long history in the wood pulping industry; however, limitations and interferences have been identified with both tests when measuring lignin content.

Due to its complex structure, lignin has historically been a challenging polymer to quantify [6-9]. Lignin is a heterogeneous polymer primarily composed of three different hydroxycinnamyl alcohols (also referred to as monolignols or phenylpropane units) in varying proportions and linked by various covalent linkages [7-9]. Wood chemists have developed a relatively good understanding of the differences between hardwood and softwood lignin. For example, softwood lignin contains predominantly coniferyl alcohol monolignols (single methoxyl group) that allow for extensive crosslinking in the biopolymer matrix and are part of the reason softwoods require the most energy to pulp [7,8]. In addition to containing less overall lignin in the wood, hardwoods have significantly more sinapyl alcohol groups, which limit the number of potential bonding sites on the aromatic portion of phenylpropane unit. Higher amounts of sinapyl alcohol groups decrease the amount of carbon-to-carbon linkages between the aromatic rings of hardwood lignin (e.g., 5–5') versus softwood lignin; such linkages are one of the most recalcitrant to cleave during alkaline pulping [9]. Lignin in grasses and other nonwood species are different from wood-based lignins because they contain significant quantities of a third monolignol, *p*-coumaryl alcohol (**Fig. 1**) [10]. This change in lignin precursors is why lignin in grasses has the highest content of free phenolic groups [11], which, in combination with prevalent lignin carbohydrate ester linkages, allow nonwood lignins to dissolve readily in alkali [12]. Ferulates and *p*-coumarates also can contribute up to 10% of the overall lignin content in nonwoods [13,14], representing significant structural difference from wood lignin. These phenylpropane components are part of the structural bonding of lignin to polysaccharides [10], and most researchers consider this to be part of the lignin, which cannot be separated in a Klason analysis.

During a typical alkaline pulping process, the lignin within the biomass undergoes a series of chemical reactions, which break liable ester and ether bonds and fragment the native lignin into smaller pieces [15,16]. For wood-based lignin, delignification in alkaline pulping conditions primarily happens through cleavage of α- and β-aryl ether bonds. Other reactions occur concurrently, such as the cleavage of dibenzodioxocin structures and the recondensation of lignin fragments; however, the extent to which these reactions occur depends on the pulping conditions, which includes whether

https://doi.org/10.32964/TJ17.11.611



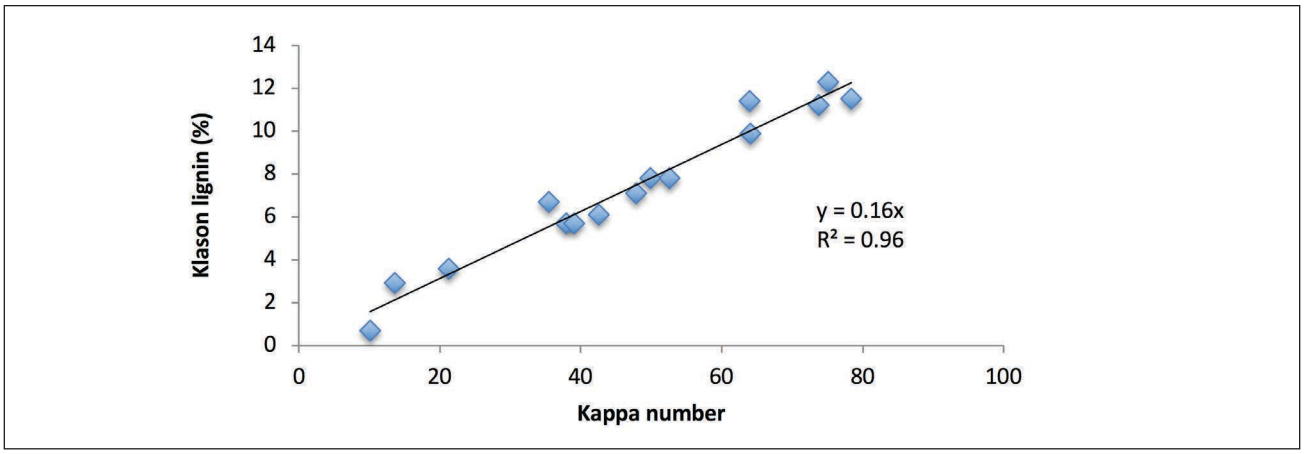
1. Primary monolignols/phenylpropane units in lignocellulosic biomass: (a) p-coumaryl alcohol, (b) coniferyl alcohol, and (c) sinapyl alcohol.

a kraft or soda pulping process was used [15]. For nonwood lignin, these reactions are less understood. Differences in monolignol content and resulting linkages increased hydroxycinnamic acid content, and changes in pulping conditions used by both newly developed and established commercial processes on grass and nonwood biomass can lead to very different results [17,18]. That being said, the analysis of the remaining lignin in the pulp is usually completed by the following methods: Klason lignin and kappa number.

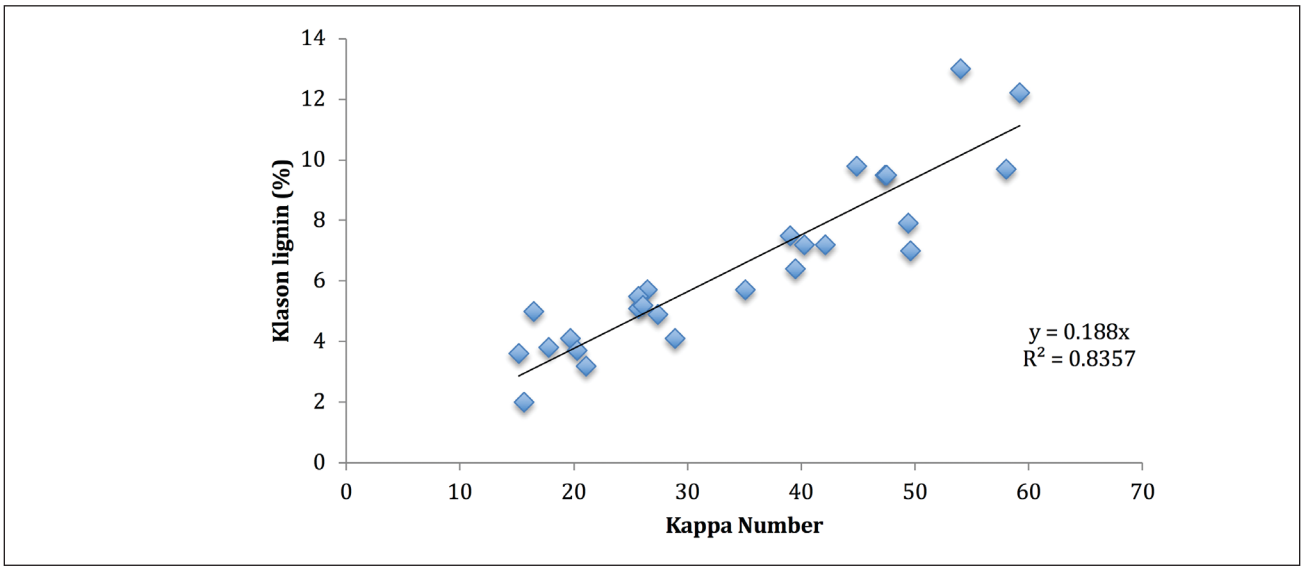
The most readily used and direct method for measuring lignin content was initially developed in the early twentieth century by Peter Johan Klason [19]. The method employs concentrated sulfuric acid solution (72%) hydrolysis of the sample at room temperature, which is followed by dilute acid hydrolysis (~3%) under boiling reflux to solubilize the carbohydrates and to precipitate the insoluble lignin that is separated, dried and weighed (TAPPI T 222 "Acid-insoluble lignin in wood and pulp"). A small portion of the lignin becomes soluble during this analysis and can be measured using UV absorption of the diluted acid hydrolysate (TAPPI UM 250 "Acid-soluble lignin in wood and pulp"). While the Klason lignin method can have interferences from extractives and other compounds [6,20], the method has been shown to be robust on many different types of biomass samples. The TAPPI T 222 Test Method has been modified by the National Renewable Energy Laboratory in their proposed Laboratory Analytical Procedures (LAPs) [21]. The NREL LAP incorporated modified extraction methods to accurately quantify the lignin in agricultural residues and other nonwood biomass [21]. The need for the use of different solvents arose because nonwood biomasses often contain different types of extractives and proteins than wood biomasses (TAPPI T 204 cm-07 "Solvent extractives of wood and pulp") [5,21]. Without the use of the appropriate solvents on the extractives contained in the biomass, these extractives would remain on the filter and be measured as "lignin" [22]. During pulping, most of the extractives become solubilized and are removed in the pulping liquor; however, some waxes present in woods and nonwoods may remain in the pulp after alkaline pulping. Ethanol-benzene (TAPPI 204 cm-07) or other organic solvents are typically used to extract high yield pulps before conducting the acid hydrolysis procedure for this reason [5]. The main drawback of the Klason method of determining lignin content is it is a very time-consuming procedure with the solvent extraction to remove extractives and with the complete acid hydrolysis of carbohydrates of the sample.

Indirect lignin analytical techniques were developed in parallel to the Klason method. The use of oxidation to measure lignin dates to as early as the 1850s [19]. While oxidative methods have struggled with selectiveness [6], by the 1950s the kappa number method had evolved to become a reliable indicator of lignin in wood-derived pulps [1-5]. In hardwood and softwood kraft pulps, there are relatively consistent linear correlations between kappa number and Klason lignin content. The TAPPI method (T 236 cm-85) and the majority of the literature will report the correlation as Klason lignin = 0.15*kappa [4,5,23-25]. However, as reported in the literature, the correlations do change as the pulp undergoes bleaching. Brogdon [24] reported that as the amount of oxidized lignin structures in the bleached residual lignin increases, namely quinones that consume less permanganate, then the Klason lignin-to-kappa correlation will shift from 0.15 to 0.18. The kappa number method is also prone to interferences from hexenuronic acids (HexA) and other oxidizable structures in the pulp [25]. The presence of these structures will contribute to the measured kappa number and will contribute to overall bleach consumption (e.g., chlorine dioxide). Hexenuronic acids are formed during alkaline pulping from the 4-*O*-methylglucuronic acid groups, which are attached to xylans of the hemicelluloses. Hexenuronic acids are typically found in significant amounts in alkaline hardwood pulps. The precursors to HexA are also found in the xylans of nonwoods [26].

The information provided in this literature review has led the author to the following question: when using methods designed for wood-based pulps, can we assume these methods will have the same level of sensitivity and reliability on a



2. Barley straw soda pulp (data from [27]).



3. Tagasaste soda pulp (data from [28]).

material with notably different initial chemical makeup? This paper examines the literature data of both the Klason lignin and kappa number on nonwood pulps at a wide range of residual lignin levels and across a variety of species. Results have been compiled from both the literature [27-36] and execution of the standard TAPPI test methods on a pulp from a proprietary pulping process (i.e., Phoenix Process) [37]. The varied pulp samples compared in this paper are all derived from nonwoods and produced via alkaline pulping processes.

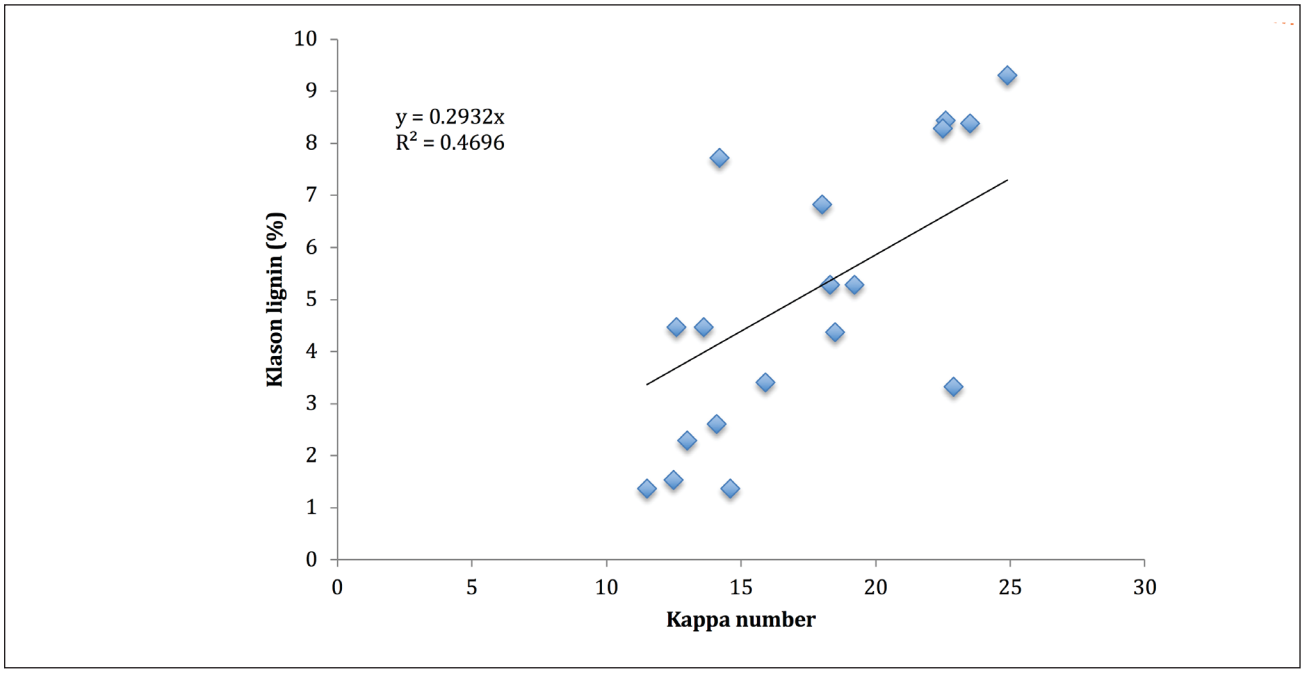
RESULTS AND DISCUSSION

In the nonwoods alkaline pulping literature, most investigators do not report both acid insoluble lignin and kappa number of the pulp. Many authors report the kappa number and state their expectation is that the lignin will follow a linear correlation (i.e., 0.15*kappa [1,5,6]). What literature that is available that reports both kappa number and Klason lignin data indicates different proportionality constants, or in some cases, lack of correlation. **Figure 2** graphs the soda pulping data of barley straw from the Vargas et al. study [27]. There is a good linear correlation between kappa number and Klason lignin content, with a proportionality factor of 0.16.

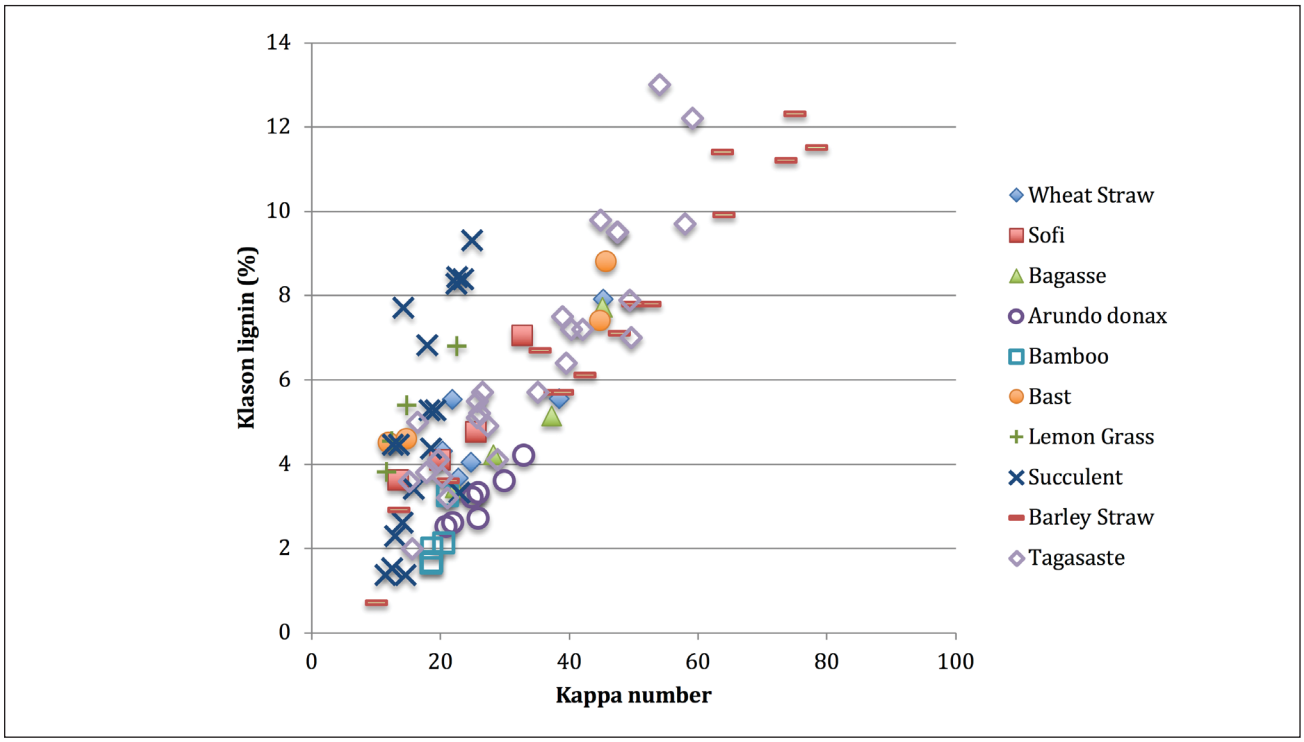
Data from Lopez et al. [28], where the authors pulped tagasaste residues at varying soda and soda-AQ conditions, were also analyzed (**Fig. 3**). The correlation is not as high (R^2 value of 0.8); however, the proportionality constant of kappa number to Klason lignin content for the nonwood tagasaste seems higher than that reported in the literature for wood-based species. For the alkaline pulp made from tagasate, the data suggest that Klason lignin would be equal to 0.19*kappa.

Data from the Andres et al. [29] study was analyzed in **Fig. 4**. These authors examined the pulping of a succulent nonwood (from the aloe family) using soda-AQ at varied temperatures, alkalinity, and time. Analysis of this data indicated a poor correlation (R^2 of 0.46) between kappa number and lignin content with a proportionality factor of 0.29.

Analysis of various literature data for nonwood chemical pulps [27-36] indicated some interesting results (**Fig. 5**).

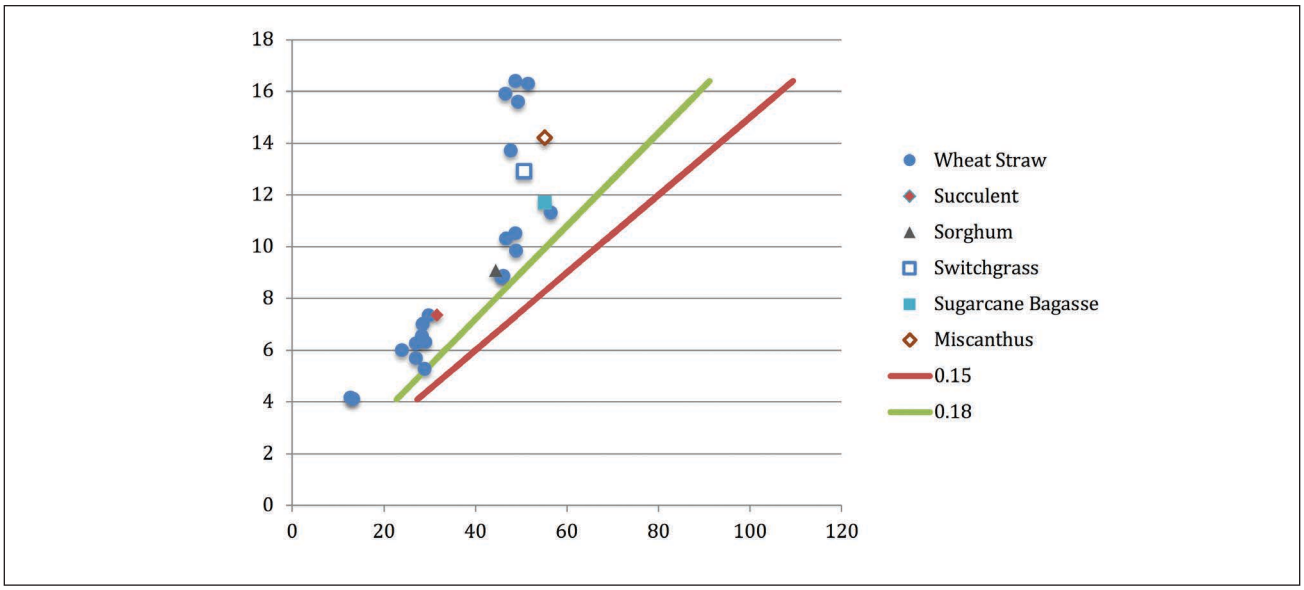


4. Succulent soda-anthraquinone (AQ) pulp (data from [29]).



5. Plot of Klason lignin versus kappa number for various nonwood chemical pulps produced by alkaline pulping processes (data from various research reports [27-36]).

These pulps were made from a variety of nonwood species that ranged from bagasse [33,35] to barley and wheat straws [27,30,31], to bamboo [32], to Arundo donax (giant reed) [34], and to other species [28,29,36]. All were produced via some derivative of an alkaline pulping process, such as kraft, soda, or soda-AQ. Including all of the data, the correlation between kappa and Klason is relatively low (R^2 of 0.55 for Klason lignin = 0.185 x kappa no.). This is not completely unexpected, as variability is expected across different labs, species, and pulping types. Lemon grass, sofi, and succulent pulps appear to particularly have a higher proportionality constant. In general, nonwood pulps appear to have a higher range of vari-



6. Kappa numbers at measured %Klason lignin values for pulps produced by proprietary pulping process (data from [37]).

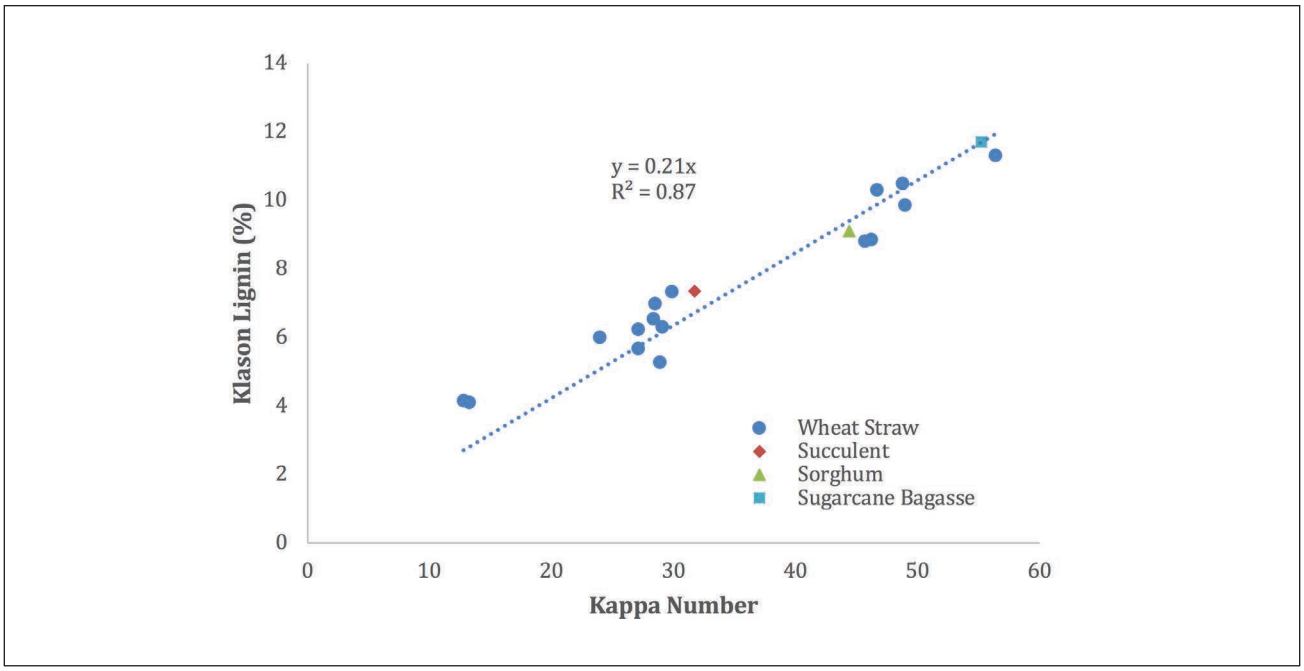
ability in comparison to wood. For example a softwood kraft pulp with 5.2% lignin should have a kappa number of 34.7 when using a 0.15 proportionality factor; however, the nonwood pulp data exhibit a wide range of kappa numbers, from 18 to 38, at ~5.2% Klason lignin content.

As noted in the review, the kappa number test is an indirect measurement method for lignin; it relies on the selective oxidation of the unsaturated carbon-carbon bonds in lignin and the consistent permanganate consumption by the unbleached residual lignin [24,25]. If these two parameters are not met and/or there are interfering non-lignin substances unaccounted (e.g., HexA [25]), then an accurate proportionality constant between kappa number and Klason lignin will not be possible.

Figure 6 plots the unpublished data from nonwood pulping studies performed by Sustainable Fiber Technologies (SFT; Renton, WA, USA) utilizing a proprietary process (i.e., Phoenix process) [37]. The pulps contained 4%–16% Klason lignin and were made from nonwood species, such as wheat straw, bagasse, miscanthus, and others. The chart also includes linear plots of kappa to Klason proportionality factors of 0.15 and 0.18. Using the data points available for all species, the R^2 of the linear correlation is around 0.7. The proportionality factor is about 0.25. The most intriguing part of this graph is what happens to Klason-kappa relationship when the Klason lignin in the pulp is above 10%; the kappa numbers of these pulps from the proprietary pulping process were between 40 and 60, even when the Klason lignin content was between 10% and 16%. Below about 10% or 12% lignin, the data are significantly more linear (**Fig. 7**). The kappa-lignin proportionality factor was higher (i.e., 0.21) than that of kraft pulps of wood species and other alkaline pulps from nonwood species.

Typically, wood-based pulps also have a larger range of error in the kappa number measurement at lignin contents above 12% (~90 kappa) [5]. The difference is that with wood-derived chemical pulps the kappa number method typically is reliable in the range needed for controlling pulp mill unit operations (e.g., pulping to target kappa number to gage bleach plant chemical demand). In SFT's process, the linear correlation appears to deteriorate above lignin contents of 10%–12%, and many of the species used will unfortunately fall above this range during processing. Therefore, the kappa test is not a practical or accurate tool to be used for process control of the proprietary pulping process when targeting an actual lignin content level.

To account for more variables and for a more accurate measure of kappa and lignin content, HexA and acid soluble lignin (ASL) were also measured on the unbleached pulp samples made by the proprietary pulping process. The HexA content of the pulps varied from 0 to 16.5 μmol/g pulp, which contributed 0 to 1.4 kappa units to the measured kappa number [25]. After accounting for these values in the data shown in Fig. 6, the impact was negligible on the R^2 and proportionality factor (not shown). ASL levels ranged from 1%–1.8% for the unbleached pulp samples, which is the typical range for wood pulps; these values were not included in the lignin values shown in Figs. 5 and 6. The Klason-to-kappa ratio used in the TAPPI method (TAPPI T 236) [4,5] and published widely *does not include* acid soluble lignin, as this can change the ratio. While a helpful characteristic to measure, the acid soluble lignin method can be affected by hydrolyzed carbohydrate compounds, such as 5-hydroxymethylfurfural, furfural, 2-furoic and 5-formyl-2-furoic acid products [5,38]. These compounds have moderate to strong UV/Vis absorbencies around 200 to 205 nm range, which is where the ASL is measured in solution. Any acid-soluble component that absorbs in this range and is not lignin can cause interferences and therefore ASL is infrequently included when comparing kappa number to Klason lignin content for this reason [49].



7. Kappa numbers at measured Klason lignin values for pulps produced by proprietary pulping process (data from [37]) that had ≤12% Klason lignin.

One other component known to affect measured Klason lignin values is ash. The literature sources used in this study are both unknown and known to both contain and be absent of ash in their Klason acid insoluble lignin. As an example of this, the barley straw data reported in Fig. 2 would have a proportionality factor of 0.18 as opposed to 0.16 if ash had not been corrected [27]. That said, the regression was still very linear (R^2 of 0.96). The SFT process pulps examined in this study, while extracted prior to acid hydrolysis, were not corrected for inorganic ash, as this has a negligible influence on wood-derived pulps and was not conducted at the testing laboratory that performed this test. Not correcting for ash for the nonwood pulps may account for part of the higher proportionality constant and for some of the variability seen in the literature data; however, it would not account for all of the differences entirely. Ash contents in nonwood-derived pulps should routinely be measured and corrected in the Klason lignin measurements since ash levels are appreciably higher in nonwood biomasses when compared to wood species.

CONCLUSION

The kappa number and Klason lignin tests, while well established in the pulping industry, were developed for pulps produced from wood species. While species, laboratories, and pulping conditions all have notable effects on the measured values obtained by these methods, it has been shown that the typical kappa-to-Klason lignin conversion factor of 0.15 is an unlikely fit for nonwood pulps. Relying on the kappa number method proportionality constant to predict Klason lignin in nonwood pulps can lead to inaccurate assumptions. As reported in this work, proportionality factors for converting kappa-to-Klason lignin can range from about 0.16 to 0.30, if a strong correlation can be measured. It is strongly encouraged that future researchers and commercial operations using nonwoods for chemical pulps separately test both Klason lignin and kappa to determine if a consistent proportionality factor exists and is reliable. If a linear regression can be fitted to the nonwood pulp data, then the proportionality factor will likely need to be tailored for each individual process, and potentially across different species, to have a reliable method to convert from kappa numbers to Klason lignin content. **TJ**

ACKNOWLEDGEMENTS

The author would like to thank Econotech Services (Delta, BC, Canada) for completing the laboratory testing on the SFT process samples, as well as all members of the SFT team for their valuable feedback and technical help throughout the study.

LITERATURE CITED

1. Tasman, J.E. and Berzins, V., *Tappi* 40(9): 691(1957).
2. Tasman, J.E. and Berzins, V., *Tappi* 40(9): 695(1957).
3. Tasman, J.E. and Berzins, V., *Tappi* 40(9) :699(1957).
4. Tasman, J.E., *Pulp Pap. Mag. Can.* 58(10): 231(1959).
5. Dence, C.W., in *Methods in Lignin Chemistry* (S.Y. Lina and C.W. Dence, Eds.), Springer-Verlag, Berlin, 1992, pp. 33-61.
6. Hatfield, R. and Fukushima, R.S., *Crop Sci.* 45(3): 832(2005).
7. Biermann, C.J., *Handbook of Pulping and Papermaking*, 2nd edn., Academic Press, San Diego, CA, USA, 1996, pp. 36-37.
8. Sjostrom, E., *Wood Chemistry: Fundamentals and Applications*, 2nd Edn., Academic Press, San Diego, 1993, pp. 71-89.

9. Heitner, C., Dimmel, D., and Schmidt, J.A., *Lignin and Lignans: Advances in Chemistry*, CRC Press, Boca Raton, FL, USA, 2010, pp. 1-48.
10. Sun, R., *Cereal Straw as a Resource for Sustainable Biomaterials and Biofuels: Chemistry, Extractives, Lignins, Hemicelluloses and Cellulose*, Elsevier, Amsterdam, Netherlands, 2010, pp. 169-207.
11. LaPierre, C., Jouin, D. and Monties, B., *Phytochem.* 28: 1401(1989).
12. Sipponen, M., "Effect of lignin structure on enzymatic hydrolysis of plant residues," Doctoral dissertation, Aalto University, Helsinki, Finland, 2015.
13. Li, M., Foster, C., Kelkar, S., et al., *Biotechnol. Biofuels* 5: 38(2012).
14. Sun, R., Sun, X.F., Wang, S.Q., et al., *Ind. Crops Prod.* 15: 179(2002).
15. Lora, J., in *Monomers, Polymers and Composites from Renewable Resources* (M. Belgacem and A. Gandini, Eds.), Elsevier Science, Amsterdam, 2008, pp. 225-241.
16. Gierer, J., *Wood Sci. Technol.* 19: 289(1985).
17. Yang, H., Zheng, X., Yao, L., et al., *BioResources* 9(1): 176(2014).
18. Calvo-Flores, F.G. and Dobado, J.A., *ChemSusChem* 3: 1227(2010).
19. Phillips, M., *Determination of Lignin*, Reinhold Publishing, New York, 1944.
20. Sherrard, E.C. and Harris, E.E., *Ind. Eng. Chem.* 24(1): 103(1932).
21. Sluiter, J. and Sluiter, A., *Summative Mass Closure - Laboratory Analytical Procedure (LAP): Review and Integration*, Technical Report NREL/TP-510-48087, National Renewable Energy Laboratory (NREL), U.S. Department of Energy, Golden, CO, USA, 2011. Available [Online] http://www.nrel.gov/docs/gen/fy11/48087.pdf <12Nov2018>.
22. Burkhardt, S., Kumar, L., Chandra, R., et al., *Biotechnol. Biofuels* 6: 90(2013).
23. Prinsen, P., Rencoret, A.G., Liitia, T., et al., *Ind. Eng. Chem. Res.* 52: 15702(2013).
24. Brogdon, B.N., *J. Pulp Pap. Sci.* 27(11): 364(2001).
25. Li, J. and Gellerstedt, G., *Nord. Pulp Pap. Res. J.* 13(2): 153(1998).
26. Wedin, H., Antonsson, S., Ragnar, M., et al., *BioResources* 7(4): 5527(2012).
27. Vargas, F., Gonzalez, Z., Rojas, O., et al., *BioResources* 10(2): 3682(2015).
28. Lopez, F., Alfaro, A., Garcia, M.M., et al., *Chem. Eng. Res. Des.* 82(A8): 1029(2004).
29. Andres, M., Sequeiros, A., Sanchez, R., et al., *Environ. Eng. Manage. J.* 14(11): 2479(2015).
30. Tozluoglu, A., Ozyurek, O., Copur, Y., et al., *BioResources* 10(4): 7834(2015).
31. Singh, S., Dutt, D., and Tyagi, C.H., *BioResources* 6(1): 154(2011).
32. Du, Y., Qin, C., Huang, X., et al., *BioResources* 10(4): 7372(2015).
33. Lin, L., Chang, F., Ko, C., et al., *BioResources* 10(2): 3625(2015).
34. Shatolov, A.A. and Pereira, H., *BioResources* 1(1): 45(2006).
35. Agnihotri, S., Dutt, D., and Tyagi, C.H., *BioResources* 5(2): 1197(2010).
36. Kaur, H., Dutt, D., and Tyagi, C.H., *BioResources* 6(1): 103(2010).
37. Burkhardt, S.J., unpublished data (Sustainable Fiber Technologies), June 2017.
38. Kaar, W.E. and Brink, D.L., *J. Wood. Chem. Technol.* 11(4): 465(1991).
39. Shin, S., Schroeder, L.R., and Lai, Y., *J. Wood. Chem. Technol.* 24(2), 139(2005).

ABOUT THIS PAPER

Cite this article as: Burkhardt, S. *TAPPI J.* 17(11):611(2018).

https://doi.org/10.32964/TJ17.11.611

DOI: https://doi.org/10.32964/TJ17.11.611

ISSN: 0734-1415

Publisher: TAPPI Press

Copyright: ©TAPPI Press 2018

About this journal

ABOUT THE AUTHORS

With Columbia Pulp in Washington State and other mills using the Phoenix Process coming online in the near future, there was a need to understand how lig-nin measurements in pulp are affected by the raw material. This paper builds on past work that chal-lenges the assumptions that standard test methods will have the same levels of accuracy and precision across all biomass sources.

The most difficult aspect of this research was par-ing through all of the data available for pulping non-wood biomass and identifying the studies that have measured both Klason lignin and kappa number sep-arately. What we discovered is that there is a not a "one size fits all" proportionality constant for kappa-to-Klason conversion with nonwood pulps. It was surprising that the overwhelming majority of non-wood pulping studies only measure kappa number and use the 0.13 or 0.15 conversion factor. This is somewhat troubling now that we understand that few species will follow that curve.



Burkhardt

This information would be particularly helpful for nonwood mills coming online, as they will want to individually work with vendors and labs to verify if the kappa number will be a reliable indicator for their process control. While more data from our process would be helpful, in the future it would be interesting to work with an inline kappa analyzer team to see if reliable mea-surements can be made in the Phoenix Process that can accu-rately correlate to overall lignin content.

Burkhardt is director of Chemical Development at Sustainable Fiber Technologies, Renton, WA, USA. Email Burkhardt at Sabrina@sustainablefibertechnologies.com.

Using multistage models to evaluate how pulp washing after the first extraction stage impacts elemental chlorine-free bleach demand

BRIAN N. BROGDON AND LUCIAN A. LUCIA

ABSTRACT: Steady-state models were constructed to predict the response of a southern U.S. softwood brownstock to three- and five-stage elemental chlorine-free (ECF) bleach sequences. The models provided insight into how typical (EO) washing efficiencies from a vacuum drum unit affected pulp brightening and total chlorine dioxide consumption. When (EO) carryover was between 15% and 30%, the chlorine dioxide needed to reach target brightness increased by 8% to 15% for the $D_0(EO)D_1(EP)D_2$ sequence (89% ISO) and by 15% to 23% for the $D_0(EO)D_1$ sequence (86% ISO) versus perfect washing. Use of (EO) filtrate as D_0 shower water, such as in split-flow countercurrent washing, caused the bleach uptake to increase by 1.5 to 3.0 kg chlorine dioxide (ClO_2)/ton pulp when compared to using cleaner D_0 shower water sources. The ClO_2 consumed by 15% to 30% (EO) washer carryover is comparable to that consumed by typical carryover levels from brownstock washing (~10 kg Na_2SO_4/ton pulp). High (EO) carryover made ECF bleaching to higher brightness targets more difficult.

Application: Multistage models are employed to estimate how typical levels of extraction washer carryover, as well as how extraction washer filtrate reuse in countercurrent washing, affects chlorine dioxide consumption and brightness development of a softwood kraft pulp when bleached with ECF sequences. These models could be adapted to simulate mill data, used to optimize bleaching operations, and used in process control strategies.

During kraft pulp bleaching, an appreciable level of dissolved organics and spent chemicals may be carried over from one stage into the next stage, which negatively affects overall bleach sequence performance [1-3]. Hence, interstage washing is a vital component of a bleaching stage that assures low-cost and consistent pulp bleaching. Elemental chlorine-free (ECF) technology is the dominant method used for bleached pulp production, mainly due to its ability to selectively brighten while preserving fiber strength and minimizing pulp yield losses. Several PAPTAC surveys [4-8] have been conducted to benchmark and to track best practices for ECF bleaching of softwood kraft pulps, some of which have specifically examined interstage pulp washing.

Among the interstage washing operations used in the bleach plant, it has been reported by PAPTAC surveys [7,8] that the majority of Canadian mills utilize vacuum drum units. Such washers are commonly employed in North American bleach plants, and operate with various countercurrent filtrate schemes as shower water. It is not uncommon for washer shower water to be partially supplemented with fresh hot water or white water. Drum washers often operate at 10% to 70% over their original design capacity [7]. These washing units typically remove 70% to 85% of the dissolved materials contained in the spent liquor leaving the bleaching stage [1].

Examination of the surveys revealed that the mills that had high relative bleach consumption tended to use higher D_1 multiple charges than their counterparts with relatively low bleach consumption (about 0.35% vs. 0.22% chlorine dioxide (ClO_2)/post-extraction kappa no.) [5]. Generally, D_1 brightening becomes less efficient when the D_1 multiple is higher than ~0.25 [4-6,8-10]. The analysis also noted that the high bleach usage mills added acid to the extracted pulp to control pH in the D_1 stage. A follow-up survey [8] revealed that extraction stage washers operated with a wash ratio (defined as the amount of washer shower water applied divided by the water in the discharged pulp mat) of 0.5 to 1.5. Almost two-thirds of the respondents use a wash ratio below 1.2. These observations suggest that there is appreciable carryover from extraction entering the D_1 stage, which is partially contributing to the elevated bleach consumption at the high bleach usage mills [8].

The bleaching literature contains numerous reports [11-18] on how interstage washing affects overall bleaching operations of chlorine-based bleach sequences. These earlier studies from the 1970s and 1980s focused on how to reduce the amount of fresh water consumed, waste effluent discharged, and energy consumed. However, there have been relatively few investigations that specifically examine how interstage washing affects bleach consumption for ECF sequences

https://doi.org/10.32964/TJ17.11.621

[19,20]. It is generally assumed by the industry that the conclusions drawn from the earlier literature with chlorine-based bleach sequences are directly applicable to today's ECF bleaching technology.

Yankowski [11] examined how interstage washing efficiencies affected the $CE_1D_1E_2D_2$ bleaching of a softwood pulp. The study calculated washing efficiencies based on dissolved solids measurements. It was observed that poor or no pulp washing after the D_1 stage and/or the E_2 stage had a minor effect on the overall bleach performance. When the E_1 washing decreased from 90% to 75%, the author observed that the D_1 brightness decreased by 3 points for a fixed D_1 bleach charge. MacDonald [12] quantified how E_1 carryover affected hypochlorite consumption in the $(CD)E_1H$ portion of the (CD) $E_1HD_1E_2D_2$ sequence. The washed E_1 pulp entering the H stage contained 1.5 to 4.4 kg dissolved lignin/ton pulp when the lignin was expressed as equivalent sodium. When the E_1 carryover was reduced from the high to the low value, the amount of hypochlorite needed decreased by 8.2 kg NaOCl/ton pulp.

Histed and co-workers [1,2,13-17] published numerous studies in the 1970s examining how direct countercurrent recycling of washer filtrates affected the bleaching of Canadian softwood kraft pulps. In one study [13], a 30-kappa brownstock was bleached to 92% Elrephro (about 89.5% ISO) using the $(D+C)E_1D_1E_2D_2$ sequence that employed 70% chlorine dioxide substitution. It was noted that the D_1 brightness decreased by almost 8 points and that the D_2 brightness decreased by 2 points when compared to no filtrate recycle. This loss was recovered when the D_1 charge was increased from 1.45% to 1.75% ClO_2. In a similar study [15], a 24-kappa brownstock was bleached with the same sequence. When filtrate recycle was employed, it was necessary to increase the (D+C) kappa factor from 0.21 to 0.24 and boost the D_1 charge from 1.42% to 1.52% ClO_2 to reach the brightness target. In a third study [17], Histed and co-workers examined how different interstage wash ratio values affected bleach consumption of the $(C+D)E_1HD_1E_2D_2$ sequence. There was little impact on hypochlorite or chlorine dioxide consumption when the wash ratios at H, D_1, and E_2 washers were decreased from 1.3 to 0.5. Lowering the wash ratio at the E_1 washer from 1.3 to 1.0 considerably increased the hypochlorite uptake in the H stage by ~10.6 kg NaOCl/ton pulp.

Waritovaara [18] explored how different filtrate recycle schemes affected the bleach consumption of a 28-kappa pine kraft pulp with the $(D/C)E_1D_1E_2D_2$ sequence. A 30% chlorine dioxide substitution level was used in the (D/C) while a wash ratio of ~1.55 was applied to each washer. The washed pulp was discharged at ~15% consistency. Direct countercurrent washing required 11% more bleach to reach 89% ISO brightness vs. not washing the pulp with recycled filtrates. Other countercurrent washing schemes, such as jump-stage countercurrent or split-flow countercurrent, had similar bleach consumptions as open interstage washing. The high wash ratio and discharge consistency ensured that there was low E_1 carryover. The higher oxidant chemical usage with direct countercurrent washing was attributed to E_1 filtrate breaking through the pulp mat at the (D/C) washer, which mixed with (D/C) seal tank filtrate and carried backwards to the brownstock dilution water of the (D/C) stage [1-3,16]. The E_1 dissolved organics consume a portion of the oxidants applied in (D/C) stage similar to black liquor carryover.

Some contemporary studies [19,20] examined direct countercurrent washing with the $D_0(EOP)D_1$ sequence. These researchers observed an increase in chlorine dioxide demand from 0% to 0.3% (on pulp) when using (EOP) filtrate to wash the D_0 pulp versus using D_1 filtrate. In another recent report, Frigieri et al. [21] examined different interstage wash ratios of 1 to 0 with a jump-stage countercurrent recycle with the $D_0(EP)D_1P$ sequence. The authors disclosed that final brightness of the oxygen-delignified eucalypt pulp declined from 92% ISO to 88% ISO when the wash ratio decreased from 1 to 0.3 while the oxidant charges in each stage were invariant.

It is apparent that first extraction stage carryover, apart from black liquor or post-oxygen carryover, can appreciably contribute to the oxidant bleach load when using chlorine-based bleach sequences, and, in particular, when extraction filtrate is reused as the shower water in the preceding washer. Nevertheless, relatively few publications have re-examined how the first extraction washer efficiency affects total bleach usage with ECF-based bleach sequence. Furthermore, most mills do not monitor interstage carryover [7,9,10,22]. It is difficult to quantify bleach washer efficiency using a simple and quick test method such as is done with brownstock washing [22]. Recently, efforts in this area [8-10,23] have related extraction carryover into the D_1 stage by using the kappa number test. The kappa number contributions from well-washed extracted pulps and their dissolved organic carryover can be correlated to the brightening response in the D_1 stage [23].

The current investigation reports the findings obtained from the spreadsheet modeling of ECF bleach sequences to determine how first extraction stage washing efficiency and filtrate reuse affects total chlorine dioxide consumption for ECF sequences. The models can predict the bleaching response after $D_0(EO)$, D_1 and D_2, and have been previously discussed [23-25]. The $D_0(EO)$ and D_1 units have the capacity to consider washer carryover entering that stage. The inputs and outputs for each unit (e.g., kappa number and/or brightness of the pulp) are coupled to each other using an analogous approach that has been reported by earlier investigators [26,27].

METHODOLOGY

Steady-state simulations of $D_0(EO)D_1(EP)D_2$ and $D_0(EO)D_1$ sequences were conducted using a hypothetical southern U.S. softwood brownstock that had a kappa number of 24 and a brightness of 23% ISO. Data from the Basta and co-workers study [28], as well as data analysis from another investigation [29], were used to calibrate the equation parameters for $D_0(EO)$ delignification, and D_1 brightening and D_2 brightening models. General conditions examined are presented in

Stage Conditions	D_0	(EO)	D_1	(EP)	D_2
Consistency, %	3.5	10	10	10	10
Temperature, °C	50	70 or 90	70	70	70
Time, min	30 – 60	60	variable	60	variable
ClO_2, % on pulp	1.00 – 3.10 (0.11 to 0.34 KF)	–	0.30 – 1.75	–	0.25
O_2, % on pulp	–	0.50 (at 0.22 MPa)	–	–	–
H_2O_2, % on pulp	–	–	–	0.20	–
NaOH, % on pulp	–	0.4·(KF)·(Kappa no.)	variable	0.50	variable
H_2SO_4, % on pulp	0.6%	–	variable	–	variable
End pH	~3	~10.5 to 11.0	~3	~11	~4

ClO_2 = chlorine dioxide; O_2 = oxygen; H_2O_2 = hydrogen peroxide; NaOH = sodium hydroxide; H_2SO_4 = sulfuric acid; and KF = kappa factor.

I. Conditions used in the model simulations of three- and five-stage elemental chlorine-free (ECF) bleach sequences for a 24-kappa softwood brownstock to reach 84% to 89% ISO and 85% to 90% ISO, respectively.

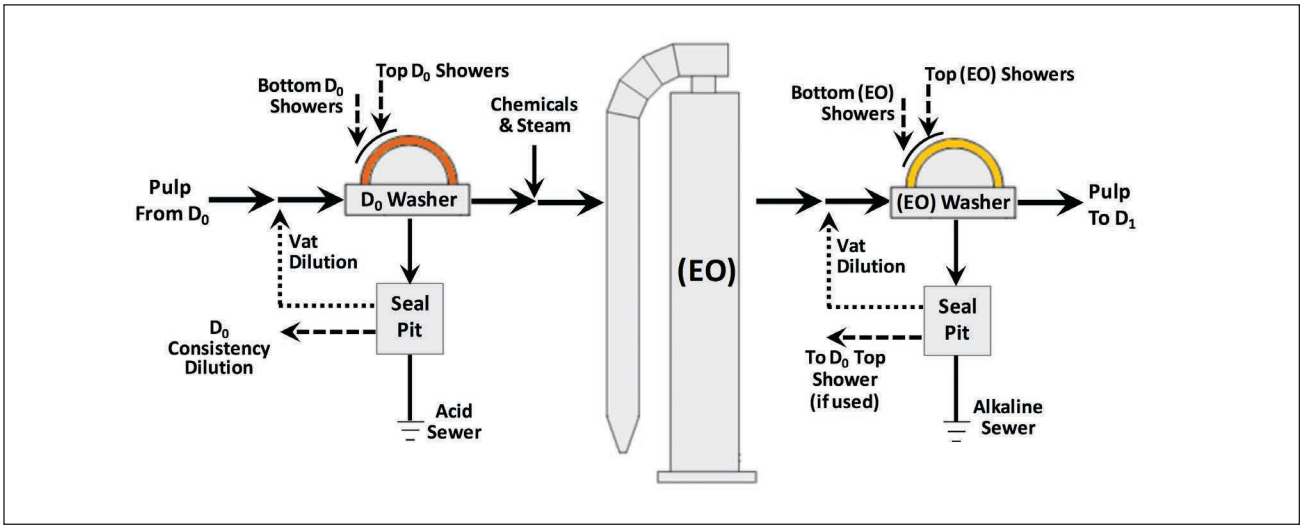
Stage	Equation	No.	Comments
D_0	D_0 Kappa =20.6-5.14·x_0	(1)	Based on Basta et al. data [28]; x_0 is % ClO_2 on pulp in D_0
(EO)	(EO) Kappa = $\frac{24}{\left(\frac{x_0 - 0.03 \cdot C_{BSW}}{2A} + 1\right)^2}$	(2)	CBSW is brownstock washer carryover (kg Na_2SO_4/ton pulp); A = 0.820 (70°C) or 0.588 (90°C)
	(EO) Brightness = B_{EO} =63.6-3.28·((EO) Kappa)	(3)	Based on Basta et al. data [28]
D_1	D_1 Brightness = B_{D1} = 92- $\frac{\beta_1}{x_1 + \frac{\beta_1}{92 - B_{EO}}}$	(4)	x_1 is % ClO_2 on pulp in D_1;
	β_1 = 4.54·(Washed Kappa)-7.43	(5)	
	Washed Kappa = (EO) Pulp Kappa + (EO) Carryover Kappa	(6)	(EO) Carryover Kappa is expressed as kappa units (on pulp) [23]
(EP)	(EP) Brightness = B_{EP} = 0.765·B_{D1} +21.8	(7)	Based on Basta et al. data [28] for a fixed 0.20% peroxide charge
D_2	D_2 Brightness = B_{D2}= 92- $\frac{\beta_2}{x_2 + \frac{\beta_2}{92 - B_{EP}}}$	(8)	x_2 is % ClO_2 on pulp in D_2;
	β_2 =0.250·B_{EP} + 23.0	(9)	Based on D_2 model [25] tuned to Basta et al. data [28]

II. Steady-state equations for the individual stages of the ECF sequences for bleaching 24-kappa brownstock.

Table I. The conditions from the laboratory study [29] are relatively consistent with current bleaching practices with North American bleach plants [4-6].

The empirical expressions for each of the bleach stages (Eqs. 1 to 9) are listed in Table II. Several relationships, such as Eqs. 1, 3 and 7, are derived from laboratory data [28]. It is presumed that the asymptotic brightness for the softwood kraft brownstock is around 92% ISO, which is based on the limiting light absorption and light scattering coefficients [25]. Unless otherwise specified, simulations were run assuming that there was negligible brownstock washer carryover into D_0 ($C_{BSW} \approx 0$ kg Na_2SO_4/ton pulp). The D_0(EO)D_1(EP)D_2 sequence utilized a milder (EO) stage at 70°C, whereas the D_0(EO)D_1 sequence used an aggressive (EO) stage at 90°C to attain 85% to 89% ISO more easily with fewer bleaching stages.

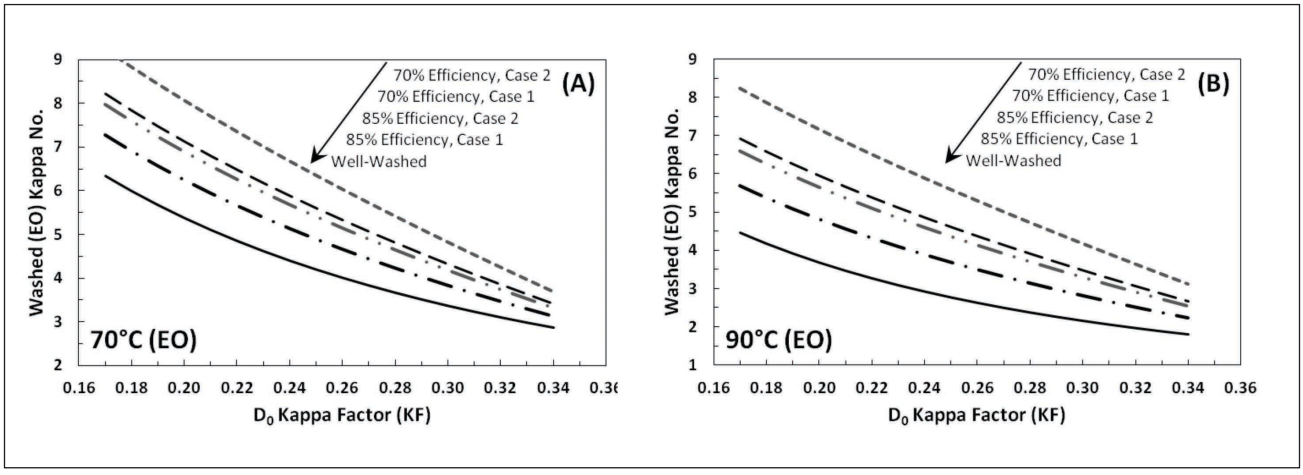
Extraction carryover was expressed in terms of kappa units on pulp [23]. This quantity is represented as the difference between the kappa number of the discharged pulp from the (EO) washer, which included its filtrate, and the kappa number of the well-washed (EO) pulp without filtrate [8,9,23].



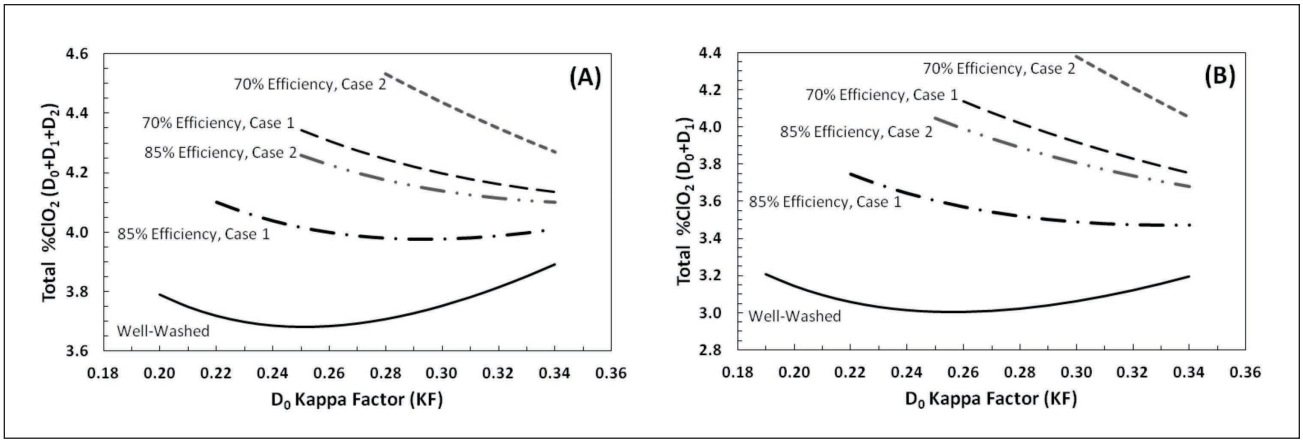
1. General water and pulp stream flows of the D_0 washer, (EO) stage, and (EO) washer.

Washing efficiencies of 85% to 70% with the (EO) washer were examined and compared to a well-washed pulp with no carryover (i.e., Control). These efficiency levels were chosen to be a representative range for vacuum drum washers [30-32], which correspond to 15% to 30% carryover, respectively. Extraction carryover was calculated from the total amount of dissolved (EO) material, expressed as kappa units (on pulp), exiting the stage but prior to washer vat dilution. The total is determined from what is generated in the (EO) stage (i.e., Eq. 1 minus Eq. 2), plus what is recycled back from the (EO) seal tank, if this filtrate is used as shower water at the D_0 washer [3]. For the simulations where (EO) filtrate is used, only one-half of the total D_0 shower water was supplemented by this source. In this split-flow arraignment, the (EO) filtrate was applied at the top D_0 shower bars to ensure that none of it broke through the pulp mat and entered into the D_0 seal tank [1-3,17]. It was assumed that any other recycled filtrates used as shower water, such as from D_1, (EP) and D_2 seal tanks, which might be used at D_0 and (EO) washers, contained dissolved substances that do not contribute to ClO_2 consumption (i.e., 0 kappa units) [1,11,17]. In addition, it was further presumed that nominal D_0 washer carryover has an insignificant effect on the total ClO_2 bleach load [33-35]. Simulations were performed using a 1.16 wash ratio, a 1.5% washer vat consistency, and a 12% discharged mat consistency.

The equations listed in Table II were run from a spreadsheet software program (Excel, version 2016; Microsoft Corp., Redmond, WA, USA), along with the material balances for the washers around the (EO) stage [3]. A solver routine in the software was used to minimize the total overall chlorine dioxide charge for a targeted brightness value and a given (EO) washer efficiency. An iterative calculation mode was used to solve material balances, which had nested recycle loops that simulate partial countercurrent washing. Iterative calculations were executed by the spreadsheet program until differences between successive computations were less than 0.01%.



2. Effect of (EO) washer efficiency and D_0 kappa factor charge on washed (EO) kappa number for the bleaching delignification: (A) $D_0(EO)D_1(EP)D_2$ with 70°C (EO), and (B) $D_0(EO)D_1$ with 90°C (EO). Case 1 refers to D_0 washer using shower water from cleaner sources, and Case 2 refers to (EO) filtrate being at the top shower bars of D_0 washer. Well-washed (i.e., Control) refers to 100% washing efficiency.



3. Effect of (EO) washer efficiency and D_0 kappa factor on the total chlorine dioxide bleach demand when bleaching with: (A) D_0(EO) D_1(EP)D_2 to 89% ISO, and (B) D_0(EO)D_1 to 86% ISO. Designations for the various cases are the same as those listed in Fig. 2.

RESULTS

Several scenarios have been examined to determine how (EO) carryover affects chlorine dioxide consumption for D_0(EO) D_1(EP)D_2 and D_0(EO)D_1 sequences. The well-washed pulp scenario assumes that there is 0% washer carryover (i.e., 100% washing efficiency). Case 1 presumes that the D_0 washer uses shower water that is relatively clean and that is free of (EO) dissolved solids (Fig. 1). The bottom D_0 showers may use hot water, white water, or D_1 filtrate, whereas the top D_0 showers may use D_1 filtrate or (EP) filtrate (if available) [7]. The bottom (EO) showers may use hot water, (EP) filtrate (if available), or D_1 filtrate; the top (EO) showers may use hot water or D_1 filtrate [7,8]. Case 2 is similar to Case 1 with one difference. In Case 2, (EO) filtrate is recycled to the top shower bars of D_0 washer; one-half of the applied shower water is (EO) filtrate [1,2,7,8,36]. The amount of (EO) dissolved solids increases in the (EO) stage. In Case 1 and Case 2, the dissolved solids in the shower water sources (other than the (EO) filtrate) are assumed to have negligible chlorine dioxide bleach consumption in the subsequent stage. The results from the spreadsheet calculations based on these scenarios are presented.

Figure 2 illustrates how the washed kappa number of the D_0(EO) pulp varies with the D_0 kappa factor (KF) charge and (EO) washer efficiency for the two cases versus the Control. If the brightness target of the D_0(EO)D_1(EP)D_2 sequence is 89% ISO, then the extracted pulp needs to have a washed D_0(EO) kappa that is between 3.8 and 4.6. This target shifts to 2.4 to 3.1 when bleaching to 86% ISO with the D_0(EO)D_1. The bleach necessary to attain these delignification targets corresponds to 0.23 to 0.27 KF (2.1% to 2.5% ClO_2 on pulp) for the Control. Depending upon the washing efficiency and washing scheme employed (Case 1 or Case 2), the incremental increase in the D_0 charge ranged from 0.04 to 0.09 KF (0.36 to 1.00% ClO_2 on pulp). The amount of carryover in the washed D_0(EO) pulps ranged from 0.4 to 0.6 kappa units when bleaching with a D_0(EO)D_1(EP)D_2 sequence to 89% ISO, and from 0.4 to 1.3 when bleaching with a D_0(EO)D_1 sequence to 86% ISO.

Figure 3 plots the total amount of ClO_2 consumed vs. the D_0 charge when bleaching to 89% ISO with the D_0(EO) D_1(EP)D_2 sequence and to 86% ISO with the D_0(EO)D_1 sequence. The minimized ClO_2 demand for the Control was approximately 36.8 kg ClO_2/ton for the five-stage sequence and approximately 30.0 kg ClO_2/ton for the three-stage sequence. Table III presents how (EO) washing efficiency and (EO) filtrate reuse affected pulp brightness when the chlorine dioxide charges are fixed at the Control levels. The D_2 brightness dropped by 0.7 to 1.4 points with the D_0(EO) D_1(EP)D_2 sequence as washing efficiency decreased with Case 1. These losses doubled when (EO) filtrate was used in a split-flow arrangement (Case 2). D_1 brightness losses for the three- and five-stage sequences ranged from 1.6 to 7.2 points. Table IV indicates how much chlorine dioxide bleach is needed in D_1 to recover the brightness losses while the chlorine dioxide charges in D_0 and D_2 (if used) remained fixed. The increase in D_1 bleach demand ranged from 3.5 to 10.5 kg ClO_2/ton to counteract the 0.7 to 1.6 kappa units of (EO) carryover.

Table V shows the minimized chlorine dioxide demand for D_0(EO)D_1(EP)D_2 and D_0(EO)D_1 at different washing efficiencies for Case 1 and 2. Balancing the ClO_2 used at D_0 and D_1 stages can afford some total bleach savings. For Case 1 where the (EO) washer is operating at 85% efficiency, the total amount of bleach saved was small (0.4 to 1.1 kg ClO_2/ton). There was an advantage of rebalancing the ClO_2 charges at D_0 and D_1 when (EO) washer efficiency was lower than 85% for Case 1, or when (EO) filtrate is recycled as D_0 shower water (Case 2). In these circumstances, the amount of chlorine dioxide saved ranged from 1.4 to 3.5 kg /ton pulp when rebalancing the bleach charges.

Figure 4 illustrates how washing efficiency and (EO) filtrate usage affected total ClO_2 needed to reach 85% to 90% ISO with the D_0(EO)D_1(EP)D_2 sequence and 84% to 89% ISO brightness with the D_0(EO)D_1 sequence. Similar bleach consumption trends were observed for these ranges as has been presented for 89% ISO and for 86% ISO scenarios.

$D_0(EO)D_1(EP)D_2$					
(EO) Washing Efficiency	(EO) Filtrate Used at D_0 Washer	D_0(EO) Washed Kappa No.	(EO) Carryover (Kappa units)	D_1 Brightness (% ISO)	D_2 Brightness (% ISO)
Well-Washed (Control)	No	4.2	0	83.9	89.0
85% Efficiency (Case 1)	No	4.9	0.7	82.3	88.3
70% Efficiency (Case 1)	No	5.6	1.4	80.3	87.6
85% Efficiency (Case 2)	Yes	5.4	1.2	80.7	87.8
70% Efficiency (Case 2)	Yes	6.3	2.1	78.5	86.9
$D_0(EO)D_1$					
(EO) Washing Efficiency	(EO) Filtrate Used at D_0 Washer	D_0(EO) Washed Kappa No.	(EO) Carryover (Kappa units)	D_1 Brightness (% ISO)	
Well-Washed (Control)	No	2.7	0	86.0	
85% Efficiency (Case 1)	No	3.6	0.9	82.1	
70% Efficiency (Case 1)	No	4.5	1.8	78.8	
85% Efficiency (Case 2)	Yes	4.3	1.6	79.6	

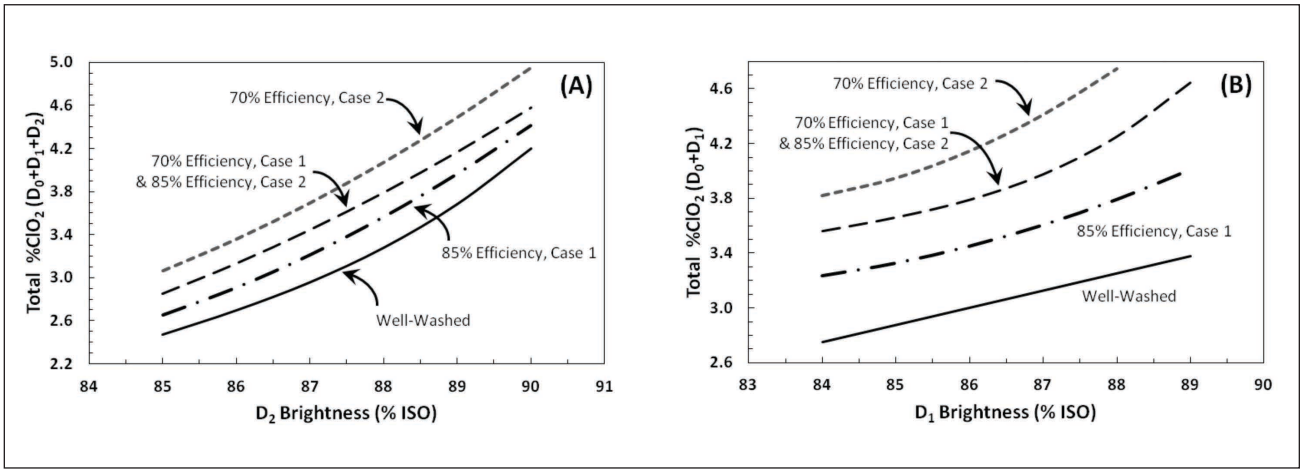
III. Influence of (EO) washer efficiency and (EO) filtrate reuse with $D_0(EO)D_1(EP)D_2$ and $D_0(EO)D_1$ sequences. Chlorine dioxide charges used in the D-stages were fixed at the levels for the well-washed pulp (Control): 2.29% D_0 (0.251 KF), 1.14% D_1 and 0.25% D_2 for $D_0(EO)D_1(EP)D_2$; and 2.32% D_0 (0.254 KF) and 0.68% D_1 for $D_0(EO)D_1$.

$D_0(EO)D_1(EP)D_2$					
(EO) Washing Efficiency	(EO) Filtrate Used at D_0 Washer	D_0(EO) Washed Kappa No.	(EO) Carryover (Kappa units)	D_1 ClO_2 to Reach 83.9% ISO	Total ClO_2 Used
Well-Washed (Control)	No	4.2	0	1.14%	3.68%
85% Efficiency (Case 1)	No	4.9	0.7	1.49%	4.03%
70% Efficiency (Case 1)	No	5.6	1.4	> 1.75%	> 4.30%
85% Efficiency (Case 2)	Yes	5.4	1.2	1.74%	4.28%
70% Efficiency (Case 2)	Yes	6.3	2.1	> 1.75%	> 4.30%
$D_0(EO)D_1$					
(EO) Washing Efficiency	(EO) Filtrate Used at D_0 Washer	D_0(EO) Washed Kappa No.	(EO) Carryover (Kappa units)	D_1 ClO_2 to Reach 86.0% ISO	Total ClO_2 Used
Well-Washed (Control)	No	2.7	0	0.67%	3.00%
85% Efficiency (Case 1)	No	3.6	0.9	1.26%	3.59%
70% Efficiency (Case 1)	No	4.5	1.8	> 1.75%	> 4.08%
85% Efficiency (Case 2)	Yes	4.3	1.6	1.72%	4.05%

IV. Influence of (EO) washer efficiency and (EO) filtrate reuse on chlorine dioxide (ClO_2) usage at the D_1 stage when bleaching to 89% ISO with $D_0(EO)D_1(EP)D_2$, and to 86% ISO with $D_0(EO)D_1$. Chlorine dioxide used in the D_0 and D_2 (if used) was fixed at the levels for the well-washed pulp (Table III). Well-washed indicates no (EO) washer carryover (i.e., 100% washing efficiency).

$D_0(EO)D_1(EP)D_2$					
(EO) Washing Efficiency	(EO) Filtrate Used at D_0 Washer	D_0(EO) Washed Kappa No.	(EO) Carryover (Kappa units)	D_1 ClO_2	Total ClO_2 Used
Well-Washed (Control)	No	3.8 to 4.6	0	0.98% to1.35%	3.68%
85% Efficiency (Case 1)	No	3.5 to 4.4	0.4 to 0.6	0.89% to 1.23%	3.99%
70% Efficiency (Case 1)	No	3.4 to 3.6	0.5 to 0.6	0.78% to 0.89%	4.14%
85% Efficiency (Case 2)	Yes	3.3 to 3.7	0.5 to 0.6	0.75% to 0.95%	4.14%
70% Efficiency (Case 2)	Yes	3.7	0.8	0.92%	4.27%
$D_0(EO)D_1$					
(EO) Washing Efficiency	(EO) Filtrate Used at D_0 Washer	D_0(EO) Washed Kappa No.	(EO) Carryover (Kappa units)	D_1 ClO_2	Total ClO_2 Used
Well-Washed (Control)	No	2.4 to 3.1	0	0.47% to 0.93%	3.01%
85% Efficiency (Case 1)	No	2.2 to 2.8	0.4 to 0.8	0.37% to 0.75%	3.48%
70% Efficiency (Case 1)	No	2.7 to 2.9	0.8 to 1.0	0.65% to 0.78%	3.77%
85% Efficiency (Case 2)	Yes	2.6 to 2.7	0.7 to 0.8	0.58% to 0.69%	3.70%

V. Influence of (EO) washer efficiency and (EO) filtrate reuse on the total chlorine dioxide usage when bleaching to 89% ISO with $D_0(EO)D_1(EP)D_2$, and to 86% ISO with $D_0(EO)D_1$. The amount of ClO_2 used in the D_0 and D_1 were allowed to vary; 0.25% ClO_2 was used in the D_2 stage.



4. Effect of (EO) washer efficiency on the minimized chlorine dioxide demand needed to reach a given brightness target when bleaching with: (A) $D_0(EO)D_1(EP)D_2$ and (B) $D_0(EO)D_1$. Designations for the various cases are the same as those listed in Fig. 2.

DISCUSSION

The results from the multistage modeling provided insights on how (EO) carryover and (EO) filtrate reuse affected ECF bleaching. Brightness losses observed from D_2 stages (Table III) seemed to concur with earlier observations for chlorine-based bleach sequences at typical interstage washing efficiencies [13-17]. Predicted D_1 brightness losses with the simulations ranged from 1.6 to 7 points when no adjustments were made for the (EO) carryover load. These predictions agree with earlier investigations [1,34,37], which generally reported a brightness drop of 0.5 to 8 points.

The washed (EO) pulps in Fig. 3 contained from 0.3 to 2.2 kappa units of (EO) carryover, depending upon the D_0 KF used, the temperature of (EO) stage, the efficiency of the (EO) drum washer, and the reuse of (EO) filtrate as shower water. Each kappa unit of (EO) carryover into the D_1 stage resulted in an additional 4.7 kg ClO_2/ton being consumed when bleaching to 89% ISO with a $D_0(EO)D_1(EP)D_2$ sequence, and an ad-

ditional 6.6 kg ClO_2/ton when bleaching to 86% ISO with a $D_0(EO)D_1$ sequence. In these two examples, the minimum ClO_2 demand was typically observed when the $D_0(EO)$ pulp had a washed kappa number between 3.8 and 4.6 for the five-stage sequence, and between 2.4 and 3.1 for the three-stage sequence. Using a higher D_0 bleach charge lowers the amount of (EO) carryover entering the D_1 for a given (EO) washer efficiency. This was due to more bleaching delignification occurring at the D_0 stage with the higher KF charges vs. the delignification occurring at the (EO) stage.

The model indicated that imperfect washing after the (EO) resulted in an additional 3 to 8 kg ClO_2/ton being expended versus perfect washing (i.e., Control). This represented an 8% to 15% increase of the total bleach needed to bleach to 89% ISO with the $D_0(EO)D_1(EP)D_2$ sequence and a 15% to 23% increase to bleach to 86% ISO with the $D_0(EO)D_1$ sequence. The amount of ClO_2 consumed by (EO) carryover is somewhat similar to the amount of bleach that is consumed by brownstock washing carryover (~10 kg Na_2SO_4/ton [4-6,24]) in the D_0 stage, which is ~3 kg ClO_2/ton.

Countercurrent usage of (EO) filtrate caused the amount of dissolved organic substances in the (EO) stage, as expressed in kappa units, to rise (Fig. 2). In Case 2 where the efficiency at the (EO) washer is 85% (i.e., 15% carryover), the reuse of (EO) filtrate caused the total bleach demand to approach that of Case 1 where the washer is operating at 70% efficiency and uses cleaner D_0 shower water sources. Case 2 resulted in an increase in the chlorine dioxide demand of 1.5 to 3.0 kg ClO_2/ton versus Case 1. Hence, recycling (EO) filtrate as shower water can result in appreciably higher chlorine dioxide consumption unless washing efficiencies after the (EO) stage are sufficiently high (≥85%), especially for short ECF bleach sequences. Similar observations have been reported by Histed et al. [1] for chlorine-based bleach sequences. These authors suggested using two washing units in series after the extraction stage to achieve >95% washing efficiency when recycling extraction filtrates. Such a countercurrent washing arraignment has been used at a softwood mill bleaching with the $D_0(EOP)D_1$ sequence that results in very low (EOP) carryover [20].

The spreadsheet simulations also illustrated how washing efficiency and countercurrent filtrate usage affected bleach consumption for various brightness targets using three- and five-stage ECF bleach sequences (Fig. 4). The bleach uptakes from 15% and 30% (EO) carryover at other brightness targets were somewhat similar to the base cases examined in greater detail (Fig. 3). Lower (EO) washing efficiencies and reuse of (EO) filtrate made it technically more difficult to attain the upper brightness targets of >87% ISO with $D_0(EOP)D_1$ sequence and >89% with $D_0(EO)D_1(EP)D_2$ sequence.

The spreadsheet models of ECF bleaching sequences, such as the one used in this study, have the potential to be used in conjunction with other computer models reported in the literature [1,36,38,39]. Combinations of such models could provide additional insights as to how various water reduction strategies in the bleach plant can affect interstage washing efficiencies, brightness targets and chemical usage, buildup of non-process elements and dissolved solids, potential scale formation, and discharged effluent properties.

CONCLUSIONS

Computer spreadsheet models were developed to forecast the response of a 24-kappa softwood kraft brownstock when subjected to $D_0(EO)D_1$ and $D_0(EO)D_1(EP)D_2$ bleach sequences. The models examined how (EO) washing efficiencies and how (EO) filtrate reuse affected the ClO_2 consumed to attain specific brightness targets. When the (EO) carryover was increased by 0.4 to 0.8 kappa units (on pulp), the chlorine dioxide demand of the $D_0(EO)D_1(EP)D_2$ sequence increased by 3 to 6 kg ClO_2/ton when bleaching to 89% ISO; when the (EO) carryover was increased by 0.4 to 1.0 kappa units, the chlorine dioxide demand of the $D_0(EO)D_1$ sequence increased by 5 to 8 kg ClO_2/ton when bleaching to 86% ISO. Bleach savings were observed when rebalancing the chlorine dioxide charge between D_0 and D_1 when the (EO) washing efficiency was <85%, or when (EO) filtrate is re-used as D_0 shower water. Employing split-flow washing with (EO) filtrate, in combination with 70% to 85% (EO) washing efficiency, resulted in an extra chlorine dioxide uptake of 1.5 to 3.0 kg/ton pulp versus when using cleaner shower water at the D_0 washer. It was more difficult to bleach to >89% ISO with the $D_0(EO)D_1(EP)D_2$ sequence and to >87% ISO with the $D_0(EO)D_1$ sequence when (EO) carryover was present at moderate levels (i.e., 15%). Hence, the advantages of split-flow countercurrent washing with (EO) filtrate, such as reduced steam and caustic usage at (EO) stage, needs to be balanced with the noted disadvantages when optimizing bleach plant operations. **TJ**

ACKNOWLEDGEMENTS

An earlier version of this work was presented at the 2018 TAPPI Pulping, Engineering, Environmental, Recycling and Sustainability (PEERS) Conference in Portland, OR, USA (October 28-31, 2018; Session 2-2). The authors gratefully acknowledge the extensive laboratory bleaching data published by Basta et al. [28] of Eka Nobel, which were used in the bleach plant modeling of this study.

LITERATURE CITED

1. Histed, J., McCubbin, N., and Gleadow, P.L., in *Pulp Bleaching—Principles and Practice* (C.W. Dence and D.W. Reeve, Eds.), TAPPI Press, Atlanta, GA, USA, 1996, pp. 647-673.
2. Histed, J.A. and Nelson, G.G., in *The Bleaching of Pulp* (R.P. Singh, Ed.), TAPPI Press, Atlanta, 1979, pp. 393-411.
3. Pryke, D.W., "Water reuse in the bleach plant," *1985 Bleach Plant Operations Seminar*, TAPPI Press, Atlanta, 1985, pp. 105-113.
4. Pryke, D.C. and Reeve, D.W., *TAPPI J.* 80(5): 153(1997).

5. Pryke, D.C. and Earl, P.F., "Softwood bleaching practices in Canada: Analysis of the 2003 PAPTAC Bleaching Committee 'best practices' survey," *TAPPI Eng., Pulping, Environ. Conf.*, TAPPI Press, Atlanta, 2005.
6. Pryke, D.C., Kanters, C.J., and Tam, T., "ECF bleaching practices in Canada, Part 2: Analysis of PAPTAC Bleaching Committee survey for softwood kraft pulps," *Int. Pulp Bleaching Conf.*, PAPTAC, Montréal, 2000.
7. Towers, M. and Turner, P.A., "Survey of bleach plant washing practices in Canadian Mills," *Pulp Washing '96*, CPPA/TAPPI, Montreal/Atlanta, 1996, pp. 23-29.
8. Earl, P.F. and Schofield, M., "Pulp washing after the first extraction stage: A survey of Canadian mills," *PAPTAC Annu. Meet., 93rd*, Montréal, 2007.
9. Pryke, D.W. and Nylen, K., *Pulp Pap. Can.* 109(1): 43(2008).
10. Steelreath, E., Earl, P.F., and Vanderheide, J., "Bleach plant optimization at the Resolute Forest Products Coosa Pines mill," *TAPPI PEERS Conf.*, TAPPI Press, Atlanta, 2014.
11. Yankowski, A.A., *Tappi* 55(6): 937(1972).
12. MacDonald, G.L.W., *Pulp Pap. Mag. Can.* 73(3): 56(1972).
13. Histed, J.A. and Nicolle, F.M.A., *Pulp Pap. Mag. Can.* 75(5): T171(1973).
14. Histed, J.A. and Nicolle, F.M.A., *Pulp Pap. Mag. Can.* 74(12): T386(1973).
15. Nicolle, F.M.A and Histed, J.A., *Pulp Pap. Can.* 76(9): T253(1975).
16. Histed, J.A. and Nicolle, F.M.A., *Tappi* 59(3): 75(1976).
17. Histed, J.A. and André, G., *Pulp Pap. Can.* 78(3): TR23(1977).
18. Wartiovaara, I., *Pap. Puu* 82(5): 319(1980).
19. Maples, G.E., Ambady, R., Caron, J.R., et al., *Tappi J.* 77(11): 71(1994).
20. Vega Canovas, R. and Maples, G., *Pulp Pap.* 69(3): 83(1995).
21. Frigieri, T.C., Ventorim, G., Savi, A.F., et al., *Environ. Technol.* 36(5): 638(2015).
22. Lunn, R., *Pulp Pap. Can.* 102(3): 46(2001).
23. Brogdon, B.N., *TAPPI J.* 15(3): 178(2016).
24. Brogdon, B.N., *TAPPI J.* 14(2): 93(2015).
25. Brogdon, B.N., *TAPPI J.* 13(3): 17(2014).
26. McDonough, T.J., Rawat, N., and Krishnagopalan, G.A., *Appita J.* 57(5): 381(2004).
27. Hart, P.W. and Connell, D., *TAPPI J.* 5(4): 23(2006).

ABOUT THE AUTHORS

This article is a continuation of the spreadsheet modeling work for ECF beaching that was previously published in *TAPPI Journal* [23-25]. In this paper, we investigate how interstage washing, particularly after the first caustic extraction stage, affects oxidant consumption and brightening during the bleaching of a softwood pulp. This topic is of interest since most North American bleach plants are utilizing older washing devices that are overloaded and washing less efficiently. The extra bleaching costs incurred by poor interstage washing are not widely known.

Much has been published about countercurrent washing schemes to minimize water usage, especially with regards to how to mitigate inorganic deposits and effluent emissions. However, the literature contains limited information on how poor pulp washing affects ECF chemical consumption and pulp brightening. Laboratory investigations examined this topic back in 1970s with a chlorine-based sequence, such as those by Jack Histed and colleagues [13-17]. However, similar studies have not been replicated for today's ECF sequences. Such laboratory studies are laborious and time consuming to conduct. An alternative method to obtain this information is through computer simulations.

This research utilizes some steady-state models that are coupled together to simulate multistage ECF sequences. These models, once tuned with basic bleaching data, have the ability to account for the impacts of washer carryover from an interstage washer on other bleaching stages with regards to oxidant consumption, kappa number reduction, and/or brightness development.

The most interesting result from our numerical modeling was that nominal levels of (EO) washer carryover (e.g., 15%) resulted in an additional chlorine dioxide demand that was similar to the bleach demand caused by typical brownstock carryover levels (e.g., 10 to 15 kg Na_2SO_4/ton pulp) into the bleach plant.

Process engineers can modify and tune the multistage ECF models employed in this study to simulate their bleach plants to estimate how improvements in interstage washing or changes to countercurrent washing schemes can affect chlorine dioxide bleach usage.



Brogdon



Lucia

Brogdon is owner of Future Bridge Consulting Services LLC, Marietta, GA, USA. Lucia is associate professor in the Department of Forest Biomaterials at North Carolina State University, Raleigh, NC, USA. Email Brogdon at Brian.Brogdon@gmail.com.

28. Basta, J., Andersson, L., Blom, C., et al.,"New and improved possibilities in D_{100} bleaching," *TAPPI Pulping Conf.*, TAPPI Press, Atlanta, 1992, pp. 547-553.
29. Brogdon, B.N., *TAPPI J*. 9(8): 27(2010).
30. Turner, P.A., Allen, L.H., Allen, S.L., et al., in *Pulp Bleaching: Principles and Practice* (C.W. Dence and D.W. Reeve, Eds.), TAPPI Press, Atlanta, 1996, pp. 569-596.
31. Germgard, U. and Steffies, F., "Pulp washing in a closed bleach plant, Part 2," *Pulp Washing '96*, CPPA/TAPPI, Montréal/Atlanta, 1996, pp. 31-36.
32. Kappel, J., Sbaschnigg, J., and Petschauer, F., "Improved washers for low effluent bleach plants," *Pulp Washing '96*, CPPA/TAPPI, Montréal/Atlanta, 1996, pp. 109-114.
33. Viirmaa, M., Dahl, O., Niinimäki, J., et al., *Appita J*. 55(6): 484(2002).
34. McDonough, T.J., Baromès, J.-C., Carter, B.R., et al., C.E., "Effects of washer efficiency on characteristics of effluents from D(EPO) D bleaching of a softwood kraft pulp," *TAPPI Environ. Conf.*, TAPPI Press, Atlanta, 1998, pp. 85-92.
35. Paleologou, M., Mahmood, T., Voss, R., et al., "Progressive system closure: A Canadian perspective," *Proc. Braz. Symp. Chem. Lignins Other Wood Compon., 7th,* Universida de Federal de Viçosa, Viçosa, Brazil, 2001, pp. 229-241.
36. Jour, P., Lindgren, K., Gutke, K., et al., *TAPPI J.* 17(6): 353(2018).
37. Parming A., Backlund B., and Bergnor, R., "A kinetic study of the reactions between dissolved organic substance and chlorine dioxide," *Intl. Pulp Bleaching Conf.*, TAPPI Press, Atlanta, 1988, pp. 161-167.
38. Rudie, A.W. and Hart, P.W., "Modeling of bleach plant washer mineral scale," *TAPPI Fall Technical Conf.*, TAPPI Press, Atlanta, 2004.
39. Rudie, A.W. and Hart, P.W., in *The Bleaching of Pulp* (P.W. Hart and A.W. Rudie, Eds.) 5th edn., TAPPI Press, Atlanta, 2012, Chap. 7, pp. 175-216.

ABOUT THIS PAPER

Cite this article as: Brogdon, B., Lucian, L. *TAPPI J.* 17(11): 621(2018). https://doi.org/10.32964/TJ17.11.621

DOI: https://doi.org/10.32964/TJ17.11.621

ISSN: 0734-1415

Publisher: TAPPI Press

Copyright: ©TAPPI Press 2018

About this journal

Understanding the pulping and bleaching performances of eucalyptus woods affected by physiological disturbance

JULIANA MARANGON JARDIM, CAROLINA MARANGON JARDIM, AND JORGE LUIZ COLODETTE

ABSTRACT: The wood quality is a factor of extreme importance when the pulping process is targeting high yield, low cost, and high pulp quality. Thus, wood knowledge is crucial for process optimization. In some northeastern Brazilian eucalyptus plantations, a physiological disturbance caused by water stress has been observed. Up to now, there have been no studies concerning the effects of such disturbances on the wood quality or on the pulping and bleaching process performance. The present work is aimed at understanding the impact of the stress on the production of bleached pulp. The wood quality of two clones (one tolerant to the disturbance and another sensitive), cultivated in sites where the disturbance is present and absent, was evaluated. Kraft pulps of kappa number 20 were produced and bleached by the sequence $D_{HT}(EP)D_1$ to a brightness of 90% ISO, which allowed for assessment of the wood pulpability and bleachability. It was concluded that the disturbance affects the wood quality, and overall it showed a negative impact on the production of bleached eucalyptus kraft pulp, with significant potential economical setbacks.

Application: This research is a case study of how bleached pulp production is affected by wood quality. Eucalyptus woods affected by physiological disturbances were studied, as well as their performance during kraft pulping and elemental chlorine-free (ECF) bleaching. Mills could use this information to better understand the wood consumption, chemicals, and energy demands on the process when using those woods in the pulp manufacturing.

Physical and chemical wood properties have a significant impact on pulp manufacture as it impacts chemical demand and yield, which ultimately affects production cost and pulp quality [1]. It is well known that the process changes as a function of the wood raw material. Therefore, knowledge of the raw material is crucial for process adequacy and optimization.

Eucalyptus wood is the main raw material used to produce bleached pulp in Brazil. The plantations success depends on the genotype's adaptability to edaphoclimatic conditions where they are cultivated. Among the main factors influencing eucalyptus growth, precipitation, temperature, and nutrition stand out. When any of these variables behave unexpectedly or inappropriately, the plant may respond negatively, affecting its growth, usually in form of a physiological stress [2-3]. Therefore, it is necessary to know the effects of site changes upon each species, since favorable conditions are specific and cannot be generalized.

Some eucalyptus plantations in South of Bahia State (Brazil) are subject to water stress and a physiological response to this disturbance has been observed in the trees. During rainfall periods, it has been observed that excess water promotes anaerobic conditions in the soil, causing root death, leading to increased ethylene and abscisic acid production and consequently increasing tree defoliation. Moreover, the high relative humidity in the air causes a reduction in the gas exchange between stomata and the atmosphere (due to the small difference in water potential between the air present in stomata and the atmosphere) and consequent reduction of photosynthetic rate. Furthermore, during intermittent periods of rainfall, the water deficit, high incident radiation, and low relative humidity in air can cause problems such as chlorophylls photo-oxidation in the leaf cells, stomatal closure, and reduction of photosynthetic rate, also leading to tree defoliation [4].

The disturbance does not kill trees sensitive to it, but it does attenuate tree growth in the field, due to the reduction of leaf area index. So far there are no studies about the effects of the disturbance on chemical and physical wood properties, or about these impacts on pulping and bleaching processes. Thus, the present work was aimed at determining the potential changes in wood quality caused by the disturbance and their consequences on pulping and bleaching performance, as well as final pulp quality.

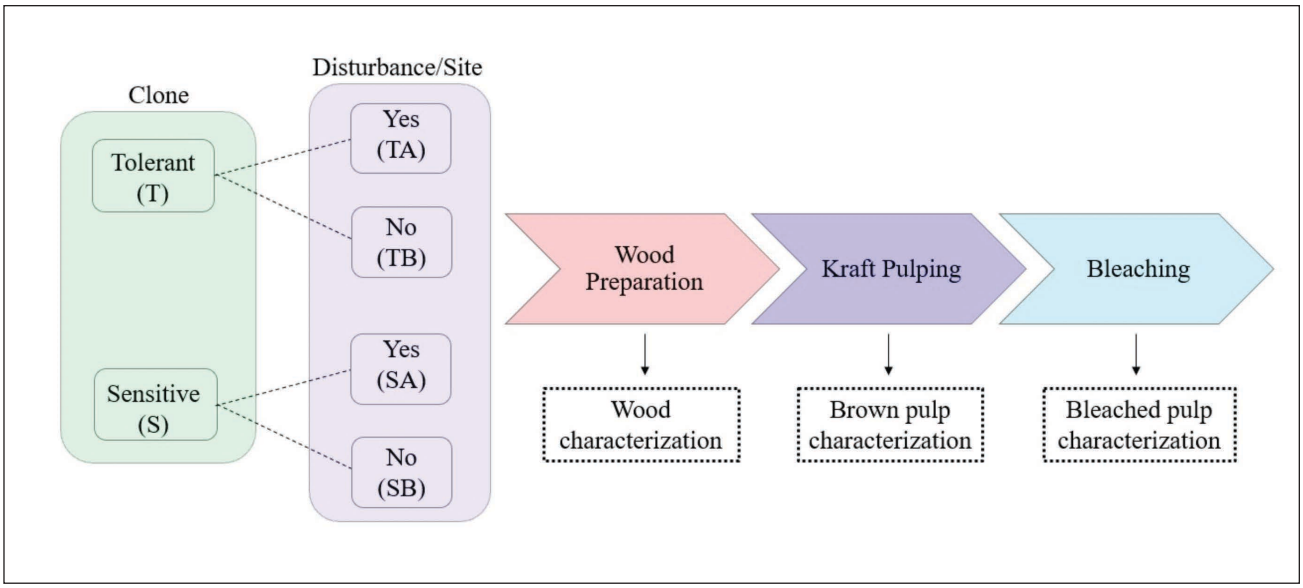
EXPERIMENTAL

Two hybrids of *Eucalyptus urophylla x Eucalyptus grandis* (8 years old) from South of Bahia State were evaluated. One clone is tolerant to the disturbance (clone T) and the other is sensitive (clone S). These clones were sampled in sites where the disturbance is present (site A) and absent (site B) (**Fig. 1**).

Wood characterization

The wood samples were chemically and physically characterized. The analyses were performed in duplicate in accordance to standard laboratory methods (**Table I**).

https://doi.org/10.32964/TJ17.11.633



1. Experimental design of the study intended to evaluate wood quality, kraft pulping response, and bleaching response of the two clones, disturbance tolerant (T) and sensitive (S), grown at two different sites (A and B).

Parameter	Standard Method
Basic wood density	ABNT NBR 11941 (2003) "Wood—Determination of basic density"
Sampling and preparing wood for analysis	TAPPI T 257 om-02 "Sampling and preparing wood for analysis"
Extractives of wood and pulp	TAPPI T 264 cm-97 "Solvent extractives of wood and pulp"
Insoluble lignin (Klason)	Gomide and Demuner 1986 [5]
Soluble lignin	Goldshimid 1971 [6]
Carbohydrates	SCAN-CM 71:09 "Pulps—Carbohydrate composition"
Uronic acids	Scott, 1979 [7]
Acetyl group	Solar et al., 1987 [8]
Ash	TAPPI T 211 om-93 "Ash in wood, pulp, paper and paperboard: combustion at 525°C"
S/G* ratio	Chen 1992 [9]
* S/G = syringyl/guaiacyl.	

I. Analytical methods used for wood characterization.

Parameter	Condition
Liquor/Wood ratio	4/1
Effective alkali, %	*
Sulfidity, %	35
Residual effective alkali, g/L	5-7
H-factor	*
Kappa number target	20
* Varied in order to achieve kappa number of 20.	

II. Pulping conditions.

Kraft pulping

Kraft pulping was performed in a 7L M/K laboratory batch digester (M/K Systems; Elk Grove, IL, USA) using 300 g of ovendry chips. Pulping experiments were replicated four times. The general pulping conditions are shown in **Table II**.

After cooking, the pulps were washed, disintegrated, screened, centrifuged, fluffed, and stored in polyethylene bags. The characterization of pulps and black liquors was done in duplicate in accordance to the analytical methods described in the **Table III**.

Oxygen delignification and bleaching

The pulps from the four replicated kraft cooks were blended and subjected to oxygen delignification in a Mark V reactor/mixer

Parameter	Standard Method
Kappa number	TAPPI T 236 cm-85 "Kappa number of pulp"
Viscosity	SCAN-CM 15:99 "Viscosity in cupriethylenediamine solution"
Brightness	TAPPI T 452 "Brightness of pulp, paper, and paperboard (directional reflectance at 457 nm)"
Hexenuronic acids	TAPPI T 282 pm-07 "Hexenuronic acid content of chemical pulp"
Carbohydrates	SCAN-CM 71:09 "Pulps—Carbohydrate composition"
Residual effective alkali	SCAN-N 33:94 "Black liquor—Residual alkali (hydroxide ion content)"
Screened yield	Gravimetric measurement
Rejects yield	Gravimetric measurement

III. Analytical methods used for brown pulp and black liquor characterization.

Conditions	Bleaching Stages			
	O	D_{HT}	(EP)	D_1
Consistency, %	11.5	11.0	11.0	11.0
Time, min	60	120	75	90
Temperature, °C	100	90	85	80
Pressure, kPa	750	-	-	-
H_2SO_4, kg/o.d. ton	-	*	-	-
NaOH, kg/o.d. ton	20.0	-	8.9	*
O_2, kg/o.d. ton	16.6	-	-	-
Kappa factor	-	0.21	-	-
ClO_2, kg/o.d. ton	-	-	-	**
$H_2O_2^-$, kg/o.d. ton	-	-	4.9	-
Final pH	-	4.0	-	5.0

H_2SO_4 = sulfuric acid; NaOH = sodium hydroxide; O_2 = oxygen; ClO_2 = chlorine dioxide; $H_2O_2^-$ = hydrogen peroxide.
* H_2SO_4 or NaOH to pH adjustment.
** Charge was variated to reach brightness of 90% ISO.

IV. Conditions of oxygen delignification and $D_{HT}(EP)D_1$ bleaching.

(Quantum Technologies Inc.; Akron, OH, USA) and then bleached with a $D_{HT}(EP)D_1$ sequence in order to reach a target brightness of 90% ISO. All of the bleaching conditions are shown in **Table IV**.

The analytical test methods performed to characterize the pulps and the resulting bleaching liquors are listed in **Table V**.

RESULTS AND DISCUSSION

Wood characterization

Observed changes in the wood properties were caused by the physiological disturbance (**Table VI**). These changes, even though to a lesser extent, were also observed in the disturbance tolerant clone.

Figure 2 shows how much, in percentage, each of the main wood parameters changed as a result of the physiological disturbance. The plotted results are a relation between the parameter measured at site A and B for each clone. An increment of 8.5% of extractives was observed for clone T at site A. A marked increase in extractives for clone S was also noticed (9.9%) for site A. The total amount of extractives in each species depends on growing conditions [11], which corroborates that these increments may be explained by the growth site. An increase of lignin for samples grown at site A was also observed. The total lignin content in clone T was increased by 3.2% and by 5% in clone S. Lignin plays an important role in the adaptation of plants when subjected to water distress [12], which indicates that the lignin increment was in response to the physiological disturbance.

Plants exposed to different environmental stresses may change lignin content and composition. In hardwood, lignin

Parameter	Standard Method
Kappa number	TAPPI T 236 cm-85 "Kappa number of pulp"
Viscosity	SCAN-CM 15:99 "Viscosity in cupriethylenediamine solution"
Brightness	ISO 2470 "Paper, board and pulps — Measurement of diffuse blue reflectance factor — Part 1: Indoor daylight conditions (ISO brightness)"
Brightness reversion	TAPPI UM 200 "Brightness loss of bleached pulp"
Hexenuronic acids	TAPPI T 282 pm-07 "Hexenuronic acid content of chemical pulp"
ClO_2 and H_2O_2 residuals	Seymour and Lavigne [10]
ClO_2 = chlorine dioxide; H_2O_2 = hydrogen peroxide.	

V. Analytical methods used for bleached pulps and bleaching effluents characterization.

Parameter	TA	TB	SA	SB
Extractives, %	6.0 ± 0.0	5.5 ± 0.0	6.3 ± 0.1	5.7 ± 0.1
Ash, %	0.2 ± 0.0	0.2 ± 0.0	0.3 ± 0.0	0.3 ± 0.0
Insoluble lignin, %	25.8 ± 0.2	25.0 ± 0.2	26.0 ± 0.0	24.8 ± 0.3
Soluble lignin, %	3.4 ± 0.0	3.3 ± 0.0	3.7 ± 0.1	3.5 ± 0.0
Arabinans, %	0.3 ± 0.0	0.3 ± 0.0	0.3 ± 0.0	0.3 ± 0.0
Galactans, %	0.8 ± 0.0	1.0 ± 0.0	0.7 ± 0.0	0.7 ± 0.0
Glucans, %	44.6 ± 0.2	45.9 ± 0.2	42.3 ± 0.0	44.2 ± 0.2
Xylans, %	10.4 ± 0.1	10.2 ± 0.0	11.6 ± 0.0	11.7 ± 0.1
Mannans, %	0.7 ± 0.0	0.5 ± 0.0	0.8 ± 0.0	0.6 ± 0.0
Acetyl groups, %	2.6 ± 0.0	2.6 ± 0.0	2.6 ± 0.0	2.6 ± 0.0
Uronic acid groups, %	3.3 ± 0.0	3.6 ± 0.0	3.4 ± 0.0	3.5 ± 0.0
S/G ratio	1.9 ± 0.0	1.7 ± 0.0	1.9 ± 0.0	1.8 ± 0.0
Basic density, kg/m³	492 ± 1	517 ± 5	503 ± 1	537 ± 6
*Means are followed by standard deviation				

VI. Wood characterization (dried wood basis) for the four samples studied (T = disturbance tolerant clone; S = sensitive clone; A and B = sites studied).

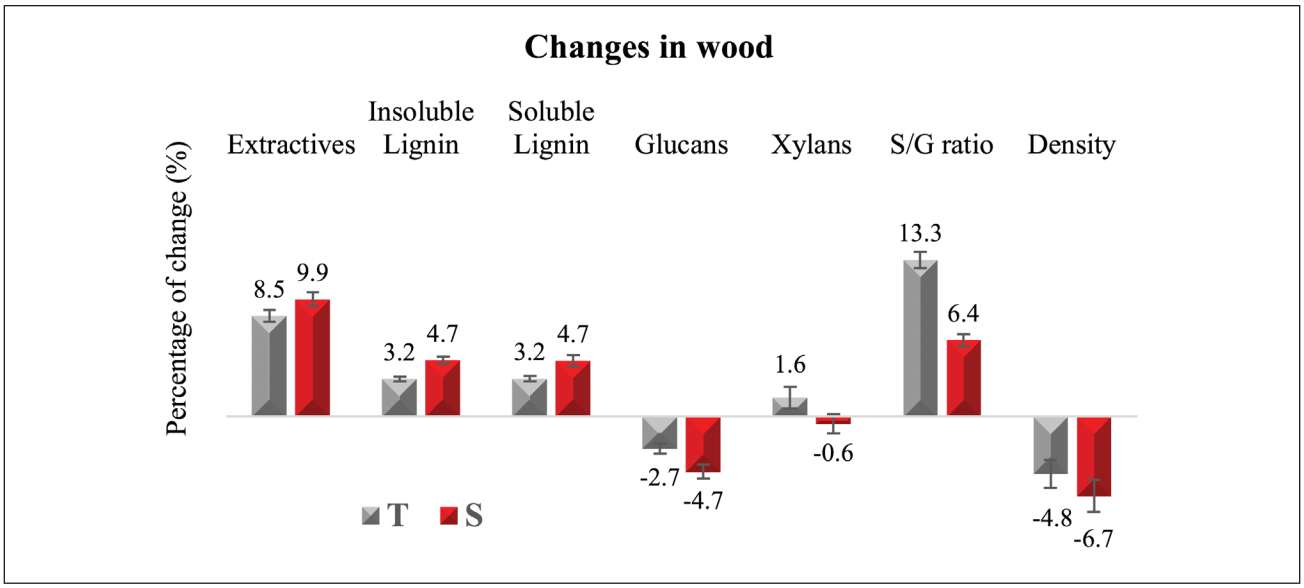
is composed of syringyl (S) and guaiacyl (G) units in varying ratios [13]. The tolerant and sensitive clones had increases in their S/G ratio by 13.3% and 6.4%, respectively, under the effect of the environmental disturbance. Moreover, the amount of holocellulose (i.e., cellulose and hemicelluloses) decreased. The greater or lower availability of growth resources can affect lignin synthesis, enlargement and thickening of the cell walls, and the ratio of lignin-to-holocellulose in the wood [14].

The basic wood density was another parameter affected by the physiological disturbance. Samples from site A showed lower wood densities. The reduction was of 6.7% for the clone sensitive and 4.8% for the clone tolerant. A drop in density of a hybrid of *Eucalyptus urophylla x E. grandis* by abiotic distress has been reported in the literature [15].

Wood chemical composition interferes with the pulping process with regards to process efficiency, yield, reagent consumption, and black liquor solids generated [16]. Therefore, the changes caused by the physiological disturbance suggest that samples from site A and B may behave differently during kraft pulping.

Kraft pulping

The different H-factors applied led to a difference in pulping yield (**Table VII**); the lower the H-factor the higher the screened yield. Samples from site A required harsher pulping conditions to reach a kappa number of 20. This may be explained by the higher extractives and lignin content of samples caused by the physiological disturbance. In general, the evaluated clones presented unusually high extractive contents, as previously reported [17]. Usually, the total extractives content in eucalyptus is around 1.9%–4.9% [18]. These components have a great importance in the pulping process as



2. Percentage of changes in wood caused by the physiological disturbance (S/G = syringyl/guaiacyl).

Sample	H Factor	EA, %	Yield**, %			SWC**, m³/o.d. ton	Black Liquor	
			Screened	Rejects	Total		REA, g/L	pH
TA	811	18.5	49.9 a	0.3 b	50.1 a	4.1 a	5.4	12.7
TB	751	18.5	50.1 a	0.4 a	50.6 a	3.9 b	5.6	12.6
SA	871	20	47.3 b	0.3 b	47.8 b	4.2 a	5.5	12.7
SB	871	19.5	47.7 b	0.3 b	48.0 b	3.9 b	5.6	12.5

SWC = specific wood consumption; EA = effective alkali; REA = residual effective alkali; T = disturbance tolerant clone; S = sensitive clone; A and B = sites studied.
* Results of pulping to reach kappa number of 20.
** Means followed by the same letters in a column do not differ significantly by the Tukey pairwise comparison test (i.e., $p < 0.05$).

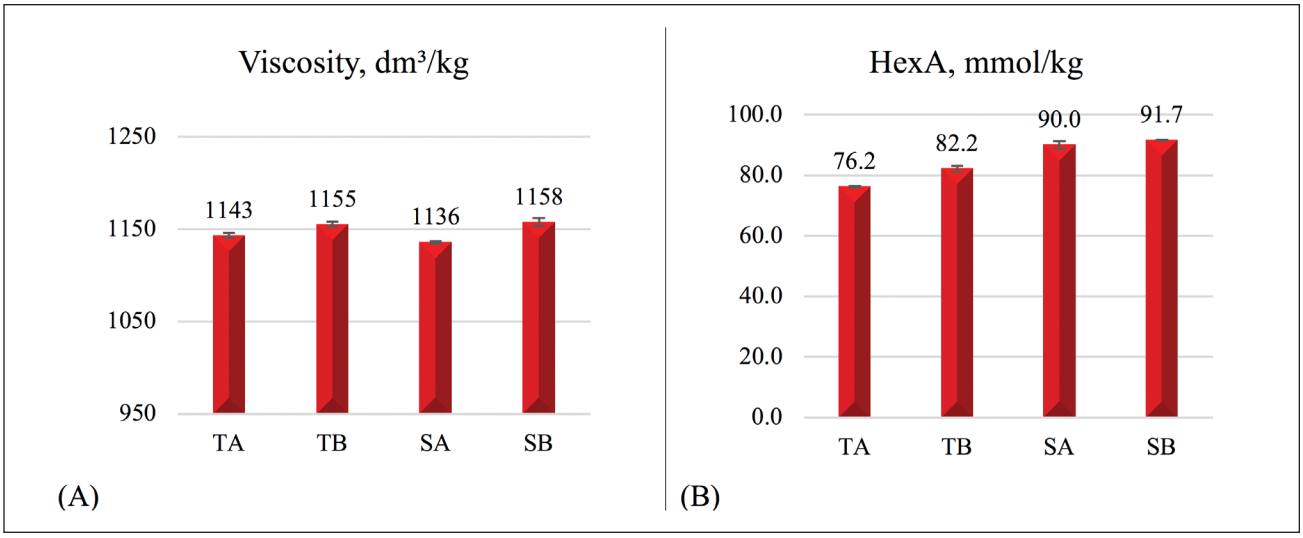
VII. Pulping results for the four samples studied.*

they can hinder liquor impregnation, consume reagents, and reduce yield [19], all of which have been observed in the present work.

Overall, the lower the lignin content, the better the performance during the pulping process; wood having a higher lignin S/G ratio should be easier to cook because S units are more reactive in kraft pulping than G units. Many researchers have reported that the S/G ratio correlates negatively with effective alkali demand and positively with pulping yield [20]. The physiological disturbance caused an increase in total lignin content and S/G ratio. It can be speculated that the increase in S/G ratio may have somewhat minimized the strong negative effect of the environmental disturbance that increased the lignin content in the wood.

Typically, higher wood densities require a higher concentration of effective alkali to achieve the same delignification degree at the same time and temperature, but in this case, the higher density was counterbalanced by lower lignin and extractives contents. Among the factors that influence pulp manufacturing costs, specific wood consumption (SWC) stands out [21,22]. SWC is usually expressed in volume (m^3) of solid wood required to produce one ton of pulp. This parameter is calculated taking into account the basic density of the raw material and pulping yield. Due to the loss of density caused by the physiological disturbance, an increase in SWC for samples from site A was observed. This increment has a negative impact since it results in higher wood demand, which is the most relevant cost to pulp manufacturing.

Viscosity of pulp is associated with the degree of polymerization for cellulose and hemicelluloses, which indirectly estimates the degradation of these carbohydrates. As can be seen in the **Fig. 3A**, the intrinsic viscosity of unbleached pulps was not significantly affected by the physiological disturbance.



3. Pulping results for the four samples studied: (A) viscosity (dm³/kg), and (B) hexenuronic acids (mmol/kg).

Sample	Arabinans	Galactans	Glucans	Xylans	Mannans
TA	n.d.	0.2 ± 0.0	80.6 ± 0.0	13.0 ±0.0	0.2 ±0.0
TB	n.d.	0.2 ± 0.0	81.1 ± 0.0	12.6 ±0.0	0.2 ±0.0
SA	n.d.	0.1 ± 0.0	78.6 ± 0.0	15.0 ±0.0	0.2 ±0.0
SB	n.d.	0.1 ± 0.0	79.4 ± 0.0	14.2 ±0.0	0.2 ±0.0

T = disturbance tolerant clone; S = sensitive clone; A and B = sites studied; n.d. = not detected.
*Means are followed by standard deviation.

VIII. Pulp characterization for the four samples studied* .

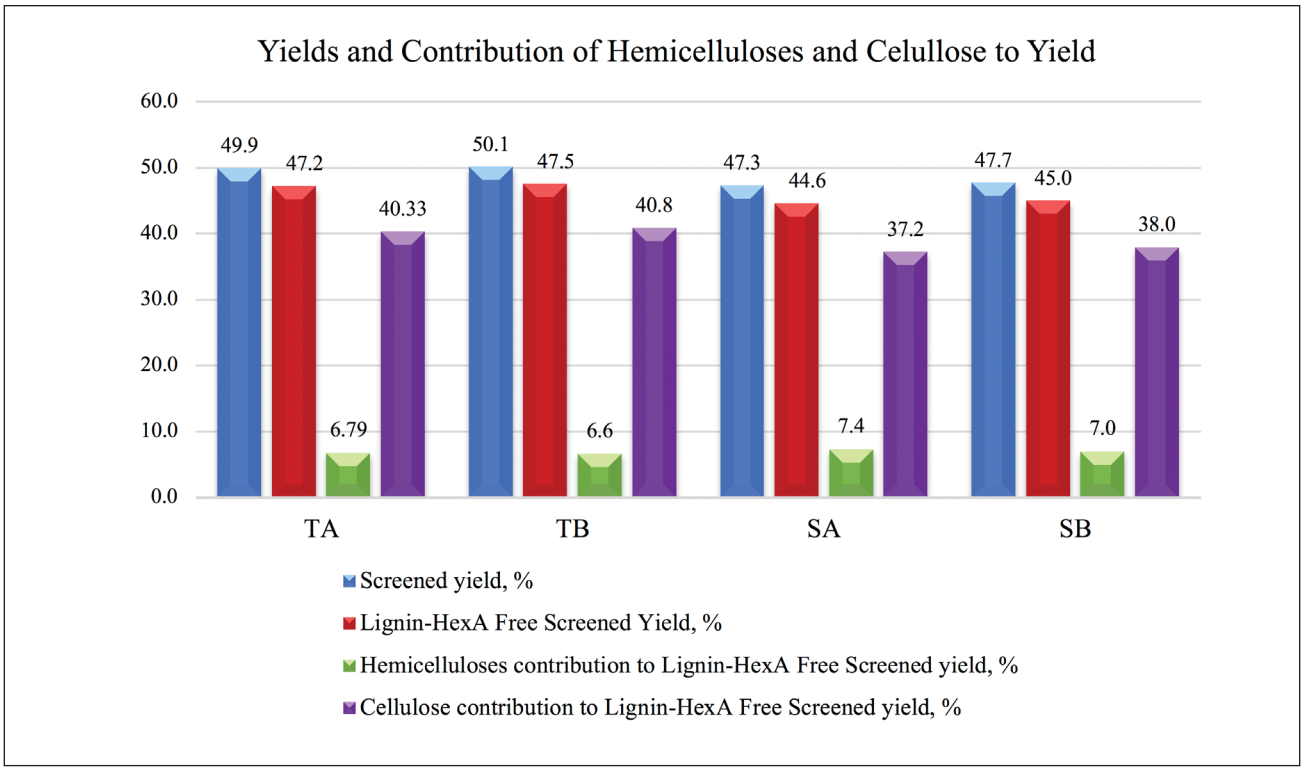
During kraft pulping, the structure of hemicelluloses is extensively modified (Fig. 3). The main detected modification is the conversion of the 4-*O*-methyl-glucuronic group, present on the sides of the xylan chains, to hexenuronic acid (HexA), via β-elimination of the methoxyl group [23]. The formation and degradation of HexA is influenced by pulping time, temperature, and effective alkali charge, as well as the interactions among these variables [24].

The higher H-factor applied during the pulping of sample TA (clone T, site A), and the higher effective alkali charge for sample SA (clone S, site A) generated lower amounts of HexA when compared with TB (clone T, site B) and SB (clone S, site B). These results are in agreement with the hypothesis that the formation and the degradation of HexAs are influenced by kraft pulping conditions [25].

Carbohydrate content in the brownstocks was investigated. Arabinans are highly degraded during the kraft pulping process, and hence, could not be detected (**Table VIII**). The hemicelluloses reacted with hydroxyl ions during pulping and dissolved into the black liquor along with lignin [26]. Besides arabinans, which were completely removed, galactans and mannans were removed at more than 80%. This significant hemicellulose loss was due to factors inherent to their chemical structure, such as their low molecular weight, low crystallinity, branching, and low stability to alkali attack [27].

Kappa number is directly related to lignin content in pulp; hence, it indirectly affects the pulping yield. In addition to lignin, HexA can also be oxidized by potassium permanganate during kappa number measurement [28]. In this sense, this study evaluated the screened yield of the pulps, and the lignin-HexA free screened yield (i.e., screened yield without lignin and HexA). Also, the contributions of hemicelluloses and cellulose to the lignin-HexA free screened yield were evaluated (**Fig. 4**).

Although samples TA and TB, as well as SA and SB, did not show a statistical difference in screened yield (Table VII), it was observed that the contributions of cellulose to lignin-HexA free screened yield of TB and SB were greater than TA and SA. Thus, the pulps from site B exhibited higher quality since they have more cellulose in their composition, which is the polymer of greatest interest in the pulping process.



4. Screened yields, lignin-hexA free screened yield, and contribution of hemicelluloses and cellulose to yield for the four samples studied.

Oxygen delignification

The unbleached pulps were subjected to oxygen delignification.The amount of oxygen delignification (Table VIII), as measured by the kappa number drop, was higher for TA and SA than for TB and SB. This can be explained by the lignin and HexA content. TA and SA have a more reactive lignin (higher S/G ratio), which means they are easier to remove. It has been reported that eucalyptus woods with higher S/G ratios afford kraft pulps that are easier to bleach at a given kappa number [29]. HexA negatively affects the calculated amount of delignification since HexAs do not react with oxygen and are measured in the kappa number test [30]. Hence, the lower HexA contents of TA and SA pulps led to a higher levels of oxygen delignification (**Table IX**).

Unbleached pulps with high intrinsic viscosity typically lose more intrinsic viscosity during delignification with oxygen [31]; this was observed in the present study. As well as the degree of delignification, the oxygen delignification selectivity with samples TA and SA was higher than with TB and SB.

Elemental chlorine-free bleaching

After oxygen delignification, the pulps were subjected to an elemental chlorine-free (ECF) sequence $D_{HT}(EP)D_1$. All bleached pulps reached a brightness of 90% ISO and a bleached kappa number lower than 1. Bleached pulps meeting market pulp brightness levels (88%–92% ISO) may also contain small amounts of leucochromophores substances, i.e., substances that may generate chromophoric structures (such as HexA) that lead to brightness reversion [32]. It has been reported that residual HexA structures reduce the brightness stability of the bleached pulp (**Fig. 5A**).

Parameter	TA	TB	SA	SB
Delignification, %	44.5	43.1	45.5	45.1
Viscosity, dm³/kg	908	910	922	931
Selectivity	0.034	0.031	0.039	0.036

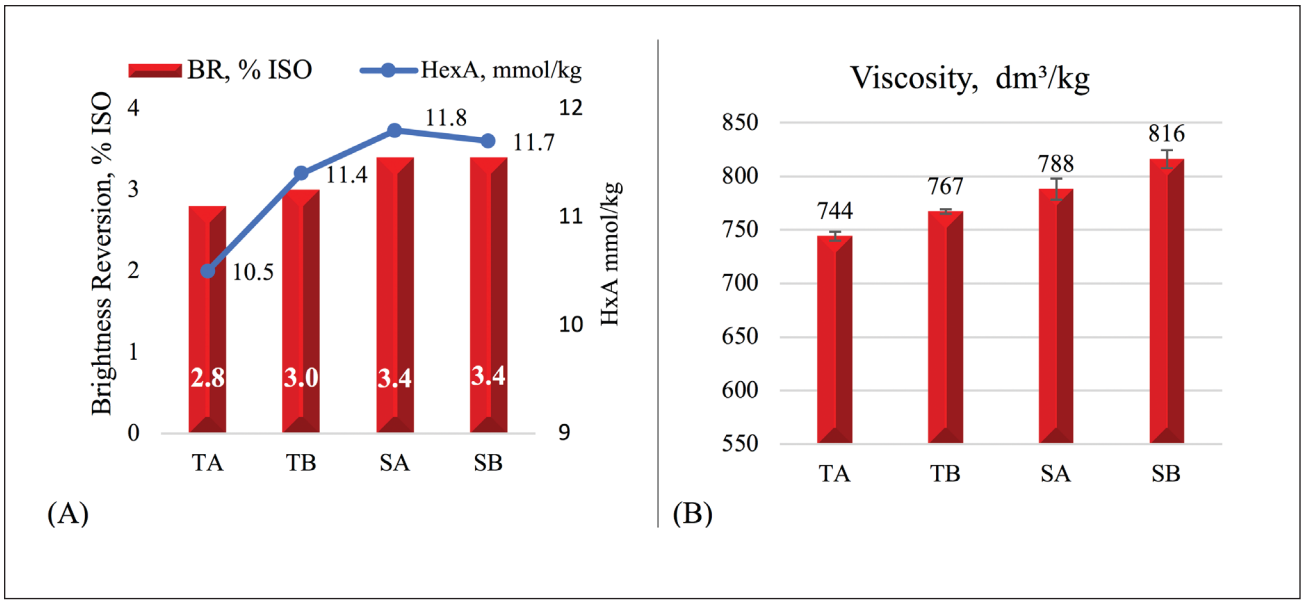
T = disturbance tolerant clone; S = sensitive clone; A and B = sites studied.

IX. Results of oxygen delignification for the four pulps studied.

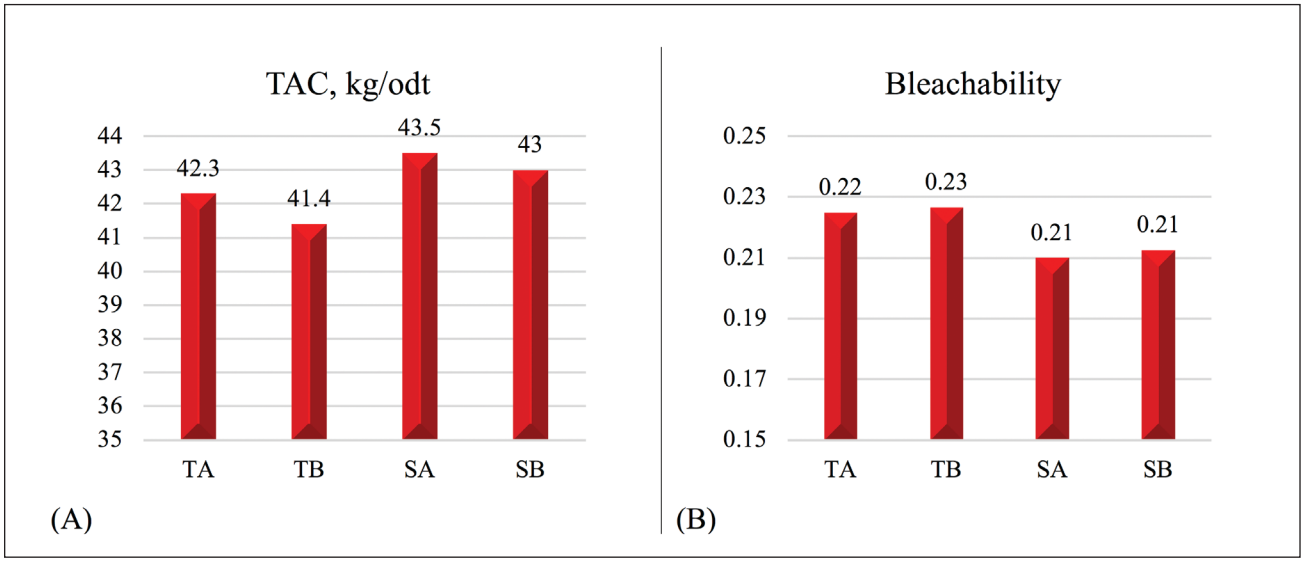
Viscosity is a quality parameter, and bleached pulp with intrinsic viscosity of 750 dm³/kg or higher is considered good for the market pulp grades. Almost all the pulps produced in this study met or exceeded this pulp quality target. Bleached pulps from site A showed slightly lower viscosity than pulps from site B (Fig.5 B).

Total active chlorine (TAC) represents the sum of chlorine dioxide and hydrogen peroxide needed to bleach the oxygen-delignified pulps to the target brightness. Thus, the lower the TAC the better, since it leads to lower bleached pulp cost. The results show that the bleaching of pulps from site A required slightly more bleaching chemicals to brighten (**Fig. 6A**).

Bleachability, which is defined as how easy or how hard a



5. Bleaching results for the four samples studied: (A) brightness reversion, % ISO vs. hexenuronic acids (mmol/kg); and (B) bleached viscosity (dm³/kg).



6. Bleaching results for the four samples studied: (A) total active chlorine (kg/o.d. ton), and (B) bleachability.

chemical pulp is to be bleached, depends on the wood's chemical composition, the extent of delignification, the conditions used during pulping, the bleaching sequence used, and the operating conditions employed [33]. Bleachability is calculated by taking into account the kappa number drop from oxygen delignification to the D_1 stage and dividing this quantity by TAC consumed during bleaching. This calculated parameter was not affected by the physiological disturbance (Fig. 6B).

CONCLUSIONS

It was determined that the physiological disturbance negatively affected wood quality by decreasing wood density and carbohydrate content and by increasing wood's lignin content and S/G ratio, as well as increasing the extractive content. Consequently, the performance during kraft pulping was hampered; i.e., there was an increase in effective alkali and H-factor demands during kraft pulping to reach the target unbleached kappa number. Moreover, the SWC was greater for pulping woods affected by the physiological disturbance. The performance of the brownstocks during the bleaching process was also impacted. The TAC to achieve brightness of 90% ISO was higher for the pulps derived from woods grown under the physiological distress. Overall, the physiological disturbance showed a negative impact in bleached eucalyptus kraft pulp production with possibly higher manufacturing costs. **TJ**

LITERATURE CITED

1. Morais, P.H.D., Longue Júnior, D., Colodette, J.L., et al., *Ciênc. Florest.* 27(1): 237(2017).
2. Larcher, W., *Ecofisiologia Vegetal*, RiMa Artes e Textos, Santa Paula, Brazil, 2000.
3. Taiz, L. and Zeiger, E., *Plant Physiology*, 3rd edn., Sinauer Associates, Sunderland, MA, USA, 2002.
4. Silva, S.R., "Physiological disturbances caused by water stress in Eucalyptus clones in Veracel: Case study and hypotheses," *VI Improvement Workshop and XLI Technical-Scientific Meeting of PTSM Genotypic Adaption to Water and Thermal Stress*, Instituto de Pesquisas e Estudos Florestais (IPEF), Piracicaba, Brazil, 2010.
5. Gomide, J.L. and Demuner, B.J., *O Papel* 47(8): 36(1986).
6. Goldschimid, O., in *Lignins: Ocurrence, Formation, Structure and Reactions* (K.V. Sarkanen and C.H. Ludwig, Eds.), John Wiley & Sons, New York, 1971, pp. 241-298.
7. Scott, R.W., *Anal. Chem.* 51(9): 936(1979).
8. Solar, R., Kacik, F., and Melcer, I., *Nord. Pulp Pap. Res. J.* 2(4): 139(1987).
9. Chen, C-L., in *Methods in Lignin Chemistry* (S.Y. Lin and C.W. Dence, Eds.), Springer-Verlag, New York, 1992, pp. 301-321.
10. Seymour, G.W. and Lavigne, J.R., in *The Bleaching of Pulp* (R.P. Singh, Ed.), 3rd edn., TAPPI Press, Atlanta, 1979, pp. 463-486.
11. Yang, G. and Jaakkola, P., "Wood chemistry and isolation of extractives from wood," Literature Study for BIOTULI Project, Saimaa University of Applied Sciences, South Karelia, Finland, 2011.
12. Kriedemann, P.E and Cromer, R.N., in *Nutrition of Eucalyptus* (P.M. Attiwill and M.A. Adams, Eds.), CSIRO Publishing, Clayton, Australia, 1996, pp. 109-122.
13. Moura, J.C., Bonine, C.A., Viana, J.O.F., et al., *J. Integr. Plant Biol.* 52(4): 360(2010).
14. Gava, J.L., "Relationship between soil attributes and quality of Eucalyptus grandis clone wood for pulp production," Master's thesis, Universidade Federal de São Paulo, São Paulo, Brazil, 2005.
15. Rodrigues, B.P., "Quality of the wood of *Eucalyptus grandis* and *E. urophylla* clone trees under abiotic stress and the impact on the pulp production," Master's thesis, Universidade Federal do Espírito Santo, Vitória, Brazil, 2013.
16. Bassa, A.G.M.C., "*Eucalyptus grandis* x *Eucalyptus urophylla*, *Eucalyptus globulus* and *Pinus taeda* wood mixtures for the production of kraft pulp through the Lo-Solids process," Master's thesis, Universidade Federal do Espírito Santo, Vitória, Brazil, 2006.
17. Jardim, C.M., Silva, F.A., Fernandes, M.B., et al., "Impacting wood extractives content through cooking additive application," *8th Int. Colloquium on Eucalyptus Pulp*, ABTCP, Sao Paulo, Brazil, 2017.
18. Jardim, J.M., Gomes, F.J.B., Colodette, J.L., et al., "Evaluation of the quality and performance of Eucalyptus clones in the production of cellulose," *49th Pulp and Paper Int. Congress & Exhibition*, ABTCP, São Paulo, Brazil, 2016.
19. Higgins, G.G., in *Eucalyptus for Wood Production* (W.E. Hillis and A.G. Brown, Eds.), CSIRO Publishing, Clayton, Australia, 1978, pp. 290-316.
20. Magaton, A.D.S., Colodette, J.L., Gouvêa, A.D.F.G., et al., *TAPPI J.* 8(8): 32(2009).
21. Nieminen, K., Paananen, M., and Sixta, H., *Ind. Eng. Chem. Res.* 53(28): 11292(2014).

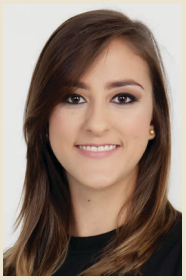
ABOUT THE AUTHORS

We chose to study the effects of the physiological disturbance on the pulping and bleaching performance because it is an issue that some Brazilian pulp and paper companies in the northeast of the country face. This research was developed as a project for my (J. Marangon Jardim's) Master's degree and is not related to previous or future research.

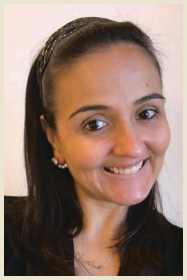
This study showed that physiological disturbance affected the wood properties and hence the pulping and bleaching performance. The most difficult aspect was understanding how the change in wood composition and properties affected the performance during the process, since some were beneficial to the process and others were harmful.

With this research, we learned how the processes are linked. It is amazing how a simple fluctuation in precipitation can impact a lot of the production. The most surprising result was that the basic wood density was decreased by the disturbance, whereas the opposite was expected.

The results obtained provide a better understanding of wood quality and hence lead to a better understanding of the processes, such as wood consumption and chemical and energy demands. This is beneficial to companies that face problems related to physiological disturbance.



J. Marangon Jardim



C. Marangon Jardim



Colodette

J. Marangon Jardim is a Ph.D. student in the Department of Forest Biomaterials at North Carolina State University, Raleigh, NC, USA. C. Marangon Jardim is a researcher at Federal University of Viçosa in Viçosa, Brazil. Colodette is full professor in the Department of Forest Engineering at Federal University of Viçosa. Email J. Marangon Jardim at jmjardim@ncsu.edu.

22. Valverde, S.R., Soares, N.S., and Silva, M.L., *Rev. Árvore* 30(6): 1017(2006).

23. Gardner, R.A.W., Little, K.M., and Arbuthnot, A., *Aust. For.* 70(1): 37(2007).

24. Vuorinen, T., Fagerstrom, P., Buchert, J., et al., *J. Pulp Pap. Sci.* 25(5): 155(1999).

25. Colodette, J.L., Gomide, J.L., Girard, R., et al., *Int. Pulp Bleaching Conf.*, Pulp and Paper Technical Association of Canada (PAPTAC), Montreal, Canada, 2000, pp. 41-48.

26. Smook, G.A., *Handbook for Pulp & Paper Technologists*, 3rd edn., Angus Wilde Publishers, Vancouver, BC, Canada, 2002.

27. Sjöström, E. and Alén, R., *Analytical Methods in Wood Chemistry, Pulping and Papermaking*, Springer-Verlag GmbH, Heidelberg, Germany, 1999.

28. Liu, J., Hu, H., and Luo, X., *BioResources* 7(1): 1134(2012).

29. Hinchee, M., Bassa, A.G.M.C., Rottmann, W., et al., "Biotech enhanced levels of syringyl lignin improves Eucalyptus pulping efficiency," *5th Int. Colloquium on Eucalyptus Pulp*, Federal University of Viçosa, Viçosa, Brazil, 2011.

30. Colodette, J.L., Gomide, J.L., Longue Junior, D., et al., *BioResources* 2(2): 223(2007).

31. Ventorim, G., Oloveira, K.D., Colodette, J.L., et al., *Scientia Forestalis* 71(8): 87(2006).

32. Costa, M.M., Oliveira, M.J., and Santos, C.A., "Effect of kappa factor on the brightness stability of the bleached kraft pulp of *Eucalyptus spp," 1st Int. Colloquium on Eucalyptus Kraft Pulp*, Federal University of Viçosa, Viçosa, Brazil, 2003.

33. Duarte, A.P., and Baptista, C., "Influence of pulping conditions on the bleachability of softwood kraft pulp," *Chem. Technol. Wood, Pulp Pap., Proc. Int. Conf.*, Slovak University of Technology, Bratislava, Slovac Republic, 2003.

ABOUT THIS PAPER

Cite this article as: Marangon Jardim, J., Marangon Jardim, C., Colodette, J. *TAPPI J.* 17(11):633(2018). https://doi.org/10.32964/TJ17.11.633

DOI: https://doi.org/10.32964/TJ17.11.633

ISSN: 0734-1415

Publisher: TAPPI Press

Copyright: ©TAPPI Press 2018

About this journal